Functional Models for Iron(II)/α-Keto Acid Dependent Enzymes

A Combined Synthetic and Analytical Approach to Elucidate the Mechanisms of TET and HPDL Enzymes

Niko Sebastian Willem Jonasson

aus Konstanz, Deutschland

2021

Functional Models for Iron(II)/α-Keto Acid Dependent Enzymes

A Combined Synthetic and Analytical Approach to Elucidate the Mechanisms of TET and HPDL

Niko Sebastian Willem Jonasson

aus Konstanz, Deutschland

2021

Erklärung

Diese Dissertation wurde im Sinne von §7 der Promotionsordnung der Ludwig-Maximilians-Universität von Frau Prof. Dr. Lena J. Daumann betreut.

Eidesstattliche Versicherung

Diese Dissertation wurde eigenständig und ohne unerlaubte Hilfe erarbeitet.

Konstanz, 18.11.2021

_____

Niko Jonasson

Dissertation eingereicht am	07.10.2021
1. Gutachterin	Prof. Dr. Lena J. Daumann
2. Gutachterin	Prof. Dr. Ivana Ivanović-Burmazović
Mündliche Prüfung am	11.11.2021

Acknowledgements

Disclosure of Participation

I was joined by the people mentioned below who contributed in the practical laboratory work of this thesis as part of their research internships and Bachelor Theses. I wish to convey my heartfelt thanks and highlight their contributions.

FEE KIELINOWSKI helped to develop synthetic routes to new ligand systems and started developing an immobilization procedure.

CAROLINE KLIEM started the project "Synthetic Epigenetics" in her Bachelor Thesis, synthesizing and investigating 5-methyl-*iso*-cytosine and derivatives thereof.

JULIANE KAMLAH initiated the investigation of nucleosides as model substrates for the activity of TET enzymes and thereby paved the way for further studies.

AILA ROTHWEILER attempted to synthesize a new quinoline based ligand system and studied the pH behavior of the $[Fe^{IV}(O)(Py_5Me_2H]^{2+}$ system.

JONAS DECHENT continued investigating the immobilization project and contributed to its reproducibility.

DOREEN KREMER joined me in the investigation of the reactivity of $[Fe^{IV}(O)(Py_5Me_2H]^{2+}$ towards oligonucleotides and the attempted synthesis of a dGp5mdC dinucleotide.

ZOE FOKAKIS helped to get the HPDL project started by developing reproducible extraction and derivatization conditions in order to analyze biological samples for HPDL metabolites.

KATHARINA SCHOLZ joined me in getting the $[Fe^{III}(OH)(Py_5Me_2H]^{2+}$ project on a solid basis, studying its synthesis and spectroscopic properties.

HANNAH WILKEN investigated side-reactions of the HPDL bioinorganic model complex studies and started the synthesis of a new iron(III)-hydroxido complex, $[Fe^{III}(OH)(Py_5(OH)_2H]^{2+}$, in her Bachelor Thesis.

JAN KRUSE optimized the synthesis of the $Py_5(OH)_2$ and $Py_5(OMe)_2$ ligands and added the new ligands $Py_5(OCD_3)_2$, $Py_5(OCF_3)_2$, and $Py_5(OCH_2F)_2$ to the library. His investigations of the oxidation of $[Fe^{II}(mecn)(Py_5(OH)_2)](OTf)_2$ led to the discovery of a new iron(IV)-oxido species.

Table of Contents

Abstract

Iron and iron enzymes are ubiquitous in nature. Besides heme-type enzymes, to which the well-known cytochrome P450 belongs, the superfamily of iron(II)/α-keto acid dependent enzymes is of utmost biological relevance. Enzymes of this class are involved in a number of important biochemical transformations including the synthesis of penicillin, the metabolism of taurine, DNA repair, or epigenetically relevant demethylation of DNA. The mechanism of action of these enzymes has been the focus of scientific investigations since 1982,[1] however, details of specific enzymatic transformations still remain elusive. In the years 2003-2005 a series of bioinorganic investigations, in part using synthetic model complexes, led to the discovery of an iron(IV)-oxido moiety as the active species in the enzymes' catalytic cycle.[2–6]

In 2009 ten-eleven translocation 5-methyl cytosine dioxygenase (TET) enzymes, members of the iron(II)/α-keto acid dependent enzyme superfamily, were discovered to play an integral part in the molecular processes of epigenetics by oxidizing the methyl group on the important epigenetic marker 5-methyl cytosine (**5mC**).[7] Whereas several biochemical investigations gave insight into the reactivity of TET enzymes, details are still unclear that warrant more thorough studies. For example, the reactivity of TET towards **5mC** and its oxidized metabolites 5-hydroxymethyl cytosine (**5hmC**) and 5-formyl cytosine (**5fC**) unexpectedly does not correspond to the trend observed in the theoretically calculated bond dissociation energies (BDEs) of these substrates.[8]

On another note, a defect in the gene coding for another iron(II)/α-keto acid dependent enzyme (4-hydroxyphenylpyruvate dioxygenase like, HPDL) was recently identified as the main cause for a neurodegenerative disorder.[9–11] Sequence, location, and some of the enzyme's biochemical behavior including its substrate have been identified. However, there is reason to believe that not all intermediates have been identified unequivocally – not mentioning the final product nor the enzymes' exact mechanism.

Therefore, the goal of this work was to synthesize, study, and modify synthetic, iron-based model complexes for the study of the aforementioned enzymes. Once obtained, these functional models were then to be applied in detailed investigations with (model) substrates of both TET and HPDL. Expansion of the functional model complex platform in order to gain a more diverse portfolio of such iron-based model complexes represents an additional goal.

The literature-known complex $[Fe^{IV}(O)(Py_5Me_2H)]^{2+}$ (**C-6**; Py_5Me_2H = 2,6-bis(1,1-bis(2-pyridyl)ethyl)pyridine, **L-1**) is the basis of the functional model complex platform developed within the scope of this work.[12] Reaction with the nucleobase **5mC** gave the expected TET metabolites **5hmC**, **5fC**, and 5-carboxy cytosine (**5caC**), as shown by GC-MS analysis. The

mechanism of this reaction was elucidated by UV-vis kinetic investigations which allowed for the determination of the rate law as well as the identification of the rate-limiting step, hydrogen atom transfer (HAT) by the iron(IV)-oxido moiety from the methyl group of the substrate (chapter III.4).[13] Subsequently, the substrate's complexity was increased to nucleosides (chapter III.5) and finally short oligonucleotides (10-mer). In a collaboration with the Carell research group at LMU Munich within the SFB1309 "Chemical Biology of Epigenetic Modifications" it was shown that **C-6** is indeed capable of selectively oxidizing a **5mC** residue within an oligonucleotide context. Side-product analysis was performed by MALDI-MS (matrix assissted laser desorption/ionization-mass spectrometry), which showed the formation of small amounts of end-of-strand decomposition, however, no interior strand breaks were observed (chapter III.7).[14] These findings lay the ground-work for ongoing investigations of the application of **C-6** in epigenetic sequencing of DNA. The TET project was complemented by a joint SFB1309 investigation of the behavior of **C-6** towards a series of natural and non-natural nucleobase substrates in collaboration with the Zipse research group at LMU Munich. Here, it was shown that BDEs are a good predictor for the reactivity of the functional model complex **C-6** towards C-H bonds, particularly in a nucleobase context (chapter III.8).[15]

Furthermore, the iron(III)-hydroxido complex $[Fe^{III}(OH)(\textbf{L-1})]^{2+}$ (**C-4**) was successfully identified as the intermediate *and* product in the reaction of **C-6** with organic substrates. Subsequent investigation of **C-4** gave first insight into its reactivity in rebound reactions (chapter IV). In addition to these investigations on the application of **C-6**, the platform of iron-based functional model complexes was expanded: the ligand system Py_5Me_2H was modified at several locations, initial experiments towards the immobilization of **C-6** on solid supports were successful, and a series of new iron(IV)-oxido, iron(III)-hydroxido, and iron(II) complexes were synthesized (chapter V). The findings presented in this work will give multiple opportunities to further continue on the bioinorganic analysis of iron(II)/α-keto acid dependent enzymes.

Metabolomic studies on biological samples obtained from *E. coli* cultures overexpressing HPDL as well as mammalian cell cultures shed light on the substrate consumption, product formation, and the mechanism of HPDL. Model complex studies with **C-6**, its iron(III)-hydroxido derivative **C-4**, and several other iron compounds gave further insight into the complex interaction of HPDL with its substrates and intermediates (chapter VI).

Zusammenfassung

Eisen und eisenhaltige Enzyme sind in der Natur allgegenwärtig. Neben den Häm-Enzymen, zu denen das relativ bekannte Cytochrom P450 gehört, ist die Superfamily der Eisen(II)/α-Ketosäure-abhängigen Enzyme von äußerster biologischer Bedeutung. Enzyme dieser Klasse sind an einer Reihe wichtiger biochemischer Transformationen beteiligt, z.B. in der Synthese von Penicillin, dem Abbau von Taurin, DNA Reparatur, oder epigenetisch relevanter DNA Demethylierung. Der Mechanismus dieser Enzyme ist seit 1982 im Fokus wissenschaftlicher Untersuchungen, allerdings sind Details bestimmter enzymatischer Transformationen nach wie vor unbekannt. Zwischen 2000-2003 wurde in einer Reihe bioanorganischer Untersuchungen, zum Teil durch die Nutzung synthetischer Modellkomplexe, eine Eisen(IV)-oxido Einheit als die aktive Spezies im katalytischen Zyklus der Enzyme ausgemacht.

2009 wurde erkannt, dass Ten-Eleven Translocation 5-Methylcytosine Dioxygenase (TET) Enzyme, welche auch Teil der Eisen(II)/α-Ketosäure abhängigen Enzym-Superfamily sind, eine integrale Rolle in der molekularen Epigenetik spielen: TET Enzyme oxidieren die Methylgruppe im wichtigen epigenetischen Marker 5-Methylcytosin (**5mC**). Diverse biochemische Untersuchungen konnten Einblick in die Reaktivität von TET Enzymen geben, wohingegen einige unklare Details weitere Forschung rechtfertigen. So korreliert zum Beispiel die Reaktivität von TET gegenüber **5mC** und seinen oxidierten Metaboliten 5-Hydroxymethylcytosin (**5hmC**) und 5-Formylcytosin (**5fC**) überraschenderweise nicht mit dem Trend der entsprechenden theoretisch berechneten Bindungsdissoziationsenergien (BDEs).

Des Weiteren wurde vor Kurzem ein Defekt in dem Gen, das ein weiteres Eisen(II)/α-Ketosäure abhängiges Enzym (4-hydroxyphenylpyruvate dioxygenase like, HPDL) kodiert, als Ursache einer neurodegenerativen Krankheit identifiziert. Sequenz, Lokation, sowie ein Teil der biochemischen Aktivität, inklusive des Substrats, des Enzyms wurden bisher identifiziert. Es gibt allerdings Anzeichen, dass nicht alle Intermediate eindeutig identifiziert wurden – ganz zu schweigen vom Produkt sowie dem genauen Mechanismus des Enzyms.

Daher war das Ziel dieser Arbeit synthetische, eisenbasierte Modellkomplexe für die zuvor erwähnten Enzyme zu synthetisieren, untersuchen und zu modifizieren. Sobald vorhanden sollten diese funktionalen Modellkomplexe in detaillierten Untersuchungen mit (Modell-)Substraten sowohl von TET als auch HPDL eingesetzt werden. Die Erweiterung der Plattform solcher eisenbasierter Modellkomplexe stellte ein weiteres Ziel dieser Arbeit dar.

Der literaturbekannte Komplex $[Fe^{IV}(O)(Py_5Me_2H)]^{2+}$ (**C-6**; Py_5Me_2H = 2,6-Bis(1,1-bis(2-pyridyl)ethyl)pyridin, **L-1**) ist die Basis der Plattform funktionaler Modellkomplexe, die in dieser

Arbeit entwickelt wurde. Die Reaktion mit **5mC** ergab die erwarteten TET Metabolite **5hmC**, **5fC**, und 5-Carboxycytosin (**5caC**), wie mittels GC-MS Analyse gezeigt werden konnte. Der Mechanismus dieser Reaktion wurde mithilfe von UV-vis Kinetik-Untersuchungen aufgeklärt: Hierbei wurde das zugehörige Geschwindigkeitsgesetz aufgestellt und die Abstraktion eines Wasserstoffatoms (hydrogen atom transfer, HAT) von der Methylgruppe des **5mC**s durch die Eisen(IV)-oxido-Einheit als geschwindigkeitsbestimmender Schritt identifiziert (Kapitel III.4). Im Anschluss wurde die Substratkomplexität erhöht, dabei wurden Nucleoside (Kapitel III.5) sowie kurze Oligonucleotide (10-mer) verwendet. In einer Kollaboration mit der Carell-Arbeitsgruppe der LMU München innerhalb des SFB1309 „Chemical Biology of Epigenetic Modifications" konnte gezeigt werden, dass **C-6** tatsächlich selektiv einen **5mC**-Rest innerhalb eines Oligonucleotids oxidiert. Analyse der Nebenprodukte mittels MALDI-MS (matrix assissted laser desorption/ionization-mass spectrometry) zeigte, dass kleinere Mengen Zersetzung am Ende des Oligonucleotid-Strangs auftraten, jedoch wurden keine internen Strangbrüche beobachtet (Kapitel III.7).[14] Diese Ergebnisse legen die Grundlage für weitere, laufende Untersuchungen bezüglich der Anwendung von **C-6** im epigenetischen Sequenzieren von DNA. Das TET-Projekt dieser Arbeit wurde schließlich von einer weiteren Kooperation innerhalb des SFB1309 komplementiert: **C-6** wurde bezüglich seiner Reaktivität gegenüber einer Reihe natürlicher und nicht-natürlicher Nucleobasen-Substrate mit Unterstützung der Zipse-Arbeitsgruppe der LMU München untersucht. In diesem Teilprojekt konnte gezeigt werden, dass sich BDEs als gute Vorhersagegrundlage für die Reaktivität von **C-6** gegenüber C-H Bindungen, besonders im Nucleobasen-Kontext, eignen (Kapitel III.8).[15]

Desweiteren konnte der Eisen(III)-hydroxido Komplex [Fe^{III}(OH)(**L-1**)]$^{2+}$ (**C-4**) als Intermediat und Produkt der Reaktion von **C-6** mit organischen Substraten identifiziert werden. Angeschlossene Untersuchungen von **C-4** in Rebound-Reaktionen ergaben erste Hinweise auf dessen Reaktivität (Kapitel IV). Zusätzlich zu diesen Untersuchungen von **C-6** konnte die Plattform eisenbasierter, funktionaler Modellkomplexe erweitert werden: Das Ligandensystem Py$_5$Me$_2$H wurde an mehreren Stellen modifiziert, erste Untersuchungen bezüglich der Immobilisierung von **C-6** auf festen Trägermaterialien durchgeführt, sowie eine Reihe weiterer Eisen(IV)-oxido-, Eisen(III)-hydroxido- und Eisen(II)-Komplexe synthetisiert (Kapitel 0). Diese Erkenntnisse ergaben diverse Möglichkeiten zur weiteren bioanorganischen Untersuchung von Eisen(II)/α-Ketosäure-abhängigen Enzymen.

Metabolomics-Studien an biologischen Proben, die von HPDL-überexprimierenden *E. coli*-Kulturen sowie Säugetier-Zellen gewonnen wurden, gaben Hinweise auf den Substratverbrauch, die Produktbildung, sowie den Mechanismus von HPDL. Modellkomplex-Untersuchungen mit **C-6**, seinem Eisen(III)-hydroxido Derivat **C-4**, sowie weiterer Eisenverbindungen, ergaben

darüberhinaus Erkenntnisse über die Interaktion von HPDL mit dessen Substraten und Intermediaten (Kapitel VI).

I. General Introduction

1. A Few Words on Nomenclature

Abbreviations and denominations of metal complexes, ligands, and substrates are introduced upon the first time of mentioning. **A summary of all ligands, complexes, and substrates** used in this work, as well as an explanation of the applied nomenclature, **can be found on p. 531 at the end of this document.**

Ligands, complexes, and substrates as well as substrate-like compounds are highlighted in **bold**. Synthetic intermediates or otherwise relevant intermediary structures are denominated based on the first chapter and order they appear in (e.g. 1,1-di(2-pyridyl)ethane, ***III-1***, is the first intermediate in chapter III) and are highlighted in ***bold and italic***. In case different abbreviations are used in the literature, these are indicated upon the first time of mentioning but then replaced by the numbering used in this work. A complete summary of abbreviations can be found in the appendix on p. 351. An overview of all synthetic intermediates can be found on p. 533.

The ligand termini "oxido", "hydroxido", "superoxido", etc. are used instead of the more common, but outdated, versions "oxo", "hydroxo", "superoxo" etc. in accordance with the IUPAC guidelines for nomenclature of ligands.

If solvents are coordinated to a metal ion, they are written in lowercase letters (e.g. $[Fe^{II}(mecn)(\textbf{L-1})](OTf)_2$). If their primary function is a solvent, they are written as is common in the literature (e.g. MeCN for acetonitrile, DMF for *N,N*-dimethylformamide, etc., refer to the list of abbreviations on p. 351).

In this work, the term "dioxygenase" refers to enzymes that incorporate both oxygen atoms of molecular dioxygen (O_2) into organic substrates, either one atom into α-keto glutarate (α-KG) and one atom into the primary substrate (e.g. taurine dioxygenase, TauD) or both atoms into the primary substrate (e.g. hydroxyphenylpyruvate dioxygenase, HPPD). If one oxygen atom is incorporated into the substrate and one atom is released as water, these enzymes are referred to as monooxygenases.

2. Iron(II)/α-Keto acid Dependent Enzymes

Iron Enzymes

Iron is ubiquitous in all domains of life: hemoglobin and myoglobin transport oxygen to the cells in vertebrates,[16] cytochrome P450 metabolizes a variety of compounds and is found in almost all forms of life (Chart 1**A**),[17] iron carbon monoxide dehydrogenase catalyzes the reaction of carbon monoxide to carbon dioxide in bacteria,[18] Taurine Dioxygenase assists in the decomposition of taurine to sulfite and aminoacetaldehyde (Chart 1**B**),[2] superoxide dismutase catalyzes the reaction of superoxide to hydrogen peroxide (Chart 1**C**),[19] Ferredoxins are responsible for the transport of electrons across cells, and there are countless more examples.[20]

Iron enzymes are often divided into groups by the structure of their ligands: enzymes with an iron center coordinated by porphyrin-based ligands are referred to as "heme iron enzymes" whereas all other enzymes belong to the "non-heme iron enzymes" (Chart 1).
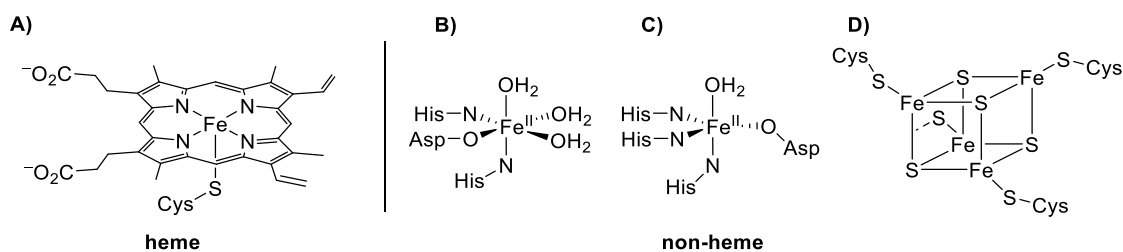
*Chart 1: Metal binding sites of **A**) Cytochrome P450[21] **B**) TauD[2] **C**) Superoxide Dismutase[19] and **D**) Ferredoxin[20]. Cytochrome P450 belongs to the heme enzymes whereas the three other enzymes are of the non-heme type.*

Iron(II)/α-Keto Acid Dependent Enzymes

Iron(II)/α-keto acid dependent dioxygenases are the largest class of non-heme iron proteins. They share two common structural motifs: a double-stranded beta-helix (DSBH) fold and a coordination site for an iron atom. The latter is formed by a conserved three-amino-acid binding site and is commonly referred to as the facial triad, as it forms one face of imaginary octahedron around the iron central atom.[22,23] Usually, the facial triad consist of two histidine and one carboxylate-bearing amino acid, such as glutamate of aspartate,[22] however, enzymes bearing three histidine residues were also discovered.[24] In most cases, α-ketoglutarate (α-KG) is used as co-factor, however, several enzymes are known that utilize different α-keto acid compounds for activation and/or as substrate.[25-27] Figure 1A shows a graphical representation of the crystal structure of TauD, a member of the iron(II)/α-KG dependent enzyme superfamily. Figure 1**B** shows a stylized representation of an iron(II)/α-KG dependent enzyme after uptake of the substrate and all co-substrates but prior to the activation of the iron center (for the activation mechanism refer to Scheme 2).

A)

B)
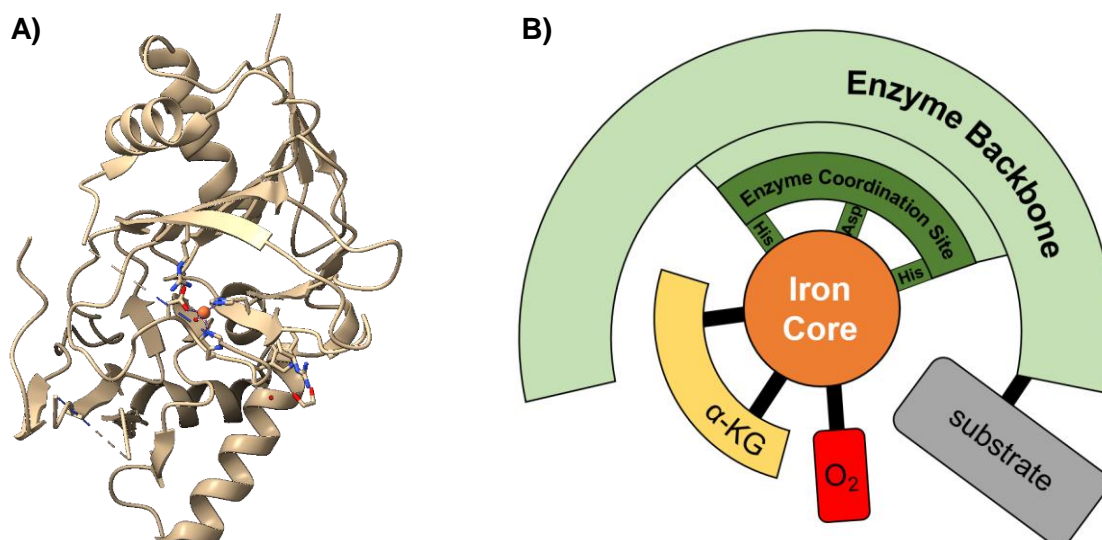
*Figure 1: **A**) Graphical representation of a crystallized monomer of TauD (PDB: 3SWT). **B**) Stylized structure of an iron(II)/α-KG dependent enzyme after uptake of substrate and co-substrates but prior to the activation reaction (refer to Scheme 2). Enzyme backbone refers to any structure of the enzyme excluding the metal binding site/enzyme coordination site or the co-factors.*

Iron(II)/α-keto acid dependent enzymes are involved in a variety of reactions such as hydroxylations, demethylations, desaturations, ring expansions, or ring closures. In addition, hydroxylation of heteroatoms, such as phosphorus, has also been observed.[28] Enzymes in a sub-class, iron(II)/α-KG dependent halogenases, use halides and dioxygen to halogenate substrates (Scheme 1).[29,30]

The probably best studied enzyme in this class is taurine dioxygenase (TauD, Scheme 1, first reaction). Meticulous biochemical and bioinorganic investigations revealed a mechanism that involves the formation of highly reactive iron(IV)-oxido species.

Substrate	Co-Substrates/Enzyme	Product(s)	Biochemical Reaction
taurine	iron(II) / α-KG / O₂ — TauD	+ HSO₃⁻	C hydroxylation
6mA	iron(II) / α-KG / O₂ — AlkBH1	A	N demethylation
5mC	iron(II) / α-KG / O₂ — TET	C	C demethylation
Flavanone	iron(II) / α-KG / O₂ — flavone synthase I	Flavone	desaturation
tripeptide	iron(II) / O₂ — IPNS	penicillin	ring closure
penicillin G	iron(II) / α-KG / O₂ — DAOCS	deacetoxycephalosporin	ring expansion
Phosphinic Acid	iron(II) / α-KG / O₂ — HtxA	Phosphonic Acid	P hydroxylation
L-threonine	iron(II) / α-KG / O₂ — SyrB2	4-Cl-L-threonine	halogenation

Scheme 1: Overview over several biochemical transformations catalyzed by iron(II)/-keto acid dependent enzymes. α-KG = α-ketoglutarate; TauD = Taurine Dioxygenase; TET = Ten Eleven Translocation 5-Methylcytosine Dioxygenase, DAOCS = Deacetoxycephalosporin C Synthase, IPNS = Isopenicillin N Synthase, SyrB2 = Syringomycin biosynthesis enzyme 2.

The Mechanism of Activation for α-KG Dependent Enzymes

The activation of the enzyme comprises the first part of the mechanism (Scheme 2, *I-1 – I-4*) and consists of the uptake of molecular dioxygen, α-KG, and the substrate R-H as well as subsequent oxidation of the iron center to the reactive iron(IV)-oxido species (*I-6*). The exact order of steps (*I-1 – I-4*) is still debated, especially the order of coordination of the co-substrates dioxygen and α-KG as well as uptake of the substrate remains controversial. In Scheme 2 three variants are shown.

4
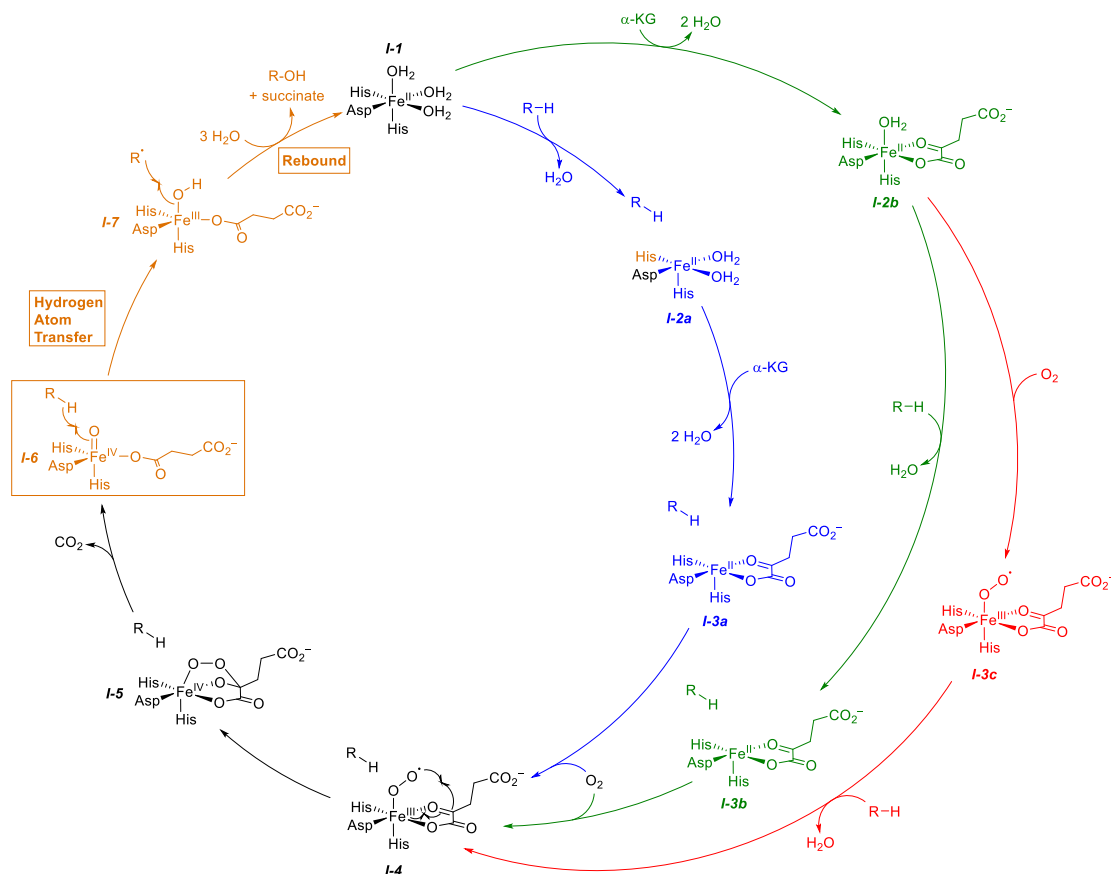
*Scheme 2: Consensus mechanism of the activation and reaction of an iron(II)/α-KG dependent dioxygenase, where R-H represents an organic substrate with a C-H bond.[1–6] Species **I-4** and **I-5** were never observed directly but are regularly discussed as intermediates.[31,32] Three pathways for the sequential uptake of α-KG, dioxygen, and the substrate R-H are discussed: first substrate, then α-KG, then dioxygen (blue, pathway **a**), first α-KG, then substrate, then dioxygen (green, pathway **b**), or first α-KG, then dioxygen, then substrate (red, pathway **c**).[33] R-H = substrate, R-OH = product.*

In path **a** (blue, innermost circle), the substrate is taken up first, replacing a water molecule (***I-2a***). The substrate is not bound directly to the iron center but is held in place by a secondary coordination sphere. Then, α-KG coordinates to the central atom and replaces the last two water molecules, resulting in species ***I-3a***. Uptake of molecular oxygen completes the coordination process and yields species ***I-4***. In pathways **b** and **c** (green and red, respectively) α-KG is taken up first to give species ***I-2b***. Then, either the substrate (path **b**, inner circle, ***I-3b***) or molecular dioxygen (red, outermost circle, ***I-3c***) is incorporated into the active site's structure. Coordination of dioxygen to ***I-3b*** or uptake of the substrate R-H into structure ***I-3c*** yields species ***I-4*** in both cases.

In addition to these three pathways, a concerted scheme is also debated in modern literature. Solomon and co-workers published their work on Deacetoxycephalosporin C Synthase (DAOCS, Scheme 1) in early 2020. The authors discuss two possibilities for the iron oxidation mechanism during enzyme activation: concerted vs. sequential. Scheme 3 gives an overview of the postulated mechanisms as they would apply for DAOCS. In the concerted mechanism (Scheme 3, upper pathway, compare to Scheme 2) both substrate and co-factor bind prior to oxidation of the iron

center by dioxygen. In the sequential pathway, the cofactor binds first, then the iron center is oxidized and then the substrate binds (Scheme 3, lower pathway).
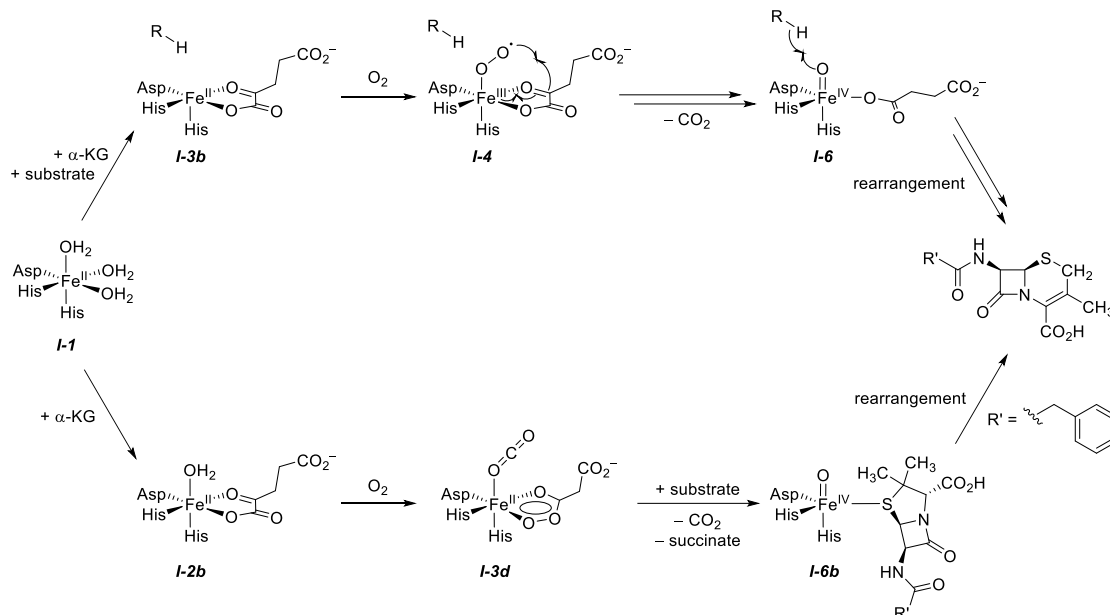
Scheme 3: Postulated concerted (upper) vs. sequential (lower) pathways in the activation of DAOCS, a non-heme iron(II)/-KG dependent enzyme.

The mechanism postulated by Solomon *et al.* also presents an alternative route for the subsequent step: oxidation of the iron center. In the classical consensus mechanism (Scheme 2) an iron(III)-superoxido species (***I-4***) is formed after uptake of all co-substrates. In a ring-closure mechanism this then reacts to the bridged iron(IV)-peroxido species (Scheme 2, ***I-5***). Release of carbon dioxide then generates the iron(IV)-oxido species ***I-6***. Solomon *et al.*, however, propose the formation of a planar peroxido structure (***I-3d***) in which carbon dioxide and succinate peroxide are coordinated to an iron(II) species. Uptake of the substrate releases carbon dioxide and succinate to form an iron-substrate complex (***I-6b***).

In addition to the order in which substrate, α-KG, and dioxygen enter the active site the exact structure of the iron(IV)-oxido species (5-coordinate vs. 6-coordinate) has been the subject of discussion for more than 20 years since the original publications by Hausinger, Krebs and Bollinger.[2–4,34] Guo and co-workers have recently published their studies on the epoxidation of olefins by an enzyme called AsqJ which also belongs to the iron(II)/α-KG dependent dioxygenases superfamily.[35] Two main pathways are known when epoxidations occur in nature: oxygen atom transfer (OAT) into an olefin bond or the formal cleavage of a C-H and adjacent O-H bond followed by C-O bond formation. The OAT can follow three different pathways (shown in Scheme 4): a concerted mechanism or one of two stepwise mechanism, one with a radical and one with a cationic intermediate. For enzymes, evidence for all three mechanisms can be found.[36–41]
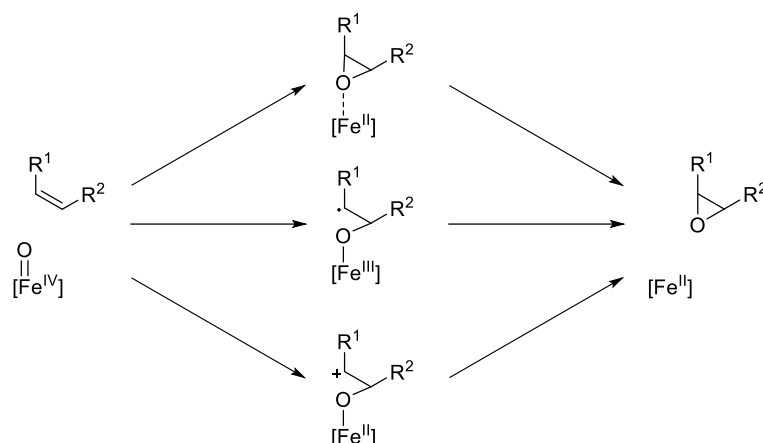
Scheme 4: Pathways for OAT epoxidation: concerted (top), radical (middle), or cationic (bottom).[35]

For heme enzymes, the spin-state has been found to play a critical role when differentiating between a stepwise or concerted mechanism. Computational evidence suggests that the doublet spin state (S = 1/2) results in concerted epoxidation whereas the quadruplet state (S = 3/2) results in a stepwise mechanism.[38,39] Non-heme iron(IV)-oxido mimics are typically found to show electrophilic behavior in epoxidation reactions.[42–44] For a heme-type manganese(V)-oxido complex, a V-shaped Hammett plot was observed which indicates a change in mechanism when going from electron donating groups to electron withdrawing groups. This would mean a change in the nature of the metal-oxido complex from electrophilic to nucleophilic.[45] In reactions with a heme-type iron(IV)-oxido complex, however, no significant influence of the *para*-substituent was observed.[46]

For AsqJ, Li and co-workers find a similar behavior, para-substitution of the natural substrate (R =H, F, CF₃, OMe) does not change the reaction rate/formation rate of the iron(IV)-oxido intermediate.[35]
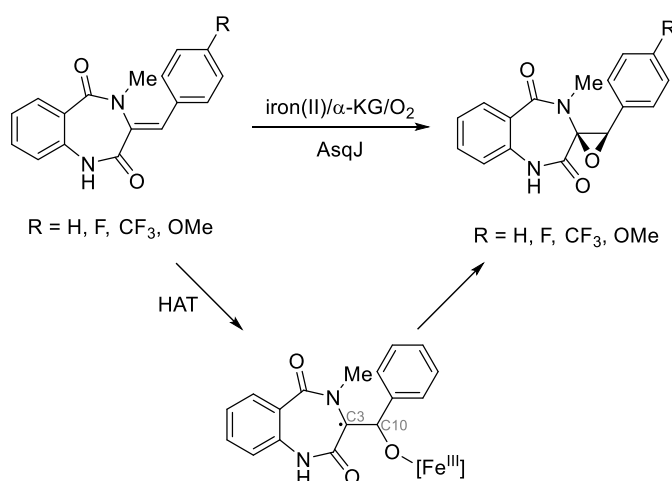
Figure 2: Epoxidation of benzodiazepinediones by AsqJ/iron(II)/α-KG/O₂ and the observed alkoxide intermediate R = OMe is the natural substrate.[35]

The authors conclude that this is due to no significant charge separation, which would exclude a cationic pathway. However, they observe the formation of iron(III)-alkoxide intermediate which

would indicate a stepwise mechanism (Figure 2). Using EPR and Mößbauer spectroscopy in addition to x-ray diffraction and computational studies, the iron(III) center was determined to be five-coordinate and antiferromagnetically coupled to a radical on the C3 position of the substrate. This is further corroborated by crystal structures that show a larger distance between the iron center and C3 than C10. After the epoxidation is completed, the collected data is interpreted as such: the epoxide stays coordinated to the iron center and only dissociates later through a hydrogen bond network. The authors also discuss the way α-KG/succinate bind to the iron center in relation to the facial triad of amino acids (Figure 3), the so-called offline and online binding modes.[35]
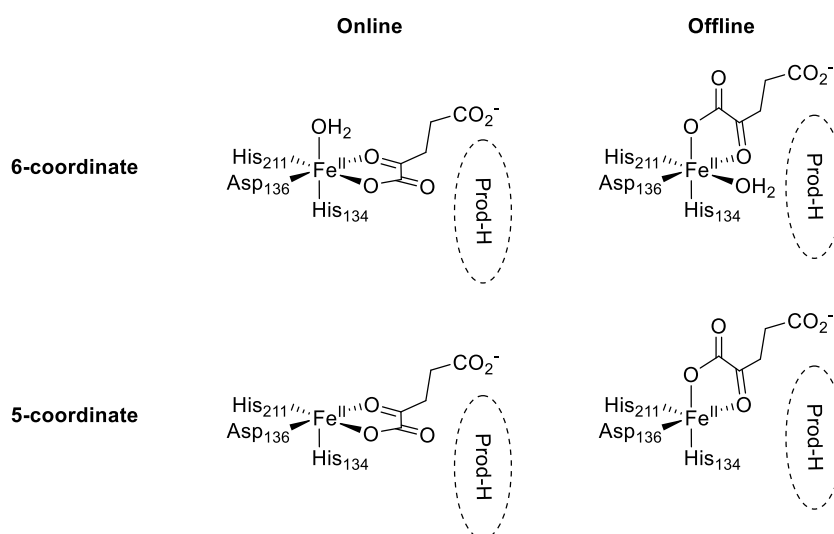
Figure 3: Online and offline binding mode of α-KG in a 5-membered or 6-membered iron coordination sphere.

Li *et al.* conclude that in the case of AsqJ both the quaternary complex of AsqJ/α-KG/iron/substrate and the product complex are 6-coordinate species. Their calculations suggest that addition of dioxygen to the complex most likely occurs in the online binding mode. However, the crystal structures obtained show an offline binding mode. The preference of oxygen to bind in the online mode was attributed to the presence of the substrate, which creates a hydrophobic environment facilitating oxygen uptake.[35]

The Mechanism of Activation for Other α-Keto acid Dependent Enzymes

In addition to the above mentioned α-KG dependent enzymes, several enzymes are known to utilize other, but structurally similar, compounds for activation of the iron center in the active site. Two such examples are 4-hydroxyphenylpyruvate dioxygenase (HPPD) and 4-hydroxymandelate synthase (HMS), both are enzymes that use 4-hydroxy phenylpyruvate (**4-HPP**) as co-factor and substrate (Scheme 5).[25–27]
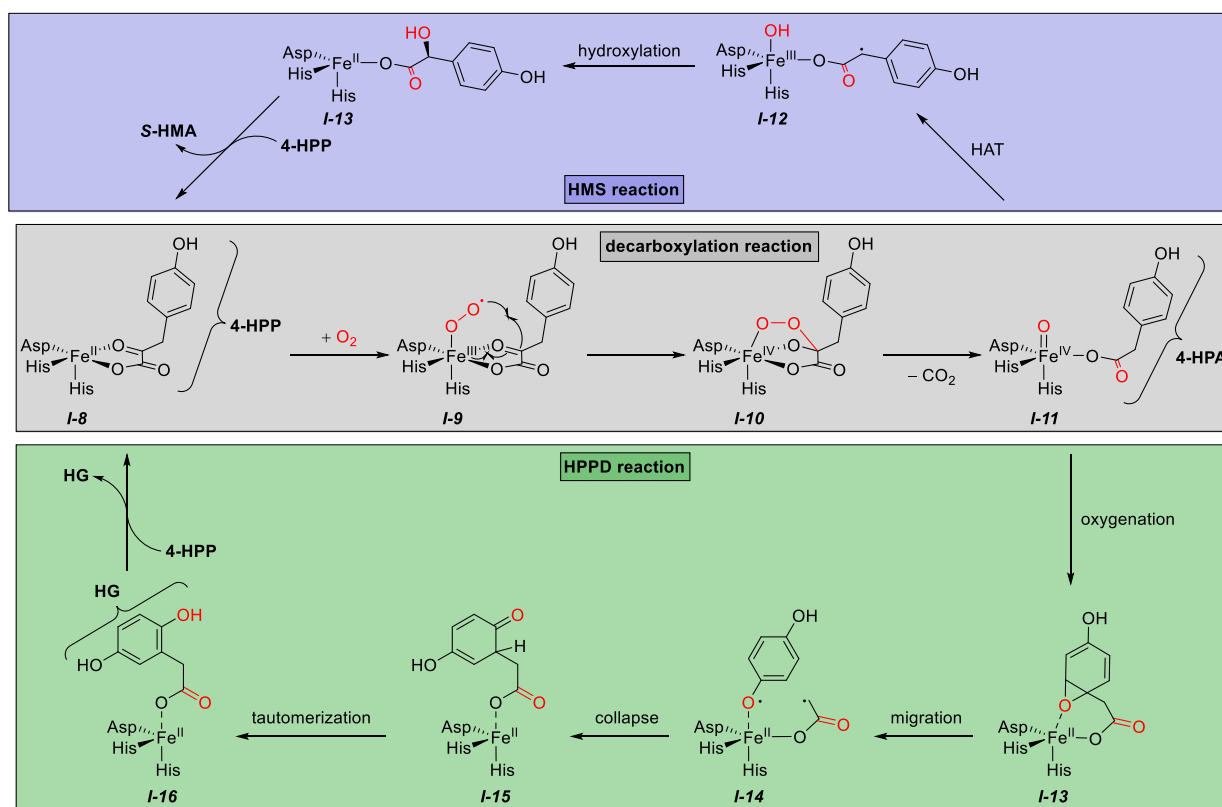
*Scheme 5: Overview of the catalytic cycles of 4-hydroxyphenylpyruvate dioxygenase (HPPD) and 4-hydroxymandelate synthase (HMS), divided by the first half-reaction (decarboxylation, black arrows) that produces 4-hydroxyphenyl acetate (**4-HPA**) from 4-hydrophenylpyruvate (**4-HPP**) in both cases and the subsequent distinct half-reactions including hydrogen atom transfer (HAT, blue arrows in upper HMS pathway) and oxygenation/migration (green arrows in lower HPPD pathway). The products are S-(4-hydroxy)mandelic acid (**S-HMA**, HMS reaction) and homogentisate (**HG**, HPPD reaction).[25–27]*

The first half-reaction is the same for both HPPD and HMS, and also similar to the first part of the mechanism shown in Scheme 2 for α-KG dependent enzymes: the α-keto acid (in the case of HPPD and HMS **4-HPP**) coordinates to the iron center (**I-8**), dioxygen coordinates to form an iron(III)-superoxido species (**I-9**), followed by oxidative ring closure (**I-10**) and subsequent loss of carbon dioxide to form the reactive iron(IV)-oxido species **I-11** and 4-hydroxyphenyl acetate (**4-HPA**, grey box "decarboxylation reaction").[25–27]

In the HMS half-reaction, a "regular" hydrogen atom transfer (HAT) reaction yields iron(III)-hydroxido species **I-12**. The hydroxyl moiety is transferred in a rebound reaction to the benzylic position of the substrate and *S*-(4-hydroxy)mandelic acid (**S-HMA**) is formed, which is subsequently expelled from the enzyme's active site. In the HPPD half-reaction, the aromatic ring is oxygenated, forming species **I-13**. Migration (**I-14**) and collapse yield the ketone form of homogentisic acid/homogentisate (**HG**, **I-15**) which tautomerizes to the phenol form (**I-16**) and is then released from the enzyme. [25–27] More information on iron(II)/α-keto acid dependent enzymes and its relevance to this work is provided in chapter VI.1.

HAT and Rebound

The second part of the mechanism shown in Scheme 2 and the two half reactions in Scheme 5 comprise the "actual" enzymatic reaction (Scheme 2, steps **VI-I;** Scheme 5 "HMS reaction" and "HPPD reaction"). In the following, the standard pathway valid for most α-KG dependent enzymes as well as HMS will be discussed in more detail: it is composed of a two-step sequence in which an iron(III)-hydroxido intermediate and a carbon-bound radical (***I-18***) are formed intermittently to subsequently form the product R-OH and regenerate the iron(II) species ***I-19*** (Figure 4**A**).

For TauD it was shown by kinetic isotope experiments that the HAT step is rate limiting for this reaction. This was achieved by replacing hydrogen atoms in taurine with deuterium atoms and comparing the reaction rates of both substrates with TauD, the ratio between the observed reaction rates is the kinetic isotope effect (KIE). For TauD, a KIE of ~50 was determined, which is a clear indication that a reaction involving the hydrogen/deuterium atoms is the rate limiting step.[2,4] As in TauD, it has been shown for TET enzymes *via* KIE experiments involving TET and a (deuterated) biotin-**5mC** complex that the HAT step is rate limiting.[47]
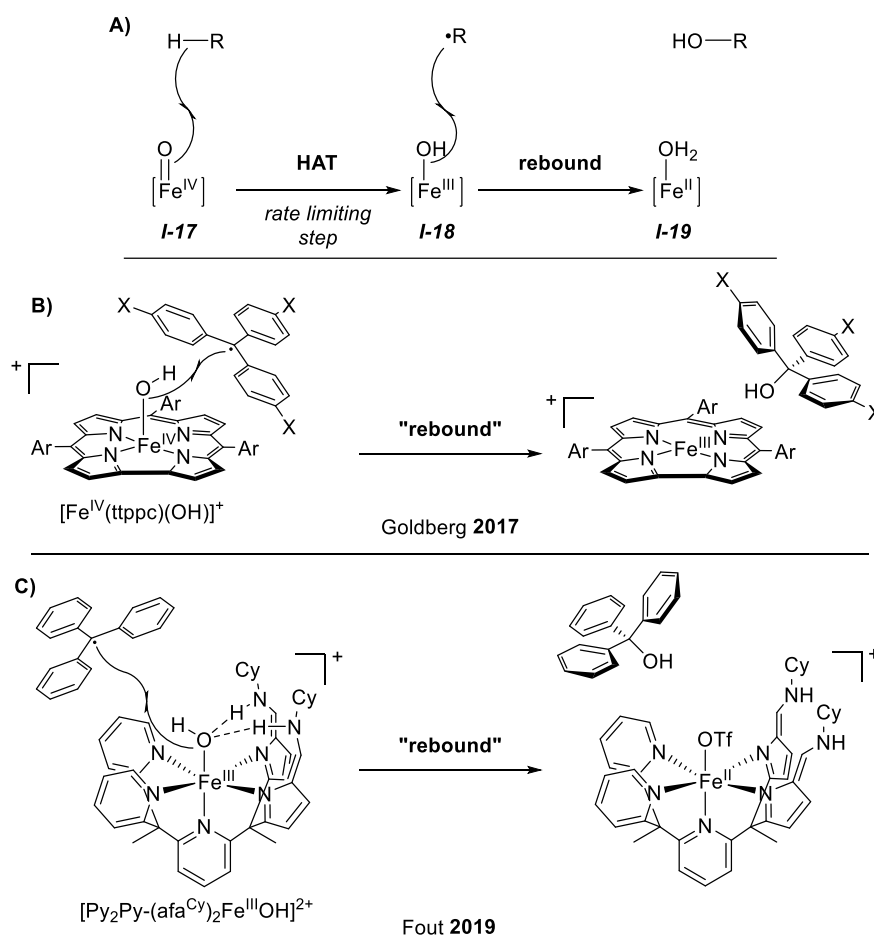
Figure 4: **A**) Schematic representation of the HAT - rebound reaction sequence in heme and non-heme iron enzymes. **B**) Synthetic model for the rebound step in heme enzymes by Goldberg, published in 2017.[48] **C**) Synthetic model for the rebound step in non-heme enzymes by Fout, published in 2019.[49] X = OMe, -Ph, -t-Bu, -Cl, Ar = 2,4,6-triphenyl)phenyl, ttppc = tris(2,4,6-triphenyl)-phenyl corrole, Cy = cyclohexane, Py_2Py-$(afa^{Cy})_2$ = 2,2',2'-methylbis-pyridyl-6-(2,2',2'-methylbis-5-cyclohexylazafulvene)-pyridine, OTf = $^-O_3SCF_3$.

In contrast to the HAT, the second step, rebound, has remained mostly unstudied by bioinorganic chemists for decades. For heme enzymes, the intermediate produced by HAT from the substrate is commonly referred to as Compound-II (Cpd-II) and has been identified as an iron(IV)-hydroxido species supported by a dianionic heme ligand. This Cpd-II had been trapped and spectroscopically studied in heme enzymes that contain negatively charged axial ligands.[50–53] In 2017, Zaragoza *et al.* published their report on a synthetic iron(IV)-hydroxido complex ($[Fe^{IV}(ttpc)(OH)]^+$, ttpc = tris(2,4,6-triphenyl)-phenyl corrole) and its interaction with a series of synthetic organic radicals (Figure 4**B**). This is the first example of directly recreating the rebound step using a synthetic compound.[48]

However, only a short while later Drummond *et al.* published a similar report on their non-heme iron(III)-hydroxido complex ($[Fe^{III}(OH)(Py_2Py-(afa^{Cy})_2)]^{2+}$ $Py_2Py-(afa^{Cy})_2$ = 2,2′,2′-methylbis-pyridyl-6-(2,2′,2′-methylbis-5-cyclohexylazafulvene)-pyridine). This complex more closely resembles non-heme iron enzymes, as it lacks a heme-type ring ligand (porphyrin/corrole) but is instead comprised of three pyridine and two azafulvene donors. Similar to the results of Zaragoza *et al.*, $[Fe^{III}(OH)(Py_2Py-(afa^{Cy})_2)]^{2+}$ reacts with an organic radical (triphenylmethyl radical) by transferring its hydroxide moiety (Figure 4**C**).[49]

It has to be noted that these examples are rare, as synthesis of an iron(III)-hydroxido species is generally considered difficult due to its preference to form μ-oxido-bridged dimers (*vide infra* for details).

For other synthetic systems, divergent reactivities concerning the two-step sequence HAT-rebound have been observed (Scheme 6). In addition to reactions mirroring those of enzymes (hydroxylation or desaturation, Scheme 6, pathways **a** and **b**, respectively), dissociation of the intermediate and organic radical has been observed (Scheme 6 pathway **c**) for the synthetic compounds $[M^{IV}(O)(Bn-TPEN)]^{2+}$ (Bn-TPEN = N-benzyl-N,N′,N′-tris(2-pyridylmethyl) ethane-1,2-diamine) and $[M^{IV}(O)(N_4Py)]^{2+}$ (N_4Py = N,N-bis(2-pyridylmethyl)-N-bis(2-pyridyl) methylamine) with M = manganese or iron.[54]
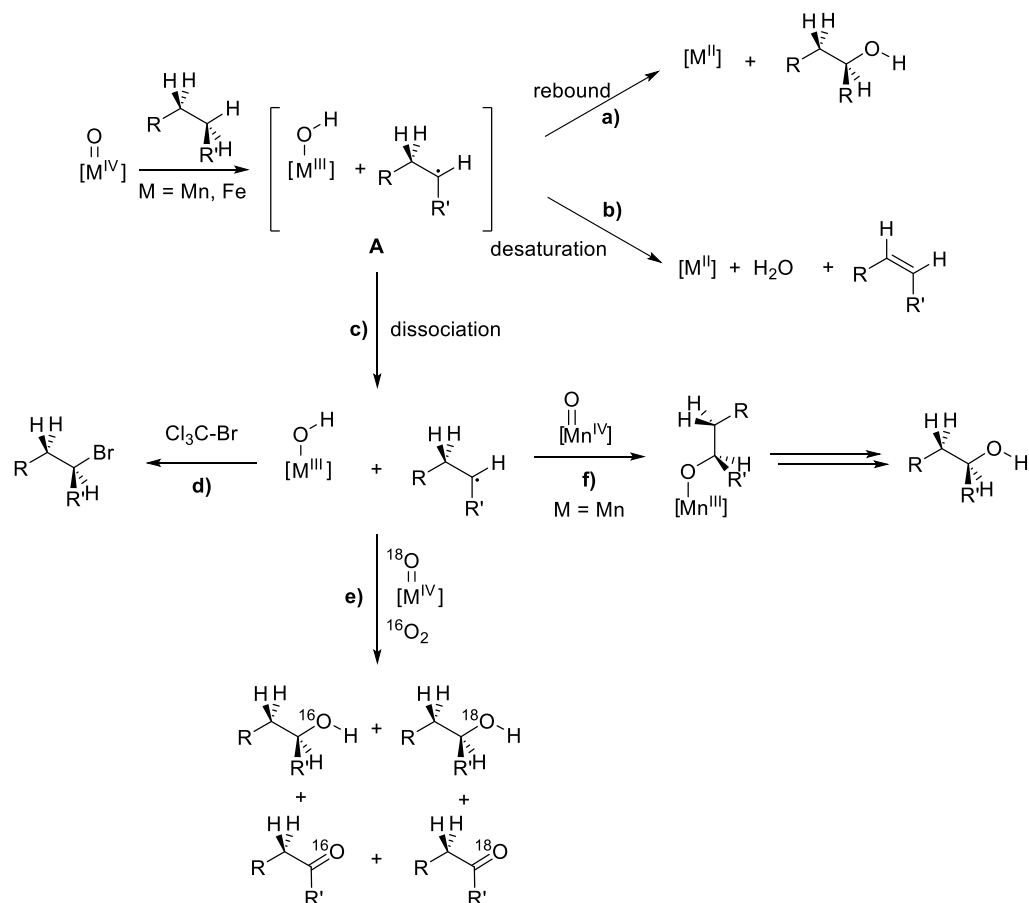
*Scheme 6: Reaction of a metal(IV)-oxido compound (metal = iron or manganese) with an organic substrate to form a metal(III)-hydroxido species and a carbon-centered organic radical. Structure **A** can further react via a rebound mechanism (path **a**), undergo desaturation (path **b**) or dissociate (path **c**). The dissociated radical can then be trapped by bromotrichloromethane (path **d**), react with (^{18}O-labeled) molecular oxygen (path **e**) or, in the case of manganese, react with a second equivalent of metal(IV)-oxido to form the corresponding alcohol (path **f**).[54,55]*

After dissociation, several observations were made: a radical scavenger such as bromotrichloromethane was observed to be able to intercept the organic centered radical to exclusively form the brominated product (pathway **d**).[55] Interestingly, the addition of another equivalent of metal(IV)-oxido compound (^{18}O labeled) under an atmosphere of oxygen ($^{16}O_2$) produced a mixture of ^{16}O- and ^{18}O-alcohol and ketone products (pathway **e**). In the case of M = manganese, the presence of another equivalent of manganese(IV)-oxido complex led to the formation of a manganese-alkoxido species which then dissociates to the hydroxylated product (pathway **f**).[54]

This shows that whereas enzymatic reactions occur *via* the HAT-rebound sequence, synthetic iron(IV)-oxido complex do not necessarily follow the same principal. This indicates the necessity for secondary interactions between the enzyme's backbone and the substrate resulting in a truly "caged radical" – in contrast to the "free radicals" formed in solutions of synthetic complexes and substrates.

Biochemical Relevance

This bioinorganic view onto the above described enzymatic reactions (Scheme 1), however, reveals only one major mechanism of action: hydrogen atom transfer (HAT) followed by a rebound step. This two-step reaction sequence is then often followed by a secondary reaction, determined by the substrates' structure: hydroxylated **6mA** is for example demethylated, hydroxylated flavanone desaturates *via* loss of water (Figure 5).
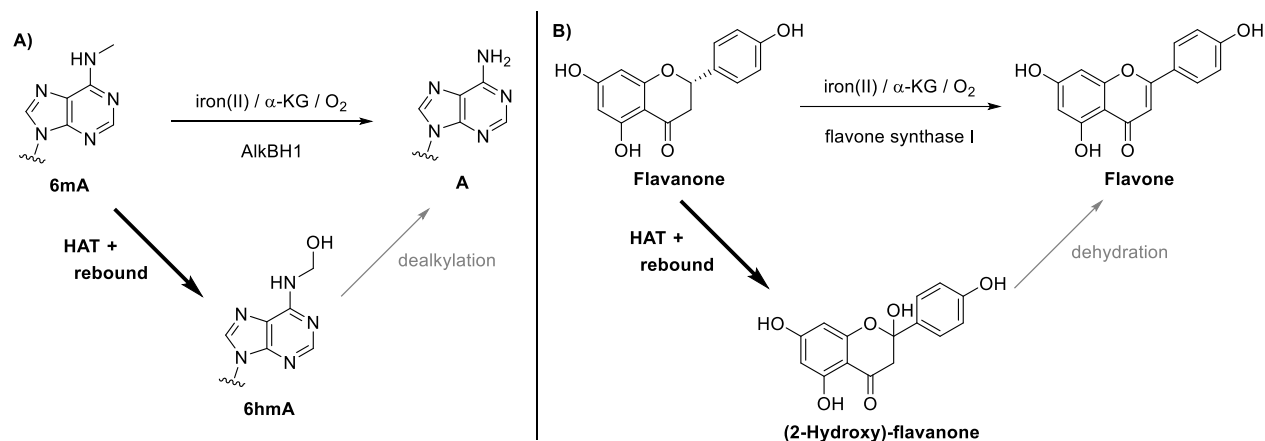
*Figure 5: A) Demethylation of **6mA** to **A** via hydroxylation and subsequent dealkylation.[56–58] **B**) Desaturation of flavanone to flavone via hydroxylation and subsequent loss of water. The step catalyzed by the respective enzyme, AlkBH1 and flavone synthase 1, is marked in bold.[59,60]*

Another example for this reaction pattern is DAOCS, in this case two secondary reactions take place in between HAT and rebound: first, one of the geminal methyl groups is transformed into a radical *via* HAT. This then undergoes ring expansion to form a more stable secondary radical (Scheme 7).

However diverse the overall reactions are, the active site of the enzyme is only capable of catalyzing one type of reaction, the insertion of an oxygen atom into a C-H bond.
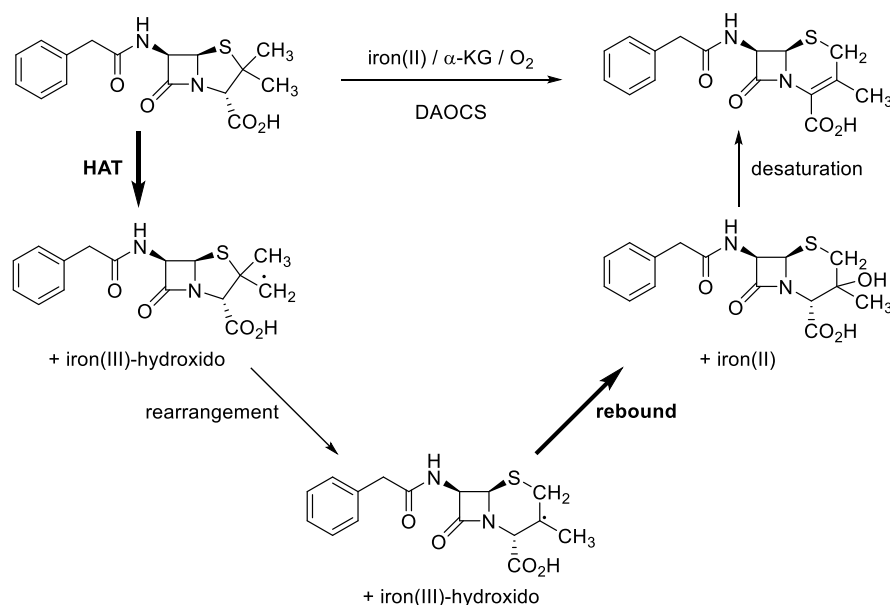
Scheme 7: Enzymatic conversion of penicillin G to deacetoxycephalosporin G by DAOCS in the presence of an iron(II) source, α-KG, and molecular oxygen.

Halogenases

Halogenases present a variation of the previously discussed "HAT/rebound hydroxylation" sequence by introducing a halogen atom through exploitation of the rebound step (Scheme 3). Halogenases can belong to the heme or non-heme type, both use an iron(IV)-oxido intermediate in order to abstract a hydrogen atom from a non-activated C-H bond to subsequently halogenate the intermittent carbon-centered radical. In particular, non-heme iron(II)/α-KG dependent enzymes have been found to catalyze such chlorination reactions.[29,30,61,62] In the first step, the iron(IV)-oxido moiety abstracts a hydrogen atom from the substrate and an iron(III)-hydroxido-halogenido intermediate is formed. Rebound involving the halogenide ligand leads to halogenation of the substrate (Scheme 8, mechanism shown for SyrB2).
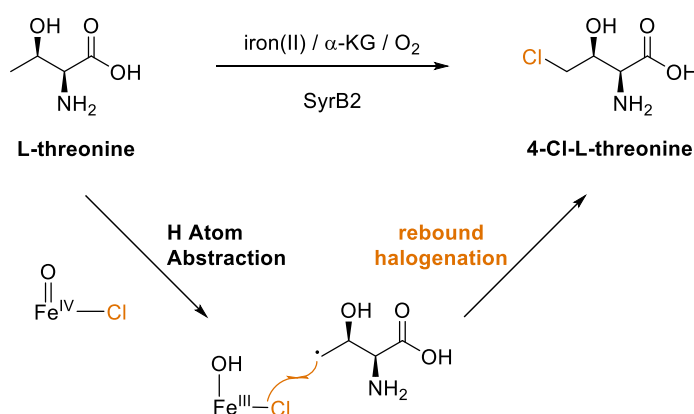
Scheme 8: Halogenation of L-threonine by SyrB2 via an iron(III)-hydroxido-chlorido intermediate that is formed by hydrogen atom abstraction and then reacts via rebound halogenation to form the product.[29,30]

This reaction mechanism is similar to the hydroxylation pathway of heme and non-heme hydroxylases (such as cytochrome P450, TauD, TET, etc.) and has been modeled by Comba and Wunderlich using synthetic iron(IV)-oxido complexes (Figure 6).[63] The synthetic iron(IV)-oxido complex $[Fe^{IV}(O)(L)Cl]^+$ (L = 3,7-dimethyl-9-oxo-2,4-bis(2-pyridyl)-3,7-diazabicyclo[3.3.1]nonane-1,5-dicarboxylate methyl ester) is capable of abstracting a hydrogen atom from cyclohexane generating an organic centered radical and an iron(III)-hydroxido-chlorido intermediate (Figure 6**A**). Rebound hydroxylation leads to cyclohexanol (Figure 6**B**) whereas rebound halogenation yields chlorocyclohexane (Figure 6**C**).[63]

oxidant	yield B	yield C
TBHP	53%	44%
H_2O_2	2%	19%
IB	0.1%	40%

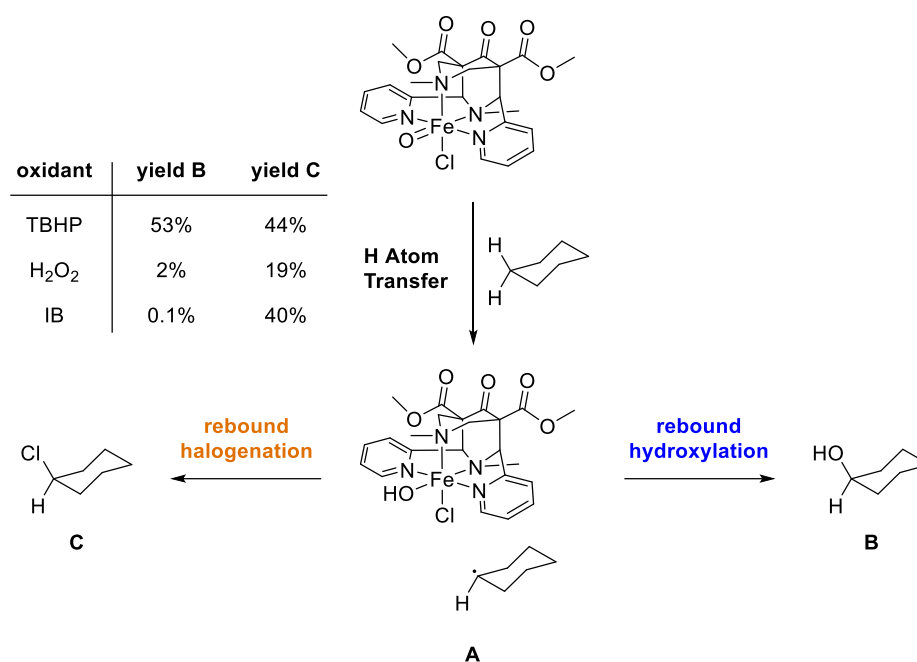*Figure 6: Reaction mechanism of the synthetic iron(IV)-oxido complex [FeIV(O)(L)Cl]+. L = 3,7-dimethyl-9-oxo-2,4-bis(2-pyridyl)-3,7-diazabicyclo[3.3.1]nonane-1,5-dicarboxylate methyl ester. TBHP = t-butylhydroperoxide, IB = iodosylbenzene.[63]*

Depending on the nature and amount of oxidant the product distribution between halogenated and hydroxylated product is shifted: use of TBHP led to a slight excess of cyclohexanol (53% vs. 44% chlorocyclohexane), hydrogen peroxide shifted this ratio towards chlorocyclohexane, while iodosylbenzene (IB) led to almost exclusive formation of the halogenated product (0.1% cyclohexanol vs. 40% chlorocyclohexane, Figure 6).

Side Reactions

Iron(II)/α-keto acid dependent enzymes have been observed to react *via* unproductive side reactions. In the aforementioned report on DAOCS, Solomon and co-workers found evidence that the substrate does not bind directly to the metal center but is rather held in place by the enzyme backbone. However, unlike other non-heme iron(II)/α-KG dependent enzymes, DAOCS forms both a five-coordinate and six-coordinate species if only α-KG but no substrate is present. This was confirmed by the authors using variable temperature-variable field MCD, Mößbauer spectroscopy, and X-ray absorption spectroscopy. Their experiments show that the binding of the co-factor α-KG to the iron center results in the formation of 45% five-coordinate species (Scheme 9**A**). This five-coordinate species was found to react faster than the six-coordinate species, likely because a water ligand needs to be replaced in the latter structure. Upon reaction of the five-coordinate structure with dioxygen (Scheme 9**A**), an iron(IV)-oxido species is formed very slowly, which then rapidly reacts with the protein to form an iron(III)-hydroxido species. This iron species is incapable of expandase activity and results in unproductive one-electron oxidation of the penicillin substrate, the radical formed on the protein is dissipated into the backbone. Thus,

15

the authors deemed such a sequential mechanism to not play a productive role in iron(II)/α-KG

enzymes.
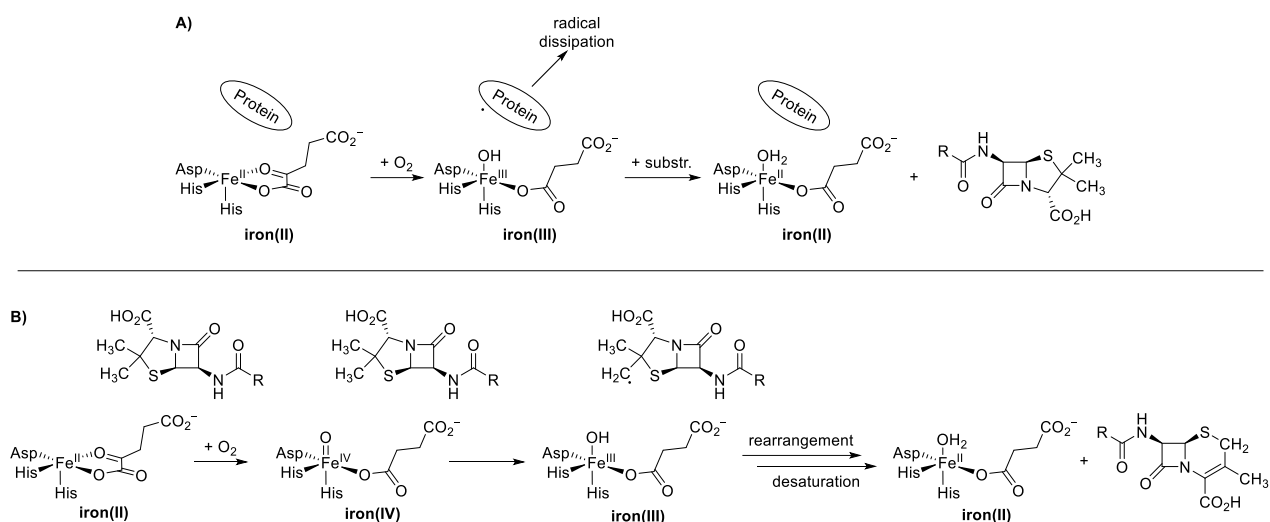
Scheme 9: **A**) Unproductive sequential (first α-KG coordination, then O_2 coordination, then substrate uptake) mechanism for DAOCS; **B**) productive concerted mechanism (both α-KG and substrate are coordinated, then O_2 uptake) that leads to the cephalosporin product. Adapted from Solomon et al.[64]

If both α-KG and the substrate are present, simultaneous binding occurs and a five-coordinate

species is formed, this then reacts with oxygen to form the active iron(IV)-oxido species (Scheme

9**B**), which is then capable of reacting with the substrate and therefore performing expandase

activity. Reaction with the substrate results in the formation of an iron(III)-hydroxido species,

not an iron(III)-oxido species (which had been proposed previously[65]). Now, both radical

substrate species and the iron(III)-hydroxido species decay simultaneously (*via* a desaturation

reaction of the substrate) and form the cephalosporin product. These results demonstrate that a

concerted coordination mechanism is required for productive DAOCS activity.[64]

Since neither the interconversion of these species nor any hydroxylation side reactions were

observed, the rearrangement step needs to be very rapid (at least an order of magnitude faster

than the HAT step). The rapid rearrangement might provide an explanation for the lack of

hydroxylation reactions, as the substrate is removed from the ferric intermediate on a time scale

that the hydroxyl group cannot be transferred prior.[64]

3. Iron(III) and Iron(IV) Complexes

Iron(III) complexes

As described above, monomeric iron(III)-hydroxido complexes are thought to be the reactive intermediates in a number of natural, enzymatic transformations.[66] Specifically, they are proposed to form intermittently in non-heme iron(II)/α-KG dependent enzymes upon HAT to then react *via* a rebound mechanism. In lipoxygenases, another class of non-heme iron enzymes, iron(III)-hydroxido species are proposed to play an integral part in the oxidation of polyunsaturated fatty acid residues such as linoleic acid (Scheme 10**A**).

Scientific interest the investigation of synthetic iron(III)-hydroxido complexes is high, as these compounds might serve as model systems for natural enzymes, e.g. for lipoxygenases by oxidizing 9,10-dihydroanthracene (DHA) to anthracene (Scheme 10**B**, structural similarities in linoleic acid and DHA are marked in bold).
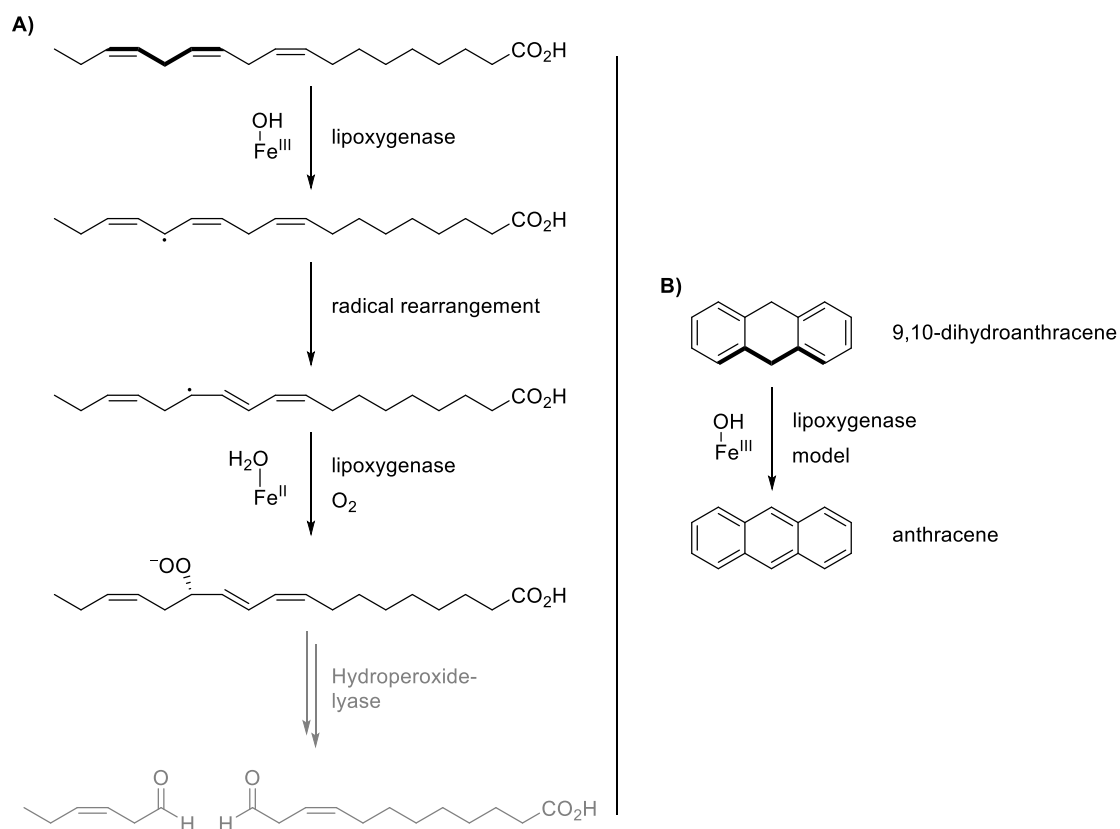
*Scheme 10: **A)** Hydrogen atom abstraction of a methylene group in linoleic acid, subsequent radical rearrangement, and transfer of dioxygen to generate the peroxide catalyzed by a lipoxygenase (13S-lipoxygenase). Subsequent protonation and C-C bond cleavage leads to cis-3-hexenal, the odor of freshly cut grass.[67] **B)** Model reaction for lipoxygenase activity: oxidation of 9,10-dihydroanthracene (DHA) to anthracene by a synthetic iron(III)-hydroxido lipoxygenase model complex. The structural similarities in linoleic acid and DHA are marked in bold.[68]*

Several examples of non-heme type synthetic iron(III)-hydroxido species have been reported in the past decades, Chart 2 gives selected examples by Masuda,[69] Borovik,[70,71] Goldsmith & Stack,[68] Que,[72] and Fout.[64] A main focus in this area of research was the reactivity of the hydroxido ligand towards organic substrates. In particular, the bond dissociation energy (BDE)

plays a crucial role in determining whether an iron(III)-hydroxido complex is able to transfer its hydrogen atom onto an organic radical.[70,73]
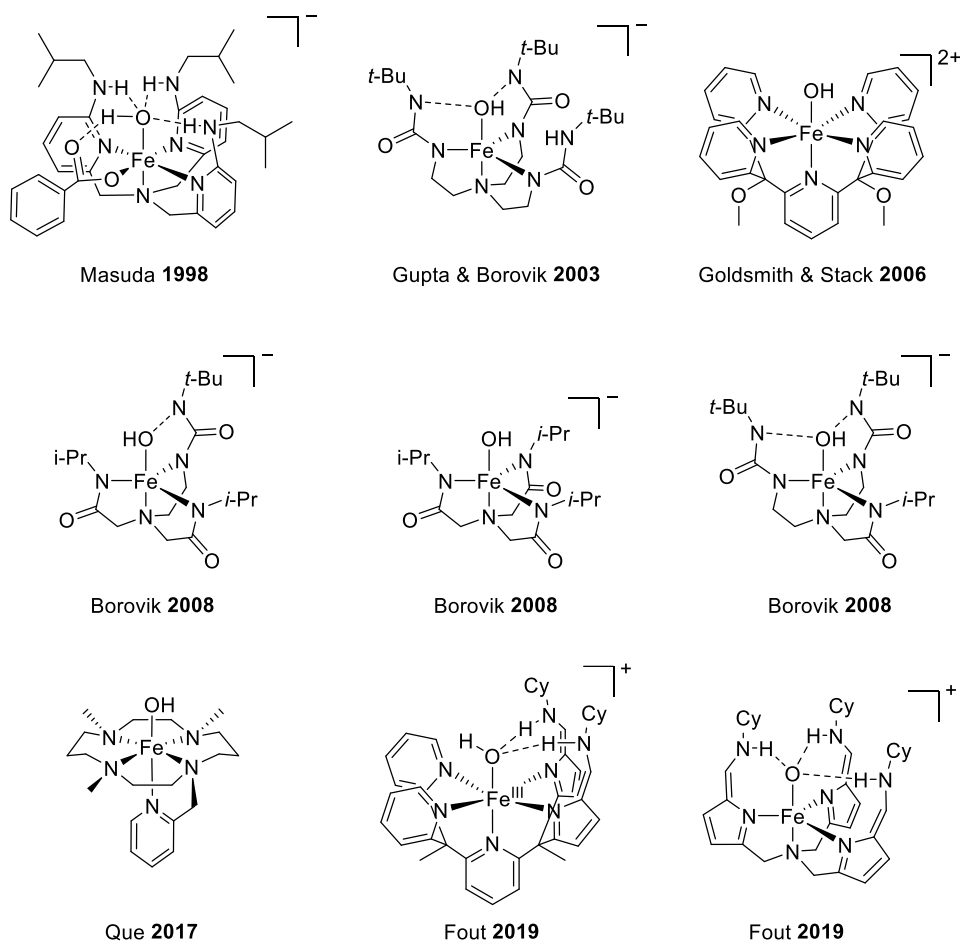
Chart 2: Overview over a selection of iron(III)-hydroxido or iron(III)-oxido complexes synthesized in the past 22 years.[49,64,68,70–72] Fe^{III}(OH)(TMC-py)(OTf)$_2$ was not isolated but observed in solution. TMC-py = 1-(pyridyl-2'-methyl)-4,8,11-trimethyl-1,4,8,11-tetrazacyclotetradecane, OTf = $^-O_3SCF_3$.

The synthesis of monomeric iron(III)-hydroxido complexes is challenging due to their preference for dimerization, leading to oxido-bridged iron(III) dimers.[72] Even a relatively recent publication by Que *et al.* states that "The small number of reports in this field may be attributed to the challenges posed by such complexes due to their (thermal) instability." The examples shown in Chart 2 often bear bulky ligands that might prevent dimerization, however, the complexes reported by Goldberg, Stack, and Que are much less sterically hindered than those of Masuda, Borovik and Fout.

Common methods for characterization are x-ray crystallography, UV-vis spectroscopy, cyclic voltammetry, and kinetic studies involving radicals (synthetic analog of the rebound step) or radical precursors such as TEMPO-H or DHA. These kinetic studies usually serve the purpose of determining the Fe-O and O-H bond strengths, which is a good indicator for the complex's ability to oxidize organic substrates.

*Iron(III)-hydroxido Complexes of **L-1***

In addition to the above-mentioned ligand systems, **L-1** has been employed in the synthesis of iron complexes. In 2014, Xiang *et al.* reported on the catalytic activity of [Fe^{II}(mecn)(**L-1**)](ClO$_4$)$_2$ (which is a derivative of **C-1**, a complex used in this work) with hydrogen peroxide in oxidizing cyclohexanol, cyclopentanol, benzyl alcohol, and other organic substrates (Figure 7).
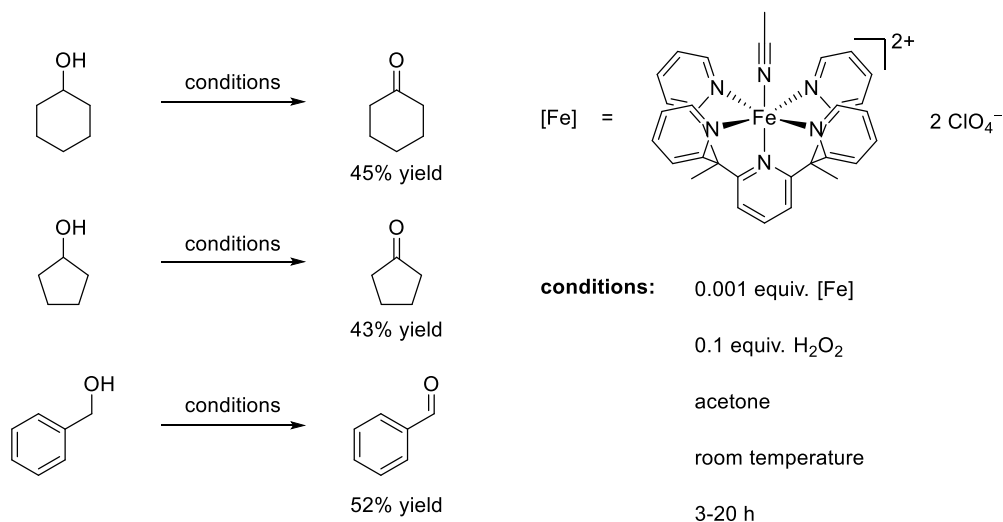
Figure 7: Alcohol oxidations performed by Xiang et al. under the given conditions. As precatalyst [Fe(mecn)(**L-1**)](ClO$_4$)$_2$ was used.[74]

The authors propose that the iron(III)-hydroxido species [Fe^{III}(OH)(**L-1**)]$^{2+}$ (**C-4**) is formed by reaction of the iron(II) precursor [Fe^{II}(mecn)(**L-1**)](ClO$_4$)$_2$ with hydrogen peroxide in acetone (Scheme 11). The evidence provided, however, was slim: the assignment was based on a color change and low resolution-mass spectrometry.[74]
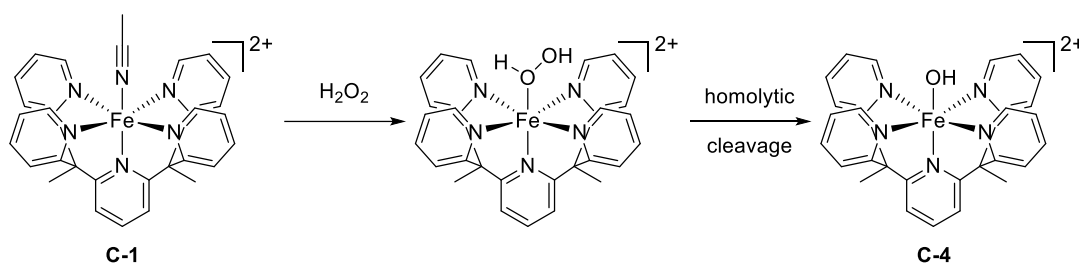
Scheme 11: Reaction of [Fe^{II}(mecn)(**L-1**)]$^{2+}$ with hydrogen peroxide to form [Fe^{II}(O$_2$H$_2$)(**L-1**)]$^{2+}$ and subsequently [Fe^{III}(OH)(**L-1**)]$^{2+}$ via homolytic cleavage of the O-O bond, as proposed by Xiang et al.[74]

Chantarojsiri *et al.* also mention **C-4** as a possible intermediate in the chemical or electrochemical oxidation of **C-1**/**C-2** to **C-5**/**C-6**. The authors propose that **C-1** or **C-2** are oxidized in pure water or a mixture of acetonitrile and water in a two-step sequence to the iron(III))-hydroxido intermediate **C-4** and subsequently to **C-6** (or **C-5** if cerium(IV) ammonium nitrate is used and the compound isolated, not shown, Scheme 12). By using ^{18}O labeled water the solvent was identified as the source of the oxygen atom that is finally incorporated as the oxido moiety. More details can be found in the next subchapter (p. 21f).[12]
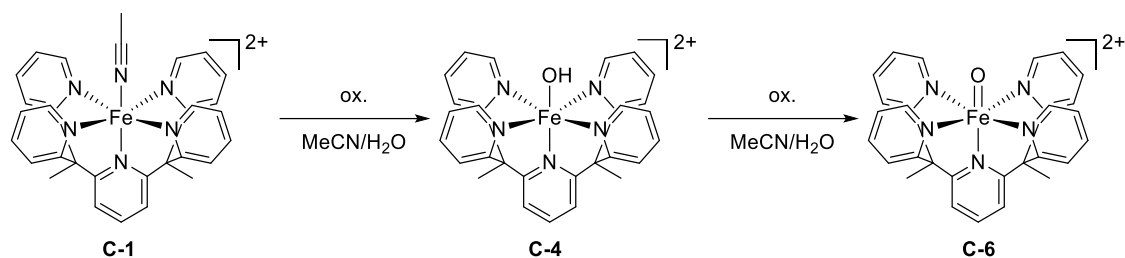
*Scheme 12: Two-step oxidation of [Fe^{II}(mecn)(**L-1**)]$^{2+}$ (**C-1**) using either cerium(IV) nitrate ([Ce(NO$_3$)$_6$]$^{2-}$) or tris(2,2'-bipyridine)ruthenium(II) ([Ru(bpy)$_3$]$^{2+}$, bpy = 2,2'-bipyridine) to form [Fe^{III}(OH)(**L-1**)]$^{2+}$ (**C-4**) and subsequently [Fe^{IV}(O)(**L-1**)]$^{2+}$ (**C-6**) in acetonitrile/water, as proposed by Chantarojsiri et al.[12] bpy = 2,2'-bipyridine.*

Iron(IV)-oxido Complexes

High valent iron(IV)-oxido species have been in the focus of the bioinorganic community since the initial reports on the structure and reactivity of TauD (*vide supra*). Since then, several iron(IV)-oxido compounds were synthesized and studied concerning their behavior in oxygen atom transfer (OAT, Scheme 13**A**) and hydrogen atom transfer (HAT, Scheme 13**B**) reactions.
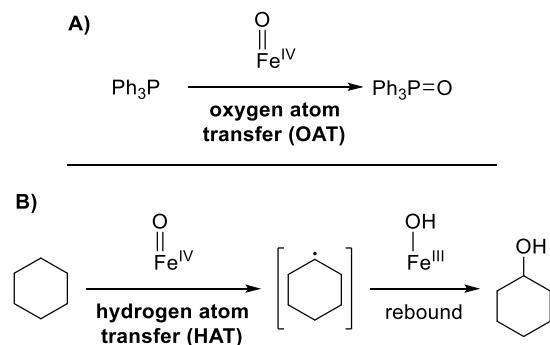
*Scheme 13: **A**) Oxygen atom transfer (OAT) from an iron(IV)-oxido species to triphenyl phosphine yielding triphenylphosphine oxide. **B**) Hydrogen atom transfer from cyclohexane to an iron(IV)-oxido species resulting in an organic-centered radical and an iron(III)-hydroxido species. These then react via a rebound step to form cyclohexanol.*

Especially the reaction in Scheme 13**B** is of importance in the field of bioinorganic chemistry, as it is proposed as the main reaction mechanism of iron(II)/α-keto acid dependent enzymes (refer to chapter I.2).

Iron(IV)-oxido species are often generated from their iron(II) precursors *via* oxidation using hydrogen peroxide, peracids, ozone, alkyl hydroperoxides, dioxygen, or cerium(IV) compounds. A notable exception is the iron(IV)-oxido species recently reported by Meyer *et al.*: ([Fe^{IV}(O)(L)]$^{2+}$, L is a macrocyclic tetracarbene of the *N*-heterocyclic carbene (NHC) type, see Figure 8). This compound was generated by disproportionation of the corresponding dinuclear [(L)Fe^{III}-(μ-O)-Fe^{III}(L)]$^{4+}$ species. More details are provided in chapter IV.1.
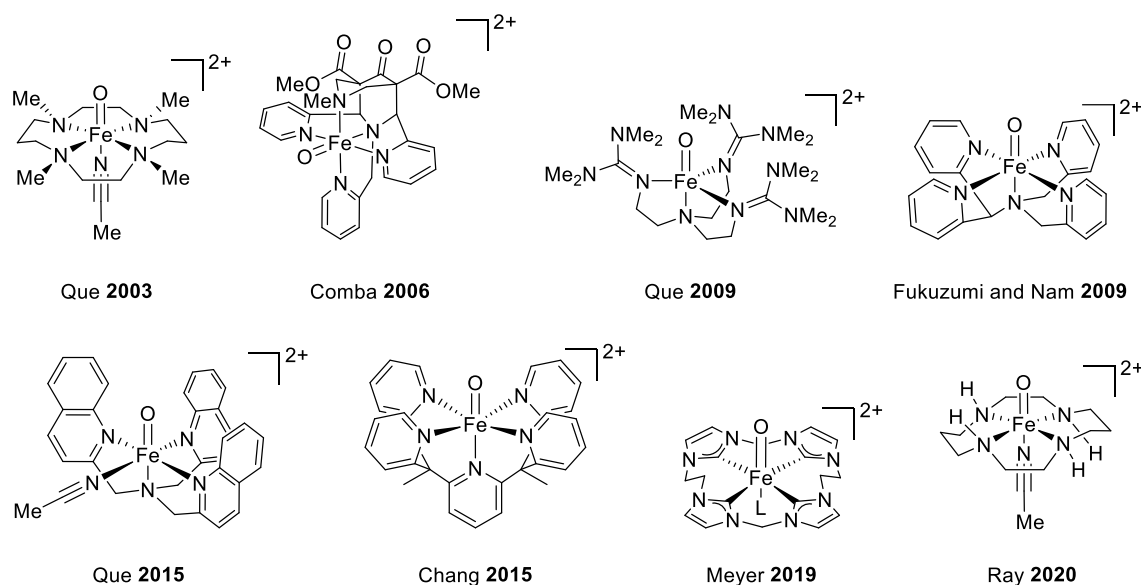
Figure 8: A selection of iron(IV)-oxido complexes reported on between 2003 and 2020.[12,75–81]

Especially the use of dioxygen is of relevance, as it closely resembles the natural mechanism for activation of an enzyme's active site (refer to chapter I.2). Recently, the research group of Kallol Ray made significant progress in this area and published their study on the stoichiometric formation of an iron(IV)-oxido complex with only molecular dioxygen as oxidant.[81] The authors had previously published a report on the same ligand and the corresponding iron(II) and iron(IV)-oxido complexes in 2019.[82] However, a side reaction was occurring: when the ligand, cyclam (1,4,8,11-tetraazaundecan), was reacted with iron(II) triflate, the corresponding iron(II) complex *I-20* formed in its *cis*-configuration (previously published, Scheme 14, pathway **A**). However, from the same solution the isomeric *trans* iron(II) complex *I-22* (Scheme 14, pathway **B**) was also isolated. Whereas *I-20* is a paramagnetic high-spin species, *I-22* displays diamagnetic properties and was assigned to exist in its low-spin state by the authors.
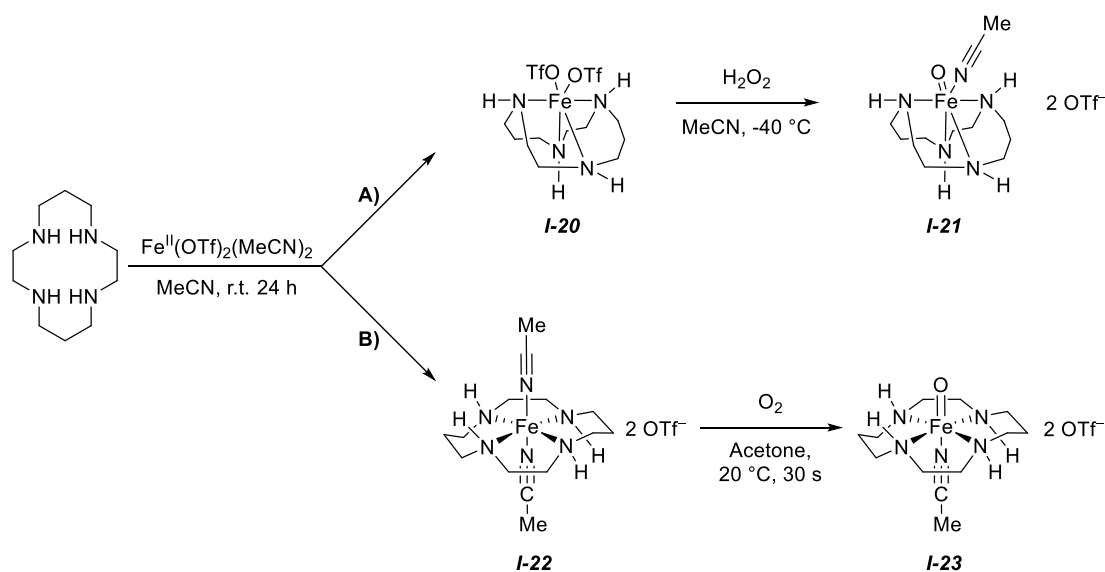
Scheme 14: One ligand - two different iron(II) complexes: formation of cis *(**A**) and* trans *(**B**) isomers of an iron(II)-cyclam complex and their corresponding iron(IV)-oxido complexes [Fe^{IV}(O)(cyclam)(mecn)]$^{2+}$.*

21

Oxidation of the *cis*-isomer **I-20** with hydrogen peroxide in acetonitrile led to the formation of the iron(IV)-oxido species **I-21** (Scheme 14, upper pathway), which is known for its preference of epoxidation of olefins over allylic hydroxylation.[82] The *trans* isomer **I-22**, however, reacts readily with dioxygen (or air) to form the corresponding *trans* iron(IV)-oxido complex **I-23** (Scheme 14, lower pathway). When comparing the reaction rate of the formation of **I-23** from **I-21**, Ray *et al.* noticed an *inverse* first order dependence on the oxygen concentration. After determining the rate law and identifying the iron(III)-superoxido complex **I-24** (Scheme 15) as an intermediate, the authors formulated an activation mechanism that bears semblance to the soluble methane monooxygenases (sMMOs, another class of iron enzymes): **I-22** reacts with molecular dioxygen to form quantitatively superoxido intermediate **I-24**. Small amounts decompose again to re-form **I-22**, which can then react with **I-24** *via* transfer of an oxygen atom to give **I-23**. This hypothesis was further corroborated by the observation that **I-24** is a very strong oxidant that transfers its oxygen atom very rapidly.
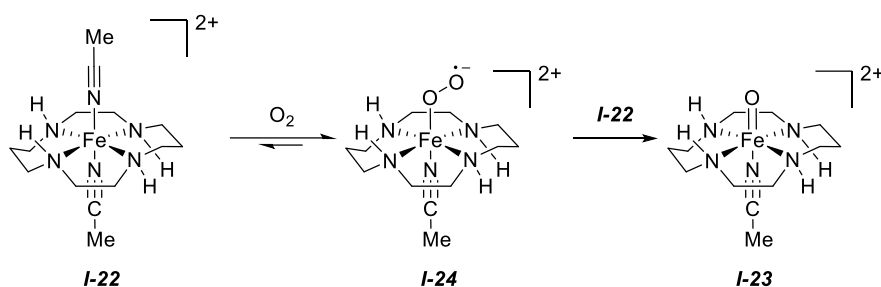
*Scheme 15: Proposed activation of **1B** by molecular oxygen.*

sMMOs are dinuclear iron enzymes, the oxidation from the +2 to +4 xidation state is believed to occur through an oxido-brigded μ-O-iron(III) complex.[83] Such a structure is resembled, if at all, by the transition state in the system reported by Ray *et al.* Nonetheless, the use of molecular oxygen in order to activate an iron(II) complex to the active iron(IV)-oxido species is a significant development in the field of iron(IV)-oxido research.

For the present work, the findings of Chantarojsiri *et al.* are of particular importance, as the reported iron(IV)-oxido complex $[Fe^{IV}(O)(\mathbf{L\text{-}1})]^{2+}$ (**C-6**) is a main focus. Chantarojsiri *et al.* report on the synthesis of the iron(II) precursors **C-1** and **C-2** and subsequent oxidation to **C-5**/**C-6** using cerium(IV) ammonium nitrate (CAN, Figure 9**A**). A similar reaction had been observed by Fukuzumi and Nam in 2009, when $[Fe^{II}(N_4Py)](ClO_4)_2$ (N_4Py = *N*,*N*-bis(2-pyridylmethyl)-*N*-bis(2-pyridyl)methylamine) was reacted with CAN to give $[Fe^{IV}(O)(N_4Py)]^{2+}$ (Figure 9**A**).[78] Chantarojsiri *et al.* also report on photochemical oxidation of **C-1** and **C-2** to **C-6** by addition of $[Ru(bpy)_3]^{2+}$ (bpy = 2,2'-bipyridine) and $K_2S_2O_8$ and irradiation using a blue fluorescence light bulb. By conducting these experiments in ^{18}O labeled water and subsequently measuring high resolution mass spectra and infrared spectra, Chantarojsiri *et al.* were able to assert water as the

source of the oxygen atom in **C-6**. Cyclovoltammetry measurements revealed that the redox process between iron(II) and iron(III) species is proton-coupled.[12]
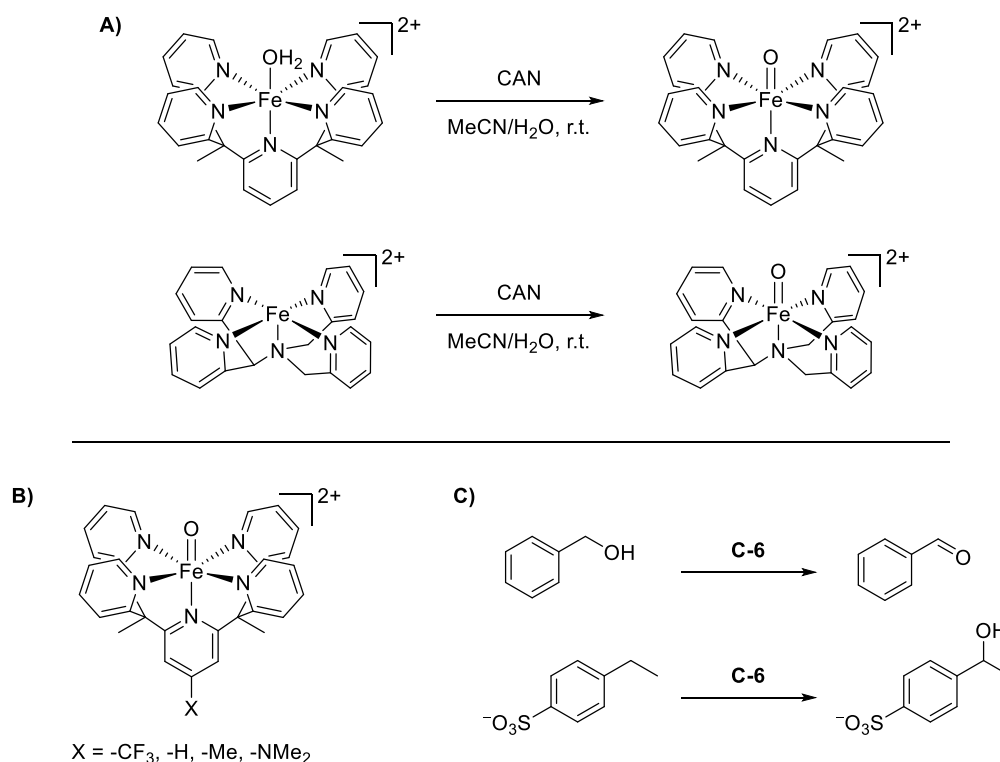

*Figure 9: **A**) Synthesis of **C-6** and [Fe^{IV}(O)(N₄Py)]²⁺ from the respective iron(II) precursors and cerium(IV) ammonium nitrate (CAN).[78] **B**) Axially modified iron(IV)-oxido complexes reported by Chantarojsiri et al. **C**) Oxidation reactions by **C-6** as reported by Chantarojsiri et al.[12]*

Chantarojsiri *et al.* also synthesized several ligand derivatives with axial modifications such as a trifluoromethyl and a methyl group, as well as a dimethylamine moiety (Figure 9**B**). The iron(IV)-oxido complex carrying the dimethylamine moiety was found to decompose quickly even at low temperature and was only observed fleetingly, this was attributed to auto-decomposition. Reactivity measurements of **C-6** with organic substrates such as benzyl alcohol *p*-ethylbenzenesulfonic acid in water revealed the oxidative capabilities of **C-6**: oxidation occurs both with unmodified aliphatic C-H bonds on the ethyl side chain in *p*-ethylbenzenesulfonic acid as well as the hydroxymethyl group in benzyl alcohol (Figure 9**C**). A plot of the observed reaction rates between **C-6** and its derivatives and the aforementioned substrates vs. the Hammett parameters of the axially modified iron(IV)-oxido complexes revealed a positive correlation, *i.e.* the electron poor trifluoromethyl modified complex was observed to react the fastest.[12]

Interestingly, Xiang *et al.* proposed the iron(III)-hydroxido species **C-4** to be capable of performing the same reactions (oxidation of aliphatic C-H bonds and hydroxymethyl groups, among others) as **C-6** (compare Figure 7 to Figure 9**C**). The reactions reported by Xiang *et al.* were performed in acetone whereas Chantarojsiri *et al.* used water as solvent. As Chantarojsiri *et al.* speculate on **C-4** being an intermediate, and therefore also a possible contaminant, in the

synthesis of **C-6**, further investigations are necessary to clearly assign the observed reactivities to a distinct iron species.

Synthetic iron(IV)-oxido chemistry

A very different application of iron(IV)-oxido research is the use of synthetic iron(IV)-oxido complexes as (late-stage) oxidants in the total synthesis of pharmacologically relevant substrates. [84] "Late-stage modification" refers to procedures that allow the modification of complex organic molecules during one of the last synthetic steps.[84–86] This enables derivatization of a base structure that can be produced on a large scale, which in turn facilitates the overall synthetic process. This base structure has usually already shown some of the desired activity (e.g. antibacterial or inhibitory activity) and is chosen for ease of derivatization. This method is commonly applied in pharmacological synthesis as it allows for the screening of large libraries of similar structure. A related method is the so-called "convergent synthesis": in this method, a complex structure is assembled from a range of commercially available building blocks that are coupled together in a series of standardized reactions. Changing one of the building blocks usually does not affect the synthetic pathway significantly but provides a new derivative.
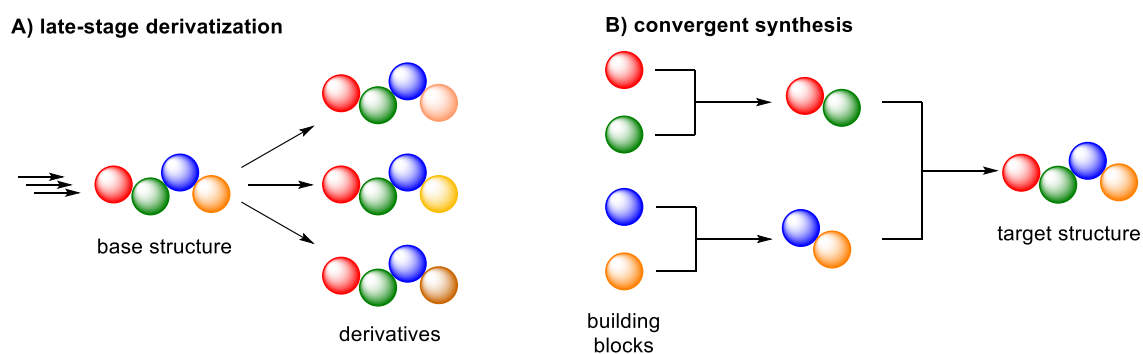
*Figure 10: Two methods for the preparation of large libraries of target compounds: **A)** late-stage derivatization – a base structure is synthesized (often* via *multiple steps) and then derivatized to gain access to a large amount of similar structures; **B)** a target structure is synthesized by coupling simple building blocks – changing a building block then gives access to a derivative.*

A special case of late-stage derivatization is the oxidation of sp³-hybridized/aliphatic C-H bonds by small molecule catalysts. Until as recently as 2007 it was commonly thought that the difference between two aliphatic bonds is not large enough to be distinguished in synthetic reactions.[87,88] However, recent discoveries have made such a distinction possible and have therefore provided a powerful tool for the derivatization of complex molecules.

*Figure 11: Examples for the change in oxidation state at a sp³ hybridized carbon center (marked with a red circle) center has on **A**) the smell and taste of a molecule or **B**) its antibacterial activity.*

In particular, iron(IV)-oxido chemistry has enabled such aliphatic C-H activation. Other metals commonly used for these reactions are manganese and ruthenium. The three most common ligand types of metal-oxido chemistry are porphyrins (derived from heme enzymes, *vide supra*), salen derivatives, and tetradentate aminopyridine ligands (Figure 12).

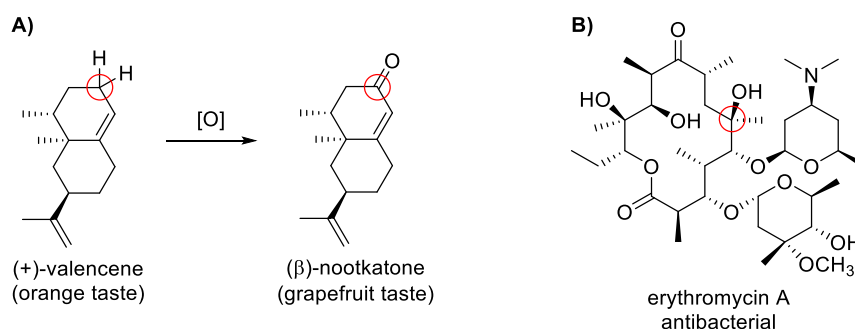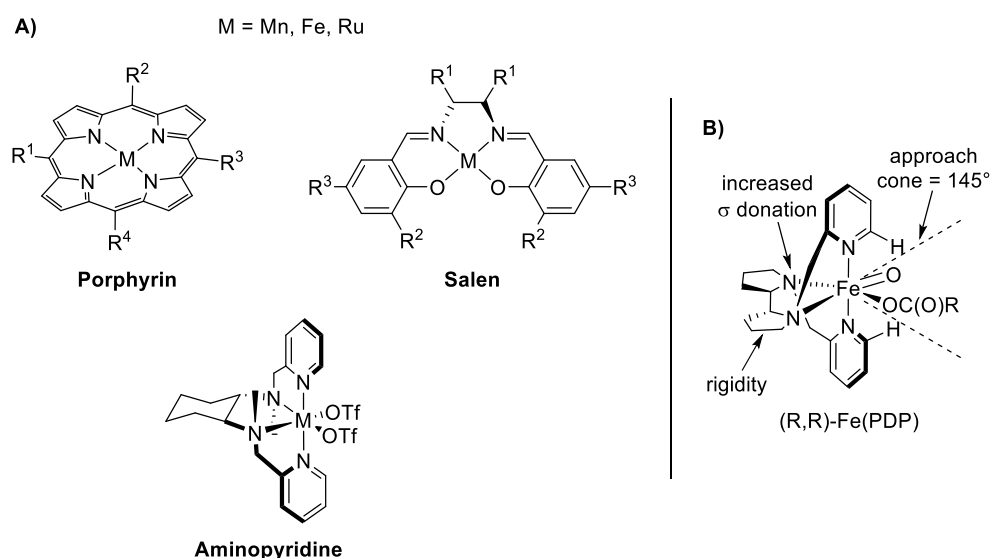*Figure 12: **A**) Three of the most common ligand types of metal-oxido chemistry: porphyrin, salen and aminopyridine **B**) A representative iron(IV)-oxido complex: [Fe^{IV}(O)(O$_2$CR)(PDP)]$^+$ (PDP = (2R,2'R-(−)-[N,N'-Bis(2-pyridylmethyl)]-2,2'-bipyrrolidine).[86]*

The Fe(PDP) iron(IV)-oxido complex (also called White-Chen-Catalyst) shown in Figure 12 is based on an aminopyridine scaffold that supplies rigidity while the amino moieties provide significant σ-donation to the central atom. This leads to significant increase in reactivity and selectivity compared to other systems of this ligand class. Fascinatingly, this complex shows oxidative selectivity that is not only based on bond dissociation energies. Reactions with methyl cyclopropanes (= radical clocks, refer to chapter IV.1 for details) do not yield ring-opening products, indicating that the rebound reaction proceeds on a much faster time scale (lifetime < 1 x 10^{11} s). The fact that the nature of the atmosphere (argon vs. air) does not result in different product ratios corroborates the hypothesis that no or only short-lived intermediates are

present.[86] Additionally, the retention of the stereoinformation of the substrate in Scheme 16 is another indication that the intermediate is at best short-lived.
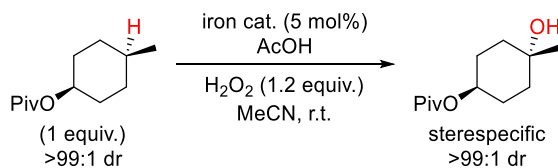
Scheme 16: Representative reaction of the above mentioned iron complex [Fe^{II}(MeCN)$_2$(PDP)](SbF$_6$)$_2$ with a cyclohexane substrate that is oxidized to the corresponding cyclohexanol derivative under stereoretention.[86] Piv = pivaloyl, dr = diastereomeric ratio.

Although common in nature, enantioselective reactions remain a challenging subject in synthetic chemistry. However, significant advances have been made in the past decades and powerful synthetic tools were created by the catalysis community. In the specific case of iron(IV)-oxido oxidations, enantioselectivity may be introduced in one of two steps: hydrogen atom transfer from the substrate to the metal oxido unit (Scheme 17**A**) or in the rebound step, in which a hydroxyl unit is transferred from the metal to the organic radical (Scheme 17**B**).
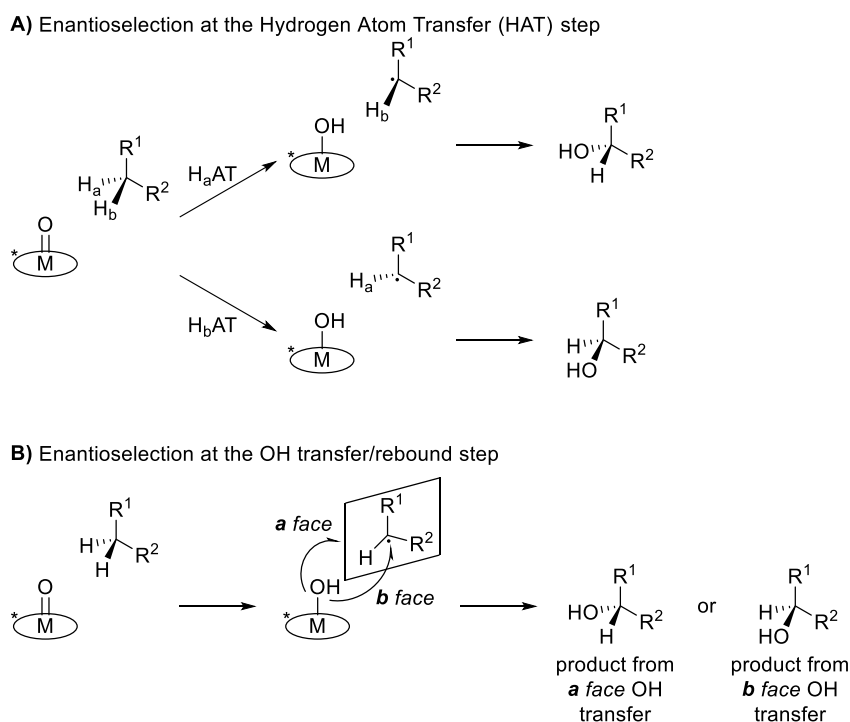
*Scheme 17: Different mechanisms for enantioselection: **A**) at the hydrogen atom transfer (HAT) step or **B**) at the OH transfer/rebound step.*

Depending on the electronic structure of the substrate, one of the two pathways is more likely. Substrates containing benzylic and allylic C-H bonds tend to follow pathway **A**, as the organic radical is comparably stable and long-lived. Methylene C-H moieties in alkyl moieties on the other hand usually follow pathway **B**.

An example of such an iron(IV)-oxido complex displaying enantioselective catalytic activity is shown in Scheme 18. Reaction with a range of benzylic substrates gives the respective chiral alcohols in moderate yields and with a moderate enantioselectivity.
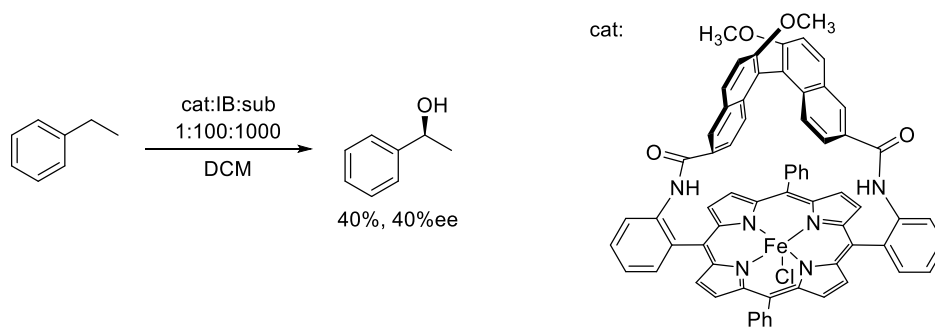
Scheme 18: Example for a chiral iron catalyst that is oxidized to its iron(IV)-oxido derivative by iodosobenzene (IB) and then capable of enantioselective oxidation of ethyl benzene to the corresponding alcohol. DCM = dichloromethane, ee = enantiomeric excess.

II. Motivation and Aim

Iron enzymes are ubiquitous in nature, however, many aspects remain poorly understood. For example, the exact nature of the interaction between the iron(II)/α-KG dependent TET enzymes and their substrate, DNA, is still matter of debate. Additionally, the iron(II)/α-keto acid dependent enzyme HPDL seems to be involved in a neurodegenerative disease, its function and mechanism of action, however, are not determined as of yet.
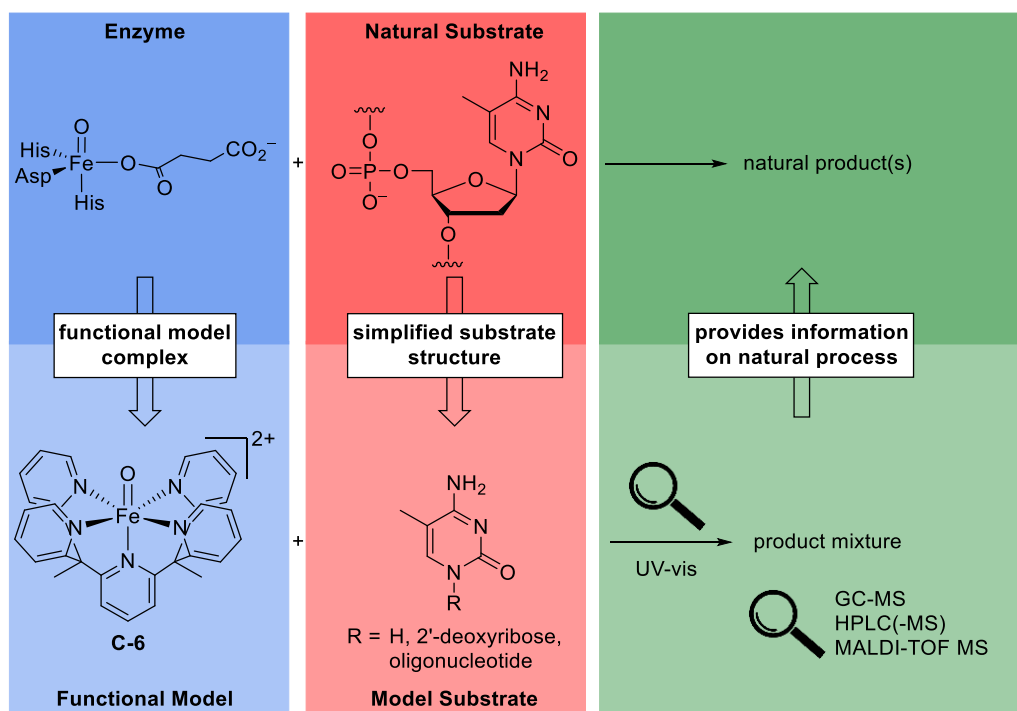
*Figure 13: TET mimic **C-6** as an example for the bioinorganic approach to answer biological/biochemical questions: study of the product distribution and reaction mechanism of a functional model complex with a simplified model substrate provides information on the natural process.*

The goal of the iron(IV)-oxido project in the research group of Prof. Lena Daumann at LMU Munich, which this work is a part of, is to identify and study suitable functional model complexes that mimic the behavior of iron(II)/α-keto acid dependent enzymes. The first step on this path was achieved in early 2018, when the iron(IV)-oxido complex [Fe^{IV}(O)(**L-1**)]$^{2+}$ (**C-6**) was observed to oxidize the nucleobase 5-methyl cytosine (**5mC**), part of the natural substrate of TET enzymes (Figure 14, grey box), to its natural metabolites 5-hydroxymethyl cytosine (**5hmC**), 5-formyl cytosine (**5fC**), and 5-carboxy cytosine (**5caC**).

Figure 14: The reaction in the grey box had been observed in previous works, expanding upon this finding was the main focus of this work.

Therefore, the focus of this work was the study of C-6 and its interaction with a variety of substrates: epigenetically relevant nucleobases, nucleosides, and oligonucleotides as well as synthetic nucleobases and intermediates in the proposed mechanism of HPDL (Figure 14, red box). To this end, new product analysis methods needed to be found and developed (Figure 14, lower green box). Furthermore, the ligand library was to 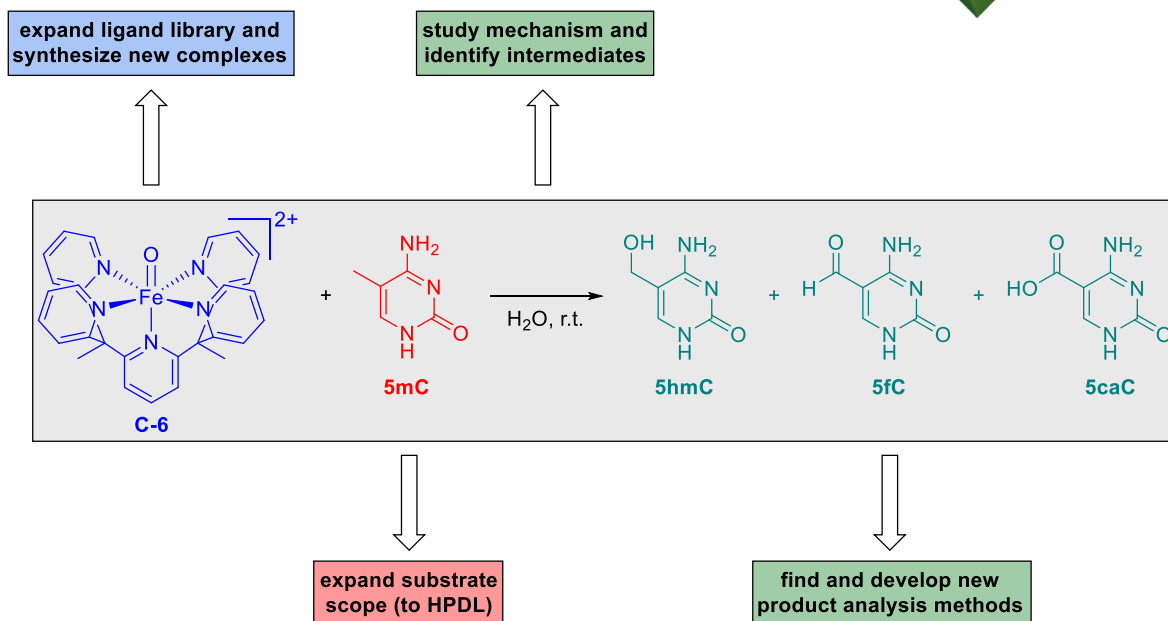be expanded and additional iron complexes were to be synthesized in order to identify new functional model complexes (Figure 14, blue box). Particular focus was set on the study of the reaction mechanism and hence the identification and study of intermediates in the reaction of C-6 with organic substrates (Figure 14, upper green box).

The results of these investigations are presented in four chapters: in chapter III the use of **C-6** as a functional model complex for TET enzymes is discussed, additional investigations that spawned from these results are also included. A major discovery herein was the isolation of **C-4** as a product of the reaction of **C-6** with an organic substrate, these studies are presented in chapter IV. Investigation of immobilizing ligands based on **L-1** onto solid supports as well as attempts of expanding the ligand and complex library are discussed in chapter V. In chapter VI, the results of the collaborative investigation of the HPDL enzyme are presented.

In addition to these, chapter VII summarizes the results obtained from mass spectrometric analysis of redox dyes (phenazine methosulfate, etc.) commonly used in the study of methanol dehydrogenases.

III. [Fe^{IV}(O)(Py$_5$Me$_2$H)]$^{2+}$ as a TET Biomimetic

1. Introduction and State of the Art

DNA and Genetics

Standard terran deoxyribonucleic acid (DNA) is a natural polymer composed of a phosphate-2'-deoxyribose backbone (Figure 15**C**) and four nucleobases: adenine (**A**), guanine (**G**), thymine (**T**), and cytosine (**C**, Figure 15**A**). These are referred to as canonical nucleobases and are connected to the backbone at position 1 of the nucleobase and the 1' position of 2'-deoxyribose *via* a glycosylic bond (Figure 15**C**). DNA can adopt different conformations, its most common structure is a double-strand (dsDNA) in the form of a right handed double-helix (B-DNA, Figure 15**B**), which was first discovered by Franklin, Wilkins, Watson, and Crick in the midst of the 20th century. In this B-DNA, the two strands are positioned anti-parallelly, *i.e.* a 5' and a 3' end are present at both ends of the DNA structure (Figure 15**B** and **C**). Base-pairing of adenine and thymine as well as guanine and cytosine (Figure 15**D**) contributes to the formation of this double-helix, however, stacking interactions between nucleobases are the main reason for its stability.
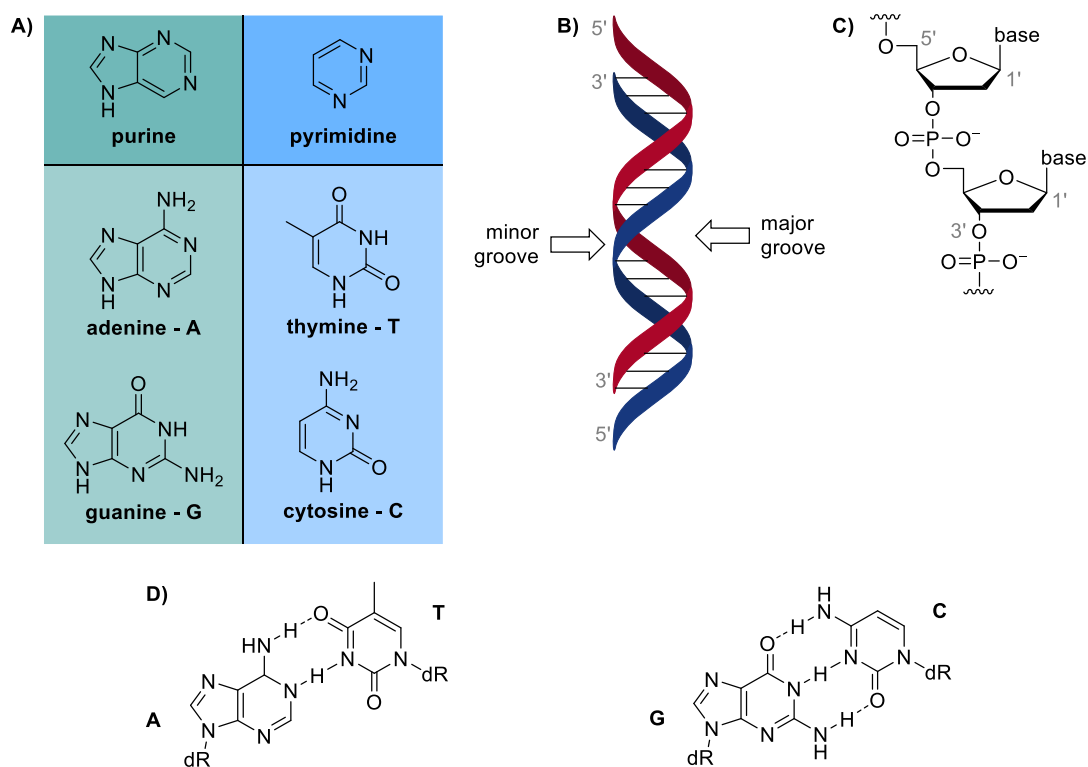
*Figure 15: **A**) Heterocycles pyrine, pyrimidine and the DNA bases derived thereof: adenine (**A**), guanine (**G**), thymine (**T**), and cytosine (**C**). **B**) The most common structure of DNA: a double-helix. The black lines indicate the pairing of the nucleobases. **C**) Structure of the phosphate-2'-deoxyribose backbone of DNA. **D**) Base paring in DNA: adenine pairs with thymine* via *two hydrogen bonds, guanine with cytosine* via *three hydrogen bonds.*

The specific properties of the components of DNA lead to the formation of two indentations, the major (width: 2.2 nm) and minor groove (width: 1.2 nm, Figure 15**B**). Proteins that interact with specific sequences of dsDNA, such as the transcription complex that copies DNA to RNA for

protein synthesis, often do so by making contact with the nucleobases exposed in the major groove.[89]

In eukaryotic cells, DNA is coiled up and wrapped around small basic proteins, called histones, forming the so-called chromatin. DNA carries hereditary information of all life-forms (and DNA viruses). This information in encoded in the form of genes: specific areas of DNA that can be read and the contained information converted into a protein. The study of these mechanisms is commonly referred to as genetics.

Genetics has long been thought to be the only mechanism for lifeforms to store and pass on information. However, in the last decades more and more attention has come to additional mechanisms capable of storing hereditary information as questions arose that could not be answered by the traditional system of genetics. For example, cell differentiation and properties that are only inherited from the father or the mother. During differentiation of embryonic stem cells, the chromatin (*i.e.* the complex of DNA and packaging proteins such has histones) is reorganized in order to establish expression programs specific for each cell type. It has been shown that this process is closely linked to DNA methylation, in particular the (de)methylation of cytosine.[90] This research field is commonly referred to as epigenetics.

Epigenetics and DNA Modification

Epigenetics is the study of heritable changes of the phenotype that do not involve changes in the sequence of the DNA bases.[91] The Greek prefix ἐπῐ (= *epi*) in epigenetics refers to changes that are made "on top of" or "in addition to" genetics. It is generally accepted that epigenetic mechanisms are the reason for differentiation of cells or even the regulation of a species' development.[92] For example, it has been shown that the different kinds of nutrition for honey bee larvae determine their developmental fate: whereas bee larvae that are only briefly fed with geleé royale (royal jelly) and then quickly switched to a honey and pollen diet develop into worker bees, whereas the larvae that are fed geleé royale exclusively develop into queens.[93] In particular, it was shown that DNA methylation is the reason for this differential development.[94] DNA methylation is one of three commonly mentioned epigenetic pathways: chromatin remodeling,[95–97] chemical modification of histones,[98–103] and, as already indicated, chemical modification of DNA.

Chromatin remodeling refers to a dynamic modification of the chromatin that influences the way DNA and transcription proteins interact and therefore how genetic information is accessed. One major pathway is ATP-dependent restructuring, ejection, or movement of nucleosomes, the 147 base-pair (bp) long structures of DNA wrapped around a histone.[104] Chromatin remodeling is also achieved by chemical modification of histones, e.g. by methylation, acetylation,

phosphorylation, or ubiquitination.[99] Environmental factors can have profound impact on these processes: Ciafré *et al.* reported that exposure of a fetus to ethanol (drinking alcohol) during the gestation alters the chromatin structure, it did in fact redraw the entire gene expression pattern.[105]

Whereas these mechanisms affect the way DNA is structured and accessed, chemical modification of DNA results in the formation of non-canonical nucleobases. Some examples of modified nucleobases are shown in Chart 3. However, not all of these modified bases are the result of epigenetic modification or occur in eukaryotes: 6-methyladenine (**6mA**),[106] 7-methylguanine (**7mG**),[107] 4-methylcytosine (**4mC**)[108] are, for example, found in bacterial or phage DNA. On the other hand, 8-oxo-guanine (**8-oxo-G**),[109,110] 3-methylcytosine (**3mC**), and 1,*N*6-etheno-adenine (**εA**) are common DNA lesions that occur when DNA is oxidatively damaged (**8-oxo-G**) or when endo- or exogeneous alkylation agents are present (**3mC** and **εA**).[111,112]
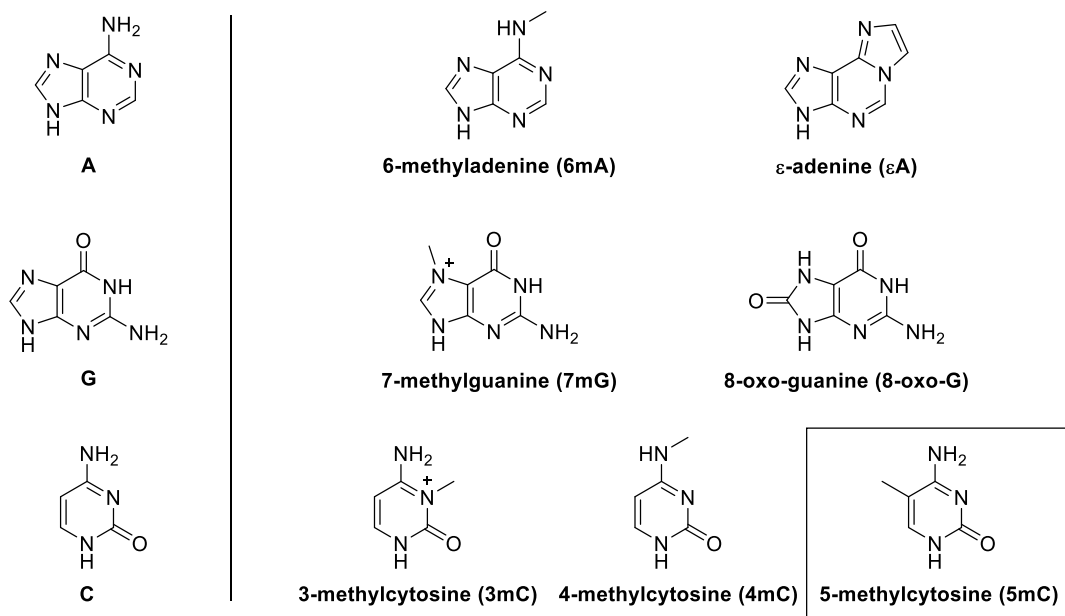

Chart 3: Canonical bases *A*, *G*, and *C* and their modified derivatives 6-methyladenine (*6mA*),[106] 1,N6-etheno-adenine (*εA*),[112] 7-methylguanine (*7mG*),[107] 8-oxo-guanine (*8-oxo-G*),[109,110] 3-methylcytosine (*3mC*),[111] 4-methylcytosine (*4mC*),[108] and 5-methylcytosine (*5mC*).[113] Not all of these derivatives are epigenetically relevant or occur in eukaryotes.

The most relevant epigenetic modification of eukaryotic DNA is 5-methyl cytosine (**5mC**). **5mC** is therefore often referred to as the "fifth base", as an addition to the four canonical bases **A**, **G**, **T**, and **C**. In some phage DNA (*Xanthomonas phage XP-12* or *halobacterium virus phiH*), the entire **C** content is replaced by **5mC**.[114] In human DNA, **5mC** is mostly found in CpG dinucleotides, ~75-80% of which are typically methylated.[113,115] Mammalian DNA is generally depleted of such CpG dinucleotides, however, certain areas show an intense clustering of CpG – these areas are referred to as CpG islands.[116] In the human genome, around 25,000 of such CpG islands can be found, 75% of these clusters are less than 850 bp long.[117] CpG islands are thought to play an integral role in gene regulation, ~75% are found within promotor regions or gene bodies, where they serve as

secondary promotors.[118,119] Generally, **5mC** levels are stable at ~5% of all cytosine residues, however, in embryonic cells a more dynamic situation is observed.[120] **5mC** is generally believed to have regulatory function by functioning as an "epigenetic switch": methylation of a cytosine residue in a promotor region prevents read-out of the corresponding gene, it is "turned off" or "silenced" (Figure 16). Removal of the methylation mark then restores the original situation and the gene is accessible for transcription again.[121–125]
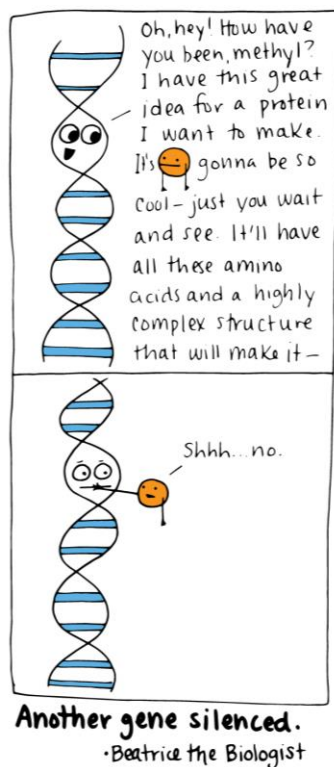

Figure 16: Caricature of the methylation of DNA, which is sometimes referred to as "gene silencing", by Beatrice the Biologist.[126]

The manner, amount, and structure of DNA methylation of a certain organism is often referred to as its "methylome", in parallel to the more widely used term "genome" referring to the structure of the organisms' genes. The entire structure of an organisms' epigenetic modifications is then referred to as "epigenome".

5mC is generated in DNA by a group of enzymes called DNA methyl transferases (DNMTs) under the consumption of *S*-adenosyl methionine (SAM, black dashed arrow in Figure 17). Different DNMTs carry out different functions: DNMT3a and DNTM3b introduce new methylation marks (so-called *de novo* methylation),[127,128] whereas DNTM1 is proposed to carry out maintenance methylation, *i.e.* restore methylation on both daughter strands after DNA replication.[129,130] DNMT1 knockout studies in mice have shown the importance of methylation maintenance, as mice without DNMT1 die early in embryogenesis.[131]

Two general pathways for demethylation are commonly discussed: *active* and *passive demethylation*. In *passive demethylation*, **5mC** is replaced by **C** during cell division, as **5mC** codes

as **C** (black dashed arrow in Figure 17). *Active demethylation* refers to the oxidative removal of the methyl moiety.[132–134] Here, two main pathways are proposed that both start with the TET-assisted oxidative hydroxylation of **5mC** to **5hmC**,[7,135] then to **5fC**, and finally to **5caC** (bold burgundy arrows in Figure 17).[136] This three-step sequence has been intensely studied, however, several details are still elusive. For example, Hu *et al.* noticed a discrepancy between the calculated bond dissociation energies (BDEs) and observed turnover of **5mC**, **5hmC**, and **5fC** by TET2 – lower BDE values should indicate a faster reaction (Figure 17).[8] For details on the enzymatic mechanism in general, refer to chapter I.2, for details on this particular circumstance, *vide infra*.
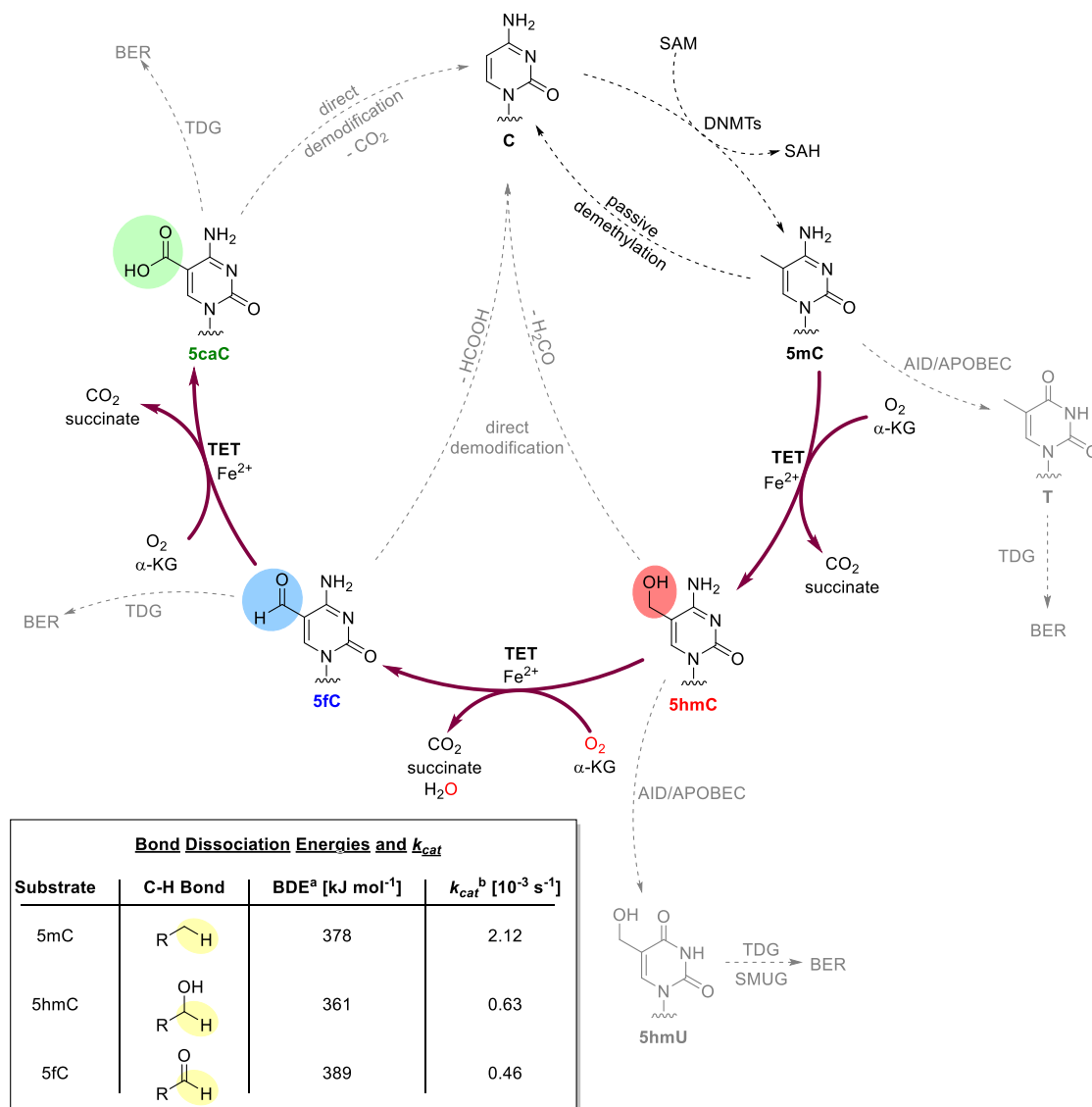

Bond Dissociation Energies and k_{cat}			
Substrate	C-H Bond	BDE^a [kJ mol^{-1}]	k_{cat}^{b} [10^{-3} s^{-1}]
5mC	R⌒H	378	2.12
5hmC	R⌒H (OH)	361	0.63
5fC	R⌒H (O)	389	0.46

*Figure 17: The general consensus mechanism of methylation of **C** to **5mC** by DNMTs using SAM and the subsequent demodification mechanism by TET and base excision repair/direct demodification. Highlighted in burgundy are the enzymatic transformations of **5mC** to **5hmC**, **5fC**, and **5caC** performed by TET under consumption of molecular dioxygen and α-KG.[120,133,137] The bond dissociation energies (BDEs) for **5mC**, **5hmC**, and **5fC** and their respective turnover constant with TET2 (k_{cat}) are given. ^{a} calculated by Hu et al. ^{b} measured by Hu et al. for TET2. SAM = S-adenosyl methionine, DNMTs = DNA methyl transferases, SAH = S-adenosyl homocysteine, TET = ten eleven translocation 5-methyl cytosine dioxygenase, AID/APOBEC = activation-induced cytidine deaminase/apolipoprotein B mRNA-editing enzyme complex, TDG = thymine DNA glycosylase, SMUG = strand-selective monofunctional uracil-DNA glycosylase 1, BER = base excision repair.[7,120,133–137]*

5hmC, **5fC**, or **5caC** are then proposed to be directly demodified (grey dashed arrows in Figure 17) under loss of formaldehyde, formic acid,[138] or carbon dioxide,[137] respectively.[120] Alternatively, the cells "standard" repair method for the removal of (unwanted) modified DNA nucleobases, base excision repair (BER), is capable of removing **5fC** and **5caC**. Both **5mC** and **5hmC** have been reported to be deaminated to **T** and **5hmU**, respectively, by activation-induced cytidine deaminase/apolipoprotein B mRNA-editing enzyme complex (AID/APOBEC) and subsequent BER, assisted by thymine DNA glycosylase (TDG) or strand-selective monofunctional uracil-DNA glycosylase 1 (SMUG).[139–142] However, it has also been shown that the deamination of **5mC** to **T** can lead to so-called point mutations, as **T** is a stable DNA base usually not recognized by BER. This is suspected to play a role in cancer development.[143]

TET-assisted oxidative modification of **5mC** to **5hmC**, **5fC**, and **5caC** is the focus of this work, therefore, a more detailed analysis of TET enzymes and the (bio)chemistry of **5mC** and its oxidized derivatives is provided.

A Closer Look at TET enzymes

Three related TET enzymes are known in mammals: TET1, TET2, and TET3. All show **5mC** oxidase activity, however, their structures differ slightly (Figure 18).[144] The responsible genes, *TET1*, *TET2*, and *TET3*, are expressed as different isoforms: at least three isoforms are known for TET2 and TET3, and at least two isoforms are known for TET1.[145,146] As iron(II)/α-KG dependent enzymes, TET proteins contain a double-stranded β-helix (DSBH) domain including a binding site for iron, which is located in a cysteine rich domain.[23,147] In addition, a CXXC zinc finger domain, used for binding the DNA substrate,[148] is found in TET1 and TET3, but is absent in TET2.[149,150] However, the neighboring gene of *TET2*, *IDAX*, encodes for such a CXXC domain and the corresponding CXXC4 protein is thought to interact with TET2 for DNA binding.[150] This separation of enzymatic domain from the substrate-recognition part of the protein contributes to making TET2 a good target for *in vitro* analyses, as interactions of the enzyme with substrates other than natural DNA can be investigated.

As α-KG is mainly produced in mitochondria and TET enzymes are commonly found in the nucleus, it remained an open question for some time how the transfer of α-KG occurs. A recent study on neurons by Traube *et al.* showed that TET3 redirects the mitochondrial enzyme glutamate dehydrogenase to the nucleus, which suggests an on-sight production of α-KG.[151]
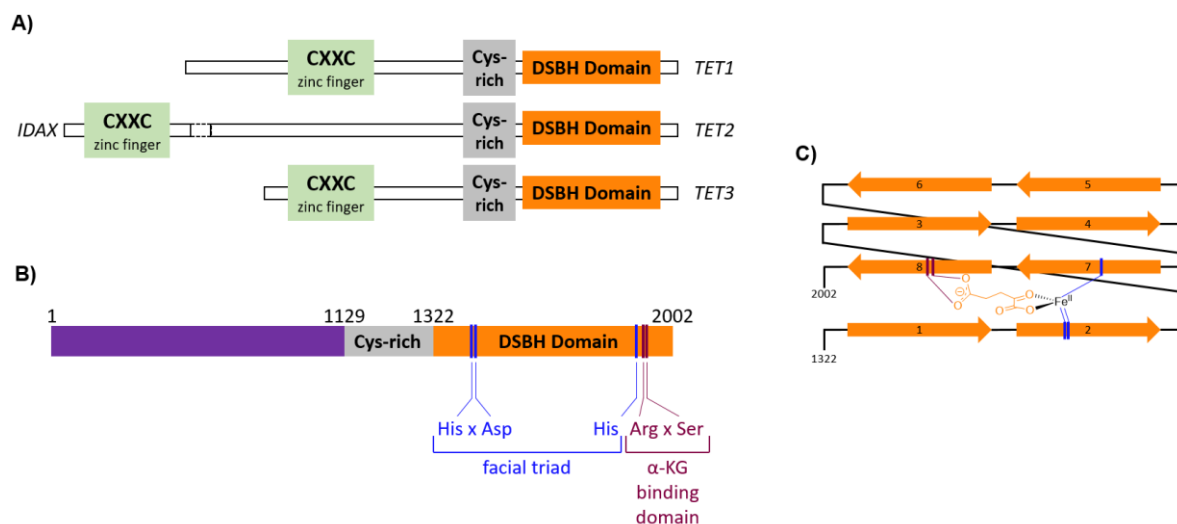
*Figure 18: **A)** Graphical representation of the primary sequences of the three tet genes in humans* TET1, TET2 *(including the neighboring* IDAX *gene), and* TET3. *The conserved structures of the CXXC zinc finger domain, the Cys-rich domain, and the DSBH domain are indicated. **B)** Graphical representation of the structure of the TET2 protein, significant amino acid locations, conserved structures, and the binding sites for iron (facial triad, in blue) and α-KG (Arg x Ser motif, in burgundy) are indicated. **C)** Graphical representation of the DSBH domain in TET2. The locations and binding motifs of the iron and α-KG cofactors are indicated.*[149,150,152]

The active site of TET enzymes contains an iron ion that is coordinated by the facial triad, a common structural motif in iron(II)/α-KG dependent enzymes (refer to chapter I.2). The three amino acids (two histidines, one carboxylate-containing; aspartate in the case of TET2) coordinate to one face of the octahedron around the iron central atom. α-KG coordinates *via* one of its carboxyl functions and the neighboring ketone moiety, the final coordination site is filled by a water molecule (Figure 19**B**).[8,153]
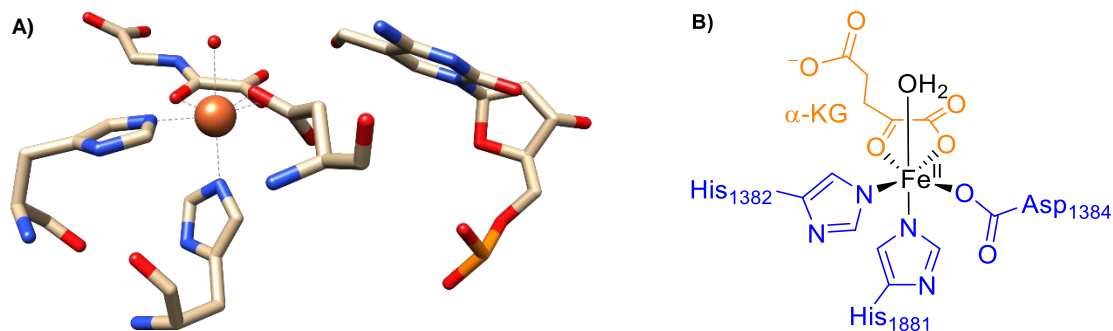

Figure 19:A) Graphical representation of the active site in a crystal structure of a TET2-5hmC complex. Instead of the natural co-factor α-KG a synthetic analog N-*oxalyl glycine (NOG) is coordinated. PDB: 5DEU **B)** Structural model of the same active site. The facial triad (in blue, 2 His 1 Asp residue) and α-KG coordinate the iron center. The coordination sphere is completed by a water molecule.*

Hu *et al.* obtained crystal structures of TET2-substrate complexes by co-crystallizing TET2, a short DNA oligomer containing a **5mC**, **5hmC**, or **5fC** residue, and *N*-oxalylglycine (NOG).[8,153] NOG was used instead of α-KG as it prevented activation of the iron center and therefore enabled crystallization. The authors then studied the orientation of the substrate within the protein, particularly the distance between the iron ion in the active site and the closest abstractable hydrogen atom on the methyl, hydroxymethyl, or formyl group in **5mC**, **5hmC**, or **5fC**,

respectively. The distance in the **5hmC**-containing structure was found to be the shortest (3.74 Å), followed by that in the **5mC**-containing structure (3.85 Å), while the distance between the formyl-hydrogen in **5fC** and the iron center was found to be the largest (4.98 Å). Similarly, the bond dissociation energies calculated by the authors (refer to the BDE values stated in the table in Figure 17) were found to follow the same pattern: BDE(**5hmC**) < BDE(**5mC**) < BFE(**5fC**).[8] These observations would indicate that substrates containing a **5hmC** moiety are turned over the fastest while a **5fC**-containing substrate reacts the slowest (for details on the general enzymatic mechanism refer to chapter I.2). However, kinetic measurements of the turnover of these substrates revealed a different pattern: **5mC** is turned over the fastest, followed by **5hmC**, and finally **5fC** (refer to the k_{cat} values stated in the table in Figure 17).[8] The reason for this behavior still remains an open question, however, our own bioinorganic approach gave some insight (refer to chapter III.4).[13]

*A Closer Look at **5mC**, **5hmC**, **5fC**, and **5caC***

5mC was first indirectly discovered in an attempt to identify the bacterial toxin responsible for tuberculosis by Ruppel in 1898. The isolated nucleic acid showed the presence of **T**, **G**, **C**, and an unknown, methylated nucleobase.[154] After initial quarrels about the identity of this unknown nucleobase,[155,156] Hotchkiss found unequivocal evidence for **5mC**'s existence by isolating it by paper chromatography from calf thymus.[157] Wyatt then determined the exact structure in 1950.[158,159] In the past decades, **5mC** has been the target of numerous investigations. Probably the most remarkable result was the discovery that the presence of **5mC** in promotor regions leads to heritable gene silencing in higher eukaryotes,[160] this opened up the field of epigenetic DNA methylation research. **5mC** is also reported to occur in RNA, however, its exact function is not clear and subject of current investigation.[161]

As mentioned above, DNMTs use SAM to methylate **C** residues in DNA. The corresponding mechanism for DNMT1 is shown in Scheme 19: first, a cysteine residue is covalently bound to position 6 of **C** while a proton is transferred from a neighboring glutamic acid residue to the *N*3 position of **C** (structure **A**). Then, deprotonation of this *N*3 position leads to nucleophilic attack of the carbon atom at the 5 position in **C** on the methyl group in SAM (structure **B**). Deprotonation of *H*5 by a hydroxide ion expels cysteine and generates **5mC** (structures **C** and **D**).[162]
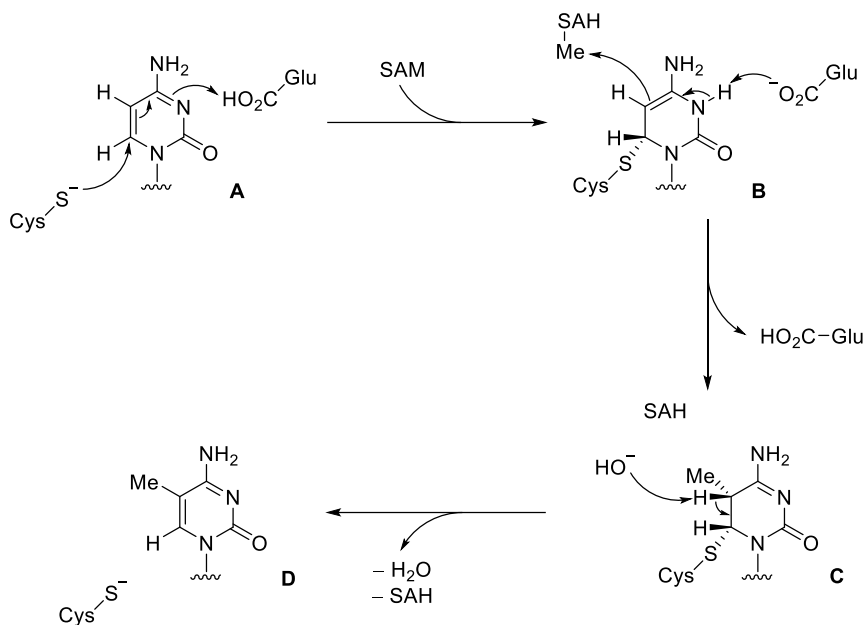
*Scheme 19: Methylation of **C** residues by DNA methyl transferase 1 (DNMT1) using S-adenosylmethionine (SAM), glutamic acid (Glu), and cysteine (Cys).[162]*

The resulting **5mC** is then subject to different pathways: as **5mC** is recognized as **C** during DNA replication, cell division dilutes the amount present in the genomes of the daughter cells. This is referred to as *passive demethylation* (Figure 15). As mentioned above, *active demethylation* involves the action of one or several enzymes.

It has been shown that **5mC** is converted to **5hmC**,[135] then **5fC**, and finally to **5caC**[136] by TET enzymes (Figure 15). The amounts of these oxidized derivatives in the human genome differ greatly between **5caC** (~0.001% of all cytosine residues), **5fC** (~0.02%), and **5hmC** (0.2-0.7%, Figure 19).[136,163] These values are also subject to change based on the cell type.[164,165]


*Figure 20: A world map demonstrating the distribution of oxidized cytosine derivatives in DNA. If the entire landmass of Earth corresponds to all cytosine residues in DNA, the area of the United States of America (excluding Alaska) would correspond to all methylated cytosine residues (**5mC**, 4 – 6%), while the area of Italy would correspond to **5hmC** residues (0.2 – 0.7%). Belgium and Luxembourg would then represent the amount of **5fC** and **5caC** respectively (0.02% and 0.001%). These values are dependent on age and origin of the tissue, therefore this visual representation is only a rough approximation.[91,166,167]*

A long-standing belief in epigenetics has been that a dynamic change in **5mC** levels is important for successful nuclear reprogramming and cell differentiation.[168] In contrast to the above

described CpG islands, methylation of **C** can also occur in a non-CPG context in embryonic stem cells (ESCs)[169,170] and some other cell types.[171,172]

A recent study on the active turnover of **5mC**, **5hmC**, and **5fC** in stem cells found that global turnover rate of **5mC** is 3-6% higher than can be accounted for by passive DNA methylation during cell division. By applying stable-isotope labelling and an MS-based quantification procedure it was also found that **5mC** and **5hmC** are both turned over when the cells are in an intermittent state between naïve and pluripotent. **5fC** is also turned over quite rapidly, taken together with the information that **5mC** and **5hmC** are oxidized this means that a dynamic equilibrium governs the amount of **5fC** present in this state of the cell.[13]

A common sequencing technique used for differentiation of **5mC** from **C** in genomic DNA strands is the bisulfite method, which exploits the difference in reactivity of bisulfite (SO$_3^{2-}$) towards **5mC** and **C**: whereas **C** deaminates to **U**, **5mC** is unaffected. During subsequent PCR sequencing, **U** is recognized as **T** and **5mC** as **C** (Scheme 20). By comparing sequencing results before and after bisulfite treatment, methylated **C** residues can be identified.[173] However, **5hmC** residues cannot be distinguished from **5mC**: **5hmC** reacts with bisulfite to form **cytosine-5-methylsulfonate**, which is also recognized as **C**.[174] **5fC** and **5caC** are converted to **U** and therefore recognized as **T** during sequencing, thus making them indistinguishable from **C** (not shown).[174,175] These difficulties in the exact sequencing of **C**, **5mC**, and its oxidized derivatives has led to the development of several new sequencing techniques,[176–179] some of them applying TET enzymes.[180,181]
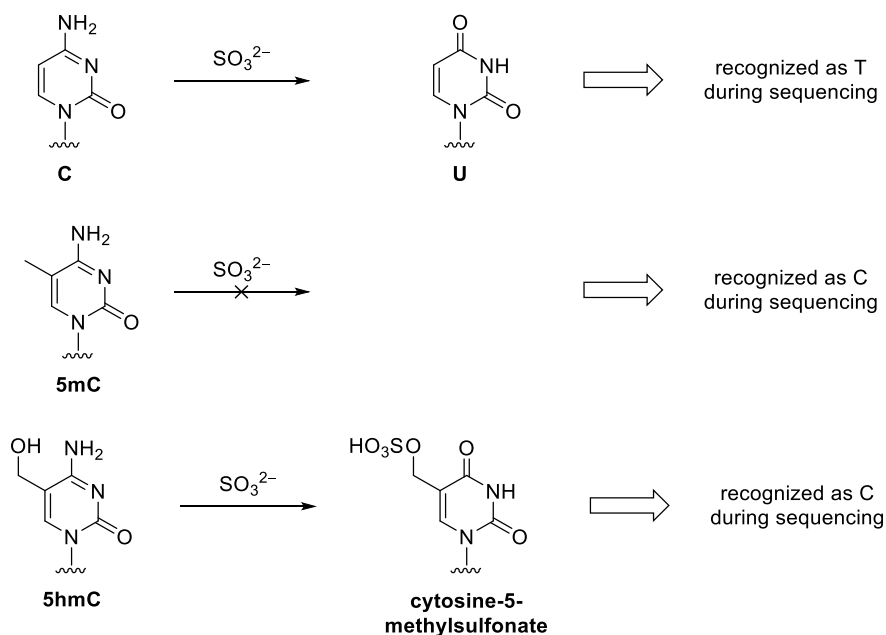

*Scheme 20: Reaction of **C**, **5mC** and **5hmC** with bisulfite to **U**, **5mC**, and **cytosine-5-methylsulfonate**, respectively. **U** is recognized as **T** during PCR sequencing, **5mC** and **cytosine-5-methylsulfonate** as **C**.*[173,174]

5hmC, **5mC**'s first oxidation product, was first discovered in bacteriophages in 1952,[182,183] in the beginning of the 21st century it was then also found in human and mouse brains as well as in

ESCs.[7,184] Nowadays, it is believed that **5hmC** occurs in practically all mammalian cells, the highest levels are detected in cells of the central nervous system. During development, **5hmC** levels increase and then stay constant during adulthood.[185–188] **5hmC** is sometimes referred to as the "sixth base" and has been implicated in epigenetic regulation during embryonic development and stem cell function.[168]

5hmC is usually only formed through oxidative hydroxylation of **5mC** by TET enzymes (Figure 17).[7,135] However, *in vitro*, it has been shown that DNMTs are capable of introducing formaldehyde to **C** yielding **5hmC**. Interestingly, the same DNMTs were also capable of removing the hydroxyl modification from **5hmC**. In addition to formaldehyde, acetaldehyde and propionaldehyde residues were successfully added to **C** resulting in the corresponding secondary α-hydroxy alcohols (Scheme 21).[189]
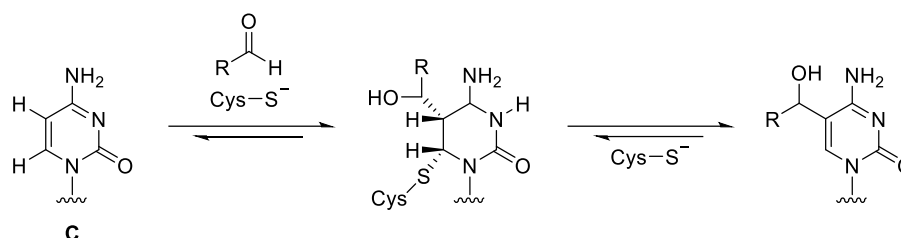
*Scheme 21: Introduction of aldehyde residues to **C** residues by DNA methyl transferases. R = -H, -CH₃, -CH₂CH₃.[189]*

5fC was discovered in 2011 by Pfaffeneder *et al.* in embryonic stem cells and has since then been thoroughly investigated.[190] In particular, the proposed direct demodification (deformylation) to yield directly **C** without the need for BER has caught the attention of researchers.[133,138]

As briefly mentioned above, the BER mechanism employs thymine DNA glycosylases (TDG) to excise the entire modified nucleobase, generating an abasic site. This is then either directly replaced by a new cytidine residue or a larger portion of the DNA is excised and then replaced in its entirety (Figure 21**A**, upper pathway, in red). This has been reported for **5fC** and **5caC**.[191,192]
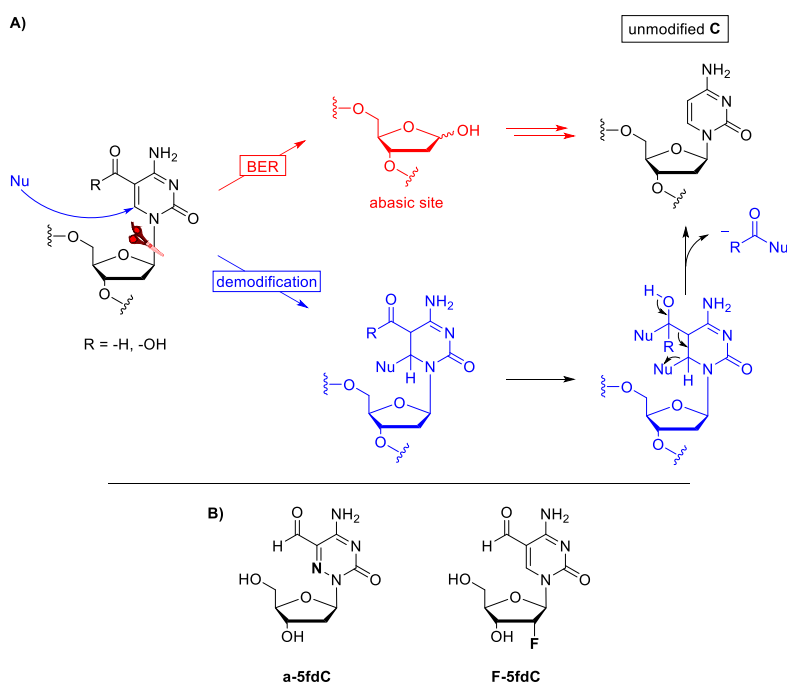
*Figure 21: **A**) **5fC/5caC** residues in a DNA context and two pathways to regenerate unsubstituted cytosine (**C**): BER (upper pathway, in red) and direct demodificaiton (lower pathway, in blue, attack of nucleophiles necessary). R = -H, -OH; Nu = nucleophile; BER = base excision repair. **B**) Synthetic nucleoside probes used by Schön et al.: **a-5fdC** and **F-5fdC** [138]*

On the other hand, direct demodification of **5fC**, or **5cC** would also lead back to an unmodified cytosine residue (Figure 21, lower pathway, in blue). The theoretical plausibility of this concept had been shown previously with the Carell research group regularly providing more insight in the mechanism involving (modified) **5fC**.[133,138] However, data on the *in vivo* deformylation of **5fC** still remains scarce. In early 2020, Schön *et al.* published a communication on their success in synthesizing the nitrogen-substituted **5fdC** derivative 6-*aza*-5-formyl-deoxycytidine (**a-5fdC**, Figure 21**B**) and its use in determining the pathway of deformylation of **5fC**.[138]

The direct demethylation pathway has been proposed to involve the attack of a nucleophile on the *C*6 position of the nucleobase,[138] similar to the methylation mechanism catalyzed by DNMTs (Scheme 19).[162,193] Introduction of a nitrogen atom at the 6-position of the nucleobase would make a nucleophilic attack impossible. If then no deformylation is observed (relative to another substrate in which deformylation was observed under the same conditions), this would corroborate this hypothesis of a nucleophilic attack being necessary for the removal of the formyl group. Indeed, by comparing the integration into DNA and subsequent deformylation behavior of two modified nucleobases (**a-5fdC** and 2'-fluoro-5-formyl-deoxycytidine F-**5fdC**, Figure 21**A**) the Carell research group hoped to gain insight into this process.[138]

After feeding cells with derivatives of the shown structures the cells were lysed, the DNA extracted, digested, and the obtained nucleosides quantified by UHPLC-MS. The authors observed significant incorporation of **a-5fdC** into the DNA, whereas **F-5fdC** was only observed to be incorporated in minute amounts, if at all. However, for **F-5fdC** the deformylated product **F-dC**

was observed in significant amounts (Scheme 22**A**) whereas no such derivative of **a-5fdC** was detected (Scheme 22**B**).
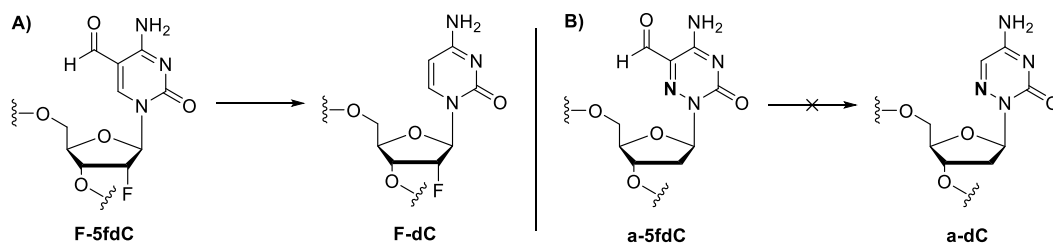
*Scheme 22: Deformylation for the fluorinated derivative **F-5fdC** to **F-dC** was observed whereas no such demodification was observed for the aza-derivative **a-5fdC**.*

The authors interpret these results in the following manner: both **F-5fdC** and **a-5fdC** are incorporated into DNA at random positions during DNA replication, as both are recognized as **5mdC**. Then **F-5fdC** is deformylated as "normal" **5fdC** would and, because of the nitrogen atom at position 6, **a-5fdC** is not. This difference in reactivity serves as evidence for the necessity of a nucleophilic attack on *C*6 in order to initiate deformylation.[138] However, as both **a-5fdC** and **F-5fdC** are non-natural nucleosides and might behave differently to **5fdC** in cells, these results have to be interpreted with caution. Nonetheless, this result is remarkable and offers insight into the proposed deformylation of **5fC**.

An SFB1309 collaboration of Romeo Dubini of the Rovó group and Alexander Schön of the Carell group gave insight into the influence of **5fC** on DNA base pairing. Using NMR spectroscopic methods, the authors identified the influence **5fC** has on the stability of dsDNA, noting a 2 K decrease of the melting point of a 40-mer DNA oligonucleotide. It was noted that both dsDNA dissociation and association of ssDNA to form dsDNA seem to be affected, the former increased while the latter decreased. The authors attribute this both to the hydrogen bonding of the formyl group with the exocyclic amine of the cytosine residue and the electron withdrawing effect of the carbonyl group (Figure 22**A**, in red).[194]
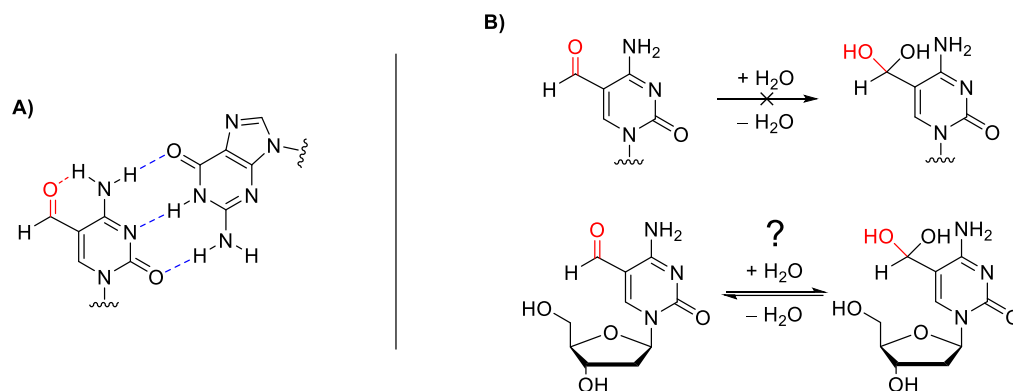

*Figure 22: **A)** The formyl group on **5fC** (in red) is proposed to influence the hydrogen bonding network of Watson-Crick base pairing (in green) because of its electron withdrawing group and the hydrogen bonding to the exocyclic amine of the cytosine residue. **B)** Reported absence of hydrate formation in **5fC**-containing oligonucleotides and proposed hydrate formation of free **5fdC** nucleosides.*

Also, no hydrate formation of the aldehyde within the dsDNA structure was observed. This is a remarkable result as it removes some of the doubt that was expressed towards the calculations of the BDE by Hu *et al.* (as to why the formyl isomer was used for calculations and not the hydrate).[8,194]

Shaofei *et al.* have recently shown that reversible crosslinks between peptides or proteins and **5fC** can inhibit transcription but do not introduce transcription errors. This might be one of the pathways in which epigenetic information is stored: **5fC** residues crosslink with histone proteins and thereby turn off specific genes.[195]

Eli Naydenova and Johannes Dietschreit of the Ochsenfeld research group, which is also a member of the SFB1309, published their recent theoretical work on the reaction mechanism involved in the cleavage of the glycosylic bond of **5fC** by TDG during BER. They provide evidence that the mechanism requires reorganization of the substrate, is not acid-catalyzed, and proceeds through an oxocarbenium-like transition state (Scheme 23).[196]
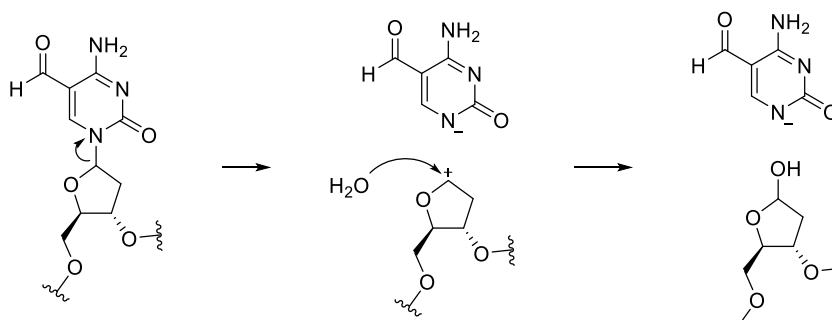

*Scheme 23: Proposed reaction mechanism of the cleavage of the glycosylic bond of **5fC** by TDG involving an oxocarbenium ion intermediate (drawn) or oxocarbenium-like transition state (not drawn).*

5caC, the last of the oxidized derivatives of **5mC**, was discovered as a product of TET activity in 2011 by Ito *et al.*[136] The role of **5caC** as an epigenetic marker on its own – not just as an intermediate during removal of **5mC** – is still under debate. It has, for example, been shown that the presence of **5caC** (and **5fC**) affects the behavior of the transcription factor RNA polymerase II (RNAPII), which would indicate some biological function of **5caC**.[197] Removal of **5caC** is thought to proceed mostly through TDG assisted BER.[140,198] TDG on the other hand has been shown to interact with DNMTs,[199] AID,[141] and transcription factors.[200] Influence of 5caCs presence on the dynamics of methylation and demethylation is therefore possible.

In addition, direct demodification by loss of carbon dioxide is debated as another likely mechanism for regeneration of unmodified **C**.[133] In July 2020, a new report was published on the direct decarboxylation of **5caC** by Feng *et al.* By exposing synthetic, modified oligomeric DNA strands (40mers) to human cells they conclusively showed that direct decarboxylation plays a significant role in the removal of the methyl moiety on **5mC**. The incorporation of sulfur atoms (instead of oxygen) into the backbone of the oligomer as well as ^{15}N labelling of the nucleobase

allowed for the unequivocal identification of the starting material oligomers containing a **5caC** residue as well as the demodified oligomers containing **5mC** due to the significant mass difference (Scheme 24). Digestion of the oligomers to the nucleotide level and detailed mass spectrometric analyses completed their investigation.[137]
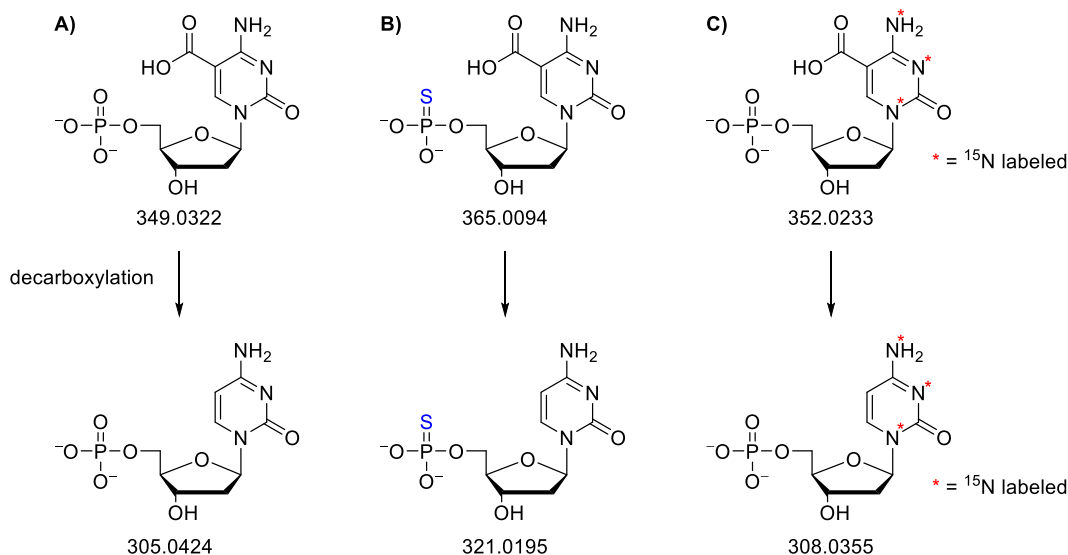
*Scheme 24: **A**) Natural **5cadC** decarboxylates to natural **dC** (mass: 305.0424); **B**) sulfur-modified **5cadC** decarboxylates to sulfur-modified **dC** (mass: 321.0195, sulfur modification in blue); **C**) ¹⁵N-labeled **5cadC** decarboxylates to ¹⁵N labeled **dC** (mass: 308.0355, ¹⁵N label marked with ***). The differences in mass can be used for identification and assignment.*

Using tandem LC-MS/MS spectrometry the authors were able to gain time-dependent data on the amount of substrate and decarboxylated product. As multiple oxygen atoms in the phosphate backbone of the substrate had been replaced by sulfur atoms, the authors were not just able to observe the direct demodification product but they were also able to discriminate between short-patch BER (single nucleotide is replaced, *i.e.* one sulfur atom replaced by oxygen) and long-patch BER (multiple nucleotides are replaced around the abasic site, *i.e.* multiple sulfur atoms replaced by oxygen). Whereas this study is an exemplary case of study design and scientific approach these findings have to be regarded carefully. Decarboxylation of a modified oligomer within a cell lysate does not necessarily mean that decarboxylation happens in the same manner in genomic DNA within functioning cells. However, this study does represent a significant advance in the field of epigenetics and helps to further complete the picture of **5mC** removal in human cells.[137]

Other DNA Modifications and Dealkylation Enzymes

The discovery of oxidized **5mC** derivatives sparked a "gold rush" search for additional DNA modifications of mammalian DNA, which resulted, for example, in the discovery of N^6-methyladenine (**6mA**).[201,202] **6mA** had previously been recognized as a modification in bacterial genomes and there were conflicting reports about its occurrence in mammalian DNA. Schiffers *et al.* published a study where they did not find evidence for **6mA** (or **4mC**) in mouse embryonic

stem cells and tissues.[203] However, a recent study by Musheev *et al.* did indeed find evidence not only for the occurrence but also the mode of incorporation of **6mA** in mammalian DNA. The authors confirm low levels of **6mA** in mammalian DNA and argue that most of it originates in RNA, from which it is excised, salvaged, and then misincorporated into DNA.[204]

The detection of the very low levels of **6mA** in mammalian DNA is complicated as the enzymes typically used for digestion are usually contaminated with bacterial DNA – which is known to contain **6mA**. Musheev *et al.* therefore labeled *S*-adenosyl methionine (SAM, methyl transfer agent which also methylates **C** to generate **5mC**, Scheme 19) with ¹³C and deuterium isotopes (so called Met-4 label) and followed the labeled **Met-4-6mA**, thereby being able to distinguish contaminated from uncontaminated **6mA** signals. They detected very low levels of **6mA** (0.00006-0.00013% of total **A**) in human embryonic kidney cells, HeLa (common carcinogenic and immortal cell line used in laboratories all over the world, named after patient Henrietta Lacks, from who the first cells were taken without her consent[205]) cells, and mouse embryonic stem cells.[204] These levels are 3-4 orders of magnitude lower than **5mC** levels and comparable to those of **5caC**.[206] In C2C12 mouse myoblasts and mouse 3T3 fibroblasts much higher levels (0.0013-0.05% of total **A**) were detected.[204]
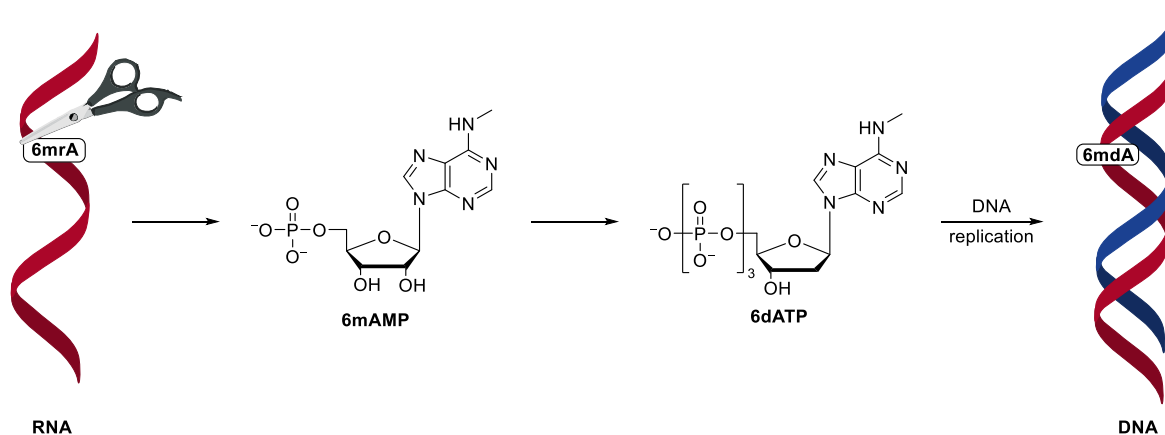

Figure 23: Excision of ribo-6mdC from RNA, subsequent salvage and misincorporation into DNA. Adapted from Musheev et al.[204]

Concerning the origin of **6mA** in DNA, the authors argue that as **6mA** is vastly more abundant in RNA than in DNA, RNA might be the source.[207] Continuous degradation of cellular RNA releases nucleotide monophosphates that are then recycled by rephosphorylation and can be reduced by ribonucleotide reductase to the corresponding deoxyribonucleotides.[208,209] Musheev *et al.* therefore fed isotopically labeled ribo-**6mA** to HEK293T lines and followed the appearance of a labeled **6mA** signal in genomic DNA (gDNA), noticing a 1000-fold increase. Interestingly, morphology and cell growth remained unaffected. By also using a labeled adenosine nucleotide (dAMP-10, isotope label in base and ribose unit) the authors were able to distinguish between their proposed "salvage pathway" and a hypothetical "DNA methyl transferase" pathway which

would directly methylate the labeled **dA** that is already present in DNA. They found no evidence for such a hypothetical DNA methyltransferase pathway, corroborating their proposal of nucleotide misincorporation.[204] Whereas these results are indeed remarkable and shed new light on **6mA** biochemistry, there are some shortcomings. The authors state "In summary, we confirm and quantitate the occurrence of **m^{6}dA [6mdA**, author's note] in gDNA in mammalian cells [...]", however, this statement is not entirely correct: the molecule they used was *isotopically labeled* **6mA**, which is indeed a different molecule. Studies on deuterium labeled **5mC** have shown that this label does decrease the reaction rate of TET enzymes which effectively decreases removal of **5mC**.[8] Therefore, it is likely that the removal of the methyl group in **6mA** is also hindered by deuterium labelling leading to significant accumulation of **6mA** – which might never happen under normal conditions.

In addition to TET enzymes, AlkBH2, AlkBH3, and EcAlkB are also capable of oxidizing **5mC** to **5hmC**, **5fC**, and **5caC**, at least *in vitro*, as was shown by Bian *et al*.[210] AlkB stands for α-ketoglutarate-dependent hydroxylase and is used herein as a general term for this class of enzymes. The "H" suffix indicates a human enzyme, the prefix "Ec" indicates it is found in *E. coli* bacteria. AlkB enzymes are involved in DNA repair mechanisms where they remove alkylation damage (mostly methylation) by hydroxylating the respective alkyl residue, the main substrates are **1mA** and **3mC** (Figure 24**A**).
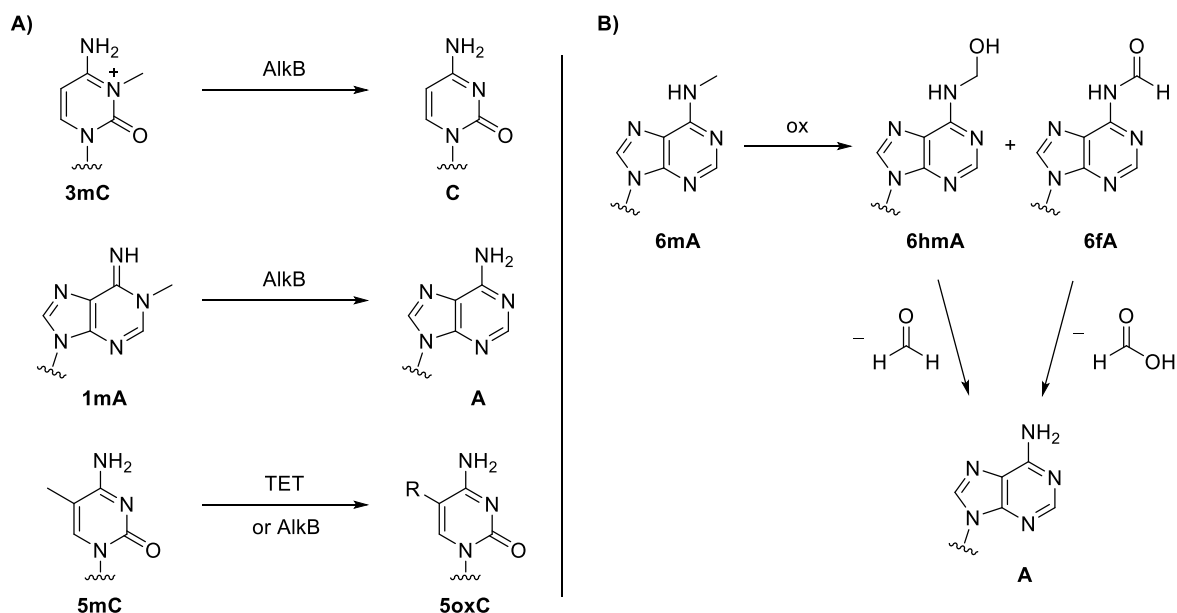
*Figure 24: **A**) Demethylation of **3mC** or **1mA** upon the action of AlkB enzymes to **C** and **A**, respectively. **5mC** is oxidized to its oxidized derivatives **5oxC** (R = -CH$_2$OH, -CHO, -CO$_2$H). **B**) Demethylation of **6mA** to **A** via oxidation to 6-hydroxymethyladenine (**6hmA**) and 6-formyladenenine (**6fA**) as proposed in the literature.[56–58]*

Whereas the general mechanism of AlkB is similar to that of TET (both belong to the superfamily of iron(II)/α-KG dependent non-heme enzymes), the chemical natures of the substrates are

distinct: **1mA** and **3mC** are *N*-methylated species, the methyl group of **5mC** is bound to a carbon atom. Considering this, it is rather surprising that AlkB is able to hydroxylate **5mC** at all.

Dealkylation of *N*-methylated nucleobases, for example **6mA**, is proposed to occur through oxidation of the methyl group resulting in the corresponding hydroxymethyl and formyl derivatives (for **6mA**: 6-hydroxymethyladenine (**6hmA**) and 6-formyladenenine (**6fA**)). These species then undergo demodification to **A** by loss of formaldehyde or formic acid, respectively (Figure 24**B**).[56–58]

Hammam *et al.* have reported on the first discovery of a hydroxymethylated cytosine in a eukaryotic virus (*Plasmodium falciparum*, a malaria pathogen). In addition to detecting less 5-methylcytosine (**5mC**) than was previously reported, they discuss the finding of a new oxidized methylcytosine modification that they called "**5hmC**-like". According to their experiments, this new modification has the same mass as but is more hydrophobic than **5hmC**. Additionally, the authors detected a hydroxymethylated cytosine derivative *via* chemical means but do not find a signal in LC-MS corresponding to **5hmC**: however, a new, shifted signal in the same retention time region was detected. The authors report on finding a similarly shifted signal that has the same m/z ratio as **5mC** and propose this to be the biological precursor of the "5hmC-like" modification. The authors speculate on the structure of these new modifications and propose that the hydroxymethyl group is shifted to position 4 on the cytosine ring (Chart 4).[211]
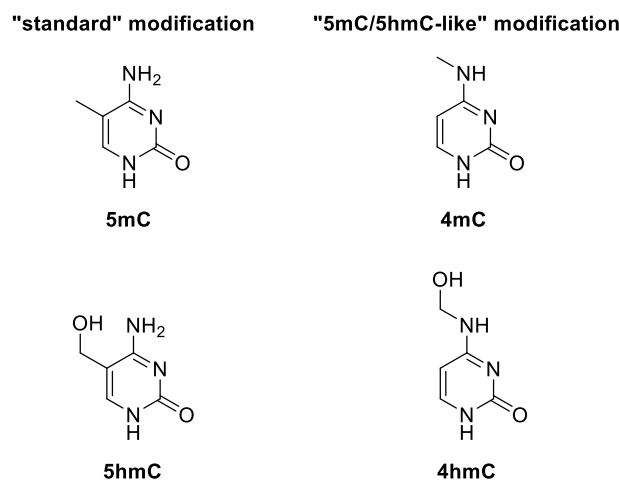
Chart 4: *5mC* and *5hmC* in addition to the proposed structure of the "5hmC-like" modification.

P. falciparum reportedly has an AT-rich genome lacking CpG islands,[212] it is therefore not unsurprising to find the **5hmC**-like modification mostly (> 95%) in the gene body instead of in the promotor region. Hammam *et al.* also report that the ratio of methylation to hydroxymethylation in *P. falciparum* is lower than that commonly found in eukaryotic cells but do not provide any explanations to why that is. The authors have also not been able to find a TET homologue responsible for the production of the 5hmC-like modification.[211]

As stated above, **5mC** usually occurs together with **G** in CpG dinucleotides. One of the most common DNA lesions is **8-oxo-G**, which is formed by oxidation of **G**.[109,110] A recent study of David *et al.* gives insight onto the interaction of **8-oxo-G** in base pairing.[110,213] **G** usually pairs with **C** (Chart 5A), whereas **8-oxo-G** is found to pair with **A** (Chart 5B). This pairing of **8-oxo-G** to **A** is responsible for a **G** to **T** transversion, as DNA repair mechanisms recognize the **8-oxo-G:A** mispair and replace **8-oxo-G** with **T**, the canonical partner of **A** (Chart 5D). David and co-workers recently published their study on the role of MutY glycosylase in the recognition of **8-oxo-G:A** mispairs. The authors noticed that identification of **8-oxo-G:A** lesions was highly sensitive to any modification of the **8-oxo-G** structure, for example the removal of the exocyclic 2-amino group in **8-oxo-G** (marked in red in Chart 5), which results in the 8-oxo-inosine (**8-oxo-I**):A mispair (Chart 5C).[213] In particular, the authors report that the *syn* orientation of **8-oxo-G** leads to the exocyclic 2-amine protruding into the major groove, which results in a structure distinct from canonical base pairs.
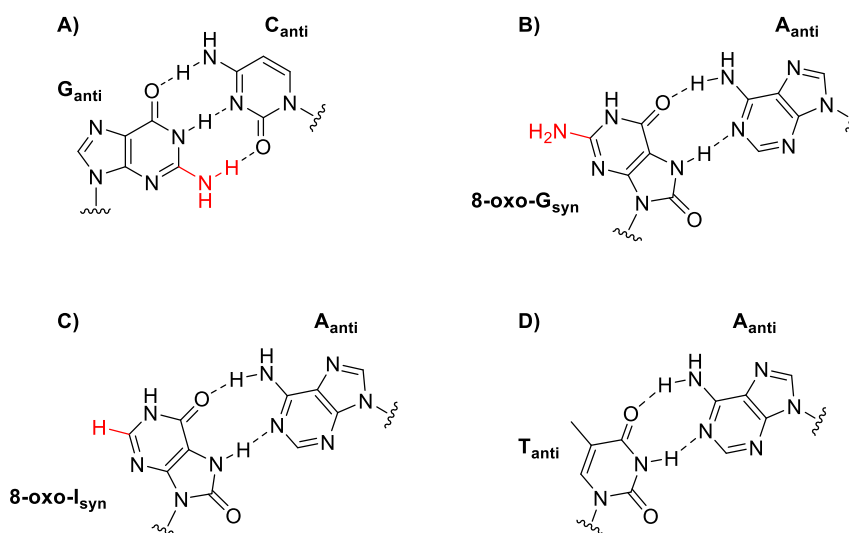
*Chart 5: DNA base pairing of **A) G** and **C; B) 8-oxo-G** and **A; C) 8-oxo-I** and **A; D) T** and **A**.*

Modeling of several structures had suggested that the H309 (H296 in *E. coli*) amino acid in the C-terminus region of MutY might play a role as a sensor for the 2-amino group of **8-oxo-G**.[214–216] The authors of this study then used a combination of methods to study the effects of H296A mutation and removal of the 2-amino group in **8-oxo-G** (resulting in **8-oxo-I**). A significant decrease was noted when David *et al.* compared the activity of WT MutY on **8-oxo-G:A**-containing DNA 30mers to that of WT MutY on **8-oxo-I:A** DNA 30mer oligonucleotides. This gave the first clue towards the interplay of H296 and the 2-amino group. When a H296A mutant was used in combination with an **8-oxo-G:A** containing oligomer, the activity was about as low as that of the wildtype (WT) with an **8-oxo-I:A** substrate. If both components are modified (H296A mutant and **8-oxo-I:A** DNA oligomer), hardly any activity at all was observed. This led

the authors to conclude that both components (H296 and the 2-amino group) are necessary for confident MutY detection of **8-oxo-G:A** mispairs.[213]

Another modified nucleobase has come to recent attention because of the Covid-19 pandemic: 1-methyl-*pseudo*-uridine (**1mrΨ**, Chart 6). Both the Pfizer/BioNTech (Comirnaty, BNT162b2) and the Moderna (Spikevax, mRNA-1273) mRNA vaccines have **1mrΨ** incorporated into their structure.[217] These mRNA vaccines function by providing the exposed cells with the information (mRNA) for building a virus spike protein *via* normal ribosome function (translation). This spike protein is then recognized by the immune system, this information is then stored, hence immunity is gained. It has been shown that incorporating **1mrΨ** into mRNA drastically increases stability, immunogenicity (ability of a foreign substance to produce an immune response), and translation capacity.[218]
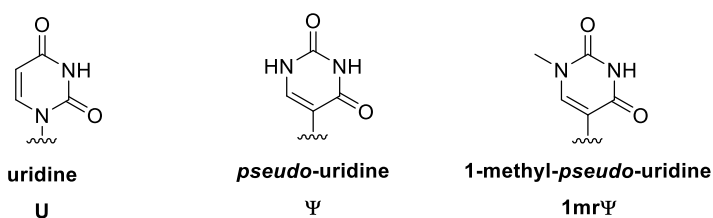
*Chart 6: Uridine (**U**), pseudo-uridine (**Ψ**), 1-methyl-pseudo-uridine (**1mrΨ**).*

The use of **1mrΨ** might well have been the reason for the success of Comirnaty and Spikevax over the mRNA vaccine by CureVac (CVnCoV), as this does not carry the **1mrΨ** modification.[219–222] The immongenicity of CvnCoV was reported to be much lower, which led the researchers to increase the dose – this then in turn resulted in more side-reactions. The dose therefore had to be lowered again, which resulted in a low overall efficacy of only 47% for CvnCoV.

Synthetic DNA: "Hachimoji"

The use of DNA as a storage medium has been investigated for a long time but has received increased attention in recent years.[223–225] This trend has even reached the entertainment industry: the popular streaming service Netflix stored the first episode of its new German series "Biohackers" on DNA with the help of the research groups of Reinhard Heckel (TU Munich) and Robert Grass (ETH Zurich). The information capacity of DNA is extremely high, the entire series of "Biohackers" would fit onto 1 pg of DNA using current technology, theoretically even higher values (2000x) are possible.[226] Although information stored on DNA is not as accessible as that stored on a conventional computer hard drive, modern sequencing and data analysis techniques allow for read out within one day.[227]

However, researchers are looking to increase the information density even further – for example by incorporating synthetic nucleotides into DNA. One such attempt was recently achieved by Benner *et al.*, expanding the regular four-nucleobase structure to an eight-nucleobase system

(called "hachimoji" DNA from Japanese 八 "*hachi*" – *eight* 文字 "*moji*" – *letters*, Chart 7). A more detailed introduction is given in chapter III.8.[228]
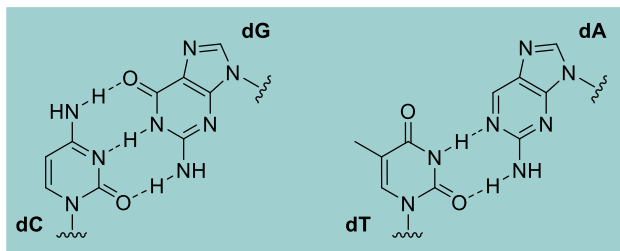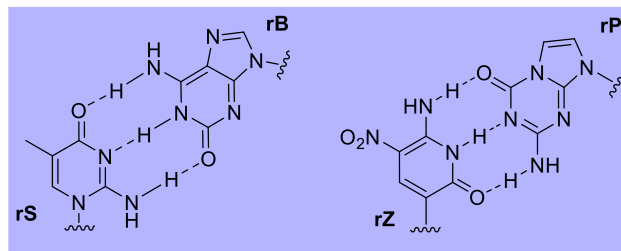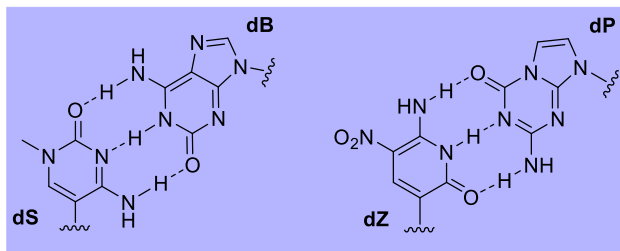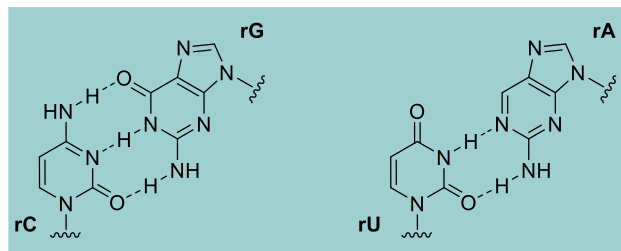
Chart 7: Standard terran (in turquoise) and synthetic (in violet) DNA/RNA base pairs in "hachimoji" DNA/RNA. The suffix "d" in front of DNA bases indicates the presence of 2'-deoxyribose in the nucleoside, the suffix "r" indicates the presence of ribose in the nucleoside.[228]

2. Motivation and Aim

TET enzymes are critically involved in the epigenetically relevant demethylation reaction of **5mC** to **C** by oxidizing the methyl group on **5mC**. As a member of the superfamily of non-heme iron(II)/α-KG dependent dioxygenases, TET enzymes are proposed to react *via* an iron(IV)-oxido intermediate (Figure 25**A**). TETs reactivity towards substrates bearing **5mC**, **5hmC**, and **5fC** residues was studied by Hu *et al.* in 2015. The authors found reactivities for these different substrates that did not correspond to the trend in the calculated BDEs of the respective C-H bonds.

	5mC	5hmC	5fC
k_{cat} [10^{-3} s^{-1}]	2.12	0.63	0.46
BDE [kJ mol^{-1}]	378	361	389
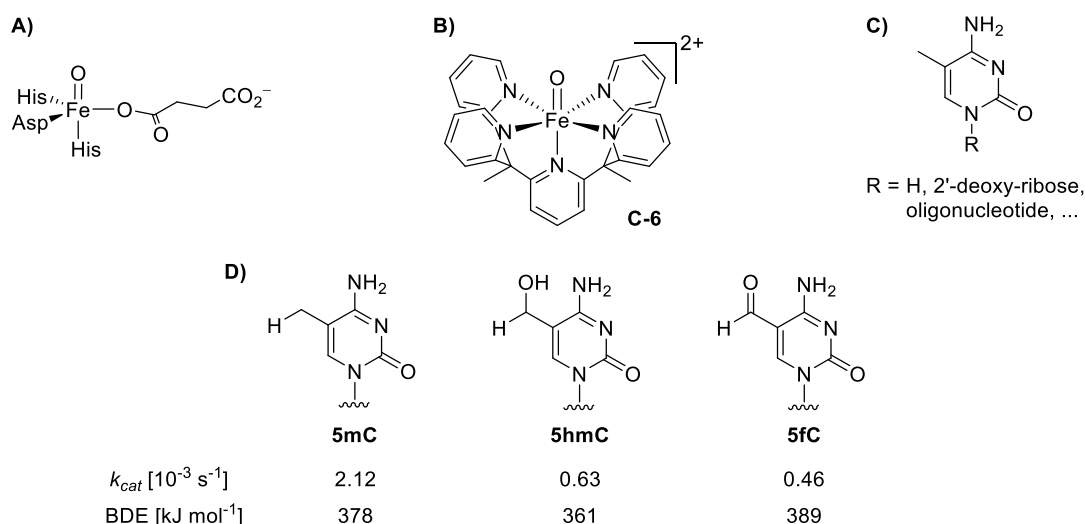
*Figure 25: **A)** Structure of the active species in non-heme iron(II)/α-KG dependent dioxygenases **B)** Functional Model complex [Fe^{IV}(O)(Py$_5$Me$_2$H)]$^{2+}$ (**C-6**, Py$_5$Me$_2$ = 2,6-bis(1,1-bis(2-pyridyl)ethyl)pyridine, **L-1**) used in this work. **C)** The primary substrates used in this work: **5mC** and its oxidized derivatives **5hmC** and **5fC**. K$_{cat}$ and BDE values were measured and calculated, respectively, by Hu et al.[8]*

Furthermore, the selective oxidation of **5mC** or any of its oxidized derivatives within a DNA context remains a highly desired transformation with potential use in sequencing applications. The gold-standard, oxidative bisulfite sequencing,[173] is highly destructive[229,230] and intrinsically incapable of distinguishing **5mC** from **5hmC** or **C** from **5fC/5caC**.[174,175,231–233]

Therefore, the goal of this work was to identify and subsequently investigate a fully-synthetic, biomimetic iron(IV)-oxido complex to shed further light on TET enzymes' reaction mechanism and lay the foundation for potential sequencing applications.

In previous studies, the synthetic iron(IV)-oxido complex **C-6** had shown potential in oxidizing **5mC** to the natural metabolites **5hmC**, **5fC**, and **5caC**.[167] Synthesis and initial investigation of **C-6** was published by Chantarojsiri *et al.* in 2015.[12] Therefore, the first part of work was to corroborate the previously obtained results for the biomimetic reaction of **C-6** with **5mC** and, if successful, expand upon these to include nucleosides and oligonucleotides as substrates.

3. Synthesis of the Functional Model Complex C-6

As mentioned in chapter I.3, Chantarojsiri *et al.* published their report on a water-soluble, air-stable iron(IV)-oxido complex ([Fe^{IV}(O)(Py$_5$Me$_2$-H)]$^{2+}$, **C-6** Py$_5$Me$_2$-H = 2,6-bis(1,1-bis(2-pyridyl)ethyl)pyridine (**L-1**, in the literature referred to as PY5Me$_2$)) capable of performing HAT reactions similar to the oxidation of **5mC** to **5hmC**, **5fC** and **5caC**.[12] In my Master Thesis I could show that **C-6** indeed shows promising behavior as a mimic for TET enzymes.[167] Therefore, **C-6** was investigated in its behavior towards a series of natural and synthetic substrates including **5mC**, **5hmC**, **5fC**, **T**, 1-methylcytosine (**1mC**), 1-methyluracil (**1mU**), 5-methyl-iso-cytosine (**5miC**), **5mdC**, and short oligonucleotides containing a **5mC** residue.
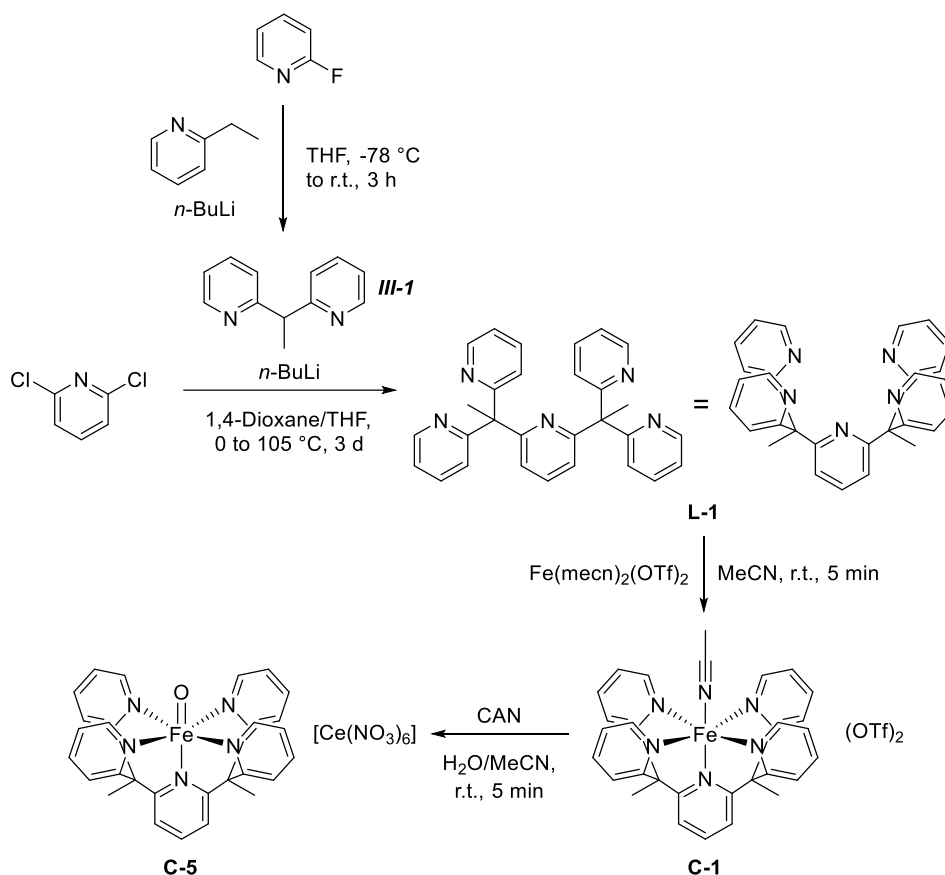
*Scheme 25: Four-step synthesis of **C-5** from 2-ethyl-pyridine, 2-fluoro-pyridine, 2,6-dichloro-pyridine, and Fe(mecn)$_2$(Otf)$_2$, adapted from the literature.[12,13,234] **L-1** is referred to in the literature as PY5Me$_2$.*

The first four steps in the synthesis of **C-6** (Scheme 25) are known in the literature and have been discussed in detail in my Master Thesis, they were also published in 2019 as modified literature procedures.[13] However, during the synthesis of 1,1-di(2-pyridyl)ethane side reactions were observed: when the reaction is heated to reflux, as described in the original literature procedure by Cong *et al.*,[234] 1,1,1-tri(2-pyridyl)ethane (**III-2**) was observed as the main product (Scheme 26). **III-2** was then isolated and characterized using ^{1}H and ^{13}C NMR spectroscopy, high-resolution mass spectrometry, IR spectroscopy and GC-MS to confirm the structural assignment. Cong *et al.* do not mention this side reaction, whether this is due to the different reaction scales (Cong *et al.*:

1 mol vs. this work: 0.05 mol) or some other factor cannot be determined at this point. It is noteworthy that the reaction was first observed when a new bottle of the starting material 2-ethyl pyridine was used. However, since then several bottles were used and the side reaction was observed in all cases.
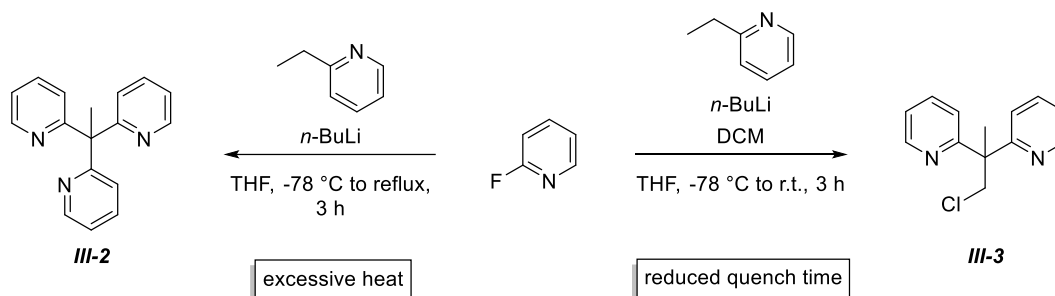
*Scheme 26: Side reactions to **III-2** and **III-3** observed in the synthesis of 1,1-di(2-pyridyl)ethane.*

In an attempt to shorten the time required for workup, the solvent used for liquid/liquid extraction, dichloromethane, was added very quickly (~1-5 min) after the water ice that was used for quenching the reaction. This led to the formation of 1-chloro-2,2-di(2-pyridyl)-propane (**III-3**, Scheme 26), which was also isolated and characterized. This side reaction can easily be bypassed by allowing the reaction to react with the added water ice for at least 15 min.

C-5 was then synthesized in a five-step reaction sequence starting from 2-ethyl-pyridine and 2-fluoro-pyridine (Scheme 25 and Scheme 27). Single crystals of **C-5** suitable for x-ray crystallography were obtained by addition of cerium(III) chloride (3 equiv.) to a solution of **C-6** in a mixture of acetonitrile/water (3:1) at 4 °C. The obtained crystallographic data is in line with recently published investigation by Que *et al*.[235]
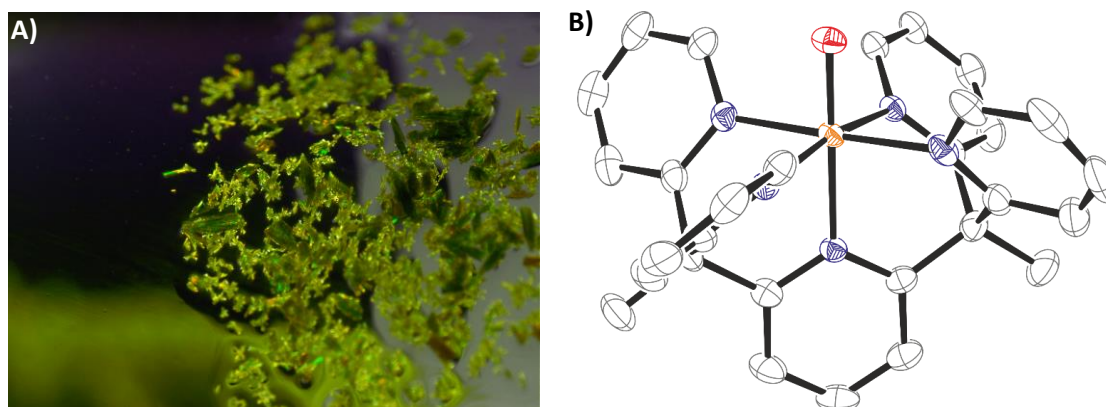
*Figure 26: **A**) Picture of green needles of **C-6** (([Fe^{IV}(O)(Py₅Me₂H)][Ce(NO₃)₆]). **B**) Graphical representation of the crystal structures of the cation of **C-5** ([Fe^{IV}(O)(Py₅Me₂H)]²⁺). Ellipsoids are drawn at 50% probability; hydrogen atoms and counter ions have been omitted for clarity (refer to the appendix p. 501 for a complete structure). Crystals were obtained from a solution of **C-5** and CeCl₃ ([**C-5**] = 15 mM, [CeCl₃] = 45 mM) in an acetonitrile/water (3:1) mixture that was stored at 4 °C.*

During my Master Thesis it was also observed that the counter ion of **C-5**, [Ce(NO₃)₆)]²⁻ is capable of oxidizing **5mC** to **5fC** and therefore needs to be removed. This was achieved by addition of 5.0 equivalents of ammonium fluoride and 1.0 equivalents of potassium hydroxide. The absence of

any residual cerium (<0.5% of the initial concentration) was confirmed by inductive coupled plasma-optical emission spectroscopy (ICP-OES). This method was published in 2019.[167]
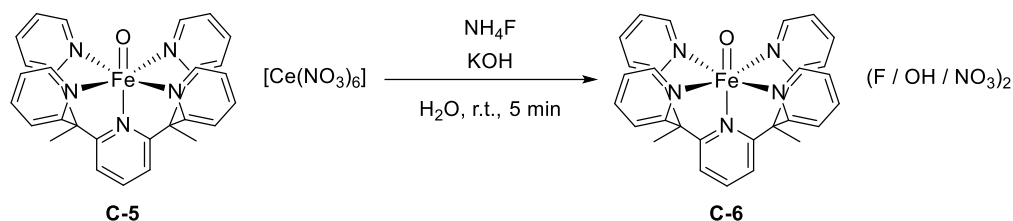
Scheme 27: *Exchange of the cerium ion in **C-5** by addition of ammonium fluoride and potassium hydroxide to obtain **C-6**.*

The influence of the amounts of ammonium fluoride and potassium hydroxide was then studied in more detail, confirming that the indicated amounts of potassium hydroxide and ammonium fluoride present the lowest concentrations possible to assure complete removal of cerium from the solution (Figure 27). This practical method reliably produces a 10 mM solution of **C-6**, which was used as such for all further investigations.
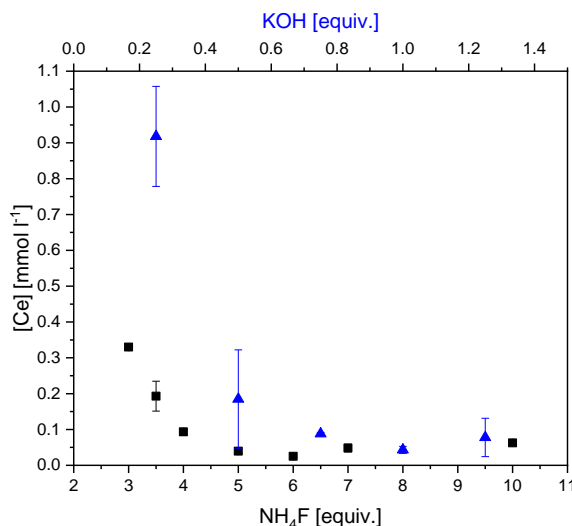
*Figure 27: Measured concentration of cerium in reactions of **C-6** with varying amounts of potassium hydroxide (KOH; in blue; 5.0 equiv. of NH$_4$F] or potassium hydroxide (NH$_4$F; in black; 1.0 equiv. of KOH). Conditions: [**C-6**] = 10 mM, H$_2$O, T = 23 °C. Published in 2019.[13]*

4. Stage 1: Nucleobases

The path to find a reliable and practical model complex, or better model system, to mimic TET enzymes began with the study of nucleobases, as these present the simplest substrate model system for **5mC**-containing DNA strands. Later, the substrate scope was extended to nucleosides and oligonucleotides. The synthesis of a dinucleotide was initially attempted to serve as an intermediate between nucleosides and oligonucleotides, however, this was then postponed due to large amount of time required to optimize synthesis. The last step in this context would be expansion of the substrate scope to actual genomic DNA, this, however, was not attempted as of yet (Figure 28).
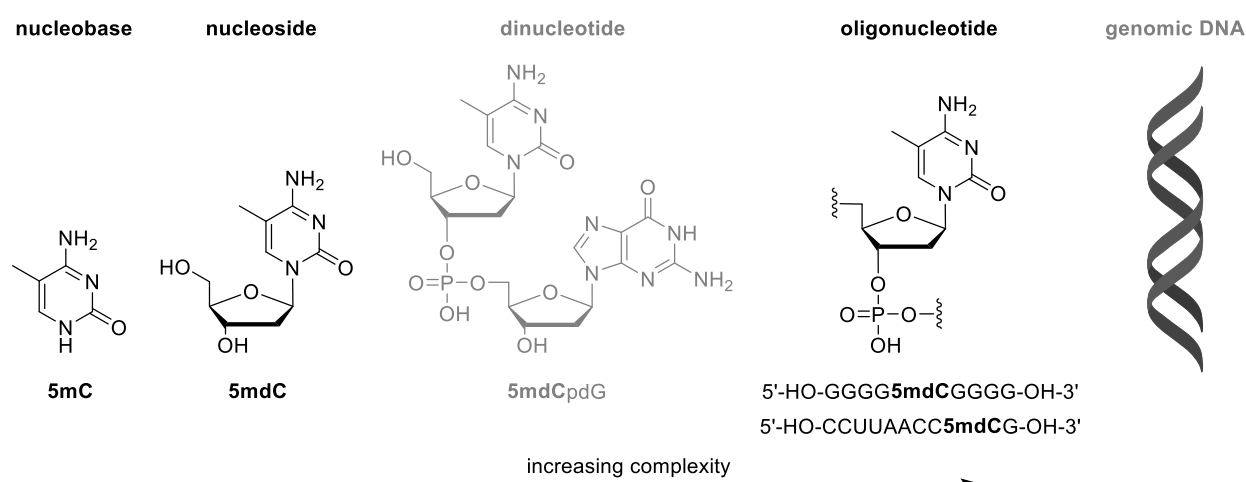
Figure 28: *Increasing complexity in the substrates used for the development of a functional model of TET enzymes. Black structures were used in this work, grey substrates were not. They are included here for context.*

In this project I was joined by Johann de Graaff in his Master Thesis, who started a preliminary investigation of the synthesis of **D$_3$-5mC** as a substrate, his contributions are mentioned below. A significant portion of the results discussed herein were published in 2019, this is, when applicable, mentioned.[13]

Identifying a Model system and Suitable Conditions

In order to identify whether **C-6** is a model system capable of mimicking TET enzymes, **C-6** was reacted with **5mC** in aqueous solution at room temperature and the product mixture analyzed by GC-MS (Scheme 28), after derivatization using *N,O*-bis(trimethylsilyl)trifluoroacetamide (BSTFA). TMS-derivatization is required for these substrates/products to ensure volatility of the compounds which is required for GC-MS measurement.
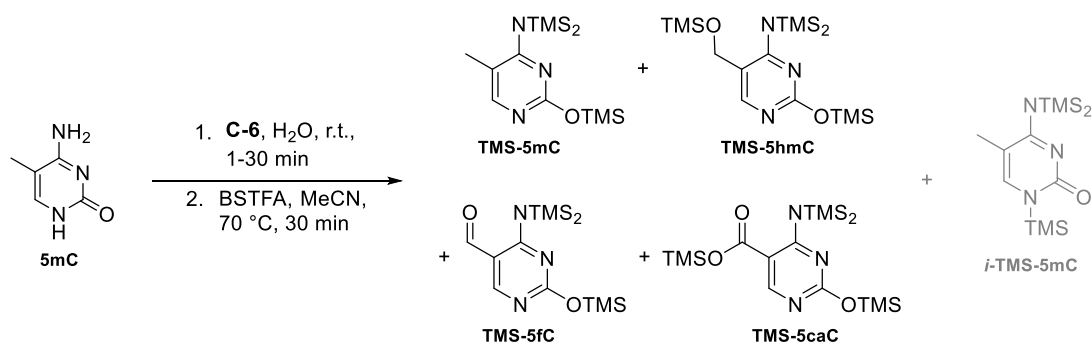
*Scheme 28: Reaction of **C-6** with **5mC** and subsequent derivatization procedure using BSTFA (N,O-bis(trimethylsilyl)trifluoroacetamide). The detected isomer **i-TMS-5mC** is not formed because of **C-6**, as it is also detected in control samples that did not contain **C-6**.*

In this reaction all expected products, the nucleobase-equivalents of the natural metabolites of TET enzymes, were detected as their TMS derivatives): **5hmC**, **5fC**, **5caC** in addition to starting material **5mC** (Figure 29). This was confirmed by comparison with synthetic reference samples (refer to chapter III.9 for details on their synthesis*). In addition to these expected products only one additional significant signal was observed. This could be assigned to an isomer of the TMS-derivatized structure of **5mC**, most likely the *N*1 position is TMS derivatized in this compound (for a reference trace refer to the appendix, p. 359, for a detailed discussion please refer to the literature[13]).
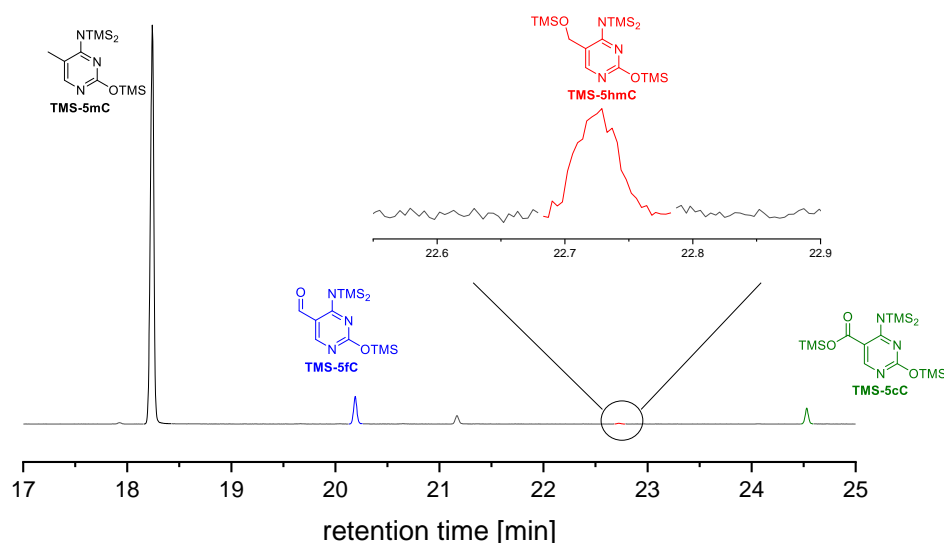
*Figure 29: Excerpt of a representative GC-MS trace of the reaction of **C-6** with **5mC**. Starting material and products are shown as their TMS-derivatized structures. The small signal at 21.2 min corresponds to the isomer **i-TMS-5mC**. GC-MS method **C**. Conditions: [**5mC**] = 2 mM, [**C-6**] = 2 mM, H$_2$O, T = 23 °C.*

In order to obtain quantifiable results, so that the amounts of substrates and products recovered can be tracked during the reaction, an internal standard (IS) was added to the reaction solution. Uracil (**U**) was found to be inert towards **C-6** and displayed a similar behavior to the substrates during filtration and derivatization, therefore it presented a good choice as IS (refer to the appendix p. 363 and refer to the literature[13] for respective GC-MS traces).

Using these conditions time-resolved reactions were conducted to study the development of the product distribution (Figure 30). At the applied conditions ([**5mC**] = 2 mM, [**C-6**] = 2 mM, H$_2$O, T = 23 °C), the amount of **5mC** was found to decrease immediately upon start of the reaction and then reach steady levels after 10 min. Only small amounts of **5hmC** were detected during the entire studied time frame, whereas the amounts of **5fC** and **5caC** were observed to increase steadily. Although the monitored time frame does not allow for an exact prediction, **5fC** levels seem to reach a steady level at 15 min, as a saturation-type fit was found to describe the behavior with good confidence (R² > 0.99).
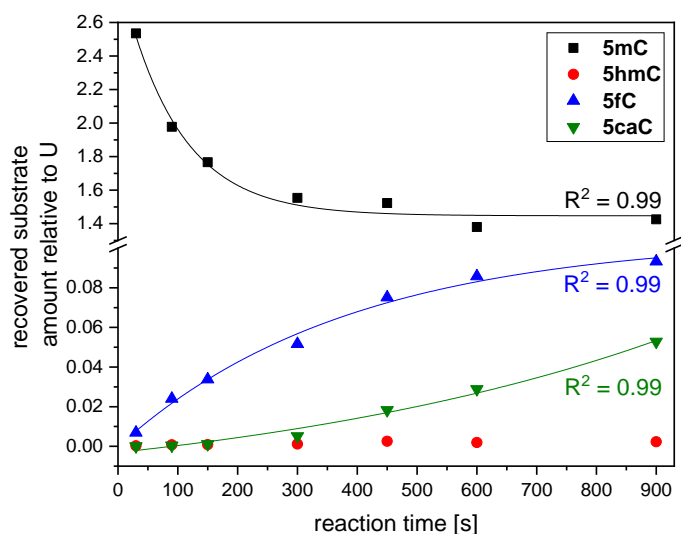
Figure 30: Recovered amounts of **5mC, 5hmC, 5fC,** and **5caC** in a time resolved reaction of **5mC** with **C-6**. Exponential fits describe the behavior of **5mC, 5fC** and **5caC** with good confidence. Levels of **5hmC** were too low for meaningful analysis. Conditions: [**5mC**] = 2 mM, [**C-6**] = 2 mM, H₂O, T = 23 °C.

This data already offers significant qualitative insight into the dynamics of this three-step reaction (Figure 31) and allows for a comparison with the respective BDEs. The low levels of **5hmC** are due to its high reactivity: its reaction to **5fC** is significantly faster than its own formation from **5mC**, yielding $v_{5hmC} \gg v_{5mC}$. This corresponds well to the BDE of **5hmC** being lower than that of **5mC** (361 vs. 378 kJ mol⁻¹, respectively).[8] For the relationship between **5mC** and **5fC**, the situation is more complicated, as three scenarios are generally possible and any detailed interpretation of the data would be speculation at this point: depending on the amount of **5mC** present and the relationship between v_{5fC} and v_{5mC}, **5fC** would accumulate (until **5mC** is depleted; $v_{5fC} < v_{5mC}$), reach a steady state (until **5mC** is depleted; $v_{5fC} \approx v_{5mC}$), or reach a maximum and then decrease before **5mC** is depleted ($v_{5fC} > v_{5mC}$). However, it can be stated that the reaction of **5fC** to **5caC** is significantly slower than that from **5hmC** to **5fC**, yielding $v_{5fC} \ll v_{5hmC}$. This is also in accordance with the calculated BDEs, as that of **5fC** is higher than that of **5hmC** (389 vs. 361 kJ mol⁻¹, respectively).[8] The development of **5caC** is rather straight-forward, as it simply

accumulates as long as **5fC** and **C-6** are present. The behavior of the intermediates was studied in more detail when nucleosides were used as substrates (refer to chapter III.5).
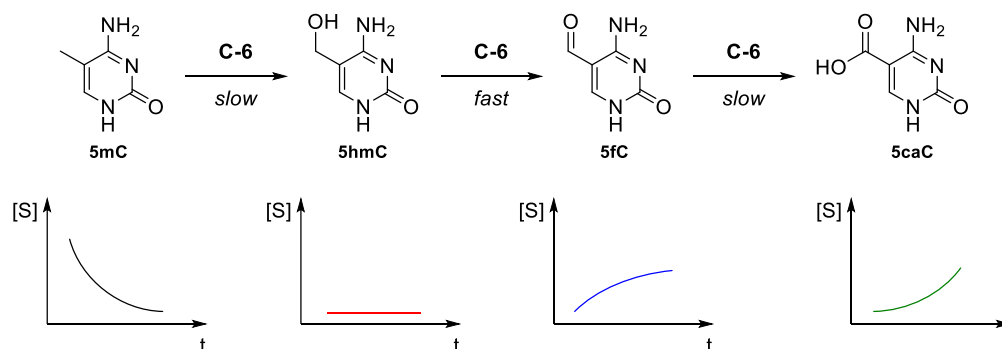

*Figure 31: Three-step reaction of **5mC** with **C-6** to **5hmC**, **5fC**, and **5caC**. The observed developments of product concentration and qualitative reaction rates summarized therefrom are indicated.*

Similar GC-MS experiments were conducted with **5hmC** and **5fC** as substrates, both yielding the expected results: **5hmC** is oxidized to **5fC** and **5caC** while **5fC** is oxidized to **5caC** (Figure 32). For details on the synthesis of **5hmC** please refer to chapter III.9, **5fC** was kindly provided by Eva Korytiaková of the Carell group at LMU Munich (refer to chapter III.9 for synthesis attempts). In the reactions of **5fC** with **C-6** potassium hydroxide was added to the mixture due to the poor solubility of **5fC** in unbuffered water at neutral pH. Potassium hydroxide was chosen as base, as it is already present in the reaction solution of **C-6**. The implications and results of this addition of base on the reaction rate are discussed in further detail below (refer to chapter III.9).
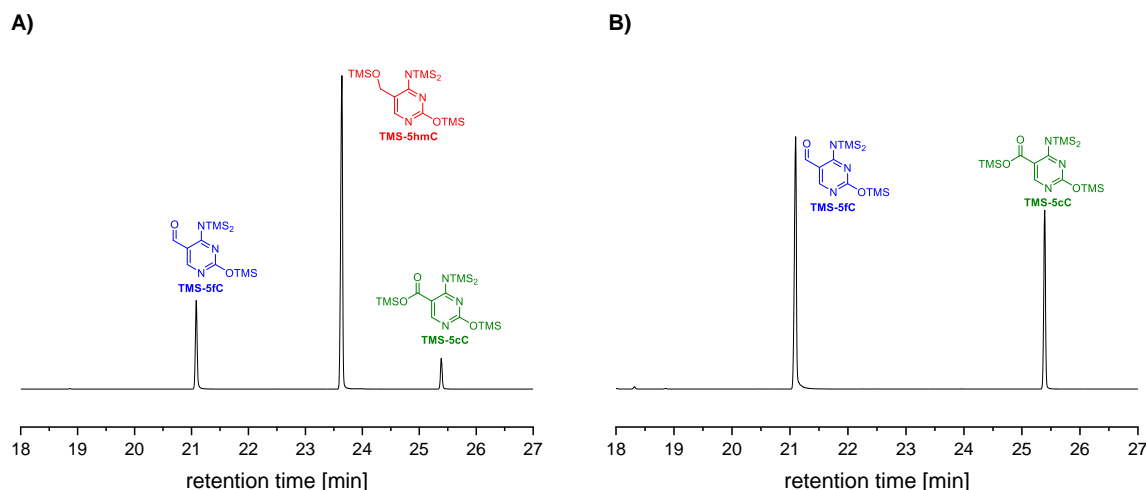
*Figure 32: **A)** Excerpt of the GC-MS trace of a representative reaction **5hmC** with **C-6**. Conditions: [**5hmC**] = 10 mM, [**C-6**] = 10 mM, H$_2$O, T = 23 °C **B**) a representative reaction **5fC** with **C-6**. GC-MS method **C**. Conditions: [**5fC**] = 10 mM, [**C-6**] = 10 mM, [KOH$_{added}$] = 10 mM, H$_2$O, T = 23 °C.*

In conclusion, **C-6** shows promising behavior as a model system for TET enzymes: reactions can be performed in water at near physiological conditions and the expected products in reactions

with a simplified substrate were observed. A closer analysis of the observed reaction rates was performed as the next step.

UV-Vis Kinetics to Obtain the Rate Law

In addition to these qualitative GC-MS measurements quantitative UV-Vis kinetic studies were performed using **5mC** and **5hmC** as substrates. When reactions of **C-6** with these substrates were monitored using UV-vis spectroscopy, a clear decrease of the absorption at λ = 718 nm was observed (Figure 33). As the absorption at this wavelength is attributed to the iron(IV)-oxido moiety in **C-6**, this decrease was deemed a good method to monitor the kinetics of the reaction.
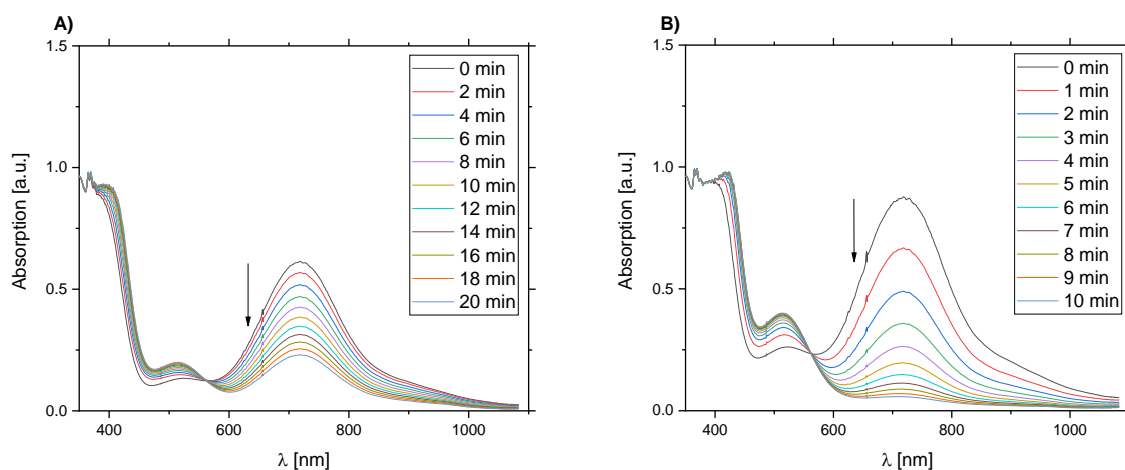
*Figure 33: Excerpts of UV-Vis traces of time-dependent measurements of the reaction of **C-6** with **A) 5mC** and **B) 5hmC**. An isosbestic point at λ = 560 nm can be observed in both cases. Conditions: [**S**] = 3 (**A**) or 5 (**B**) mM, [**C-6**] = 3 (**A**) or 5 (**B**) mM, H₂O, T =23 °C.*

To determine reaction rates and rate constants the decrease in the characteristic absorption of **C-6** at λ = 718 nm was therefore monitored and the method of initial rates applied (Figure 34).
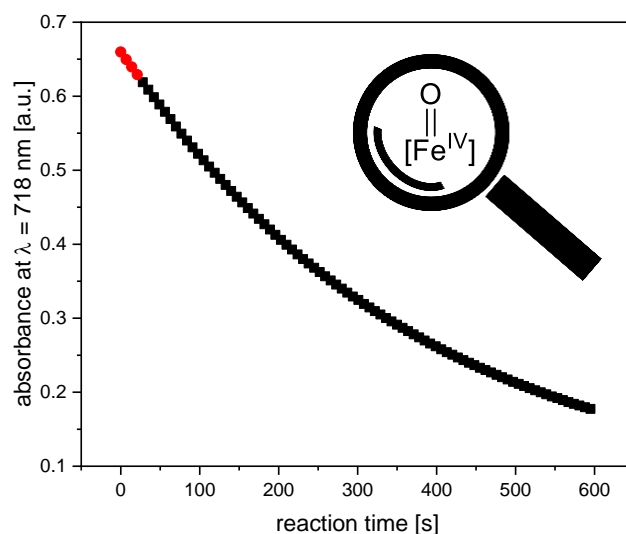
*Figure 34: Representative decrease of the absorption at λ = 718 nm upon reaction of **C-6** with **5mC**. Data points were collected every Δt = 7 s, the first four data points (red circles) were used for kinetic analysis.*

With **5mC** as substrate two series of four experiment sets were performed: In one experiment set, the concentration of **C-6** was kept constant at four different concentrations (1.25 mM, 2.50 mM, 3.75 mM, 5.00 mM) while the amount of **5mC** was varied between 0.2-1.6 equiv. In the other experiment set, the concentration of **5mC** was kept constant at (1.25 mM, 2.50 mM, 3.75 mM, 5.00 mM) while the amount of **C-6** was varied between 0.2-1.6 equiv. Each individual experiment was performed three times and the obtained results averaged.
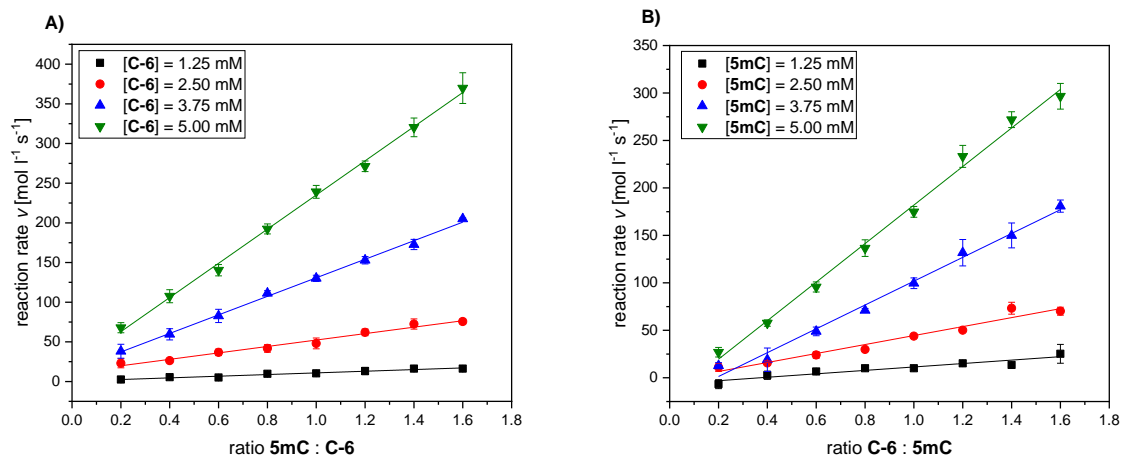
*Figure 35: **A)** Initial rates for eight different ratios of **5mC:C-6** at four different concentrations of **C-6**. **B)** Initial rates for eight different ratios of **C-6:5mC** at four different concentrations of **5mC**. Each experiment was performed as a triplicate measurement and the results averaged. Conditions: [**5mC**] = 0.25-8 mM, [**C-6**] = 0.25-8 mM, H$_2$O, T = 30 °C.*

A linear relationship was observed for each experiment set (Figure 35), indicating that both **5mC** and **C 6** enter, under the applied conditions, the rate law of the reaction in first order giving the second-order rate law **Eq. 1**.

$$v = k_{5mC}[\mathbf{5mC}]^1[\mathbf{C-6}]^1$$

Eq. 1

This was confirmed when the linear fits of each experiment set above were plotted vs. the respective concentrations and linear correlations were observed (Figure 36).
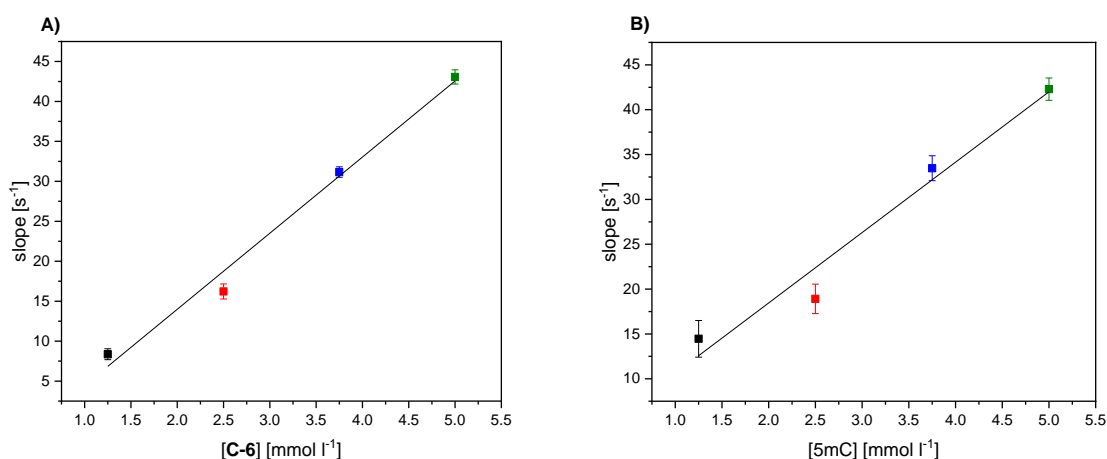
*Figure 36: **A)** Dependence of the measured reaction rates in Figure 35**A** on [**C-6**]. **B)** Dependence of the measured reaction rates in Figure 35**B** on [**5mC**]. Error values were calculated from linear regression of the data presented in Figure 35**A** and **B**. Conditions: [**5mC**] = 0.25-8 mM, [**C-6**] = 0.25-8 mM, H$_2$O, T = 30 °C.*

Additionally, the **5mC** concentration was increased up to 21 equiv. at [**C-6**] = 1.25 mM to screen for saturation behavior and decreased to 0.02 equiv. to compare it to the results obtained for **5hmC** (Figure 38).
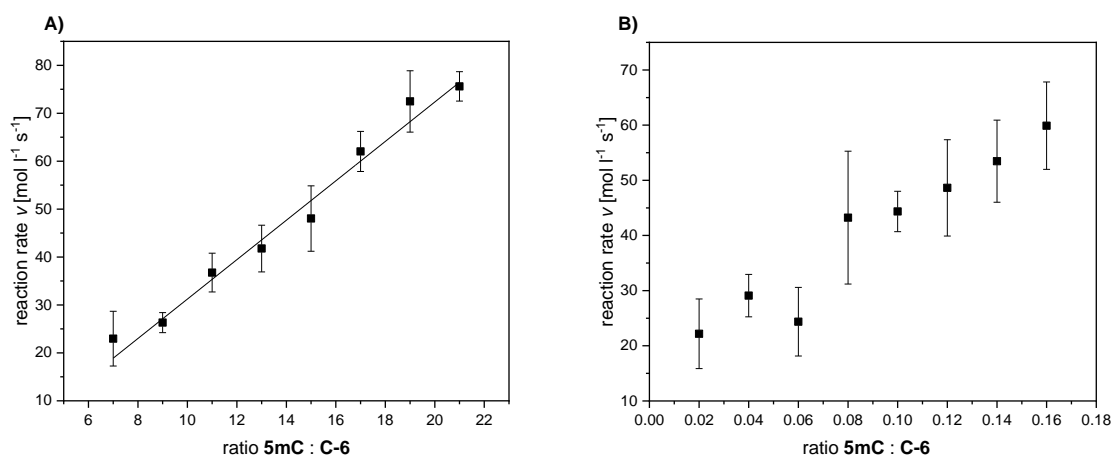

*Figure 37: **A**) Initial rates of the reaction of **C-6** (1.25 mM) with **5mC** (7-21 equiv.) **B**) Initial rates of the reaction of **C-6** (5 mM) with **5mC** (0.02-0.16 equiv.). Conditions: [**S**] = 0.1-8 mM [**C-6**] = 1.25/5 mM, H₂O, T = 30 °C.*

Similar studies were performed with **5hmC** as substrate. The reaction rate of **5hmC** was found to be much higher than that of **5mC** and a saturation-type behavior was observed in the concentration range previously employed for **5mC** measurements (Figure 38, red dots). Therefore, the concentration was decreased 10-fold, resulting in a linear correlation between measured rate and **5hmC** concentration (Figure 38, brown triangles).
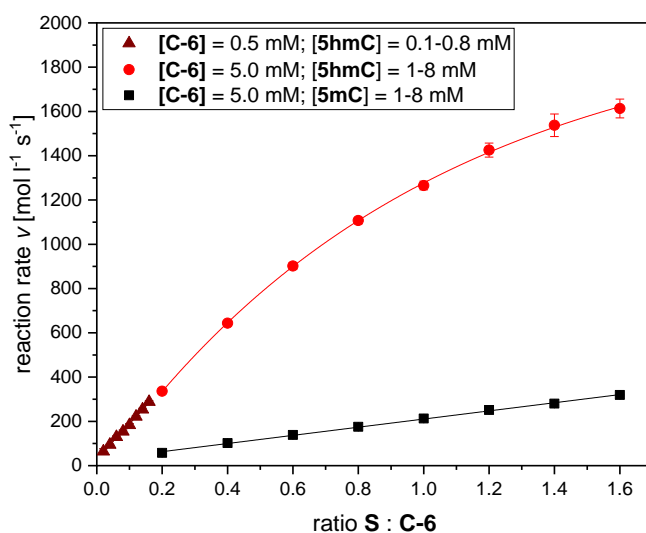
*Figure 38: Initial rates for eight different ratios of **5hmC:C-6** at two different concentrations of **C-6**: [**C-6**] = 5 mM (red circles), [**C-6**] = 0.5 mM (brown triangles). For comparison, the measured initial rates for **5mC** are also shown (black cubes). **S** = substrate. Each experiment was performed as a triplicate measurement and the results averaged. Conditions: [**S**] = 0.1-8 mM, [**C-6**] = 0.25-8 mM, H₂O, T = 30 °C.*

The observed high reaction rate of **5hmC** confirms the previous interpretation that **5hmC** reacts faster than **5mC** under the applied conditions (*vide supra*) and is therefore also in good agreement with the calculated BDEs of **5hmC** and **5mC** (361 vs. 378 kJ mol⁻¹, respectively). Additionally, the

rate law for the reaction of **5hmC** with **C-6** can be formulated as a second-order rate law within the monitored concentration range (**Eq. 2**).

$$v = k_{5mC}[5hmC]^1[C-6]^1$$

It has to be noted that the ratio of substrate:**C-6** was much lower in these experiments than is usually employed in such kinetic investigations. Therefore, no true pseud-zeroth-order-kinetics were measured. However, these conditions were employed due to the solubility of the components as well as the low absorbance at λ = 718 nm of **C-6** which limited the concentration to concentrations above ~0.5 mM for any meaningful analysis.

In addition to **5mC** and **5hmC**, **5fC** was also used as substrate for the reaction with **C-6**. As mentioned above, **5fC** is poorly soluble in unbuffered water at neutral pH, therefore, one equivalent of base (potassium hydroxide) had to be added to assure complete dissolution. As the reaction conditions are changed, a control measurement was performed to compare the initial rates of the reaction of **5mC** with **C-6** with and without added base. It was found that the addition of one equivalent of potassium hydroxide increases the reaction rates significantly (Figure 39**A**). Therefore, the observed reaction rates found for **5fC** with **C-6** are always compared to reaction rates measured for **5mC** and **5hmC** with one equivalent of potassium hydroxide added.

The initial rates measured for the reaction of **5fC** with **C-6** show a linear correlation with [**5fC**] for low concentrations ([**5fC**] = 1-5 mM; 0.2-1.0 equiv. of **5fC** relative to **C-6**) and a saturation behavior for higher concentrations ([**5fC**] = 6-8 mM; 1.2-1.6 equiv. of **5fC** relative to **C-6**). Additionally, the rates were observed to be higher than those of **5mC** but slightly lower than those of **5hmC** (within the linear range; Figure 39**B**).
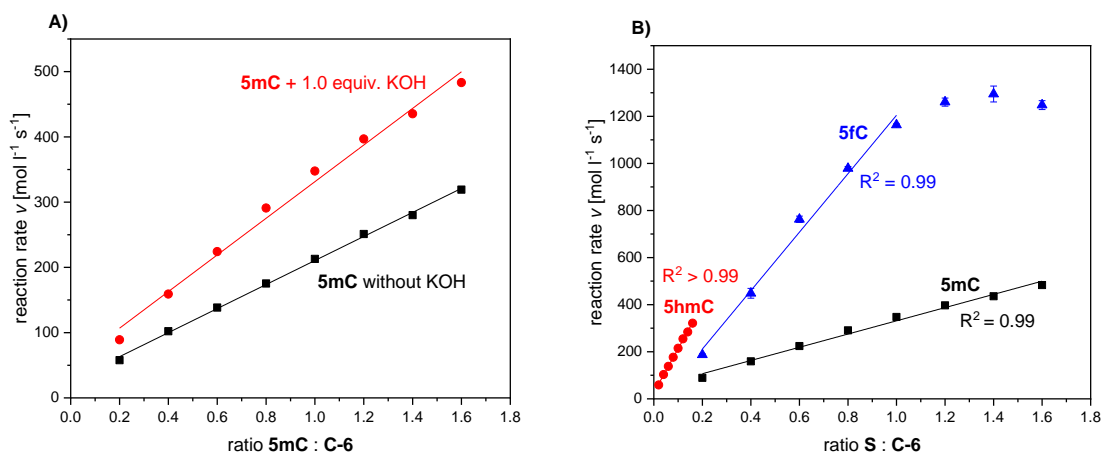

*Figure 39: **A**) Comparison of the initial rates of the reaction of **5mC** with **C-6** without added potassium hydroxide (black cubes) and with 1.0 equiv. of potassium hydroxide (red circles). **B**) Initial rates for **5mC**, **5hmC**, and **5fC** in reactions with **C-6**. For **5mC** and **5fC** concentrations were between [**S**] = 1-8 mM at a **C-6** concentration of [**C-6**] = 5 mM. For **5hmC**, the **C-6** concentration was decreased to [**C-6**] = 5 mM with [**5hmC**] = 0.1-0.8 mM. Each experiment was performed as a triplicate measurement and the results averaged. Conditions: [**S**] = 0.1-8 mM, [**C-6**] = 5 mM, H_2O, T = 30 °C.*

This observation is in direct contradiction with the calculated BDEs, these suggest that **5fC** should react slower than **5mC**.[8] However, the presence of base might have a significant impact on the

reaction mechanism resulting in this unexpected behavior. Additionally, it was observed that while the absorption at λ = 718 nm does decrease upon reaction of **5fC** with **C-6** (1.0 equiv.) in the first 100 s, it then increases again (Figure 40).
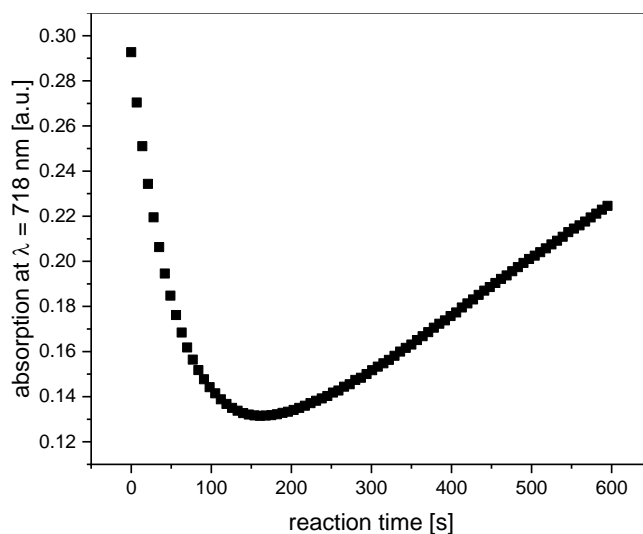

*Figure 40: Absorption at λ = 718 nm during the reaction of **5fC** with **C-6**. Conditions: [**5fC**] = 5 mM, [**C-6**] = 5 mM, [KOH] = 5 mM, H₂O, T = 30 °C.*

This was attributed to a precipitate that formed during the reaction, which indicates that additional reactions take place. Due to limited amounts of **5fC** that were available no further studies could be performed. However, the influence of the pH value on the reaction of **5mC** with **C-6** was further investigated (refer to chapter III.9).

A Closer Look at the Mechanism

As mentioned in chapter I.2, the so-called hydrogen atom transfer (HAT) reaction, in which the iron(IV)-oxido moiety abstracts a hydrogen atom from the organic substrate, is considered a major reaction pathway for iron(II)/α-KG dependent enzymes, such as TET,[3,8,147] as well as synthetic iron(IV)-oxido complexes.[236,237] This step yields an iron(III)-hydroxido species (**C-4**) and a carbon-centered organic radical. Both species then recombine in a rebound-type reaction to form the hydroxylated product and an iron(II) complex (**C-2**; Scheme 29).
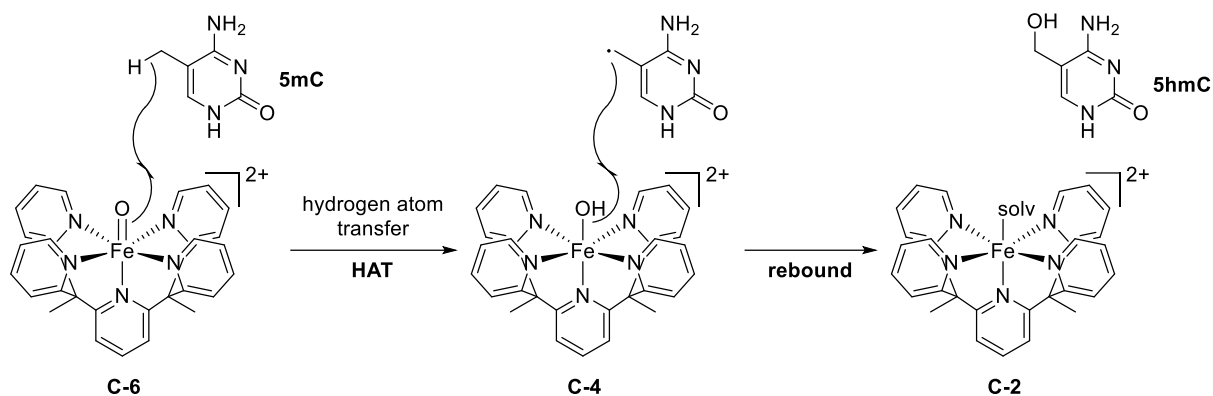
*Scheme 29: Postulated reaction mechanism of **5mC** with **C-6** via a hydrogen atom transfer (HAT) step to form an iron(III)-hydroxido intermediate **C-4** and a carbon-centered radical. These species then recombine in a rebound reaction to form the product **5hmC** and an iron(II) species **C-2**. solv = solvent, **C-2** refers to the structure with H$_2$O as solvent.*

Hu *et al.* used deuterated substrates to show that the HAT step is the rate limiting step for TET2, providing further evidence to support the HAT/rebound mechanism.[8] To confirm the validity of **C-6** as model system for TET enzymes and to provide evidence for the mechanism postulated in Scheme 29, **D$_3$-5mC** and **D$_2$-5hmC** were synthesized and used as substrate (for synthetic details please refer to chapter III.9).

When the reaction rates were compared, a clear trend was observed: deuterated substrates react significantly slower than their undeuterated counterparts.
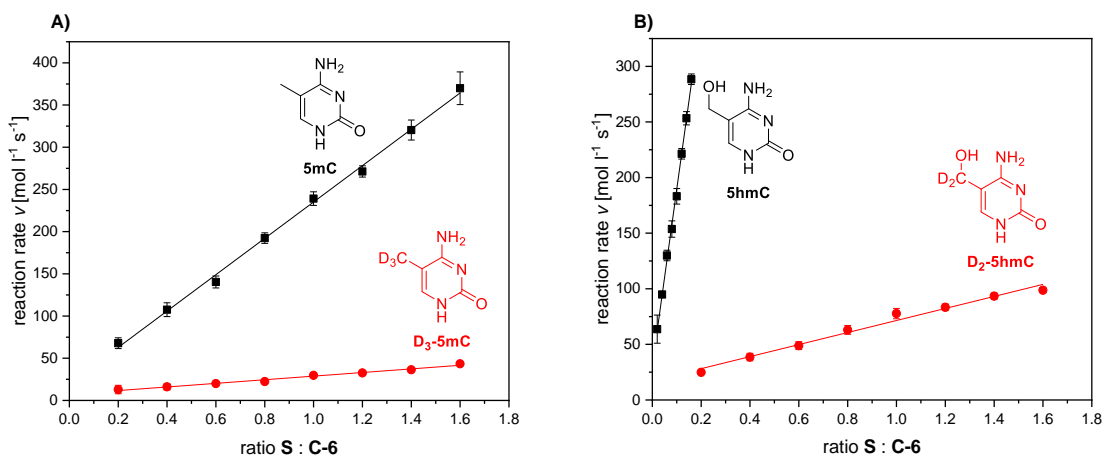
*Figure 41: **A)** Comparison of the initial rates of the reaction of **C-6** with **5mC** (black cubes) and **D$_3$-5mC** (red circles). **B)** Comparison of the initial rates of the reaction of **C-6** with **5hmC** (black cubes) and **D$_2$-5hmC** (red circles). For **5mC**, **D$_3$-5mC** and **D$_2$-5hmC** concentrations were between [S] = 1-8 mM at a **C-6** concentration of [**C-6**] = 5 mM. For **5hmC**, the **C-6** concentration was decreased to [**C-6**] = 0.5 mM with [**5hmC**] = 0.1-0.8 mM. Each experiment was performed as a triplicate measurement and the results averaged. Conditions: [S] = 0.1-8 mM, [**C-6**] = 5 mM, H$_2$O, T = 30 °C.*

The kinetic isotope effect (KIE) values were calculated from the ratio between rate constants of deuterated and undeuterated substrates according to **Eq. 3**, the results are found in Table 1.

$$KIE = \frac{k_H}{k_D}$$

Eq. 3

For both **5mC/D$_3$-5mC** and **5hmC/D$_2$-5hmC** large KIE values were observed. Although the reaction rates used for calculation of the rate constants, and therefore also the KIE value, were recorded at different substrate concentrations of **5hmC** and **D$_2$-5hmC**, interpretation was deemed

possible as the KIE is very large: the reaction of **C-6** with either **5mC** or **5hmC** proceeds *via* a rate limiting step that involves the hydrogen atoms on the methyl or hydroxymethyl moiety, respectively. This is in accordance with the postulated mechanism shown in Scheme 29 and previous findings on the reactivity of synthetic iron(IV)-oxido complexes[236,237] as well as iron(II)/α-KG dependent enzymes as TauD[3] and TET.[8] The discussed results were published in 2019.[13]

Table 1: Measured rate constants k$_S$ *(C-6) for **5mC**, **5hmC**, **D$_3$-5mC**, and **D$_2$-5hmC**[13] in comparison with BDEs of **5mC**, **5hmC**, and **5fC**,* k$_{cat}$ *values calculated by Hu* et al. *for TET2 in reaction with DNA oligonucleotides containing **5mC**, **5hmC**, and **5fC**,[8] as well as observed KIE values.*

	5mC	5hmC	5fC	D$_3$-5mC	D$_2$-5hmC
k_S (C-6) [l mol^{-1} s^{-1}]	7.37 ± 1.57	63.56 ± 12.81	-	0.86 ± 0.25	2.16 ± 0.52
BDE [kJ mol^{-1}]	378	361	389	-	-
k_{cat} (TET2) [10^{-3} s^{-1}]	2.12	0.63	0.46	-	-
KIE	-	-	-	9	29

However, even though the mechanism of the reaction of **C-6** with a nucleobase substrate seems to be similar to that observed for TET enzymes, a significant difference is observed. The rate constants k_S for **C-6** correlate with the calculated BDEs, whereas the corresponding k_{cat} values for TET2 do not.[8] This means that the observed reactivity in TET2 cannot be attributed to the reactivity of the iron(IV)-oxido moiety but rather to a secondary coordination sphere that specifies the nature of the substrate-enzyme interactions and thereby controls the reaction's speed.

5. Stage 2: Nucleosides

The next step in this project was to expand the substrate scope of **C-6** as a TET mimic to nucleoside structures, coming one step closer to the natural substrate of TET enzymes. After I had performed preliminary experiments and syntheses, I was joined in this project by David Schmidl for his Master Thesis. The preliminary results performed by myself are described in the following, a significant portion of the results obtained by David Schmidl, Eva Korytiaková of the Carell Research group at LMU Munich, and myself was then published in 2021.[14] This will be mentioned when applicable.

Reference Sample Synthesis

As **5mdC** and **5hmdC** are commercially available, only **5fdC** and **5cadC** needed to be synthesized to serve as reference samples. **5fdC** was synthesized according to literature procedures first published by Globisch *et al.*[185] and were optimized for higher yield. The synthesis of **5fdC** will be described in the following, whereas synthesis of **5cadC** was performed by David Schmidl in his Master Thesis.[238]
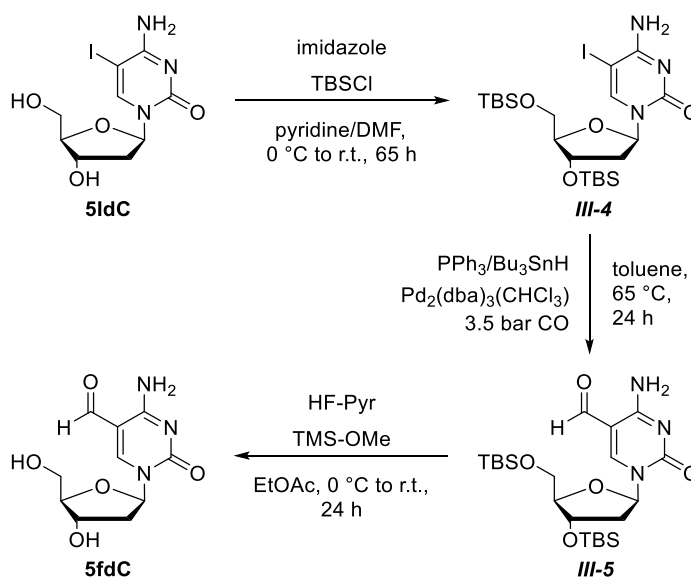
*Scheme 30: Three-step synthesis of **5fdC** from 5-iodo-2'-deoxyribo-cytidine (**5IdC**), adapted from Globisch et al.[185]*

In the first step in the synthesis of **5fdC**, 5-iodo-2'-deoxyribo-cytidine (**5IdC**) is reacted with imidazole and *tert*-butyl-dimethyl-silyl chloride (TBSCl) to obtain **III-4**. The solvent system was changed from pure dimethylformamide to a 3:1 mixture of pyridine:dimethylformamide, which resulted in a yield increase from 80% to 99%. The next step, a carbonylative Stille coupling to obtain **III-5**, was performed as described by Globisch *et al.* in the laboratories of the Carell group at LMU Munich with the help of Eva Korytiaková.[185] Subsequent deprotection of the silyl groups and HPLC purification gave the desired **5fdC**.

With **5mdC**, **5hmdC**, and **5fdC** as reference samples at hand, the reactivity of **C-6** towards **5mdC** was investigated. In contrast to nucleobases, nucleosides present more than one aliphatic hydrocarbon moiety, which are likely to react with **C-6** (Figure 42 left). Therefore, a comparison of the relevant BDEs provides a first estimate of the expected reactivity (Figure 42 right).
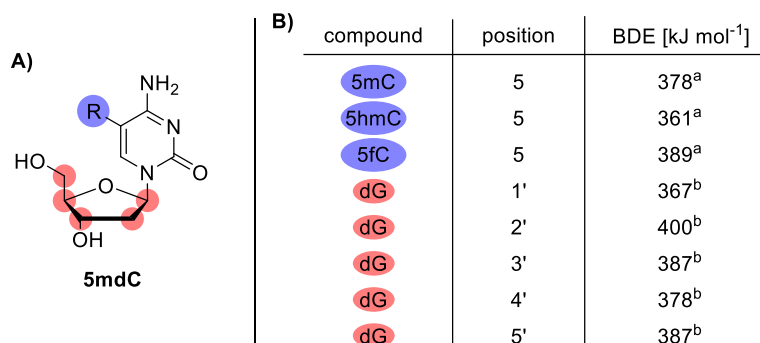

compound	position	BDE [kJ mol^{-1}]
5mC	5	378[a]
5hmC	5	361[a]
5fC	5	389[a]
dG	1'	367[b]
dG	2'	400[b]
dG	3'	387[b]
dG	4'	378[b]
dG	5'	387[b]

*Figure 42: **A**) Structure of 5-methyl-2'-deoxyribo-cytidine, the epigenetically relevant position R is marked in blue, the possible sites for side reactions on the 2'-deoxyribose backbone are marked in red. **B**) Calculated BDEs of C-H bonds in the nucleobases **5mC, 5hmC**, and **5fC** as well as in 2'-deoxyribo-guanosine. ^{a} Calculated by Hu et al.[8] ^{b} Calculated by Steenken et al.[239]*

Steenken *et al.* calculated BDE values for the C-H bonds on the 2'-deoxyribose unit for 2'-deoxyguanosine and these are used here, for lack of data on a more similar derivative.[239] These values show that most of the C-H bonds on the carbohydrate backbone are thermodynamically prone to oxidation by **C-6**: the values for the 1', 3', 4', and 5' position are below that of **5fC** (Figure 42 right), which has been shown to react with **C-6** (*vide supra*).

The 1' position was calculated to have an especially low BDE of 367 kJ mol^{-1}, which is almost as low as the one calculated for the hydroxymethyl group on **5hmC** (361 kJ mol^{-1}). Both the 3', 4', and 5' position show BDE value that is within the expected range for oxidation, however, positions 3' and 4' are sterically significantly more hindered than the 5' position. Therefore, oxidation at the 1' and 5' positions is expected to occur when **5mdC** is exposed to **C-6** oxidation at positions 3' and 4' is deemed unlikely, but possible.

As GC-MS is not an optimal method for nucleoside detection, due to decomposition during derivatization and injection (please refer to the literature), HPLC was chosen for product analysis. Therefore, a method was developed that allowed for separation of the expected main products **5mdC**, **5hmdC** and **5fdC** (Figure 44). In the commercial sample of **5hmdC** a small impurity was observed (Figure 44, retention time = 3.5 min) This method was later optimized by David Schmidl,[238] but served its purpose at this stage in the project.
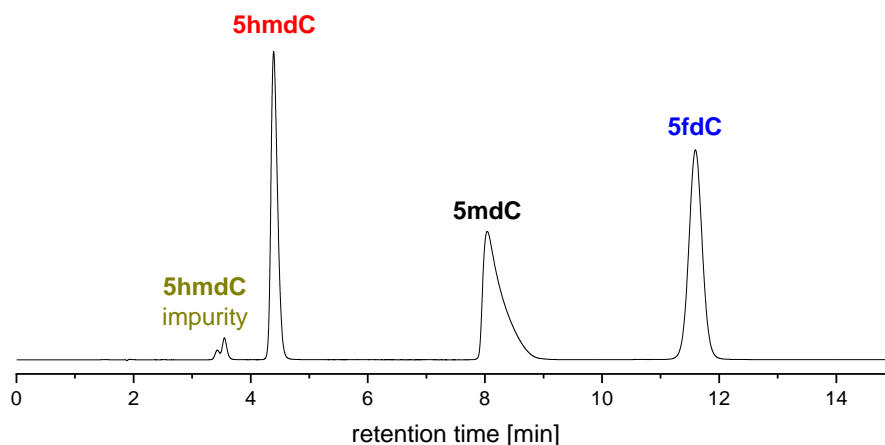
*Figure 43: HPLC trace (λ = 260 nm) of the reference samples **5mdC**, **5hmdC** and **5fdC**. HPLC conditions: C18, 95% water/5% methanol, isocratic, 15 min. The signal observed at a retention time of ~3.5 min (**5hmdC** impurity) stems from an impurity present in the commercial sample of **5hmdC**. This was later identified as 5-hydroxymethyl -cytidine (**5hmrC**) by David Schmidl.[238]*

With this method at hand, **C-6** was reacted with **5mdC** and **5hmdC** in aqueous solution and analyzed for the formed products (Figure 44). The color of both reactions changed from green to brown, with the **5hmdC**-containing reaction changing faster. This indicates consumption of **C-6** and thereby reaction with the substrates. In both reactions, significant amounts of the starting material were observed after 1 min and 10 min reaction time. Additionally, the expected oxidation products, **5hmdC** and **5fdC** in case of **5mdC** as starting material and **5fdC** in the case of **5hmdC**, were observed. This was confirmed by spiking **5hmdC** and **5fdC** reference samples into these reactions (refer to the appendix, p. 365ff). Even small amounts of the nucleobase **5hmC** were observed in both reactions, as was **5fC** in the reaction of **C-6** with **5hmdC**.
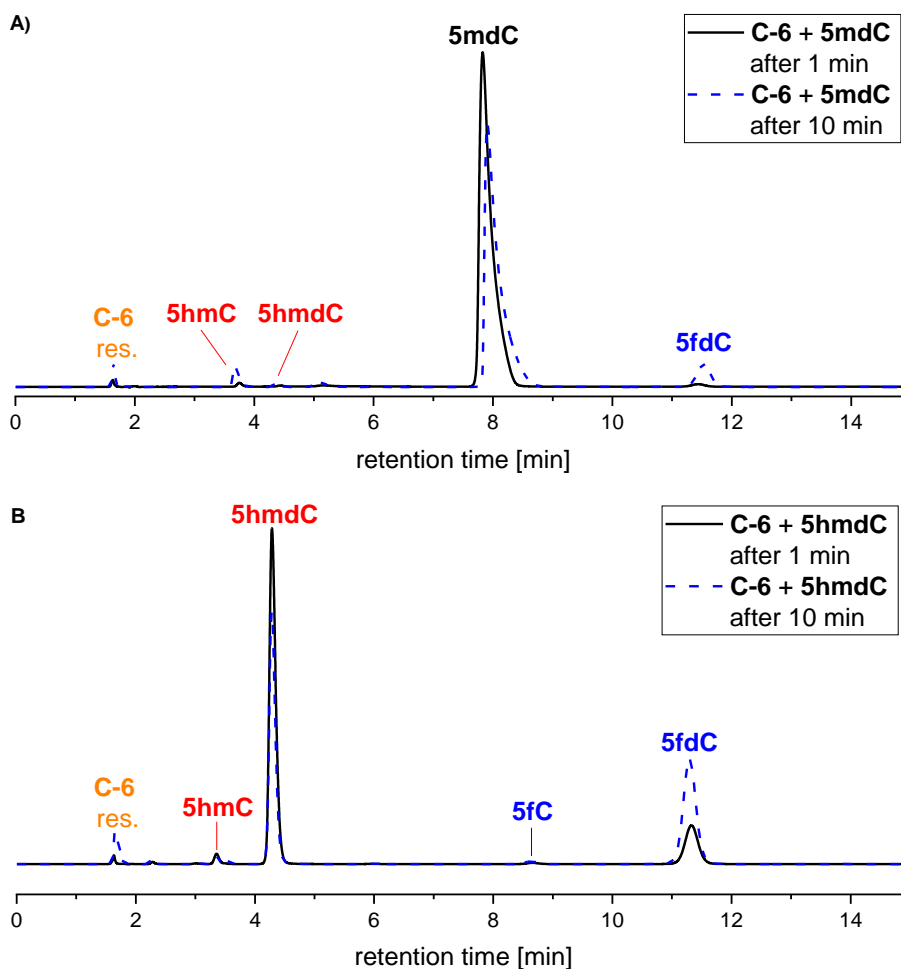
*Figure 44: **A)** Superimposed excerpts of a representative HPLC trace (λ = 260 nm) of the recovered products of a reaction of **C-6** with **5mdC** after 1 min (black solid) and after 10 min reaction time (blue dashed). **B)** Superimposed excerpts of a representative HPLC trace (λ = 260 nm) of the recovered products of a reaction of **C-6** with **5hmdC** after 1 min (black solid) and after 10 min reaction time (blue dashed). HPLC conditions: C18, 95% water/5% methanol, isocratic, 15 min. Assignments were made based on retention time and spiking of the expected products. "**C-6** res." refers to residual signals of **C-6** after filtration. Conditions: [**C-6**] = 5 mM, [**S**] = 3.75 mM, H$_2$O, T = 23 °C.*

The assignments shown in Figure 44 account for almost all of the observed signals, with only three significant signals remaining unassigned: 2.3 min, 3.5 min, and 5.1 min. As the expected products **5hmdC** and **5fdC** as well as all corresponding nucleobases were observed, it is likely that **5cadC** and **5caC** were also formed. At this point it was not possible to corroborate this hypothesis, as no reference samples of **5cadC** and **5caC** were present in large enough amounts to allow for comparative measurements. However, David Schmidl was able to show in his Master Thesis that both **5cadC** and **5caC** are indeed formed under the applied conditions.[238]

High resolution-mass spectrometry (HR-MS) of collected preparative HPLC fractions confirmed the assignments of the major signals in Figure 44 (**5mdC**, **5hmdC**, **5fdC**). Coupled MS/MS experiments further confirmed these results, as signals corresponding to the m/z values of the nucleobases were found in the respective HPLC peak. However, HPLC-MS/MS of the signal in Figure 44 assigned to **5hmdC** (retention time = 4.2 min) indicates that at least two substances are present. An m/z value of 258 was detected, which corresponds to the m/z value of **5hmdC**,

however, when subjected to fragmentation in an MS/MS experiment, two m/z values were detected: 126 and 142. These correspond to **5mC** and **5hmC**, respectively, indicating that oxidation had occurred both on the cytosine unit (Scheme 31 upper pathway) as well as the 2-deoxyribose scaffold (Scheme 31 lower pathway). This would mean that oxidation indeed occurs on the 2-deoxyribose unit, as indicated by BDE values (*vide supra*). However, assignment as to which carbon atom on the deoxyribose backbone is oxidized was not possible at this point. In general, this side-reaction was observed to be very small compared to the amount of **5fdC** (compare Figure 44).
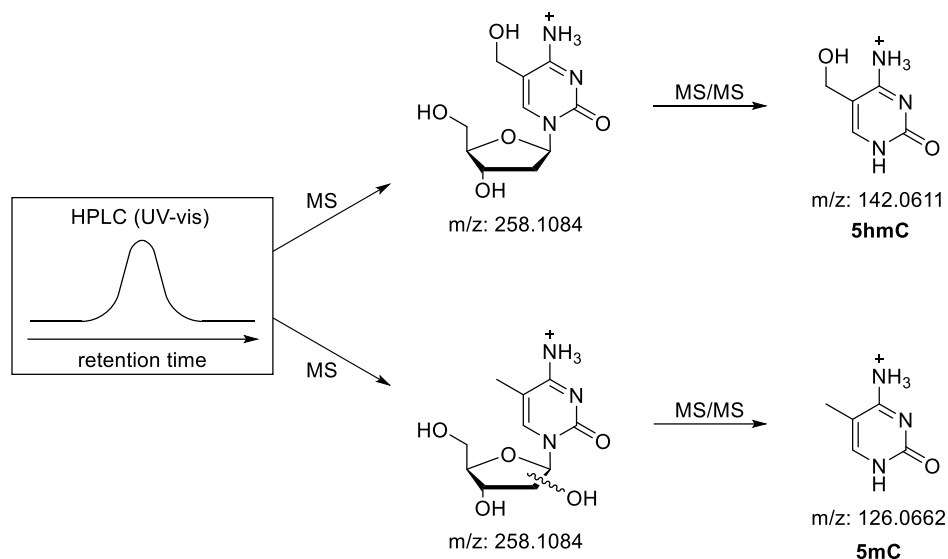
*Scheme 31: HPLC separation and subsequent MS/MS experiments of a reaction mixture of **C-6** and **5mdC**. The wavy bond in the lower structure indicates that a hydroxyl moiety is bound to the 2-deoxyribose scaffold at an unspecified position.*

In conclusion, these results show that **C-6** does indeed oxidize the 5-position of **5mdC** and **5hmdC** to the corresponding hydroxylated products. The most significant side-reaction is release of corresponding nucleobases (Scheme 32). It remains unclear, whether nucleobases are <u>only</u> formed from the corresponding nucleoside or whether they are <u>also</u> formed by a reaction of **5mC** with **C-6**. Both pathways were observed within the scope of this work (Figure 44: reaction of **5mdC** to **5mC**/**5hmdC** to **5hmC**; Figure 29: reaction of **5mC** to **5hmC**, **5fC**, and **5caC**), it is, however, impossible to state which of the pathways is responsible for the observed nucleobases in Figure 44.
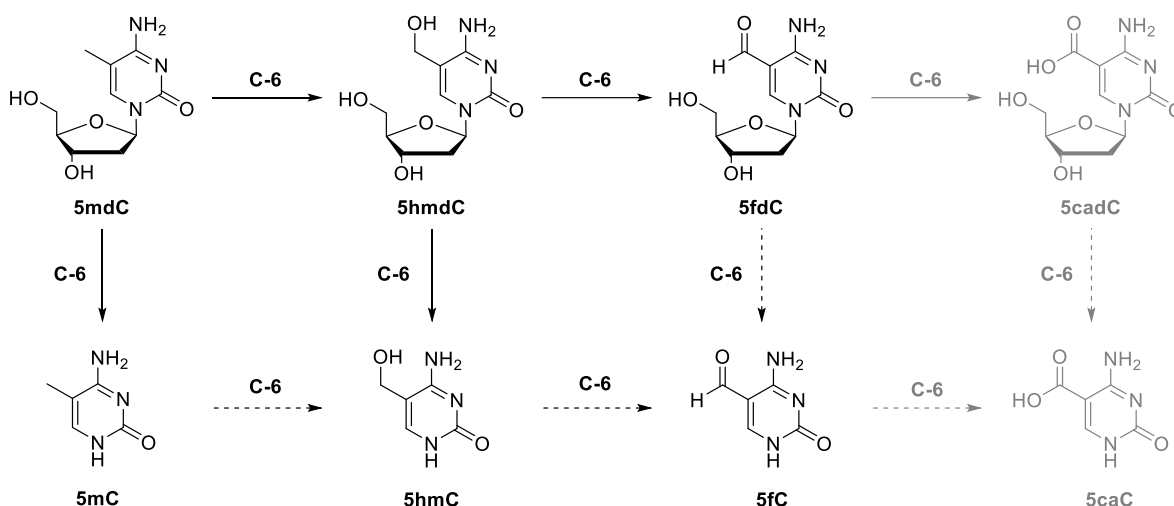
*Scheme 32: Observed (black in this work, grey in other works[14,238]) intermediates in the reaction of **5mdC** with **C-6**. Dashed arrows show reactions that might occur, solid arrows show reactions that are very like to have occurred.*

As for the mechanism of nucleobase release from the corresponding nucleosides, two pathways are likely. On the one hand, hydrolysis of the glycosidic bond would result in the formation of the free nucleobase as well as 2'-deoxyribose (Scheme 33 upper pathways). On the other hand, oxidative hydroxylation of the 1' position and subsequent release of the nucleobase would result in the formation of 2'-deoxy-γ-ribonolactone (Scheme 33 lower pathway). This question was later addressed by David Schmidl and the results published in 2021: it is highly likely that only 1' oxidation, the lower pathway in Scheme 33, is responsible for the formation of nucleobases in reactions of **C-6** with nucleosides.[14]
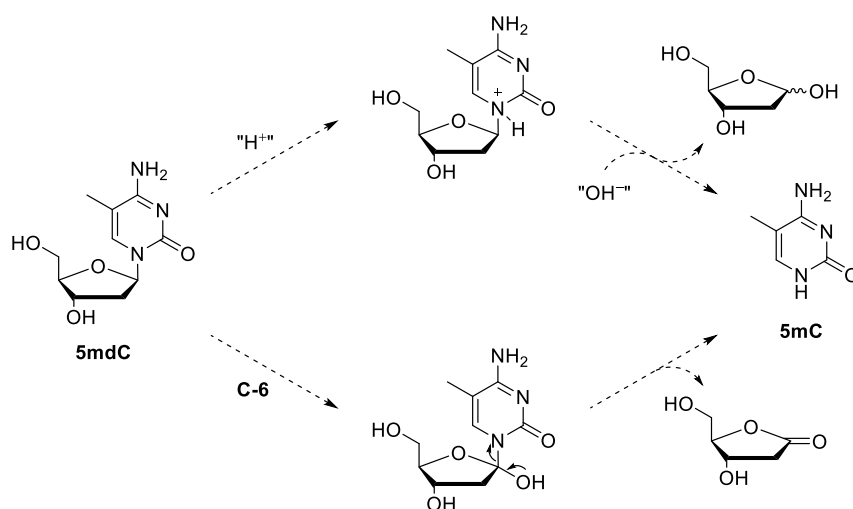
*Scheme 33: Postulated pathways for the release of a nucleobase, in this example **5mC**, from a nucleoside, here **5mdC**. The upper pathway describes acid-catalyzed hydrolysis, whereas the lower pathway relies on oxidative hydroxylation of the 1' position in **5mdC**.*

In addition to qualitative product analysis, the development of product formation was also analyzed. This was performed in a semi-quantitative manner by analyzing the development of the absorption at λ = 260 nm at the respective retention times. As expected, the amount of **5mdC** was observed to decrease over the monitored reaction time (10 min) while the amount of **5fdC**

increased. The amount of **5hmdC** was observed to remain constant at low levels, as was observed for nucleobases (refer to chapter III.4). These measurements were then continued and optimized to allow for exact quantification by David Schmidl and the obtained results published in 2021.[14,238]
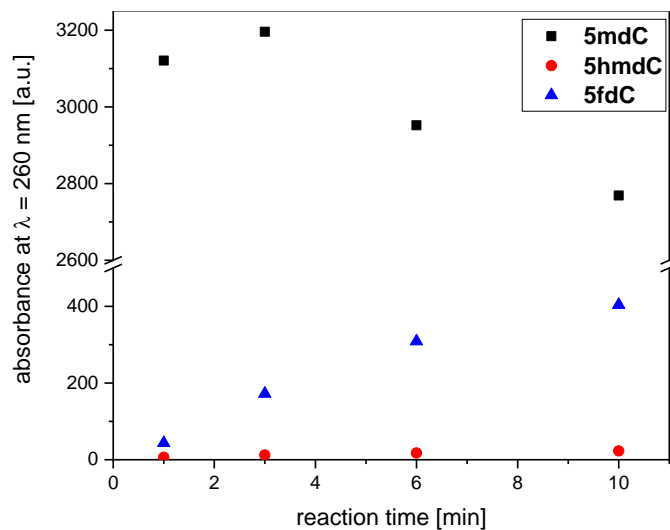
*Figure 45: Development of the amounts of **5mdC, 5hmdC,** and **5fdC** in a reaction of **C-6** with **5mdC** over time. Conditions: [**C-6**] = 5 mM, [**5mdC**] = 5 mM, H_2O, T = 23 °C.*

6. Stage 3: Dinucleotides

As these results were promising the next step in the expansion of the substrate scope was attempted: dinucleotides. These would still represent relatively small and simple substrates, compared to actual genomic DNA. Suitable dinucleotides are not commercially available, therefore, synthesis of these dinucleotides was attempted. However, due to the large amount of time this project required, it was soon aborted in favor of using short commercially available oligonucleotides (9-mers and 10-mers) as substrate. The synthetic procedures undertaken are described in the following (Scheme 34).
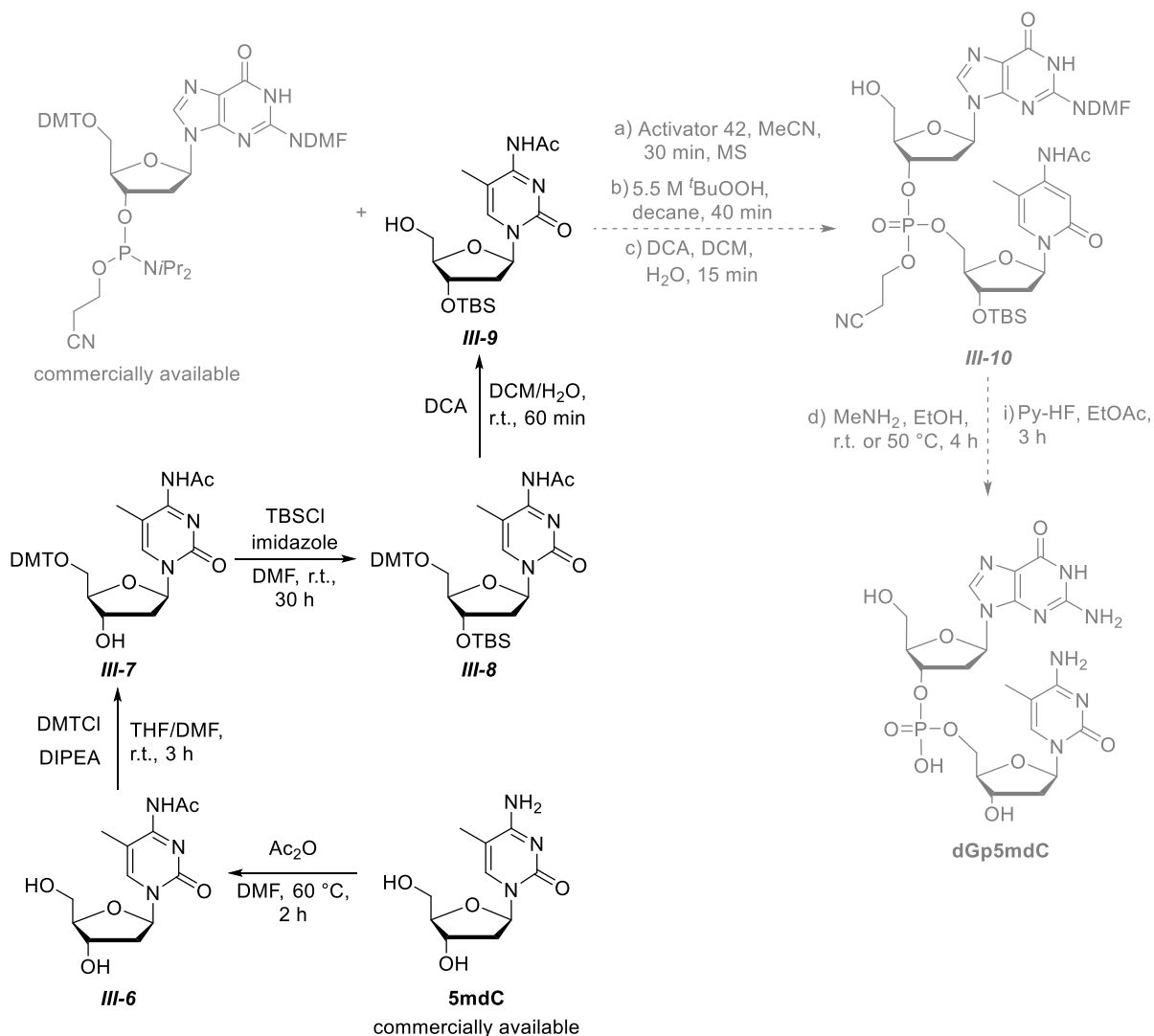
Scheme 34: Synthesis route to partially protected **5mdC** nucleoside and subsequent coupling with a guanosine phosphoramidite. Black structures were isolated, solid arrows indicate completed reactions, dashed arrows indicated attempted but incomplete reactions. Ac = acetyl, DMT = dimethoxy trityl, TBS = tetra-butyl-di-methyl silyl, DCA = dichloro acetic acid, DMF = dimethylformamide (in this context as protecting group as well as solvent), DIPEA = di-iso-propyl ethyl amine, iPr = iso-propyl, Activator 42 = 5-[3, 5-bis(trifluormethyl)phenyl]-1-H-tetrazole, Py-HF = hydrogen fluoride pyridine.

Dinucleotides have been synthesized from a partially protected nucleoside and a corresponding phosphoramidite.[240] As **5mC** residues often occur within a CpG dinucleotide context,[241] and the phosphoramidite derivative of **dG** is commercially available but not of **5mdC**, **dGp5mdC** (Scheme 34) was chosen as a target structure. Therefore, a partially protected **5mdC** derivative needed to

be synthesized. This was achieved by acylation of the exocyclic amine of the **5mC** moiety, subsequent protection of the 5' position using dimethoxy trityl (DMT) chloride, followed by *tert*-butyl dimethyl silyl (TBS) protection of the 3' hydroxyl moiety, and selective deprotection of the 5' position. The first two steps were also performed in reversed order.

| | T = 50 °C, t = 2 h | 50 | 50 |
| | T = 60 °C, t = 1 h | 100 | 0 |
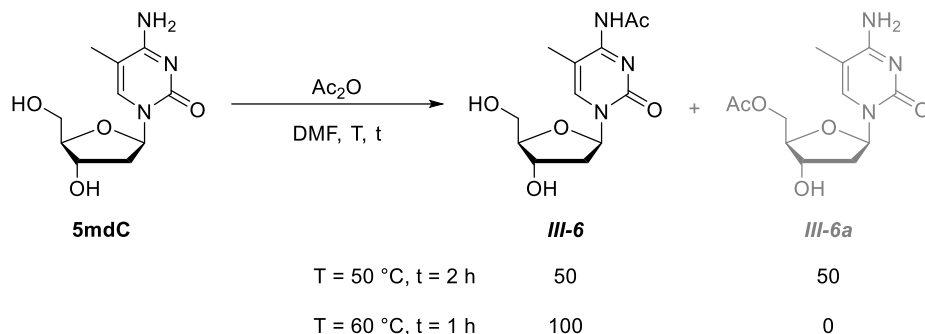
*Scheme 35: Acetylation of **5mdC** using acetic acid anhydride in dimethylformamide (DMF) yielding the desired product **III-6** in addition to the 5'-O-acylated side-product **III-6a**, performed according to a procedure by Mizuta et al.[242] DMF = N,N-dimethylformamide.*

N_4-acetylation was performed according to a literature known procedure,[242] however, the 5'-*O*-acylated side-product ***III-6a*** was obtained in addition to the desired product ***III-6*** in 50% relative yield (Scheme 35). When the reaction temperature was increased to 60 °C and the reaction time reduced to one hour the reaction proceeded in a more selective fashion (Scheme 35). However, even under optimized conditions, traces of the starting material were observed in the crude product.
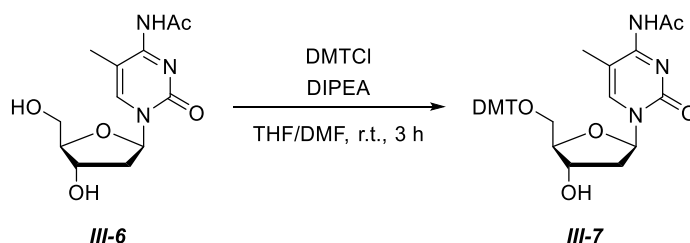
*Scheme 36: Synthesis of a DMT and acetyl protected intermediate **III-7** according to a procedure of Shahsavari et al.[243] by treatment of **III-6** with dimethoxy trityl chloride (DMTCl) and di-iso-propyl ethyl amine (DIPEA) in a mixture of tetrahydrofuran (THF) and dimethylformamide (DMF).*

This mixture of **5mdC** and ***III-6*** was then used for the second step, protection of the 5' hydroxyl moiety using DMTCl according to a procedure published by Shahsavari *et al.* (Scheme 36, reaction of **5mdC** with DMTCl and DIPEA is not shown).[243] Unfortunately, only low yields (~13%) were isolated of ***III-7***. This was attributed to unwanted deprotection of the 5' position during the acidic conditions of column chromatography which had been observed using LC-MS and ¹H NMR spectroscopic analysis of the obtained chromatography fractions. This was even observed when pyridine or triethyl amine were added to the eluent during column chromatography.

As mentioned above, the two steps described here can also be conducted in reverse order, leading to an increased overall yield (Scheme 37, ~17% vs. ~5%).
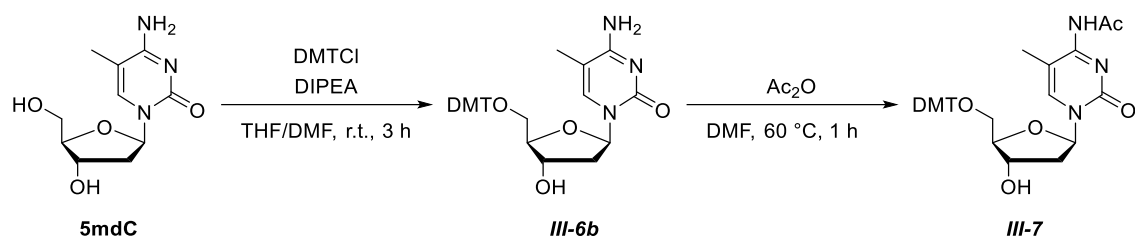
Scheme 37: Synthesis of intermediate **III-6b** *from* **5mdC** *by DMT protection using dimethoxy trityl chloride (DMTCl) and di-iso-propyl ethyl amine (DIPEA) in a mixture of tetrahydrofuran (THF) and dimethylformamide (DMF) and subsequent N-acetylation to* **III-7** *using acetic acid anhydride in DMF in 17% total yield.*

Intermediate **III-7** was subsequently TBS protected on the 3' hydroxyl moiety using *tert*-butyl dimethyl silyl chloride (TBSCl) and imidazole according to a literature procedure.[244] However, the amount of TBSCl had to be increased to from the literature amount of 2.5 equiv. to 5.0 equiv. in order to observe product formation using LC-MS. However, only minor amounts of the desired product **III-8** were observed, therefore, the reaction was stirred overnight. Unfortunately, LC-MS indicated not only the formation of **III-8** but also the presence of several side-products (Scheme 38 and Table 2).
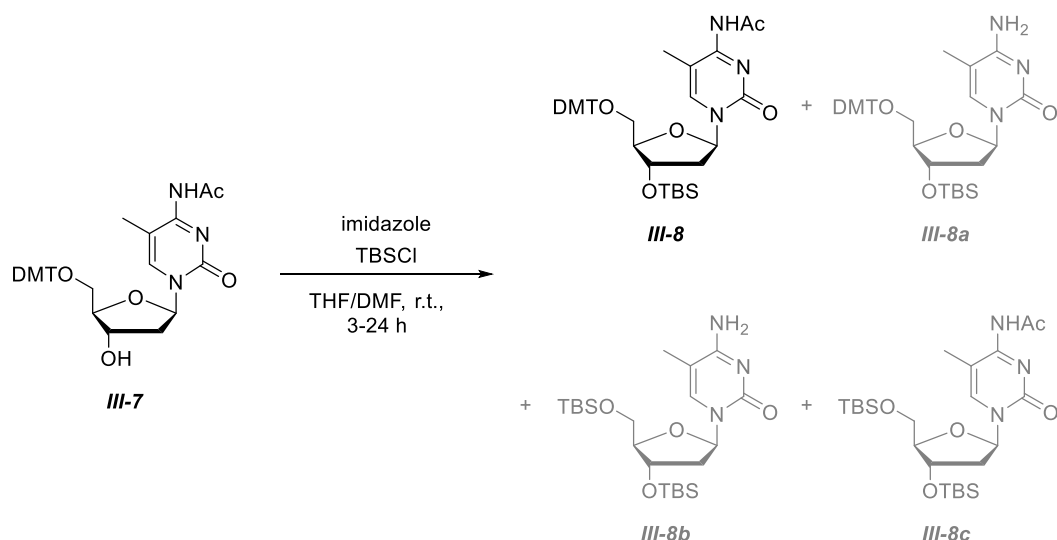
Scheme 38: TBS protection of **III-7** *using tert-butyl dimethyl silyl chloride (TBSCl) and imidazole in a mixture of tetrahydrofuran (THF) and dimethylformamide (DMF) yielding* **III-8** *in addition to three tentatively assigned side-products* **III-8a**, **III-8b**, *and* **III-8c**.

A decrease in the reaction time to 3 h did significantly reduce the amounts of side-products, however, the crude yield of **III-8** was also only 50%. Column chromatography on silica was observed to cause decomposition of **III-8**, mostly by loss of the acetyl protecting group (yielding **III-8a)**.

*Table 2: Calculated and observed m/z ratios for **III-8** and tentatively assigned side-products.*

Compound	Calculated m/z	Observed m/z
III-8	700.3	700.2
III-8a	658.3	658.5
III-8b	470.3	470.5
III-8c	512.3	512.5

Nonetheless, the desired product was obtained and was therefore subsequently treated with dichloroacetic acid to deprotect the 5' position by acidic cleavage of the DMT protecting group. Addition of dichloroacetic acid to a solution of ***III-8*** in dichloromethane results in a color change to red indicating the removal of the DMT group.
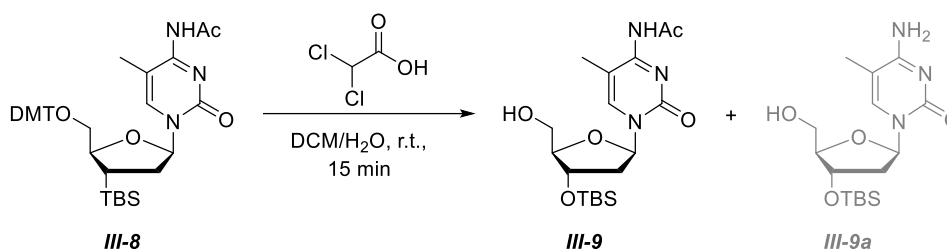
*Scheme 39: Final step in the synthesis of the N,3' protected **5mdC** derivative **III-9** and side-product **III-9a** by treating **III-8** with dichloroacetic acid in dichloromethane (DCM).*

Even though ***III-9*** was isolated in 72% yield, only very small amounts were obtained. Therefore, it was decided to use the TBS-protected side-product ***III-9a*** as well as unmodified **5mdC** in coupling the phosphoramidite derivative of guanosine (Scheme 40), even though both are not ideal starting materials for this transformation due to the multiple sites of phosphoramidite coupling. A procedure described by Ching *et al.* was used for both reactions.[240]
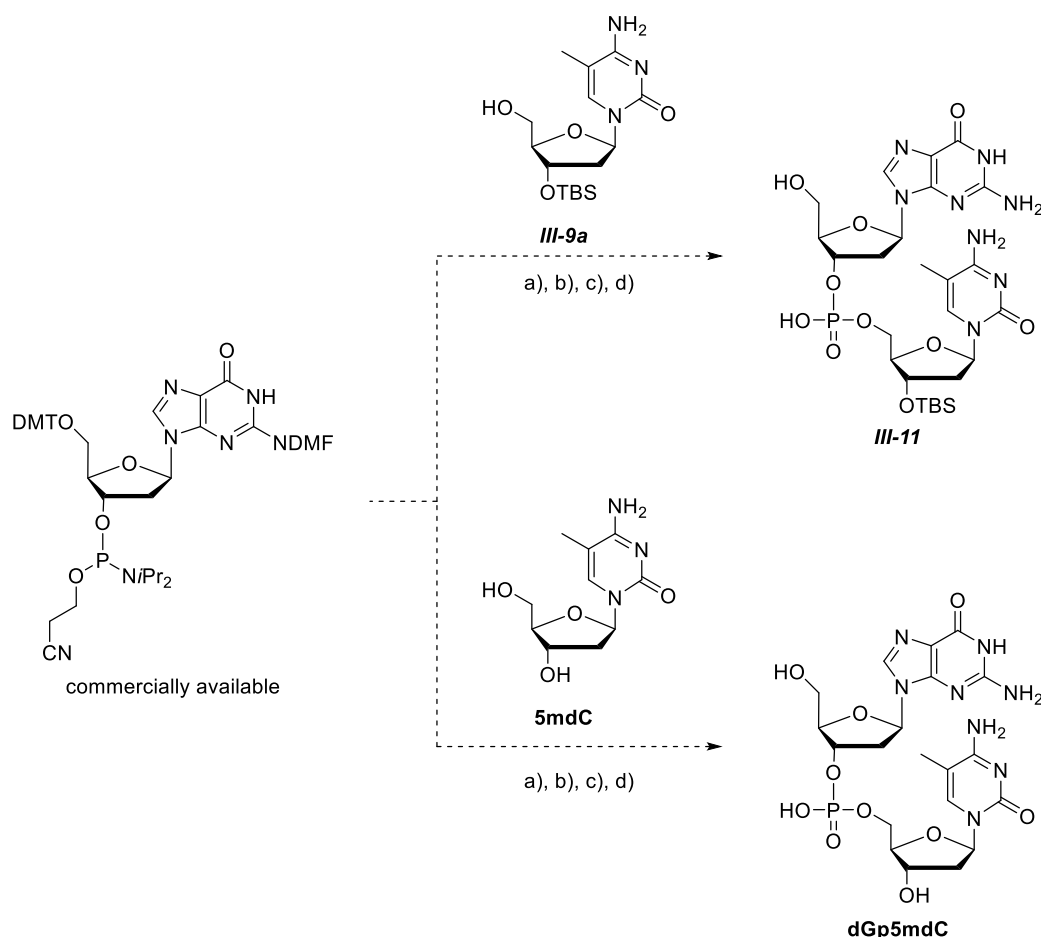
*Scheme 40: Attempted coupling of the commercially available phosphoramidite derivative of guanosine with **III-9a** and **5mdC**. A) Activator 42, MeCN, r.t., t = 30 min, molecular sieve (3 Å), b) 5.5 M tert-BuOOH, decane, r.t., 40 min, c) 3% DCA in DCM, H$_2$O, r.t., 15 min, d) NH$_3$ (aq.), MeOH, 50 °C, 6 h. DMT = dimethoxy trityl, DMF = dimethylformamide (as protecting group), iPr = iso-propyl, TBS = tert-butyl dimethyl silyl, Activator 42 = 5-[3, 5-bis(trifluormethyl)phenyl]-1-H-tetrazole, DCA = dichloroacetic acid, DCM = dichloromethane.*

Unfortunately, LC-MS analysis of the obtained product mixtures of both starting materials, ***III-9a*** and **5mdC**, did not reveal signals corresponding to the desired products. This was expected, as the respective starting materials do contain several sites for coupling with the phosphoramidite group and a *N,3'*-protected substrate should be used for coupling.

As the acetyl protecting group proved labile under the applied conditions, the use of the benzoyl protecting group was briefly investigated (Scheme 41). This was successful and presents a good starting point for an additional route to a *N,3'*-protected starting material for coupling with a suitable phosphoramidite.
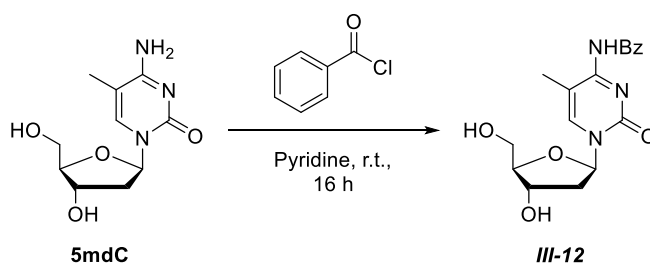
*Scheme 41: Benzoyl protection of **5mdC** using benzoyl chloride in pyridine yielding **III-12**. Bz = benzoyl.*

7. Stage 4: Oligonucleotides

David Schmidl continued the investigation of nucleosides as substrates for **C-6**, therefore I started investigating small oligonucleotide structures. This project is a part of the SFB "Chemical Biology of Epigenetic Modifications" and the culmination of a long-standing cooperation between myself and Eva Korytiaková of the Carell research group at LMU Munich. A part of the results obtained were published in 2021.[14]

Oligonucleotides as Substrates

As **5mdC** occurs mostly in CpG dinucleotides in nature,[245,246] similar structures were chosen as model substrates (Table 3). **O-1** was chosen due to its simplicity, however, it later presented significant challenges, therefore **O-2** was chosen. **O-2** is composed of **dA**, **dC**, deoxyuridines (**dU**) and **dG**, as the corresponding nucleobases do not contain aliphatic hydrocarbons that are prone to be attacked by **C-6**. The methyl group of **T** is a target for oxidation by **C-6** (refer to chapter III.8), **dU** was chosen. The CpG dinucleotide motif was also included in the design. **O-2C** is the complementary strain of **O-2**, **O-2-ctr.** and **O-2-ctrl.-P** served as control strains, see below for further details.

Table 3: Oligonucleotide substrates sequences used in this work.

Compound	Sequence (5' to 3')
O-1	HO-GGGG**5mC**GGGG-OH
O-2	HO-CCUUACC**5mC**G-OH
O-2C	HO-CGGGUUAAGG-OH
O-2-ctrl.	HO-CCUUAACCCG-OH
O-2-ctrl.-P	HO$_3$PO-CCUUAACCCG-OH

Oligonucleotide structures offer several points of attack for **C-6** beside the methyl group on **5mC**, similar to nucleosides (refer to chapter III.5). In addition to the deoxyribose backbone, other nucleobases might also be a target for **C-6** oxidation, even though no aliphatic hydrocarbons are present. In particular, **8-oxo-G**, a common oxidative DNA lesion,[109,110] might form upon exposure to **C-6**. Therefore, these reactions would need to be analyzed carefully for the occurrence of side-products.
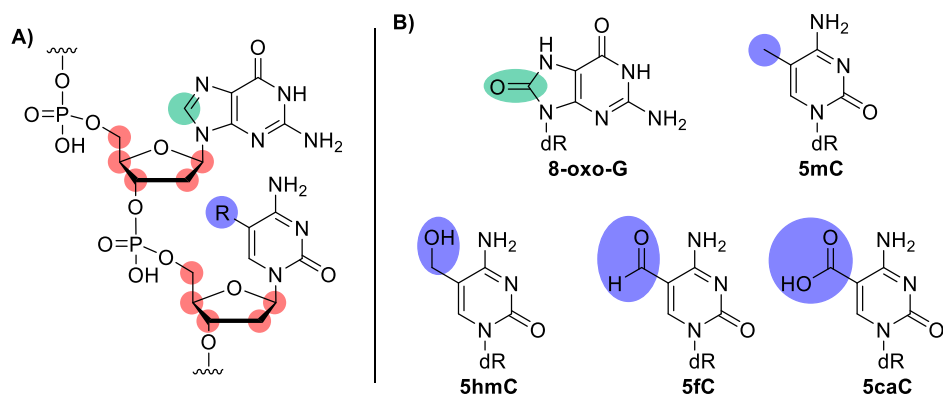
*Chart 8: **A)** Excerpt of an oligonucleotide structure, potential sites for **C-6** mediated oxidations are marked (blue = 5 position on cytosine, green = position 8 on guanine, red = 1', 2', 3', 4', and 5' positions on the deoxyribose backbone. **B)** Potential nucleobase products of **C-6** mediated oxidation with marked sites corresponding to the structure on the left.*

Prior to reacting any oligonucleotide substrates with **C-6**, alternative work-up procedures were explored. The standard work-up procedure employed for nucleobase and nucleoside substrates involved filtering the reaction mixture through silica in order to remove iron complexes from the solution and quench the reaction. Rigorous washing of the silica is required to ensure that all products are eluted. The amount of substrate was envisioned to be significantly decreased when using oligonucleotides (0.125-0.5 mM) compared to nucleobase and nucleoside substrates (1-8 mM). Therefore, a standard oligonucleotide work-up filter (Zymo Research Oligo Clean & Concentrator Kit) was tested for its ability to separate iron complexes from oligonucleotides. The oligonucleotide substrate was largely unaffected by this process, unfortunately, significant amounts of the iron complexes were still detected in the filtered sample (Figure 46).
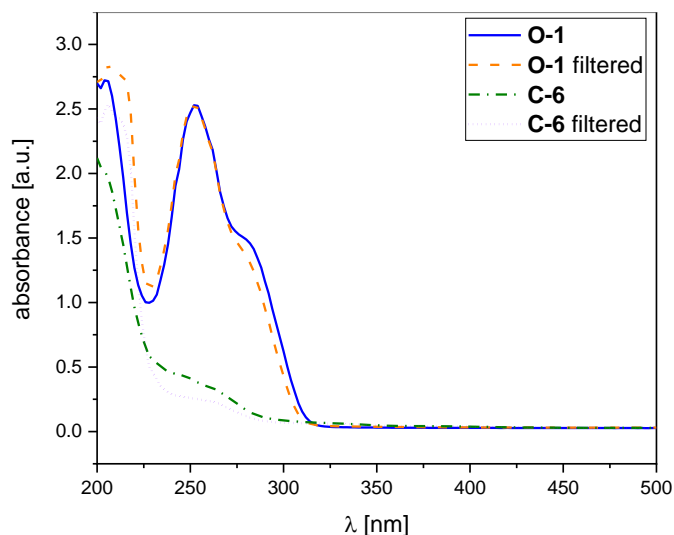
*Figure 46: Superimposed excerpts of UV-Vis spectra obtained for unfiltered (blue solid: **O-1**/green dashed-dotted: **C-6**) and filtered (orange dashed: **O-1 filtered**/ violet dotted: **C-6 filtered**) samples. Conditions: [**O-1/C-6**] = 0.2 mM, H₂O, T = 25 °C.*

Decreasing the amount of iron complex to [**C-6**] = 0.05 mM or filtering the sample twice did not improve the method (not shown, refer to the appendix, Figure 193 and Figure 194, p.372), this approach was therefore discontinued. By significantly decreasing the amount of silica (100 μl compared to 1.5 ml) of the previously applied procedure while simultaneously increasing the

amount of water used for washing (~5-fold increase relative to the used concentration) the work-up procedure was adapted to satisfactory levels. However, in the case of **O-1** significant loss of substrates was observed: after reaction with **C-6** and subsequent work-up only ~50% oligonucleotide were recovered to be used for further analysis (determined *via* UV-vis quantification, refer to the appendix, Table 22, p. 370). Fortunately, **O-2** was recovered reproducibly in amounts > 80%. It was therefore decided to continue with this modified work-up procedure.

 In a first set of experiments, **O-1** was treated with one or four equivalents of **C-6**, the resulting product mixture digested, and the obtained nucleoside mixture analyzed using a triple quadrupole mass spectrometer (Figure 47). **5mdC**, the oxidized **5mdC** derivatives **5hmdC**, **5fdC**, and **5cadC**, as well as **8-oxo-dG** were of interest.
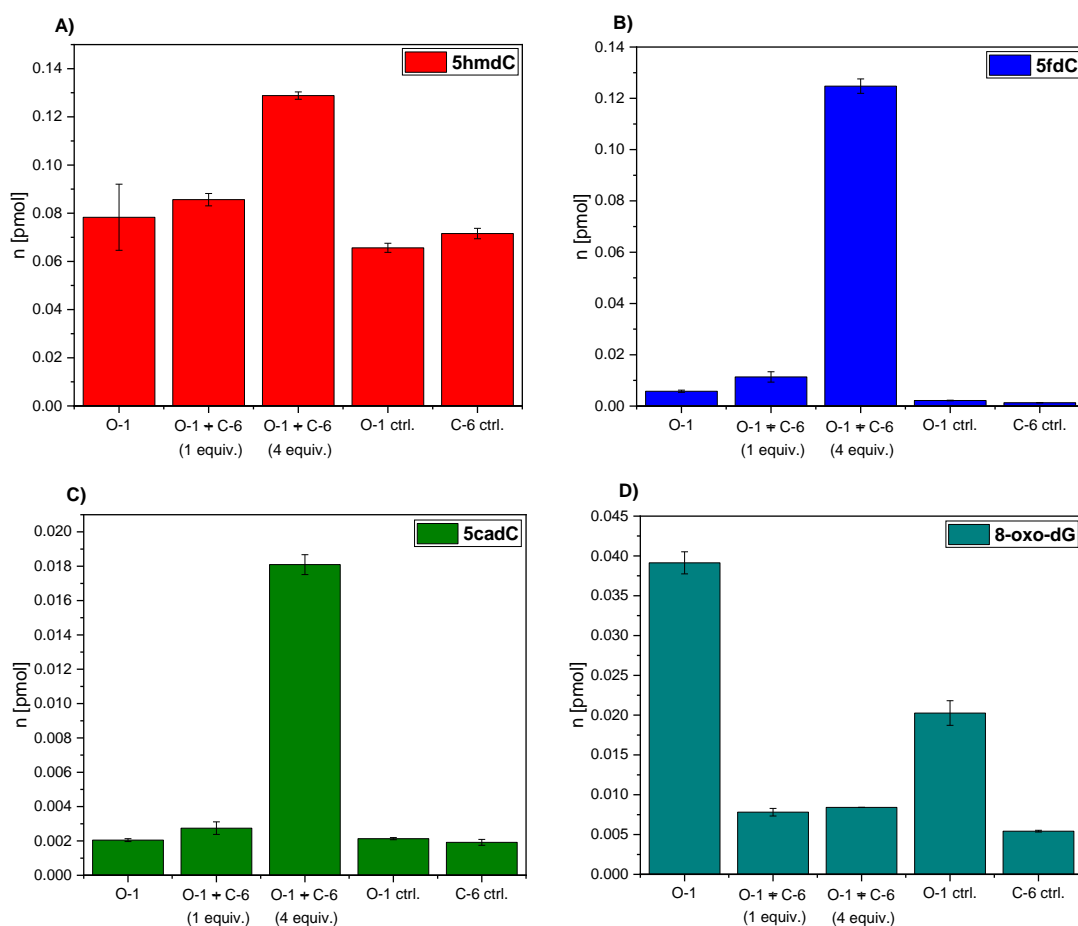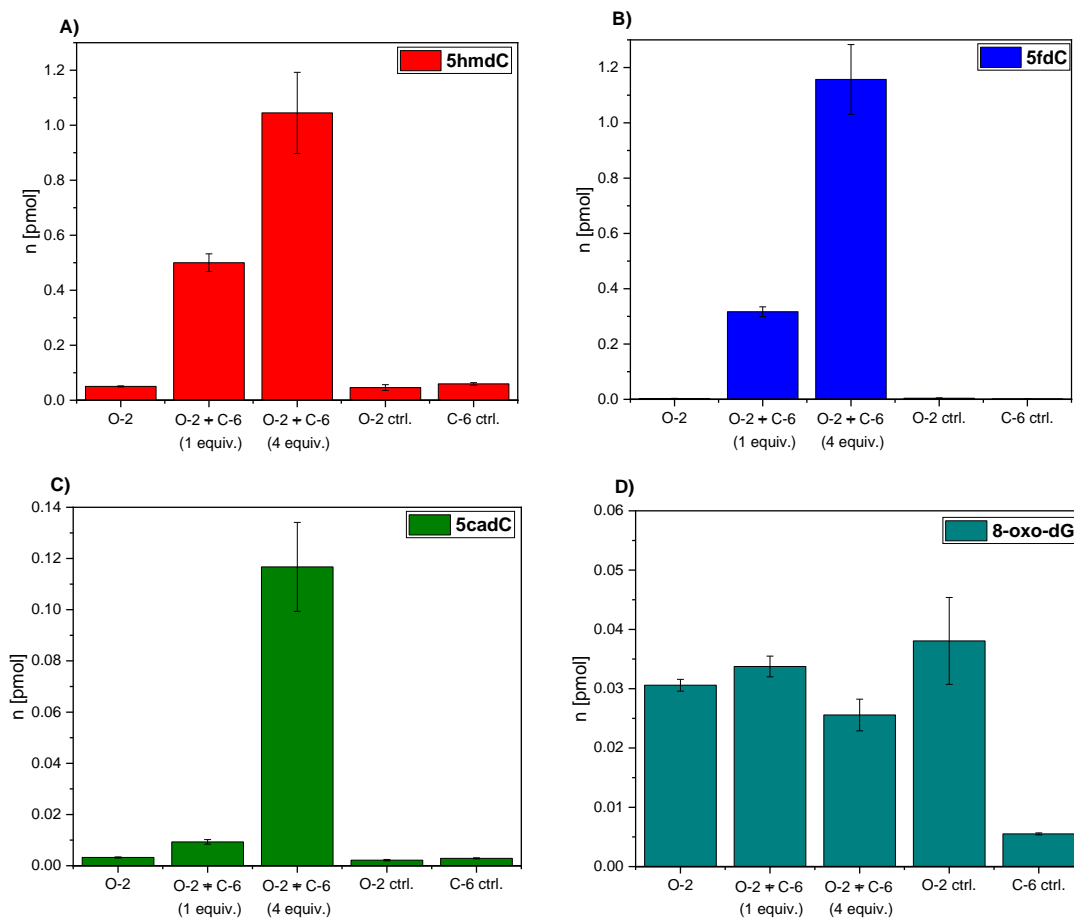

*Figure 47: Detected levels of **5hmdC (A)**, **5fdC (B)**, **5cadC (C)**, and **8-oxo-dG (D)** in **O-1** samples. **O-1** refers to the untreated oligo, "**O-1 + C-6** (1 equiv.)" to a ratio of 1:1 **O-1:C-6**, "**O-1 + C-6** (4 equiv.)" to a ratio of 1:4 **O-1:C-6**, "**O-1** ctrl" and "**C-6** control" refer to samples in which **O-1** or **C-6**, respectively, were treated as the reaction samples. Conditions: [**O-1**] = 0.25 mM, [**C-6**] = 0.25 or 1 mM, H$_2$O, T = 23 °C, t = 30 min. Error bars represent standard deviation between technical replicates.*

In both samples of **O-1** that were treated with **C-6** a rise in **5hmdC** levels compared to the untreated **O-1** sample is observed, however, arguably small. In the case of **5fdC** and **5cadC**, on the other hand, a significant increase was observed when four equivalents of **C-6** were used, a slight increase when one equivalent of **C-6** was used. **5mdC** levels were observed to decrease, but no

clear trend was observed (not shown, refer to the appendix, Figure 191, p. 371). This is probably due to the large overall levels of **5mdC** (compared to **5hmdC**, **5fdC**, or **5cadC**, ~10-70-fold), therefore, small chenges are not easily detectable. The levels of **8-oxo-dG** were found to be small for all samples and no trend was observed. It was therefore concluded that **8-oxo-dG** is likely not formed upon treatment of **O-1** with **C-6**. Further evidence for this hypothesis was provided by exposing **G** as well as **dG** to **C-6** and analyzing the product mixture using high-resolution mass spectrometry. In the case of **G**, no signal corresponding to **8-oxo-G** was observed (Scheme 42). In the case of **dG**, a signal with a mass-to-charge ratio corresponding to **8-oxo-dG** (284.0995) was detected. However, MS/MS analysis of this compound revealed only the presence of **G** (Scheme 42). Taken together with the results presented in chapter III.5, oxidation of the 2'-deoxyribose unit was assumed as the most likely explanation.
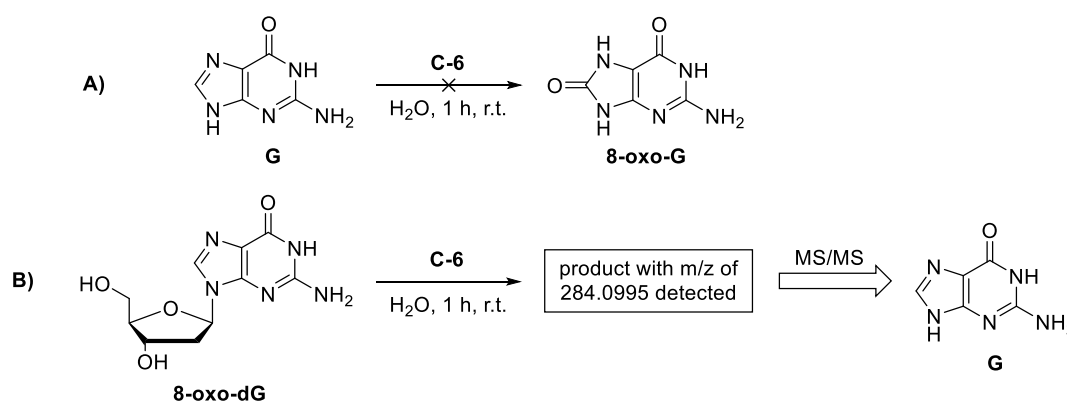
Scheme 42: **A)** Reaction of G with **C-6**. **B)** Reaction of dG with **C-6** that gave a product with a mass-to-charge ratio of 284.0995. MS/MS experiments of this compound revealed only the presence of G.

The low levels of **5hmdC** are in line with the results obtained when using nucleobases and nucleosides, as discussed above: the **5hmC** residue seems to be preferentially turned over by **C-6** yielding low amounts, whereas **5fdC** and **5cadC** accumulate. It is noteworthy that the detected **5cadC** levels are ~7-fold lower than those of **5hmdC** and **5fdC**.

These are remarkable results showing that oligonucleotide structures containing a **5mC** residue indeed serve as a substrate for **C-6** and that a significant amount of the reactivity is directed towards the methyl group on **5mC**. However, as only 50% of the substrate were recovered after work-up (refer to the appendix p. 370 for experimental details and UV-vis quantification of the obtained oligonucleotide amounts) and no clear trend in **5hmdC** levels is observable, further improvements on substrate and experimental procedure were necessary.

Therefore, **O-2** was chosen as the next substrate and treated with **C-6** in the next set of experiments. The structure of **O-2** is not only more similar to natural DNA, but also behaved more favorably during the work-up procedure with > 80% recovery of the used substrate. Analysis of the digested substrate showed a rise in **5hmdC**, **5fdC**, and **5cadC** levels upon **C-6** treatment (Figure 48). The presence of a **5hmC-**, **5fC-**, and **5caC**-containing 10-mer oligonucleotide product

was also confirmed using matrix assisted laser desorption-time of flight mass spectrometry (MALDI-TOF MS, *vide infra*, Figure 53).

*Figure 48: Detected levels of **5hmdC** (**A**), **5fdC** (**B**), **5cadC** (**C**), and **8-oxo-dG** (**D**) in **O-2** samples. "**O-2**" refers to the untreated oligo, "**O-2** + **C-6** (1 equiv.)" to a ratio of 1:1 **O-2:C-6**, "**O-2** + **C-6** (4 equiv.)" to a ratio of 1:4 **O-2:C-6**, "**O-2** ctrl" and "**C-6** control" refer to samples in which **O-2** or **C-6**, respectively, were treated as the reaction samples. Conditions: [**O-2**] = 0.25 mM, [**C-6**] = 0.25 or 1 mM, H$_2$O, T = 23 °C, t = 30 min. Error bars represent standard deviation between technical replicates.*

In contrast to **O-1**, an increase in **5hmdC** levels compared to the untreated sample (**O-2**) or control measurement (**O-2** ctrl.) was clearly observable, when **O-2** was exposed to **C-6**. **5fdC** and **5cadC** levels both increased significantly. **5hmdC** and **5fdC** levels were observed to be in a comparable range at ~10 times those of **5cadC**. In the case of **5cadC**, the use of four equivalents of **C-6** produced more than a four-fold increase in **5cadC** levels.
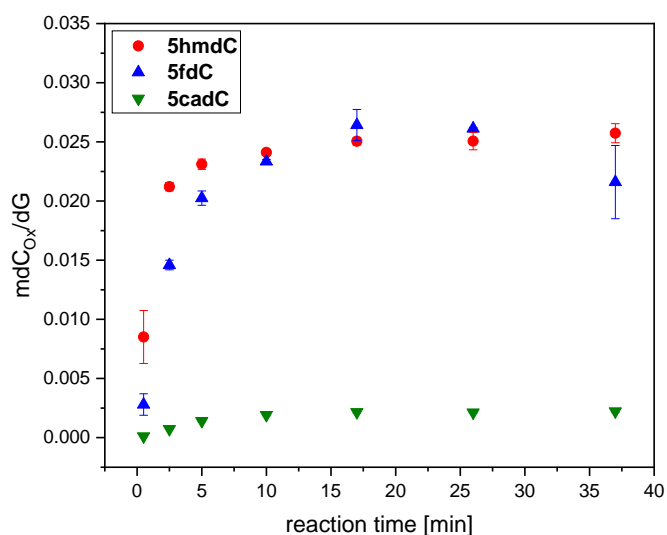
*Figure 49: Observed levels of **5hmdC**, **5fdC**, and **5cadC** relative to **dG**, when **O-2** was treated with **C-6**. Conditions: [**O-2**] = 0.125 mM; [**C-6**] = 0.5 mM, H$_2$O, T = 23 °C. Each measurement was performed as three technical replicates and averaged, the results of two such experiments were averaged and the error values calculated therefrom.*

The reaction was also monitored over time, with samples taken after regular intervals over the course of 37 min (Figure 49 and Figure 50). **5hmdC** levels were observed to increase sharply within the first 5 min of the reaction and then reaching steady levels after ~10 min. **5fdC** levels also increased within the first minutes, albeit not as fast. The maximum level was observed at ~17 min, then a slow decrease was observed to take place. However, the error bar of the last data point is rather large, so no definite statement can be made. **5cadC** levels were observed to increase slowly over the first minutes and then reach a steady level. After ~10-15 min most reactivity seems to have stopped.
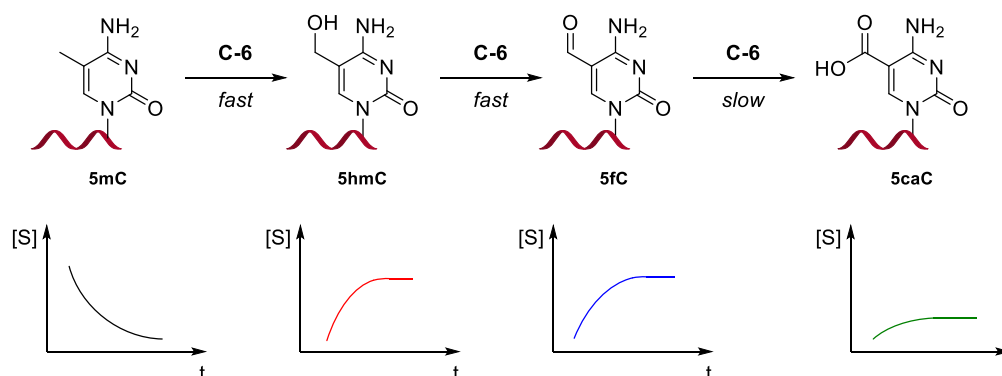
*Figure 50: Three-step reaction of an oligonucleotide containing a **5mC** residue with **C-6** to the respective oligonucleotides containing **5hmC**, **5fC**, and **5caC** residues. The observed developments of product concentration and qualitative reaction rates summarized therefrom are indicated.*

These observations are rather surprising as they significantly differ from those observed for nucleobases, nucleosides, and **O-1**: Here, accumulation of **5hmdC** was not observed, which was explained by its low BDE. The BDE is unlikely to have changed significantly for **O-2**, but as **5hmdC** did accumulate when **O-2** was used as substrate, an additional effect must be responsible for this

observation. Additionally, only low levels of **5cadC** are detected, indicating that the reaction from **5fdC** to **5cadC** is suppressed.

A possible explanation for both observations would be the formation of hydrogen bonds between the hydroxyl/formyl group and the exocyclic amine of the cytosine moiety (**5fdC**: Figure 51, **5hmdC** not shown, refer to the appendix, p. 373). Hydrogen bond formation was reported for a **5fC** moiety in a 20-mer oligonucleotide studied by Dubini *et al.* in a collaboration project of the Rovó and Carell groups within SFB1309 (refer to chapter III.1).[194] Further investigation, for example by geometry optimization calculations, would be necessary to provide further evidence for this hypothesis.
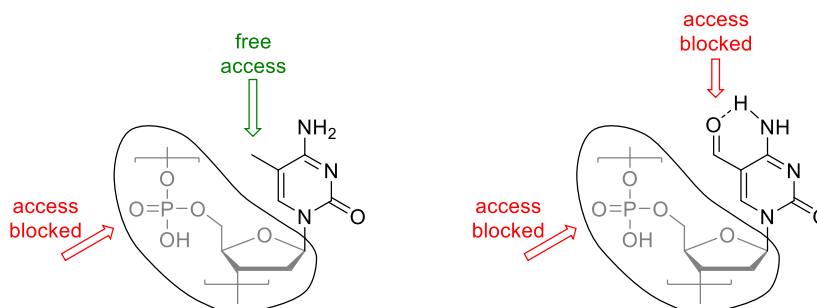
*Figure 51: Spatial access to the methyl/formyl group in a **5mC/5fC** containing oligonucleotide, the situation in **5hmC** is not shown (refer to the appendix p. 373).*

Furthermore, the high reactivity of **O-2** towards **C-6** is rather surprising: the nucleoside **5mdC** was observed by David Schmidl to react for >70 min with **C-6** at concentrations of [**5mdC**] = 1 mM and [**C-6**] = 5 mM.[14,238] The reaction of **O-2** and **C-6** was observed to be complete within 15 min at a concentration of [**O-2**] = 0.125 mM and [**C-6**] = 1 mM, accounting for a ~37-fold increase in reactivity. An explanation for this increased reactivity might be electrostatic attraction of the positively charged **C-6** ion by the negatively charged phosphate backbone of **O-2**. Additionally, π-stacking interactions of the ligand **L-1** in **C-6** with nucleobase moieties in **O-2** might provide a second reason for the increased reactivity.

Side-Product Analysis

To confirm that the observed reactivity is indeed the main reaction between **O-2** and **C-6**, several analytical techniques were employed to screen for side products. In a first experiment, the undigested product mixture of **O-2** was analyzed using triple quadrupole mass spectrometry for any traces of the relevant nucleosides. Detection of significant levels of nucleosides would have implied that the oligonucleotide is decomposed during reaction with **C-6**. However, no traces of **dA**, **dU**, **dC**, **dG**, **5mdC**, **5hmdC**, **5fdC**, **5cadC**, or **8-oxo-dG** were detected. The digested product mixture was then analyzed using HPLC-MS, but no significant signals were detected in addition to those corresponding to the expected nucleosides (**dA**, **dU**, **dC**, **dG**, **5mdC**, **5hmdC**, **5fdC**, **5cadC** or **8-oxo-dG**).
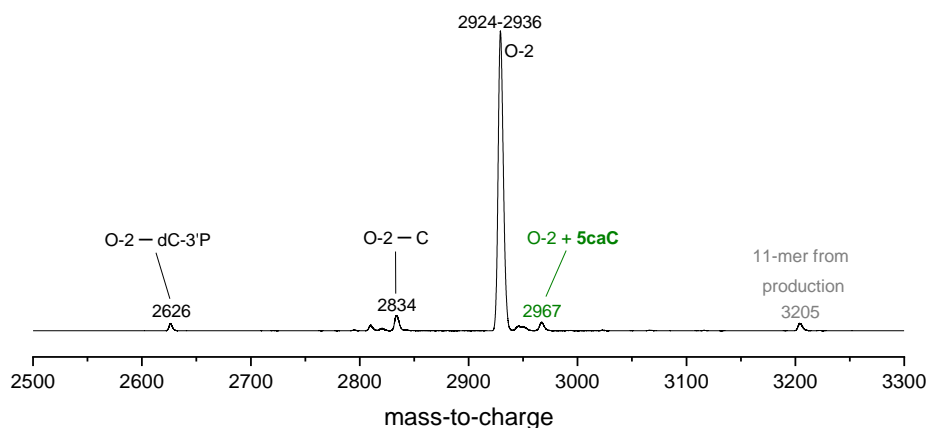
*Figure 52: Excerpt of a MALDI-TOF MS spectrum of the reaction of **O-2** with **C-6**. Relevant signals are denominated. Reaction conditions: [**O-2**] = 0.25 mM, [**C-6**] = 1 mM, H$_2$O, T = 23°C.*

Next, MALDI-TOF MS analysis was performed. It needs to be stated that due to the large analytes (mass of **O-2**: 2933 amu) in addition to deviation of the used instruments (~3 m/z) broad signals were obtained. For the untreated **O-2** sample a signal between 2924-2936 m/z was observed. Therefore, exact assignment of structures is difficult, but nonetheless general observations were made that fit well with the previously discussed results.

The MALDI-TOF MS spectrum of the untreated **O-2** sample showed that both a 9-mer as well as an 11-mer impurity were present, albeit at very low levels (2626 and 3205 m/z, not shown, refer to the appendix, Figure 196, p. 373). In the reaction of **O-2** with one equivalent of **C-6** several additional signals were observed (Figure 52 and Figure 53), e.g. a slight increase in the signal at 2626 m/z.
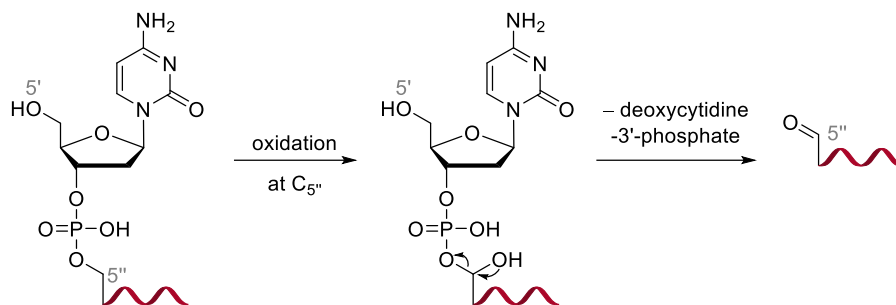
Scheme 43: Postulated mechanisms responsible for the loss of a deoxycytidine-3'-phosphate fragment at the 5' end of the oligonucleotide substrate.

A possible explanation for this would be oxidation at the 5' carbon atom of the second-to-last nucleotide (Scheme 43, denominated C$_{5''}$) on the 5' end of the oligonucleotide strand. Formation of a formyl group on this C$_{5''}$ carbon atom would result in the loss of a deoxycytidine-3'-phosphate fragment (291 m/z).
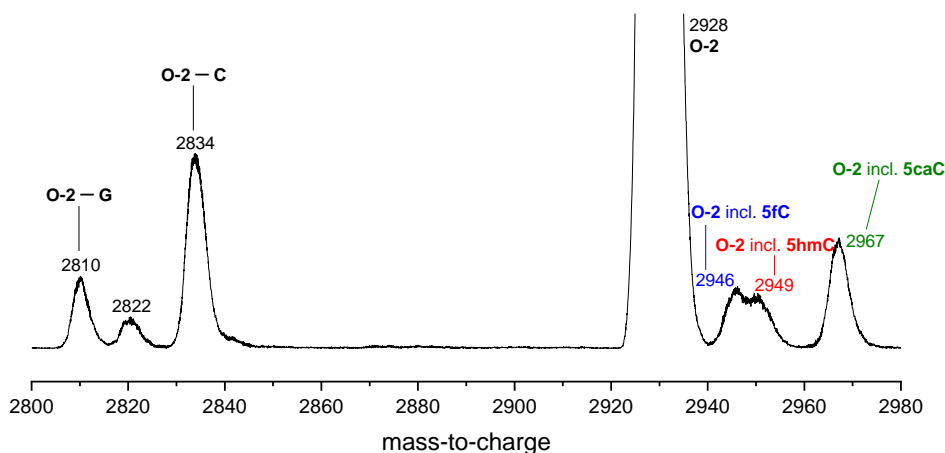
*Figure 53: Zoomed-in excerpt of a MALDI-TOF MS spectrum of the reaction of **O-2** with **C-6**. Assigned signals are denominated, **O-2** incl. **5hmC/5fC/5caC** refers to the desired oligonucleotide product in which the **5mC** moiety has reacted to the natural metabolites. Reaction conditions: [**O-2**] = 0.25 mM, [**C-6**] = 1 mM, H_2O, T = 23°C.*

In addition, signals were detected at -95 m/z and -135 m/z relative to that of **O-2** (Figure 53), these would correspond to loss of a **C** or **G** nucleobase fragment while simultaneously an oxygen atom is gained. Oxidation of the 1' position of the terminal nucleotides on either end of the strain, **dC** on the 5' end, **dG** on the 3' end, with subsequent loss of the nucleobase and formation of a lactone would be a likely mechanism (Scheme 44**A** and **B**). This hypothesis is supported by the observation of 2'deoxy-γ-ribonolactone as well as **5mC** in reactions of **C-6** with **5mdC** (Scheme 44**C**, experiments performed together with David Schmidl, results published in 2021[14]).
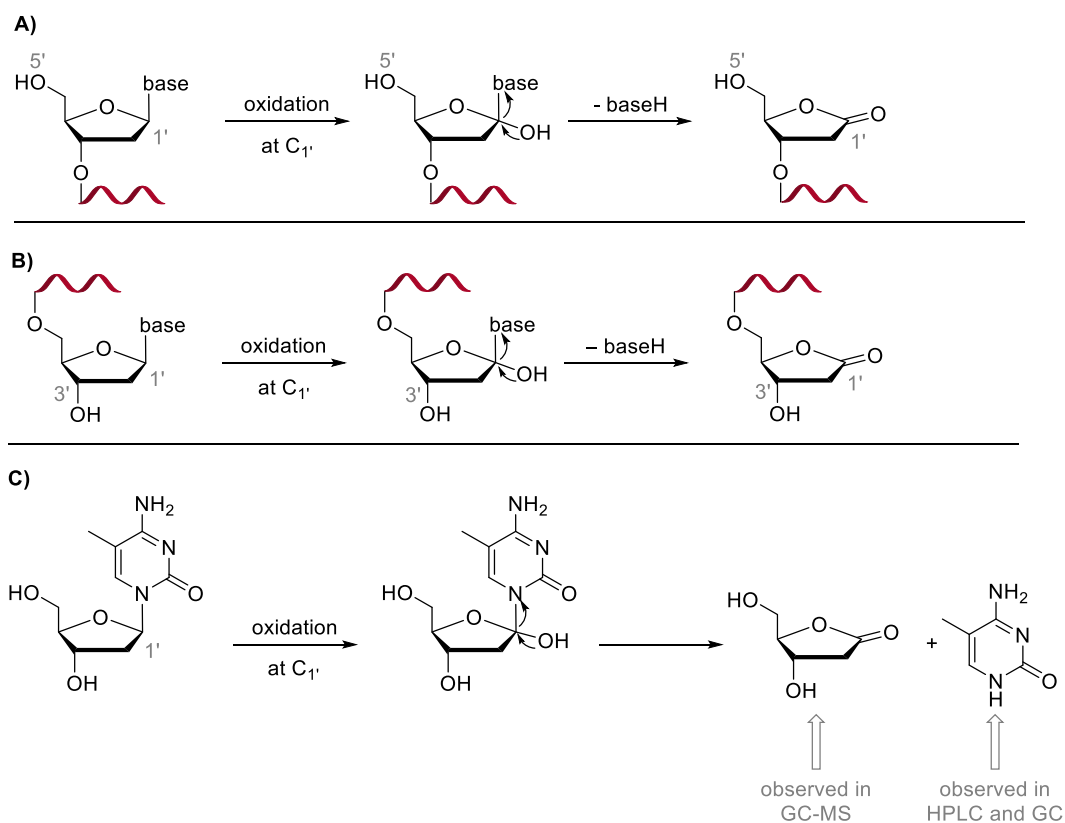
*Scheme 44: Postulated mechanisms responsible for the loss of a nucleobase fragment (baseH) at the 5' (**A**) or 3' end (**B**) of the oligonucleotide substrate **C**) Observed C1' oxidation in the reaction of **C-6** with **5mdC**.[14,238]*

Originally only for side-product analysis intended, MALDI-TOF MS confirmed the previously discussed results of successful **5mC** oxidation: signals corresponding all expected structures **O-2** incl. **5hmC**, **O-2** incl. **5fC**, and **O-2** incl. **5caC** were observed (Figure 53).

The use of four equivalents of **C-6** resulted in significantly more side reactions, the consecutive loss of two nucleobase fragment was observed (not shown, refer to the appendix, Figure 197, p. 374).

Whereas side-reactions were indeed observed in MALDI-TOF MS experiments, no interior strand breaks or other significant side reactions seem to have occurred. The only side reactions that were observed only involved the strand ends of the oligonucleotide. In larger oligonucleotide structures, which represent one of the next targets in this project, these would then be negligible compared to interior **5mC** oxidation.

Double-Stranded DNA

The next step to increase substrate complexity would be the use of double-stranded DNA. To that end, the base-pairing properties of the two complementary strands **O-2** and **O-2C** was tested as a first measure. Agarose gel electrophoresis confirmed that the two strands paired, as a UV-active band was observed for **ds-O** but none for the single strand **O-2** (Figure 54).
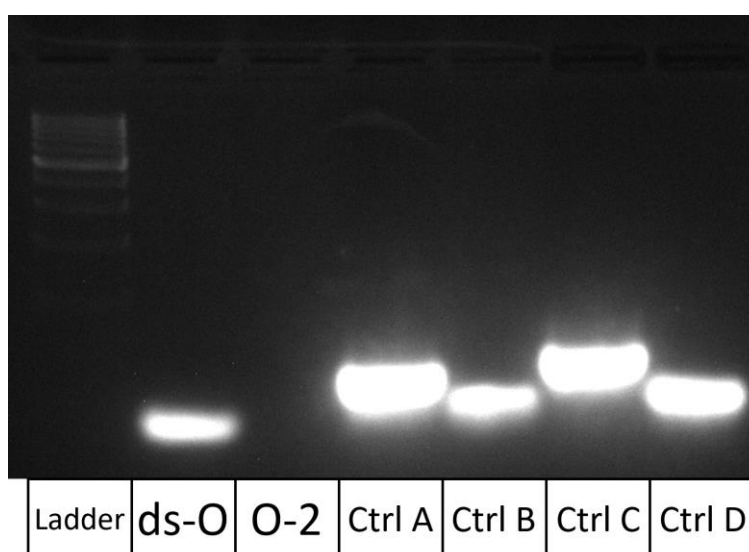
*Figure 54: Agarose gel (5%) of **ds-O** (**O-2** + **O-2C** + NaCl), **O-2** (**O-2** + NaCl), Ctrl A (20-mer dsDNA + 5 mM NaCl), Ctrl B (20-mer ssDNA + NaCl), Ctrl C (30-mer dsDNA + NaCl), Ctrl D (30-mer ssDNA + NaCl). Concentration of each added single-stranded DNA sample was [ssDNA] = 0.25 mM. [NaCl] = 5 mM. dsDNA was prepared by mixing two complementary ssDNA strands at [ssDNA] = 0.25 mM and [NaCl] = 5 mM at room temperature, heating to 95 °C, then slowly cooling to room temperature.*

In the next step, the melting curve of the **ds-O** sample determined by measuring the absorbance between λ = 190-350 nm (Figure 55**A**) and plotting the absorbance at λ = 260 nm vs. the applied temperature (Figure 55**B**, blank squares). Calculating the first derivative gave the melting point as a local maximum (Figure 55**B**, red triangles) at T = 27 °C. At the melting point temperature, DNA exists in a mixture of 50% annealed and 50% unannealed strands. As the determined melting

point of **ds-O** is very close to the temperature at which the experiments with **C-6** are conducted (22-23 °C), incomplete annealing was assumed.
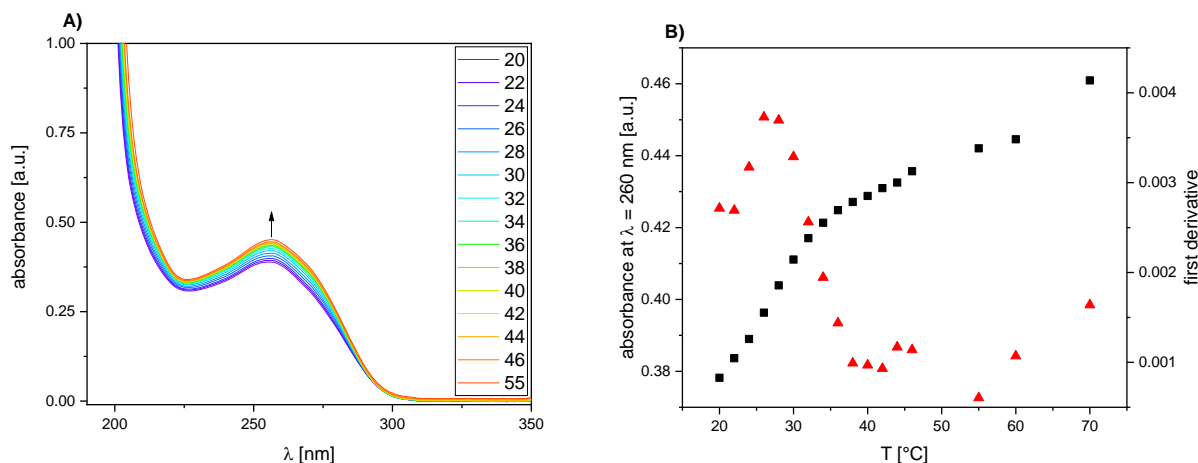
*Figure 55: **A**) UV/Vis spectra of **ds-O** in water at variable temperatures. **B**) Absorbance values at λ = 260 nm (black squares) and their derivatives (red triangles). Annealing conducted at [**ds-O**] = 0.125 mM. UV-Vis measurement conducted at [**dsO**] = 6.25 µM.*

This limitation in mind, **ds-O** was reacted with **C-6** and the levels of nucleosides **5mdC**, **5hmdC**, **5fdC**, and **5cadC** determined. Significantly lower levels were determined for all relevant oxidized modifications than if the single-stranded oligonucleotide **O-2** substrate was used. As a control measurement, the complementary strand **O-2C** was also reacted with **C-6**, here, no significant levels for **5hmC**, **5fdC**, and **5cadC** were detected (Figure 56).

A significant reduction in **5mC** oxidation was observed. This is interpreted as a first indication that **C-6** does not oxidize **5mC** moieties as well in a double-stranded DNA context as in a single-stranded sample. The residual observed activity likely stems from single-stranded substrate that had not annealed.
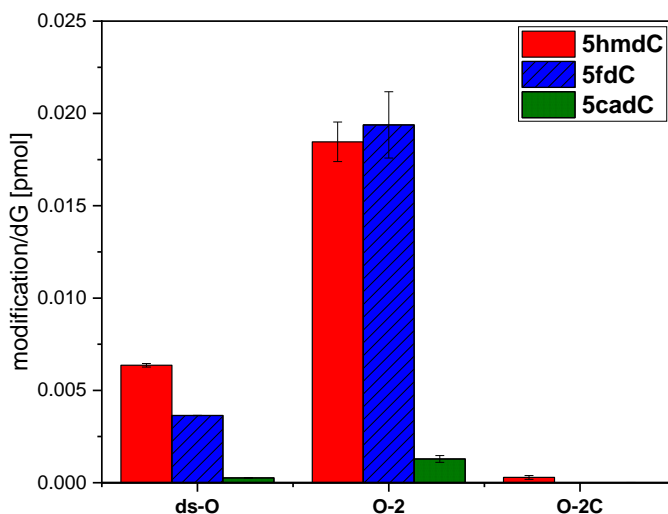
*Figure 56: Detected relative levels of **5hmdC** (red), **5fC** (blue striped), and **5cadC** (green dotted) in samples that were annealed to double-stranded DNA (**ds-O**) and subsequently treated with **C-6**, and the respective control experiments (**O-2** = **O-2** treated with **C-6**, **O-2C** = **O-2C** treated with **C-6**); Conditions: [**S**] = 0.125 mM, [**C-6**] = 0.5 mM, H$_2$O, T = 23 °C, t = 30 min. Error bars represent standard deviation between technical replicates.*

Preliminary Conclusion

It was shown that **C-6** serves as a functional model for TET enzymes on **nucleobase**, **nucleoside**, and even short **oligonucleotide** substrates. The reaction is **specific**; no side reactions are observed on the nucleobase moiety. When using nucleosides as substrates, the most prevalent **side reaction is oxidation of the 1' carbon** atom resulting in the formation of nucleobase and 2'-deoxy-γ-ribono-lactone. Oligonucleotides are only **degraded on the strand ends**; **no internal strand breaks** were detected. Nucleobases **A** and especially **G** are inert toward **C-6**, the **formation** of **8-oxo-dG** was **not observed**. Double-stranded DNA is significantly less reactive than single-stranded DNA.
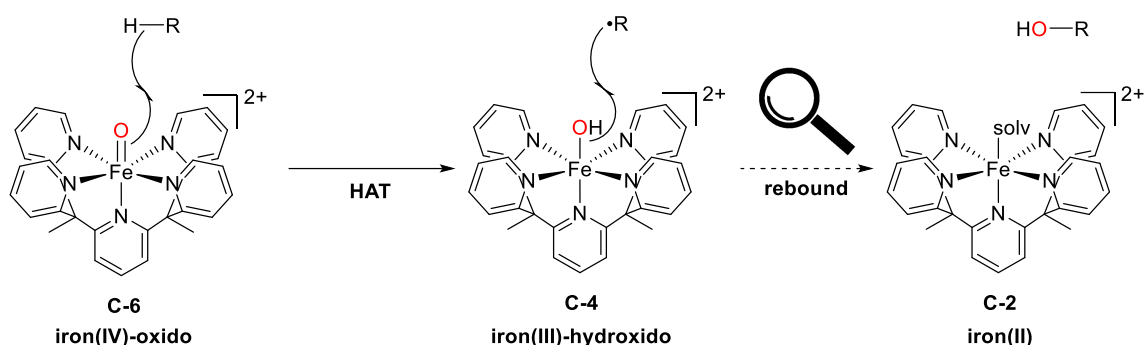
Scheme 45: Reaction mechanism of **C-6** with an aliphatic C-H bond via a hydrogen atom transfer (HAT) reaction to an iron(III)-hydroxido intermediate and subsequent, postulated, rebound mechanism. solv = solvent, **C-2** refers to the structure with H_2O as solvent.

Kinetic data shows that **C-6** reacts *via* a **two-step mechanism**: first a hydrogen atom is transferred from the substrate to the oxido moiety in the **rate limiting hydrogen atom transfer** (HAT) step. The resulting iron(III)-hydroxido moiety is then presumed to react with the carbon-centered organic radical to form the product in a rebound type reaction.

Whereas the first step is supported by determination of the rate law and kinetic isotope effect studies, the second step lacks evidence and further investigation is necessary. Identification of the iron(III)-hydroxido intermediate, its synthesis, and subsequent characterization represent starting points for this endeavor. Preliminary results and identification of iron-based side products can be found in chapter IV.
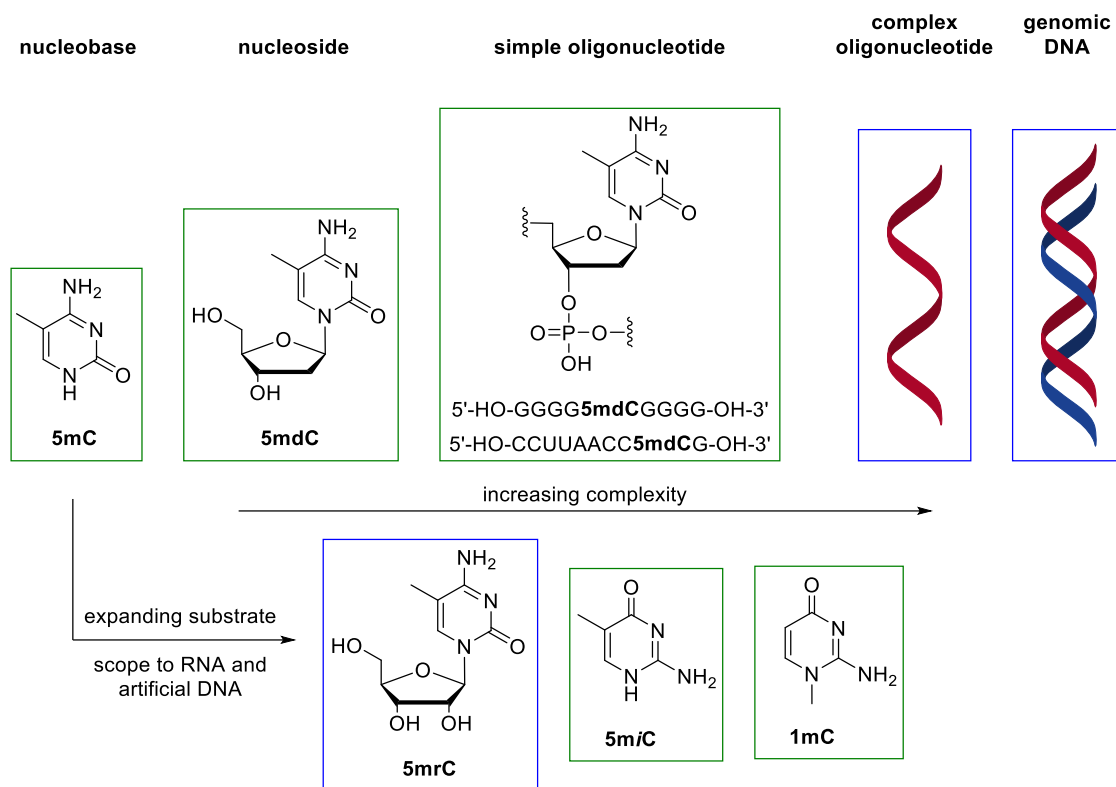
Figure 57: Increasing complexity in the substrates used for the development of a functional model of TET enzymes. Substrates within green boxes were successfully used in biomimetic studies in this work. The blue boxes indicate targets for further investigations.

Next, more complicated oligonucleotides, both as single- and double-strands, should be investigated. Furthermore, the corresponding RNA nucleosides should be investigated for the influence of the 2'-hydroxyl function of the reactivity of **C-6** towards the methyl moiety on **C**. The latter project was started by David Schmidl and is continued by Annika Menke.

Within this work, expanding the nucleobase substrate scope to include artificial nucleobases such as 5-methyl-*iso*-cytosine (**5m*i*C**) and 1-methyl-cytosine (**1mC**) was attempted. Reaction kinetics of **C-6** towards a broader range of substrates (Figure 57) were conducted to provide further insight into the fundamentals of natural and synthetic DNA bases. Both mentioned substrates, and several more, were investigated in a collaboration project of Rachel Janßen (Daumann group), Annika Menke (Daumann group), Fabian Zott (Zipse group), and myself (refer to chapter III.8).

8. Synthetic Epigenetics and the Nucleobase Comparison Project

Why Synthetic Epigenetics?

Two of the main goals of synthetic DNA research are to 1) increase information storage density in DNA and 2) study characteristics of natural DNA. Similar to *natural* epigenetics adding a layer of information to *natural* DNA, *synthetic* epigenetics could expand *synthetic* DNA analogs' information density even further. For standard terran DNA, significant progress was achieved by Mayer *et al.* in 2016: the authors reported on an epigenetics-based procedure to encode three layers of information into a single strand of DNA: "normal" sequencing yields one result (a picture of Charles Darwin), bisulfite sequencing yields another result (a picture of Alan Turing), coupled $KRuO_4$/bisulfite sequencing yields yet another result (a picture of Rosalind Franklin, Figure 58).[247] By expanding the genetic code, even more information could be encoded – and still more by combining an artificially expanded DNA with an epigenetic-inspired system.
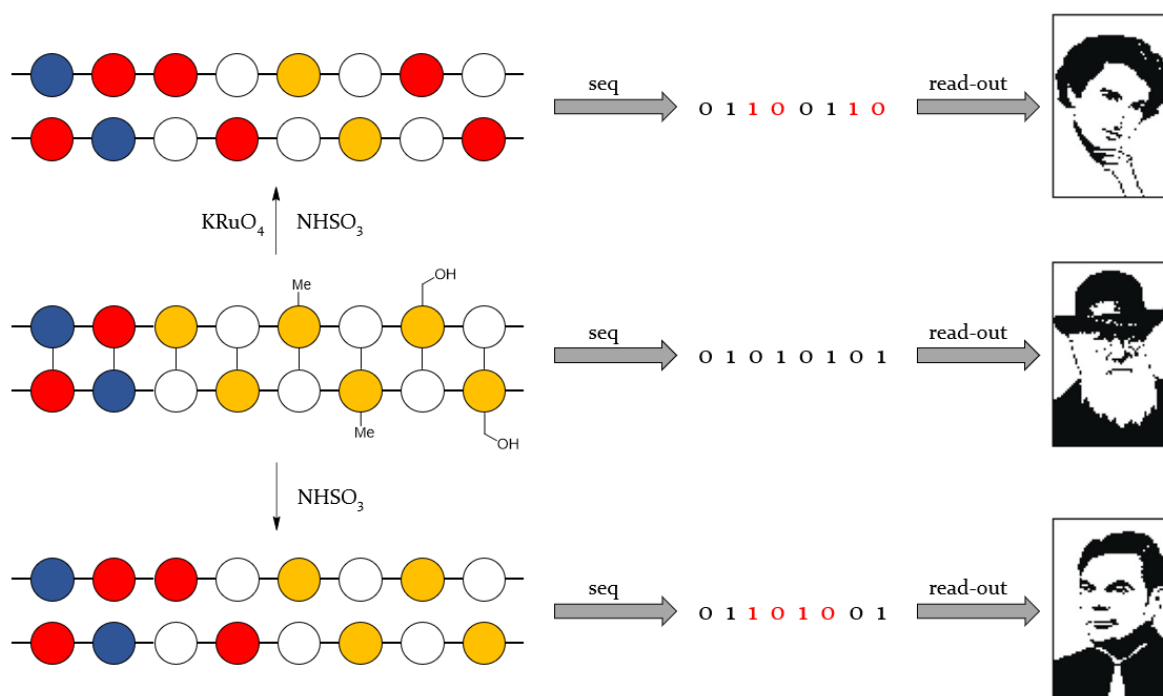
Figure 58: Storing three layers of information in a single strand of DNA: sequencing of the initial strand yields one result, bisulfite sequencing another, and coupled oxidative-bisulfite sequencing yet another. Adapted from Mayer et al.[247]

As mentioned in chapter III.1, standard terran DNA consists of the four canonical bases **A**, **T**, **G**, and **C** as well as some modified versions thereof. However, scientists have been attempting to further increase the number of nucleotides that form DNA-like structures.[248–251] One recent, remarkable example is "*hachimoji*" (from Japanese 八 "*hachi*" – *eight* 文字 "*moji*" – *letters*) DNA/RNA by Steven Benner and his research group that builds on decades of artificial DNA research.[228] In *hachimoji* DNA/RNA the natural alphabet is expanded to an eight-letter system that forms four orthogonal base pairs. *Hachimoji* DNA does not perturb natural characteristics of DNA, meets the requirements for Darwinian evolution, and was even transcribed to the corresponding RNA. One of the synthetic base pairs in *hachimoji* system is the *iso-*

guanine/*pseudo*-cytosine (DNA) or *iso*-guanine/*iso*-cytosine (RNA) pair (Figure 59), which will be of interest for this work.
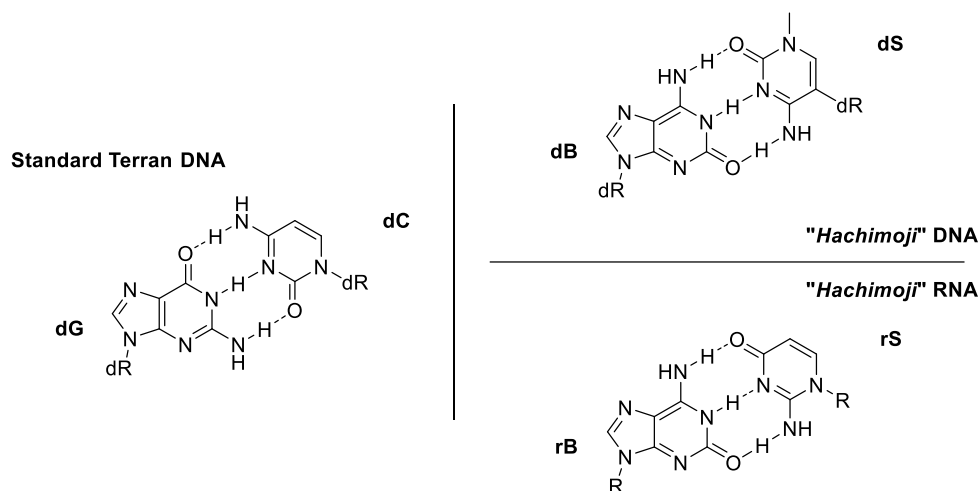
*Figure 59: Standard terran DNA base pairing of **G/C** compared to selected examples of synthetic "hachimoji" DNA (**dB/dS**) and RNA (**rB/rS**). **dR** refers to a 2'-deoxyribose backbone, **R** to a ribose backbone.*

Albeit the same letter (**S**) is used for both nucleobases in Benner's original work, the bases pairing with *iso*-guanine (**B**) are structurally different. **dS** refers to 2'-deoxyribo-*N*-methyl-*pseudo*-cytidine, **S** on the other hand refers to ribo-*iso*-cytidine (Figure 59). As the focus in this work is on nucleobases, new designations are chosen. On a nucleobase level, discrimination based on the pattern of the heteroatomic substituents is a sensible approach for classification. **C** is used as a basis, swapping the exocyclic amine at position 4 with the carbonyl of the urea moiety at position 2 then results in *iso*-cytosine. This is equivalent for **5mC**/5-methyl-*iso*-cytosine (**5miC**).

Substitution within a nucleoside/nucleotide context provides another method for nomenclature. Cytosine is usually bound to (2'-deoxy)ribose at its 1*N*-position *via* a glycosidic bound, if it is, however, bound *via* a C-C bond at the 5-position, it is referred to as *pseudo*-cytosine. The 1*N*-methylated derivative is therefore referred to as 1m*p*C (Chart 9A). Equivalent nomenclature is valid for uracil: when bound to a (2'-deoxy)ribose backbone by a C-C Bond it is referred to as *pseudo*-uracil. In the case of thymine, the corresponding carbon bound *pseudo* structure is referred to as 1-methyl-*pseudo*-uridine **1mΨ** (Chart 9**B** and chapter III.1).
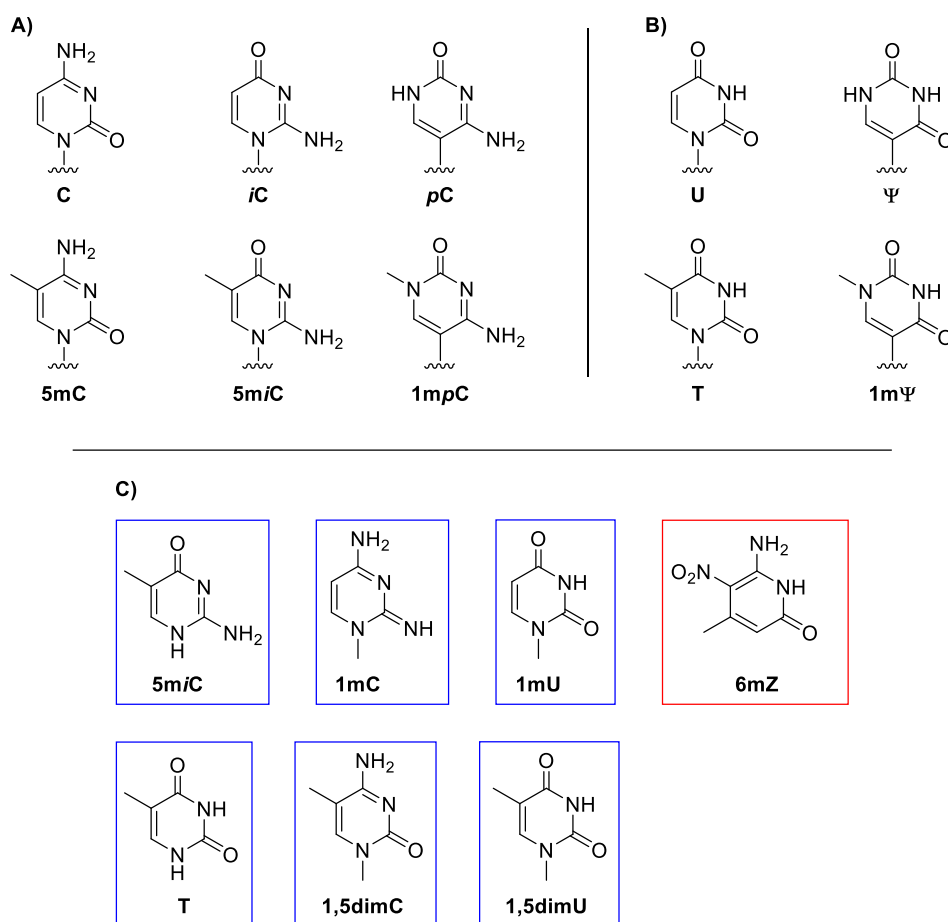
Chart 9: A) *First row: C and its derivatives* iso-*cytosine* (*iC*) *and* pseudo-*cytosine* (*pC*). *Second row:* **5mC** *and the corresponding derivatives 5-methyl-*iso-*cytosine* (**5miC**) *and 1-methyl-*pseudo-*cytosine* (**1mpC**). **B)** *First row:* **U** *and its derivative* pseudo-*uracil* (**Ψ**). *Second row:* **T** *and the corresponding derivative 1-methy-*pseudo-*uracil* (**1mΨ**). *Structures are shown as nucleobases bound to (synthetic) DNA, but are referred to by their nucleobase designation.* **C)** *Non-canonical, methylated nucleobases. Structures that were studied in this work are marked in blue boxes, the structure* **6mZ** *(6-amino-4-methyl-5-nitropyridin-2(1H)-one, name derived from original designation* **Z**, *6-amino-5-nitropyridin-2(1H)-one, according to Benner* et al.*)*[228] *in the red box presents a target for further investigations.*

From these structures, suitable substrates for investigation of a synthetic epigenetics system were identified and investigated: **5miC**, **1mC**, **1mU**, 1,5-dimethyl cytosine (**1,5dimC**), and 1,5-dimethyl uracil (**1,5dimU**) (Chart 9C, blue boxes). **6mZ** (6-amino-4-methyl-5-nitropyridin-2(1H)-one, Chart 9C, red box) is also based on *hachimoji* DNA (base **Z**, **6-amino-5-nitropyridin-2(1H)-one**, nomenclature according to Benner *et al.*) and might present a target for further investigations.

Initial Investigations

5miC was chosen as the first substrate to be investigated. Synthesis of **5miC** was achieved using a literature procedure first published by Stoss *et al.*[252] In addition, attempts were made to synthesize the expected oxidation products 5-hydroxymethyl-*iso*-cytosine (**5hmiC**), 5-formyl-*iso*-cytosine (**5fiC**), and 5-carboxy-*iso*-cytosine (**5caiC**) as reference samples for later analysis (Scheme 46). Unfortunately, these attempts were not met with success (a discussion of these syntheses can be found in chapter III.9). However, the reactivity of **C-6** towards **5miC** was

investigated and **5hm*i*C**, **5f*i*C**, and **5ca*i*C** were identified as oxidation products (Scheme 46, Figure 202).
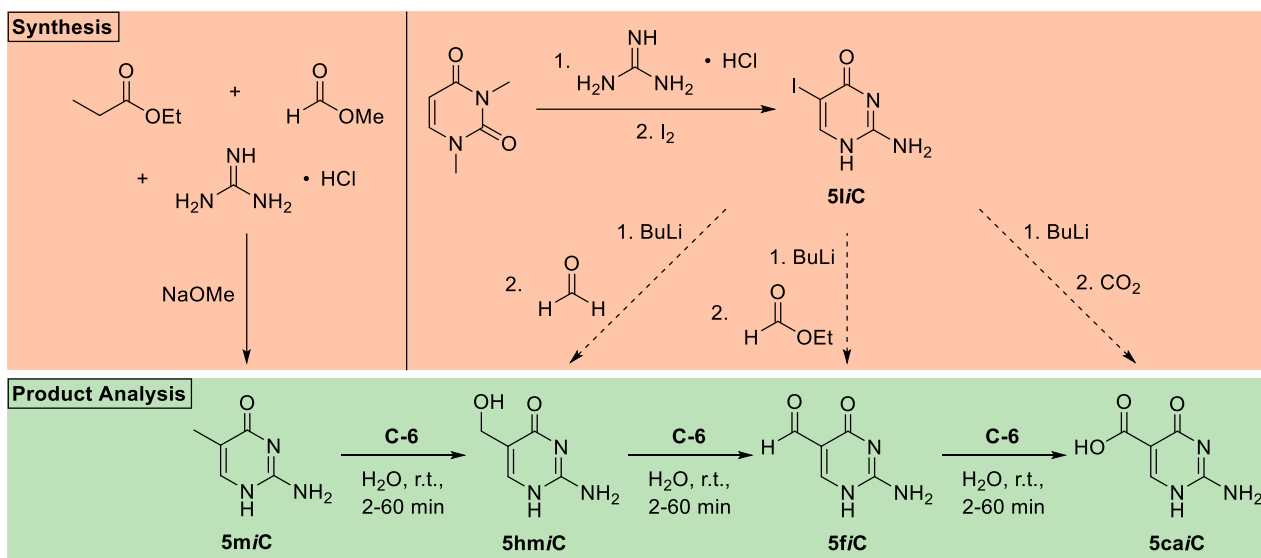
Scheme 46: Syntheses of **5m*i*C** and **5I*i*C** were performed according to literature known procedures. Subsequent derivatization of 5IiC was attempted to synthesize **5hm*i*C**, **5f*i*C**, and **5ca*i*C** as reference sample for GC-MS product analysis of the reaction of **5m*i*C** with **C-6**.

In a first experiment, **C-6** was reacted with **5m*i*C** in water at room temperature, similar to the reactions of **5mC** discussed in chapter III.4. In the obtained GC-MS spectra, **5f*i*C** and **5ca*i*C** were identified as products. While **5f*i*C** was already observed after 2 min reaction time, significant levels of **5ca*i*C** could only be identified after 60 min reaction time (refer to appendix, Figure 202, p. 377). **5hm*i*C** could not be observed using GC-MS, but was later observed by Rachel Janßen using UHPLC-MS.[15,253] It can therefore be concluded that **5m*i*C** reacts in an analogue fashion to **5mC** when exposed to **C-6**.

The Nucleobase Comparison Project

I was then joined by two colleagues, Annika Menke and Rachel Janßen, for the further investigation of **5m*i*C** and **1mC**. **1mU** was also synthesized and studied as a substrate for **C-6** (refer to chapter III.9 for synthetic details). Fabian Zott of the Zipse research group at LMU supplied a first batch of 1mU, a sample **1,5dimU** as well as valuable calculations to support our measurements. The results of this collaborative project, which was part of the SFB1309 "Chemical Biology of Epigenetic Modifications", were published in 2021.[15]

Rachel Janßen investigated the reactions of **1mC** and **1,5dimC** with **C-6** and found that the 1*N*-methyl group of **1mC** reacts very slowly to the corresponding oxidized derivatives (Scheme 47, detected *via* direct HPLC-MS measurement of the reaction solution). These then decompose during lyophilisation (a necessary step during work-up) to **C**, which was observed in UHPLC-MS

measurements. This also applies to **1,5dimC**: whereas most reactivity is observed at the carbon-bound methyl group yielding **5hm-1mC**, **5f-1mC**, and **5ca-1mC**, the partially demethylated derivatives **5mC** and **5caC** were also observed, due to the same mechanism described for **1mC** (refer to the appendix, Scheme 115, p. 377).[15,253]
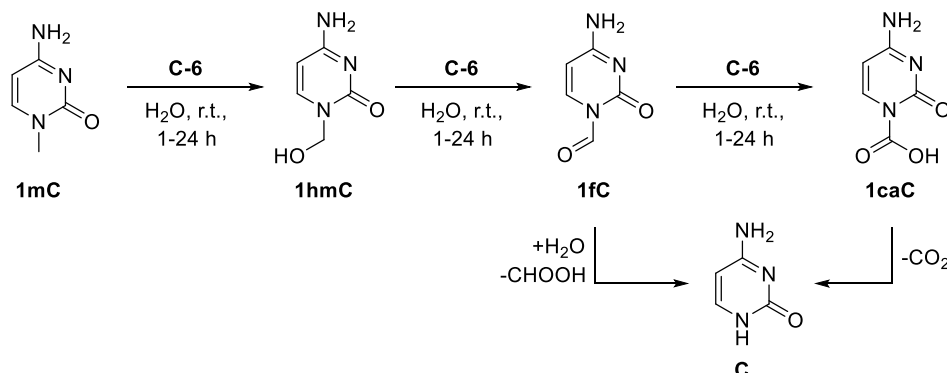
*Scheme 47: Reaction sequence of **1mC** with **C-6** to give **1hmC, 1fC, 1caC**. Deformylation/decarboxylation of the latter two yields **C**.*

These product analyses at hand, Annika Menke and I measured the reaction rates v and rate constants k_S of a series of **C**- and **U**-derived substrates (Chart 10). The rate constants were then compared to calculated values of the respective BDEs.
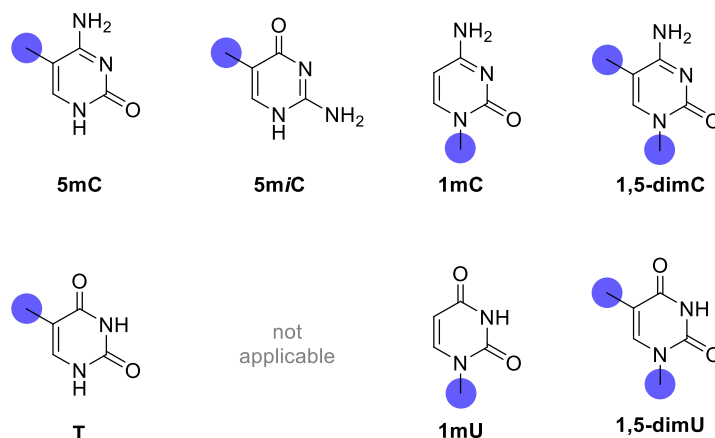
*Chart 10: **C**- and **U**-derived substrates investigated in the collaboration project of the Daumann and Zipse groups. The relevant methyl groups are marked with a blue circle.*

Reaction rates v were measured by using the same methodology that was employed to study **5mC** (refer to chapter III.4): the absorbance at $\lambda = 718$ nm was monitored and the method of initial rates applied, then the reaction rates were calculated by linear regression.

For all substrates, a decrease in the absorbance at $\lambda = 718$ nm was observed. For **1mC** and **1mU**, this decrease was observed to be significantly slower than for all other substrates (Figure 60**A**). A linear increase in reaction rate upon increase of **C-6** was observed for all substrates (Figure 60**B**).
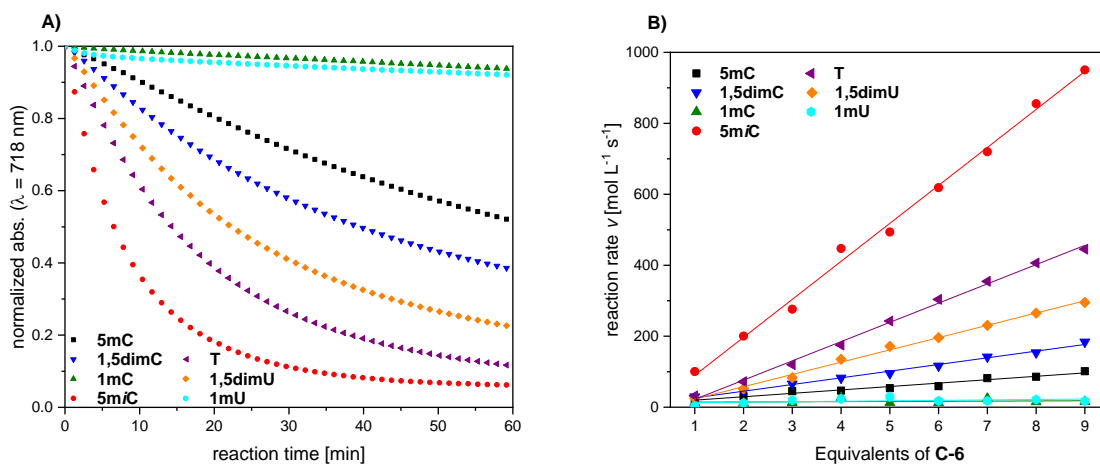
*Figure 60: Observed decrease in the absorbance at λ = 718 nm in reactions of **C-6** with **5mC** (black squares), **5miC** (red dots), **1mC** (green triangles), **1,5dimC** (blue inverted triangles), **1,5dimU** (orange diamonds), **T** (purple twisted triangles) and **1mU** (cyan dots).*

The substituents on the pyrimidine backbone of the substrates seem to significantly influence the reactivity: **U**-derived structures **T**, **1mU**, **1,5dimU** were observed to react faster than their respective **C**-derived counterparts **5mC**, **1mC**, and **1,5dimU**, respectively, whereas the *iso*-cytosine-derived substrate **5miC** reacts even faster. Interestingly, the nitrogen-bound methyl group in the dimethylated substrates **1,5dimC** and **1,5dimU** seems to have opposite effects on the reactivity, depending whether **C** or **U** is the base structure: **1,5dimC** was observed to react faster than its mono-methylated counterpart **5mC** whereas 1,**5dimU** reacts faster than **T**. **1mC** was observed to react significantly slower than all other substrates, **1mU** shows a faster initial decrease but then shows a similar rate to **1mC**.

The "factor of the impact of **C-6**" *f* on the reaction rate *v* was calculated for selected substrates by the following equation (**Eq. 4**):

$$f = \frac{v(x \; equiv. \; of \; \boldsymbol{C-X})}{v(1 \; equiv. \; of \; \boldsymbol{C-X})}$$

<div align="right">**Eq. 4**</div>

For a reaction that is kinetically controlled by the amount of **C-6** present in the reaction a linear correlation at the angle bisector is expected. Lower values for *f* indicate that the substrate is controlling the reaction rate.
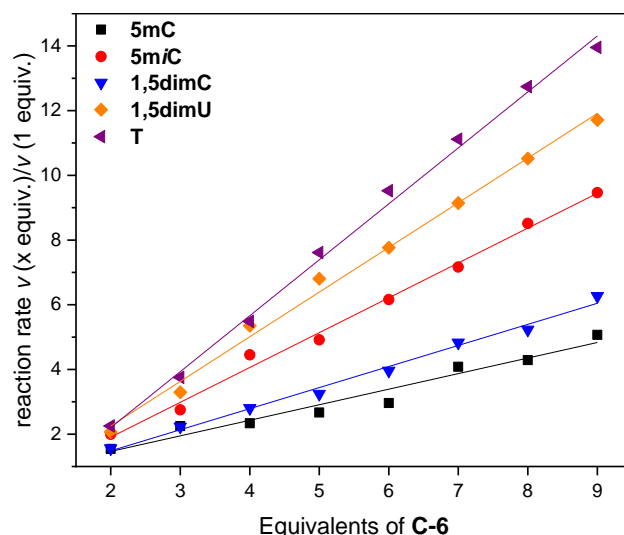
*Figure 61: Plot of "the factor of impact of **C-6**" f (Eq. 4) vs. the added equivalents of **C-6**. Values for **5miC** (red dots) are observed at the angle bisector, those for **5mC** (black squares) and **1,5dimC** (blue inverted triangles) below it, those for **T** (purple twisted triangles) and **1,5dimU** (orange diamonds) above it. Conditions: [S] = 1 mM, [**C-6**] = 1-9 mM, H$_2$O, t = 5 min, 30 °C.*

Linear correlations were observed for all substrates, confirming that indeed no saturation behavior takes place. However, only **5miC** expresses the mentioned expected behavior, its f values are situated on the angle bisector. Interestingly, the **C**-derived substrates **5mC** and **1,5dimC**) show f values that are lower indicating that these reactions are kinetically controlled by the substrate. On the other hand, both **U**-derived substrates (**T** and **1,5dimU**) display higher f values. Due to their low reaction rates, **1mC** and **1mU** were excluded from this analysis.

The second-order rate law (**Eq. 5**) found for the reaction of **5mC** with **C-6** was assumed valid for all reactions and used to calculate the corresponding rate constants k_S. This assumption was supported by the linear behavior of the observed reaction rates v upon increase of **C-6** (Figure 60**B**), however, dependence on the substrate concentration was not tested.

$$v = k_s[\boldsymbol{S}][\boldsymbol{C-6}]$$ **Eq. 5**

The values for k_S range from 2.5-98.7 l mol^{-1} s^{-1} and correlate inversely to the BDEs calculated for the respective methyl group (Figure 62, relevant methyl groups are marked). The BDEs of the nitrogen-bound methyl groups in the dimethylated substrates **1,5dimC** and **1,5dimU** were calculated to be 413.9 and 414.9 kJ mol^{-1}, respectively. Due to the observed reactivity of **1,5dimC** and **1mC** (*vide supra*), reactivity at the 1N-methyl group was assumed to be minimal. The carbon-bound methyl group can therefore be assumed responsible for the observed reactivity of **1,5mC** and **1,5dimU**.

	1mC	**1mU**	**5mC**	**1,5dimC**	**1,5dimU**	**T**	**5miC**
k_S [l mol^{-1} s^{-1}]	2.5 ± 0.4	5.9 ± 1.6	10.7 ± 0.8	19.2 ± 0.8	34.3 ± 0.9	48.6 ± 0.3	98.7 ± 1.2
BDE [kJ mol^{-1}]	414.8	416.0	387.3	386.5	385.7	383.1	379.4

faster reaction
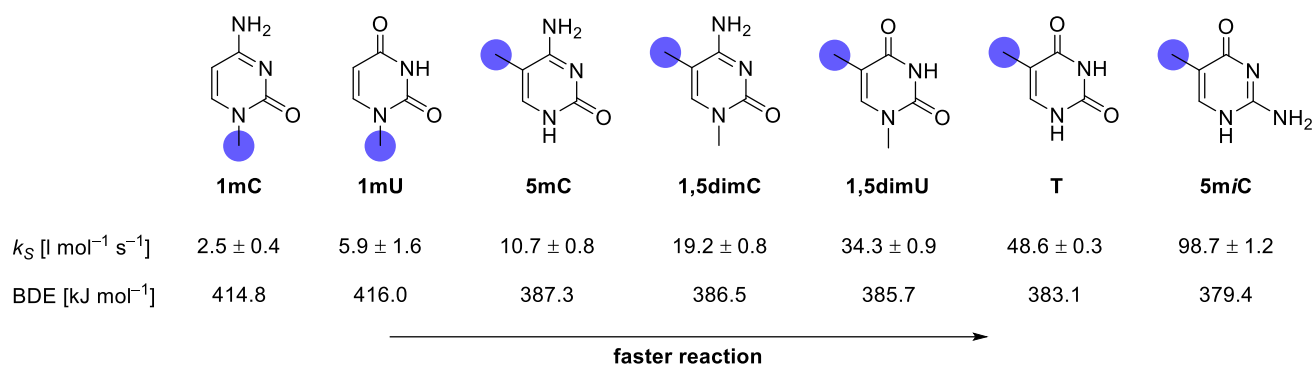
*Figure 62: Measured rate constants k_S of the reaction of the substrate with **C-6** and calculated BDEs, the relevant methyl groups used for calculations are marked. BDEs were calculated by Fabian Zott using on the SMD(H$_2$O)/DLPNO-CCSD(T)/CBS//(U)B3LYP-D3/6-31+G(d,p) level of theory.[15]*

The observed rate constants generally correlate with the calculated BDE values: the lower the BDE, the higher the rate constant. The only exception from this is **1mU**, which has a slightly higher BDE than **1mC** and should therefore be expected to react slower – however, its calculated rate constant k_S is slightly higher (5.9 vs. 2.5 l mol^{-1} s^{-1}). On the other hand, the long-term decrease in absorbance at λ = 718 nm in the reaction of **1mU** with **C-6** is very similar to that of **1mC** – only the first few minutes differ significantly. The deviation of **1mU** from the expected BDE-k_S correlation might therefore be the result of improperly chosen data analysis methods, as these first minutes were used for the calculation of the reaction rate v and the rate constant k_S. Nonetheless, the deviation is rather small and fits well within the general trend observed for all substrates.

The substrates' BDE values of the methyl groups indicated in Figure 62 were plotted vs. the rate constants k_S on a logarithmic scale (Figure 63). A linear Bell-Evans-Polanyi correlation was observed for the substrates that react primarily at their carbon-bound methyl group (**5mC**, **1,5dimC**, **1,5dimU**, **T**, and **5miC**). The only outliers in this graph are **1mC** and **1mU**, which can be explained by these being the only substrates that react solely at a nitrogen-bound methyl group.
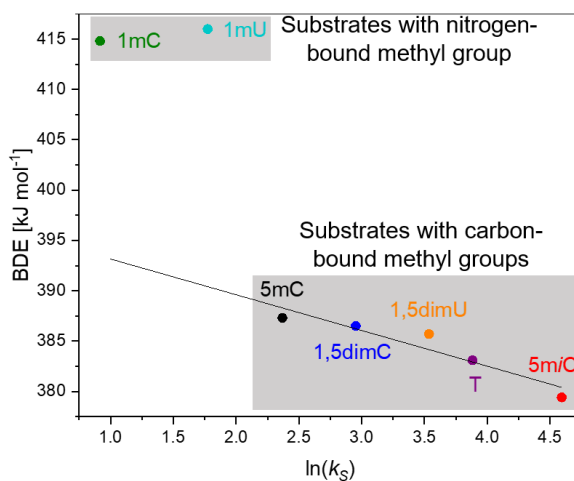
*Figure 63: Bell-Evans-Polanyi plot of the calculated BDE values in aqueous phase against the observed rate constants k_S on a logarithmic scale (R^2= 0.891). Substrates are grouped by those that react primarily at their carbon-bound methyl group (**5mC**, **1,5dimC**, **1,5dimU**, **T**, **5miC**) and the substrates that react at their nitrogen-bound methyl group (**1mC** and **1mU**).*

These results are remarkable, as they show that BDEs can be used to accurately predict the reactivity of **C-6** towards methylated nucleobases. Using these results, a synthetic epigenetics system could be devised that incorporates two different methyl substituents. These can be oxidized sequentially using **C-6**, yielding different read-outs upon sequencing.

For example, a sequence comprised of a substrate with a high reactivity (green circles in Figure 64) and one with low reactivity (yellow methylated circles in Figure 64) could be envisioned. Treatment of this synthetic DNA sample with **C-6** (or an optimized derivative thereof) for a short amount of time would result in the conversion of the substrate with high reactivity, whereas the low reactivity residues are not affected (Figure 64 upper sequence). This then results in a different read-out (a picture of the Matterhorn) compared to the original sequence (a picture of Kilimanjaro). If the sample is exposed to an oxidizing agent for a longer time period, however, both moieties are converted (Figure 64 lower sequence) and yet another read-out is obtained (a picture of the Tre Cime).
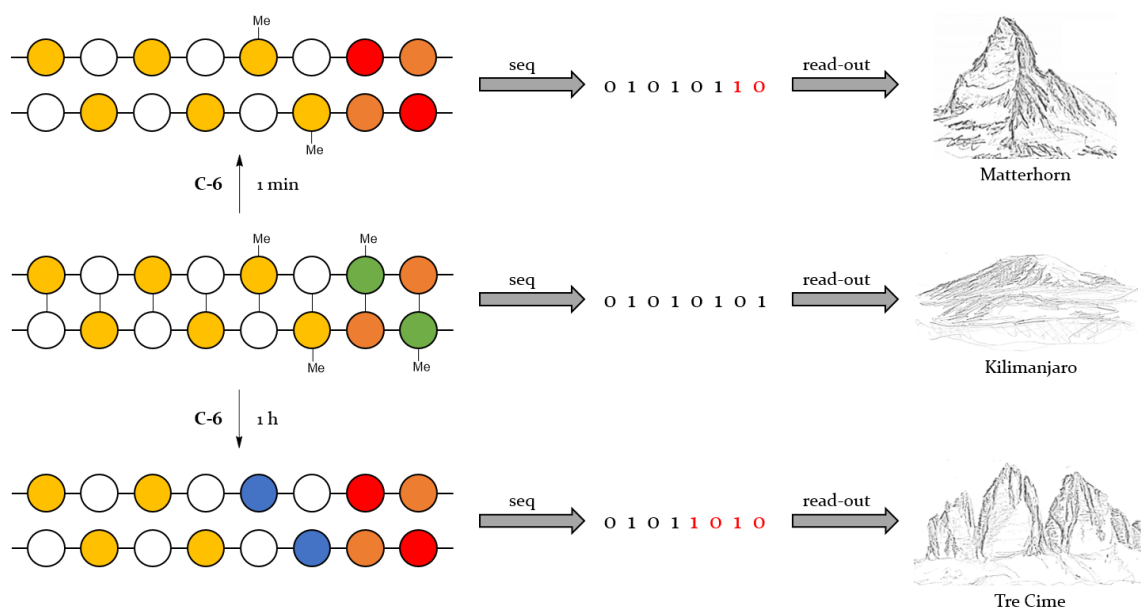
*Figure 64: Schematic representation of how differences in reaction rates with **C-6** might be exploited to store several layers of information: treatment of the original substrate with **C-6** for 1 min results only in conversion of one of methyl moieties (green methylated circles convert to red circles, upper sequence), whereas treatment for 1 h results in the conversion of both methyl moieties (green methylated circles convert to red circles and yellow methylated circles convert to blue circles, lower sequence). After read-out, different information is obtained. Scheme idea adapted from Mayer et al.[247]*

9. Miscellaneous: Syntheses and pH Dependence

Syntheses of Naturally Occurring Nucleobases

D$_3$-5mC synthesis was performed using literature known reactions that were modified slightly for higher yield.[254–257] Johann de Graaff started this project in his Master Thesis,[258] I then later optimized upon his initial work, starting with undeuterated reagents and later repeating all steps with deuterated reagents.

In the first step, 5-bromo-2,4-dimethoxypyrimidine is lithiated and then treated with methyl iodide (or D$_3$-methyl iodide) according to a procedure first published by Slatkin *et al.*[254] When performing this step, a side-product with a mass-to-charge ratio of roughly two times that of the desired product was observed (322.1955 m/z observed vs. 154.0742 m/z expected). This side-product also showed multiple distinct signals in ^{1}H NMR spectroscopy in a range where methoxy groups are expected (4.2-3.8 ppm) and was therefore tentatively assigned as a dimeric structure of the desired product. The occurrence of this dimer was attributed to relatively high concentrations (~0.5 M) and a long lithiation time frame (60 min). Therefore, lithiation was performed within a so-called Helmchen-Double-Schlenk-Flask (refer to the appendix p. 378),[259] which ensured isothermal addition of a diluted solution of *n*-butyl lithium (0.25 M) to a more dilute solution of the starting material (initial: 0.23 M, after addition of *n*-butyl lithium: 0.12 M). This resulted in an increase of ***III-13*** in yield from previously ~50% to ~67%.
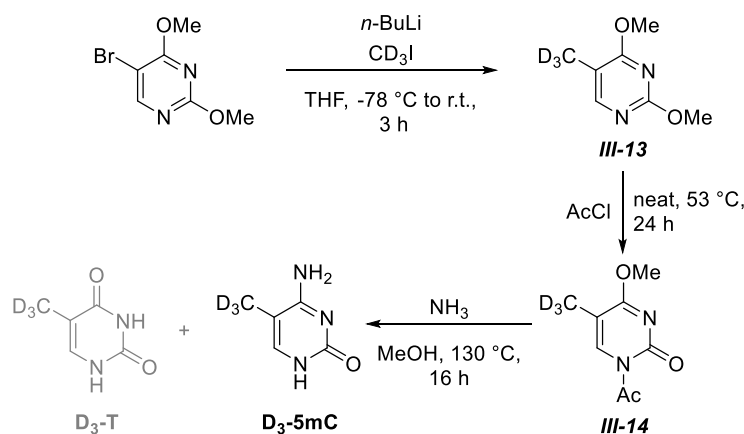
*Scheme 48: Three-step synthesis of **D₃-5mC** and D₃-thymine (**D₃-T**) as a side product, starting from 5-bromo-2,4-dimethoxypyrimidine, adapted from Slatkin* et al.,[254] *Ballweg,[255] Wong and Fuchs,[256] and Dvorakova et al.[257] n-BuLi = n-butyl lithium, THF = tetrahydrofuran, AcCl = acetyl chloride.*

In the next step, ***III-13*** was reacted with acetyl chloride according to procedures first published by Ballweg as well as Wong and Fuchs.[255,256] It was found that this reaction proceeds best under neat conditions in a sealed container at the temperature indicated in the literature (53 °C, boiling point of acetyl chloride at 1 atm). The final step was then performed according to literature procedures in a sealed pressure tube,[255,257] that was placed in a pre-heated oil bath immediately after addition of the methanolic solution of ammonia to the starting material ***III-14***. Pre-heating the oil bath was observed to be vital, as otherwise large amounts of D$_3$-thymine (**D$_3$-T**) are formed.

The products **D$_3$-5mC** and **D$_3$-T** were then separated using HPLC (C18, 100% water grading to 1% acetonitrile in 99% water) and used as such for further experiments. These syntheses were published in 2019,[13] with the exception of the isolation of **D$_3$-T**, which was achieved later.

5hmC was synthesized by an adapted method previously published by Patel *et al.* in 2015.[260] This method was already discussed in my Master Thesis[167] and only the last step was repeated during my Ph.D. thesis. This last step was then also repeated using lithium aluminum deuteride (LiAlD$_4$) instead of lithium aluminum hydride (LiAlH$_4$) in order to obtain **D$_2$-5hmC** as a substrate for TET mimic studies.
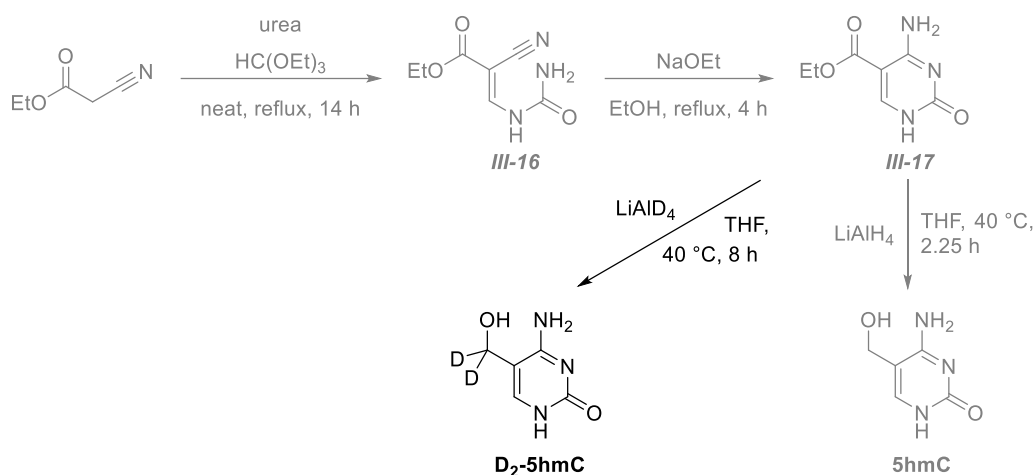
Scheme 49: Three-step synthesis of **5hmC** and **D$_2$-5hmC**, starting from ethyl-2-cyanoacetate, adapted from Patel et al.[260] The greyed-out reactions were only performed during my Master Thesis and are mentioned here only to provide context.[167] THF = tetrahydrofuran.

The reaction time with lithium aluminum deuteride needs to be elongated to four-fold that of lithium aluminum hydride to achieve acceptable yields (24% after HPLC). **5hmC** and **D$_2$-5hmC** were isolated using HPLC (C18, 100% water grading to 1% acetonitrile in 99% water). These procedures were published in 2019.[13]

With significant amounts of **5hmC** at hand, the next step was attempted: synthesis of **5fC** by oxidation using potassium perruthenate, as published by Patel *et al.*[260] This synthetic step follows the same procedure that is employed in oxidative bisulfite sequencing.[261]
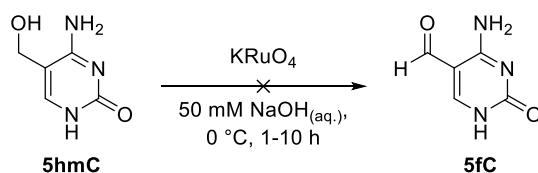
Scheme 50: Attempted synthesis of **5fC** by reaction of **5hmC** with potassium perruthenate.

However, when the product mixture was analyzed using GC-MS, several species were detected including **U**, **5mC**, and **5caC**, with **5fC** being only a minor component (Figure 65). Additionally, HPLC separation of this complex mixture proved unsuccessful due to the multitude of species present and their small differences in retention time.
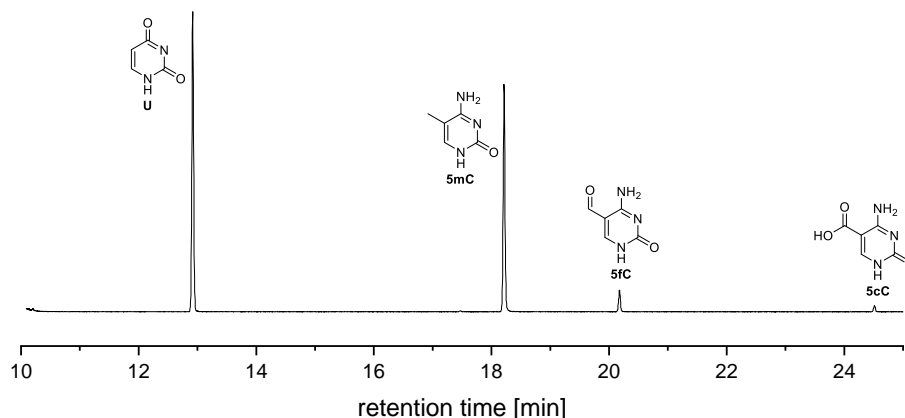
*Figure 65: Excerpt of the GC-MS trace of the reaction of **5hmC** with KRuO$_4$, reaction condictions as previously published by Patel et al. GC-MS method **C**.*

Hence, reaction of **5mC** with **C-6** was tested as a method to synthesize **5fC**, as **5fC** was usually observed as a major product. In a first attempt, one equivalent of **5mC** was reacted with **C-6** and the mixture analyzed by GC-MS, showing that most of the starting material had not yet been converted to **5fC** (Figure 66).
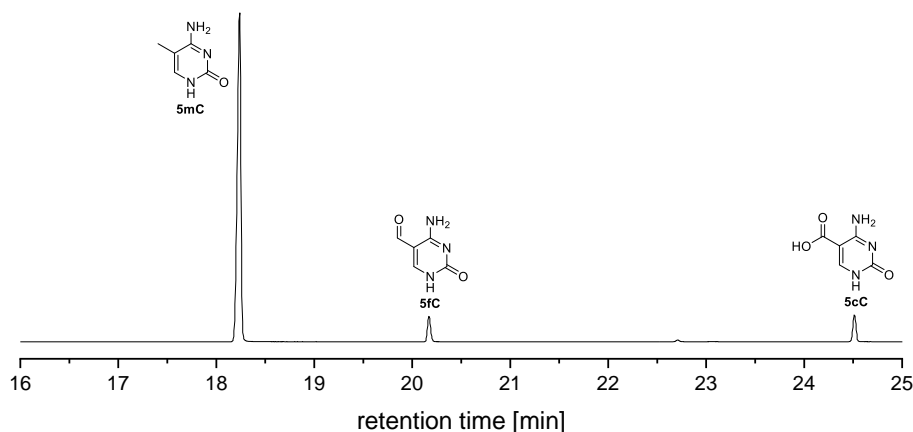
*Figure 66: Excerpt of the GC-MS trace of the reaction of **C-6** with 1.0 equiv. of **5mC**. GC-MS method **C**.*

Unfortunately, HPLC separation proved unsuccessful as too much **5mC** is present resulting in mixtures of **5fC** and **5mC** in the collected fractions (**5mC** and **5fC** have very similar elution properties, this had also been observed by Patel *et al.*[260]).

It was therefore attempted to react the product mixture as obtained from the previous reaction with another equivalent of **C-6** in order to decrease the amount of **5mC** present which should facilitate HPLC separation.

The obtained chromatogram contained almost no signals, only traces **5mC**, **5fC**, and **5caC** were detected (not shown, refer to the appendix, Figure 204, p. 379). As silica is always present in the reaction mixture due to the work-up procedure (refer to the appendix p. 356), this was suspected to have interfered with the second reaction step.

As a next step, cleaving the glycosylic bond in the TBS and THP protected **5fdC** derivative (provided by Eva Korytiaková of the Carell group at LMU Munich) using concentrated hydrochloric acid was attempted (Scheme 51). This procedure had previously been employed on the 2-fluoro **5fdC** derivative by Eva Korytiaková and therefore presented a suitable path to explore.
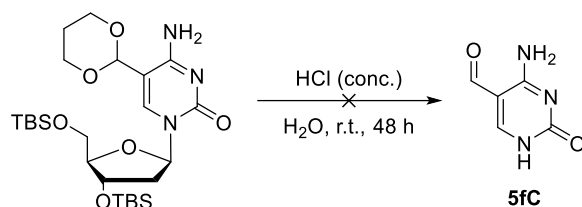
Scheme 51: Attempted cleavage of the glycosylic bond in a TBS and THP protected **5fdC** derivative.

However, LC-MS analysis of the obtained product mixture did not confirm formation of the free nucleobase **5fC**.

For the measurements described above, a sample of **5fC** provided by Eva Korytiaková was used. As this sample was sufficient for the procedures and measurements described in this work, synthetic attempts to obtain **5fC** were suspended. Analytical data on **5fC** is provided on p. 320.

Synthesis of Artificial Nucleobases

To expand the substrate scope of **C-6**, the above-mentioned synthetic nucleobases were synthesized. As mentioned in chapter III.8, **5miC** was synthesized according to a literature procedure by Stoss *et al.*[252] To this end, ethyl propionate was reacted with methyl formiate and sodium methanolate in DMF. Subsequently, a guanidine hydrochloride solution in methanol was added and the mixture refluxed for two hours. **5miC** was then obtained in 78% yield, however, Annika Menke later realized that the obtained compound was contaminated with ^{1}H NMR-inactive salts. Recrystallization from water gave the pure compound (yield not determined).
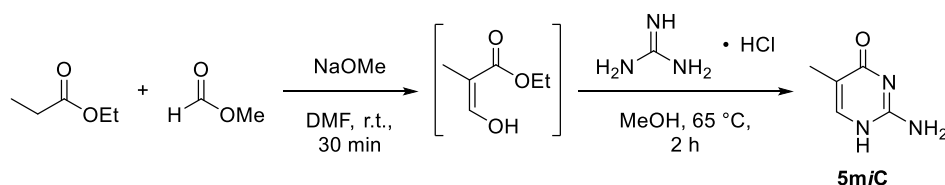
Scheme 52: Synthesis of **5miC**, procedure adapted from Stoss et al.[252] The shown intermediate was not isolated.

In order to obtain **5hmiC**, **5fiC**, and **5caiC** as reference samples, their synthesis was attempted by substitution of 5-iodo-*iso*-cytosine (**5IiC**) with suitable electrophiles. **5IiC** was synthesized according to a modified literature procedure by Doi *et al.* from 1,3-dimethyl-uracil (**1,3dimU**) using guanidine hydrochloride and iodine (Scheme 53).[251] **5IiC** was isolated in 74% yield.
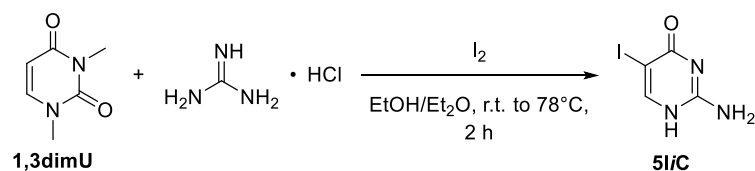
*Scheme 53: Synthesis of **5IiC** according to a procedure by Doi et al. from **1,3dimU**.[251]*

With **5IiC** at hand, a "protection-lithiation-substitution-deprotection" reaction sequence was devised (Scheme 54). Protection of the amine groups in **5IiC** was attempted using the trimethylsilyl (TMS) or *tert*-butyl dimethyl silyl (TBS) groups. Subsequently, lithiation using either *n*-butyl lithium or *tert*-butyl lithium was attempted. Reaction of this intermediate with methyl iodide, formaldehyde, ethyl formate, or carbon dioxide and subsequent deprotection would then give **5miC**, **5hmiC**, **5fiC**, or **5caiC**. Synthesis of **5miC** was attempted as a method of establishing a synthetic protocol, as a reference sample of **5miC** was available (Scheme 52).
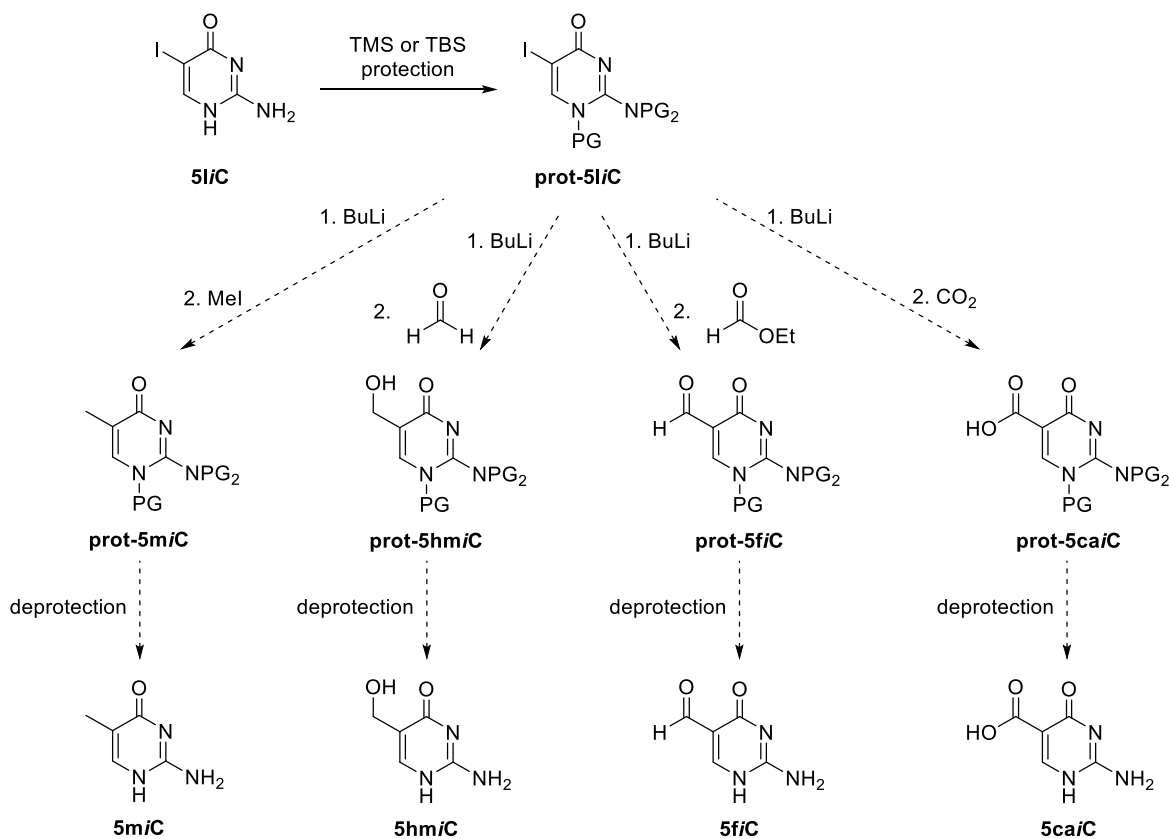
*Scheme 54: Attempted synthesis of **5miC, 5hmiC, 5fiC**, and **5caiC** from **5IiC** via a four step sequence: protection, lithiation, substitution, deprotection. PG = protecting group, prot-S = protected substrate, BuLi = either* n-*butyl lithium or* t-*butyl lithium.*

5IiC was successfully reacted with *N,O*-bis(trimethylsilyl)trifluoroacetamide (BSTFA) to give the three-fold TMS protected intermediate **TMS-5IiC** (Scheme 55A). This was confirmed by GC-MS analysis of the product mixture. Unfortunately, this intermediate did not prove stable, it was observed to decompose at room temperature and even 4 °C, and could therefore not be isolated in pure form. Hence, TBS protection using *tert*-butyl-dimethyl-silyl chloride and imidazole in a pyridine/dimethylformamide mixture was attempted (Scheme 55B). However, no product

formation was observed at 70 °C and 3.5 h reaction time. In a second attempt, the reaction temperature was increased to 130 °C and the reaction monitored for up to 70 h, however, no product was observed using GC-MS, HPLC-MS, or TLC.
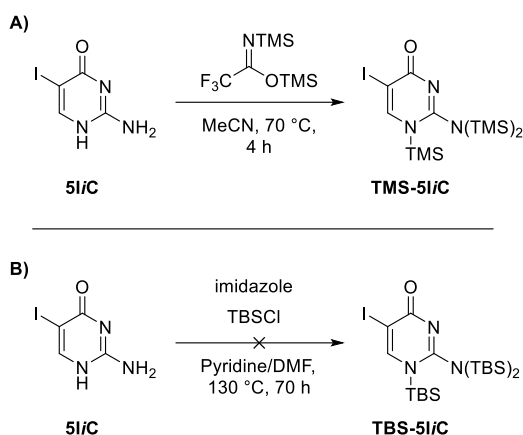
*Scheme 55: Synthesis of **TMS-5IiC** and attempted synthesis of **TBS-5IiC** from **5IiC**. TBSCl = tert-butyl-dimethyl-silyl chloride, DMF = dimethylformamide.*

Therefore, **TMS-5I*i*C** was used as crude reaction product for further reactions. Lithiation was attempted using *n*-butyl lithium, then methyl iodide or ethyl formate where added as liquids, while formaldehyde (generate from para-formaldehyde) or carbon dioxide were bubbled through the solution. GC-MS and ¹H NMR analysis of these reactions showed the formation of additional signals, however, none could be assigned to the desired products. Therefore, investigation of this method of synthesis was discontinued.

5hmC had been successfully synthesized according to a procedure by Patel *et al.* via the intermediates **III-16** and **III-17** (Scheme 49 and Scheme 56**A**). Therefore, an analogous reaction sequence was attempted for the synthesis of **III-19** *via* **III-18** in which urea is replaced by guanidine hydrochloride and ethyl cyanoacetate by diethyl malonate (Scheme 56**B**). Unfortunately, neither NMR spectroscopy nor mass spectrometry gave any indication of the formation **III-18**. This reaction was therefore discontinued and ethyl cyanoacetate was reacted with guanidine hydrochloride (Scheme 56**C**).
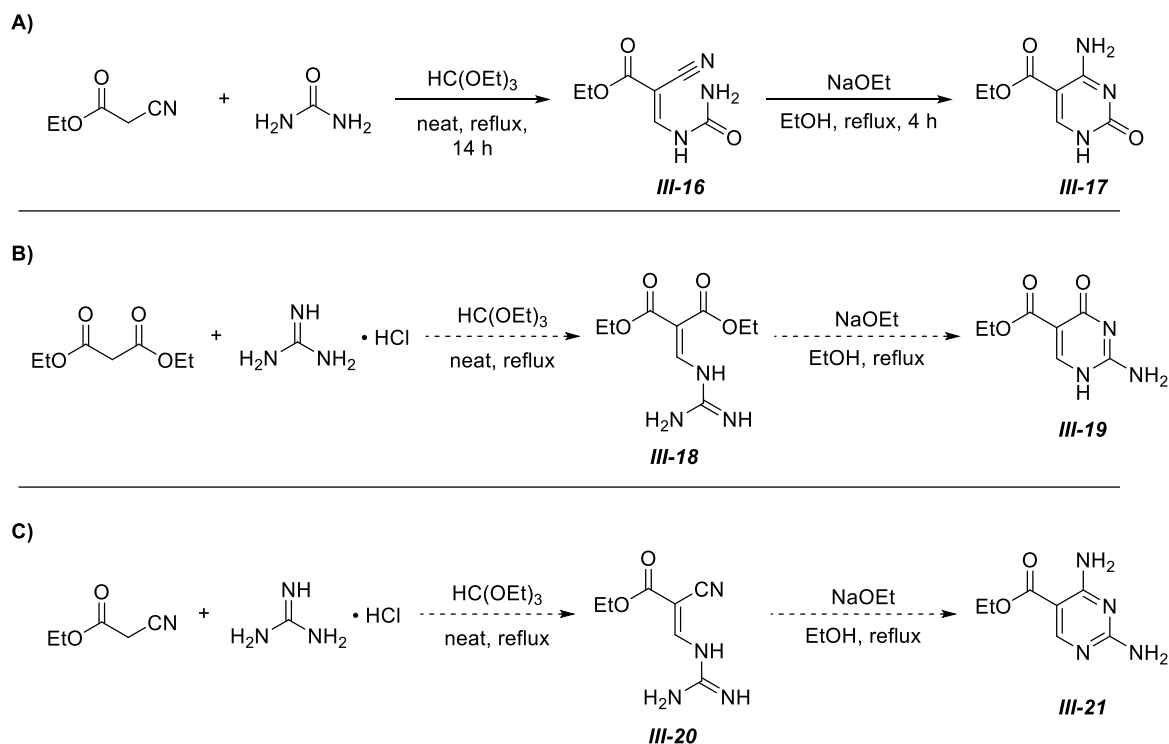
Scheme 56: **A**) Literature known synthesis of ethyl-5-carboxy-cytosine (Et-5caC, **III-17**) as comparison. **B**) Attempted synthesis of ethyl-5-carboxy-iso-cytosine (Et-5caiC, **III-19**) for further transformation to **5hmiC**, **5fiC** or **5caiC**. **C**) Attempted synthesis of intermediate for further transformation to **5hmiC**, **5fiC** or **5caiC** via selective transformation of the 4-amino group.

From this reaction, a product was obtained that was characterized using ^{1}H and ^{13}C NMR spectroscopy, mass spectrometry, and elemental analysis. Whereas ^{1}H and ^{13}C NMR spectroscopy show the expected signals for **III-20** (Figure 67 and appendix, Figure 205, p. 376), HR-MS and elemental analysis data did not correspond to the expected values.

The obtained ^{1}H NMR spectrum in DMSO-d$_6$ contains four signals **A**, **B**, **C** and **D** (Figure 67). Upon addition of D$_2$O to this sample, signal **B** almost completely vanishes, indicating an acidic proton. Signals **C** and **D** display a split and integral pattern corresponding to an ethyl group. The overall relative integral pattern (1:7:4:6) does not correspond to the desired product. The ^{13}C NMR spectrum in DMSO-d$_6$ contains seven signals, which would correspond to the desired product. The observed chemical shifts are very similar to those observed for the intermediate in the reaction shown in Scheme 56**A**. In HR-MS (negative mode) a signal at 235.07228 m/z was observed that could not be assigned to any structure. The values for C, H, and N found using elemental analysis did not correspond to the desired product or sodium, guanidinium, or hydrochloride salts thereof (calculated: C 45.64, H 6.57, N 30.42, found: C 48.48, H 5.82, N 23.89. In total, the analytical results were inconclusive and further investigation was suspended.
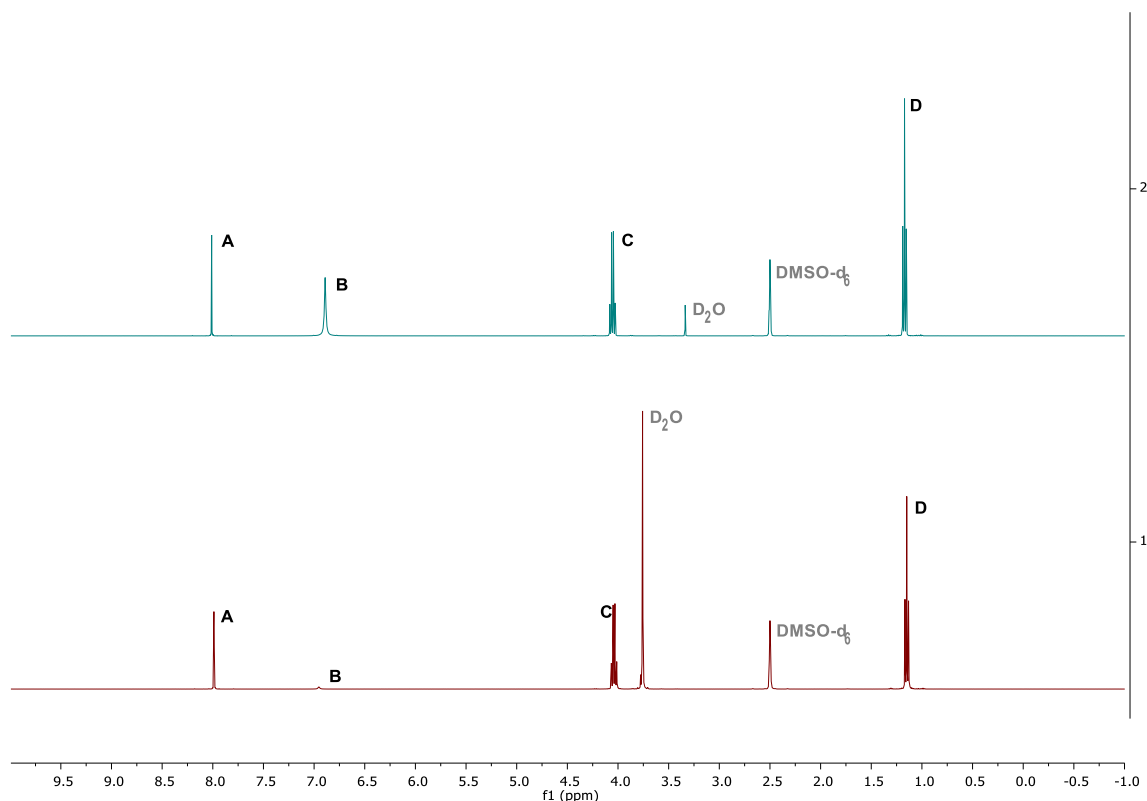
Figure 67: ^{1}H NM spectra of the product obtained from the first reaction described in Scheme 56C. The upper spectrum was recorded in DMSO-d$_6$, the lower spectrum in DMSO-d$_6$ with a drop of D$_2$O. T = 298 K.

An additional synthesis route was tested to obtain a 5-bromo-substituted pyrimidine intermediate ***III-22*** suitable for further derivatization. The first step of this route was successful: substitution of the methyl thioether moiety in the starting material 5-bromo-2-(methylthio)pyrimidin-4-ol with *p*-anisidine gave ***III-22*** with small imputrities of 5-bromo-2-(methylthio)pyrimidin-4-ol. As I was joined by Annika Menke in this project, she continued the investigation of this route.
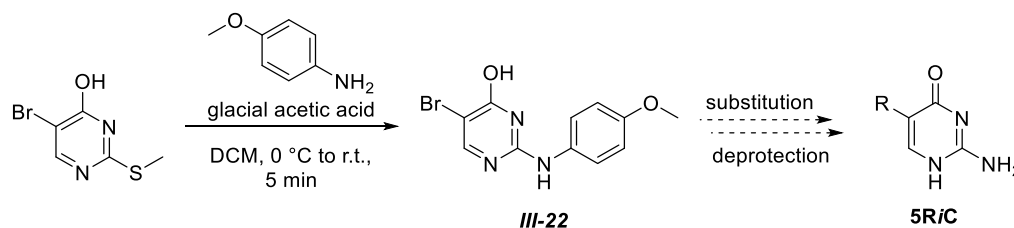
*Scheme 57: Synthesis of **5RiC** compounds* via **III-22** *starting from 5-bromo-2-(methylthio)pyrimidin-4-ol. R = -CH$_3$, -CH$_2$OH, -CHO, -CO$_2$H.*

Synthesis of 1-methyluracil (1mU)

1mU was synthesized for use in the nucleobase comparison project (refer to chapter III.8), according to a procedure by Micklitz *et al.*[262] **U** was reacted with bis(trimethylsilyl)amine (HMDS), trimethylsilyl chloride (TMSCl), and methyl iodide. In contrast to the literature, a mixture of **1mU** and **U** was obtained through recrystallization and HPLC purification was necessary to obtain the desired product.
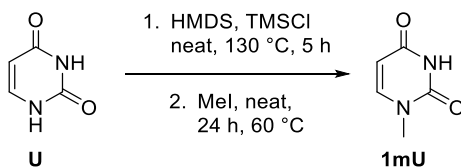
*Scheme 58: Synthesis of **1mU** from **U** according to a synthesis procedure by Micklitz et al.[262]*

pH Dependence

As mentioned in chapter III.4, the reaction of **5mC** (or **5hmC**/**5fC**) was observed to be dependent on the amount of potassium hydroxide that was added. This was studied in more detail in an attempt to discern the exact nature of pH dependence.

The pH value of a [**C-6**] = 5 mM solution (prepared by mixing the standard 10 mM stock solution with an equal amount of water) was found to be 4.77±0.10. Then, the pH value was monitored during the reaction of **5mC** with **C-6**, but without potassium hydroxide, and was found to decrease steadily (Figure 68A). Subsequently, the influence of added potassium hydroxide on the pH value of the reaction solution was studied. To this end, the stock solution of **C-6** was prepared as described above, however, the amount of added potassium hydroxide was varied. In Figure 68B, 1.0 equiv. of potassium hydroxide correspond to the "standard" formula, 2.0 equiv. then corresponds to 1.0 additional equiv. of potassium hydroxide and so forth.
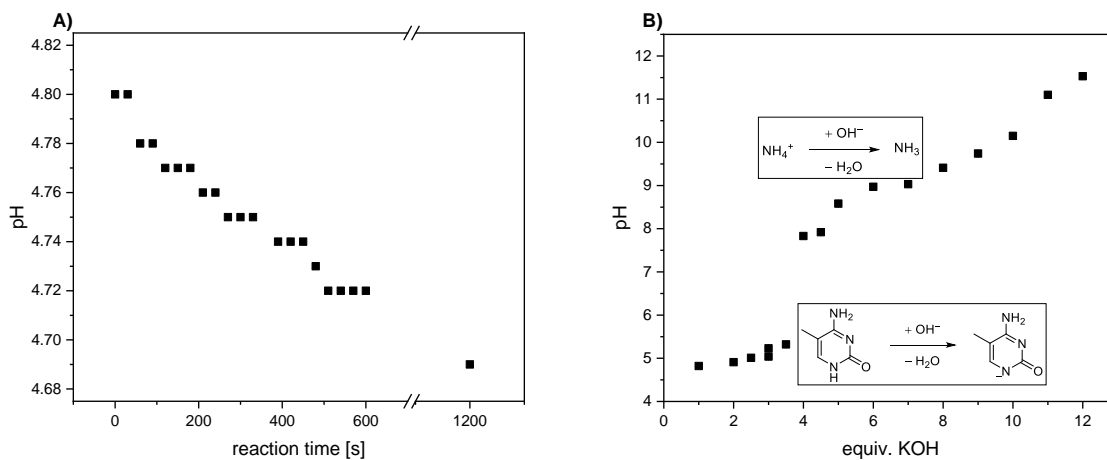
*Figure 68: **A)** Measured pH values during the reaction of **5mC** with **C-6**. Conditions: [**5mC**] = 5 mM, [**C-6**] = 5 mM, [KOH] = 5 mM, H₂O, T = 23 °C. **B)** Measured pH values upon addition of potassium hydroxide to a solution of **5mC** and **C-6** (including the standard 25 mM ammonium fluoride, present from preparation of **C-6**). Buffer reactions are indicated. Conditions: [**5mC**] = 5 mM, [**C-6**] = 5 mM, [KOH] = 10-120 mM, H₂O, T = 23 °C.*

The presence of up to 3.5 equiv. of potassium hydroxide does not strongly influence the pH value, however, a significant increase was observed between 3.5 and 4.0 equiv. and another, smaller, increase can be observed between 10.0 and 11.0 equiv (Figure 68**B**). These were attributed to the completed abstraction of the proton on the endocyclic amine of **5mC** (3.5 to 4.0 equiv. increase) and the completed deprotonation of the ammonium ion (10.0 to 11.0 equiv. increase). From the plateaus "left" of the respective increases the pK$_A$ was calculated (4.9 and 9), which correspond well to the literature known pK$_A$ values of **C** (4.45)[263] and ammonium (9.25).[264] The pK$_A$ values of **5mC** are not known, hence that of **C** is used here for comparison.
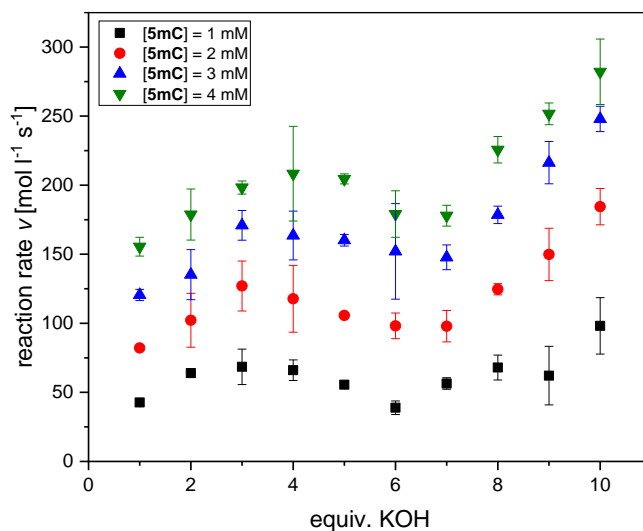
Figure 69: Observed reaction rates in reaction of **C-6** with **5mC** at four different concentrations of **5mC** ([**5mC**] = 1-4 mM) for different amounts of added KOH (1-10 equiv.). Conditions: [**5mC**] = 1-4 mM, [**C-6**] = 5 mM, H₂O, T = 23 °C.

With this at hand, the influence this pH change/addition of base had on the reactivity of **5mC** was investigated (Figure 69). Unfortunately, the data collected did not prove as straight forward as hoped. Whereas an overall increase in the reaction rates was observed, the increase did not follow any easily discernable pattern. During addition of 1.0-4.0 equiv. potassium hydroxide, the rate increased steadily in a linear fashion. It then decreases from 4.0-6.0 equiv. only to then increase further until 10.0 equiv. Lower concentrations of **5mC** (1.0 mM, Figure 69; 0.5 mM and 1.5 mM, not shown) lead to the development of an additional feature between 7.0-9.0 equiv. of potassium hydroxide. This was not observed for higher concentrations (2-4 mM).
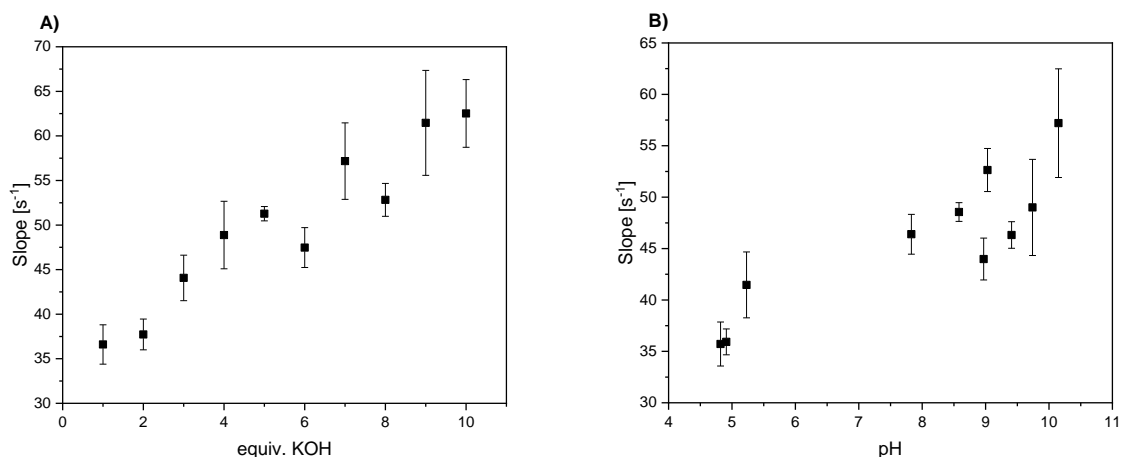
*Figure 70: Obtained reaction rate dependences ("slope") plotted against the added KOH equivalents (left graph) or the resulting pH value (right graph). Conditions: [**5mC**] = 1 mM, [**C-6**] = 5 mM, H$_2$O, T = 23 °C.*

The dependence of the reaction rate on the **5mC** concentration ("slope") was plotted against the added amount of potassium hydroxide (Figure 70**A**) or the measured pH (Figure 70**B**). A similar behavior as with the reaction rates was observed with an initial increase, then a decrease around 5.0-7.0 equiv. and an additional increase for higher amounts of potassium hydroxide. During addition of 1.0-5.0 equiv. potassium hydroxide, the rate dependence on the **5mC** concentration increases steadily, even in a linear manner. Then it decreases from 5.0-6.0 equiv. only to then increase further until 10.0 equiv. The last two values seem to suggest a plateau/saturation limit, however, the error values are quite large and therefore no definite conclusions can be drawn.

If the slope is plotted against the pH, two clusters can be observed. One is located around pH values between 4.8 and 5.4 and another for pH values between 7.8 and 10.3. can be attributed to the two buffer systems described previously (Figure 68). Unfortunately, this means that no significant conclusions can be drawn from the presented data.

In conclusion, the previously observed behavior of the reaction rate to increase upon addition of potassium hydroxide was corroborated, however, due to the systems complexity no more detailed information was obtained. Blocking the endocyclic amine group of **5mC** by addition of a trifluormethyl group might simplify the system so that a more direct correlation of HAT reaction rate and pH can be drawn.

*Additional Investigations of **C-6** and its Interactions with **5mC** and **5hmC***

A publication by Fukuzumi and Nam in 2010 about the interaction of Sc^{3+} and [Fe^{IV}(O)(TMC)]$^{2+}$ (TMC = 1,4,8,11-tetramethyl-1,4,8,11-tetraaza-cyclotetradecane) prompted the question, whether **C-6** also shows interaction with Sc^{3+} ions.[265] Fukuzumi and Nam showed that the iron-oxygen bond length is significantly elongated in a complex containing [Fe^{IV}(O)(TMC)]$^{2+}$ and Sc^{3+}, when compared to the free [Fe^{IV}(O)(TMC)]$^{2+}$ (1.753 vs. 1.643 Å). The Sc-O bond was found to be much

shorter than a typical Sc-OH bond, which suggests a strong interaction between scandium and the oxo moiety.[265]
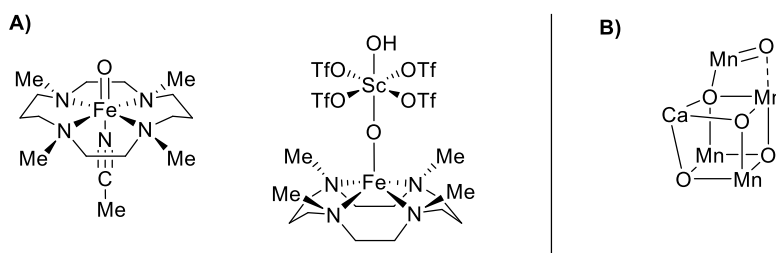
*Figure 71: **A)** [Fe^{IV}(O)(TMC)(MeCN)]²⁺ and [(TMC)Fe^{IV}(O)-Sc(Otf)₄(OH)]. In [Fe^{IV}(O)(TMC)(MeCN)]²⁺ the methyl groups point downward (away from the oxido moiety), in [(TMC)Fe^{IV}(O)-Sc(Otf)₄(OH)] the methyl groups point upwards (towards the oxido moiety). The coordination geometry on the iron is distorted square-pyramidal with the iron center sitting slightly above the plane spanned by the four nitrogen atoms of the TMC ligand.[265] **B)** Proposed structure of the oxygen evolving complex in photosystem II.[266]*

Kenneth Karlin argued in a Nature Chemistry article that such an interaction of a positively charged ion with an oxido-moiety could facilitate the reduction from iron(IV) to iron(III) which would help speed up reactions in enzymes that use such a high-valent iron(IV)-oxido moiety as catalytically active species. Karlin also mentions photosystem II, a structure made up of a manganese(V)-oxido moiety coupled to a cuboidal complex containing three manganese and one calcium ions. The calcium ion might then, as scandium does in the work of Fukuzumi and Nam with iron(IV)-oxido, activate the manganese(V)-oxido group, facilitating the reaction of photosystem II.[267] Such interactions of Lewis acids and oxido moieties therefore represent an interesting field of study when investigating functional model systems for enzymatic processes.
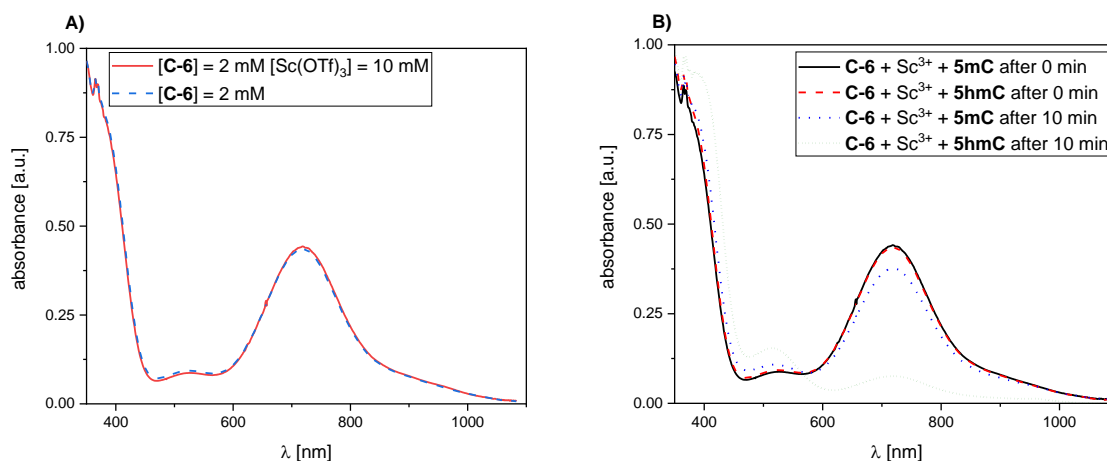
*Figure 72: **A)** Excerpts of UV-Vis spectra of **C-6** with (blue dashed) and without Sc³⁺ (red solid). **B)** Representative excerpts of UV-Vis spectra of mixtures containing **C-6** and Sc(Otf)₃, in addition to either **5mC** or **5hmC**. Conditions: [**C-6**] = 2 mM, [Sc(OTf)₃] = 10 mM, [**S**] = 2 mM, H₂O, T = 23 °C.*

Figure 72**A** shows an excerpt of a 2 mM aqueous solution of **C-6** with and without added Sc³⁺ (10 mM), however, no significant change in the iron(IV)-oxido absorption feature at λ = 718 nm was observed. This indicates that no interaction occurs between the oxido moiety and Sc³⁺. A comparison of UV-Vis spectra of reaction mixtures containing **C-6** (2 mM) and Sc³⁺ (10 mM) and

either **5mC** (2 mM) or **5hmC** (2 mM) showed no significant differences to spectra collected of reaction solutions without Sc^{3+} (Figure 72**B**).

Additional Investigations of C-6 and its Interactions with T and D$_3$-T

In addition to studies on methylated/oxo-methylated **C** derivatives (chapter III.4) as well as the nucleobase comparison project (chapter III.8), a short investigation into the behavior of **T** was performed. As mentioned above (Scheme 48) **T** (or **D$_3$-T**) was obtained as a side product in the synthesis of **D$_3$-5mC**. Therefore, the KIE between the reactions of **C-6** with **T** and **D$_3$-T** was investigated by using the experimental setup described above.
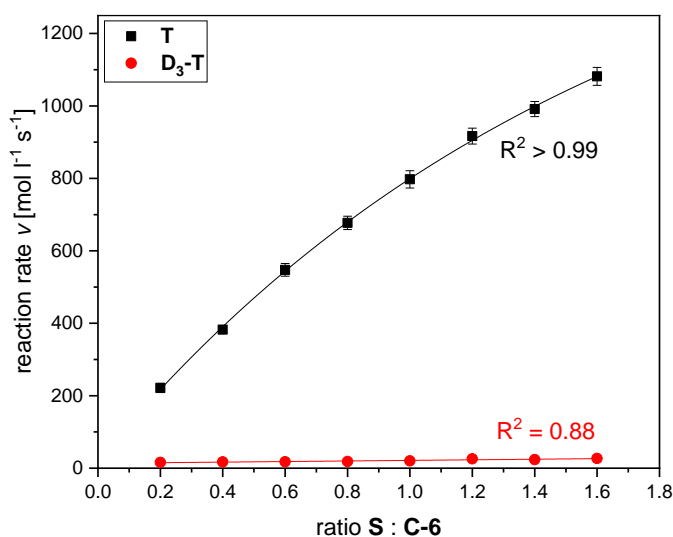
*Figure 73: Initial rates of the reaction of **C-6** with **T** and **D$_3$-T**. The values for **T** show a non-linear behavior that can be described with a saturation-type fit. **D$_3$-T** follows a linear behavior, albeit significant variations were observed, probably due to the low overall rates and resulting fluctuations in absorption at λ = 718 nm. Conditions: [**S**] = 1-8 mM [**C-6**] = 5 mM, H$_2$O, T = 30 °C.*

The measured reaction rates *v* of the reaction of **C-6** with **T** show a saturation type behavior (R^2 > 0.99), similar to the one observed for **5hmC**. The reaction rates for **D$_3$-T** show a linear behavior, however, significant variations were observed. These were attributed to the observed fluctuations in the measured absorbance at λ = 718 nm, as these play a more significant role when very low reaction rates are measured. Nonetheless, a linear behavior was observed for **D$_3$-T** in the chosen concentration range (R^2 = 0.88).

Even though a saturation behavior was observed for **T** as substrate, the rate constants k_S were calculated from a linear regression of the observed rates. This, of course, presents a significant inaccuracy but still allows for a semi-quantitative comparison with other substrates such as **5mC** or **5hmC** as well as calculation of the KIE. The obtained values are shown in Table 4, the rate constants of **5mC** and **5hmC** are included for sake of comparison. The rate constant of **C-6** with **T** is significantly higher than that of **5mC** (17-fold), whereas the rate constant of **D$_3$-T** was observed to be very small. This is rather surprising, as **T** is structurally very similar to **5mC**.

Table 4: Measured rate constants k$_S$ (C-6) for T and D$_3$-T, the resulting KIE, as well as k$_S$ (C-6) values of 5mC and 5hmC for comparison.

S	k$_S$ [l mol^{-1} s^{-1}]	KIE
T	24.51	-
D$_3$-T	0.32	~76
5mC	7.37	-
5hmC	63.56	-

The KIE for **T/D$_3$-T** is much larger than for **5mc** (KIE ≈ 9)[13] or **5hmC** (KIE ≈ 29)[13] and far exceeds the usual range of KIE values obtained at room temperature (usually 6-9, seldom ~20). Such large KIEs also often imply secondary reaction mechanisms such as tunneling.[268]

IV. [Fe^{III}(OH)(Py$_5$Me$_2$H)]$^{2+}$ and Iron(IV)-oxido/Iron(II) Comproportionation

1. Introduction and State of the Art

Comproportionation of Iron(IV)-oxido and Iron(II) Species

An often unregarded reactivity of iron(IV)-oxido complexes is their ability to comproportionate with iron(II) species. This results in the formation of two equivalents of an iron(III) species. Few examples are known for non-heme derived systems[55] (Scheme 59**A**). The opposite reaction, disproportionation, is also known, especially in heme-derived[269,270] or closely related NHC-derived[80] systems (Scheme 59**B**). In the case of the latter, an equilibrium between an μ-oxido-bridged iron(III) dimer on the one hand and an iron(IV)-oxido species/iron(II) species on the other hand was observed (Scheme 59**C**).

A) Comproportionation in a non-heme complex

iron(IV)-oxido   iron(II)   iron(III) hydroxido
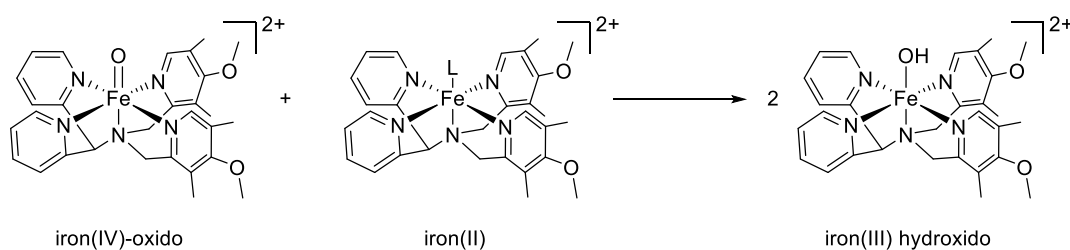
B) Disproportionation in a heme-derived complex

iron(IV)-oxido   iron(IV) radical cation   iron(III)
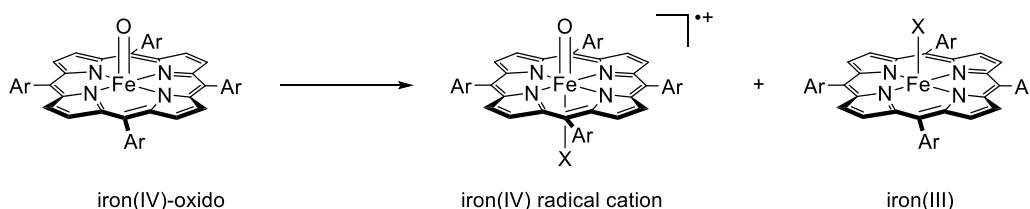
C) Com- and disproportionation equilibrium in an NHC-derived complex
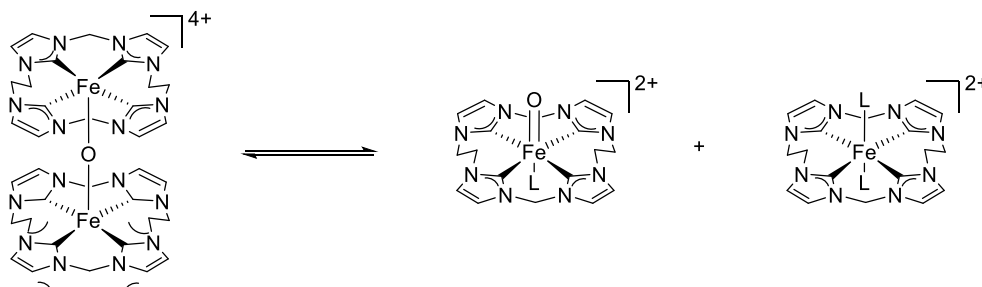
Scheme 59: **A)** *Comproportionation reaction in a non-heme derived iron(IV)-oxido complex.*[55] **B)** *Disproportionation reaction in a heme-derived iron(IV)-oxido complex.*[269,270] **C)** *Com- and Disproportion equilibrium in an NHC-derived complex.*[80]

The comproportionation reaction depicted in Scheme 59**A** occurs after one equivalent of the iron(IV)-oxido complex reacted with the substrate to form an iron(III)-hydroxido intermediate and subsequently transferred the hydroxyl moiety to the organic radical of the substrate, as

described in chapter I, Figure 4. As this is the standard pathway, the amount of iron(II) species should be significant in all reactions involving iron(IV)-oxido complexes and organic substrates. Comproportionation should therefore never be ruled out as a competing side reaction.

Radical Clocks

A radical clock is a molecule that undergoes rapid reorganization if a radical is formed at a certain position of the compound. For example, methyl cyclopropanes undergo a ring-opening rearrangement (Scheme 60). Radical clocks such as methyl propanes and methyl cubanes have been used to study rebound behavior.[271,272]
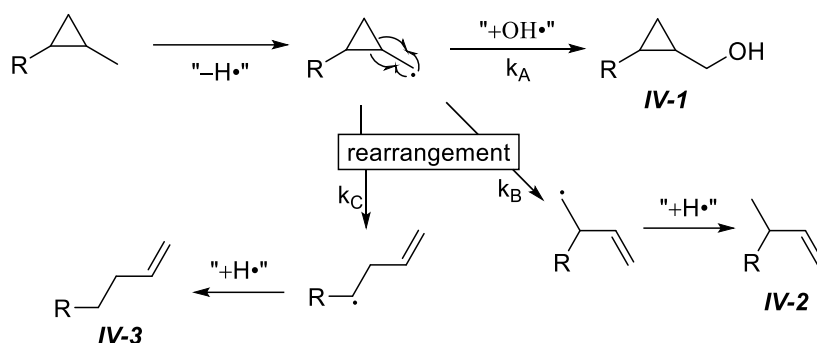
Scheme 60: Hydrogen atom abstraction from the methyl group of a substituted methyl cyclopropane and follow-up reactions. The upper pathway involves the addition of a hydroxyl radical (in the case of iron chemistry, this would be considered the rebound step) whereas the two lower pathways describe possible spontaneous ring-opening rearrangements.

By analysis of the product distribution, a statement can be made about the reaction rate of the hydroxylation/rebound, if the reaction rates of the rearrangement reactions are known. In the case of methyl cyclopropanes, these typically range between $k = 10^7\text{-}10^8$ s^{-1}.[273,274] If therefore only products ***IV-2*** or ***IV-3*** are observed, the reaction rate k_A of the hydroxylation/rebound is lower than $10^7\text{-}10^8$ s^{-1}. If only the hydroxylated product ***IV-1*** is observed, then $k_A > 10^7\text{-}10^8$ s^{-1}.

2. Motivation and Aim

Scheme 61 shows the proposed reaction mechanism of the reaction of **C-6** with a substrate bearing an aliphatic C-H bond. The first step, hydrogen atom transfer (HAT), has been investigated in some detail, e.g. by deuterating the substrate and studying the kinetic isotope effect (refer to chapter III). The second step, proposed as a rebound-type mechanism, was not yet studied for this system.
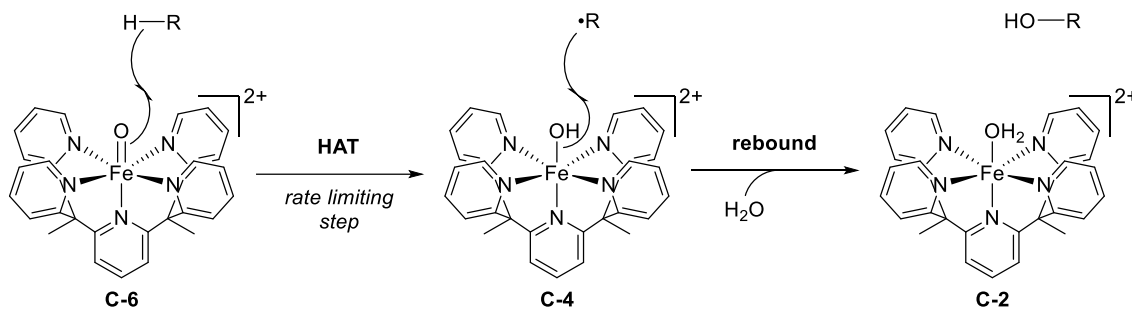
*Scheme 61: Proposed reaction mechanism of **C-6** with an organic substrate R-H in a two step sequence: HAT followed by rebound, as previously published by Jonasson and Daumann.[13]*

Therefore, the goal of this sub-project was to observe C-4 in reaction mixtures of C-6 with organic substrate. If successful, synthesis of C-4 was to be attempted, which would enable the study of the crucial rebound step by reacting C-4 with a stable organic radical, as has been reported by Goldberg[48] and Fout[49] (refer to chapter I, p. 10). Synthesis of C-4 would also offer the possibility to confirm the results published by Xiang *et al.* (refer to chapter I.3). If so, this would also indicate that C-4 might possess lipoxygenase activity, hence, a detailed investigation will be conducted.

3. Identification of [Fe^{III}(OH)(Py$_5$Me$_2$H)]$^{2+}$ as a Reaction Product

When a flask containing residue of a reaction of **C-6** with **5mC** was left to slowly evaporate, orange-brown crystals were obtained. These crystals proved suitable for x-ray crystallography and the structure shown in Figure 74 was obtained. David Schmidl obtained similar crystals from an old reaction solution of **C-6** and **5mdC** during his Master Thesis i.[238]
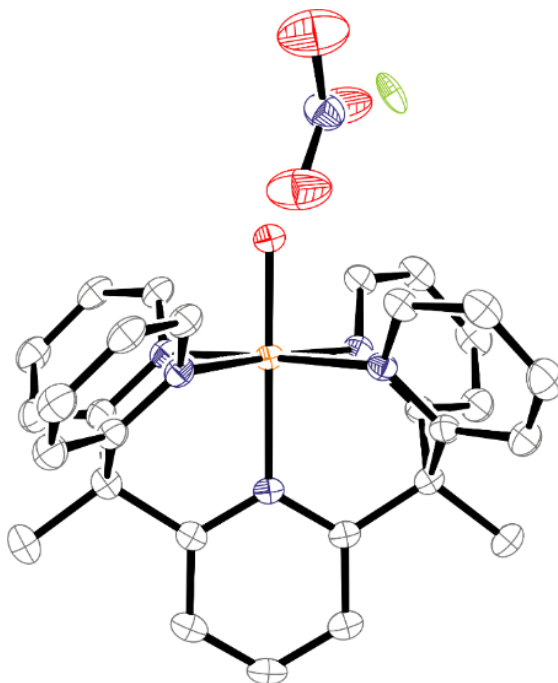
*Figure 74: Graphical representations of the crystal structure of [Fe^{III}(OH)(Py$_5$Me$_2$-H)](NO$_3$)$_{1.81}$F$_{0.19}$. Ellipsoids are drawn at 50% probability, hydrogen atoms and co-crystalized solvent molecules have been omitted for clarity. A complete structure and crystallographic details can be found in the appendix p. 497. Crystals were obtained from slow evaporation of an aqueous solution of **C-6** and **5mC** at room temperature.*

The bond lengths and angles of this compound were compared to those of the literature known iron(II) species (**C-2**) and iron(IV)-oxido species (**C-5/C-6**) and other iron(III)-hydroxido species. For example, Borovik *et al.* and Fout *et al.* reported Fe-O bond lengths of 1.86-1.93 Å for their high-spin iron(III)-hydroxido species.[64,71] The Fe-O bond length of the compound in Figure 74 is significantly shorter than this at 1.79 Å (Table 5, compound in Figure 74 referred to as **C-4**). An explanation for this would be that both systems of Borovik and Fout contain a secondary coordination sphere that forms hydrogen bonds to the hydroxyl group, possibly elongating the iron-oxygen bond (chapter I.3, Chart 2).[12,39] However, the bond length in the iron(II) complex **C-2** is significantly longer at 2.01 Å, that of the **C-6** significantly shorter at 1.66 Å (Table 5).

These comparisons suggest that the compound shown in Figure 74, **C-4**, is a low-spin iron(III)-hydroxido complex. These are rare, as dimerization to a µ-oxido-bridged structure is often observed. Goldsmith and Stack report for the related complex **C-18** ([Fe^{III}(OH)(Py$_5$(OMe)$_2$)]$^{2+}$, refer to chapter V.4 for details) the formation of a high-spin iron(III)-hydroxido species which undergoes a spin-flip to the corresponding low-spin species upon cooling to 77 K.[68]

Table 5. Selected bond lengths and angles in single crystals of C-2, C-4 and C-5. Py$_{eq.}$ = pyridines in the equatorial plane, Py$_{ax.}$ = axial pyridine. For values involving equatorial pyridines the average value is provided.

Iron(II)-aqua C-2		Iron(III)-hydroxido C-4		Iron(IV)-oxido C-5	
Fe-OH$_2$	2.01 Å	**Fe-O**H	1.79 Å	**Fe-O**	1.66 Å
Fe-N(Py$_{eq}$)	2.01 Å	**Fe-N**(Py$_{eq}$)	2.00 Å	**Fe-N**(Py$_{eq}$)	2.00 Å
Fe-N(Py$_{ax}$)	1.95 Å	**Fe-N**(Py$_{ax}$)	2.03 Å	**Fe-N**(Py$_{ax}$)	2.07 Å
N(Py$_{eq.}$)-**Fe-O**	89.8°	**N**(Py$_{eq.}$)-**Fe-O**	91.1°	**N**(Py$_{eq.}$)-**Fe-O**	92.3°
N(Py$_{ax.}$)-**Fe-O**	180.0°	**N**(Py$_{ax.}$)-**Fe-O**	179.8°	**N**(Py$_{ax.}$)-**Fe-O**	179.7°
N(Py$_{eq.}$)-**Fe-N**(Py$_{eq.}$)	90.1°	**N**(Py$_{eq.}$)-**Fe-N**(Py$_{eq.}$).	90.0°	**N**(Py$_{eq.}$)-**Fe-N**(Py$_{eq.}$)	90.1°
N(Py$_{eq.}$)-**Fe-N**(Py$_{ax.}$)	90.2°	**N**(Py$_{eq.}$)-**Fe-N**(Py$_{ax.}$)	88.9°	**N**(Py$_{eq.}$)-**Fe-N**(Py$_{ax.}$)	87.6°

A closer comparison of bond lengths and bond angles reveals a clear trend from iron(II)-aqua to iron(IV)-oxido. **Fe-O** bonds, as mentioned above, decrease, whereas **Fe-N**(Py$_{ax.}$) bonds (**N**(Py$_{ax.}$) refers to the axial pyridine moiety) increase. In addition, the average bond angle between the equatorial pyridine moiety (**N**(Py$_{eq.}$)) and the oxygen moiety increases from 89.8° (**C-2**) to 92.3° (**C-5**), while simultaneously the angle between the axial pyridine and the equatorial pyridine moieties decreases from 90.2° to 87.6° (**C-2** to **C-5**, respectively). From this data it is evident, that the iron ion "moves up" within the coordination cage when the oxidation state changes from +2 to +3 to +4, it is in fact located slightly above the plane formed by the four equatorial pyridine moieties (Figure 75**B**).
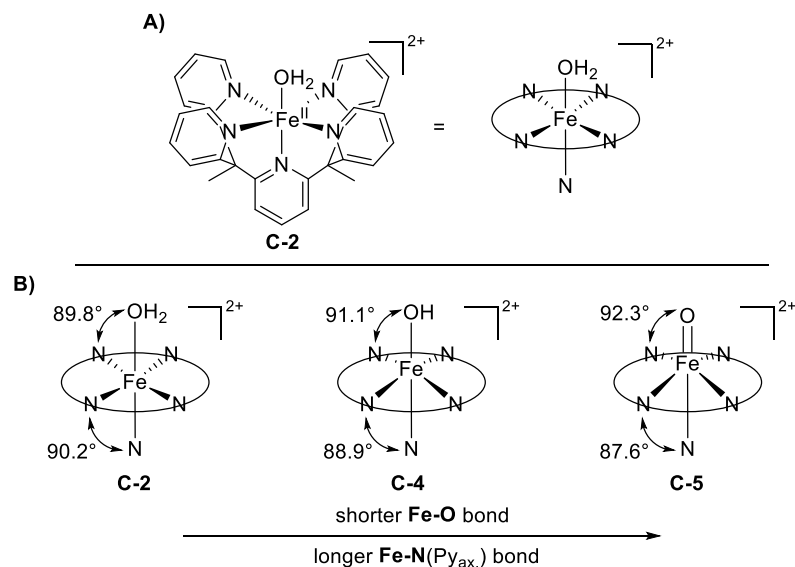
*Figure 75: **A**) Simplified graphical representation of the coordination environment of the iron(II) central ion in **C-2**. **B**) Graphical representation of the changes in coordination geometry between **C-2**, **C-4**, and **C-5**.*

The spin-state of **C-4** is not the only peculiar observation: If the mechanism in Scheme 61 is correct, an iron(II) species is expected as the reaction product, not an iron(III)-hydroxido compound. This is underlined by the statement of Chantarojsiri *et al.*, who first synthesized and studied **C-5**/**C-6**, about the mechanism of oxidation of **C-1** and **C-2** to **C-5**: "as Fe(IV)-oxo [**C-5**,

authors note], directly generated in the presence of Fe(II) starting material [**C-2**, authors note], can undergo an intermolecular reaction to produce a μ-oxo Fe^{III} sink that cannot be oxidized to Fe(IV)-oxo."[12]

To confirm that **C-4** is indeed formed during the reaction, HR-MS analyses of the reaction mixture of **C-6** with **5mC** were conducted. In these, clearly, the iron(III)-hydroxido species was detected – but no traces of an iron(II) compound (Figure 76).
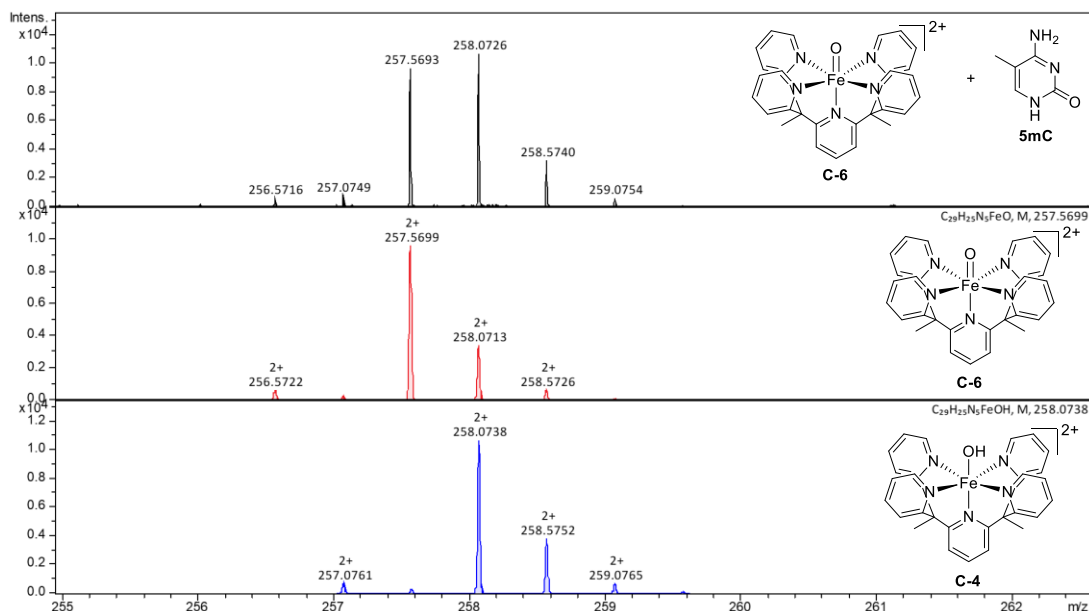
*Figure 76: In situ HR-MS spectrum of the reaction of **C-6** with **5mC** (upper spectrum) and simulated spectra of **C-6** and **C-4** (middle and lower spectrum, respectively).*

These observations make it clear that either the proposed two-step mechanism of HAT and rebound step is not correct or some secondary reactions leading to the observed species take place. A possible secondary reaction and an explanation for the formation of **C-4** would be a comproportionation reaction between **C-2** formed during the reaction with the substrate and residual **C-6** (Scheme 62). As mentioned above, similar reactions have been reported in the literature.[55,80,275,276] This hypothesis was then to be confirmed by UV-vis and HR-MS experiments after a reference sample of **C-4** was synthesized (refer to chapter IV.4 for synthetic details).
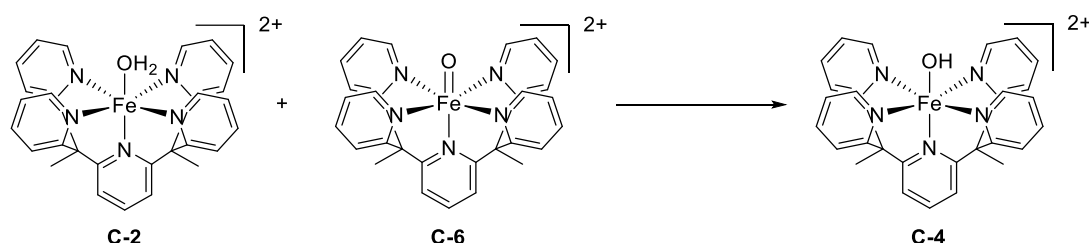
*Scheme 62: Proposed comproportionation of **C-2** with residual **C-6** leading to **C-4**. Counter ions have been omitted for clarity.*

Having a reference sample of **C-4**, UV-vis studies were conducted to study the proposed comproportionation reaction by mixing aqueous solutions of **C-2** and **C-6** in equimolar amounts (**C-6** was chosen rather than **C-5** to exclude any involvement of the hexanitrato cerate(IV) counter

ion). This resulted in a fast color change from brown (**C-2**) and green (**C-6**) to a clear red-orange. This was counted as a first indication of the formation of **C-4** as its aqueous solution is also red-orange. Comparison of the collected UV-vis trace with that of a reference sample of **C-4** supports this conclusion: in the relevant region of the UV-vis trace (λ = 300-500 nm) the spectra of the mixture and the reference sample are nearly identical (Figure 77**A**, full spectra can be found in the appendix, p. 380).
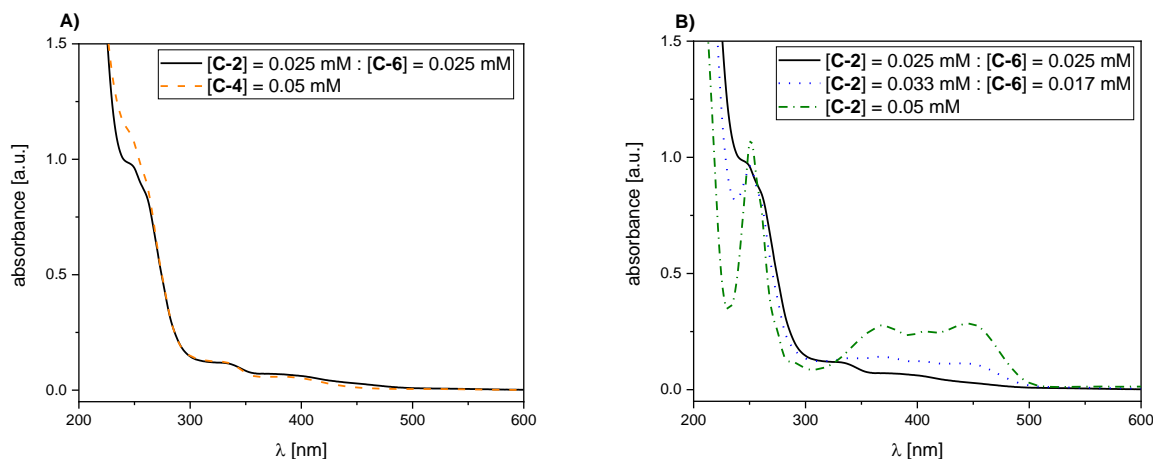
*Figure 77: **A**) Excerpts of UV-vis spectra of a 1:1 mixture of **C-2** and **C-6** (0.025 mM:0.025 mM, black solid) compared to a reference sample of **C-4** (0.05 mM, orange dashed). **B**) Excerpts of UV-vis spectra of mixtures of **C-2** and **C-6**: 1:1 (0.025 mM:0.025 mM, black solid) and 2:1 (0.017 mM:0.033 mM, blue dotted), as well as a reference sample of **C-2** (0.05 mM, green dotted/dashed).*

Figure 77**B** shows a comparison of the UV-vis spectra of two mixtures (1:1, black and 2:1, blue) of **C-2** and **C-6** as well as a reference sample of **C-2** (green). In the 2:1 mixture residual traces of **C-2** can be observed.

Furthermore, HR-MS spectra were collected to confirm the presence of the iron(III)-hydroxido species in this comproportionation reaction. Table 6 gives an overview over the observed species. The concentration range was chosen so that a final concentration of iron of c = 0.5 mM was reached upon mixing.

*Table 6: Observed species in HR-MS experiments of a reaction of **C-2** with **C-6** (1:1, [**C-2**]/[**C-6**] = 0.25 mM) and a **C-4** reference sample ([**C-4**] = 0.05 mM). All measurements were conducted in pure water at a flow rate of 100 μl/min.*

species	Calcd. m/z	C-2 + C-6	C-4 reference
[Fe^{III}(OH)(**L-1**)]$^{2+}$	258.07435	258.07415	258.07355
[Fe^{II}(OTf)(**L-1**)]$^{+}$	648.09796	648.09900	648.09609
[Fe^{III}(OH)(**L-1**)(OTf)]$^{+}$	665.10070	665.10191	665.09883
Li[Fe^{III}(OH)(**L-1**)(OTf)$_2$]$^{+}$	821.06873	-	821.06664

All signals that were found and assigned to an iron species in the **C-4** reference sample were also found in the **C-2**:**C-6** mixture with the exception of the Li[Fe^{III}(OH)(**L-1**)(OTf)$_2$]$^{+}$ species (this was probably observed in the reference measurement because likely lithium ions were present in the

mass spectrometer from previous measurements). Whereas the data definitely confirms the presence of the expected iron(III) species in the mixture, the detected iron(II) species [Fe^{II}(OTf)(**L-1**)]$^+$ is noteworthy. In both samples, mixture and **C-4** reference sample, this species was detected. However, in the reference sample the intensity was much lower than in the mixture sample. An explanation for this species could be that a) iron(II) is always present when the **C-4** is synthesized or b) iron(II) is formed upon measurement in the mass spectrometer. The second interpretation is likely, as in previous synthesis attempts the iron(II) species were isolated when an organic solvent was used (*vide infra*). As the mass spectrometer used for these experiments (Thermo Finnigan LTQ FT Ultra Fourier Transform Ion Cyclotron Resonance mass spectrometer with acetonitrile/water as the carrier solvent, operated by Dr. Werner Spahl at the department of chemistry) is usually operated with a mixture of acetonitrile and water, residual amounts of acetonitrile are likely present. Indeed, Mößbauer analysis of the **C-4** showed that the sample used was indeed pure iron(III)-hydroxido (refer to chapter IV.4).
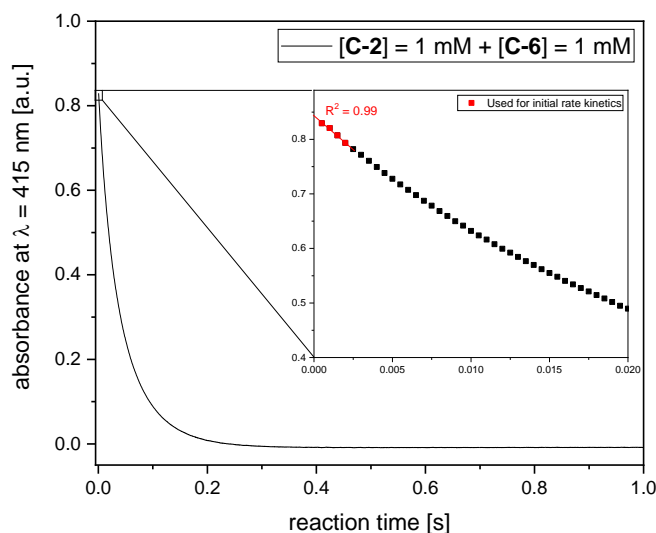
*Figure 78: Stopped-flow UV-vis measurement of the comproportionation of **C-2** and **C-6** at λ = 445 nm including a zoomed-in version of the first 0.02 s. Red data points were used for initial rate kinetics. Conditions: [**C-2/C-6**] = 1 mM, H$_2$O, T = 24 °C.*

Stopped-flow UV-vis measurements of the proposed comproportionation reaction confirmed the previously observed high reaction rate. When solutions of **C-2** and **C-6** were mixed ([**C-2/C-6**] = 1 mM), a fast decrease in the absorption at λ = 445 nm was observed (**C-4** does not show significant absorption at this wavelength). The reaction seems to be complete within 0.4 s, the reaction rate was calculated using the method of initial rates at v = 2.43 * 10^4 mol l^{-1} s^{-1}. This means that the comproportionation between **C-2** and **C-6** is much faster (~800-1000 fold) than the reactions observed between **C-6** and the tested substrates **5mC**, **5hmC**, **T**, etc.

At this point it can safely be concluded that **C-2** and **C-6** form **C-4** in a comproportionation reaction. Such reactions have, on occasion, been described for related iron complexes (refer to chapter IV.1) However, it remains an open question whether this behavior is universal for all iron(IV)-oxido systems. Furthermore, studies on the activity of **C-4** towards organic reactions

122

need to be conducted to assess its role in the reaction of **C-6** with substrates. Additionally, **C-4** has been proposed as the active species in the catalytic reaction of **C-2** (the perchlorate derivative thereof) with hydrogen peroxide and organic substrates such as cyclohexane and benzyl alcohol by Xiang *et al.* in 2015.[74] Confirming this hypothesis would shed further light on the behavior of iron complexes bearing the **L-1** ligand.

4. Synthesis and Analysis of [Fe^{III}(OH)(Py$_5$Me$_2$H)]$^{2+}$

Synthesis Optimization

When the hypothesis of comproportionation was postulated, a reference sample of **C-4** was required. Unfortunately, efforts to synthesize and isolate **C-4** directly from ligand **L-1** and a metal precursor (Fe(OTf)$_3$), instead of crystallizing it from a reaction solution, proved unsuccessful initially. The only compounds isolated were the corresponding iron(II) acetonitrile complexes, sometimes as single crystals suitable for x-ray crystallography (Figure 79**A**-**E**, x-ray crystallographic structures not shown, refer to the appendix p. 489 (**C-1**, **A**) p. 491 (**C-1**, **B**), p. 493 (**C-1b**, **C**), p.495 (**C-3**, **E**)). This is rather surprising, as the iron ions in the mixture must then be reduced – opposite to what is usually observed for solutions of iron(II) or iron(III) under ambient conditions, these typically react towards iron(III).
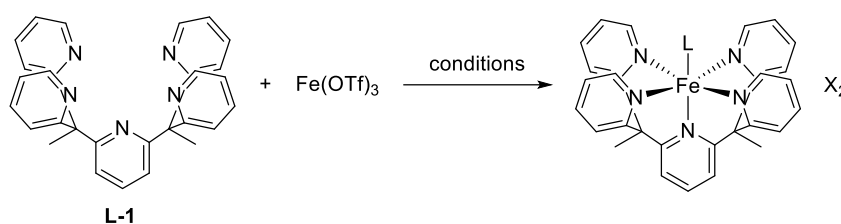
reaction	conditions	L	product
A	acetonitrile	mecn	C-1
B	acetonitrile/H$_2$O, NaNO$_3$	mecn	C-1
C	acetonitrile/H$_2$O, NaPF$_6$	mecn	C-1b
D	acetone/H$_2$O, NaNO$_3$	mecn	C-1
E	H$_2$O/pyridine	Py	C-3
F	H$_2$O	OH	C-4

*Figure 79: Attempted syntheses of **C-4** from **L-1** and Fe(OTf)$_3$. X = OTf$^-$, NO$_3^-$, PF$_6^-$. Py = pyridine.*

As **C-4** had been isolated previously from purely aqueous solutions of **C-6** and organic substrates, the solvent was then changed to pure water. In this manner, **C-4** was isolated in pure form (Figure 79**F**).

After **C-4** was synthesized successfully, the procedure was optimized to the following: ligand **L-1** was ground to a fine powder and then suspended in water. Fe(OTf)$_3$ was added as a solid and the mixture sonicated for 10 min. This resulted in the formation of a red solution containing a red precipitate. The precipitate was filtered off and NaOTf was added to the solution, which was stored at 4 °C to yield crystals of **C-4** x H$_2$O suitable for x-ray crystallography (structure not shown, refer to the appendix p. 499). The previously obtained precipitate was dissolved in water and recrystallized at 40 °C. The obtained solid was characterized as **C-4** x 2 H$_2$O by elemental analysis. Lyophilization and subsequent recrystallization from water afforded **C-4** x 3 H$_2$O. Drying the solids in an oven at 100 °C over night decreased the amount of crystal water to 1.0 equivalents, however, longer exposure to high temperatures led to decomposition of the product. Increasing

the temperature of the reaction did not have any effect on the yield but did produce larger crystals upon cooling.
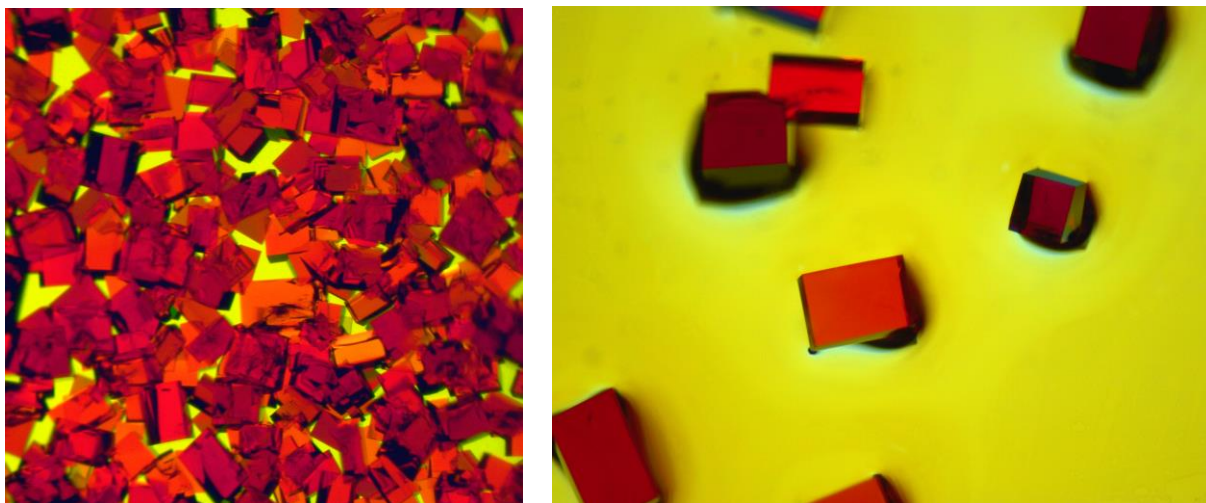
*Figure 80: Pictures of crystals of **C-4**, obtained from an aqueous solution of **C-4** at 4 °C.*

As a deprotonation step is required to form the hydroxide ligand, pyridine was added as a base in order to increase yield (Figure 79**E**). This resulted in the formation of brown crystals that were suitable for x-ray crystallography and characterized as [Fe^{II}(py)(**L-1**)](OTf)$_2$ (**C-3**, Figure 81). As with acetonitrile, addition of pyridine seems to result in reduction of the iron ions to iron(II). Use of Fe(ClO$_4$)$_3$ as iron(III) precursor led to the formation of [Fe^{III}(OH)(**L-1**)](ClO$_4$)$_2$, as observed *via* HR-MS and elemental analysis (not shown, refer to experimental section p. 264). No single crystals could be isolated of this species after several crystallization attempts.

Addition of NaBF$_4$ or NaPF$_6$ to solutions containing **L-1** and FeCl$_3$ in water did not yield any pure substances but a mixture of differently colored precipitates that were not analyzed further.
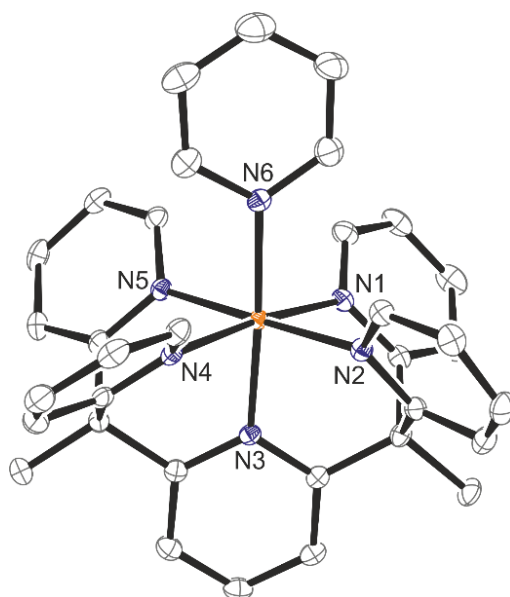
*Figure 81: Visual representation of the cation in **C-3**. Ellipsoids are drawn at 50% probability; hydrogen atoms and counter ions were omitted for clarity. Refer to the appendix p. 495 for a complete structure and crystallographic details.*

Analysis of **C-4**

C-4 was then analyzed using EPR (Figure 82**A**), Mößbauer spectroscopy (Figure 82**B**), as well as cyclic voltammetry (Figure 83). The EPR and Mößbauer spectra are in accordance with low spin iron(III) complex in a distorted octahedral ligand environment.
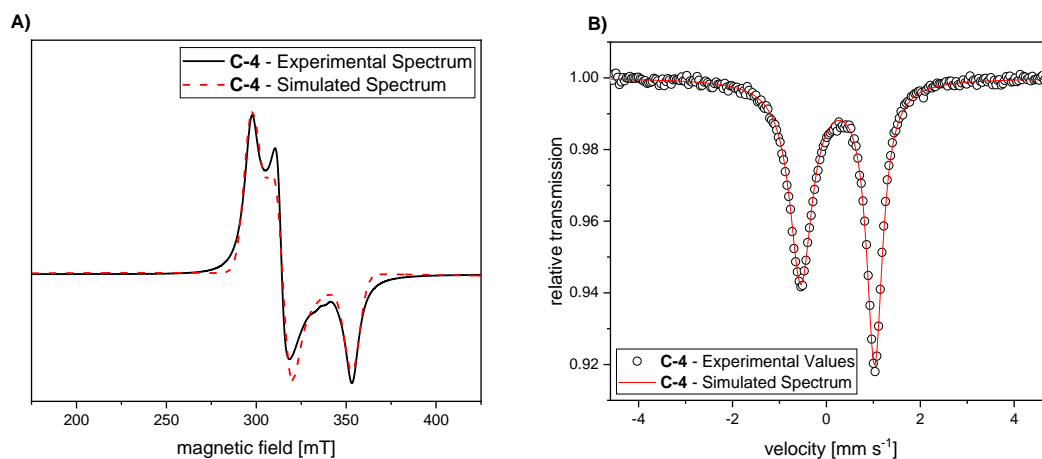
*Figure 82: **A**) X-band EPR spectrum (black solid) of a powdered sample of **C-4** at 296 K, simulated spectrum (red dashed) by Dr. Katherine Fisher. **B**) Mößbauer spectrum of **C-4** at 80 K, measurement and simulation by Serhiy Demesheko.*

Cyclic voltammetry measurements of **C-4** in wet acetonitrile under equilibrium conditions showed three reversible peaks (Figure 83). Notably, the observed intensity changes differently for the two signals between 0.3 to 0.7 V when the scan rate is increased. The left peak (**1**), attributed to the $[Fe^{II}(OH)(L-1)]^+/[Fe^{III}(OH)(L-1)]^{2+}$ couple, increases less than the right peak (**2**), which was attributed to the $[Fe^{II}(OH_2)(L-1)]^{2+}/[Fe^{III}(OH_2)(L-1)]^{3+}$ couple. The rightmost peak (**3**) was attributed to the $[Fe^{II}(mecn)(L-1)]^{2+}/[Fe^{III}(mecn)(L-1)]^{3+}$ couple. These measurements show that the electron transfer is proton coupled, which has previously been reported for **C-1**, an iron(II) derivative of **C-4**.[12]
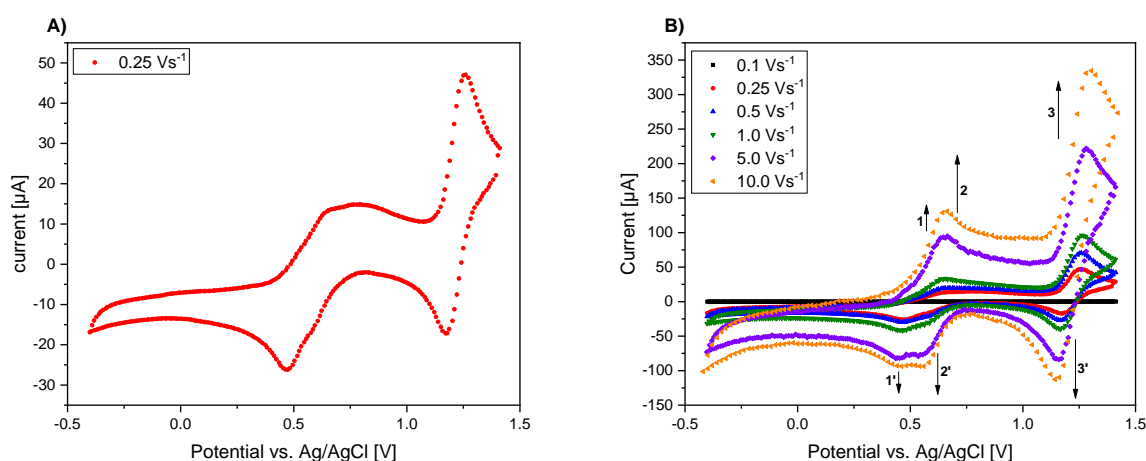
*Figure 83: **A**) Cyclic voltammogram of **C-4** at 0.25 Vs^{-1}. **B**) Cyclic voltamograms of **C-4** at different scan rates. Measurements were conducted in wet acetonitrile under equilibrium conditions.*

The ^{18}O-labeled complex $[Fe^{III}(^{18}OH)(L-1)](OTf)_2$ (**C-4**) was synthesized and the incorporation of the ^{18}O label confirmed using Raman spectroscopy. To this end, **C-4** was synthesized under identical conditions using $H_2^{16}O$, $H_2^{18}O$, and a mixture of $H_2^{16}O/H_2^{18}O$ (Figure 84**A**). The obtained

solids were studied using Raman spectroscopy: around 600 cm⁻¹, two distintinctive signals were observed in samples of ¹⁶O-**C-4** and ¹⁸O-**C-4**, that were assigned to the respective Fe-O bond (Figure 84**B**).
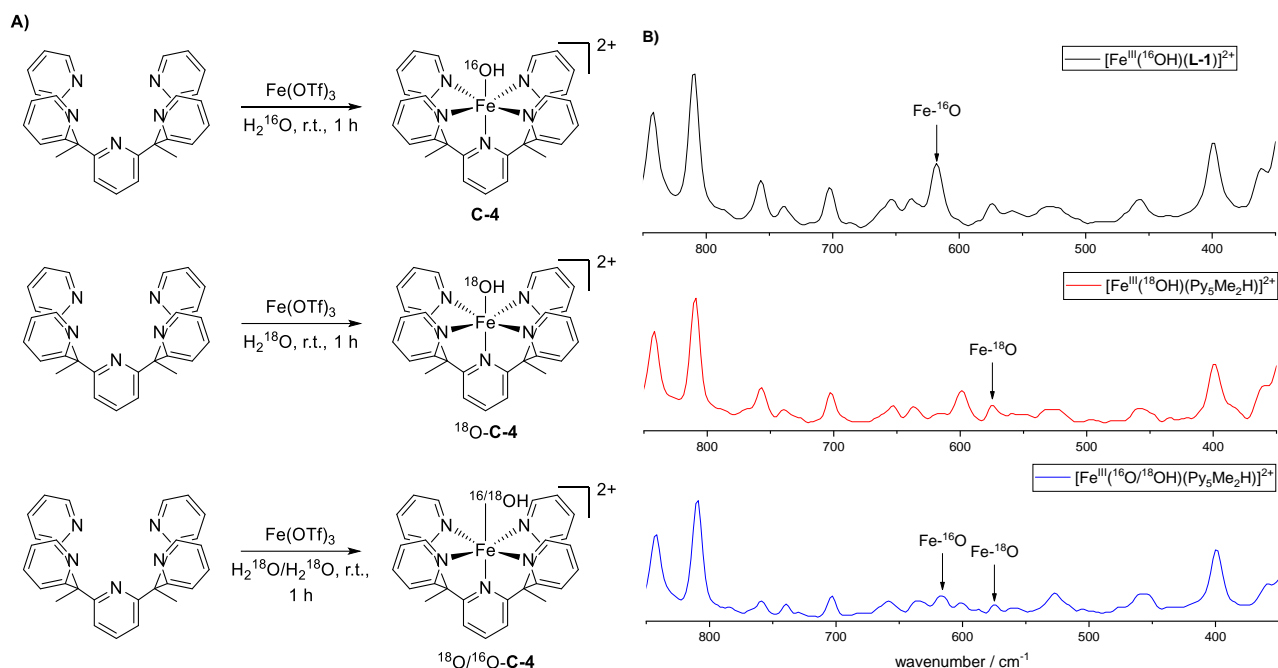
*Figure 84: **A**) Synthesis of different derivatives of **C-4** from **L-1**: [Fe^{III}(¹⁶OH)(**L-1**)](OTf)$_2$, [Fe^{III}(¹⁸OH)(**L-1**)](OTf)$_2$, and mixture of [Fe^{III}(¹⁸/¹⁶OH)(**L-1**)](OTf)$_2$. **B**) Excerpts of Raman spectra of the corresponding derivatives of C-4, the respective signal corresponding to the Fe-¹⁶O or Fe-¹⁸O bond is indicated.*

Then, the complex's behavior in water and ¹⁸O-labeled water was studied using LR-MS. It was found that the hydroxide ligand of **C-4** exchanges rapidly with water. When 18O was added during the MS-measurement, a signal corresponding to ¹⁸O-**C-4** was observed. This rapid exchange of the hydroxido ligand is unfortunate, as it does not allow for easy tracking experiments in which the ¹⁸O label is followed. In such experiments it would therefore be necessary to work under strict exclusion of water (refer to chapter IV.0, p. 132ff).
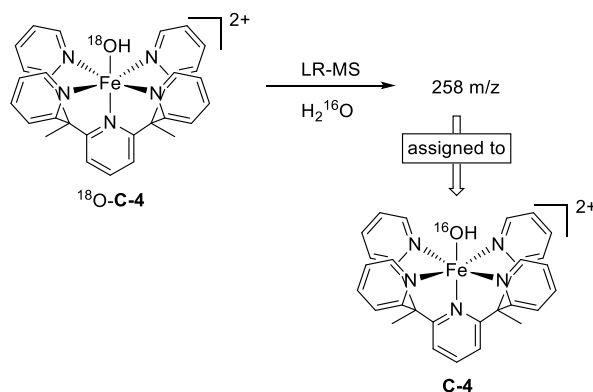
*Figure 85: LR-MS measurement of ¹⁸O-**C-4** in ¹⁶O water.*

5. Reactivity Studies with Organic Substrates

C-4 represents an interesting research target in its reactions with several organic substrates. First of all, iron(III) species have been implicated in the reaction mechanisms of a variety of iron enzymes, both of heme and non-heme type (refer to chapter I.2). Synthetic iron(III)-hydroxido complexes have been used to study the proposed rebound step, however, not many such systems are known (refer to chapters I.2 and 0). Investigation of **C-4** in reactions with stable radicals, such as the trityl radical, or radical clocks to determine the reaction kinetics would provide additional data on this biologically relevant step.

As mentioned above, Xiang *et al.* proposed **C-4** as the intermediate in the catalytic oxidations of benzyl alcohol and cyclohexane, as described in chapter I.3.[74] Confirmation or invalidation of their hypothesis would give insight into the reactivity of **C-4** in general: is this iron(III)-hydroxido species capable of oxidizing organic substrates? If yes, does it also react with the previously studied substrates **5mC**, **5hmC**, **5mdC**, etc.?

*Reactions with Benzyl Alcohol, Cyclohexane, **5mC**, and **5hmC***

From the publications of Xiang *et al.* (oxidation of organic substrates by proposed iron(III)-hydroxido complex) and Chantarojsiri *et al.* (oxidation of organic substrates by iron(IV)-oxido complex) and the observations described in this work (refer to chapter III for substrate reactions of **C-6** and chapter IV.3 for comproportionation of **C-6** and **C-2**) a reaction map including all possible reactions was constructed (Scheme 63): a substrate R-CH$_2$-H is oxidized by one equivalent of **C-6** in a "regular" iron(IV)-oxido reaction (blue bold arrow), yielding R-CH$_2$-OH and an equivalent of **C-2** (black curved arrow). This process can be repeated twice yielding R-CHO and R-CO$_2$H as well as two more equivalents of **C-2** (blue bold arrows). **C-2** comproportionates with **C-6** to form **C-4** (lower green dashed arrows).
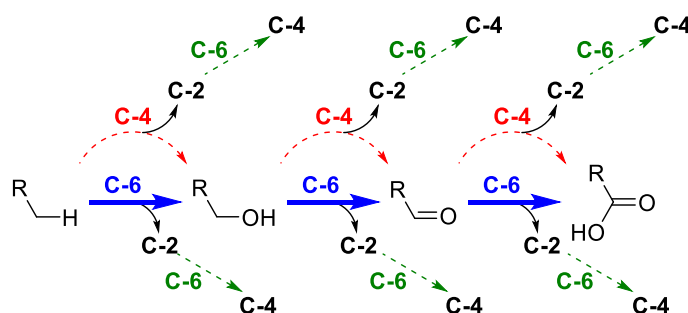
*Scheme 63: Reported reactions for a substrate R-CH$_2$-H: Oxidation by **C-6** leads to R-CH$_2$-OH, R-CHO, and R-CO2H (blue bold arrows). In each step an equivalent of **C-2** is formed, which comproportionates with another equivalent of **C-6** (lower green straight dashed arrows). Parallelly, R-CH$_2$-H can be oxidized by **C-4** (red curved dashed arrows), also generating an equivalent of **C-2** which comproportionates with **C-6** to **C-4** (upper green straight dashed arrows). R = aliphatic or aromatic hydrocarbons.*

As now **C-4** is present, this can also react with the substrates R-CH$_2$-H, R-CH$_2$-OH, and R-CHO (red dashed arrows). In these reactions, **C-2** is formed which subsequently comproportionates with **C-6** to form **C-4** (upper green dashed arrows). Due to the comproportionation reaction of **C-**

6 with **C-2**, significant levels of **C-4** are expected in reaction solutions of **C-6** with organic substrates (refer to chapter IV.3).

As mentioned above, Xiang *et al.* had previously postulated that **C-4** is the active species in the oxidation of benzyl alcohol to benzaldehyde in acetone. It is therefore within reason to expect reactivity of **C-4** with the epigenetically relevant substrates **5mC**, **5hmC**, and/or **5fC** of chapter III. Therefore, the reactivity of **C-4** towards **5mC** and **5hmC** was investigated in an attempt to assign the observed oxidative reactivity clearly to one iron species.

Table 7 gives an overview of the conducted reactions. Reactions **A/B** and **F/G** were intended to give reference spectra of successful oxidation reactions. Reactions **C** and **H** would give the required information of **C-4** oxidation using a pure **C-4** sample. Reactions **D/E** as well as **I/J** resemble the conditions in reactions of **C-6** with organic substrates as mixtures of different iron species are present. A series of control reactions of all individual components complemented this experimental setup. The reactions were then analyzed using GC-MS as described in chapter III.4.

*Table 7: Experiments with **5mC** (top section) and **5hmC** (middle section) in combination with **C-2**, **C-4**, and **C-6**. Control reactions are shown in the lower section. Conditions: [**C-2**] = 0.5-1 mM, [**C-4**] = 1 mM, [**C-6**] = 1-2 mM, H$_2$O, t = 30 min, T = 24 °C.*

No.	[5mC] [mM]	[5hmC] [mM]	[C-2] [mM]	[C-4] [mM]	[C-6] [mM]
A	1	-	-	-	1
B	1	-	-	-	2
C	1	-	-	1	-
D	1	-	-	1	1
E	1	-	0.5	-	1.5
F	-	1	-	-	1
G	-	1	-	-	2
H	-	1	-	1	-
I	-	1	-	1	1
J	-	1	0.5	-	1.5
5mC ctrl.	1	-	-	-	-
5hmC ctrl.	-	1	-	-	-
C-2 ctrl.	-	-	1	-	-
C-4 ctrl.	-	-	-	1	-
C-6 ctrl.	-	-	-	-	1

As expected, the control reactions containing only the iron complexes showed no signals in the relevant range. The control measurements containing **5mC** or **5hmC** showed the expected signals.

Table 8 gives a qualitative overview of the obtained results as well as the quantitative ratio of **5fC** to **5mC** or **5hmC**. As expected, the amount of **5fC** increased from sample **A** to sample **B** and sample **F** to **G** as more **C-6** was present. Samples **C** and **H** showed no oxidation products. Samples **D** and **I** showed slightly decreased activity compared to samples **A** and **F**, respectively, even though the same amount of **C-6** was present. Whether this is within the error of the method of measurement or because of interactions of the nucleobases with **C-4** cannot be determined at this point. Samples **E** and **J** also showed slightly lower **5fC:S** (S = **5mC** or **5hmC**) ratio than was expected, even if it is assumed that the 0.5 equiv. of **C-2** comproportionated with 0.5 equiv. of **C-6**, leaving only 1.0 equiv. of **C-6** for substrate for oxidation. Samples **D** and **E** as well as **I** and **J** are virtually indistinguishable which supports the comproportionation hypothesis.

*Table 8: Results of the experiments discussed above. (S = **5mC** or **5hmC**)*

No.	Qualitative Analysis	Quantitative Analysis Ratio 5fC:S
A	Regular reactivity	0.05
B	Regular reactivity	0.10
C	No reactivity	0.00
D	Regular reactivity	0.04
E	Regular reactivity	0.04
F	Regular reactivity	0.80
G	Regular reactivity	4.37
H	No Reactivity	0.00
I	Slightly lower reactivity	0.30
J	Lower reactivity	0.56

In the case of **5hmC** (Table 8, lower section), a similar trend is observed although the quantitative analysis reveals larger deviations. Whether this is due to the higher reactivity of **5hmC** (small differences in composition lead to large differences in product formation) or an interaction of **5hmC** with the iron(III)-hydroxido complex could not be determined at this point. UV-Vis or HR-MS studies of the interaction of **5hmC** with **C-4** might provide some insight.

Using these results, the general reaction scheme shown in Scheme 63 was simplified for the applied conditions (S = **5mC** or **5hmC**, H$_2$O, t = 30 min, T = 24°C). Under these conditions, only substrate oxidation by **C-6** was observed in addition to the previously discussed comproportionation reaction. **C-4** was found to be inert towards **5mC** or **5hmC**.
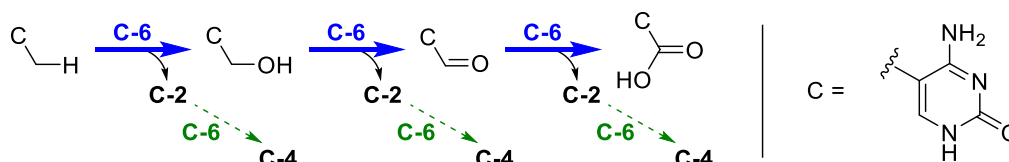
*Scheme 64: Simplified reaction scheme for a substrate R-CH$_2$-H: Oxidation by **C-6** leads to R-CH$_2$-OH, R-CHO, and R-CO2H (blue bold arrows). In each step an equivalent of **C-2** is formed, which comproportionates with another equivalent of **C-6** (green straight dashed arrows).*

As these findings are in contradiction to those of Xiang *et al.*,[74] the reaction conditions described by Xiang *et al.* were recreated and similar reactions with **C-4** conducted to compare the results of the catalytic activity of **C-1**/H$_2$O$_2$ with pure **C-4**.

solvent:	acetone or water
reaction time:	3 h
internal standard:	chlorobenzene (acetone) phenol (water)
[Fe]	**C-1** + H$_2$O$_2$
	C-4
	Fe(mecn)$_2$(OTf)$_2$ + H$_2$O$_2$
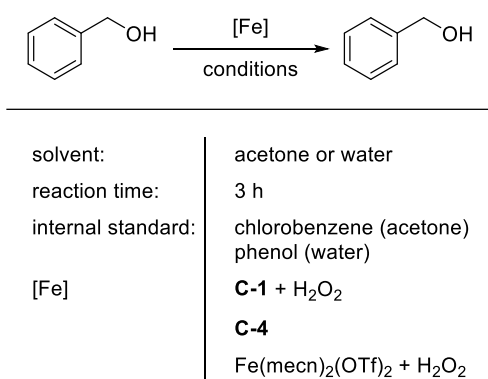
Scheme 65: Reaction of benzyl alcohol with different iron compounds (and hydrogen peroxide) in acetone or water.

To this end, benzyl alcohol was reacted with a mixture of a catalytic amount of **C-1** and hydrogen peroxide or pure **C-4** in acetone or water. In addition, a mixture of Fe(mecn)$_2$(OTf)$_2$ and hydrogen peroxide was also reacted with benzyl alcohol to obtain Fenton chemistry conditions (Scheme 65). The obtained product mixtures were analyzed using GC-MS: the observed signals were identified using reference samples and EI mass spectra, then integrated and the integration values compared those of the added internal standards (IS). The results are presented in Table 9.

*Table 9: Observed conversions of benzyl alcohol by iron complexes **C-1** and **C-4** as well as iron(II) salt Fe(mecn)$_2$(OTf)$_2$. When **C-1** or Fe(mecn)$_2$(OTf)$_2$ were used, H$_2$O$_2$ was added as oxidant. "Control" refers to a reaction without iron complex but at otherwise equivalent conditions. Note that due to the different solubility of the substrate in the respective solvent, different concentrations were chosen. However, the ratios iron compound/substrate and H$_2$O$_2$/substrate were kept the same. As internal standards chlorobenzene (in acetone) or phenol (in water) were used. Conditions: (**C-1**/substrate) = 0.1 mol%, (H$_2$O$_2$/substrate) = 10 mol%, (**C-4**/substrate) = 10 mol%, (Fe(mecn)$_2$(OTf)$_2$ = 0.1 mol%, (internal standard/substrate) = 5 mol%, v = 3 ml, t = 3 h. n.d. = not determined.*

Reaction No.	Iron Compound (+ Additive)	Solvent	Conversion Reaction	Control
A	**C-1** + H$_2$O$_2$	Acetone	52%	20%
B	**C-4**	Acetone	6%	10%
C	**C-1** + H$_2$O$_2$	H$_2$O	7%	9%
D	**C-4**	H$_2$O	9%	8%
E	Fe(mecn)$_2$(OTf)$_2$ + H$_2$O$_2$	H$_2$O	5%	n.d.

In none of the reactions was any difference observed between the control reaction or the reaction containing an iron compound except for reaction **A**, in which **C-1** was mixed with H$_2$O$_2$ in acetone – *i.e.* the original conditions applied by Xiang *et al.*[74] Most interesting is that in reaction **B**, in which **C-4** – the postulated intermediate formed from **C-1** and H$_2$O$_2$ – no additional reactivity was observed. These results clearly do not support the hypothesis of Xiang *et al.* that **C-4** is the active species in the catalytic oxidation of benzyl alcohol.

Concerning the samples performed in water, no reactivity was observed. This is in line with the results presented above. Interestingly, in all reactions a significant background reaction was observed. This is likely due to molecular oxygen – and not hydrogen peroxide – oxidizing benzyl alcohol in solution, as reactivity was also observed in reactions **B** and **D**. Further experiments should therefore be performed under exclusion of air to control for this reactivity. Due to the low observed conversion in reaction **E** no control measurement was performed.

A set of additional experiments was conducted in which a sample of **C-4** (in water) or a mixture of **C-2** and **C-4** (in water) was mixed with acetone (10 vol%). Over the course of t = 10 min, neither sample showed significant change (not shown). However, both baselines slightly shifted and some gas bubbles were visible in the cuvette. HR-MS analysis of the sample of **C-4** with acetone did not show any significant difference to the sample without acetone. This would be in line with the results of Xiang *et al.*,[74] who performed their experiments with the iron(II) complex [Fe^{II}(MeCN)(**L-1**)](ClO$_4$)$_2$ with hydrogen peroxide in acetone.

Synthesis and Investigation of Gomberg's Dimer (GD)

First, reaction of **C-4** with a stable, organic radical was to be studied. Therefore, Gomberg's dimer (**GD**) was synthesized as it provides easy access to the trityl radical (***IV-4***, Scheme 66).
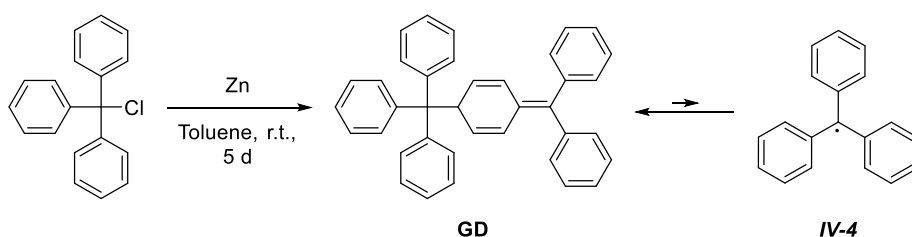
Scheme 66: Synthesis of Gomberg's dimer from trityl chloride and zinc,[277] the equilibrium of the dimer and trityl radicals is shown.

Synthesis of Gomberg's Dimer was achieved by reacting trityl chloride with zinc, as described previosly by Heurich *et al.*[277] EPR spectra of a solution in benzene show the presence of a radical species (***IV-4***, Figure 86**A**) and its decomposition upon exposure to daylight (Figure 86**B**, red line). This is in line with the literature, which states that a solution of **GD** in benzene contains ~2% of trityl radical ***IV-4*** at room temperature (Scheme 66).[278]
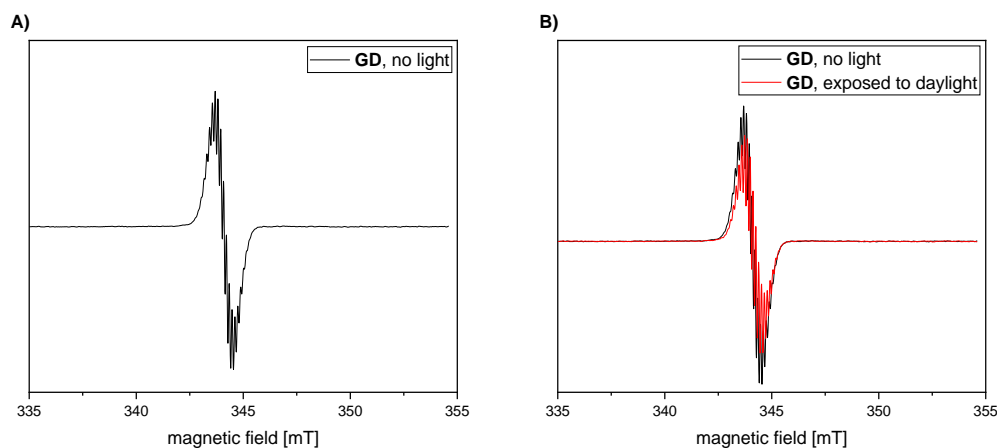
*Figure 86: **A)** EPR spectrum of a solution of Gomberg's dimer (**GD**) in benzene **B)** Overlayed EPR spectra of a solution of Gomberg's dimer (**GD**) in benzene prior to (black line) and after exposure to daylight for 10 min (red line). Spectra were collected at 296 K.*

Reaction of trityl radical with the ^{18}O labeled complex **C-4** should then form the ^{18}O labeled product triphenylmethanol, if a rebound-type reaction occurs (Figure 87). Unfortunately, **C-4** is insoluble in benzene or tetrahydrofuran, two common solvents used for this reaction.[48,49] Therefore, a solution of **GD** in dry benzene and a solution **C-4** in dry acetonitrile were prepared and mixed in a glove box under vigorous stirring. A sample was taken after 1 min reaction time and analyzed *via* GC-MS for the presence of the expected reaction products (Figure 87).
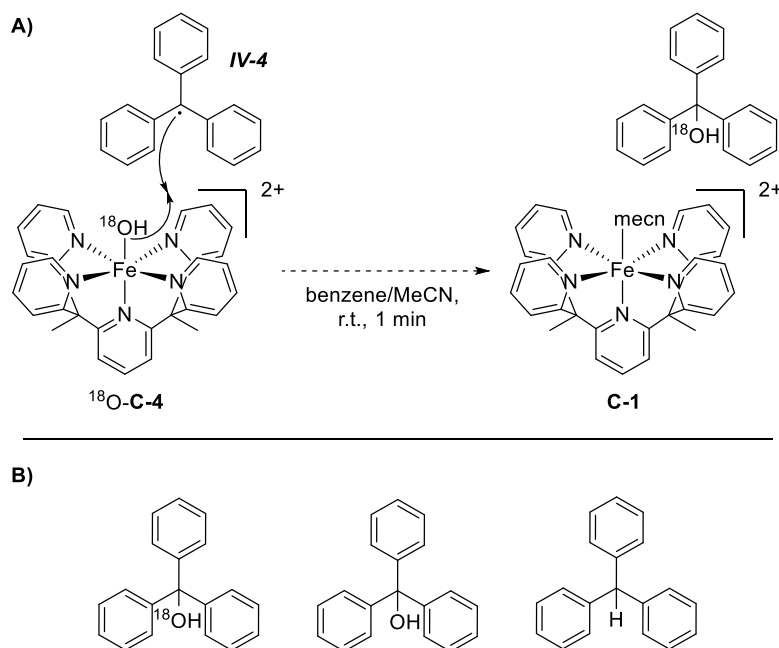
*Figure 87: **A)** Proposed reaction between ^{18}O-**C-4** and the trityl radical **IV-4** produced from Gomberg's dimer (**GD**). **B)** Envisioned expected product and likely side-products triphenylmethanol and triphenylmethane, respectively.*

In a first set of experiments using the unlabeled complex **C-4**, triphenylmethanol and triphenylmethane were identified in the GC-MS traces of both the reaction containing **C-4** (Figure 88**A**) and the control reaction (only acetonitrile, no **C-4**, Figure 88**B**). This indicates that **GD** must reacted with residual traces of water in the solvents (or other hydroxylating contaminants), even though benzene and acetonitrile were bought as dry solvents, degassed, and handled exclusively

133

in the glovebox. However, the detected amounts of triphenylmethane and triphenylmethanol in the samples indicate that when **C-4** was present, significantly more triphenylmethanol had formed. The ratio between the signals at $t_R = 10.7$ min (triphenylmethane) and $t_R = 12.3$ min (triphenylmethanol) was determined to be 1.8 for the reaction with **C-4** and 0.8 for the control reaction, this corresponds to a ~220% increase. These results show that **C-4** is indeed capable of transferring its hydroxyl moiety to an organic radical.
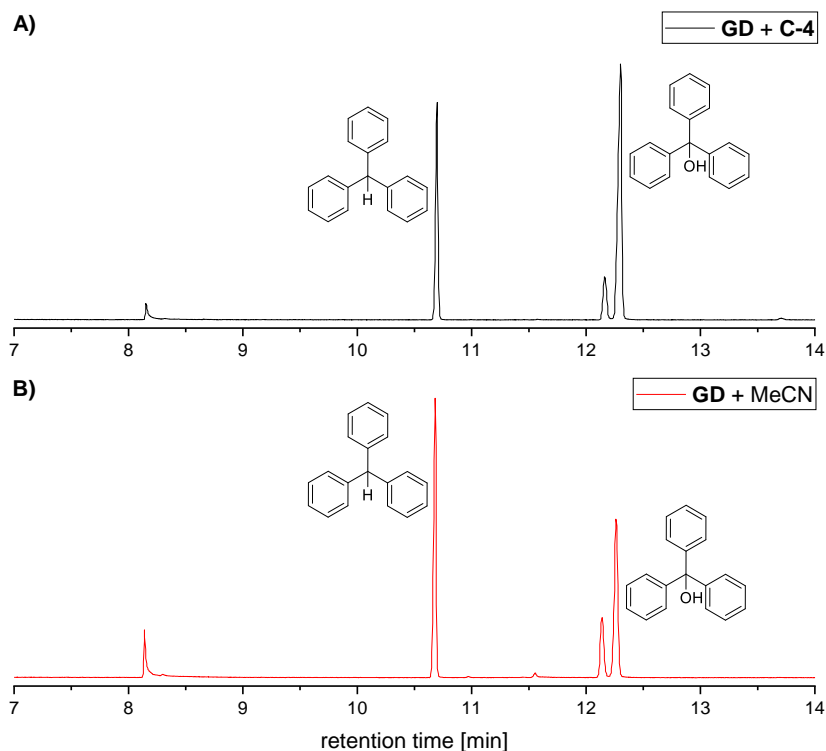
*Figure 88: Excerpt of GC-MS traces of **A**) a solution of **GD** in benzene mixed with a solution of **C-4** in acetonitrile and **B**) a control reaction of a solution of GD in benzene with pure acetonitrile. Signals at $t_R = 10.7$ min and $t_R = 12.3$ min were assigned based on retention time and EI mass spectrometry as well as comparison with the NIST 2020 database. GC-MS method **A**. Conditions: [**C-4**] = 5 mM, [**GD**] = 5 mM, benzene/acetonitrile, T = 24 °C.*

However, due to the large amount of triphenylmethane present, further experiments are necessary to confirm this finding. As the glovebox in our laboratory is operated in wet box mode, there is likely a significant amount of water vapor present. Therefore, these experiments were repeated under strict exclusion of water (Figure 89). In these cases, the increase of triphenylmethanol when **C-4** was added compared to the control reaction was even more pronounced with a ~300% increase. However, still a significant amount of triphenylmethane was observed. This could be due to a reaction between the trityl radical ***IV-1*** and **C-4** in which the O–H bond is broken instead of the Fe–O bond. Further experiments, e.g. involving other stable radicals such as (2,2,6,6-tetramethylpiperidin-1-yl)oxyl (TEMPO) or the labeled complex ^{18}O-**C-4**, are necessary to investigate this hypothesis.
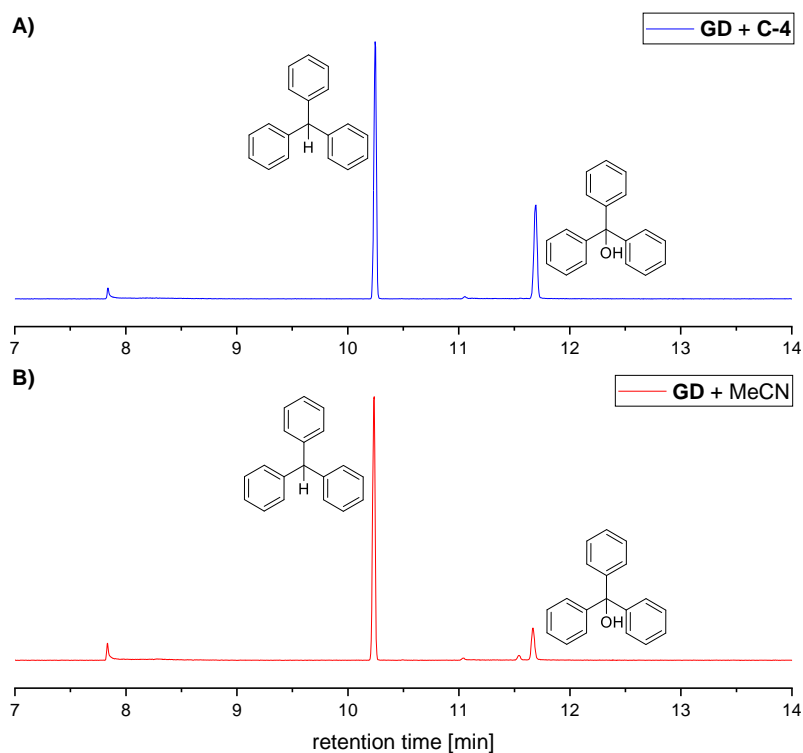
*Figure 89: Excerpt of GC-MS traces of **A**) a solution of GD in benzene mixed with a solution of **C-4** in acetonitrile and **B**) a control reaction of a solution of GD in benzene with pure acetonitrile. Signals at t_R = 10.2 min and t_R = 11.7 min were assigned based on retention time and EI mass spectrometry as well as comparison with the NIST 2020 database. GC-MS method **A**. Conditions: [**C-4**] = 2.5 mM, [GD] = 2.5 mM, benzene/acetonitrile, T = 22 °C.*

Radical Clocks

Another possibility to investigate the rebound mechanism is the use of a so-called radical clock. As mentioned above, a radical clock is a compound that undergoes rapid reorganization if a radical is formed at the right position of the molecule (refer to chapter IV.1, p. 116). To this end, synthesis of methyl 2,2-dichloro-3-methylcyclopropane-1-carboxylate from methyl crotonate after a modified literature procedure was attempted (Scheme 67).[279] The two chloride moieties were envisioned to block an otherwise competitive C-H bond and might therefore result in a cleaner product mixture. Unfortunately, the cyclopropanation reaction yielded only very little product (mostly starting material and side-products were observed *via* GC/MS), which could not be isolated from the complex mixture, therefore the synthesis was discontinued.
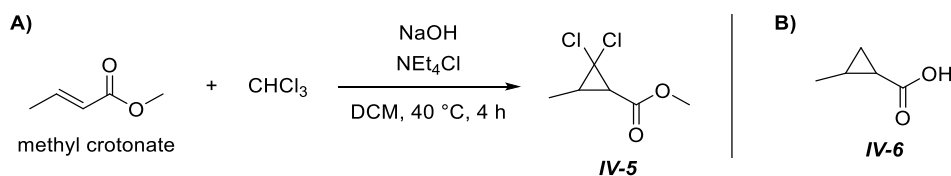
*Scheme 67: **A**) Dichloro-cyclopropanation* via *the dichloro carbene generated from CHCl$_3$/KOH. **B**) 2-methylcyclopanecarboxylic acid (**IV-6**).*

2-methylcyclopanecarboxylic acid (**IV-6**, Scheme 67) is commercially available and was used instead. As **C-6** is soluble only in water but analysis of **IV-6** and its reaction products is best done

135

via GC-MS and analysis of aqueous systems is difficult at best, a mixed phase system was employed: **C-6** complex was dissolved in water which is layered with an organic solvent containing the radical clock. A purely aqueous system could not be used due to the volatile nature of the radical clock and the expected reaction products, as the solution would need to be dried and re-dissolved in an organic solvent prior to GC-MS measurement.

In a first attempt, diethyl ether was tested as organic solvent for these experiments. Diethyl ether was therefore layered over an aqueous solution of **C-6**. Unfortunately, the color of the aqueous layer quickly changed from green to brown, indicating a reaction between **C-6** complex and diethyl ether. Thus, benzene was tested as solvent, which does not possess any aliphatic carbon-hydrogen bonds and should therefore be inert. Indeed, the green color of the solution of **C-6** did not change over the course of several hours. GC-MS analysis of the benzene layer also did not show any new signals indicating a stable system.

Subsequently, a series of experiments and control experiments were performed, an overview is shown in Table 10. The color indicated is the one observed at the end of the reaction (15 h). The solutions were stirred vigorously to allow for sufficient mixing of the components. When the reactions were deemed complete, the layers were separated and the benzene layer transferred to a vial and used without further processing for GC-MS measurement.

*Table 10: Experiments with **C-6** and the radical clock **IV-6**. Conditions: [**C-6**] = 10 mM, [**IV-6**] = 10 mM, H₂O/benzene, T = 23 °C.*

Nr.	H₂O [ml]	Fe^{IV}(O) [mM]	Benzene [ml]	*IV-6* [mM]	Color
A	0	0	1	10	Colorless
B	1	0	1	0	Colorless
C	1	0	1	10	Colorless
D	1	10	1	0	Slightly Brown
E	1	10	1	10	Red/Orange

The GC-MS traces of **B** and **D** show only a single signal that was assigned to benzene. The GC-MS traces of experiments **A**, **C**, and **E** show signals corresponding to *IV-6* and benzene, as expected. GC-MS trace of **E** unfortunately does not show any other signals, even though a color change was observed from green to red/orange, which would indicate reactivity of **C-6** complex with a compound present in the mixture. It therefore remains unclear whether the expected products did not form in the first place, decomposed during GC-MS measurement, or were only dissolved in the aqueous layer.

Addition of BSTFA to the benzene layer after the layers were separated might provide a solution: any products formed would be derivatized to their corresponding TMS ethers or esters possibly improving GC-MS analysis.

In addition, methyl cubane derivatives could be used as radical clocks. These compounds have been used in the literature for studying the rebound mechanism in heme-type iron enzyme

cytochrome P450.[280] As with methyl cyclopropanes, the formation of hydroxylated products indicates a fast rebound reaction, whereas observation of ring-opening reactions indicates a slow(er) rebound reaction (Scheme 68).
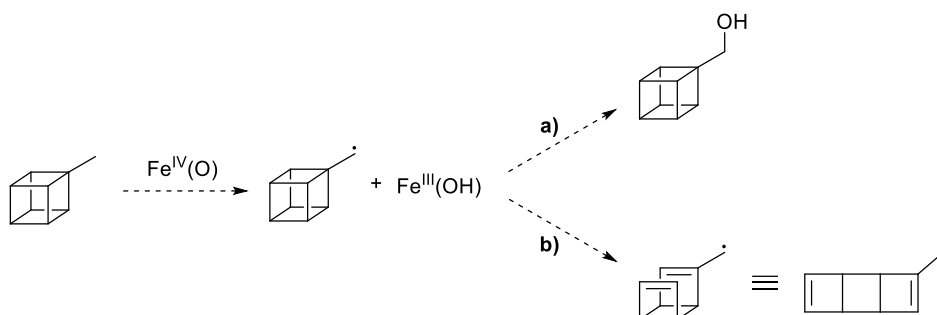
Scheme 68: Possible application of methyl cubane as a radical clock: after HAT by an iron(IV)-oxido species a radical is formed that is either **a**) hydroxylated or **b**) rearranges. Modified from Choi et al.[280]

6. Miscellaneous: Auto-Decomposition

As mentioned above, the iron(IV)-oxido complex **C-6** displays auto-decomposition in aqueous solution at room temperature. A possible reaction pathway would be hydroxylation of the two methyl groups on the ligand resulting in the formation of **IV-7** (Scheme 69). In this process one equivalent of **C-2** is formed which then comproportionates with one equivalent of **C-6**, effectively reducing the amount of **C-6** by two equivalents for each decomposition reaction.

Additionally, the formation of bridged μ-oxido iron(III) dimers has been observed for iron(IV)-oxido species and might contribute to the observed decomposition,[236] however, HR-MS of solutions of **C-6** never showed signals corresponding to such a bridged μ-oxido-dimer (not shown).
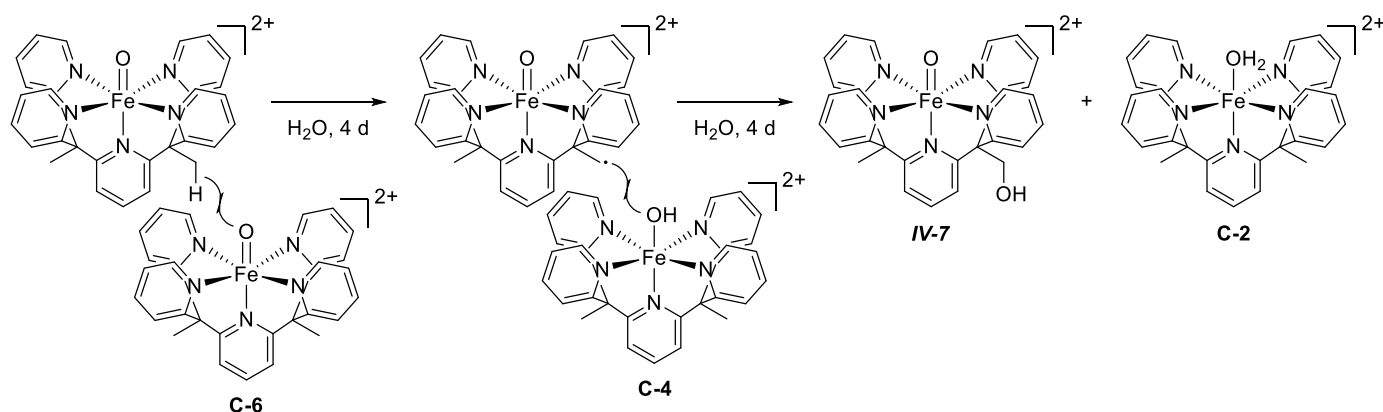
Scheme 69: Postulated mechanism for auto-decomposition of **C-6** resulting in the formation of **IV-7**.

The pathway proposed in Scheme 69 would follow a concentration dependent rate law, as two equivalents of **C-6** are necessary for the decomposition process. In order to confirm this, long-term UV-vis spectroscopy kinetics were conducted for three different concentrations (2.0 mM, 1.0 mM, 0.5 mM, Figure 90).
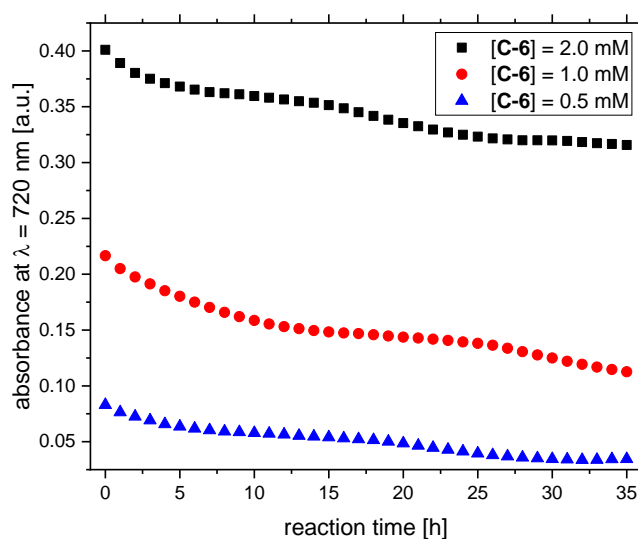
Figure 90: Long-term decomposition study of **C-6** monitoring the absorbance at λ = 720 nm. Conditions: [**C-6**] = 0.5-2.0 mM, H$_2$O, T = 23 °C.

The measured absorbance values show considerable variation (this was attributed to the change in room temperature during the measurements), still, linear fits over the entire data set were performed with good coefficients of determination (R^2 = 0.95). The slope values obtained hereby all fall within the same range, the slope values for [**C-6**] = 2.0 mM and [**C-6**] = 1.0 mM are even within 1σ of one another (s = –0.00216 and s = –0.00233, respectively) but, as of yet, do not allow for a clear interpretation. The decomposition reaction seems to be concentration independent, which does not support the above postulated mechanism. However, another set of experiments in which the temperature is held constant and additional concentrations are used should be conducted to shed more light on the auto-decomposition reaction. Organic contaminants in the water could also be the reason for the observed decrease in absorption at λ = 718 nm, this hypothesis also needs to be investigated further.

To investigate whether **C-6** decomposes by attacking its own ligand backbone, a solution containing the free ligand **L-1** and **C-6** was studied using LR-MS. This showed only slow decomposition, even after days at room temperature the solution remained green and LR-MS analysis showed only minor amounts of oxidized **L-1** (< 1%). Of course, the electronic properties of the free ligand are different from the complex and these results should therefore be interpreted with caution.

Another experiment that would shed light on the nature of decomposition reaction would be the synthesis of the methyl-deuterated ligand Py$_5$-D$_6$-Me$_2$H **IV-10** and its corresponding iron(IV)-oxido complex [Fe^{IV}(O)(Py$_5$-D$_6$-Me$_2$H)]$^{2+}$ **IV-12**. Due to the observed kinetic isotope effect in reactions of **C-6** (refer to chapter III.4), the reaction involving the methyl groups should be much slower in this case.

In addition to slowing auto-decomposition, the reactivity of the deuterated complex **IV-13**, Scheme 71) might differ from that of its undeuterated parent compound. This effect has been shown by Heinze *et al.*, who synthesized several deuterated versions of the ligand ddpd (ddpd = N,N'-dimethyl-N,N'-dipyridine-2-yl-pyridine-2,6-diamine) and observed vastly different results in their study of the luminescent properties of the corresponding cobalt complexes.[281] They studied different deuteration patterns, Scheme 70 gives an overview of their performed reactions in order to obtain these.
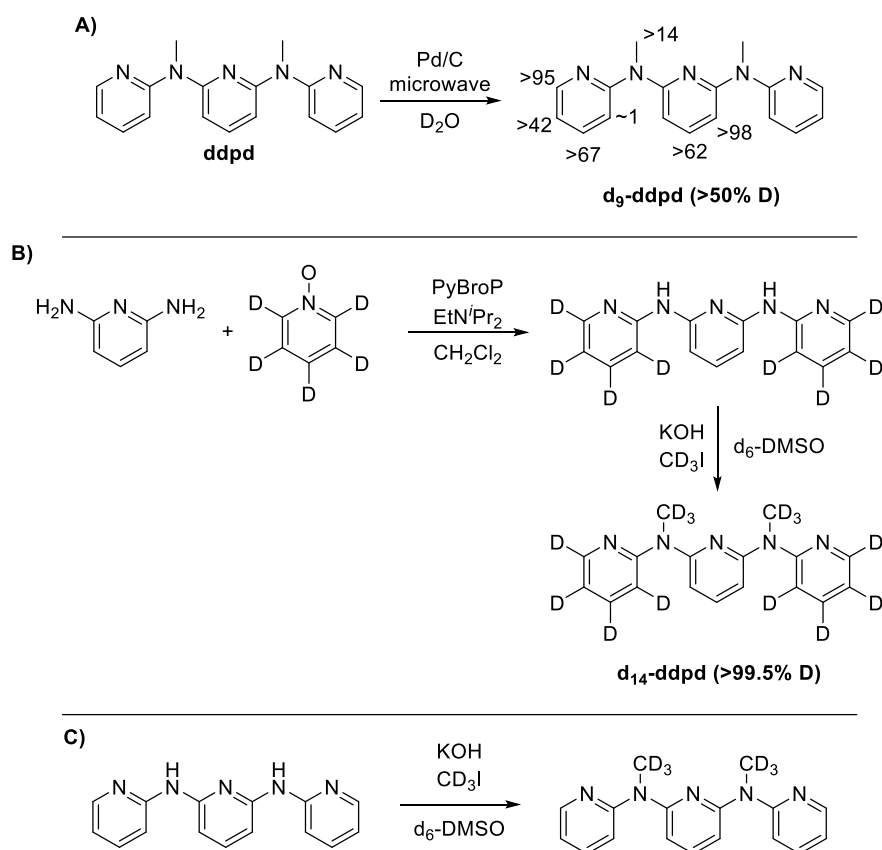
Scheme 70: Synthesis of differentially deuterated derivatives of ddpd as published by Heinze et al.[281]

Especially the reactions shown in Scheme 70**A** and Scheme 70**B** represent interesting concepts for adaptation to the Py$_5$Me$_2$H/**L-1** system. Unfortunately, deuteration of the methyl groups of **L-1** is more difficult than in ddpd, as the methyl group is connected to a carbon center and can therefore not be introduced as easily. However, slight adaptions of the established synthesis route of **L-1** might enable synthesis of ***IV-10*** (Scheme 71).
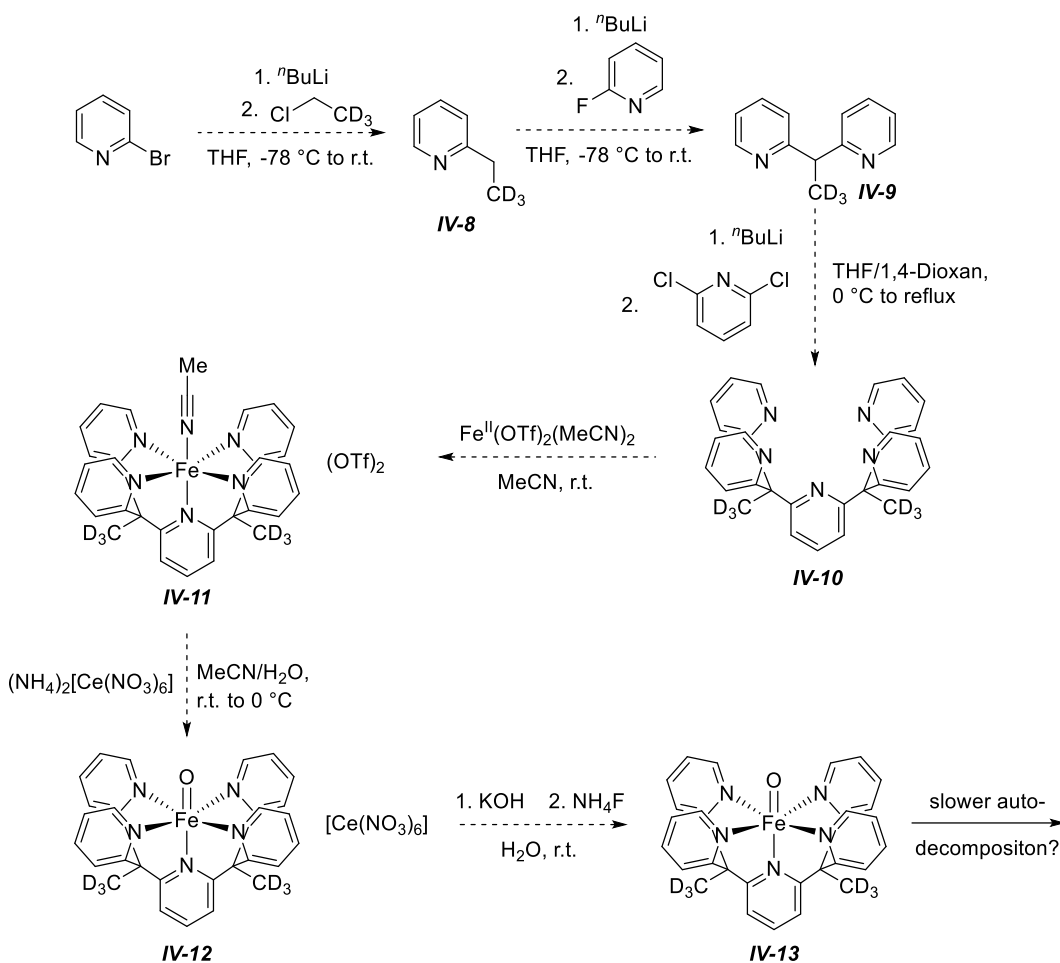
Scheme 71: Synthesis of Py₅-D₆-Me₂H (**IV-10**) and its corresponding iron(II) (**IV-11**) and iron(IV)-oxido (**IV-12 and IV-13**) complexes.

First, deuterated 2-ethyl pyridine would have to be synthesized (Scheme 73). To this end, 2-bromo pyridine was reacted with *n*-butyl lithium and (at this stage undeuterated) chloroethane was added. However, using GC-MS only the twice and thrice substituted products were observed (see Figure 91).
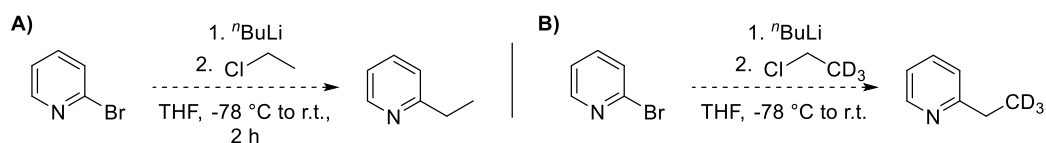
Scheme 72: **A)** Reaction of 2-bromo pyridine with n-*butyl lithium and chloroethane.* **B)** Proposed reaction of 2-bromo pyridine with n-*butyl lithium and deuterated chloroethane.*
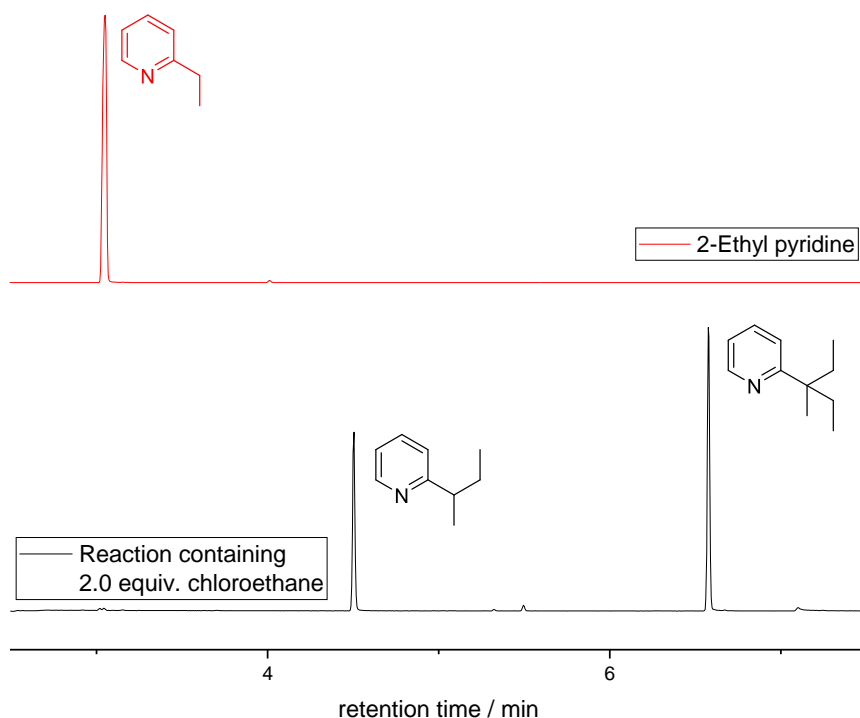
Figure 91: GC-MS traces of a reference sample of 2-ethylpyridine (upper trace) and a reaction mixture containing 1.0 equiv. 2-bromo pyridine, 1.2 equiv. n-BuLi, and 2.0 equiv. chloroethane (lower trace). Here, only small amounts of the desired 2-ethyl pyridine were observed. GC-MS method A.

An alternative approach might be the procedure published by Bell *et al.* in 1987 using an arylchloride, a Grignard reagent, and a copper(I) salt (refer to chapter V.7 for a more detailed discussion of this reaction).[282] The authors did not use this specific substrate but rather 2-chloroquinoline/ethyl magnesium bromide/copper(I) cyanide or 2-bromopyridine/methyl magnesium bromide/copper(I) bromide, therefore some modifications would be necessary (Scheme 73). Due to time constraints this project was discontinued at this stage.
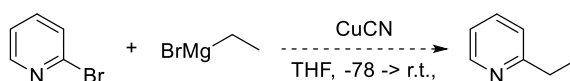
Scheme 73: Proposed synthetic procedure to obtain 2-ethyl pyridine from 2-bromo pyridine and ethyl magnesium bromide.

V. Immobilization, Py₄PhMe₂H, Py₄OHMe₂H, and Other Ligand Systems

1. Introduction and State of the Art

Immobilization

Immobilization of a catalyst onto a solid surface may provide advantages over the homogenous system by facilitating removal of the catalytically active unit from the reaction mixture. Thereby, the (often expensive) catalyst is recovered and may be recycled, saving money and reducing contamination of the product. The latter is especially important in industries where high purity of the desired compound is required, *i.e.* in pharmaceutical or analytical chemistry.

Multiple ways are known in the literature for immobilizing (inorganic) catalysts on solid support systems: adsorption (Chart 11**A**), encapsulation (Chart 11**B**), electrostatic interaction (Chart 11**C**), and covalent tethering (Chart 11**D**).[283] Of course, the distinction between adsorption *via* hydrogen bond and electrostatic interactions can be difficult in some cases.
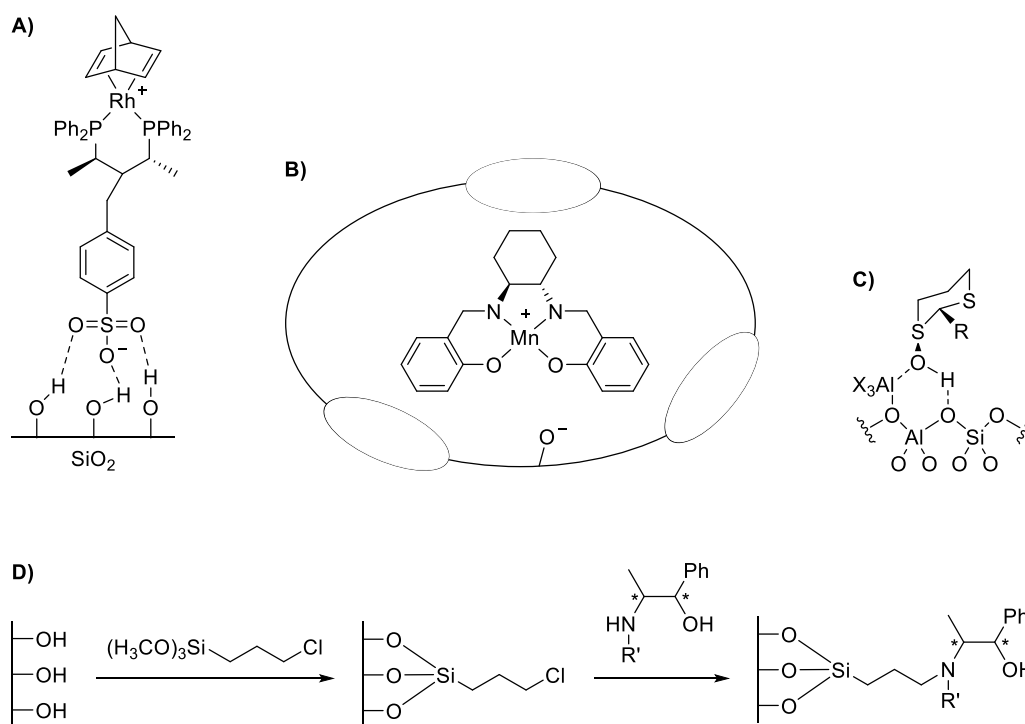
*Chart 11: Different ways to immobilize ligands or metal complexes on solid supports: **A)** adsorption (a Rh(I) complex is immobilized by hydrogen bond interactions of a sulfonic acid moiety on the ligand with the silanol functions of the silica),[284] **B)** encapsulation (a salen-derived Mn(III) complex is encapsulated in zeolite Y,[285] **C)** electrostatic interaction (the proposed interaction of a dithiane catalyst in zeolite USY, R = -H, -CH₃, -Ph),[286] and **D)** covalent tethering (epihedrine is immobilized by forming Si-O bonds between silica and a linker and by forming an amide bond between the linker and the amine moiety on a functionalized ephedrine, R' = CH₃, -C₂H₅, -C₃H₇).[283,287]*

Generally, the stability of these immobilized metal complexes differs by the method of immobilization: covalent tethering and electrostatic interaction typically yield the most stable compounds, whereas adsorption often leads to complexes that are leached off more easily. On the other hand, adsorption is considered the most facile method. Encapsulation is on the other hand is considered an elegant approach, however, often represents significant synthetic challenges.[283]

Immobilized catalysts can then be used in "regular" batch reactions or in continues flow regimes. In the latter application, a solution of the substrate (and additives) is passed through a chamber containing the catalyst, where the desired reaction occurs. This method may offer several advantages, e.g. easy separation of the product from the catalyst, lower waste production, portability, recycling of the catalyst, and/or a better safety profile.[288]
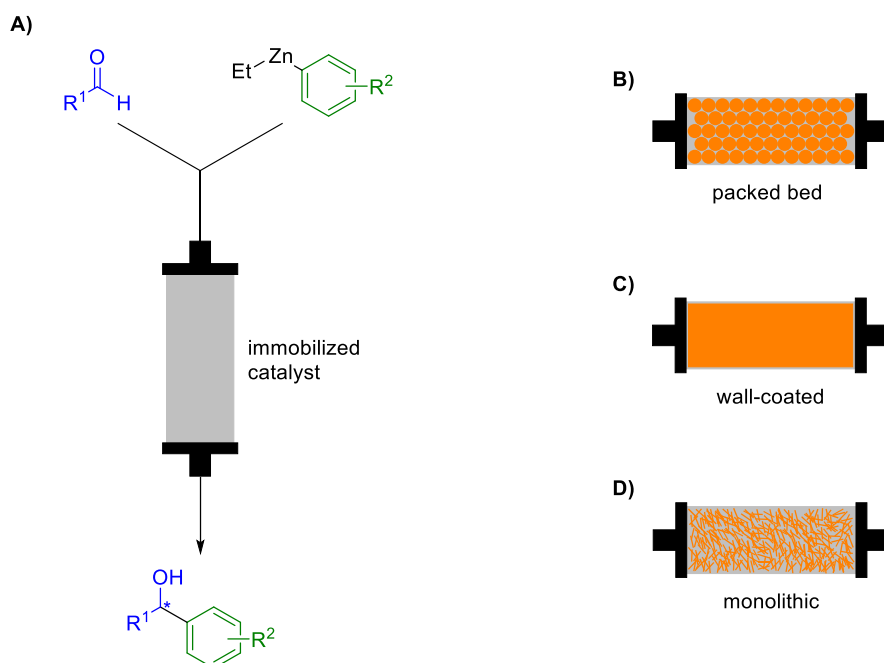
*Figure 92: **A**) Graphic representation of the incorporation of an immobilized catalyst in a continues flow reactor, adapted from Pastre et al.[288] **B**) Graphic representation of a packed-bed reactor setup. **C**) Graphic representation of a wall-coated reactor setup. **D**) Graphic representation of a monolithic reactor setup. Adapted from Verboom et al.[289]*

Three methods are commonly discussed for the design of the "catalysis chamber": 1) packed-bed, 2) wall-coated, and 3) monolith. In monolithic systems, a porous support material is modified to contain the active catalyst. This design allows for a greater tolerance of high flow rates and efficient mass transfer, generally yielding higher productivities. On the other hand, monolithic designs may suffer from pore clogging. Wall-coated systems are known for their well-defined fluid dynamics, as mass transfer resistance is minimized. However, the catalyst loading is generally lower, as typically only one layer of catalyst is applied. For packed-bed systems, a large selection of solid support materials can be used: organic resins, custom polymers, as wells as inorganic materials (silica, alumina, zeolites, etc.) are typically chosen. In this approach, high catalyst loadings can be obtained and the catalyst can be easily characterized and quantified. However, fluid dynamics, pressure issues, as well as heat transfer represent significant challenges.[289]

In general, these microreactors often enabled an increase in both selectivity and yield while simultaneously creating a safer experimental environment compared to traditional batch chemistry by sealing the reaction chamber. Nonetheless, leaching of metal catalysts is often observed and needs to be addressed to obtain a highly efficient system.[289]

Immobilization of Py₅Me₂-X Derived Ligands

In 2018, Kerstin Rickmeyer conducted her Master Thesis in the research group of Prof. Dr. Lena Daumann and started the investigation of the immobilization of Py₅Me₂-X derived ligands on resin supports. To this end, ligand **L-10** was synthesized using a literature known procedure previously published by Chantarojsiri *et al.*[12,290]
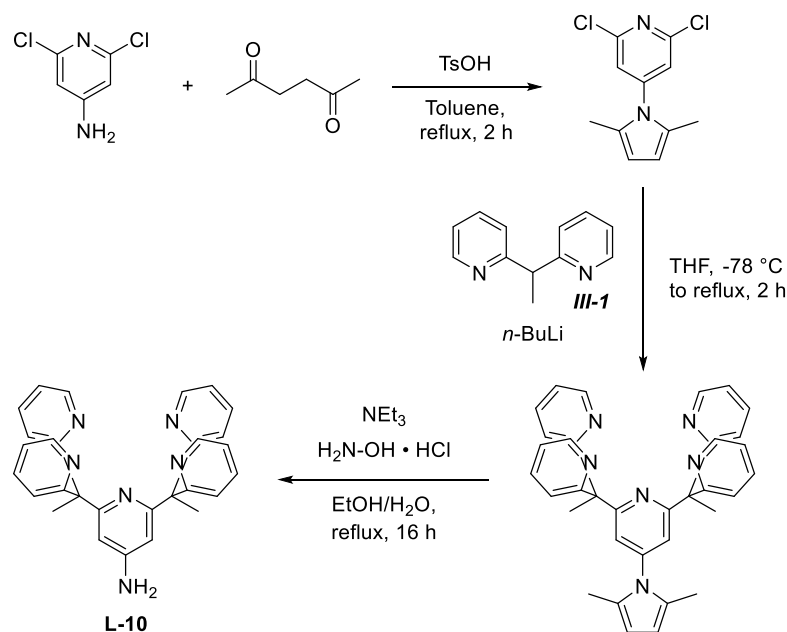
Chart 12: Synthesis of **L-10** as performed by Kerstin Rickmeyer.[290]

Unfortunately, immobilization of **L-10** onto Merrifield (Figure 93) or Tentagel (not shown) resin *via* nucleophilic substitution was unsuccessful. This was attributed to the steric and electronic properties of the ligand: the direct proximity of the amine group to the electron poor pyridine ring decreases its nucleophilicity, making successful coupling to the resin unlikely.
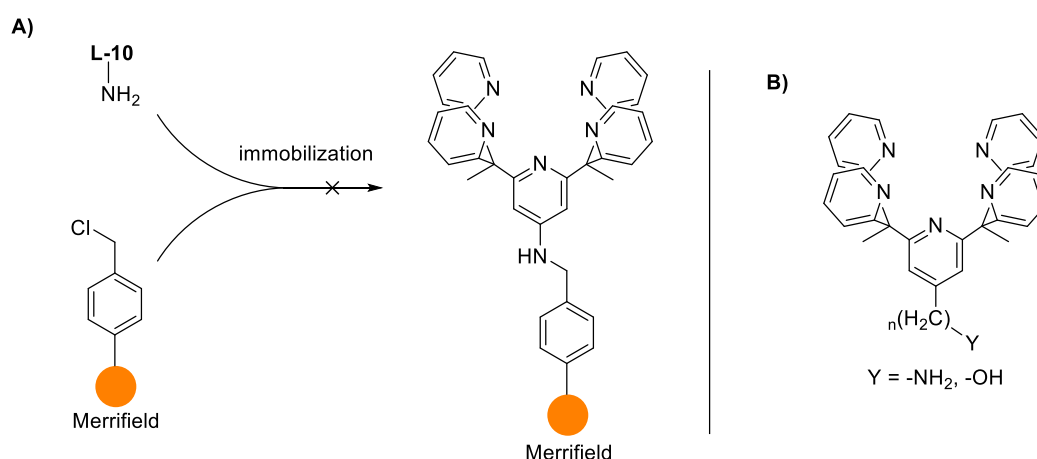
Figure 93: **A)** Attempted immobilization of **L-10** on Merrifield resin as performed by Kerstin Rickmeyer. **B)** New ligand design containing a (CH₂)ₙ linker and an amine or alcohol moiety for resin coupling.

Therefore, new ligands were envisioned that contain an alkyl linker in between the amine moiety and the pyridine ring, possibly improving the nucleophilicity and coupling properties.

This next step was partly investigated by Fee Kielinowski, who conducted her admission work (Zulassungsarbeit Lehramt) under my supervision.[291] In this project, ligand **L-11** was first synthesized (refer to chapter V.3).

New Ligand Systems

Multiple nitrogen-based ligand systems forming non-heme iron(II), iron(III), and iron(IV) complexes are known, a selection of ligands or common base structures is shown in Chart 13**A**. Chart 13**B** gives two examples of ligands that are based on one of the mentioned base structures in Chart 13**A**, **tren**. In chapter I.3, several examples of iron(III) and iron(IV)-oxido complexes of these ligand systems are mentioned.

A)

N,N-bis(2-aminoethyl)
ethane-1,2-diamine

tren

1,4,8,11-Tetramethyl-1,4,8,11-
tetraazacyclotetradecan

TMC

2,6-bis-(bis(2-pyridyl)
methoxymethane)pyridine

PY5 / L-3

3,7-dimethyl-9-oxo-2,4-bis(2-pyridyl)-3,7-
diazabicyclo[3.3.1]nonane-1,5-dicarboxylate
methyl ester

bispidine

B)

N4Py

TQA
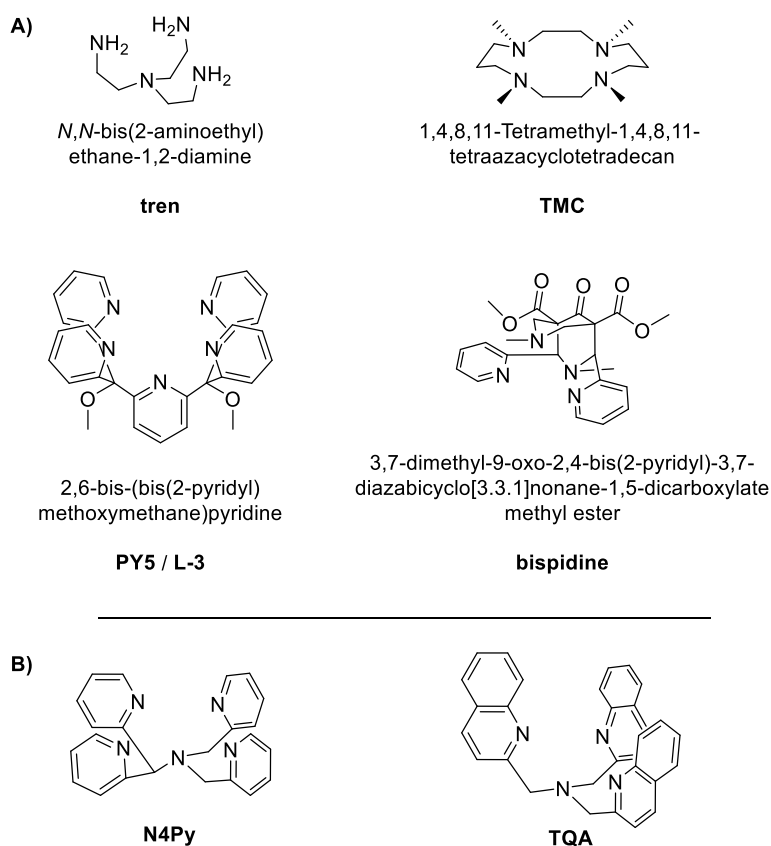
*Chart 13: **A**) Overview of common ligand systems used for the generation of non-heme iron complexes, their IUPAC designation as well as the common abbreviation are mentioned. In the case of 2,6-bis-(bis-(2-pyridyl)methoxy methane)pyridine the designation used in this work (**L-3**) is also indicated. **B**) Modified ligands based on the **tren** base structure.*

Typically, (distorted) octahedral coordination geometries are observed in iron(II), iron(III), and iron(IV)-oxido complexes. In the case of **TMC** or **bispidine** based ligands as well as in **L-3**, this is expected, as the ligand enforces this geometry. In **tren** based systems, the geometry depends on the exact shape of and number of donor groups in the ligand. In the **tren**-based N4Py ligand, the four pyridine moieties together with the central amine group led to a distorted octahedral geometry (Chart 14**A**), in the quinoline-modified ligand system TQA (tris(2-quinolylmethyl)amine), a molecule of acetonitrile is necessary to complete a distorted octahedron

(Chart 14**B**), whereas the bulky TMG₃tren ligand leads to a trigonal bipyramidal structure (Chart 14**C**).
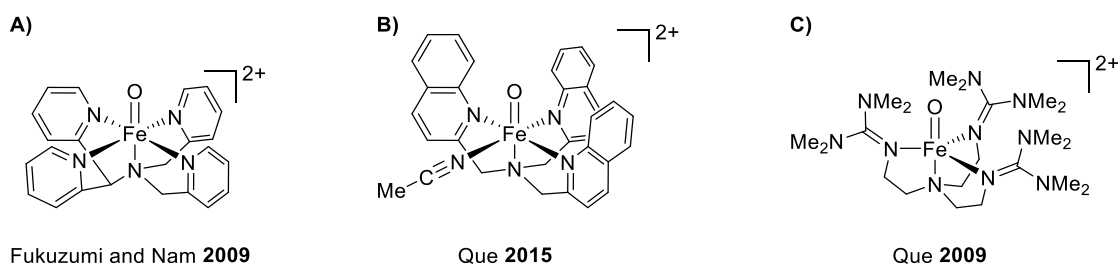
*Chart 14: Iron(IV)-oxido complexes bearing the **A**) N4Py (distorted octahedral geometry), **B**) TQA (tris(2-quinolylmethyl)amine, distorted octahedral geometry), or **C**) TMG₃tren (distorted trigonal bipyramidal geometry) ligand.*

Whereas the mentioned ligand systems exclusively contain nitrogen atoms as donor groups, natural non-heme enzymes coordinate the iron central ion with a mixture of nitrogen and oxygen donors (Chart 15). In the proposed resting state (Chart 15**A**) as well as after α-KG coordination (Chart 15**B**) an octahedral coordination geometry is commonly assumed. Activation leads to the formation of an iron(IV)-oxido species, which is typically described as a trigonal bipyramid (Chart 15**C**). Both the Asp residue and the α-KG co-factor coordinate *via* oxygen atoms.
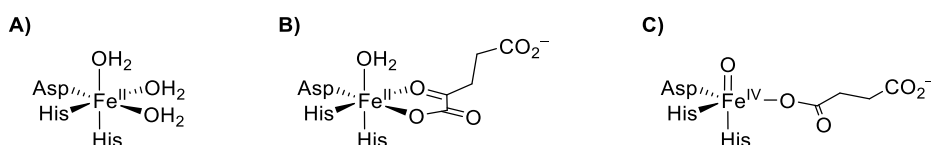
*Chart 15: Proposed structure of the active site in α-KG dependent enzymes **A**) prior and **B**) after coordination of α-KG as well as **C**) after formation of the active iron(IV)-oxido species.*

The spin state of the iron(IV)-oxido active species in enzymes is reported as high spin with $S = 2$,[3,33,292–294] a state that is seldom reached in synthetic systems and, even if, these systems rarely display strong HAT reactivity.[77,295–297] However, the above mentioned $[Fe^{IV}(O)(TQA)]^{2+}$ complex by Que *et al.* also exists in the "natural" quintet spin state and is indeed capable of performing HAT reactions. Theoretical calculations indicate that the high-spin quintet state is more reactive than the corresponding triple ($S = 1$) state.[79,298–302]

In particular, Comba *et al.* propose a change in spin state during HAT reaction for the **bispidine** based iron(IV)-oxido complexes shown in Figure 94. An 18 kJ mol⁻¹ energy difference separates the triplet ground state from the excited quintet state. However, for a reaction to occur between the complex and a suitable substrate, the complex' spin state changes to the excited state, from which a reaction is much more likely. Comba *et al.* describe this behavior as the complex existing in the "entatic state".[303]
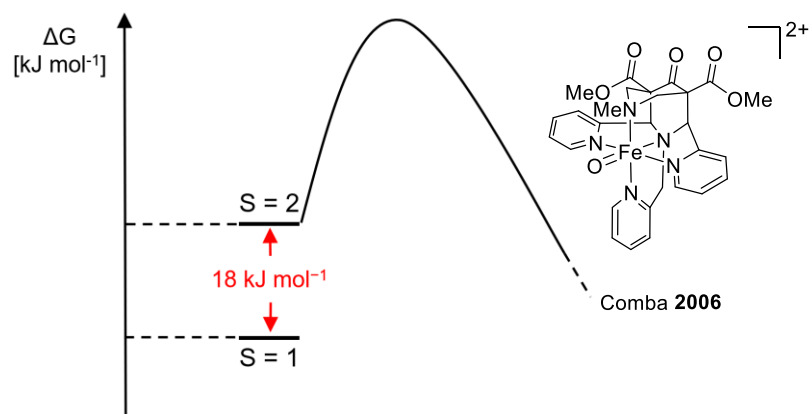
Figure 94: Energy profile of [Fe^{IV}(O)(bispidine)]$^{2+}$ complex, first synthesized in 2006, as published by Comba et al.[303]

2. Motivation and Aim

As described in chapter III, the use of **C-6** as a functional model was met with success: oxidation of the epigenetic marker **5mC** to its naturally occurring derivatives **5hmC**, **5fC**, and **5caC** was observed for nucleobase, nucleoside, and oligonucleotide substrates. The reaction conditions were optimized for these substrates and kinetic constants determined as well as side products analyzed.

Separation of iron complexes from the desired organic products was performed by filtration through silica. Whereas this method did work satisfactory, dissolved silica in the sample made further analysis difficult. Additionally, auto-oxidation of **C-6** was observed in aqueous solutions at room temperature (refer to chapter IV.6).

Immobilization of **C-6** onto a resin might provide a solution to both problems: **C-6** and its resin-bound decomposition products that formed upon reaction with a substrate could easily be removed from the reaction mixture *via* filtration of the resin. In addition, immobilization of **C-6** would make direct contact between two molecules of **C-6** impossible, likely reducing auto-oxidation.
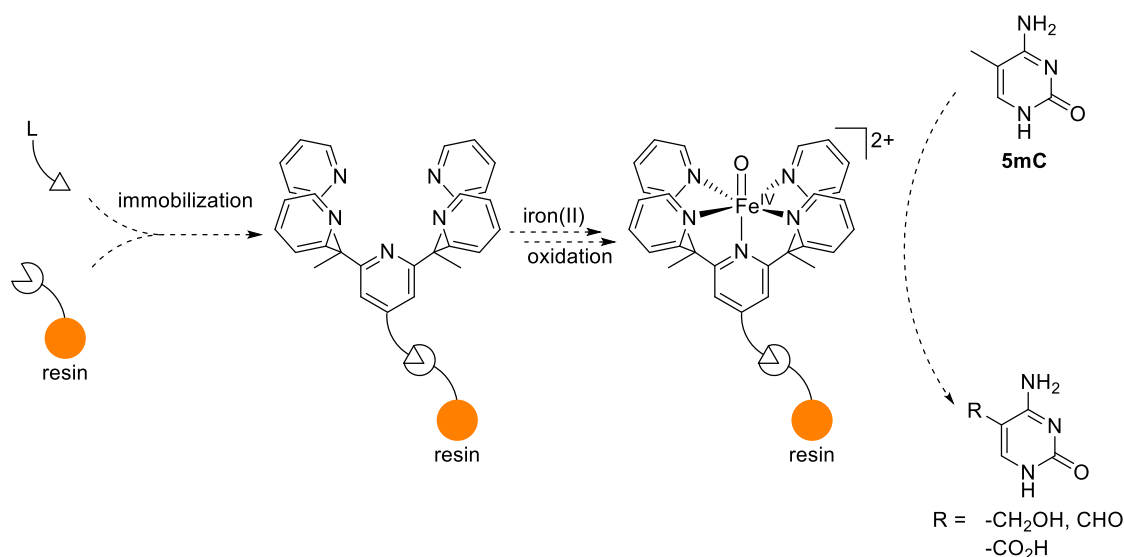
*Scheme 74: Planned immobilization of a ligand (L) on a resin, subsequent iron(II) incorporation and oxidation to the corresponding iron(IV)-oxido species. If successful, substrates such as **5mC** will be tested in oxidation reactions.*

In our group, several attempts were made to immobilize suitable ligand systems on Merrifield and Tentagel resins. Significant progress was made when a methylene linker was introduced between the central pyridine moiety and the linking amine moiety (Chart 16).

In this work, synthesis of such methylene linked ligand systems was to be performed and, if successful, the obtained ligands coupled to Merrifield and Tentagel resins and subsequently converted to the corresponding iron(II) and iron(IV)-oxido species.

Furthermore, additional ligand systems were to be investigated for their suitability as function model complexes for iron(II)/α-keto acid dependent enzymes. Even though the natural ligand environment in iron(II)/α-keto acid dependent enzymes includes oxygen donor functions, few ligand systems containing oxygen atoms as donor groups are known, that produce stable iron(III)-hydroxido or even iron(IV)-oxido complexes. In addition, iron(IV)-oxido complexes with a free coordination site were reported to be capable of mimicking halogenase activity.[63]
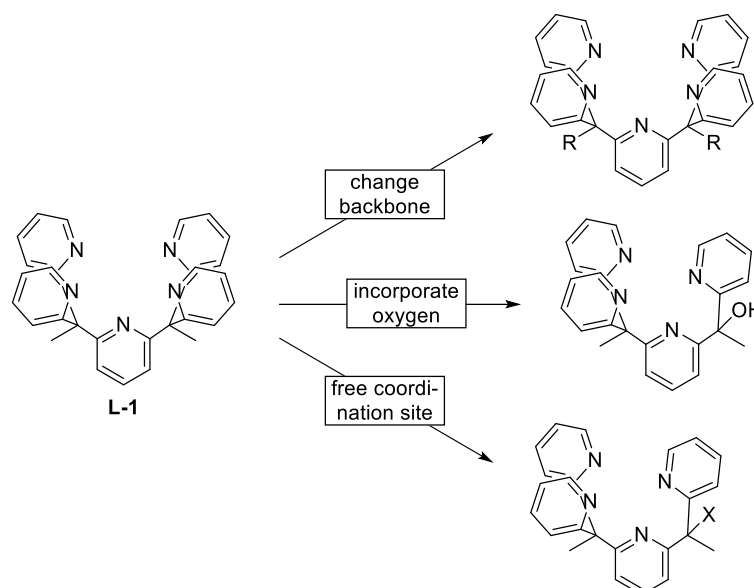
*Figure 95: Ligand **L-1** and planned changes on the ligands scaffold and donor functions.*

Therefore, a goal of this work was to expand the ligand library on the basis of L-1 to include ligands with oxygen donors as well as a free coordination site. Due to the success in using C-6 as a functional model, the penta-pyridine scaffold was to be used as basis and modified on a single site. Additionally, exploring ligands with a different backbone composition, as the literature known PY5 / L-3 ligand, would provide another set of iron complexes that could be studied as functional models.

3. Immobilization of Py_5Me_2-X Ligands and Iron Complex Formation

New Ligand Systems

Due to the difficulties experienced by Kerstin Rickmeyer using **L-10** for immobilization on Merrifield and Tentagel resin, ligands **L-11** and **L-14** were investigated: both provide more flexibility through the methylene link. Additionally, the amine and alcohol moieties are further removed from the pyridine ring and separated *via* an aliphatic linker, which should decrease the pyridine's electron withdrawing effect. The alcohol moiety in **L-14** might offer other reactivities than the amine moiety in **L-11**, therefore its inclusion into these studies seemed prudent.
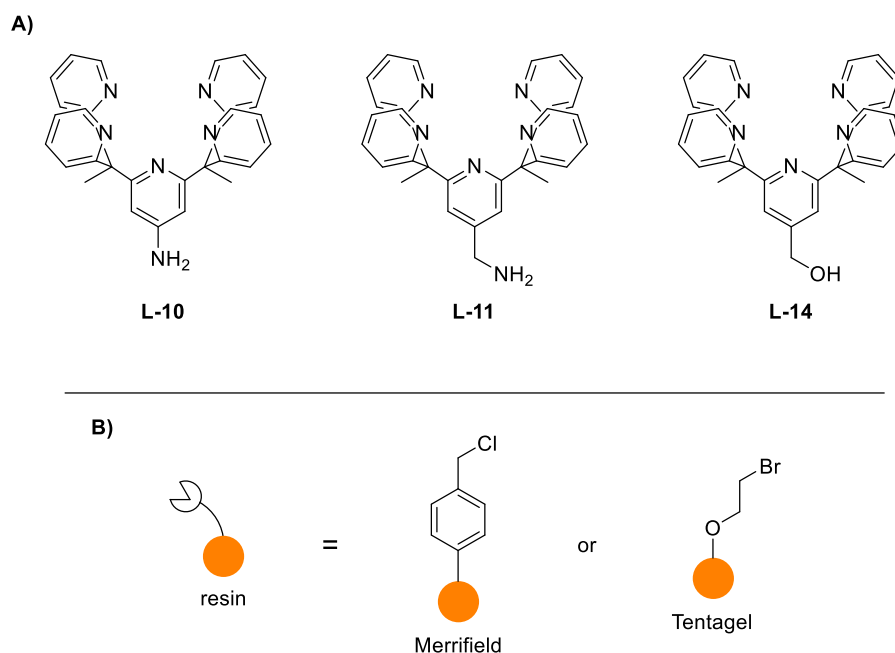
Chart 16: **A***) Ligands of the Py₅Me₂X-type used for immobilization in this and previous work.* **L-10** *was investigated by Kerstin Rickmeyer,* **L-11** *and* **L-14** *were investigated by Fee Kielinowski and in this work.* **B***) Resins used in this and previous works: Merrifield and Tentagel. The functional groups used for immobilization are shown.*

Synthesis of **L-11**

Synthesis of **L-11** was achieved through a five-step sequence starting from (2,6-dichloropyridin-4-yl)methanol (Scheme 75). Reaction of the starting material with phthalimide, triphenyl phosphine, and di-*iso*-propyl azodicarboxylate (DIAD) in tetrahydrofuran in a Mitsunobu-type reaction gave intermediate *V-1* in 81% yield. Addition of methyl amine in ethanol provided *V-2* in 83% yield in a Gabriel-type synthesis. Protection of the amine moiety using 2,5-hexanedione in an acid-catalyzed reaction according to a literature procedure by Chantarojsiri *et al.* yielded *V-3* (72%). ***III-1*** was reacted with *n*-butyl lithium in a mixture of 1,4-dioxane and tetrahydrofuran, then *V-3* was added. Refluxing the reaction mixture for three days afforded *V-4* in 83% yield. This reaction was performed according to a literature procedure by Chantarojsiri *et al.*[12] Deprotection of the amine moiety was achieved by addition of hydroxyl amine and **L-11** was obtained (71%).

Some of these syntheses were further optimized by Fee Kielinowski during her admission work (Zulassungsarbeit).[291]
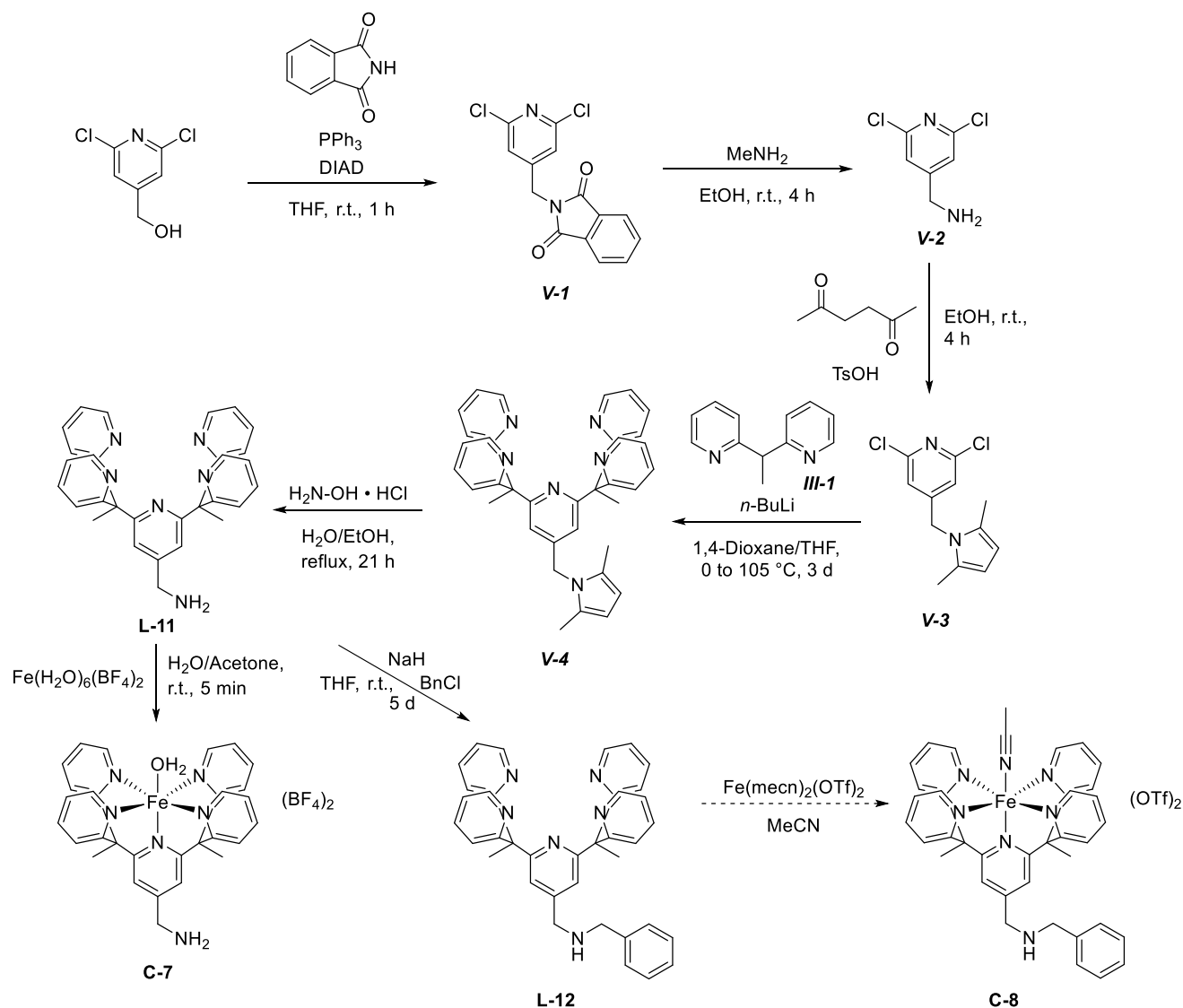
*Scheme 75: Synthesis of **L-11**, **L-12**, **C-7**, and proposed synthesis of **C-8** from 2,6-dichloropyridin-4-yl)methanol. DIAD = di-*iso*-propyl azodicarboxylate, THF = tetrahydrofuran, TsOH = p-*toluenesulfonic acid,* n-*BuLi =* n-*butyl lithium, BnCl = benzyl chloride.*

Next, **L-11** was reacted with an iron(II) salt ($Fe^{II}(H_2O)_6(BF_4)_2$) to investigate whether this ligand forms iron complexes. **C-7** was indeed obtained in 73% yield, unfortunately, no single crystals suitable for x-ray crystallography were obtained. The assignment of this structure was based on elemental analysis, HR-MS, and IR spectroscopy. Nonetheless, the data obtained could used to analyze the spectroscopic data obtained from immobilization reactions.

L-11 was also reacted with sodium hydride and benzyl chloride in tetrahydrofuran to afford **L-12** (34%). **L-12** resembles the chemical environment of a Merrifield-immobilized ligand more closely than **L-11** due to the presence of the benzyl group. Unfortunately, the isolated amount of **L-12** did not suffice for the synthesis of corresponding iron complexes, a potential synthesis procedure is indicated in Scheme 75 (dashed arrow). This and other synthetic procedures to obtain the

152

corresponding iron complexes of **L-12** should be the focus of further investigations. The obtained product can then be, if the syntheses are successful, used for comparison of the obtained analytical data of immobilization experiments (*vide infra*).

Synthesis of L-14

Ligand **L-14** was synthesized in a three-step sequence starting from (2,6-dichloropyridin-4-yl)methanol (Scheme 76). Protection of the alcohol moiety was achieved by addition of chloromethyl methyl ether (MOMCl) to a solution of the starting material in dichloromethane with added Hünig's base (di-*iso*-propyl ethyl amine, DIPEA), intermediate ***V-5*** was obtained in 80% yield. Analogous to the syntheses of other ligands of the Py_5Me_2-X type, ***III-1*** was reacted with *n*-butyl lithium in a mixture of 1,4-dioxane and tetrahydrofuran, subsequently ***V-5*** was added and the mixture refluxed for three days to afford **L-13** in 26% yield. Then, the alcohol moiety in **L-13** was deprotected by addition of aqueous hydrochloric acid to obtain **L-14** (50%).
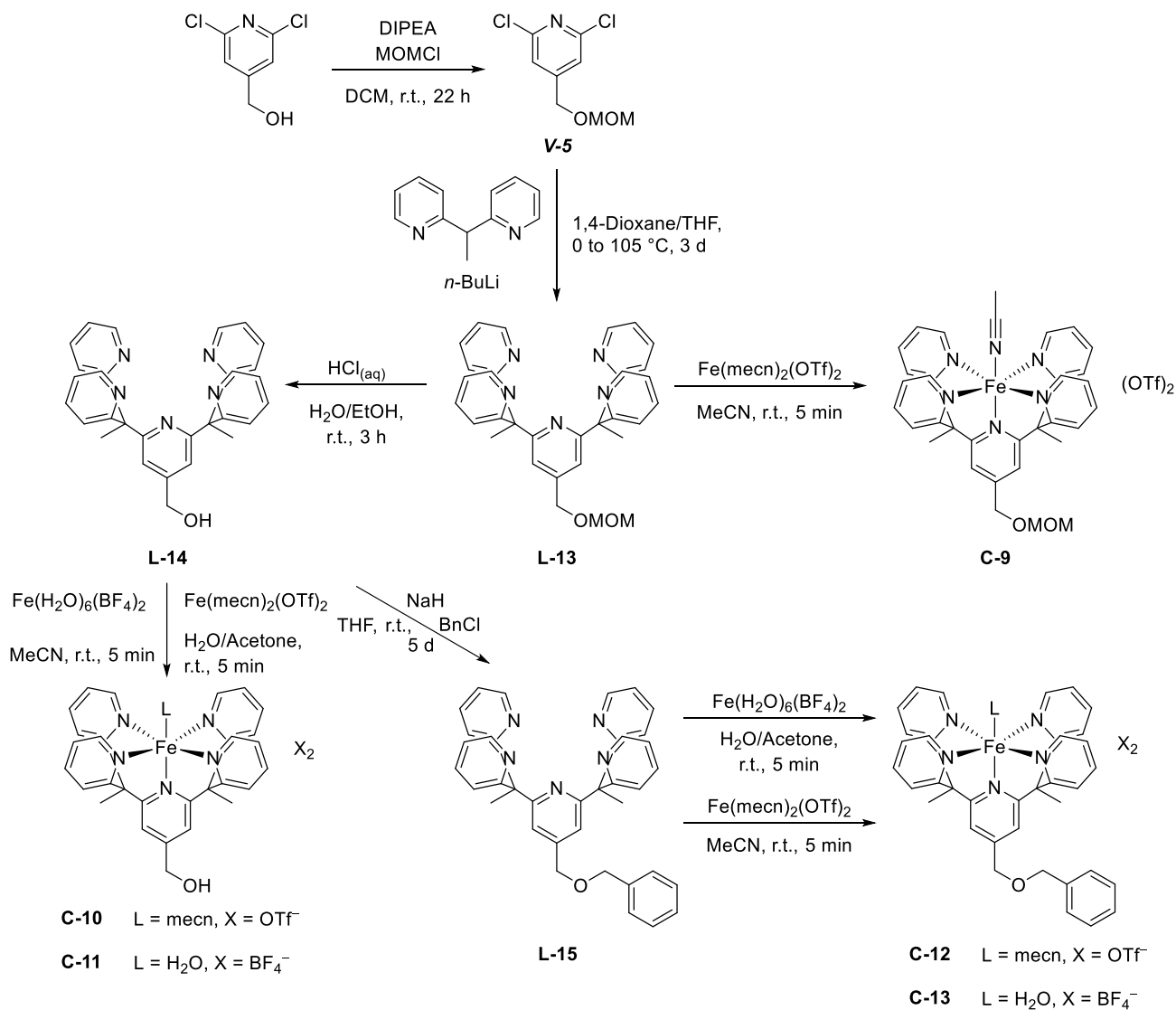
Scheme 76: Synthesis of *L-13*, *L-14*, *L-15*, *C-9*, *C-10*, *C-11*, *C-12*, and *C-13* from 2,6-dichloropyridin-4-yl)methanol. DIPEA = di-iso-*propyl ethyl amine, MOMCl = chloromethyl methyl ether, *n-BuLi = n-butyl lithium, BnCl = benzyl chloride.

Parallelly, **L-13** was also reacted with the iron(II) salt Fe(mecn)₂(OTf)₂ to obtain **C-9** (74% yield). Similarly, **L-14** was reacted with Fe(mecn)₂(OTf)₂ and Fe(H₂O)₆(BF₄)₂ to afford **C-10** and **C-11** in 76% and 73% yield, respectively. Single crystals of **C-11** suitable for x-ray crystallography were obtained by slow diffusion of diethyl ether into a solution of **C-11** in acetone/water at room temperature (Figure 96**A**).

Ligand **L-14** was then further reacted with sodium hydride and benzyl chloride in tetrahydrofuran to afford **L-15** in 84% yield. **L-15** was reacted with both Fe(mecn)₂(OTf)₂ and Fe(H₂O)₆(BF₄)₂ to afford **C-12** and **C-13**, respectively. Both complexes were obtained in 49% yield. Single crystals of **C-12** suitable for x-ray crystallography were obtained by slow diffusion of diethyl ether into a solution of **C-12** in acetonitrile at room temperature (Figure 96**B**).
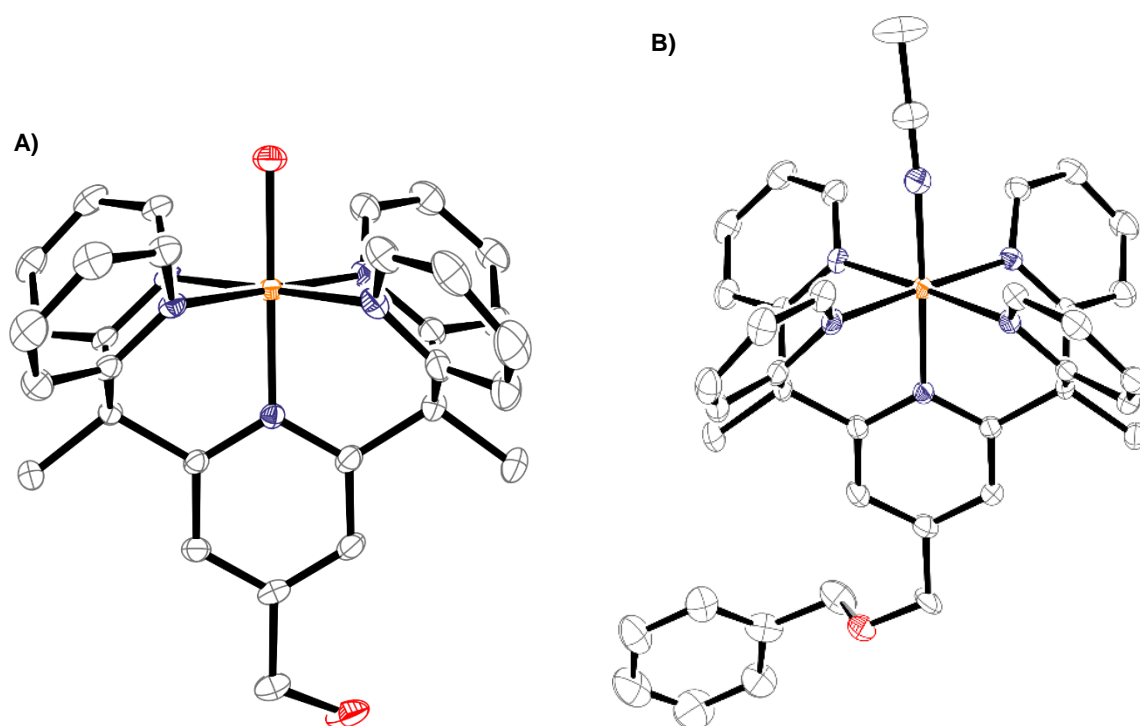
*Figure 96: Graphical representation of the crystal structures of **A**) **C-11** and **B**) **C-12**. Ellipsoids are drawn at 50% probability; hydrogen atoms and counter ions have been omitted for clarity (refer to the appendix p. 503 (**C-11**) and p. 505 (**C-12**) for complete structures and crystallographic details). Crystals were obtained from slow diffusion of diethyl ether into a solution of **C-11** in acetone/water or **C-12** in acetonitrile at room temperature.*

Both crystal structures of **C-11** and **C-12** show a distorted octahedral coordination geometry, similar to those observed for **C-1** and **C-2**. The bond lengths measured for both **C-11** and **C-12** fit well with those previously reported for **C-1** and **C-1** (Table 11).

*Table 11: Bond lengths in complexes **C-1**, **C-2**, **C-11**, and **C-12**. The relevant bond is indicated in bold, the corresponding donor group mentioned in brackets. Py$_{eq}$ = pyridines in the equatorial plane, Py$_{ax}$ = axial pyridine. For values involving equatorial pyridines the average value is provided.*

Bond	C-1 [Å]	C-2 [Å]	C-11 [Å]	C-12 [Å]
Fe-N(C-Me)	1.94	-	1.94	-
Fe-O(H$_2$)	-	2.01	-	2.00
Fe-N(Py$_{eq}$)	2.01	2.01	2.01	2.01
Fe-N(Py$_{ax}$)	1.97	1.95	1.98	1.95

The analytical data obtained from complexes **C-9** to **C-13** can already be used as comparison in immobilization experiments. However, further studies should focus on the synthesis of iron(III) and iron(IV)-oxido complexes of ligands **L-11** to **L-15**, as to provide more reference materials of these key intermediates.

*Immobilization of **L-11** on Merrifield*

Immobilization of **L-11** and **L-14** on Merrifield and Tentagel resins was attempted, following a procedure developed by Kerstin Rickmeyer and Fee Kielinowski.

Fee Kielinowski had shown previously that **L-11** can be immobilized on Merrifield. This procedure was to be tested for reproducibility. To this end, ligand **L-11** was dissolved in dichloromethane and added to a suspension of Merrifield resin and potassium carbonate. The mixture was shaken for several days, then the resin was filtered or centrifuged off and washed with dichloromethane, methanol, and water (Scheme 77). IR spectroscopy shows the emergence of new bands that correspond to those measured in ligand **L-11** (not shown, refer to the appendix p. 381), as previously observed by Fee Kielinowski. Characteristic signals of ligand **L-11** that cannot be found in the unreacted resin but in **V-6** are $\tilde{\nu}$ = 1153, 1431, 1463 and 1584 cm^{-1}.

The amount of **L-11** was varied between 5-10 equiv. and the scale of the reaction increased from 100 mg to 250 mg of resin. The relative amount of ligand was calculated from the loading of chloride residues on Merrifield, which was given as 1.3 mmol g^{-1} by the supplier (Sigma Aldrich). The amount of potassium carbonate was kept constant at 20 equiv. Table 12 gives an overview of the conducted experiments and elemental analyses of the obtained products.

*Table 12: Experimental parameters, measured elemental analysis data, and occupancy x for the immobilization of **L-11** on Merrifield.*

L-11	m$_{Merrifield}$ [mg]	Cl [wt%]	N [wt%]	Occupancy x
5 equiv.	100	-	1.63	-
10 equiv.	100	3.87	3.52	0.277
10 equiv.	250	-	3.92	-

The amount of nitrogen detected gives a good indication on the success of the immobilization procedure, as Merrifield resin itself does not contain any nitrogen atoms. It was found that 10 equiv. of **L-11** reliably result in ~3.5 wt% of nitrogen in the sample, a decrease to 5 equiv. **L-11** while keeping all other parameters the same, resulted in a significantly lower amount of nitrogen in the sample (~1.6%). An increase of the scale to 250 mg produced a slight increase of the measured nitrogen amount.

Using the measured values for the amount of chlorine and nitrogen present, the relative occupancy x was determined using **Eq. 6**.

$$x = \frac{\frac{m(N)}{6M(N)}}{\frac{m(N)}{6M(N)} + \frac{m(Cl)}{M(Cl)}} \qquad \textbf{Eq. 6}$$

m(*element*) is the observed amount in elemental analysis, M(*element*) the corresponding molecular mass. This analysis shows that only ~28% of all benzyl chloride sites are actually substituted by the ligand, further improvement on the immobilization procedure therefore seems possible and prudent.
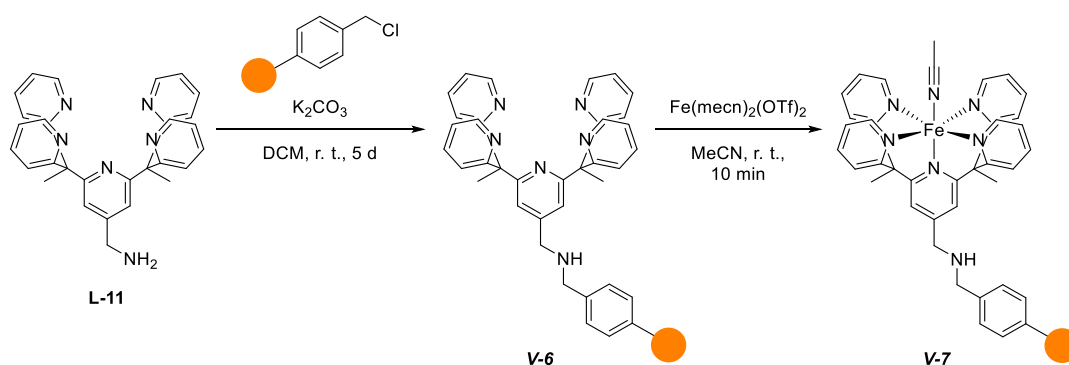
*Scheme 77: Immobilization of **L-11** on Merrifield resin and subsequent incorporation of iron(II).*

Nonetheless, the obtained resins were used for further investigations, *i.e.* the incorporation of iron(II) ions into the immobilized ligand. Preliminary work had been done by Fee Kielinowski, however, additional experiments were deemed necessary to confirm synthesis of the desired species and the reproducibility of the method. The immobilized resins were therefore suspended in acetonitrile and Fe(mecn)$_2$(OTf)$_2$ was added. IR spectroscopy of the washed and dried products confirmed successful incorporation of the iron(II) ion into the ligand framework, as bands are

156

visible in the spectra of the treated resin beads that correspond to the reference complex **C-1** (Figure 97**A**). Comparison of the solid-state UV-vis spectra of the treated resins (***V-7***) with the reference complex **C-1** confirmed these results (Figure 97**B**). ICP-OES measurement of the beads gave an iron content of 0.075 mmol g^{-1}, which would correspond to an occupancy of 5.8% of functional sites. This is significantly lower than the measured ligand occupancy (*vide supra*), further improvements on the incorporation of iron(II) should therefore be performed.
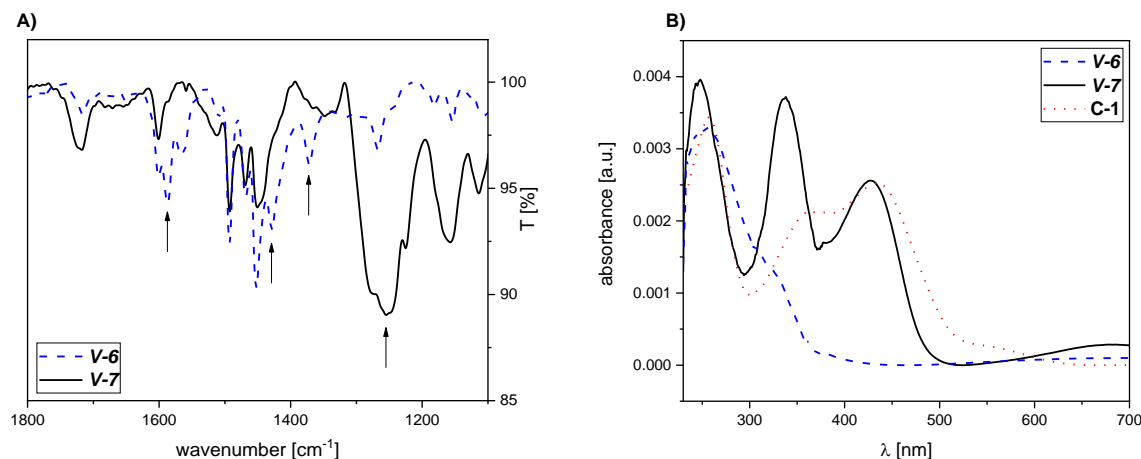
*Figure 97: **A**) Excerpts of IR spectra of Merrifield resin beads with immobilized ligand **L-11** (**V-6**) before (blue) and after (**V-7**, black) treatment with Fe(mecn)$_2$(OTf)$_2$. Distinct differences are marked with arrows. **B**) Excerpts of solid-state UV-vis spectra of Merrifield resin with immobilized **L-11** (**V-6**) before (blue dashed) and after treatment with Fe(mecn)$_2$(OTf)$_2$ (**V-7**, black solid) including a reference of **C-1** (red dotted). Full spectra can be found in the appendix p. 382.*

These results show that immobilization of **L-11** and subsequent formation of the corresponding immobilized iron(II) complex is possible, yielding ***V-7***. However, monitoring the obtained compound using solid-state UV-vis spectroscopy also showed decomposition of the obtained resin beads at room temperature (Figure 98). The red-shift of the observed band at λ = 430 nm to λ = 466 nm would indicate formation of an iron(III) species, however, further measurements, e.g. using Mößbauer spectroscopy, are necessary to confirm this hypothesis.
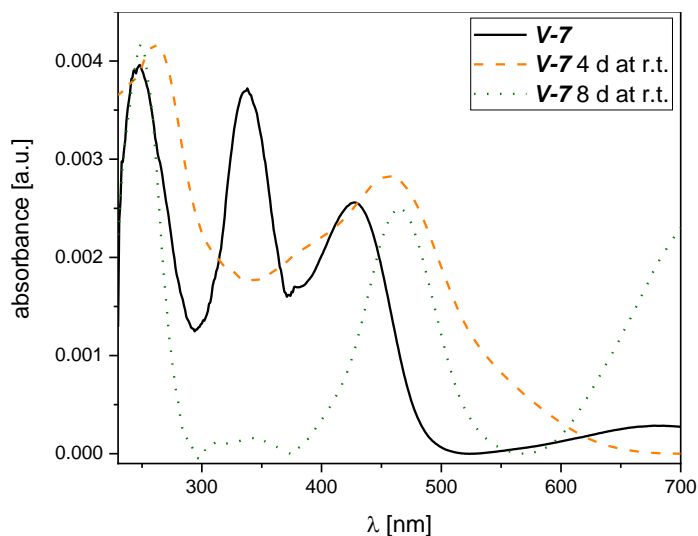
*Figure 98: Excerpts of solid-state UV-vis spectra of the resin carrying immobilized **L-11** that was treated with Fe(mecn)$_2$(OTf)$_2$ (**V-7**, black solid) after 4 d (orange dashed) or 8 d (green dotted) at room temperature. Full spectra can be found in the appendix p. 383.*

The incorporation of iron(II) ions into the immobilized ligand **L-11** on Merrifield should therefore be performed immediately prior to further reactions and the samples should not be stored at room temperature. The influence of storage at –20 °C on the stability of the samples needs to be investigated.
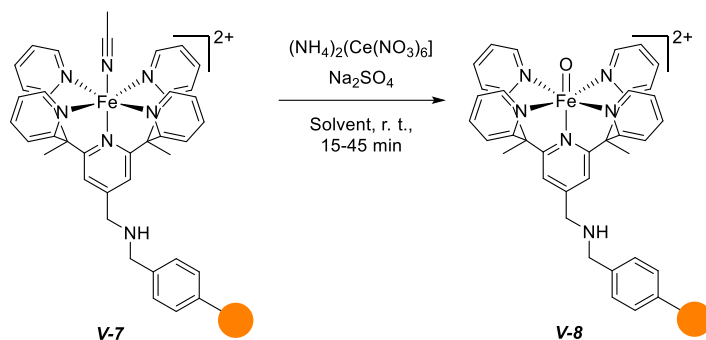
*Scheme 78: Attempted oxidation of **V-7** to the corresponding iron(IV)-oxido species using cerium(IV) ammonium nitrate. As solvent either water or a mixture of acetonitrile/water (3:1) was used.*

Nonetheless, oxidation of **V-7** to the corresponding iron(IV)-oxido species using cerium(IV) ammonium nitrate was attempted. In a first experiment, a mixture of acetonitrile and water (3:1) was used as solvent, as had been used for the generation of the soluble derivative **C-6**. Indeed, the suspension was observed to turn green after addition of cerium ammonium nitrate, indicating formation of an iron(IV)-oxido species. However, after ~5-10 min the suspension turned orange. This indicates decomposition of the supposed iron(IV)-oxido species, possibly by reaction with acetonitrile. Therefore, the solvent was exchanged for pure water and the reaction time was shortened to 15 min. Additionally, the resin beads were washed with water and an aqueous solution of sodium sulfate in order to exchange any $[Ce(NO_3)_6)]^{2-}$ counterions for sulfate. This is necessary, as $[Ce(NO_3)_6)]^{2-}$ is itself capable of oxidizing **5mC** and other substrates (refer to chapter III.3). Under these conditions, a band at $\lambda = 700\text{-}800$ nm can be observed in solid-state UV-vis spectroscopy. This is a strong indication of the formation of an iron(IV)-oxido species and the obtained spectrum shows remarkable resemblance to that of **C-6** (Figure 99). Full reference spectra of **C-1** and **C-6** can be found in the appendix p. 384.
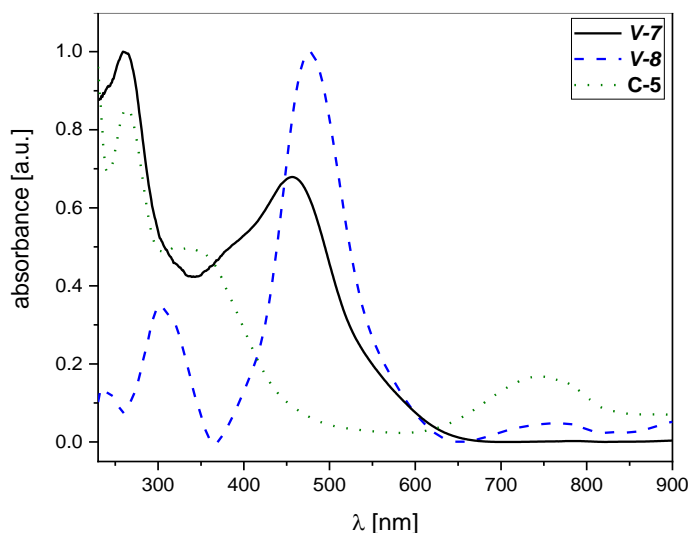
*Figure 99: Excerpts of solid-state UV-vis spectra of intermediate **V-7** before (black solid) and after treatment with cerium(IV) ammonium nitrate (CAN, **V-8**, blue dashed) and **C-5** as reference sample (green dotted). Full spectra can be found in the appendix p. 383.*

ICP-OES measurements of the supernatant and the washing solutions also confirmed that only small amounts of iron were washed out of the resins during the oxidation reaction and almost none during washing with sodium sulfate. However, a significant amount of cerium was detected in the washing steps with sodium sulfate (after the sample had been washed three times with water, refer to the appendix p. 384). This indicates that sulfate indeed replaces $[Ce(NO_3)_6)]^{2-}$ as counterion.

These results at hand, a first test of the reactivity of the sample was attempted. ***V-8*** was suspended in water and **5mC** or *p*-ethylbenzenesulfonic acid were added. The mixture was incubated for 15 min to 48 h and samples were taken. These were filtered, lyophilized, and subsequently either derivatized using BSTFA for GC-MS measurement of directly measured using ^{1}H NMR spectroscopy. Unfortunately, none of the samples showed the presence of any of the expected reaction products, instead, the starting materials were observed as the sole product.
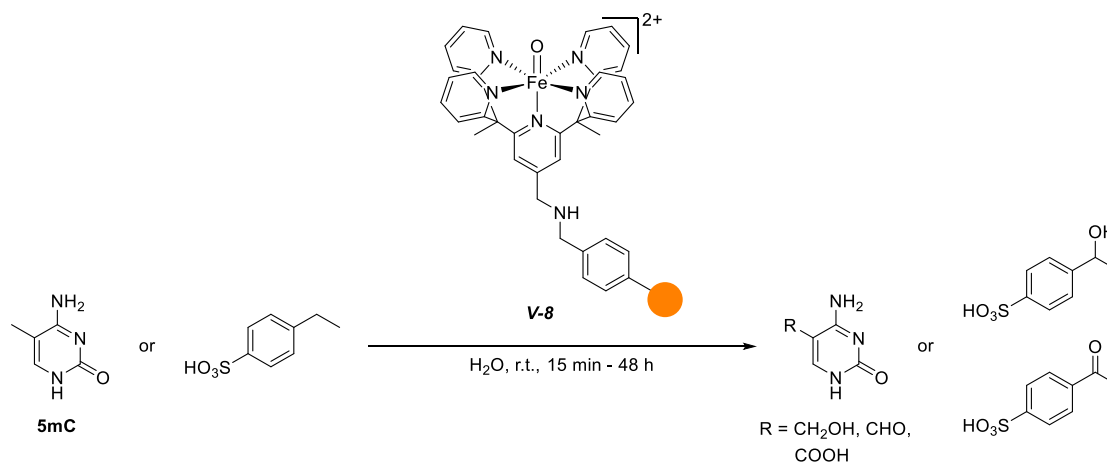
*Scheme 79: Attempted oxidation of **5mC** or p-ethylbenzenesulfonic acid to the oxidation products by **V-8**. R = -CH$_2$OH, -CHO, -CO$_2$H.*

159

These results are promising, as they show that **L-11** can be reliably immobilized on Merrifield yielding **V-6**. This can be transformed to its iron(II)-containing derivative **V-7** and subsequently be oxidized to the iron(IV)-oxido species **V-8**. Further studies on the stability of **V-7** and **V-8** as well as the oxidative capabilities of **V-8** are, however, necessary.

*Immobilization of **L-14** on Tentagel*

Similar to the above described experiments, preliminary studies on the immobilization of ligand **L-14** on Tentagel were performed. However, instead of potassium carbonate, sodium hydride was used to deprotonate the ligand's alcohol moiety.
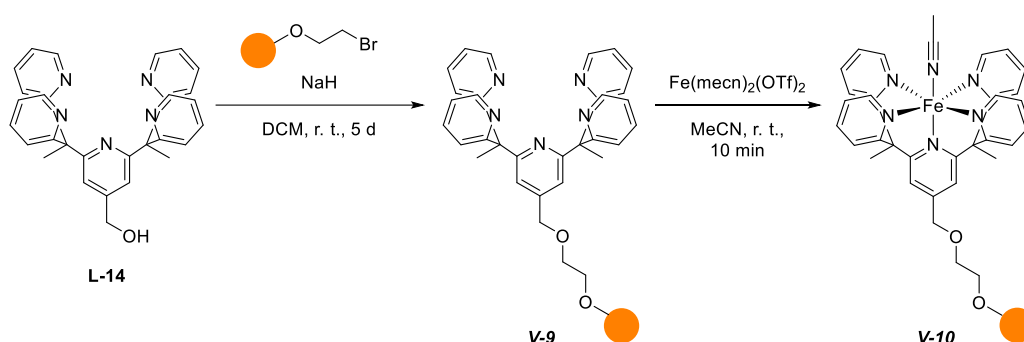
*Scheme 80: Immobilization of **L-14** on Merrifield resin and subsequent incorporation of iron(II).*

IR spectroscopic data of the washed beads shows the successful coupling of the ligand to the resin (Figure 100). Characteristic peaks found in the ligand but not the pure Tentagel resin are $\tilde{\nu}$ = 1427, 1466, 1565 and 1587 cm⁻¹. Elemental analysis of the sample showed the presence of 2.26 wt% of nitrogen and no bromine. From this, occupancy of coupling sites (Tentagel: 0.4 mmol g⁻¹) was calculated to be ~81%, which is significantly more than was observed for the coupling of **L-11** to Merrifield resin. This also indicates that side-reactions replacing the bromide moiety occurred, accounting for the missing ~19% occupancy. Still, this is a remarkably high number.
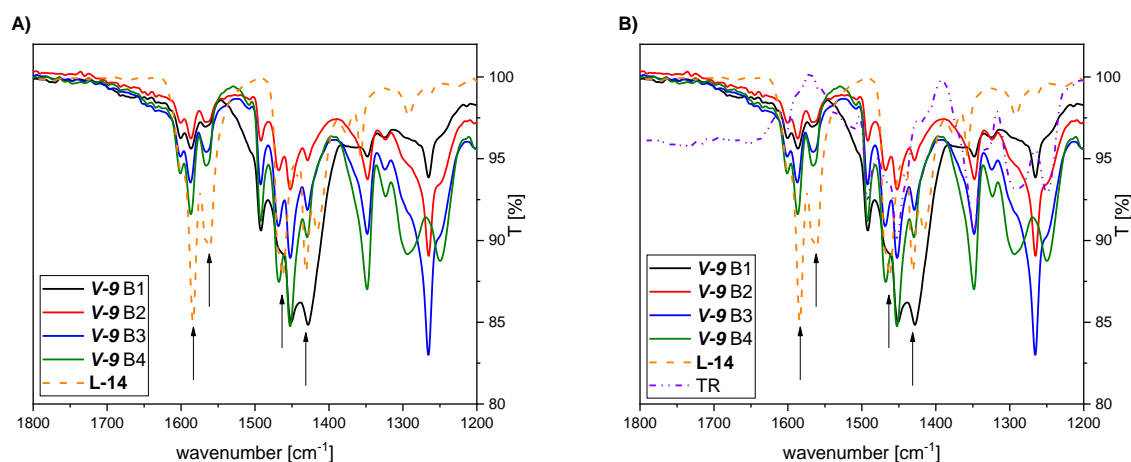
*Figure 100: Excerpts of IR spectra of four batches (B1-B4) of **V-9** in comparison to **A) L-14** and **B) L-14** and Tentagel resin /TR). Full spectra can be found in appendix p. 382.*

Incorporation of iron(II) ions into **V-9** was also attempted by suspending the resin beads in acetonitrile and adding Fe(mecn)₂(OTf)₂. Solid-state UV-vis spectroscopy of the obtained product indicates the formation of an iron species (Figure 101), which is supported by ICP-OES measurements, which give an amount of 18 mg g⁻¹ iron in the sample. This corresponds to 81% occupancy, which would mean that every ligand moiety has indeed reacted to the corresponding iron(II) complex and confirms the previously calculated ligand occupation.

The slight red-shift observed for the absorption band of **V-10** in Figure 101, however, indicates the formation of an iron(III) species. Further measurements, e.g. using Mößbauer spectroscopy, are necessary to assess the identity of the formed compound.
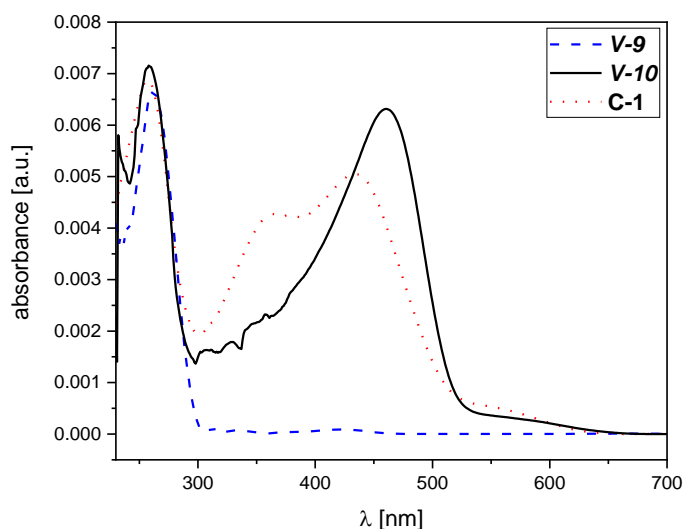
*Figure 101: Excerpts of solid-state UV-Vis spectra of immobilized **L-14** before (**V-9**, blue dashed) and after treatment with Fe(mecn)₂(OTf)₂ (**V-10**, black solid), and **C-1** (red dotted) as reference sample. Full spectra can be found in the appendix p. 384.*

Oxidation of the iron(II) center to the corresponding iron(IV)-oxido species was attempted according to the first procedure used for Merrifield resin (*vide supra*). Unfortunately, solid-state UV-Vis spectroscopy of the obtained sample does not show the presence of a band at λ = 700-800 nm which would be indicative of an iron(IV)-oxido species. In fact, the solid-state UV-vis spectrum indicates decomposition of the compound, as no significant absorption was measured between λ = 300-900 nm.
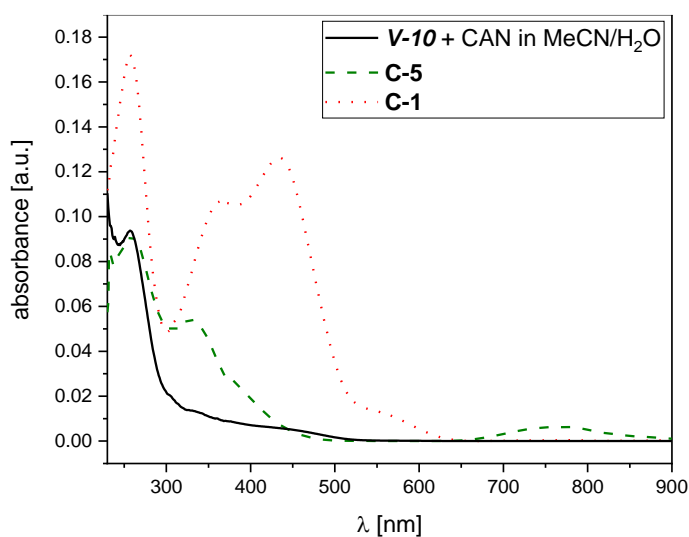
*Figure 102: Solid-state UV-vis spectra of intermediate **V-10** after treatment with cerium(IV) ammonium nitrate (black solid) and **C-1** (red dotted) and **C-5** (green dashed) as reference samples.*

As solvent a mixture of acetonitrile and water (3:1) was used, which had also not proven useful in the case of Merrifield resin. Also, the reaction time was rather long (30 min), which might have led to decomposition of the desired product. Due to lack of starting material, no further investigations were conducted. However, the preliminary results of immobilization of **L-14** on Tentagel and subsequent iron(II) incorporation are promising and the studies of this immobilization system should be continued.

Preliminary Conclusion

Synthesis of a series of **ligands of the Py₅Me₂-X type** and **their corresponding iron(II) complexes was achieved**. The presented IR spectra confirm that **immobilization** of **L-11** and **L-14** on Merrifield and Tentagel resin, respectively, can be achieved **reproducibly**, yielding the intermediates **V-6** and **V-9**. **Incorporation of iron(II)** into **V-6** was **successful**, as shown by solid state UV-vis spectroscopy of intermediate **V-7**. In the case of **V-9**, **incorporation of iron** was **successful**, however, the nature of the obtained iron species is still unclear and further measurements are necessary (Scheme 81).
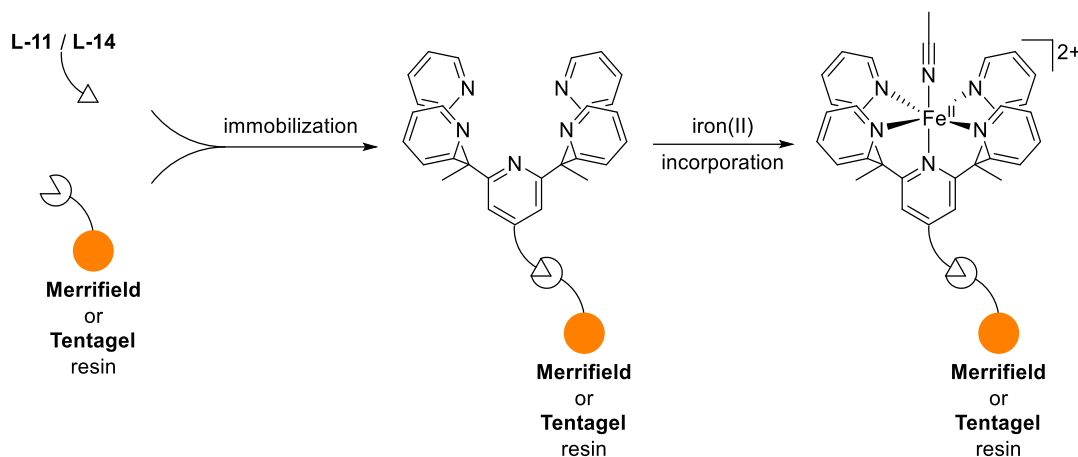
*Scheme 81: Performed immobilization of ligands **L-11** and **L-14** on Merrifield and Tentagel resin, respectively, and subsequent iron(II) incorporation.*

Oxidation of **V-7** to the corresponding iron(IV)-oxido species **V-8** was attempted and initial solid-state UV-vis measurements **indicate successful formation**. However, the obtained sample of **V-8** was incapable of oxidizing **5mC** or *p*-ethylbenzenesulfonic acid.

Thus, further experiments are necessary to confirm the proposed structures and compositions of the mentioned intermediates, especially the iron-containing compounds **V-7**, **V-8**, and **V-10** need verification. In particular, Mößbauer spectroscopy could provide a useful tool to a) confirm the presence of iron ions in the obtained resins and b) identify the oxidation state of the iron ion in question. Furthermore, close examination using IR and solid-state UV-vis spectroscopy will provide more insight into the processing occurring in Py₅Me₂-X type ligands immobilized on Merrifield and Tentagel resins.
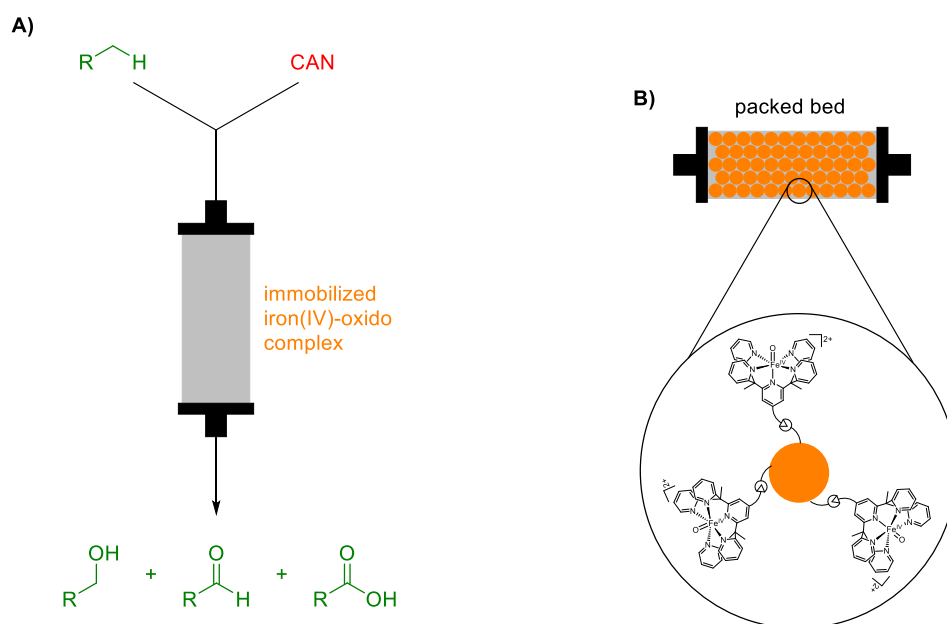
*Figure 103: **A**) Integration of an immobilized iron(IV)-oxido complex (orange) in a continuous flow regime to selectively oxidize substrates (R-CH₃, green) to the corresponding products R-CH₂OH, R-CHO, or R-CO₂H. Intermittently, the system is flushed with a solution of oxidant, in this case cerium(IV) ammonium nitrate (CAN, red) in order to regenerate the iron(IV)-oxido species. Adapted from Pastre et al.[288] **B**) Packed-bed design of a reactor chamber containing the immobilized iron(IV)-oxido complex.*

If successful, the immobilized iron(IV)-oxido complexes might be integrated in a continuous flow regime, as discussed above (Figure 103**A**). This could be achieved by employing a packed-bed approach (Figure 103**B**) in which the complex is immobilized on a resin support which is then integrated into the reaction chamber of a continuous flow apparatus.

4. The Py₅(OR)₂ Ligand System

The following chapter describes the attempts to expand the ligand library by changing the backbone of **L-1**. These investigations were based on the work of Goldsmith and Stack, who first synthesized **L-3**.[68]

Synthesis of **L-2** *and Corresponding Iron Complexes*

In order to expand the ligand library and gain access to other iron(II), iron(III), and possibly iron(IV)-oxido complexes, **L-2** was synthesized from diethyl pyridine-2,6-dicarboxylate *via* **V-11**. To this end, 2-bromo lithium was reacted with *n*-butyl lithium and subsequently diethyl pyridine-2,6-dicarboxylate was added, according to a procedure by Goldsmith *et al*.[68] **V-11** (in the literature referred to as PY3) was isolated in yields between 50-67%. It was found that larger reaction volumes led to higher yields of this reaction. Recrystallization from acetone/diethyl ether yielded single crystals of **V-11** suitable for x-ray crystallography (Figure 104). As evident from the structure, the three pyridine moieties are rotated out of the plane of the carbonyl functions.
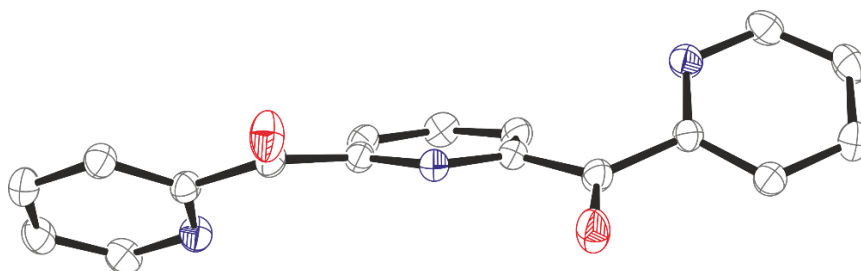
*Figure 104: Graphical representation of the crystal structure of **V-11**. Ellipsoids are drawn at 50% probability; hydrogen atoms have been omitted for clarity. Crystals were obtained from a solution of **V-11** in acetone/diethyl ether at −20 °C. A full structure and crystallographic details can be found in the appendix p. 507.*

V-11 was then further reacted by addition to a solution of lithiated pyridine (prepared from 2-bromo pyridine and *n*-butyl lithium) to afford **L-2** (in the literature sometimes referred to as PY5OH) in 38% yield (Scheme 82).
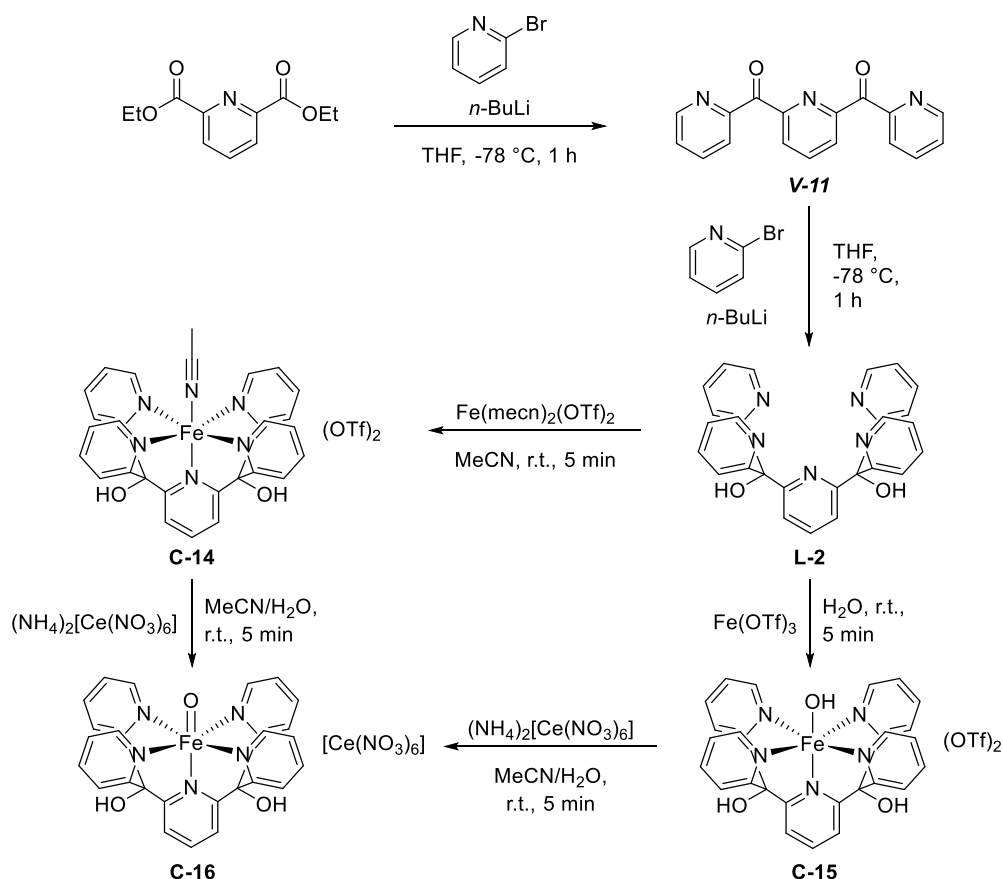
*Scheme 82: Synthesis of **L-2** in two steps from diethyl pyridine-2,6-dicarboxylate via **V-11** according to a modified literature procedure. Subsequent synthesis of **C-14**, **C-15**, and **C-16** from **L-2**; **C-14** and **C-16** according to modified literature procedures.[12] n-BuLi = n-butyl lithium, THF = tetrahydrofuran.*

In the next step, **L-2** was dissolved in acetonitrile and Fe(mecn)$_2$(OTf)$_2$ was added. The solution turned immediately a deep red and red-brown crystals of **C-14** were obtained upon vapor diffusion of diethyl ether, according to a procedure published by Chantarojsiri *et al*. **C-14** was characterized using ^{1}H and ^{13}C NMR, HR-MS, elemental analysis, UV-vis, and IR. However, characterization of the electronic properties of **C-14** *via* cyclovoltammetry or related methods is still necessary. Unfortunately, the quality of the crystals obtained was not good enough for a high-resolution x-ray crystallographic analysis. However, the obtained structure was resolved well enough to confirm the coordination geometry indicated in Scheme 82 in contrast to coordination *via* the alcohol moieties (structure not shown). **C-14** is closely related to the previously reported iron(II) complex [Fe^{II}(mecn)(**L-2**)](BF$_4$)$_2$.[304]
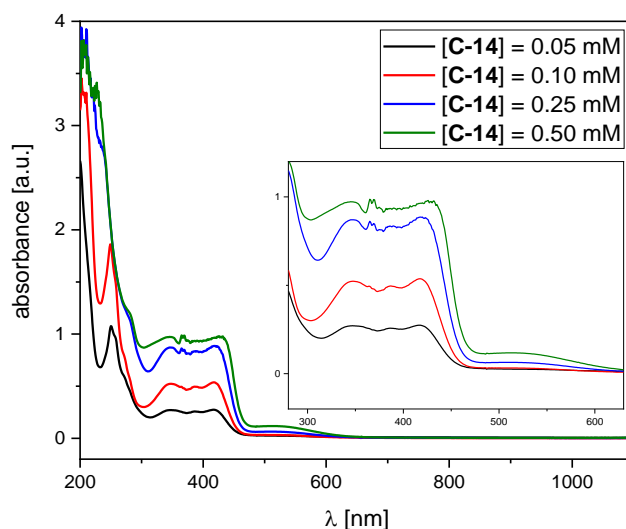
*Figure 105: UV-vis spectra of **C-14** in acetonitrile at room temperature.*

When **L-2** was suspended in water and Fe(OTf)$_3$ was added, a red-orange solution was obtained from which **C-15** crystallized as red disks or needles. Unfortunately, the crystals were not of suitable quality for x-ray crystallographic analysis (Figure 106**A**). High resolution-mass spectrometric analysis of the obtained compound showed signals and an isotope distribution pattern corresponding to **C-15**.

EPR spectroscopic analysis of **C-15** showed a signal similar to that of **C-4** (see Figure 82, p. 126), a closer comparison of EPR parameters of these compounds is found in the appendix (Table 25, p. 386). On the basis of this comparison, **C-15** was assigned as a low-spin distorted octahedrally coordinated iron(III)-hydroxido species.
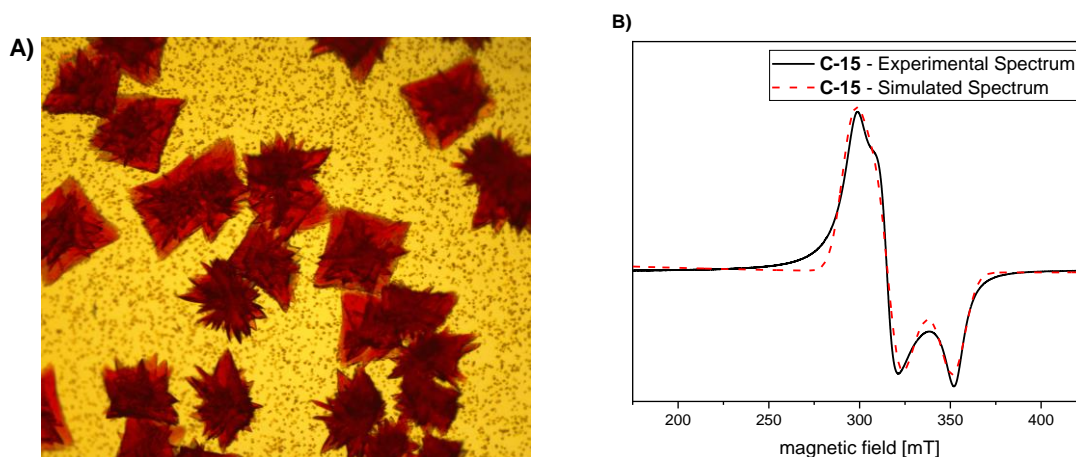
*Figure 106: **A**) Pictures of crystals of **C-15** obtained from an aqueous solution of **C-15** at 4 °C. **B**) X-band EPR spectrum (black solid) of **C-15**, collected at 298 K, simulated spectrum (red dashed) by Dr. Katherine Fisher.*

C-14 was treated with cerium ammonium nitrate (CAN) which afforded a green solid, identified as **C-16** (*via* UV-vis and CHNS elemental analysis as well as HR-MS, refer to experimental section p. 289 for details), analogous to the reaction of **C-1** to **C-5**. Additionally, a solution of **C-15** was treated with a solution of CAN, which resulted in the formation of a green species with an

167

absorption feature at λ = 730 nm (Figure 107), this was attributed to the iron(IV)-oxido moiety in **C-16**.
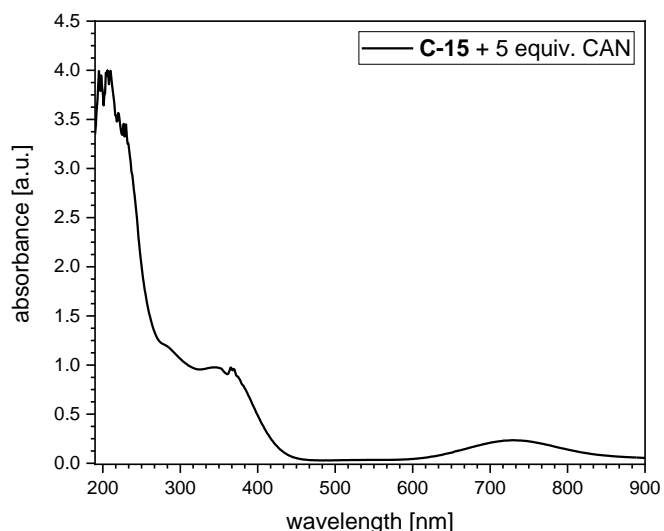
*Figure 107: UV-vis spectrum of a solution of C-15 that was treated with 5 equiv. of cerium(IV) ammonium nitrate. Conditions: [**C-15**] = 0.5 mM, [CAN] = 2.5 mM, H₂O, T = 24 °C.*

The rate of formation of this species was also studied using UV-vis spectroscopy and comparted to the formation of **C-5** from **C-4**: to this end, aqueous solutions of **C-4** and **C-15** were mixed with aqueous solutionso of CAN and the absorbance at λ = 515 nm and λ = 720/730 nm recorded (Figure 108). In these measurements, the reaction of **C-15** with CAN was observed to be significantly faster that the reaction of **C-4** with CAN.
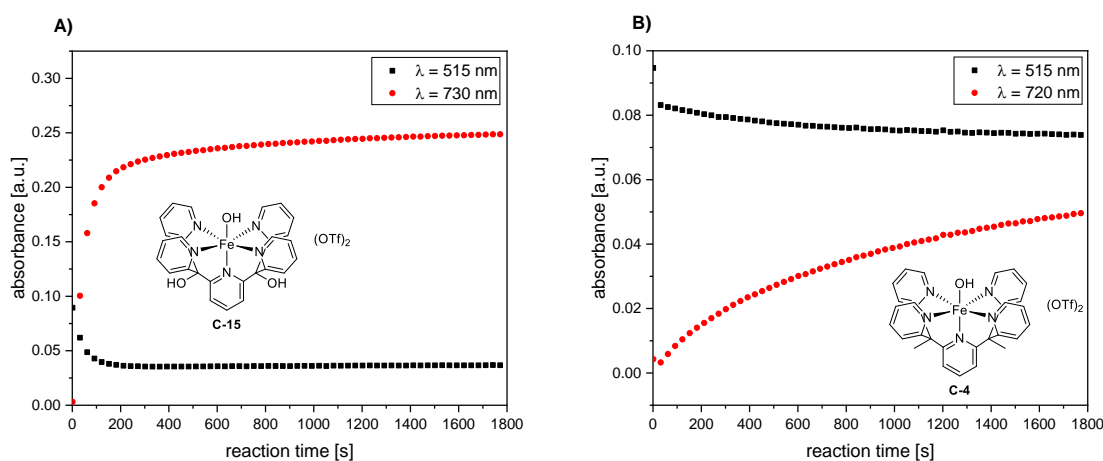
*Figure 108: **A**) UV-vis absorption at λ = 730 nm (red dots) and λ = 515 nm (black squares) upon reaction of **C-15** with cerium(IV) ammonium nitrate. **B**) UV-vis absorption at λ = 720 nm (red dots) and λ = 515 nm (black squares) upon reaction of **C-4** with cerium(IV) ammonium nitrate. Conditions: [**C-4/C-15**] = 1 mM, [CAN] = 3 mM, H₂O, T = 24 °C.*

HR-MS analysis of a reaction solution of **C-15** with 3 equiv. of CAN showed conversion to **C-16** (Figure 109). However, significant amounts of the starting material were detected during the measurement. Whether this is due to incomplete conversion or reaction of **C-16** with traces of methanol (used for purging the injection system) and subsequent formation of **C-15** is unclear.
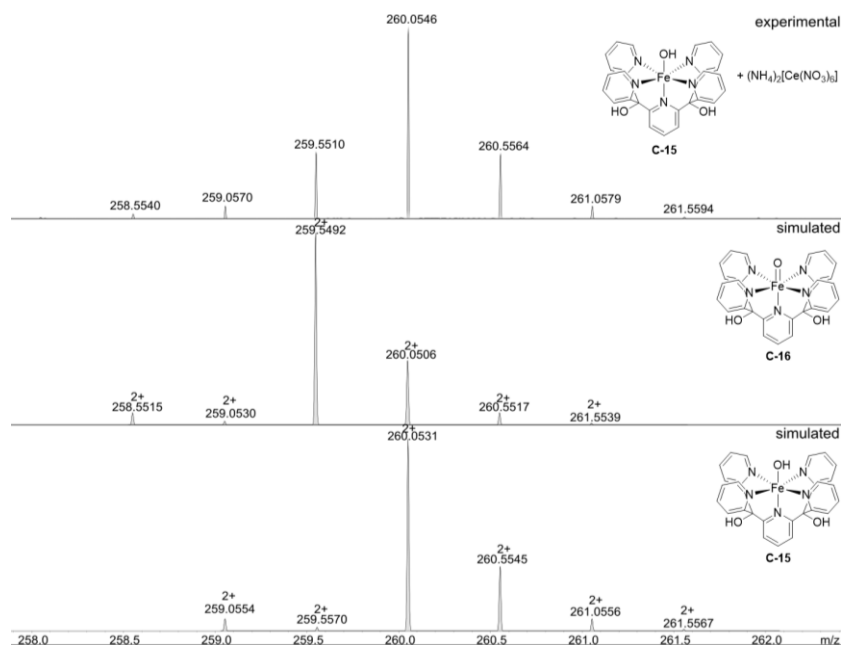
*Figure 109: In situ HR-MS spectrum of the reaction of **C-15** with 3 equiv. of CAN (upper spectrum) and simulated spectra of **C-16** and **C-15** (middle and lower spectrum, respectively). HR-MS spectrum measured by Laura Senft. Conditions: [**C-15**] = 1 mM, [CAN] = 3 mM, H₂O, T = 24 °C*

*Reactivity Studies with **C-15** and **C-16***

As with **C-4**, **C-15** was reacted with Gomberg's Dimer (**GD**) in order to probe for rebound activity. The results are very similar to those of the reaction of **C-4** with GD (refer to chapter IV.5): the amount of triphenylmethanol increased significantly upon addition of **C-15** to a solution of GD in benzene (Figure 110).
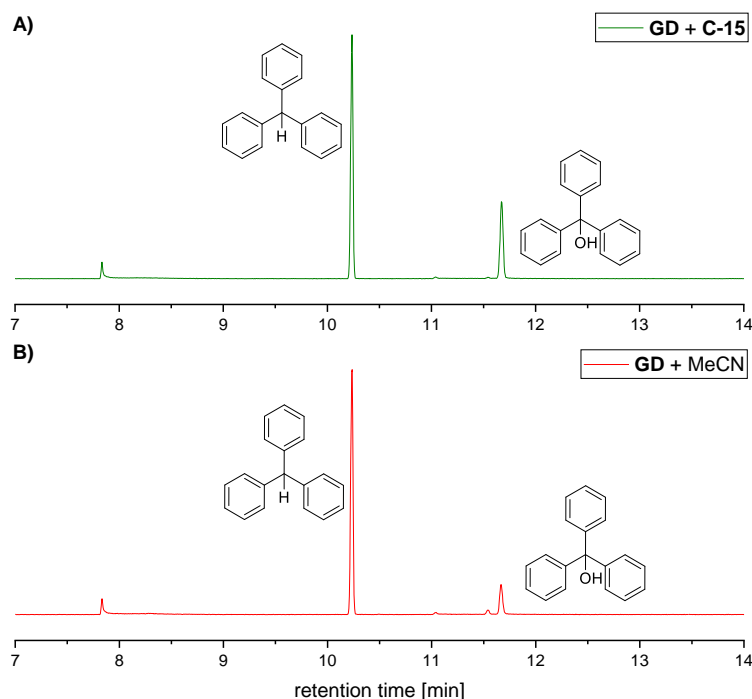
*Figure 110: Excerpt of GC-MS traces of **A**) a solution of GD in benzene mixed with a solution of **C-15** in acetonitrile and **B**) a control reaction of a solution of GD in benzene with pure acetonitrile. Signals at t_R = 10.2 min and t_R = 11.7 min were assigned based on retention time and EI mass spectrometry as well as comparison with the NIST 2020 database. GC-MS method **A**. Conditions: [**C-15**] = 2.5 mM, [GD] = 2.5 mM, benzene/acetonitrile, T = 22 °C.*

Further studies involving an ^{18}O labeled derivative of **C-15** are necessary in order to confirm the transfer of the hydroxyl moiety from **C-15** to GD.

Expanding the Ligand Library

L-2 was then also treated with sodium hydride and methyl iodide to afford **L-3**, according to the previously published procedure by Stack *et al.*[305] Similarly, **L-2** was treated with sodium hydride and other electrophiles: CD₃I to afford **L-4**, CH₂FI to afford **L-5**, and F₃CSO₂OCF₃ to afford **L-6**. The reaction time had to be increased for the reactions with CD₃I and CH₂FI to ensure complete consumption of the starting material.
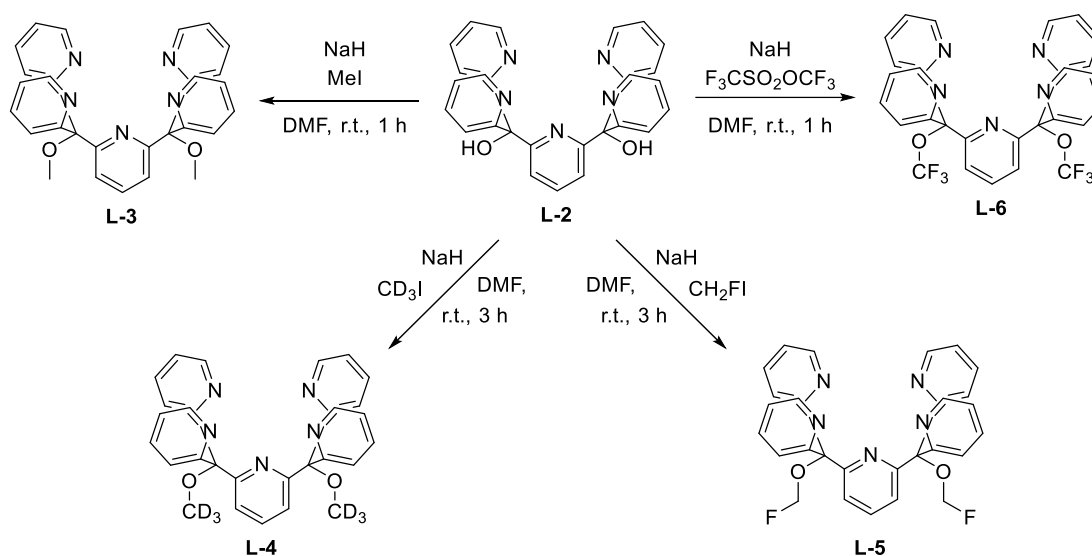
*Scheme 83: Synthesis of ligands **L-3**, **L-4**, **L-5**, and **L-6** from **L-2** according to a modified literature procedure.[305] DMF = N,N-dimethylformamide. CH₂FI was provided by Alexander Gisnapp of the Karaghiosoff group at LMU Daumann.*

The ¹H NMR spectrum of the partially deuterated ligand **L-4** is virtually identical to that of the reference compound **L-3** (Figure 111). Of course, the signal for the methyl group in **L-3** is absent in the spectrum of **L-4** (not shown, refer to the appendix p. 435 and p. 438).
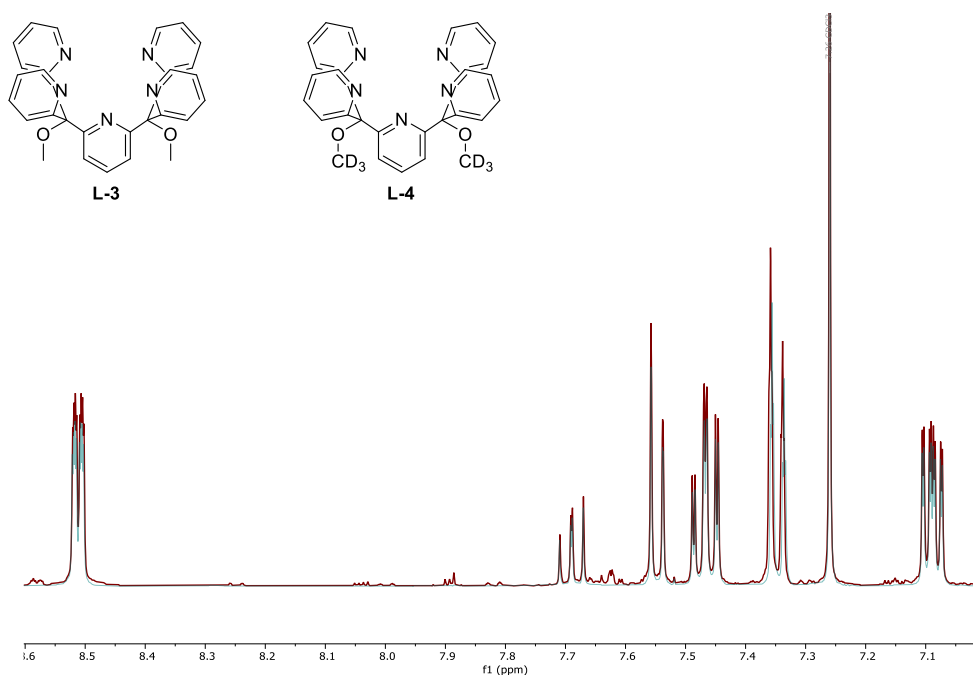
Figure 111: Excerpts of superimposed ^{1}H NMR spectra of **L-3** (brown) and **L-4** (turqoise).

When the ^{1}H NMR spectra of the fluorinated compounds **L-5** and **L-6** are compared, a larger difference is observed. In the aromatic region, several signals are shifted (Figure 112). In addition, in the region of δ = 5.65-5.40 ppm two singlets are found (not shown) for **L-5** whereas **L-6** displays no signals outside of δ = 8.60-7.00 ppm (refer to the appendix p. 442 for a full ^{1}H NMR spectrum).
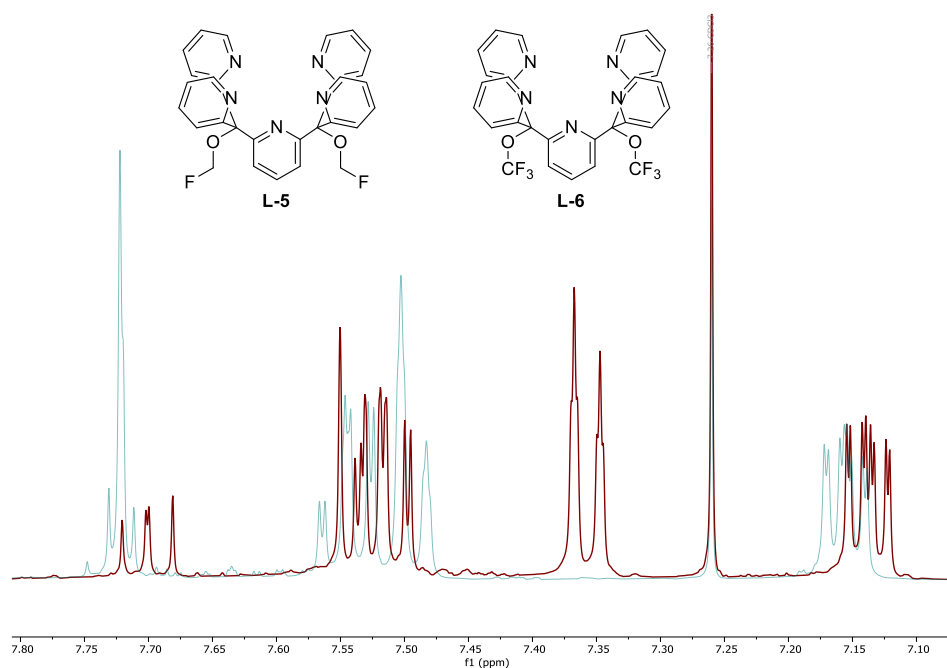
Figure 112: Excerpts of superimposed ^{1}H NMR spectra of **L-5** (brown) and **L-6** (turqoise).

In addition, both fluorinated compounds **L-5** and **L-6** were observed to decompose under column chromatography conditions (Figure 113). Whereas the signals assigned to L-5 are still observable in the aromatic region (δ = 8.60-7.00 ppm) after column chromatography, an increase in unassigned, minor signals was noted.
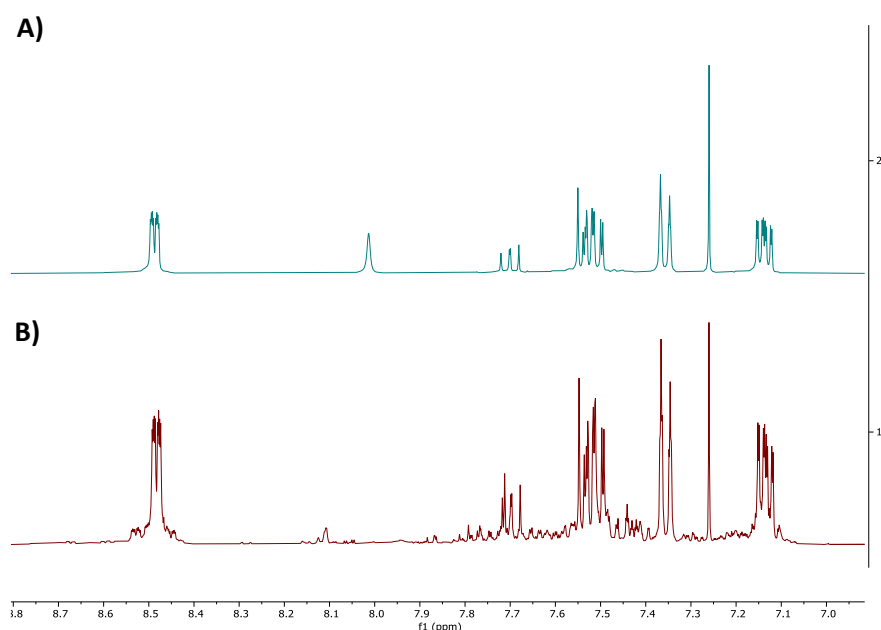
*Figure 113: Excerpts of ^{1}H NMR spectra of **L-5**. **A**) crude product directly after synthesis and **B**) after column chromatography and storage at ambient conditions for 21 d. The signal at δ = 8.00 ppm was assigned to residual N,N-dimethylformamide.*

Nonetheless, **L-3** – **L-5** were used for complexation reactions. Analogous to **L-2**, synthesis of iron(II) and iron(III) compounds was attempted by addition of Fe(mecn)$_2$(OTf)$_2$ and Fe(OTf)$_3$ in acetonitrile or water, respectively.

In the case of **L-3**, synthesis of the corresponding iron(II) complex **C-17** was performed according to a procedure by Goldsmith and Stack or Chantarojsiri *et al.*[68] Both procedures yielded the same product, the procedure described by Chantarojsiri *et al.* should be preferred in future investigations due to its simplicity (the ligand is dissolved in acetonitrile, the metal precursor is added, diethyl ethyer is diffused into the solution which yields the product as long needles, all steps are performed under ambient conditions). The obtained product was then oxidized using iodosylbenzene (IB) to obtain **C-18**, as previously reported by Goldsmith and Stack.[68] However, the obtained compound had an oily texture and did not crystallize/solidify. When **L-3** was directly treated with Fe(OTf)$_3$, the same observation was made. This behavior was attributed to residual traces of the ligand or, in the case of oxidation with IB, the presence of unreacted IB or decomposition products thereof (e.g. iodobenzene).
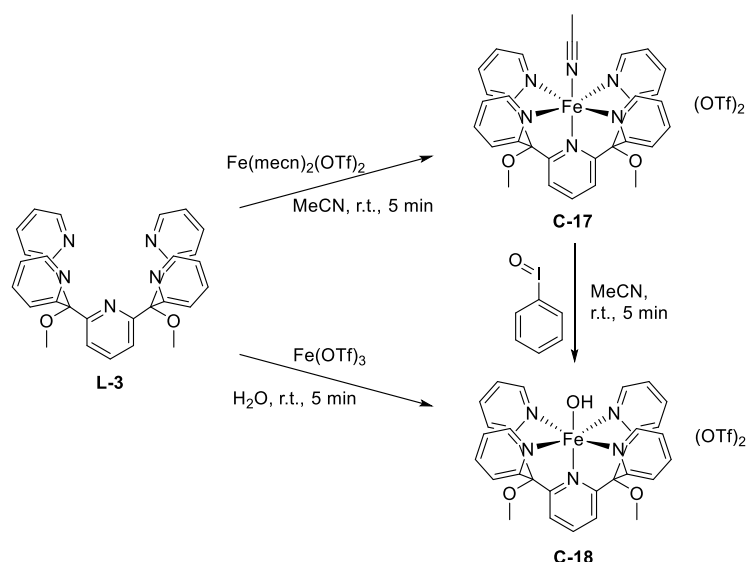
*Scheme 84: Synthesis of **C-17** and **C-18** from **L-3** by addition of Fe(mecn)₂(OTf)₂ or Fe(OTf)₃ to a solution/suspension of the ligand in acetonitrile or water, respectively. Subsequent oxidation of **C-17** by iodosylbenzene also yielded **C-18**. Synthesis of **C-17** and **C-18** via oxidation using iodosylbenzene were conducted according to the literature procedure by Goldsmith and Stack.[68]*

The corresponding deuterated complex **C-19** was obtained from the reaction of **L-4** with Fe(mecn)₂(OTf)₂ in acetonitrile at room temperature as red-brown needles (Scheme 85). This complex is an interesting candidate for the synthesis of a new iron(IV)-oxido complex as the deuterated methyl group makes the complex likely less prone to auto-oxidation (refer to chapter IV.6). This was not attempted within the scope of this work.
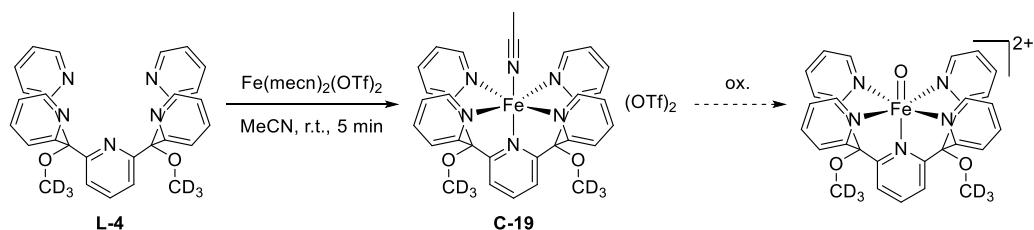
*Scheme 85: Synthesis of **C-19** and proposed oxidation to the corresponding iron(IV)-oxido complex. Synthesis of **C-19** according to a modified procedure by Chantarojsiri et al.[12]*

A comparison of the ¹H NMR spectra of **C-14**, **C-17**, and **C-19** shows the differences and similarities of these complexes: Whereas the ¹H NMR spectrum of **C-14** is markedly different from that of **C-17**, the ¹H NMR spectra of **C-17** and **C-19** are nearly identical, as is expected. Notably the signals in the ¹H NMR spectrum of **C-14** are sharper than those in the spectra of **C-17** and **C-19**. Whether this is due to the presence of paramagnetic impurities, such as iron(III) complexes, or a more degrees of freedom, due to the methyl groups, cannot be stated at this moment. Measuring ¹H NMR spectra at low temperature would give insight into this question.
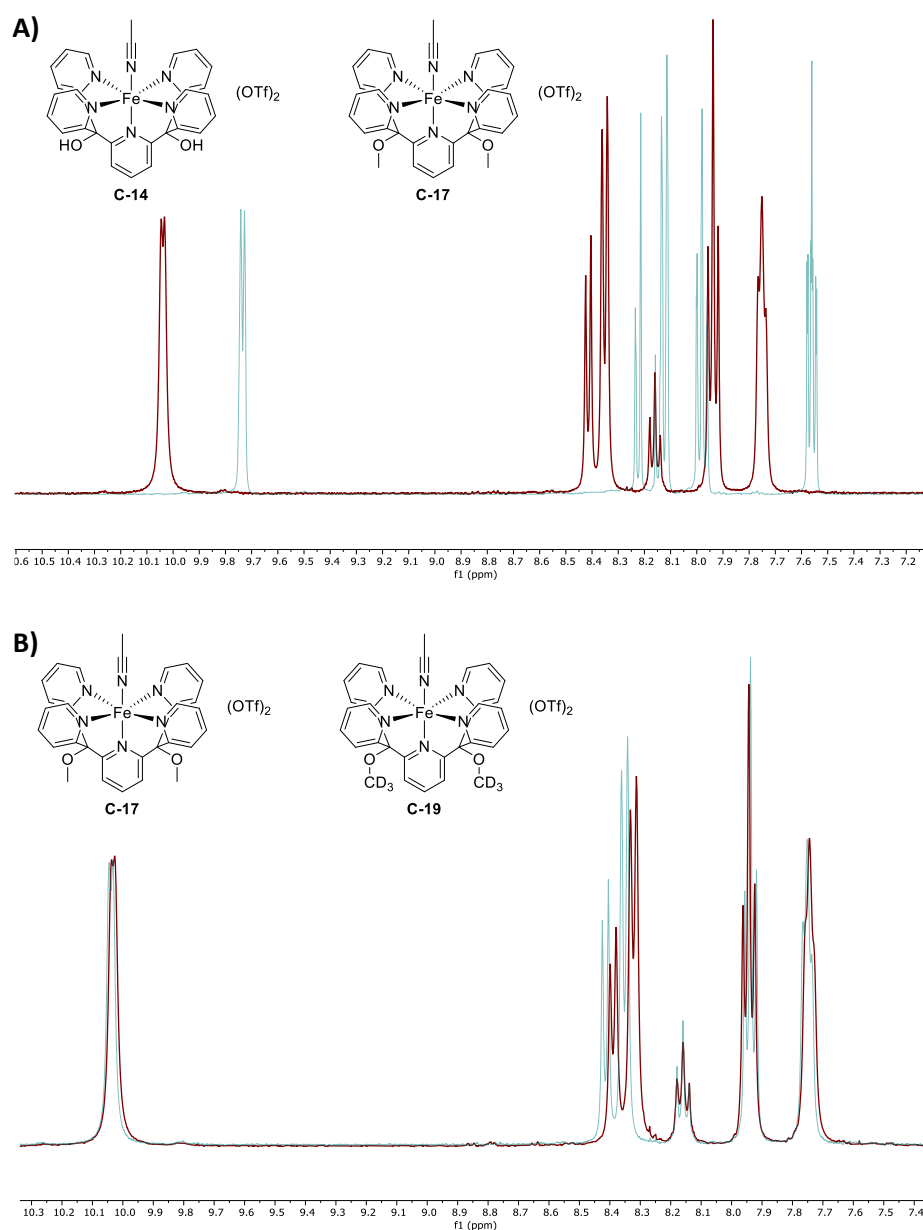
*Figure 114: **A**) Overlay of excerpts of the ¹H NMR spectra of **C-14** (turquoise) and **C-17** (brown) in CD₃CN at room temperature. **B**) Overlay of excerpts of the ¹H NMR spectra of **C-17** (turquoise) and **C-19** (brown) in CD₃CN at room temperature.*

Synthesis of the corresponding iron(II) acetonitrile complexes of **L-5** and **L-6** failed despite several attempts (Scheme 86). This was attributed to the observed decomposition of both ligands. In the future, complexation reactions immediately after isolation of the ligands might provide a solution to circumvent this problem, as the complexes themselves might be more stable than the free ligands.
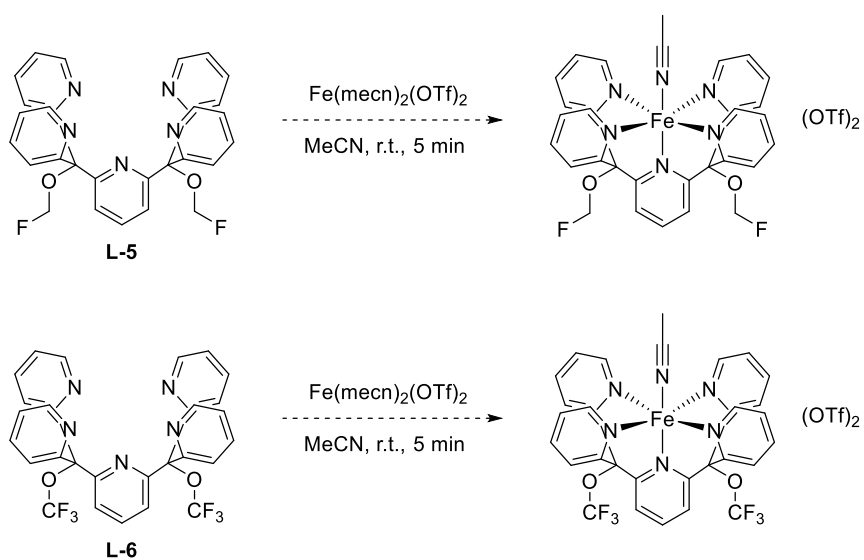
*Scheme 86: Attempted syntheses of iron(II) complexes from **L-5** or **L-6** by addition of Fe(mecn)₂(OTf)₂ to a solution of the ligand in acetonitrile, according to a modified procedure by Chantarojsiri et al.[12]*

5. The Py₄OHMe₂H Ligand and its Complexes

The following chapter describes the attempts to expand the ligand library towards an oxygen-containing ligand: **L-7**.

Synthesis of **L-7**

Synthesis of **L-7** was achieved through a three-step synthesis starting from 2-bromo-6-(2-methyl-1,3-dioxolan-2-yl)pyridine. In the first step, ***III-1*** was reacted with *n*-butyl lithium in tetrahydrofuran and the starting material was added, analogous to the previously described syntheses of similar ligand systems (refer to chapters III.3 and IV.3). ***V-12*** was obtained as the crude product, its dioxolan protecting group was then removed by addition of aqueous hydrochloric acid to afford ***V-13*** in 75% yield over two steps. Subsequently, 2-bromopyridine was reacted with *n*-butyl lithium and ***V-13*** was added, **L-7** (Py₄OHMe₂H) was isolated in 58% yield. Reaction of **L-7** with Fe(mecn)₂(OTf)₂ gave the corresponding iron(II) complex **C-20.** Reaction with Fe(H₂O)₆(BF₄)₂ resulted in the formation of μ-oxido-bridged complex **C-21**, as was confirmed by HR-MS and elemental analysis (refer to p. 181 for details).
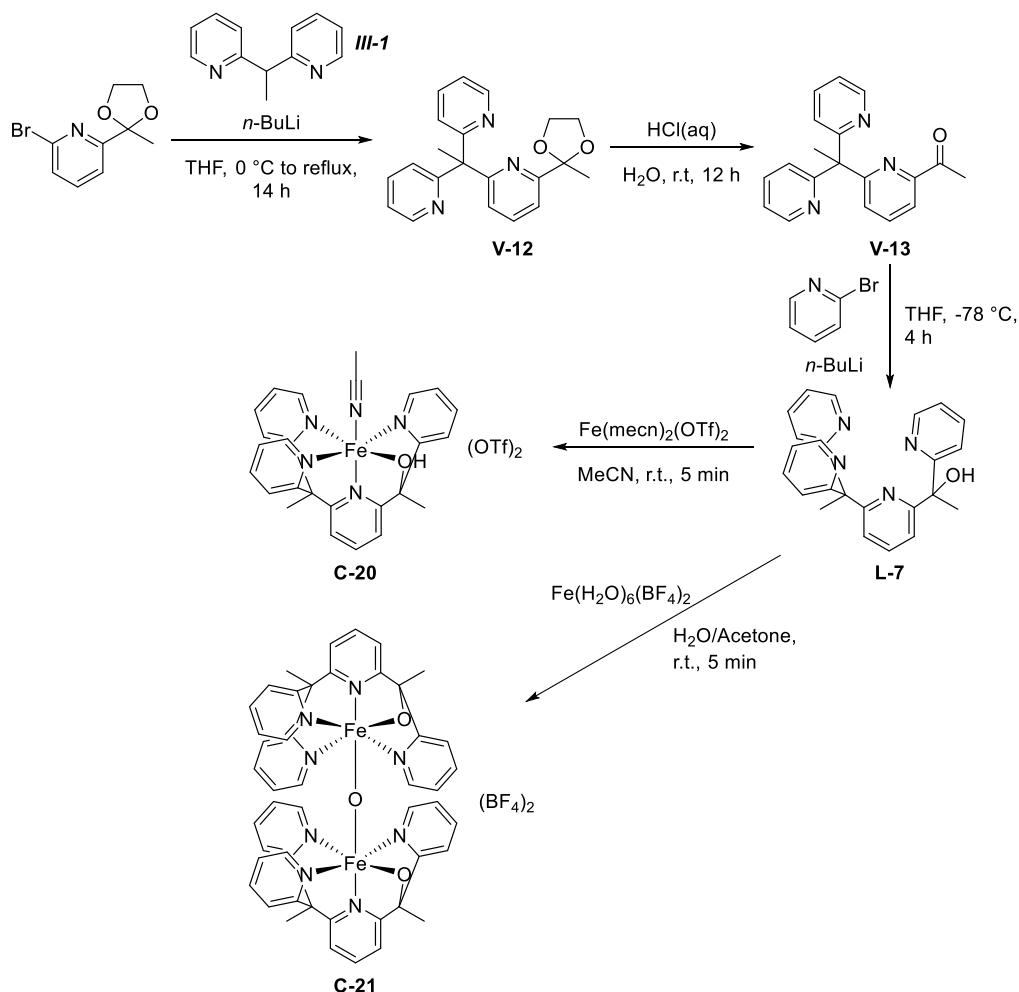
*Scheme 87: Synthesis of **L-7**, **C-20**, and **C-21** from 2-bromo-6-(2-methyl-1,3-dioxolan-2-yl)pyridine. THF = tetrahydrofuran, MsCl = methanesulfonyl chloride, DCM = dichloromethane. Synthesis of **V-12** and **V-13** according to a modified procedure by Drummond et al.[49]*

The obtained crystals of **C-20** were suitable for x-ray crystallography (Figure 115**A** and **B**) and coordination of the oxygen atom can clearly be observed. The iron center is coordinated in a distorted octahedral fashion, as was expected from previous experiments. However, the bond lengths of the donor atoms to the iron core differ considerably: The Fe-O bond is the longest at 2.025 Å whereas the two axial nitrogen atoms are much closer to the iron center (around 1.92 Å). Moreover, the oxygen atom is situated outside of the equatorial plane, as can be observed in Figure 115. This is also reflected in the bond angles, as for example the angle between the acetonitrile nitrogen atom and the oxygen atom was measured to be 96.3°. The angle between the two axial ligands is 174.5° and shows that the iron atom is situated slightly off-center.
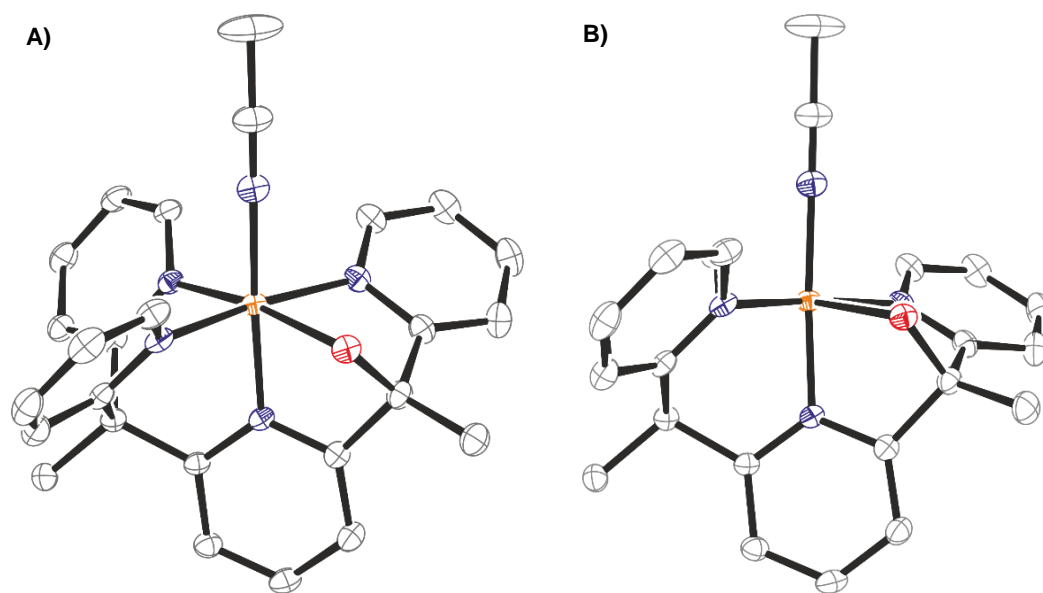
Figure 115: **A)** *Graphical representation of the crystal structure of* **C-20**. **B)** *Side-on view of* **C-20**. *Ellipsoids are drawn at 50% probability; hydrogen atoms and counter ions have been omitted for clarity. Crystals were obtained from slow diffusion of diethyl ether into a solution of* **C-20** *in acetonitrile. A full structure and crystallographic details can be found in the appendix p. 507.*

As x-ray crystallography is mostly not suitable for detecting protons, the crystal structure does not provide any insight into whether the alcohol moiety on **L-7** remains protonated upon coordination. However, a comparison of the ¹H NMR spectra of **L-7** and the corresponding iron(II) complex **C-20** shows strong evidence in favor of a protonated alcohol moiety (Figure 116). The most upfield shifted signal visible in Figure 116 (upper spectrum **L-7**: δ = 6.02 ppm, lower spectrum **C-20**: δ = 6.85 ppm) was assigned to the alcohol proton. Addition of D$_2$O to [Fe^{II}(**L-7**)(MeCN)]$^{2+}$ in CD$_3$CN resulted in decomposition of the complex and thus could not be used to confirmed the assignment of this signal.
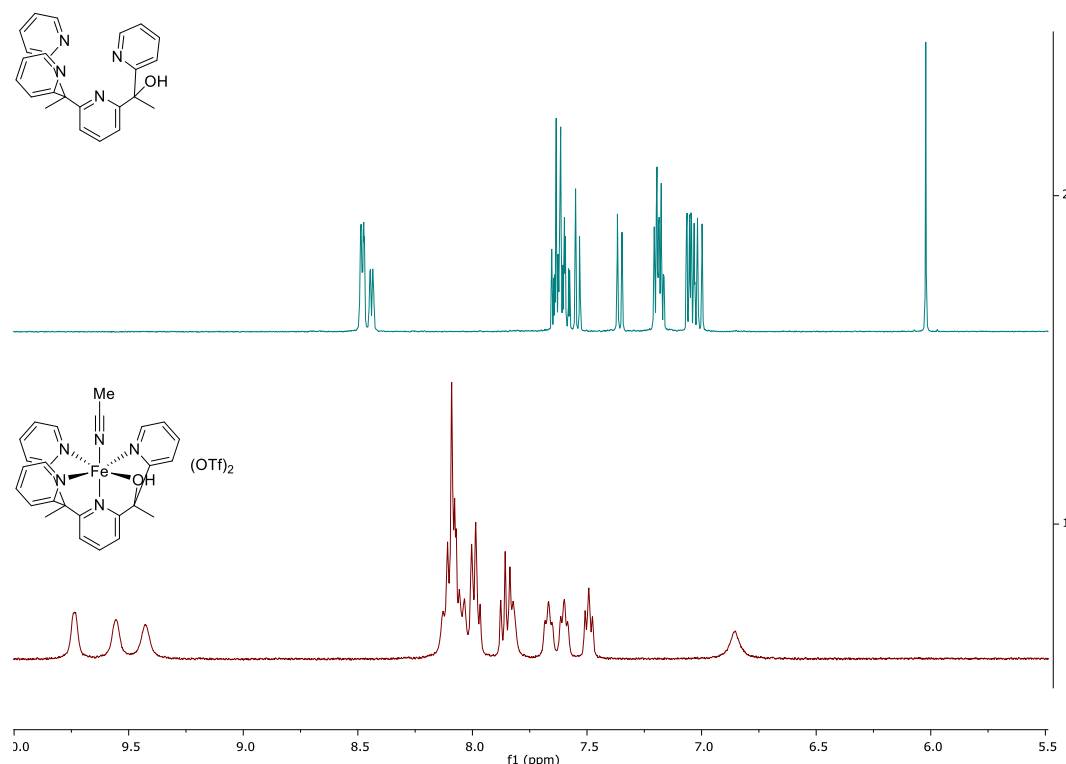
*Figure 116: Excerpts of the ¹H NMR spectra of the free ligand **L-7** (upper spectrum) and its corresponding iron(II) complex **C-"=** (lower spectrum). Both spectra were recorded at 298 K in CD₃CN.*

A downfield shift was observed for all protons including the alcohol proton. Notably, all signals in the spectrum of **C-20** show line broadening, which might be due to the presence of a paramagnetic substance, possibly an iron(III) species, in the solution. This was not observed for the corresponding complex of the Py₅Me₂-H/**L-1** ligand system (**C-1**, refer to the appendix p. 420).
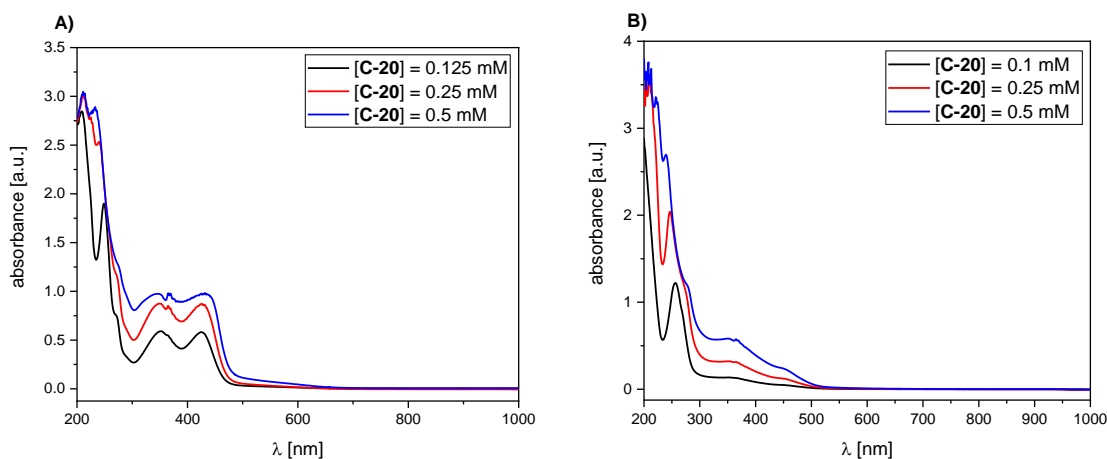
*Figure 117: UV-vis spectra of **C-20** recorded in **A)** acetonitrile and **B)** water.*

UV-vis spectroscopic analysis of this compound showed absorption features in the region from λ = 200-700 nm, both as solution in acetonitrile and water. The absorption at λ = 200-300 nm was mostly attributed to the pyridine moieties of the ligand. In acetonitrile, an absorption feature consisting of two bands at λ = 352 nm and λ = 426 nm was observed with ε_{352} = 4727 l mol⁻¹ cm⁻¹ and ε_{426} = 4660 l mol⁻¹ cm⁻¹. In the case of water as solvent, the absorption was much lower and a

single broad band between λ = 300-500 nm with a peak at λ = 352 nm (ε_{352} = 1350 l mol^{-1} cm^{-1}) and a shoulder at λ = 276 nm were observed.
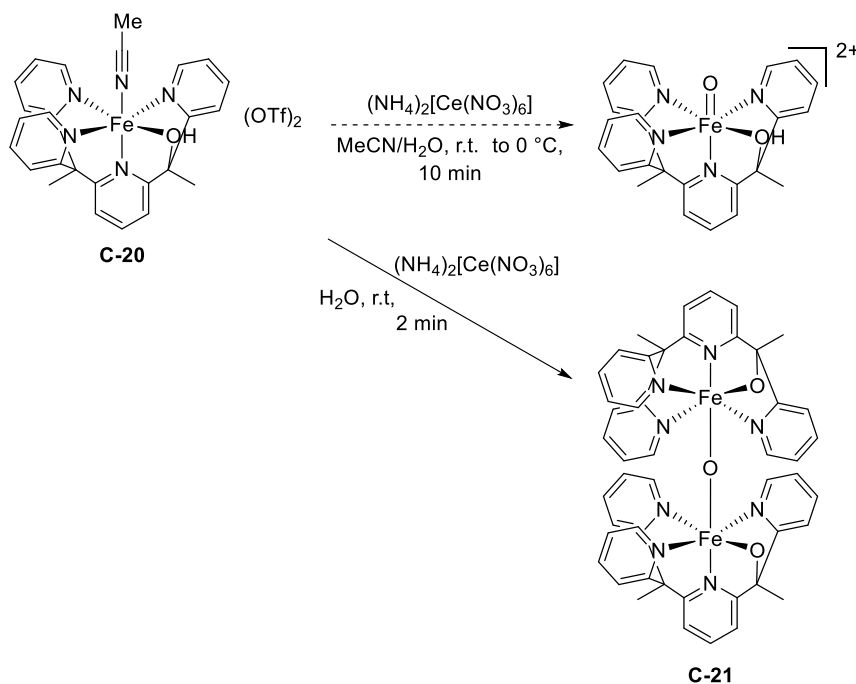
Scheme 88: *Oxidation attempt of **C-20** using cerium(IV) ammonium nitrate (CAN) to the corresponding iron(IV)-oxido species resulted in the formation of **C-21**. HR-MS measurements were performed by Laura Senft of the Ivanović-Burmazović group at LMU Munich.*

Oxidation of this iron(II) complex using cerium(IV) ammonium nitrate in a mixture of acetonitrile/water (3:1) resulted in a color change from yellow/brown to red solution, however, no precipitate formed, as was observed for the reaction of **C-1** with cerium ammonium nitrate. UV/Vis spectroscopic analysis of the obtained solution showed no absorption feature in the range of λ = 700-800 nm, which would be typical for iron(IV)-oxido complexes.[12,76,79] However, a shoulder was detected at λ = 530 nm which could be a sign of the corresponding iron(III)-hydroxido species. This signal was also detected when iodosylbenzene (IB) or diacetoxyiodosylbenzene (DAcIB) were used.
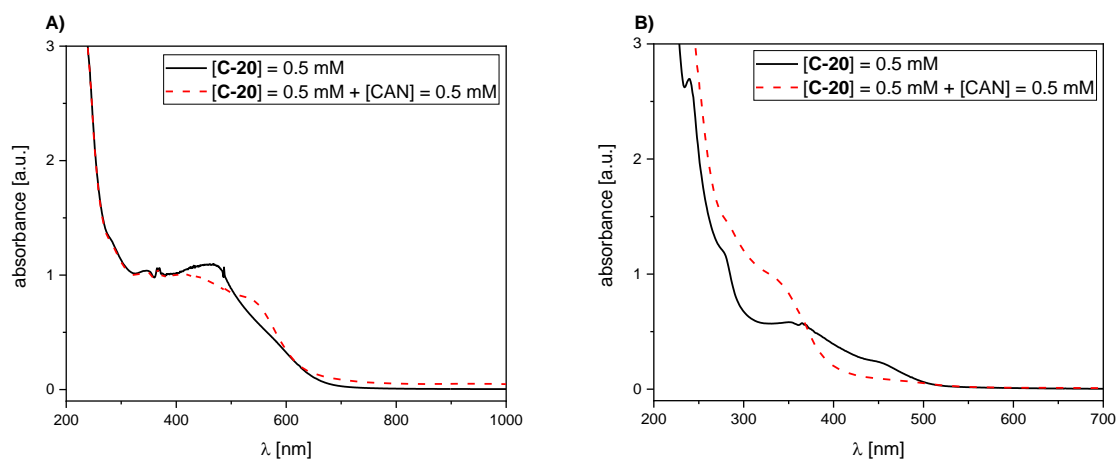
*Figure 118: **A)** Excerpts of UV-vis spectra of **C-20** before (black solid) and after (red dashed) addition of cerium(IV) ammonium nitrate (CAN) in a mixture of acetonitrile and water (3:1). **B)** Excerpts of UV-vis spectra of **C-20** before (black solid) and after (red dashed) addition of cerium(IV) ammonium nitrate (CAN) in water. Full spectra can be found in the appendix p. 387.*

Analysis of the reaction mixture using HR-MS confirmed the presence of an iron(III) species, however, the obtained data suggests the formation of μ-oxido-bridged dimer. This assignment is based on the observation of a signal at 445.1060 m/z which would correspond to the calculated m/2 exact mass of **C-21** (Scheme 88). Additionally, the calculated isotope distribution pattern of **C-21** fits the observed measurement (Figure 119). The analytical data obtained from this reaction is equivalent to that obtained from the reaction of **L-7** with Fe(H₂O)₆(BF₄)₂ as described above. This circumstance indicates that the either oxidation of the iron(II) complex of **L-7** *or* mixture of such a complex with an organic solvent (e.g. acetone or acetonitrile) for a prolonged time period leads to the oxidation of the iron centers under formation of an iron(III)-μ-oxido-bridged dimer. Interestingly, this assignment would also indicate that the alcohol moiety has been deprotonated, which is likely according to the hard and soft acids and bases (HSAB) principle: the harder iron(III) ion prefers the harder alkoxy ligand.
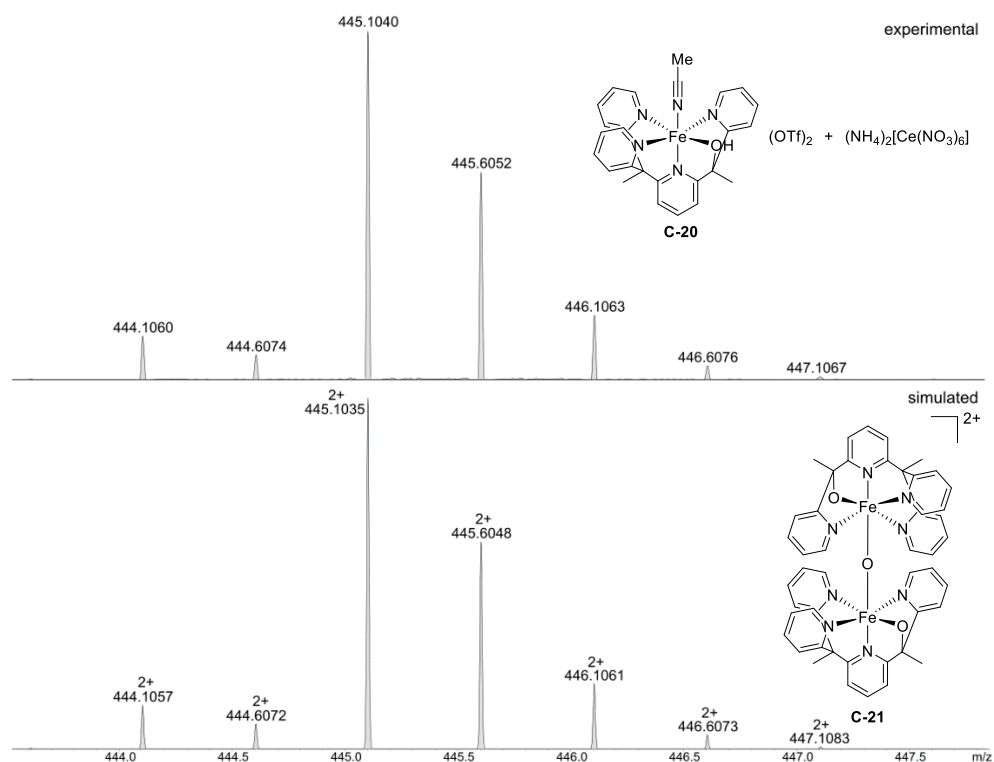
*Figure 119: HR-MS measurement of the oxidation reaction of **C-20** with 3 equiv. of cerium(IV) ammonium nitrate (upper spectrum). Calculated isotope distribution patterns for **C-21** (lower spectrum). HR-MS measurements were performed by Laura Senft of the Ivanović-Burmazović group at LMU Munich.*

Such μ-oxido-bridged iron(III) complexes are not observed in complexes of the **L-1** ligand, the exchange of one of the pyridine donors for an oxygen donor therefore seems to be the reason for this behavior. Crystallization and subsequent x-ray crystallographic analysis of **C-21** would provide insight into the exact structure. The tilted geometry of the acetonitrile ligand in **C-20** might suggest that steric interactions of the two ligand frameworks could be responsible for the successful formation of **C-21** in the case of ligand **L-7**.

Reactivity experiments

C-21 was formed in situ using IB and then reacted with DHA in acetonitrile,the resulting product mixture was analyzed using GC-MS (Figure 120**A**). In this reaction, anthracene and anthraquinone were observed as products, in addition to the starting material (Figure 120**B**, black solid trace). In a control reaction that contained only IB and DHA, the same products anthracene and anthraquinone, although in lower amounts were observed.

A)

B)
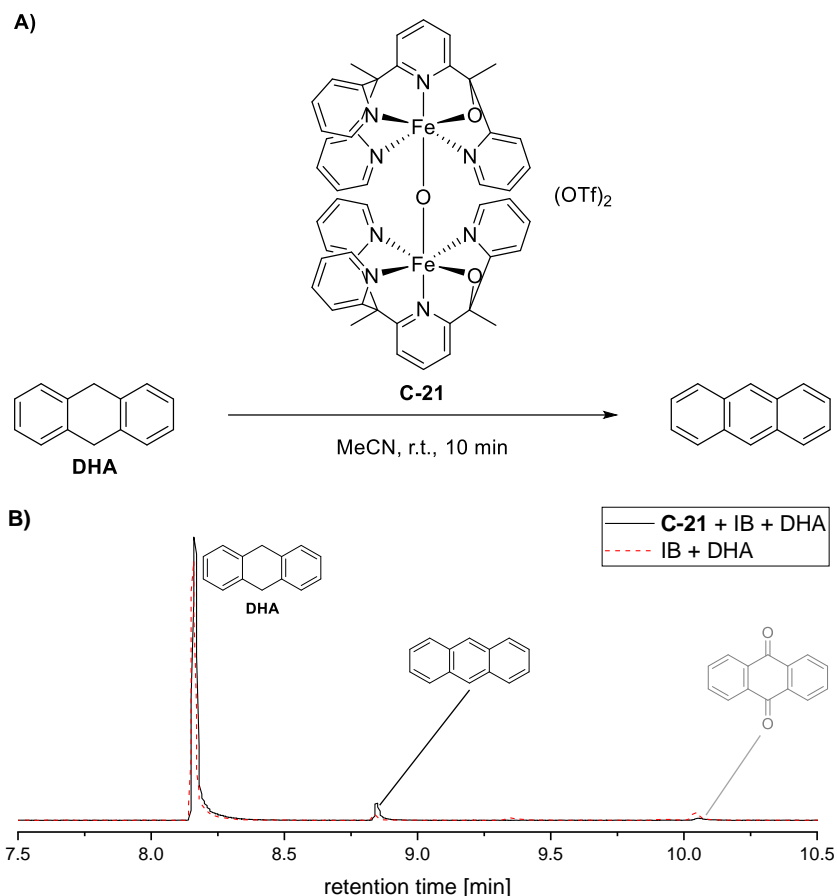
*Figure 120: **A)** Reaction of **C-21** with DHA in acetonitrile. **C-21** was synthesized in situ from **C-20** and iodosylbenzene (IB). **B)** Excerpt of the GC-MS trace of the reaction of **C-21** (fromed in situ from **C-20** and IB) with DHA in acetonitrile. The products DHA, anthracene, and anthraquinone are marked. For a complete trace and references traces refer to the appendix p. 388f. GC-MS method **A**. Conditions: [**C-21**] = 5 mM, [IB] = 10 mM, DHA = 50 mM, MeCN, T = 25 °C.*

Unfortunately, these results cannot be interpreted unequivocally. Thus, further experiments on the reactivity of **C-21** towards DHA, cyclohexadiene, cyclohexane, or other common substrates are necessary to confirm these initial results.

*Attempted Synthesis of **L-8***
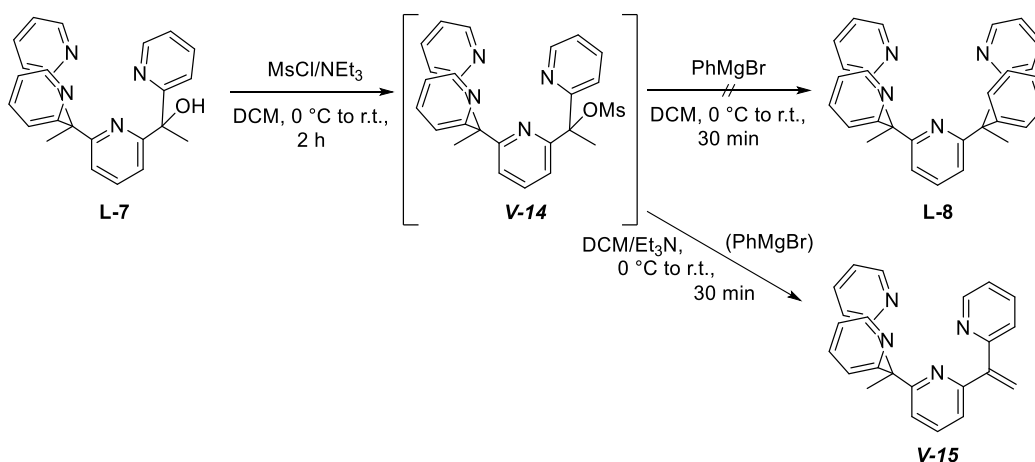
*Scheme 89: Attempted synthesis of **L-8** via mesylation of **L-7** and subsequent addition of phenyl magnesium bromide. **V-15** was obtained, even if no phenyl magnesium bromide is added. MsCl = methanesulfonyl chloride, DCM = dichloromethane, PhMgBr = phenyl magnesium bromide.*

Converting the hydroxyl group of ligand **L-7** into the corresponding mesylate (***V-14***) and addition of phenyl magnesium bromide did not give the desired substitution product **L-8** (Py$_4$PhMe$_2$H) but led to elimination forming ***V-15***. Even if PhMgBr is not added but instead an excess of MsCl (10.0 equiv.) is used, the eliminated product forms. Unfortunately, ***V-15*** was observed to decompose even at –20 °C. Still, this compound should also be studied concerning its complexation behavior with iron(II) precursors. The ligand might enforce a trigonal bipyramidal structure which has been proposed to be the geometry of the enzymes active site when it is in its active iron(IV)-oxido form (refer to chapters 0 and V.1).[15]

6. Py$_4$PhMe$_2$H and Py$_3$PhMe$_2$H Ligands

The following chapter describes the attempts to synthesize a ligand that provides a free coordination site when coordinated to iron: **L-8**.

Synthesis of **L-8** *and* **L-9**

When synthesis of **L-8** by converting **L-7** into the corresponding mesylate and subsequent substitution by a phenyl moiety was unsuccessful (chapter V.5, Scheme 89) another pathway was investigated. Scheme 90 gives an overview of the conducted syntheses: 2,6-dichloropyridine was reacted with ***III-1*** and 2-(1-phenylethyl)pyridine (***V-16***) to obtain a mixture of **L-1**, **L-8**, and **L-9**.
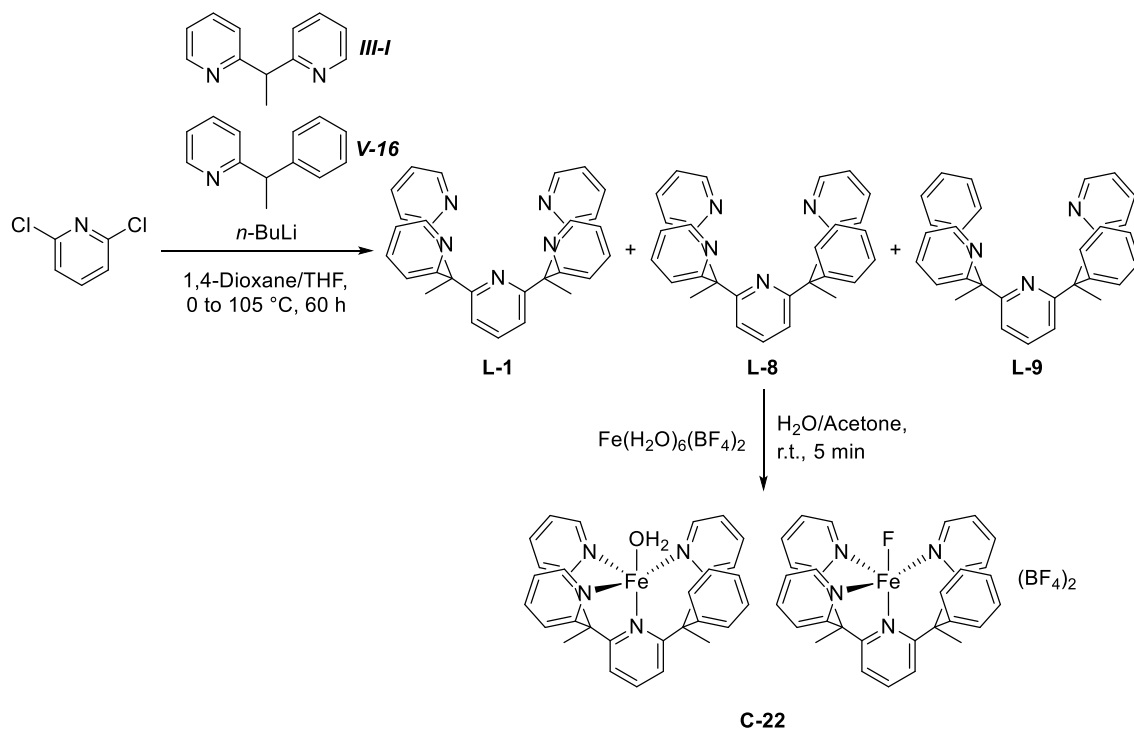
*Scheme 90: Synthesis of **L-1, L-8, L-9** and **C-22** from 2,6-dichloropyridine, **III-I**, and **V-16**.*

V-16 was synthesized analogous to ***III-I*** by reacting 2-ethyl pyridine with *n*-butyl lithium and fluorobenzene (Scheme 91).
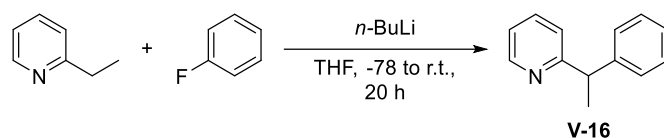
Scheme 91: Reaction of 2-ethyl pyridine, n-*butyl lithium and fluorobenzene to obtain* **V-16**.

As a side product of this reaction, the twice substituted 2-(1,1-diphenylethyl)pyridine was obtained. This was observed *via* GC-MS (Figure 121) and LC-MS. This is very similar to the synthesis of 1,1-bis(2-pyridyl)ethane, a similar side reaction was also observed in this case (refer to chapter III.3). This side reaction can be averted by conducting the reaction in a more dilute concentration (0.2 M instead of 0.5 M), reducing the reaction temperature to r.t. (23 °C), and using an excess (3 equiv.) of 2-ethyl pyridine. This afforded the desired product **V-16** in 90% yield.
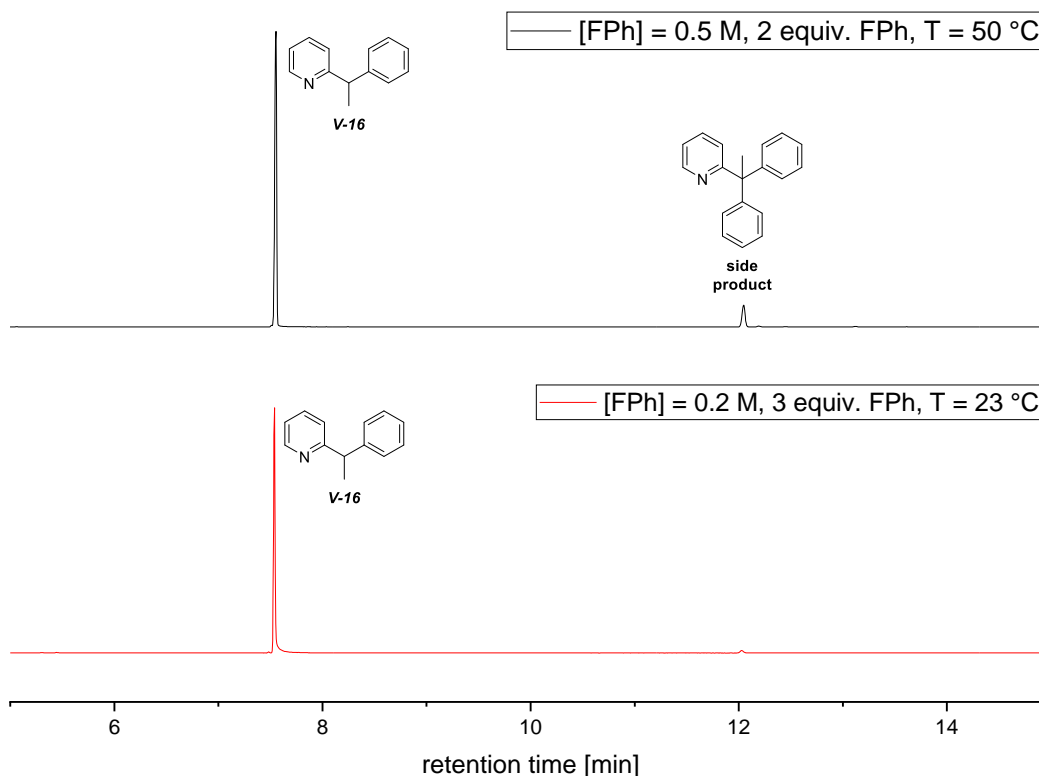
Figure 121: GC/MS traces of reactions containing the starting material, the desired product **V-16**, *and a side product (upper trace) and a reaction where the side product is only present in trace amounts) after work-up. The starting material can then easily be removed under high vacuum. FPh = fluorophenol.*

In the next step, a 1:1.2 mixture of **III-I** and **V-16** was treated with *n*-butyl lithium and 2,6-dichloro pyridine was added. This resulted in a mixture of several species, including the desired ligand **L-8**, the previously known ligand **L-1**, and the two-fold 2-(1-phenylethyl)pyridine substituted species Py$_3$Ph$_2$Me$_2$H (**L-9**). All assignments were made on the basis of HR-MS and ^{1}H NMR spectroscopy (not shown, refer to the appendix p. 259f for **L-1** and p. 307f for **L-8**, and **L-9**). Additionally, the half-substituted intermediates **V-17** and **V-18** were observed (Scheme 92) in LC-MS measurements

of the reaction mixture and obtained column fractions. ¹H NMR spectroscopy confirmed the assignment for **V-17**, for **V-18** no pure sample was obtained.
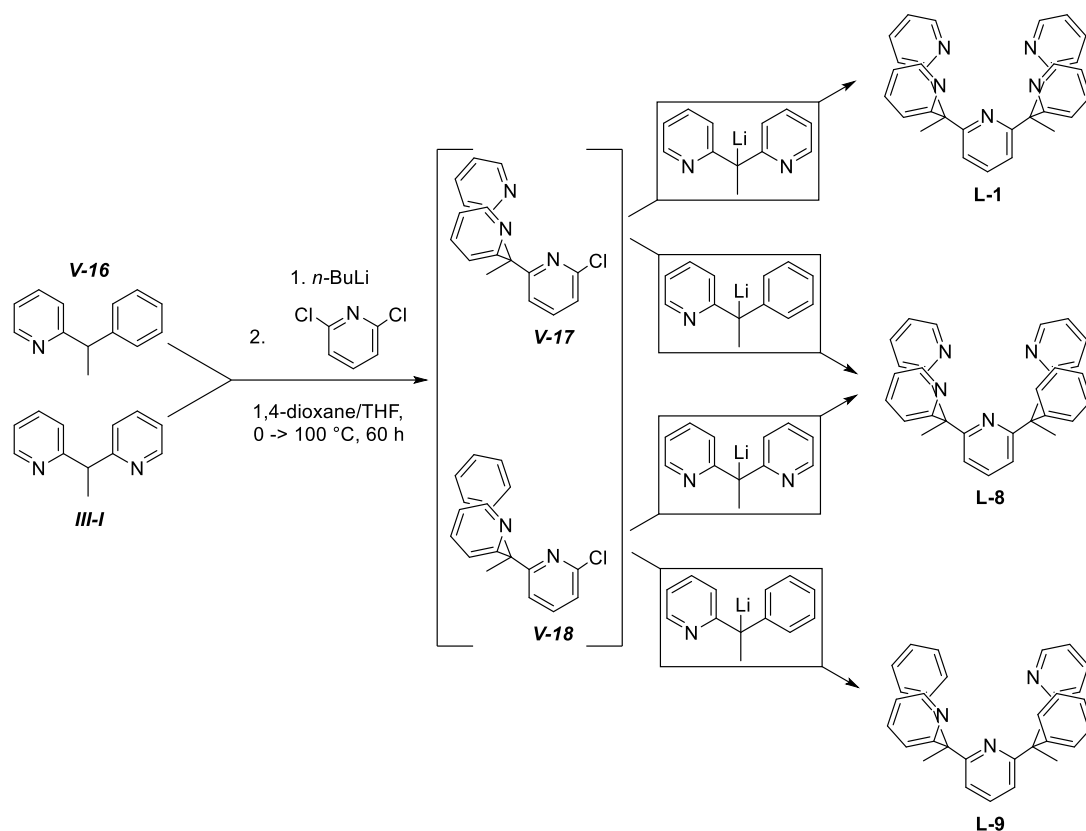
*Scheme 92: Proposed mechanism of the synthesis of the ligands **L-1**, **L-8**, and **L-9** via the intermediates **V-17** and **V-18**. n-BuLi = n-butyl lithium, THF = tetrahydrofuran.*

The three ligands **L-1**, **L-8**, and **L-9** are formed roughly in equal amounts (as observed in the UV trace during flash column chromatography), which is rather surprising, as two paths should lead to **L-8** whereas only one path leads to either **L-1** or **L-9**. Additionally, an excess of **V-16** was used (1.2 equiv. compared to **III-I**), which should increase the amounts of **L-8** and **L-9** formed during the reaction. This suggests another mechanism might be involved, more data needs to be collected for any definite statement. Unfortunately, a recrystallization step is required for **L-1**, **L-8**, and **L-9** after column chromatography which further reduces the yield of this reaction.

Column chromatography and subsequent re-crystallization from diethyl ether gave **L-8** in 5-10% yield. The obtained crystals were also suitable for x-ray crystallography, Figure 122 shows the graphical representation of the ligands structure. A crystal structure of **L-1** was also obtained (refer to the appendix, p. 487).
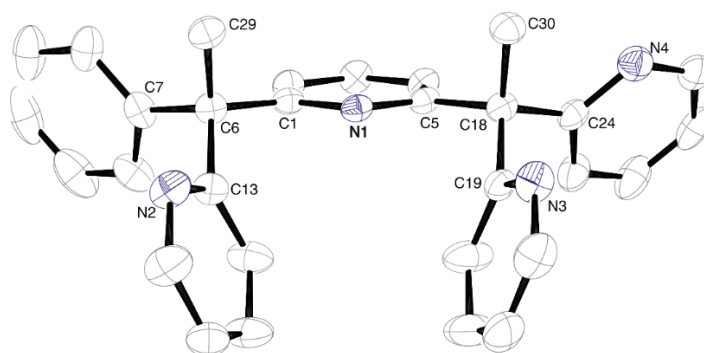
*Figure 122: Graphical representation of the crystal structure of **L-8**. Ellipsoids are drawn at 50% probability; hydrogen atoms have been omitted for clarity (refer to the appendix p. 511 for crystallographic details). Crystals were obtained from a solution of **L-8** in diethyl ether at −20 °C.*

The bond angles between the two sp³ carbons (C6 and C18) and their respective binding partners are slightly distorted from the tetrahedral angle of 109.5°. However, when compared to **L-1**, no significant differences are noted (Table 13): both in **L-1** and **L-8** bond angles deviate ~2° from 109.5°. The largest difference from this tetrahedral bond angle is observed for the angle of the methyl groups in **L-8** at 106.6° and 106.0° for the phenyl and pyridyl side, respectively.

*Table 13. Comparison of bond angles in crystals of **L-1** and **L-8**.*

L-8 Phenyl Side		L-8 Pyridyl Side		L-1 -	
C1-C6-C7	110.8°	C5-C18-C24	111.9°	C1-C6-C7	110.0°
C1-C6-C13	110.0°	C5-C18-C19	109.7°	C1-C6-C12	108.0°
C1-C6-C29	106.6°	C5-C18-C30	106.0°	C1-C6-C28	110.9°
C7-C6-C13	108.0°	C24-C18-C19	107.1°	C7-C6-C12	111.9°
C7-C6-C29	111.4°	C24-C18-C30	111.4°	C7-C6-C28	110.1°

Upon addition of Fe(mecn)₂(OTf)₂ to an acetonitrile solution of **L-8**, the color of the solution turned from yellow to a light brown, instead of the dark red that is usually observed for Py₅Me₂-X ligands (refer to chapters 0 and V.3). LR-MS analysis of the obtained solution shows a signal at 647 m/z, a corresponding tentative structure is shown in Scheme 93.
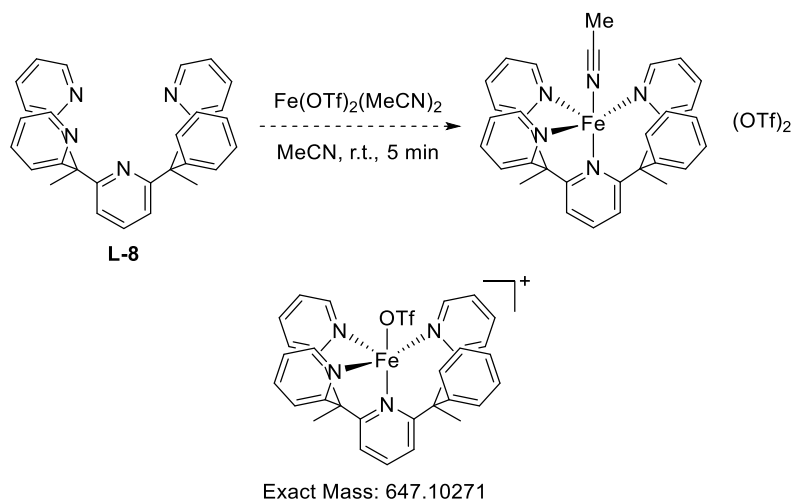
*Scheme 93: Reaction of **L-8** with iron(II) triflate according to a modified literature procedure.[12] A tentative structure for the observed LR-MS signal is shown.*

Unfortunately, diffusion of diethyl ether into the reaction solution did not yield any crystals but an oily, dark brown substance that did not yield usable ^1H NMR spectra. This is likely the result of oxidation of the iron(II) central ion, *vide infra* for details.
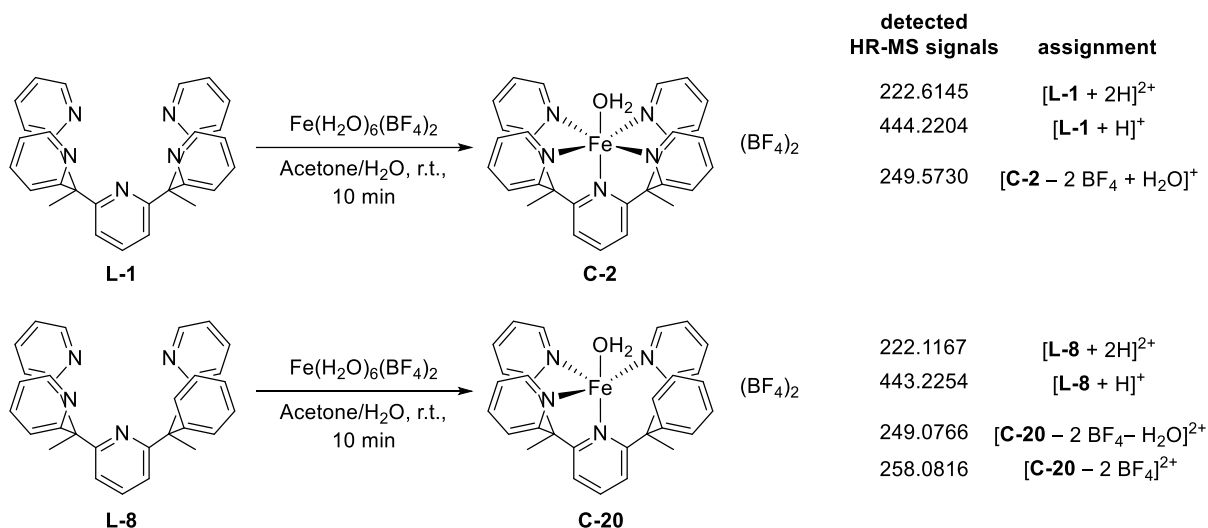
*Figure 123: Reaction of **L-1** or **L-8** with Fe(H₂O)₆(BF₄)₂ in acetone/water at room temperature and subsequent high resolution mass spectrometric analysis. HR-MS measurements of **C-2** and **C-20** were performed by Laura Senft of the Ivanović-Burmazović group at LMU Munich.*

Use of $Fe^{II}(H_2O)_6(BF_4)_2$ rather than $Fe(mecn)_2(OTf)_2$ resulted in the formation of a green compound that shows similar UV-vis and high-resolution mass spectra (compare the signals assigned to $[C\text{-}X - 2\ BF_4 - H_2O]^+$ with X = **2**, **20** in Figure 123) to the corresponding **L-1** complex **C-2** ([Fe(**L-1**)(OH₂)](BF₄)₂), which has been described in the literature and was synthesized as reference (for synthetic details refer to p. 262).[12] The tentative structure of **C-22** shown in Figure 123 for **C-20** was then confirmed by x-ray crystallography (Figure 125), which shows the formation of a dimer of $[Fe^{II}(\textbf{L-8})(OH_2)]^{2+}$ and $[Fe^{II}(\textbf{L-8})(F)]^{2+}$. Elemental analysis also shows a composition that corresponds to the dimer structure with two co-crystallized water molecules (not shown, refer to experimental section p. 309).
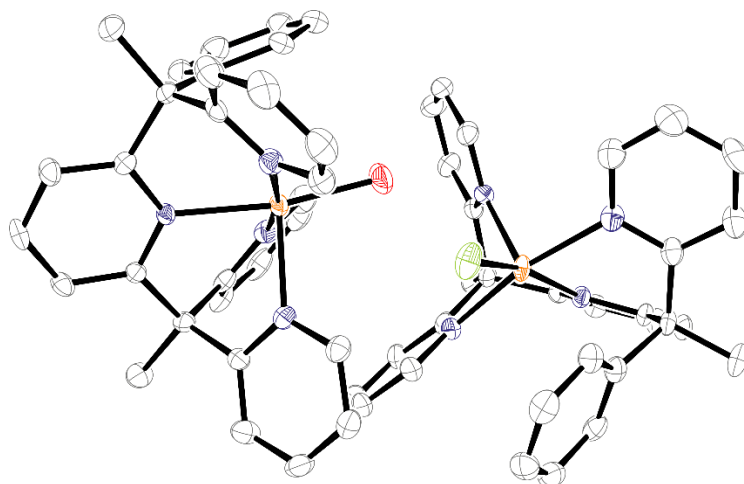
*Figure 124: Graphical representation of the crystal structure of **C-22** [Fe^{II}(**L-8**)(F)][Fe^{II}(**L-8**)(OH$_2$)]$^{3+}$. Ellipsoids are drawn at 50% probability; hydrogen atoms, counterions and co-crystalized solvent molecules have been omitted for clarity, refer to the appendix p. 511 for a complete structure and crystallographic details. Crystals were obtained from slow diffusion of diethyl ether into a solution of **C-22** in acetone/water at room temperature.*

The fluoride ligand is most probably the result of hydrolysis of the tetrafluoroborate ion, a commonly observed side reaction of tetrafluoroborate in water. A separate crystallization attempt resulted in exchange of the fluoride ion for OH⁻ [Fe^{II}(**L-8**)(OH)][Fe^{II}(**L-8**)(OH$_2$)]$^{3+}$, however, these crystals were of low quality and unsuitable for a complete analysis.
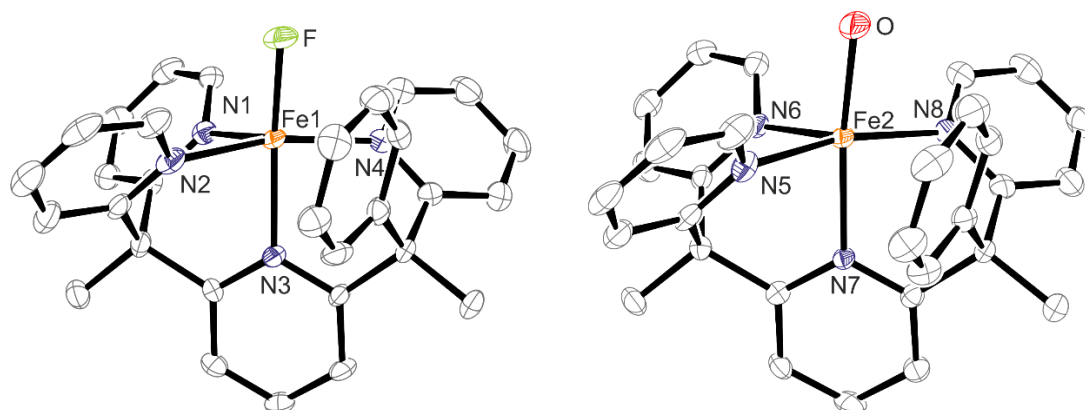
*Figure 125: Graphical representation of the crystal structure of **C-22** [Fe^{II}(**L-8**)(OH$_2$)]$^{2+}$ and [Fe^{II}(**L-8**)(F)]$^{2+}$. Ellipsoids are drawn at 50% probability; hydrogen atoms, counterions and co-crystalized solvent molecules have been omitted for clarity, refer to the appendix p. 511 for a complete structure and crystallographic details. Crystals were obtained from slow diffusion of diethyl ether into a solution of **C-22** in acetone/water at room temperature.*

The bond angles in the crystal structure are similar for both monomers: the geometry is that of a distorted octahedron that is missing a corner where the phenyl group is situated, resulting in a tetragonal pyramidal coordination geometry. Both the fluoride and the water ligand coordinated to the iron center are tilted towards this unoccupied coordination site (Table 14, Figure 125), as are the two neighboring pyridine units in the equatorial plane. This geometry is unsurprising, as the ligand enforces it, but still remarkable as the iron is only five-coordinate in a pseudo-octahedral coordination sphere.

When compared to the corresponding cation in **C-2**, [Fe^{II}(OH$_2$)(**L-1**)]$^{2+}$, significant differences can be noted: the angle between the axial pyridine and the water/fluoride ligand is distorted in the

case of **C-22** (169° or 167° compared to 180° in **C-2**) as well as the angle between two equatorial pyridines on opposite sites of the iron central ion (N2-Fe-N4 for X = F⁻ and N5-Fe2-N8 for X = OH_2 in **C-22**, N1-Fe-N1' in **C-2**).

The Fe-O bond length in **C-2** is 2.007 Å, in **C-22** it is very similar at 2.000 Å. The Fe-F bond length was measured at 1.897 Å.

Table 14. Bond angles in the two monomers of **C-22** compared to **C-2** (refer to Figure 125 for labelling of **C-22** and the appendix p. 388 for labelling of **C-2**).

C-22 X = F⁻		C-22 X = OH_2		C-2	
F-Fe-N1	104.7°	O-Fe2-N5	95.6°	O-Fe-N1	88°
F-Fe-N2	93.2°	O-Fe2-N6	102.0°	O-Fe-N2	91.6°
F-Fe-N4	96.2°	O-Fe2-N8	92.5°	-	-
F-Fe-N3	167.1°	O-Fe2-N7	169.9°	O-Fe-N3	180.0°
N1-Fe-N2	84.0°	N5-Fe2-N6	83.7°	N1-Fe-N2	83.4°
N1-Fe-N4	100.8°	N6-Fe2-N8	103.3°	N1-Fe-N2'	96.7°
N2-Fe-N4	167.8°	N5-Fe2-N8	167.8°	N1-Fe-N1'	176°
N1-Fe-N3	87.1	N5-Fe2-N7	84.2°	N1-Fe-N3	92.0°
N2-Fe-N3	83.2	N6-Fe2-N7	87.9°	N2-Fe-N3	88.3°
N4-Fe-N3	85.8	N7-Fe2-N8	86.1°	-	-

This structural description becomes even more obvious when a top view is chosen (Figure 126), the three remaining pyridine donors in the former equatorial plane form a t-shape, not an equilateral triangle. The distance from the center of the phenyl ring to the iron center is around 3.2 Å, whereas the distance from the closest C-C bond in the phenyl ring to the iron atom is approximately 2.63 Å. This short distance might suggest a coordinative bond between the C-C bond and the iron center, however, such a bond should have an impact on the geometry of the phenyl ring. As the ring is not distorted and all bond lengths and angles are similar, an η^2/ η^6-bond of two or all of the carbon atoms, respectively, in the phenyl ring to the iron center seems unlikely.
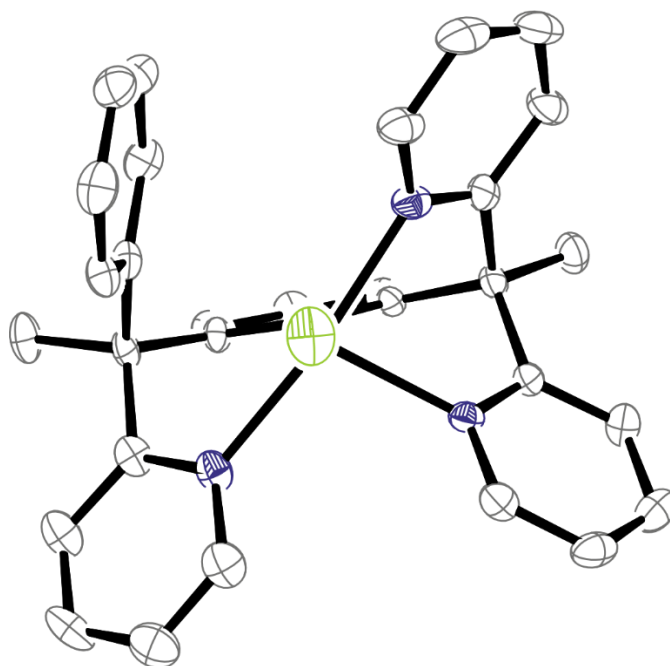
*Figure 126: Top view of one of the monomers in **C-22** ([Fe^{II}(**L-8**)(F)]$^{2+}$). Ellipsoids are drawn at 50% probability; hydrogen atoms, counterions and co-crystalized solvent molecules have been omitted for clarity, refer to the appendix p. 511 for a complete structure and crystallographic details. Crystals were obtained from slow diffusion of diethyl ether into a solution of **C-22** in acetone/water at room temperature.*

The UV/Vis spectrum of **C-2** shows a strong absorption between λ = 300-510 nm with a maximum at λ = 450 nm (ε = 4300 l mol^{-1} cm^{-1}). The doublet fine structure at λ = 365-370 nm is an artifact produced by the instrument (Agilent 8453 Diode Array). In the spectrum of **C-22** a much weaker absorption feature is observed at λ = 450 nm (ε = 1800 l mol^{-1} cm^{-1}).
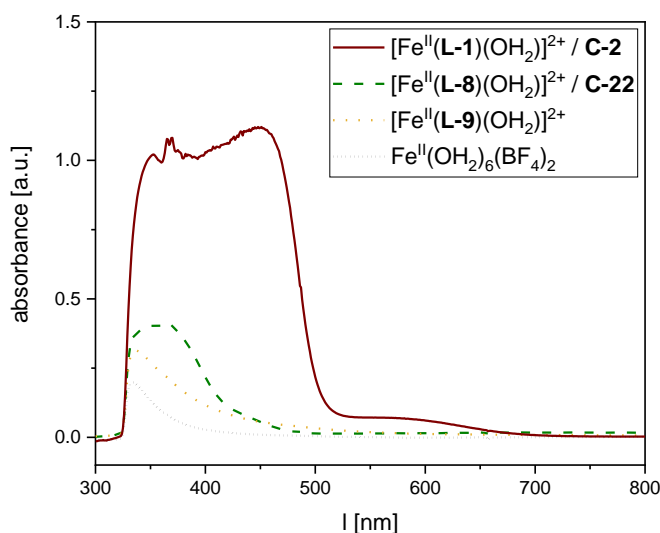
*Figure 127: Excerpts of UV-vis spectra of **C-2**, **C-22**, a mixture of **L-9** and Fe^{II}(H$_2$O)$_6$(BF$_4$)$_2$, and Fe^{II}(H$_2$O)$_6$(BF$_4$)$_2$ as reference. Full spectra can be found in the appendix p. 387.*

Ligand **L-9** was also reacted with Fe^{II}(H$_2$O)$_6$(BF$_4$)$_2$ (not shown) and the obtained solution analyzed using UV-vis spectroscopy (Figure 127) and HR-MS. The observed absorption is even lower (ε = 1225 l mol^{-1} cm^{-1}), even more blue-shifted (λ = 340 nm).

Oxidation of **C-22** using cerium(IV) ammonium nitrate was also attempted (Scheme 94), in contrast to the literature procedure pure water was chosen as solvent, due to the experiences during the immobilization project (refer to chapter V.3).

	calculated m/2 for [V-X]²⁺	257.5767	257.0728
	detected HR-MS signals	257.5752	257.0737
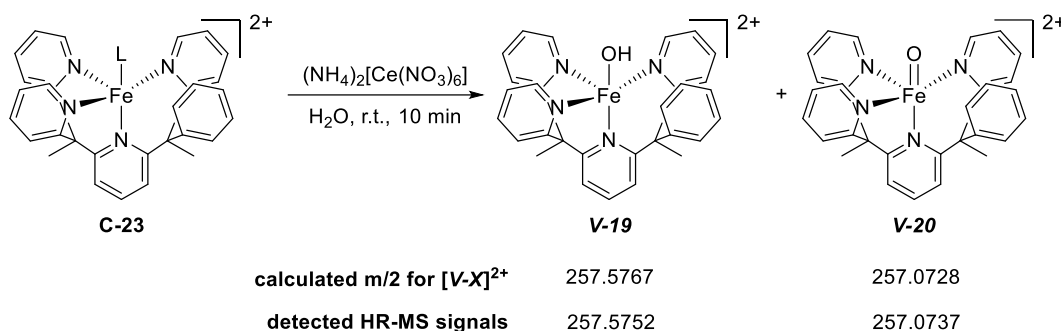
*Scheme 94: Oxidation attempt of **C-22** using cerium(IV) ammonium nitrate to the corresponding iron(III)-hydroxido and iron(IV)-oxido species **V-19** and **V-20**, respectively. HR-MS measurements were performed by Laura Senft of the Ivanović-Burmazović group at LMU Munich.*

HR-MS analysis of the reaction mixture did indeed indicate the formation of the desired iron(IV)-oxido species **V-20**. In addition, the formation of the corresponding iron(III)-hydroxido species **V-19** was also observed. Both assignments were corroborated by analysis of the isotope distribution pattern in HR-MS (Figure 128).
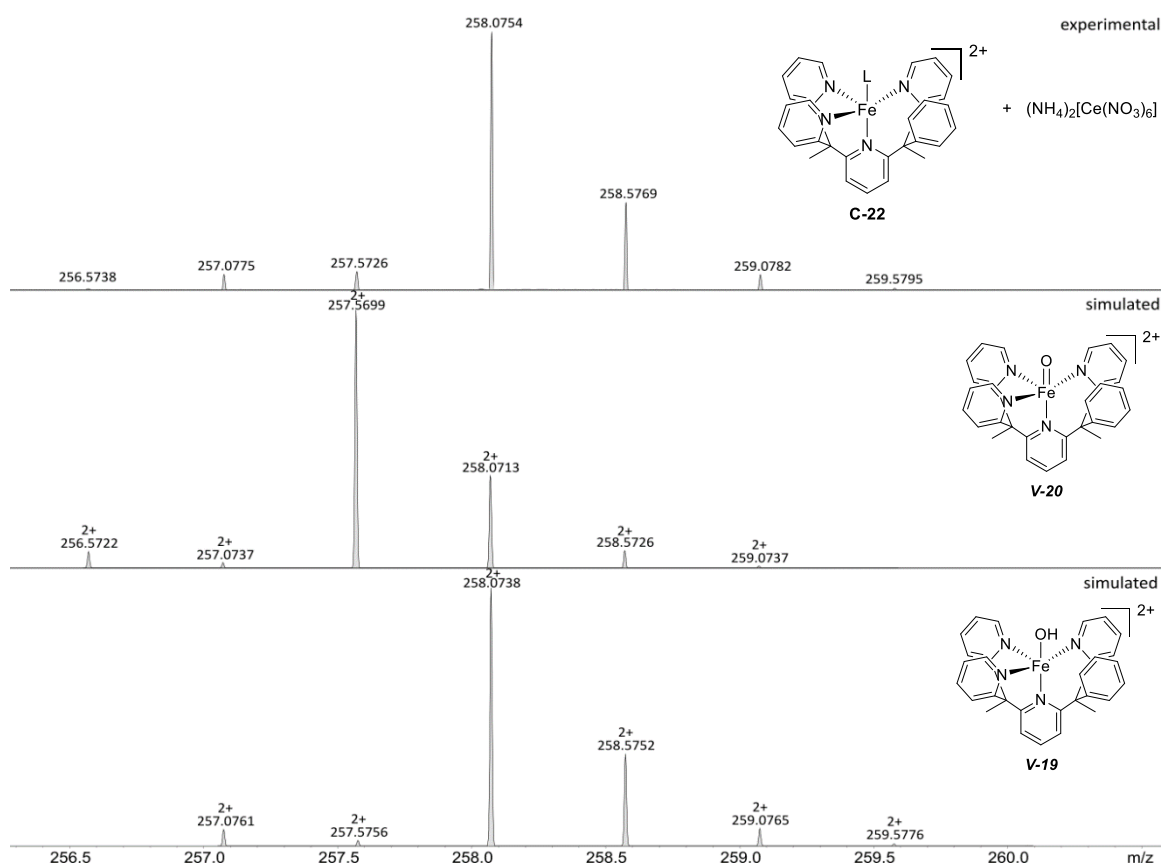
*Figure 128: HR-MS measurement of the oxidation reaction of **C-22** with 3 equiv. of cerium(IV) ammonium nitrate (upper spectrum). Calculated isotope distribution patterns for **V-20** and **V-19**, middle and lower spectrum, respectively. HR-MS measurements were performed by Laura Senft of the Ivanović-Burmazović group at LMU Munich.*

Unfortunately, attempts to isolate **V-19** or **V-20** have proven unsuccessful as of yet. Further investigations, such as changing the solvent to pure acetonitrile and lowering of the reaction temperature or the *in situ* generation of **V-19** or **V-20** and subsequent reaction with a suitable substrate, are necessary to complete the picture of this newly synthesized iron(IV)-oxido species.

7. Q$_4$Me$_2$H – Combining Py$_5$Me$_2$H and TQA into One Ligand

The following chapter describes the attempts to synthesize an iron(IV)-oxido complex that more closely resembles the electronic properties of iron(II)/α-KG dependent enzymes, i.e. the spin state of S = 2.

Synthesis Attempts of Q$_4$Me$_2$H

As shown in Figure 129, the proposed ligand Q$_4$PyMe$_2$H represents a combination of two existing ligands: Py$_5$Me$_2$H (**L-1**) and TQA (tris(2-quinolylmethyl)amine). In this work, the corresponding iron(IV)-oxido complex to **L-1** (**C-6**, previously described by Chantarojsiri *et al.*) has been successfully used as a <u>functional</u> model for TET, a member of the iron(II)/α-KG dependent enzyme superfamily. On the other hand, the iron(IV)-oxido complex [Fe^{IV}(O)(mecn)(TQA)]$^{2+}$ first synthesized by Que *et al.*, represents a very good <u>electronic</u> model for iron(II)/α-KG enzymes (e.g. TauD), as it exists in the same spin state (quintet, S = 2).[79]
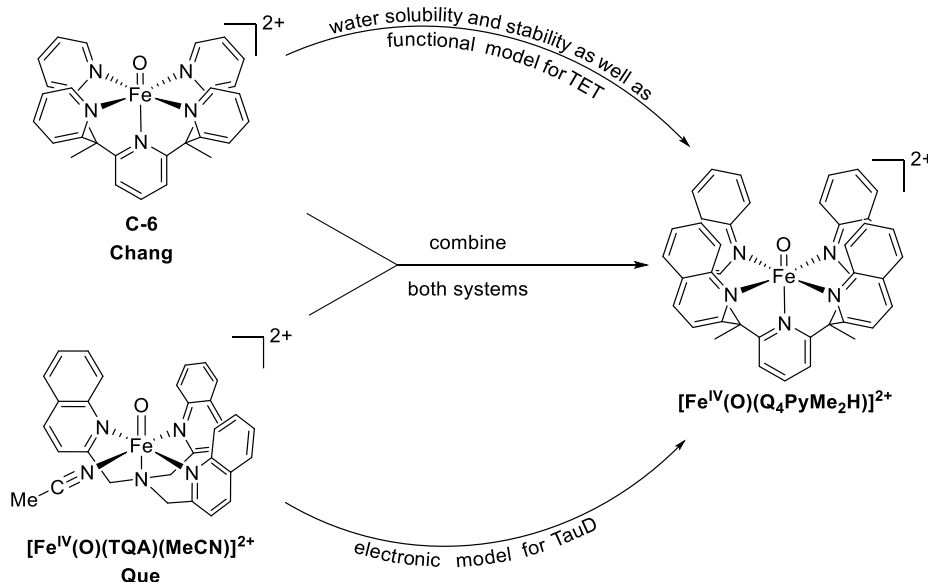
Figure 129: Combination of two literature-known iron(IV)-oxido ligand systems into a new ligand design.[12,13,79]

Despite the preliminary work of Chantarojsiri *et al.* and the advances in the understanding of the interaction of **C-6** with organic substrates, certain aspects of this functional model complex remain unclear or need to be refined. As described in chapter IV.3, a comproportionation reaction of **C-6** and **C-2** occurs under the reaction conditions of **C-6** with organic substrates. Also, a (slow) decomposition process of the iron(IV)-oxido complex in aqueous solution was observed (0). A combination of the ligand systems **L-1** and TQA could shed more light on the mechanism involved in iron(IV)-oxido mediated C-H activation and might also give insight into the comproportionation and decomposition reactions observed for **C-6**.

Additionally, the steric demand of the quinolyl residues on the proposed Q$_4$PyMe$_2$H ligand might prevent **5hmC** and **5fC** from reaching the active iron(IV)-oxido moiety, thus reducing the

reactivity of the iron(IV)-oxido complex to specifically hydroxylate only **5mC**. This could provide a valuable tool for sequencing DNA that contains **5mdC** and its oxidized derivatives (refer to chapters III.1 and 0 for details).

Scheme 95 shows the performed syntheses from commercially available starting material 2-chloroquinoline to intermediate **V-22**. The synthesis of **V-21** was reported by Patel *et al.* in 1987.
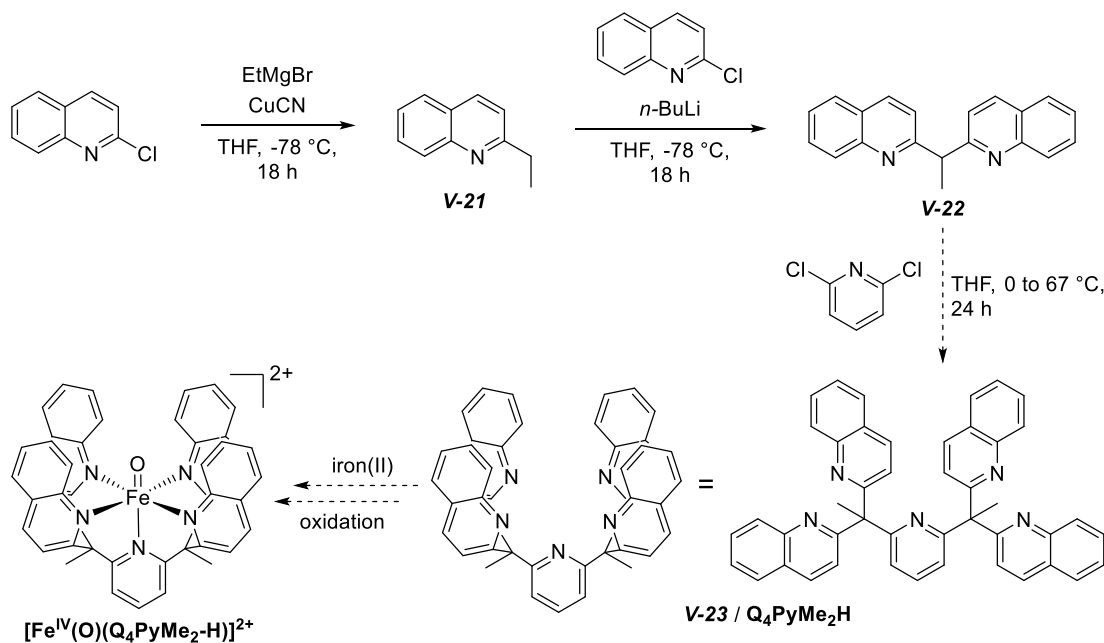
Scheme 95: Performed (solid) and attempted (dashed) syntheses in order to obtain [Fe^{IV}(O)(Q₄PyMe₂H)]$^{2+}$.

Intermediate **V-21** was indeed obtained, however, the yields were far lower than previously reported (25% vs. 50%). **V-21** was then reacted with *n*-butyl lithium and 2-chloroquinoline was added subsequently. LR-MS monitoring of the reaction solution indicated the formation of **V-22**, however, the thrice-substituted side product was detected in significant amounts. Additionally, a signal at 539.28 m/z was detected, which could correspond to the four times substituted side product. As optimization of the reaction conditions was not successful, a palladium-catalyzed cross-coupling (Negishi) reaction was tested, but also to no avail. Despite several attempts, the use of two different palladium pre-catalysts (Pd(dppf)Cl₂ and Pd(PPh₃)₂Cl₂), identification of the product in the reaction mixture using LC-MS, the product could not be isolated in pure form.
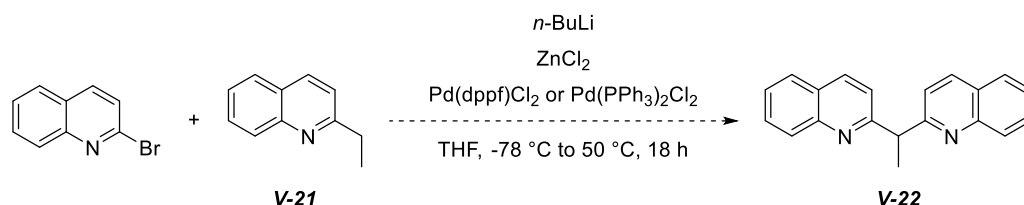
*Scheme 96: Attempted synthsis of **V-22** from **V-21** and 2-bromoquinoline* via *a Negishi cross-coupling reaction.*

VI. Elucidating the Mechanism of Action of HPDL

1. Introduction and State of the Art

Hydroxyphenyl Pyruvate Dioxygenase Like (HPDL) Enzyme

In 2020-2021 three publications linked the *HPDL* gene to hereditary neurodegenerative diseases. In particular, bi-allelic variants of *HPDL* were found in patients suffering from hereditary spastic paraplegia (HSP), a group of 80 different types of disorders, that can involve a wide range of molecular and metabolic aetiologies including metabolic dysfunction, myelin abnormalities, and organellar dysfunction that can affect the endoplasmic, lysosomes, and mitochondria.[9–11,306–309]

HPDL is a single-exon 1.8 kb gene located on chromosome 1p34.1 and is expressed as one transcript. The resulting 371 amino acid long protein, HPDL, is suspected of binding iron(II) as well as of dioxygenase activity, due to its structural similarities to 4-hydroxyphenyl pyruvate dioxygenase (HPPD) and hydroxymandelate synthase (HMAS). The amino-terminal domain is suspected in aiding in dimerization of the protein.[11] The *HPPD* gene, encoding for HPPD, is linked to two diseases which result in neurological symptoms as well as the accumulation of tyrosine in bodily fluids coupled with massive excretion of tyrosine derivatives 4-hydrophenyl pyruvic acid (**4-HPP**, substrate of HPPD), 4-hydroxyphenyl lactic acid (4-HPLA, reduced form of **4-HPP**), and 4-hydroxyphenyl acetic acid (**4-HPA**, intermediate in HPPD metabolism).[310,311] However, Wiessner *et al.* did not find abnormal tyrosine or tyrosine metabolite levels in blood, urine, and sometimes spinal fluid of all 34 patients with biallelic HPDL variants (except for one case of borderline high **4-HPA**). The authors therefore concluded that HPDL likely catalyzes a different reaction but may have dioxygenase activity.[11]

In silico calculations by Wiessner *et al.* predicted HPDL to possess a mitochondrial targeting signal. Indeed, separation of cellular compartments from HeLa (human cervical carcinoma, named after the patient Henrietta Lacks) cells showed endogenous HPDL in the mitochondrial fraction. Subfractionation and proteinase K treatment indicated that HPDL is located in the outer mitochondrial membrane, which is consistent with the aforementioned calculations.[11]

These results sparked the investigations described herein, as until recently no substrate of HPDL or information on its involvement in any biosynthetic pathway was known. However, a recent publication by Banh *et al.* shed some initial light and is discussed in the following.[312]

Mechanism of Action

In humans, tyrosine is transformed into 4-hydroxyphenyl pyruvate (**4-HPP**) by tyrosine transaminase (also known as tyrosine aminotransferase).[313] **4-HPP** then serves as an activator for the iron(II)/α-keto acid dependent enzymes HPPD (found in humans and bacteria) and HMAS (found only in bacteria) by aiding in the oxidation of the iron(II) center to its active iron(IV)-oxido species (refer to chapter I and Scheme 97**B**). In this initial catalytic step 4-hydrophenyl

195

acetate (**4-HPA**) is formed, which is then further transformed to homogentisate (**HG**) in the case of HPPD or *S*-hydroxymandelic acid (**S-HMA**) in the case of HMAS (refer to chapter I for details).[314–316]
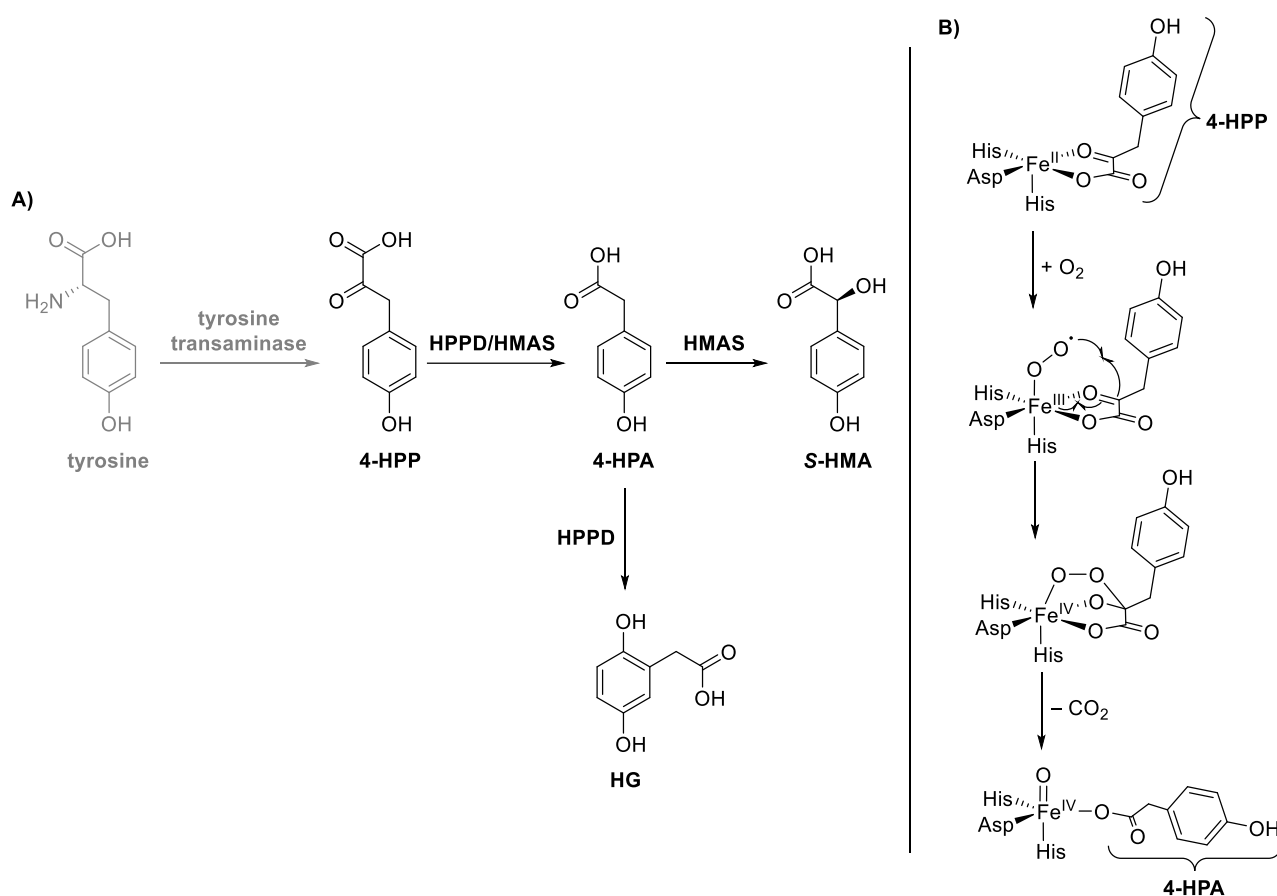
Scheme 97: **A**) *Excerpt of the tyrosine catabolism pathway including the suspected 4-hydroxyphenylpyruvate dioxygenase (HPPD) and hydroxymandelate synthase (HMAS) pathways.*[317–319] **B**) *Activation of the iron(II) center in HPPD or HMAS by* **4-HPP** *yielding* **4-HPA** *and an iron(IV)-oxido species.*

Following up on the genetic studies mentioned above, that did localize HPDL and identify its general dioxygenase function, Banh *et al.* identified **S-HMA** as a product of tyrosine metabolism by using ^{18}O and ^{13}C isotope labels. The authors also mention that a comparison of HPDL, HPPD, and HMAS on protein and cDNA level revealed that the two human enzymes HPPD and HPDL show 80% sequence similarity to HMAS,[312], however, only ~20-30% of the amino acid sequences are homologous.

As mentioned above, HPPD produces **HG** but not **S-HMA**. However, site directed mutagenesis in the sequence of HPPD at the active site (F337V or F337I) led to significant production of **S-HMA**.[318,319] A similar observation by Ali *et al.* revealed the importance of a handful of critical amino acids forming substrate specific contacts in the active site reaction chamber, when performing a computational study on the iron(II)/α-KG dependent enzymes OrfP and VioC. Both enzymes are known to hydroxylate arginine, but whereas VioC yields monohydroxylated hydroxyarginine, OrfP yields 3*R*,4*R*-dihydroxoarginine. The authors attributed the differential

activity to small changes in the amino acid residues lining the active site cavity.[320,321] Protein sequence alignment by Banh *et al.* showed that HPDL possesses an isoleucine residue at what would correspond to the 337 position in HPPD, which is the exact position where mutation in HPPD to isoleucine led to **S-HMA** production. This makes **S-HMA** a likely product of HPDL catalysis.[312]

The authors also identified Coenzyme Q10 (CoQ10, an essential part of the electron transport chain in mitochondria) as a possible product of this non-canonical tyrosine catabolism under involvement of HPDL (Scheme 98). However, it was also found that CoQ10 biosynthesis is only impaired under specific culture conditions – indicating the presence of a secondary pathway.[312]
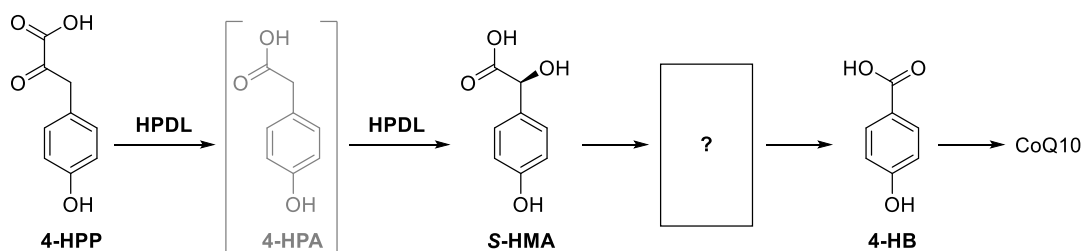
*Scheme 98: Transformation of **4-HPP** to **S-HMA** by HPDL, subsequent proposed conversion to **4-HB** and CoenzymeQ10 (CoQ10). **4-HPA**, the intermediate in the HPPD and HMAS catalytic pathways, is proposed as an intermediate here as well.[312]*

CoQ10 is proposed to be synthesized from 4-hydroxybenzoic acid (**4-HB**) which in turn is suspected to be formed from 4-hydroxybenzaldehyde (**4-HBz**) by an aldehyde dehydrogenase (Aldehyde Dehydrogenase 3 Family Member A1 - ALDH3A1, Scheme 98).[322]

HPPD also occurs in plants and is known to play a part in biosynthesis of plastoquinone. Plastoquinone plays an important role in the electron transport chain through the thylakoid, allowing plants and cyanobacteria to convert water into oxygen through the action of photosystem II.[323]
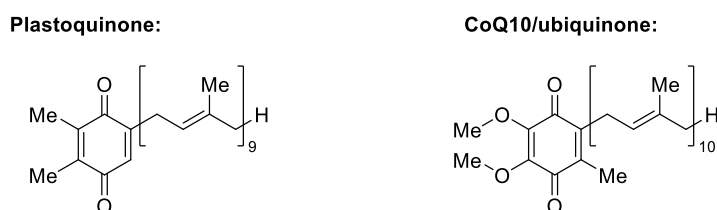
Figure 130: Structures of plastoquinone and CoQ10/ubiquinone.

Even though plastoquinone and CoQ10 share a lot of structural and functional similarities, to date no connection between the function of HPPD and HPDL has been proposed – they are usually just linked due to their structural similarities. However, the mentioned observations warrant more detailed investigations into the role of HPDL in the biosynthesis of CoQ10.
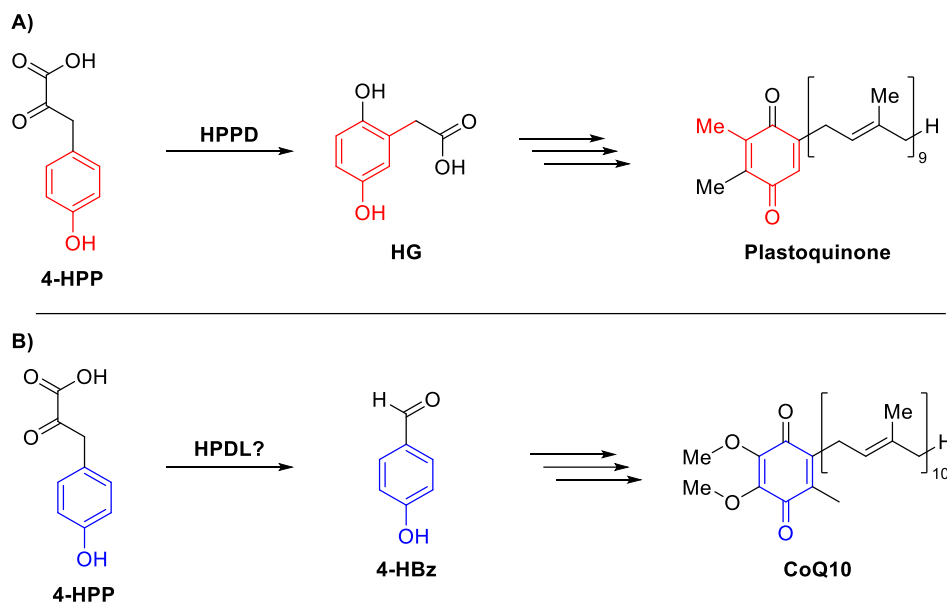
*Scheme 99: **A)** Involvement of HPPD in the biosynthesis of plastoquinone, retained structures are highlighted in red. **B)** Postulated role of HPDL in the biosynthesis of CoQ10, possibly retained structures are highlighted in blue.[324]*

In 2010, Paine *et al.* proposed a mechanism relying on a bridged peroxido species for the C-C bond cleavage in mandelate by an iron-based functional model complex. This bioinorganic work was inspired by the previously proposed mechanism for the enzyme CloR, which plays a role in the biosynthesis of the natural antibiotic clorobiocin. In this pathway, a derivative of **4-HPP**, 3-dimethylallyl-4-hydroxyphenylpyruvate (**3-DMA-4-HPP**), is converted to the the corresponding benzoic acid derivative 3-dimethylallyl-4-hydroxybenzoic acid (**3-DMA-4-HB**) in a two-step sequence *via* 3-dimethylallyl-4-hydroxymandelic acid (**3-DMA-4-HMA**) (Figure 131**A**).[325]

Paine *et al.* synthesized an iron(II) complex based on the ligand 6-Me$_3$-TPA (TPA = tris-pyridylamine) and a simplified substrate: mandelate ((Figure 131**A**, structure **I**). Upon exposure of this complex to molecular dioxygen, one of the pyridyl donors dissociates from the metal center to allow for the coordination of dioxygen resulting in the superoxide **II**. Hydrogen atom transfer (HAT) yields the hydroperoxido species **III**. Then, rearrangement either yields the keto-derived structure **IV** which is attacked by the hydroperoxido moiety or this hydroperoxido moiety directly attacks the carbon centered radical in **III**. In either pathay, the bridged peroxido species **V** is formed which subsequently decarboxylates to give the product **VI**.[326]

This mechanism provides a good basis for further investigations of the C-C bond cleavage in α-keto acids such as **S-HMA** in the context of the proposed mechanism of HPDL.
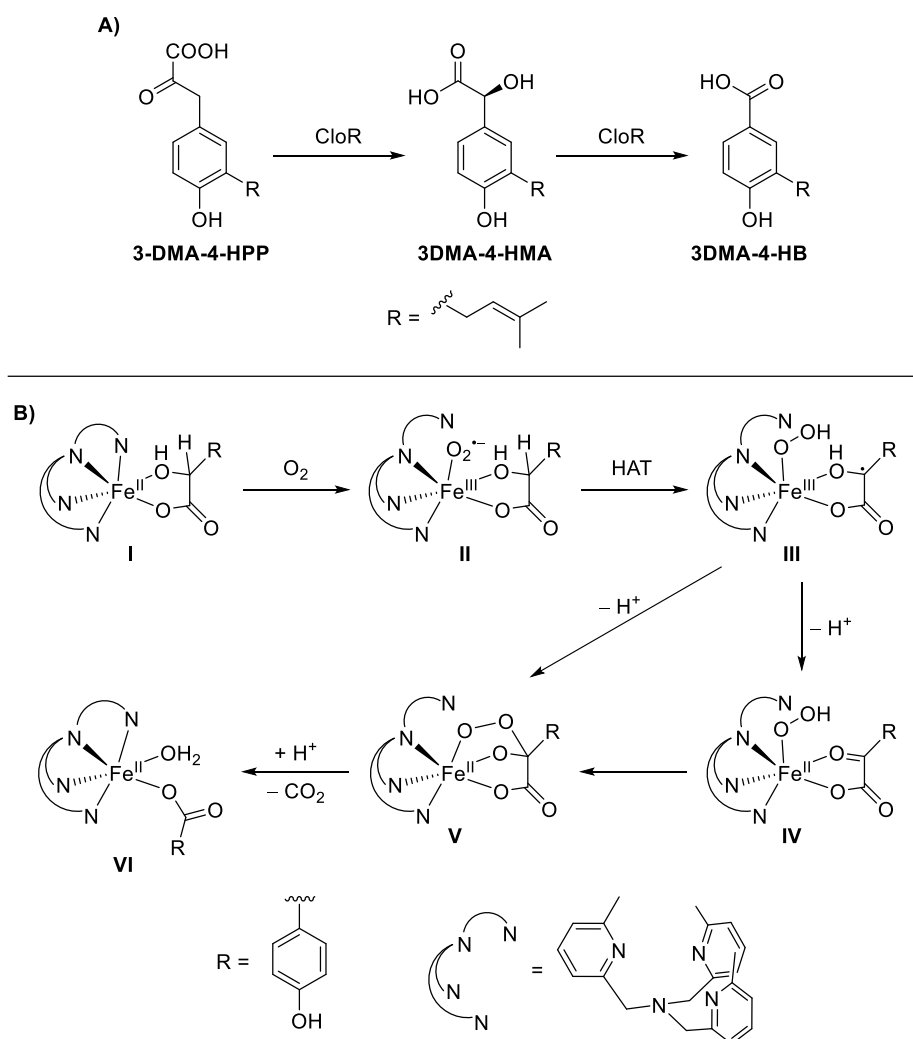
Figure 131: *A) Proposed mechanism of CloR. B) Reported C-C bond cleavage mechanism of [Fe^{II}(6-Me$_3$-TPA)(mandelate]$^{2+}$ upon exposure to oxygen.*[326]

2. Motivation and Aim

Biallelic variations in the *HPDL* gene were associated with neurodegenerative diseases. The corresponding protein HPDL shows structural similarity to HPPD and HMAS and is likely involved in the biosynthesis of CoQ10, an important part of the electron transport chain in mitochondria.[9–11] Also, **4-HPP** was recently identified as its substrate and **S-HMA** as a product and/or intermediate (Scheme 100).[312]
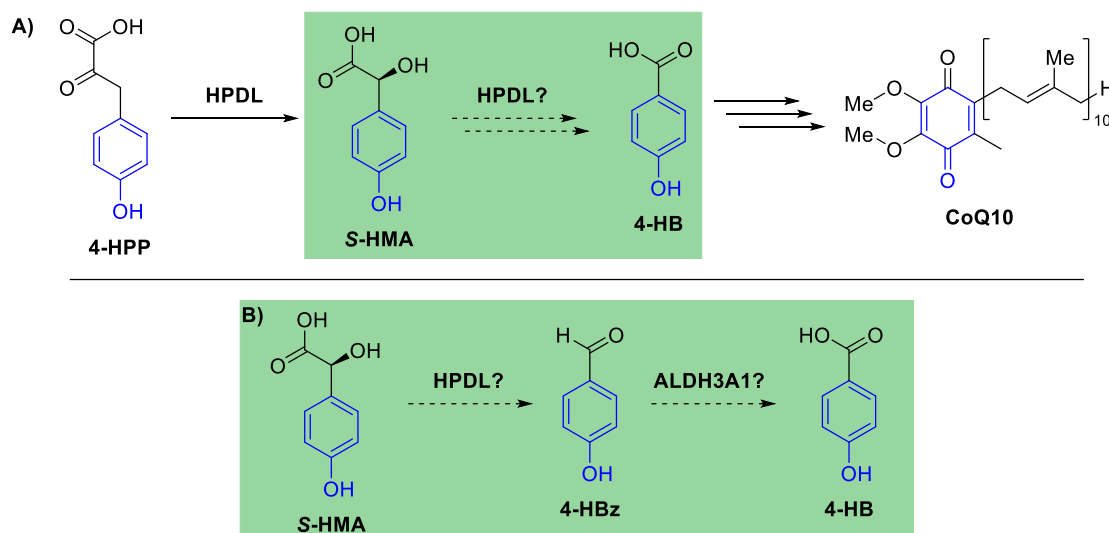
*Scheme 100: **A)** Postulated HPDL involvement in the biosynthesis of CoQ10: transformation of **4-HPP** to **S-HMA** and proposed reaction to CoQ10. **B)** Proposed HPDL-mediated formation of **4-HBz** from **S-HMA** followed by aldehyde oxidation by ALDH3A1 (most relevantsteps are marked with a green box). ALDH3A1 = Aldehyde Dehydrogenase 3 Family Member A1.[312]*

However, the intermittent steps from **S-HMA** to **4-HB** still remain elusive. Possibly, **4-HBz** is formed as an intermediate and subsequently converted to **4-HB**, the known precursor of CoQ10.[312] The method applied by Banh *et al.* would not reveal an ^{18}O label in **4-HBz**, as it likely forms a hydrate in water, diluting the ^{18}O label (Scheme 101).
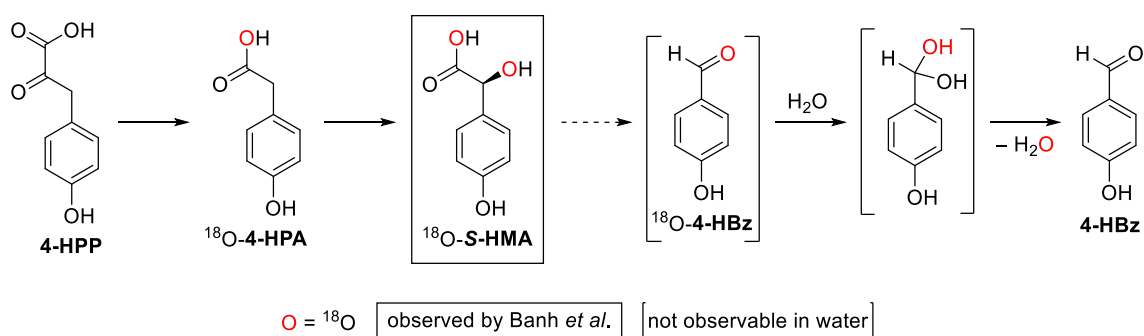
*Scheme 101: Reaction of **4-HPP** to ^{18}O-**4-HPA** and ^{18}O-**S-HMA** as postulated by Banh et al. If ^{18}O-**4-HBz** forms from ^{18}O-**4-HMA**, the ^{18}O label is diluted by reaction of the aldehyde with water (i.e. hydrate formation).[312]*

The goal of this work was the elucidation of the involvement of HPDL in the biosynthesis pathway of CoQ10. Particular focus was set on the identification of 4-HBz as product. This was to be achieved by investigation of the reaction mechanism by means of A) metabolomics and B) functional model complex studies involving iron(IV)-oxido (C-6) and iron(III)-hydroxido (C-4) complexes.

200

3. Metabolomics

The first step in the analysis of biological HPDL samples was the search of an analytical method suitable for the identification and quantification of the (suspected) HPDL substrates, intermediates, and products (in the following referred to as "HPDL metabolites". Subsequently, metabolomic analysis of samples obtained from *E. coli* cultures (with transformed *HPDL* wild-type and mutant constructs, for the exact sequences please refer to the appendix p. 390f) as well as mammalian cells was performed.
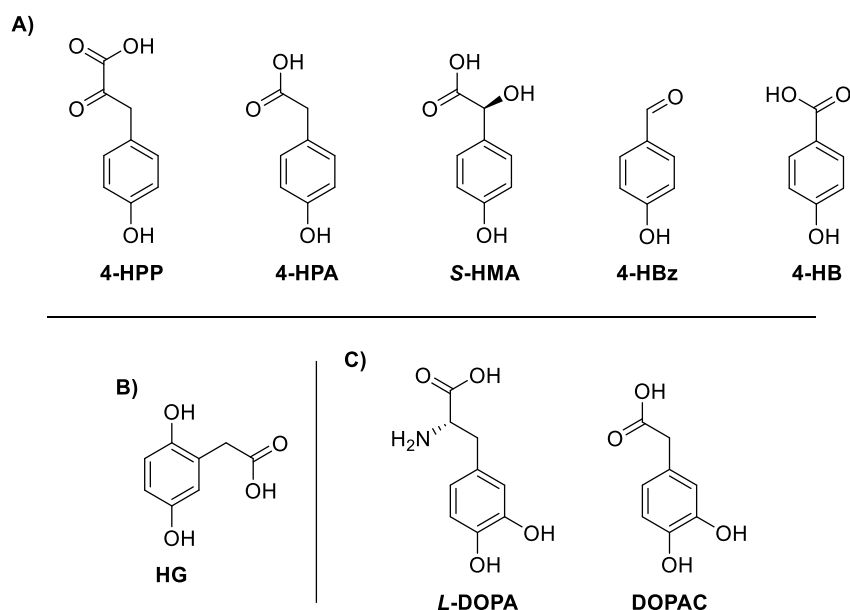
*Chart 17: Summary of **A**) HPDL metabolites **B**) HPPD products and **C**) internal standards in stability and extraction tests as well as biological sample analysis. L-DOPA = L-3,4-dihydroxyphenylalanine, DOPAC = 3,4-dihydroxyphenylacetic acid.*

Internal standards were only used in derivatization studies and not in the study of biological samples, here absolute quantification was chosen as the preferred method (*vide infra*). **S-HMA** is formed in nature as a pure enantiomer, however, a racemic mixture of both **S**- and **R-HMA** was used as reference sample in GC-MS and HPLC measurements. All preparations of biological samples were performed by Dr. Rolf Stucka at the Laboratory Molecular Myology at LMU Munich (Friedrich-Baur-Institute).

Identification of an Analytical Method to Measure HPDL Metabolites

A common method for the analysis of small molecules is GC-MS. In the case of HPDL metabolites derivatization using *N,O*-Bis(trimethylsilyl)trifluoroacetamide (BSTFA) is necessary prior to analysis due to decomposition of the compounds during injection/vaporization. Scheme 102 shows the derivatization of **4-HPA** as a representative example. In the following signals corresponding to a TMS-derivatized compound observed in GC-MS are simply referred to by the underivatized compound for reasons of clarity.
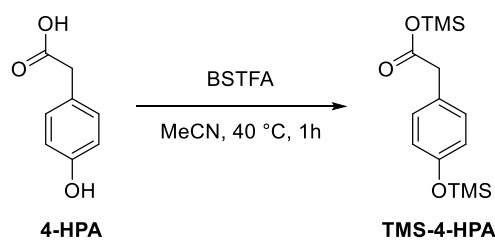
*Scheme 102: Derivatization of **4-HPA** to **TMS-4-HPA** using BSTFA in acetonitrile at 40 °C for 1 h. BSTFA = N,O-bis(trimethylsilyl)trifluoroacetamide.*

Several experiments were necessary to decrease the number of observed side reactions. Reducing the reaction temperature from 70 to 50 °C and shortening the reaction time from 35 min to 15 min lead to some improvement (Figure 132). However, still additional peaks were observed in the GC-MS traces, indicating side reactions.
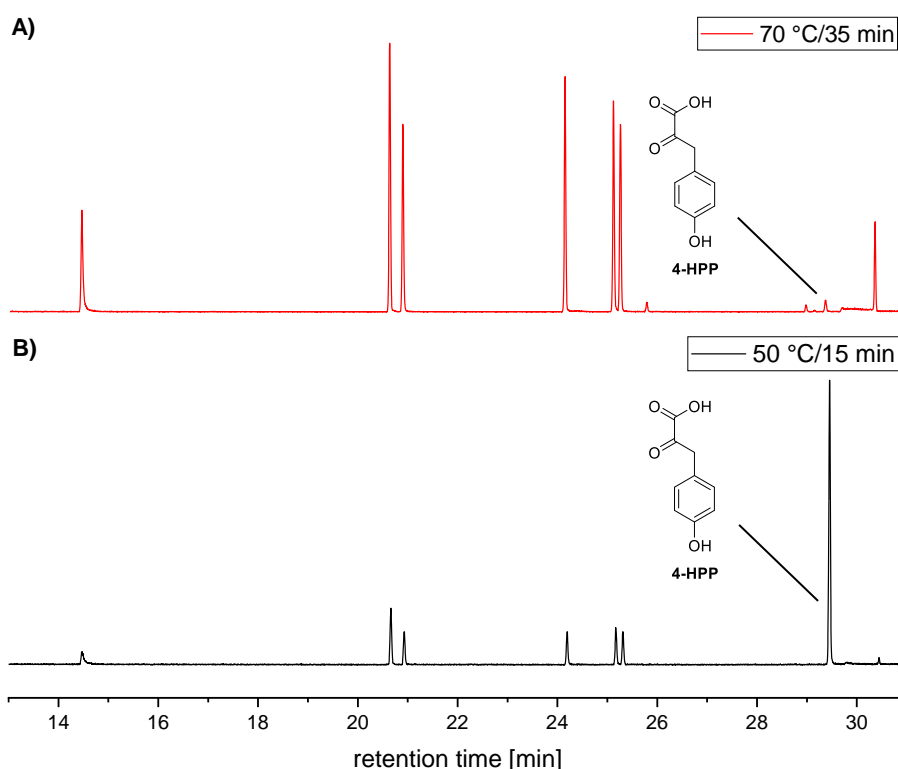
*Figure 132: Comparison of two conditions for derivatization: **A)** 35 min at 70 °C (red) **B)** 15 min at 50 °C (black). Only the signal corresponding to **4-HPP** is marked as it represents the largest difference between the spectra. For a complete assignment of all signals and full traces refer to the appendix p. 393. GC-MS method **C**.*

Derivatization at 40 °C for 1 h was found to lead to the least amount of decomposition of the HPDL metabolites and was therefore chosen as the standard procedure. In Figure 133 a GC-MS trace of the most relevant HPDL metabolites **4-HBz**, **4-HB**, **4-HPA**, and **4-HPP** is shown, collected EI-MS spectra can be found in the appendix p. 396-398.
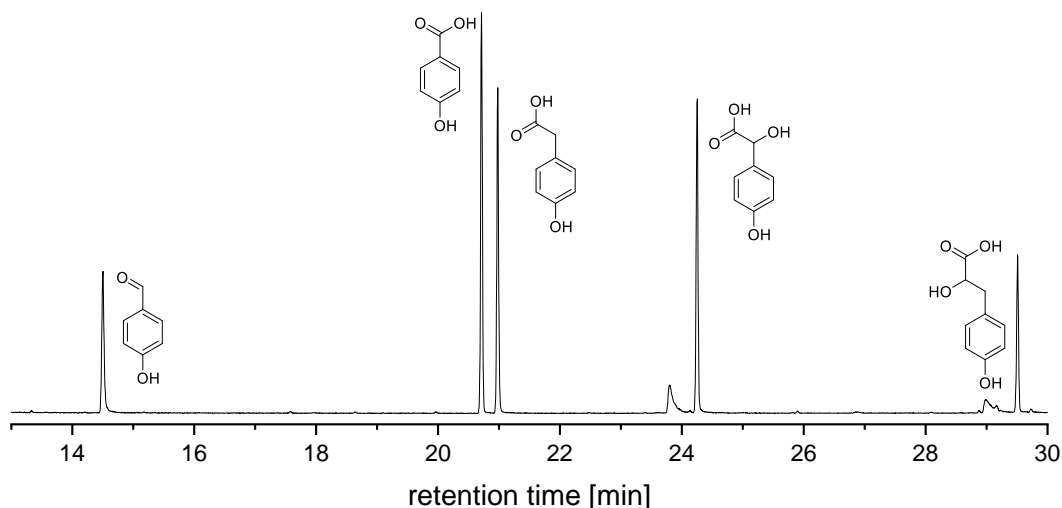
*Figure 133: Excerpt of a GC-MS trace of selected HPDL metabolites (from left to right): **4-HBz, 4-HB, 4-HPA, 4-HMA,** and **4-HPP**. GC-MS method **C**.*

As an alternative to GC-MS, HPLC was tested as a method for the separation of HPDL metabolites. However, in the conducted HPLC measurements the retention times of the peaks of the HPDL metabolites were much more sensitive to the contents of the injected solution than in the GC-MS measurements. For example, the retention time of **4-HPP** when injected with and without the other references changed from t_R = 19.4 min to t_R = 18.6 min, respectively). This means that no clear interpretations can be drawn from these measurements, as the retention times might be different in the mixture of the reference samples and in the sample of the HPDL supernatant.

Still, analysis of the untreated supernatant collected from an *E. coli* culture transformed with *HPDL* seems to indicate the presence of **4-HBz** and also possibly **S-HMA**. Due to the poor separation of **4-HB and 4-HPA**, however, GC-MS was chosen as the preferred method for analysis.
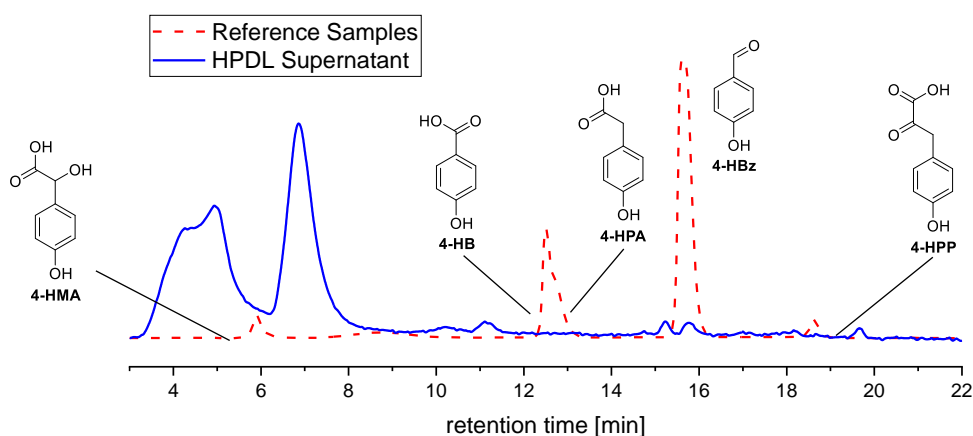
Figure 134: Excerpt of the HPLC trace of supernatant collected from an E. coli *culture transformed with* HPDL *(blue solid trace) and a mixture of the HPDL metabolites **4-HBz, 4-HB, 4-HPA, 4-HMA,** and **4-HPP** (red dashed trace). Full traces can be found in the appendix p. 393.*

GC-MS analysis of samples of untreated supernatant collected from an *E. coli* culture transformed with *HPDL* (Figure 135**A**) showed only few signals at all. Analysis of a similar sample collected

from an *E. coli* culture transformed with *HPPD* (Figure 135**B**) showed more signals, however, in neither trace were any of the expected metabolites observed (reference mixture as red dashed trace in both Figure 135**A** and **B**).
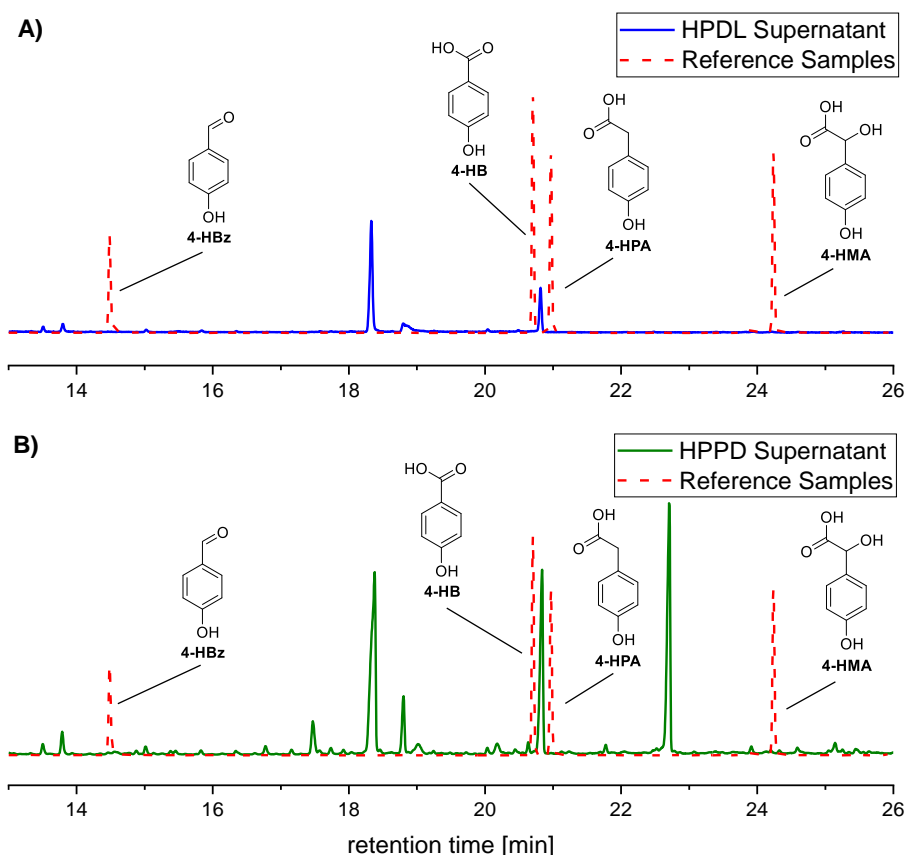
*Figure 135: **A**) Excerpt of the GC-MS trace of the dried, derivatized supernatant of* E. coli *cultures with transformed* HPDL *(solid blue trace) compared to a trace of reference samples (dashed red trace). **B**) Excerpt of the GC/MS trace of dried, derivatized supernatant of* E. coli *cultures with transformed* HPPD *(solid green trace) compared to a trace of reference samples (dashed red trace). Reference samples are indicated in both traces. Full traces can be found in the appendix p. 398. GC-MS method **C**.*

This was attributed to the low concentration of the expected HPDL metabolites in the samples. Therefore, an extraction procedure was developed.

In a first step, stock cultures of HPDL metabolites were prepared and acidified using acetic acid (as 1:1 mixture with water) to a pH of 6. Next, a liquid/liquid extraction was performed using a mixture of dichloromethane and *iso*-propanol (3:1). Acidification of the aqueous layer was necessary due to the acidic nature of **4-HPP**, **4-HPA**, **4-HMA**, **4-HB**, ***L*-DOPA** (L-3,4-dihydroxyphenylalanine, an internal standard commonly used), **DOPAC** (3,4-dihydroxyphenylacetic acid, another internal standard commonly used), and **HG**. The obtained organic layer was then dried and the remaining solid derivatized using BSTFA in acetonitrile, as mentioned before (for a detailed description of the procedure refer to the appendix p. 390).

During tests of this workflow decomposition reactions were observed when using stock solutions of the metabolites **4-HPP**, **4-HPA**, **4-HMA**, **4-HB**, **4-HBz**, **L-DOPA**, **DOPAC**, and **HG**. This was especially the case when the aqueous layer was not acidified. As some of the substrates (e.g. **4-**

HPP) can form enols or enolates, these side-reactions are unsurprising. When the pH was kept below 6 and the time between mixing and extracting kept short, however, most substrates could be extracted from the aqueous layer using the above-mentioned conditions without significant side reactions.

Applying this extraction protocol to biological samples (supernatants of *E. coli* cultures) lead to the identification of the HPDL metabolites **4-HBz**, **4-HB**, and **4-HPA** in the GC-MS trace, based on retention time and EI mass spectrum (Figure 136). Spiking experiments confirmed this assignment, as the addition of **4-HBz**, **4-HB**, and **4-HPA** lead to an increase of the signal strength while the mass spectra were unaffected (Figure 136, mass spectra not shown). In addition, small amounts of **S-HMA** were detected (not shown). Whereas levels of **4-HBz**, **4-HB**, and **4-HPA** were in a range quantifiable by the applied method, levels of **S-HMA** were too low and were therefore disregarded in all further measurements.
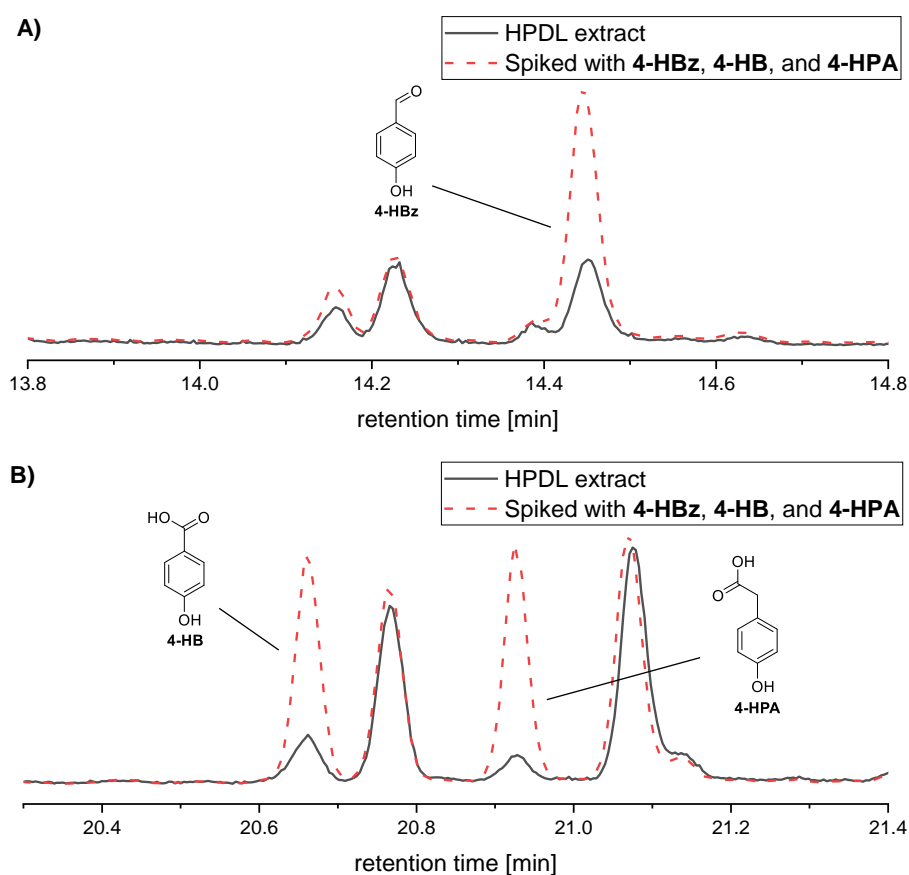
*Figure 136: Excerpts of a GC-MS trace directly obtained from an extract of cell cultures (black solid trace) and the same extract that was spiked with an acetonitrile solution of derivatized **4-HBz, 4-HB**, and **4-HPA** (red dashed trace). **A**) Shows the region between a retention time of 13.8-14.8 min where **4-HBz** was identified. **B**) Shows the region between a retention time of 20.3-21.4 min where **4-HB** and **4-HPA** were identified. Full traces can be found in the appendix p. 399. GC-MS method **C**.*

Quantification of HPDL Metabolites

When HPDL metabolites had been identified successfully in biological samples, a quantification procedure was developed. To this end, calibration curves of **4-HBz**, **4-HB**, and **4-HPA** were collected and the conversion factors calculated (for details, please refer to the appendix p. 390). Note that due to the chosen quantification method obtained values for HPDL metabolite concentrations may vary due to the state of the used instrument. Whereas the obtained values do not show great variations, values should only be compared to those measured in a similar time frame. In this work, only datasets measured in one experimental series are presented within one graph.

The extraction method was subsequently optimized for the optimal acid content by measuring the pH value of the supernatant and adding different amounts of acetic acid. Figure 137 gives an overview of the results obtained from a variation of the pH between 4.8 and 8.6 (this is the pH value as it is measured in the supernatant without any further processing).
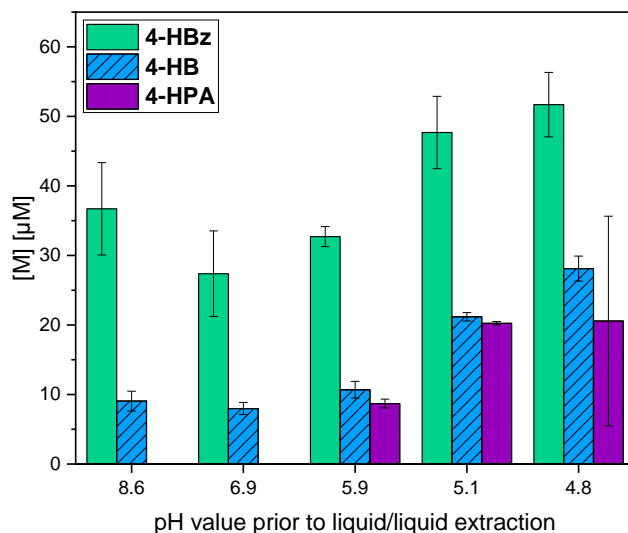
*Figure 137: Overview of the amounts of **4-HBz** (green), and **4-HB** (blue, striped), and **4-HPA** (violet, dotted) that were detected in supernatant extracts obtained from* E. coli *cultures transformed with* HPDL *after addition of different amounts of acetic acid prior to liquid/liquid extraction. Note that these measurements give absolute values and should only be compared within the shown series. Error values were obtained as standard deviations from three separate work-up/measurement-procedure of each sample.*

Whereas the extraction of **4-HBz** does not seem to be overly affected by the presence of acid, **4-HB** and **4-HPA** show a strong dependency on the pH. As both are carboxylic acids, this is unsurprising and validates this method. Only at a pH lower than 5.9 significant levels of **4-HPA** can be detected, these then seem to steady out at around a pH of 5. Therefore, in following experiments a pH value of 4.8-5 was chosen. Figure 138 gives an overview of the workflow applied for the analysis of biological samples (both from *E. coli* and mammalian cell cultures).

Figure 138: Overview over the workflow used for detection of HPDL/HPPD metabolites. The first two steps, marked in green, were performed by Dr. Rolf Stucka.

Side-Product Analysis

In the biological samples several signals were observed that did not correspond to any of the expected HPDL metabolites. By comparison with the NIST2020 database as well as reference samples of a series of compounds (amino acids, indol, etc.) several signals could be assigned to a structure. The identified compounds are presented as their underivatized form for clarity.

In addition to a selection of amino acids (from left to right: valine, leucine, isoleucine, proline, phenylalanine, cysteine), indol, HPDL metabolites (from left to right **4-HBz**, **4-HB**, **4-HPA**), several unsaturated fatty acids (palmitic and stearic acid) were found. In addition, (*Z*)-nonadec-9-enamide was identified based on a comparison with the NIST database.
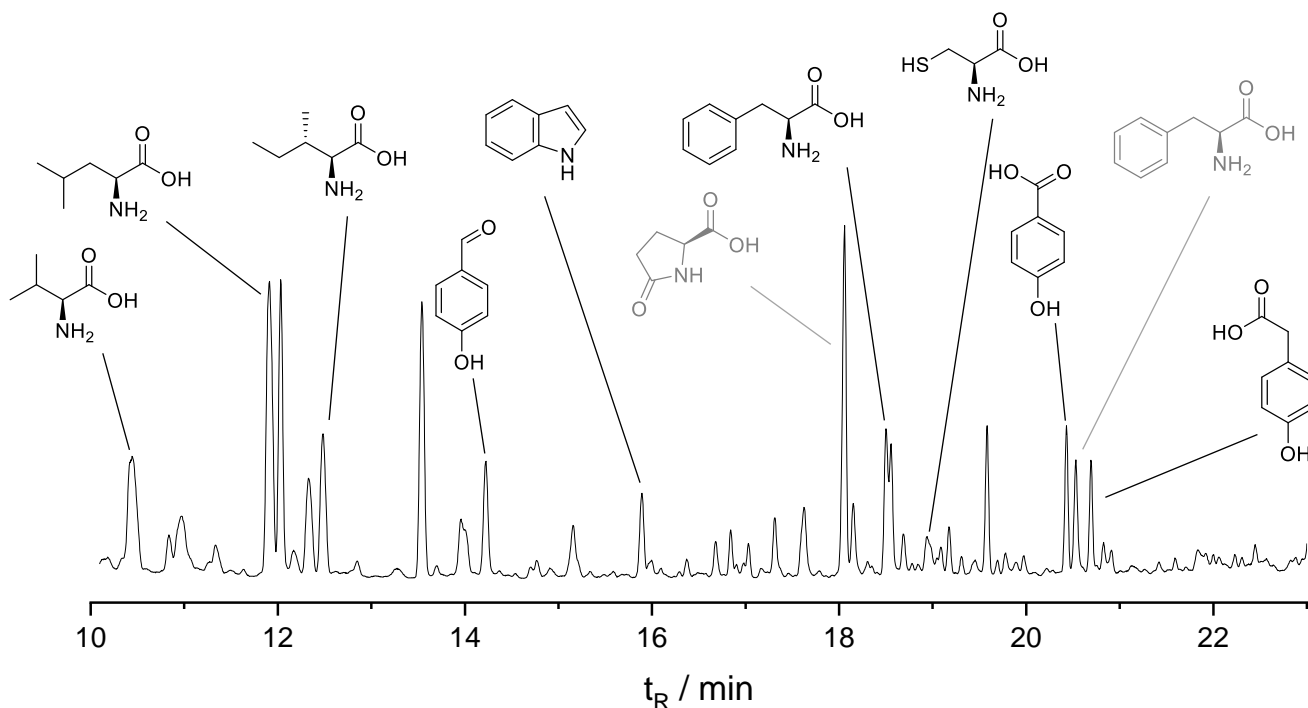
Figure 139: Identified compounds in GC-MS traces obtained from E. coli *cultures transformed with* HPDL. *Black compounds were identified on the basis of retention time and mass spectra of a reference sample. Tentative assignments of grey compounds are based on comparison with the NIST2020 database at a probability > 85%. GC-MS method **C**.*
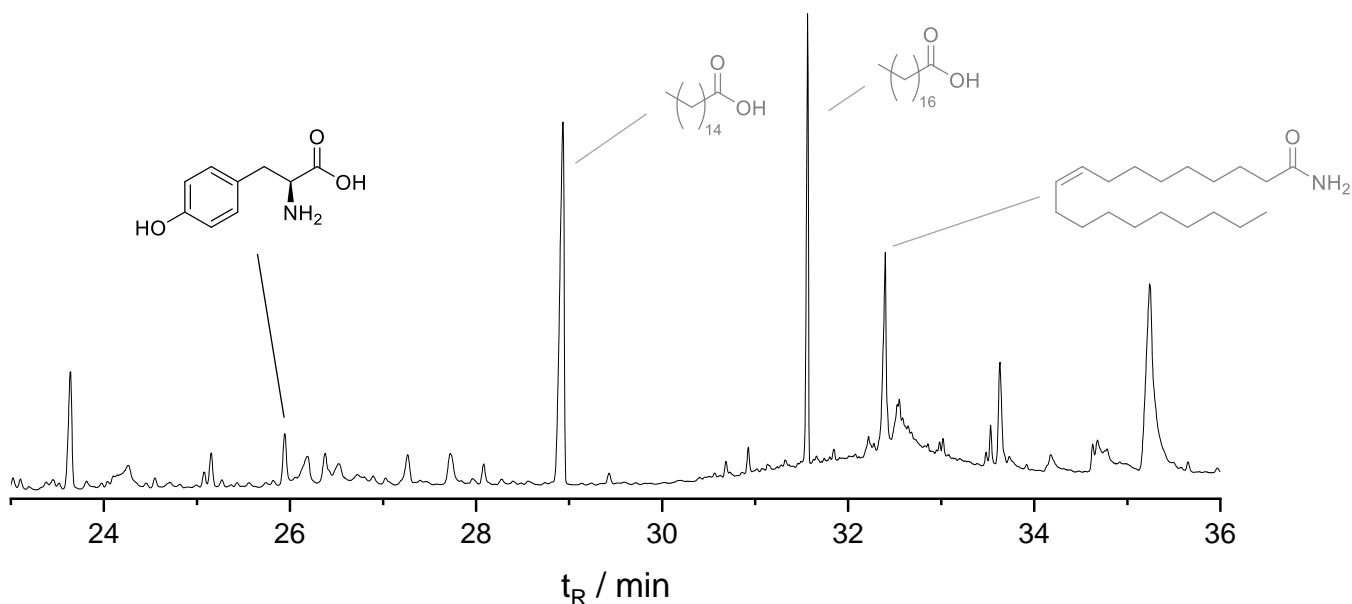
Figure 140: Identified compounds in GC-MS traces obtained from E. coli *cultures transformed with* HPDL. *Black compounds were identified on the basis of retention time and mass spectra of a reference sample. Tentative assignments of grey compounds are based on comparison with the NIST2020 database at a probability > 85%. GC-MS method **C**.*

The presence of these compounds in biological samples is unsurprising and the signals were ignored in all further measurements.

Measurements of HPDL Metabolites in Standard E. coli *Samples*

Next, a series of experiments were performed to quantify the amount of **4-HBz**, **4-HB**, and **4-HPA** in *E. coli* samples transformed with *HPDL*. pET28 was used as bacterial expressionvector and the cultures treated with kanamycin to ensure uptake of the *HPDL* gene (for the cDNA sequence refer to the appendix p. 391). *E. coli* cultures expressing HPDL or HPPD as well as samples with the empty vector pET28 and medium control samples were measured. For these experiments, the workflow shown in Figure 138 was used.

Figure 141 provides a first overview over the quantification experiments conducted using HPDL (HPDL-5 and HPDL-8) and HPPD as well as pET28 empty vector control samples.
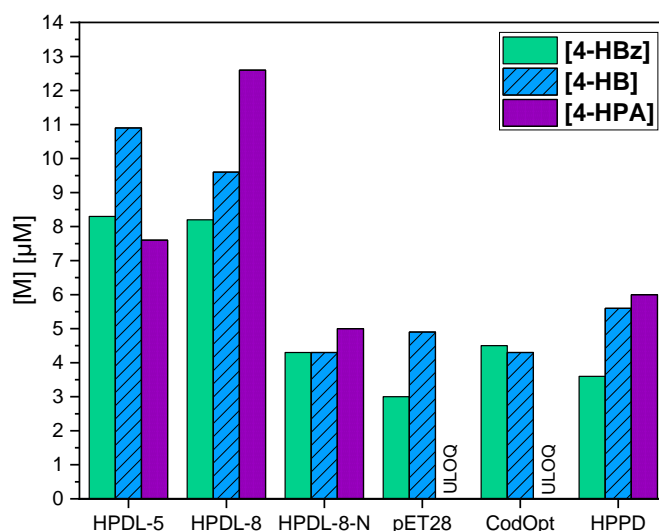
*Figure 141: Overview of the amounts of **4-HBz** (green), **4-HB** (blue, striped), and **4-HPA** (violet, dotted) that were detected in HPDL (HPDL-5, HPDL-8), empty vector control (pET28, HPDL-8-N, CodOpt), and an HPPD sample. Note that the Coomassie SDS-PAGE of HPDL-8-N and CodOpt showed no expression of HPDL enzyme, both can therefore be considered as negative controls. ULOQ = under limit of quantification. Note that these measurements give absolute values and should only be compared within the shown series.*

Comparison of the values in Figure 141 reveals that **4-HBz** and **4-HB** are found in significantly larger amounts in HPDL samples (two independent clones, HPDL-5 and HPDL-8) than in the pET28 empty vector control or HPPD sample. Note that the CodOpt sample did not show any expression of HPDL enzyme in a Coomassie stained SDS-PAGE, this classifies this clone as "pET28 like" retrospectively. The low levels detected for the clone HPDL-8-N can be explained by the often-observed behavior of *HPDL*-transformed *E. coli* cultures: initially, the transformed gene is expressed and (some) enzymatic activity is observed. Then after some time, the bacteria stop expression of HPDL (leading to little expression as detected by SDS-PAGE in the case of HPDL-8-N) yielding a clone that does contain some amounts of enzymatic products but does not show a large expression of enzyme. This was likely the case for HPDL-8-N, which would explain the relatively low levels of **4-HBz**, **4-HPA**, and **4-HB**.

4-HPA is only found in HPDL and HPPD samples and was observed to be more (HPDL-8) or roughly equally as abundant (HPDL-5) as in HPPD.

Neither metabolite is found in the medium control sample (not shown) which indicates that the amount of **4-HBz** and **4-HB** observed in the pET28 sample is due to endogenously produced **4-HBz** and **4-HB** by *E. coli*. Indeed, *E. coli* do possess a pathway for producing **4-HBz** and **4-HB**, so this fits well into the above-described results.[327]

The fact that **4-HBz**, **4-HB** and **4-HPA** were found in *E. coli* cultures transformed with *HPDL* but not in the empty vector controls does indeed indicate involvement of HPDL in the transformation of **4-HPP** to **4-HB**.

Measurements of HPDL Metabolites in E. coli *Samples with HPDL Mutants*

A central problem in the study of HPDL has been the difficult to impossible isolation of an active sample of enzyme. This was attributed to the enzymes preference for coagulation, probably due to the transmembrane domain of the enzyme, and the resulting difficulty to redissolve the isolated enzyme.[328] For this reason, samples produced by *E. coli* cultures are used instead of *in vitro* experiments performed with isolated protein. Isolation of HPDL itself, however, would allow such *in vitro* studies and therefore gain a deeper understanding of substrate consumption, kinetics, detection of intermediates, modes of inhibition, and much more. Hence, Dr. Rolf Stucka attempted to modify the cDNA sequence used for expression of HPDL in *E. coli* cultures by removing part of the *N*-terminus including the sequence assigned to the **t**ransmembrane domain of and the **m**itochondria target signal of the enzyme (HPDL-TM). If the enzymatic function of the protein is retained, this could result in an enzyme mutant suitable for isolation and thus *in vitro* experiments.

Coomassie SDS-PAGE shows a strong expression in *E. coli* and GC-MS analysis of the culture's supernatant indicates significant levels of **4-HBz**, **4-HB**, and **4-HPA** production (Figure 142).
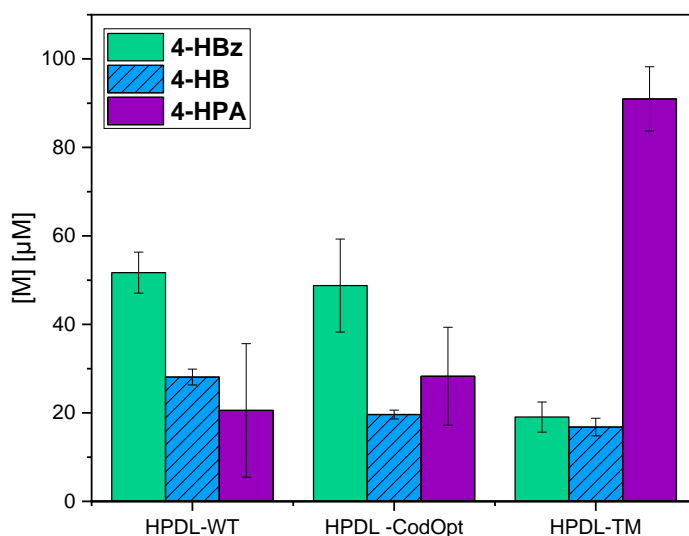
*Figure 142: Comparison of detected metabolite levels of **4-HBz** (green), **4-HB** (blue, striped), and **4-HPA** (violet, dotted) in samples obtained from* E. coli *cultured transfeormed with a modified* HPDL *gene (HPDL-TM and HPDL-CodOpt) as well as the initial, wild-type* hpdl *gene (HPDL-WT). Note that these measurements give absolute values and should only be compared within the shown series. Error values were obtained as standard deviations from three separate work-up/measurement-procedure of each sample.*

The amount of **4-HPA** detected in the new mutant HPDL enzyme (HPDL-TM) is significantly larger than in the wild-type (about four-fold) while **4-HBz** levels of HPDL-TM are decreased compared to the wild-type (HPDL-WT) and codon-optimized (HPDL-CodOpt) sample. As *E. coli* do not possess a known pathway to transform **4-HPA** to **4-HBz** (**4-HBz** is formed *via* a different pathway from chorismic acid[327]), an increase of **4-HPA** combined with a decrease of **4-HBz** indicates that the new mutant of HPDL is not as capable in performing the reaction from **4-HPA** to **4-HBz** as is the wild-type. An explanation for this behavior would be that removing the

210

mitochondria target signal and transdomain part of the enzyme hindered dimerization of the enzyme – which then resulted in a loss-of-function for the second part of the enzymatic reaction (conversion of **4-HPA** to ***S*-HMA** and then **4-HBz**) whereas the first part (activation by conversion of **4-HPP** to **4-HPA**) stays intact.

Even though this effect was not expected, the increase in **4-HBz** and **4-HPA** levels upon changing of HPDLs sequence again supports the hypothesis that HPDL is involved in the transformation of **4-HPP** to **4-HB**.

Another approach taken in this project was inspired from a recent study on a family of related enzymes: arginine hydroxylases OrfP and VioC.[321] As briefly mentioned above (refer chapter VI.1), these enzymes share the same active site structure (*i.e.* facial triad, iron center, α-KG cofactor) but differ slightly in the amino acids that line the substrate cavity. As mentioned in chapter VI.1, this also applies for the enzymes HPPD, HMAS, and HPDL. Accordingly, HPPD can be modified to resemble the active site structure of HMAS which indeed led to an increase in ***S*-HMA** as product.[318,319]

These studies led to the design of an experimental setup to identify which amino acids within the mentioned enzymes are responsible for the differentiation in reactivity.
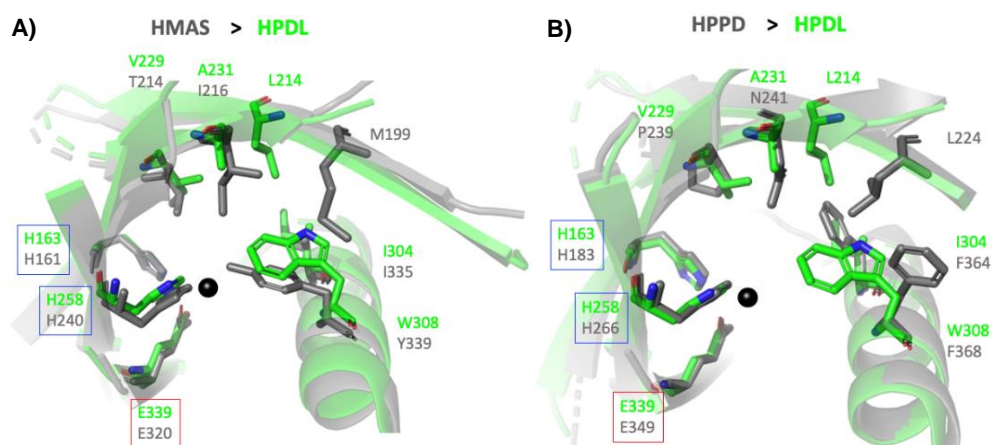
*Figure 143: Overlay of visual representations of the active site cavities of **A**) HMAS (PDB: 2R5V) and a hypothetic structure of HPDL as well as **B**) human HPPD (PDB: 5EC3) and a hypothetical structure of HPDL. The human HPPD, HPDL and HMAS structures are shown as ribbon diagrams. Previously identified structural aspects, such as the active binding groove formed by a single helix carrying the aromatic residues and the shielding antiparallel five β-sheets are shown as ribbon diagrams. Structural calculations performed by Dr. Britta Möhl, Institute of Virology, Technical University of Munich. For enlarged pictures and details on the structural modelling calculations refer to the appendix p. 402f.*

Although the crystal structure of human HPDL has not been solved yet, the sequence homology between the human proteins, 24,5% for HPPD and HPDL and 27,41% for HMAS and HPDL, allowed homology modeling of human HPDL. The homology model of human HPDL were generated using SWISS-MODEL program[329] based on the crystal structures of human HPPD (PDB: 5EC3) and HMAS (PDB: 2R5V). The structural sequence alignment of human HPPD, HMAS and HPDL based on the crystal structures of HPPD and HMAS was performed using T-COFFEE Expresso (Figure 143).[330] The alignment revealed that overall the active binding center is similar

but that the substrate binding groove is enlarged in HPDL. The hypothetical structure of human HPDL generated by SWISS-MODEL shows an overall similar substrate binding groove arranged by the same order of a single helix carrying the aromatic residues and five antiparallel β-sheets flanking the groove.

Generally speaking, the active site cavity of HPDL is very hydrophobic and provides little interaction with the substrate. In particular, the active site pouch of HMAS contains a threonine residue where HPDL features an alanine (position 229 in HPDL). Very close to this residue (position 231), HPDL possesses an alanine residue whereas HMAS has an *iso*-leucine side-chain. These two differences are found within a larger, conserved structure of ...**L²²⁹XL²³¹XE**... (conserved positions are bold, variable positions marked with their amino acid number in HPDL) that can be found in HPDL, HPPD, and HMAS. This suggests that the surrounding, conserved amino acids are necessary for the overall structure of the active site whereas the flexible positions could play a role in determining the reactivity of the enzyme by interacting with the substrate. Another conserved site is situated on the opposite side of the active site: ...**NI³⁵⁴XAK³⁵⁸XI**... As the residue at position 354 is not situated close to the iron center, it was disregarded for the time being, rather position 358 was chosen for site directed mutagenesis. HPDL carries a tryptophan residue here whereas HMAS features a tyrosine side chain. As the active site chamber of HPDL is hydrophobic in nature, likely little to no interaction with the hydrophilic part of the substrate is possible. However, the tryptophane residue or the hydrophobic chains of the amino acids lining the wall of the active site might interact with the benzene ring of the substrate(s) by π-stacking or van-der-Waals interactions, respectively. This hypothesis would well coincide with the hypothesis that HPDL carries out two separate transformation steps (**4-HPP** to **4-HPA** and **4-HPA** to **4-HBz**), as the hydrophilic part of the substrate changes whereas the hydrophobic part stays the same.

In an attempt to change the enzymes product distribution towards that of HMAS (*i.e.* more **S-HMA** and less to none **4-HBz**) it was decided to mutate the positions V229T, A231I, and W358Y using two primers (one containing the mutations V229T and A231 and one containing the W358Y mutation). These experiments were performed by Dr. Rolf Stucka.

A pET28 plasmid containing the modified HPDL gene was indeed obtained. The mutant (V229T, A231I, and W358Y) is referred to as **HPDL>HMAS** in the following (refer to the appendix p. 391 for the complete amino acid sequence). Dr. Rolf Stucka then successfully transformed the corresponding plasmid into *E. coli*, the supernatants collected after cultivation of HPDL>HMAS clones in medium with additional tyrosine were then analyzed for **4-HPA**, **S-HMA**, **4-HBz**, and **4-HB**. If the interpretation of the active site structure is correct and the conducted experiments successful, a shift in the product distribution from **4-HBz** and 4-**HB** to **S-HMA** would be expected,

as the latter is the main product of HMAS but was previously only detected in miniscule amounts in supernatants of HPDL samples.
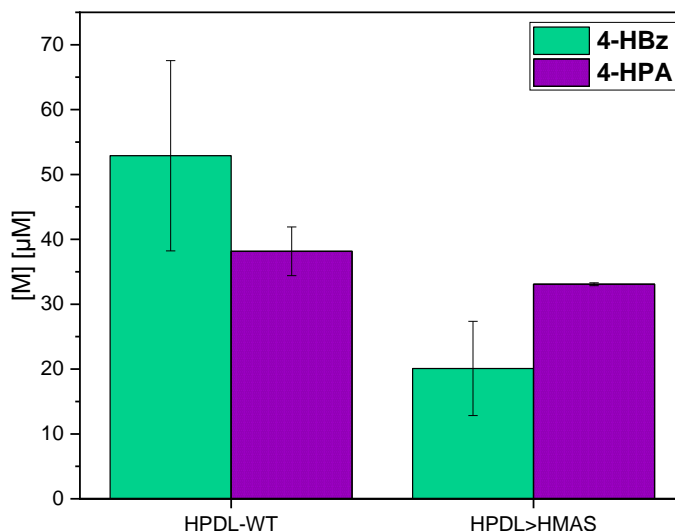
Figure 144: Comparison of detected metabolite levels of **4-HBz** (green) and **4-HPA** (violet, dotted) in samples obtained from E. coli cultured transformed with the wildtype HPDL gene as well as the modified HPDL>HMAS gene. Note that these measurements give absolute values and should only be compared within the shown series. Error values were obtained as standard deviations from three separate work-up/measurement-procedure of each sample.

Indeed, the observed levels of **4-HBz** in samples of HPDL>HMAS are lower than those in samples of the wild-type HPDL-WT (Figure 144). The amount of **4-HPA** was also (slightly) decreased, however, the ratio **4-HBz**/**4-HPA** changes significantly towards more **4-HBz** which was expected and subsequently interpreted as a shift in product distribution and therefore as a successful outcome of the site directed mutagenesis experiment. Unfortunately, in neither sample were any traces of **S-HMA** detected. However, as **S-HMA** was never detected in any of these samples, this is unsurprising. Likely, **S-HMA** is either used by *E. coli* or decomposes in the culture medium or during work-up. Applying the extraction/HPLC-MS method developed by Banh *et al.* could allow for the isolation, identification, and quantification of **S-HMA** which would then further corroborate these studies.

Isotope Labeling Studies

To gain further insight into the postulated pathway of HPDL, *E. coli* cultures transformed with (several variants of) *HPDL* were fed isotopically labeled tyrosine (**Tyr***). When **Tyr*** is then converted to the isotopically labeled derivatives of **4-HPP**, **4-HPA**, **S-HMA**, **4-HBz** and **4-HB**, these can be identified using GC-MS due to the difference in m/z values (Scheme 103).

m/z difference	9	8	8	7	7
usually detected	No	Yes	Yes[1]	Yes	Yes

[1] = small amounts, not quantifed
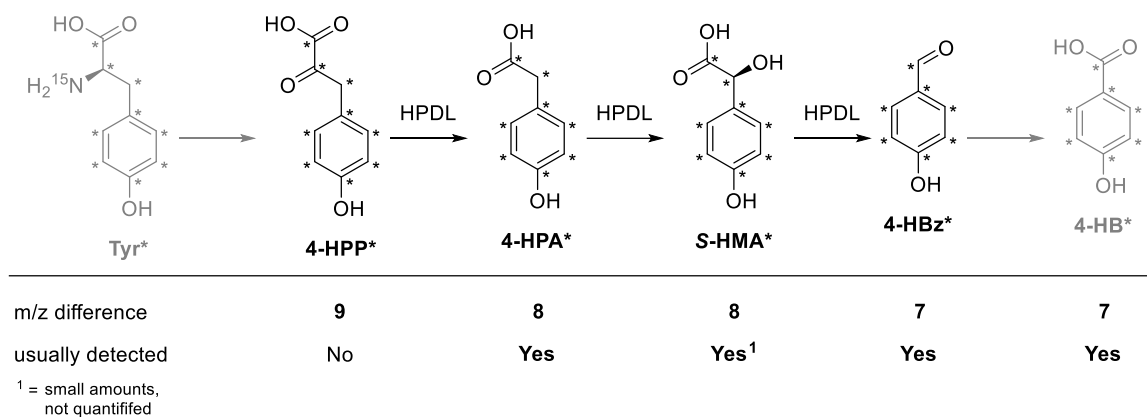
Scheme 103: HPDL metabolism as well as prior and posterior enzymatic modifications (in grey) of ^{13}C-labeled **Tyr***. Low-resolution m/z difference as well as whether the compound is usually detected in biological HPDL samples is indicated.

Indeed, signals corresponding to the isotopically labeled compounds were observed in GC-MS measurements. In addition to the isotopically *labeled* compounds, signals corresponding to the *unlabeled* compounds were also detected. The distribution (in %) of these detected signals is presented in Table 15.

Table 15: Relative amounts of isotopically labeled HPDL metabolites **4-HBz**, **4-HB**, and **4-HPA** detected.

Sample	% 4-HBz*	% 4-HB*	% 4-HPA*
HPDL-WT	75	25	75
HPDL-CodOpt	75	25	75
HPDL>HMAS	60	20	60

None of the substrates was detected as 100% of the labeled compound, which indicates the involvement of secondary pathways that do not use tyrosine as initial substrate. In addition, lower levels (20-25%) of isotopically labeled **4-HB** were found than for **4-HBz** and **4-HPA** (60-75%). This indicates that while the pathway tyrosine → **4-HPP** → (**S-HMA**) → **4-HBz** → **4-HB** is responsible for the major part of **4-HPA** and **4-HBz**, significant amounts of **4-HB** are produced *via* other pathways. The interpretation of **4-HB** levels as an indicator for HPDL activity must therefore be regarded very carefully.

In all measurements, the relative amounts of labeled **4-HBz** and **4-HPA** are equal. This implies that only one (relatively direct) pathway is responsible for the conversion of **4-HPA** to **4-HBz**, which would fit the hypothesis that HPDL is involved in this transformation.

Interestingly, the relative amounts of isotopically labeled compounds are lower in the HPDL mutant HPDL>HMAS. This indicates lower activity of HPDL>HMAS than the wild-type. However, taken together with the results shown in Figure 144, two interpretations are possible: 1) HPDL>HMAS is as active as the wildtype, but **S-HMA** is produced preferentially resulting in low levels of **4-HBz** and **4-HPA** or 2) HPDL>HMAS is less active (concerning **4-HBz** production) than

the wildtype, resulting in lower levels of **4-HBz** and **4-HPA**. Taken together with the results presented above, this the second interpretation seems more likely at this point.

*Inhibitor/Crystallization Aid – **4-HPN***

A different approach taken in this work to elucidate the nature of the HPDL enzyme was the synthesis of an inhibitor/crystallization aid based on the structure of **4-HPP**, the proposed substrate for HPDL and HPPD. This project is based on findings from research on TET enzymes during the past years: in 2013 Hu *et al.* published the results of a crystallization experiment which gave evidence for the orientation of **5mdC**-containing DNA in the active site pouch of TET2 (Scheme 104**A**). These crystals were obtained by using *N*-oxalylglycine (NOG) instead of α-keto glutarate (α-KG) as co-substrate: whereas NOG coordinates to the iron central atom of the active site similar to α-KG, oxidation to the catalytically active iron(IV)-oxido species is hampered. From this data the "real" structure of TET2 enzyme active site was proposed (Scheme 104**B**).[153]
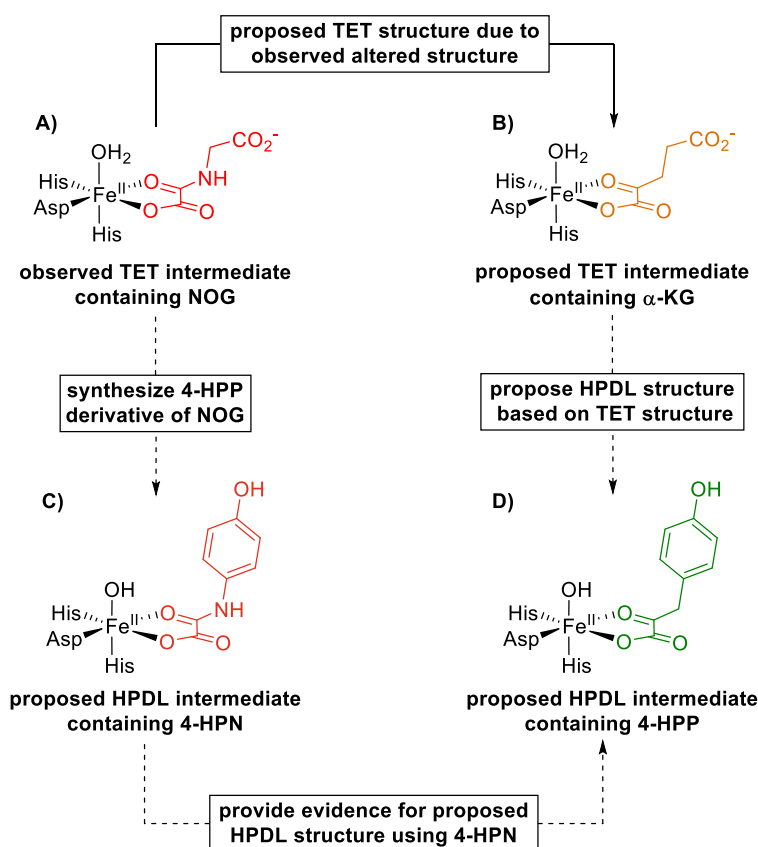
*Scheme 104: Observed structure of TET2 and NOG (**A**) led to the proposal for the structure of TET2:α-KG complex (B). As the amino acids forming the active site of HPDL have been reported to be similar, a similar structure of the active site can be proposed (**D**). By synthesizing 2-((4-hydroxyphenyl)amino)-2-oxoacetic acid (**4-HPN**) and subsequently crystallizing HPDL with **4-HPN** (D) further evidence to corroborate this proposal could be obtained.*

Based on the similarity of the amino acids making up the active sites of TET and HPDL a similar active site structure can be proposed for HPDL (Scheme 104**C**). As of yet, no crystal structure of HPDL has been reported (Sep 2021). A derivative of the proposed natural substrate of HPDL, **4-HPP**, which contains an amide moiety instead of a methylene group next to the carbonyl group

215

(similar to NOG compared to α-KG) might have an inhibitory effect similar to that of NOG and probably could help in obtaining a crystal structure of HPDL. To this end, 2-((4-hydroxyphenyl)amino)-2-oxoacetic acid (**4-HPN**) was synthesized in a five-step synthetic sequence (Scheme 105).
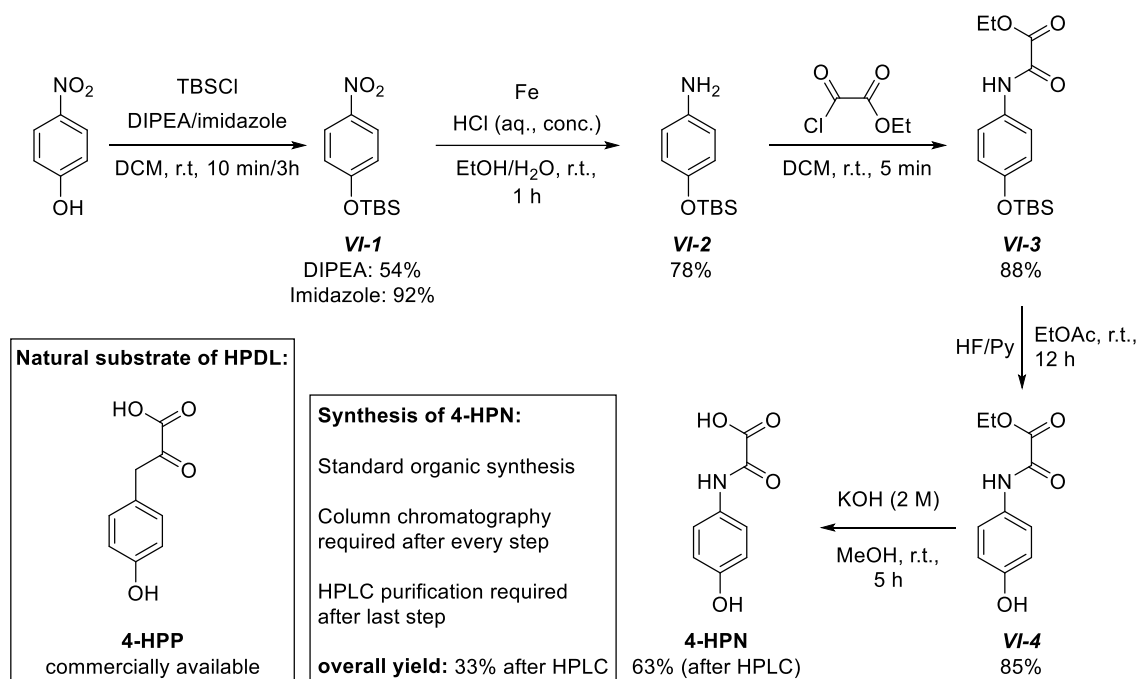
Scheme 105: Synthesis of *4-HPN* starting with 4-nitro phenol in a five-step sequence.

At first, the hydroxyl moiety of 4-nitro phenol was protected using tert-butyl-dimethyl-silyl chloride (TBSCl) and Hünig's base (di-*iso*-propyl ethyl amine, DIPEA) to obtain intermediate *VI-1* in 54% yield. Whereas both thin layer chromatography (TLC) as well as GC-MS show 100% conversion of the starting material only a about half of the expected product was isolated after column chromatography. Changing the base to imidazole resulted in a longer reaction time to achieve full conversion (3 h) but also a much higher yield (92%).

Reduction of the nitro group using iron and aqueous hydrochloric acid gave intermediate *VI-2* in 78% yield. It has to be noted that a reaction time of 1 h (scale: 1-2 mmol) is required for complete conversion, even though TLC indicates complete consumption of the starting material after 5 min. If the reaction is stopped earlier, only a fraction of the desired product can be isolated. Also, triethyl amine has to be added during the work-up procedure which results in a color change to green and the precipitation of a fluffy, colorless-greenish solid. When no triethyl amine was added, the product *VI-2* was not isolated after column chromatography. This circumstance was tentatively attributed to coordination of triethylamine and thus displacement of *VI-2* from the iron ions in solution.

Addition of ethyl 2-chloro-2-oxoacetate gives *VI-3* within 1 min reaction time in 84% yield. Sequential deprotection of the TBS moiety using hydrogen fluoride in pyridine (yielding *VI-4*,

85%) and KOH in methanol gives the desired product **4-HPN** (63% after HPLC). The overall yield was determined to be 33% after HPLC purification. Unfortunately, **4-HPN** was observed to be unstable during the standard derivatization procedure (BSTFA, MeCN, 40 °C, 1 h) or during the GC-MS measurement itself, as only fragments were detected.

Dr. Rolf Stucka performed an initial series of inhibitory studies in HPPD in order to show the principle of inhibitory action in this much better studied enzyme. He found that **4-HPN** does indeed inhibit the function of HPPD. This was observed by feeding between 1.25-25 mM **4-HPN** to *E. coli* cultures transformed with *HPPD* and observing the emergence of a brown pigment which is a direct result of HPPD activity (**HG** is well known to be converted into this brown pigment in *E. coli*). The cultures with added **4-HPN** (Figure 145 entries 3-7) show significantly lighter shades of brown and lower absorption at λ = 580 nm, indicating an inhibitory effect. When 50 mM of **4-HPN** were added the cultures ceased to grow.

	1	2	3	4	5	6	7
Tyr (mM)	-	+ 2.5	+ 2.5	+ 2.5	+ 2.5	+ 2.5	+ 2.5
4-HPN (mM)	-	-	+ 1.25	+ 2.5	+ 5.0	+ 12.5	+ 25.0
Color Abs. (λ = 580 nm)	100	295	190	130	126	105	95
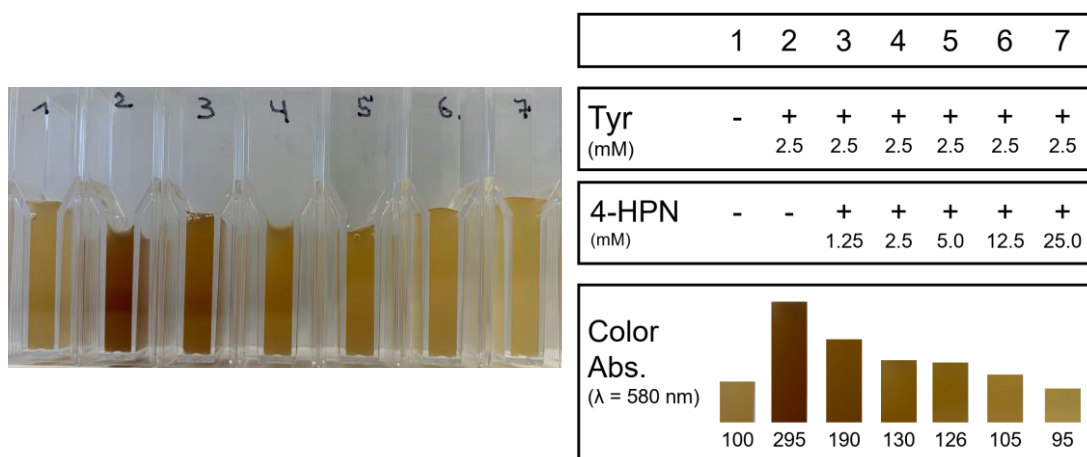
Figure 145: Picture of E. coli *cultures containing variable amounts of **4-HPN** as well as the experimental setup and UV-vis analysis at λ = 580 nm. Experiments and evaluation performed by Dr. Rolf Stucka.*

Dr. Rolf Stucka then continued on performing inhibitory experiments with *E. coli* cultures that overexpress HPDL instead of HPPD. In a first series, the codon for wild-type HPDL was used (Figure 146**A**). In a second experiment, the above-mentioned HPDL-TM with a shortened N-terminus was used. The obtained supernatants were then analyzed for HPDL metabolites **4-HBz**, **4-HB** and **4-HPA** in both cultures, that without added **4-HPN** and that with 25 mM **4-HPN**.
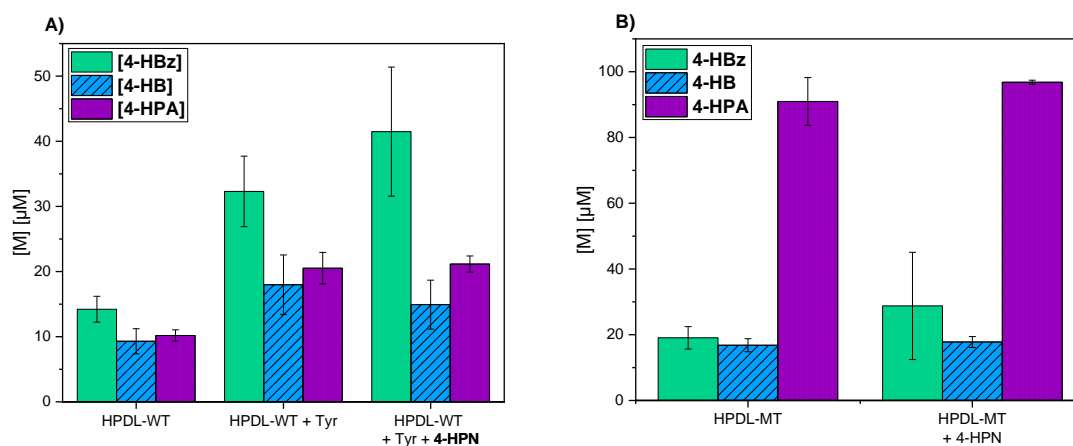
*Figure 146: Comparison of detected metabolite levels (**4-HBz** (green), **4-HB** (blue, striped), **4-HPA** (violet, dotted)) in supernatant samples obtained from* E. coli *cultures expressing **A**) the HPDL-WT or **B**) the HPDL-TM, both with and without **4-HPN**. If added, then [L-tyrosine] = 2.5 mM and [4-HPN] = 25 mM. Note that these measurements give absolute values and should only be compared within the shown series. Error values were obtained as standard deviations from three separate work-up/measurement-procedure of each sample.*

As can be observed in Figure 146, the detected levels of **4-HBz**, **4-HB**, and **4-HPA** are similar for all samples that contain any HPDL variant and tyrosine regardless of added **4-HPN**. This means that **4-HPN** has no inhibitory effect on HPDL-WT and HPDL-TM.
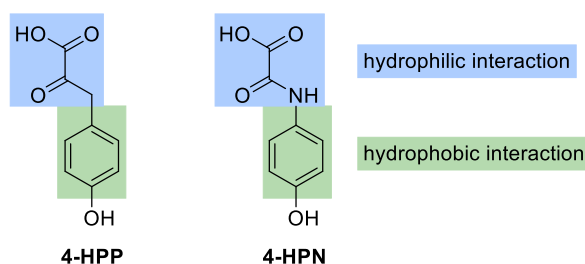
*Figure 147: Structures of **4-HPP** and **4-HPN**, parts of the molecules providing hydrophilic (blue) and hydrophobic (green) interaction.*

This result is actually in line with the previous observations: the modeling and directed mutagenesis studies suggest that the active site cavity of HPDL provides very little interaction with the hydrophilic part of the substrate – which is the location which differentiates **4-HPN** from the natural substrate **4-HPP**. As **4-HPN** is even more hydrophilic due to the amide moiety, an even lower uptake compared to **4-HPP** is possible, which would then result in no observable inhibitory effects. On the other hand, HPPD's active site cavity does provide moieties for hydrophilic interaction which does allow for the localization of **4-HPN** inside the active site enabling inhibition of the enzyme's activity.

To date, all attempts of crystallizing HPDL without denaturing the protein have failed. However, crystallization experiments using **4-HPN** crystallization aid may provide another possibility to study HPDL.

Measurements of HPDL Metabolites in Mammalian Cell Samples

In addition to samples obtained from *E. coli* cultures that were transformed with the *HPDL* gene, samples were also obtained from mammalian cell lines. In particular, HEK (human embryonic kidney), P19 (mouse embryonic carcinoma) and HeLa cells were used. In addition, Dr. Rolf Stucka obtained mouse cerebellum, cerebrum, and liver cells from livestock department at LMU Munich (refer to the appendix p. 403 for details). Mammalian cells contain little native HPDL, therefore, *HPDL* was transfected in some experiments (indicated in the corresponding figure caption). In particular, HEK cells do not contain detectable levels of HPDL as found by Dr. Rolf Stucka.

In all cases, the cells were broken apart and the mitochondria isolated. These were then either transfected with *HPDL* or incubated directly with/without the proposed HPDL substrate **4-HPP**. In some cases (indicated where applicable), the samples were fractionated into two fractions: 1) outer membrane (OM)/inter membrane space (IMS) and 2) inner membrane (IM) and matrix. Cell culture experiments were performed by Dr. Rolf Stucka. Then, the samples were treated similarly to the above described: the collected supernatants were acidified with acetic acid, extracted using 3:1 dichlormethane:*iso*-propanol, dried, derivatized, and analyzed using GC-MS (refer to the appendix p. 390 for a more detailed description).

In contrast to samples obtained from *E. coli* cultures these mammalian cell samples contained less **4-HB.** This is likely due to the high reactivity (and toxicity) of parabens (to which **4-HB** is the base structure) in mammalian organisms.[331] Therefore, in most of the following analyses **4-HB** is excluded. The samples also contained less contamination of other volatile compounds (Figure 148).
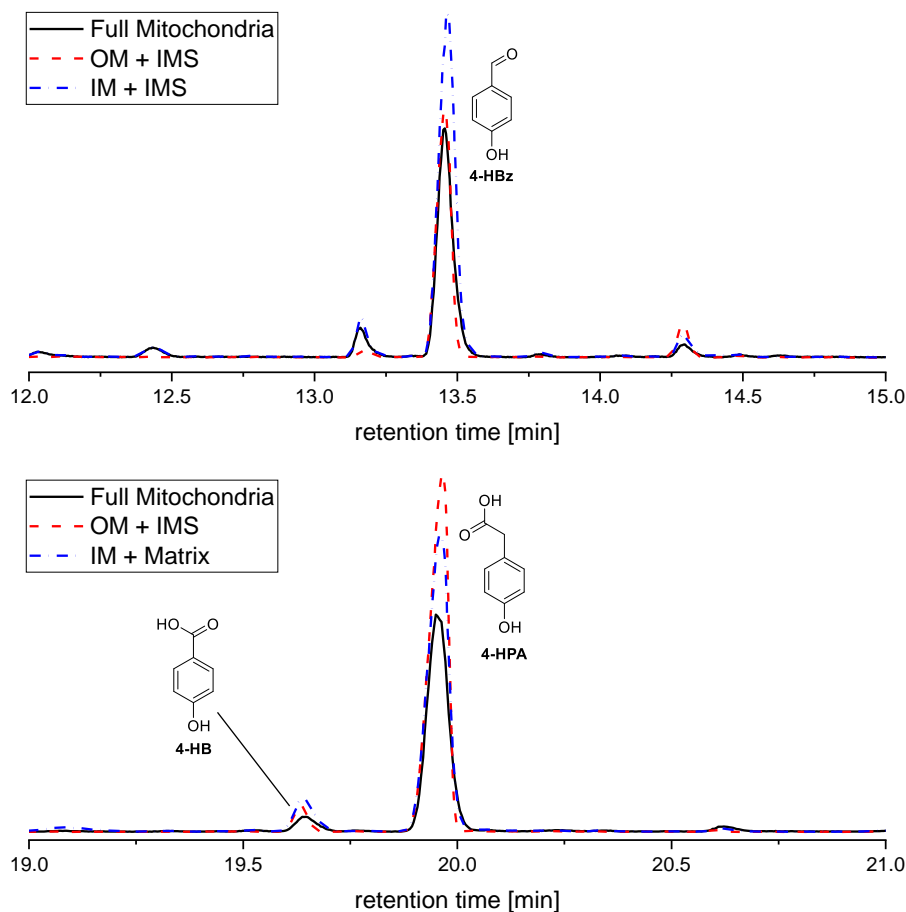
*Figure 148: Excerpts of GC-MS traces of extracted, dried, and derivatized samples taken from HEK cell mitochondria: Full mitochondria (black, solid), outer membrane + inter membrane space (OM+IMS, red, dashed), inner membrane + matrix (IM + matrix, blue, dashed and dotted). Signals corresponding to **4-HBz**, **4-HB**, and **4-HPA** are indicated. GC-MS method **C**.*

In an attempt to localize HPDL through metabolomic analysis, samples containing mitochondria obtained from mammalian cells (specified in the figure description) were either treated as a whole or divided into subfractions: the inner membrane (IM)/matrix fraction and the outer membrane (OM)/intermembrane space (IMS) fraction. The individual samples were then incubated, either with or without **4-HPP**. Cell culture and fractionation experiments were performed by Dr. Rolf Stucka.

It was generally noted, that **4-HBz**, **4-HB**, and **4-HPA** levels differ among the collected fractions. For **4-HBz**, levels are similar in the full mitochondria and OM/IMS fraction, both are significantly smaller than the level detected in the IM/matrix fraction. In the case of **4-HPA**, levels were determined to be largest in the OM/IMS fraction, second largest in the IM/matrix fraction, and lowest in the full mitochondria sample. The difference in **4-HBz** and **4-HPA** levels is smallest in the IM/matrix fraction, which could indicate that here most of the intermediate **4-HPA** is converted into the product **4-HBz**. On the other hand, most **4-HPA** is found in the OM/IMS fraction.

As HEK cells do not contain native HPDL and these cells were not transfected with additional HPDL, these results point towards a secondary pathway for the production of **4-HBz** and **4-HPA**.

Due to the process of solubilizing, it is likely that parts of the IM/matrix fraction ended up in the OM/IMS fraction, but not *vice versa*. Coupled with the higher **4-HBz** levels in the IM/matrix fraction this proposed secondary pathway is possibly located in the inner membrane of the mitochondria. However, it is also possible that the compounds produced by this secondary pathway are capable of traversing to other layers in the mitochondria which makes localization of any metabolite production stites using this method difficult.
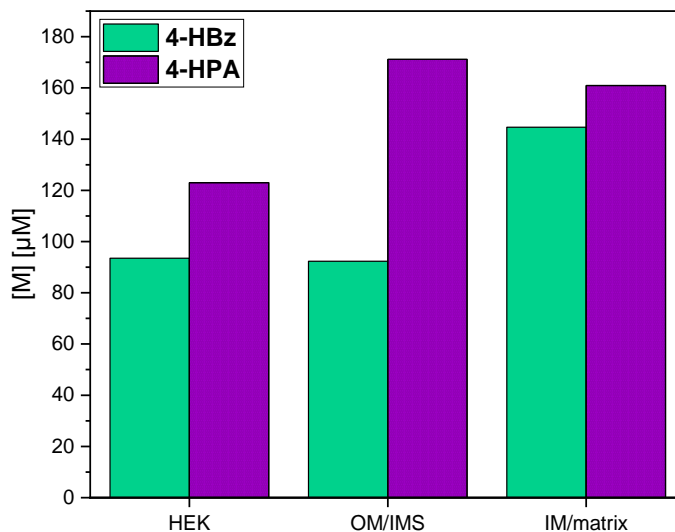
*Figure 149: Detected levels of **4-HBz** (green) and **4-HPA** (violet, dotted) in samples obtained from HEK cell cultures. The mitochondria of these cells were isolated and incubated with [**4-HPP**] = 2.5 mM (HEK) or separated into fractions (OM/IMS or IM/matrix) that were also incubated with [**4-HPP**] = 2.5 mM. Note that these measurements give absolute values and should only be compared within the shown series.*

4-HBz and **4-HPA** levels were also determined in P19 (mouse embryonic carcinoma) and HeLa (human cervical carcinoma) mitochondria. These mitochondria samples were obtained from cells that were either incubated without additives ("*cell type* no add", not shown, refer to the appendix p. 401) with **4-HPP** ("*cell type* + 4-HPP", Figure 150), transfected with additional *HPDL* ("*cell type* + HPDL*", not shown, refer to the appendix p. 401), or transfected with additional *HPDL* and incubated with **4-HPP** ("*cell type* + HPDL + 4-HPP", Figure 150). Even though the x-axis description refers to cell types, only the mitochondria of these respective cell types were used.
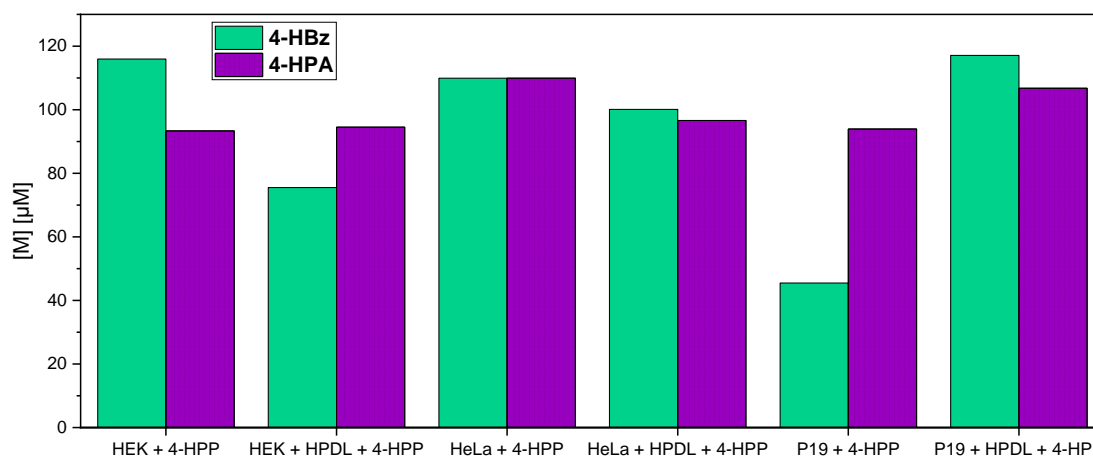
*Figure 150: **4-HBz** (green) and **4-HPA** (violet, dotted) levels in mitochondria samples obtain from HEK, HeLa, and P19 cells. The mitochondria isolated from the indicated cell type were either incubated with [**4-HPP**] = 2.5 mM ("cell type + 4-HPP") or transfected with HPDL and then incubated with [**4-HPP**] = 2.5 mM. ("cell type + HPDL + 4-HPP"). Tissue preparation, incubation, and collection of supernatants performed by Dr. Rolf Stucka.*

In the case of mitochondria obtained from HEK cells, which do not contain native HPDL, less **4-HBz** was detected when additional *HPDL* was transfected. In mitochondria samples from P19 cells (intermediate native HPDL levels) an increase in **4-HBz** production was noted upon transfection with additional *HPDL* and incubation with **4-HPP** compared to only incubating the samples with **4-HPP**. In HeLa cells (highest native HPDL levels) no significant change was noted. These observations suggest that the proposed secondary pathway for **4-HBz** and **4-HPA** production is very active in HEK cells and is disrupted by additional HPDL, whereas P19 cells are very susceptible to an increase in HPDL levels resulting in increased **4-HBz** and **4-HPA** production. As HeLa cells already contain (relatively) high levels of native HPDL, transfection with additional HPDL does not produce any observable change in product formation.

This suggests that HPDL function is highly dependent on the cell type used in these experiments. In a separate experiment to localize/identify the proposed secondary pathways, the IM/matrix fraction obtained from HEK cells was treated with proteinase K and the **4-HBz** and **4-HPA** levels determined. It was observed that addition of sodium dodecyl sulfate (SDS, a denaturing agent) increased **4-HBz** and **4-HPA** formation, whereas addition of SDS and proteinase K lead to a relative, but only minor, decrease (Figure 151). Proteinase K decomposes proteins and peptides that are accessible to it. In the case of the IM/matrix fraction, only proteins located within the IM are therefore accessible to decomposition by proteinase K. The decrease in **4-HBz** and **4-HPA** levels in the proteinase K treated sample could therefore be attributed to the involvement of an enzyme that is located in the IM. However, as the observed changes are minute this interpretation has to be regarded with great care.
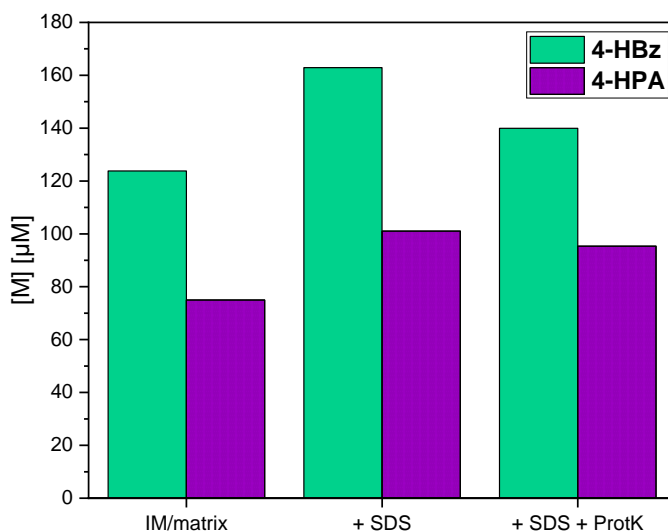
*Figure 151: Detected levels of **4-HBz** (green) and **4-HPA** (violet, dotted) in the IM/matrix fraction before (IM/matrix) and after addition of SDS (+ SDS) and SDS/proteinase K (+ SDS +ProtK). Note that these measurements give absolute values and should only be compared within the shown series. SDS = sodium dodecyl sulfate.*

As mutations in the *HPDL* gene are linked to a neurodegenerative disease and HPDL was indeed found to be expressed in higher levels in rat cerebellum, mouse brain (cerebrum and cerebellum) was studied.[11] As a reference sample, mouse liver was used.
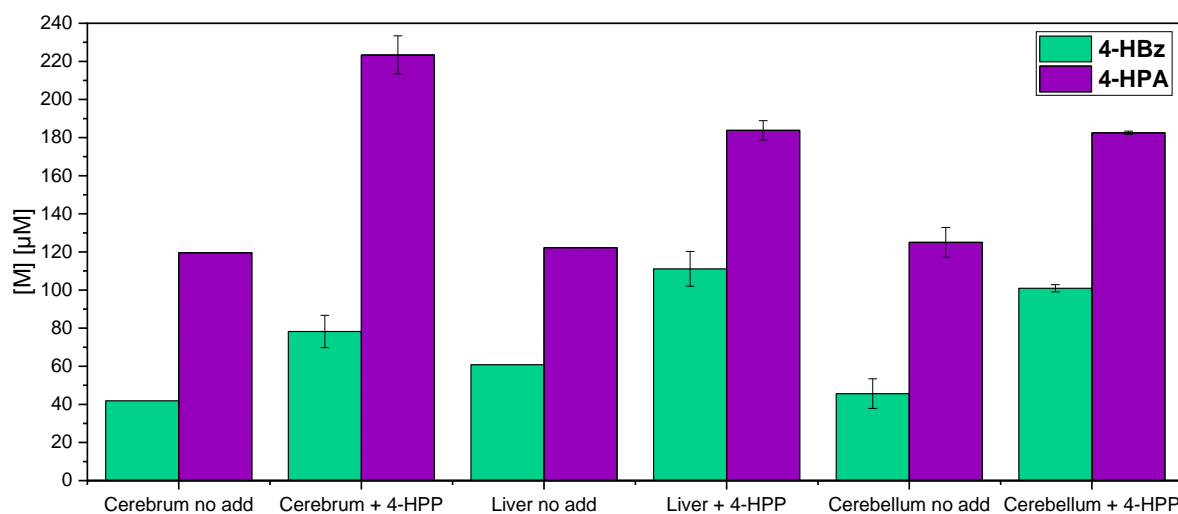
*Figure 152: Comparison of detected metabolite levels (**4-HBz** (green) and **4-HPA** (violet, dotted)) in supernatant samples obtained from mouse tissue samples of the cerebrum, the liver or the cerebellum. The mitochondria of these cells were then isolated and measured as such ("tissue type no add") or incubated with [**4-HPP**] = 2.5 mM ("tissue type + 4-HPP"). In the case of cerebrum and liver, error values stem from two independent mitochondria preparations that were incubated with **4-HPP**. In the case of cerebellum, error values stem from two (Cerebellum no add) or four (Cerebellum + 4-HPP) mitochondria preparations. Tissue preparation, incubation, and collection of supernatants performed by Dr. Stucka. Note that these measurements give absolute values and should only be compared within the shown series.*

Analysis of **4-HBz** and **4-HPA** levels in these mouse brain and liver cells yielded slightly different results for each tissue sample but a general overall trend was observed: when mitochondria are incubated with **4-HPP** levels of **4-HBz** and **4-HPA** increase (Figure 152). This indicates that all cell types possess a pathway to metabolize **4-HPP** to **4-HBz** and **4-HPP**. Taken together with the results presented above and found in the literature, HPDL is a likely candidate.

The levels observed in the samples that were not incubated with **4-HPP** were attributed to a mixture of native **4-HPP** and the proposed secondary pathway.

Interestingly, the the levels of **4-HBz** are significantly lower than those of **4-HPA**. Previously, this had only been found in samples were a loss-of-function of HPDL was observed/postulated. These samples obtained from mouse tissue were incubated in a closed 1.5 ml reaction vessel (0.5 ml sample, 1 ml air) instead of in well-ventilated containers, as were used in all previous experiments, lack of a sufficient supply of oxygen might therefore have led to this change in product distribution. As HPDL is a member of the dioxygenases and therefore requires molecular dioxygen for its correct function, the observed loss-of-function due to low levels of oxygen was counted as further evidence for the involvement of HPDL in the production of **4-HBz** and **4-HPA**. Future experiments should therefore also include a comparison of samples that were incubated with sufficient ventilation and samples that were incubated under anaerobic conditions.

Preliminary Conclusion

From the data presented in this subchapter on studies performed in *E. coli* cultures, mammalian cell lines, and organ samples it becomes apparent that HPDL is likely involved in the transformation of **4-HPP** to **4-HBz**, however, details are still elusive. The finding of high levels of **4-HBz** and **4-HPA** in HEK cells, which are essentially devoid of HPDL, suggests an alternative, HPDL-independent pathway for the biosynthesis of **4-HBz** and **4-HPA**.

In the described experiments, the intermediates **4-HBz** and **4-HPA** were regularly detected, however, the postulated successive compound **4-HB** was detected only on occasion in quantifiable amounts. This is also seen *in vivo* and probably reflects a tight downregulation of this putative harmful intermediate.[312]

Absolute and relative levels of the metabolites **4-HBz** and **4-HPA** were observed to differ upon Changing the enzymes structure. This was counted as evidence for the involvement of HPDL in the proposed transformation.

4-HPN, a compound closely related to the substrate **4-HPP** was found to inhibit the closely related HPPD but no inhibition of HPDL was noted.

4. Iron(IV)-oxido and Iron(III)-hydroxido Model Systems

The proposed reaction of **4-HPA** to **4-HBz**, potentially catalyzed by HPDL, was also studied using synthetic iron model complexes in order to gain further insight into the reactivity of this iron(II)/α-keto acid dependent enzyme. In all of the experiments described below, the racemic mixture of **4-HMA** was used instead of the naturally occurring **S-HMA**.

In a first experimental series iron(III)-hydroxido complex **C-4** and iron(IV)-oxido complex **C-6** were reacted with **4-HPA**, **4-HMA**, and **4-HBz** (Scheme 106). The obtained GC-MS trace of the reaction of **4-HPA** with **C-6** showed the presence of **4-HPA**, **4-HMA**, **4-HBz**, and **4-HB** as well as traces of an additional product tentatively identified as 2-(2,4-hydroxyphenyl)acetic acid. This side-product is rather surprising, as oxidation of a benzene ring is not regularly observed for **C-6** (refer to chapters 0, III, and IV as well as the literature[12]). The GC-MS trace of the reaction of **C-6** with **4-HMA** showed the presence of **4-HMA**, **4-HBz**, and **4-HB** and an additional signal that was assigned to 2-(4-hydroxyphenyl)-2-oxoacetic acid (**4-HMK**), the ketone derivative of **4-HMA**. This is an expected side product as such alcohol oxidations are regularly observed in iron(IV)-oxido chemistry (refer to chapters 0, III, and IV). The GC-MS trace of the reaction of **C-6** with **4-HBz** showed the presence of **4-HBz** and **4-HB**. The GC-MS traces obtained from the reaction of **C-4** with either **4-HPA** or **4-HMA** showed the presence of **4-HBz** in addition to the starting materials. Otherwise, no reactivity of **C-4** was noted. Neither **C-4** nor **C-6** were observed to react with **4-HB**. The GC-MS traces of the discussed reactions can be found in the appendix p. 405ff.
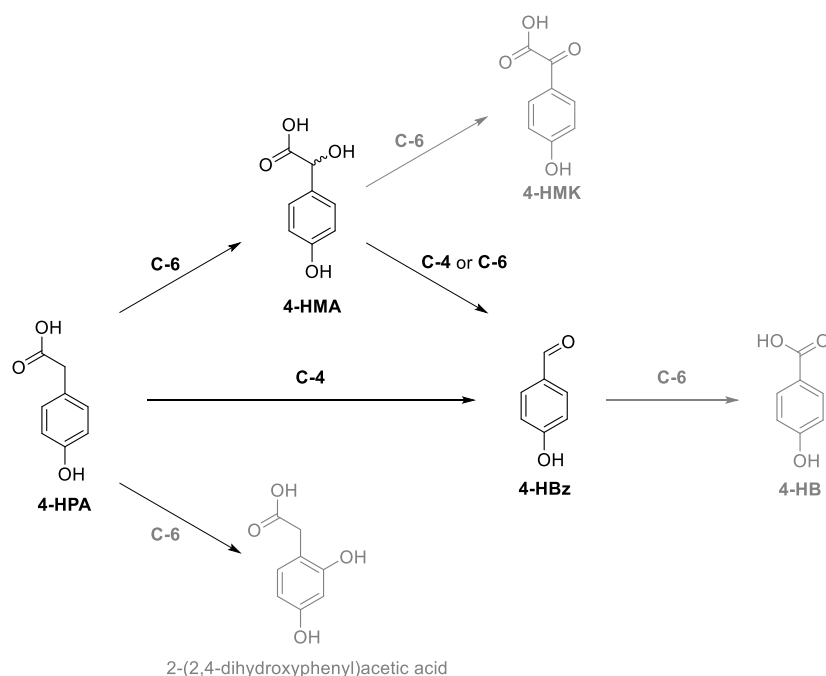
*Scheme 106: Functional model complex studies of the reactivity of **C-4** and **C-6** towards **4-HPA**, **4-HMA** and **4-HBz**. Reactions not assigned to HPDL activity are greyed out. Conditions: [**C-4/C-6**] = 8 mM, [M] = 2 mM, H₂O, 24 °C, t = 30 min. M = **4-HPA**, **4-HMA**, **4-HBz**.*

225

The hydroxylation of **4-HPA** yielding **4-HMA** is well within the expected reactivity for **C-6**, as is the reaction of aldehyde **4-HBz** to the corresponding acid **4-HB**, as these are reactions regularly observed for iron(IV)-oxido complexes (refer to chapters, 0, III, IV, and the literature[12]).

Much more interesting to the research question of this work is the step from **4-HMA** to **4-HBz**, which involves the oxidative cleavage of a carbon-carbon bond. Surprisingly, both **C-6** as well as **C-4** complex were observed to perform this reaction (Figure 153**A** and **B**).
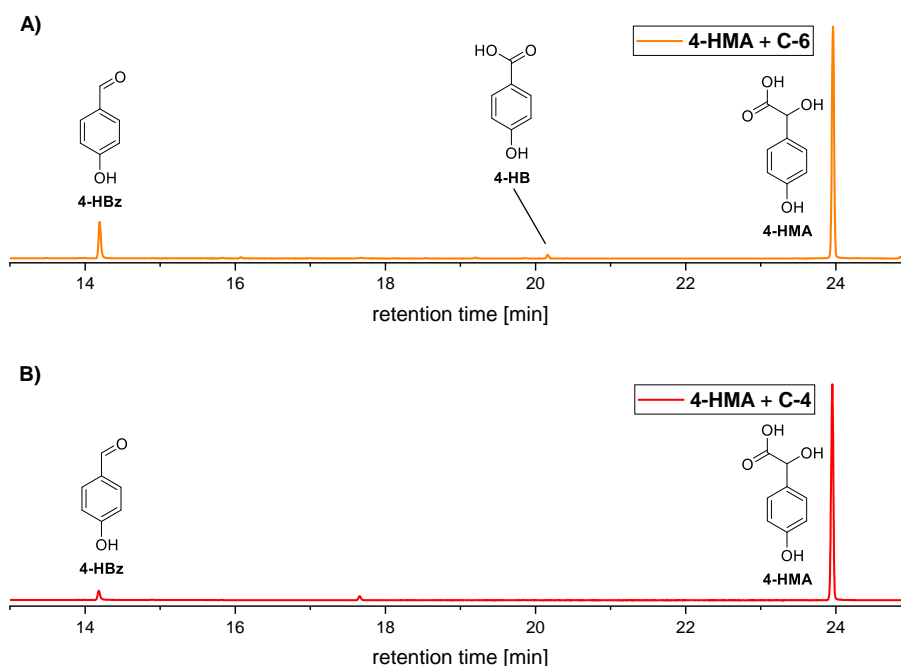
*Figure 153: **A**) Excerpt of the GC-MS trace of the reaction of **4-HMA** with **C-6** (Reaction **2**). **B**) Excerpt of the GC-MS trace of the reaction of **4-HMA** with **C-4** (Reaction **5**). Conditions: [**4-HMA**] = 2 mM, [**C-6/C-4**] = 4 mM, H_2O, 24 °C, t = 30 min. GC-MS method **C**.*

In order to obtain more data on this remarkable reactivity, a series of control reactions involving iron(II) and iron(III) salts was conducted (Scheme 107). **4-HPA**, **4-HMA**, and **4-HBz** were reacted with either $Fe^{II}(mecn)_2(OTf)_2$ or $Fe^{III}(OTf)_3$ alone or with a mixture of $Fe^{II}(mecn)_2(OTf)_2/H_2O_2$ to achieve Fenton chemistry conditions. These Fenton conditions led to unspecific decomposition of all substrates (GC-MS traces not shown).
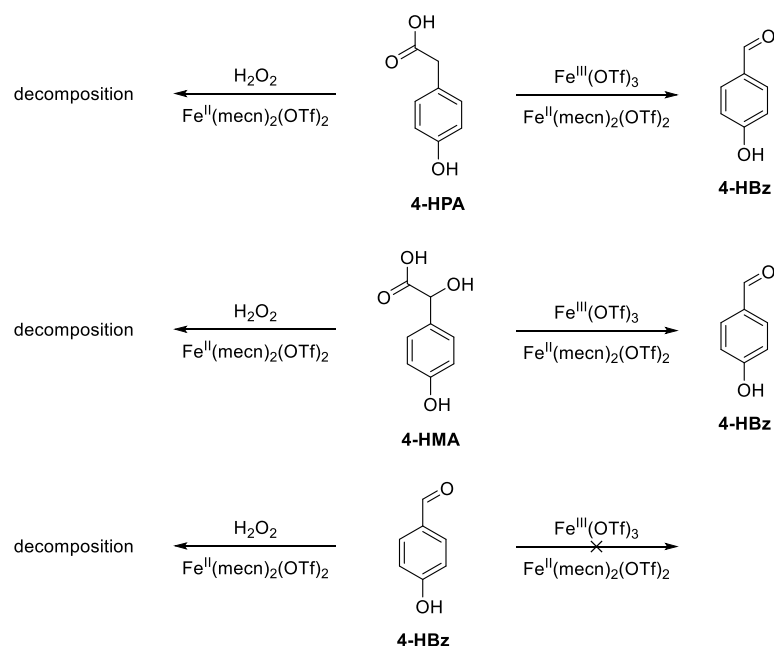
*Scheme 107: Reactions of **4-HPA**, **4-HMA**, **4-HBz** with the iron salts Fe^{II}(mecn)$_2$(OTf)$_2$ (+ H$_2$O$_2$) and Fe^{III}(OTf)$_3$. All reactions were performed under ambient conditions. Conditions: [Fe^{2+}/Fe^{3+}] = 8 mM, [M] = 2 mM, H$_2$O, 24 °C, t = 30 min. M = **4-HPA**, **4-HMA**, **4-HBz**.*

In all reactions containing **4-HPA** or **4-HMA** with either Fe^{II}(mecn)$_2$(OTf)$_2$ or Fe^{III}(OTf)$_3$ **4-HBz** was detected using GC-MS. In the case of Fe^{III}(OTf)$_3$, this is surprising and shows, that the ligand environment of **C-4** is not necessary for this reaction. For Fe^{II}(mecn)$_2$(OTf)$_2$, this observed reactivity is unusual, as the reaction from either **4-HPA** or **4-HMA** to **4-HBz** requires an oxidation step – a reactivity usually not ascribed to iron(II). However, as these experiments were performed under ambient conditions, the iron(II) ions in solution were probably oxidized to iron(III) by dioxygen from the air.

Therefore, another series of experiments was conducted to control for the influence of air on the observed reactivities (Scheme 108). It was found that the absence of oxygen only affected the reactivity of Fe^{II}(mecn)$_2$(OTf)$_2$: no additional products beside the starting material (either **4-HPA**, **4-HMA**, or **4-HBz**) were detected. The outcome of all other reactions (either Fe^{III}(OTf)$_3$ or **C-4**) remained unchanged. **C-6** was excluded from these experiments, as preparation of **C-6** in the glove box is cumbersome.
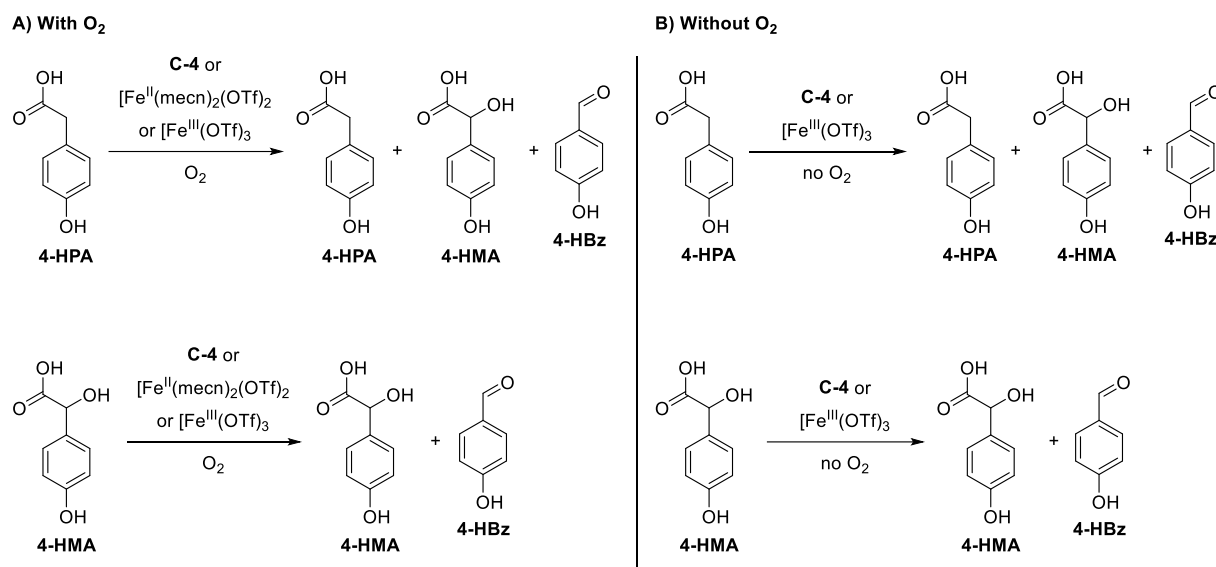
*Scheme 108: Overview of the reactivity of **4-HPA** and **4-HMA** with **C-4**, Fe^{II}(mecn)_2(OTf)_2, and Fe^{III}(OTf)_3 **A)** with and **B)** without molecular oxygen. For the corresponding GC-MS traces please refer to the appendix p. 405ff. Conditions: [**C-4**/Fe^{2+}/Fe^{3+}] = 8 mM, [M] = 2 mM, H_2O, 24 °C, t = 30 min. M = **4-HPA**, **4-HMA**, **4-HBz**.*

In these experiments it was found that the iron(II) salt Fe^{II}(mecn)_2(OTf)_2 does indeed not react with any of the tested substrates if oxygen is excluded from the reaction. However, both **C-4** and Fe^{III}(OTf)_3 still reacted with **4-HPA** and **4-HMA** forming the previously observed products (**4-HMA** in the case of **4-HPA** as starting material and **4-HBz** for both starting materials).

As mentioned above, **C-6** was also observed to mediate the reaction from **4-HMA** to **4-HBz**. However, another explanation of this observed behavior might be that the reaction is actually performed by traces of **C-4**, which has been observed under several conditions to perform this reaction. As shown in chapter IV.3, **C-4** is formed from **C-6** in the presence of any organic substrate by a comproportionation reaction with the intermittently formed **C-2**. Therefore, the following reaction scheme would be possible without **C-6** mediating the transformation of **4-HMA** to **4-HBz** directly: **4-HMA** could have reacted with **C-6** to form **4-HMK** and **C-2**. **C-2** then comproportionated with another equivalent of **C-6** to form **C-4**. **C-4** then reacts with **4-HMA** to **4-HBz**, as has been observed in reactions including only **C-4** and **4-HMA**. This likely results in the formation of **C-2**, which could comproportionate again to form more **C-4**. Similarly, **4-HBz** reacts with residual **C-6** to form **4-HB**, which also generates **C-2** (Scheme 109).

As **C-2** is a likely product of the reaction of **C-4** with **4-HPA**/**4-HMA**, the reaction could well become auto-catalytic after an initial lag period. To confirm this, further experiments are necessary, e.g. the detection of **C-2** in reactions of **4-HMA** with **C-4** to **4-HBz**.
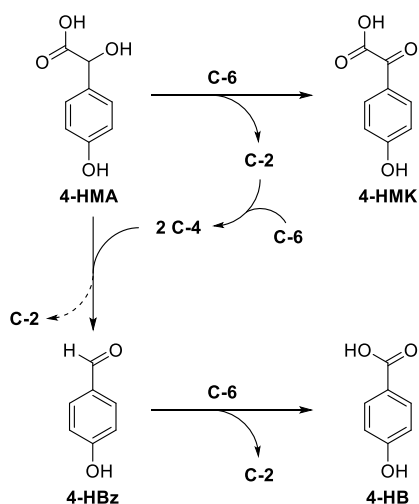
*Scheme 109: Reaction of **4-HMA** with **C-6** to form **4-HMK** and **C-2**. **C-2** comproportionates with another equivalent of **C-6** to form **C-4**. **C-4** reacts with **4-HMA** to form **4-HBz** which is subsequently converted to **4-HB**, forming another equivalent of **C-2**.*

Taken together it becomes obvious that the reaction from either **4-HPA** or **4-HMA** can be mediated by an iron(III) compound, or more specifically an iron(III)-hydroxido complex (**C-4** or $Fe^{III}(OTf)_3$). This is a remarkable result and requires further experiments: for example, additional iron(III)-hydroxido or iron(III)-oxido complexes, such as **C-15** (refer to chapter V.4), **C-21** (refer to chapter V.5), or iron(III)-hydroxido complexes of **L-3, L-4, L-5**, and **L-6** (refer to chapter V.4) should be synthesized and tested in this transformation. Especially the efficacy in the mediation of this reaction should be monitored, this could give valuable insight into such reactivity. In general, kinetic investigations of this type of reactions might provide useful insight, for example into the proposed auto-catalytic nature of the reaction of traces of **C-4** in reactions of **C-6** with **4-HPA/4-HMA**.

Sligar *et al.* postulated that iron(III) species of heme enzymes might also be catalytically active – in addition to the more commonly mentioned iron(IV)-oxido species. Additionally, Paine et al. proposed a mechanism based on the interaction of an iron(II) species with molecular dioxygen for the C-C-bond cleavage of α-keto acids (refer to chapter VI.1).[326] However, as the data presented in this subchapter does not indicate the necessity for molecular dioxygen but rather suggests the involvement of an iron(III)-hydroxido species, another mechanism is possible and even likely. A hypothetical mechanism was postulated (Scheme 110) based on the results described in the present chapter and chapter IV. The proposed mechanism might provide orientation of an explanation of the reactivity observed for **4-HMA** with iron(III)-hydroxido species.
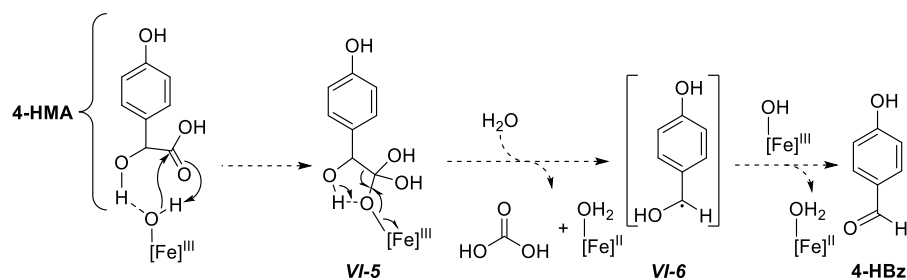
*Scheme 110: Postulated mechanism for the reaction of an iron(III)-hydroxido species with **4-HMA** based on the work of Sligar[332] as well as results described in the present chapter and chapter IV.*

In the first step, the iron(III)-hydroxido moiety attacks the carboxy carbon atom on **4-HMA**, a proton is transferred from the iron species to the substrate (***VI-5***). Now, the carbon-carbon bond in the substrate as well as the iron-oxygen bond are homolytically broken, resulting in the formation of a carbon-centered radical (***VI-6***). This radical does bear some resemblance to the structure **III** in Figure 131 on p. 199. Another iron(III)-hydroxido species could then react with ***VI-6*** in a rebound reaction to form (a hydrated version of) the product **4-HBz**.

Of course, at this point this proposed mechanism is highly speculative. However, it might provide a basis for further studies (for an overview of proposed future experiments see chapter VIII).

VII. PMS, PES, and Wurster's Blue – A Short Mass Spectrometric Investigation

1. Introduction and State of the Art

Lanthanides in Biochemistry

For a long time, lanthanides were believed to be mostly biologically irrelevant – this was often attributed to their low bioavailability, as most lanthanide salts (e.g. phosphates) are insoluble in water. However, in the first half of the last decade, several revolutionary discoveries were made: multiple bacterial strains (*Methylobacterium radiotolerans, Methylorubrum (formerly Methylobacterium) extorquens* AM1*, Bradyrhizobium sp.*, and *Methylacidiphilum fumariolicum* SolV) were observed to grow in a strictly lanthanide dependent manner (Table 16). These bacteria are methylotrophs, meaning they utilize reduced one-carbon substrates such as methane or methanol as an energy source. Oxidation of methane is usually achieved with the help of methane monooxygenases whereas oxidation of methanol is facilitated by methanol dehydrogenases (MDH).

A significant discovery was made when lanthanide levels in the Gulf of Mexico were analyzed after the DeepWater Horizon (DWH) oil platform catastrophe in 2010. Interestingly, levels of several lanthanides were found to be depleted compared to levels prior the catastrophe (Table 16). This was later attributed to a bloom of bacteria that utilized the escaped natural gas and in turn depleted levels of La, Ce, Pr, and Nd in the region.[333]

Table 16: Growth of M. extorquens *AM1 or* M. fumariolicum *SolV in the presence of several lanthanides[334–336] and depletion of lanthanide levels in the Gulf of Mexico after the Deep Water Horizon (DWH) catastrophe in 2010.[333] AM1 =* Methylorubrum extorquens *AM1; SolV =* Methylacidiphilum fumariolicum *SolV. Adapted from L. Daumann.[337]*
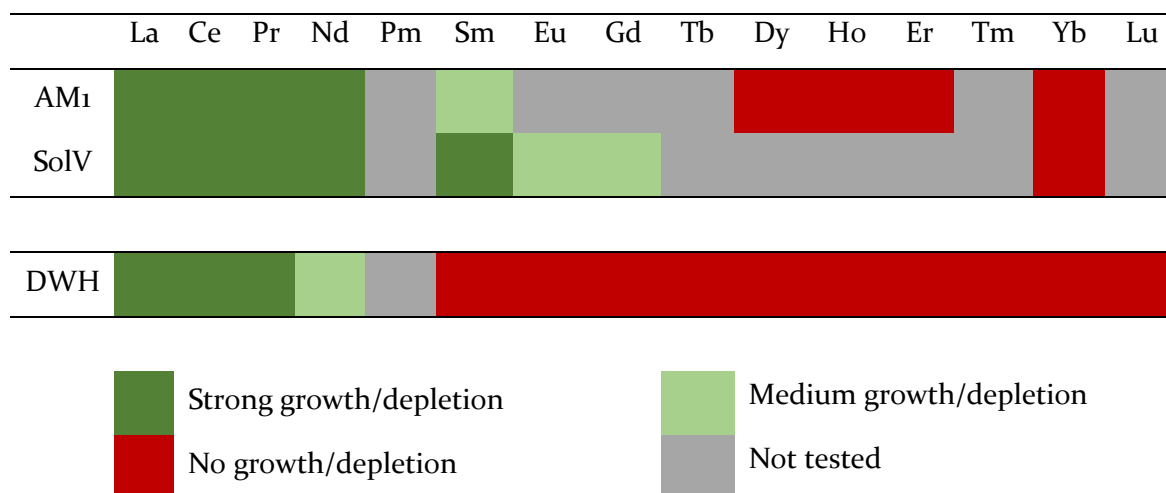
MDH Enzymes

MDH enzymes catalyze the oxidation of methanol to formaldehyde (Figure 154**A**), using a metal ion (Ca²⁺ or Ln³⁺) and pyrroloquinoline quinone (PQQ) as co-factors. In the case of lanthanides, formaldehyde is further oxidized to formic acid.[335,337–340] MDH enzymes have been known since 1964, however, only calcium had been identified as a co-factor until recently.[338,339] In 2004, a

231

study by Lim and Franklin implied that lanthanides might also serve as metals for MDH enzymes – this was, however, disregarded due to lanthanides low bioavailability.[341] With the discovery of lanthanide-dependent bacteria, interest was rekindled and a publication by Pol *et al.* revealed what had been suspected: MDH enzymes are capable of using lanthanide ions as co-factor (Figure 154**B**).[340,342] Calcium-dependent MDH enzymes were found to be encoded by the *mxaF* gene,[338,339] whereas lanthanide dependent MDH enzymes are expressed from the *xoxF* gene.[343,344] Genetic analyses revealed that the *xoxF* gene is found in a wide range of microorganisms[337] – it is even more widespread and probably evolutionary older that its *mxaF* counterpart.[345] Some microorganisms were found to carry both the *mxaF* and *xoxF* gene; upregulation of *xoxF* with simultaneous downregulation of *mxaF* in the presence of nanomolar concentrations is referred to as the "lanthanide switch".[337,346–349]
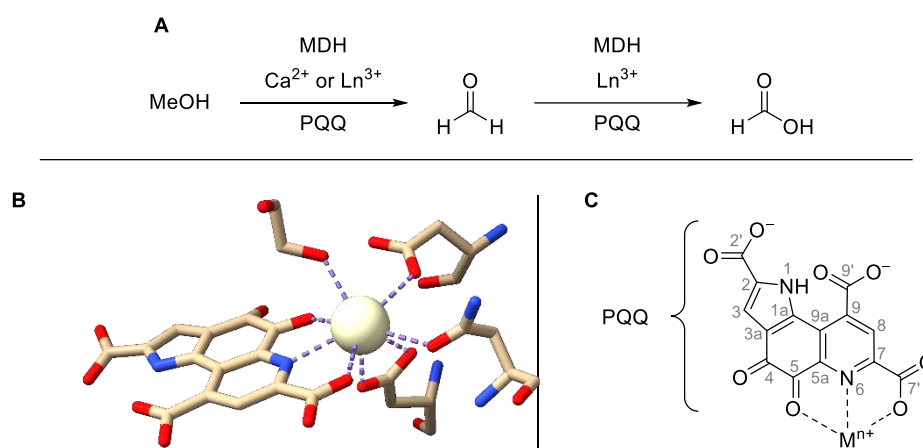
*Figure 154: **A**) Enzymatic transformation of methanol (MeOH) to formaldehyde and formic acid by the MDH enzyme with calcium or lanthanide ions and pyrroloquinoline quinone (PQQ).[338,339,345] **B**) Graphical representation of the active site in one of the monomers in the crystal structure of Ce-MDH from SolV. The structure was optimized for Ce, however, different lanthanide ions were identified in the enzymes active site due to the use of mudpot water for bacteria cultivation. PDB ID: 4MAE **C**) Structure of the co-factor PQQ binding to a non-specified metal. Numbering system according to Unkefer et al.[350]*

Two mechanisms are currently discussed for the MDH mediated oxidation of methanol to formaldehyde: the hemiketal mechanism (Scheme 111**A**) and the hydride transfer mechanism (Scheme 111**B**). In the hemiketal mechanism, methanol directly attacks the carbon atom at position 5 (for the numbering system refer to Figure 154**C**) forming a hemiketal (***VII-1***, Scheme 111**A**). Rearrangement involving the pyrrole moiety leads to the formation of an enolate (***VII-2***) which abstracts a proton from methanol to release the product formaldehyde and form the reduced form of the PQQ co-factor, PQQH₂ (***VII-3***). In the hydride transfer mechanism, methanol is deprotonated *via* a nearby aspartate residue and a hydride is transferred to position 5 of PQQ (***VII-4***). Subsequent rearrangement and deprotonation/protonation steps led to the formation of PQQH₂ (***VII-6***, last proton transfer step not shown).[345,351–357]

For *xoxF*, computational and functional model complex studies suggested the hydride transfer mechanism to be more likely, however, more data, especially in an enzymatic context, is still necessary to confirm this.[358,359]
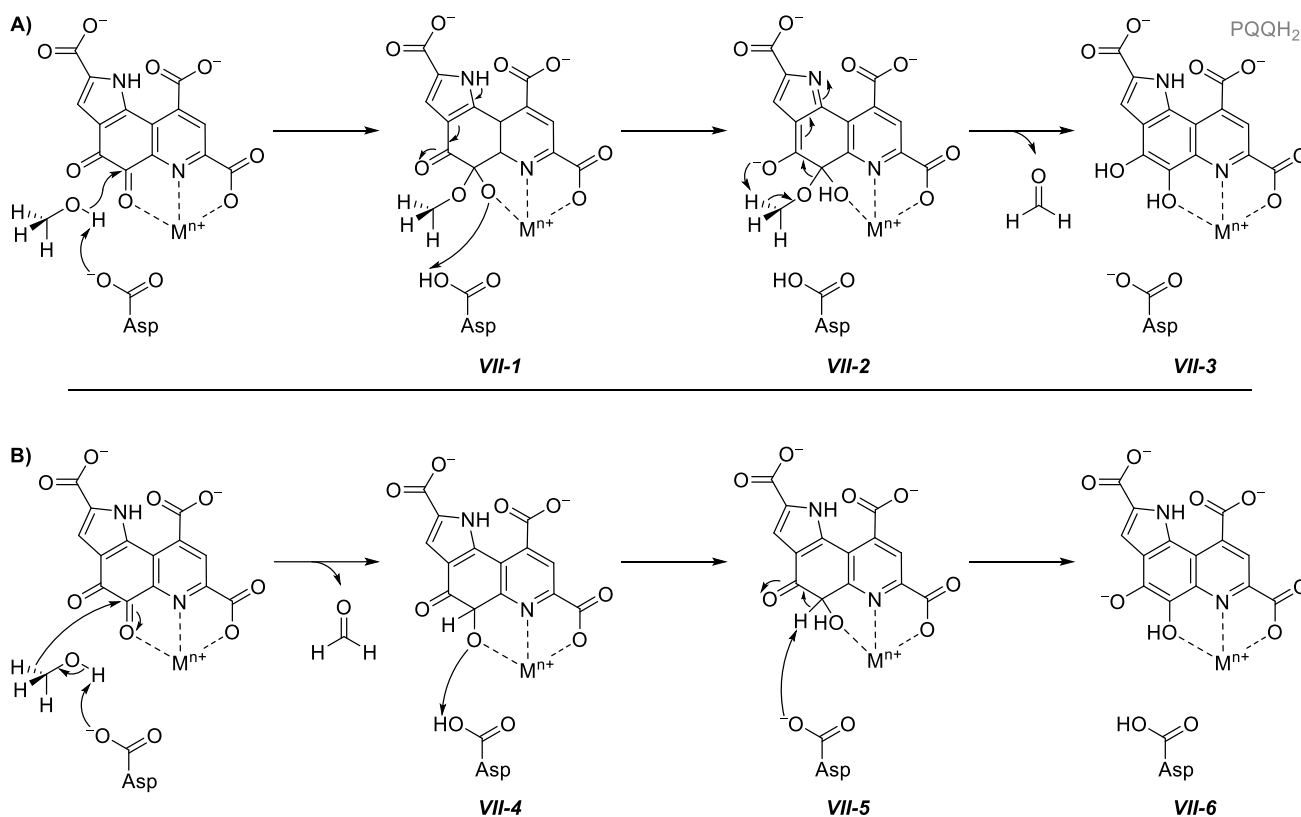
Scheme 111: **A)** Hemiketal mechanism for the PQQ/MDH mediated oxidation of methanol to formic acid. Deprotonation and subsequent protonation of the pyrrole nitrogen is not shown for sake of clarity. **B)** Hydride transfer mechanism for the PQQ/MDH mediated oxidation of methanol to formic acid.[345,358–360]

Artificial Electron Acceptors

In nature, PQQH$_2$ is subsequently oxidized to PQQ by the electron carrier cytochrome c$_L$.[345] In *in vitro* studies of MDH enzymes, a range of electron acceptors (EAs) have been used, including the synthetic phenazine derivatives phenazine methosulfate (**PMS**) or phenazine ethosulfate (**PES**),[335,338,339] Wurster's Blue (*N,N,N',N'*-tetramethyl-*p*-phenylenediamine radical, **WB**)[361,362] beside the natural cytochrome c$_L$.[339,362–364] The use of artificial EAs such as **PMS** and **PES** is coupled to the redox dye 2,6-dichlorophenolindophenol (DCPIP), its oxidized form ***VII-8*** (Figure 155) shows a strong absorption at λ = 600 nm, which can be used in UV-vis assays to determine the activity of MDH. Figure 155 shows how the oxidation of the substrate methanol to formaldehyde by MDH leads to reduction of PQQ to PQQH$_2$. The subsequent regeneration of PQQH$_2$ to PQQ is then achieved by **PES** or **PMS**, which are reduced to the corresponding phenazine derivative ***VII-7***, which is then in turn oxidized by ***VII-8*** (shown in blue for its distinctive blue color) to yield DCPIP. If **WB** is used as an oxidative agent to regenerate PQQ, no additional dye needs to be added, as **WB** itself shows a strong absorption at λ = 550-650 nm.[365]
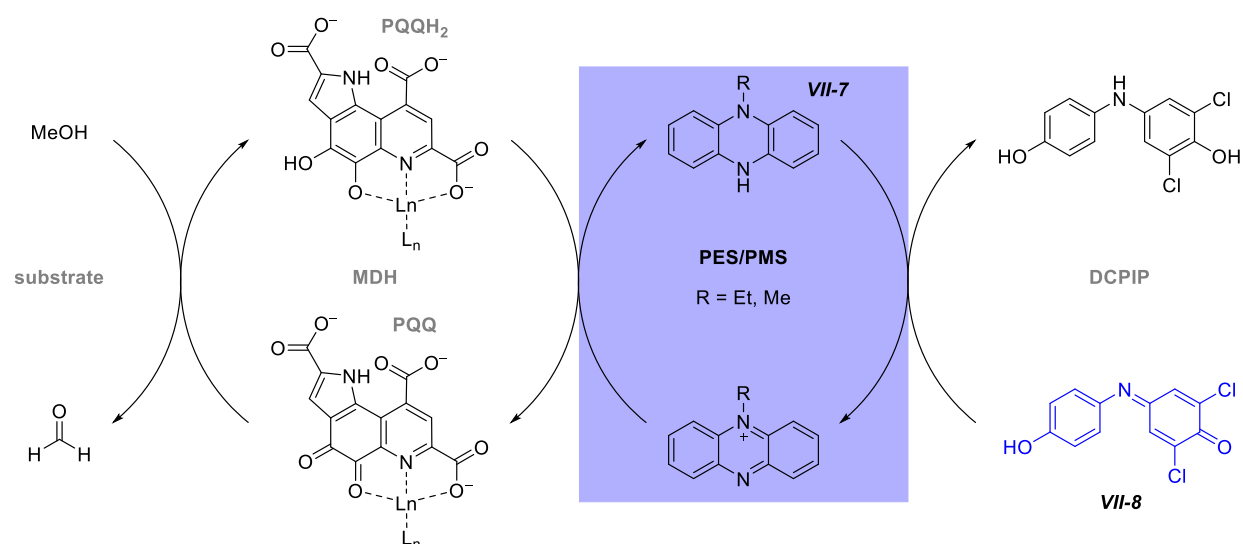
Figure 155: Proposed in vitro *reaction mechanisms in the study of MDH enzymes: the substrate methanol (MeOH) is oxidized by MDH to formaldehyde, thereby PQQ is transformed to PQQH$_2$. This is then oxidized by the artificial electron acceptors PMS or PES (R = Me or Et, respectively). DCPIP, a redox dye, is then coupled to this step and the absorption of the oxidized DCPIP (**VII-8**, in blue) is monitored in UV-vis experiments. MDH = methanol dehydrogenase, PQQ = pyrroloquinoline quinone, PQQH$_2$ = 4,5-dihydroxy-1H-pyrrolo[2,3-f]quinoline-2,7,9-tricarboxylate, PES = phenazine ethosulfate, PMS = phenazine methosulfate, DCPIP = 2,6-dichlorophenolindophenol.*

2. Motivation and Aim

Artificial EAs such as **PMS**, **PES**, and **WB** (Chart 18) enable the facile study of MDH enzymes *in vitro*, as no additional enzymes (such as cytochrome c_L) must be isolated and stored. However, several side-reactions were reported when **PMS** or **PES** were used in MDH assays. Day and Anthony noted in 1990 that "An important and often confusing characteristic of most MDH is their activity in the absence of added substrate.". They also state that "This activity requires the presence of activator (ammonia), […], and its initial rate is the same as that with added substrate".[366]
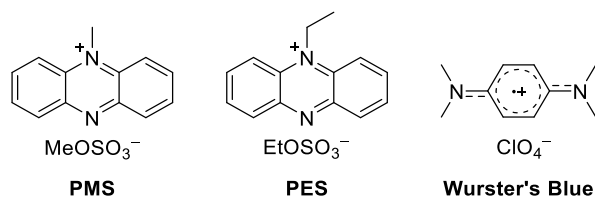
Chart 18: Artificial electron acceptors (EAs) in MDH assays studied in this work.

Therefore, studying the behavior of **PMS**, **PES**, and **WB** during preparation, storage, and under assay conditions would contribute to finding more reliably assay conditions and hence obtain clearer data on the activity of MDH. Analysis using HR-MS after exposure to several different conditions (oxygen, common additives such as ammonia and potassium cyanide, heat) would give insight into background reactions and decomposition of these artificial EAs (Figure 156). These HR-MS experiments would be completed by EPR and UV-vis assay measurements, performed by my colleagues Bérénice Jahn and Helena Singer.
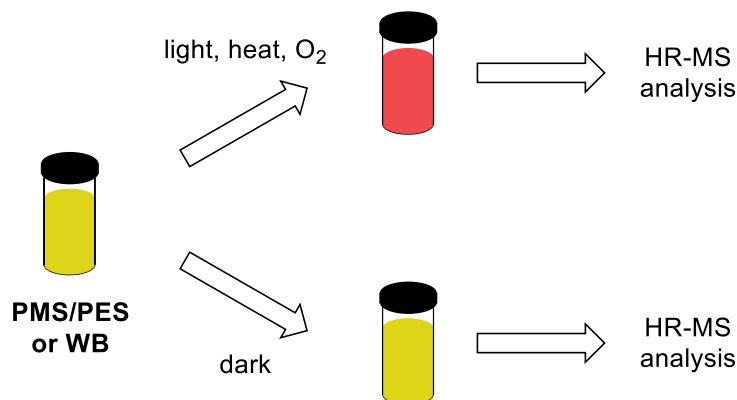
Figure 156: Experimental setup for the HR-MS analysis of PES/PMS/WB samples after exposure to light, heat, O₂ and comparison with a sample that was kept in the dark as much as possible.

3. Phenazine Methosulfate and Phenazine Ethosulfate – PMS and PES

Phenazine Methosulfate – PMS

PMS was dissolved in unbuffered water and exposed to eight different conditions in two sets of experiments of four samples each: aerobic (O_2 was added) and anaerobic (samples strictly handled under an atmosphere of nitrogen). Two samples of each set were kept in the dark, whereas the other two samples were exposed to daylight. Of each two sample sets, one was cooled to 0 °C whereas the other was heated to 45 °C (the assay temperature most often used in our laboratories). The samples were taken after 1 h and 2.5 h, diluted, stored at 0°C in the dark until they were injected into a Thermo Fisher Orbitrap. In these measurements up to four distinct signals were detected: 188.128 m/z, 195.092 m/z, 210.110 m/z, and 211.086 m/z. These were tentatively assigned to **PMS** (195.092 m/z) and pyocyanin (211.087 m/z, Figure 157**B**), a literature-known decomposition product of **PMS**.[367] To confirm this assignment, pyocyanin was synthesized according to McIlwain *et al.* (for experimental details, refer to the appendix p. 349).[367] The signals at 188.128 m/z and 210.110 m/z were not assigned to any known compound.
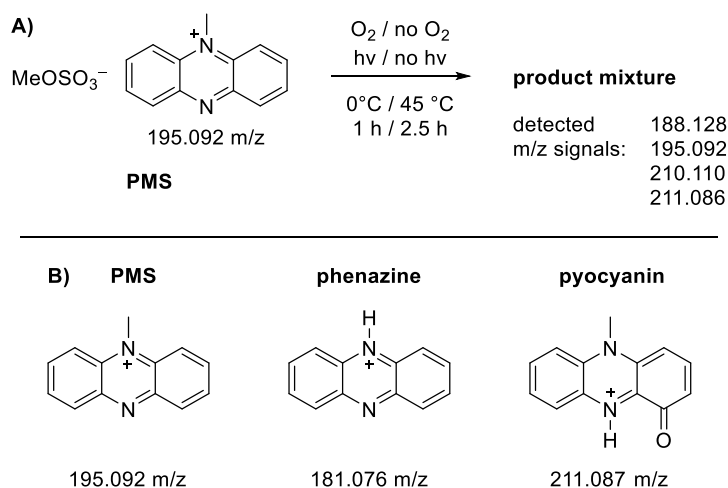
*Figure 157: **A)** **PMS** was exposed to different conditions and the product mixture analyzed using mass spectrometry. **B)** Structures and exact masses of the cations of **PMS**, phenazine (as its protonated derivative), and pyocyanin (as its protonated derivative). **PMS** = phenazine methosulfate.*

The results of these HR-MS experiments are shown in Table 17, the most intensive signal is highlighted in bold and given 100% abundance, all other signals are given in relation. No direct quantitative evaluation can be performed due to possibly different ionization potentials, but qualitative trends can be observed and described.

Generally, it was observed that the anaerobic samples show a greater variety in detected m/z signals than the aerobic samples. Whereas in most cases of the aerobic samples one or two signals are dominant and the other signals are detected within 0%-30% relative abundance, in the case of the anaerobic experiments a broader distribution is observed.

*Table 17: Results of the exposure of **PMS** to the conditions described in Figure 157.*

reaction time [h]	temperature [°C]	m/z signals	Relative Abundance [%]				Tentative Assignment
			aerobic		anaerobic		
			light	dark	light	dark	
1	0 °C	188.128	7	3	23	19	-
		195.092	96	**100**	**100**	**100**	**PMS**
		210.110	7	0	40	33	-
		211.086	**100**	5	4	6	pyocyanin
	45°C	188.128	78	12	70	40	-
		195.092	30	**100**	79	**100**	**PMS**
		210.110	46	12	**100**	70	-
		211.086	**100**	4	63	78	pyocyanin
2.5	0 °C	188.128	7	3	14	15	-
		195.092	3	**100**	52	**100**	**PMS**
		210.110	5	1	23	31	-
		211.086	**100**	7	**100**	8	pyocyanin
	45°C	188.128	28	2	23	17	-
		195.092	6	**100**	11	**100**	**PMS**
		210.110	23	0	28	27	-
		211.086	**100**	5	**100**	7	pyocyanin

Regarding exposure to daylight, a trend can be observed for all experiments: when a sample is kept in the dark, the signal assigned to **PMS** is the most dominant, often with only marginal amounts detected at the other three m/z ratios. Whereas if a sample is exposed to daylight, the signal assigned to pyocyanin is usually the most abundant, often by a great margin. The only exception is the anaerobic sample exposed to daylight that was kept at 0 °C for 1 h, here the signal **PMS** remains the most intensive. After a reaction time of 2.5 h, the signal at 210.110 m/z becomes the most abundant, which is also not observed for any other sample.

In the literature **PMS** has often been characterized as light sensitive; the presented data clearly supports this claim.[367] The collected data also shows that raised temperatures seem to accelerate the light-induced decomposition, even though the trend is not as clear. Moreover, the absence of oxygen seems to have only a minimal effect on PMS stability, as the **PMS** signal at 195.092 m/z is one of the minor signals in all samples handled under an inert atmosphere but exposed to light (column 3 of Table 17). However, it can be noted that the exclusion of oxygen leads to a more even distribution of obtained signals across the four detected m/z ratios.

In a second series of mass spectrometry experiments, we investigated the influence of the individual components of the **PMS** assay. As mentioned above, potassium cyanide and ammonia are often added to MDH for storage or activation.[362] However, both cyanide and ammonia have been reported to react with **PMS**.[367]

Exact Mass: 210.103   Exact Mass: 220.087
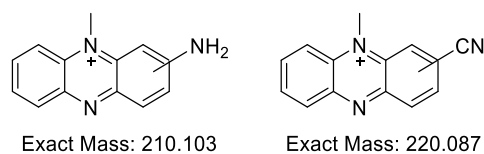
*Chart 19: Products of the reaction of **PMS** with ammonia and cyanide, according to the literature.[367]*

Firstly, **PMS** was reacted with ammonia and cyanide at room temperature, both in the dark and in daylight. Samples were collected after 100 min and 300 min and analyzed using HR-MS. Across all samples, four distinct signals were detected: 181.076 m/z, 195.092 m/z, 210.089 m/z, and 211.086 m/z. The signal at 181.076 m/z was assigned to phenazine, this was corroborated by measuring a commercial sample of phenazine. The signals at 195.092 m/z and 211.086 m/z were, as previously, assigned to **PMS** and pyocyanin, respectively. The obtained results can be found in Table 18.

*Table 18: Results of the reaction of **PMS** with potassium cyanide (KCN) and ammonia (NH$_3$).*

reaction time [min]	reactant	m/z signals	Relative Abundance [%]		Tentative Assignment
			light	dark	
100	KCN	181.076	30	98	phenazine
		195.092	15	**100**	**PMS**
		210.089	13	23	-
		211.086	**100**	18	pyocyanin
	NH$_3$	181.076	71	**100**	phenazine
		195.092	4	34	**PMS**
		210.089	0	0	-
		211.086	**100**	9	pyocyanin
300	KCN	181.076	95	**100**	phenazine
		195.092	23	0	**PMS**
		210.089	31	1	-
		211.086	**100**	7	pyocyanin
	NH$_3$	181.076	91	**100**	phenazine
		195.092	0	0	**PMS**
		210.089	0	0	-
		211.086	**100**	7	pyocyanin

In addition to these four signals, another signal was detected at 220.087 m/z which can be ascribed to the structure shown in Chart 19 on the right. This was detected in the reaction of **PMS** with potassium cyanide at room temperature in daylight, both after 100 min and 300 min this signal was observed as a minor peak with around 40-50% relative abundance. A signal corresponding to the left structure in Chart 19, as has been described in the literature, was detected in the reaction of **PMS** with ammonia in the light after 100 min and 300 min, though only as a minor signal with a relative abundance of 6% and 16%, respectively.[367] If light was excluded, neither of these two signals was detected.

In all cases the signal at 181.076 m/z is detected as a major peak, corresponding to the demethylation product phenazine. Additionally, a signal corresponding to pyocyanin (211.086 m/z) was detected in all samples, although most prevalent in the experiments exposed to light.[367]

All of these experiments taken together paint a clear picture of **PMS** stability in aqueous systems. Exposure to light leads to at least partial if not complete decomposition of PMS giving mostly pyocyanin. Handling PMS under exclusion of light drastically enhances stability, even in an oxidizing atmosphere and in elevated temperatures. However, if either ammonia or cyanide are added, PMS was observed to decompose under loss of the methyl group, probably giving phenazine.

Phenazine Ethosulfate – PES
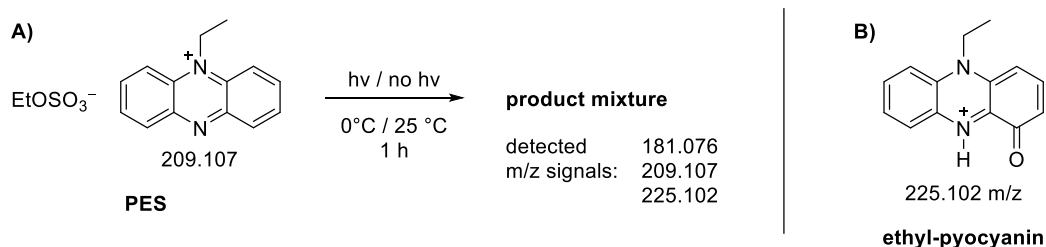
Figure 158: *A) HR-MS experiments of the decomposition of **PES** under different conditions. B) Proposed structure of ethyl-pyocyanin, a decomposition product of **PES**. **PES** = phenazine ethosulfate.*

As mentioned above, **PES** is also used as an artificial EA. Thus, the behavior of **PES** in aqueous solutions under the influence of daylight was also investigated (Figure 158). Similar to the experiments with **PMS**, aqueous solutions of **PES** were exposed to daylight and performed control reactions in the dark, both at room temperature and at 0 °C. Experiments on the effect of oxygen and longer reaction times were deemed unnecessary, as more realistic assay conditions were to be simulated and the influence of oxygen had been shown to be negligible on the decomposition of **PMS** (*vide supra*).

Table 19: *Results of the reaction of **PES** in daylight and in the dark at different temperatures.*

reaction time [min]	temperature [°C]	m/z signals	Relative Abundance [%]		Tentative Assignment
			light	dark	
60	0	181.076	-	0	phenazine
		209.107	-	**100**	**PES**
		225.102	-	2	Et-pyocyanin
	25	181.076	<1	<1	phenazine
		209.107	27	**100**	**PES**
		225.102	**100**	2	Et-pyocyanin

PES was previously reported to be more stable than **PMS** and less prone to dealkylation.[367] As can be seen in Table 19, the collected HR-MS data fits this observation: PES decomposes mainly to a species with 225.102 m/z, while phenazine (181.076 m/z) is detected only in traces. The observed signal at 225.102 m/z was tentatively assigned to ethyl-pyocyanin (proposed structure shown in Figure 158).

Additionally, HR-MS analysis was conducted of a complete assay mixture containing 1 mM **PES**, 100 μM DCPIP, and 20 μM EuCl$_3$ which was dissolved in 20 mM PIPES. The sample was conditioned at 45 °C for 15 min and always kept in the dark, as would be if it was to be used for assay experiments with MDH enzymes. As can be seen in Figure 159, hardly any oxidation (~1%) and no de-ethylation of **PES** was observed under these conditions.
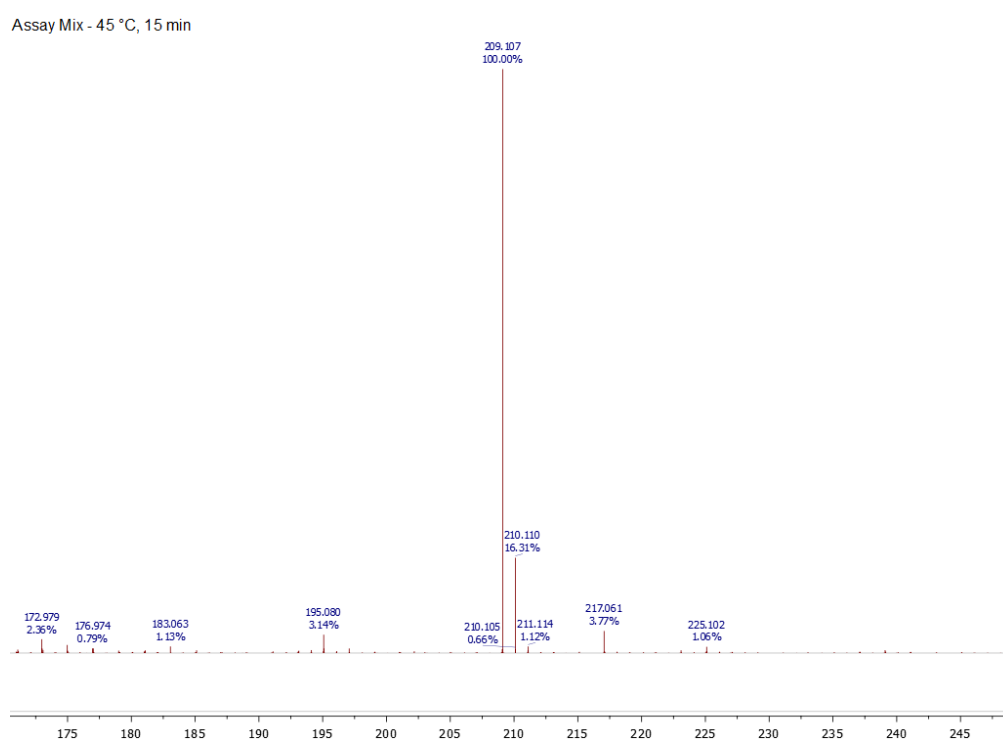
Figure 159: Mass spectrum collected of an assay mixture that had been conditioned at 45 °C for 15 min under exclusion of light, as is the normal procedure for these types of assays.

4. Wurster's Blue – WB

In addition to the phenazine-base artificial EAs **PMS** and **PES**, Wurster's Blue (WB) was also investigated in its decomposition behavior. **WB** refers to the mono-cationic radical of *N,N,N',N'*-tetramethyl-p-phenylenediamine, it was synthesized as the corresponding perchlorate salt (Figure 160**A**). Of particular interest was the storage stability of **WB** in aqueous solution, therefore, HR-MS measurements were performed after 150 min and 21 d of storage while the sample was kept in the dark for the entire time.
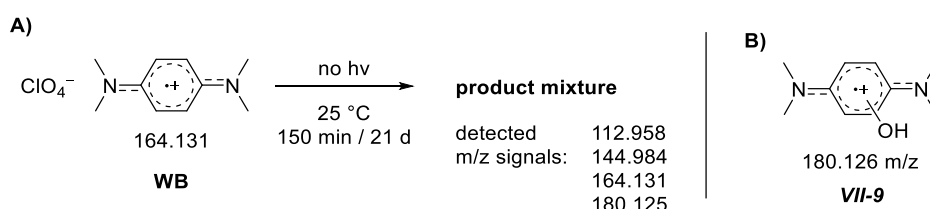
*Figure 160: **A**) HR-MS experiments of the decomposition of **WB** under different conditions. **B**) Proposed structure for a decomposition product of **WB** (**VII-9**).*

As evident from Table 20, the samples of **WB** showed some decomposition after 150 min of storage, however, this is significantly more pronounced after 21 d. After 150 min, a signal was detected at 180.125 m/z which was tentatively assigned to the structure shown in Figure 160**B**. This signal was then only observed in traces after 21 d of storage, this is proposed to be the result of further decomposition.

This analysis shows that aqueous solutions of **WB** cannot be stored in water at room temperature for significant amounts of time. Stock solutions should be prepared on a daily level and stored at 0 °C during the measurements.

*Table 20: HR-MS results of the storage of **WB** for 150 min and 21 d.*

reaction time	temperature [°C]	m/z signals	Relative Abundance [%]	Tentative Assignment
150 min	**25**	112.958	9	
		144.984	15	
		164.131	**100**	**WB**
		180.125	14	*VII-9*
21 d	**25**	112.958	58	
		144.984	**100**	**WB**
		164.131	6	
		180.125	>1	*VII-9*

VIII. Summary and Outlook

The main aim of this work was successfully accomplished: the study of the synthetic iron(IV)-oxido complex **C-6** as a functional model for TET enzymes. During these studies, the iron(III)-hydroxido species **C-4** was identified as the intermediate *and* product of the reaction of **C-6** with organic substrates – as the thereby formed iron(II) complex comproportionates with **C-6** to form **C-4**. In addition, the model complex platform was expanded to include several new iron(IV)-oxido, iron(III)-hydroxido, and iron(II) complexes to further investigate iron(II)/α-keto acid dependent enzymes, in particular TET and HPDL. These results were described in chapters III-VI, a short summary and outlook is given below. A summary of the massspectrometric investigation of the artificial electron acceptors PMS, PES, and WB is also presented below.

TET Functional Model

The main project of this work was to use the previously identified functional model complex **C-6** in detailed studies with the epigenetically relevant substrate **5mC**, its derivatives, and other related compounds and thereby gain insight into the functionality of TET enzymes. The first step of this project consisted of studying the reactivity of **C-6** towards the free nucleobase **5mC** using GC-MS and UV-vis kinetics. In these investigations, a second-order rate law was found for this reaction and the HAT, performed by the iron(IV)-oxido moiety, identified rate-limiting step (Figure 161).
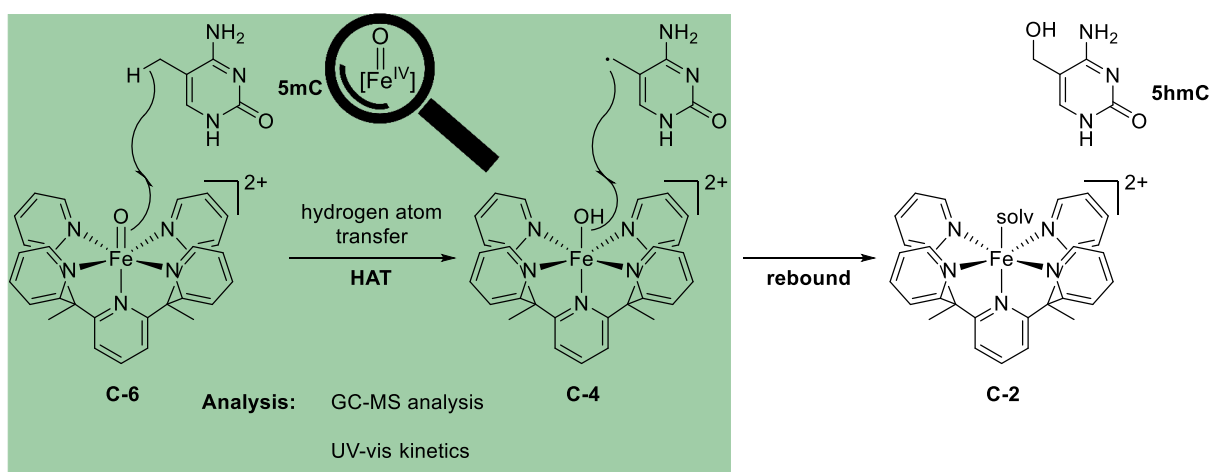
*Figure 161: Reaction of **C-6** with **5mC** in a two-step sequence: first hydrogen atom transfer (HAT) yields **C-4** and a carbon centered radical, these then recombine in rebound reaction to form the final product **5hmC** and **C-2**.*

In the next step of this project, the substrate scope was expanded to nucleosides and oligonucleotides. In a collaboration project with the Carell research group at LMU Munich it was shown that **C-6** does indeed preferentially oxidize the methyl or hydroxylmethyl groups on **5mC** or **5hmC**-containing substrates, respectively, compared to any other positions on the deoxyribose unit. However, oxidation of the 1' and 5' position in the deoxyribose backbone was observed as a

side reaction (Figure 162). In the case of oligonucleotides, only end-of-strand decomposition occurs and no internal strand breaks were detected.

nucleobase   **nucleoside**   **oligonucleotide**

5mC   **5mdC**

5'-HO-GGGG**5mdC**GGGG-OH-3'
5'-HO-CCUUAACC**5mdC**G-OH-3'
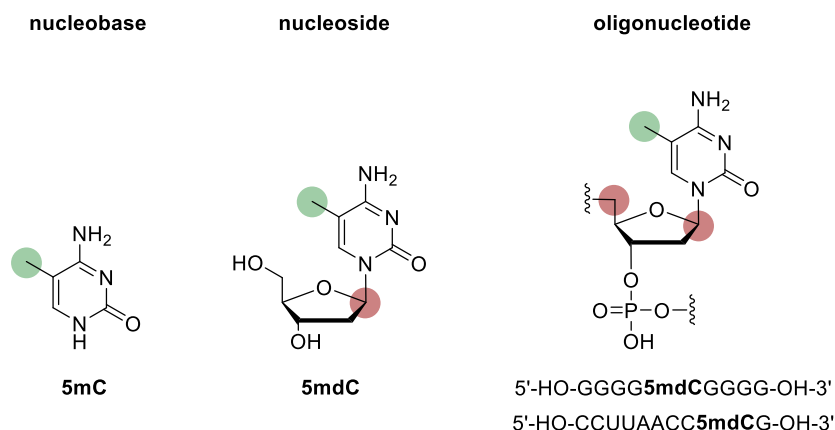
*Figure 162: Increasing substrate complexity: from nucelobase to nucleoside and oligonucleotide. The 5-position of the **5mC** residue is marked in green, the observed locations of side reactions (1' position in nucleosides, 1' and 5' position in oligonucleotides) are marked in red.*

The substrate scope was then expanded even further to include **T** and the non-natural cytosine-derived substrates **5miC** and **1mC**. In a collaboration with the Zipse research group at LMU Munich BDEs were identified as good predictors for the reactivity of C-6 towards carbon-bound methyl groups (Figure 163).
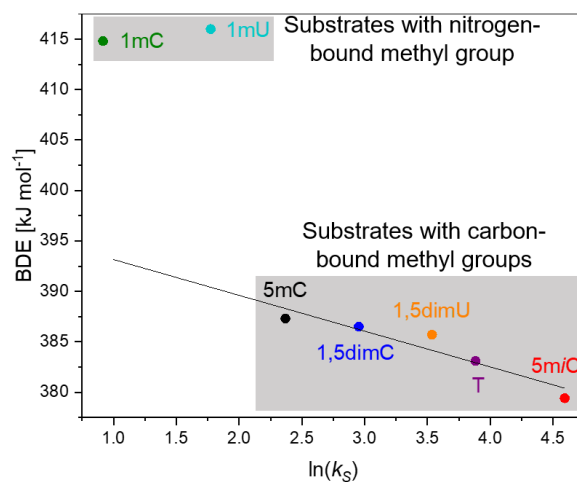
*Figure 163: Bell-Evans-Polanyi plot of the calculated BDE values in aqueous phase against the observed rate constants k_S on a logarithmic scale ($R^2 = 0.891$). Substrates are grouped by those that react primarily at their carbon-bound methyl group (**5mC, 1,5dimC, 1,5dimU, T, 5miC**) and the substrates that react at their nitrogen-bound methyl group (**1mC** and **1mU**).*

*[Fe^{III}(OH)(**L-1**)]$^{2+}$ and Other Iron Complexes*

The iron(III)-hydroxido complex **C-4** was identified as the reaction product of **C-6** and organic substrates. This unintuitive result is the reason of a comproportionation reaction of **C-6** with **C-2** – the intermittently occurring product of the reaction with **C-6** with an organic substrate (Scheme 112).
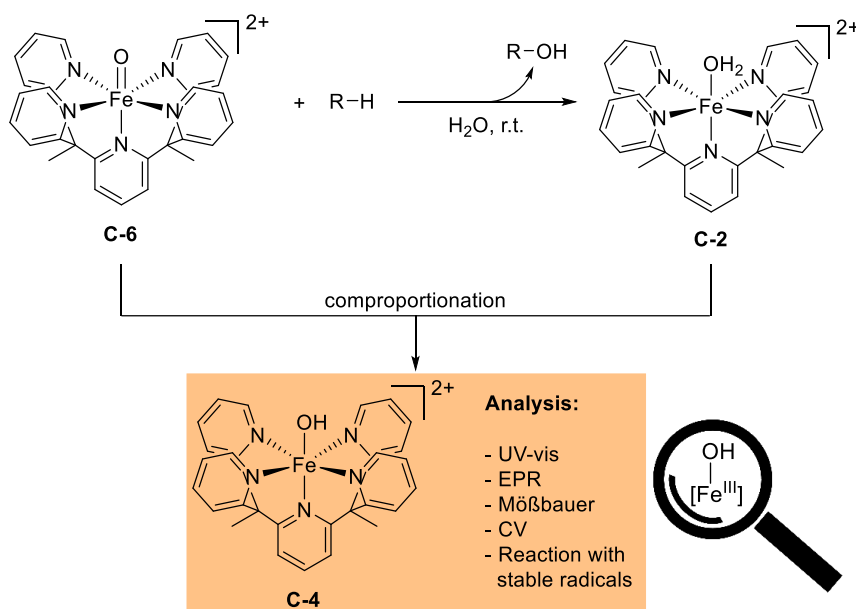
*Scheme 112: Reaction of **C-6** with an organic substrate R-H yielding **C-2** and R-OH. **C-2** and **C-6** comproportionate to form **C-4**.*

C-4 was then synthesized independently from ligand **L-1** and Fe(OTf)$_3$, characterized thoroughly, and studied for its oxidative reactivity towards organic substrates. As **C-4** is also proposed as the intermediate in the reaction of **C-6** with an organic substrate,[13] it was studied for its behavior towards the stable trityl radical as a model for the rebound reaction. Whereas this was met with success and **C-4** can be considered a model complex for the proposed iron(III)-hydroxido intermediate in iron(II)/α-keto acid dependent further investigations are necessary: the cyclic voltammetry investigations presented in this work need to be complemented with mesurements performed under exclusion of water, other stable radical substrates (such as TEMPO) should be tested as substrates, and radical clocks might provide another methods to determine the reaction kinetics of the proposed rebound reaction.

Immobilization

The immobilization of the Py$_5$Me$_2$-X type ligands **L-11** and **L-14** on Merrifield was successful and its reproducibility was shown. Incorporation of iron(II) ions into the immobilized ligand was observed and initial studies on the oxidation to iron(IV)-oxido species were performed. However, further investigations are necessary: as of yet no reaction between an immobilized iron(IV)-oxido complex and an organic substrate was observed and oxidation of the immobilized iron(II) species was not reproducible and needs further investigation.
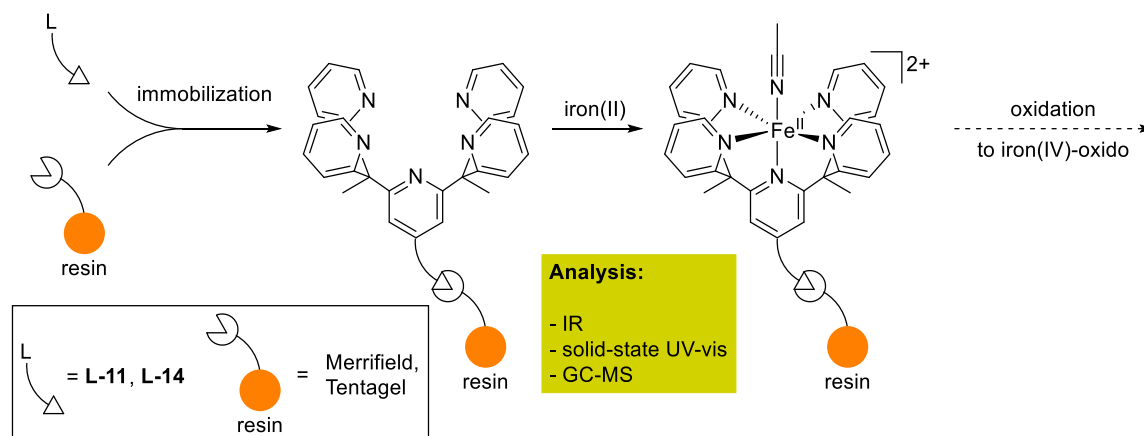
Figure 164: Immobilization of L-11 and L-14 on Merrifield or Tentagel resin and subsequent incorporation of iron(II). Oxidation to the corresponding iron(IV)-oxido species was attempted but not observed reproducibly.

In addition, a series of measures are proposed for future studies: due to the ease of synthesis, **L-14** should be placed at the center of future investigations (Scheme 113). Likely, **L-11** can be synthesized in a two-step reaction, similar to the transformation of 2,6-dichloro-4-methanol to *V-2* (refer to Scheme 75) in an attempt to decrease the synthetic expenditure (Scheme 113**A**). Incorporation of a sulfonic acid (Scheme 113**B**) or a hydrophob group/extended aromatic system (Scheme 113**C**) could allow for immobilization via adsorption (refer to Chart 11). Conversion of the alcohol moiety to a chloride or bromide function could enable the coupling to solid support materials that possess alcohol, acid, or amine moieties (Scheme 113**D**). Finally, coupling of *L-14* to a alky-chloride modified silica support might provide an immobilized iron(IV)-oxido complex less prone to auto-oxidation as a side reaction (Scheme 113**E**).
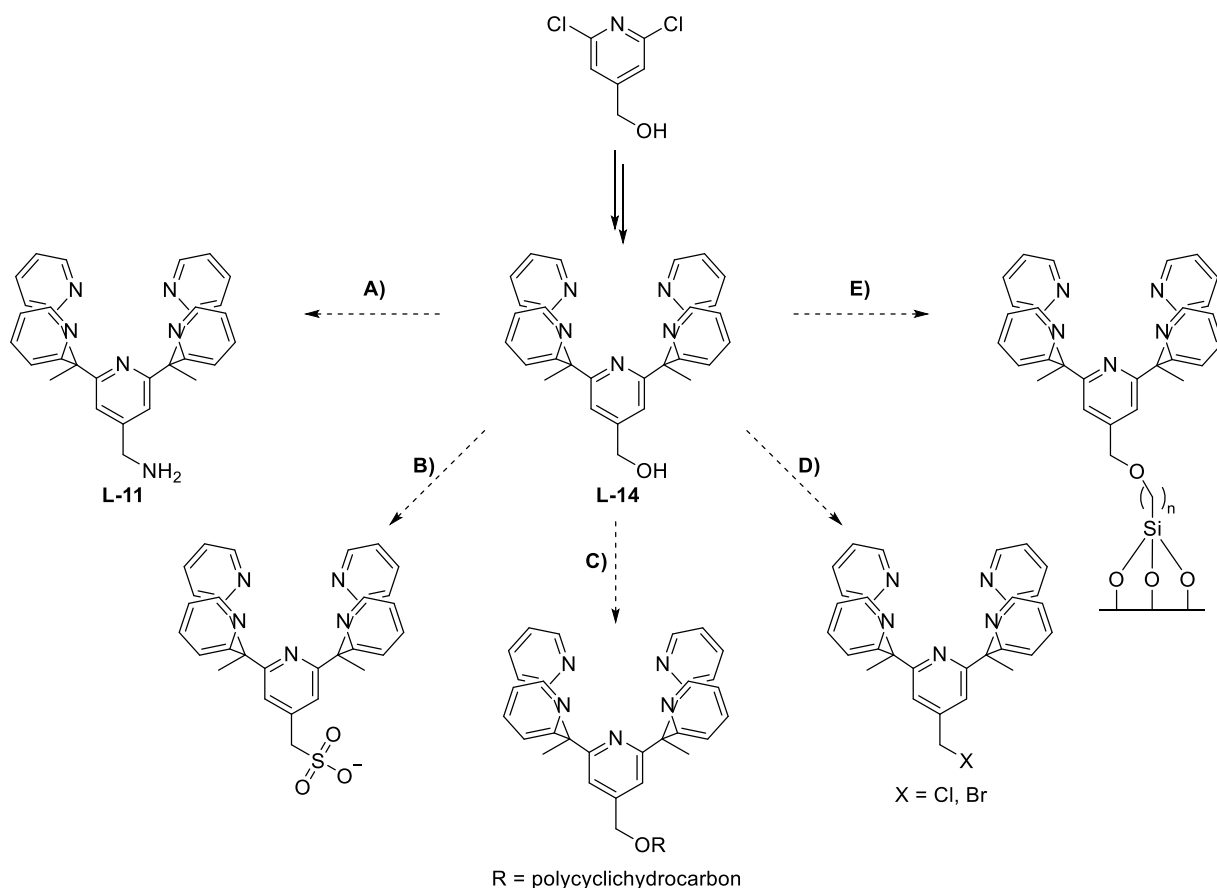
*Scheme 113: Placement of **L-14** as the central starting material for future immobilization investigations: **A)** conversion of **L-14** to **L-11** via a Mitsonubo and Gabriel reaction could reduce the synthetic expenditure. **B)** Incorporation of a sulfonic acid group could enable immobilization via electrostatic interactions (refer to Chart 11). **C)** Incorporation of a hydrophobic group/extendend aromatic system could enable immobilization via Van-der-Waals or π-stacking interactions. **D)** Exchange of the alcohol moiety on **L-14** by a chloride function could allow for the coupling to additional solid support systems containing alcohol, acid, or amine moieties. **E)** L-11 could be coupled to silica similar to the reaction presented in Chart 11**D**.*

Additional Iron Complexes

The ligand system Py_5Me_2H (**L-1**) was succesfully modified which provided the new ligands Py_4OHMe_2H (**L-7**) and Py_4PhMe_2H (**L-8**), and $Py_3Ph_2Me_2H$ (**L-9**). In addition, the literature-known ligand system consisting of $Py_5(OH)_2$ (in the literature referred to as PY5-OH, in this work referred to as **L-2**) and $Py_5(OMe)_2$ (in the literature referred to as PY5, in this work referred to as **L-3**) was expanded to included the ligands $Py_5(OCH_2F)_2$ (**L-4**), $Py_5(OCH_2F)_2$ (**L-5**) and $Py_5(OCF_3)_2$ (**L-6**).
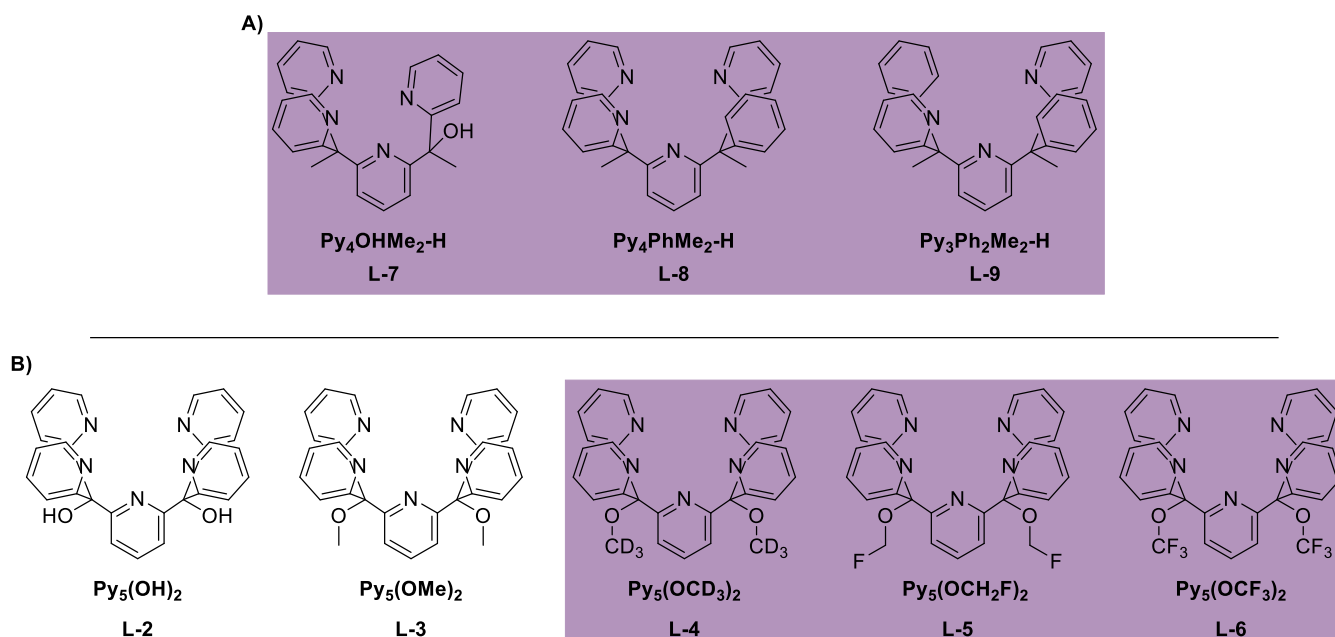
*Figure 165: **A**) Ligands **L-7**, **L-8**, and **L-9** based on the Py_5Me_2H (**L-1**) ligand system. **B**) Ligands **L-3**, **L-4**, **L-5**, and **L-6** based on $Py_5(OH)_2$ (**L-2**). Newly synthesized ligands are highlighted in violet.*

Using these ligands, a series of iron(II), iron(III)-hydroxido, and iron(IV)-oxido complexes were synthesized. These represent suitable starting points for further application as functional model complexes in the study of iron-based enzymes including the superfamily of iron(II)/α-keto acid dependent enzymes.

Elucidating the Mechanism of HPDL

The experiments described in this chapter do indeed provide evidence for the involvement of HPDL in the transformation of **S-HMA** to **4-HBz**: on the one hand, metabolite analysis of biological samples show varying concentrations of **4-HBz** depending on the enzyme used, the reaction conditions, and cell type. On the other hand, bioinorganic functional model studies using **C-4**, **C-6**, and several other iron compounds showed that iron(III) ions are capable of mediating the transformation in question. Whereas both results cannot be considered irrefutable proof, they provide the basis for further investigations.

As a first experiment, **S-HMA** should be fed to bacteria or cell cultures in biological experiments and the metabolites analyzed. If available, ^{13}C-labeled **S-HMA** could be used in order to track its fate even more closely (Scheme 114 light blue).
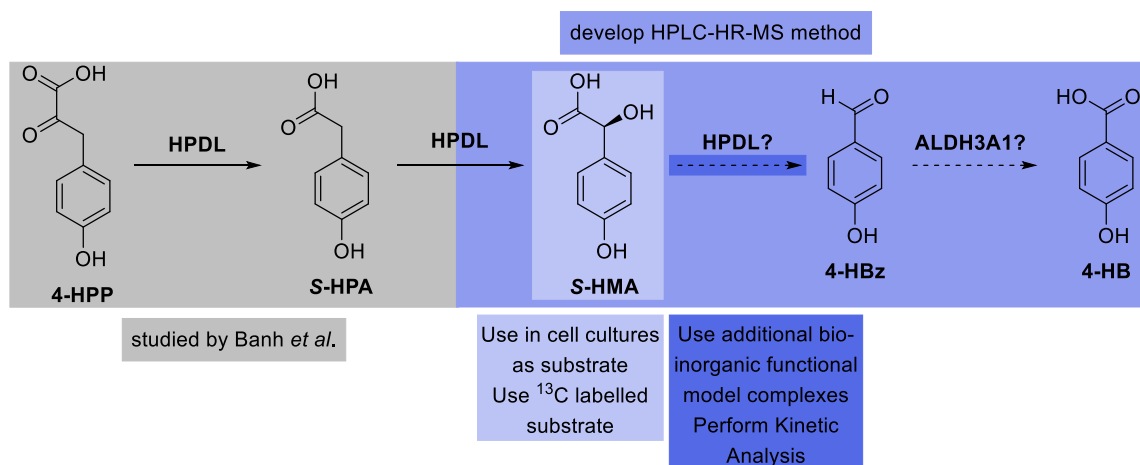
Scheme 114: Involvement of HPDL in the biosynthesis of CoQ10 (not shown): transformation of **4-HPP** to **S-HMA** as discovered by Banh et al. and proposed transformation of **S-HMA** to **4-HBz** with subsequent aldehyde oxidation by ALDH3A1. ALDH3A1 = Aldehyde Dehydrogenase 3 Family Member A1.

The development of a suitable HPLC method (in the best case coupled with HR-MS) could provide another tool to study the metabolite distribution. (Scheme 114 blue)

Further functional model studies, both with **C-4** and other iron(III) compounds, e.g. **C-15**, could also provide more evidence for the postulated mechanism. Close kinetic investigation of these reactions could give insight into the mechanism, as in the proposal shown in Scheme 110 two equivalents of **C-4** are used for the transformation of **S-HMA** to **4-HBz** – the kinetics of this reaction could therefore give valuable insight (Scheme 114 dark blue).

PMS, PES, and Wurster's Blue

HR-MS analysis of aqueous solutions of **PMS**, **PES**, and **WB** showed that all artificial EAs show significant decomposition reactions when either exposed to light and/or handled at temperatures above 0 °C for extended amounts of time. However, analysis of an assay mixture containing **PES** showed no significant decomposition reactions, implying that the handling and storage under exclusion of light and storage at 0 °C does indeed prevent most decomposition. Nevertheless, stock solutions of these compounds should be prepared freshly and regularly checked for decomposition.

My colleagues Bérénice Jahn and Helena Singer complemented these findings with EPR and UV-vis studies. The results of our collaborative work, including some of the data presented above, were published in 2020.[365] HR-MS analysis of aqueous solutions of **PMS**, **PES**, and **WB** showed that all artificial EAs show significant decomposition reactions when either exposed to light and/or handled at temperatures above 0 °C for extended amounts of time. However, analysis of an assay mixture containing **PES** showed no significant decomposition reactions, implying that the handling and storage under exclusion of light and storage at 0 °C does indeed prevent most decomposition. Nevertheless, stock solutions of these compounds should be prepared freshly and regularly checked for decomposition.

My colleagues Bérénice Jahn and Helena Singer complemented these findings with EPR and UV-vis studies. The results of our collaborative work, including some of the data presented above, were published in 2020.[365]

IX. Experimental Section

1. Materials and Methods

1.1. Solvents and Chemicals

Chemicals were purchased from commercial sources (*Sigma Aldrich, ABCR, Acros Organics, Alfa Aesar, TCI Chemicals, Oakwood Chemicals*) or the LMU Munich chemical supply and used without further purification. Trifluoromethyl triflate was synthesised in the group of Prof. Kornath, fluoromethyl iodide was synthesised in the group of Prof. Karaghiosoff at the Department of Chemistry at LMU.

Acetone, ethyl acetate, methanol, dichloromethane, *iso*-hexane, and diethyl ether were obtained from the LMU Munich chemical supply. Ethyl acetate, diethyl ether, dichloromethane, and *iso*-hexane were distilled *via* rotary evaporation prior to use.

1.2. Methods and Manipulations

All manipulations were carried out under ambient conditions if not stated otherwise. Air- and moisture-sensitive chemicals and absolute solvents were transferred *via* stainless-steel cannula or syringe. Organic solutions were concentrated by rotary evaporation at 40 °C. Analytical thin layer chromatography (TLC) was performed on pre-coated (silica gel, 0.25 mm, 60 Å pore-size, 230–400 mesh, Merck KGA) aluminum plates or which were impregnated with a fluorescent indicator (254 nm) or. TLC plates were visualized by exposure to ultraviolet light.

1.3. GC-MS

An Agilent 7920 GC coupled to an Agilent 5970 EI mass spectrometer was used equipped with a silica capillary column (30 m x 0.25 mm) coated with cross-linked 5% phenyl/95% methylpolysiloxane. The injector temperature was set to 280 °C and the temperature of the ion source 230 °C. In case of derivatized samples, the below-mentioned method was used. In case of non derivatized samples, one of two methods was used. Method **A**) Substrates *III-1*, *V-16*, **GD**, DHA. The initial oven temperature was 80 °C, held there for 1 min, ramped to 230 °C at 20 K/min and then held there for 8 min. Method **B**) Substrate: Benzyl Alcohol. The initial oven temperature was 80 °C, held there for 1 min, ramped to 230 °C at 20 K/min and then held there for 4 min.

1.4. General Derivatization and Measurement Procedure for GC-MS Samples

Method **C**) Substrates: All BSTFA-derivatized samples. Reference samples were used as received, reaction samples were dried under high vacuum ($< 1{*}10^{-2}$ mbar) prior to derivatization. Each sample was suspended in acetonitrile, BSTFA was added and the mixture was heated (exact amounts, temperature and incubation time are given in the respective procedure). The samples were syringe filtered (PTFE, 0.45 µm) and injected (exact amount given in the respective procedure) onto the aforementioned GC-MS instrument. The initial oven temperature was 80 °C, held there for 2 min, ramped to 240 °C at 5 K/min and then held there for 20 min.

1.5. NMR Spectroscopy

^{1}H NMR and ^{13}C NMR spectra were recorded, unless otherwise stated, at room temperature on Jeol ECP 270 (400MHz), Jeol ECX 400 (400 MHz) and Bruker Avance III (400MHz) instruments operating at 400 MHz for proton nuclei and 100 MHz for carbon nuclei. ^{1}H- chemical shifts are reported in δ units relative to residual proton signals in CDCl$_3$ (δ_H = 7.26), CD$_3$CN (δ_H = 1.94), (δ_H = 2.05), CD$_3$OD (δ_H = 3.31), D$_2$O (δH = 4.79) or D$_6$-DMSO (δ_H = 2.50). ^{13}C chemical shifts are given in δ units relative to CDCl$_3$ (central line of triplet: δ_C = 77.16), CD$_3$CN (δ_C = 1.32) or D$_6$-DMSO (δ_C = 39.52).[368] The following abbreviations were used: s = singlet, d = doublet, t = triplet, dd = doublet of doublets, dt = doublet of triplets, m = multiplet, br = broad. Coupling constants (*J*) are given in Hertz. The software used for data processing was MNova Version 12.0.1-20560.

For literature-known compounds, ^{1}H NMR spectra were measured and compared to to values provided in the literature. This is indicated in the respective analysis section of a specific compound. For new compounds, 1D measurements (^{1}H, ^{13}C, and ^{2}H or ^{19}F if applicable) as well as 2D measurements (COSY, HSQC, HMBC) were conducted and the collected data was then used in conjunction with predicted spectra (ChemDraw 2019 & 2020, MNova Version 12.0.1-20560) for assignments. Positions of C and H atoms are indicated in the structure of the respective compound as numbers starting at 1, these are used for assignment of ^{1}H and ^{13}C spectra, if such assignments were possible. If applicable, "N*H*" or "O*H*" etc. is used for denomination instead of the number-based system, italic font refers to the indicated atom. "Ph" and "Py" refers to unspecified ^{1}H or ^{13}C atoms in a phenyl or pyridine moiety, respectively.

1.6. EPR Spectroscopy

EPR measurements were performed using a BRUKER EMXNano X-band (9.5 GHz) spectrometer at room temperature. All 1D continuous wave (CW) EPR experiments were conducted using a microwave power of 1.0 mW. Modulation amplitudes and frequencies of 0.4 mT and 100 kHz were used, respectively. A time constant of 1.28 ms and a sweep time of 10 min were also used. CW spectra were processed using MATLAB® and EasySpin® software. The CW EPR spectra were processed using the *pepper* function. After spectra were processed using the software, parameters were extracted by fitting the spectra obtained using a non-linear least squares regression model (Nelder/Mead downhill simplex algorithm) where the overall RMSD value for the entire system was minimized to as close to zero as possible.

1.7. ICP-OES Measurements and Elemental Analysis

Inductively coupled plasma optical emission spectroscopy (ICP-OES) was conducted by the central analysis department on a VARIAN-VISTA instrument with an autosampler. Samples were digested in hot nitric acid and then diluted with MilliQ water to a final HNO$_3$ concentration of 3%.

Elemental Microanalyses (C, H, N, S) were performed with an Elementar vario EL.

1.8. UV-vis and IR Spectroscopy

UV-Vis Spectroscopy measurements were conducted with an Agilent 8453 Diode Array Spectrophotometer with a thermostatted cuvette holder. 10 mm quartz Suprasil cuvettes from Hellma were used in all experiments.

FT-Infrared Spectroscopy was carried out with a Jasco FT/IR-460Plus with ATR Diamond Plate.

1.9. Mass Spectrometry

Electrospray Ionzation mass spectrometry (ESI-MS) and electron ionization mass spectroscopy (EI-MS) measurements for characterization of organic compounds and complexes was carried out by Dr. Werner Spahl at the department of chemistry. ESI spectra were recorded with a Thermo Finnigan LTQ FT Ultra Fourier Transform Ion Cyclotron Resonance mass spectrometer with acetonitrile/water as the carrier solvent.

EI spectra were recorded with a Thermo Q Exactive GC, a Thermo Finnigan MAT 95 or a Jeol MStation mass spectrometer.

Further, Cryospray-Ionization Mass Spectrometry (CSI-MS) measurements were performed by Laura Senft on an UHR-TOF Bruker Daltonik (Bremen, Germany) maXis plus, an ESI-quadrupole time-of-flight (qToF) mass spectrometer capable of a resolution of at least 60.000 (FWHM), which was coupled to a Bruker Daltonik Cryospray unit. Detection was in positive ion mode, the source voltage was 3.5 kV and the flow rate was 240 µL/hour. The temperature of the spray gas (N_2) and the temperature of the dry gas (N_2) to aid solvent removal were both kept at 5 °C. The mass spectrometer was calibrated prior to every experiment *via* direct infusion of Agilent ESI-TOF low concentration tuning mixture, which provided an m/z range of singly charged peaks up to 2700 Da in both ion modes. Processing of the obtained spectra was done with Bruker DataAnalysis 5.2.

1.10. Preparative HPLC

Preparative HPLC was performed on an Agilent 1260 Infinity II HPLC system equipped with a manual injector, a preparative binary pump (G7161A), a multi-wavelength detector (G7165A), a fraction collector (G1364E) and a C18 column (Dr. Maisch, 250x20mm 5 µm). As solvents water with 0.1% TFA and acetonitrile with 0.1% TFA were used, these were prepared freshly immediately prior to use.

1.11. Analytical HPLC and HPLC-MS

Analytical HPLC was performed on a semi-preparative VWR Chromaster HPLC (VWR) equipped with an Autosampler, a binary pump, and a heatable column compartment carrying an ACE-1210-1546 C18-PFP column (150 x 4.6 mm, 5 µm) operated at a flow rate of 1 ml/min. As solvent, a mixture of 5% methanol in 95% water was used in an isocratic method.

1.12. Nucleoside Quantification

Internal standards (isotopically labeled dC*, 5mdC*, 5hmdC*, 5fdC*, 5cadC*, dA*, dG*, dT*, and 8-oxo-dG*) were added to a sample and the samples then digested using Degradase Plus from Zymo Research, and subsequently measured on a tandem UHPLC-MS system (UHPLC system: Agilent Technologies, model no. 1290 Infinity II LC; MS system: Triple quadrupole LC/MS system with iFunnel technology (Agilent Technologies, model no. 6490)). The exact method was described here.[369]

1.13. X-ray crystallography

Data collection and structure elucidation was performed by Dr. Peter Mayer at the Chemistry Department of the Ludwig-Maximilians University Munich. The x-ray intensity data were collected on a Bruker D8 Venture TXS system equipped with a multilayer mirror optics monochromator and a Mo Kα rotating-anode X-ray tube (l mbda = 0.71073 Å). The frames were integrated with the Bruker SAINT software package usinga narrow-frame algorithm.[283] Data were corrected for absorption effects using the Multi-Scan method (SADABS).[284] The structure was solved and refined using the Bruker SHELXTL Software Package.[285]

2. General Procedures

2.1. General Procedure for the Exchange of [Ce(NO₃)₆]²⁺

C-5 → **C-6**
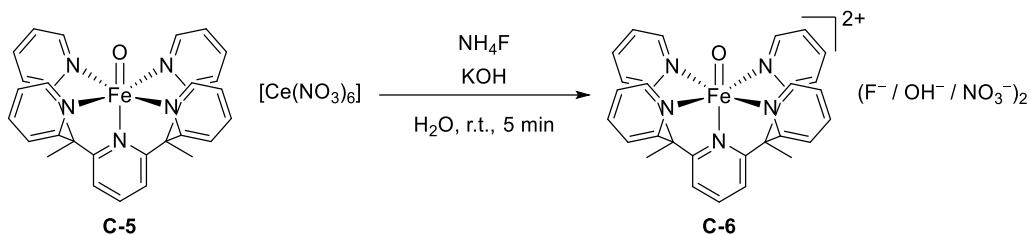
This procedure was first described in *Chem. Eur. J.* **2021**, *52*, 12091.[13]

The required amount of **C-5** was dissolved in unbuffered, MilliQ grade water so that a concentration of 15 mM was reached. The solution was vortexed and sonicated for 30 s. Then, 1.0 equiv. of an aqueous solution of potassium hydroxide ([KOH] = 1 M) and 5.0 equiv. of an aqueous solution ammonium fluoride ([NH₄F] = 1 M) were added and then diluted so that a final concentration of 10 mM of the iron compound **C-6** is reached. The solution was vortexed for 30 s and then centrifuged at 600 rpm for 3 min. The supernatant was collected and used as such for further experiments or diluted accordingly.

*2.2. General Procedure for the Immobilization of **L-11** on Merrifield Resin*
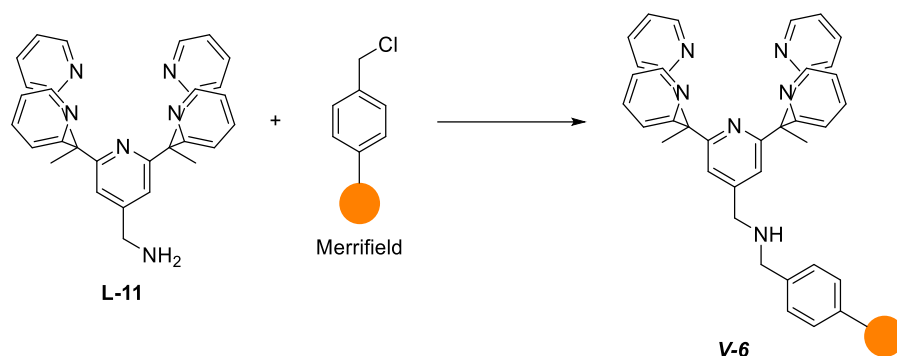
L-11 (614 mg, 1.30 mmol, 10 equiv.) was dissolved in DCM (2.5 ml) in a Falcon tube. Subsequently, potassium carbonate (359 mg, 2.60 mmol, 20 equiv.) and Merrifield® resin (100 mg, 0.13 mmol, 1.0 equiv.) were added. The Falcon tube was sealed using parafilm and vortexed on a daily basis for 5 d. Then the suspension was diluted with methanol and subsequently filtered through a sintered glass frit. The resulting solid was washed with methanol, water, and again methanol thoroughly. The product **V-6** was dried under high vacuum and obtained as a yellow granular solid.

Excess **L-11** was retrieved by partly concentrating the filtrate *in vacuo*. The remaining aqueous solution was extracted with DCM (3 × 25 mL). The combined organic layers were dried over anhydrous magnesium sulfate, solvents removed *in vacuo* and dried under high vacuum.

Solid-state UV/Vis:

λ = 256 nm

IR (thin film):

$\tilde{\nu}$ = 3026, 2924, 2359, 2341, 1587, 1493, 1452, 1372, 1268, 1154, 1029, 916, 844, 750, 699, 659 cm^{-1}.

Elemental Analysis:

Found: C 84.99., H 6.88., N 3.41, Cl 3.79.

2.3. General Procedure for the Incorporation of iron into V-6
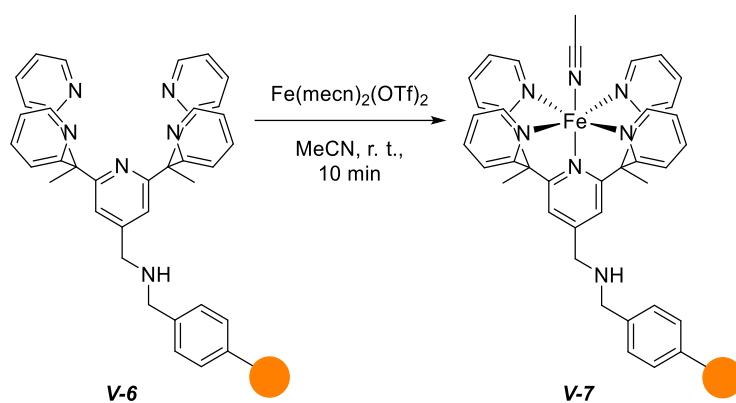
V-6 (64.0 mg, 83 µmol theor.) was suspended in 2.5 ml acetonitrile. Iron(II) triflate (50.0 mg, 114 µmol, 1.4 equiv.) was added and the suspension was vortexed. The reaction was allowed to rest for 10 min and then filtered through a sintered glass frit. The residue was washed with diethyl ether and dried under high vacuum. Product **V-7** was obtained as brown beads.

Solid-state UV/Vis:

λ = 259, 457 nm

IR (thin film):

$\tilde{\nu}$ = 3025, 2919, 1601, 1493, 1469, 1443, 1241, 1159, 1029, 904, 829, 758, 697 cm^{-1}.

ICP-OES:

Found Fe: 4.2 mg/g

3. Synthetic Procedures – Ligands and Metal Complexes

3.1. Synthesis of *III-1*
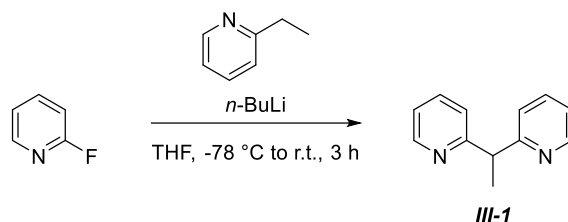
According to a modified literature procedure:[234]

A flame-dried flask was charged with 2-ethylpyridine (6.27 ml, 5.88 g, 54.84 mmol, 2.1 equiv.) under inert atmosphere (nitrogen) and 50 ml of absolute tetrahydrofuran and then cooled to –78 °C. When a solution of *n*-butyl lithium (2.5 M in hexane, 20.80 ml, 52.01 mmol, 2.0 equiv.) was added dropwise, the solution turned a deep red. The mixture was stirred for 60 min at –78 °C, then 2-fluoropyridine (2.21 ml, 2.50 g, 25.8 mmol, 1.0 equiv.) was added dropwise, the solution stirred at –78 °C for an additional 10 min and the cooling bath removed. The reaction mixture was allowed to warm to room temperature and then stirred at room temperature for 3 h. 30 g ice were added slowly, at which point the mixture turned yellow. Additional 30 ml MilliQ grade water were added and the solution stirred vigorously for 10 min. The layers were separated and the aqueous layer was extracted with dichloromethane (3 x 50 ml). The combined organic layers were dried over anhydrous magnesium sulfate and the solvents removed *in vacuo* to yield a yellow to orange oil as the crude product. Excess 2-ethylpyridine was removed under reduced pressure to yield the product *III-1* as a yellow to orange oil in 84% yield (3.79 g).

R_F = 0.23 (silica, UV, 80% ethyl acetate - hexanes)

¹H NMR (400.0 MHz, CDCl$_3$, 295 K):
δ = 8.55 (ddd, *J* = 4.9 Hz, *J* = 1.9 Hz, *J* = 0.9 Hz, 2H), 7.60 (td, *J* = 7.7 Hz, *J* = 1.8 Hz, 2H), 7.28 (dd, *J* = 7.9 Hz, *J* = 1.0 Hz, 2H), 7.11 (ddd, *J* = 7.5 H, *J* = 4.9 Hz, *J* = 1.2 Hz, 2H), 4.48 (q, *J* = 7.2 Hz, 2H), 1.76 (d, *J* = 7.2 Hz, 3H) ppm.

¹³C NMR (100.0 MHz, CDCl$_3$, 295 K):
δ = 163.9, 149.3, 136.6, 122.5, 121.5, 49.9, 19.8 ppm.

NMR data is in accordance with the literature.[234]

HR-MS (ESI):
Calculated for C$_{12}$H$_{13}$N$_2$ [M+H]$^+$: 185.10787 m/z
Found: 185.10723 m/z

3.2. Synthesis of L-1
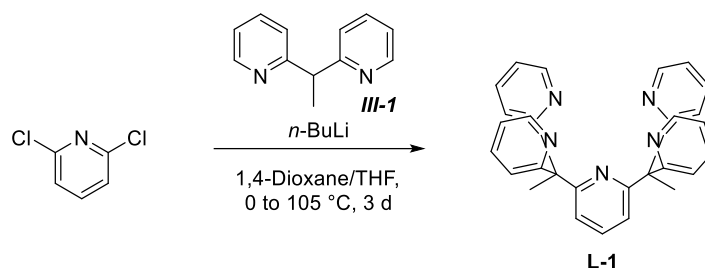
According to a modified literature procedure:[12]

A flame-dried flask was charged with ***III-1*** (2.00 g, 10.9 mmol, 3.0 equiv.), 36 ml of absolute 1,4-dioxane under inert atmosphere (nitrogen) and 4 ml of absolute tetrahydrofuran and cooled to 0 °C. When a solution of *n*-butyl lithium (2.5 M in hexane, 4.34 ml, 10.9 mmol, 3.0 equiv.) was added, the solution turned a dark red. The solution was stirred for 45 min at 0 °C, at which time 2,6-dichloropyridine (535.5 mg, 3.62 mmol, 1.0 equiv.) was added all at once. The reaction mixture was allowed to warm to room temperature and then heated to reflux for 60 hours (bath temperature 105 °C). When the solution had turned from deep red to light brown and thin layer chromatography showed no change during a time span of 6 h, the mixture was allowed to cool to room temperature. 20 ml water were added and the mixture extracted with dichloromethane (3 x 70 ml). The combined organic layers were then dried over anhydrous magnesium sulfate and the solvents removed *in vacuo*. 40 ml methanol were added and the solvents removed *in vacuo* to remove residual 1,4-dioxane. A deep red oil was obtained as the crude product. Diethyl ether was added until a yellow precipitate began to form which was filtered off, washed with diethyl ether (1 x 10 ml) and dried to yield the product **L-1** as a yellow solid in 91% yield.

R_F = 0.10 (silica, UV, 80% ethyl acetate - hexanes)

¹H NMR (400.0 MHz, CDCl$_3$, 295 K):
δ = 8.51 (ddd, *J* = 4.8 Hz, *J* = 1.9 Hz, *J* = 0.9 Hz, 4H), 7.54 (t, *J* = 7.9 Hz, 1H), 7.39 (ddd, *J* = 8.1 Hz, *J* = 7.5 Hz, *J* = 1.9 Hz, 4H), 7.05 (d, *J* = 7.9 Hz, 2H) 7.04 (ddd, *J* = 7.5 Hz, *J* = 4.8 Hz, *J* = 1.1 Hz, 4H), 6.84 (dt, *J* = 8.0 Hz, *J* = 1.0 Hz, 4H), 2.21 (s, 6H) ppm.

¹³C NMR (100.0 MHz, CDCl$_3$, 295 K):
δ = 166.2, 166.3, 148.5, 136.8, 135.6, 124.1, 121.0, 120.0, 60.1, 26.8 ppm.

NMR data is in accordance with the literature.[12]

HR-MS (ESI):
Calculated for C$_{29}$H$_{26}$N$_5$ [M+H]$^+$: 444.21882 m/z
Found: 444.21811 m/z

IR (thin film):

$\tilde{v}$ = 3053, 2992, 1566, 1466, 1428, 1365, 1293, 1153, 1102, 1078, 1067, 1046, 991, 962, 903, 875, 799, 786, 768, 752, 699, 654 cm^{-1}.

3.3. Synthesis of C-1

L-1 → Fe(mecn)$_2$(OTf)$_2$, MeCN, r.t., 5 min → **C-1** (OTf)$_2$
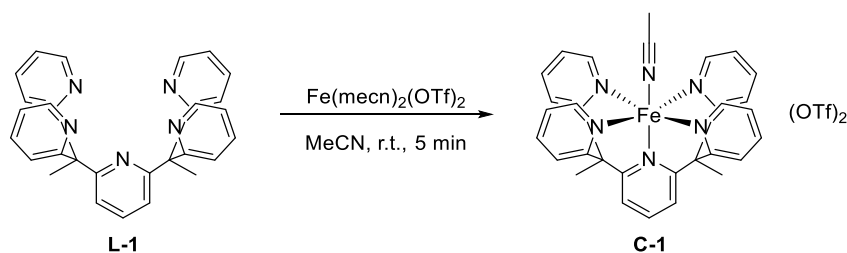
According to a modified literature procedure:[12]

Ligand **L-1** (300.0 mg, 0.679 mmol, 1.0 equiv.) was dissolved in 15 ml acetonitrile under a nitrogen atmosphere. Iron(II)bis(acetonitrile)bis(triflate) (294.9 mg, 0.679 mmol, 1.0 equiv.) was added as a solid, turning the solution deep red. The mixture was then stirred for an additional 5 min and then diethyl ether was diffused into the solution under ambient conditions to give the product as brown crystals in 91% yield (516.0 mg).

^{1}H NMR (400.0 MHz, CD$_3$CN, 295 K):
δ = 9.81 (d, J = 5.9 Hz, 4H), 8.03 (s, 3H), 7.93 (d, J = 3.8 Hz, 8H), 7.54 (m, 4H), 2.75 (s, 6H), 1.96 (s, 3H) ppm.

^{13}C NMR (100.0 MHz, CD$_3$CN, 295 K):
δ = 165.0, 163.0, 158.2, 140.1, 139.7, 124.3, 123.8, 122.1, 118.3, 55.7, 24.2 ppm.

NMR data is in accordance with the literature.[12]

HR-MS (ESI):
Calculated for C$_{30}$H$_{25}$F$_3$FeN$_5$O$_3$S [Fe(Py$_5$Me$_2$-H)(MeCN)(OTf)]$^+$: 648.09796 m/z
Found: 648.09648 m/z
Calculated for C$_{31}$H$_{28}$FeN$_6$ [Fe(Py$_5$Me$_2$-H)(MeCN)]$^{2+}$: 270.08625 m/z
Found: 270.08562 m/z

Elemental Analysis:
Calculated for C$_{33}$H$_{28}$F$_6$FeN$_6$O$_6$S$_2$: C 47.27, H 3.37, N 10.02, S 7.65.
Found: C 47.03, H 3.33, N 9.94, S 7.86.

IR (thin film):
$\tilde{v}$ = 1598, 1469, 1442, 1415, 1281, 1251, 1225, 1149, 1070, 1028, 865, 791, 761, 702 cm^{-1}.

3.4. Synthesis of **C-2**

L-1 → **C-2**

Fe(H$_2$O)$_6$(BF$_4$)$_2$

H$_2$O/Acetone,
r.t., 5 min

(BF$_4$)$_2$
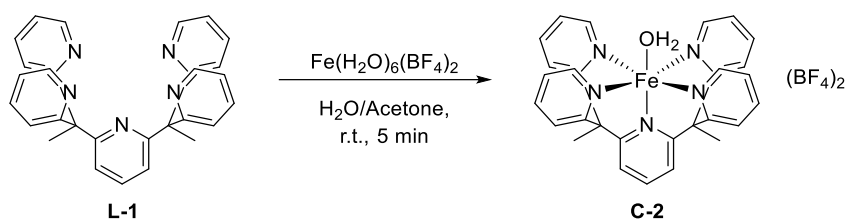
According to a modified literature procedure:[12]

Ligand **L-1** (90.0 mg, 0.190 mmol, 1.0 equiv.) was dissolved in 4.0 ml acetone. Hexaqua iron(II) bis(tetrafluoroborate) (64.2 mg, 0.190 mmol, 1.0 equiv.) was dissolved in 0.5 ml water and then added to the solution of the ligand, turning the solution red-brown. The mixture was stirred for 5 min and then diethyl ether was diffused into the solution to give the product as a red-brown powder in 73% yield (100.0 mg).

HR-MS (ESI):
Calculated for C$_{29}$H$_{25}$FFeN$_5$ [Fe(**L-1**)(F)]$^+$: 518.14434 m/z
Found: 518.14454 m/z
Calculated for C$_{31}$H$_{28}$FeN$_6$ [Fe(**L-1**)(MeCN)]$^{2+}$: 270.08625 m/z
Found: 270.05525 m/z
Calculated for C$_{31}$H$_{28}$FeN$_6$ [Fe(**L-1**)]$^{2+}$: 249.5730 m/z
Found: 249.5730 m/z

Elemental Analysis:
Calculated for C$_{29}$H$_{27}$B$_2$F$_8$FeN$_5$O: C 50.41, H 3.94, N 10.15.
Found: C 50.43, H 3.80, N 10.11.

IR (thin film):
$\tilde{\nu}$ = 3398, 1653, 1597, 1465, 1442, 1412, 1390, 1283, 1069, 993, 863, 768 cm^{-1}.

3.5. Synthesis of **C-3**
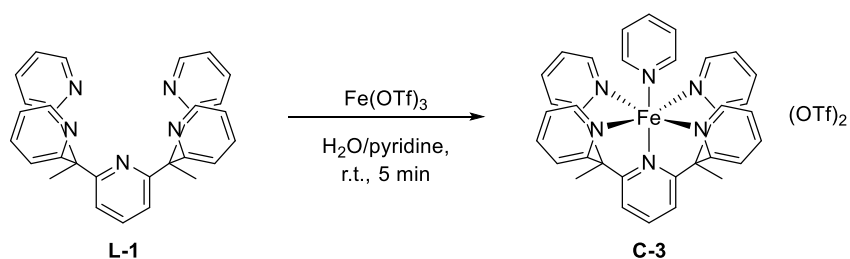
Ligand **L-1** (100.0 mg, 0.225 mmol, 1.0 equiv.) was suspended in 2 ml water and the suspension vortexed for 30 s and then sonicated for 60 s. Iron(III) triflate (226.8 mg, 0.451 mmol, 2.0 equiv.) was dissolved in 2 ml water and then added to the suspension of the ligand, turning the solution orange-red. The mixture was sonicated and vortexed for 60 s each. Pyridine (100 µl, 1.24 mmol, 2.8 equiv.) was added, the mixture vortexed and sonicated for 60 s each. Then, the mixture was then heated to 80 °C for 1.5 h. The red-brown solution with red-brown precipitate was centrifugated (600 rpm, 5 min) and the supernatant collected. Deep red crystalline needles formed over night in the solution at room temperature (no yield determined). The obtained needles were submitted for x-ray diffraction measurements, therefore no further analytical data was obtained.

3.6. Synthesis of **C-4**
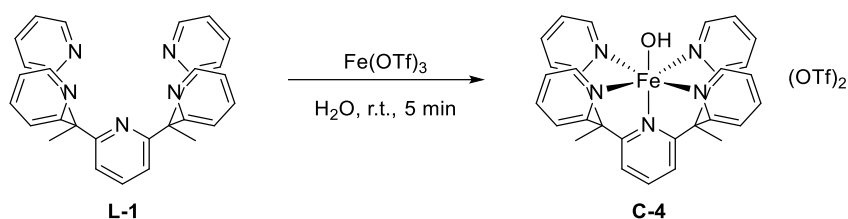
Ligand **L-1** (1.00 g, 2.25 mmol, 1.0 equiv.) was suspended in 40 ml water. Iron(III) triflate (1.51 mg, 3.00 mmol, 1.3 equiv.) was added as a solid. The mixture turned orange-red upon mixing, the mixture was sonicated for 1 h at 40 °C which led to a color change to deep red. Additional iron(III) triflate (0.56 g, 1.11 mmol, 0.8 equiv.) was added and the mixture was sonicated briefly. The mixture was filtered through a sintered glass frit and sodium triflate (775.0 mg, 4.50 mmol) was added as a solid to the filtrate. The mixture was stored at 4 °C for 3 d. The formed crystals were washed with water and dried *in vacuo* to give **C-4** (no yield determined). The precipitate obtained from filtering was collected and recrystallized from water (40 °C) to yield **C-4** x 2 H$_2$O (no yield determined).

HR-MS (ESI):
Calculated for C$_{29}$H$_{26}$FeN$_5$O [Fe(OH)(**L-1**)]$^{2+}$: 258.07434 m/z
Found: 258.07355 m/z

Elemental Analysis:
Calculated for C$_{31}$H$_{26}$F$_6$FeN$_5$O$_7$S$_2$: C 45.71, H 3.22, N 8.60, S 7.87.
Found: C 44.17, H 3.36, N 8.07, S 7.78.
 Calculated for C$_{31}$H$_{30}$F$_6$FeN$_5$O$_9$S$_2$ (**C-4** x 2 H$_2$O): C 43.78, H 3.56, N 8.23, S 7.54.
Found: C 43.53, H 3.42, N 8.06, S 7.99.

IR (thin film):
$\tilde{v}$ = 3424, 3091, 1657, 1599, 1462, 1447, 1390, 1256, 1224, 1154, 1103, 1026, 914, 868, 847, 782, 764, 742, 664 cm^{-1}.

3.7. Synthesis of **C-5**

C-1   **C-5**
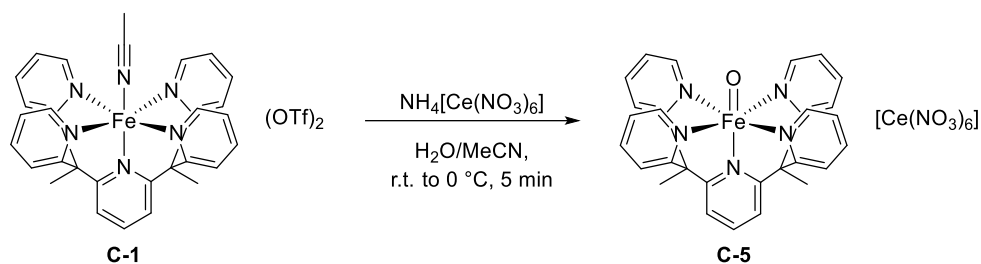
According to a modified literature procedure:[12]

C-1 (100 mg, 0.119 mmol, 1.0 equiv.) was dissolved in 1.5 ml of 3:1 acetonitrile:water. Cerium(IV) ammonium nitrate (347.1 mg, 0.633 mmol, 5.3 equiv.) was added as a solid and the mixture sonicated for 60 s. As a pale green precipitate began to form the reaction mixture was placed in an ice bath to complete the precipitation. The solid was collected on a sintered glass frit, washed with 1.5 ml of ice cold 3:1 acetonitrile:water and dried *in vacuo* to yield product **C-5** as a pale green solid (107.2 mg, 87%) .

Elemental Analysis:
Calculated for $C_{29}H_{25}CeFeN_{11}O_{19}$: C 33.90, H 2.45, N 14.99.
Found: C 33.81, H 2.58, N 15.20.

ICP-OES:
Fe: 52.3 mg/g ≙ 0.937 mmol/g
Ce: 131.5 mg/g ≙ 0.939 mmol/g
Molecular ratio of Fe:Ce = 1:1

IR (thin film):
$\tilde{v}$ = 1600, 1496, 1277, 1033, 864, 822, 804, 784, 760, 742 cm⁻¹.

UV-vis (H_2O):
λ = 720 nm (ε = 349 l mol⁻¹ cm⁻¹).

3.8. Synthesis of V-1
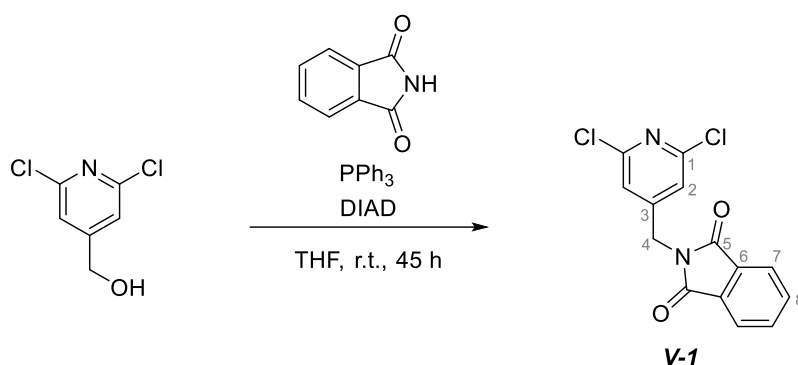
A flask was charged with 2,6-dichloropyridine-4-methanol (1.00 g, 5.62 mmol, 1.0 equiv.), triphenylphosphine (1.77 g, 6.74 mmol, 1.2 equiv.), and phthalimide (0.99 g, 6.74 mmol, 1.2 equiv.). 30 ml of tetrahydrofuran were added and the mixture stirred for 5 min at room temperature while a colorless solid remained undissolved. Diisopropyl azodicarboxylate (DIAD, 1.32 ml, 1.36 g, 6.74 mmol, 1.2 equiv.) was added dropwise, the solution turning slowly orange. The previously insoluble colorless solid disappeared upon addition of DIAD. The solution was stirred for 4 h at room temperature, heated to 30 °C for 1 h and stirred for an additional 40 h at room temperature. A colorless solid precipitated which was filtered off and washed with 3 x 10 ml diethyl ether. The filtrate was concentrated under reduced pressure and stirred for another 1 h at room temperature. A colorless solid precipitated which was filtered off and washed with 3 x 5 ml diethyl ether. The precipitates were combined and dried under reduced pressure to give the product *V-1* in 81% yield (1.40 g) as a colorless solid, sufficiently pure for further use.

R_F = 0.68 (silica, UV, 100% ethyl acetate)

^{1}H NMR (400.0 MHz, CDCl$_3$, 295 K):
δ = 7.91 (dd, J = 5.5 Hz, J = 3.0 Hz, 2H, H-7), 7.78 (dd, J = 5.5 Hz, J = 3.1 Hz, 2H, H-8), 7.27 (s, 2H, H-2), 4.80 (s, 2H, H-4) ppm.

^{13}C NMR (100.0 MHz, CDCl$_3$, 295 K):
δ = 167.6 (C-5), 151.2 (C-3), 150.6 (C-1), 134.7 (C-8), 131.8 (C-6), 124.0 (C-7), 122.4 (C-2), 39.7 (C-4) ppm.

HR-MS (EI):
Calculated for C$_{14}$H$_8$Cl$_2$N$_2$O$_2$ [M]$^+$: 305.9963 m/z
Found: 305.9958 m/z
Calculated for C$_{14}$H$_8$^{37}Cl^{35}ClN$_2$O$_2$ [M]$^+$: 307.9933 m/z
Found: 307.9943 m/z

Elemental Analysis:
Calculated for C$_{14}$H$_8$Cl$_2$N$_2$O$_2$: C 54.75, H 2.63, N 9.12, Cl 23.08.
Found: C 54.78, H 2.58, N 9.16, Cl 23.01.

IR (thin film):

$\tilde{\nu}$ = 2190, 1767, 1696, 1643, 1583, 1545, 1416, 1376, 1324, 1166, 1108, 1096, 985, 946, 907, 884, 812, 759, 727, 714, 676 cm^{-1}.

3.9. Synthesis of V-2
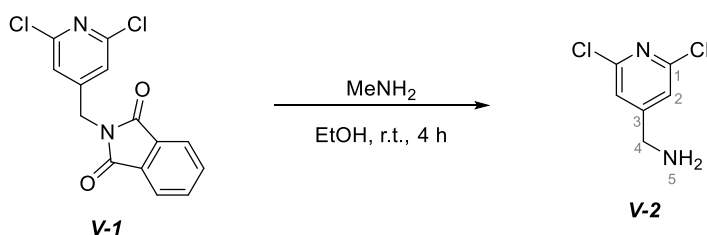
According to a modified literature procedure:[370]

A flask was charged with **V-1** (0.25 g, 0.81 mmol, 1.0 equiv.) and 7.5 ml of methylamine solution in absolute ethanol (33%, 7.50 ml, 1.87 g, 60.25 mmol, 74.0 equiv.) were added which resulted in a clear, yellow solution. The solution was stirred for 4 h, after which no more starting material was detected using thin layer chromatography (UV, 100% EtOAc, starting material R_F = 0.68). The solvents were removed under reduced pressure to give a colorless solid. This was taken up in 20 ml of 15% aqueous acetic acid, sonicated for 5 min, and washed with 3 x 20 ml dichloromethane. The aqueous layer was basified to pH = 12 with 1 M aqueous sodium hydroxide solution and then extracted with 6 x 20 ml dichloromethane:*iso*-propanol 3:1. This organic layer was dried over anhydrous magnesium sulfate and the solvents were removed under reduced pressure to give the product **V-2** in 83% yield (120 mg) as a colorless solid.

R_F = 0.04 (silica, UV, 100% ethyl acetate)

¹H NMR (400.0 MHz, CDCl$_3$, 295 K):
δ = 7.25 (s, 2H, H-2), 3.91 (s, 2H, H-4) ppm.

¹³C NMR (100.0 MHz, CDCl$_3$, 295 K):
δ = 158.3 (C-3), 150.7 (C-1), 121.3 (C-2), 44.5 (C-4) ppm.

HR-MS (ESI):
Calculated for C$_6$H$_6$Cl$_2$N$_2$ [M+H]$^+$: 176.99863 m/z
Found: 176.99813 m/z

Elemental Analysis:
Calculated for C$_{14}$H$_8$Cl$_2$N$_2$O$_2$: C 40.71, H 3.42, N 15.82, Cl 40.05.
Found: C 40.95, H 3.34, N 15.57, Cl 39.85.

IR (thin film):
$\tilde{v}$ = 3360, 3286, 2737, 2190, 1588, 1538, 1443, 1388, 1250, 1158, 1094, 1077, 990, 886. 862, 802 cm^{-1}.

3.10.   Synthesis of V-3
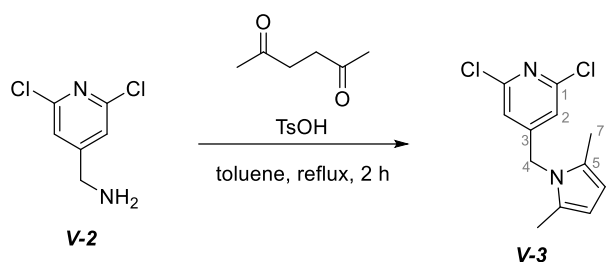
According to a modified literature procedure:[12]

A flask was charged with **V-2** (0.25 g, 1.41 mmol, 1.0 equiv.), *para*-toluenesulfonic acid hydrate (0.027 g, 0.141 mmol, 0.1 equiv.), 50 mg of powdered molecular sieves and 2.5 ml of toluene. 2,5-hexane-di-one (0.199 ml, 0.193 g, 1.69 mmol, 1.2 equiv.) was added dropwise and the reaction mixture heated to 110 °C for 2 h, at this point thin layer chromatography (silica, ethyl acetate:hexanes 10%:90%) confirmed full consumption of the starting material. The hot reaction mixture was filtered through a PTFE syringe filter (PTFE, 0.45 µm), the filter washed with 1 ml toluene and the mixture was allowed to cool to room temperature. Column chromatography (silica, ethyl acetate and hexanes, starting at 5% ethyl acetate for 5 column volumes, then grading to 10% ethyl acetate over 10 column volumes and continuing for additional 5 column volumes at 10% ethyl acetate) gave the product **V-3** as a colorless crystalline solid in 72% yield (0.26 g).

R_F = 0.67 (silica, UV, 10% ethyl acetate in hexanes)

^{1}H NMR (400.0 MHz, CDCl$_3$, 295 K):
δ = 6.74 (s, 2H, H-2), 5.89 (s, 2H, H-6), 4.95 (s, 2H, H-4), 2.11 (s, 6H, H-7) ppm.

^{13}C NMR (100.0 MHz, CDCl$_3$, 295 K):
δ = 154.2 (C-3), 151.4 (C-1), 127.6 (C-5), 120.1 (C-2), 106.8 (C-6), 45.4 (C-4), 12.5 (C-7) ppm.

HR-MS (EI):
Calculated for C$_{12}$H$_{12}$Cl$_2$N$_2$ [M]$^+$: 254.0378 m/z
Found: 254.0378 m/z

Elemental Analysis:
Calculated for C$_{12}$H$_{12}$Cl$_2$N$_2$: C 56.49, H 4.74, N 10.98, Cl 27.79.
Found: C 56.44, H 4.68, N 10.88, Cl 27.64.

IR (thin film):
$\tilde{v}$ = 3059, 2926, 2192, 1587, 1549, 1523, 1438, 1402, 1377, 1329, 1299, 1249, 1211, 1169, 1101, 1022, 985, 924, 906, 884, 841, 819, 769, 750 cm^{-1}.

3.11.   Synthesis of *V-4*
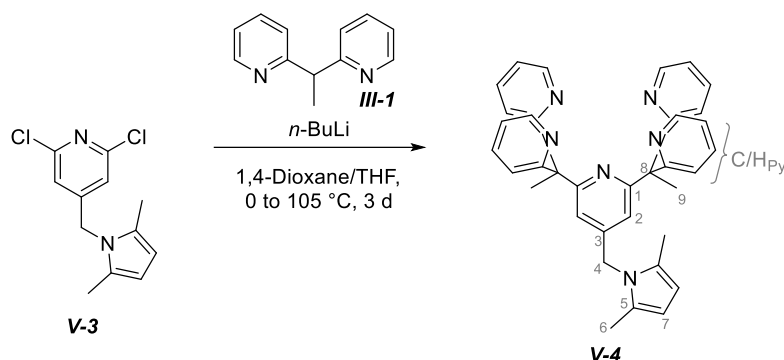
According to a modified literature procedure:[12]

A flame-dried flask was charged with ***III-1*** (2.17 g, 11.76 mmol, 3.0 equiv.), 36 ml of absolute 1,4-dioxane and 4 ml of absolute tetrahydrofuran under inert atmosphere (nitrogen) and cooled to 0 °C. When a solution of *n*-butyl lithium (2.5 M in hexane, 5.49 ml, 13.72 mmol, 3.5 equiv.) was added, the solution turned a dark red. The solution was stirred for 35 min at 0 °C, at which time ***V-3*** (1.0 g, 3.92 mmol, 1.0 equiv.) was added all at once. The reaction mixture was stirred for another 5 min at 0 °C and then allowed to warm to room temperature. The mixture was then heated to reflux (bath temperature 105 °C) for 3 d. The mixture was then allowed to cool to room temperature and 25 ml water were added slowly and the mixture extracted with dichloromethane (3 x 50 ml). The combined organic layers were dried over anhydrous magnesium sulfate and the solvents removed *in vacuo*. A deep red oil was obtained as the crude product. Column chromatography (silica, 10% triethylamine 90% hexanes grading to 10% triethylamine 40% ethyl acetate 50% hexanes) gave the product ***V-4*** as a yellow solid (83%, 1.8 g).

¹H NMR (400.0 MHz, CDCl₃, 295 K):
δ = 8.50 (ddd, J = 4.8 Hz, J = 1.9 Hz, J = 0.9 Hz, 4H, H$_{Py}$), 7.39 (ddd, J = 8.0 Hz, J = 7.5 Hz, J = 1.9 Hz, 4H, H$_{Py}$), 7.04 (ddd, J = 7.5 Hz, J = 4.8 Hz, J = 1.1 Hz, 4H, H$_{Py}$), 6.78 (dt, J = 7.5 Hz, J = 4.8 Hz, 2H, H$_{Py}$), 6.47 (s, 2H, H-2), 5.67 (s, 2H, H-4), 4.84 (s, 2H, H-7), 2.14 (s, 6 H, H-6), 1.99 (s, 6H, H-9) ppm.

¹³C NMR (100.0 MHz, CDCl₃, 295 K):
δ = 166.1 (C$_{Pyquart}$), 164.9 (C-1), 148.5 (C$_{Py}$), 148.2 (C-5) 135.6 (C$_{Py}$), 127.7 (C-3), 124.0 (C$_{Py}$), 121.0 (C$_{Py}$), 117.5 (C-2), 106.0 (C-4), 60.13 (H-8), 46.4 (C-7), 26.8 (C-6), 12.5 (C-9) ppm.

HR-MS (EI):
Calculated for C₃₆H₃₅N₆ [M+H]⁺: 551.29232 m/z
Found: 551.29529 m/z

Elemental Analysis:
Calculated for C₃₆H₃₄N₆: C 78.52, H 6.22, N 15.26.
Found: C 78.50, H 6.45, N 15.11.

3.12.   Synthesis of L-11
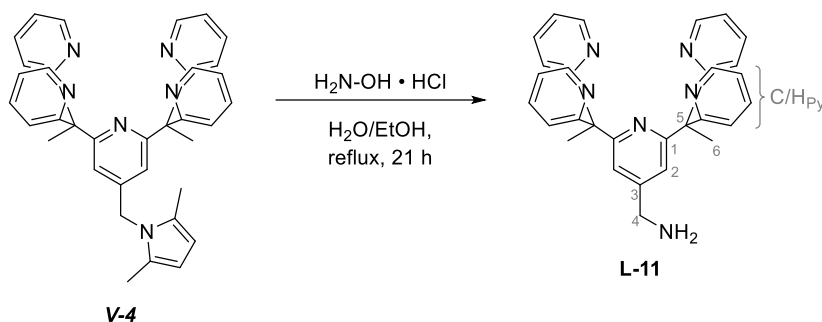
According to a modified literature procedure:[12]

A round bottom flask was charged with **V-4** (1.80 g, 3.27 mmol, 1.0 equiv.), 8 ml ethanol, 2 ml water resulting in a clear yellow solution. Hydroxylamine hydrochloride (0.204 g, 2.94 mmol, 0.9 equiv.) was added and the reaction stirred for 10 min at room temperature. The mixture was then heated to reflux (bath temperature 80 °C) for 21 h. The mixture was then allowed to cool to room temperature, diluted with 20 ml of hydrochloric acid (2 M in water) and washed with diethyl ether (2 x 30 ml). The organic layer was discarded, the aqueous layer basified to pH = 11-12 using a solution of sodium hydroxide (6 M in water) and extracted with dichloromethane (3 x 30 ml). The combined dichloromethane layers were dried over anhydrous magnesium sulfate and the solvents removed *in vacuo*. A deep red oil was obtained as the crude product and then dissolved in dichloromethane (10 ml). Addition of diethyl ether (10 ml) led to precipitation of a colorless solid which was collected on a sintered glass frit and dried *in vacuo* to give the product **L-11** in 71% yield (1.1 g).

¹H NMR (400.0 MHz, CDCl₃, 295 K):
δ = 8.51 (ddd, J = 4.8 Hz, J = 1.9 Hz, J = 0.9 Hz, 4H, H$_{py}$), 7.39 (s, J = 8.1 Hz, J = 7.5 Hz, J = 1.9 Hz, 4H, H$_{py}$), 7.11-7.00 (m, 6H, H$_{py}$/H-2), 6.83 (dt, J = 8.0 Hz, J = 1.0 Hz, 4H, H$_{py}$), 3.79 (s, 2H, H-4), 2.20 (s, 6H, H-6) ppm.

¹H NMR (400.0 MHz, CD₃OD, 295 K):
δ = 8.41 (ddd, J = 4.9 Hz, J = 1.9 Hz, J = 0.9 Hz, 4H, H$_{py}$), 7.54 (s, J = 8.1 Hz, J = 7.5 Hz, J = 1.9 Hz, 4H, H$_{py}$), 7.19 (ddd, J = 7.5 Hz, J = 4.9 Hz, J = 1.1 Hz, 4H, H$_{py}$), 7.16 (s, 2H, H-2), 6.82 (d, J = 8.1 Hz, 4H, H$_{py}$), 4.56 (s, 2H, H-4), 2.17 (s, 6H, H-6) ppm.

¹³C NMR (100.0 MHz, CDCl₃, 295 K):
δ = 167.1 (C$_{py\text{-quart}}$), 165.2 (C-1), 153.5 (C-3), 149.1 (C$_{py}$), 137.6 (C$_{py}$), 125.7 (C$_{py}$), 122.7 (C$_{py}$), 118.9 (C-2), 63.9 (C-4), 61.1 (C-5), 27.13 (C-6) ppm.

HR-MS (EI):
Calculated for C₃₆H₃₅N₆ [M+H]⁺: 473.24537 m/z
Found: 473.24479 m/z

IR (thin film):

$\tilde{\nu}$ = 3047, 2997, 2989, 2976, 2936, 1583, 1561, 1462, 1431, 1461, 1377, 1357, 1293, 1155, 1108, 1091, 1048, 991, 927, 879, 838, 808, 772, 759, 745, 667 cm^{-1}.

3.13.   Synthesis of **C-7**

L-11   **C-7**
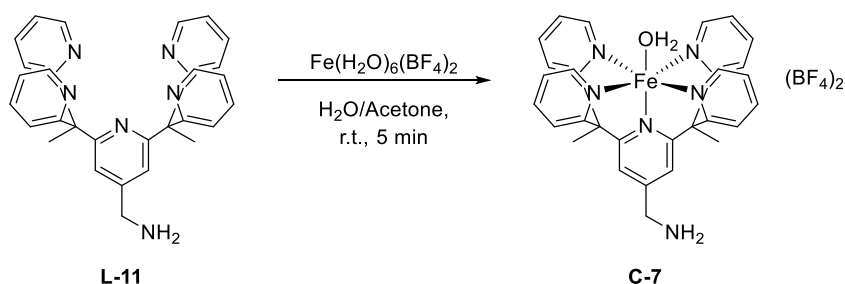
According to a modified literature procedure:[12]

Ligand **L-11** (90.0 mg, 0.190 mmol, 1.0 equiv.) was dissolved in 4.0 ml acetone. Hexaqua iron(II) bis(tetrafluoroborate) (64.3 mg, 0.190 mmol, 1.0 equiv.) was dissolved in 0.5 ml water and then added to the solution of the ligand, turning the solution red-brown. The mixture was stirred for 5 min and then diethyl ether was diffused into the solution to give the product **C-7** as a red-brown powder in 73% yield (100 mg).

HR-MS (ESI):
Calculated for $C_{32}H_{31}FeN_7$ [Fe(mecn)(Py$_5$Me$_2$-CH$_2$-NH$_2$)]$^{2+}$: 284.59952 m/z
Found: 284.59914. m/z
Calculated for $C_{30}H_{28}FeN_6$ [Fe(Py$_5$Me$_2$-CH$_2$-NH$_2$)]$^{2+}$: 264.08625 m/z
Found: 264.08588 m/z

Elemental Analysis:
Calculated for $C_{30}H_{30}B_2F_8FeN_6O$: C 50.04, H 4.20, N 11.67.
Found: C 50.23, H 4.47, N 11.32.

IR (thin film):
$\tilde{v}$ = 1596, 1466, 1441, 1390, 1046, 909, 759 cm^{-1}.

3.14.   Synthesis of **L-12**
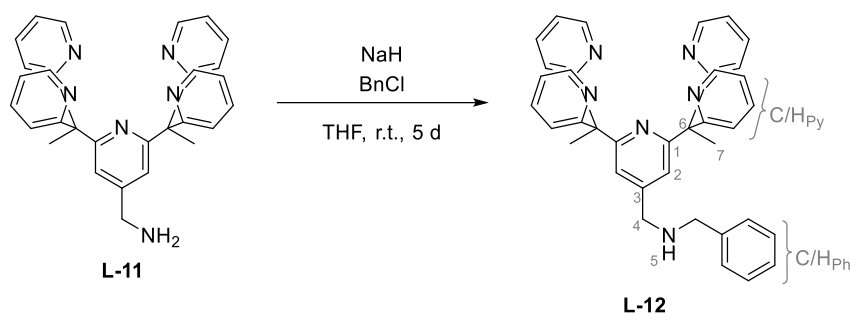
Ligand **L-11** (100.0 mg, 0.212 mmol, 1.0 equiv.) was dissolved in 5 ml absolute tetrahydrofuran and 2 ml absolute dichloromethane. Sodium hydride (60wt.-% in mineral oil, 60.00 mg, 1.500 mmol, 7.1 equiv.) and benzyl chloride (250.0 µl, 275.0 mg, 1.300 mmol, 6.2 equiv.) were added and the mixture stirred for 5 days at room temperature. When thin layer chromatography (silica, UV, 10% triethyl amine, 40% ethyl acetate, 50% hexanes) indicated complete consumption of the starting material, the solvents were removed *in vacuo*. *Iso*-hexane (5 ml) was added and the emulsion stirred for 10 min at room temperature. The hexane layer was removed, the remaining oil suspended in water and extracted with dichloromethane (3 x 10 ml). The combined organic layers were dried with anhydrous magnesium sulfate and the solvents removed *in vacuo* to give the crude product as a yellow oil. Column chromatography (silica, 10% triethyl amine and grading from 20-40% ethyl acetate/70-50% hexanes) gave the product **L-12** as a colorless oil (34%).

¹H NMR (400.0 MHz, CDCl$_3$, 295 K):
δ = 8.68 (ddd, J = 4.8 Hz, J = 1.9 Hz, J = 0.9 Hz, 4H, H$_{py}$), 7.56 (ddd, J = 8.1 Hz, J = 7.4 Hz, J = 1.9 Hz, 4H, H$_{py}$), 7.49-7.36 (m, 5H, H$_{Ph}$), 7.21 (ddd, J = 7.5 Hz, J = 4.8 Hz, J = 1.1 Hz, 4H, H-2), 7.00 (dt, J = 8.1 Hz, J = 1.1 Hz, 4H, H$_{py}$), 3.89 (s, 2H, H-5), 3.89 (s, 2H, H-4), 2.38 (s, 6H, H-7) ppm.

¹³C NMR (100.0 MHz, CDCl$_3$, 295 K):
δ = 166.4 (C$_{Py\text{-}quart}$), 164.4 (C-1), 150.1 (C-3), 148.5 (C$_{Py}$), 140.1 (C$_{Ph\text{-}quart}$), 135.6 (C$_{Py}$), 128.5 (C$_{Ph}$), 128.3 (C$_{Ph}$), 127.2 (C$_{Ph}$), 124.2 (C$_{Py}$), 121.0 (C$_{Py}$), 119.4 (C-2), 60.13 (C-6), 53.6 (C-4), 52.5 (C-5), 26.9 (C-7) ppm.

HR-MS (ESI):
Calculated for C$_{37}$H$_{35}$N$_6$ [Py$_5$Me$_2$-CH$_2$-NHBn+H]$^+$: 563.29232 m/z
Found: 563.29145 m/z

3.15. Synthesis of V-5

V-5
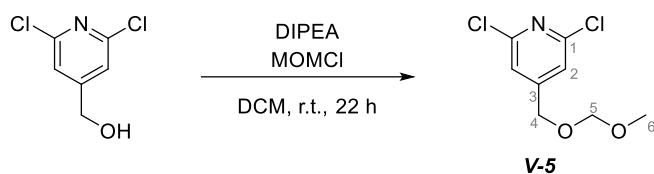
A flask was charged with 2,6-dichloropyridine-4-methanol (1.00 g, 5.62 mmol, 1.0 equiv.) and 10.0 ml dichloromethane. Di-*iso*-propyl-ethyl-amine (DIPEA) (2.87 ml, 2.18 g, 16.85 mmol, 3.0 equiv.) was added and the mixture cooled to 0 °C. Chloromethyl methyl ether (MOMCl) (1.07 ml, 1.13 g, 14.04 mmol, 2.5 equiv.) was added dropwise and the reaction mixture stirred at 0 °C for 10 min. Subsequently, the mixture was allowed to warm to room temperature and stirred for additional 22 h. At this point thin layer chromatography (UV, 50% ethyl acetate in hexanes) showed no more starting material, thus the clear red reaction mixture was diluted with 3 ml dichloromethane, poured into diluted hydrochloric acid (~3%) and stirred for 10 min at room temperature. The yellow layers were separated, the aqueous layer extracted with dichloromethane (3 x 20 ml). The combined organic layers were dried over anhydrous magnesium sulfate and the solvents removed *in vacuo* to yield the crude product as a yellow oil. Column purification (silica, 20% ethyl acetate in hexanes grading to 40% ethyl acetate) gave the product *V-5* as a colorless oil in 80% yield (1.0 g).

R_F = 0.78 (UV, 50% ethyl acetate in hexanes)

^{1}H NMR (400.0 MHz, CDCl$_3$, 295 K):
δ = 7.26 (d, J = 0.8 Hz, 2H, H-2), 4.73 (s, 2H, H-5), 4.58 (t, J = 0.8 Hz, 2H, H-4), 3.41 (s, 3H, H-6) ppm.

^{13}C NMR (100.0 MHz, CDCl$_3$, 295 K):
δ = 153.6 (C-3), 150.7 (C-1), 120.8 (C-2), 96.4 (C-5), 66.4 (C-4), 55.8 (C-6) ppm.

HR-MS (EI):
Calculated for C$_8$H$_{10}$Cl$_2$NO$_2$ [M+H]$^+$: 222.00886 m/z
Found: 222.00836 m/z

Elemental Analysis:
Calculated for C$_{14}$H$_8$Cl$_2$N$_2$O$_2$: C 43.27, H 4.09, N 6.31, Cl 31.93.
Found: C 43.42, H 3.91, N 6.27, Cl 31.56.

3.16. Synthesis of L-13
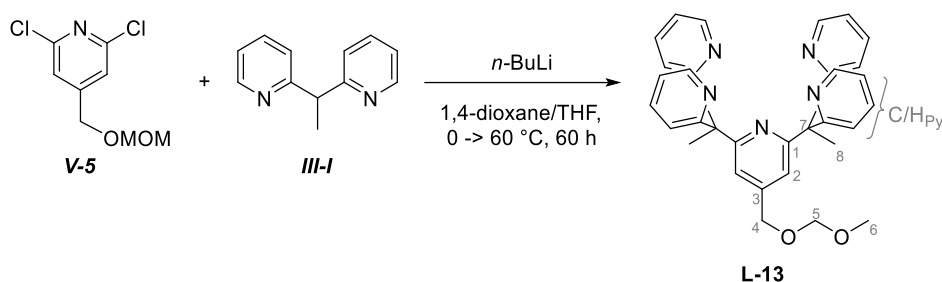
According to a modified literature procedure:[12]

A flame-dried flask was charged with 1,1-di-(2-pyridyl)-ethane (0.217 g, 1.18 mmol, 3.0 equiv.), 3 ml of absolute 1,4-dioxane and 1 ml of absolute tetrahydrofuran under inert atmosphere (nitrogen) and cooled to 0 °C. When a solution of *n*-butyl lithium (2.5 M in hexane, 0.55 ml, 1.37 mmol, 3.5 equiv.) was added the solution turned a dark red. The solution was stirred for 35 min at 0 °C, at which time *V-5* (100.0 mg, 0.39 mmol, 1.0 equiv.) was added all at once. The reaction mixture was stirred for another 5 min at 0 °C and then allowed to warm to room temperature. The mixture was then heated to 100 °C for 60 h. The mixture was allowed to cool to room temperature and diluted with 10 ml ethyl acetate. 3 g ice and 10 ml water were added and the mixture vigorously stirred for 15 min at room temperate. The layers were separated and the organic layer washed with 10 ml brine and 10 ml water. The combined aqueous layers were then extracted with ethyl acetate (3 x 30 ml). The combined organic layers were dried over anhydrous magnesium sulfate and the solvents removed *in vacuo*. A red/orange oil was obtained as the crude product. Column chromatography (silica, 20% triethylamine, 20% ethyl acetate in hexanes grading to 20% triethylamine, 70% ethyl acetate in hexanes) gave the product **L-13** as a pale yellow oil in 26% yield (300 mg).

¹H NMR (400.0 MHz, CDCl₃, 295 K):
δ = 8.50 (ddd, J = 4.8 Hz, J = 1.9 Hz, J = 0.9 Hz, 4H, H$_{py}$), 7.38 (ddd, J = 8.1 Hz, J = 7.4 Hz, J = 1.9 Hz, 4H, H$_{py}$), 7.08 (s, 2H, H-2), 7.04 (ddd, J = 7.5 Hz, J = 4.8 Hz, J = 1.1 Hz, 4H, H$_{py}$), 6.81 (dt, J = 8.1 Hz, J = 1.0 Hz, 4H, H$_{py}$), 4.64 (s, 2H, H-5), 4.51 (s, 2H, H-4), 3.31 (s, 3H, H-6), 2.21 (s, 6H, H-8) ppm.

¹³C NMR (100.0 MHz, CDCl₃, 295 K):
δ = 166.3 (C$_{py\text{-}quart}$), 164.5 (C$_1$), 148.5 (C$_{py}$), 148.0 (C-3), 135.6 (C$_{py}$), 124.2 (C$_{py}$), 121.0, (C$_{py}$), 118.2 (C-2), 96.3 (C-5), 68.4 (C-4), 60.1 (C-7), 55.6 (C-6), 26.8 (C-8) ppm.

HR-MS (EI):
Calculated for C₃₆H₃₅N₆ [M+H]⁺: 551.29232 m/z
Found: 551.29529 m/z

3.17. Synthesis of C-9

L-13   **C-9**
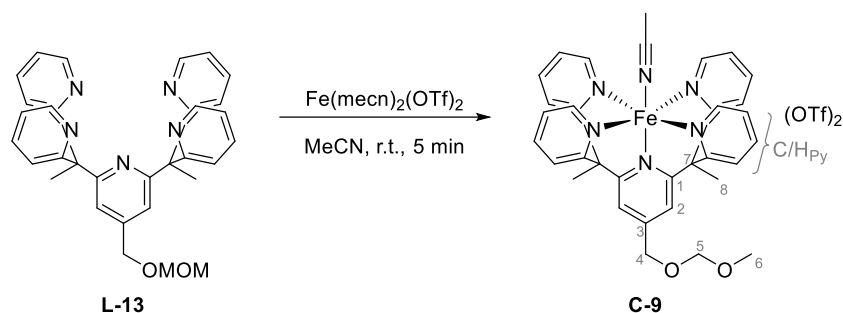
According to a modified literature procedure:[12]

Ligand **L-13** (100.0 mg, 0.193 mmol, 1.0 equiv.) was dissolved in 4.5 ml acetonitrile. Iron(II) bis(acetonitrile) bis(triflate) (84.2 mg, 0.193 mmol, 1.0 equiv.) was added as a solid, turning the solution deep red. The mixture was then stirred for an additional 5 min and then diethyl ether was diffused into the solution under ambient conditions to give the product **C-9** as brown crystals in 74% yield (130.0 mg).

¹H NMR (400.0 MHz, CD$_3$CN, 295 K):
δ = 9.84 (dt, J = 5.9 Hz, J = 1.1 Hz, 4H, H$_{Py}$), 8.00 (s, 2H, H-2), 7.93 (d, J = 3.7 Hz, 8H, H$_{Py}$), 7.55 (dt, J = 5.9 Hz, J = 4.6 Hz, 4H, H$_{Py}$), 4.76 (s, 2H, H-5), 4.72 (s, 2H, H-4), 3.35 (s, 3H, H-6), 2.76 (s, 6H, H-8), 1.96 (s, 3H, CH_3-CN) ppm.

¹³C NMR (100.0 MHz, CD$_3$CN, 295 K):
δ = 164.6, 163.0, 158.2 (C$_{py}$), 152.9, 139.7 (C$_{py}$), 124.3 (C$_{py}$), 123.8 (C$_{py}$), 120.1 (C-2), 97.4 (C-5), 67.6 (C-4), 56.0 (C-6), 55.6 (C-7), 24.2 (C-8) ppm.

HR-MS (ESI):
Calculated for C$_{33}$H$_{31}$F$_3$FeN$_5$O$_5$S [Fe(Py$_5$Me$_2$-CH$_2$-OMOM)(OTf)]$^+$: 722.13474 m/z
Found [Fe(Py$_5$Me$_2$-CH$_2$-OMOM)(OTf)]$^+$: 722.13434 m/z
Calculated for C$_{34}$H$_{34}$FeN$_6$O$_2$ [Fe(Py$_5$Me$_2$-CH$_2$-OMOM)(MeCN)]$^{2+}$: 307.10463 m/z
Found [Fe(Py$_5$Me$_2$-CH$_2$-OMOM)(MeCN)]$^+$: 307.10416 m/z

Elemental Analysis:
Calculated for C$_{36}$H$_{38}$F$_6$FeN$_6$O$_{10}$S$_2$ [M x 2 H$_2$O]: C 45.58, H 4.04, N 8.86, S 6.76.
Found: C 45.92, H 4.02, N 8.73, S 7.20.

IR (thin film):
$\tilde{v}$ = 1737, 1620, 1600, 1576, 1469, 1440, 1373, 1253, 1225, 1148, 1060, 1027, 963, 918, 879, 831, 796, 771, 758 cm^{-1}.

3.18.   Synthesis of L-14

L-13   **L-14**
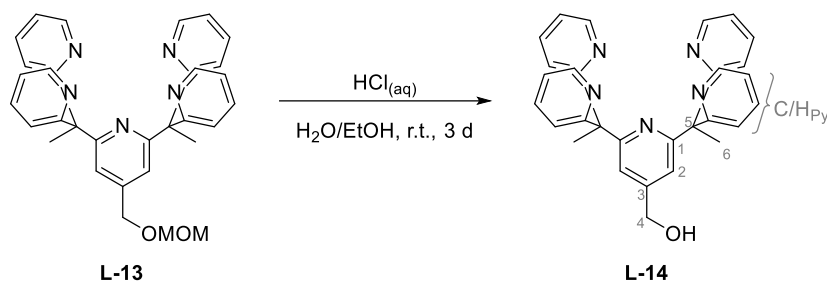
A round bottom flask was charged with crude **L-13** (0.36 g, 0.35 mmol, 1.0 equiv.), 7 ml of ethanol and aqueous hydrochloric acid (5 M, 7 ml, 35.00 mmol, 100.0 equiv.). The solution was stirred for 3 h at room temperature. The solvents were removed *in vacuo* to yield the crude product as a pale orange oil. Column chromatography (silica, 20% triethylamine, 40% ethyl acetate grading to 20% triethylamine, 60% ethyl acetate in hexanes) gave the product **L-14** as a colorless solid (50% yield, 83 mg).

R_F = 0.23 (silica, UV, 20% triethyl amine, 40% ethyl acetate, 40% hexanes)

¹H NMR (400.0 MHz, CD₃OD, 295 K):
δ = 8.42 (ddd, J = 4.9 Hz, J = 1.9 Hz, J = 0.9 Hz, 4H, H_{Py}), 7.54 (ddd, J = 8.1 Hz, J = 7.5 Hz, J = 1.9 Hz, 4H, H_{Py}), 7.22-7.14 (m, 6H, H-2, H_{Py}), 6.83 (dt, J = 8.1 Hz, J = 1.0 Hz, 4H, H_{Py}), 4.56 (s, 2H, H-4), 2.07 (s, 3H, H-6) ppm.

¹³C NMR (100.0 MHz, CD₃OD, 295 K):
δ = 167.1 ($C_{py-quart}$), 165.2 (C-1), 153.5 (C-3), 149.1 (C_{py}), 137.6 (C_{py}), 125.7 (C_{py}), 122.7 (C_{py}), 118.9 (C-2), 63.9 (C-4), 61.1 (C-5), 27.1 (C-6) ppm.

HR-MS (EI):
Calculated for $C_{30}H_{28}N_5O$ [M+H]⁺: 474.22939 m/z
Found [M+H]⁺: 474.22916 m/z

IR (thin film):
$\tilde{v}$ = 3150, 2995, 2933, 2839, 1737, 1588, 1565, 1466, 1426, 1359, 1286, 1230, 1151, 1091, 1073, 1060, 1046, 992, 876, 780, 744, 655 cm⁻¹.

3.19.   Synthesis of C-10

L-14   **C-10**
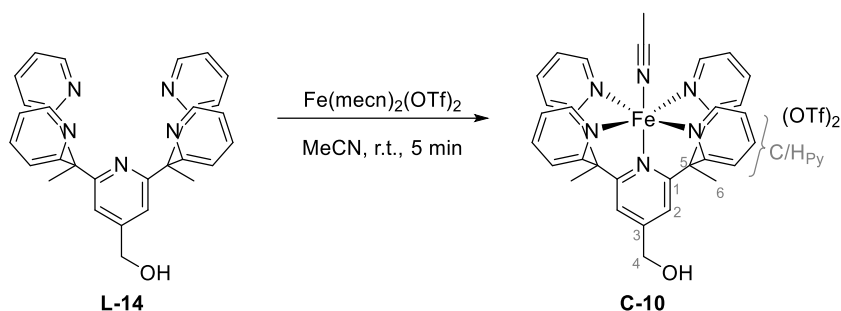
According to a modified literature procedure:[12]

Ligand **L-14** (50.0 mg, 0.106 mmol, 1.0 equiv.) was dissolved in 2.5 ml acetonitrile. Iron(II) bis(acetonitrile) bis(triflate) (46.0 mg, 0.106 mmol, 1.0 equiv.) was added as a solid, turning the solution deep red. The mixture was then stirred for an additional 5 min, filtered through a PTFE syringe filter (0.45 μm) and then diethyl ether was diffused into the solution under ambient conditions to give the product **C-10** as a red powder in 76% yield (70 mg).

¹H NMR (400.0 MHz, CD$_3$CN, 295 K):
δ = 9.79 (d, J = 5.8 Hz, 4H, H$_{Py}$), 7.99 (s, 2H, H-2), 7.95 (d, J = 3.5 Hz, 8H, H$_{Py}$), 7.53 (dt, J = 5.9 Hz, J = 4.5 Hz, 4H, H$_{Py}$), 4.77 (d, J = 5.5 Hz, 2H, H-4), 3.70 (dt, J = 5.8 Hz, 1H, H-5), 2.75 (s, 6H, H-6), 1.96 (s, 3H, **CH$_3$**-CN) ppm.

¹³C NMR (100.0 MHz, CD$_3$CN, 295 K):
δ = 164.3 (C-1), 163.1 (C$_{py\text{-}quart}$), 158.2 (C$_{py}$), 156.4 (C-3), 139.7 (C$_{py}$), 124.3 (C$_{py}$), 123.8 (C$_{py}$), 119.5 (C-2), 62.5 (C-4), 55.7 (C-5), 24.1 (C-6) ppm.

HR-MS (ESI):
Calculated for C$_{31}$H$_{27}$F$_3$FeN$_5$O$_4$S [Fe(Py$_5$Me$_2$-CH$_2$-OH)(OTf)]$^+$: 678.10853 m/z
Found: 678.10903 m/z
Calculated for C$_{32}$H$_{30}$FeN$_6$O [Fe(Py$_5$Me$_2$-CH$_2$-OH)(MeCN)]$^{2+}$: 285.09153 m/z
Found: 285.09122 m/z

3.20.   Synthesis of **C-11**
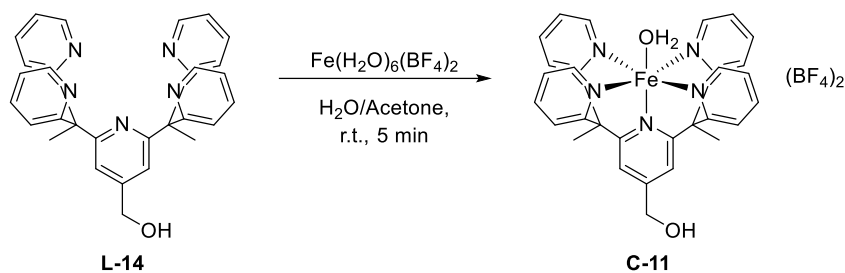
According to a modified literature procedure:[12]

Ligand **L-14** (90.0 mg, 0.190 mmol, 1.0 equiv.) was dissolved in 4.0 ml acetone. Hexaqua iron(II) bis(tetrafluoroborate) (64.2 mg, 0.190 mmol, 1.0 equiv.) was dissolved in 0.5 ml water and then added to the solution of the ligand, turning the solution red-brown. The mixture was stirred for 5 min and then diethyl ether was diffused into the solution to give the product **C-11** as a red-brown powder in 73% yield (100.0 mg).

HR-MS (ESI):
Calculated for $C_{31}H_{27}F_3FeN_5O_4S$ $[Fe(Py_5Me_2\text{-}CH_2\text{-}OH)(OTf)]^+$: 678.10853 m/z
Found: 678.10903 m/z
Calculated for $C_{32}H_{30}FeN_6O$ $[Fe(Py_5Me_2\text{-}CH_2\text{-}OH)(MeCN)]^{2+}$: 285.09153 m/z
Found: 285.09145 m/z

Elemental Analysis:
Calculated for $C_{30}H_{29}B_2F_8FeN_5O_2$ x H_2O: C 48.76, H 4.23, N 9.48.
Found: C 49.07, H 4.35, N 9.35.

IR (thin film):
$\tilde{\nu}$ = 1622, 1599, 1467, 1437, 1394, 1049, 882, 829, 797, 759 cm^{-1}.

3.21. Synthesis of L-15

L-14   **L-15**
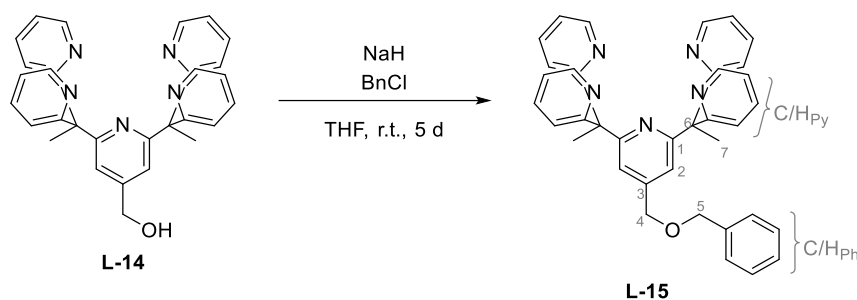
A flame dried flask was charged with sodium hydride (60wt.-% in mineral oil, 60.80 mg, 1.520 mmol, 4.00 equiv.) and 1 ml dry hexanes was added and the suspension stirred for 5 min at room temperature. The solvent was carefully removed *via* syringe and the procedure repeated. Ligand **L-14** (180.0 mg, 0.380 mmol, 1.0 equiv.) was dissolved in 8 ml absolute tetrahydrofuran and was then added to the sodium hydride. Benzyl chloride (250.0 µl, 275.0 mg, 1.300 mmol, 6.17 equiv.) was added and the mixture stirred for 5 days at room temperature. When thin layer chromatography (silica, UV, 10% triethyl amine, 40% ethyl acetate, 50% hexanes) indicated complete consumption of the starting material, the solvents were removed *in vacuo*. The remaining oil was suspended in water and extracted with ethyl acetate (3 x 20 ml). The combined organic layers were dried with anhydrous magnesium sulfate and the solvents removed *in vacuo* to give the crude product as a yellow oil. Column chromatography (silica, 10% triethyl amine and grading from 20-40% ethyl acetate/70-50% hexanes) gave the product **L-15** as a colorless oil (84%, 180 mg).

R_F = 0.38 (silica, UV, 20% triethyl amine, 40% ethyl acetate, 40% hexanes)

^{1}H NMR (400.0 MHz, CDCl$_3$, 295 K):
δ = 8.41 (ddd, J = 4.8 Hz, J = 1.9 Hz, J = 0.9 Hz, 4H, H$_{py}$), 7.39 (ddd, J = 8.1 Hz, J = 7.5 Hz, J = 1.9 Hz, 4H, H$_{py}$), 7.36-7.25 (m, 5H, H$_{Ph}$), 7.07 (s, 2H, H-2), 7.04 (ddd, J = 7.5 Hz, J = 4.8 Hz, J = 1.1 Hz, 4H, H$_{py}$), 6.83 (dt, J = 8.0 Hz, J = 1.0 Hz, 4H, H$_{py}$), 4.50 (s, 2H, H-5), 4.47 (s, 2H, H-4), 2.21 (s, 6H, H-7) ppm.

^{13}C NMR (100.0 MHz, CDCl$_3$, 295 K):
δ = 166.2 (C$_{Py-quart}$), 164.4 (C-1), 148.4 (C$_{Py}$), 148.1 (C-3), 137.8 (C$_{Ph-quart}$), 135.5 (C$_{Py}$), 128.4 (C$_{Ph}$), 127.7 (C$_{Ph}$), 124.1 (C$_{Py}$), 120.9 (C$_{Py}$), 118.1 (C-2), 72.6 (C-4), 70.9 (C-5), 60.1 (C-6), 26.8 (C-7) ppm.

HR-MS (ESI):
Calculated for C$_{37}$H$_{34}$N$_5$O [Py$_5$Me$_2$-CH$_2$-OBn+H]$^+$: 564.27634 m/z
Found: 564.27671 m/z

Elemental Analysis:
Calculated for C$_{37}$H$_{33}$N$_5$O: C 78.84, H 5.90, N 12.42.
Found: C 76.92, H 6.06, N 11.85.

IR (thin film):

$\tilde{\nu}$ = 3053, 2998, 2932, 1585, 1563, 1496, 1466, 1428, 1362, 1294, 1152, 1102, 1074, 1047, 1029, 992, 960, 917, 877, 843, 784, 745, 699, 671 cm^{-1}.

IR (thin film):

3.22.   Synthesis of **C-12**
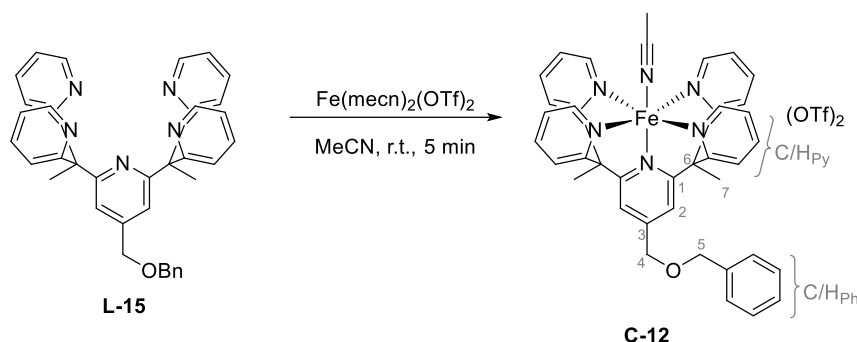
According to a modified literature procedure:[12]

Ligand **L-15** (50.0 mg, 0.089 mmol, 1.0 equiv.) was dissolved in 2.0 ml acetonitrile. Iron(II) bis(acetonitrile) bis(triflate) (38.7 mg, 0.089 mmol, 1.0 equiv.) was added as a solid, turning the solution deep red. The mixture was then stirred for an additional 5 min, filtered through a PTFE syringe filter (0.45 μm) and then diethyl ether was diffused into the solution under ambient conditions to give the product **C-12** as red-brown needles in 49% yield (42 mg).

¹H NMR (400.0 MHz, CD$_3$CN, 295 K):
δ = 9.81 (d, J = 5.9 Hz, 4H, H$_{Py}$), 7.93 (m, 10H, H-2/H$_{Py}$), 7.55 (td, J = 5.7 Hz, J = 3.2 Hz, 4H, H$_{Py}$), 7.32 (d, J = 7.4 Hz, 2H, H$_{Ph}$), 7.21 (t, J = 7.6 Hz, 2H, H$_{Ph}$), 7.10 (tt, J = 7.4 Hz, J = 1.4 Hz, 1H, H$_{Ph}$), 4.74 (s, 2H, H-4), 4.61 (s, 2H, H-5), 2.72 (s, 6H, H-7), 1.96 (s, 3H, C**H$_3$**-CN) ppm.

¹³C NMR (100.0 MHz, CD$_3$CN, 295 K):
δ = 164.4 (C-1), 163.0 (C$_{Py-quart}$), 158.2 (C$_{Py}$), 153.2 (C-3), 139.7 (C$_{Py}$), 139.0 (C$_{Ph}$), 129.3 (C$_{Ph}$), 129.0 (C$_{Ph}$), 128.7 (C$_{Ph}$), 124.3 (C$_{Py}$), 123.8 (C$_{Py}$), 120.3 (C-2), 73.9 (C-4), 70.5 (C-5), 55.6 (C-6), 24.1 (C-7) ppm.

HR-MS (ESI):
Calculated for C$_{38}$H$_{33}$F$_3$FeN$_6$O$_4$S [Fe(Py$_5$Me$_2$-CH$_2$-OBn)(OTf)]$^+$: 768.15548 m/z
Found: 768.15697 m/z
Calculated for C$_{39}$H$_{36}$FeN$_6$O [Fe(Py$_5$Me$_2$-CH$_2$-OBn)(MeCN)]$^+$: 330.11500 m/z
Found: 330.11493 m/z

Elemental Analysis:
Calculated for C$_{41}$H$_{36}$F$_6$FeN$_6$O$_7$S$_2$: C 51.36, H 3.79, N 8.77, S 6.69.
Found: C 50.85, H 4.12, N 8.77, S 6.73.

IR (thin film):
$\tilde{v}$ = 1708, 1623, 1600, 1469, 1444, 1353, 1253, 1223, 1146, 1029, 905, 878, 833, 763, 741, 670 cm⁻¹.

3.23.   Synthesis of **C-13**
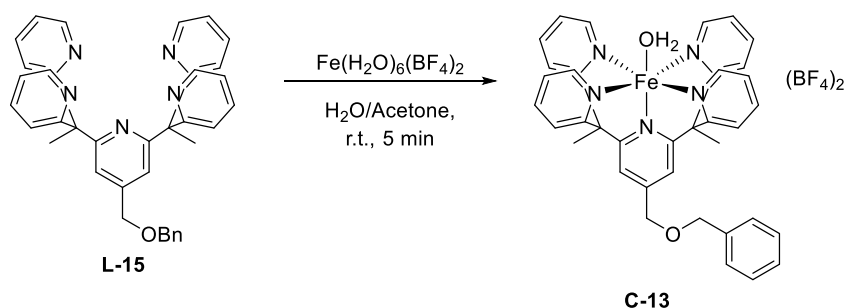
According to a modified literature procedure:[12]

Ligand **L-15** (50.0 mg, 0.089 mmol, 1.0 equiv.) was dissolved in 2.5 ml acetone. Hexaqua iron(II) bis(tetrafluoroborate) (29.9 mg, 0.089 mmol, 1.0 equiv.) was dissolved in 0.25 ml water and then added to the solution of the ligand, turning the solution red-brown. The mixture was stirred for 5 min and then diethyl ether was diffused into the solution to give the product **C-13** as a red-brown powder in 49% yield (35.5 mg).

HR-MS (ESI):
Calculated for $C_{37}H_{33}FFeN_5O$ [Fe(Py$_5$Me$_2$-CH$_2$-OBn)(F)]$^+$: 638.20186 m/z
Found: 638.10224 m/z
Calculated for $C_{39}H_{36}FeN_6O$ [Fe(Py$_5$Me$_2$-CH$_2$-OBn)(MeCN)]$^+$: 330.11500 m/z
Found: 330.11492 m/z

Elemental Analysis:
Calculated for $C_{37}H_{37}B_2F_8FeN_5O_3$ [M+H$_2$O]: C 53.60, H 4.50, N 8.45.
Found: C 53.29, H 4.36, N 8.36.

IR (thin film):
$\tilde{\nu}$ = 1621, 1598, 1467, 1436, 1392, 1362, 1289, 1035, 880, 756 cm^{-1}.

3.24.   Synthesis of *V-11*
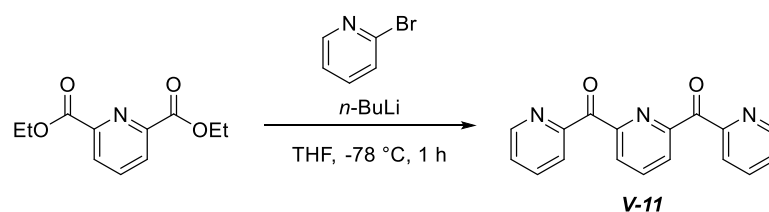
According to a modified literature procedure:[68]

A flame-dried flask was charged with 2-bromo pyridine (2.62 ml, 4.25 g, 26.88 mmol, 3.0 equiv.) and 100 ml of absolute tetrahydrofuran were added. After cooling the mixture to −78 °C, a solution of *n*-butyl lithium (2.5 M in hexanes, 10.75 ml, 1.72 g, 26.88 mmol, 3.0 equiv.) was added dropwise, resulting in a color change to yellowish brown. The mixture was stirred at −78 °C for 10 min and then a solution of 1-(6-(1,1-dipyridin-2-yl)ethyl)pyridin-2-yl)ethan-1-one (0.224 M in tetrahydrofuran, 40.0 ml, 2.0 g, 8.96 mmol, 1.0 equiv.) was added dropwise, the solution's color slowly changed to a very dark green. The reaction was stirred at −78 °C for 40 min, then 50 ml methanol were added slowly to quench the reaction. The mixture was allowed to warm to room temperature, 100 ml of aqueous hydrochloric acid (3 M) were added, and organic solvents removed via rotary evaporation (90 mbar at 40 °C) the mixture transferred to a separatory funnel. Additional 10 ml of aqueous hydrochloric acid (3 M) were added and the mixture washed with dichloromethane (2 x 25 ml), this organic layer was discarded. The aqueous layer was basified to pH 12 with an aqueous solution of sodium hydroxide (19 M) and extracted with dichloromethane (3 x 100 ml). These combined organic layers were dried over anhydrous magnesium sulfate and the solvents removed *in vacuo* to yield the crude product. Recrystallization at room temperature from acetone/diethyl ether gave the pure product *V-11* as a colorless crystalline solid in 67% yield (1.74 g).

R_F = 0.13 (silica, UV, 10% triethyl amine, 50% ethyl acetate, 40% hexanes)

¹H NMR (400.0 MHz, CDCl₃, 295 K):
δ = 8.75 (ddd, *J* = 4.7 Hz, *J* = 1.7 Hz, *J* = 0.9 Hz, 2H), 8.31 (d, *J* = 8.0 Hz, 2H), 8.19 (dt, *J* = 7.9 Hz, *J* = 1.1 Hz, 2H), 8.11 (dd, *J* = 8.2 Hz, *J* = 7.4 Hz, 1H), 7.79 (td, *J* = 7.8 Hz, *J* = 1.8 Hz, 2H), 7.45 (ddd, *J* = 7.6 Hz, *J* = 4.7 Hz, *J* = 1.2 Hz, 2H) ppm.

NMR data is in accordance with the literature.[68]

HR-MS (ESI):
Calculated for $C_{17}H_{12}N_3O_2$ [M+H]⁺: 290.09295 m/z
Found: 290.09271 m/z

3.25. Synthesis of L-2
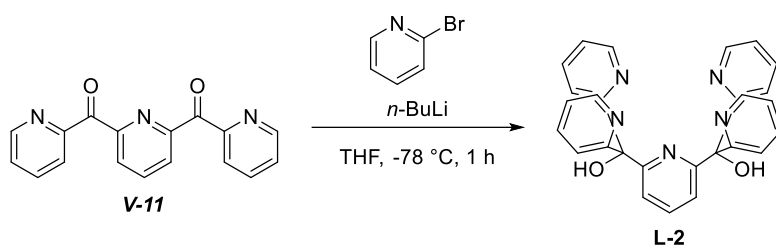
According to a modified literature procedure:[68]

A flame-dried flask was charged with 2-bromo pyridine (0.36 ml, 0.58 g, 3.66 mmol, 2.12 equiv.) and 80 ml of absolute tetrahydrofuran were added. After cooling the mixture to –78 °C, a solution of n-butyl lithium (2.5 M in hexanes, 1.49 ml, 0.24 g, 3.72 mmol, 2.15 equiv.) was added dropwise, resulting in a color change to yellowish brown. The mixture was stirred at –78 °C for 10 min and then a solution of **V-11** (57.5 mM in tetrahydrofuran/1,4-dioxane (4:1), 30.0 ml, 0.5 g, 1.73 mmol, 1.0 equiv.) was added dropwise, the solution's color changed first to red then to a very dark green. The reaction was stirred at –78 °C for 60 min, then allowed to warm to room temperature. When LC-MS confirmed complete consumption of **V-11**, 50 ml methanol were added slowly to quench the reaction. Then 100 ml of aqueous hydrochloric acid (3 M) were added, the organic solvents removed *via* rotary evaporation (90 mbar @ 40 °C), and the mixture transferred to a separatory funnel. Additional 10 ml of aqueous hydrochloric acid (3 M) were added and the mixture washed with dichloromethane (2 x 25 ml), this organic layer was discarded. The aqueous layer was basified to pH 12 with an aqueous solution of sodium hydroxide (19 M) and extracted with dichloromethane (3 x 100 ml). These combined organic layers were dried over anhydrous magnesium sulfate and the solvents removed *in vacuo* to yield the crude product. Recrystallization at room temperature from acetone/diethyl ether gave the pure product **L-2** as a colorless solid in 38% yield (290.0 mg).

R_F = 0.04 (silica, UV, 10% methanol, 90% dichloromethane)

¹H NMR (400.0 MHz, CDCl$_3$, 295 K):
δ = 8.49 (ddd, J = 4.9 Hz, J = 1.8 Hz, J = 1.0 Hz, 4H), 7.73-7.71 (m, 3H), 7.52 (ddd, J = 8.0 Hz, J = 7.3 Hz, J = 1.8 Hz, 4H), 7.44 (dt, J = 8.0 Hz, J = 1.1 Hz, 4H), 7.17-7.13 (m, 6H) ppm.

NMR data is in accordance with the literature.[68]

HR-MS (ESI):
Calculated for C$_{27}$H$_{22}$N$_5$O$_2$ [M+H]$^+$: 448.17735 m/z
Found: 448.17693 m/z

This procedure was part of the Bachelor Thesis of Hannah Wilken, 2021, and the Internship Report of Jan Kruse, 2021, both conducted under my supervision.

3.26. Synthesis of C-14
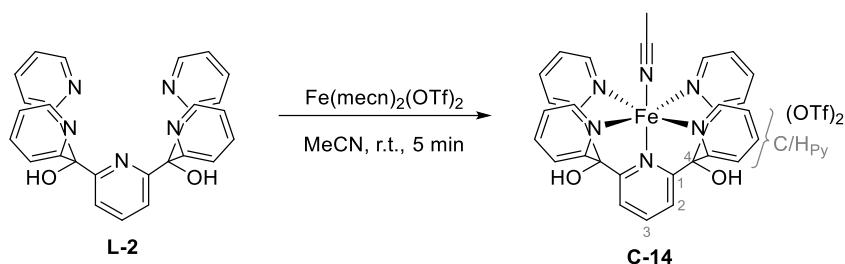
According to a modified literature procedure:[12]

Ligand **L-2** (51.0 mg, 0.114 mmol, 1.0 equiv.) was dissolved in 2.55 ml acetonitrile. Iron(II)bis(acetonitrile)bis(triflate) (49.7 mg, 0.114 mmol, 1.0 equiv.) was added as a solid, turning the solution deep red. The mixture was then stirred for an additional 5 min and then diethyl ether was diffused into the solution under ambient conditions to give the product **C-14** as brown crystals in 77% yield (80.0 mg).

¹H NMR (400.0 MHz, CD$_3$CN, 295 K):
δ = 9.73 (d, J = 5.8 Hz, 4H, H$_{Py}$), 8.17 (m, 5H, H$_{Py}$/H-2/H-3), 7.98 (ddd, J = 8.1 Hz, J = 7.4 Hz, J = 1.4 Hz, 4H, H$_{Py}$), 7.56 (ddd, J = 7.4 Hz, J = 5.8 Hz, J = 1.5 Hz, 4H, H$_{Py}$), 6.85 (s, 2H, OH), 1.96 (s, 3H, CH_3CN) ppm.

¹³C NMR (100.0 MHz, CD$_3$CN, 295 K):
δ = 164.5 (C$_{Py-quart}$), 163.1 (C-1), 158.1 (C$_{Py}$), 140.7 (C-2), 140.0 (C$_{Py}$), 124.9 (C$_{Py}$), 122.4 (C$_{Py}$), 121.0 (C-3), 80.7 (C-4) ppm.

HR-MS (ESI):
Calculated for C$_{30}$H$_{25}$F$_3$FeN$_5$O$_3$S [Fe(Py$_5$(OH)$_2$)(OTf)]$^+$: 652.05649 m/z
Found: 652.05432 m/z

Elemental Analysis:
Calculated for C$_{33}$H$_{30}$F$_6$FeN$_6$O$_7$S$_2$ (**C-14** x H$_2$O): C 43.27, H 3.05, N 9.77, S 7.45.
Found: C 43.25, H 3.12, N 9.79, S 7.91.

IR (thin film):
$\tilde{v}$ = 3288, 1738, 1603, 1469, 1444, 1373, 1276, 1244, 1224, 1157, 1096, 1028, 887, 800, 762, 712, 661 cm^{-1}.

UV-vis (MeCN):
λ = 347 nm (ε = 5315 l mol^{-1} cm^{-1}).
λ = 420 nm (ε = 5415 l mol^{-1} cm^{-1}).

3.27.   Synthesis of C-15
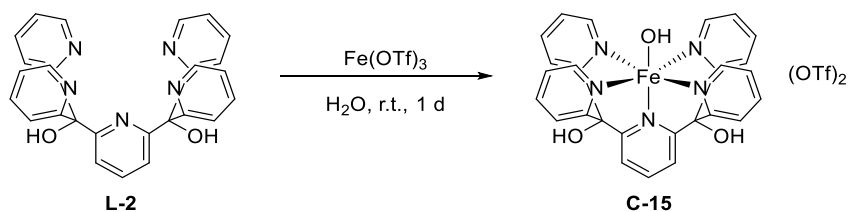
A scintillation vial was charged with finely ground **L-2** (200.0 mg, 0.447 mmol, 1.0 equiv.) and 1.1 ml of water. Iron(III) triflate (247.3 mg, 0.492 mmol, 1.1 equiv.) was added and the suspension mixed by pumping of an Eppendorf pipette. The mixture was sonicated for 60 s, shaken, and again sonicated for 60 s resulting in a dark red suspension. The mixture was then syringe-filtered (PTFE, 0.45 µm) to give a clear red-orange solution. This was placed in a fridge at 4 °C for 3 d until dark red crystals had formed. The supernatant was removed, the crystals washed with water (2 x 0.5 ml, brief sonication) and subsequently dried *in vacuo* to give the pure product **C-15** (no yield determined).

HR-MS (EI):
Calculated for $C_{27}H_{22}FeN_5O_3$ [Fe(OH)(Py$_5$(OH$_2$)$_2$)]$^{2+}$: 260.0536 m/z
Found: 260.0548 m/z

Elemental Analysis:
Calculated for $C_{29}H_{24}F_6FeN_5O_{10}S_2$ [Fe(OH)(Py$_5$(OH$_2$)$_2$)](OTf)$_2$ x H$_2$O:
C 41.64, H 2.89, N 8.37, S 7.67.
Found: C 41.71, H 2.92, N 8.24, S 7.94.

IR (thin film):
$\tilde{v}$ = 3450, 3264, 1739, 1604, 1458, 1445, 1364, 1278, 1243, 1222, 1152, 1097, 1027, 927, 810, 795, 766, 741, 675, 662 cm^{-1}.

This procedure was part of the Bachelor Thesis of Hannah Wilken, 2021, and the Internship Report of Jan Kruse, 2021, both conducted under my supervision.

3.28.   Synthesis of **C-16**

C-14   **C-16**
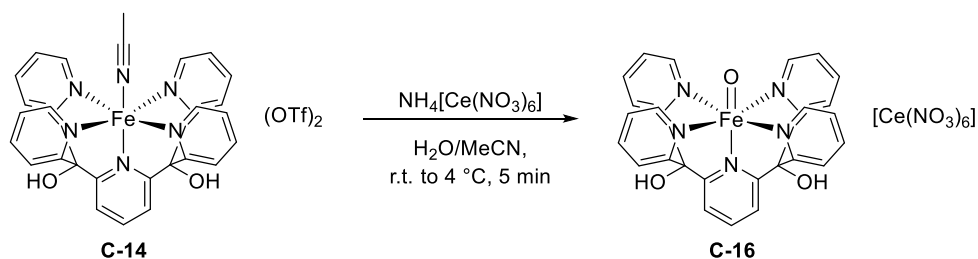
According to a modified literature procedure:[12]

C-14 (80 mg, 0.950 mmol, 1.0 equiv.) was dissolved in 1.2 ml of 3:1 acetonitrile:water. Cerium(IV) ammonium nitrate (276.4 mg, 0.504 mmol, 5.3 equiv.) was added as a solid and the mixture sonicated for 60 s. As a pale green precipitate began to form the reaction mixture was placed in the refridgerator at 4 °C to complete the precipitation. The solid was collected *via* centrifugation (600 rpm), washed with 10.5 ml of ice cold 3:1 acetonitrile:water and dried *in vacuo* to yield product **C-16** as a pale green solid (no yield determined).

Elemental Analysis:
Calculated for $C_{27}H_{23}CeFeN_{11}O_{22}$ (M x H_2O): C 30.90, H 2.21, N 14.68.
Found: C 30.71, H 2.54, N 15.05.

HR-MS (ESI)**:**
Calculated for $C_{27}H_{21}FeN_5O_3$ [$Fe^{IV}(O)(Py_5(OH)_2)$]$^{2+}$: 259.5497 m/z
Found: 259.5492 m/z

IR (thin film):
$\tilde{v}$ = 1605, 1504, 1463, 1278, 1170, 1098, 1029, 830, 805, 780, 763, 742, 661, 626, 614 cm^{-1}.

3.29. Synthesis of **L-3**
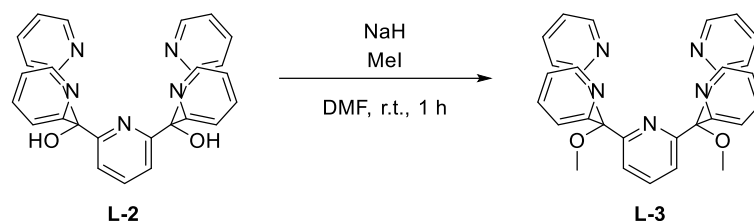
According to a modified literature procedure:[305]

A flame-dried flask was charged with **L-2** (500.0 mg, 1.12 mmol, 1.0 equiv.) and 50 ml of absolute *N,N*-dimethylformamide were added. Sodium hydride (60wt.-%, suspension in mineral oil, 98.3 mg, 2.46 mmol, 2.2 equiv.) was added in two portions, resulting in a color change to red and then green upon stirring for 5 min at room temperature. Methyl iodide (0.35 ml, 348.9 mg, 2.46 mmol, 2.2 equiv.) was added dropwise, the solution's color slowly changed to a pale red. The reaction was stirred at room temperature for 1 h, then 50 ml methanol were added slowly to quench the reaction. Then 100 ml of aqueous hydrochloric acid (3 M) were added, the organic solvents removed *via* rotary evaporation (90 mbar at 40 °C) and the mixture transferred to a separatory funnel. Additional 10 ml of aqueous hydrochloric acid (3 M) were added and the mixture washed with dichloromethane (2 x 25 ml), this organic layer was discarded. The aqueous layer was basified to pH 12 with an aqueous solution of sodium hydroxide (19 M) and extracted with dichloromethane (3 x 100 ml). These combined organic layers were dried over anhydrous magnesium sulfate and the solvents removed in vacuo to yield the crude product. Recrystallization at room temperature from acetone/diethyl ether gave the pure product **L-3** as a colorless solid in 35% yield (180.0 mg).

R_F = 0.22 (silica, UV, 20% triethylamine, 50% ethyl acetate, 30% hexanes)

¹H NMR (400.0 MHz, CDCl$_3$, 295 K):
δ = 8.51 (ddd, *J* = 4.8 Hz, *J* = 1.9 Hz, *J* = 0.9 Hz, 4H), 7.69 (dd, *J* = 8.4 Hz, *J* = 7.3 Hz, 1H), 7.54 (d, *J* = 8.2 Hz, 2H), 7.47 (ddd, *J* = 8.1 Hz, *J* = 7.4 Hz, *J* = 1.8 Hz, 4H), 7.35 (dt, *J* = 8.1 Hz, *J* = 1.1 Hz, 4H), 3.15 (s, 6H) ppm.

NMR data is in accordance with the literature.[305]

HR-MS (ESI):
Calculated for C$_{29}$H$_{26}$N$_5$O$_2$ [M+H]$^+$: 476.20865 m/z
Found: 476.20836 m/z

This procedure was part of the Bachelor Thesis of Hannah Wilken, 2021, and the Internship Report of Jan Kruse, 2021, both conducted under my supervision.

3.30.   Synthesis of **C-17**
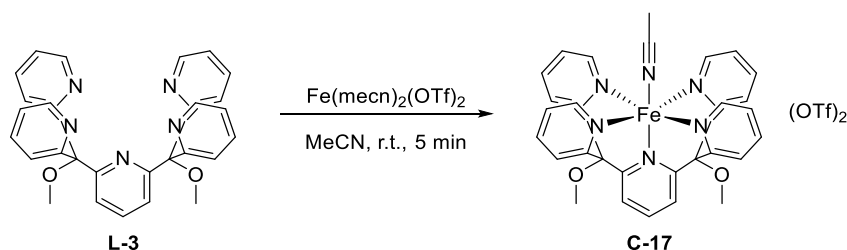
According to a modified literature procedure:[12]

Ligand **L-3** (49 mg, 0.103 mmol, 1.0 equiv.) was dissolved in 1.5 ml acetonitrile and iron(II)bis(acetonitrile)bis(triflate) (44.9 mg, 0.103 mmol, 1.0 equiv.) was added as a solid, turning the solution deep red. The mixture was then stirred for an additional 5 min and then diethyl ether was diffused into the solution under ambient conditions to give the product as brown crystals in 77% yield (69 mg).

Due to the original authors description of decomposition of **C-17** under high vacuum, traces of diethyl ether were still present in product.[68]

¹H NMR (400.0 MHz, CD₃CN, 295 K):
δ = 10.04 (d, *J* = 5.8 Hz, 4H), 8.41 (d, *J* = 8.0 Hz, 2H), 8.35 (d, *J* = 8.1 Hz 4H), 8.16 (t, *J* = 8.0 Hz, 1H), 7.94 (t, *J* = 7.8 Hz, 4H), 7.75 (t, *J* = 6.2 Hz, 4H), 4.05 (s, 6H) ppm.

δ = 164.2, 162.8, 159.2, 140.8, 140.2, 127.0, 126.0, 125.0, 15.6 ppm.

NMR data is in accordance with the literature.[68]

HR-MS (ESI):
Calculated for $C_{30}H_{25}F_3FeN_5O_5S$ [Fe(Py₅(OMe)₂)(MeCN)(OTf)]⁺: 680.08779 m/z
Found: 680.08557 m/z

3.31.   Synthesis of **L-4**
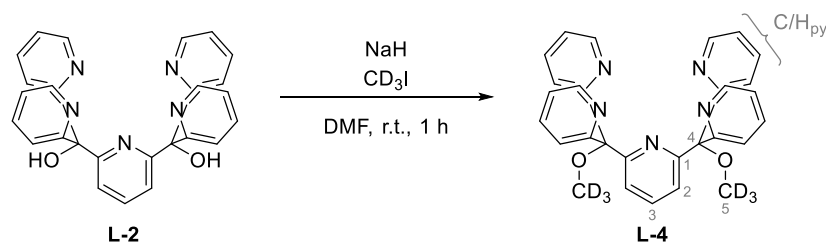
According to a modified literature procedure:[305]

A flame-dried flask was charged with **L-2** (295.0 mg, 0.658 mmol, 1.0 equiv.) and 50 ml of absolute *N*,*N*-dimethylformamide were added. Sodium hydride (60wt.-%, suspension in mineral oil, 164.0 mg, 4.100 mmol, 6.2 equiv.) was added, resulting in a color change to dark green and later to red upon stirring for 10 min at room temperature. D_3-methyl iodide (0.21 ml, 489 mg, 3.38 mmol, 5.1 equiv.) was added dropwise, the solution's color slowly changed to a pale red. The reaction was stirred at room temperature for 3 h, then 50 ml methanol were added slowly to quench the reaction. 20 ml of aqueous hydrochloric acid (3 M) were added, and organic solvents removed *via* rotary evaporation (90 mbar @ 40 °C) the mixture transferred to a separatory funnel. Additional 10 ml of aqueous hydrochloric acid (3 M) were added and the mixture washed with dichloromethane (2 x 25 ml), this organic layer was discarded. The aqueous layer was basified to pH 12 with an aqueous solution of sodium hydroxide (19 M) and extracted with dichloromethane (3 x 100 ml). These combined organic layers were dried over anhydrous magnesium sulfate and the solvents removed *in vacuo* to yield the crude product. Flash column chromatography (silica, 10% triethyl amine/30% ethyl acetate/60% hexanes grading to 10% triethyl amine/60% ethyl acetate/30% hexanes) gave the pure product **L-4** as a colorless solid (no yield was determined).

R_F = 0.09 (silica, UV, 10% triethylamine, 50% ethyl acetate, 40% hexanes)

¹H NMR (400.0 MHz, CDCl₃, 295 K):
δ = 8.51 (ddd, *J* = 4.8 Hz, *J* = 1.8 Hz, *J* = 0.9 Hz, 4H, H$_{py}$), 7.69 (dd, *J* = 8.4 Hz, *J* = 7.3 Hz, 1H, H-3), 7.55 (d, *J* = 7.7 Hz, 2H, H-2), 7.47 (ddd, *J* = 8.1 Hz, *J* = 7.4 Hz, *J* = 1.9 Hz, 4H, H$_{py}$), 7.09 (ddd, *J* = 7.4 Hz, *J* = 4.8 Hz, *J* = 1.2 Hz, 4H, H$_{py}$) ppm.

¹³C-NMR (100.0 MHz, CDCl₃, 295 K):
δ = 161.4 (C$_{Py-quart}$), 160.7 (C-1), 148.2 (C$_{Py}$), 136.7 (C-3), 135.3(C$_{Py}$), 124.8(C$_{Py}$), 121.6(C$_{Py}$), 121.5 (C-2), 52.1 (C-5) ppm.

HR-MS (ESI):
Calculated for $C_{29}H_{20}D_6N_5O_2$ [M+H]⁺: 482.24631 m/z
Found: 482.24556 m/z

This procedure was part of the Internship Report of Jan Kruse, 2021, conducted under my supervision.

3.32. Synthesis of C-19
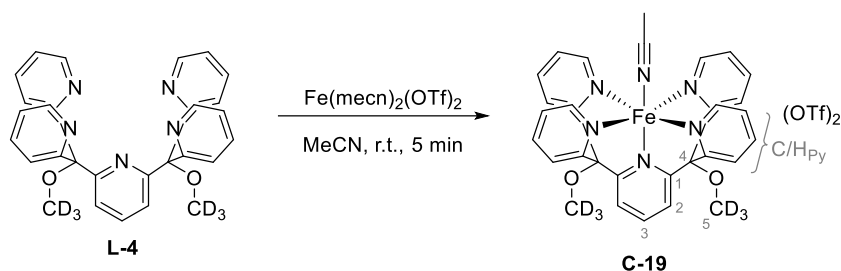
According to a modified literature procedure:[12]

Ligand **L-4** (48.0 mg, 0.100 mmol, 1.0 equiv.) was dissolved in 2.2 ml acetonitrile. Iron(II) bis(acetonitrile) bis(triflate) (43.5 mg, 0.100 mmol, 1.0 equiv.) was added as a solid, turning the solution deep red. The mixture was then stirred for an additional 5 min, syringe filtered (0.45 μm) and then diethyl ether was diffused into the solution under ambient conditions to give the product **C-19** as red-brown crystals in 85% yield (74.0 mg).

^{1}H NMR (400.0 MHz, CD$_3$CN, 295 K):
δ = 10.03 (d, J = 5.9 Hz, 4H, H$_{Py}$), 8.39 (d, J = 5.9 Hz, 2H, H-2), 8.32 (d, J = 3.8 Hz, 4H, H$_{Py}$), 8.16 (t, J = 5.9 Hz, 1H, H-3), 7.94 (t, J = 5.9 Hz, 4H, H$_{Py}$), 7.74 (s, 4H, H$_{Py}$), 1.96 (s, 3H, **CH$_3$**-CNppm.

^{2}H NMR (61.0 MHz, CD$_3$CN, 295 K):
δ = 4.03 ppm

^{13}C-NMR (100.0 MHz, CD$_3$CN, 295 K):
δ = 164.2 (C$_{Pyquart}$), 162.8 (C$_{Py}$), 140.8 (C-3), 140.2 (C$_{Py}$), 127.0 (C$_{Py}$), 126.0 (C$_{Py}$), 125.0 (H-2), 15.6 (C-4) ppm.

Even though the the obtained sample was stored under high vacuum for over 24 h, significant amounts of diethyl ether can still be observed in the NMR spectra.

HR-MS (ESI):
Calculated for C$_{30}$H$_{19}$D$_6$F$_3$FeN$_5$O$_5$S [Fe(Py$_5$(OCD$_3$)$_2$)(OTf)]$^+$: 686.12545 m/z
Found: 686.12378 m/z
Calculated for C$_{31}$H$_{22}$D$_6$FeN$_6$O$_2$ [Fe(mecn)(Py$_5$(OCD$_3$)$_2$)]$^{2+}$: 289.09999 m/z
Found: 289.09930 m/z

Elemental Analysis:
Calculated for C$_{37}$H$_{32}$D$_6$F$_6$FeN$_6$O$_6$S$_2$: C 45.22, H 3.91, N 9.59, S 7.31.
Found: C 45.32, H 3.66, N 8.94, S 6.47.

IR (thin film):
$\tilde{v}$ = 2970, 1739, 1601, 1442, 1372, 1255, 1222, 1151, 1100, 1030, 931, 815, 773, 704, 664 cm^{-1}.

3.33.   Synthesis of **L-5**
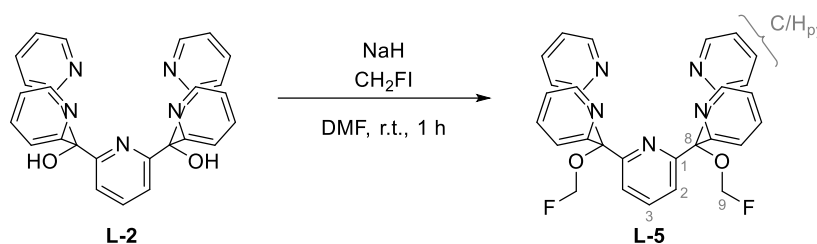
According to a modified literature procedure:[305]

A flame-dried flask was charged with **L-2** (281.0 mg, 0.628 mmol, 1.0 equiv.) and 50 ml of absolute *N,N*-dimethylformamide were added. Sodium hydride (60wt.-%, suspension in mineral oil, 153.0 mg, 3.83 mmol, 6.1 equiv.) was added in two portions, resulting in a color change to dark green and then to red upon stirring at room temperature. The mixture was then cooled to 0 °C and fluoroiodomethane (0.34 ml, 165.8 mg, 5.02 mmol, 8.0 equiv.) was added dropwise, the solution's color slowly changed to a pale red. The reaction was stirred at room temperature for 1 h, LC-MS measurements indicated complete consumption of the starting material at this point. The solution was then allowed to warm to room temperature. 20 ml of aqueous hydrochloric acid (3 M) were added, the solution washed with dichloromethane (20 ml), and the layers separated. This organic layer was discarded. The aqueous layer was basified to pH 12 with an aqueous solution of sodium hydroxide (19 M), extracted with ethyl acetate (2 x 20 ml) and the combined organic layers washed with lithium chloride solution (5% in water). Then, the organic layer was dried over anhydrous magnesium sulfate and the solvents removed *in vacuo* to yield the crude product. Flash column chromatography (silica, triethyl amine/ethyl acetate/hexanes) led to decomposition of the product.

R_F = 0.22 (silica, UV20% triethylamine, 50% ethyl acetate, 30% hexanes)

¹H NMR (400.0 MHz, CDCl₃, 295 K):
δ = 8.49 (ddd, *J* = 4.8 Hz, *J* = 1.8 Hz, *J* = 0.9 Hz, 4H, H$_{py}$), 7.54 (d, *J* = 7.6 Hz, 1H, H-2), 7.52 (ddd, *J* = 8.1 Hz, *J* = 7.4 Hz, *J* = 1.8 Hz, 4H, H$_{Py}$), 7.36 (dt, *J* = 8.1 Hz, *J* = 1.1 Hz, 4H, H$_{py}$), 7.14 (ddd, *J* = 7.5 Hz, *J* = 4.8 Hz, *J* = 1.2 Hz, 4H, H$_{py}$), 5.59 (s, 2H, H-9a), 5.45 (s, 2H, H-9b) ppm.

¹⁹F NMR (376.0 MHz, CDCl₃, 295 K):
δ = –146.6 (t, *J* = 55.8 Hz) ppm.

Due to decomposition of the product no ¹³C NMR was obtained.

LR-MS (EI):
Calculated for $C_{27}H_{19}N_5$ [M–2 x OCH_2F]$^+$: 413.16 m/z
Found: 413.86 m/z

Calculated for $C_{16}H_{11}N_3$ [M–1,1-dipyridiylethan–OCH_2F]$^+$: 245.10 m/z
Found: 245.96 m/z

This procedure was part of the Internship Report of Jan Kruse, 2021, conducted under my supervision.

LR-MS (EI):

3.34.   Synthesis of **L-6**
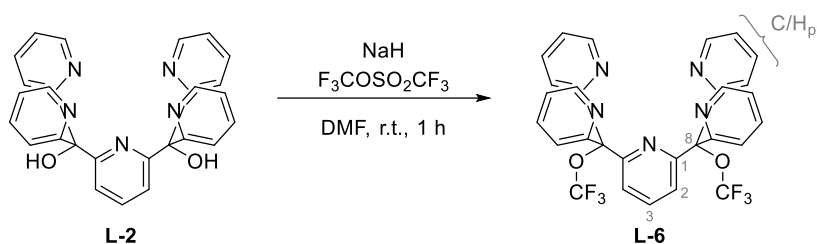
According to a modified literature procedure:[305]

A flame-dried Young ampoule was charged with trifluoromethyl triflate (58 mg, 0.27 mmol, 6.0 equiv) and cooled to -46 °C, then 0.35 ml absolute *N,N*-dimethylformamide were added. After vigorous shaking, the mixture was allowed to warm to room temperature. A separate flame-dried flask was charged with **L-2** (20.0 mg, 0.045 mmol, 1.0 equiv.) and 3 ml of absolute *N,N*-dimethylformamide were added. Sodium hydride (60wt.-%, suspension in mineral oil, 10.0 mg, 0.25 mmol, 6.0 equiv.) was added resulting in a color change to red and then green upon stirring for 5 min at room temperature. The beforehand prepared solution of trifluoromethyl triflate was added dropwise, the solution's color slowly changed to a pale red. The reaction was stirred at room temperature for 2 h during which the solutions color changed to colorless and finally yellow. The solution was diluted with 2 ml of an aqueous solution of calcium chloride and 2 ml of hydrochloric acid (3 M). Then, the mixture was washed with dichloromethane (5 ml), this organic layer was discarded. The aqueous layer was basified to pH 12 with an aqueous solution of sodium hydroxide (19 M) and extracted with ethyl acetate (3 x 20 ml). These combined organic layers were washed with 20 ml lithium chloride solution (5% in water), dried over anhydrous magnesium sulfate and the solvents removed *in vacuo* to yield the crude product. During flash column chromatography (silica, triethyl amine/ethyl acetate/hexanes) decomposition was observed.

¹H NMR (400.0 MHz, CDCl$_3$, 295 K):
δ = 8.50 (ddd, *J* = 4.9 Hz, *J* = 1.8 Hz, *J* = 1.0 Hz, 4H, H$_{py}$), 7.75-7.69 (m, 3H, H-2/H-3), 7.59 (m, 8H, H$_{Py}$), 7.16 (ddd, *J* = 7.2 Hz, *J* = 4.9 Hz, *J* = 1.4 Hz, 4H, H$_{Py}$) ppm.

¹⁹F NMR (376.0 MHz, CDCl$_3$, 295 K):
δ = −78.7 (s) ppm.

Due to decomposition of the product, no ¹³C NMR was obtained. In HR-MS measurements, only signals corresponding to the starting material were obtained. This was attributed to the observed decomposition reaction.

This procedure was part of the Internship Report of Jan Kruse, 2021, conducted under my supervision.

*3.35.   Synthesis of **V-12***
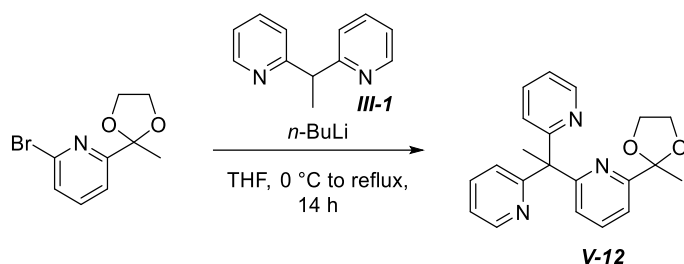
According to a modified literature procedure:[49]

A flame-dried flask was charged ***III-1*** (0.750 g, 4.07 mmol, 1.20 equiv.) and 36 ml of absolute tetrahydrofuran under inert atmosphere (nitrogen) and cooled to 0 °C. When a solution of *n*-butyl lithium (2.5 M in hexane, 2.04 ml, 5.09 mmol, 1.5 equiv.) was added the solution turned a dark red. The solution was stirred for 10 min at 0 °C, at which time 2-bromo-6-(2-methyl-1,3-dioxolan-2-yl)-pyridine (828.0 mg, 3.39 mmol, 1.0 equiv.) was added all at once. The reaction mixture was stirred for another 10 min at 0 °C and then allowed to warm to room temperature. The mixture was then heated to reflux (bath temperature 75 °C) for 5 d. The mixture was allowed to cool to room temperature and 10 g ice were added. The mixture was vigorously stirred for 15 min at room temperate and additional 20 ml water were added and the mixture extracted with dichloromethane (3 x 30 ml). The combined organic layers were dried over anhydrous magnesium sulfate and the solvents removed *in vacuo*. A red/orange oil was obtained as the crude product ***V-12*** and used as such for the next synthesis step (theoretical yield: 1.18 g/3.39 mmol).

¹H NMR (400.0 MHz, CDCl₃, 295 K):
δ = 8.56 (dtd, J = 4.8 Hz, J = 1.9 Hz, J = 1.0 Hz, 2H), 7.60-7.52 (m, 3H), 7.35 (dd, J = 7.7 Hz, J = 0.9 Hz, 1H), 7.13-7.03 (m, 3H), 4.04 (m, 2H), 3.88 (m, 2H), 2.34 (s, 3H), 1.64 (s, 3H) ppm.

NMR data is in accordance with the literature.[49]

HR-MS (EI):
Calculated for $C_{20}H_{18}N_3O_2$ [M]·⁺: 347.1634 m/z
Found: 347.1626 m/z
Calculated for $C_{20}H_{18}N_3O_2$ [M–CH₃]⁺: 332.1399 m/z
Found: 332.1400 m/z
Calculated for $C_{20}H_{18}N_3O_2$ [M–C₅H₄N]⁺: 269.1290 m/z
Found: 269.1287 m/z

3.36.   Synthesis of *V-13*
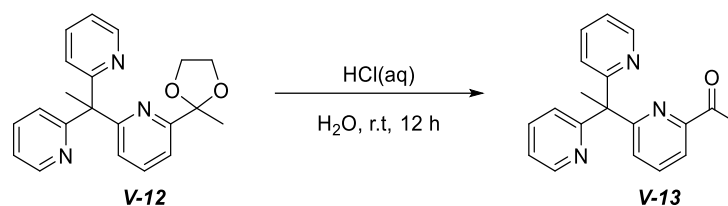
According to a modified literature procedure:[49]

A flask was charged with crude *V-12* (theoretical yield: 1.18 g/3.39 mmol) and 20 ml of aqueous hydrochloric acid (6 M) were added. The mixture was stirred for 12 h at room temperature and was then transferred into a separatory funnel. Saturated aqueous sodium bicarbonate solution was added and the mixture extracted with dichloromethane (3 x 50 ml). The combined organic layers were dried over anhydrous magnesium sulfate and the solvents removed *in vacuo* to yield the product *V-13* as a brown oil (770 mg/75% over two steps).

R_F = 0.63 (silica, UV, 10% triethyl amine, 40% ethyl acetate, 50% hexanes)

^{1}H NMR (400.0 MHz, CDCl$_3$, 295 K):
δ = 8.59 (dtd, J = 4.7 Hz, J = 1.9 Hz, J = 0.9 Hz, 2H), 7.87 (dd, J = 7. Hz, J = 1.0 Hz, 1H), 7.72 (t, J = 7.8 Hz, 1H), 7.60 (ddd, J = 8.1 Hz, J = 7.5 Hz, J = 1.9 Hz, 2H) 7.40 (dt, J = 7.9 Hz, J = 1.0 Hz, 1H), 7.14 (ddd, J = 7.5 Hz, J = 4.8 Hz, J = 1.1 Hz, 2H), 7.09 (dt, J = 8.0 Hz, J = 1.0 Hz, 2H), 2.51 (s, 3H), 2.37 (s, 3H) ppm.

NMR data is in accordance with the literature.[49]

HR-MS (EI):
Calculated for C$_{19}$H$_{17}$N$_3$O [M+H]$^{\cdot+}$: 303.1372 m/z
Found: 303.1366 m/z
Calculated for C$_{19}$H$_{17}$N$_3$O [M+H]$^{\cdot+}$: 288.1137 m/z
Found: 288.1120 m/z

3.37. Synthesis of L-7
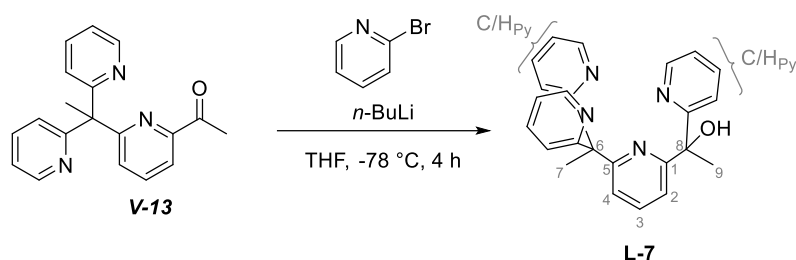
According to a modified literature procedure:[68,371]

A flame-dried flask was charged with 2-bromo pyridine (161 µl, 260.7 mg, 1.65 mmol, 1.3 equiv.) and 10 ml of absolute tetrahydrofuran were added. After cooling the mixture to –78 °C, a solution of *n*-butyl lithium (2.5 M in hexanes, 660 µl, 105.7 mg, 1.65 mmol, 1.3 equiv.) was added dropwise, resulting in a color change to yellow. The mixture was stirred at –78 °C for 10 min and then a solution of *V-13* (0.423 M in tetrahydrofuran, 3.0 ml, 385.0 mg, 1.27 mmol, 1.0 equiv.) was added slowly. The reaction was stirred at –78 °C for 60 min, then 5 ml methanol were added slowly to quench the reaction. The mixture was allowed to warm to room temperature, 10 ml of aqueous hydrochloric acid (2 M) were added, and the mixture transferred to a separatory funnel. Additional 20 ml of aqueous hydrochloric acid (2 M) were added and the mixture washed with dichloromethane (3 x 25 ml), this organic layer was discarded. The aqueous layer was basified to pH 14 with an aqueous solution of sodium hydroxide (6 M) and extracted with dichloromethane (4 x 30 ml). These combined organic layers were dried over anhydrous magnesium sulfate and the solvents removed *in vacuo* to yield the crude product. Column chromatography (silica, 10% triethylamine, 90% hexanes grading to 10% triethyl amine, 40% ethyl acetate, 50% hexanes) gave the pure product *L-7* as a colorless solid in 58% yield (283.0 mg).

R_F = 0.47 (silica, UV, 10% triethyl amine, 40% ethyl acetate, 50% hexanes)

¹H NMR (400.0 MHz, CDCl₃, 295 K):
δ = 8.59 (dtd, *J* = 4.7 Hz, *J* = 1.8 Hz, *J* = 0.9 Hz, 2H, H$_{Py}$), 8.45 (ddd, *J* = 4.9 Hz, *J* = 1.8 Hz, *J* = 1.0 Hz, 1H, H$_{Py}$), 7.60-7.52 (m, 4H, H$_{Py}$/H-3), 7.49 (ddd, *J* = 8.0 Hz, *J* = 7.4 Hz, *J* = 1.8 Hz, 1H, H$_{Py}$) 7.39 (dt, *J* = 8.0 Hz, *J* = 1.1 Hz, 1H, H$_{Py}$), 7.14 (dddd, *J* = 7.5 Hz, *J* = 4.8 Hz, *J* = 1.1 Hz, *J* = 0.7 Hz, 3H, H$_{Py}$), 7.03-6.95 (m, 3 H, H$_{Py}$/H-2/H-4), 6.38 (s, 1H, -O*H*), 2.34 (s, 3H, H-7), 1.84 (s, 3H, H-9) ppm.

¹³C NMR (100.0 MHz, CDCl₃, 295 K):
δ = 166.1 (C-5/C$_{Py-quart}$), 165.9 (C-1/C$_{Py-quart}$), 164.3 (C-1/C$_{Py-quart}$), 163.7 (C-1/C$_{Py-quart}$), 163.3 (C-1/C$_{Py-quart}$), 148.8 (C$_{Py}$), 148.8 (C$_{Py}$), 147.2 (C$_{Py}$), 137.2 (C-3), 136.6 (C$_{Py}$), 135.9 (C$_{Py}$), 135.8 (C$_{Py}$), 123.8 (C-2/C-4), 123.8 (C$_{Py}$/C-2/C-4), 121.9 (Cx), 121.3 (Cx), 121.3 (CG), 121.2 (CH), 121.0 (CE), 117.7 (CC1), 76.1 (C-8), 60.2 (C-6), 29.3 (C-9), 27.2 (C-7) ppm.

HR-MS (ESI):
Calculated for $C_{24}H_{23}N_4O$ [M+H]$^+$: 383.18719 m/z
Found: 383.18668 m/z
Calculated for $C_{24}H_{22}N_4ONa$ [M+Na]$^+$: 405.16913 m/z
Found: 405.16850 m/z

Elemental Analysis:
Calculated for $C_{24}H_{22}N_4O$: C 75.37, H 5.80, N 14.65.
Found: C 74.60, H 5.66, N 14.20.

^{1}H NMR (400.0 MHz, CD$_3$CN, 295 K):
δ = 8.48 (ddt, J = 4.8 Hz, J = 2.1 Hz, J = 1.1 Hz, 2H), 8.44 (ddd, J = 4.9 Hz, J = 1.8 Hz, J = 1.0 Hz, 1H), 7.66-7.57 (m, 4H), 7.54 (dd, J = 7.9 Hz, J = 0.9 Hz, 1H) 7.36 (dt, J = 8.0 Hz, J = 1.1 Hz, 1H), 7.23-7.14 (m, 3H), 7.05 (dd, J = 7.8 Hz, J = 0.9 Hz, 1H), 7.03 (ddt, J = 13.8 Hz, J = 8.1 Hz, J = 1.0 Hz, 2H), 6.02 (s, 1 H, -OH), 2.24 (s, 3H, H$_7$), 1.75 (s, 3H, H$_9$) ppm.

^{13}C NMR (100.0 MHz, CD$_3$CN, 295 K):
δ = 167.0, 167.0, 165.3, 165.1, 164.5, 149.3, 149.3, 148.3, 138.1, 137.8, 136.8, 136.8, 124.7, 124.6, 123.1, 122.4, 122.3, 121.7, 76.9, 61.0, 29.4, 27.4 ppm.

IR (thin film):
$\tilde{v}$ = 3332, 3057, 2974, 2931, 1583, 1568, 1469, 1454, 1359, 1300, 1256, 1160, 1144, 1104, 1088, 1071, 1061, 1046, 1000, 992, 941, 913, 896, 862, 834, 814, 783, 777, 747, 690 cm^{-1}.

3.38. *Synthesis of* **C-20**
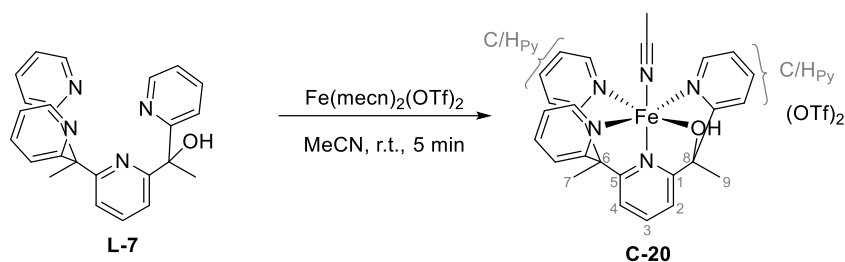
According to a modified literature procedure:[12]

Ligand **L-7** (50.0 mg, 0.131 mmol, 1.0 equiv.) was dissolved in 2.55 ml acetonitrile. Iron(II) bis(acetonitrile) bis(triflate) (57.0 mg, 0.131 mmol, 1.0 equiv.) was added as a solid, turning the solution deep red. The mixture was then stirred for an additional 5 min and then diethyl ether was diffused into the solution at 4 °C to give the product **C-20** as red-brown crystals in 71% yield (71.8 mg).

¹H NMR (400.0 MHz, CD$_3$CN, 295 K):
δ = 9.74 (br, 1H, H$_{Py}$), 9.56 (br, 1H, H$_{Py}$), 9.43 (br, 1H, H$_{Py}$), 8.15-7.94 (m, 7H, H$_{Py}$/H-2/3/4), 7.90-7.79 (m, 2H, H$_{Py}$/H-2/3/4), 7.67 (t, J = 6.5 Hz, 1H, H$_{Py}$), 7.60 (t, J = 6.4 Hz, 1H, H$_{Py}$), 7.49 (t, J = 6.5 Hz, 1H, HPy), 6.86 (s, 1H, -OH), 2.84 (s, 3H, H-7), 2.31 (s, 3H, H-9), 1.96 (s, 3H, CH_3CN) ppm.

¹³C NMR (100.0 MHz, CD$_3$CN, 295 K):
δ = 159.9 (C$_{Py}$), 159.1 (C$_{Py}$), 155.9 (C$_{Py}$), 139.6 (C$_{Py}$/H-2/3/4), 139.4 (C$_{Py}$/H-2/3/4), 138.8 (C$_{Py}$/H-2/3/4), 124.3 (C$_{Py}$/H-2/3/4), 20.3 (C-7), 20.0 (C-9) ppm.

No other signals could be distinguished from the background noise.

HR-MS (ESI):
Calculated for C$_{25}$H$_{22}$F$_3$FeN$_4$O$_4$S [Fe(**L-7**)(OTf)]$^+$: 587.06633 m/z
Found: 587.06718 m/z
Calculated for C$_{26}$H$_{24}$FeN$_5$O [Fe(**L-7**)(MeCN)]$^+$: 478.13303 m/z
Found: 478.13339 m/z

Elemental Analysis:
Calculated for C$_{28}$H$_{27}$F$_6$FeN$_5$O$_8$S$_2$ ([Fe(Py$_4$OHMe$_2$-H)(MeCN)](OTf)$_2$ x 1 H$_2$O): C 42.28, H 3.42, N 8.80, S 8.06.
Found: C 42.14, H 3.39, N 8.67, S 7.74.

IR (thin film):
$\tilde{v}$ = 1603, 1464, 1441, 1254, 1234, 1219, 1154, 1025, 762 cm^{-1}.

3.39.   Synthesis of **C-21**
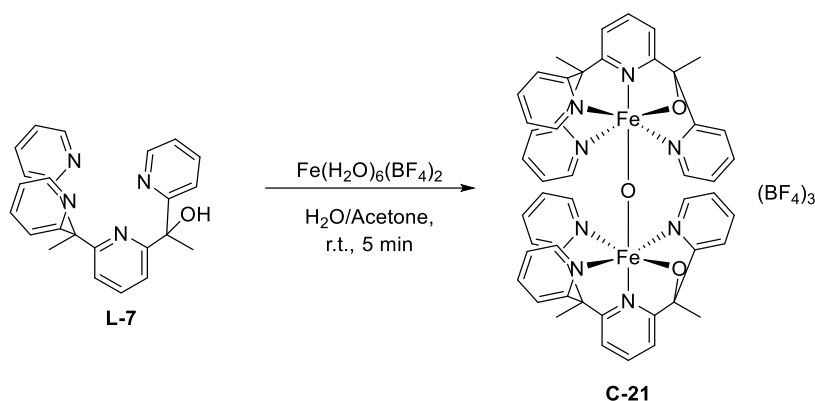
According to a modified literature procedure:[12]

Ligand **L-7** (70.0 mg, 0.183 mmol, 1.0 equiv.) was dissolved in 4.0 ml acetone. Hexaqua iron(II) bis(tetrafluoroborate) (61.8 mg, 0.83 mmol, 1.0 equiv.) was dissolved in 0.5 ml water and then added to the solution of the ligand, turning the solution red-brown. The mixture was stirred for 5 min and then diethyl ether was diffused into the solution to give the product **C-21** as a red-brown powder in 73% yield (100.2 mg).

HR-MS (ESI):
Calculated for $C_{48}H_{42}Fe_2N_8O_3$ $[Fe_2(O)(Py_4OMe_2H)_2]^{4+}$: 445.10394 m/z
Found: 445.10347 m/z

Elemental Analysis:
Calculated for $C_{48}H_{42}B_3F_{12}Fe_2N_8O_3$: C 50.09, H 3.68, N 9.74.
Found: C 50.07, H 4.02, N 9.32.

IR (thin film):
$\tilde{v}$ = 1738, 1597, 1541, 1456, 1378, 1305, 1227, 1053, 1016, 927, 809, 761, 699 cm⁻¹.

*3.40.   Synthesis **V-15***
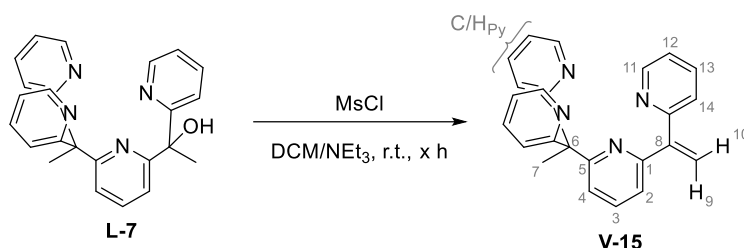
A flame-dried flask was charged with ligand **L-7** (50.0 mg, 0.131 mmol, 1.0 equiv.), 5 ml of absolute dichloromethane and 1 ml of absolute triethylamine and then cooled to 0 °C. Mesyl chloride (0.2 ml, 299.5 mg, 2.610 mmol, 20.0 equiv.) was added dropwise, the mixture allowed to warm to room temperature and then stirred for 12 h, during this time a colorless/yellow precipitate formed. 25 ml ethyl acetate and 20 ml water were added successively and the solution was then stirred vigorously for 10 min at room temperature. The layers were separated and the aqueous layer extracted with 3 x 25 ml ethyl acetate. The combined organic layers were dried over anhydrous sodium sulfate and the solvents removed *in vacuo* to give the crude product as a yellow oil. Column chromatography (silica, 20% triethyl amine, 5% ethyl acetate, 75% hexanes grading to 20% triethyl amine, 20% ethyl acetate, 60% hexanes) gave the pure product **V-15** (due to decomposition of the product, no yield was determined).

¹H NMR (400.0 MHz, C_6D_6, 295 K):
δ = 8.50 (ddd, *J* = 4.8 Hz, *J* = 1.9 Hz, *J* = 1.0 Hz, 1H, H-11), 8.47 (ddd, *J* = 4.8 Hz, *J* = 1.9 Hz, *J* = 1.0 Hz, 2H, H_{Py}), 7.14-7.07 (m, 5H), 7.00 (tt, *J* = 7.4 Hz, *J* = 2.0 Hz, 2H) 6.99 (t, *J* = 1.9 Hz, 1H), 6.62 (ddd, *J* = 7.5 Hz, *J* = 4.8 Hz, *J* = 1.2 Hz, 1H), 6.57 (ddd, *J* = 7.4 Hz, *J* = 4.8 Hz, *J* = 1.2 Hz, 2H), 6.27 (d, *J* = 1.2 Hz, 1H, H-9/H-10), 6.03 (6.27 (d, *J* = 1.2 Hz, 1H, H-9/H-10), 1.74 (s, 3H, H-7) ppm.

Due to decomposition of the product, no ¹³C NMR spectrum or 2D spectra were obtained. Therefore, not all peaks in the ¹H NMR spectrum could be assigned unequivocally.

HR-MS (ESI):
Calculated for $C_{24}H_{21}N_4$ [M+H]⁺: 365.17662 m/z
Found: 365.17612 m/z

3.41. Synthesis of *V-16*
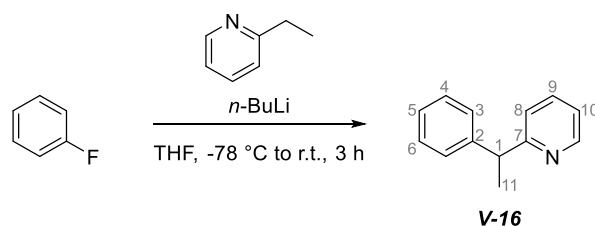
V-16

According to a modified literature procedure:[234]

A flame-dried flask was charged with 2-ethylpyridine (3.57 ml, 3.34 g, 31.22 mmol, 3.0 equiv.) under inert atmosphere (nitrogen) and 50 ml of absolute tetrahydrofuran and cooled to –78 °C. When a solution of *n*-butyl lithium (2.5 M in hexane, 12.49 ml, 31.22 mmol, 3.0 equiv.) was added dropwise, the solution turned deep red. The mixture was stirred for 30 min at –78 °C, then fluorobenzene (0.97 ml, 1.00 g, 10.41 mmol, 1.0 equiv.) was added dropwise, the solution stirred at –78 °C for an additional 10 min and the cooling bath removed. The reaction mixture was allowed to warm to room temperature and then stirred at room temperature for 3 h. 60 ml MilliQ grade water were added and the solution stirred vigorously for 10 min. The layers were separated and the aqueous layer was extracted with dichloromethane (3 x 50 ml). The combined organic layers were dried over anhydrous magnesium sulfate and the solvents removed *in vacuo* to yield an orange oil as the crude product. Excess 2-ethylpyridine was removed under reduced pressure to yield the product as a red oil in 89% yield (1.70 g).

R_F = 0.79 (silica, UV, 10% triethyl amine, 30% ethyl acetate, 60% hexanes)

^{1}H NMR (400.0 MHz, CDCl$_3$, 295 K):
δ = 8.56 (ddd, J = 4.9 Hz, J = 1.9 Hz, J = 1.0 Hz, 1H, H-6), 7.56 (td, J = 7.7 Hz, J = 1.9 Hz, 1H, H-4), 7.30 (d, J = 4.6 Hz, 4H, H-8/9/10), 7.25-7.16 (m, 1H, H-5/8/9/10), 7.14-7.05 (m, 2H, H-3/8/9/10), 4.30 (q, J = 7.2 Hz, 1H, H-1), 1.71 (d, J = 7.2 Hz, 3H, H-11) ppm.

^{13}C NMR (100.0 MHz, CDCl$_3$, 295 K):
δ = 165.2 (C-2), 149.3 (C-6), 145.3, 136.5 (C-4), 128.6 (C-8/9/10), 127.8 (C-8/9/10), 126.4 (C-5), 122.3 (C-7/8/9/10), 121.3 (C-3), 47.5 (C-1), 20.9 (C-11) ppm.

HR-MS (ESI):
Calculated for C$_{13}$H$_{14}$N [M+H]$^+$: 184.11262 m/z
Found: 184.11210 m/z

Elemental Analysis:
Calculated for C$_{13}$H$_{13}$N: C 85.21, H 7.15, N 7.64.
Found: C 85.01, H 6.95, N 8.10.

IR (thin film):

$\tilde{\nu}$ = 2968, 2932, 1589, 1568, 1494, 1472, 1451, 1431, 1370, 1283, 1148, 1044, 1028, 994, 910, 806, 746, 698 cm^{-1}.

3.42. Synthesis of **L-1***,* **L-8***, and* **L-9**
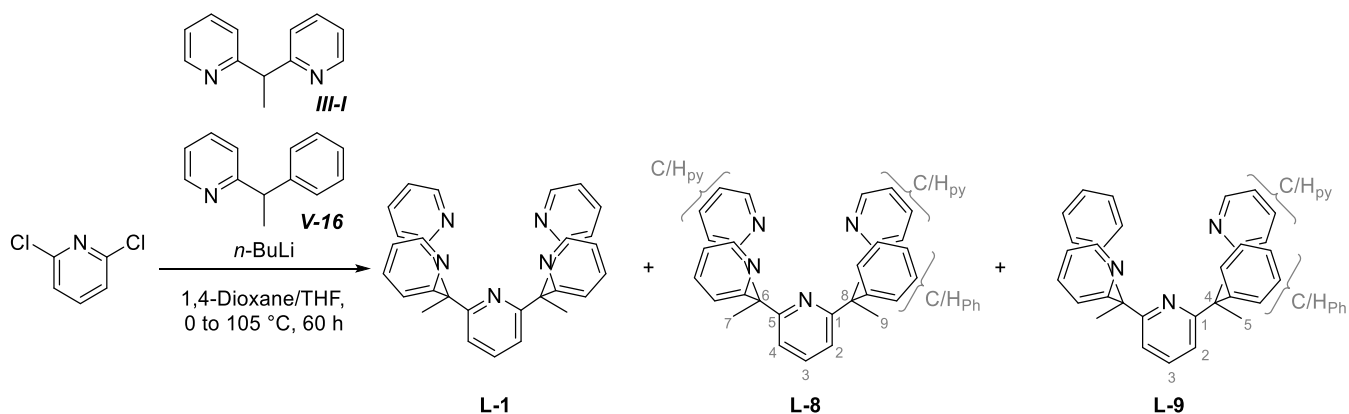
According to a modified literature procedure:[12]

A flame-dried flask was charged with ***III-1*** (3.84 g, 20.83 mmol, 1.0 equiv.) and ***V-16*** (4.58 g, 25.00 mmol, 1.2 equiv.), 200 ml of absolute 1,4-dioxane, 50 ml of absolute tetrahydrofuran and was then cooled to 0 °C. When a solution of *n*-butyl lithium (2.5 M in hexane, 25.00 ml, 62.50 mmol, 3.0 equiv.) was added, the solution turned a dark red. The solution was stirred for 45 min at 0 °C, at which time 2,6-dichloropyridine (3.08 g, 20.38 mmol, 1.0 equiv.) was added all at once. The reaction mixture was allowed to warm to room temperature and then heated to reflux for 60 hours (bath temperature 105 °C). When the solution had turned from deep red to light brown and thin layer chromatography showed no change during a time span of 6 h, the mixture was allowed to cool to room temperature. 100 ml water were added and the mixture extracted with dichloromethane (4 x 200 ml). The combined organic layers were then dried over anhydrous magnesium sulfate and the solvents removed *in vacuo*. 40 ml methanol were added and the solvents removed *in vacuo* to remove residual 1,4-dioxane. A deep red oil was obtained containing the desired product as well as side products including the two-fold 1,1-bis(2-pyridyl)ethane substituted **L-1** and the two-fold 2-(1-phenylethyl)pyridine substituted **L-9**. Column chromatography (silica, 10% triethyl amine, 90% hexanes grading to 10% triethyl amine, 40% hexanes, 40% ethyl acetate) gave the crude products with only minor impurities. Recrystallization from diethyl ether gave the products as colorless/off-white solids in 13% (**L-9**), 5% (**L-8**), and 20% (**L-1**) yield.

L-1 – Py₅Me₂H
R_F = 0.33 (silica, UV, 20% triethylamine, 50% ethyl acetate, 30% hexanes)

L-8 – Py₄PhMe₂H
R_F = 0.74 (silica, UV, 20% triethylamine, 50% ethyl acetate, 30% hexanes)

L-9 – Py₃Ph₂Me₂H

R_F = 0.78 (silica, UV, 20% triethylamine, 40% ethyl acetate, 40% hexanes)

¹H NMR L-8 (400.0 MHz, CDCl₃, 295 K):
δ = 8.52 (ddd, J = 4.8 Hz, J = 1.9 Hz, J = 1.0 Hz, 3H, H$_{Py}$), 7.52 (t, J = 7.9 Hz, 1H, H-3), 7.46-7.31 (m, 3H, H$_{Py/Ph}$), 7.23-7.13 (m, 3H, H$_{Ph}$), 7.09-6.95 (m, 7H, H$_{Py}$/H-2/4), 6.92-6.81 (m, 3H, H$_{Py/Ph}$), 2.22 (s, 3H, H₇), 2.14 (s, 3H, H₉) ppm.

¹³C NMR L-8 (100.0 MHz, CDCl₃, 295 K):
δ = 167.1 (C$_{Py-quart}$), 166.4 (C$_{Py-quart}$), 166.3 (C$_{Py-quart}$), 165.0 (C-1/5), 164.2 (C-1/5), 148.5 (C$_{Py}$), 148.5 (C$_{Py}$), 148.4, 148.1, 136.6, 135.7, 135.6, 135.5, 128.7, 127.9, 126.0, 124.3, 124.2, 124.1, 121.1, 121.0, 120.9, 120.1, 119.9, 60.2 (C-6), 57.7 (C-8), 28.0 (C-9), 26.9 (C-7).

The unspecified signals could not be assigned unequivocally due to the complex structure of the molecule.

¹H NMR L-9 (400.0 MHz, CDCl₃, 295 K):
δ = 8.54 (ddd, J = 4.8 Hz, J = 1.9 Hz, J = 0.9 Hz, 2H, H$_{Py}$), 7.50 (t, J = 7.9 Hz, 1H, H-3), 7.39 (ddd, 2H, J = 8.1 Hz, J = 7.4 Hz, J = 1.9 Hz, H$_{Py}$), 7.22-7.14 (m, 6H, H$_{Ph}$), 7.05 (ddd, J = 7.5 Hz, J = 4.8 Hz, J = 1.1 Hz, 2H, H$_{Py}$), 7.02-6.96 (m, 6H, H$_{Ph}$/H-2), 6.89 (dt, J = 8.1 Hz, J = 1.0 Hz, 2H, H$_{Py}$), 2.16 (s, 6H, H-5) ppm.

¹³C NMR L-9 (100.0 MHz, CDCl₃, 295 K):
δ = 167.0 (C$_{Py-quart}$), 164.9 (C-1), 148.4 (C$_{Py}$), 148.2 (C$_{Ph-quart}$), 136.4 (C-3), 135.5 (C$_{Py}$), 128.7 (C$_{Ph}$), 127.8 (C$_{Ph}$), 126.0 (C$_{Ph}$), 124.4 (C$_{Py}$), 120.9 (C$_{Py}$), 119.9 (C-2), 57.5 (C-4), 28.04 (C-5).

Elemental Analysis (L-8):
Calculated for C₃₀H₂₆N₄: C 81.42, H 5.92, N 12.66.
Found: C 81.45, H 5.85, N 12.64.

Elemental Analysis (L-9):
Calculated for C₃₁H₂₇N₃: C 84.32, H 6.16, N 9.52.
Found: C 84.06, H 5.97, N 9.23.

HR-MS L-8 (ESI):
Calculated for C₃₀H₂₇N₄ [M+H]⁺: 443.22357 m/z
Found: 443.22310 m/z

HR-MS L-9 (ESI):
Calculated for C₃₁H₂₈N₃ [M+H]⁺: 442.22832 m/z
Found: 442.22807 m/z

IR (thin film, L-8):
$\tilde{\nu}$ = 3051, 2980, 2933, 1739, 1582, 1567, 1495, 1467, 1444, 1427, 1360, 1292, 1217, 1150, 1100, 1071, 1046, 992, 905, 853, 815, 796, 786, 753, 702 cm⁻¹.

IR (thin film, L-9):
$\tilde{\nu}$ = 2997, 2934, 1738, 1583, 1567, 1495, 1470, 1440, 1427, 1359, 1296, 1215, 1150, 1097, 1080, 1069, 1052, 1027, 993, 908, 846, 815, 794, 772, 746, 730, 701 cm⁻¹.

For analytical data on **L-1** refer to p. 259.

3.43.   Synthesis of **C-22**
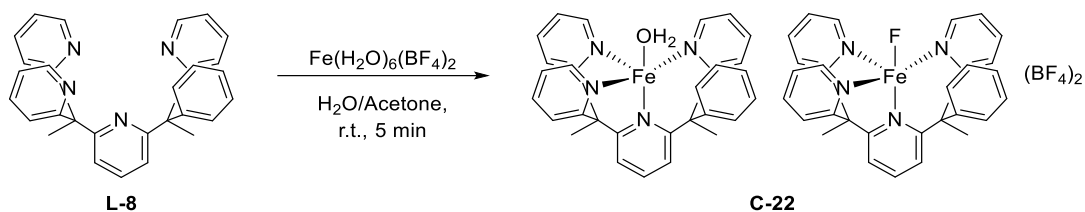
According to a modified literature procedure:[12]

Ligand **L-8** (80.0 mg, 0.181 mmol, 1.0 equiv.) was dissolved in 4.0 ml acetone in a scintillation vial. Hexaqua iron(II) bis(tetrafluoroborate) (61.0 mg, 0.181 mmol, 1.0 equiv.) was dissolved in 0.5 ml water and then added to the solution of the ligand, turning the solution apple green. The mixture was stirred for 5 min and then diethyl ether was diffused into the solution to give the product **C-22** as apple green crystals in 28% yield (35.1 mg).

HR-MS (ESI):
Calculated for $C_{30}H_{28}FeN_4O$ [$Fe(Py_4PhMe_2-H)(OH_2)$]$^{2+}$: 258.0806 m/z
Found: 258.0801 m/z
Calculated for $C_{30}H_{26}FeN_4$ [$Fe(Py_4PhMe_2-H)$]$^{2+}$: 249.0753 m/z
Found: 258.0748 m/z

Elemental Analysis:
Calculated for $C_{60}H_{58}B_3F_{13}Fe_2N_8O_3$ ([$Fe(Py_4PhMe_2-H)(F)$][$Fe(Py_4Ph_2Me_2-H)(OH_2)$](BF_4)$_3$(H_2O)$_2$:
C 54.17, H 4.39, N 8.42.
Found: C 54.46, H 4.02, N 8.62.

IR (thin film):
$\tilde{v}$ = 1708, 1598, 1456, 1441, 1392, 1304, 1051, 1017, 927, 857, 826, 809, 787, 761 cm^{-1}.

3.44.   Synthesis of V-21
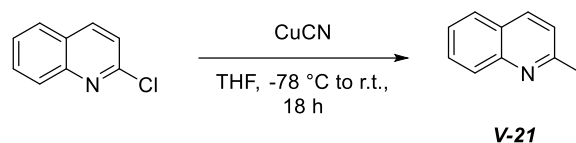
According to a modified literature procedure:[282]

Copper(I) cyanide (2.19 g, 24.5 mmol, 4.00 equiv.) was dissolved in absolute tetrahydrofuran (40 ml). The solution was cooled to –78 °C and a solution of ethylmagnesium bromide (3.0 M in hexane, 16.3 ml, 6.52 g, 48.9 mmol, 8.00 equiv.) was added. Upon cooling, the reaction mixture solidified. The reaction mixture was allowed to warm to room temperature and then stirred for 30 min at room temperature. The reaction mixture was then again cooled to –78 °C (upon which it solidified). Separately, 2-chloroquinoline (1.00 g, 6.11 mmol, 1.0 equiv.) was dissolved in absolute tetrahydrofuran (5 ml) under ultrasonification. This solution of 2-chloroquinoline was added to the reaction solution and the cooling bath was removed. The reaction mixture was left to stir overnight at room temperature and was then quenched by addition of an aqueous solution of ammonium hydroxide (20 ml) and basified by addition of an aqueous sodium hydroxide solution (2 M, 5 ml). The resulting solution was extracted three times with diethyl ether, the organic extracts were combined, dried over anhydrous magnesium sulfate and concentrated *in vacuo*. The crude product was purified *via* column chromatography, whereby the following solvent mixtures were used:

1) Hexane/triethylamine (95%/5%)
2) Hexane/triethylamine (95%/5%) to hexane/triethylamine/ethyl acetate (85%/5%/10%)
3) Hexane/triethylamine/ethyl acetate (96%/3%/1%) to (93%/3%/4%)
4) *n*-pentane/diethyl ether (95%/5%) to (85%/15%)

Using solvent mixture 1, *V-21* was obtained as a yellow oily solid in 36% yield (350 mg)

^{1}H NMR (400.0 MHz, CDCl$_3$, 295 K):
δ = 8.1-8.0 (m, 2H), 7.77 (d, *J* = 8.3 Hz, 1H), 7.68 (ddd, *J* = 8.4 Hz, *J* = 6.9 Hz, *J* = 1.5 Hz, 1H), 7.48 (ddd, *J* = 8.1, *J* = 6.9, *J* = 1.2 Hz, 1H), 7.31 (dd, *J* = 8.4, *J* = 1.0 Hz 1H), 3.01 (q, *J* = 7.6 Hz, 2H), 1.40 (t, *J* = 7.7 Hz, 3H) ppm.

NMR data is in accordance with the literature.[372,373]

LR-MS (ESI):
Calculated for C$_{11}$H$_{12}$N [M+H]$^+$: 158.1 m/z
Found: 158.2 m/z

This procedure was part of the Internship Report by Aila Rothweiler, 2019, conducted under my supervision.

*3.45.   Synthesis of **V-22***
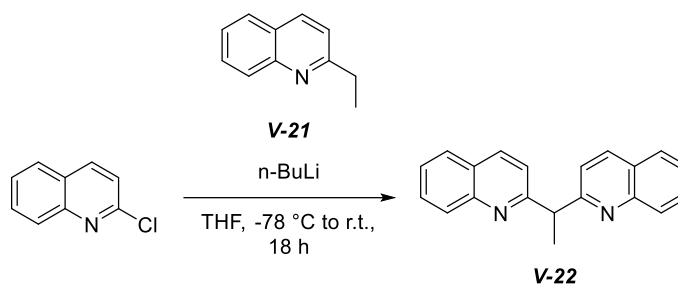
According to a modified literature procedure:[12]

V-21 (50.0 mg, 318 μmol, 3.00 equiv.) was dissolved in absolute tetrahydrofuran (40 ml) and the reaction mixture was cooled to –78 °C. When a solution of *n*-butyl lithium (2.5 M in hexane, 140 μl, 22.4 mg, 350 μmol, 3.30 equiv.) was added, the solution turned deep red. The reaction mixture was stirred for 20 min at –78 °C. Separately, 2-chloroquinoline (17.3 mg, 106 μmol, 1.00 equiv) was dissolved in absolute tetrahydrofuran and then added to the reaction mixture at –78 °C. The reaction mixture was further stirred for 10 min at –78 °C, after which the aceton/dry ice cooling bath was switched for a water ice bath and the reaction mixture was stirred for 30 min at 0 °C. Subsequently, the reaction was quenched by addition of water. The resulting solution was extracted three times with dichloromethane, the organic extracts were combined, dried over anhydrous magnesium sulfate and concentrated *in vacuo*. The crude product was purified *via* column chromatography, whereby the following solvent mixtures were attempted:

1) Iso-hexane/triethylamine   (95%/5%)   to   Iso-hexane/triethylamine/ethyl   acetate (90%/5%/5%)

2) n-Pentane (100%) to n-pentane/diethyl ether (85%/15%) 3)n-Pentane/diethyl ether (98%/2%) to (89%/12%)

Obtained ^{1}H NMR spectra were not clear enough to identify desired product, therefore the yield of ***V-22*** was not determined. As this project was discontinued, no further measures were undertaken to isolate ***V-22*** and obtain clean ^{1}H NMR spectra.

LR-MS (ESI):
Calculated for $C_{20}H_{17}N_2$ [M+H]$^+$: 285.1 m/z
Found: 285.2 m/z

This procedure was part of the Internship Report by Aila Rothweiler, 2019, conducted under my supervision.

4. Synthetic Procedures – Nucleobases

4.1. Synthesis of *III-13*

III-13
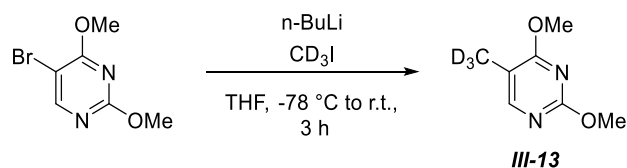
According to a modified literature procedure:[254]

The reaction side of a Helmchen-Double-Schlenk-Flask (HDSF, refer to the appendix, Figure 203, p. 378) was charged with 5-bromo-2,4-dimethoxypyrimidine (1.00 g, 4.57 mmol, 1.0 equiv.) and 20 ml absolute tetrahydrofuran. The addition side of the HDSF was charged with a solution of *n*-butyl lithium (2.5 M in hexanes, 1.83 ml, 4.57 mmol, 1.0 equiv.) which was diluted with additional 18 ml of absolute tetrahydrofuran. The HDSF was then cooled to –78°C, at this point the solution of *n*-butyl lithium was added dropwise to the reaction side resulting in a pale yellow reaction mixture. The mixture was stirred for 30 min at –78 °C, at which point iodomethane-d₃ (0.36 ml, 827.24 mg, 5.71 mmol, 1.25 equiv.) was added dropwise. The reaction mixture was stirred for 30 min at –78 °C, then an excess of dry ice was added directly to the reaction mixture. The cooling bath was removed and the mixture allowed to warm to room temperature over 3 h. 10 ml of water were added slowly and the mixture was stirred vigorously for 10 min at room temperature. The mixture was then extracted with dichloromethane (6 x 20 ml), the combined organic layers dried over anhydrous magnesium sulfate, the solvents removed *in vacuo* to give the crude product as a pale yellow solid. Column chromatography (silica, grading from 0% to 10% ethyl acetate in hexanes over a total of 30 column volumes) yielded the product *III-13* (which sublimes easily at high vacuum) as a colorless solid in 67% yield (401 mg).

¹H NMR (400.0 MHz, CDCl₃, 295 K):
δ = 8.01 (s, 1H), 4.03 (s, 3H), 4.01 (s, 3H) ppm.

²H NMR (61.0 MHz, CDCl₃, 295 K):
δ = 1.96 ppm.

¹³C NMR (100.0 MHz, CDCl₃, 295 K):
δ = 169.5, 164.0, 156.8, 110.8, 54.4, 53.6, 11.1, 10.9 (h) ppm.

HR-MS (EI):
Calculated for $C_7H_7D_3N_2O_2$ [M]$^{•+}$: 157.0924 m/z
Found: 157.0931 m/z

This procedure was previously published in *Chem. Eur. J.* **2019**.[13]

*4.2. Synthesis of **III-14***

III-13   III-14
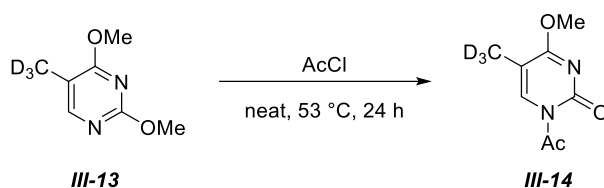
According to a modified literature procedure:[255,256]

A Young ampoule was charged with ***III-13*** (70.0 mg, 0.445 mmol, 1.0 equiv.) and acetyl chloride (0.985 ml, 1.08 g, 13.81 mmol, 31.0 equiv.) was added. The reaction mixture was heated to 53 °C for 20 h in the closed ampoule and then allowed to cool to room temperature. The solvents were then removed in vacuo to yield ***III-14*** (74 mg, 90%) sufficiently pure for use in the following synthesis step.

^{1}H NMR (400.0 MHz, CDCl$_3$, 295 K):
δ = 8.05 (s, 1H), 4.03 (s, 3H), 2.79 (s, 3H) ppm.

^{2}H NMR (61.0 MHz, CDCl$_3$, 295 K):
δ = 1.94 ppm.

^{13}C NMR (100.0 MHz, CDCl3, 295 K):
δ = 172.4, 171.8, 155.1, 137.1, 107.6, 55.4, 27.1, 11.7 (h) ppm.

HR-MS (EI):
Calculated for C$_8$H$_7$D$_3$N$_2$O$_3$ [M]$^{\cdot+}$: 185.0880 m/z
Found: 185.0874 m/z

This procedure was previously published in *Chem. Eur. J.* **2019**.[13]

4.3. Synthesis of **D₃-5mC** *and* **D₃-T**
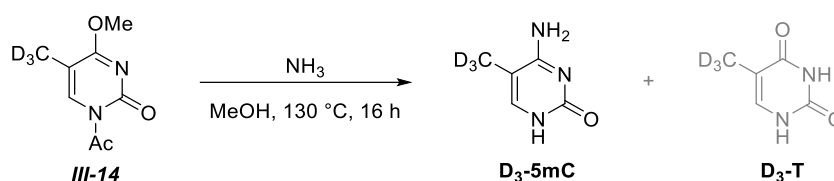
According to a modified literature procedure:[255,257]

A 15 ml pressure tube (ACE®) was charged with ***III-14*** (260.0 mg, 1.40 mmol, 1.0 equiv.). A solution of ammonia (7.0 M in methanol, 5.2 ml, 36.40 mmol, 26.0 equiv.) was added under evolution of gas. The pressure tube was then immediately placed in a pre-heated oil bath (130 °C) and stirred at this temperature for 16 h. The mixture was then allowed to cool to room temperature, at which point a colorless solid precipitated, which was collected, washed with methanol (2 x 1 ml) and dried to give the product in 38% yield (68 mg). The supernatants were also collected and placed in a freezer resulting in the precipitation of a colorless solid, which was collected and washed with methanol (1 x 1 ml). The solids were collected and dissolved in 6 ml aq. NH_4COO buffer (pH = 4). Two HPLC purification steps (step one: silica C-18, 100% A grading to 80% A/20% B in 45 min, retention time of product 20 min, solvent A: aq. NH_4COO at pH = 4, solvent B: 80% MeCN in aq. NH_4COO; step two: 100% H_2O grading to 1% MeCN in H_2O in 25 min, retention time of product **D₃-5mC** 8 min) gave 24 mg of the product, resulting in a total yield of 51% (92 mg) of **D₃-5mC**. **D₃-T** was obtained at 14 min, no yield was determined.

D₃-5mC:
¹H NMR (400.0 MHz, D_2O, 295 K):
δ = 7.34 (s, 1H), 3.37 (s, 1H) ppm.

¹³C NMR (100.0 MHz, D_2O, 295 K):
δ = 164.9, 157.0, 138.0, 101.0, 46.6 ppm.

D₃-T:
¹H NMR (400.0 MHz, D_6-DMSO, 295 K):
δ = 10.98 (s, 1H), 10.57 (s, 1H), 7.24 (d, *J* = 5.7 Hz, 1H), 3.37 (s, 1H) ppm.

²H NMR (61.0 MHz, D_6-DMSO, 295 K):
δ = 1.67 ppm.

¹³C NMR (100.0 MHz, D_6-DMSO, 295 K):
δ = 164.9, 151.5, 137.7, 107.5 ppm.

Due to the large deuterium splitting, the signal for the methyl group could not be distinguished from the background noise.

¹H NMR (400.0 MHz, D_2O, 295 K):
δ = 7.37 ppm.

²H NMR (61.0 MHz, D_2O, 295 K):
δ = 1.81 ppm.

¹³C NMR (100.0 MHz, D_2O, 295 K):
δ = 139.0, 109.9 ppm.

No other signals could be distinguished from the background noise.

HR-MS (ESI):
Calculated for $C_5H_4D_3N_2O_2$ [M+H]⁺: 130.06958 m/z
Found: 130.06920 m/z
Calculated for $C_5H_2D_3N_2O_2$ [M–H]⁻: 128.05393 m/z
Found: 128.05437 m/z

A part of this procedure was previously published in *Chem. Eur. J.* **2019**.[13]

4.4. Synthesis of *III-16*

III-16
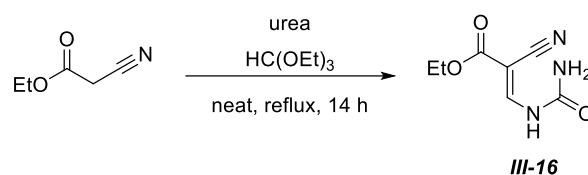
According to a modified literature procedure:[260]

A round-bottom flask was charged with urea (2.50 g, 41.63 mmol, 1.00 equiv.), ethyl cyanoacetate (4.50 ml, 4.78 g, 42.29 mmol, 1.02 equiv.) and triethyl orthoformate (11.10 ml, 9.89 g, 66.73 mmol, 1.60 equiv.). The mixture was heated to reflux (bath temperature 105 °C) for 14 h. A grey precipitate formed, the green solution was filtered off and the precipitate was washed with 50 ml ethanol and 50 ml acetone to give the product *III-16* as a grey solid in 52% yield (3.99 g).

¹H NMR (400.0 MHz, D₆-DMSO, 295 K):
δ = 10.55 (d, J = 12.8 Hz, 1H), 8.08 (d, J = 12.8 Hz, 1H), 7.60 (br, 1H), 7.37 (br, 1H), 4.23 (q, J = 7.1 Hz, 2H), 1.26 (t, J = 7.1 Hz, 3H) ppm.

¹³C NMR (100.0 MHz, D₆-DMSO, 295 K):
δ = 164.7, 151.8, 151.7, 117.1, 77.6, 61.0, 14.1 ppm.

HR-MS (ESI):
Calculated for $C_7H_8LiN_3O_3$ [M+Li]⁺: 190.08040 m/z
Found: 190.10751 m/z
Calculated for $C_7H_8N_3O_3$ [M-H]⁻: 182.05657 m/z
Found: 182.05708 m/z

IR (thin film):
$\tilde{v}$ = 3347, 3245, 3192, 3006, 2233, 1749, 1685, 1595, 1459, 1398, 1373, 1349, 1311, 1272, 1256, 1173, 1108, 1021, 1003, 956, 849, 775, 742, 707 cm⁻¹.

This procedure was previously published in *Chem. Eur. J.* **2019**.[13]

*4.5. Synthesis of **III-17***
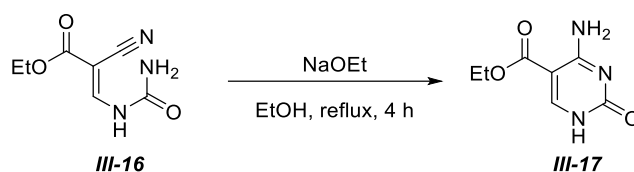
According to a modified literature procedure:[260]

A round-bottom flask was charged with ***III-16*** (1.70 g, 9.28 mmol, 1.00 equiv.) and 5.00 ml ethanol. A solution of sodium ethoxide (2.68 M in ethanol, 5.20 ml, 0.94 g, 13.94 mmol 1.50 equiv.) was added dropwise and the reaction mixture was heated to reflux (bath temperature 85 °C) for 1 h. Another 7.0 ml ethanol were added and the reaction was stirred for an additional 3 h. A grey precipitate formed, the red-brown solution was filtered off, and the precipitate washed with 30 ml ethanol. The residue was dissolved in 80 ml of water and then acidified to pH ≈ 5.5 with glacial acetic acid. A colorless solid precipitated from the yellow solution and was filtered off, and the precipitate washed with ethanol and diethyl ether (25 ml each) to give the product as a colorless solid. In addition, the ethanol phase from the first filtration step was acidified to pH ≈ 5.5 with glacial acetic acid. The colorless solid that precipitated was collected, washed with diethyl ether and dried to give the product ***III-17*** as a colorless solid. The combined products resulted in 59% yield (1.08 g).

^{1}H NMR (400.0 MHz, D$_6$-DMSO, 295 K):
δ = 11.31 (br, 1H), 8.19 (s, 1H), 7.81 (br, 2H), 7.61 (s, 6H), 4.21 (q, *J* = 7.1 Hz, 2H), 1.26 (t, *J* = 7.1 Hz, 6H) ppm.

^{13}C NMR (100.0 MHz, D$_6$-DMSO, 295 K):
δ = 164.8, 93.4, 60.3, 14.1 ppm. (These were the only signals distinguishable from background noise.)

HR-MS (ESI):
Calculated for C$_7$H$_9$N$_3$O$_3$ [M+H]$^+$: 184.07222 m/z
Found: 184.07170 m/z
Calculated for C$_7$H$_8$N$_3$O$_3$ [M-H]$^-$: 182.05657 m/z
Found: 182.05710 m/z

IR (thin film):
$\tilde{v}$ = 3414, 3166, 2986, 2601 (br), 1865, 1701, 1642, 1620, 1570, 1468, 1395, 1368, 1308, 1245, 1156, 1122, 1111, 1020, 962, 932, 874, 847, 795, 764, 717, 662, 652 cm^{-1}.

This procedure was previously published in *Chem. Eur. J.* **2019**.[13]

4.6. Synthesis of 5hmC
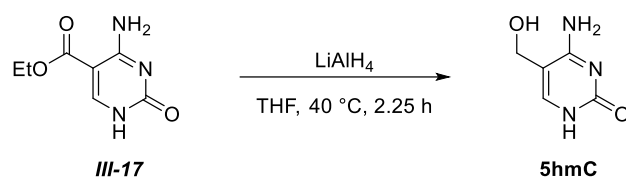
III-17 → **5hmC**

According to a modified literature procedure:[260]

A flame-dried flask was charged with **III-17** (366 mg, 2.00 mmol, 1.0 equiv.) and a solution of lithium aluminum hydride (1.0 M in tetrahydrofuran, 9.99 ml, 379.19 mg, 9.99 mmol, 5.0 equiv.) was added dropwise under evolution of gas. The reaction mixture was heated to 40 °C for 2.25 h. 5 ml of water were slowly added, which resulted in heavy foaming. The mixture was filtered, washed with additional 50 ml of water and the aqueous layer was concentrated. High performance liquid chromatography (C18, 100% water grading to 1% acetonitrile in water) and subsequent removal of the solvents *in vacuo* gave the product **5hmC** as a colorless solid in 71% yield (200 mg).

¹H NMR (400.0 MHz, D₂O, 295 K):
δ = 7.70 (s, 1H), 4.42 (d, J = 0.5 Hz, 2H) ppm.

HR-MS (ESI):
Calculated for $C_5H_8N_3O_2$ [M+H]⁺: 142.06110 m/z
Found: 142.06122 m/z
Calculated for $C_{10}H_{15}N_6O_4$ [2M+H]⁺: 283.11493 m/z
Found: 283.11496 m/z
Calculated for $C_5H_6N_3O_2$ [M-H]⁻: 140.04655 m/z
Found: 140.04648 m/z

4.7. Synthesis of D$_2$-5hmC
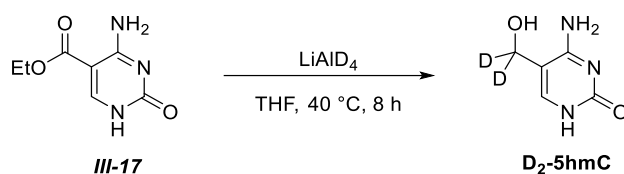
III-17

According to a modified literature procedure:[260]

A flame-dried flask was charged with lithium aluminum deuteride (150.00 mg, 3.57 mmol, 4.51 equiv.) and 4 ml of absolute tetrahydrofuran. After cooling the resulting suspension to 0 °C, **III-17** (145 mg, 0.792 mmol, 1.0 equiv.) was added in one portion, resulting in gas evolution. The reaction mixture was stirred at 0 °C for 10 min, allowed to warm to room temperature and then heated to 40 °C for 8 h. The reaction was allowed to cool to room temperature and 5 ml of water were slowly added resulting in gas evolution and foaming. The mixture was filtered, washed with additional 50 ml of water and the aqueous layer was concentrated. High performance liquid chromatography (C18, 100% water grading to 1% acetonitrile in water) and subsequent removal of the solvents *in vacuo* yielded the product **D$_2$-5hmC** as a colorless solid (27 mg, 24%).

¹H NMR (400.0 MHz, D$_6$-DMSO, 295 K):
δ = 10.31 (br, 1H), 7.25 (s, 1H), 7.03 (br, 1H), 6.49 (br, 1H), 4.87 (br, 1H), ppm.

²H NMR (61.0 MHz, D$_6$-DMSO, 295 K):
δ = 4.11 ppm.

¹³C NMR (100.0 MHz, D$_6$-DMSO, 295 K):
δ = 156.7, 104.42 ppm.

No other signals could be distinguished from background noise.

HR-MS (ESI):
Calculated for C$_5$H$_5$D$_2$N$_3$O$_2$ [M+H]$^+$: 144.07366 m/z
Found: 144.07376 m/z
Calculated for C$_5$H$_6$N$_3$O$_2$ [M-H]$^-$: 142.05910 m/z
Found: 142.05904 m/z

4.8. Analytical Data of **5fC**
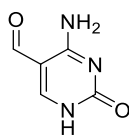
¹H NMR (400.0 MHz, D$_6$-DMSO, 295 K):
δ = 10.31 (br, 1H), 7.25 (s, 1H), 7.03 (br, 1H), 6.49 (br, 1H), 4.87 (br, 1H), ppm.

¹³C NMR (100.0 MHz, D$_6$-DMSO, 295 K):
δ = 156.7, 104.42 ppm.

No other signals could be distinguished from background noise.

HR-MS (ESI):
Calculated for C$_5$H$_6$N$_3$O$_2$ [M+H]$^+$: 140.04600 m/z
Found: 140.04557 m/z
Calculated for C$_5$H$_4$N$_3$O$_2$ [M–H]$^-$: 138.03035 m/z
Found: 138.03078 m/z

4.9. Synthesis of **5m***i***C**
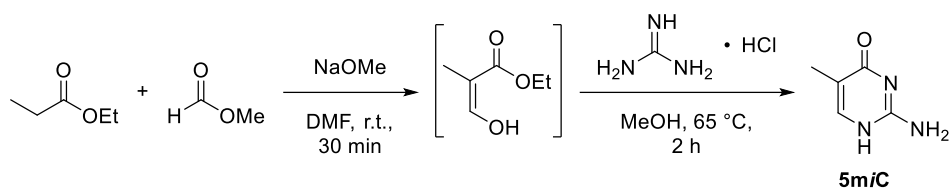
According to a modified literature procedure:[252]

A flask was charged with sodium methoxide (2.82 g, 52.20 mmol, 2.01 mmol) and 4 ml of dimethylformamide. Ethyl propionate (4.50 ml, 3.98 g, 38.95 mmol, 1.50 equiv.) was added. Then, methyl formate (1.60 ml, 1.57 g, 26.11 mmol, 1.01 equiv.) was added dropwise over a period of 2 h. The solution was stirred for an additional 30 min at room temperature. Then, a solution of guanidine hydrochloride (2.83 M in methanol, 9.2 ml, 2.49 g, 26.07 mmol, 1.00 equiv.) was added rapidly and the mixture refluxed (bath temperature 95 °C) for 2 h. The solution was allowed to cool to 30 °C and the pH was adjusted to 6 using concentrated hydrochloric acid. The mixture was stored at 4 °C for 15 h, the precipitate filtered off through a sintered glass frit, washed with methanol and dried in vacuo to yield the crude product as a colorless solid. Recrystallization from water afforded the pure product **5m***i***C** (no yield was determined).

¹H NMR (400.0 MHz, D_6-DMSO, 295 K):
δ = 11.06 (br, 1H), 7.39 (d, *J* = 1.2 Hz, 1H), 6.45 (br, 2H), 1.74 (d, *J* = 1.0 Hz, 3H) ppm.

¹³C NMR (100.0 MHz, D_6-DMSO, 295 K):
δ = 156.1, 110.2, 12.3 ppm.

No other signals could be distinguished from the background noise.

¹H NMR (400.0 MHz, D_2O, 295 K):
δ = 7.47 (s, 1H), 1.89 (d, *J* = 1.1 Hz, 3H) ppm.

¹³C NMR (100.0 MHz, D_2O, 295 K):
δ = 12.1 ppm.

No other signals could be distinguished from the background noise.

HR-MS (ESI):
Calculated for $C_5H_8N_3O$ [M+H]$^+$: 126.06674 m/z
Found: 126.06624 m/z
Calculated for $C_5H_6N_3O$ [M–H]$^-$: 124.05109 m/z
Found: 124.05149 m/z

This procedure was part of the Bachelor Thesis of Caroline Kliem, 2019, conducted under my supervision.

4.10.   Synthesis of TMS-5m*i*C
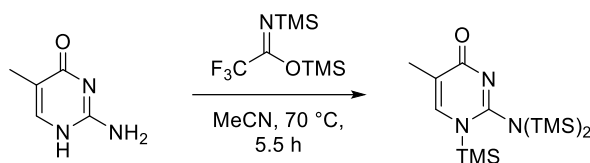
A flask was charged with **5m*i*C** (20.9 mg, 0.2 mmol, 1.0 equiv.), acetonitrile (0.8 mL) and N,O-Bis(trimethylsilyl)trifluroacetamide (BSTFA) (0.9 mL, 864.0 mg, 3.4 mmol, 20.1 equiv.). The reaction mixture was stirred at 70 °C for 5.5 h, then the solvent was removed *in vacuo* to yield the product as a yellow oil (60.6 mg, 106%) that was stored at room temperature and still contains acetonitrile as confirmed *via* ¹H NMR spectrometry. In addition to the desired product, several signals were detected that could not be assigned unequivocally. Moreover, an additional constitutional isomer with a low concentration could be identified *via* ¹H NMR spectrometry.

¹H NMR (400.0 MHz, CDCl₃, 295 K):

Isomer with the higher concentration:

δ = 7.85 (d, *J* = 0.9 Hz, 1H), 1.94 (d, *J* = 0.8 Hz, 3H), 0.35 (m, *J* = 6.7 Hz, 18H) ppm. Isomer with the lower concentration:

δ = 7.96 (d, *J* = 0.9 Hz, 1H), 1.99 (d, *J* = 0.8 Hz, 3H), 0.35 (m, *J* = 6.7 Hz, 18H) ppm.

This procedure was part of the Bachelor Thesis of Caroline Kliem, 2019, conducted under my supervision. As this project was not further continued, no additional analytical characterization was conducted.

4.11.   Synthesis of 5I*i*C
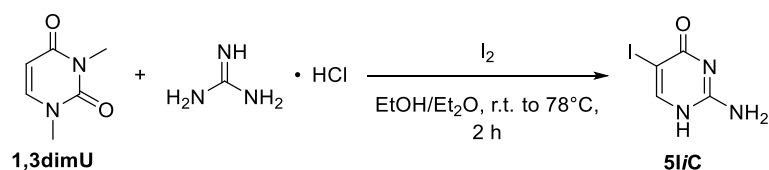
According to a modified literature procedure:[251]

A flame-dried Schlenk flask was charged with guanidine hydrochloride (2.73 g, 28.54 mmol, 4.0 equiv.) and 15 ml ethanol. A solution of sodium ethoxide (1.93 M in ethanol, 14.75 ml, 1.94 g, 28.54 mmol, 4.00 equiv.) was added dropwise and the mixture stirred for 15 min at room temperature. The suspension was filtered through a sintered glass frit and 1,3-dimethyluracil (1.00 g, 7.14 mmol, 1.00 equiv.) was added in one portion to the filtrate. The mixture was heated to reflux (bath temperature 90 °C) for 1 h. Subsequently, the solvents were removed *in vacuo*. The obtained residue was dissolved in an aqueous solution of sodium hydroxide (2 M, 30 ml). A solution of iodine (0.29 M in diethyl ether, 25 ml, 1.85 g, 7.29 mmol, 1.02 equiv. was added resulting in a biphasic mixture. The organic layer turned colorless upon addition to the aqueous solution. The aqueous layer was then washed with diethyl ether (3 x 30 ml) and subsequently neutralized with glacial acetic acid to pH 7. A colorless precipitate formed which was filtered off, washed with water and ethanol, and dried *in vacuo* to yield the product **5I*i*C** as a colorless solid (1.25 g, 74%).

¹H NMR (400.0 MHz, D₆-DMSO, 295 K):
δ = 11.26 (br, 1H), 7.93 (s, 1H), 6.70 (br, 2H) ppm.

This procedure was part of the Bachelor Thesis of Caroline Kliem, 2019, conducted under my supervision. As this project was not further continued, no additional analytical characterization was conducted.

4.12. Synthesis of TMS-5I*i*C
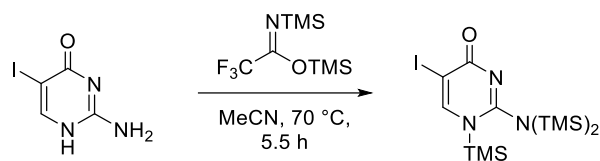
5I*i*C (312.0 mg, 1.3 mmol, 1.0 equiv.), acetonitrile (12.0 mL) and *N,O*-Bis(trimethylsilyl)trifluoroacetamide (3.6 mL, 3.5 g, 13.4 mmol, 10.2 equiv.) were stirred at 70 °C for 4 h. The solvent was removed *in vacuo* to yield **4** as a yellow oil (1240.6 mg, 208%) that was stored at room temperature and still contains acetonitrile as confirmed *via* 1H NMR spectrometry. In addition to the desired product, several signals were detected that could not be assigned unequivocally.

¹H NMR (400.0 MHz, CDCl₃, 295 K):
δ = 8.26 (s, 1H), 0.38 (s, 9H) ppm.

This procedure was part of the Bachelor Thesis of Caroline Kliem, 2019, conducted under my supervision. As this project was not further continued, no additional analytical characterization was conducted.

*4.13.   Synthesis of **III-22***
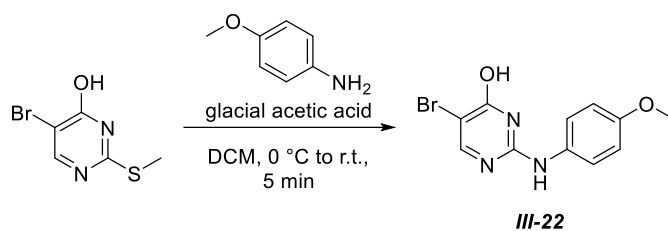
A flask was charged with 5-bromo-2-(methylthio)pyrimidin-4-ol (999.8 mg, 4.5 mmol,1.0 equiv.), *p*-anisidine (1119.4 mg, 9.1 mmol, 2.0 equiv.) and glacial acetic acid (21 mL). The mixture was refluxed (bath temperature 130 °C) for 25 h at which time the color has changed from brown to a dark purple. Water was added and the solvents were removed *via* freeze drying. Column chromatography (silica, methanol in dichloromethane, starting at 5% methanol for 5 column volumes, then grading to 10% methanol over 10 column volumes and continuing for additional 10 column volumes at 10% methanol) gave a colorless solid, which was recrystallized from dichloromethane (bath temperature 35 °C) to yield ***III-22*** as a colorless solid. The product still contains 5-bromo-2-(methylthio)pyrimidin-4-ol as confirmed *via* ^{1}H NMR spectrometry, therefore no yield was determined.

^{1}H NMR (400.0 MHz, CDCl$_3$, 295 K):
δ = 7.38 (dd, *J* = 9.0 Hz, 2H), 6.86 (dd, *J* = 9.0 Hz, 1H), 3.78 (s, 3H) ppm.

^{13}C NMR (100.0 MHz, CDCl$_3$, 295 K):
δ = 168.5, 161.7, 156.6, 131.0, 122.1, 114.3, 55.6 ppm.

No other signals could be distinguished from the background noise.

HR-MS (EI):
Calculated for C$_{11}$H$_{10}$^{81}BrN$_3$O$_2$ [M]$^{•+}$: 296.9936 m/z
Found: 296.9957 m/z
Calculated for C$_{11}$H$_{10}$^{79}BrN$_3$O$_2$ [M]$^{•+}$: 294.9956 m/z
Found: 294.9944 m/z
Calculated for C$_{10}$H$_7$BrN$_3$O$_2$ [M-CH$_3$]$^{•+}$: 279.9722 m/z
Found: 279.9789 m/z

This procedure was part of the Bachelor Thesis of Caroline Kliem, 2019, conducted under my supervision.

*4.14.   Synthesis of **1mU***
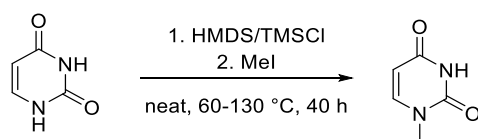
According to a modified literature procedure:[262]

A flame-dried flask was charged with uracil (2.8 g, 24.98 mmol, 1 equiv.), bis(trimethylsilyl)amine (HMDS, 50.14 ml, 39.11 g, 242.31 mmol, 9.7 equiv.) and trimethylsilyl chloride (TMSCl, 4.73 ml, 4.04 g, 37.22 mmol, 1.49 equiv.). The mixture was heated to reflux (bath temperature 130 °C) for 5 h. After one hour, the suspension turned into a clear solution. Then, the solution was allowed to slowly cool. When the bath temperature reached 60 °C, methyl iodide (15.08 ml, 34.39 g, 242.31 mmol, 9.7 equiv.) was added and the mixture heated to reflux (bath temperature 60 °C) for 24 h. The mixture was then concentrated to a volume of ~10-15 ml at 60 °C under reduced pressure. Then, the mixture was allowed to cool to room temperature and 150 ml *iso*-propanol were added. A colorless precipitate formed, the suspension was stirred for 1 h at room temperature. The precipitate was collected using centrifugation and recrystallized from water (~30-35 ml, 70 °C). The first precipitate was identified to contain mostly uracil and traces of the desired product. High performance liquid chromatography (C18, 100% water grading to 1% acetonitrile in water) and subsequent removal of the solvents *in vacuo* yielded the product as a colorless solid (yield not determined).

^{1}H NMR (400.0 MHz, D$_6$-DMSO, 295 K):
δ = 11.20 (br, 1H), 7.60 (d, *J* = 7.8 Hz, 1H), 5.51 (d, *J* = 7.8 Hz, 1H), 3.22 (s, 3H) ppm.

NMR data is in accordance with the literature.[374]

HR-MS (ESI):
Calculated for C$_5$H$_7$N$_2$O$_2$ [M+H]$^+$: 127.05075 m/z
Found: 127.05038 m/z
Calculated for C$_5$H$_5$N$_2$O$_2$ [M−H]$^-$: 125.03510 m/z
Found: 125.03553 m/z

Elemental Analysis:
Calculated for C$_5$H$_6$N$_2$O$_2$: C 47.62, H 4.80, N 22.21.
Found: C 46.92, H 4.62, N 21.85.

5. Synthetic Procedures – Nucleosides and Dinucleotides

5.1. Synthesis of III-4

III-4
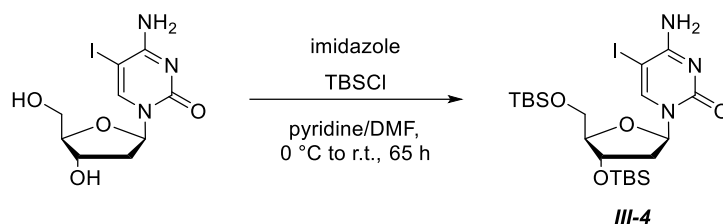
According to modified literature procedure:[375]

A flame-dried flask was charged with 5-iodo deoxycytidine (256.3 mg, 0.73 mmol, 1.0 equiv.) and imidazole (345.9 mg, 5.08 mmol, 7.0 equiv.) and dissolved in 3.3 ml absolute pyridine and 1 ml absolute tetrahydrofuran. After the reaction mixture was cooled to 0 °C, *tert*-butyldimethylsilyl chloride (656.4 mg, 4.35 mmol, 6.0 equiv.) was added. The reaction mixture was allowed to slowly to warm room temperature and was stirred for 65 h. The solvents were removed *in vacuo* and obtained solid residue dissolved in 5 mL saturated sodium hydrogen carbonate solution and 10 ml dichloromethane. The aqueous layer was extracted with dichloromethane (4 x 30 ml) and the combined organic layers were washed with water (1 x 50 ml) and brine (1 x 50 ml). The solvents were removed *in vacuo* to yield product **III-4** as a colourless solid in 99% yield (418 mg).

¹H NMR (400.0 MHz, CDCl3, 295 K):
δ = 8.09 (s, 1H), 6.24 (t, J = 6.51 Hz, 1H), 3.97 (t, J = 2.76 Hz, 1H), 3.89 (dd, J = 11.43 Hz, J = 2.58 Hz, 1H), 3.75 (dd, J = 11.42 Hz, J = 2.58 Hz, 1H), 2.47 (ddd, J = 13.33 Hz, J = 5.97 Hz, J = 3.13 Hz, 1H), 1.96 (m, 1H), 0.93 (s, 9H), 0.88 (s,9H), 0.14 (s, 3H), 0.13 (s, 3H), 0.06 (s, 3H), 0.06 (s, 3H) ppm.

HR-MS (ESI):
Calculated for $C_{21}H_{41}IN_3O_4Si_2$ [M+H]⁺: 582.16748 m/z
Found: 582.16692 m/z

NMR data is in accordance with the literature.[375]

This procedure was part of the Internship Report of Juliane Kamlah, 2019, conducted under my supervision.

5.2. Synthesis of *III-5*
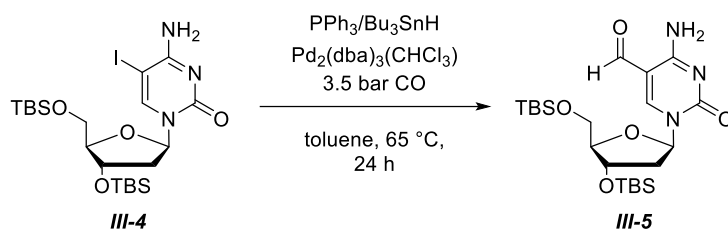
According to modified literature procedure:[376]

A high-pressure glass autoclave vessel was charged with **III-4** (1.0 g, 1.72 mmol, 1.0 equiv.), Pd₂(dba)₃(CHCl₃) (178.0 mg, 0.172 mmol, 0.1 equiv.) and triphenyl phosphine (270.6 mg, 1.03 mmol, 0.6 equiv.) under inert atmosphere (argon). The reaction mixture was dissolved in 19 ml toluene and the autoclave flushed three times with CO to remove residual air. The reaction mixture was stirred at a CO pressure of 3.5 bar and 65 °C. With a syringe pump tributyltin hydride (0.546 ml, 2.06 mmol, 1.2 equiv.) in 1 ml toluene solution was added through a septum at 0.45 µl per hour. After complete addition the reaction was stirred additional 9 hours at 60 °C. Subsequently the CO was discharged and the solvent evaporated *in vacuo*. After filtration and column purification the product **III-5** was isolated as a colourless solid in 81% yield (671 mg).

¹H NMR (400.0 MHz, CDCl3, 295 K):
δ = 9.56 (s, 1H), 8.76 (s, 1H), 8.70 (s, 1H), 7.45 (m, 1H), 6.19 (t, *J* = 6.1 Hz, 1H), 4.36 (m, 1H), 4.09 (m, 1H), 3.97 (dd, *J* = 11.8 Hz, *J* = 2.5 Hz, 1H), 3.79 (dd, *J* = 11.8 Hz, *J* = 2.5 Hz, 1H), 2.62 (ddd, *J* = 13.8 Hz, *J* = 5.9 Hz, *J* = 3.8 Hz, 1H), 2.12 (m, 1H), 0.90 (s, 9H), 0.89 (s, 9H), 0.10 (s, 3H), 0.09 (s, 6H), 0.07 (s, 3H) ppm.

NMR data is in accordance with the literature. [376]

This procedure was part of the Internship Report of Juliane Kamlah, 2019, conducted under my supervision.

5.3. Synthesis of 5fdC

III-5   **5fdC**
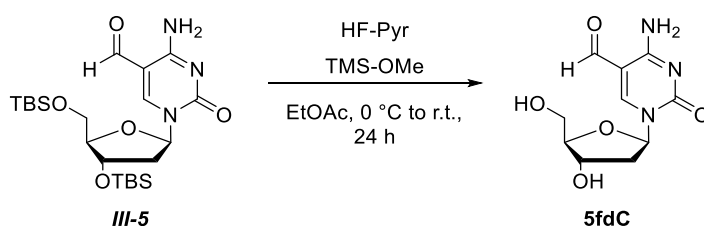
According to modified literature procedure:[376]

In a polypropylene tube twice TBS-protected **III-5** (256.3 mg, 0.729 mmol, 1.0 equiv.) was dissolved in 13.8 ml absolute ethyl acetate. Then, 70% hydrogen fluoride pyridine (1.54 ml, 5.08 mmol, 7.0 equiv.) was added and the solution stirred for 16 h at room temperature. Then, methoxytrimethyl silane (3.16 ml, 4.35 mmol, 6.0 equiv.) was added and the mixture stirred at room temperature for an additional 8 h. The solvents were removed *in vacuo* and the obtained solid redissolved in water. The aqueous layer was washed with dichloromethane (3 x 50 ml) and ethyl acetate (1 x 50 ml). The water was removed *in vacuo* to yield the product **5fdC**, which was subjected to HPLC purification (C18, 100% water grading to 10% acetonitrile in water). No yield was determined.

¹H NMR (400.0 MHz, CDCl3, 295 K):
δ = 9.56 (s, 1H), 8.76 (s, 1H), 8.70 (s, 1H), 7.45 (m, 1H), 6.19 (t, J = 6.1 Hz, 1H), 4.36 (m, 1H), 4.09 (m, 1H), 3.97 (dd, J = 11.8 Hz, J = 2.45 Hz, 1H), 3.79 (dd, J = 11.77 Hz, J = 2.45 Hz, 1H), 2.62 (ddd, J = 13.76 Hz, J = 5.91 Hz, J = 3.80 Hz, 1H), 2.12 (m, 1H), 0.90 (s, 9H), 0.89 (s, 9H), 0.10 (s, 3H), 0.09 (s, 6H), 0.07 (s, 3H) ppm.

HR-MS (ESI):
Calculated for $C_5H_5N_2O_2$ [M–H]⁻: 254.07770 m/z
Found: 254.07815 m/z

This procedure was part of the Internship Report of Juliane Kamlah, 2019, conducted under my supervision.

*5.4. Synthesis of **III-6***
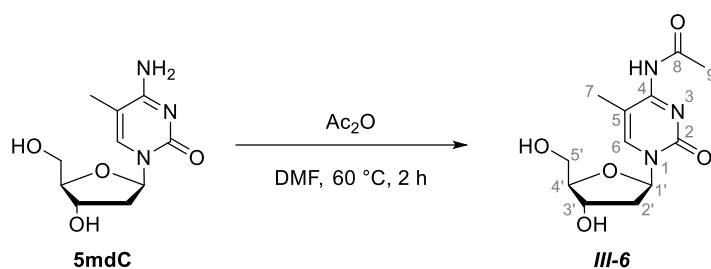
According to modified literature procedure:[242]

5mdC (1.17 g, 4.85 mmol, 1.0 equiv.) was dissolved in 50 ml dimethylformamide. To this solution was added acetic anhydride (504 µl, 5.33 mmol, 1.1 equiv.) and the mixture was stirred at 60 °C for 2 h. The reaction was quenched by addition of methanol (30 ml) and the solvents were removed under reduced pressure. The crude product was purified by flash column chromatography (silica, grading from 2% to 10% methanol in dichloromethane) to obtain product **III-6** in 41% yield (569 mg).

R_F = 0.10 (silica, UV, 2% methanol in 98% dichloromethane)

¹H NMR (400.0 MHz, CDCl3, 295 K):
δ = 8.10 (s, 1H, H-6), 6.11 (t, J = 6.4 Hz, 1H, H-1'),5.24 (d, J = 4.2 Hz, 1H, OH-3'), 5.08 (s, 1H, OH-5'), 4.20 (dd, J = 5.9 Hz, J = 3.3 Hz, 1H, H-3'), 3.83 (q, J = 3.7 Hz, 1H, H-4'), 3.64 – 3.53 (m, 2H, H-5'), 2.23 (s, 3H, H-9), 2.09 – 1.92 (m, 2H, H-2'), 1.91 (s, 3H, H-7) ppm.

LR-MS (ESI):
Calculated for $C_{12}H_{18}N_3O_5$ [M+H]⁺: 284.3 m/z
Found: 284.2 m/z

This procedure was part of the Internship Report of Doreen Reuter, 2019, conducted under my supervision. As this project was not further continued, no additional analytical characterization was conducted.

*5.5. Synthesis of **III-7** from **III-6***
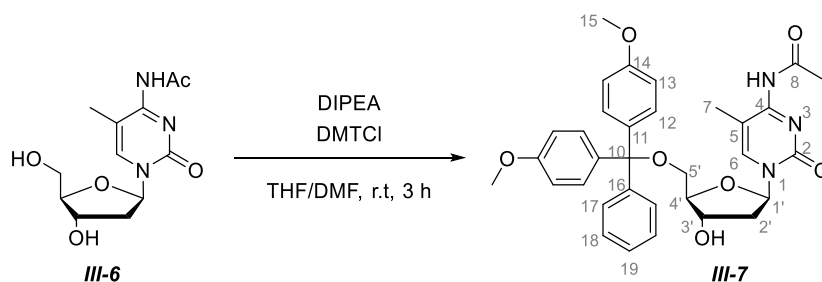
According to modified literature procedure.[243]

4,4′-Dimethoxytrityl chloride (680.3 mg, 2.01 mmol, 1.2 equiv.) was dissolved in absolute tetrahydrofuran (5 ml), and added to a solution of **III-6** (100 mg, 1.67 mmol, 1.0 equiv.) and *N,N*-di-*iso*-propylethylamine (DIPEA, 570 µl, 4.77 mmol, 2.0 equiv.) in a mixture of 5 ml absolute tetrahydrofuran and 2 ml absolute dimethylformamide at room temperature. After stirring for 3 h, the reaction mixture was poured into a separatory funnel containing 5% sodium bicarbonate solution (15 ml), and extracted with ethyl acetate (3 x 10 ml). The layers were separated and the organic layer dried over anhydrous magnesium sulphate, filtered, and concentrated *in vacuo*. After purification by flash column chromatography (silica, grading from 0 to 10% methanol in dichloromethane) the product **III-7** was obtained. No yield was determined.

¹H NMR (400.0 MHz, CDCl₃, 295 K):
δ = 8.06 (s, 1H, H-6), 7.35-7.27 (m, 2H, H-18), 7.27-7.08 (m, 7H, H-12, H-17, H-19), 6.85-6.69 (m, 4H, H-13), 6.14 (t, *J* = 6.2 Hz, 1H, H-1′), 4.40 (q, *J* = 4.4 Hz, 1H, H-3′), 4.04-3.94 (m, 1H, H-4′), 3.68 (s, 6H, H-15), 3.42-3.35 (m, 1H, H-5′), 3.28 (dd, *J* = 10.5 Hz, *J* = 3.5 Hz, 1H, H-5′), 2.50-2.41 (m, 1H, H-2′), 2.28 (s, 3H, H-9), 2.22 (dt, *J* = 13.6 Hz, J = 6.5 Hz, 1H, H-2′), 1.50 (s, 3H, H-7) ppm.

LR-MS (ESI):
Calculated for C₃₃H₃₆N₃O₇ [M+H]⁺: 586.7 m/z
Found: 586.4 m/z

This procedure was part of the Internship Report of Doreen Reuter, 2019, conducted under my supervision. As this project was not further continued, no additional analytical characterization was conducted.

5.6. Synthesis of III-8
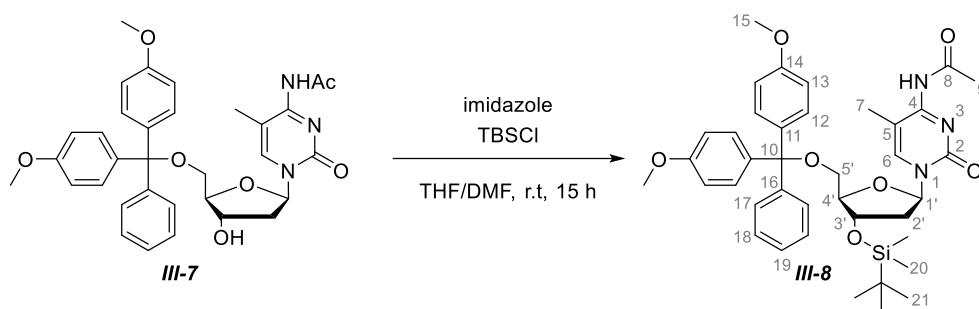
III-7 (490 mg, 0.837 mmol, 1.0 equiv.) was dissolved in a mixture of 10 ml of absolute tetrahydrofuran and 5 ml of absolute dimethylformamide. Imidazole (114 mg, 1.67 mmol, 2.0 equiv.) and *tert*-butyldimethylsilyl chloride (504 mg, 3.35 mmol, 4.0 equiv.) were added to the solution and the reaction mixture was stirred at room temperature for 15 h. The solvents were removed under reduced pressure, then a saturated solution of sodium bicarbonate solution (15 ml) and a solution of lithium chloride (5% in water, 15 ml) were added. The aqueous layer was extracted with ethyl acetate (3 x 20 mL), the layers separated, and the organic layer dried over magnesium sulfate, filtered, and the solvent removed *in vacuo*. The crude product was purified by flash column chromatography (silica, 0% - 20% methanol in dichloromethane) and product **III-8** was obtained in 50% yield (291 mg).

¹H NMR (400.0 MHz, CDCl$_3$, 295 K):
δ = 7.74 (t, *J* = 1.2 Hz, 1H, H-11′), 7.47-7.40 (m, 2H, H-18), 7.08 – 7.02 (m, 4H, H-12), 6.85-6.78 (m, 3H, H-17, H-19), 6.63-6.57 (m, 4H, H-13), 6.40 (t, *J* = 6.6 Hz, 1H, H-1′) 4.38 (dt, *J* = 6.5 Hz, *J* = 3.4 Hz, 1H, H-3′), 3.85 (d, *J* = 3.1 Hz, 1H, H-4′), 3.65 (dd, *J* = 11.4 Hz, *J* = 2.9 Hz, 1H, H-5′), 3.53 (dd, *J* = 11.4 Hz, J = 2.8 Hz, 1H, H-5′), 3.34-3.31 (m, 2H, H-2′), 3.28 (s, 6H, H-15), 0.94*¹ (s, 9H, H-21), 0.91*¹ (d, *J* = 1.5 Hz, 9H, H-21), 0.87 (s, 3H, H-7), 0.04*² (d, *J* = 2.7 Hz, 6H, H-20), 0.00*² (d, *J* = 2.9 Hz, 6H, H-20).

LR-MS (ESI):
Calculated for C$_{12}$H$_{18}$N$_3$O$_5$ [M+H]$^+$: 284.3 m/z
Found: 284.2 m/z

Two signals were observed that could be assigned to the methyl or *tert*-butyl groups on the TBS group, these are marked with *¹ for the methyl groups and *² for the tert-butyl group.

This procedure was part of the Internship Report of Doreen Reuter, 2019, conducted under my supervision. As this project was not further continued, no additional analytical characterization was conducted.

*5.7. Synthesis of **III-9***
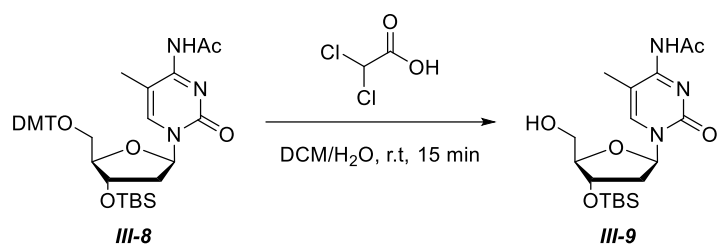
According to modified literature procedure:[377]

A solution of ***III-6*** (50.0 mg, 0.071 mmol, 1.0 equiv.) in dichloromethane (1 ml) was treated with a 3% solution of dichloroacetic acid in dichloromethane (1 ml). Water (12 µl) was added until the solution turned bright red and clear. After 15 min the reaction was quenched with methanol (5 ml) and pyridine (5 ml). The solvents were removed *in vacuo* and the crude product was purified by flash column chromatography (silica, grading from 0 to 10% methanol in dichloromethane) to give product ***III-9*** in 72% yield (20.4 mg).

LR-MS (ESI):
Calculated for $C_{18}H_{32}N_3O_5Si$ [M+H]$^+$: 398.6 m/z
Found: 398.4 m/z

This procedure was part of the Internship Report of Doreen Reuter, 2019, conducted under my supervision. As this project was not further continued, no additional analytical characterization was conducted.

*5.8. Synthesis of **III-6a***
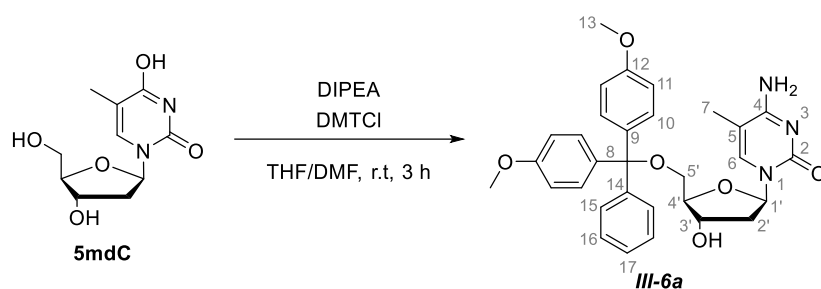
According to modified literature procedure:[243]

4,4′-Dimethoxytrityl chloride (969 mg, 2.86 mmol, 1.2 equiv.) was dissolved in 10 ml of absolute tetrahydrofuran and added to a solution of **5mdC** (575 mg, 2.38 mmol, 1.0 equiv.) and *N,N*-diisopropylethylamine (811 µl, 4.77 mmol, 2.0 equiv.) in absolute dimethylformamide (15 ml) at room temperature. After stirring for 3 h, the reaction mixture was poured into a separatory funnel containing saturated sodium bicarbonate solution (15 ml), and extracted with ethyl acetate (2 x 10 ml). The layers were separated and the organic layer dried over anhydrous magnesium sulfate, filtered, and concentrated. After purification by flash column chromatography (silica, grading from 0 to 10% methanol in dichloromethane) the product ***III-6a*** was obtained in a 37% yield (482 mg).

¹H NMR (400.0 MHz, CDCl$_3$, 295 K):
δ = 7.78 (d, *J* = 1.2 Hz, 1H, H-6), 7.45 – 7.41 (m, 2H, H-16), 7.33 – 7.21 (m, 7H, H-15, H-17), 6.90 – 6.85 (m, 4H, H-11), 6.31 (t, *J* = 6.5 Hz, 1H, H-1′), 4.49 (dt, *J* = 6.9 Hz, *J* = 3.7 Hz, 1H, H-3′), 4.02 (q, *J* = 3.2 Hz, 1H, H-4′), 3.45 (dd, *J* = 10.6 Hz, *J* = 2.8 Hz, 1H, H-5′), 3.38 – 3.34 (m, 1H, H-5′), 2.41 (ddd, *J* = 13.6 Hz, *J* = 6.2 Hz, *J* = 3.8 Hz, 1H, H-2′), 2.27 (dt, *J* = 13.4 Hz, *J* = 6.6 Hz, 1H, H-2′), 1.48 (d, *J* = 1.0 Hz, 3H, H-7) ppm.

LR-MS (ESI):
Calculated for C$_{18}$H$_{32}$N$_3$O$_5$Si [M+H]$^+$: 544.6 m/z
Found: 544.4 m/z

This procedure was part of the Internship Report of Doreen Reuter, 2019, conducted under my supervision. As this project was not further continued, no additional analytical characterization was conducted.

*5.9. Synthesis of **III-7** form **III-6a***
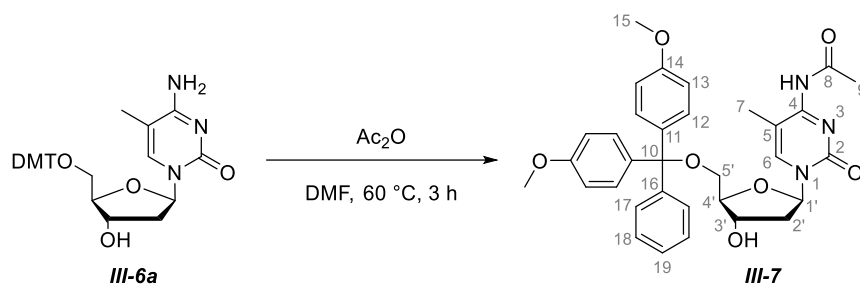
According to modified literature procedure:[243]

III-6a (92.0 mg, 0.169 mmol, 1.0 equiv.) was dissolved in 5 ml absolute dimethylformamide. To this solution was added acetic anhydride (17.6 µl, 0.186 mmol, 1.1 equiv.) and the mixture was stirred at 60 °C for 1 h. The reaction was quenched by addition of methanol (10 ml) and the solvents were removed under reduced pressure. The crude product was purified by flash column chromatography (silica, grading from 0% to 20% methanol in dichloromethane) to obtain the product **III-7** in 46% yield (45.5 mg).

¹H NMR (400.0 MHz, CDCl$_3$, 295 K):
δ = 8.06 (s, 1H, H-6), 7.35-7.27 (m, 2H, H-18), 7.27-7.08 (m, 7H, H-12, H-17, H-19), 6.85-6.69 (m, 4H, H-13), 6.14 (t, *J* = 6.2 Hz, 1H, H-1′), 4.40 (q, *J* = 4.4 Hz, 1H, H-3′), 4.04-3.94 (m, 1H, H-4′), 3.68 (s, 6H, H-15), 3.42-3.35 (m, 1H, H-5′), 3.28 (dd, *J* = 10.5 Hz, *J* = 3.5 Hz, 1H, H-5′), 2.50-2.41 (m, 1H, H-2′), 2.28 (s, 3H, H-9), 2.22 (dt, *J* = 13.6 Hz, J = 6.5 Hz, 1H, H-2′), 1.50 (s, 3H, H-7) ppm.

LR-MS (ESI):
Calculated for C$_{33}$H$_{36}$N$_3$O$_7$ [M+H]$^+$: 586.7 m/z
Found: 586.4 m/z

This procedure was part of the Internship Report of Doreen Reuter, 2019, conducted under my supervision. As this project was not further continued, no additional analytical characterization was conducted.

*5.10.   Synthesis of **III-12***
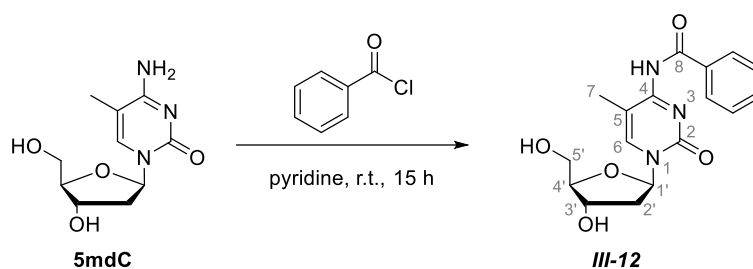
5mdC (100 mg, 0.414 mmol, 1.0 equiv.) was dissolved in absolute pyridine and cooled to 0 °C. Benzoyl chloride (96 μl, 0.829 mmol, 2.0 equiv.) was added and the reaction mixture was stirred at room temperature for 15 h. To the mixture was added ethyl acetate (10 ml), sodium bicarbonate solution (10 ml) and water (15 ml), before it was extracted with ethyl acetate (3 x 15 ml). The layers were separated and the combined organic layers were washed with ammonium chloride (2 x 20 ml) and brine (20 ml), then dried over anhydrous magnesium sulfate, filtered, and the solvent was removed *in vacuo* to give the crude product **III-12** with benzoic acid as byproduct. No yield was determined.

¹H NMR (400.0 MHz, CD₃CN, 295 K):
δ = 6.20 (dd, *J* = 7.6 Hz, *J* = 6.0 Hz, 1H, H-1′), 5.65 (dt, *J* = 6.7 Hz, *J* = 2.5 Hz, 1H, H-3′), 4.76-4.57 (m, 3H, H-4′, H-5′), 2.84 (ddd, *J* = 14.6 Hz, *J* = 6.0 Hz, J = 2.6 Hz, 1H, H-2′), 2.42 (ddd, *J* = 14.5 Hz, J = 7.6 Hz, *J* = 6.8 Hz, 1H, H-2′), 1.88 (d, *J* = 0.9 Hz, 3H, H-7) ppm.

Due to overlap with the signals of benzoic acid, the signal for H-6 and the benzyl group in the product could not be assigned unequivocally.

LR-MS (ESI):
Calculated for $C_{33}H_{36}N_3O_7$ [M+H]⁺: 586.7 m/z
Found: 586.4 m/z

This procedure was part of the Internship Report of Doreen Reuter, 2019, conducted under my supervision. As this project was not further continued, no additional analytical characterization was conducted.

5.11.   Synthesis of III-10a
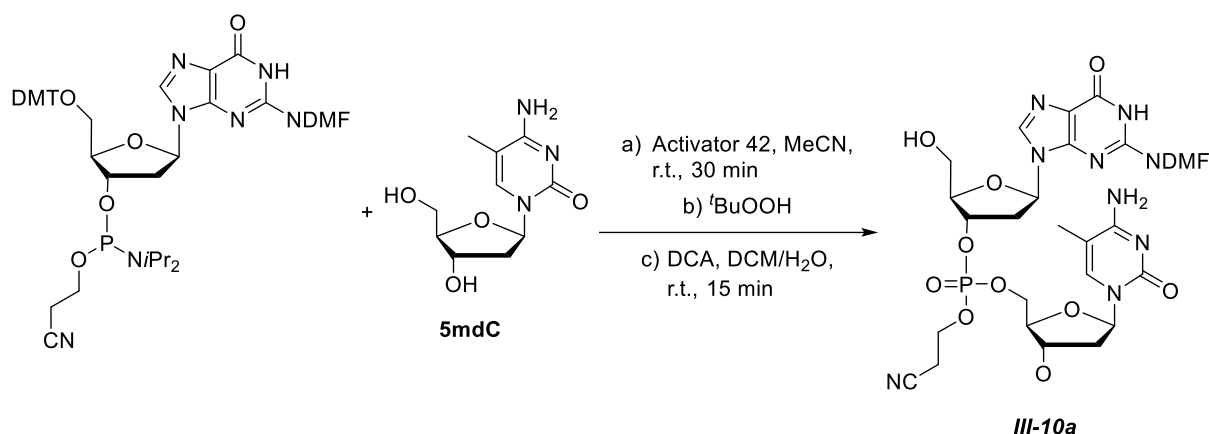
According to a modified literature procedure:

To a solution of **5mdC** (29.24 mg, 0.121 mmol, 1.00 equiv.) in a solution of Activator 42 (5-[3,5-Bis(trifluoromethyl)phenyl]-1H-tetrazole solution) (0.1 M in acetonitrile, 2.4 ml, 0.242 mmol, 2.00 equiv.) in the presence of molecular sieves (3 Å) was added the commercially available deoxy-guanosine(n,ndmf)phosphoramidite (200 mg, 0.245 mmol, 2.0 equiv.) in one portion. The mixture was stirred for 90 min at room temperature. Then a solution of *tert*-butyl hydroperoxide in decane (5.5 M, 44.08 μl, 0.242 mmol, 2.0 equiv.) was added to the mixture, which was then stirred at room temperature for 60 min. The solution was filtered and the molecular sieves washed with dichloromethane. The filtrate was concentrated *in vacuo*. The residue was treated with 3% dichloroacetic acid in dichloromethane (5 ml) in the presence of water (21 μl) at room temperature for 15 min until the solution turned bright red and clear. The reaction was quenched with methanol (15 ml) and pyridine (2 ml). The solvents were removed *in vacuo* and the obtained residue purified by column chromatography (silica, grading from 0-20% methanol in dichloromethane) to yield the product ***III-10a*** in 24% yield (30.0 mg, 44.2 μmol).

LR-MS (ESI):
Calculated for $C_{26}H_{36}N_{10}O_{10}P$ [M+H]$^+$: 679.2 m/z
Found: 679.3 m/z

Due to the limited amount of product no further characterization was performed and the obtained product used as such for further syntheses.

This procedure was part of the Internship Report of Doreen Reuter, 2019, conducted under my supervision. As this project was not further continued, no additional analytical characterization was conducted.

6. Synthetic Procedures – HPDL Project

6.1. Synthesis of VI-1

VI-1
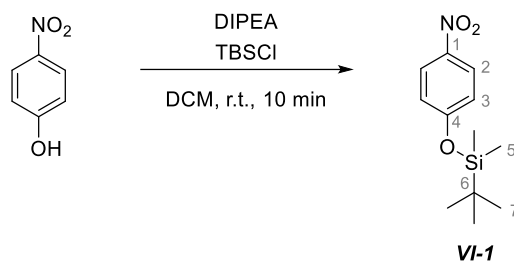
According to a modified literature procedure:[378]

4-nitrophenol (1.00 g, 7.19 mmol, 1.0 equiv.) was suspended in 20 ml dichloromethane. Di-*iso*-propyl-ethyl-amine (DIPEA, 2.98 ml, 2.26 g, 14.38 mmol, 2.0 equiv.) was added which resulted in a clear yellow solution. Upon addition of *tert*-butyldimethylsilyl chloride (1.63 g, 10.78 mmol, 1.5 equiv) the solution turned almost completely colorless again. After 5 min GC-MS analysis (Method **A**) of the reaction mixture confirmed complete consumption of the starting material. The solution was concentrated *in vacuo* to dryness. Column chromatography (silica, 2% ethyl acetate in hexanes grading to 5% ethyl acetate in hexanes) gave the product as a pale yellow crystalline solid in 54% yield (0.98 g).

R_F = 0.60 (silica, UV, 10% ethyl acetate in hexanes)

¹H NMR (400.0 MHz, CDCl$_3$, 295 K):
δ = 8.17-8.13 (m, 2H, H-2), 6.92-6.87 (m, 2H, H-3), 0.99 (s, 9H, H-7), 0.26 (s, 6H, H-5) ppm.

¹³C NMR (100.0 MHz, CDCl$_3$, 295 K):
δ = 161.8 (C-1), 142.1 (C-4), 126.0 (C-2), 120.3 (C-3), 25.7 (C-7), 18.4 (C-6), −4.2 (C-5) ppm.

NMR data is in accordance with the literature.[379]

HR-MS (EI):
Calculated for C$_{12}$H$_{19}$NO$_3$Si: 253.1134 m/z
Found: 253.1116 m/z
Calculated for [C$_8$H$_{10}$NO$_3$Si]$^{+}$: 196.0430 m/z
Found: 196.0423 m/z

*6.2. Synthesis of **VI-1** (alternative)*
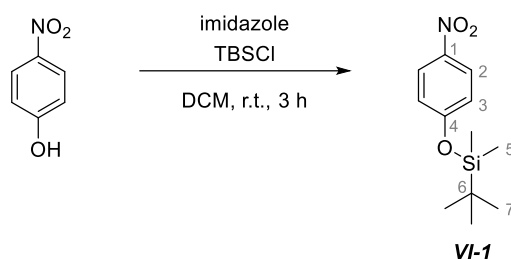
According to a modified literature procedure:[378]

4-nitrophenol (1.00 g, 7.19 mmol, 1.0 equiv.) was dissolved in 50 ml dichloromethane. Imidazole (0.73 g, 10.78 mmol, 1.5 equiv.) was added which resulted in a clear yellow solution. Upon addition of *tert*-butyldimethylsilyl chloride (1.63 g, 10.78 mmol, 1.5 equiv.) the solution turned almost completely colorless again and a colorless precipitate formed. The reaction mixture was stirred for 1 h at room temperature and thin layer chromatography (10% ethyl acetate in hexanes) indicated the presence of residual starting material. Therefore, two portions of imidazole (two times 0.39 g, 5.75 mmol, 0.8 equiv.) and two portions of *tert*-butyldimethylsilyl chloride (0.81 g, 5.39 mmol, 0.75 equiv.) were added. Thin layer chromatography confirmed complete consumption of the starting material after another 1 h at room temperature. The reaction mixture was filtered and the filtrate concentrated *in vacuo* to dryness. Three of these reactions were combined and column chromatography (silica, 2% ethyl acetate in hexanes grading to 5% ethyl acetate in hexanes) performed on the mixture. The product was isolated as a pale yellow crystalline solid in 92% yield (5.01 g combined yield).

R_F = 0.60 (silica, UV, 10% ethyl acetate in hexanes)

¹H NMR (400.0 MHz, CDCl$_3$, 295 K):
δ = 8.17-8.13 (m, 2H, H-2), 6.92-6.87 (m, 2H, H-3), 0.99 (s, 9H, H-7), 0.26 (s, 6H, H-5) ppm.

¹³C NMR (100.0 MHz, CD$_3$CN, 295 K):
δ = 161.8 (C-1), 142.1 (C-4), 126.0 (C-2), 120.3 (C-3), 25.7 (C-7), 18.4 (C-6), −4.2 (C-5) ppm.

NMR data is in accordance with the literature.[379]

HR-MS (EI):
Calculated for C$_{12}$H$_{19}$NO$_3$Si: 253.1134 m/z
Found: 253.1116 m/z
Calculated for [C$_8$H$_{10}$NO$_3$Si]$^{•+}$: 196.0430 m/z
Found: 196.0423 m/z

6.3. Synthesis of VI-2
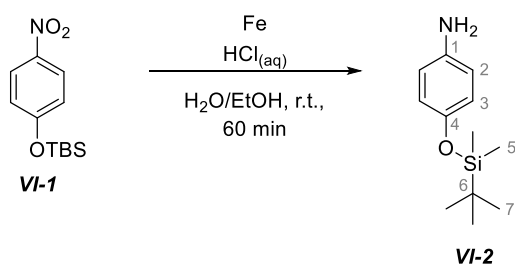
According to a modified literature procedure:[378]

A round bottom flask was charged with *tert*-butyldimethyl(4-nitrophenoxy)silane (0.36 g, 1.42 mmol, 1.0 equiv.), 12 ml ethanol, 3 ml water and reduced iron (0.87 g, 15.63 mmol, 11.0 equiv.). Concentrated aqueous hydrochloric acid (118.00 µl, 51.80 mg, 1.42 mmol, 1.0 equiv.) was added. After stirring for 10 min at room temperature the solution slowly turned orange-red, then after 60 min dark green with black particles. GC-MS analysis (GC-MS method **A**) of the reaction solution confirmed complete consumption of the starting material at this points. The reaction mixture was filtered, diluted with 10 ml methanol, and 3 ml triethyl amine were added. A dark green precipitate formed which was filtered off. The solvents were removed *in vacuo* to give the crude product as a yellow oil. Column chromatography (silica, 10% ethyl acetate in hexanes grading to 50% ethyl acetate in hexanes) gave the product as a pale brown oil in 63% yield (200 mg).

R_F = 0.12 (silica, UV, 10% ethyl acetate in hexanes)

¹H NMR (400.0 MHz, CDCl$_3$, 295 K):
δ = 6.68-6.63 (m, 2H, H-2), 6.60-6.55 (m, 2H, H-3), 3.40 (br, 2H, N*H*$_2$), 0.97 (s, 9H, H-7), 0.15 (s, 6H, H-5) ppm.

¹³C NMR (100.0 MHz, CD$_3$CN, 295 K):
δ = 148.4 (C-4), 140.4 (C-1), 120.8 (C-2), 116.5 (C-3), 25.9 (C-5), 18.3 (C-6), −4.4 (C-7) ppm.

NMR data is in accordance with the literature.[380]

HR-MS (EI):
Calculated for C$_{12}$H$_{21}$NOSi: 223.1392 m/z
Found: 223.1388 m/z
Calculated for [C$_6$H$_{12}$NOSi]$^{•+}$: 166.0688 m/z
Found: 166.0683 m/z

6.4. Synthesis of VI-3

VI-2   *VI-3*
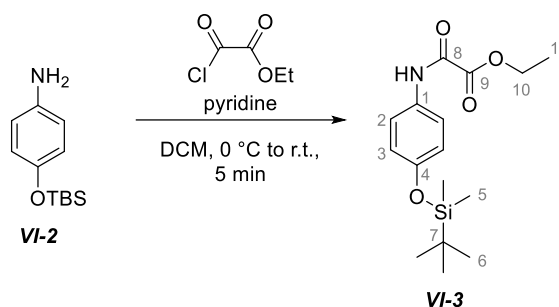
According to a modified literature procedure:[381]

A round bottom flask was charged with 4-((*tert*-butyldimethylsilyl)oxy)aniline (1.71 g, 7.65 mmol, 1.0 equiv.), pyridine (0.74 ml, 0.727 g, 9.19 mmol, 1.2 equiv.) and 8 ml dichloromethane. The reaction mixture was cooled to 0 °C and ethyl 2-chloro-2-oxoacetate (1.03 ml, 1.25 g, 9.19 mmol, 1.2 equiv.) was added dropwise. The reaction mixture was stirred for 5 min at 0 °C, at which point thin layer chromatography indicated complete consumption of the starting material and a brown precipitate had formed. The reaction mixture was allowed to warm to room temperature and diluted with 5 ml ethyl acetate. The reaction mixture was washed once with aqueous hydrochloric acid (2 M, 10 ml), once with aqueous saturated bicarbonate solution (10 ml), and once with brine (10 ml). The organic layer was dried over sodium sulfate and the solvents removed *in vacuo* to yield the crude product as a pale brown oil. Flash column chromatography (silica, 5% ethyl acetate in hexanes grading to 30% ethyl acetate) gave the product as a colorless crystalline solid in 88% yield (2.17 g).

R_F = 0.68 (silica, UV, 30% ethyl acetate in hexanes)

¹H NMR (400.0 MHz, CDCl$_3$, 295 K):
δ = 8.77 (s, 1H, N*H*), 7.52-7.47 (m, 2H, H-2), 6.86-6.81 (m, 2H, H-3), 4.41 (q, *J* = 7.1 Hz, 2H, H-10), 1.43 (t, *J* = 7.1 Hz, 3H, H-11), 0.98 (s, 9H, H-7), 0.19 (s, 6H, H-5) ppm.

¹³C NMR (100.0 MHz, CD$_3$CN, 295 K):
δ = 161.3 (C-9), 153.7 (C-8), 153.4 (C-1), 130.2 (C-4), 121.4 (C-2), 120.7 (C-3), 63.8 (C-10), 25.8 (C-7), 18.4 (C-6), 14.2 (C-11), −4.3 (C-5) ppm.

HR-MS (EI):
Calculated for C$_{16}$H$_{25}$NO$_4$Si: 323.1553 m/z
Found: 323.1548 m/z
Calculated for C$_{12}$H$_{16}$NO$_4$Si [M-*t*Bu]$^{•+}$: 266.0849 m/z
Found: 266.0846 m/z

Elemental Analysis:
Calculated for C$_{16}$H$_{25}$NO$_4$Si:
C 59.41, H 7.79, N 4.33.

341

Found: C 59.24, H 8.02, N 4.33.

IR (thin film):

$\tilde{v}$ = 3260, 3130, 2960, 2930, 2895, 2858, 1739, 1683, 1604, 1551, 1505, 1472, 1442, 1412, 1389, 1368, 1324, 1284, 1249, 1221, 1176, 1106, 1031, 941, 903, 843, 806, 778, 701, 659 cm^{-1}.

*6.5. Synthesis of **VI-4***

VI-3   **VI-4**
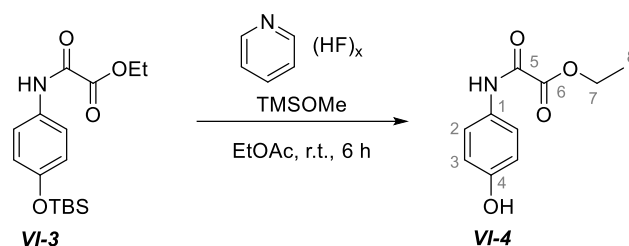
A 15 ml Falcon tube was charged with ethyl 2-((4-((*tert*-butyldimethylsilyl)oxy) phenyl)amino)-2-oxoacetate (0.115 g, 0.36 mmol, 1.0 equiv.) and 5.5 ml ethyl acetate. Hydrogen fluoride in pyridine (70% wt-% HF, 0.07 ml, 0.08 g, 0.53 mmol, 1.5 equiv.) was added and the solution stirred vigorously for 6 h at room temperature, at which point thin layer chromatography indicated complete consumption of the starting material. Methoxytrimethylsilane (1.0 ml, 0.760 g, 7.29 mmol, 20.5 equiv.) was added and the solution stirred at room temperature for 2 h. At this point 10 ml water were added, the mixture transferred to a separatory funnel and the organic layer was washed 10 ml saturated sodium bicarbonate solution and 10 ml brine. The organic layer was then dried over anhydrous sodium sulfate and the solvents removed *in vacuo* to yield the crude product as a colorless solid. Flash column chromatography (silica, 30% ethyl acetate in hexanes grading to 60% ethyl acetate) gave the product as a colorless crystalline solid in 85% yield (380 mg).

R_F = 0.12 (silica, UV, 30% ethyl acetate in hexanes)

^{1}H NMR (400.0 MHz, CDCl$_3$, 295 K):
δ = 8.77 (s, 1H, N*H*), 7.55-7.53 (m, 2H, H-2), 6.87-6.81 (m, 2H, H-3), 4.90 (s, 1H, O*H*), 4.42 (q, 2H, *J* = 7.1 Hz, 2H, H-7), 1.43 (t, *J* = 7.1 Hz, 3H, H-8) ppm.

^{13}C NMR (100.0 MHz, CDCl$_3$, 295 K):
δ = 161.3 (C-1), 121.4 (C-2), 116.0 (C-3), 63.8 (C-7), 14.2 (C-8) ppm.

No other signals could be distinguished from the background noise.

^{1}H NMR (400.0 MHz, D$_6$-DMSO, 295 K):
δ = 10.53 (s, 1 H, N*H*), 10.53 (s, 1 H, O*H*), 7.54-7.50 (m, 2H, H-2), 6.75-6.71 (m, 2H, H-3), 4.28 (q, 2H, *J* = 7.1 Hz, 2H, H-7), 1.30 (t, *J* = 7.1 Hz, 3H, H-8) ppm.

NMR data (D$_6$-DMSO) is in accordance with the literature.[382]

HR-MS (EI):
Calculated for C$_9$H$_9$NO$_4$ [M-CH$_2$]$^+$: 195.0532 m/z
Found: 195.0526 m/z
Calculated for C$_6$H$_6$NO [M-C$_2$O$_2$-CH$_2$CH$_3$]$^+$: 108.0449 m/z
Found: 108.0444 m/z

Elemental Analysis:

Calculated for $C_{10}H_{11}NO_4$:

C 57.41, H 5.30, N 6.70.

Found: C 57.38, H 5.31, N 6.61.

IR (thin film):

$\tilde{v}$ = 3332, 3294, 2987, 2383, 1730, 1669, 1622, 1603, 1557, 1514, 1470, 1447, 1393, 1370, 1296, 1265, 1219, 1185, 1109, 1094, 1019, 948, 932, 876, 830, 809, 708, 674 cm^{-1}.

6.6. Synthesis of **4-HPN**
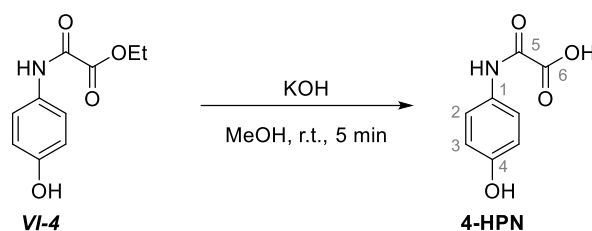
A 5 ml round bottom flask was charged with ethyl-((4-hydroxyphenyl)amino)-2-oxo acetate (0.300 g, 1.43 mmol, 1.0 equiv.) and a methanolic solution of potassium hydroxide was added (2 M, 21.51 ml, 2.41 g, 43.02 mmol, 30.0 equiv.). The solution immediately turned yellow and was then stirred for 5 min at room temperature. The reaction mixture was then neutralized using hydrochloric acid (2 M, aqueous), diluted with 20 ml water and the organic solvents removed *in vacuo*. The sample was then freeze dried, re-dissolved in water and subsequently purified using HPLC (C18, 5% MeCN in water held for 2 min, then grading to 15% MeCN in water over 10 min, 0.1% TFA in both solvents, t_R = 10 min) giving the product in 63% yield (164.0 mg).

^{1}H NMR (400.0 MHz, D_6-DMSO, 295 K):
δ = 14.03 (br, 1H, COO*H*), 10.46 (s, 1H, O*H*), 9.33 (br, 1H, N*H*), 7.57-7.50 (m, 2H, H-2), 6.75-6.69 (m, 2H, H-3) ppm.

^{1}H NMR (400.0 MHz, D_2O, 295 K):
δ = 7.44-7.38 (m, 2H, H-2), 6.97-6.92 (m, 2H, H-3) ppm.

^{13}C NMR (100.0 MHz, D_6-DMSO, 295 K):
δ = 162.4 (C-6), 156.3 (C-5), 154.3 (C-1), 129.3 (C-4), 121.9 (C-2), 115.1 (C-3) ppm.

HR-MS (ESI):
Calculated for $C_8H_6NO_4$ [M-H]$^-$: 180.02968 m/z
Found: 380.03007 m/z

Elemental Analysis:
Calculated for $C_8H_7NO_4$:
C 53.04, H 3.90, N 7.73.
Found: C 52.82, H 3.79, N 7.69.

IR (thin film):
$\tilde{v}$ = 3303, 1761, 1723, 1673, 1606, 1555, 1515, 1458, 1338, 1308, 1241, 1174, 1112, 1017, 930, 835, 829, 792, 745, 684 cm^{-1}.

7. Synthetic Procedures – Miscellaneous

7.1. Analytical Data of *III-2*
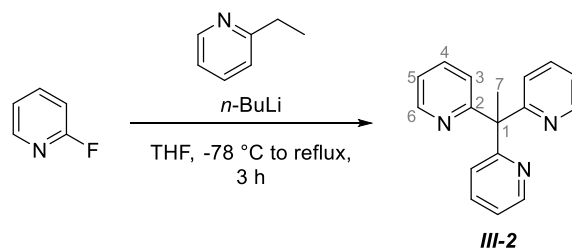
This compound was obtained as a side product in the reaction of 2-ethylpyridine with n-butyl lithium and 2-fluorpyridine as described on p. 258. Here, only analytical data is presented.

R_F = 0.43 (silica, UV, 10% triethyl amine, 30% ethyl acetate, 60% hexanes)

¹H NMR (400.0 MHz, CDCl$_3$, 295 K):
δ = 8.59 (ddd, J = 4.8 Hz, J = 1.9 Hz, J = 0.9 Hz, 3H), 7.57 (ddd, J = 8.1 Hz, J = 7.5 Hz, J = 1.9 Hz, 3H, H-4f), 7.12 (ddd, J = 7.6 Hz, J = 4.9 Hz, J = 1.1 Hz, 3H, H-3), 7.09 (ddd, J = 8.0 H, J = 1.0 Hz, 3H, H-5), 1.76 (s, 3H) ppm.

¹³C NMR (100.0 MHz, CDCl$_3$, 295 K):
δ = 166.0 (C-2), 149.0 (C-6), 136.2 (C-4), 123.6 (C-5), 121.4 (C-3), 60.25 (C-1), 27.5 (C-7) ppm.

Elemental Analysis:
Calculated for C$_{17}$H$_{15}$N$_3$: C 78.13, H 5.79, N 16.08.
Found: C 78.03, H 5.76, N 16.04.

HR-MS (ESI):
Calculated for C$_{17}$H$_{16}$N$_3$ [M+H]$^+$: 262.13442 m/z
Found: 262.13393 m/z

IR (thin film):
$\tilde{v}$ = 3058, 2999, 2980, 1585, 1567, 1467, 1433, 1423, 1372, 1294, 1160, 1148, 1116, 1106, 1076, 1048, 991, 887, 859, 775, 703 cm^{-1}.

*7.2. Analytical Data of **III-3***
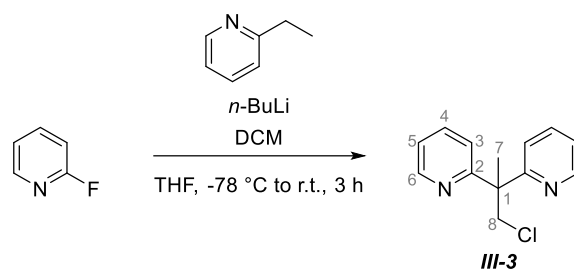
This compound was obtained as a side product in the reaction of 2-ethylpyridine with n-butyl lithium and 2-fluorpyridine as described on p. 258. Here, only analytical data is presented.

R_F = 0.74 (silica, UV, 10% triethyl amine, 30% ethyl acetate, 60% hexanes)

¹H NMR (400.0 MHz, CDCl$_3$, 295 K):
δ = 8.58 (dd, J = 5.2 Hz, J = 2.0 Hz, 2H, H-6), 7.60 (td, J = 7.9 Hz, J = 2.0 Hz, 2H, H-4), 7.18-7.05 (m, 4H, H-3/5), 4.54 (s, 2H, H-8), 1.91 (s, 3H, H-7) ppm.

¹³C NMR (100.0 MHz, CDCl$_3$, 295 K):
δ = 164.2 (C-2), 149.0 (C-6), 136.4 (C-4), 122.4 (C-3/5), 121.8 (C-3/5), 53.8 (C-8), 53.1 (C-1), 24.1 (C-7) ppm.

HR-MS (ESI):
Calculated for C$_{13}$H$_{14}$ClN$_2$ [M+H]$^+$: 233.08455 m/z
Found: 233.08411 m/z

Elemental Analysis:
Calculated for C$_{13}$H$_{13}$ClN$_2$: C 67.10, H 5.63, N 12.04, Cl 15.23.
Found: C 67.24, H 5.43, N 11.89, Cl 14.67.

IR (thin film):
$\tilde{\nu}$ = 3055, 3007, 2979, 1587, 1568, 1465, 1426, 1373, 1297, 1282, 1243, 1149, 1096, 1078, 1069, 1044, 992, 968, 938, 911, 903, 835, 791, 777, 762, 751, 745, 737, 716 cm^{-1}.

*7.3. Synthesis of **GD***

GD
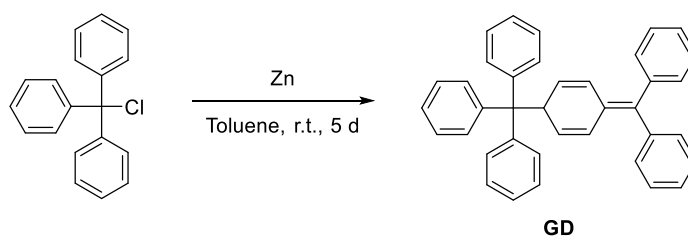
According to a modified literature procedure.[277]

A brown flame-dried flask was charged with triphenylmethyl chloride (500 mg, 1.79 mmol, 1.0 equiv.) and absolute toluene (10.7 ml). Zinc powder (609 mg, 9.33 mmol, 5.2 equiv.) was added and the mixture stirred in the dark at room temperature for 5 d. At this point, the mixture was filtered through a stainless steel canula equipped with filter paper on one end, the remaining solid washed with 1 ml of absolute toluene and the solvents removed *in vacuo* to give a yellow solid as the product GD. Due to its light sensitivity and paramagnetism, only EPR spectroscopy and GC-MS were performed as analytical techniques (refer to chapter IV.5, p. 133f).

7.4. Synthesis of pyocyanin

pyocyanin

According to a modified literature procedure.[367]

Phenazine methosulfate (50 mg, 0.16 mmol, 1.00 equiv.) was dissolved in 50 mL MilliQ water. The yellow solution was exposed to day light for 36 h resulting a deep red solution. Aqueous sodium carbonate solution (1.58 M in water, 0.500 ml, 83.7 mg, 0.79 mmol, 4.84 equiv.) was added at once, turning the solution turquoise. The solution was exposed to daylight light for another 6 h and 1 mL of an aqueous sodium carbonate solution (100 mM in water, 10.60 mg, 0.100 mmol, 0.61 equiv.) was added. The turquoise solution was extracted with chloroform (3 × 100 ml), the organic layer was dried over saturated sodium chloride solution and potassium carbonate. The solvent was reduced to a total volume of 20 mL using a rotary evaporator (250 mbar at40 °C). Crystallization from *iso*-hexane *via* vapor diffusion yielded the product **pyocyanin** as deep blue needles (20 mg, 60%).

^{1}H NMR (400 MHz, CD$_3$OD, 295 K):
δ = 8.30 (s, 1H), 8.09-7.95 (m, 2H), 7.94-7.83 (m, 1H), 7.69 (t, *J* = 7.6 H, 1H), 6.54 (dd, *J* = 33.0 Hz, *J* = 8.6 Hz, 2H), 4.19 (s, 3H) ppm.

^{13}C NMR (100 MHz, CD$_3$OD, 295 K):
δ = 144.9, 135.7, 132.0, 125.5, 114.8, 113.9, 92.8, 34.4 ppm.

These chemical shifts were collected from HMQC measurements as the signals in a normal ^{13}C NMR spectrum could not be distinguished from the background noise.

HR-MS (ESI):
Calculated for C$_{13}$H$_{11}$N$_2$O [M+H]$^+$: 211.087 m/z
Found: 211.086 m/z

X. Appendix

1. List of Abbreviations

Free nucleobases are referred to by their commonly used abbreviation (A for adenine, 5mC for 5-methyl cytosine, etc.). For DNA and DNA-like nucleosides a "d" is added before the abbreviation of the base structure (adenine A, guanine G, cytosine C, thymine T, or Uracil U) or in between modification and base structure, if applicable: 5-methyl-2'-deoxycytidine is abbreviated 5mdC. For RNA nucleosides an "r" is added at the same position: 5-methyl-cytidine is abbreviated 5mrC.

3mC	3-methyl-cytosine
3mdC	N^3-methyl-2'-deoxy-cytidine
4-HB	4-hydroxybenzoic acid
4-HBz	4-hydroxybenzaldehyde
4-HMA	4-hydroxymandelic acid
4-HPA	4-hydroxyphenyl acetic acid
4-HPN	2-((4-hydroxyphenyl)amino)2-oxoacetic acid
4-HPP	4-hydroxyphenyl pyruvic acid
4mC	N^4-methylcytosine
5cadC	5-carboxy-2'-deoxycytidine
5caU	5-carboxy-uracil
5cC	5-carboxy-cytosine
5fC	5-formyl-cytosine
5fdC	5-formyl-2'-deoxycytidine
5fU	5-formyl-uracil
5hmC	5-hydroxymethyl-cytosine
5hmdC	5-hydroxymethyl-2'-deoxycytidine
5hmrC	5-hydroxymethyl-cytidine
5hmU	5-hydroxymethyl-uracil
5mC	5-methyl-cytosine
5mdC	5-methyl-2'-deoxycytidine
8-oxo-dG	8-oxo-2'-deoxy-guanosine
8-oxo-G	8-oxo-guanine
A	adenine
Å	Ångström
a.u.	arbitrary units
AcCl	acetyl chloride
AlkB	an α-ketoglutarate-dependent dioxygenase

AlkBH	an α-ketoglutarate-dependent dioxygenase homologue
Asp	aspartate
atm	atmospheric pressure = 1013.25 mbar
BDE	bond dissociation energy
BER	base excision repair
Bn-TPEN	*N*-benzyl-*N*,*N'*,*N'*-tris(2-pyridylmethyl)ethane-1,2-diamine
BSTFA	*N*,*O*-bis(trimethylsilyl)trifluoroacetamide
Bu	butyl
C	cytosine
CD	circular dichroism
COSY	correlation spectroscopy
CpG	(2'-deoxy)cytidine-phosphate-(2'-deoxy)guanosie
Cy	cyclohexane
Cys	cysteine
d	doublet
D_2-5hmC	D_2-5-hydroxymethyl cytosine
D_3-5mC	D_3-5-methyl cytosine.
D_3-T	D_3-thymine
dA	2'-deoxy-adenosine
DAOCS	Deacetoxycephalosporin C Synthase
dC	2'-deoxy-cytidine
DCM	dichloromethane
dG	2'-deoxy-guanosine
DHA	9,10-dihydroanthracene
DIBAL-H	di-*iso*-butyl aluminum hydride
dioxane	1,4-dioxane
DIPEA	*N*,*N*-di-*iso*-propylethylamine
DMF	*N*,*N*-dimethylformamide
DMF	*N*,*N*-dimethylformamide (ligand)
DMSO	dimethylsulfoxide
dN	2'-deoxynucleotide
DNA	deoxyribonucleic acid
DNMT	DNA methyl transferase
dT	2'-deoxy-thymidine
dU	2'-deoxy-uridine

EI	electron ionization
EPR	electron paramagnetic resonance
ESI	electrospray ionization
Et	ethyl
FT IR	Fourier-transform infrared
G	guanine
GC	gas chromatography
h	septet or hour
HAT	hydrogen atom transfer
HG	homogentisate
His	histidine
HMBC	heteronuclear multiple-bond correlation spectroscopy
HMQC	heteronuclear multiple quantum correlation spectroscopy
HMS	4-Hydroxymandelate Synthase
HMS	hydroxymandelate synthase
HPDL	hydroxyphenyl pyruvate dioxygenase like
HPLC	high performance liquid chromatography
HPPD	4-hydroxyphenylpyruvate Dioxygenase
HPPD	hydroxyphenyl pyruvate dioxygenase
HR	high resolution
IB	iodosylbenzene (IB)
ICP-OES	inductively-coupled plasma optical emission spectroscopy
IPNS	Isopenicillin N Synthase
JBP	base J-binding proteins
Kcal	kilocalories
LC	liquid chromatography
LR	low resolution
M	molar, mol l^{-1}
m	multiplet or meter
MCD	magnetic circular dichroism
Me	methyl
MeCN	acetonitrile
mecn	acetonitrile (ligand)
min	minutes
MLCT	metal to ligand charge transfer

mRNA	messenger-RNA
MS	mass spectrometry
N$_4$Py	*N,N*-bis(2-pyridylmethyl)-*N*-bis(2-pyridyl)methylamine
NMR	nuclear magnetic resonance
NOG	*N*-oxalyl glycine
OAT	oxygen atom transfer
OTf	$^-O_3SCF_3$
p	quintet
PFP	pentafluorophenyl
ppm	parts per million
Pr	propyl
PTFE	polytetrafluoroethylene
py	pyridine (ligand)
Py$_2$Py-(afaCy)$_2$	2,2′,2′-methylbispyridyl-6-(2,2′,2′-methylbis-5-cyclohexylazafulvene)-pyridine
Py$_3$Ph$_2$Me$_2$H	2,6-bis(1-phenyl-1-(pyridin-2-yl)ethyl)pyridine (**L-9**)
Py$_4$OHMe$_2$H	1-(6-(1,1-di(pyridin-2-yl)ethyl)pyridin-2-yl)-1-(pyridin-2-yl)ethan-1-ol (**L-7**)
Py$_4$PhMe$_2$H	2,2'-(1-(6-(1-phenyl-1-(pyridin-2-yl)ethyl)pyridin-2-yl)ethane-1,1-diyl)dipyridine (**L-8**)
Py$_5$(OCD$_3$)H	2,6-bis((methoxy-D$_3$)di(pyridin-2-yl)methyl)pyridine (**L-4**)
Py$_5$(OCF$_3$)$_2$H	2,6-bis(di(pyridin-2-l)(trifluoromethoxy)methyl)pyridine (**L-6**)
Py$_5$(OCH$_2$F)$_2$H	2,6-bis((fluoromethoxy)di(pyridin-2-yl)methyl)pyridine (**L-5**)
Py$_5$(OH)$_2$H	pyridine-2,6-diylbis(di(pyridin-2-yl)methanol) (PY5OH/**L-2**)
Py$_5$(OMe)$_2$H	2,6-bis(methoxydi(pyridin-2-yl)methyl)pyridine (PY5/**L-3**)
Py$_5$Me$_2$H	2,6-bis(1,1-bis(2-pyridyl)ethyl)pyridine (**L-1**)
q	quartet
Q$_4$PyMe$_2$H	2,6-bis(1,1-bis(2-quinolyl)ethyl)pyridine
RNA	ribonucleic acid
RP	reversed phase
s	singlet or seconds
SAH	*S*-adenosylhomocysteine
SAM	*S*-adenosyl methionine
S-HMA	*S*-(4-hydroxymandelic acid)
SyrB2	Syringomycin Biosynthesis Enzyme 2

T	thymine
t	triplet or time
TauD	taurine/α-keto glutarate dioxygenase
TBHP	*tert*-butylhydroperoxide
TBS	*tert*-butyldimethylsilyl
TBSCl	*tert*-butyldimethylsilyl chloride
TDG	thymine DNA glycosylase
TEMPO	(2,2,6,6-tetramethylpiperidin-1-yl)oxyl
TET	ten-eleven translocation methylcytosine dioxygenase
TFA	trifluoro acetic acid
THF	tetrahydrofuran
thf	tetrahydrofuran (ligand)
TLC	thin layer chromatography
TMC-py	1-(pyridyl-2′-methyl)-4,8,11-trimethyl-1,4,8,11-tetrazacyclotetradecane
Tol	toluene
TQA	tris(2-quinolylmethyl)amine
tRNA	transfer-RNA
ttppc	tris(2,4,6-triphenyl)-phenyl corrole
Tyr	tyrosine
U	uracil
UHPLC	ultra-high-performance liquid chromatography
UV	ultraviolet
vis	visible
α-KA	α-keto acid
α-KG	α-ketoglutarat/2-oxyglutarat

2. Chapter III – Additional Data and Spectra

General Procedures

Reactions with **C-6** and respective substrates (nucleobases, nucleosides, or oligonucleotides) as well as corresponding control reactions were performed according to the following general procedure.

A 10 mM solution of **C-6** was prepared as described on p. 255. A 20 mM stock solution of the substrate was prepared and diluted to the required concentration. The required amount of **C-6** solution was added to the substrate and the reaction stirred at room temperature (T = 22-25 °C, indicated in the respective figure description or experimental details). After the required reaction time had passed a sample was taken (1000 µl for nucleobases, 200 µl for nucleosides, 50 µl for oligonucleotides) and filtered through a plug of silica (1.5 ml for nucleobases and nucleosides, 100 µl for oligonucleotides) in a plastic syringe (3 ml for nucleobases and nucleosides, 1 ml for oligonucleotides) that was connected to a flask or falcon tube (Figure 166). Additional water (3 ml for nucleobases, 4 ml for nucleosides, 800 µl for oligonucleotides) was added to flush the substrates out of the silica. The collected aqueous solution was then freeze-dried and further analyzed.

Nucleobases:	the solid sample was suspended in 250 µl acetonitrile/100 µl BSTFA, heated to 70 °C for 30 min, filtered, and injected onto a GC-MS instrument.
Nucleosides:	the solid sample was resuspended in 500 µl water, filtered, and injected onto an HPLC instrument.
Oligonucleotides:	The solid sample was resuspended in 250 µl/500 µl water, filtered, and the oligonucleotide concentration determined. Eva Korytiaková then digested the samples and injected these mixtures onto a triple quadrupole mass spectrometer.

For an optimized procedure for nucleoside analysis as well as oligonucleotide digestion and subsequent nucleoside detection please refer to the literature.[14]
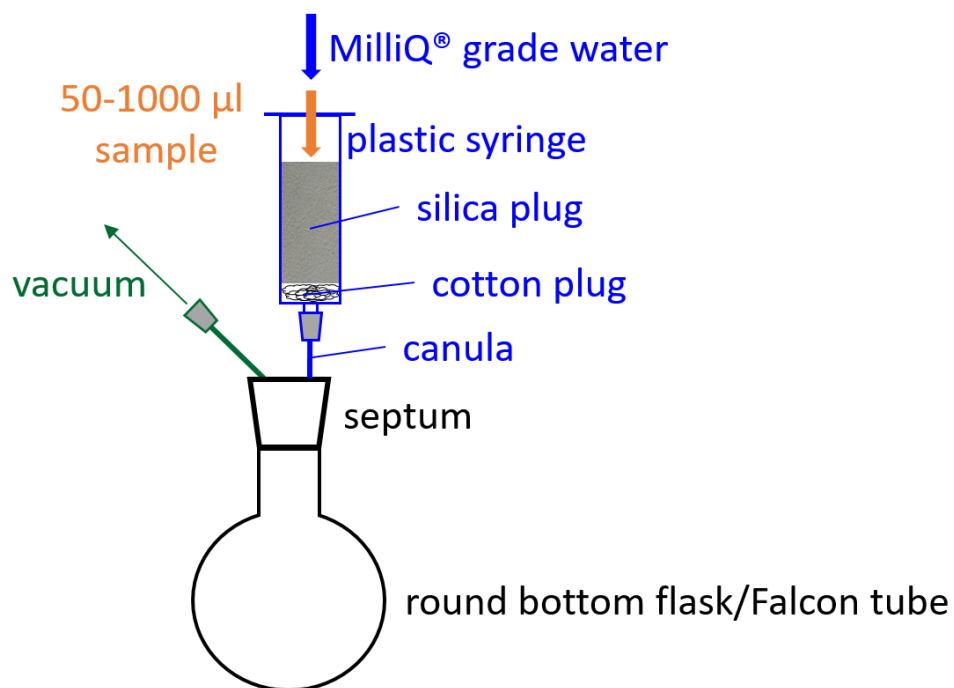
Figure 166: Schematic representation of the work-up procedure.

Subchapter 4: Nucleobases
GC-MS Reference Traces
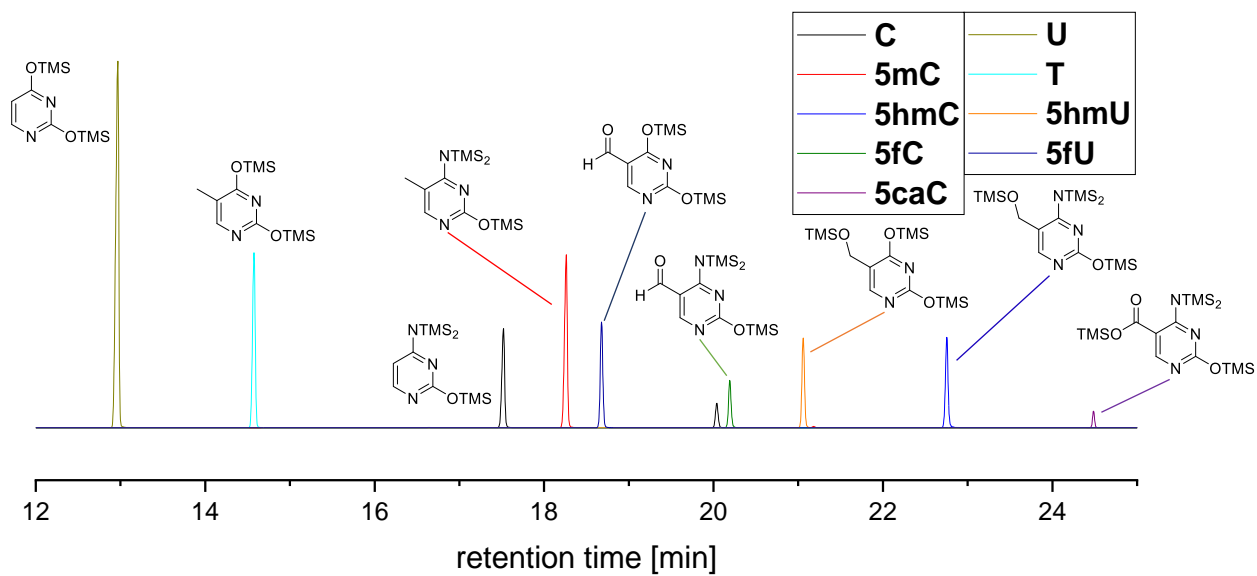
*Figure 167: Overlay of excerpts of GC-MS traces of derivatized **C, 5mC, 5hmC, 5fC, 5caC, U, T, 5hmU**, and **5fU**. The signal at a retention time of 20.1 min also corresponds to cytosine (structure not shown, refer to Figure 168). GC-MS method **C**.*
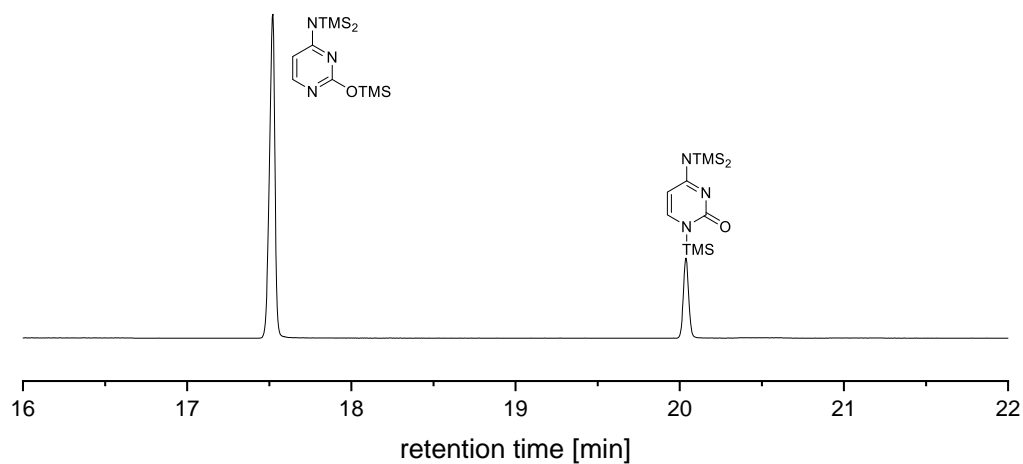
*Figure 168: Excerpt of a GC-MS trace of derivatized **C**, both observed signals were assigned to **C** (refer to the literature for a more detailed discussion).[13] GC-MS method **C**.*
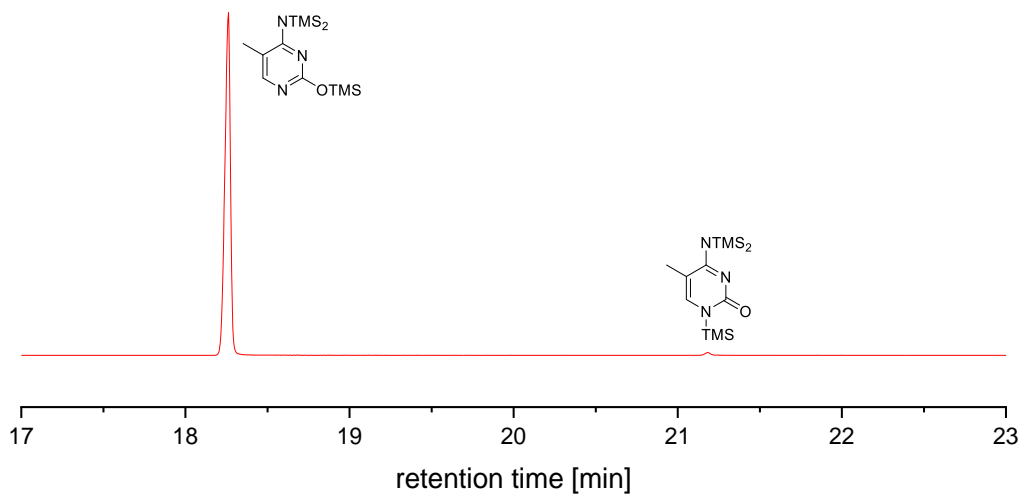
Figure 169: Excerpt of a GC-MS trace of derivatized **5mC**, both observed signals were assigned to **5mC** (refer to the literature for a more detailed discussion).[13] GC-MS method **C**.
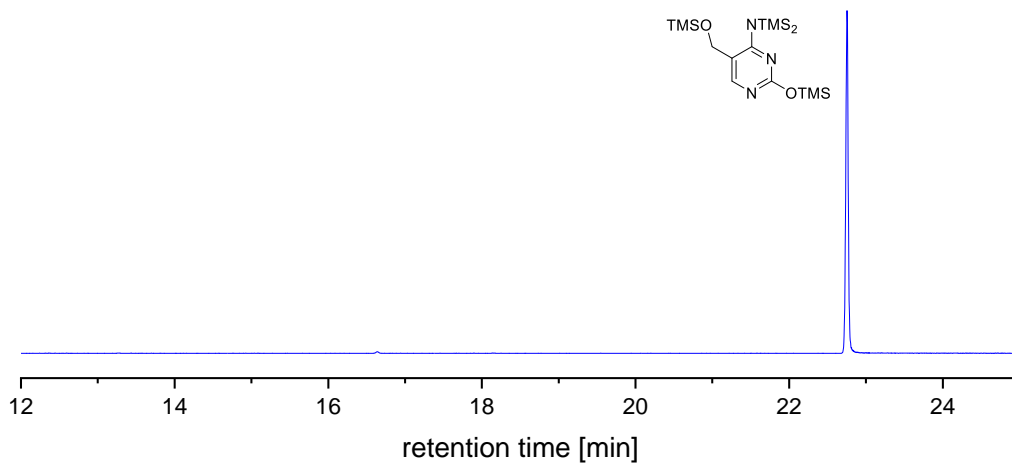
Figure 170: Excerpt of a GC-MS trace of derivatized **5hmC**. GC-MS method **C**.
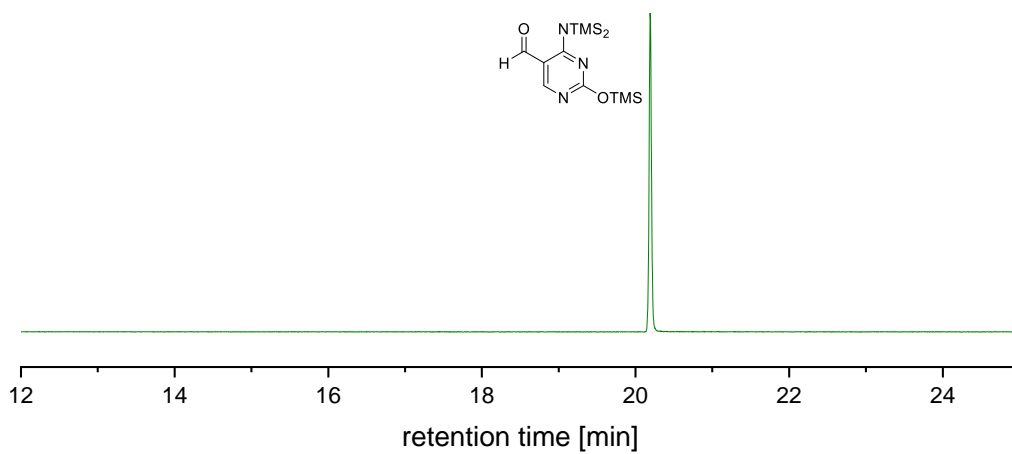
Figure 171: Excerpt of a GC-MS trace of derivatized **5fC**. GC-MS method **C**.

5caC Reference Trace

5caC was only observed in conjunction with **5hmC** in the product mixture resulting from LiAlH$_4$ treatment of ***III-17***. The MS spectrum of the additional signal observed in the mixed **5hmC/5caC** trace was analyzed and assigned to **5caC**, refer to *Chem. Eur. J.* **2019**, *25*, 12091–12097 for details. HPLC separation of a clean **5caC** sample was not achieved within the scope of the project, but later by David Schmidl, which confirmed the previous assignment.[238]
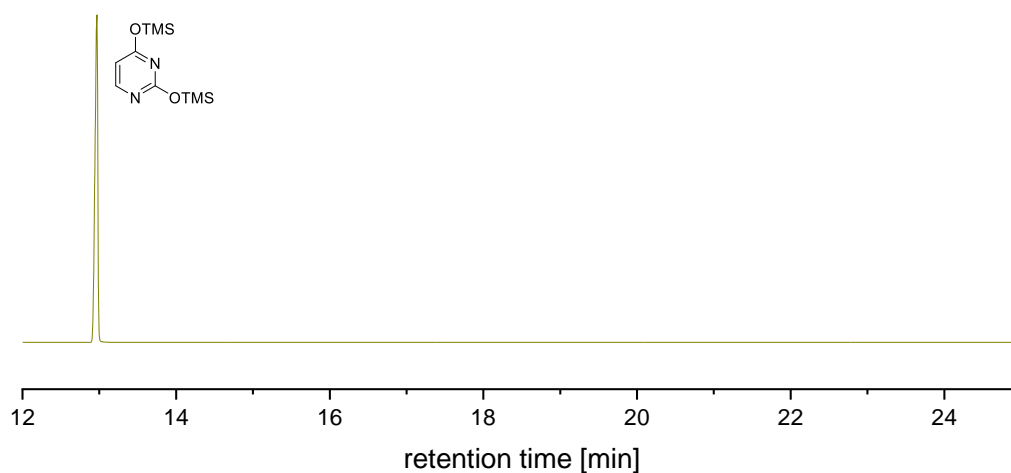
*Figure 172: Excerpt of a GC-MS trace of derivatized **U**. GC-MS method **C**.*
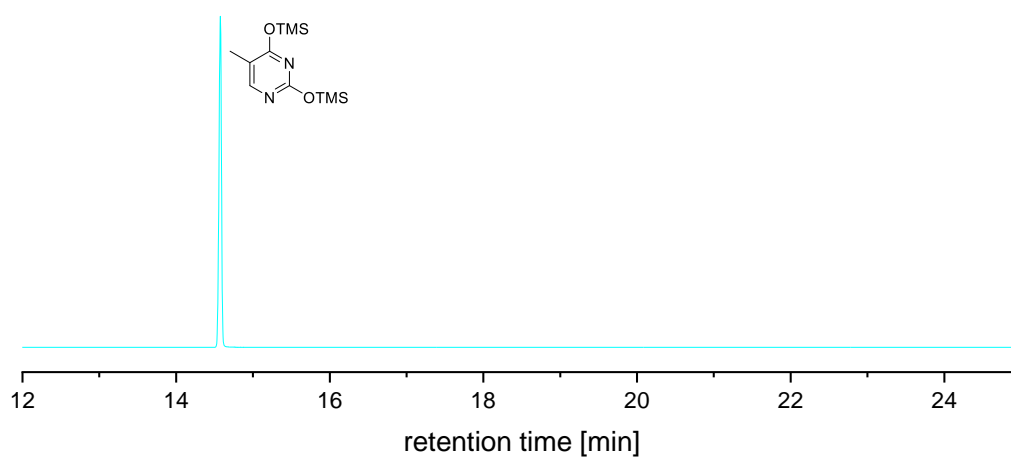
*Figure 173: Excerpt of a GC-MS trace of derivatized **T**. GC-MS method **C**.*
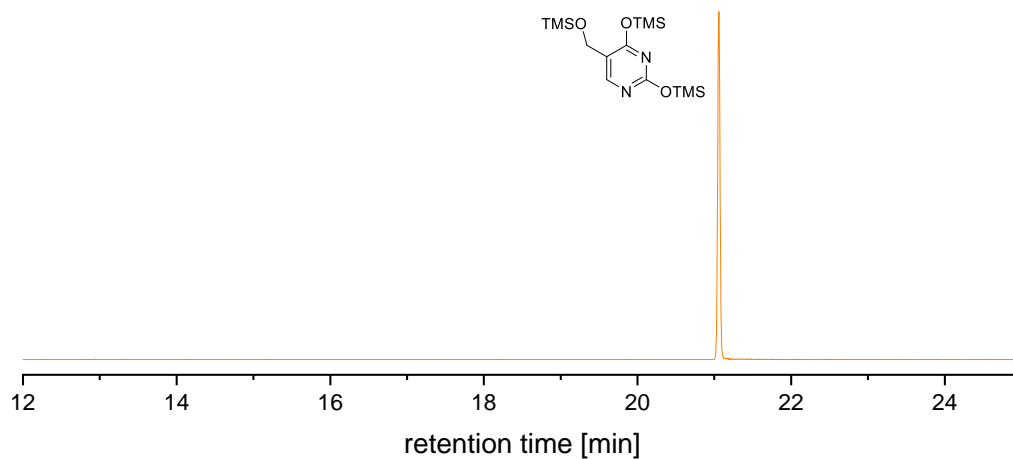
*Figure 174: Excerpt of a GC-MS trace of derivatized **5hmU**. GC-MS method **C**.*
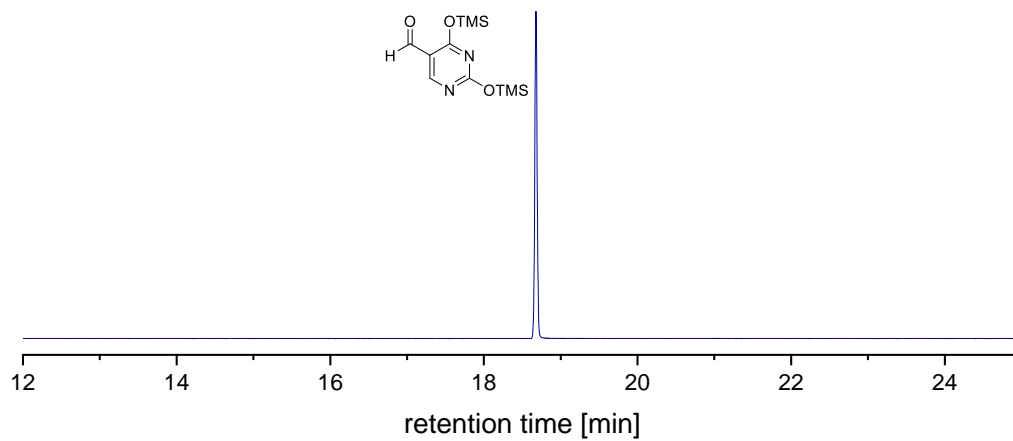
*Figure 175: Excerpt of a GC-MS trace of derivatized **5fU**. GC-MS method **C**.*

Control Experiments – GC-MS traces

Reactions were performed as described on p. 356.

Reaction conditions: [**C-6**] = 5 mM, [**S**] = 5 mM, H_2O, T = 22-24 °C, 30 min.
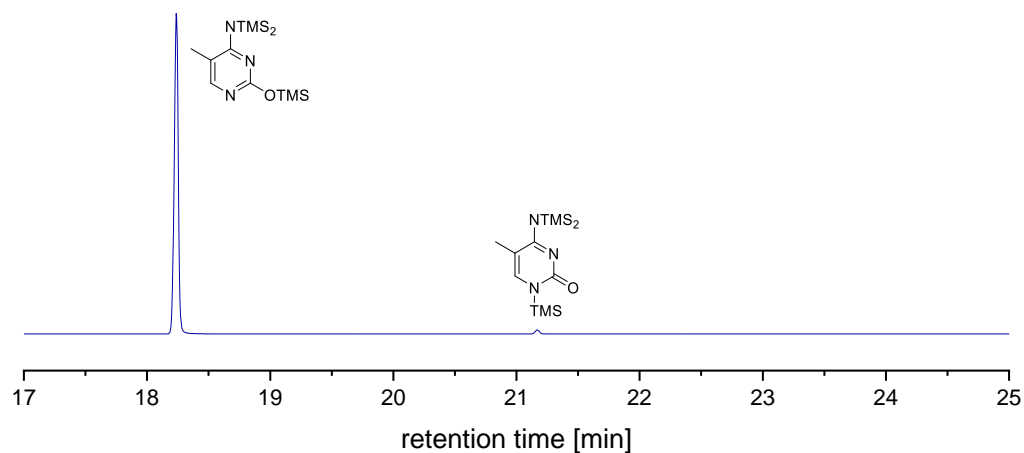
*Figure 176: Excerpt of a GC-MS trace of the reaction of **5mC** with KOH ([KOH] = 5 mM). GC-MS method **C**.*
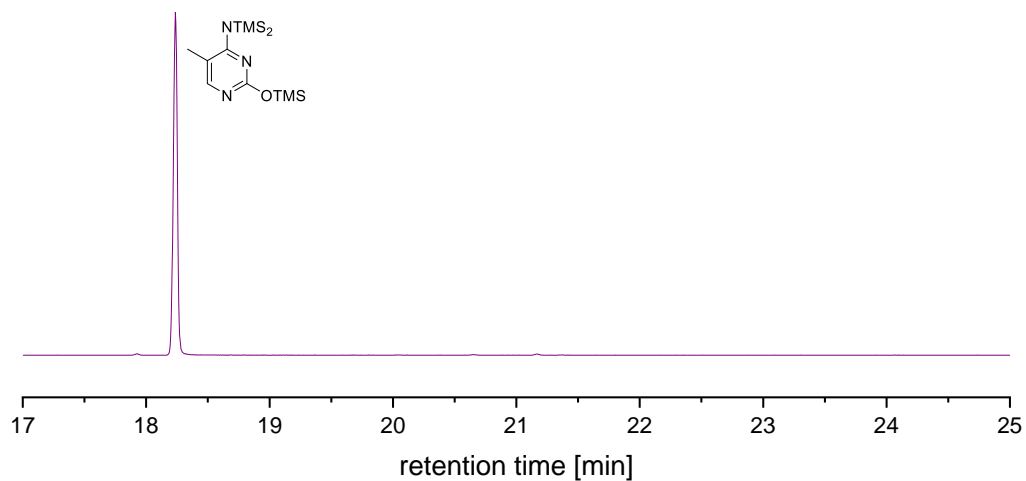
*Figure 177: Excerpt of a GC-MS trace of the reaction of **5mC** with ammonium fluoride ([NH₄F] = 25 mM). GC-MS method **C**.*
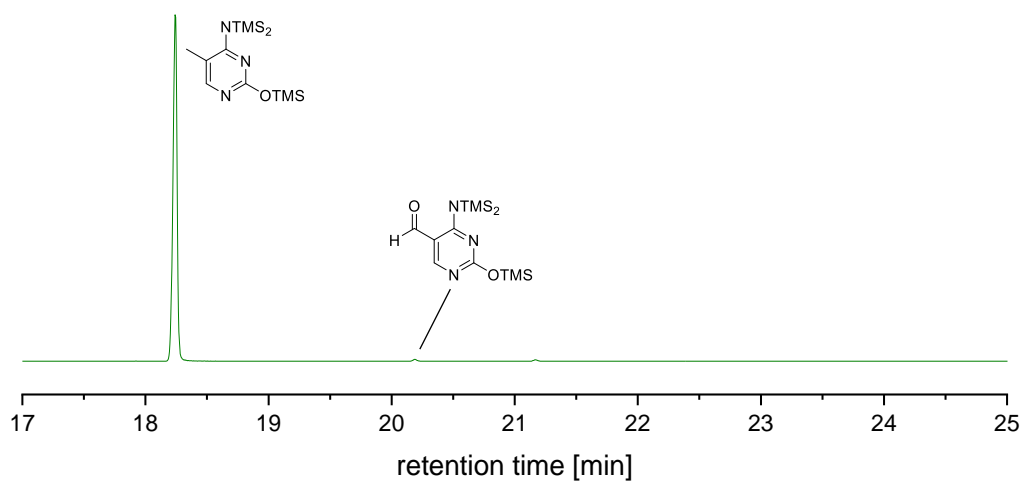
*Figure 178: Excerpt of a GC-MS trace of the reaction of **5mC** with (NH₄)₂[Ce(NO₃)₆] (CAN, [CAN] = 5 mM. GC-MS method **C**.*
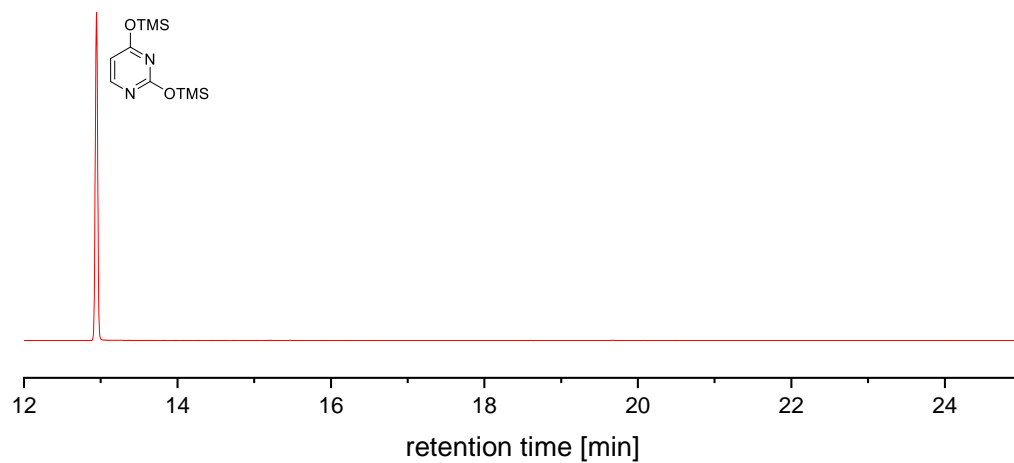
*Figure 179: Excerpt of a GC-MS trace of the reaction of **C-6** with **U**. GC-MS method **C**.*

UV-vis Experiments

UV-vis kinetic experiments were performed on a BioTek Epoch2® Plate Reader using 96-well plates. **C-6** was prepared as described on p. 255. Absorbance at $\lambda = 718$ nm was monitored for decrease every 7 s and analyzed using linear regression and the method of initial rates (*vide supra*).
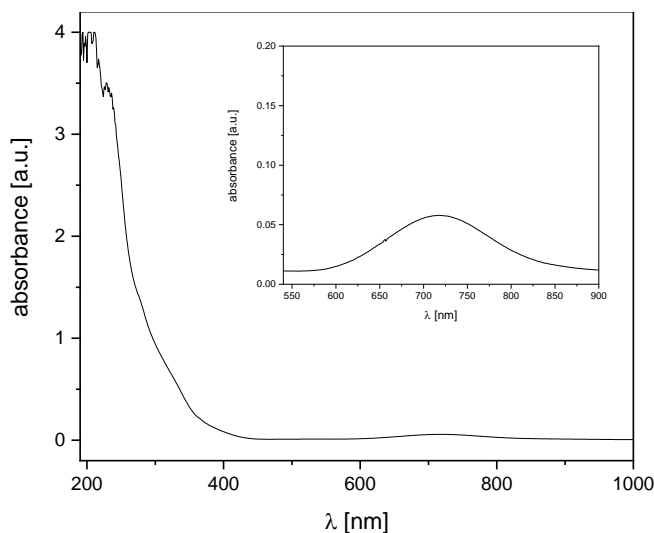
*Figure 180: Absorbance of **C-6** between $\lambda = 190\text{-}1000$ nm. Conditions: [**C-6**] = 10 mM, H_2O, T = 22 °C.*

For each set of experiments, three rows on a 96-well plate were charged with the required amounts of water and one of the reaction components, either **C-6** (using the aforementioned stock solution) or the substrate. The well plate was then placed in the tray holder and the sample compartment pre-heated to 30 °C. Subsequently, 100 µl of the complementary reaction component were added to one row, the samples mixed using the pipette (pumping 4-5 times) and the measurement started. The hereby determined slope values were then averaged and plotted against the respective substrate concentration and **S:C-6** concentration ratio. Origin 2018G was used for the evaluation of the data.

Two series of experiments were performed to investigate the behavior of **C-6** towards **5mC**. In the first series of experiments, the **5mC** concentration was kept constant at four values (1.25 mM, 2.50 mM, 3.75 mM, 5.00 mM), while the concentration of **C-6**. A total of eight measurements for each **5mC** concentration. In the second series of experiments, the **C-6** concentration was kept constant at four values (1.25 mM, 2.50 mM, 3.75 mM, 5.00 mM) and the **5mC** concentration was varied between 0.2-1.6 equiv. of the corresponding **C-6** concentration.

Subchapter 5: Nucleosides
HPLC Spiking Experiments

In these experiments, stock solutions of **5mdC**, **5hmdC**, **5fdC**, **5mC**, **5hmC**, or **5fC** were added to a reaction solution of **C-6** with **5mdC** after workup (filtration through silica). The amounts were chosen so that the signal was expected to approximately double.

HPLC conditions: C18, 95% water/5% methanol, isocratic, 15 min.

Reaction conditions: [**C-6**] = 5 mM, [**5mdC**] = 3.75 mM, H$_2$O, T = 23 °C, 10 min.
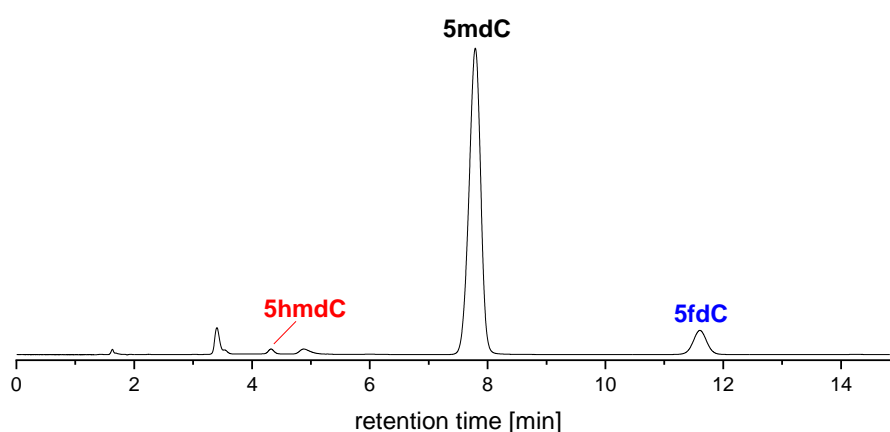
*Figure 181: HPLC trace of a reaction of **5mdC** with **C-6**.*
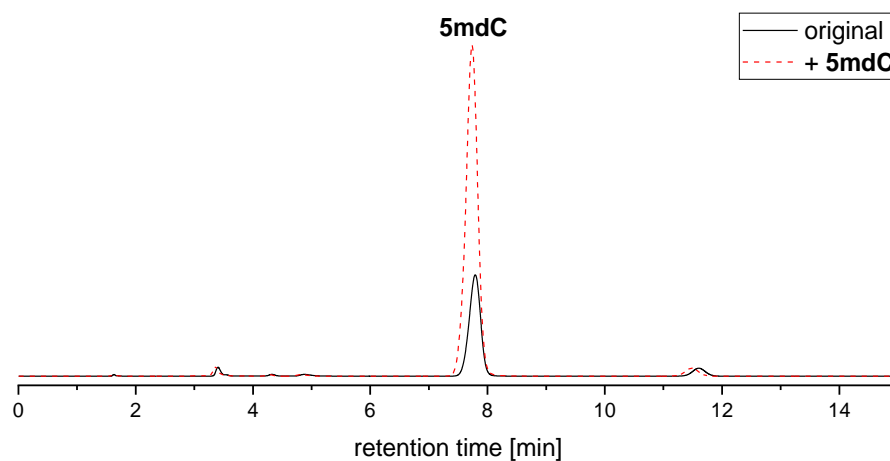
*Figure 182: HPLC traces of a reaction of **5mdC** with **C-6** (black solid) and of the same reaction spiked with **5mdC** (red dashed).*
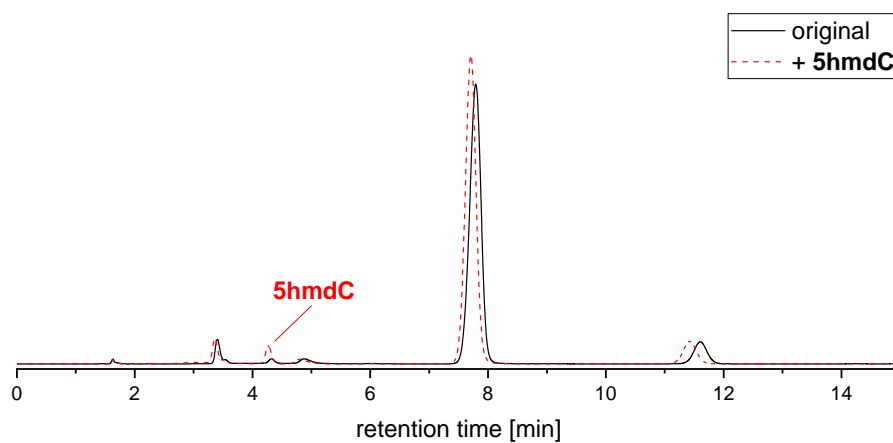
*Figure 183: HPLC traces of a reaction of **5mdC** with **C-6** (black solid) and of the same reaction spiked with **5hmdC** (red dashed).*
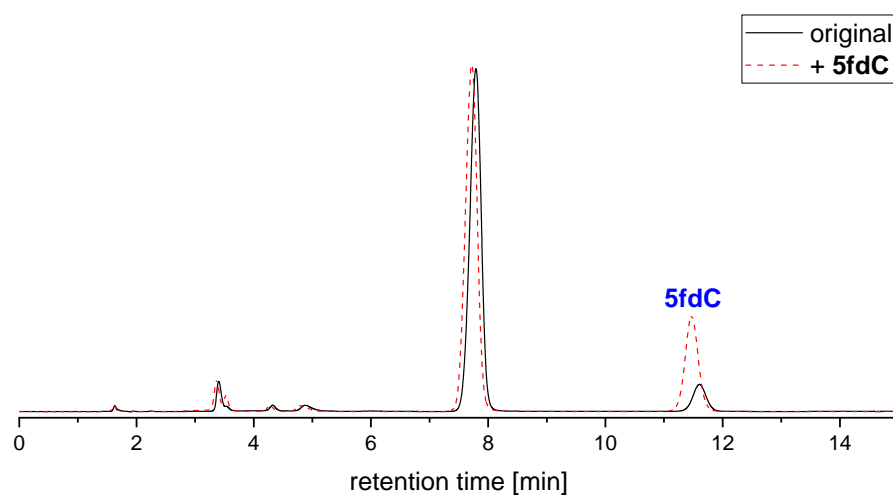
*Figure 184: HPLC traces of a reaction of **5mdC** with **C-6** (black solid) and of the same reaction spiked with **5fdC** (red dashed).*
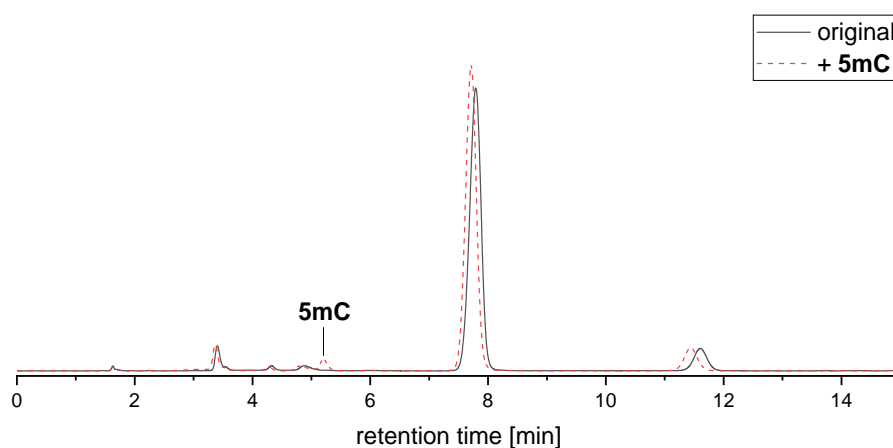
*Figure 185: HPLC traces of a reaction of **5mdC** with **C-6** (black solid) and of the same reaction spiked with **5mC** (red dashed).*
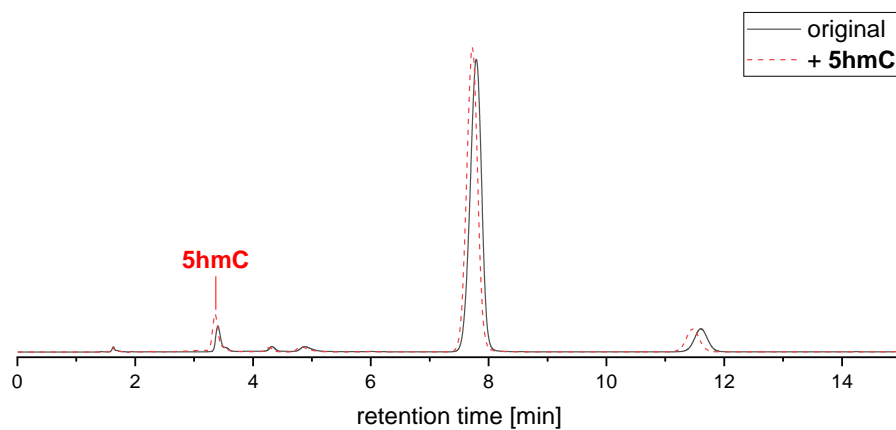
*Figure 186: HPLC traces of a reaction of **5mdC** with **C-6** (black solid) and of the same reaction spiked with **5hmC** (red dashed).*
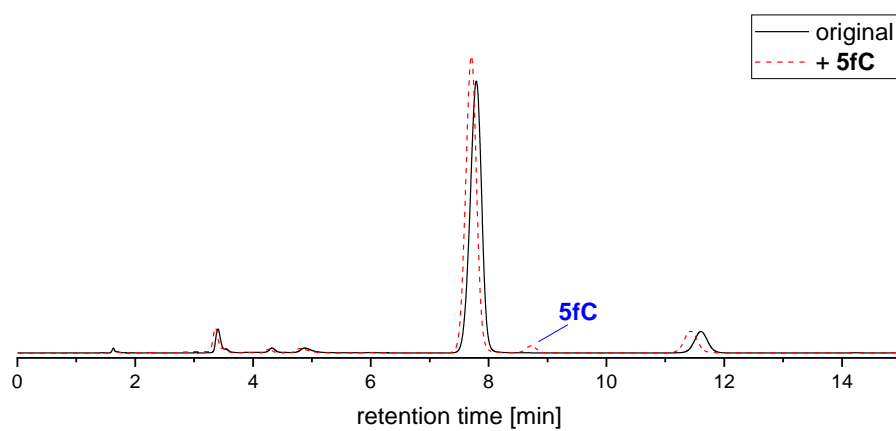
*Figure 187: HPLC traces of a reaction of **5mdC** with **C-6** (black solid) and of the same reaction spiked with **5fC** (red dashed).*

HPLC Control Experiments

In these experiments **5mdC** was reacted with $Fe(OTf)_2(mecn)_2$ and **C-1**, with and without added α-KG.

HPLC conditions: C18, 95% water/5% methanol, isocratic, 15 min.

Reaction conditions: [**C-1**]/[$Fe(OTf)_2(mecn)_2$] = 5 mM, [**5mdC**] = 3.75 mM, [α-KG] = 5 mM, H_2O, T = 23 °C, 10 min.
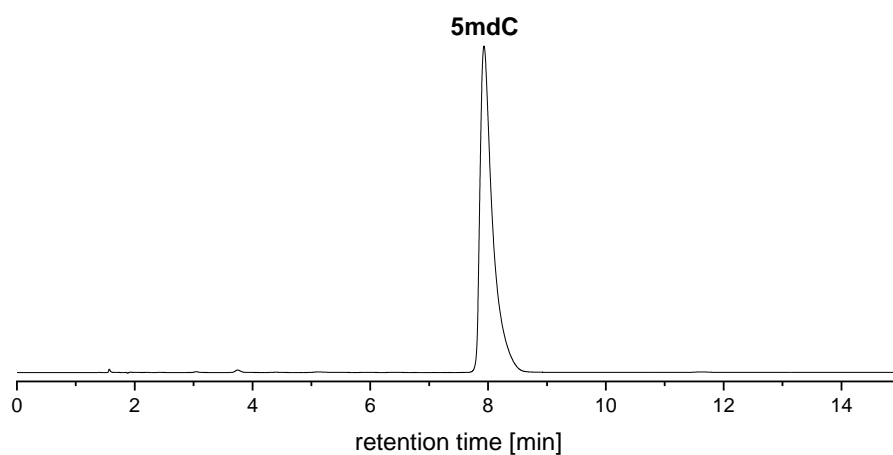
*Figure 188: HPLC trace of a reaction of **5mdC** with Fe(mecn)$_2$(OTf)$_2$.*
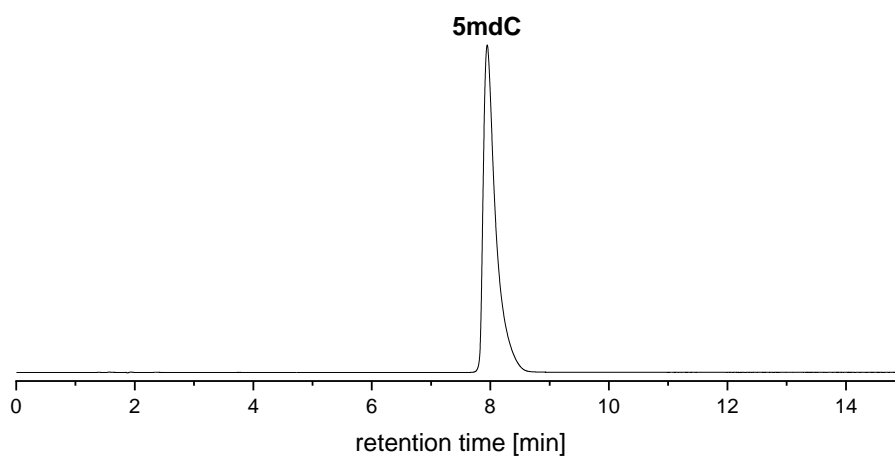
*Figure 189: HPLC trace of a reaction of **5mdC** with **C-1**.*
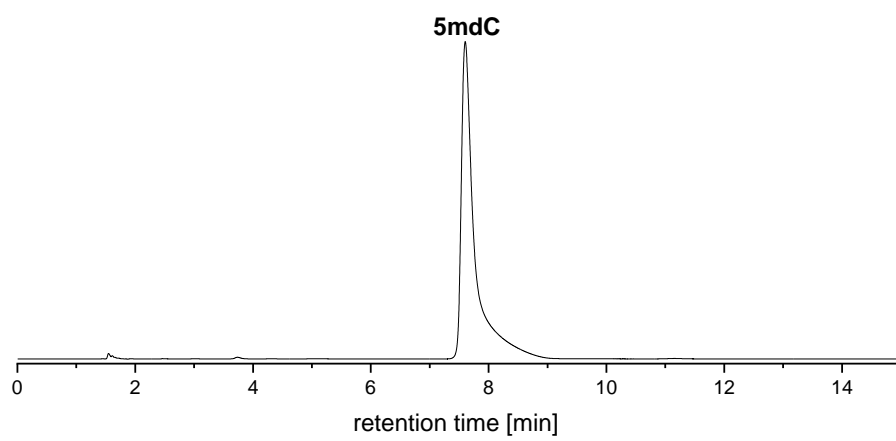
*Figure 190: HPLC trace of a reaction of **5mdC** with **C-1** and α-KG.*

Subchapter 7: Oligonucleotides
Additional Data

Reactions with oligonucleotides were performed as described on p. 356, the oligonucleotide content of the obtained aqueous solution was then determined (for results refer to Table 22 and Table 23) by UV-vis measurement and use of the extinction coefficients given in Table 21. To this end the absorption at λ = 260 nm was measured on a NanoDrop (NanoDrop Technologies, cat. no. ND-1000) and the concentration determined by the following equation (**Eq. 7**).

$$c = \frac{A_{260}}{\varepsilon_{260}}$$

Eq. 7

*Table 21: Exctinction coefficents ε_{260} of the oligonucleotide strands used in this work as given by the supplier Sigma Aldrich. In the case of **ds-O** the absorption coefficient was calculated using the molbiotools calculator (http://www.molbiotools.com/dnacalculator.html).*

Olignucleotide	Strand sequence (5'->3')	ε_{260} [mM^{-1} cm^{-1}]
O-1	HO-GGGG**5mdC**GGGG-OH	88.8
O-2	HO-CCUUAACC**5mdC**G-OH	90
O-2C	HO-GGAAUUGGGC-OH	104
O-2-ctrl.	HO-CCUUAACCCG-OH	87
O-2-ctrl.-P	HO$_3$PO-CCUUAACCCG-OH	87
ds-O	HO-CCUUAACC**5mdC**G-OH/ HO-GGAAUUGGGC-OH	166.8

*Table 22: Experimental conditions ([**O-1**], [**C-6**]), measured absorption values (A$_{260}$, λ = 260 nm, two measurements and average thereof), and resulting final oligonucleotide concentration of reactions of **O-1**, with **C-6** as well as control measurements of **O-1** and **C-6**. Samples that contained **O-1** were dissolved in such an amount of water that a final concentration of [**O-1**] = 50 µM should be reached.*

Experiment	Experimental Conditions		A$_{260}$			Concentration	
	[O-1] [mM]	[C-6] [mM]	Meas. 1	Meas. 2	Avg.	$c_{calc.}$ [µM]	c_{corr} [µM]
Untreated	0.20	0.00	1.712	1.753	1.733	19.5	-
O-1 + C-6	0.25	0.25	2.190	2.183	2.187	24.6	24.5
O-1 + C-6 2	0.25	1.00	2.787	2.692	2.740	30.9	30.8
O-1 control	0.25	0.00	3.338	3.209	3.274	36.9	36.4
C-6 control	0.00	1.00	0.000	0.015	0.008	0.1	0
H$_2$O	0.00	0.00	0.042	0.048	0.045	0.5	0

Table 23: Experimental conditions ([**O-2**], [**C-6**]), measured absorption values (A_{260}, λ = 260 nm, two measurements and average thereof), and resulting final oligonucleotide concentrations of reactions of **O-2**, a double stranded DNA sample (**ds-O**), the complementary strand to **O-2** (**O-2C**), the control strands **O-2-ctrl.** and **O-2-ctrl.-P** with **C-6** as well as control measurements of **O-2** and **C-6**. TD = time dependent measurement. *) These reactions contained additionally 2.5 mM NaCl. **) This sample was treated as all reaction samples (incubated, filtered, lyophilized, re-suspended, syringe-filtered) and used for determination of the background absorbance at λ = 260 nm. This data was previously published.[14]

Experiment	Experimental Conditions		A_{260}			Concentration	
	[O-2] [mM]	[C-6] [mM]	Meas. 1	Meas. 2	Avg.	$c_{calc.}$ [μM]	c_{corr} [μM]
Untreated	0.50	0.00	1.034	1.059	1.047	11.8	10.4
O-2 + C-6	0.25	0.25	4.017	4.073	4.045	45.6	41.5
O-2 + C-6 2	0.25	1.00	4.146	4.176	4.161	46.9	42.8
TD1-0.5 min	0.125	0.5	0.910	1.010	0.960	10.7	9.3
TD1-5 min	0.125	0.5	1.192	1.366	1.279	14.2	12.8
TD1-10 min	0.125	0.5	1.145	1.064	1.105	12.3	10.9
TD1-17 min	0.125	0.5	1.396	1.219	1.308	14.5	13.2
TD1-26 min	0.125	0.5	1.050	1.107	1.079	12.0	10.6
TD1-37 min	0.125	0.5	1.108	1.120	1.114	12.4	11.0
TD2-0.5 min	0.125	0.5	1.091	1.115	1.103	12.3	10.9
TD2-2.5 min	0.125	0.5	1.306	1.606	1.456	16.2	14.8
TD2-5 min	0.125	0.5	1.092	1.184	1.138	12.6	11.3
TD2-10 min	0.125	0.5	1.150	1.228	1.189	13.2	11.8
TD2-17 min	0.125	0.5	1.248	1.368	1.308	14.5	13.2
TD2-26 min	0.125	0.5	1.223	1.388	1.306	14.5	13.1
TD2-37 min	0.125	0.5	0.698	0.835	0.767	8.5	7.1
ds-O*	0.125	0.5	1.726	1.570	1.648	9.9	9.1
O-2*	0.125	0.5	1.002	1.145	1.074	11.9	5.7
O-2C*	0.125	0.5	0.820	0.798	0.809	7.8	4.1
O-2-ctrl.	0.25	1.0	1.693	1.460	1.577	18.1	14.0
O-2-ctrl.-P	0.25	1.0	2.612	2.520	2.566	29.5	28.1
O-2 control	0.25	0.00	4.489	4.487	4.488	50.5	46.5
C-6 control	0.00	1.00	0.366	0.346	0.356	4.0	0
H₂O**	0.00	0.00	0.138	0.109	0.124	1.4	0
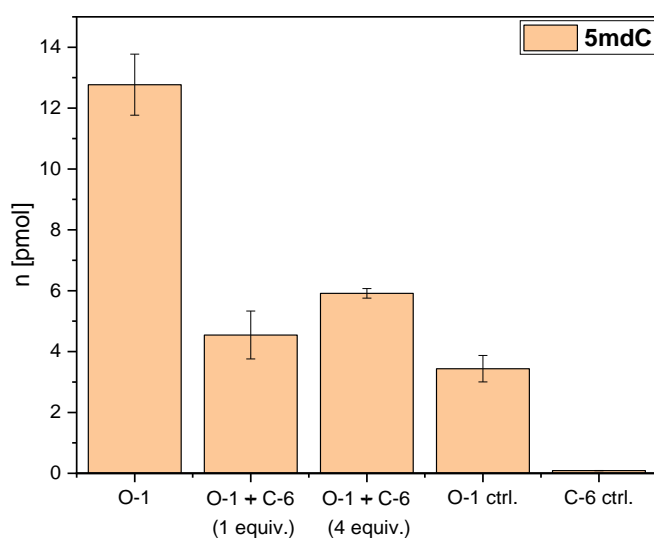
Figure 191: Detected levels of 5mdC in **O-1** samples. **O-1** refers to the untreated oligo, "**O-1** + **C-6** (1 equiv.)" to a ratio of 1:1 **O-1**:**C-6**, "**O-1** + **C-6** (4 equiv.)" to a ratio of 1:4 **O-1**:**C-6**, "**O-1** ctrl" and "**C-6** control" refer to samples in which **O-1** or **C-6**, respectively, were treated as the reaction samples. Conditions: [**O-1**] = 0.25 mM, [**C-6**] = 0.25 or 1 mM, H₂O, T = 23 °C, t = 30 min. Error bars represent standard deviation between technical replicates.
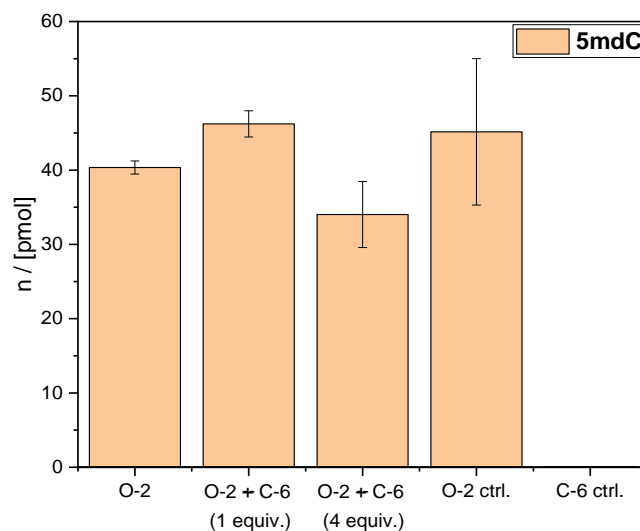
Figure 192: Detected levels of 5mdC in O-2 samples. O-2 refers to the untreated oligo, "O-2 + C-6 (1 equiv.)" to a ratio of 1:1 O-2:C-6, "O-2 + C-6 (4 equiv.)" to a ratio of 1:4 O-2:C-6, "O-2 ctrl" and "C-6 control" refer to samples in which O-2 or C-6, respectively, were treated as the reaction samples. Conditions: [O-2] = 0.25 mM, [C-6] = 0.25 or 1 mM, H_2O, T = 23 °C, t = 30 min. Error bars represent standard deviation between technical replicates.

Additional UV-vis Spectra
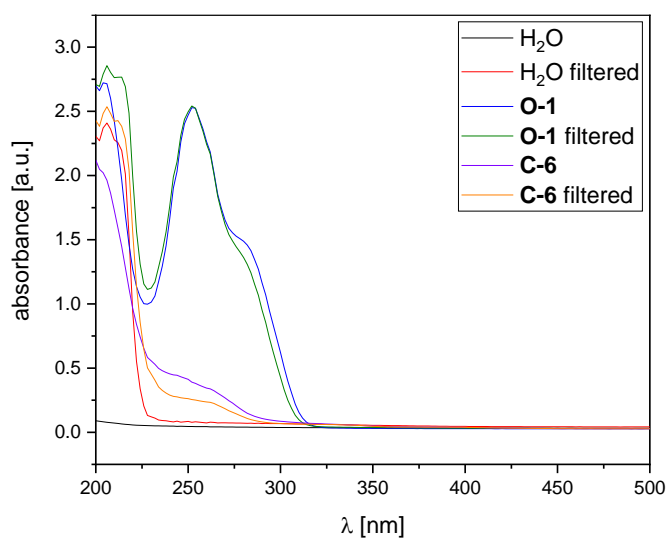
Figure 193: Superimposed excerpts of UV-Vis spectra obtained for unfiltered (H_2O/O-1/C-6) and filtered (H_2O filtered/O-1 filtered/C-6 filtered) samples. Conditions: [O-1/C-6] = 0.2 mM, H_2O, T = 25 °C. The data shown for O-1 and C-6 is the same as in Figure 46 and is only shown here as a comparison.
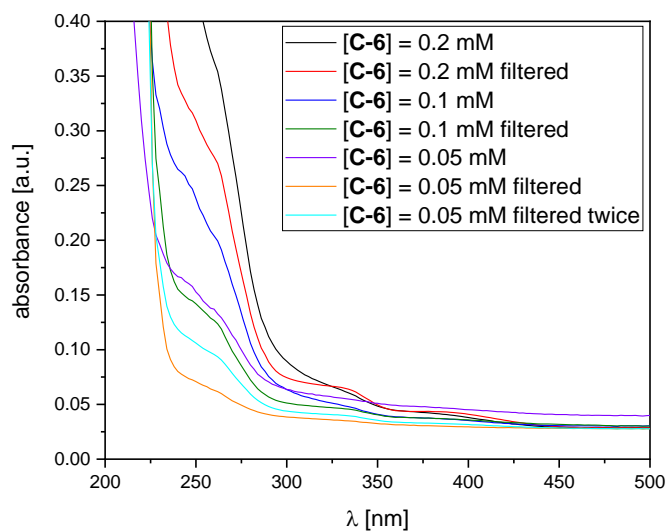
*Figure 194: Superimposed excerpts of UV-Vis spectra obtained for unfiltered and filtered samples. Conditions: [**C-6**] = 0.05-0.2 mM, H₂O, T = 25 °C. The data shown for [**C-6**] = 0.2 mM is the same as in Figure 46 and Figure 193 and is only shown here as a comparison.*

Additional Schemes
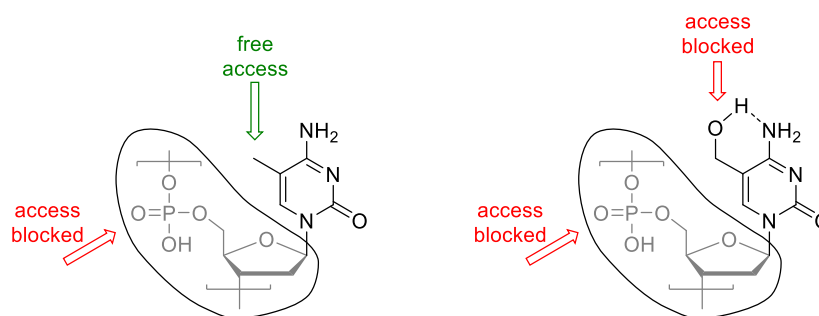
*Figure 195: Spatial access to the methyl/hydroxymethyl group in a **5mC/5hmC** containing oligonucleotide.*

Side Product Analysis – MALDI MS
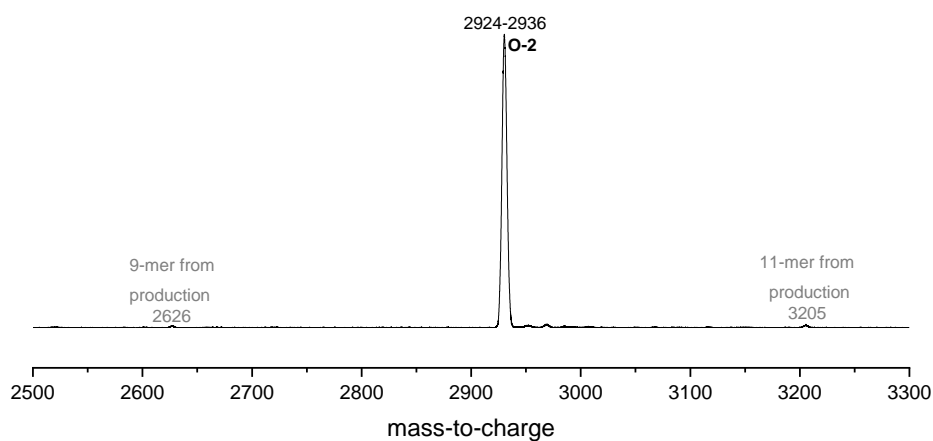
*Figure 196: Excerpt of the MALDI MS spectrum obtained for the control reaction of **O-2** without **C-6**. Small signals are observed at 2626 m/z and 3205 m/z, these were assigned to 9-mer and 11-mer contaminants stemming from production.*
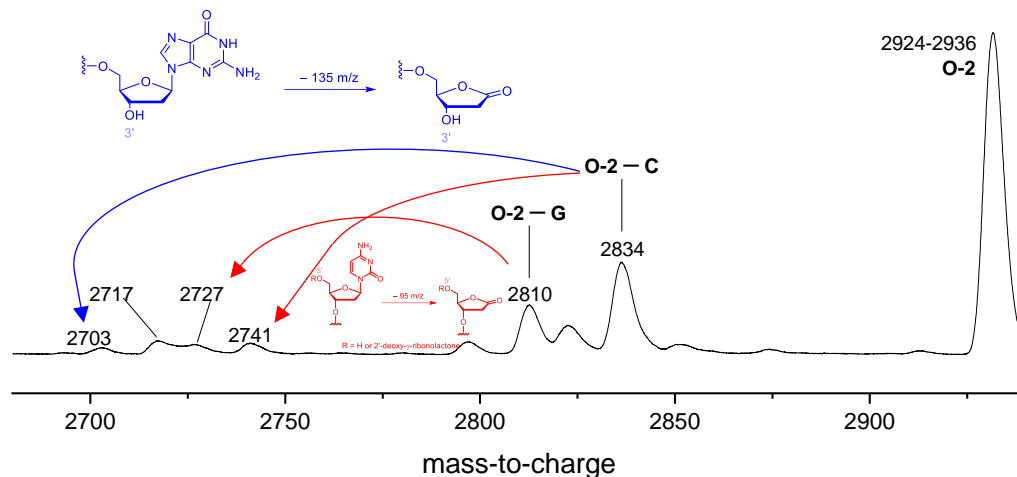
*Figure 197: Excerpt of an additional MALDI-TOF MS spectrum of the reaction of **O-2** with **C-6**. Possible fragmentation pathway resulting in loss of **G** or **C** (blue and red, respectively) are indicated. Conditions: [**O-2**] = 0.25 mM, [**C-6**] = 1 mM, H_2O, T = 23°C.*
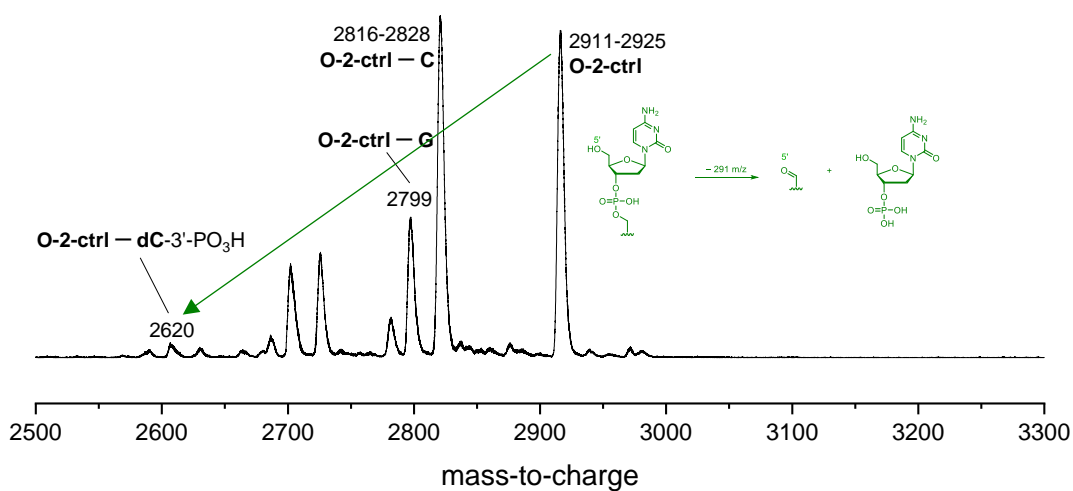
*Figure 198: Excerpt of the MALDI MS spectrum obtained for the reaction of the "control strand" **O-2-ctrl.** with 4 equiv. of **C-6**. A possible fragmentation pathway resulting in the observed signal at 2620 m/z is indicated (green). The signals between 2650-2950 m/z are shown enlarged in Figure 199.*
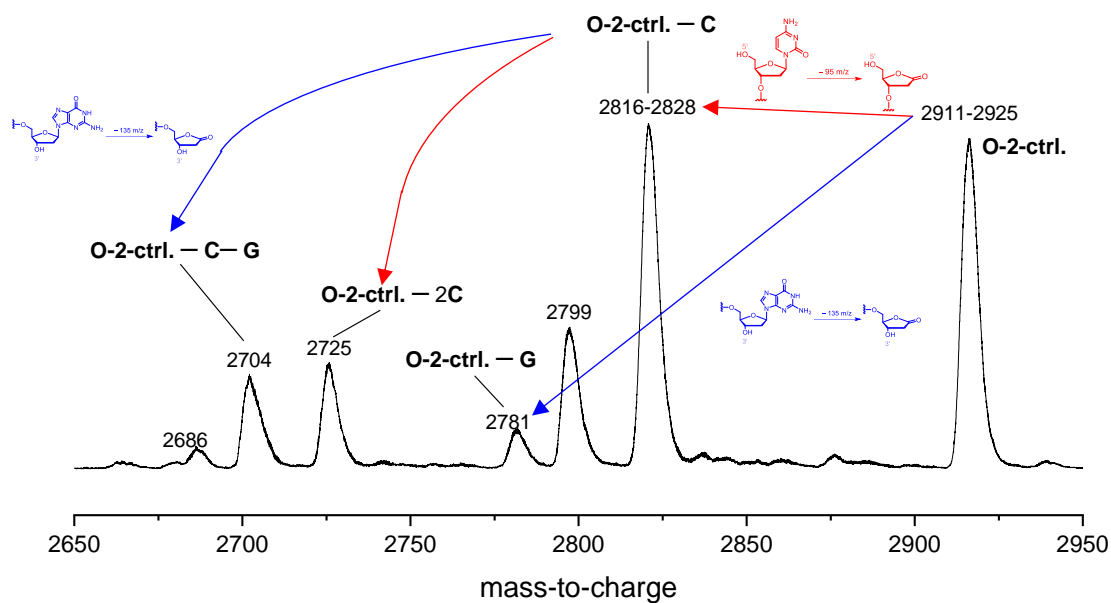
*Figure 199: Zoomed-in excerpt of the MALDI-TOF MS spectrum obtained for the reaction of the "control strand" **O-2-ctrl.** with 4 equiv. of **C-6**. Possible fragmentation pathway resulting in loss of **G** or **C** (blue and red, respectively) are indicated.*
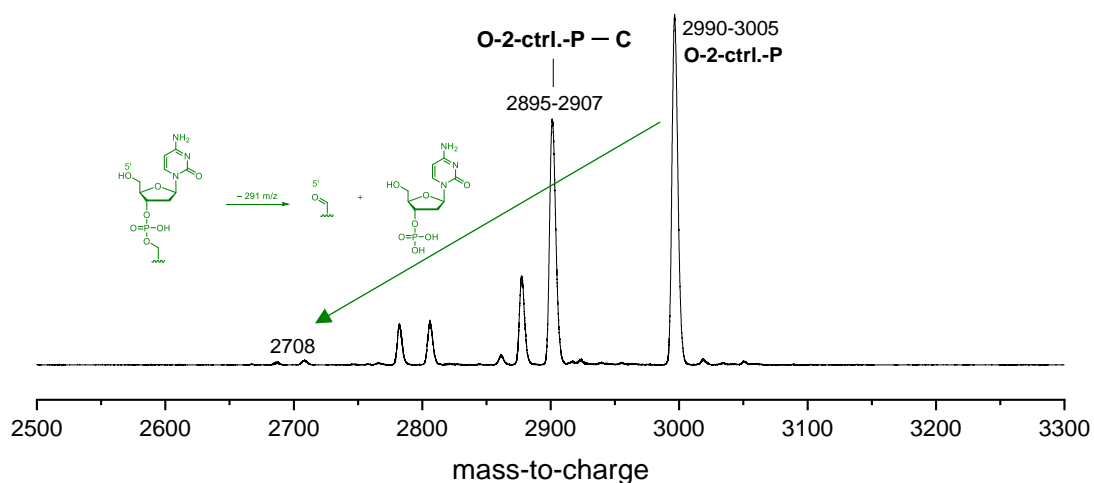
*Figure 200: Excerpt of the MALDI-TOF MS spectrum obtained for the reaction of the "control strand" **O-2-ctrl.-P** with 4 equiv. of **C-6**. A possible fragmentation pathway resulting in the observed signal at 2708 m/z is indicated (green). The signals between 2750-3050 m/z are shown enlarged in Figure 199.*
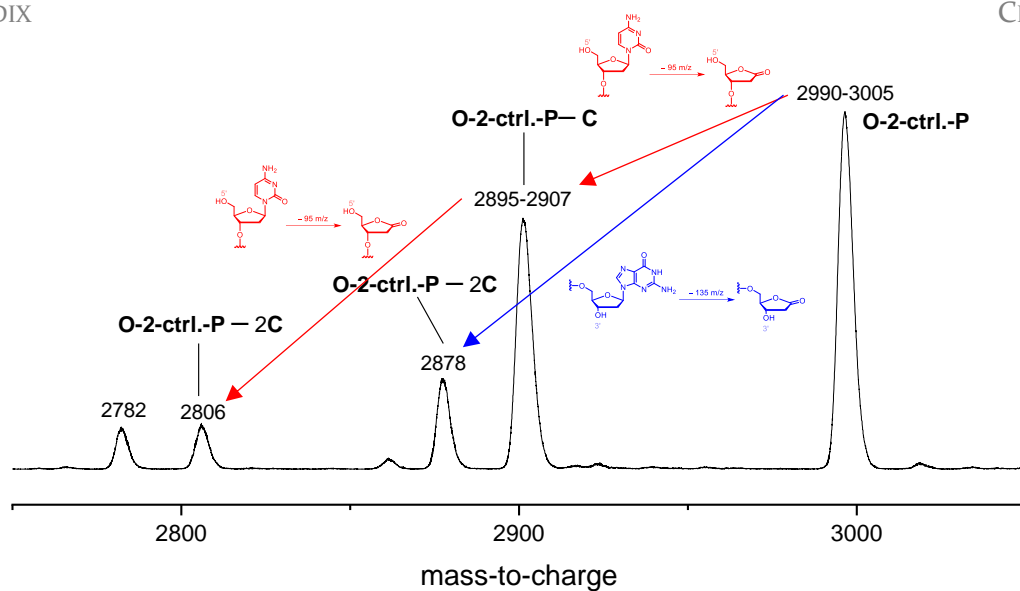
*Figure 201: Zoomed in excerpt of the MALDI-TOF MS spectrum obtained for the reaction of the "control strand" **O-2-ctrl.-P** with 4 equiv. of **C-6**. Possible fragmentation pathway resulting in loss of **G** or **C** (blue and red, respectively) are indicated. The signal at 2782 m/z is also probably formed by loss of guanine from the signal at 2895-2907 m/z (not indicated by an arrow).*

Subchapter 8 Synthetic Epigenetics
Additional Data
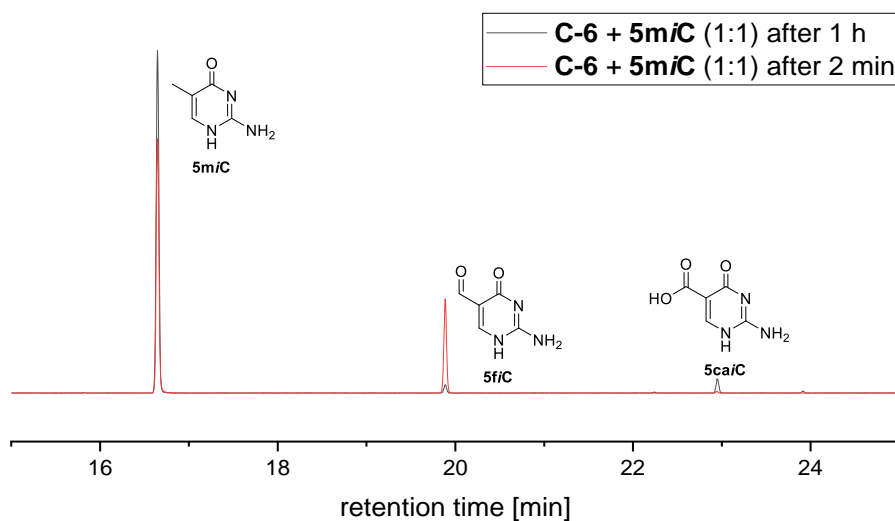
*Figure 202: Superimposed excerpt of the GC-MS traces of reactions of **C-6** with **5miC** after 1 h or 2 min. **5fiC** and **5caiC** were observed in addition to the starting material. GC-MS method **C**. Conditions: [**C-6**] = 1 mM; [**5miC**] = 1 mM, H₂O, T = 30 °C.*
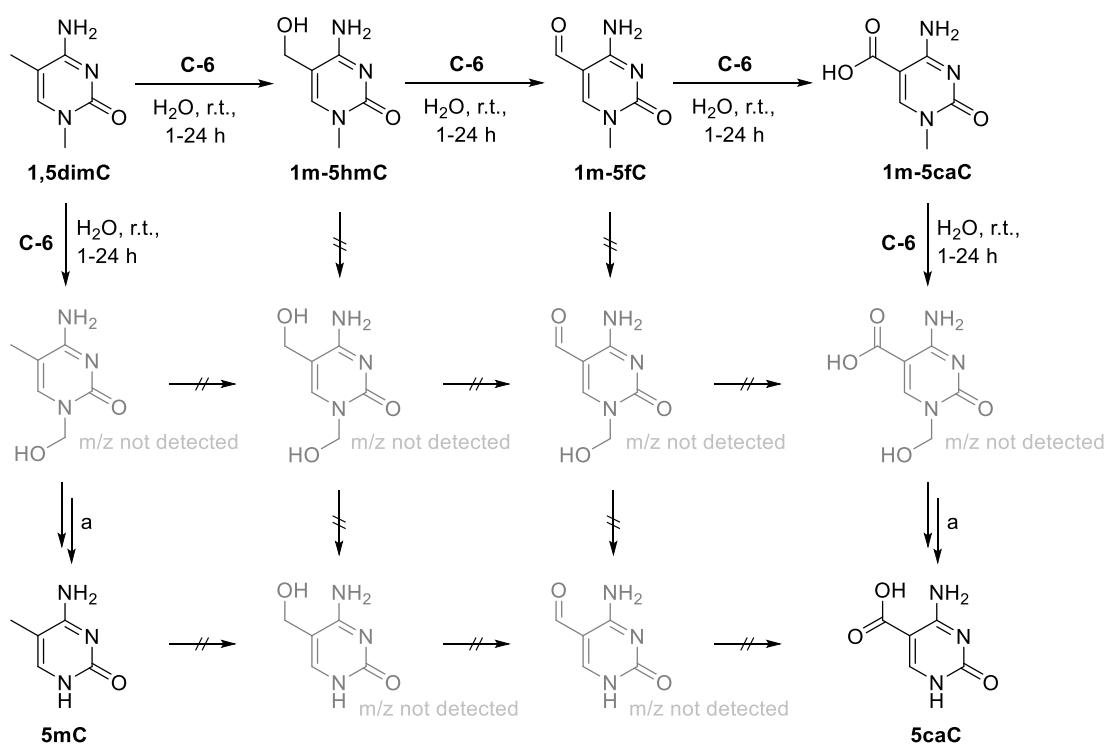
*Scheme 115: Reaction pathways of the reaction of **1,5dimC** with **C-6**, structures in black were detected after 1 h and 24 h reaction time by Rachel Janßen using UHPLC-MS. ᵃ For this step we propose a similar reaction sequence as for **1mC**.*

Subchapter 9: Miscellaneous
Helmchen-Doubleschlenk-Flask (HDSF)
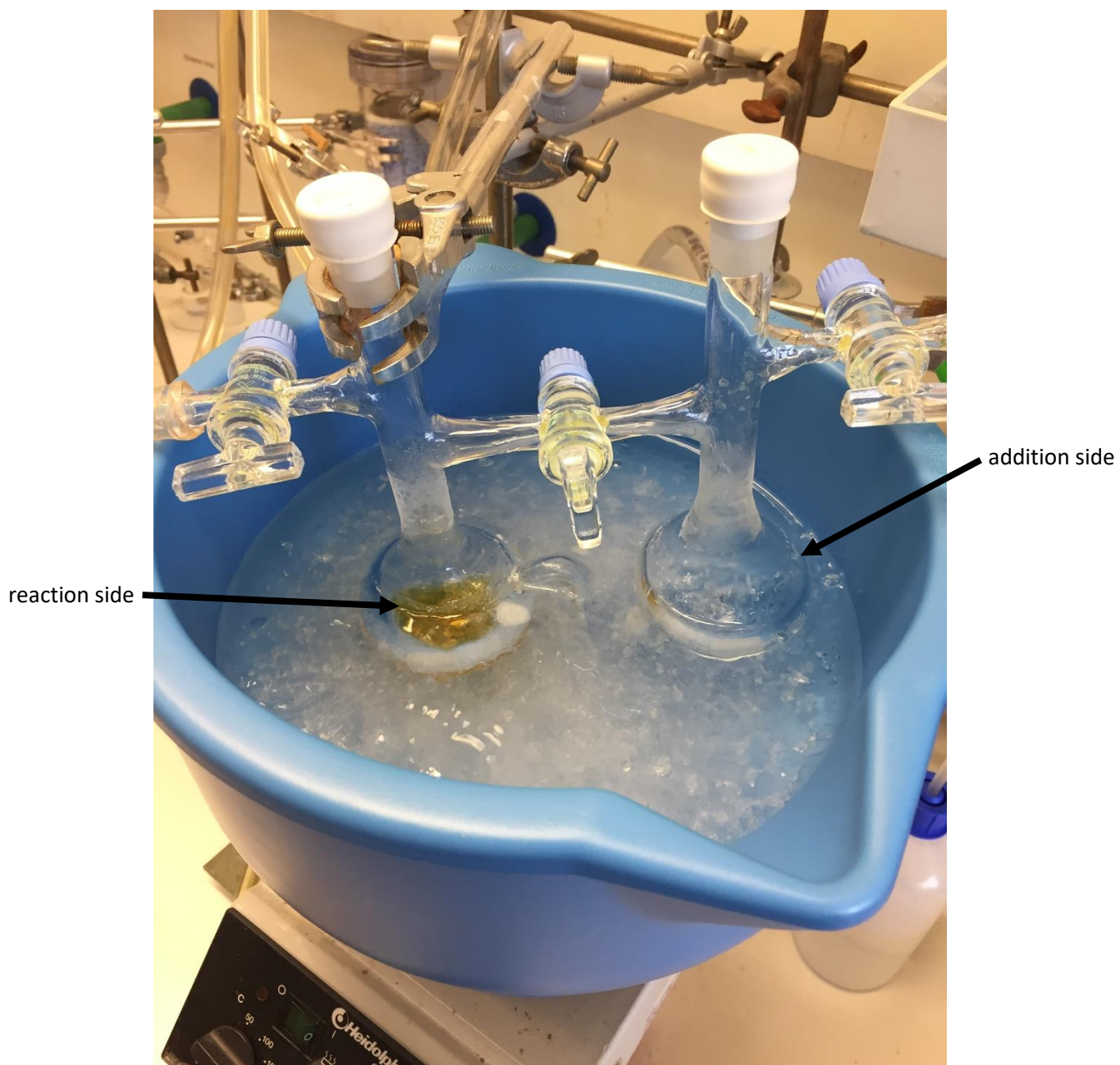
Figure 203: A picture of the Helmchen-Doubleschlenk-Flask during the synthesis of **III-13**.

Additional GC-MS Traces and NMR Spectra
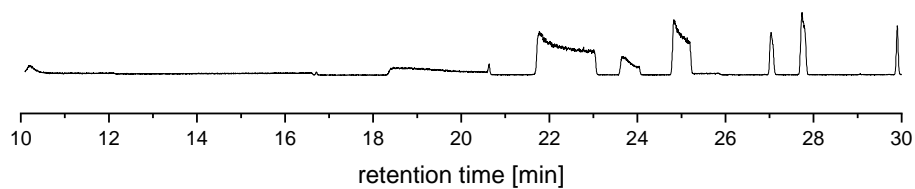
*Figure 204: Excerpt of the GC-MS trace of the reaction of **C-6** with the obtained product mixture shown in Figure 66.*
*GC-MS method **C**.*
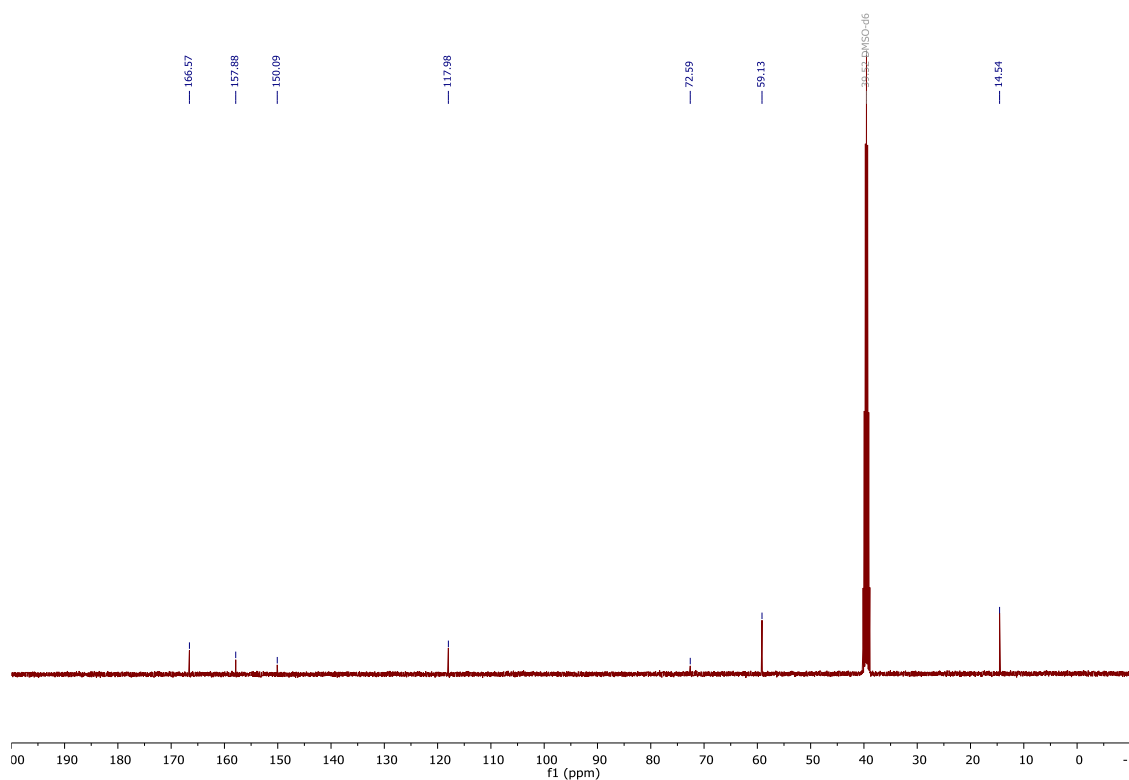
*Figure 205: ^{13}C NMR spectrum of the unidentified product of the first reaction in Scheme 56**C** in DMSO-d$_6$.*

3. Chapter IV – Additional Data and Spectra
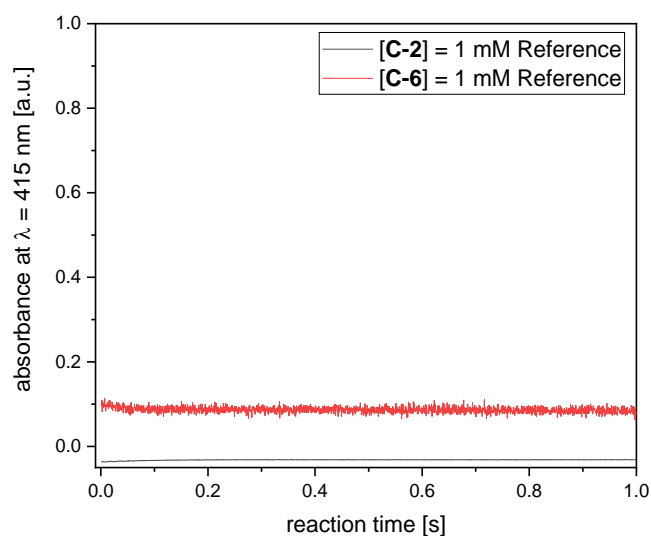
*Figure 206: Reference stopped flow UV-vis measurements of **C-2** and **C-6** at λ = 415 nm. Conditions: [**C-2/C-6**] = 1 mM, H₂O, T = 24 °C.*
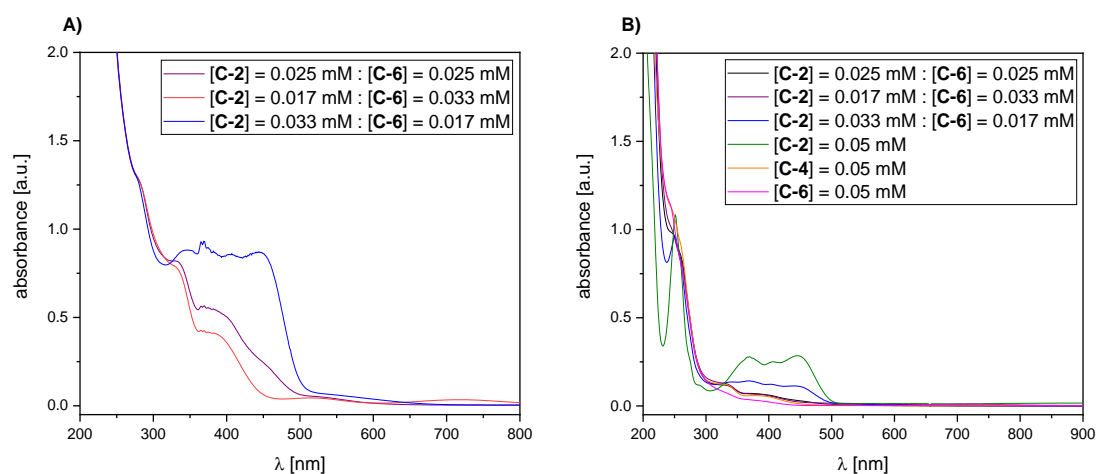
*Figure 207: **A**) UV-Vis spectra collected from aqueous solutions of three mixtures of **C-2** and **C-6** at a total iron concentration of c = 0.5 mM each. **B**) UV/Vis spectra collected from aqueous solutions of three mixtures of **C-2** and **C-6** at a total iron concentration of c = 0.05 mM each as well as reference samples of **C-2**, **C-4**, and **C-6**. Conditions: [**C-2/C-4/C-6**] = 0.17-0.5 mM, H₂O, T = 23 °C.*

4. Chapter V – Additional Data and Spectra

Subchapter 3: Immobilization
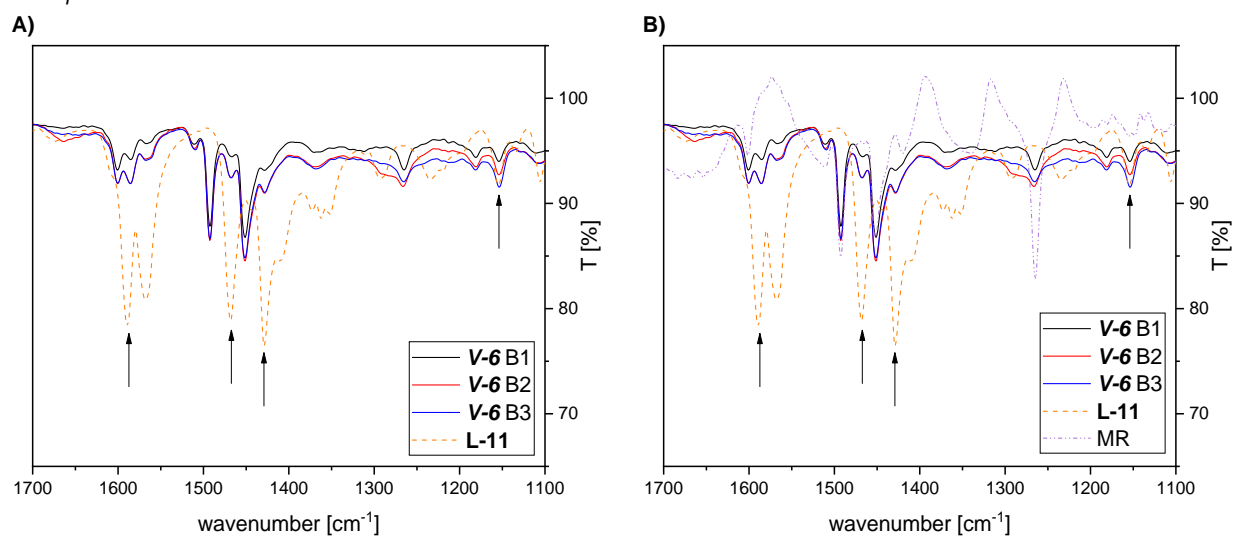
*Figure 208: Excerpts of IR spectra of three batches (B1-B3) of **V-6** in comparison to **A) L-11** and **B) L-11** and Merrifield Resin (MR).*
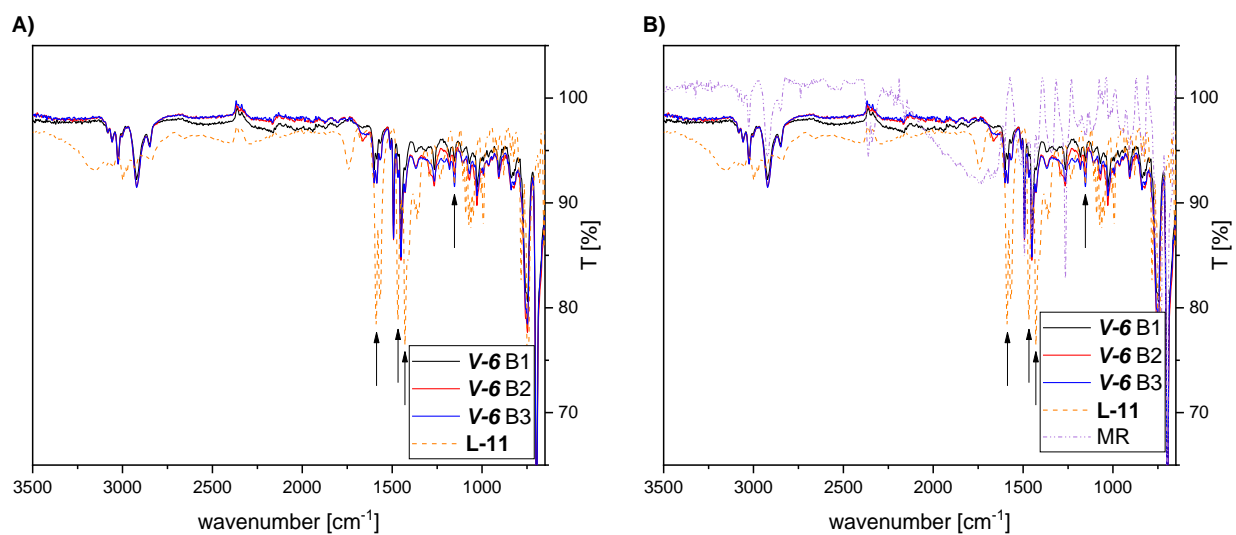
*Figure 209: Full IR spectra of three batches (B1-B3) of **V-6** in comparison to A) **L-11** and B) **L-11** and Merrifield Resin (MR).*
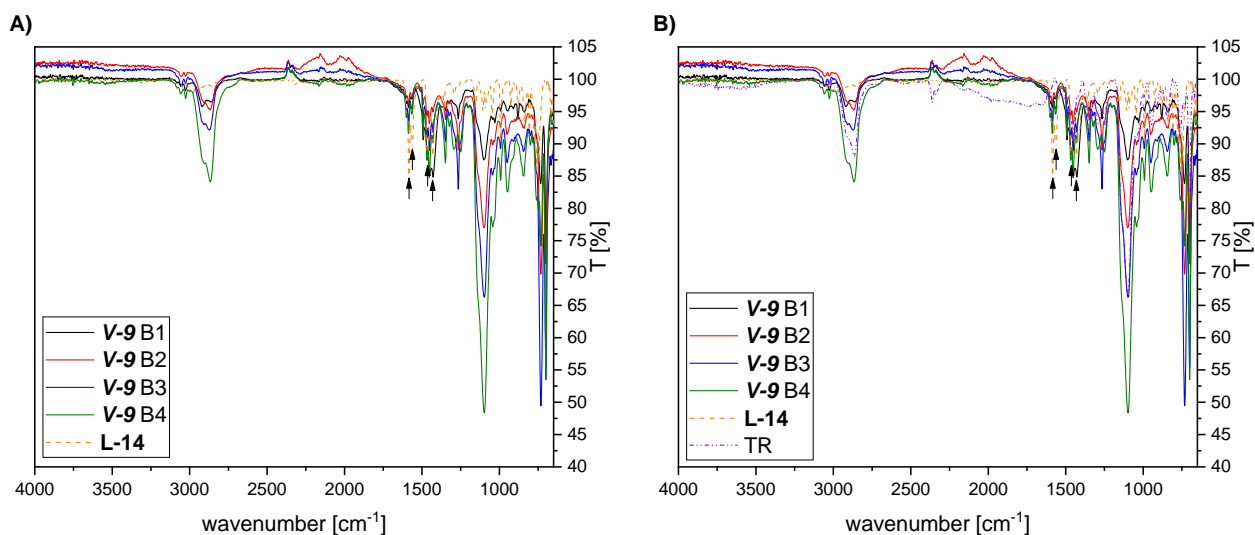
*Figure 210: Full IR spectra of three batches (B1-B4) of **V-9** in comparison to **A)** **L-14** and **B)** **L-14** and Tentagel Resin (TR).*
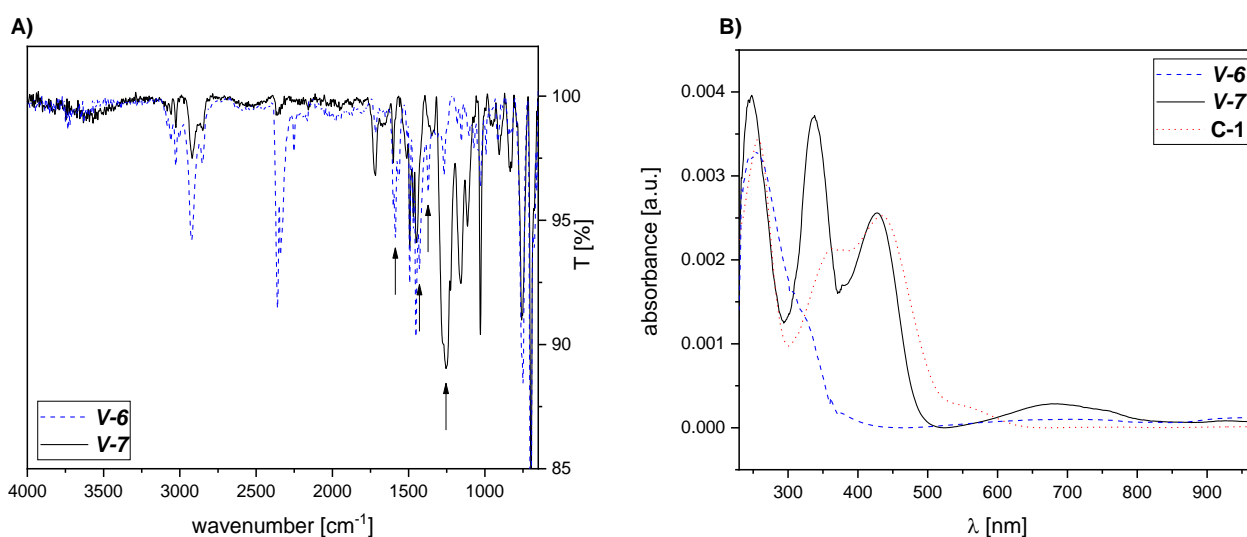
*Figure 211: **A)** Full IR spectra of Merrifield resin beads with immobilized ligand **L-11** (**V-6**) before (blue dashed) and after (**V-7**, black) treatment with Fe(mecn)$_2$(OTf)$_2$. Distinct differences are marked with arrows. **B)** Solid-state UV-vis spectra of Merrifield resin with immobilized **L-11** (**V-6**) before (blue dashed) and after treatment with Fe(mecn)$_2$(OTf)$_2$ (**V-7**, black) including a reference of **C-1** (red dotted).*
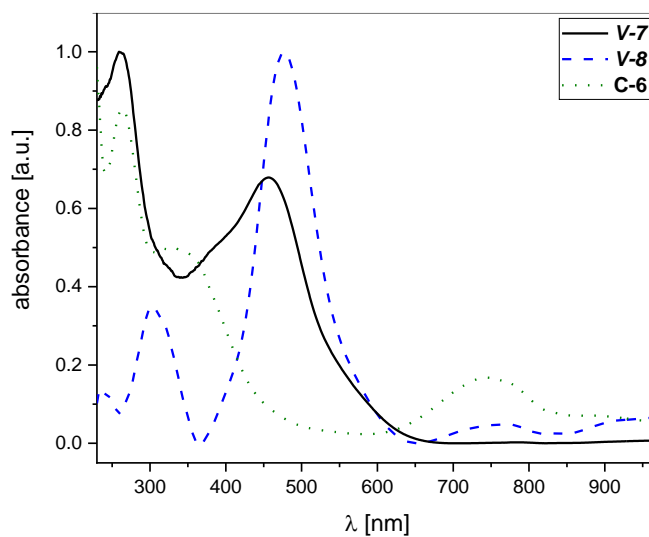
Figure 212: Full solid-state UV-vis spectra of intermediate **V-7** *before (black) and after treatment with cerium(IV) ammonium nitrate (CAN,* **V-8***, blue dashed) and* **C-6** *as reference sample (green dotted).*
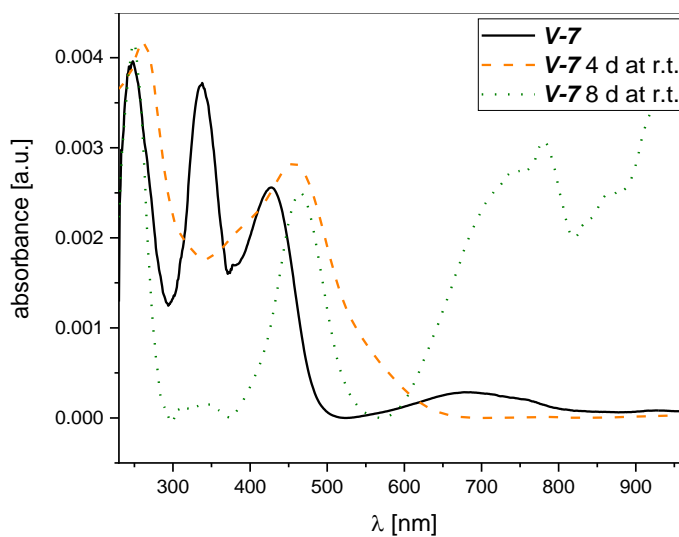
Figure 213: Full solid-state UV-Vis spectra of the resin carrying immobilized **L-11** *that was treated with Fe(mecn)$_2$(OTf)$_2$ (***V-7***, black) after 4 d (orange dashed) or 8 d (green dotted) at room temperature.*
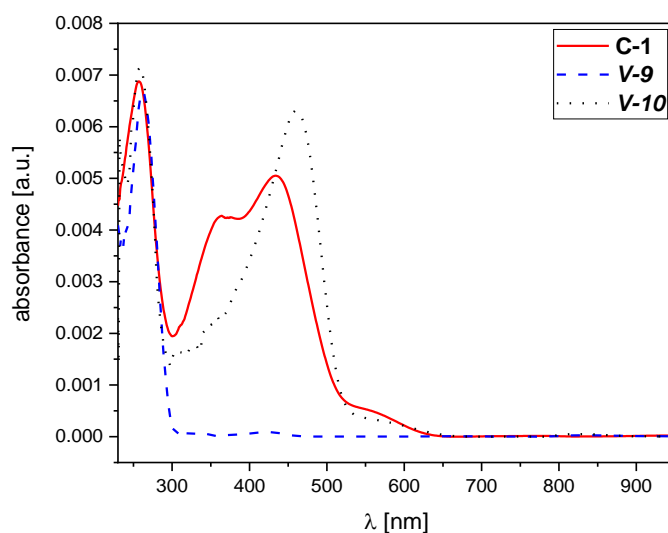
*Figure 214: Solid-state UV-vis spectra of Merrifield resin with immobilized **L-14** (**V-9**) before (blue dashed) and after treatment with Fe(mecn)$_2$(OTf)$_2$ (**V-10**, black dotted) including a reference of **C-1** (red solid)*
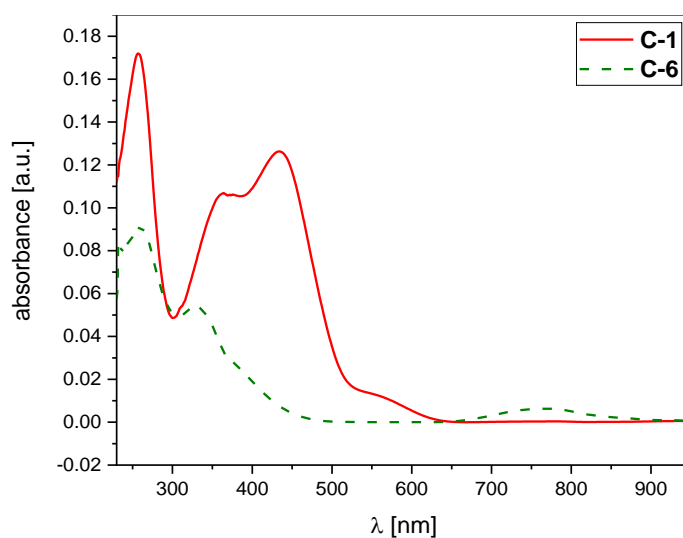
*Figure 215: Full solid-state UV-vis reference spectra of **C-1** (red solid) and **C-6** (green dashed).*

*Table 24: ICP-OES measurements of the supernatant and washing solution after oxidation of **V-7** with cerium(IV) ammonium nitrate (H$_2$O and aq. Na$_2$SO$_4$) and a reference sample of sodium sulfate.*

	Ce [μg ml^{-1}]	Ce [μg ml^{-1}]
Supernatant after oxidation	4045	20
Wash Step with aq. Na$_2$SO$_4$ (sat.)	3	0
Aq. Na$_2$SO$_4$ (sat., control)	ULOD	ULOD

Subchapter 4: The Py₅(OR)₂ Ligand System
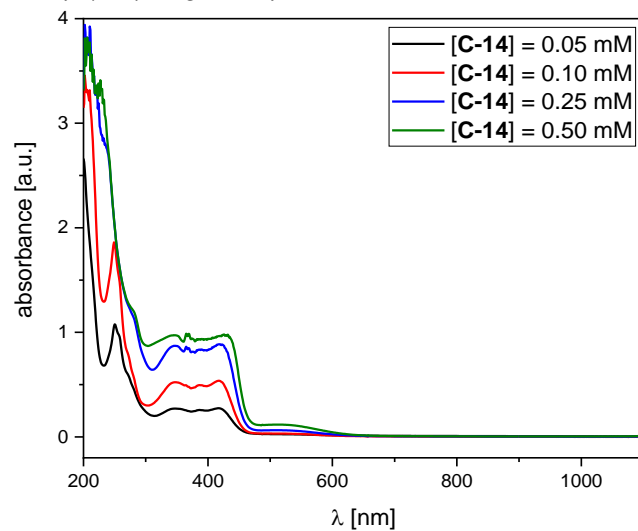
*Figure 216: UV-vis spectra of **C-14** in acetonitrile at different concentrations.*
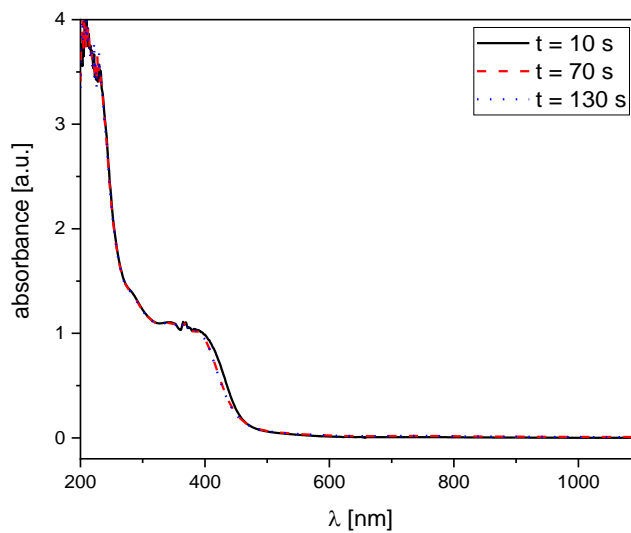
*Figure 217: UV-vis spectra of a mixture of **C-14** and cerium ammonium nitrate (CAN). Conditions: [**C-14**] = 0.25 mM, [CAN] = 1 mM, MeCN, T = 24 °C.*

385
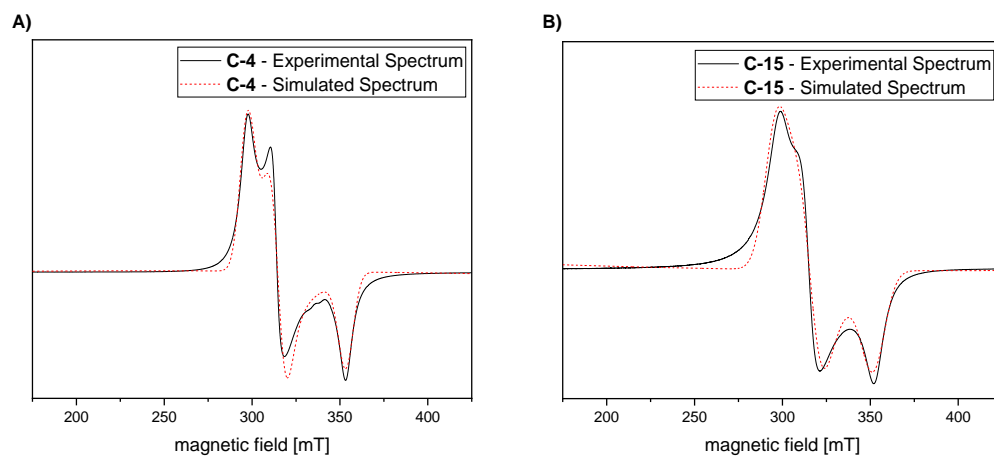
*Figure 218: **A**) X-band EPR spectrum (black solid) of **C-4**, collected at 296 K, simulated spectrum (red dashed) by Dr. Katherine Fisher. **B**) X-band EPR spectrum (black solid) of **C-15**, collected at 298 K, simulated spectrum (red dashed) by Dr. Katherine Fisher.*

*Table 25: Comparison of EPR spectroscopic data of **C-4** and **C-15**.*

	C-4	C-15
g(3)	2.318884	2.325975
g(2)	2.189958	2.183291
g(1)	1.950636	1.959197

Subchapter 5: The Py$_4$OHMe$_2$-H Ligand and its Complexes
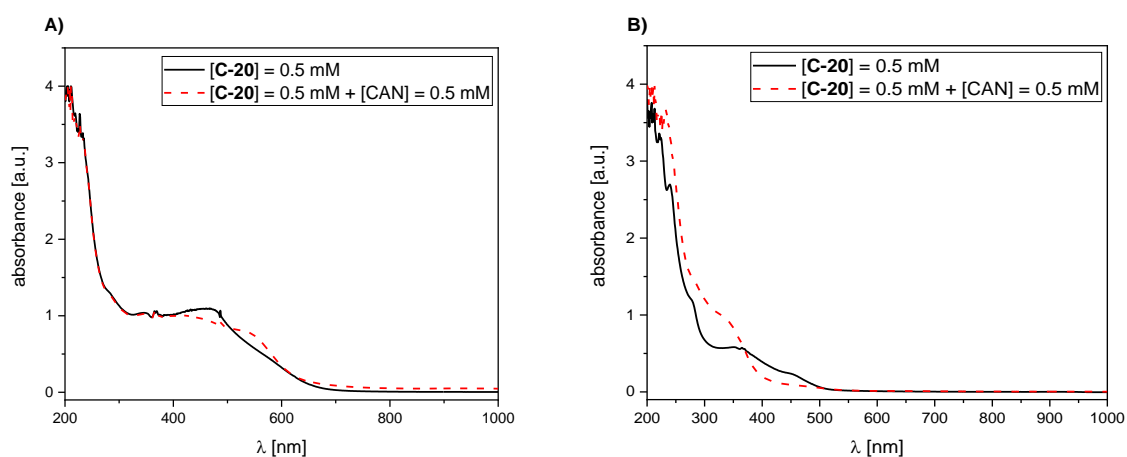
*Figure 219: **A**) UV-vis spectra of **C-20** before (black) and after (red) addition of cerium(IV) ammonium nitrate (CAN) in a mixture of acetonitrile and water (3:1). **B**) UV-vis spectra of **C-20** before (black) and after (red) addition of cerium(IV) ammonium nitrate (CAN) in water.*

Subchapter 6: Py$_4$PhMe$_2$H and Py$_3$Ph$_2$Me$_2$H Ligands
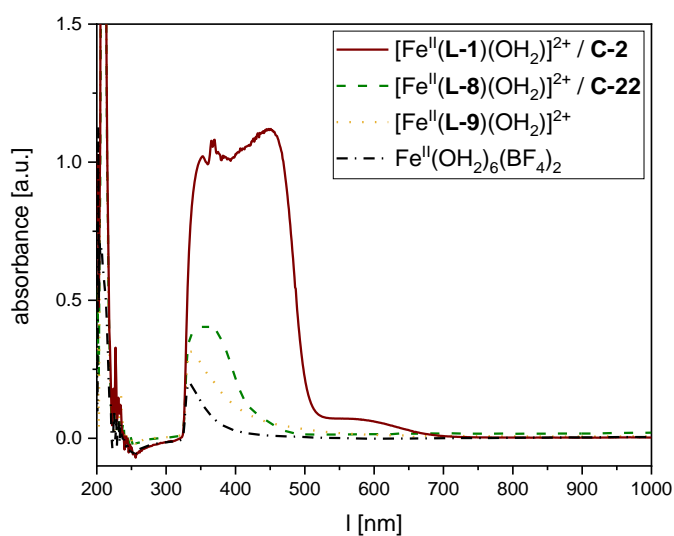
*Figure 220: UV-vis spectra of **C-2**, **C-22**, a mixture of **L-9** and Fe^{II}(H$_2$O)$_6$(BF$_4$)$_2$ (labeled as [Fe^{II}(**L-9**)(OH$_2$)]$^{2+}$), and Fe^{II}(H$_2$O)$_6$(BF$_4$)$_2$ as reference.*

387
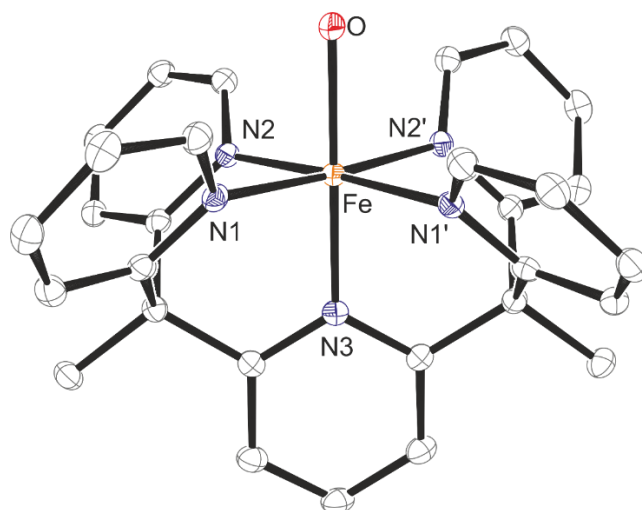
*Figure 221: Graphical representation of the cation [Fe^{II}(OH$_2$)(**L-1**)]$^{2+}$ in **C-2**. Reproduced from Chantarojsiri* et al. *for comparison.*
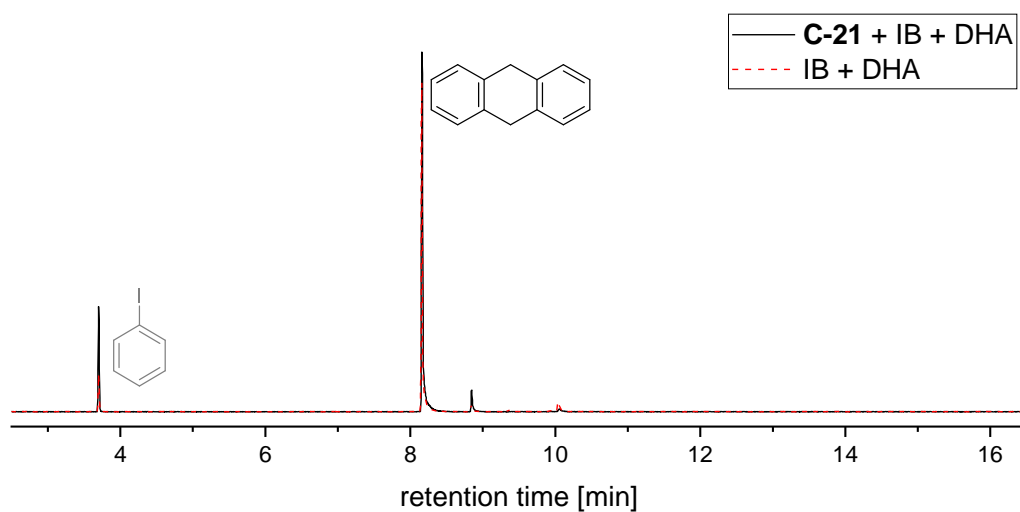
*Figure 222: GC-MS trace of the reaction of **C-21** (formed in situ from **C-20** + IB) with DHA in acetonitrile. GC-MS method **A**. Conditions: [**C-20**] = 5 mM, [IB] = 10 mM, DHA = 50 mM, MeCN, T = 25 °C.*
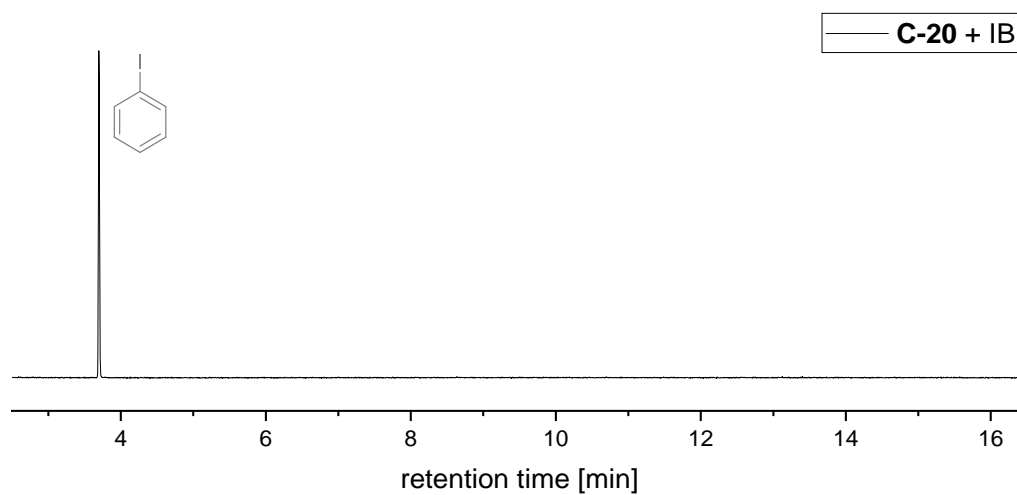
*Figure 223: GC-MS trace of the the reaction of **C-20** with IB in acetonitrile. GC-MS method **A**. The observed signal was assigned to iodobenzene based on comparison with the NIST2020 database. Conditions: [**C-20**] = 5 mM, [IB] = 10 mM, MeCN, T = 25 °C.*
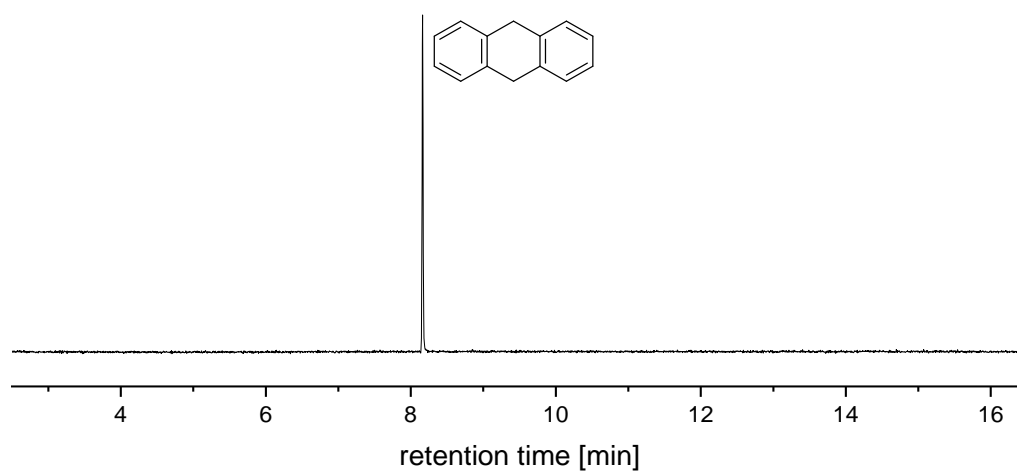
*Figure 224: GC-MS reference trace of DHA. GC-MS method **A**.*

5. Chapter VI – Additional Data and Spectra

General Procedure for HPDL Metabolite Samples

Samples were received as frozen solutions and thawed in water at room temperature. Subsequently, the pH was determined and acetic acid (as a 1:1 mixture with water) was added (15 µl per 3 ml *E. coli* sample or per 1 ml mammalian cell sample) which resulted in a decrease of the pH to ~4.5-5. To *E. coli* samples 1 ml of water and 4 ml of 3:1 dichloromethane:*iso*-propanol was added. To mammalian cell samples 1 ml of 3:1 dichloromethane:*iso*-propanol was added. The biphasic mixtures were then vigorously shaken and vortexed for 2 min. After 5 min, the layers were separated using a syringe and the organic layer dried off in a gentle stream of nitrogen. The samples were then placed under high vacuum for 40-60 min and derivatized using BSTFA: 400 µl acetonitrile/100 µl BSTFA for *E. coli* samples; 100 µl acetonitrile/50 µl BSTFA for mammalian cell samples. Subsequently the samples were injected onto the GC-MS instrument in splitless mode (1 µl, GC-MS method **C**, refer to p. 251).

Quantification Curves

Quantification curves were obtained by preparing samples of known amounts of **4-HBz**, **4-HB**, and **4-HPA** from stock solutions. These samples were then dried, derivatized with BSFTA (400 µl acetonitrile/100 µl BSTFA), and injected onto the GC-MS in splitless mode (1 µl, for details refer to page 251).

The corresponding values for slope m and y-axis section c were calculated from linear regression of the measured integral values and are given in Table 26.

*Table 26: Slope m and y-axis section c of quantification curves of **4-HBz**, **4-HB**, and **4-HPA**.*

	m	c
4-HBz	1.70×10^7	-8.33×10^4
4-HB	2.90×10^7	-3.24×10^5
4-HPA	2.08×10^7	-2.04×10^5

With these values, the amount of metabolite in each sample was calculated and then converted into the corresponding metabolite concentration depending of the amount used for the liquid/liquid extraction step (2-3 ml in *E. coli* samples, 1 ml in mammalian cell samples).

Subchapter 3: Metabolomics
HPDL Amino Acid Sequences

6.   **HPDL-WT [NP_116155]:**

MAAPALRLCHIAFHVPAGQPLARNLQRLFGFQPLASREVDGWRQLALRSGDAVFLVNE
GAGSGEPLYGLDPRHAVPSATNLCFDVADAGAATRELAALGCSVPVPPVRVRDAQGAA
TYAVVSSPAGILSLTLLERAGYRGPFLPGFRPVSSAPGPGWVSRVDHLTLACTPGSSPTLLR
WFHDCLGFCHLPLSPGEDPELGLEMTAGFGLGGLRLTALQAQPGSIVPTLVLAESLPGAT
TRQDQVEQFLARHKGPGLQHVGLYTPNIVEATEGVATAGGQFLAPPGAYYQQPGKER
QIRAAGHEPHLLARQGILLDGDKGKFLLQVFTKSLFTEDTFFLELIQRQGATGFGQGNIR
ALWQSVQEQ

7.   **HPDL-TM**

MGYRGPFLPGFRPVSSAPGPGWVSRVDHLTLACTPGSSPTLLRWFHDCLGFCHLPLSPG
EDPELGLEMTAGFGLGGLRLTALQAQPGSIVPTLVLAESLPGATTRQDQVEQFLARHKG
PGLQHVGLYTPNIVEATEGVATAGGQFLAPPGAYYQQPGKERQIRAAGHEPHLLARQGI
LLDGDKGKFLLQVFTKSLFTEDTFFLELIQRQGATGFGQGNIRALWQSVQEQ

8.   **HPDL>HMAS**

MAAPALRLCHIAFHVPAGQPLARNLQRLFGFQPLASREVDGWRQLALRSGDAVFLVNE
GAGSGEPLYGLDPRHAVPSATNLCFDVADAGAATRELAALGCSVPVPPVRVRDAQGAA
TYAVVSSPAGILSLTLLERAGYRGPFLPGFRPVSSAPGPGWVSRVDHLTLACTPGSSPTLLR
WFHDCLGFCHLPLSPGEDPELGLEMTAGFGLGGLRLTALQAQPGSIVPTLTLIESLPGAT
TRQDQVEQFLARHKGPGLQHVGLYTPNIVEATEGVATAGGQFLAPPGAYYQQPGKER
QIRAAGHEPHLLARQGILLDGDKGKFLLQVFTKSLFTEDTFFLELIQRQGATGFGQGNIR
ALYQSVQEQ

HPDL cDNA Sequences

1.   **HPDL-WT cDNA [NM_032756]**

ATGGCCGCGCCCGCCCTTCGTTTGTGCCACATCGCCTTCCACGTGCCCGCCGGGCAGCCCCTA
GCCCGGAACCTGCAGCGCCTCTTCGGCTTCCAGCCCCTGGCTTCGCGGGAGGTGGACGGCTG
GCGGCAGCTAGCCCTGCGCAGCGGCGACGCGGTCTTTTTGGTGAACGAGGGCGCAGGGTCTG
GAGAGCCGCTGTACGGCCTGGATCCGCGTCACGCCGTGCCCAGCGCCACAAACCTGTGCTTC
GACGTGGCGGACGCCGGCGCTGCAACCCGGGAGCTGGCAGCGCTGGGCTGCAGCGTGCCTGT
CCCTCCCGTTCGCGTGCGGGACGCGCAGGGTGCCGCCACTTACGCCGTGGTCAGCTCGCCTG
CCGGCATCCTCAGCCTGACCTTGCTGGAGCGCGCTGGCTACCGCGGACCCTTCCTACCCGGCT
TCAGGCCCGTGTCCTCTGCGCCTGGCCCCGGGTGGGTCAGCCGCGTGGACCACCTGACCTTG

GCCTGCACCCCCGGCAGCTCCCCCACACTTTTGCGCTGGTTCCACGACTGCCTGGGCTTTTGC
CACTTGCCGCTGAGCCCAGGTGAGGATCCCGAGCTGGGCCTCGAAATGACAGCAGGGTTTGG
GCTTGGGGGACTGAGGCTTACAGCCCTGCAGGCCCAGCCGGGCAGCATTGTCCCCACTCTTGT
TCTGGCTGAGTCCCTTCCGGGGGCGACGACACGACAGGACCAGGTGGAGCAGTTCCTGGCCC
GGCACAAGGGGCCAGGCCTGCAGCACGTGGGGCTGTATACGCCTAACATTGTGGAGGCCACT
GAGGGGGTGGCAACTGCTGGAGGCCAGTTCCTGGCTCCCCCTGGGGCATACTACCAGCAGCC
AGGAAAGGAGAGGCAGATCCGAGCTGCAGGGCACGAGCCTCATCTGCTTGCTCGACAGGGGA
TCCTGCTAGATGGTGATAAAGGCAAGTTTCTGCTTCAGGTCTTCACCAAGTCCCTTTTTACTG
AGGACACTTTCTTCCTGGAGCTGATTCAGAGGCAGGGGGCCACTGGCTTTGGTCAGGGCAAC
ATCAGAGCTCTGTGGCAGTCCGTACAGGAGCAATCTGCCAGGAGCCAGGAAGCCTAA

2. HPDL-CodOpt[328]

ATGGCAGCACCGGCACTGCGTCTGTGTCATATTGCATTTCATGTTCCGGCAGGTCAGCCGCTG
GCACGTAATCTGCAGCGTCTGTTTGGTTTTCAGCCTCTGGCAAGCCGTGAAGTTGATGGTTGG
CGTCAGCTGGCCCTGCGTAGCGGTGATGCAGTTTTTCTGGTTAATGAAGGTGCAGGTAGTGGT
GAACCGCTGTATGGTCTGGACCCTCGTCATGCAGTTCCGAGCGCAACCAATCTGTGTTTTGAT
GTTGCAGATGCGGGTGCAGCAACCCGTGAACTGGCAGCACTGGGTTGTAGCGTTCCGGTTCC
GCCTGTTCGTGTTCGTGATGCACAGGGTGCAGCCACCTATGCAGTTGTTAGCTCACCGGCAGG
TATTCTGAGCCTGACCCTGCTGGAACGTGCAGGTTATCGTGGTCCGTTTCTGCCTGGTTTTCG
TCCGGTTAGCAGCGCACCGGGTCCGGGTTGGGTTAGCCGTGTTGATCATCTGACCCTGGCATG
TACACCGGGTAGCAGCCCGACACTGCTGCGTTGGTTTCATGATTGTCTGGGTTTTTGTCATCT
GCCGCTGAGTCCGGGTGAAGATCCGGAACTGGGTCTGGAAATGACCGCAGGTTTTGGTCTGG
GTGGTCTGCGTCTGACCGCACTGCAGGCACAGCCTGGTAGCATTGTTCCGACCCTGGTTCTGG
CAGAAAGCCTGCCTGGTGCAACCACCCGTCAGGATCAGGTTGAACAGTTTCTGGCACGTCATA
AAGGTCCGGGTCTGCAGCATGTTGGTCTGTATACCCCGAATATTGTTGAAGCAACCGAAGGTG
TTGCAACCGCAGGCGGTCAGTTCCTGGCACCTCCGGGTGCATATTATCAGCAGCCAGGTAAAG
AACGCCAGATTCGTGCAGCAGGTCATGAACCTCATCTGCTGGCACGCCAGGGTATTCTGCTGG
ATGGTGATAAAGGTAAATTTCTGCTGCAGGTCTTTACCAAAAGCCTGTTTACCGAAGATACCT
TTTTTCTGGAACTGATTCAGCGTCAGGGTGCAACCGGTTTTGGCCAGGGTAATATTCGTGCAC
TGTGGCAGAGCGTTCAAGAACAGAGCGCACGTAGCCAAGAAGCATAA

GC-MS Traces
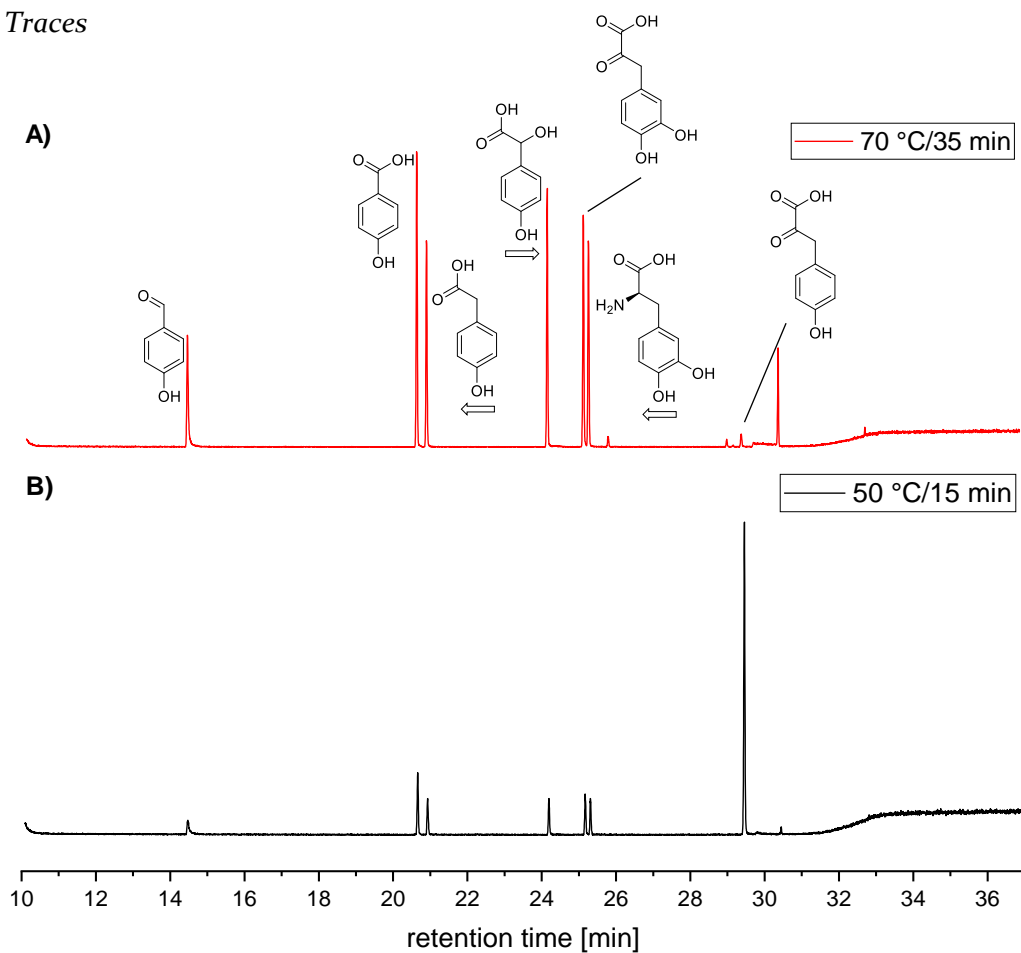
*Figure 225: Comparison of two conditions for derivatization: **A)** 35 min at 70 °C. **B)** 15 min at 50 °C.*
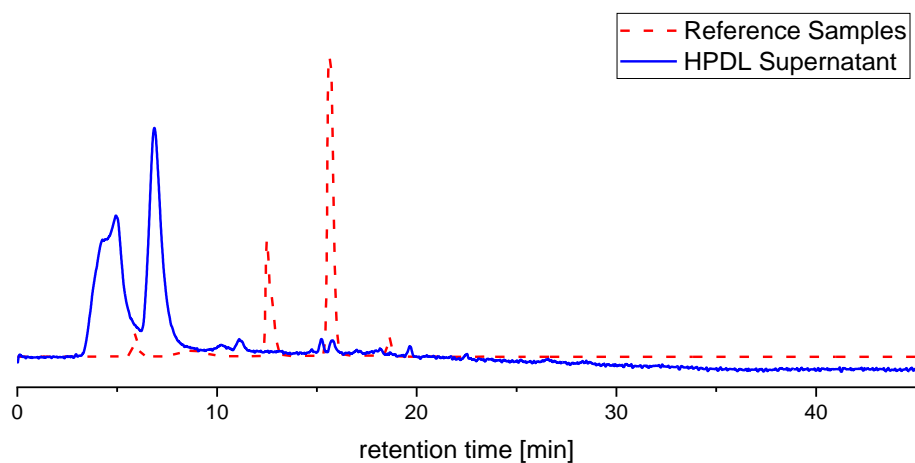
Figure 226: HPLC trace of supernatant collected from an E. coli *culture transfected with* HPDL *(blue solid trace) a mixture of the HPDL metabolites **4-HBz, 4-HB, 4-HPA, S-HMA,** and **4-HPP** (red dashed trace).*
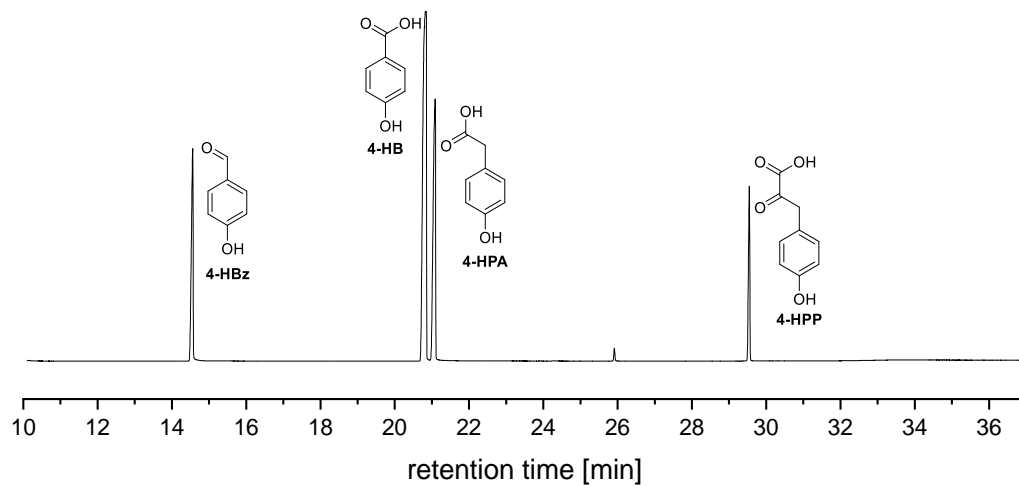
*Figure 227: Excerpt of a GC-MS trace of selected HPDL metabolites (from left to right): **4-HBz, 4-HB, 4-HPA, and 4-HPP**.*
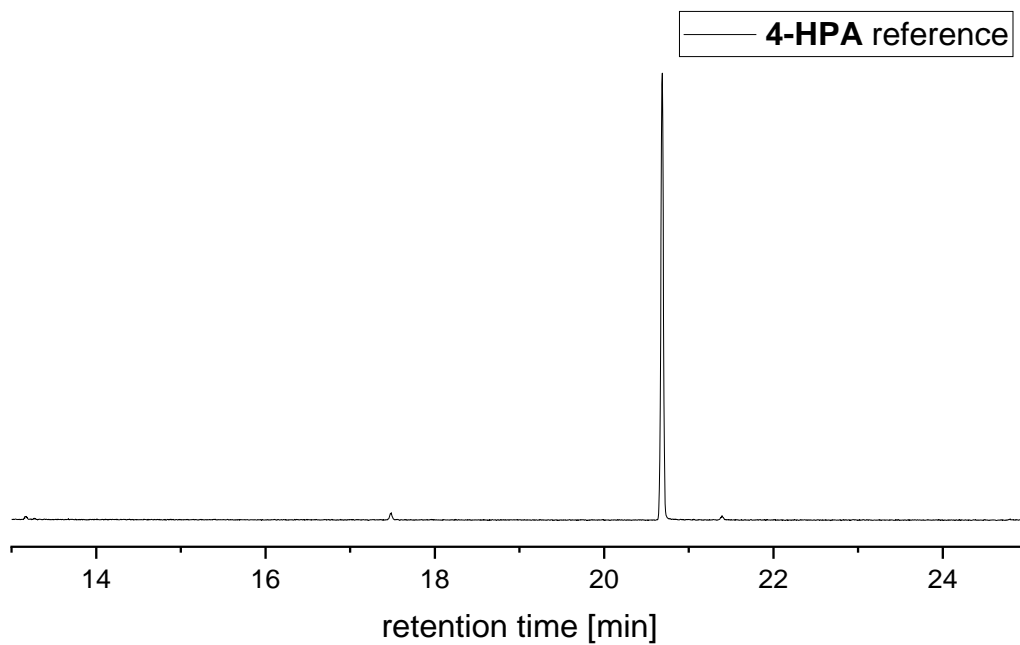
*Figure 228: Excerpt of a reference GC-MS trace of **4-HPA**.*
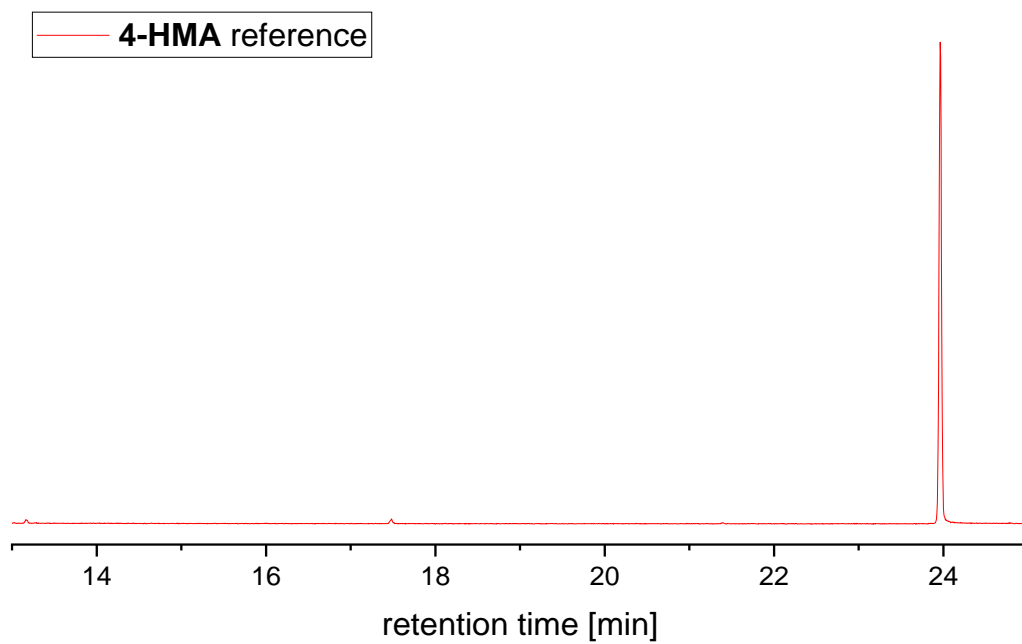
*Figure 229: Excerpt of a reference GC-MS trace of **4-HMA**.*
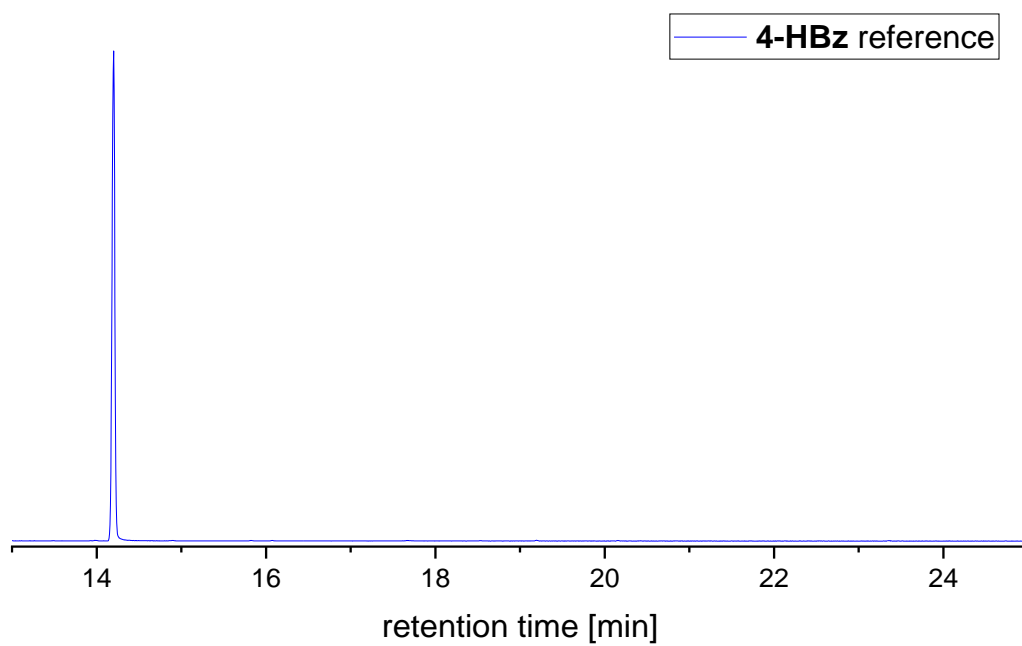
*Figure 230: Excerpt of a reference GC-MS trace of **4-HBz**.*
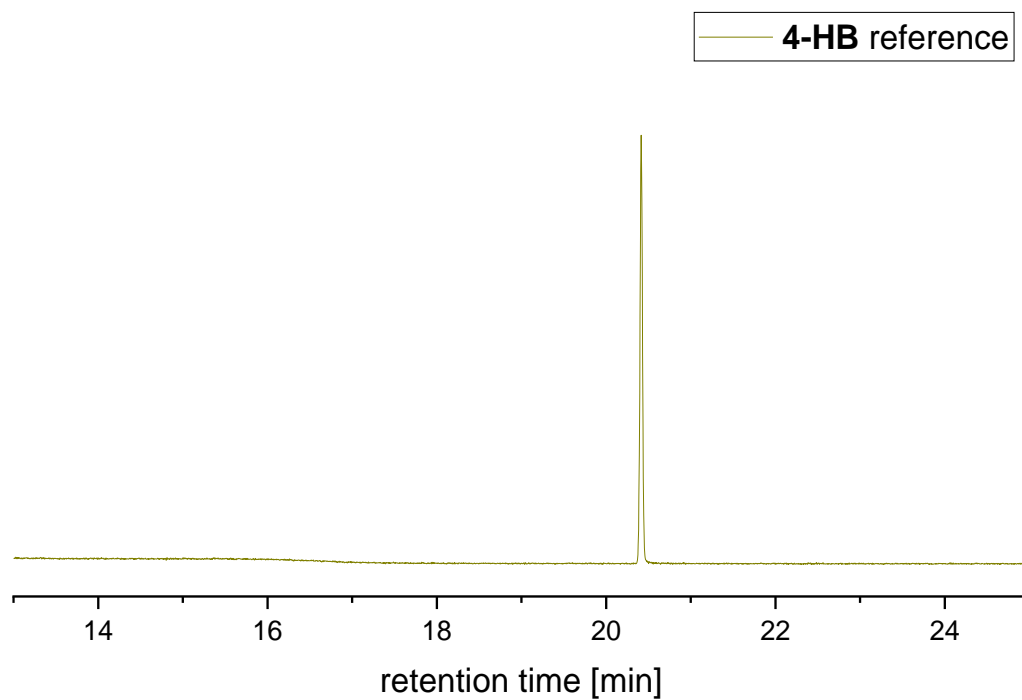
*Figure 231: Excerpt of a reference GC-MS trace of **4-HB**.*

EI MS Reference Spectra
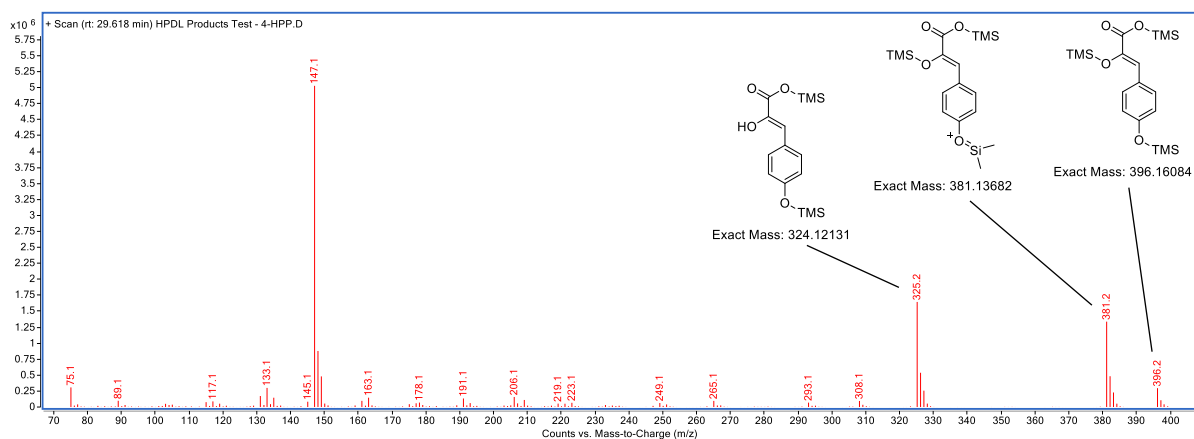
*Figure 232: EI MS spectrum of **TMS-4-HPP**.*
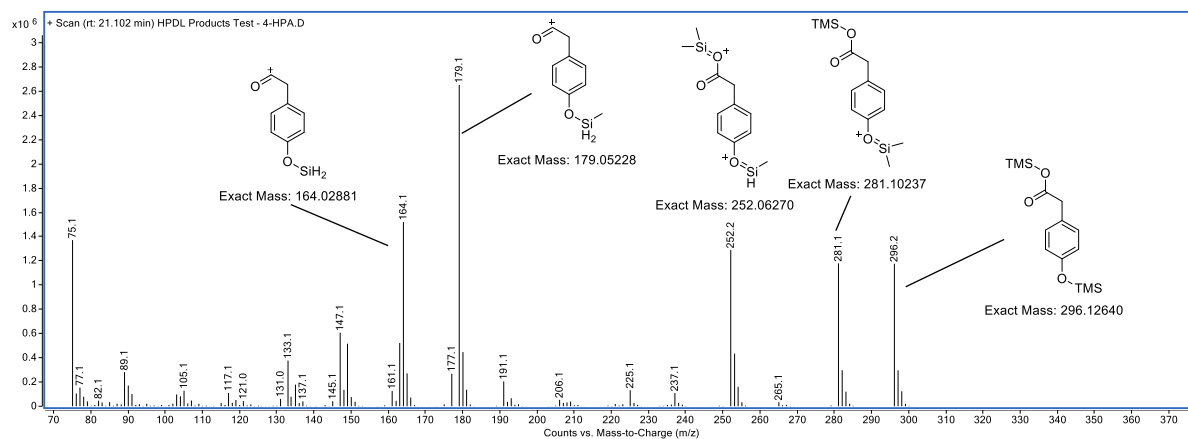
*Figure 233: EI MS spectrum of **TMS-4-HPA**.*
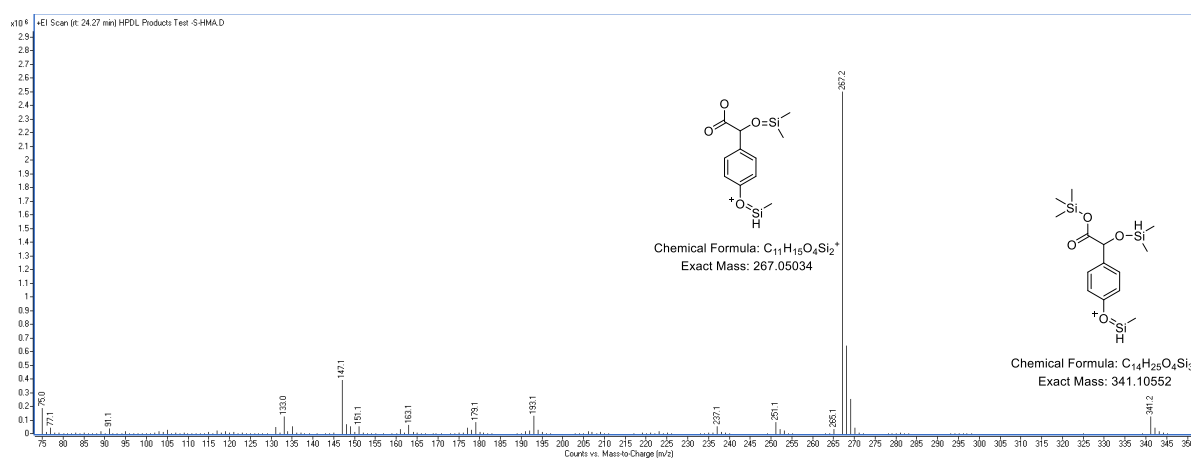
*Figure 234: EI MS spectrum of **TMS-4-HMA**.*
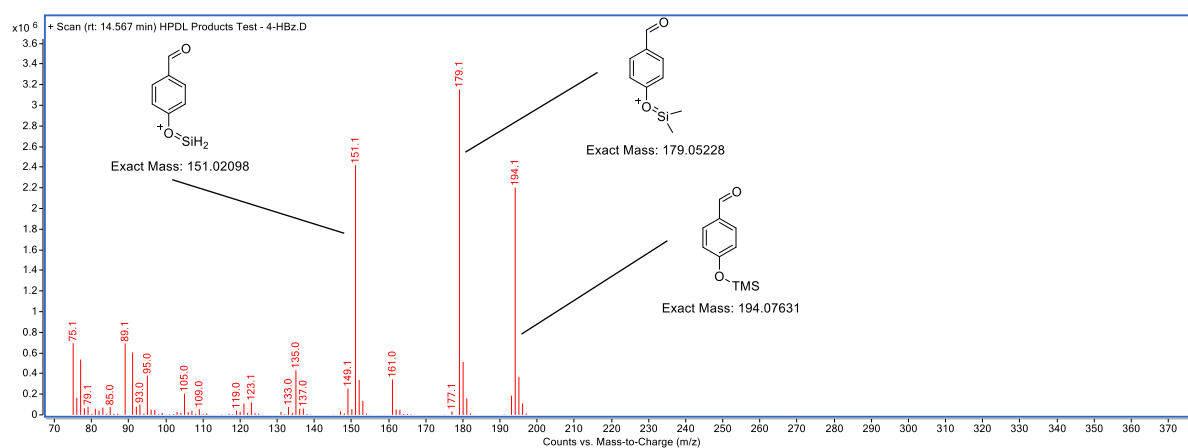
*Figure 235: EI MS spectrum of **TMS-4-HBz**.*

397
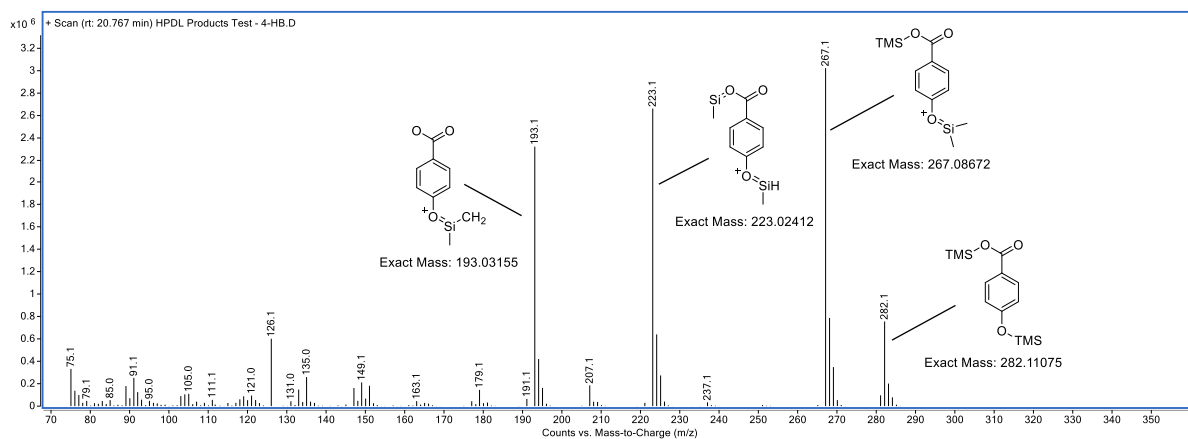
*Figure 236: EI MS spectrum of **TMS-4-HB**.*

Additional GC-MS Traces
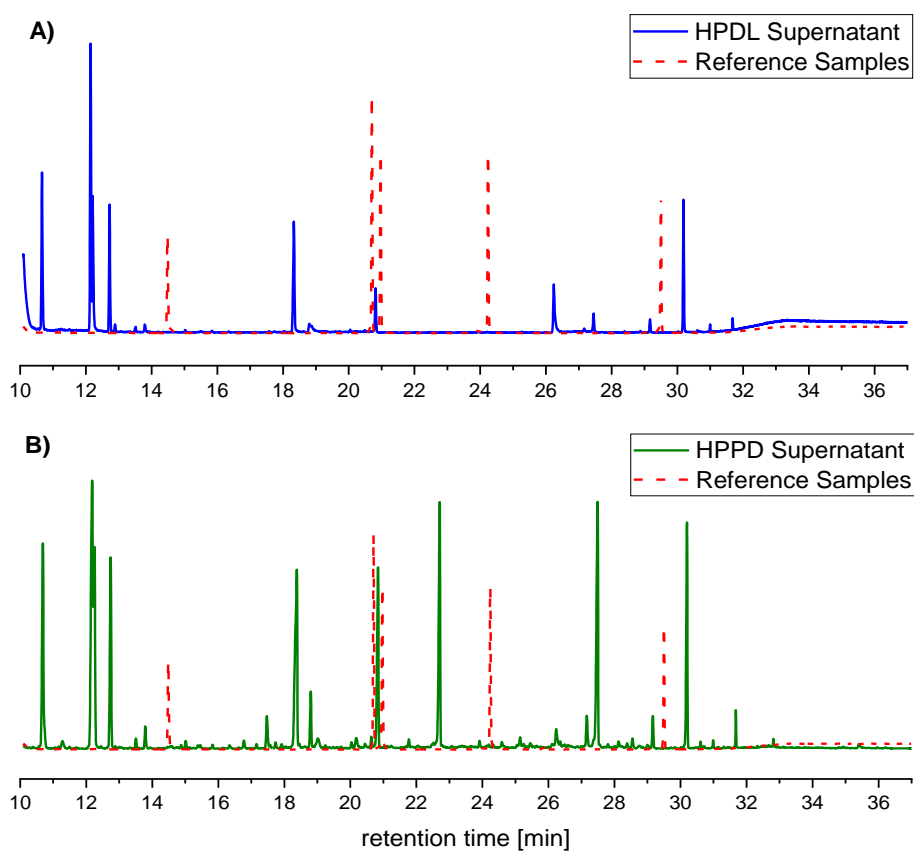
*Figure 237: **A**) GC-MS trace of the dried, derivatized supernatant of* E. coli *cultures with transformed* HPDL *(solid blue trace) compared to a trace of reference samples (dashed red trace). **B**) GC/MS trace of dried, derivatized supernatant of* E. coli *cultures with transfformed* HPPD *(solid green trace) compared to a trace of reference samples (dashed red trace). Reference samples are indicated in both traces.*
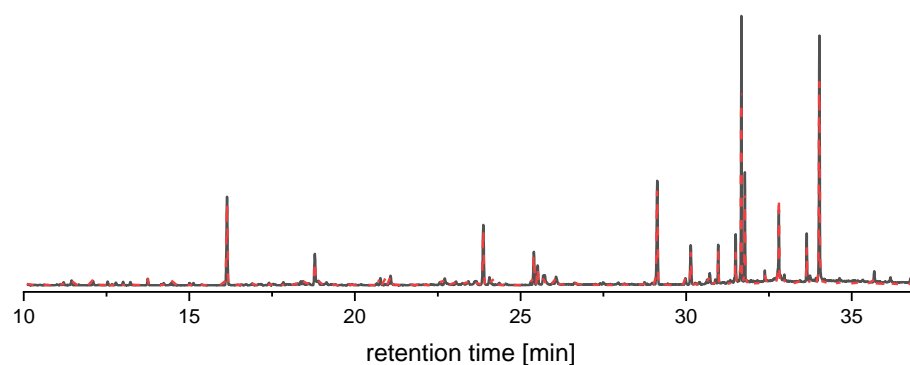
*Figure 238: GC-MS trace directly obtained from an extract of cell cultures (black solid trace) and the same extract that was spiked with an acetonitrile solution of derivatized **4-HBz**, **4-HB**, and **4-HPA** (red dashed trace).*

Isotope Labelling Experiments – EI MS Spectra
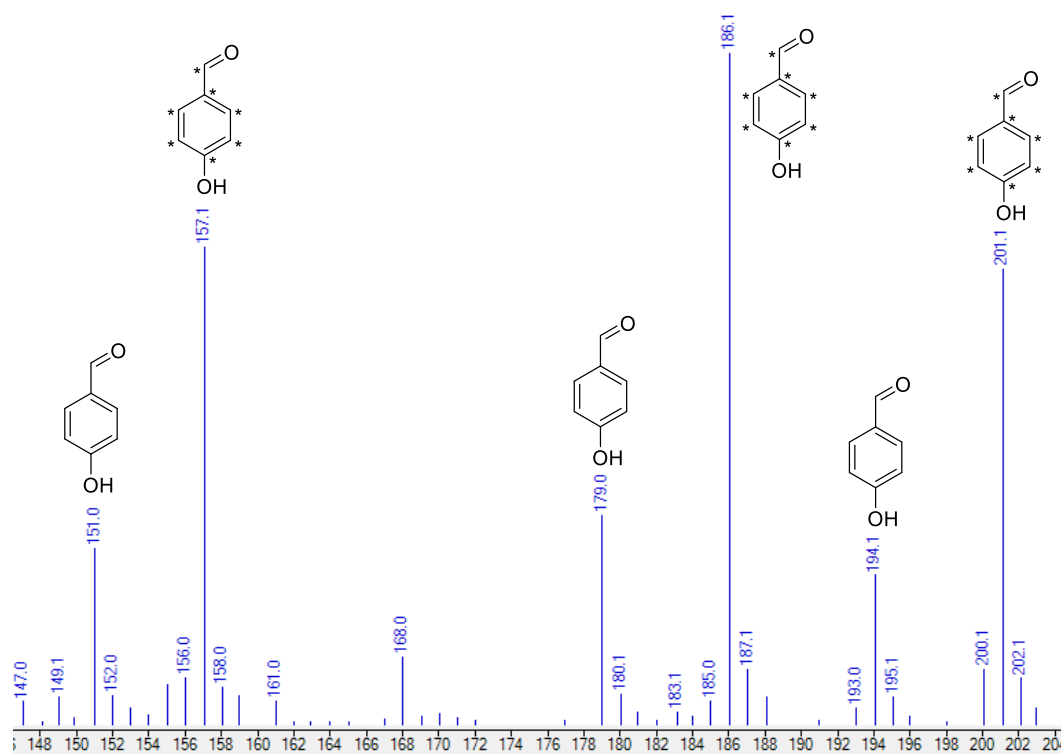
*Figure 239: EI MS spectrum at the retention time assigned to **4-HBz** of a sample collected from E. coli cultures transformed with HPDL that were fed isotopically labeled tyrosine. Parent structures of the observed peaks are shown, assignments are tentative.*
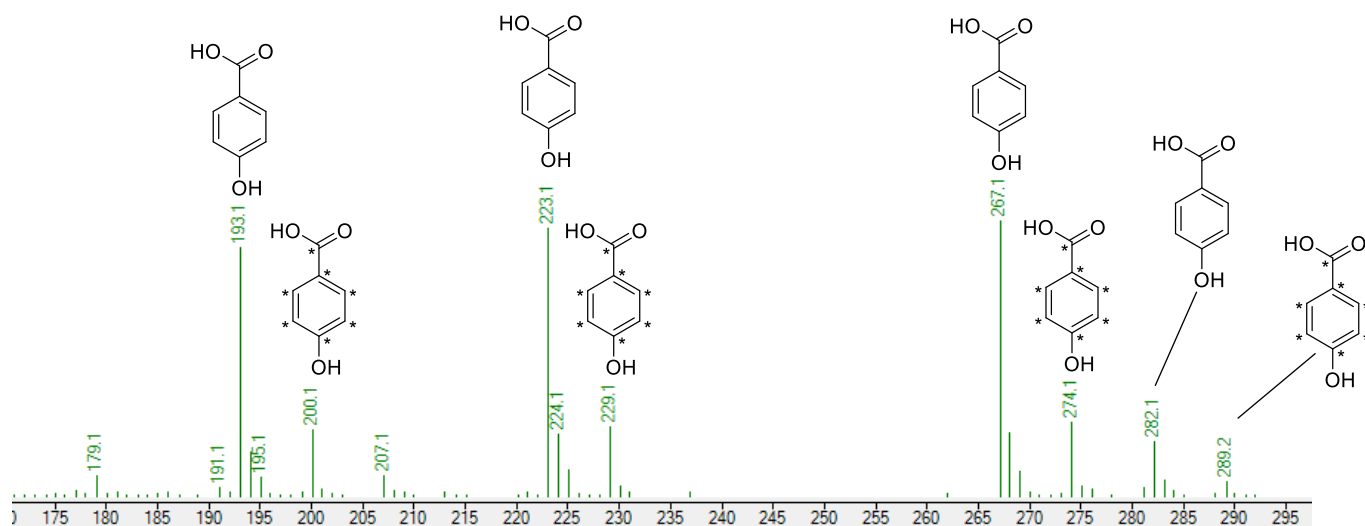
Figure 240: EI MS spectrum at the retention time assigned to **4-HB** of a sample collected from E. coli *cultures transformed with* HPDL *that were fed isotopically labeled tyrosine. Parent structures of the observed peaks are shown, assignments are tentative.*
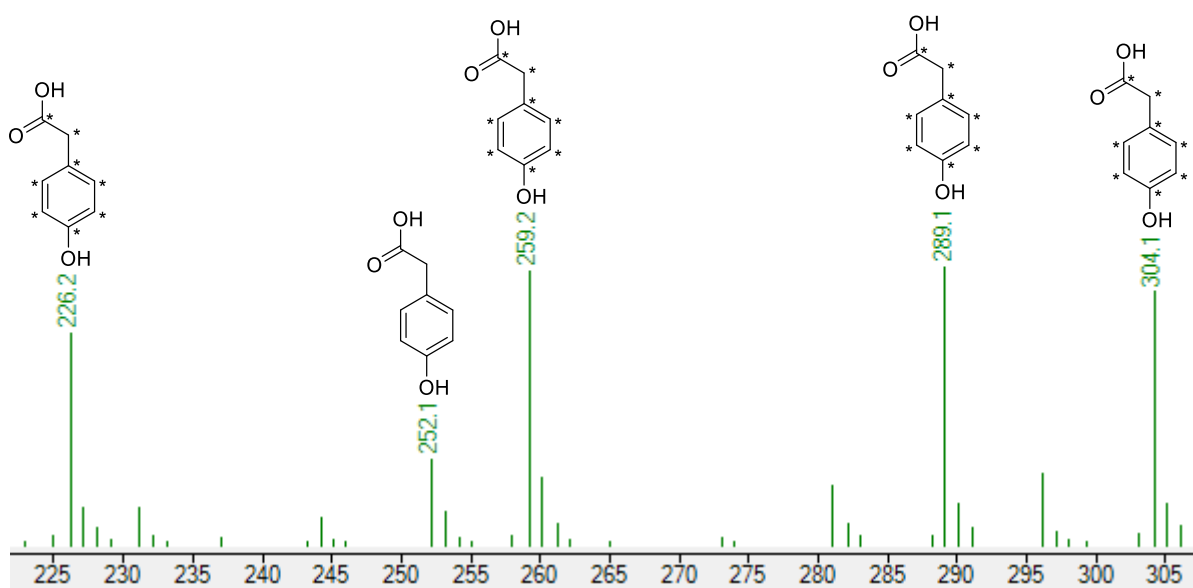
Figure 241: EI MS spectrum at the retention time assigned to **4-HPA** of a sample collected from E. coli *cultures transformed with* HPDL *that were fed isotopically labeled tyrosine. Parent structures of the observed peaks are shown, assignments are tentative.*

HPDL Metabolite Quantification in Mammalian Cells
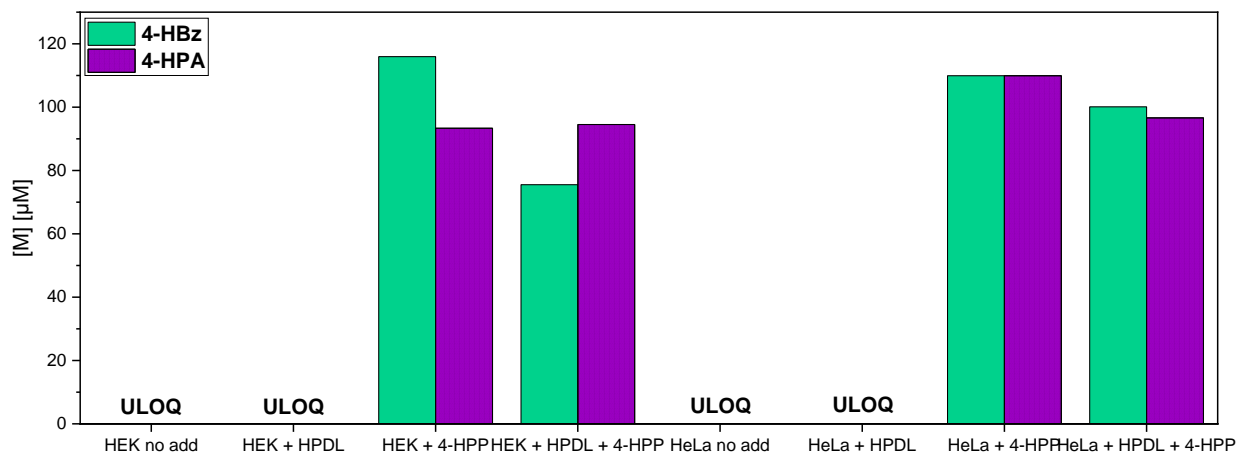
Figure 242: Comparison of detected metabolite levels (**4-HBz** (green) and **4-HPA** (violet, dotted)) in supernatant samples obtained from HEK and HeLa cell samples. The mitochondria of these cells were then isolated and incubated without additives ("cell type *no add*"), the cells transfected with additional HPDL *and the mitochondria isolated* ("cell type *+ HPLD*"), the mitochondria isolated incubated with [**4-HPP**] = 2.5 mM ("cell type *+ 4-HPP*"), or the cells transfected with additional HPDL, mitochondria isolated, and incubated with [**4-HPP**] = 2.5 mM ("cell type *+ HPDL + 4-HPP*"). Tissue preparation, incubation, and collection of supernatants performed by Dr. Rolf Stucka.
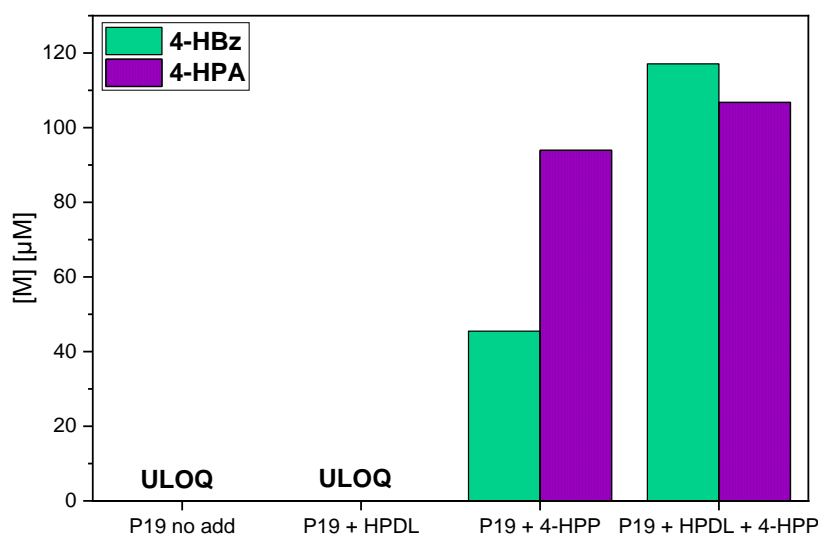
Figure 243: Comparison of detected metabolite levels (**4-HBz** (green) and **4-HPA** (violet, dotted)) in supernatant samples obtained from P19 cell samples. The mitochondria of these cells were then isolated and incubated without additives ("P19 no add"), the cells transfected with additional HPDL *and the mitochondria isolated* ("P19 + HPLD"), the mitochondria isolated incubated with [**4-HPP**] = 2.5 mM ("P19 + 4-HPP"), or the cells transfected with additional HPDL, mitochondria isolated, and incubated with [**4-HPP**] = 2.5 mM ("P19 + HPDL + 4-HPP"). Tissue preparation, incubation, and collection of supernatants performed by Dr. Rolf Stucka.

Structural Modelling
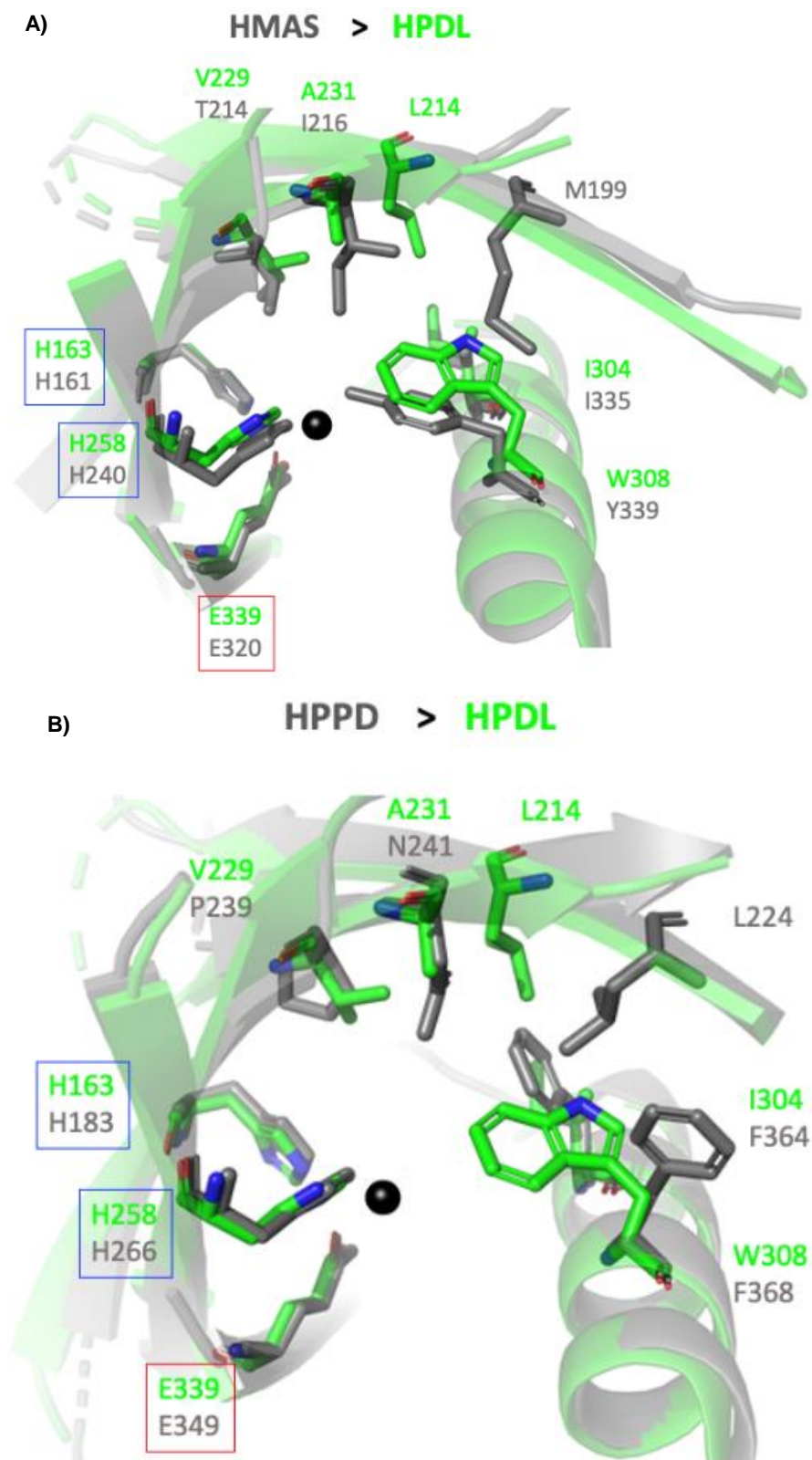
*Figure 244: Overlay of visual representations of the active site cavities of **A**) HMAS (PDB: 2R5V) and a hypothetic structure of HPDL as well as **B**) human HPPD (PDB: 5EC3) and a hypothetical structure of HPDL. The human HPPD, HPDL and HMAS structures are shown as ribbon diagrams. Previously identified structural aspects, such as the active binding groove formed by a single helix carrying the aromatic residues and the shielding antiparallel five β-sheets are shown as ribbon diagrams. Structural calculations performed by Dr. Britta Möhl, Institute of Virology, Technical University of Munich.*

The structural views of HPPD (PDB: 5EC3),[383] and HMAS (PDB: 2R5V)[315] were generated using PyMOL Molecular Graphics System, Version 2.0 (Schrödinger, LLC).

The gene sequences of HPPD, HPDL and HMAS were aligned using T-Coffee Expresso (http://tcoffee.crg.cat/apps/tcoffee/do:expresso),[330] including the PDB files of HPPD (5EC3) and HMAS (2R5V). The homology modelling of human HPDL were generated using SWISS-MODEL program.[329]

Mouse Cells

Two male mice, C57BI6/J, birth date 02.05.2021, 12 weeks of age at time of death, were used as cell donors. The mice were dissected by Dr. Rolf Stucka, the obtained cells then homogenized for 10 min, then treated with the QProteome-Kit by Quiagen, the mitochondria isolated and incubated in mitochondria storage buffer with **4-HPP** at 37 °C for 1 h. The cells were then centrifuged (14.000 rpm) and the supernatants collected. These were then treated as described above (p. 390).

Subchapter 4: Bioinorganic Model Complex Studies
General Procedure for Reactions of HPDL Metabolites with Iron Complexes or Iron Salts

A scintillation vial was charged with the required amount of a stock solution of the respective HPDL metabolite so that a final concentration of 2 mM was reached. The required amount of a stock solution of the respective iron complex or iron salt was added and the mixture stirred for 30 min. Then, the mixture was filtered through a plug of silica (1.5 ml in a 3 ml syringe, refer to Figure 245, p. 404 for a graphical representation of the setup), lyophilized, derivatized using BSTFA (400 μl acetonitrile, 100 μl BSTFA, 40 °C, 60 min), and injected onto a GC-MS (1 μl in splitless mode, GC-MS method **C**, 251).

Inert Gas Procedure

Experiments that were handled under inert gas atmosphere (N_2) were prepared in a glove box (operated in wet box mode). Filtering of the samples through silica was performed outside of the glove box, therefore, the work-up procedure described above had to be modified. To this end, a tube was connected to the syringe containing the silica. This tube was then also connected to a second flask that was filled with nitrogen to serve as surge tank. This second flask was then connected to a nitrogen supply line.

The apparatus was flushed with nitrogen for at least 10 min prior to working up the sample. Then, the sample was injected onto the silica and tube connected as fast as possible. Subsequently, negative pressure was applied through the vacuum line to filter the sample through the silica

plug. 3 ml degassed MilliQ grade water were then added to wash the remainder of the sample through the silica plug. Now, the flask containing the filtered sample was disconnected from the apparatus and the sample lyophilized and treated as described above.
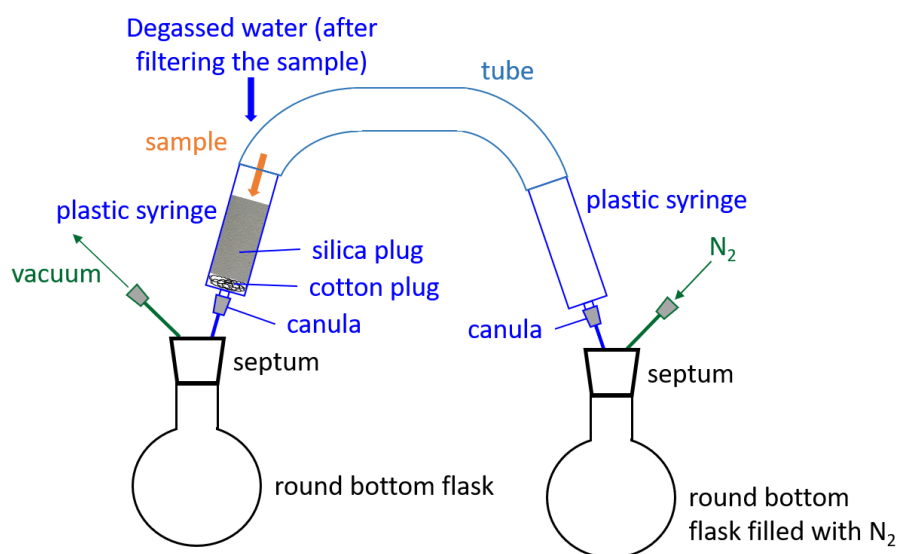
Figure 245: Graphical representation of the work-up procedure used for samples that were handled under inert gas atmosphere (N_2).

Table 27: Reaction conditions of the conducted experiments under ambient conditions.

No.	Components [mM]						
	[4-HPA]	[4-HMA]	[4-HBz]	[4-HB]	C-6	C-4	C-1
1	2	-	-	-	4	-	-
2	-	2	-	-	4	-	-
3	-	-	2	-	4	-	-
4	2	-	-	-	-	4	-
5	-	2	-	-	-	4	-
6	-	-	2	-	-	4	-
7	2	-	-	-	-	-	4
8	-	2	-	-	-	-	4
9	-	-	2	-	-	-	4
10	2	-	-	-	-	-	-
11	-	2	-	-	-	-	-
12	-	-	2	-	-	-	-
13	-	-	-	2	4	-	-
14	-	-	-	2	-	4	-
15	-	-	-	2	-	-	4

Table 28: Reaction conditions of the conducted experiments under exclusion of O_2.

No.	Components [mM]					
	[4-HPA]	[4-HMA]	[4-HBz]	Fe(mecn)$_2$(OTf)$_2$	Fe(OTf)$_3$	C-4
16	2	-	-	4	-	-
17	-	2	-	4	-	-
18	-	-	2	4	-	-
19	2	-	-	-	4	-
20	-	2	-	-	4	-
21	-	-	2	-	4	-
22	2	-	-	-	-	4
23	-	2	-	-	-	4
24	-	-	2	-	-	4

GC-MS Traces
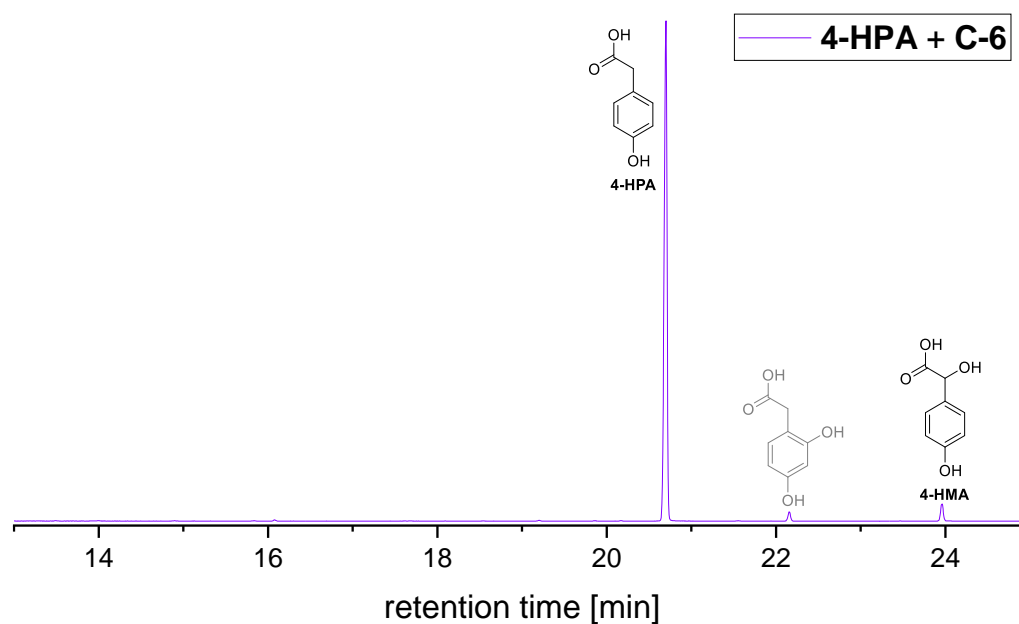
*Figure 246: Excerpt of the GC-MS trace of the reaction of **4-HPA** with **C-6** (Reaction **1**). GC-MS method **C**. Conditions: [**4-HPA**] = 2 mM, [**C-6**] = 4 mM, H_2O, 24 °C, t = 30 min. Assignment of the signal at a retention time of 22.1 min to 2-(2,4-hydroxyphenyl)acetic acid was based on comparison with the NIST 2020 database.*
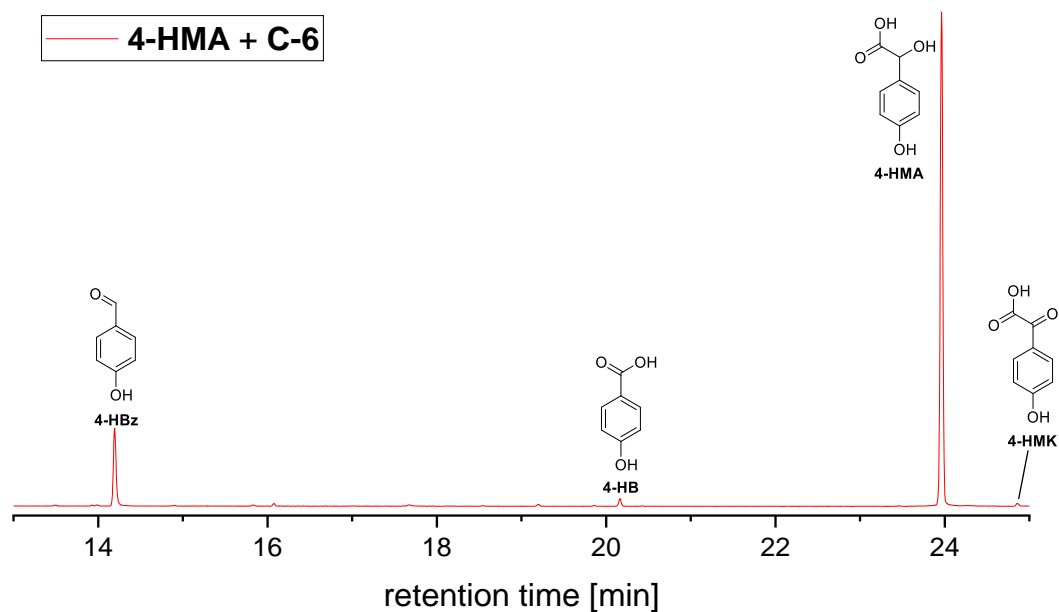
*Figure 247: Excerpt of the GC-MS trace of the reaction of **4-HMA** with **C-6** (Reaction **2**). GC-MS method **C**. Conditions: [**4-HMA**] = 2 mM, [**C-6**] = 4 mM, H₂O, 24 °C, t = 30 min. For a reference spectrum of **4-HMK** refer to p. 416.*
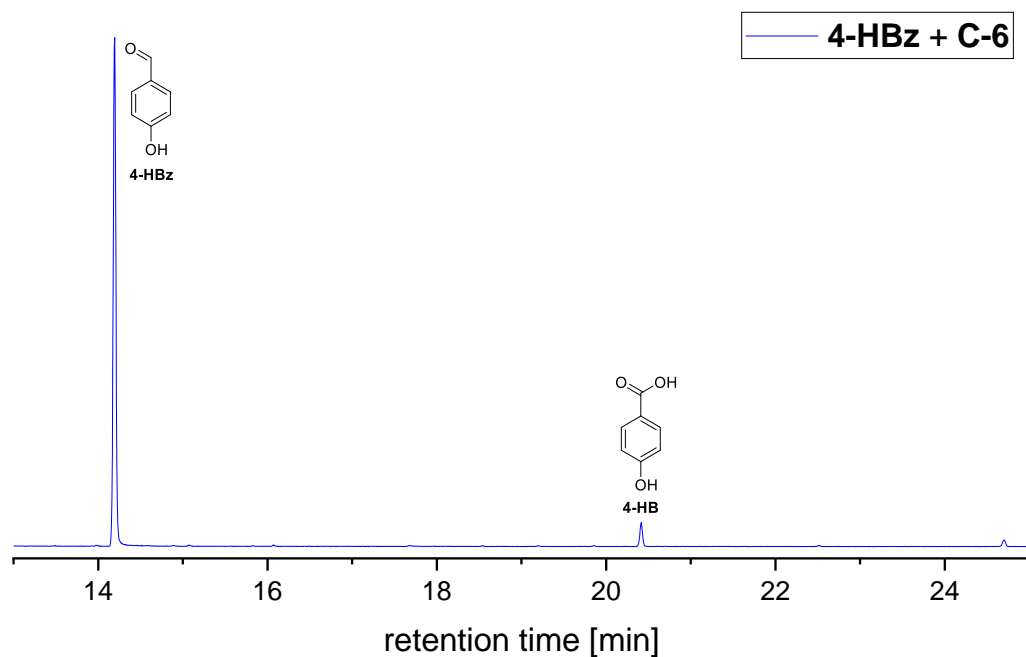
*Figure 248: Excerpt of the GC-MS trace of the reaction of **4-HBz** with **C-6** (Reaction **3**). GC-MS method **C**. Conditions: [**4-HBz**] = 2 mM, [**C-6**] = 4 mM, H₂O, 24 °C, t = 30 min.*
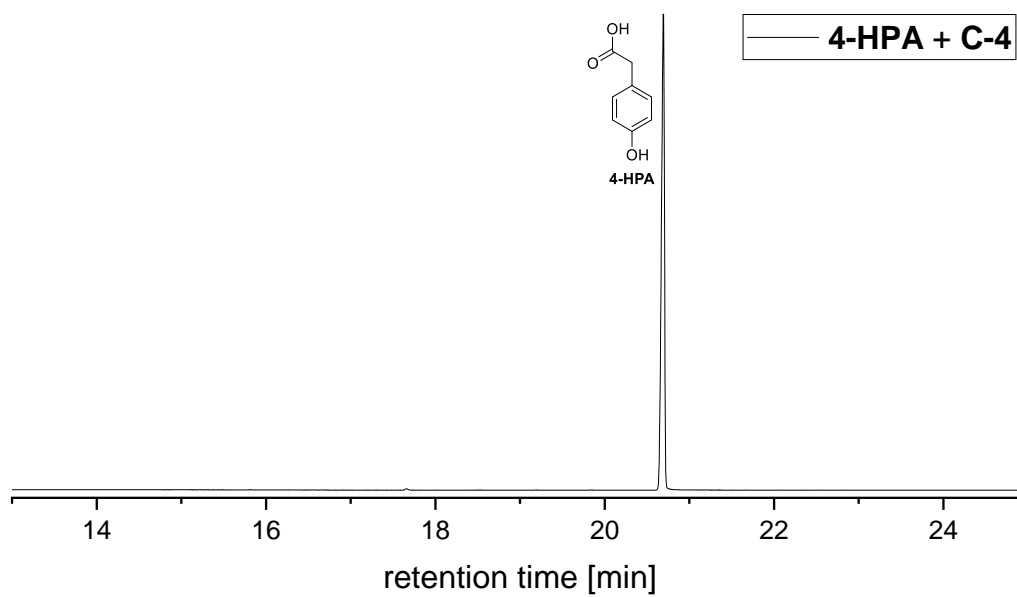
*Figure 249: Excerpt of the GC-MS trace of the reaction of **4-HPA** with **C-4** (Reaction **4**). GC-MS method **C**. Conditions: [**4-HPA**] = 2 mM, [**C-4**] = 4 mM, H₂O, 24 °C, t = 30 min.*
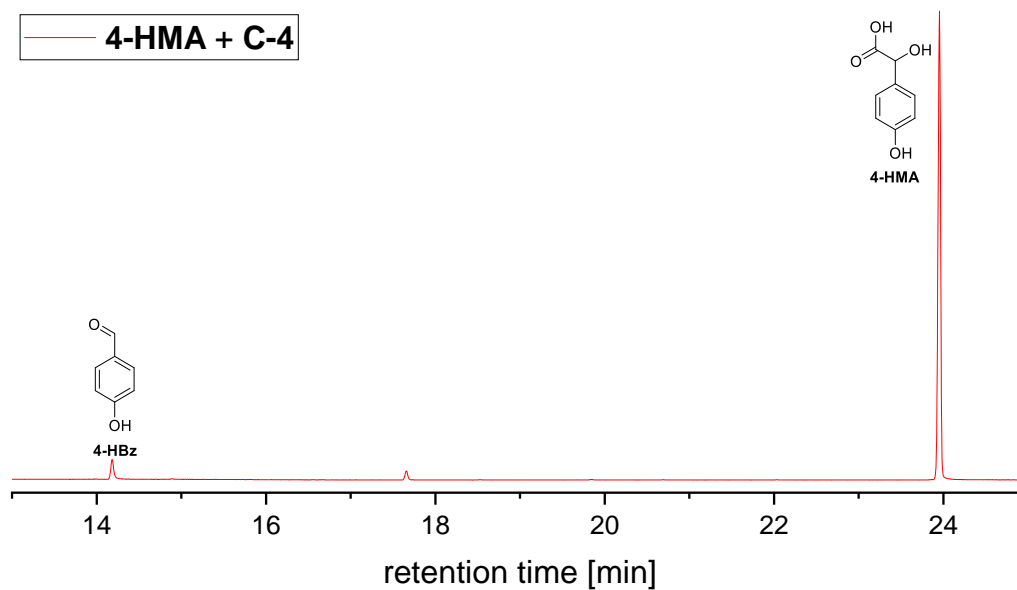
*Figure 250: Excerpt of the GC-MS trace of the reaction of **4-HMA** with **C-4** (Reaction **5**). GC-MS method **C**. Conditions: [**4-HMA**] = 2 mM, [**C-4**] = 4 mM, H₂O, 24 °C, t = 30 min.*
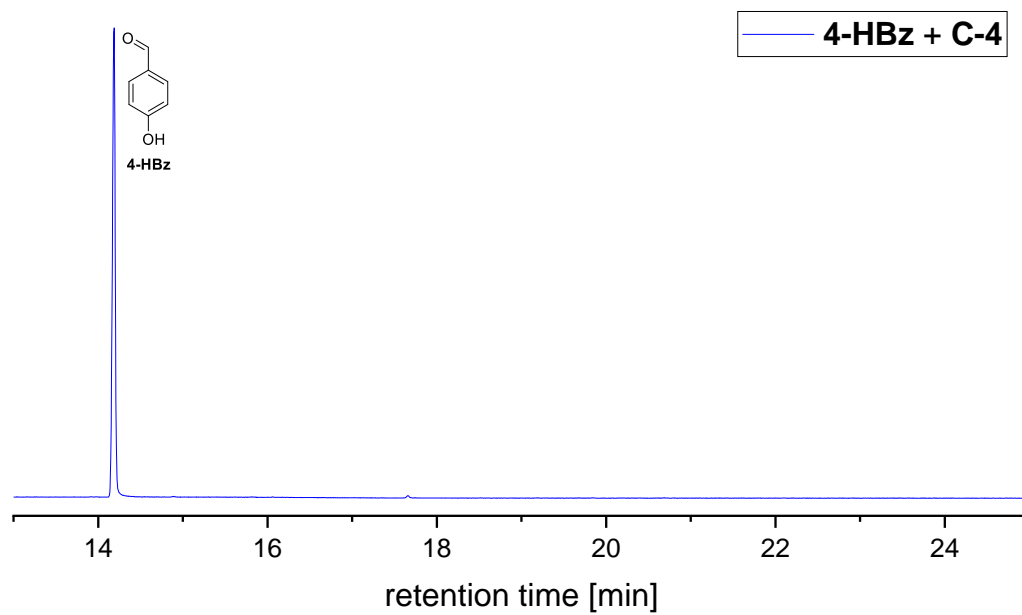
*Figure 251: Excerpt of the GC-MS trace of the reaction of **4-HBz** with **C-4** (Reaction **6**). GC-MS method **C**. Conditions: [**4-HBz**] = 2 mM, [**C-4**] = 4 mM, H₂O, 24 °C, t = 30 min.*
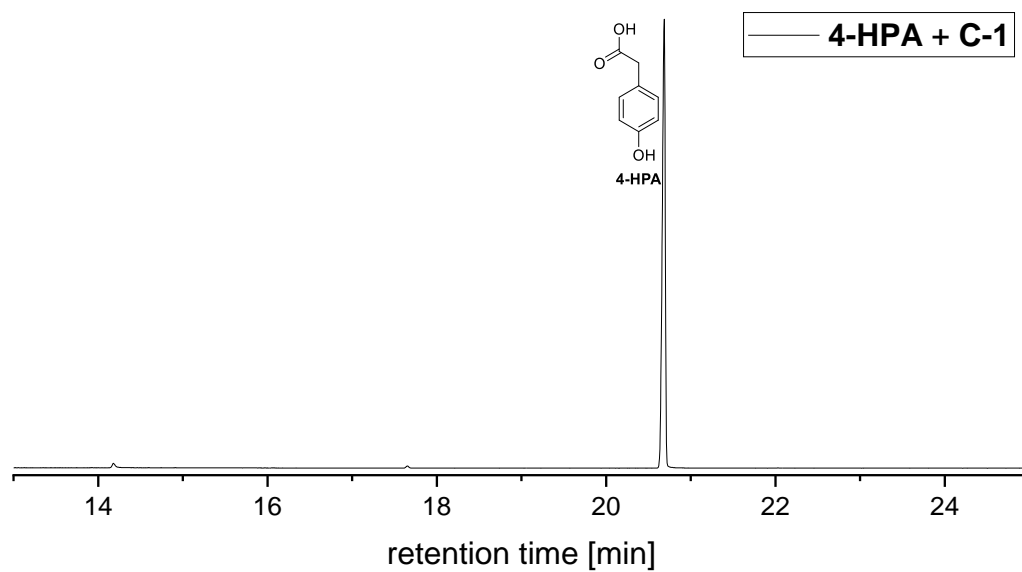
*Figure 252: Excerpt of the GC-MS trace of the reaction of **4-HPA** with **C-1** (Reaction **7**). GC-MS method **C**. Conditions: [**4-HPA**] = 2 mM, [**C-1**] = 4 mM, H₂O, 24 °C, t = 30 min.*
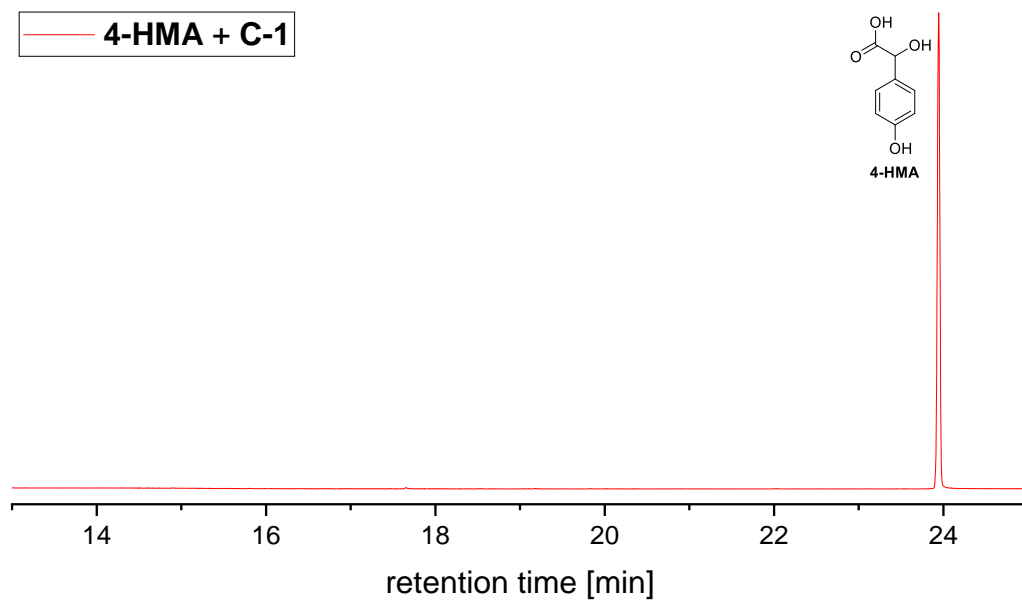
*Figure 253: Excerpt of the GC-MS trace of the reaction of **4-HMA** with **C-1** (Reaction **8**). GC-MS method **C**. Conditions: [**4-HMA**] = 2 mM, [**C-1**] = 4 mM, H$_2$O, 24 °C, t = 30 min.*
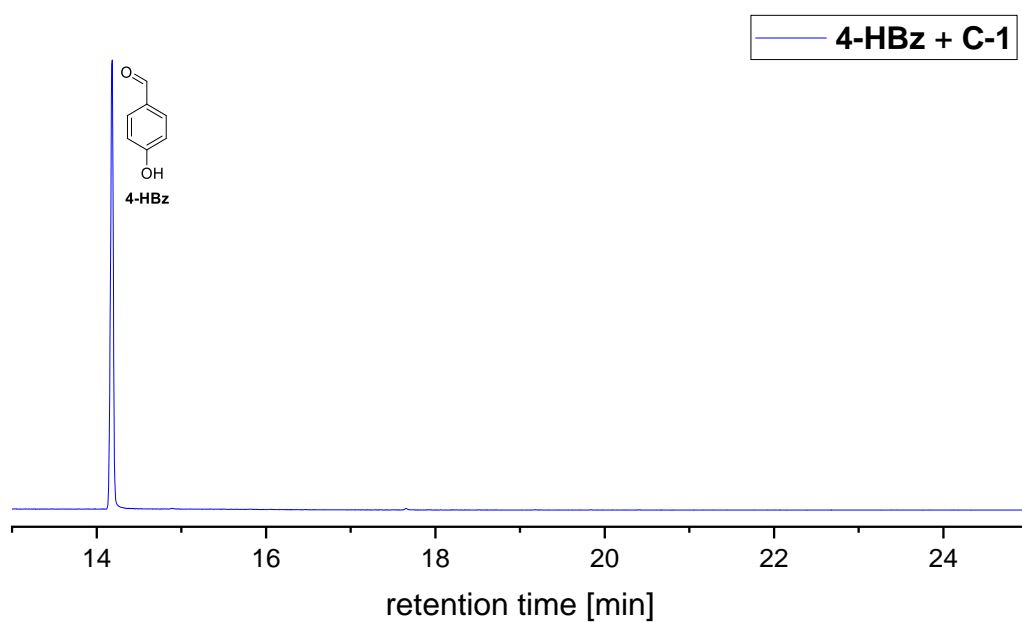
*Figure 254: Excerpt of the GC-MS trace of the reaction of **4-HBz** with **C-1** (Reaction **9**). GC-MS method **C**. Conditions: [**4-HBz**] = 2 mM, [**C-1**] = 4 mM, H$_2$O, 24 °C, t = 30 min.*
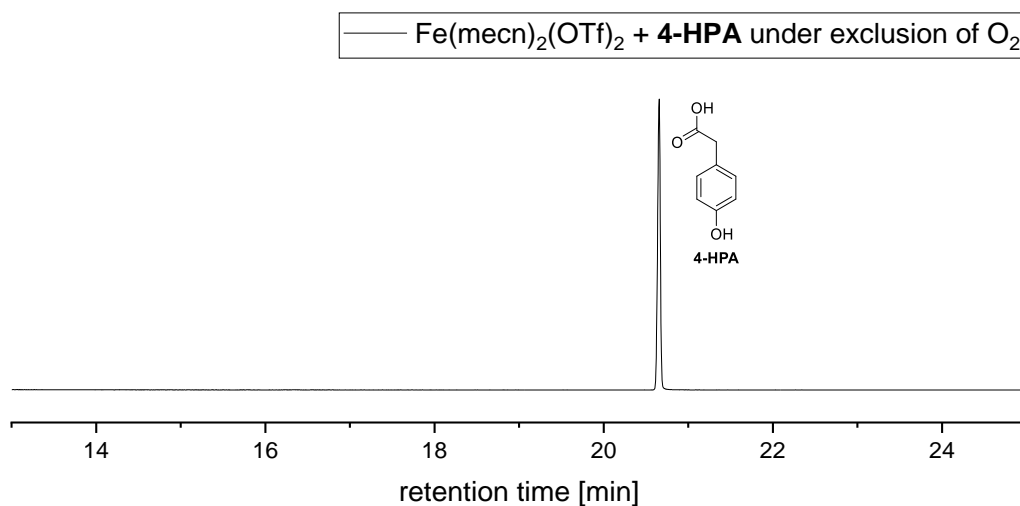
*Figure 255: Excerpt of the GC-MS trace of the reaction of **4-HPA** with Fe(mecn)₂(OTf)₂ (Reaction **16**). GC-MS method **C**. Conditions: [**4-HPA**] = 2 mM, [Fe(mecn)₂(OTf)₂] = 4 mM, H₂O, 24 °C, t = 30 min.*
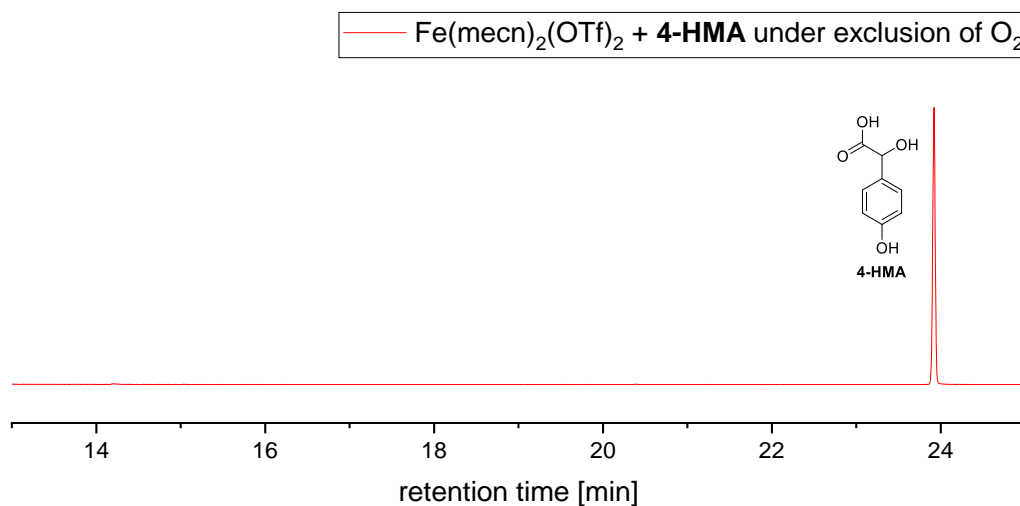
*Figure 256: Excerpt of the GC-MS trace of the reaction of **4-HMA** with Fe(mecn)₂(OTf)₂ (Reaction **17**). GC-MS method **C**. Conditions: [**4-HMA**] = 2 mM, [Fe(mecn)₂(OTf)₂] = 4 mM, H₂O, 24 °C, t = 30 min.*
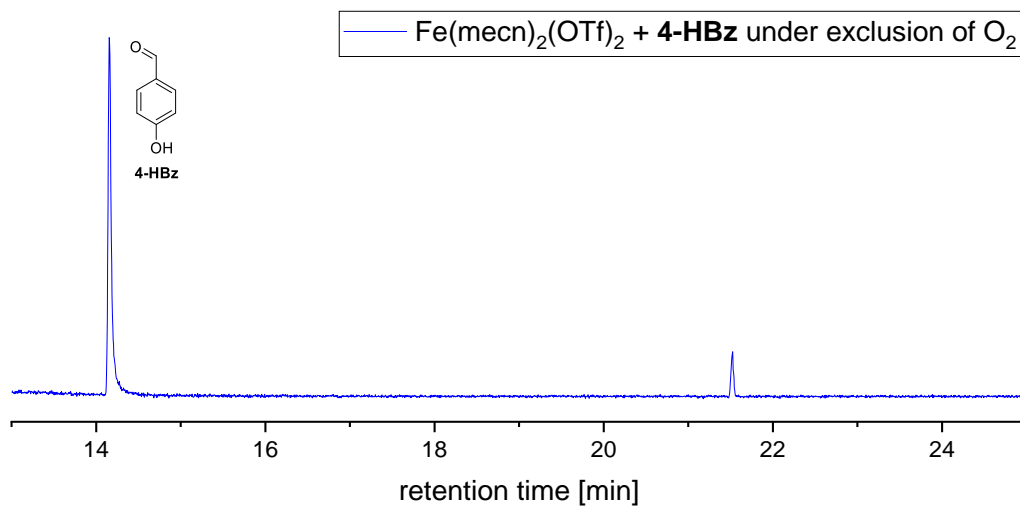
*Figure 257: Excerpt of the GC-MS trace of the reaction of **4-HBz** with Fe(mecn)$_2$(OTf)$_2$ (Reaction **18**). GC-MS method **C**.*
*Conditions: [**4-HBz**] = 2 mM, [Fe(OTf)$_3$] = 4 mM, H$_2$O, 24 °C, t = 30 min.*
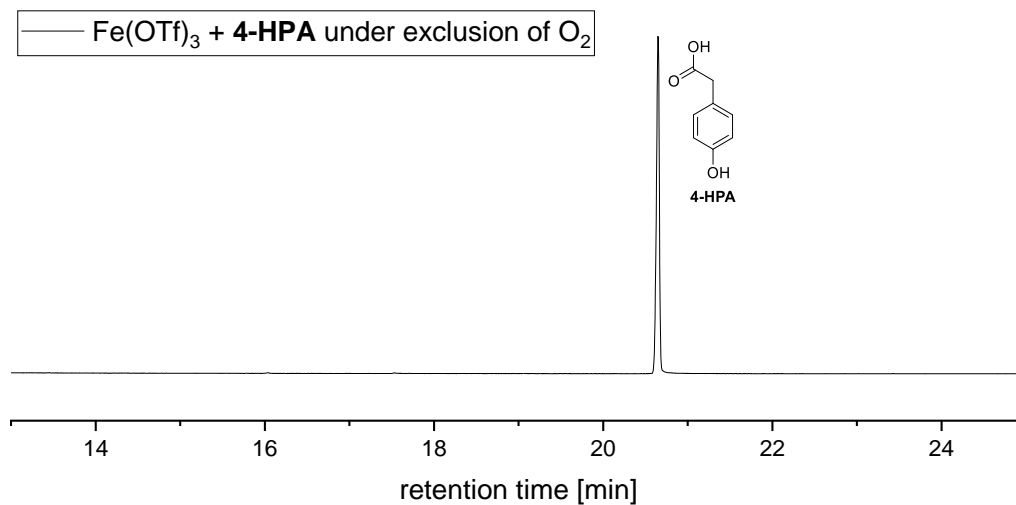
*Figure 258: Excerpt of the GC-MS trace of the reaction of **4-HPA** with Fe (OTf)$_3$ (Reaction **19**). GC-MS method **C**. Conditions:*
*[**4-HPA**] = 2 mM, [Fe(OTf)$_3$] = 4 mM, H$_2$O, 24 °C, t = 30 min.*
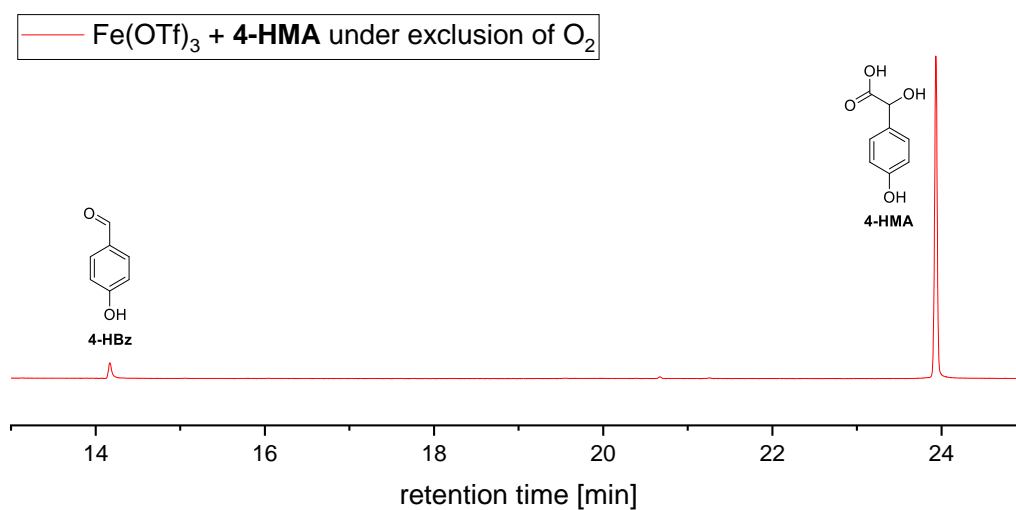
*Figure 259: Excerpt of the GC-MS trace of the reaction of **4-HMA** with Fe(OTf)$_3$ (Reaction **20**). GC-MS method **C**. Conditions:*
*[**4-HMA**] = 2 mM, [Fe(OTf)$_3$] = 4 mM, H$_2$O, 24 °C, t = 30 min.*

411
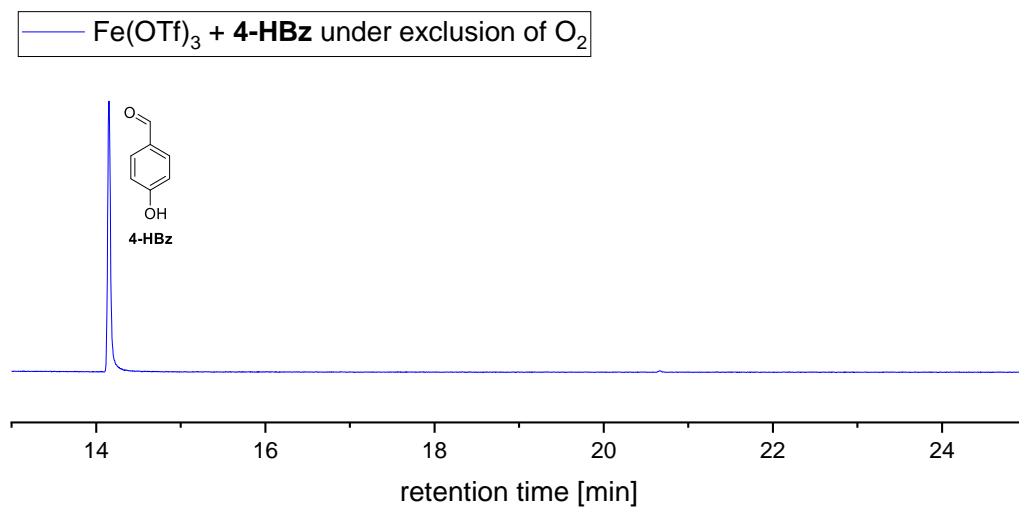
*Figure 260: Excerpt of the GC-MS trace of the reaction of **4-HBz** with Fe(OTf)₃ (Reaction **21**). GC-MS method **C**. Conditions: [**4-HBz**] = 2 mM, **C-4**] = 4 mM, H₂O, 24 °C, t = 30 min.*
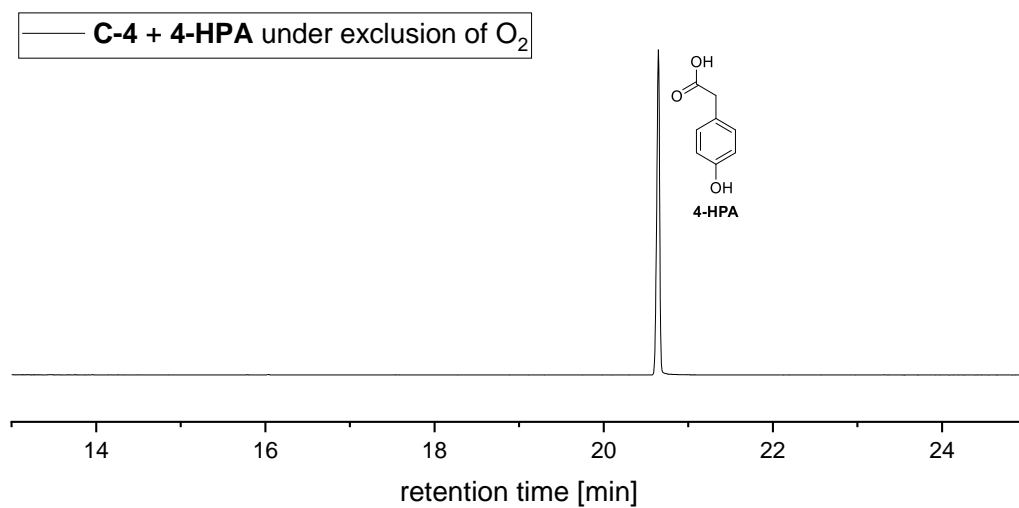
*Figure 261: Excerpt of the GC-MS trace of the reaction of **4-HPA** with **C-4** (Reaction **22**). GC-MS method **C**. Conditions: [**4-HPA**] = 2 mM, [**C-4**] = 4 mM, H₂O, 24 °C, t = 30 min.*
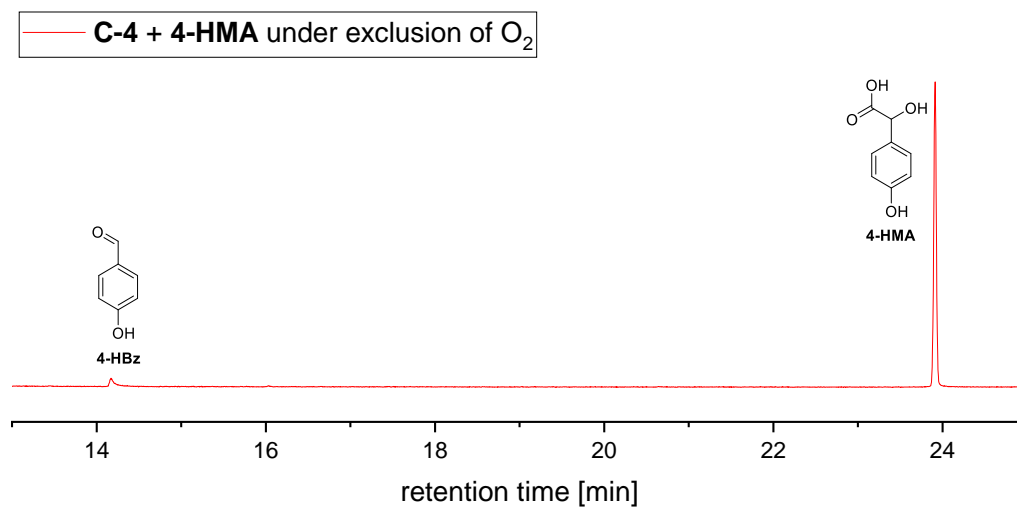
*Figure 262: Excerpt of the GC-MS trace of the reaction of **4-HMA** with **C-4** (Reaction **23**). GC-MS method **C**. Conditions: [**4-HMA**] = 2 mM, [**C-4**] = 4 mM, H$_2$O, 24 °C, t = 30 min.*
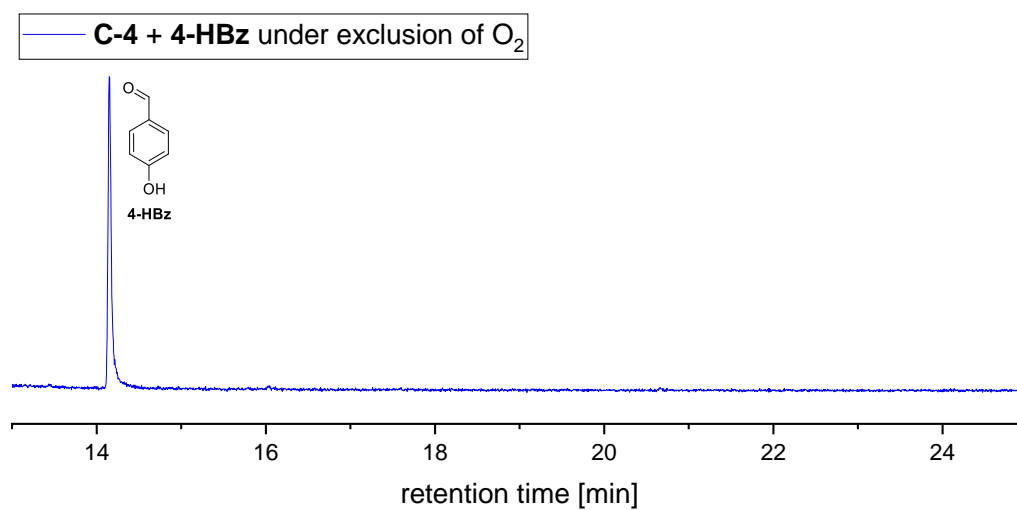
*Figure 263: Excerpt of the GC-MS trace of the reaction of **4-HBz** with **C-4** (Reaction **23**). Conditions: [**4-HBz**] = 2 mM, [Fe(mecn)$_2$(OTf)$_2$] = 4 mM, H$_2$O, 24 °C, t = 30 min.*
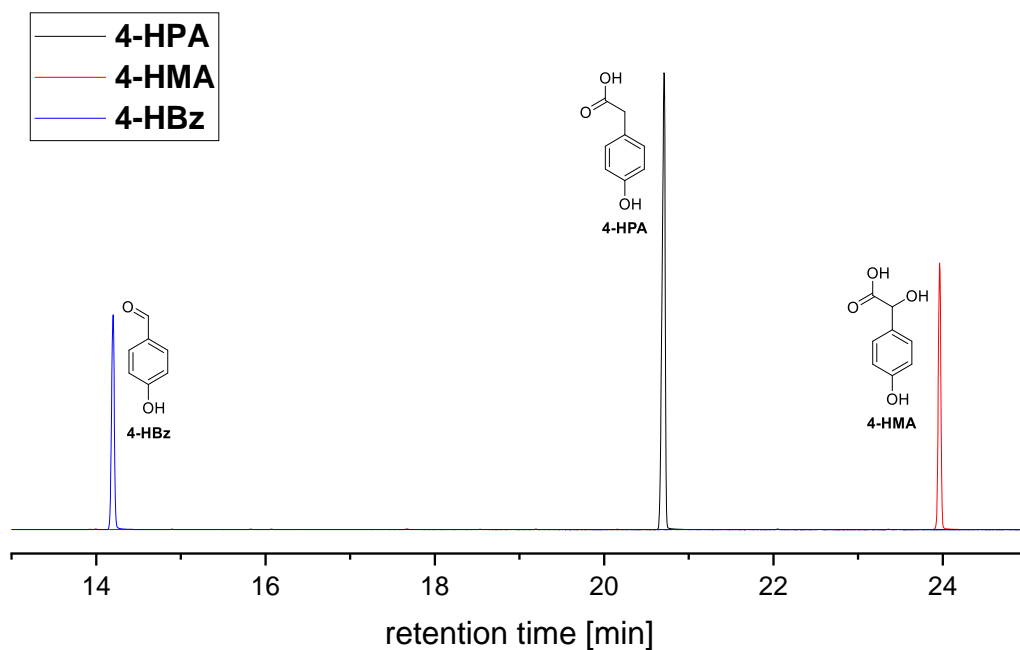
*Figure 264: Excerpt of the GC-MS trace of control reactions with **4-HPA, 4-HMA, and 4-HBz** (Reactions **10, 11, 12**, respectively). Conditions: [**M**] = 2 mM, H_2O, 24 °C, t = 30 min.*
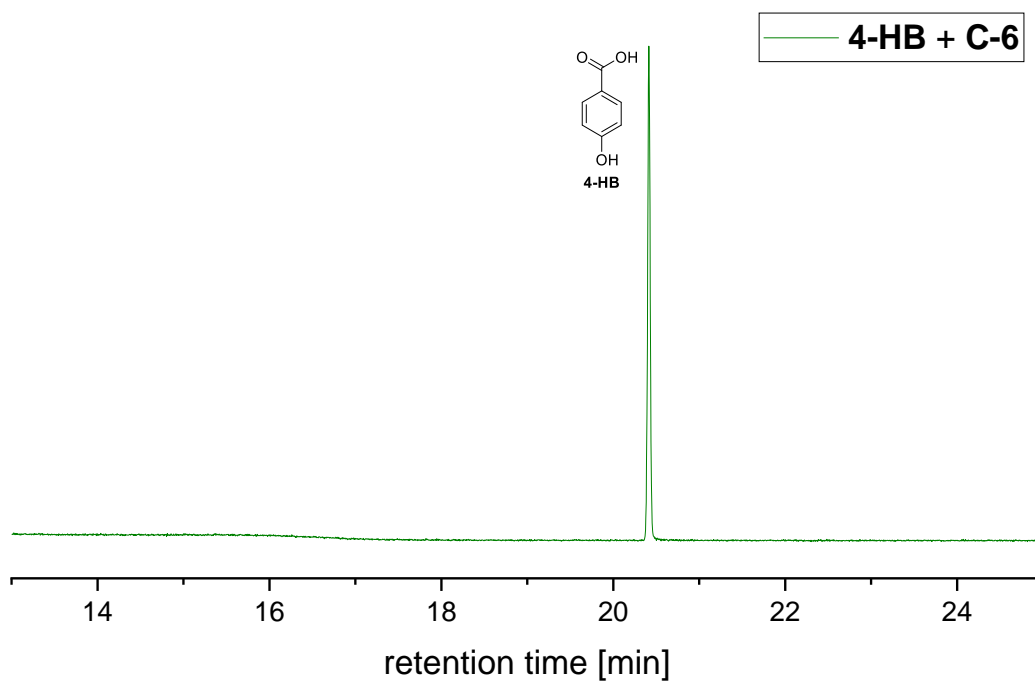
*Figure 265: Excerpt of the GC-MS trace of **4-HB** with **C-6** (Reaction **13**). Conditions: [**4-HB**] = 2 mM, [**C-6**] = 4 mM, H_2O, 24 °C, t = 30 min.*
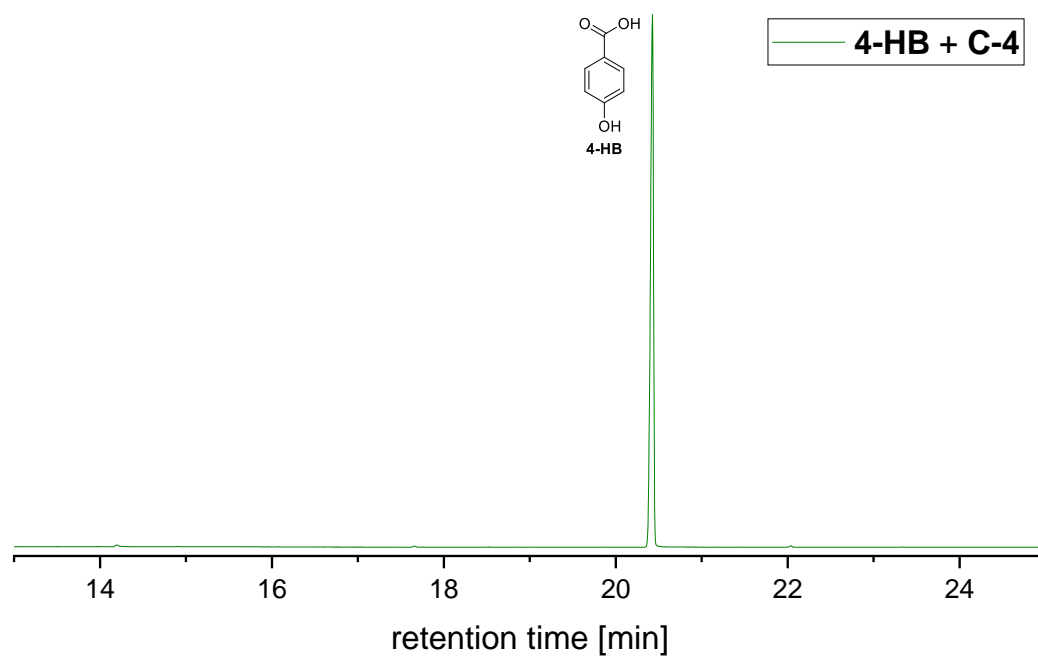
*Figure 266: Excerpt of the GC-MS trace of **4-HB** with **C-4** (Reaction **14**). Conditions: [**4-HB**] = 2 mM, [**C-4**] = 4 mM, H_2O, 24 °C, t = 30 min.*
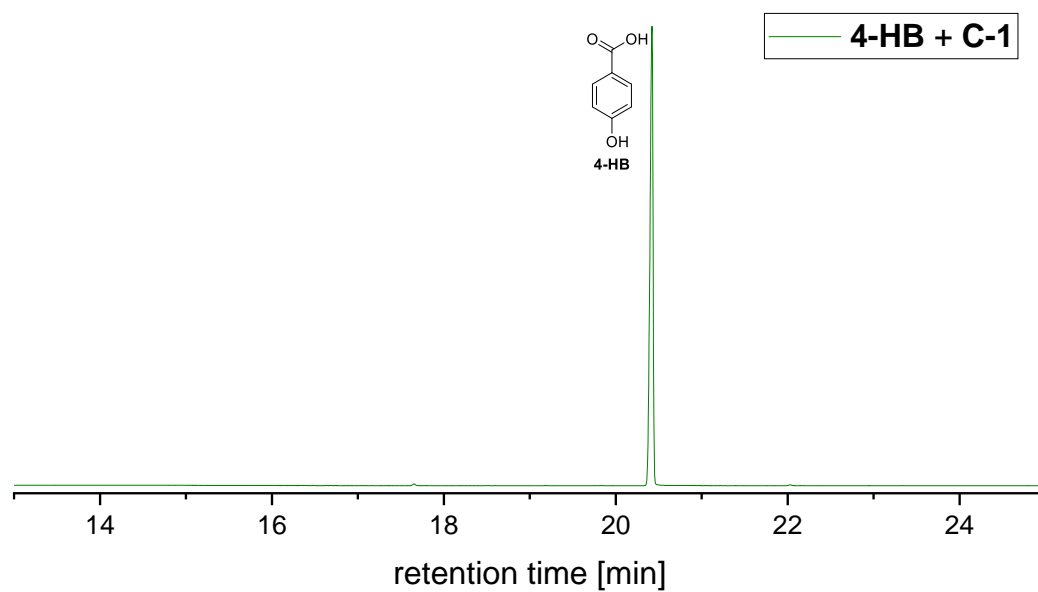
*Figure 267: Excerpt of the GC-MS trace of **4-HB** with **C-1** (Reaction **15**). Conditions: [**4-HB**] = 2 mM, [**C-1**] = 4 mM, H_2O, 24 °C, t = 30 min.*
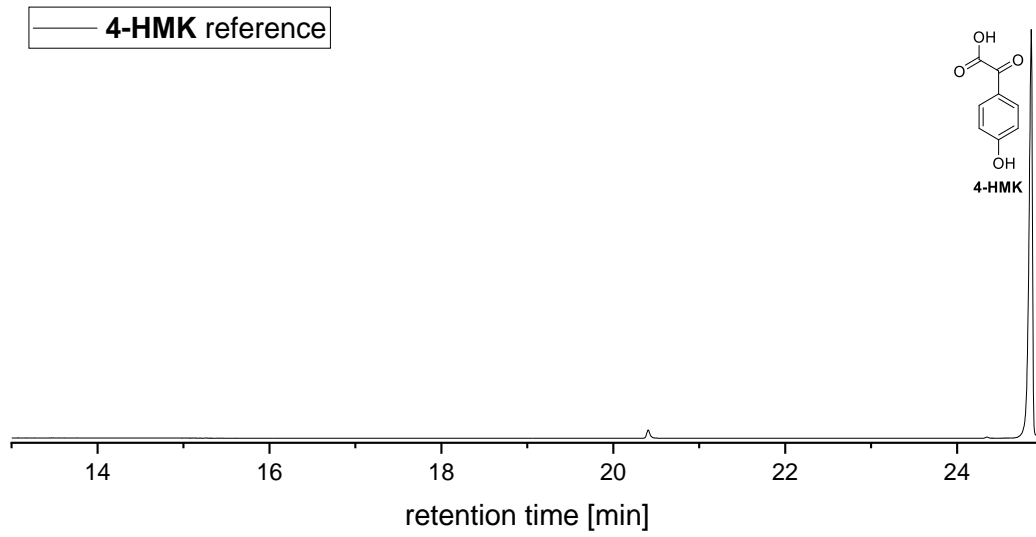
*Figure 268: Excerpt of the GC-MS trace of a reference sample of **4-HMK**.*

9. Chapter VII – Additional Data and Spectra

Subchapter 4: Wurster's Blue – WB

A)

B)

*Figure 269: ESI-HR-MS spectra of **A)** sample of Wurster's Blue that was stored for 150 min and **B)** a sample that was stored for 21 d at room temperature in amber tubes.*
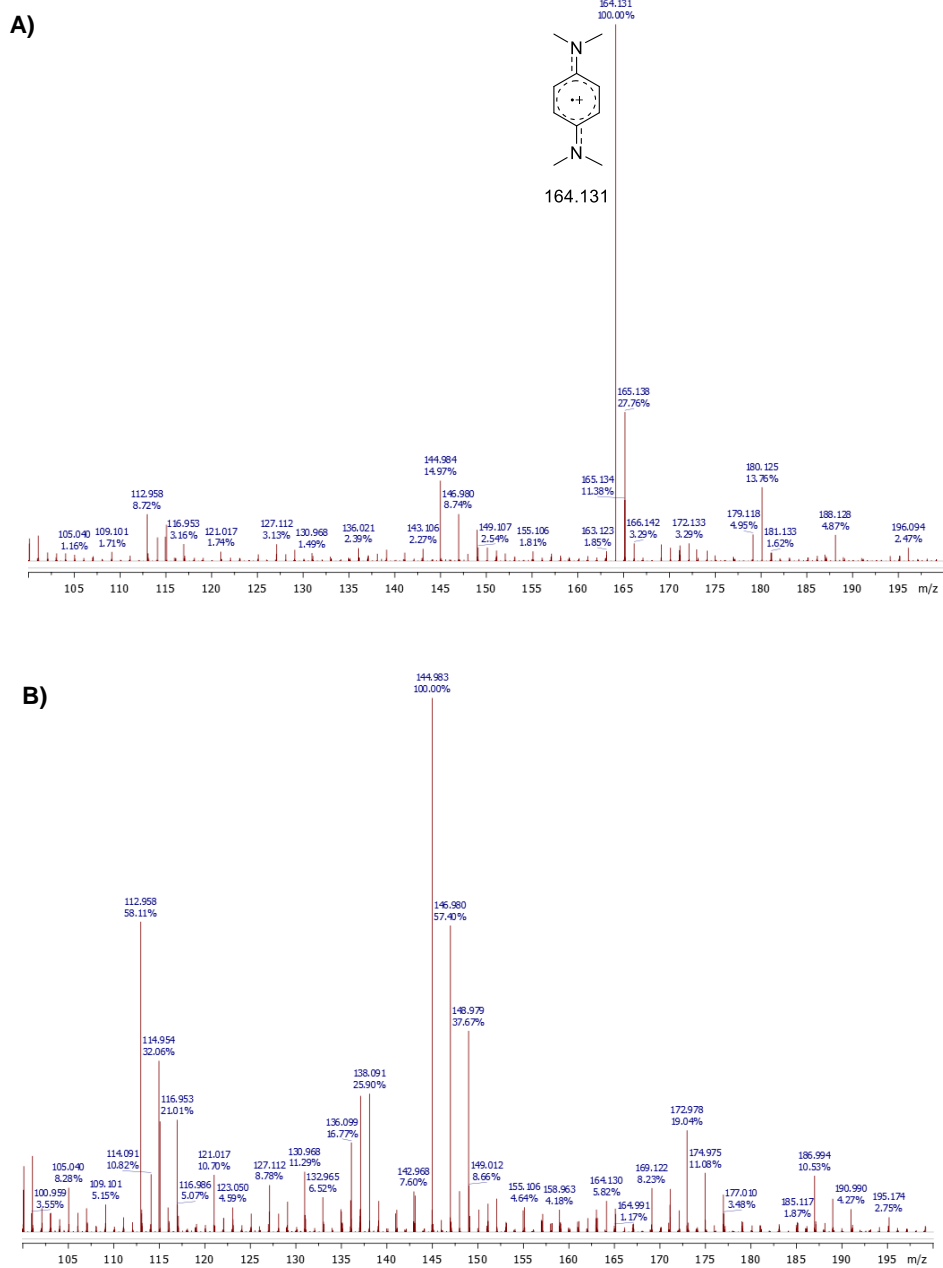
10. NMR Spectra – Ligands and Complexes

10.1. *III-1*

¹H
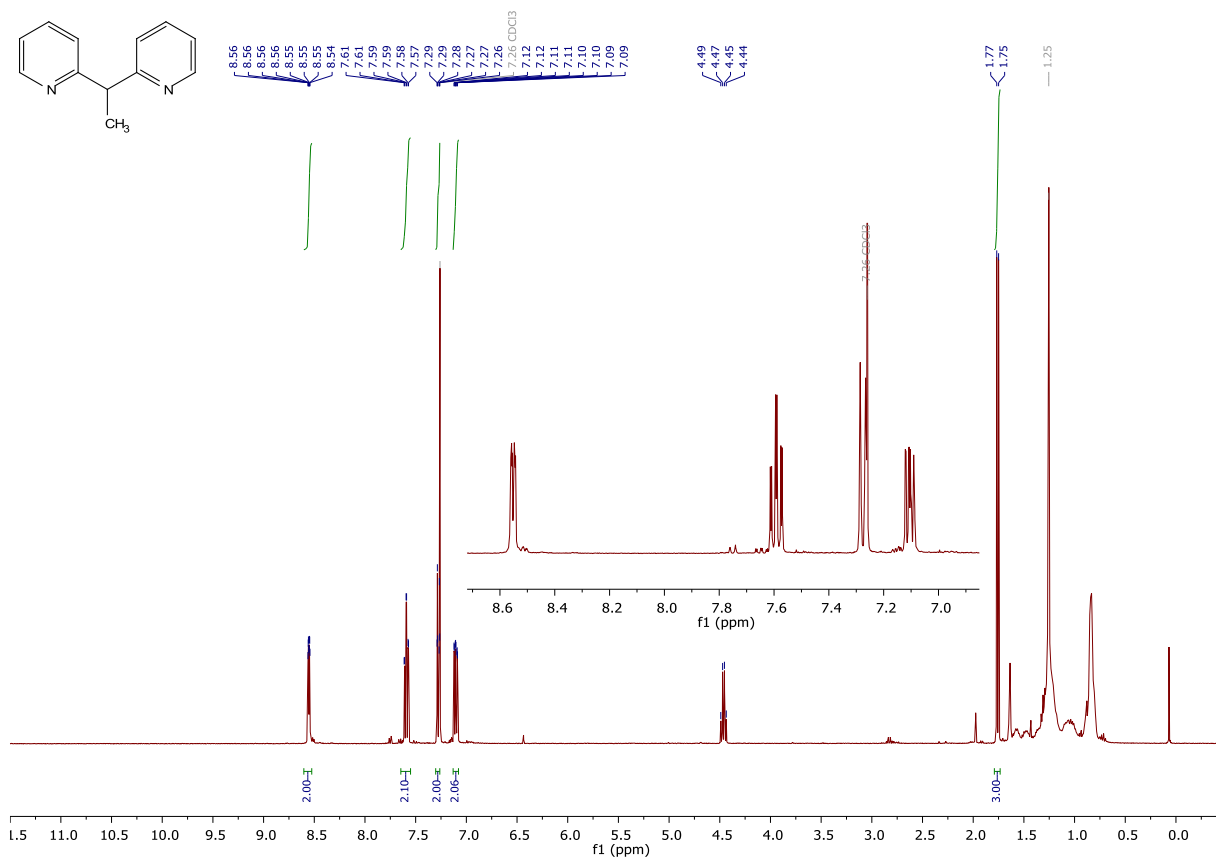
10.2. L-1

¹H – CDCl₃
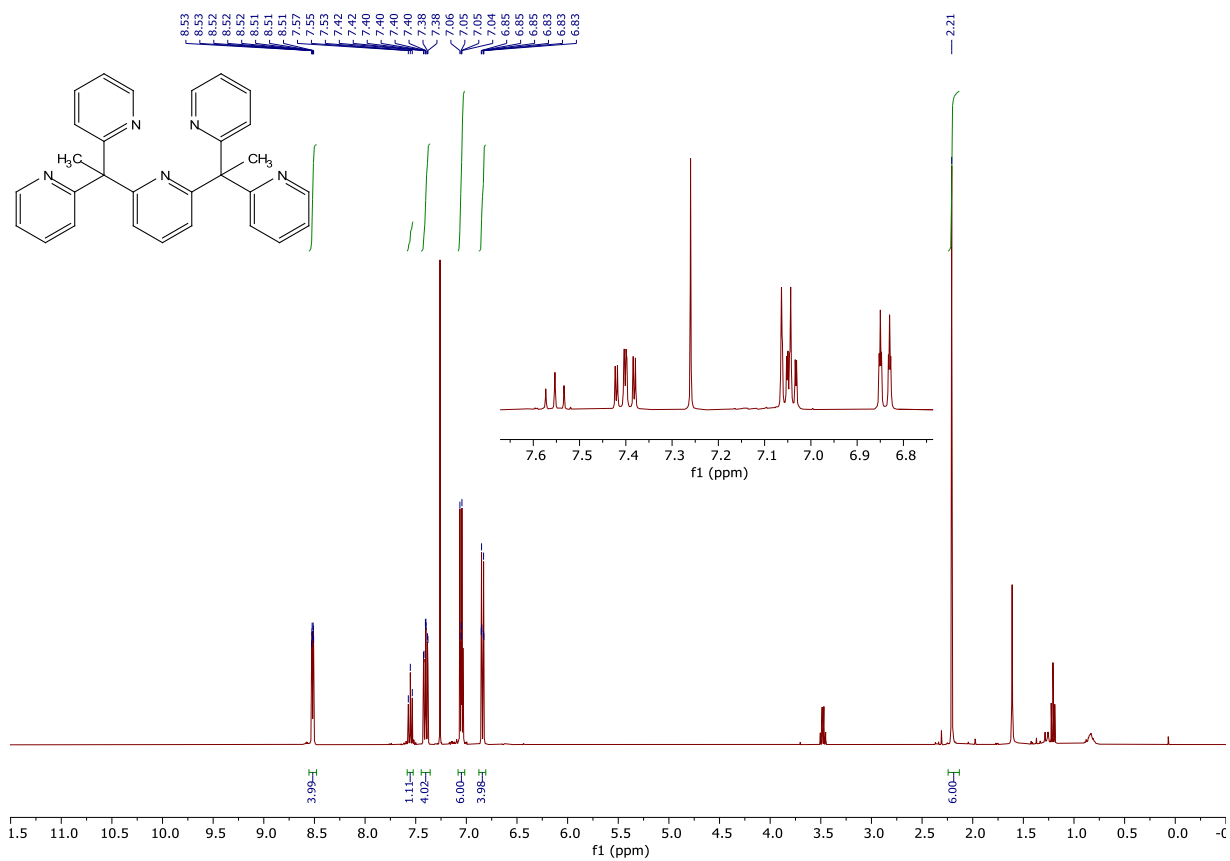
¹H – D₃-MeCN
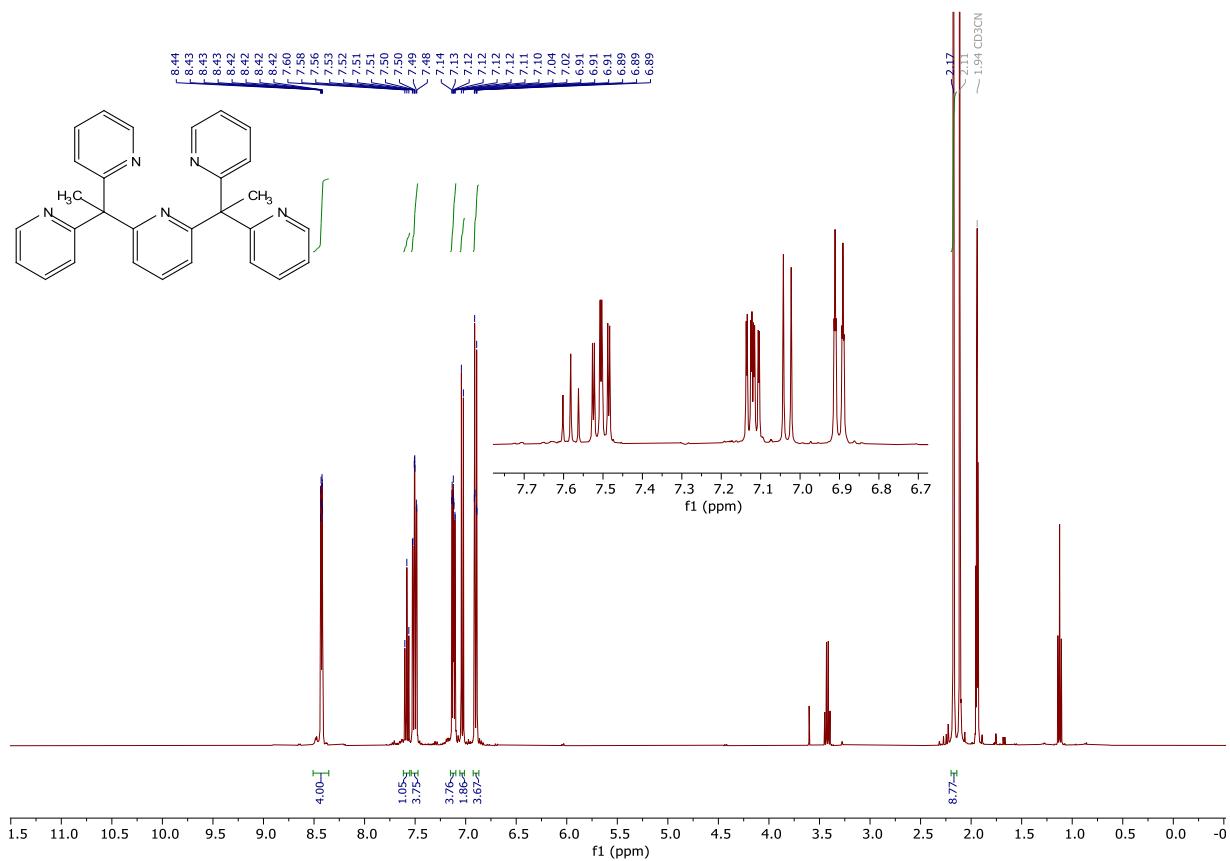
10.3.   C-1

¹H
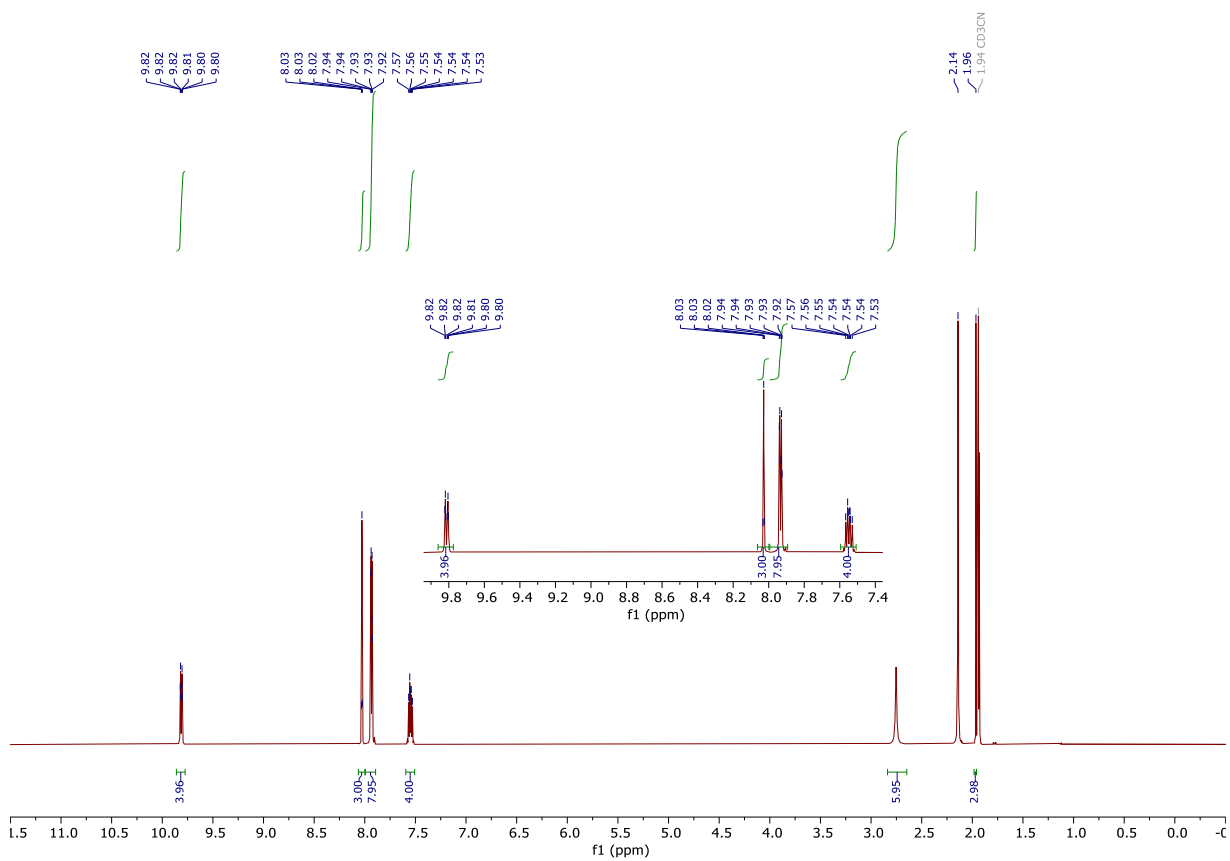
10.4. *V-1*

¹H
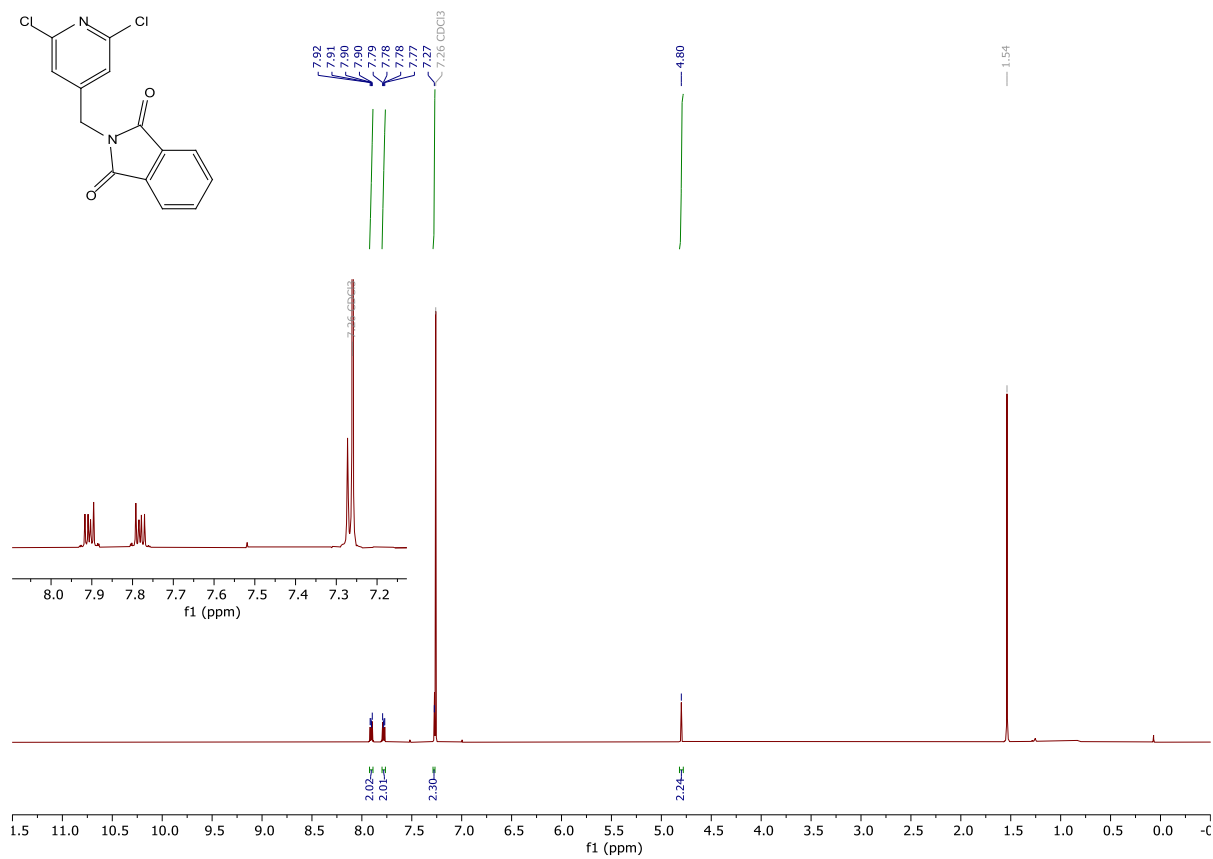
¹³C
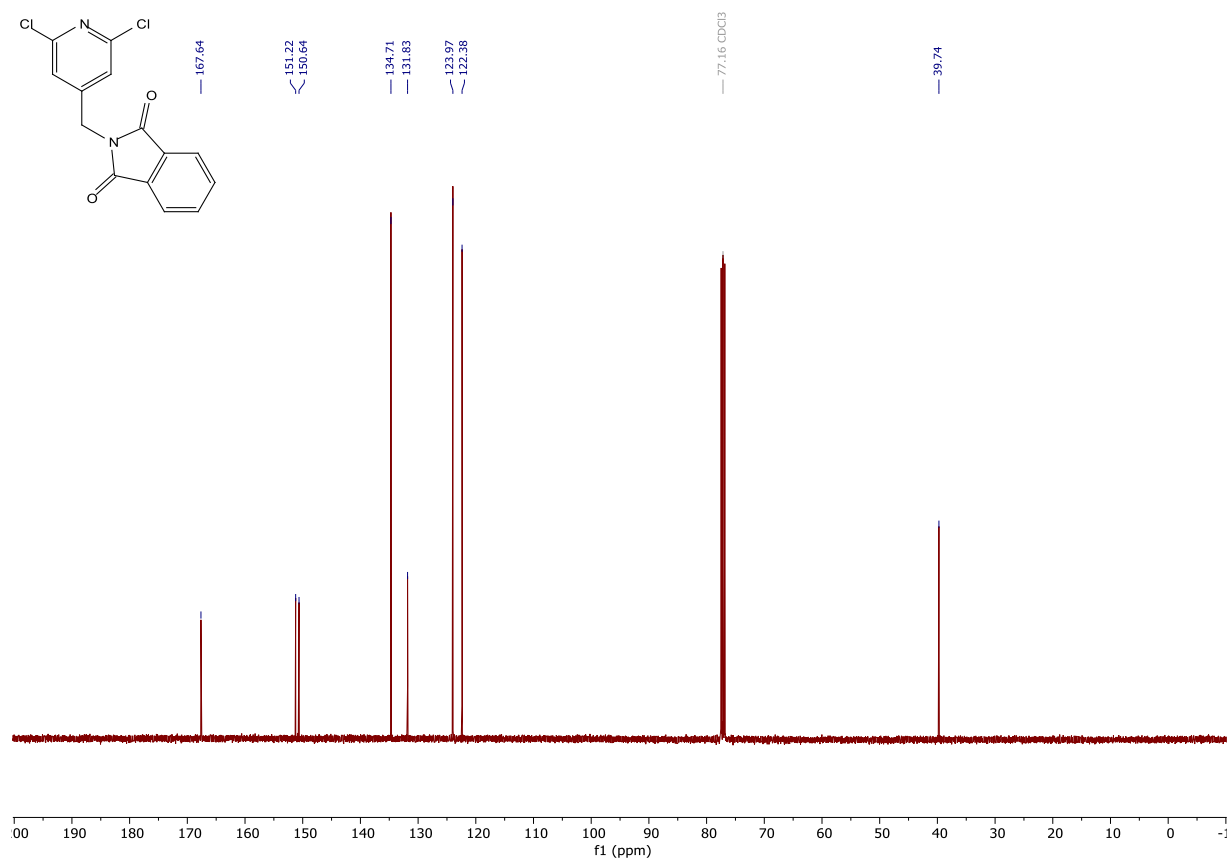
10.5. **V-2**

¹H

¹³C

10.6. V-3

¹H

¹³C

10.7. *V-4*
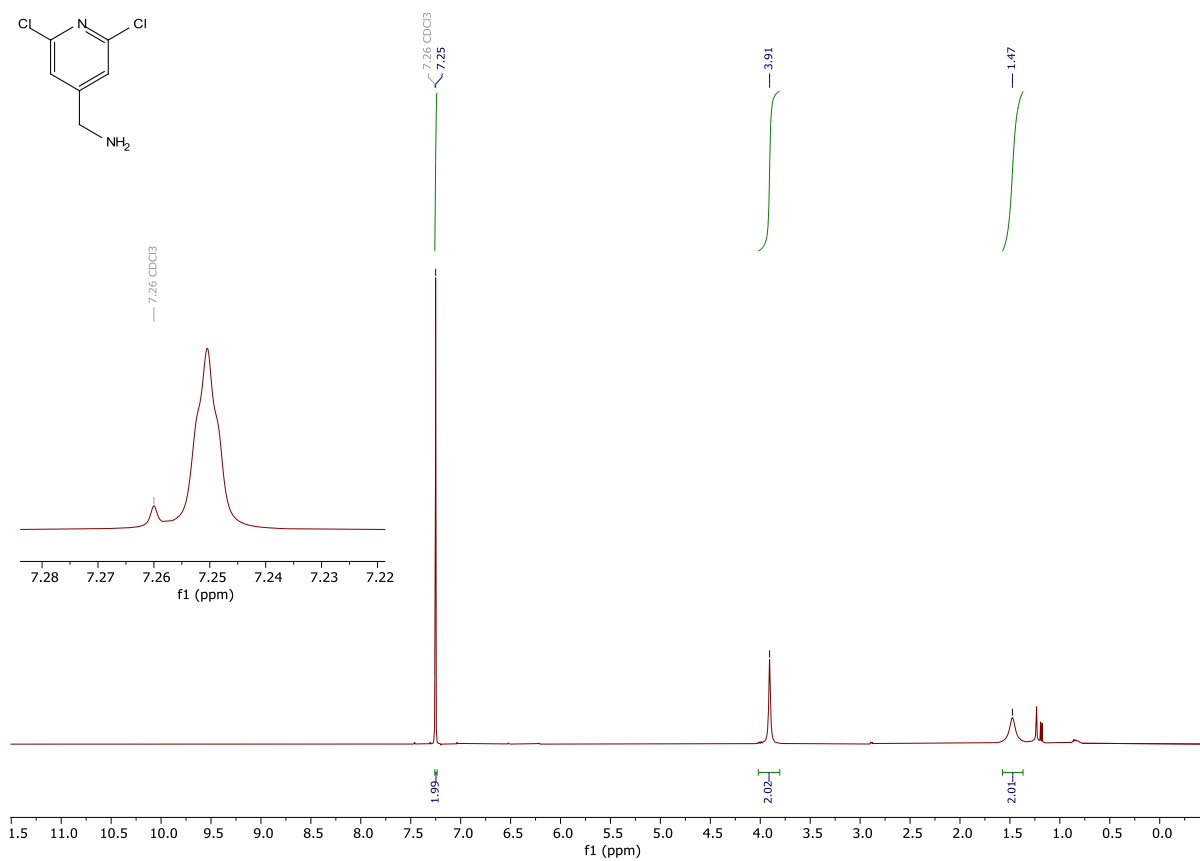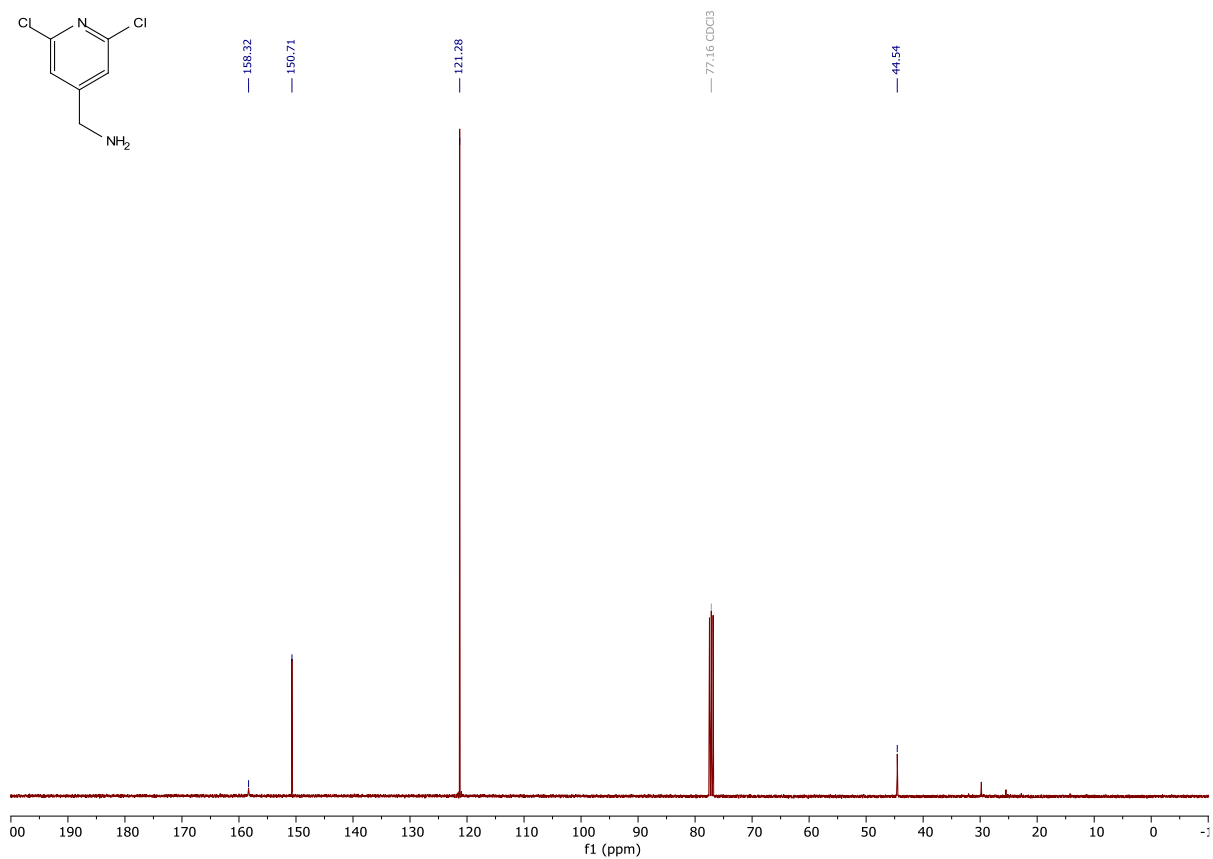
¹H
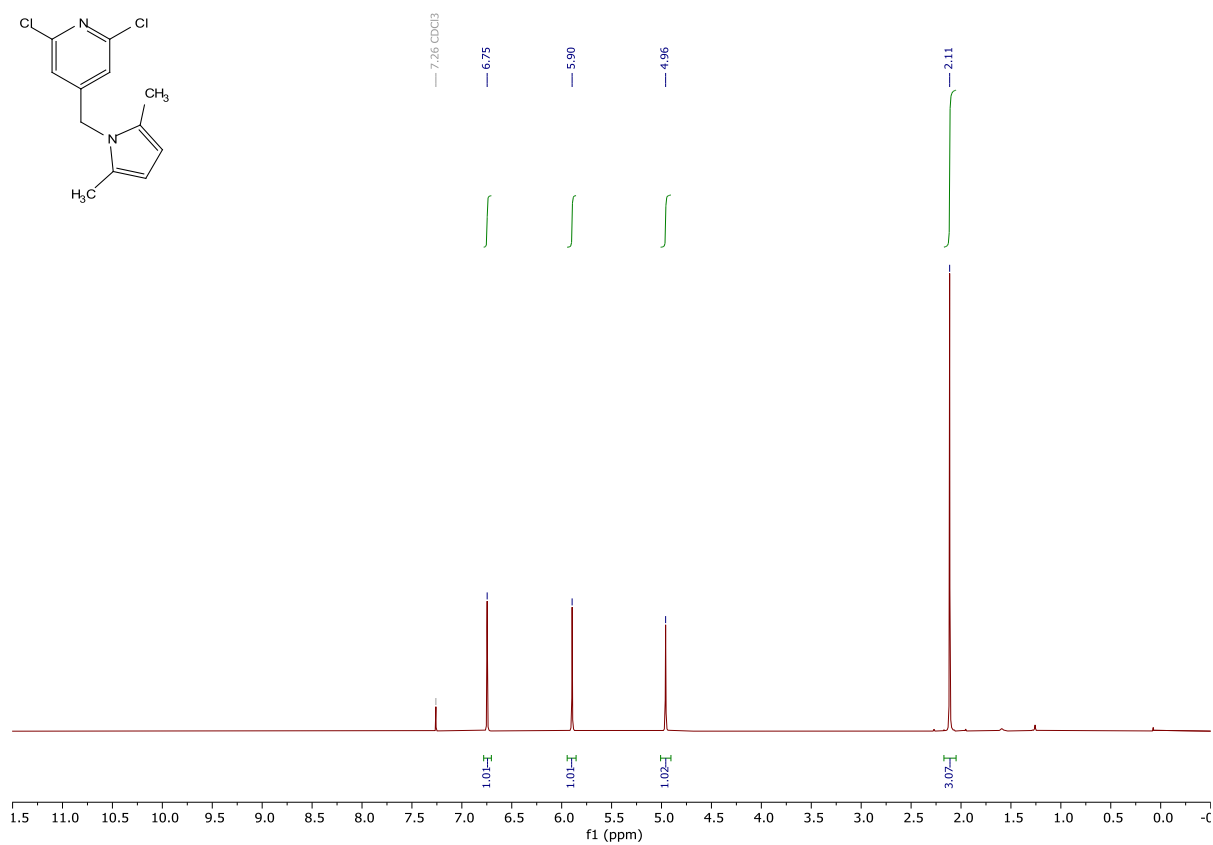
¹³C
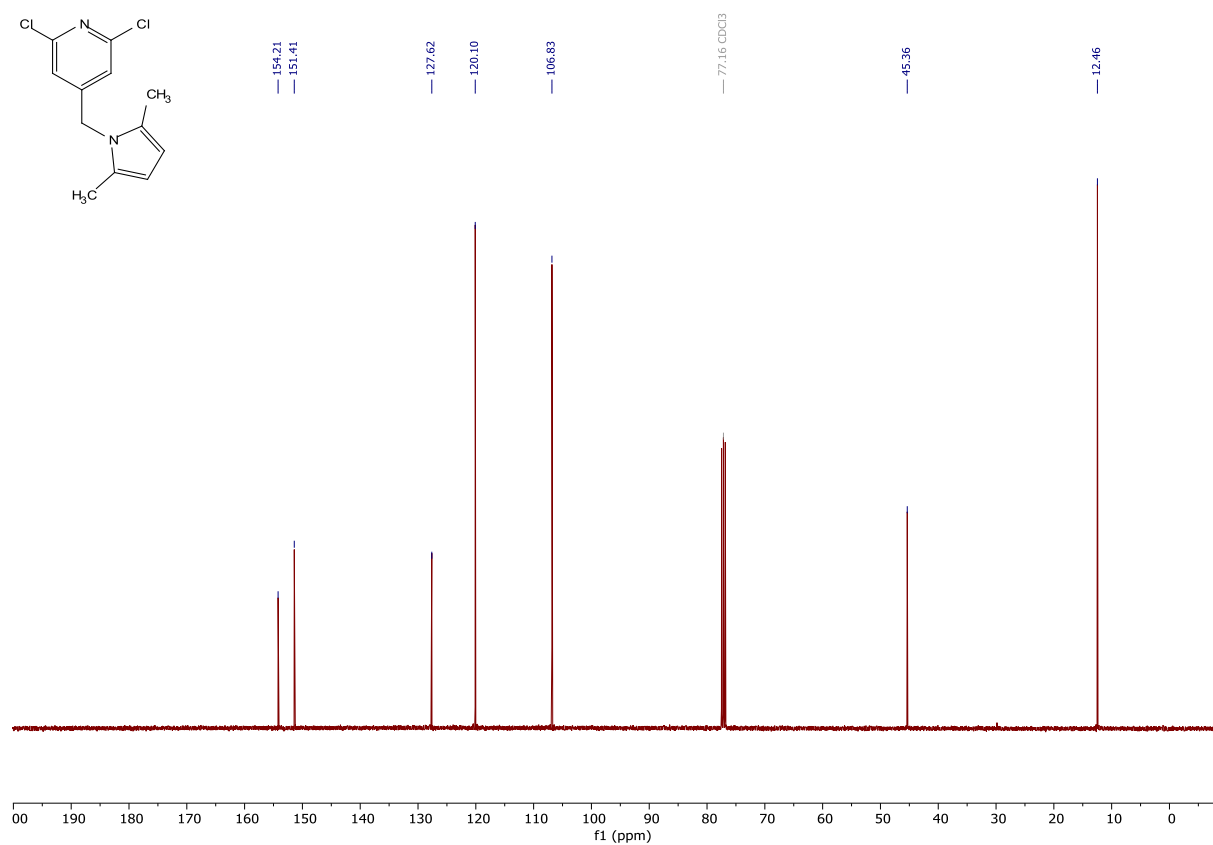
10.8. L-11

¹H
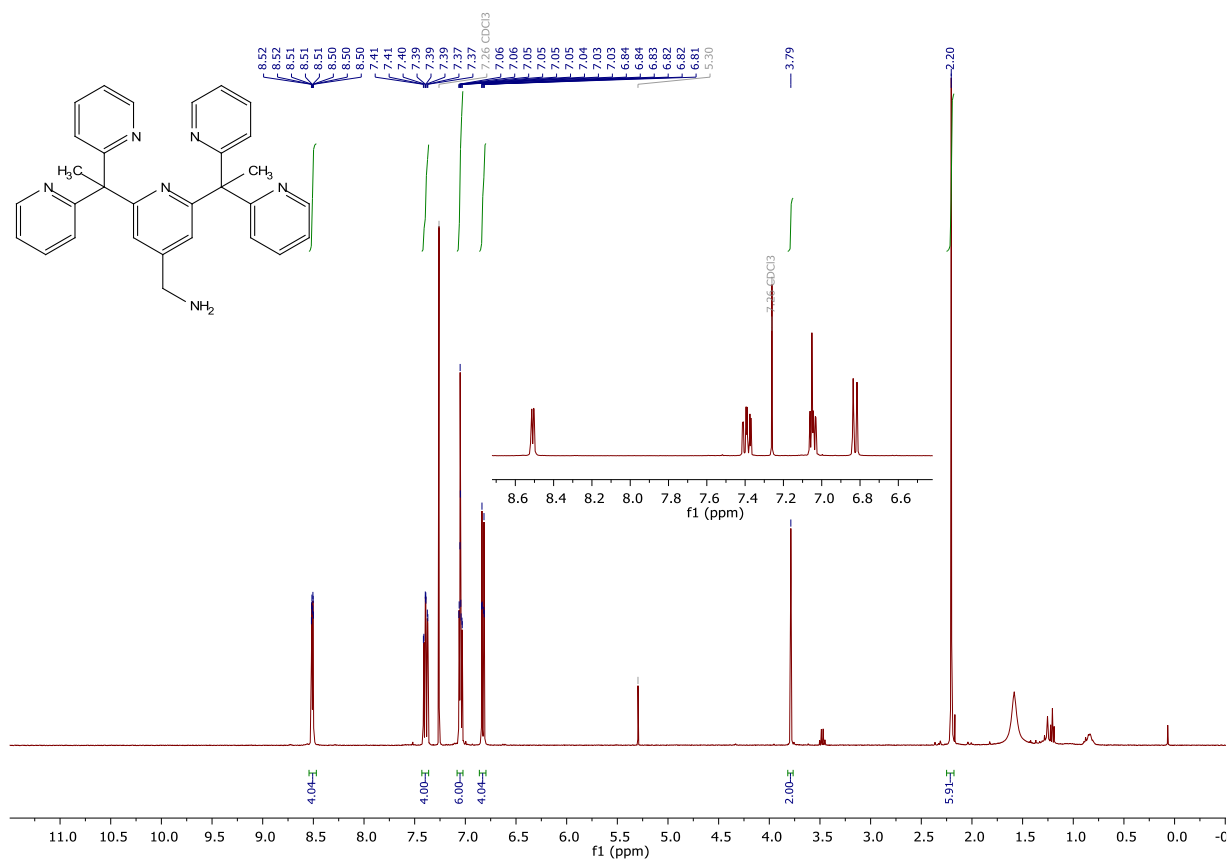
¹³C
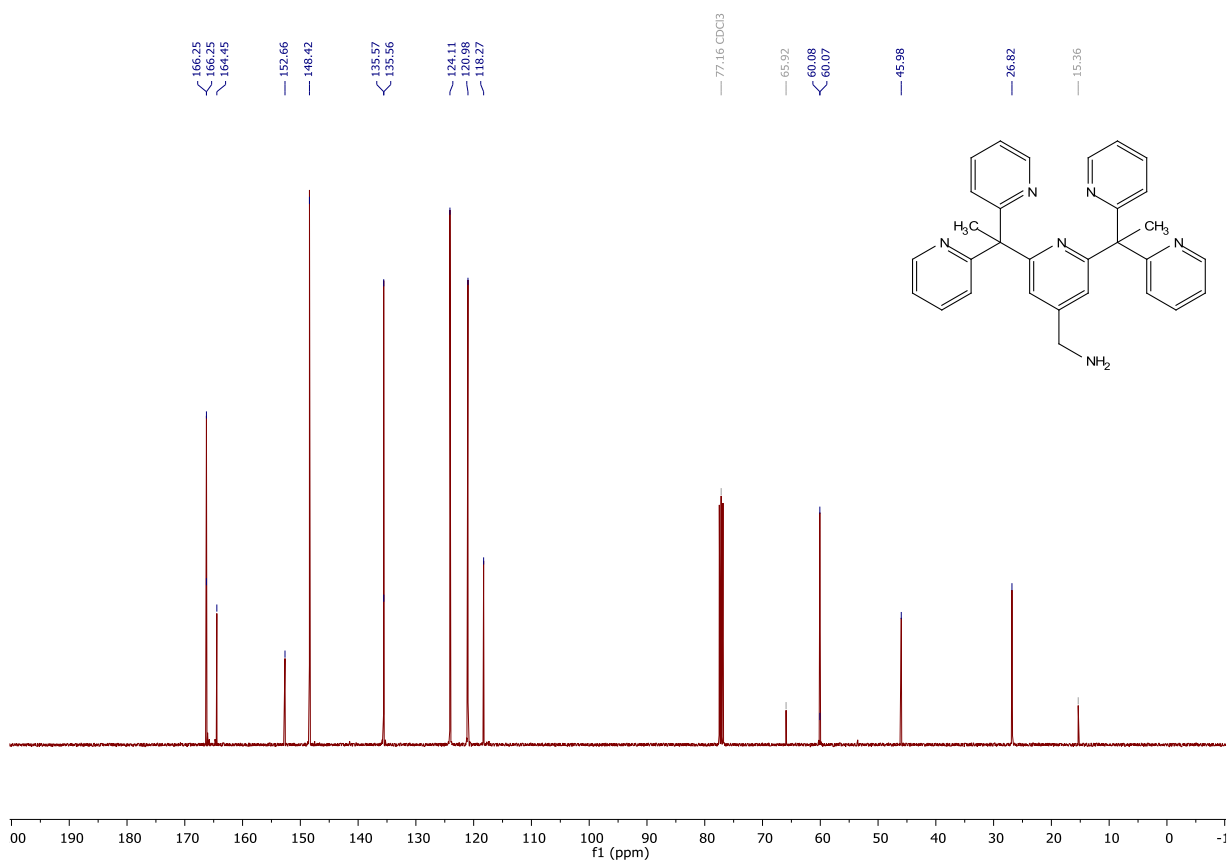
10.9. L-12

¹H
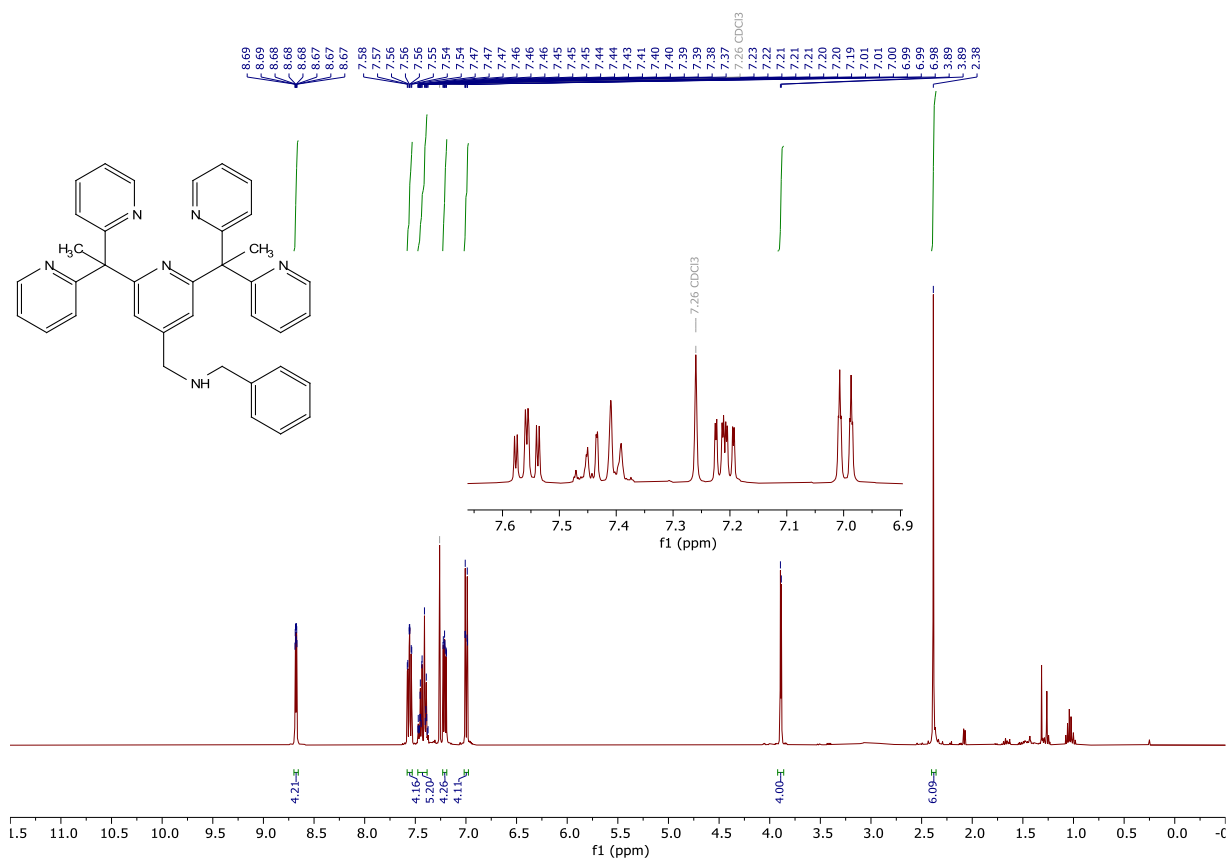
¹³C
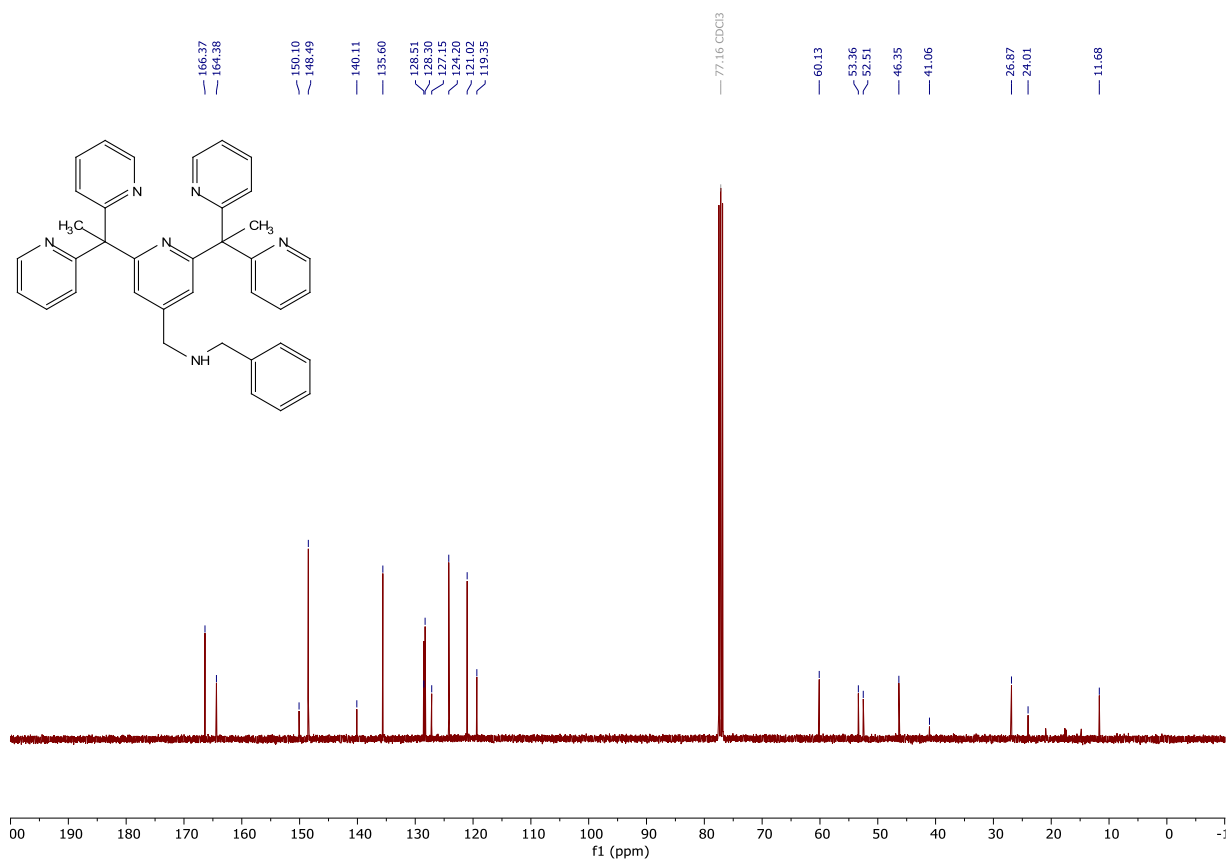
10.10. *V-5*

¹H
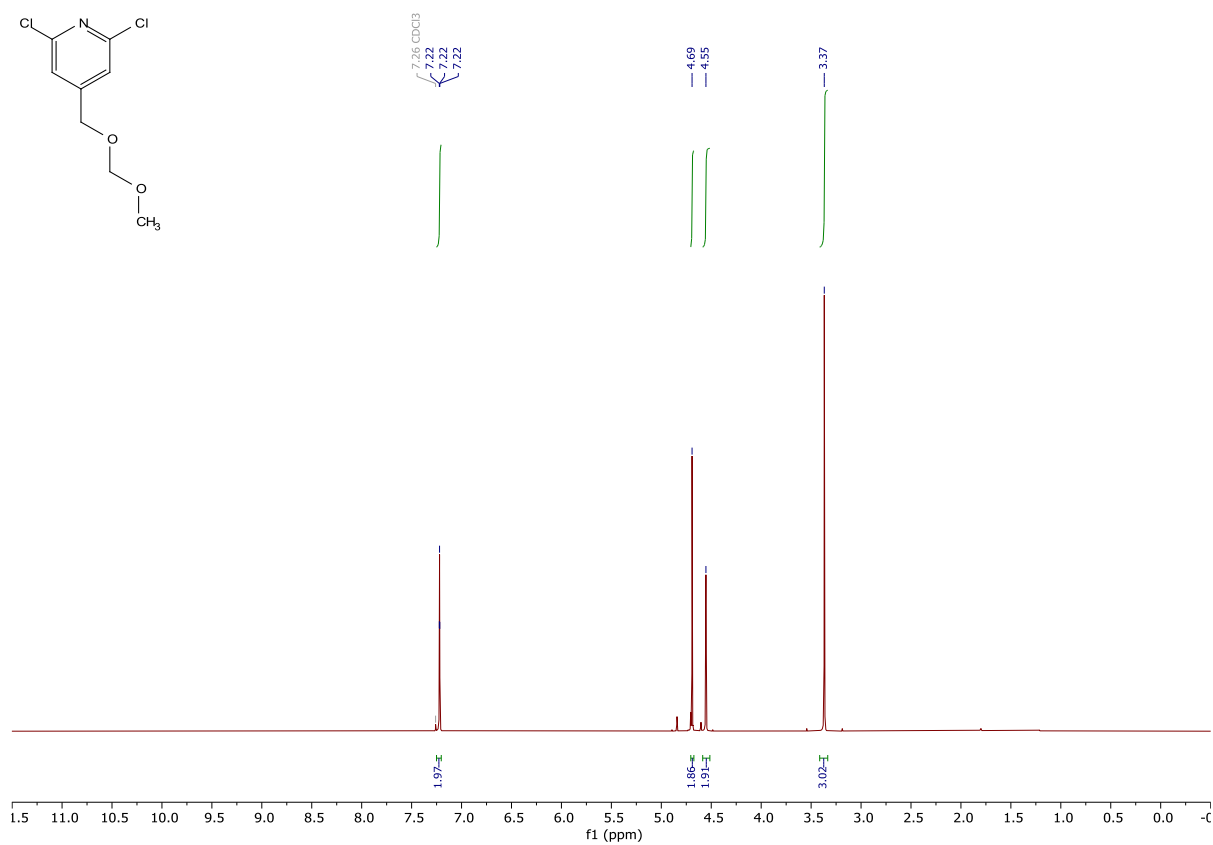
¹³C
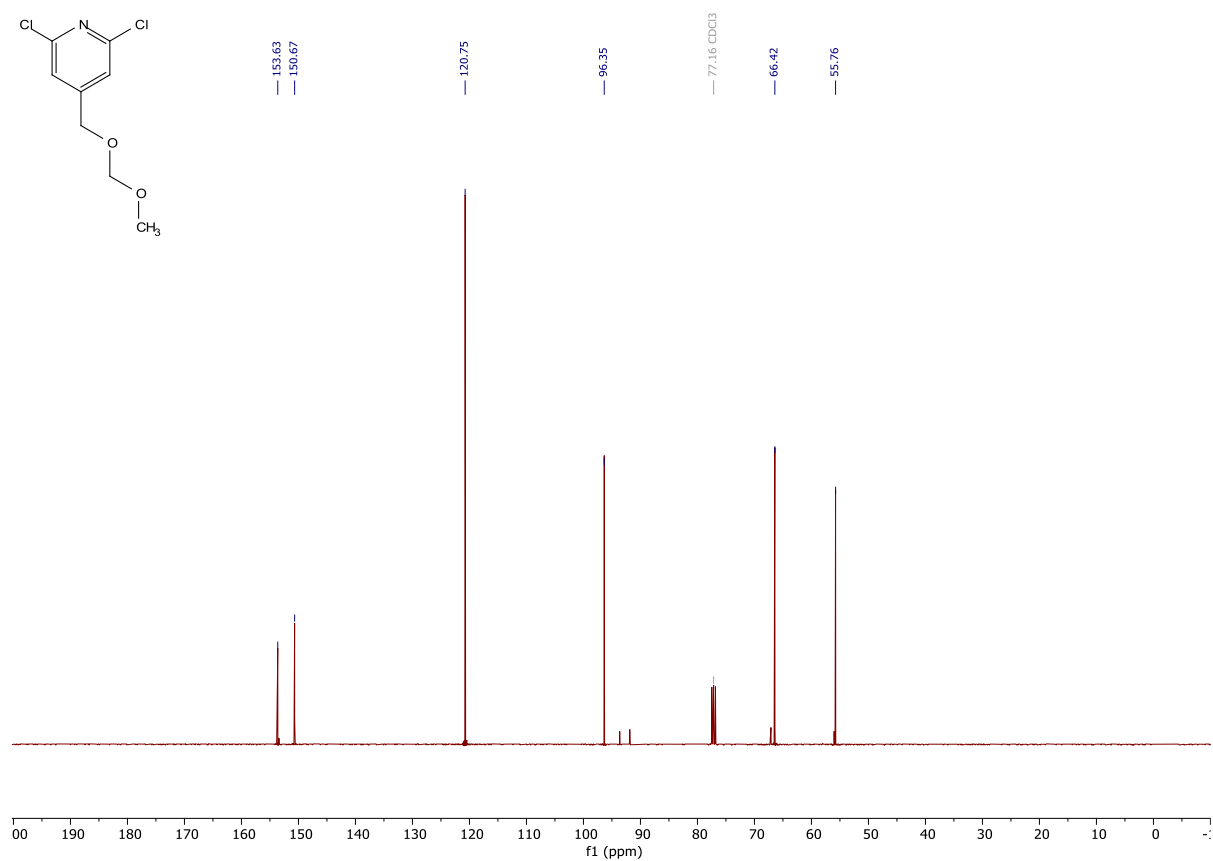
10.11. L-*13*

¹H
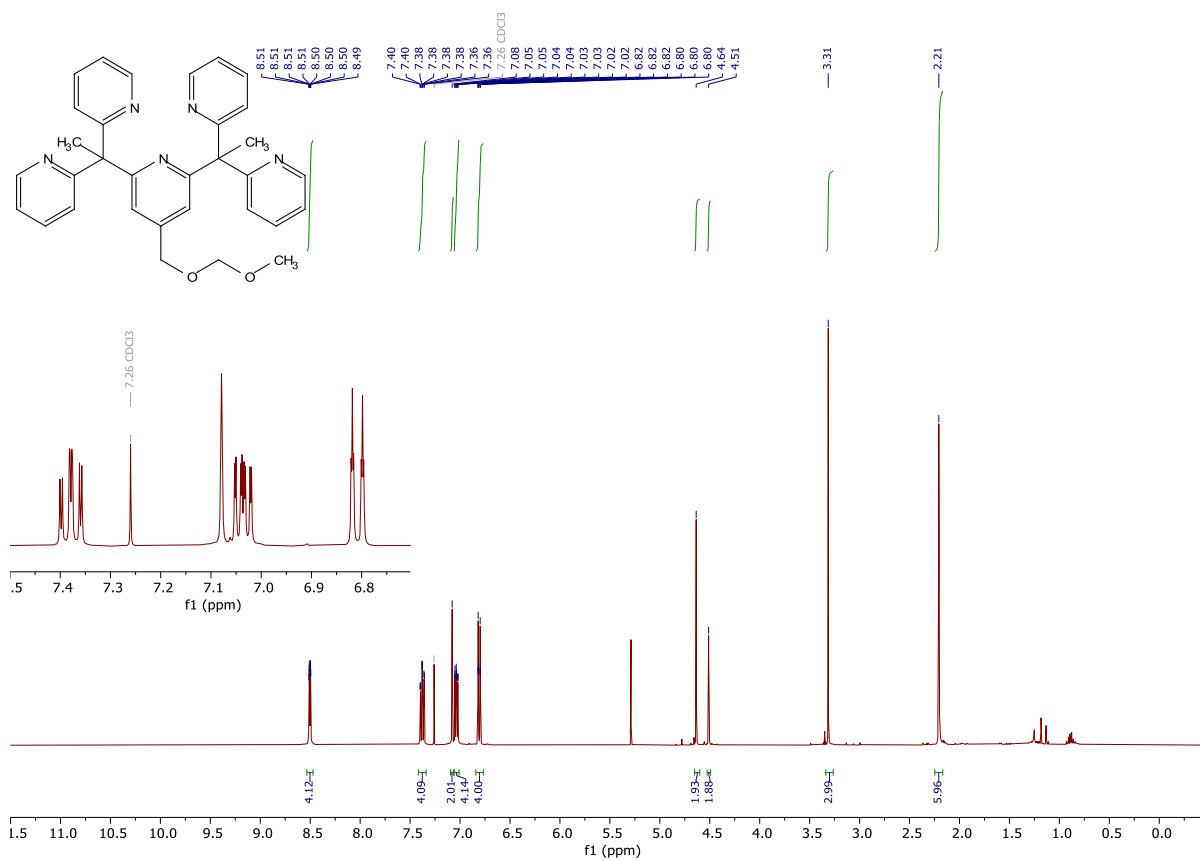
¹³C
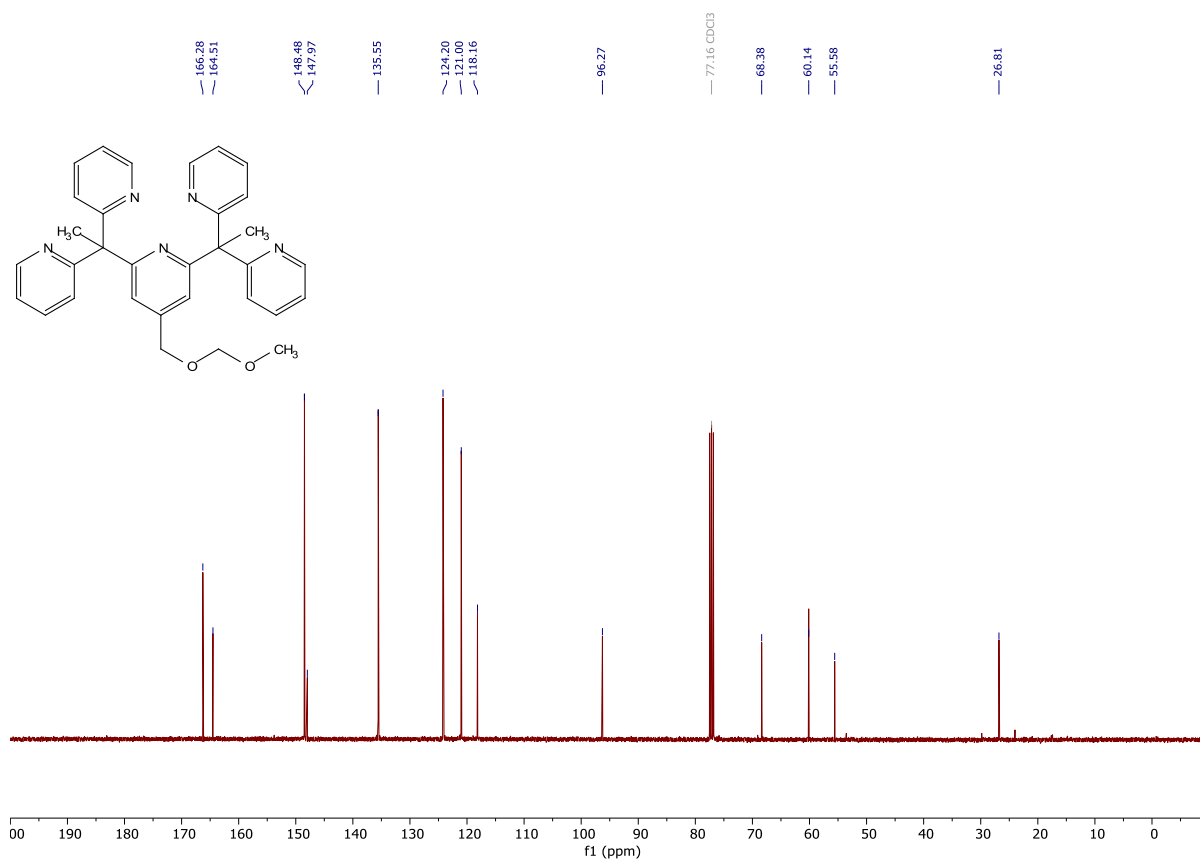
10.12. C-9

¹H
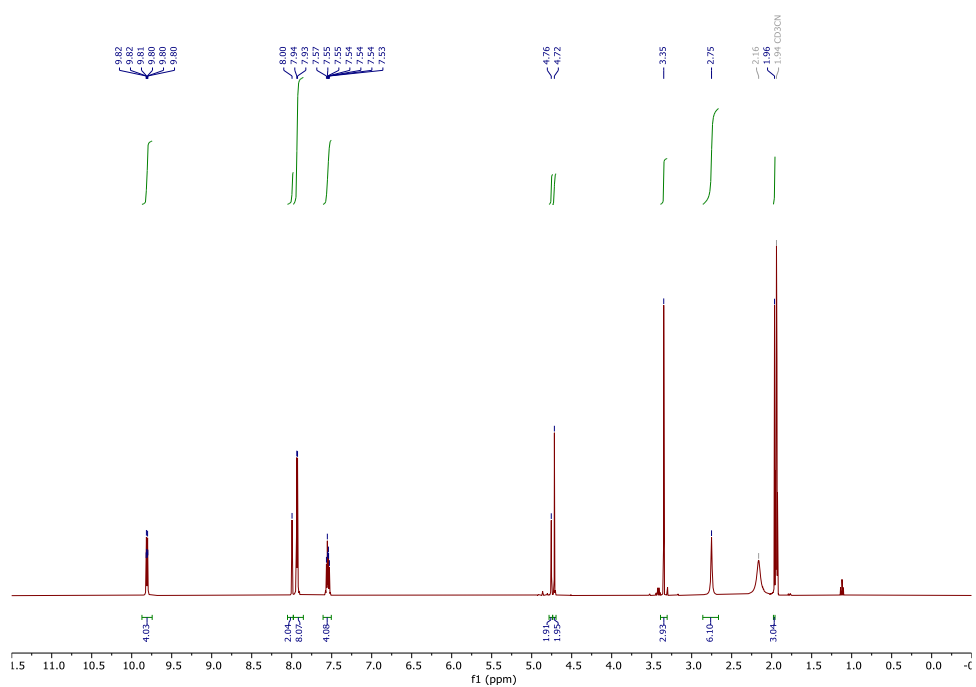
¹³C
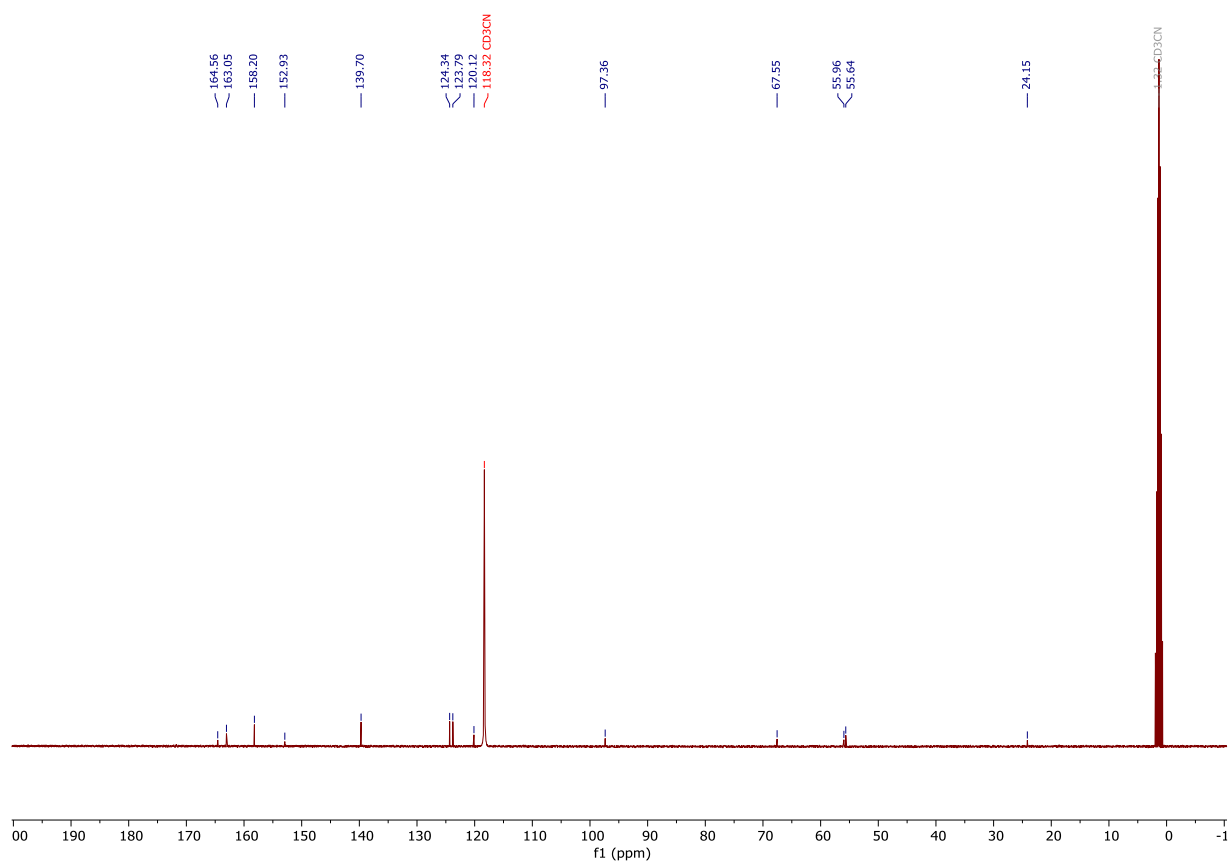
10.13. L-14

¹H
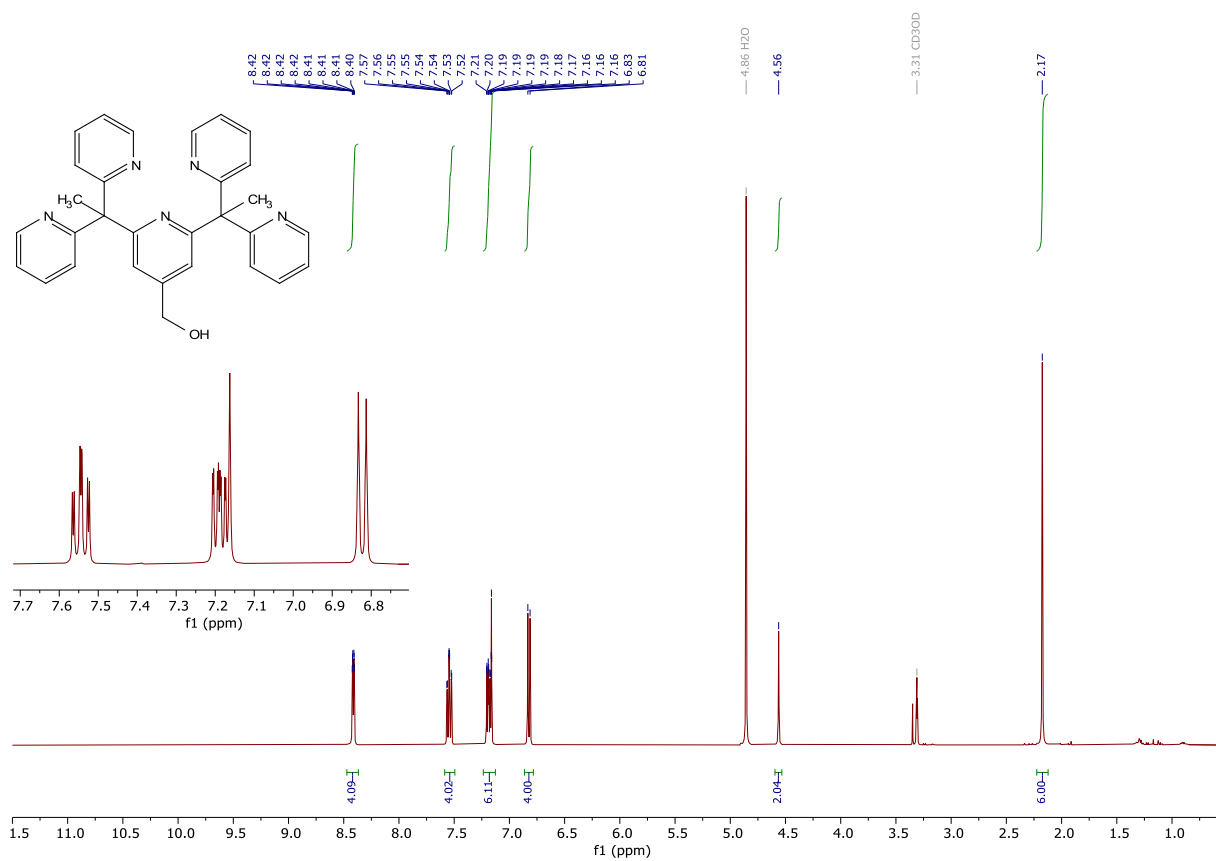
¹³C
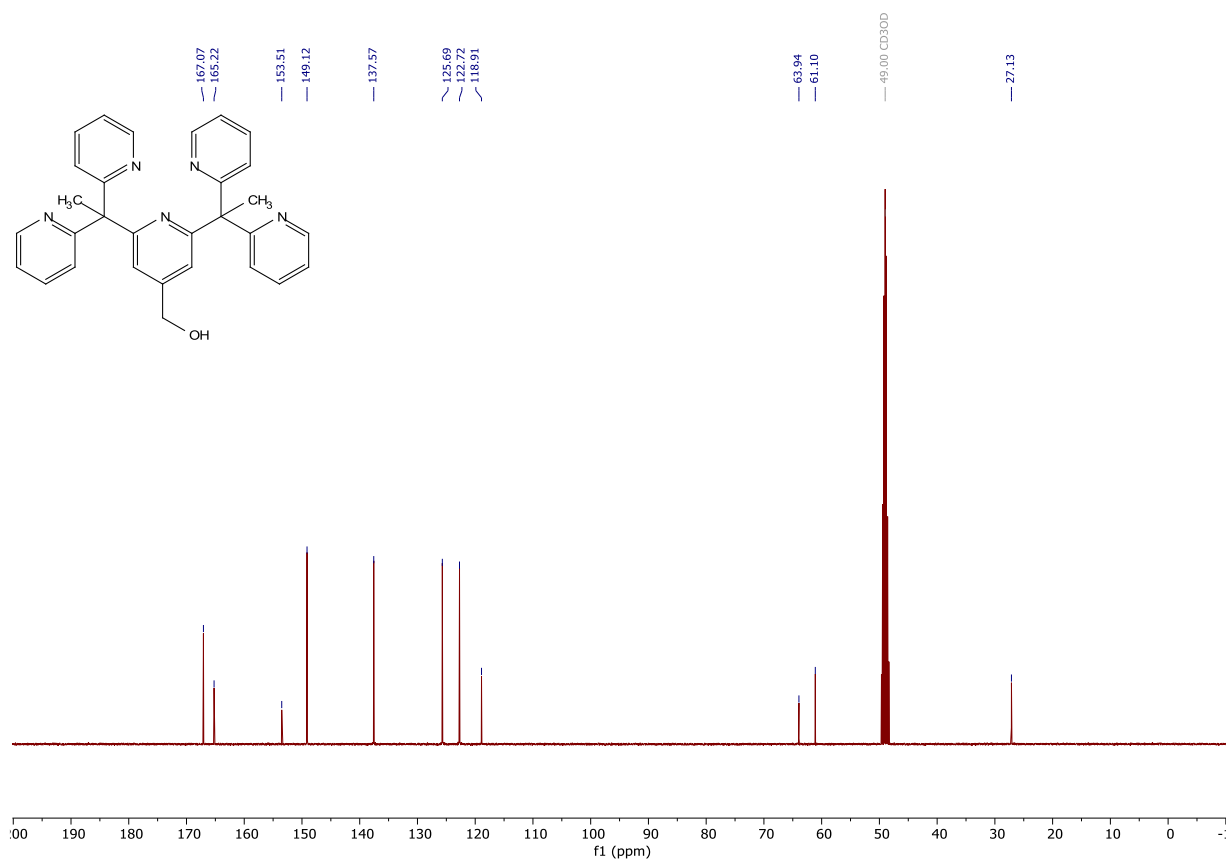
10.14. C-10

¹H
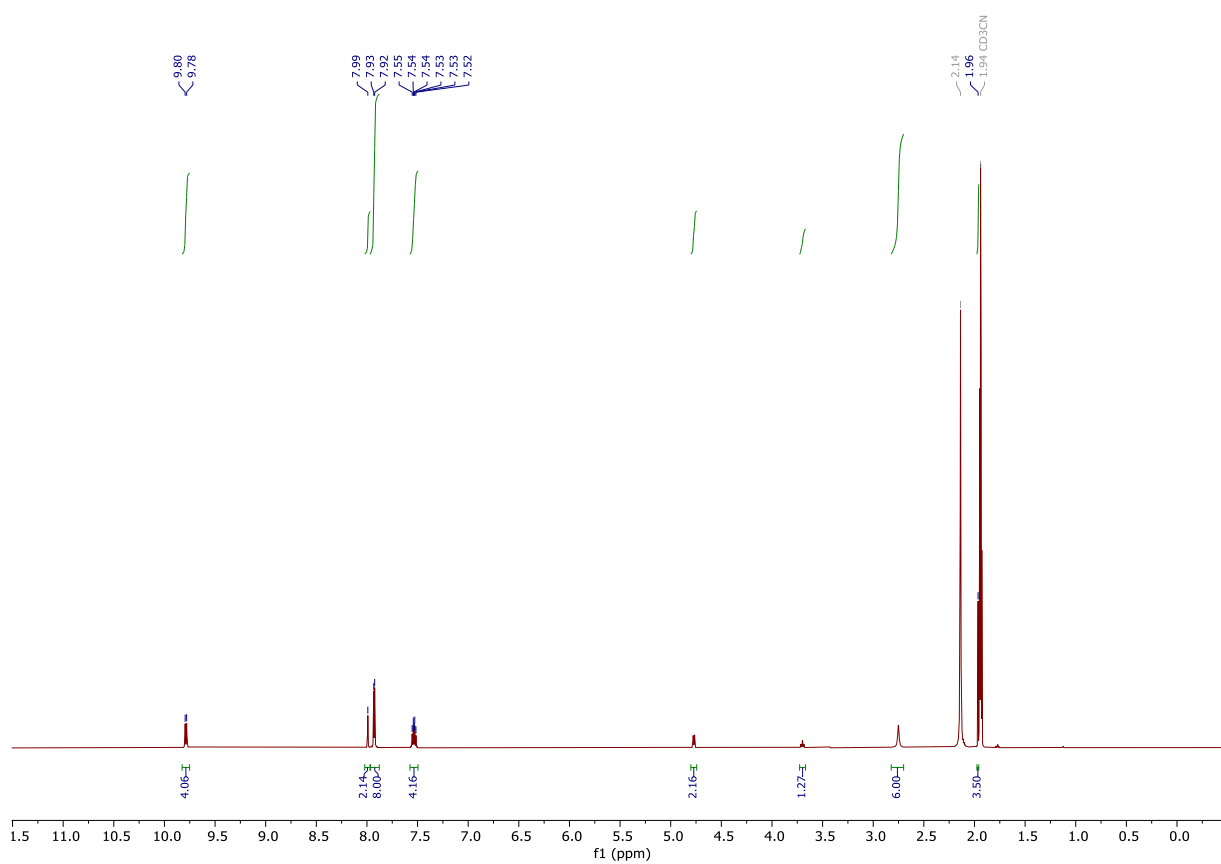
¹³C
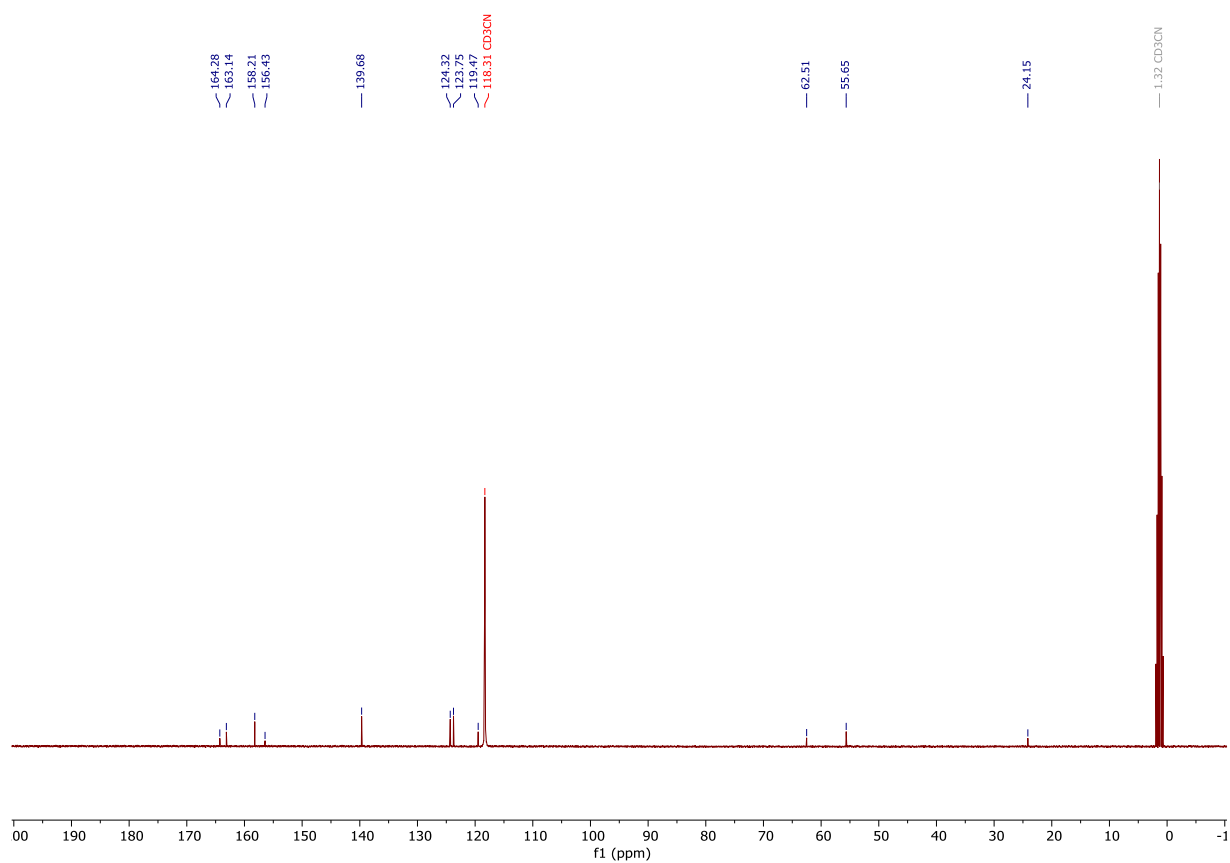
10.15. L-15

¹H

¹³C

10.16. C-12

¹H

¹³C

10.17. *V-11*

¹H NMR

10.18. L-2

¹H NMR

10.19. C-14

¹H

¹³C

10.20. L-3

¹H NMR
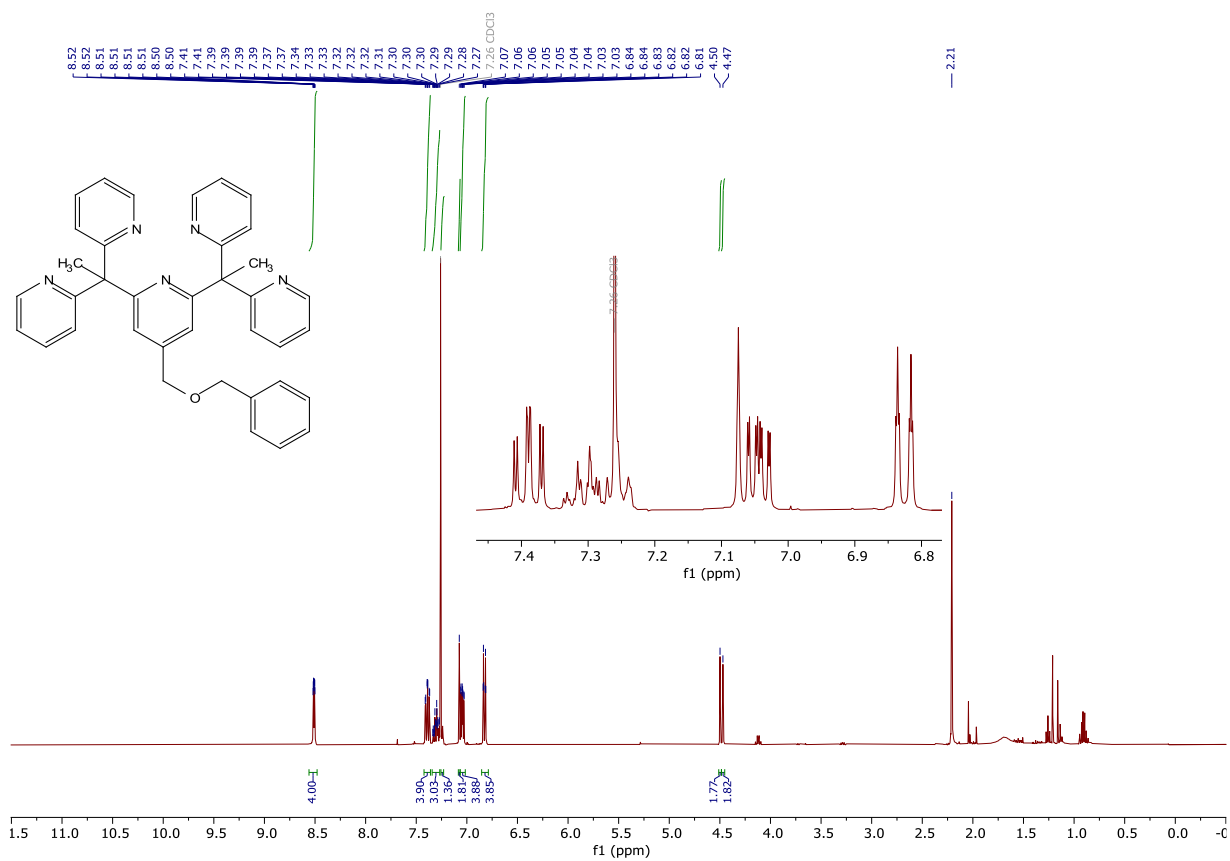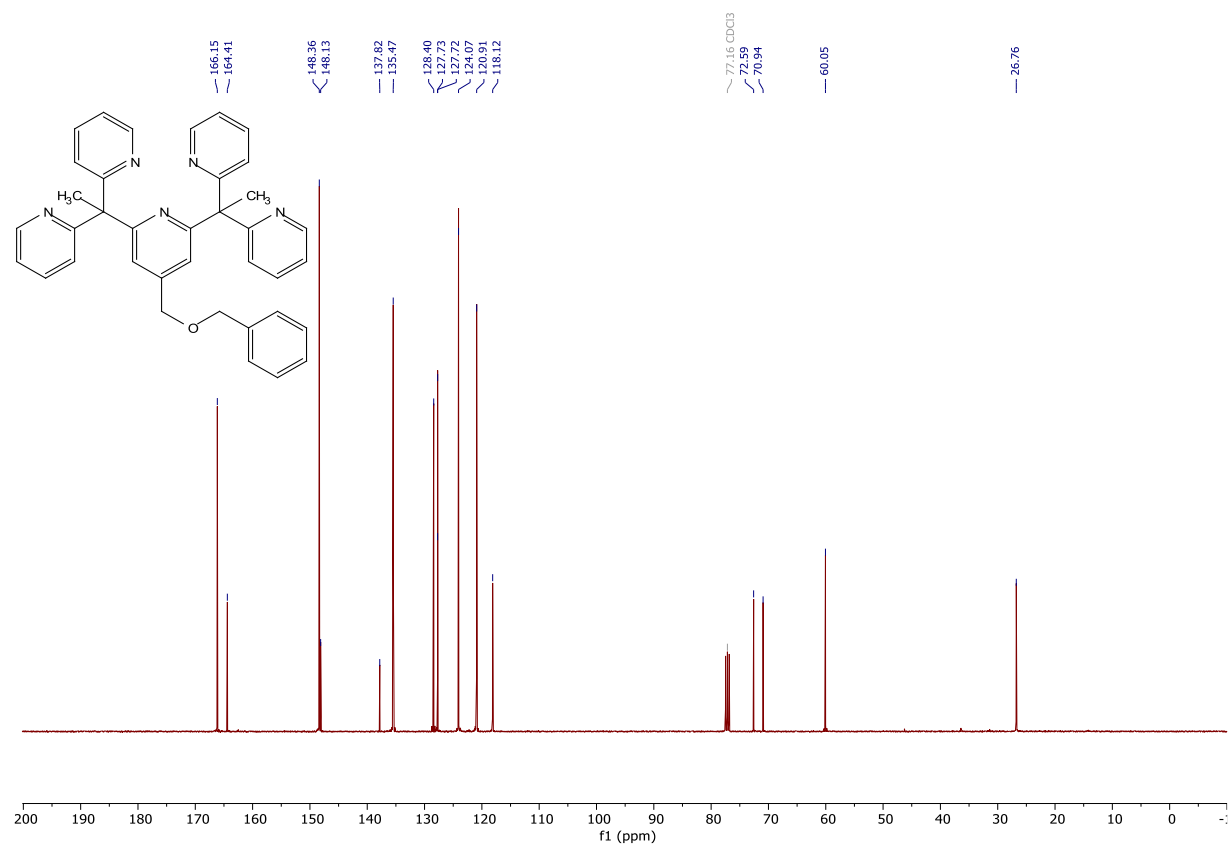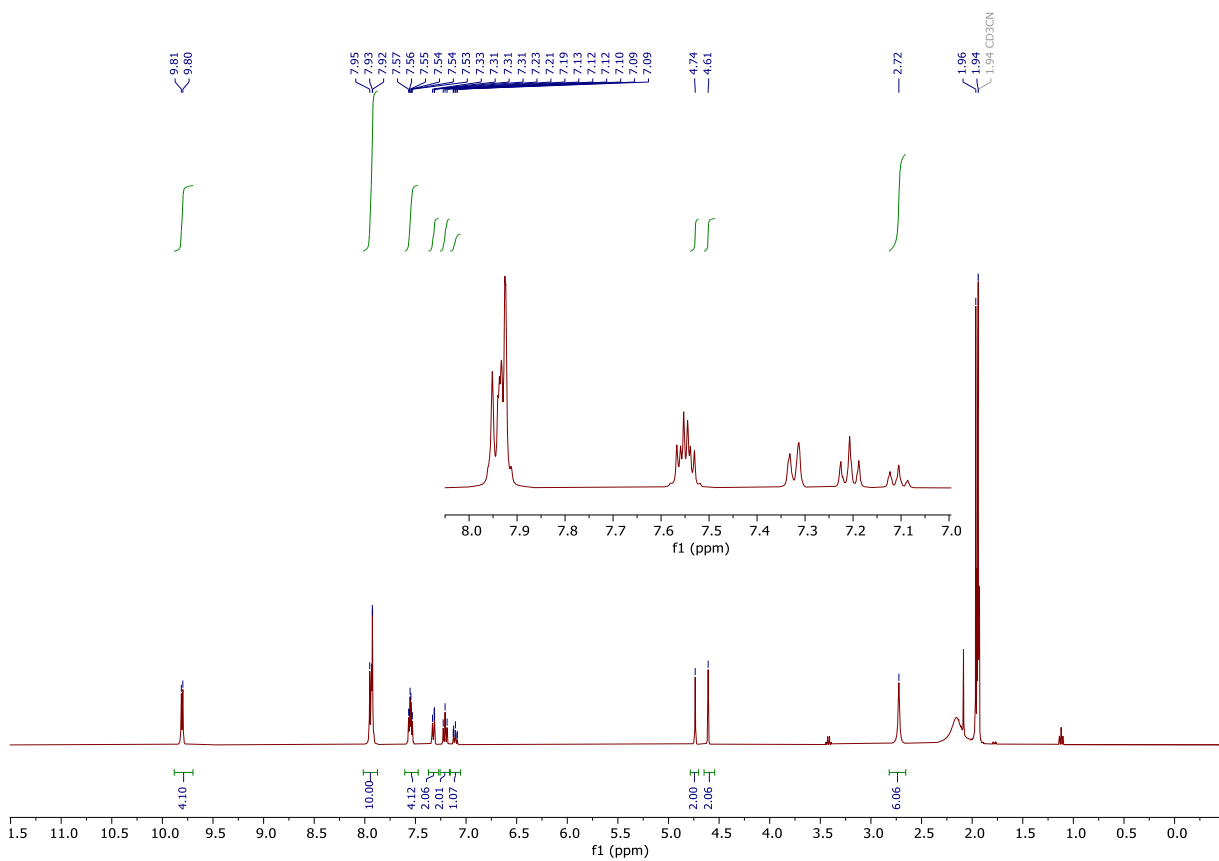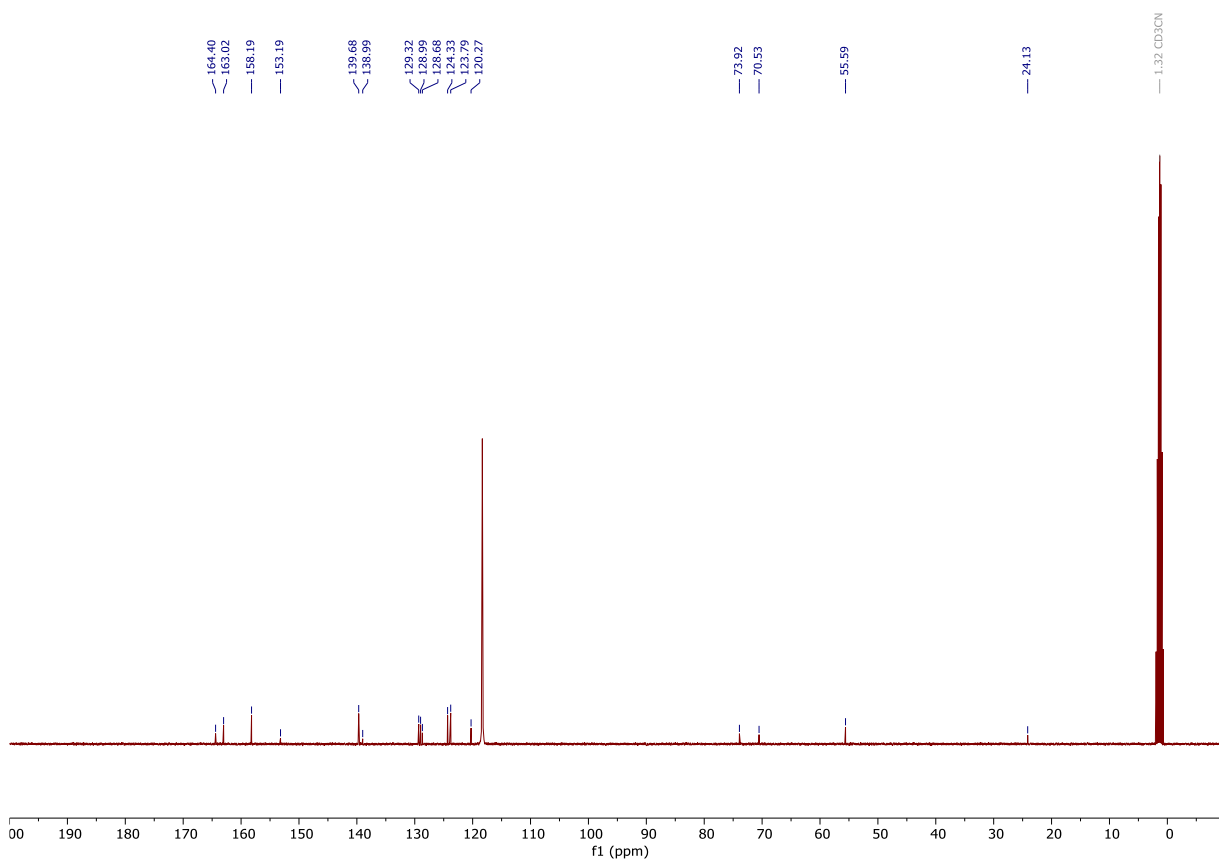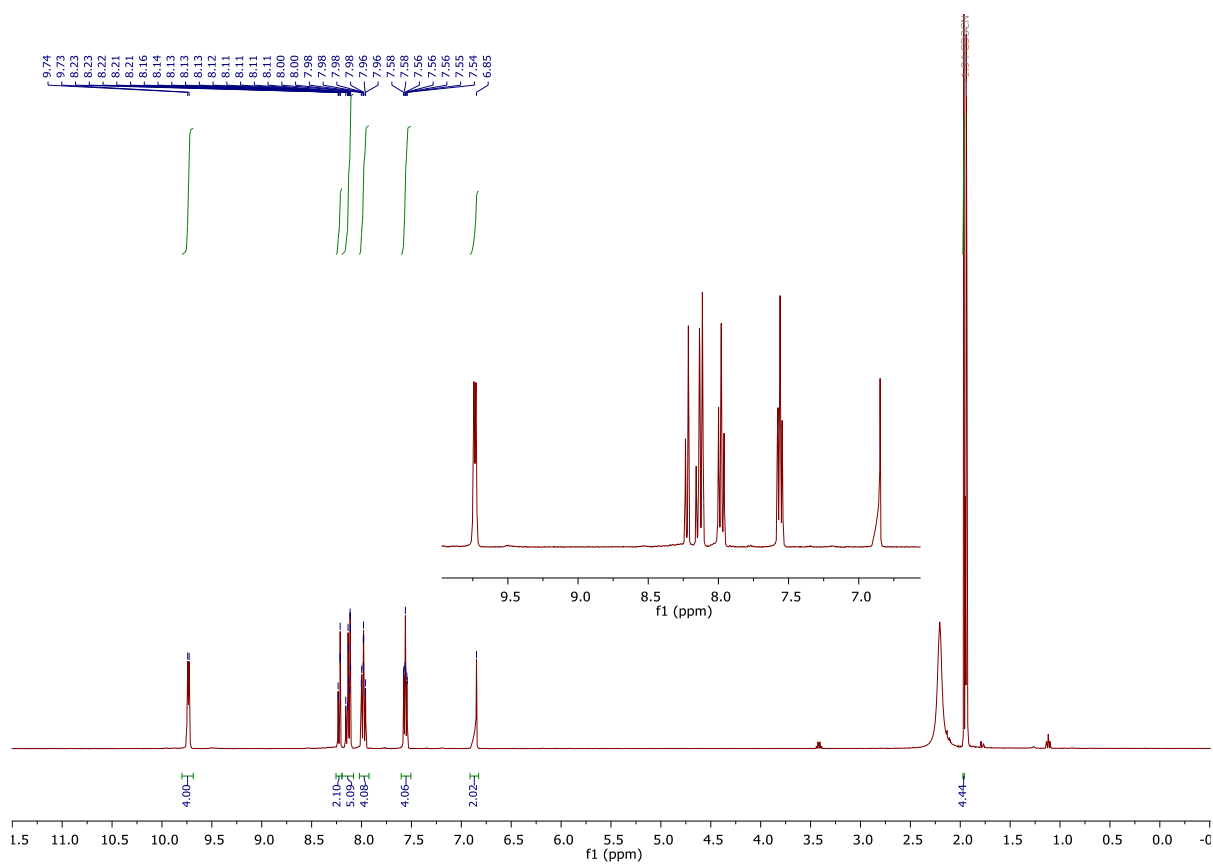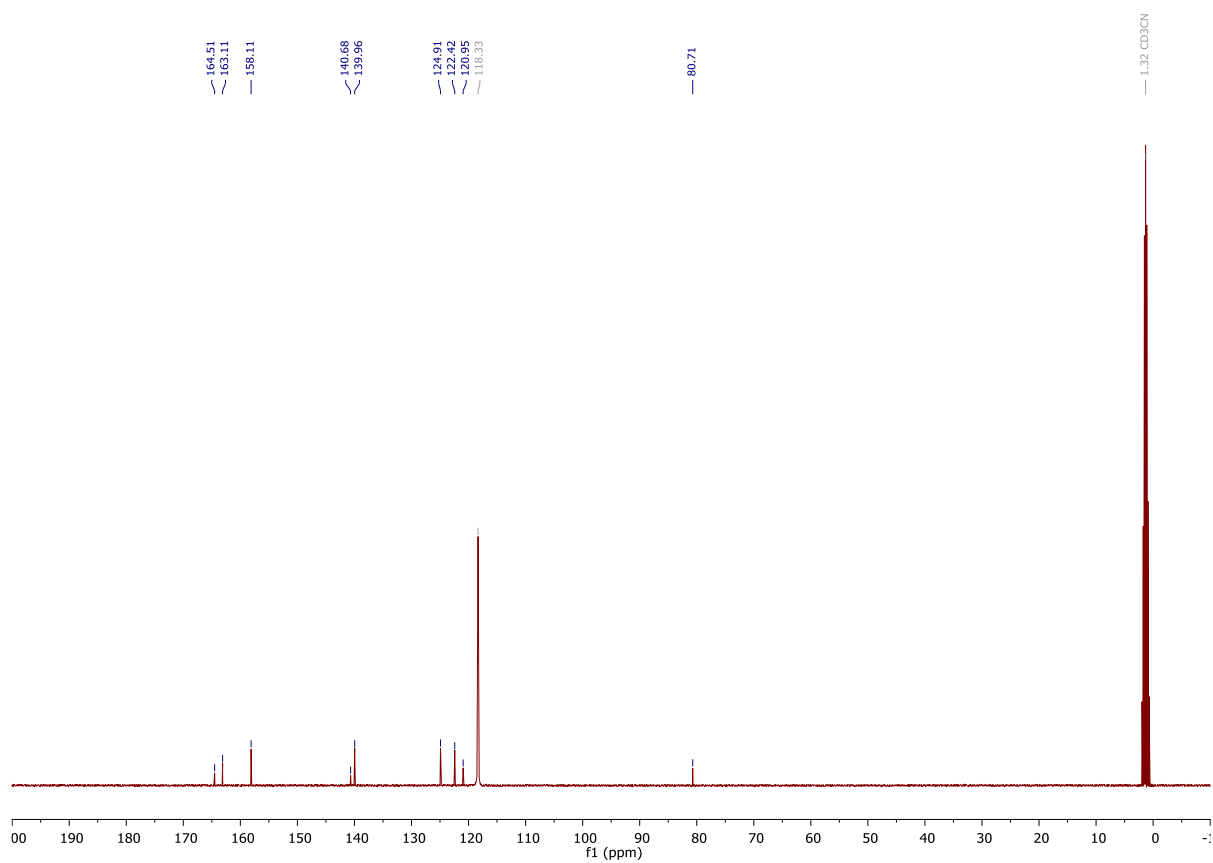
10.21. C-17

¹H
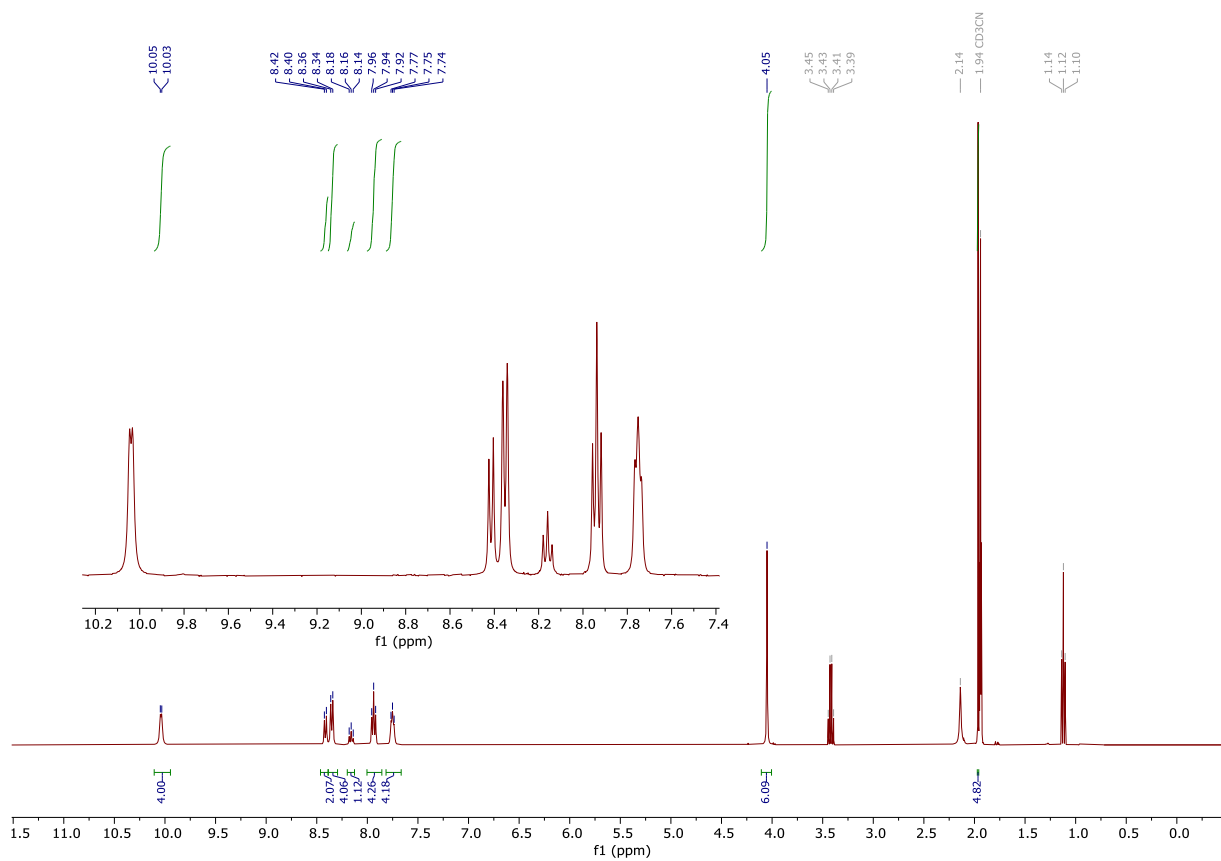
¹³C
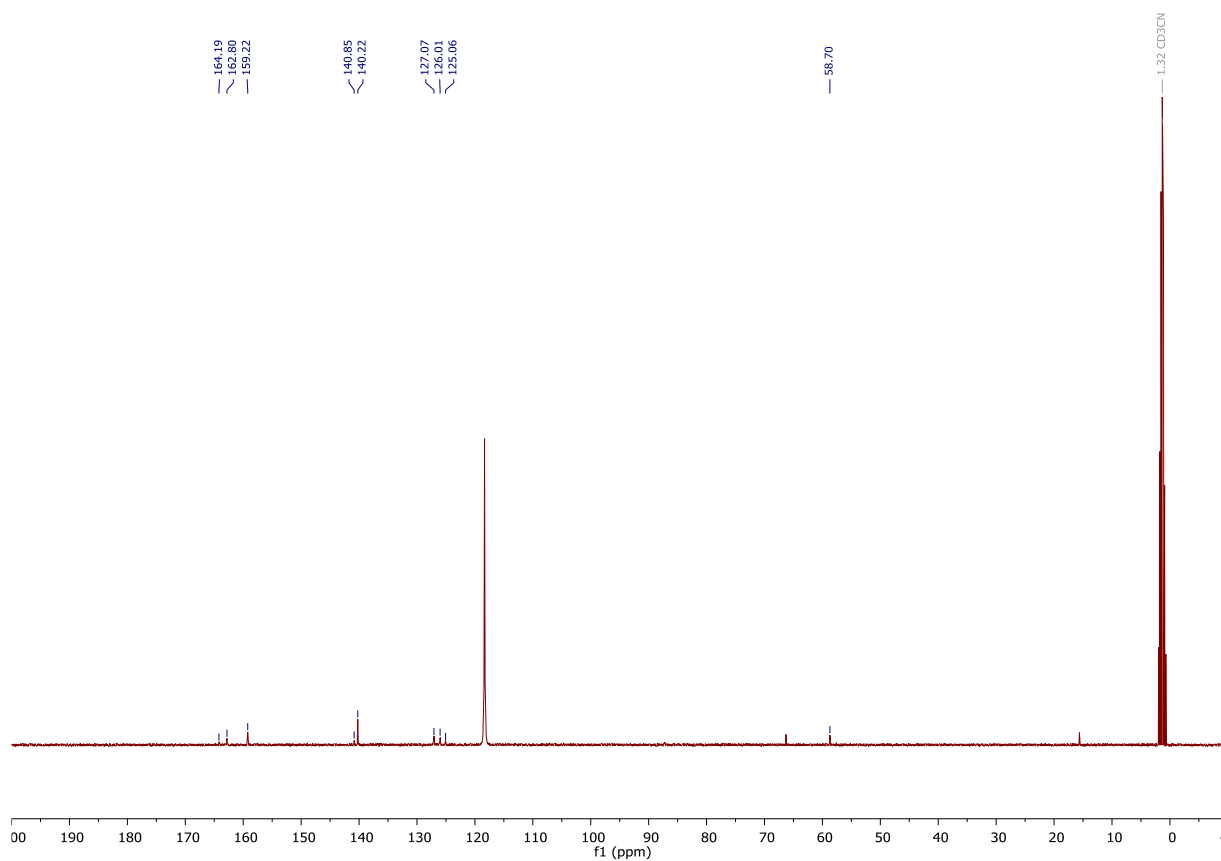
10.22. L-4

¹H
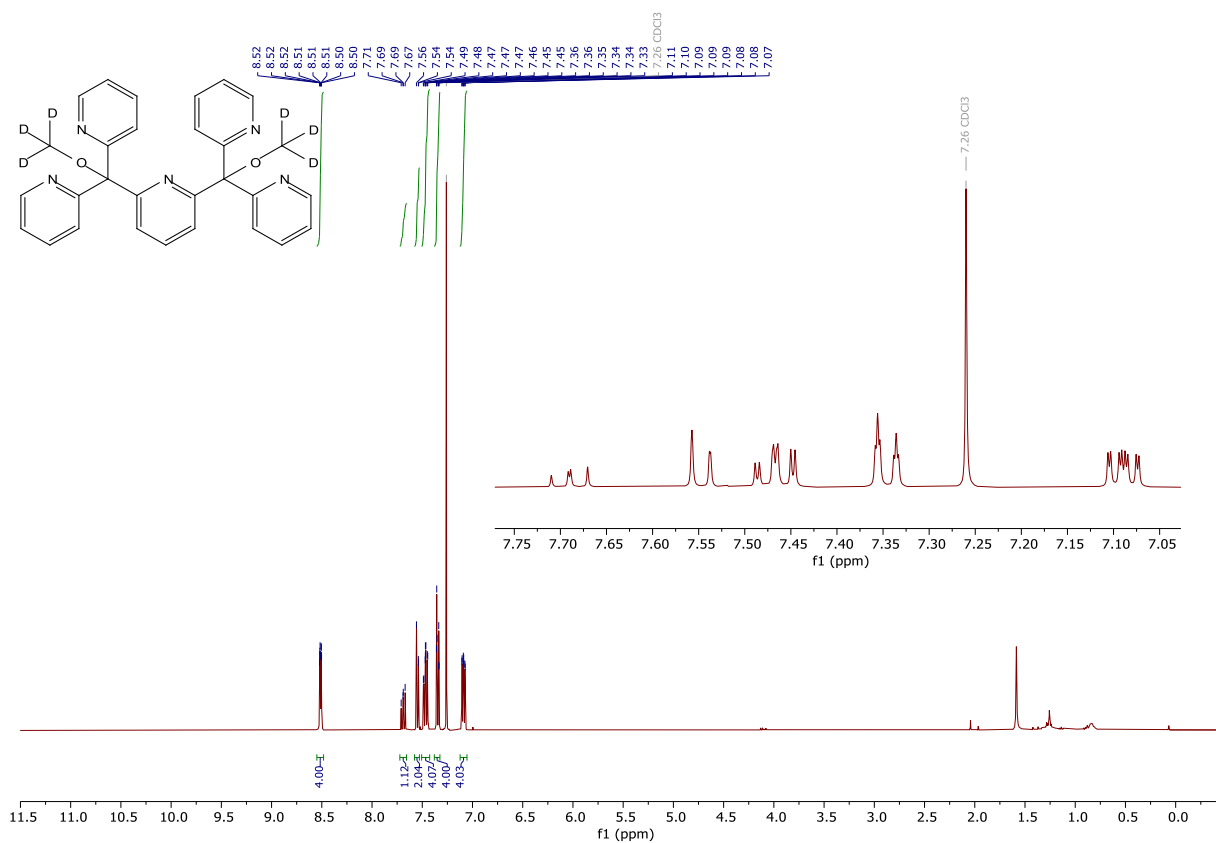
¹³C
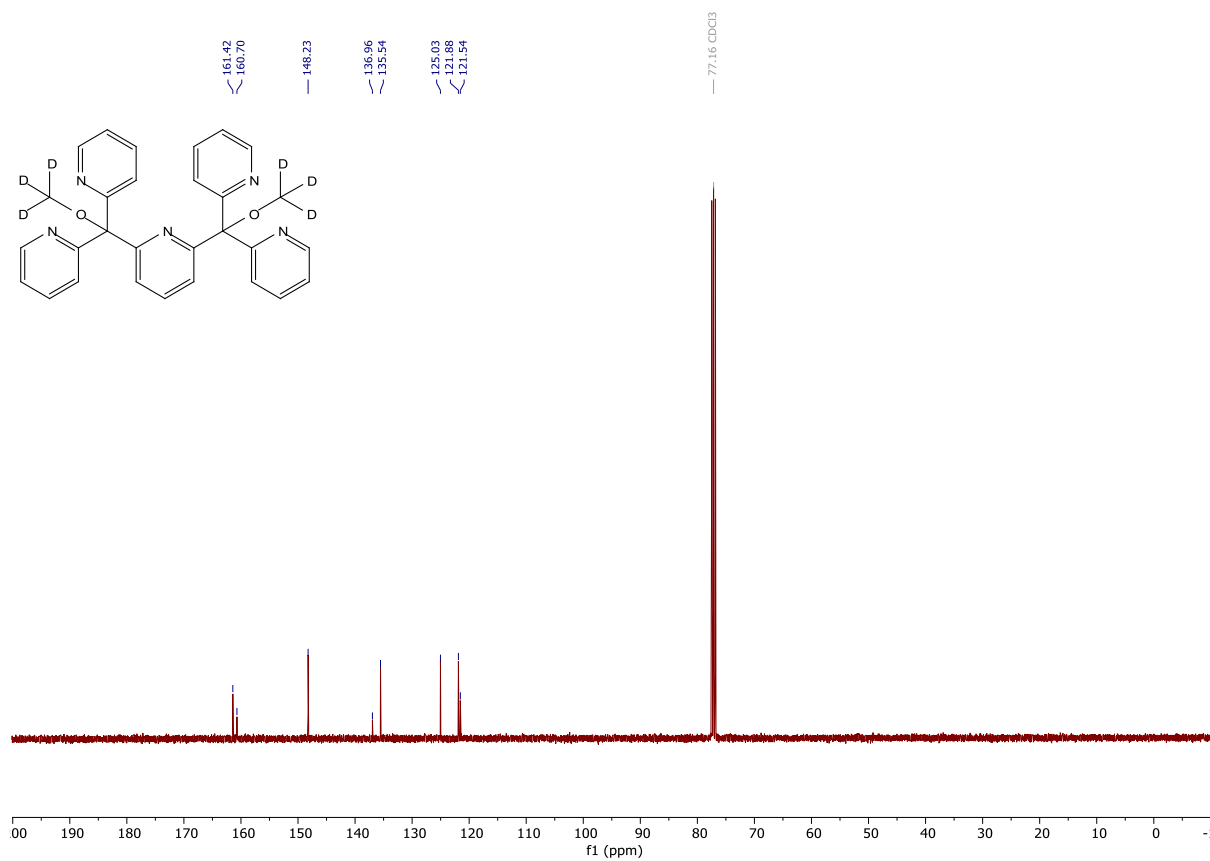
10.23. C-19

¹H
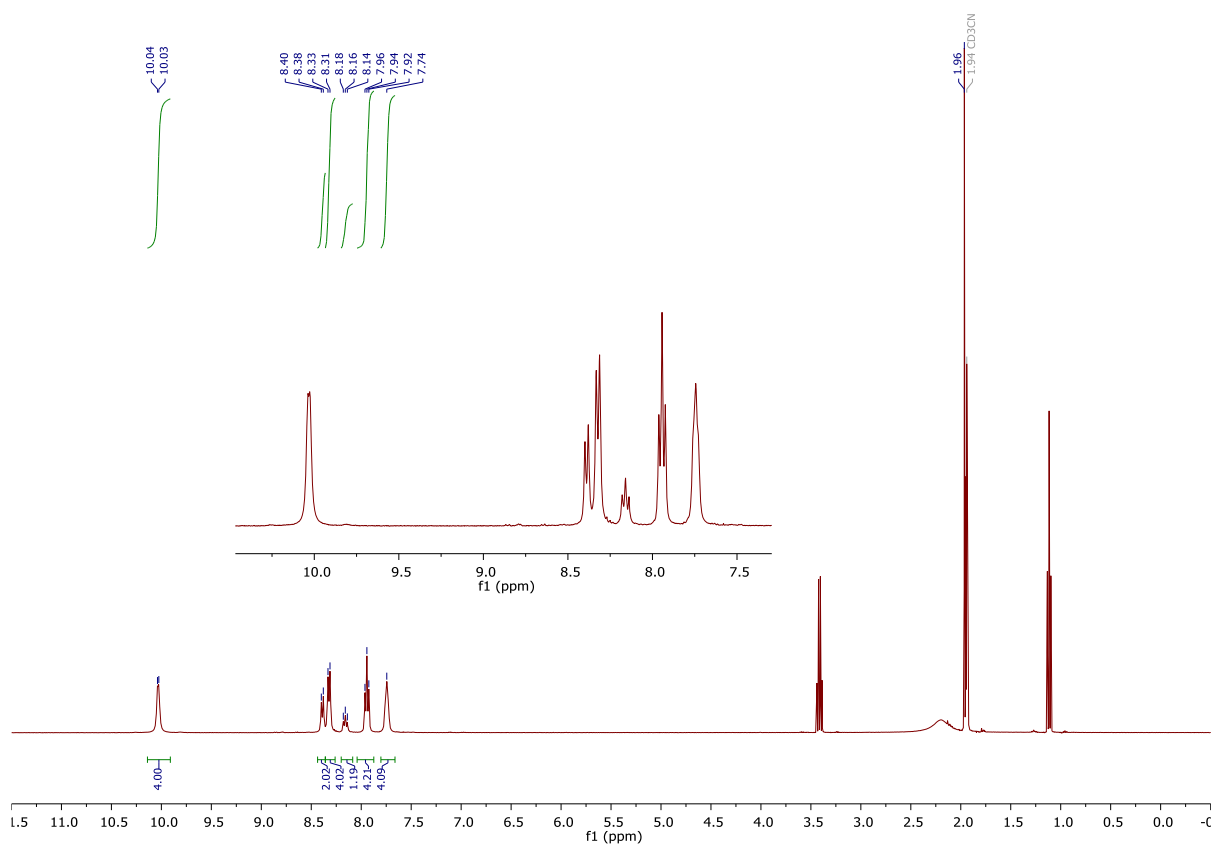
²H
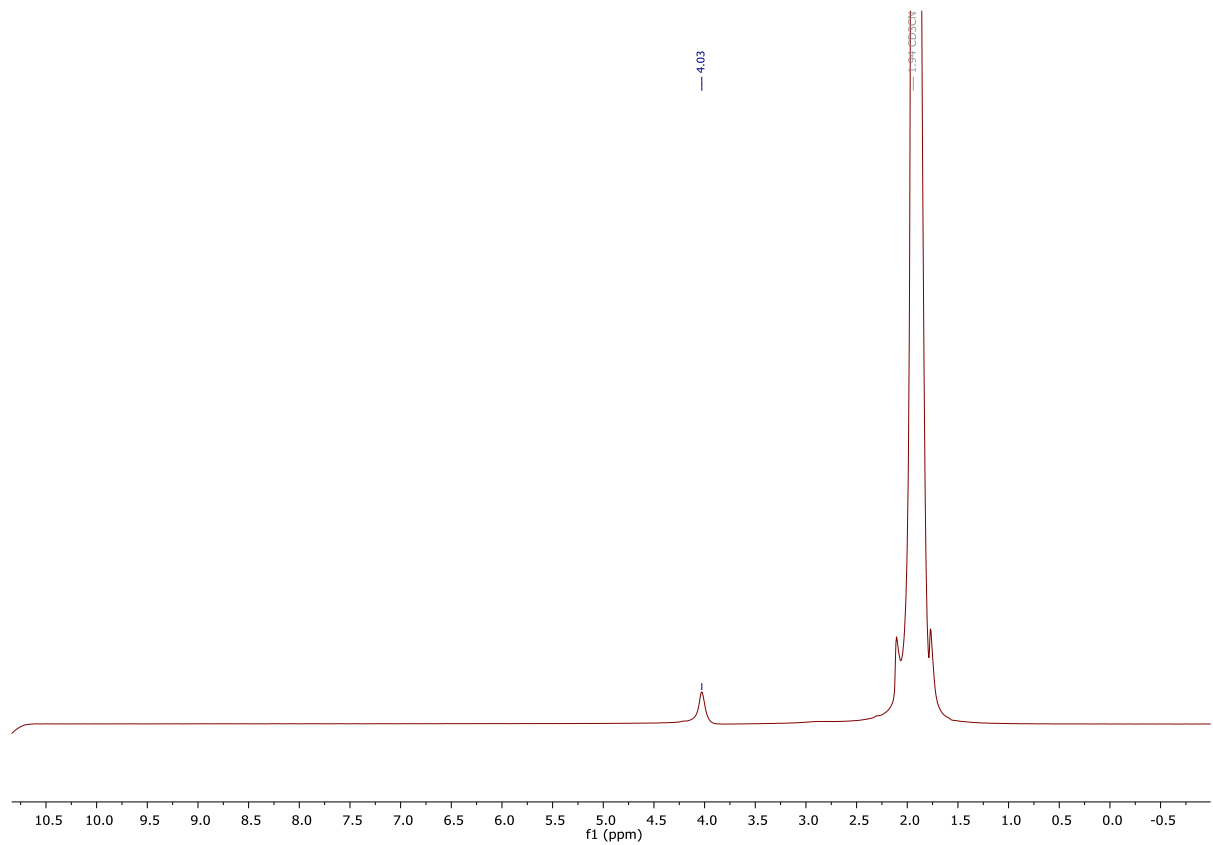
¹³C
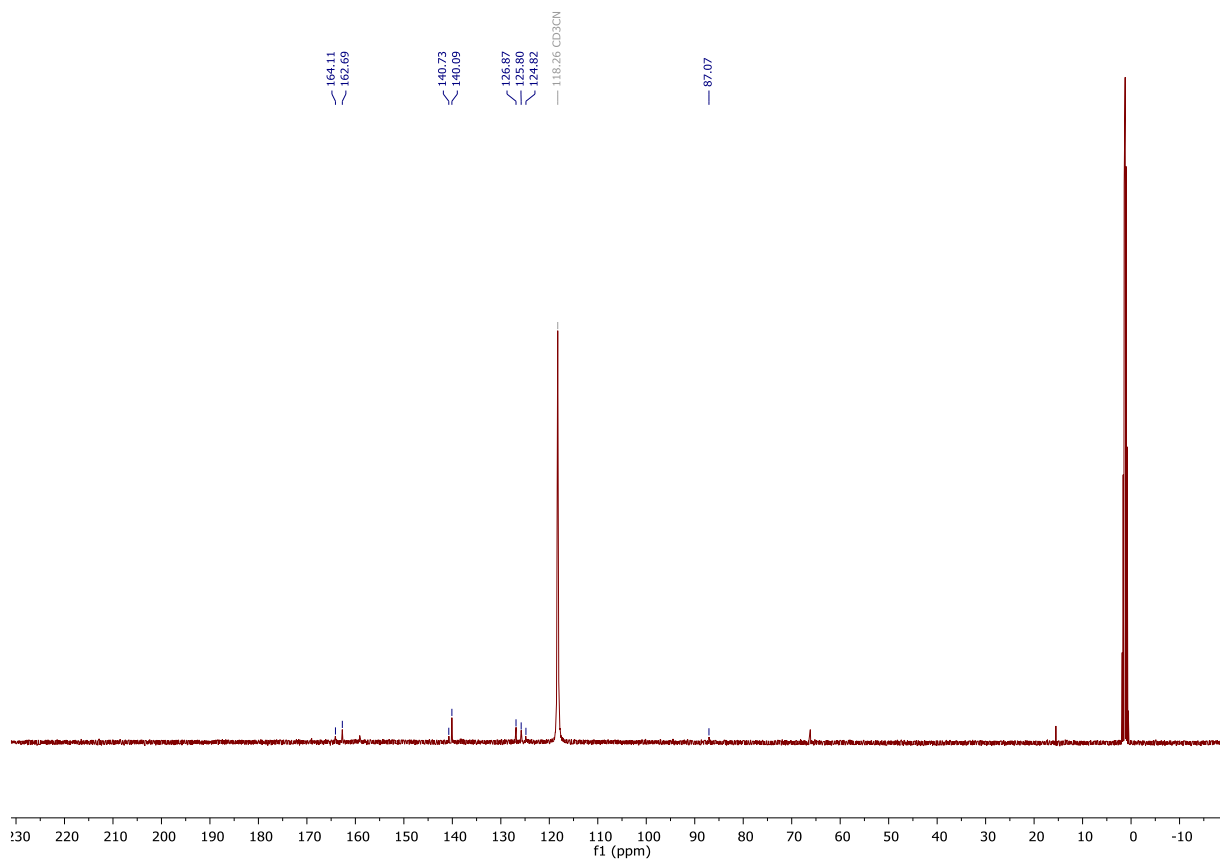
10.24. L-5

¹H – the crude product's NMR spectrum is shown here due to decomposition of **L-5** during column chromatography.
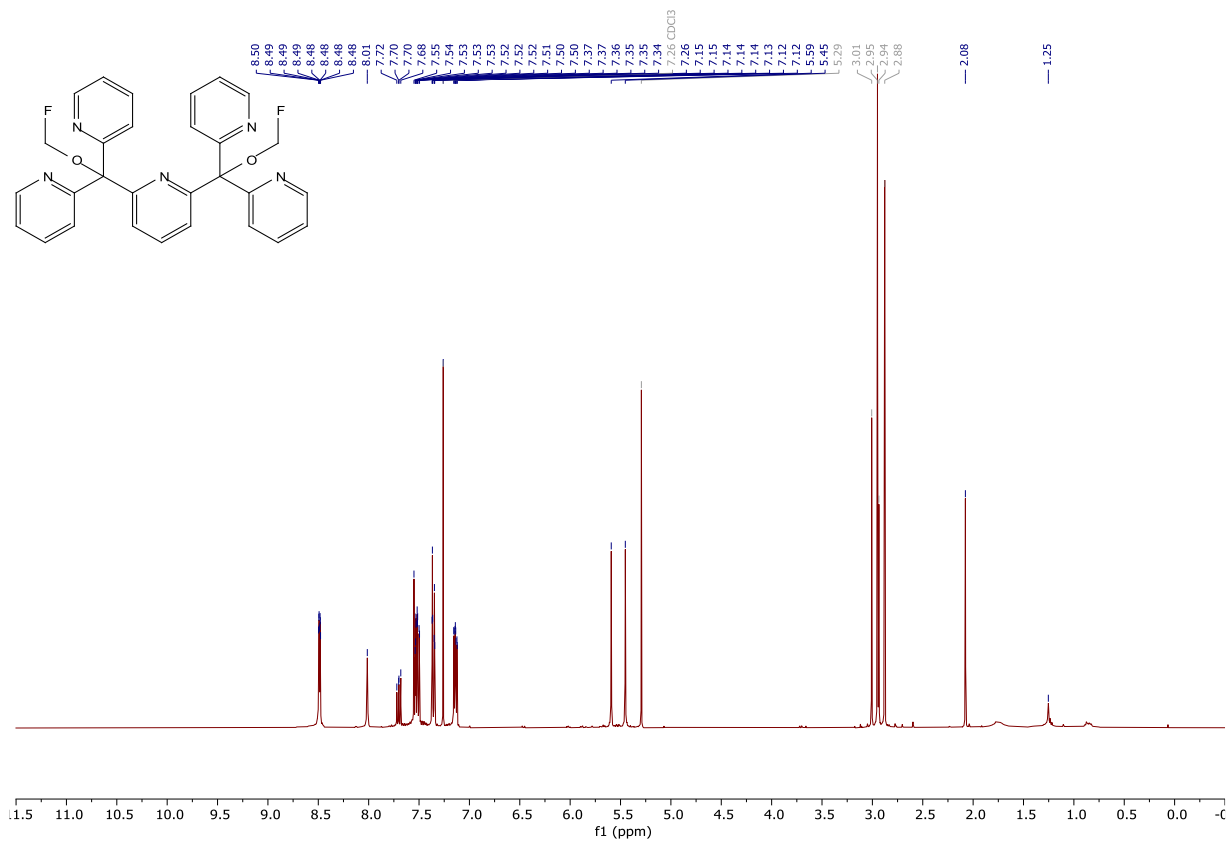
¹⁹F
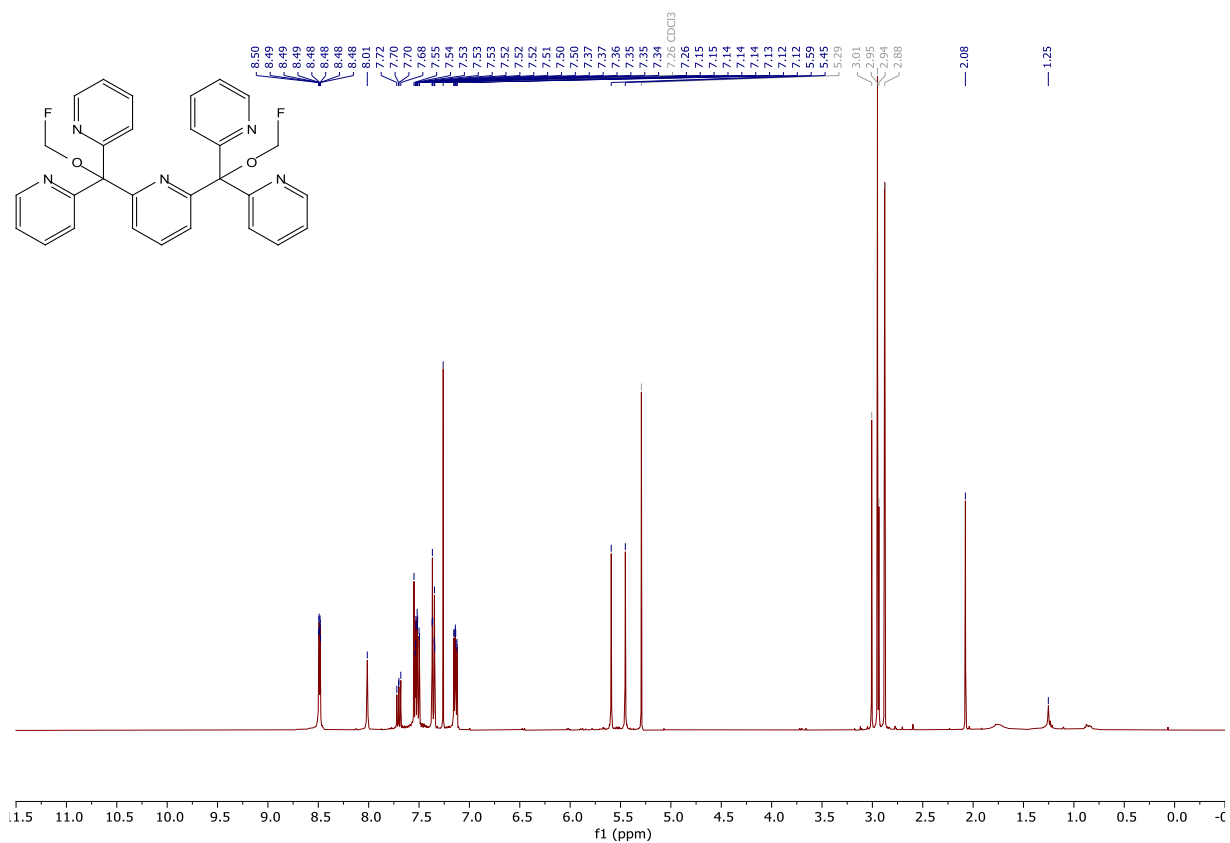
10.25. L-6

¹H – the crude product's NMR spectrum is shown here due to decomposition of **L-5** during column chromatography.

¹⁹F

10.26. V-12

¹H
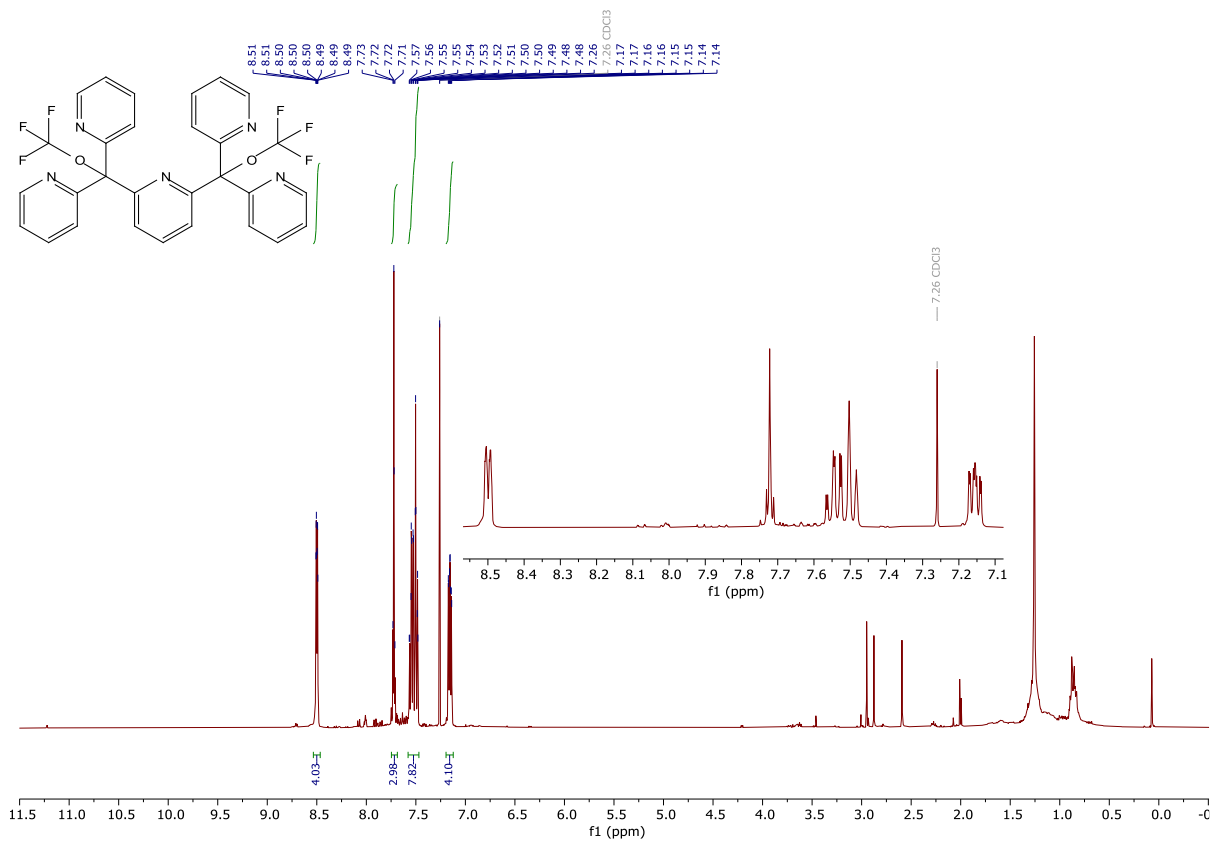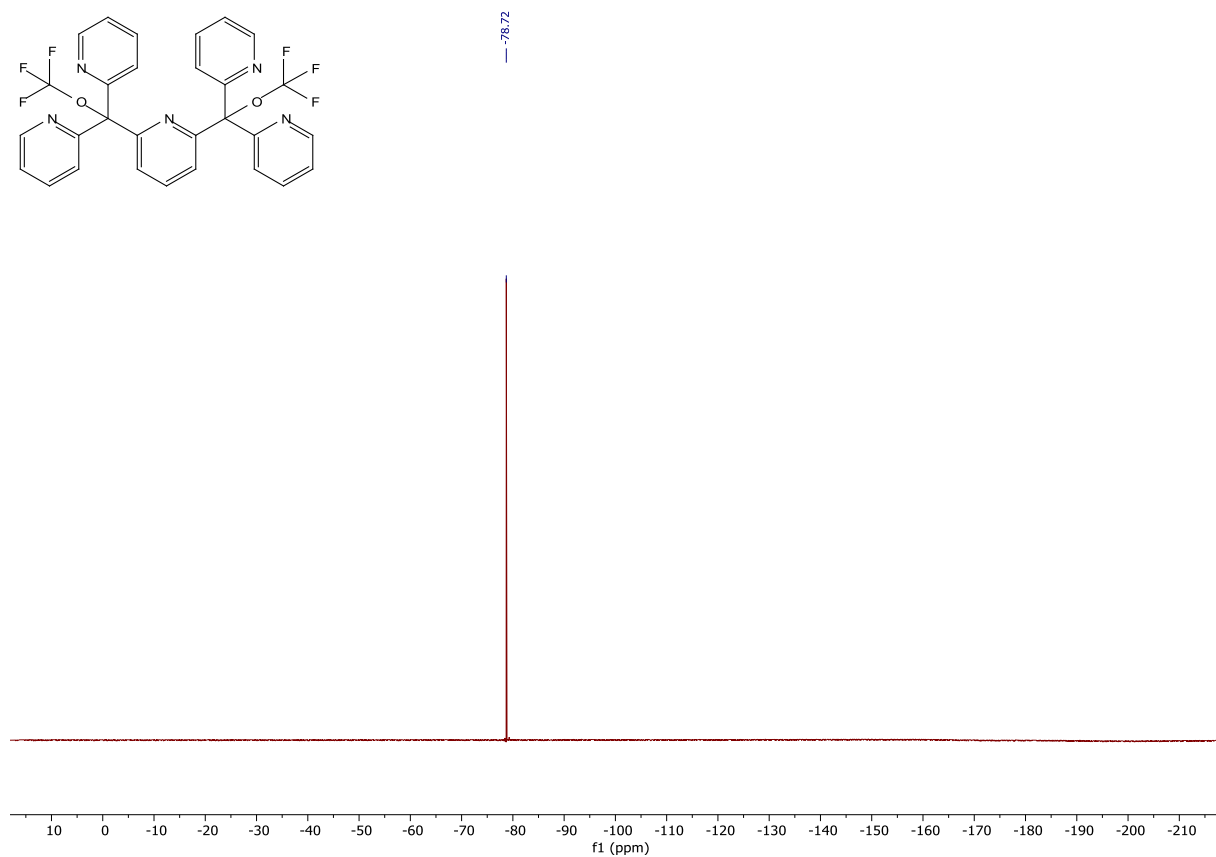
10.27. V-13

¹H
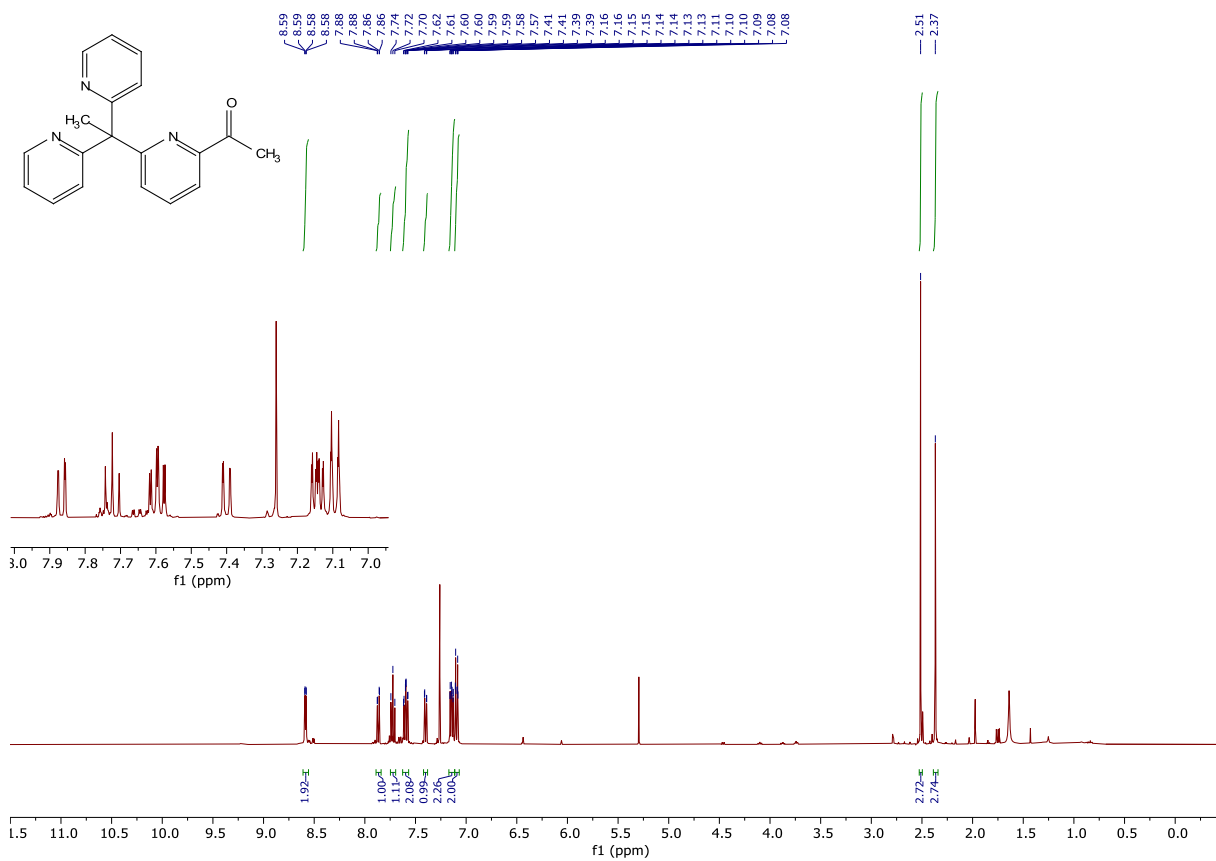
10.28. L-7

¹H
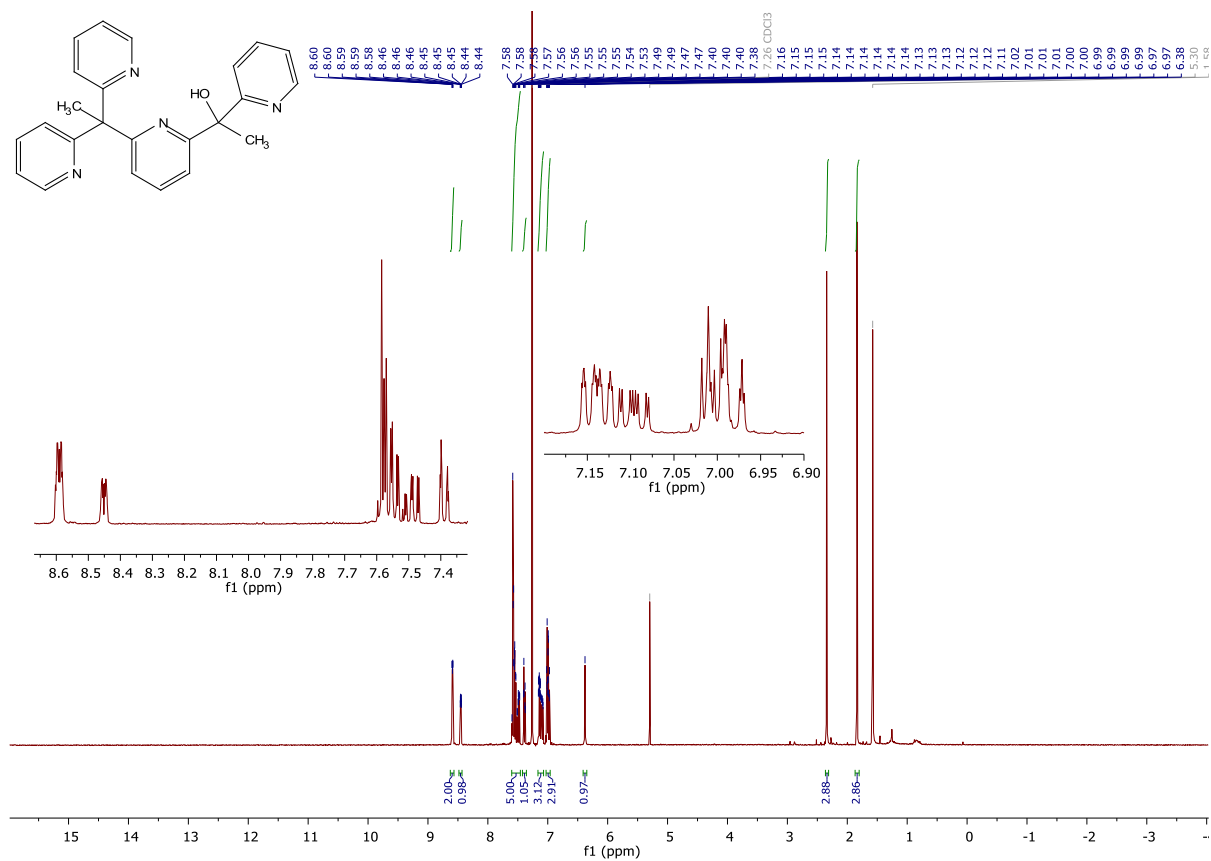
¹³C
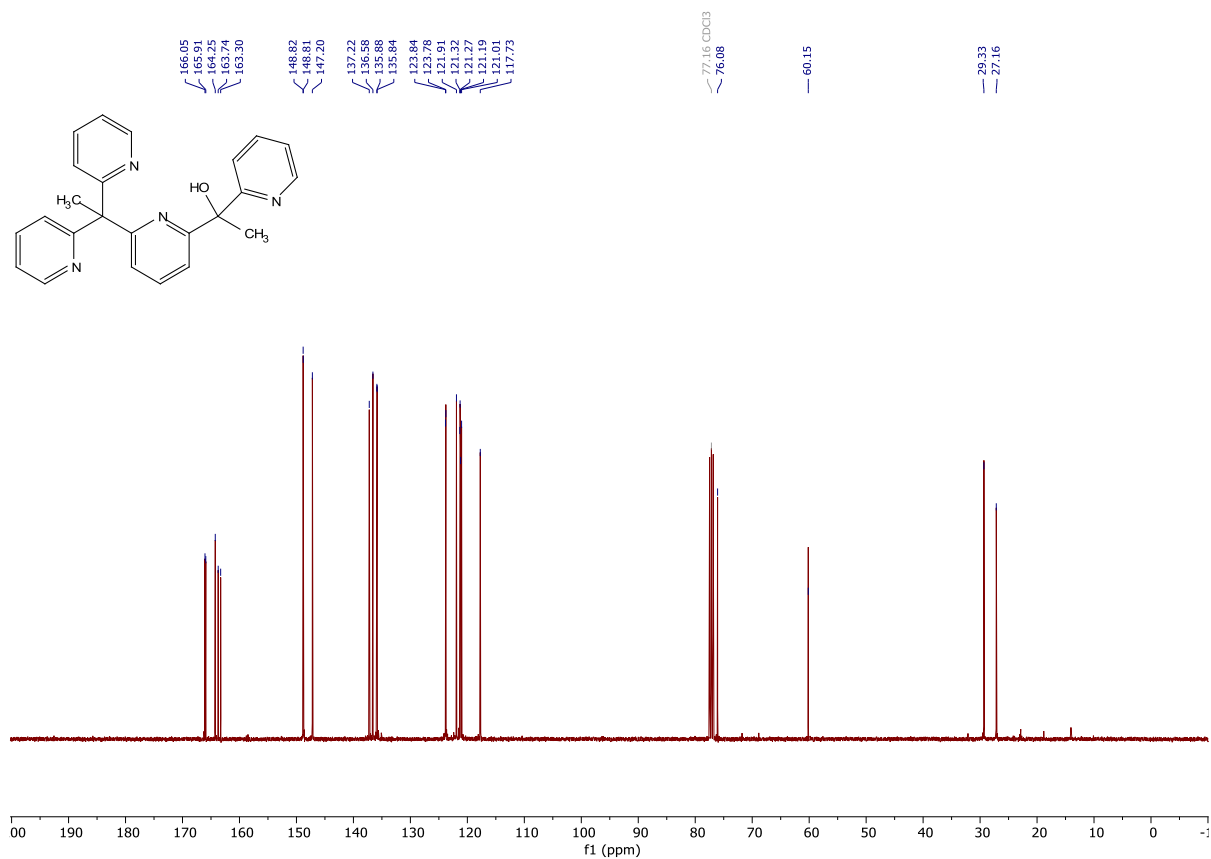
10.29. **C-20**

¹H
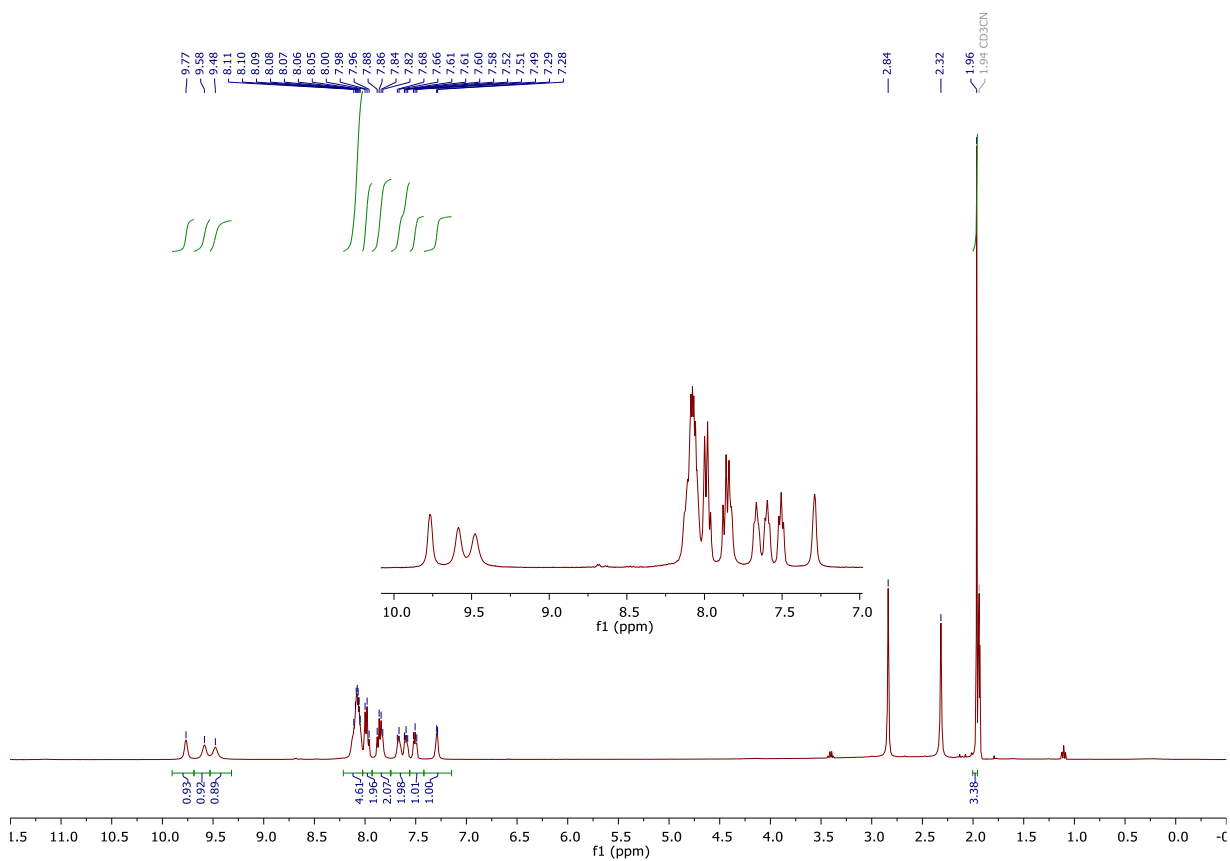
¹³C
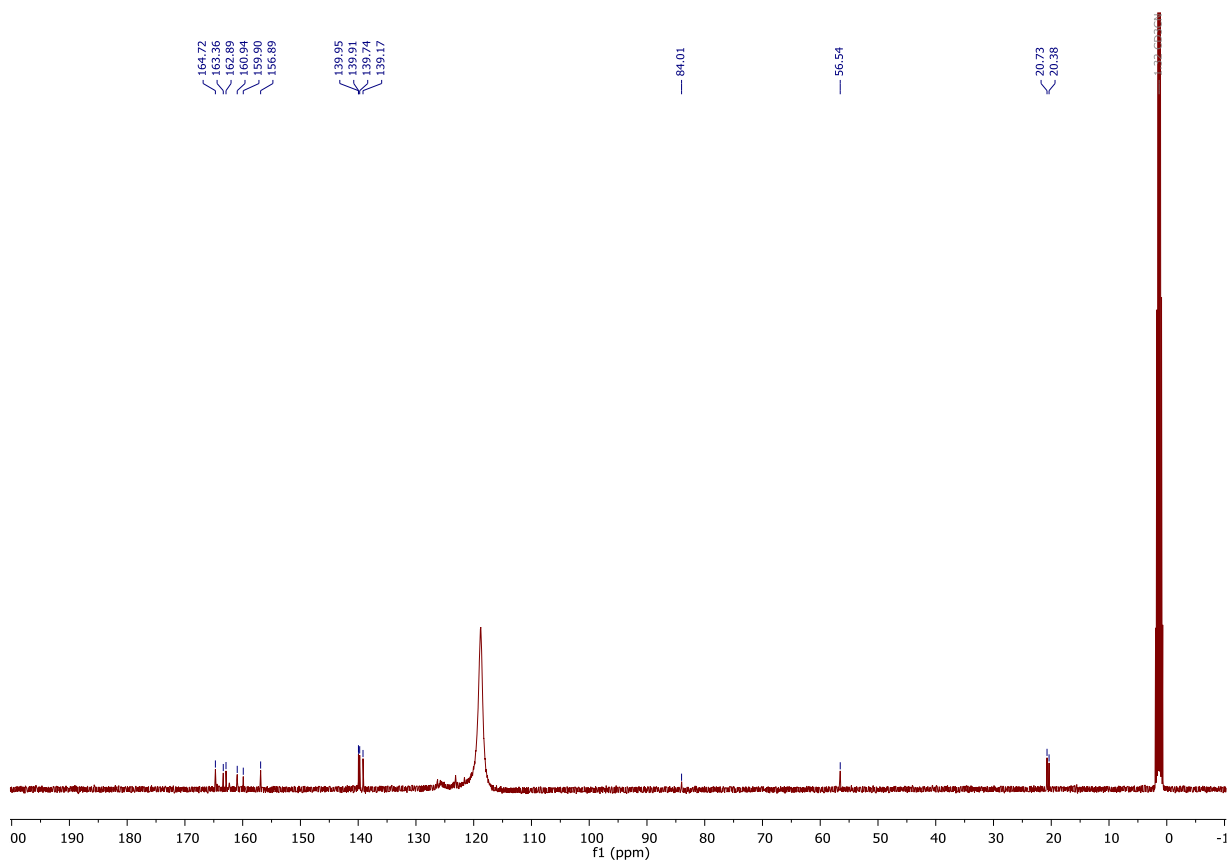
10.30. *V-15*

¹H

10.31. *V-16*

¹H

¹³C

10.32. L-8
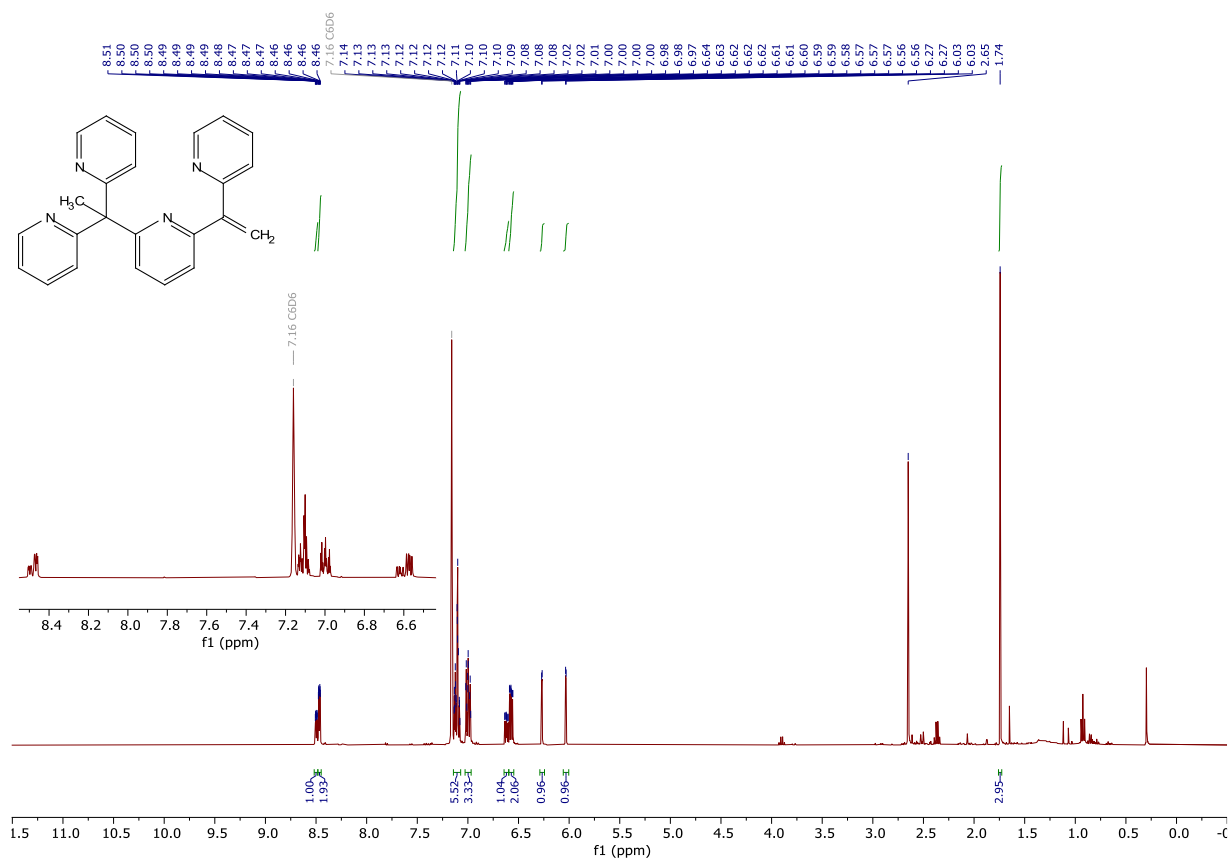
¹H
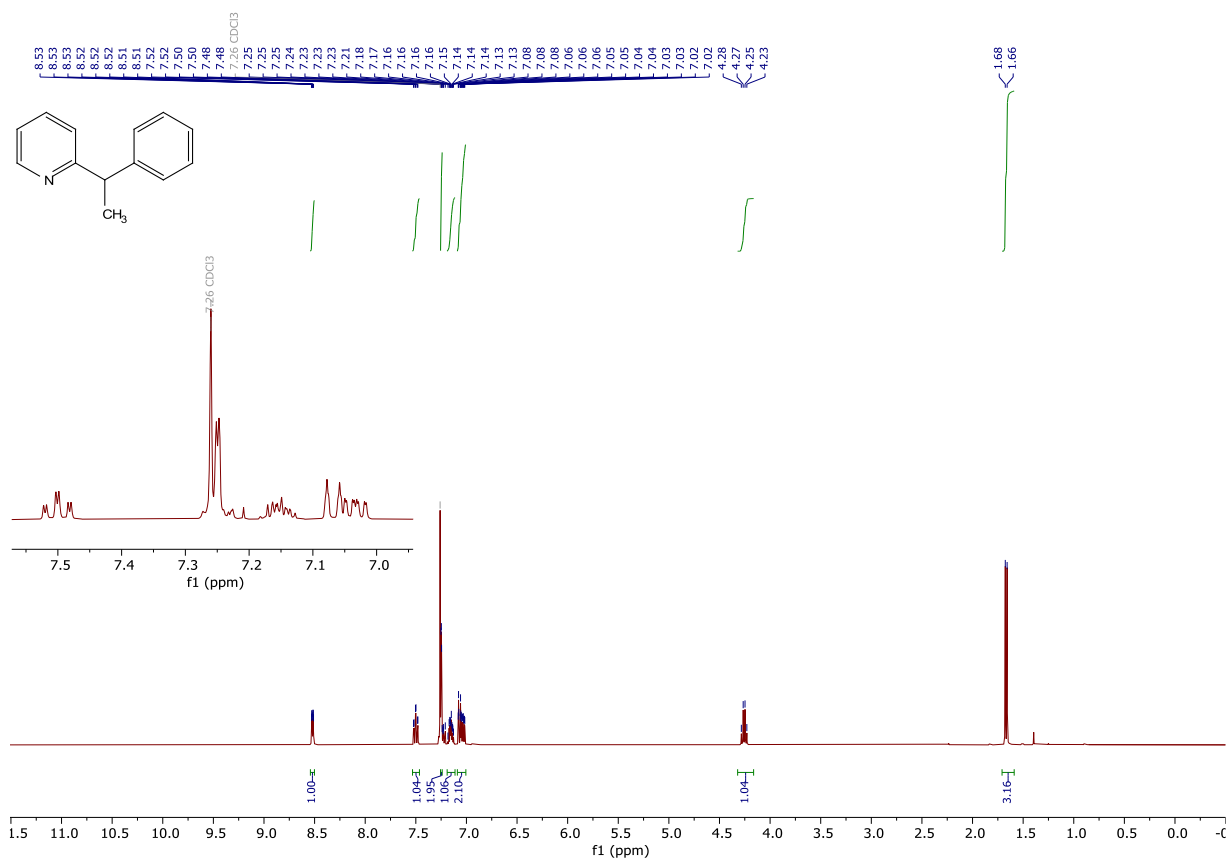
¹³C
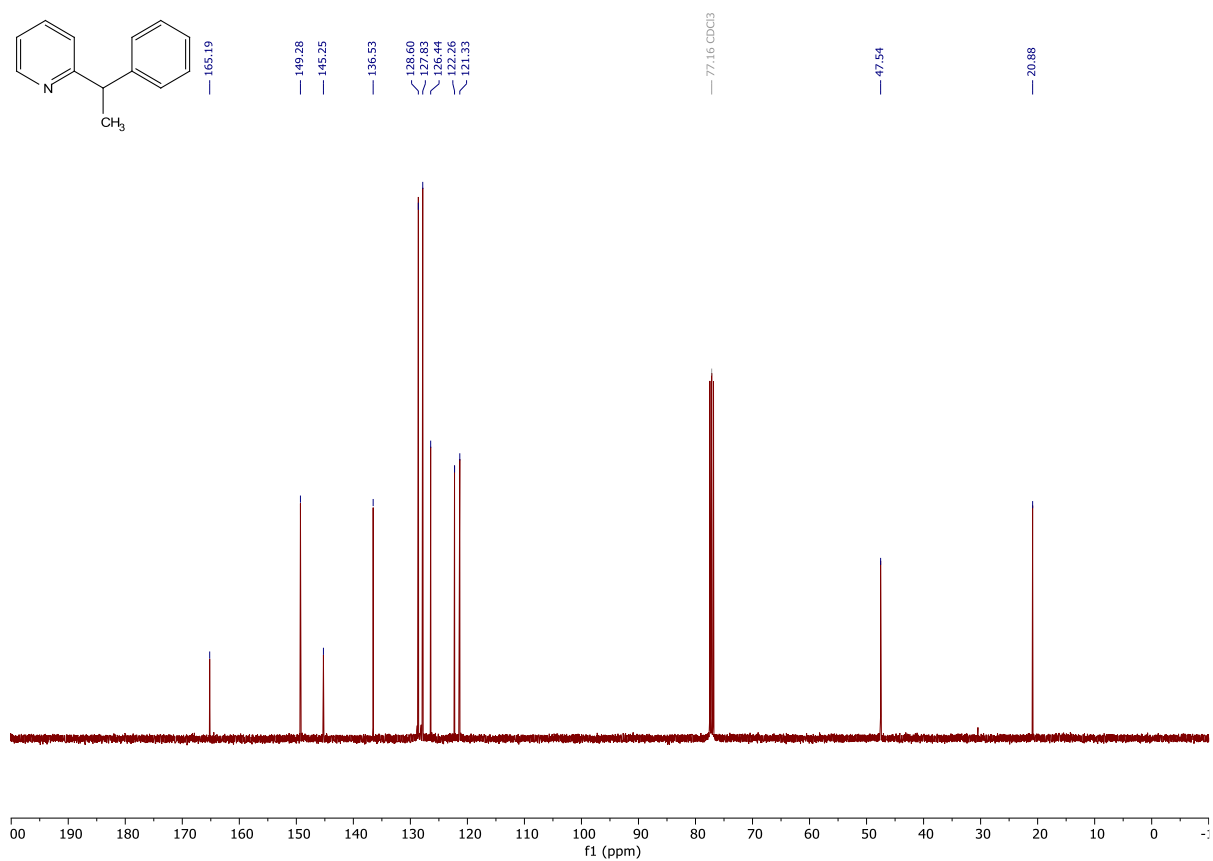
10.33. L-9

¹H
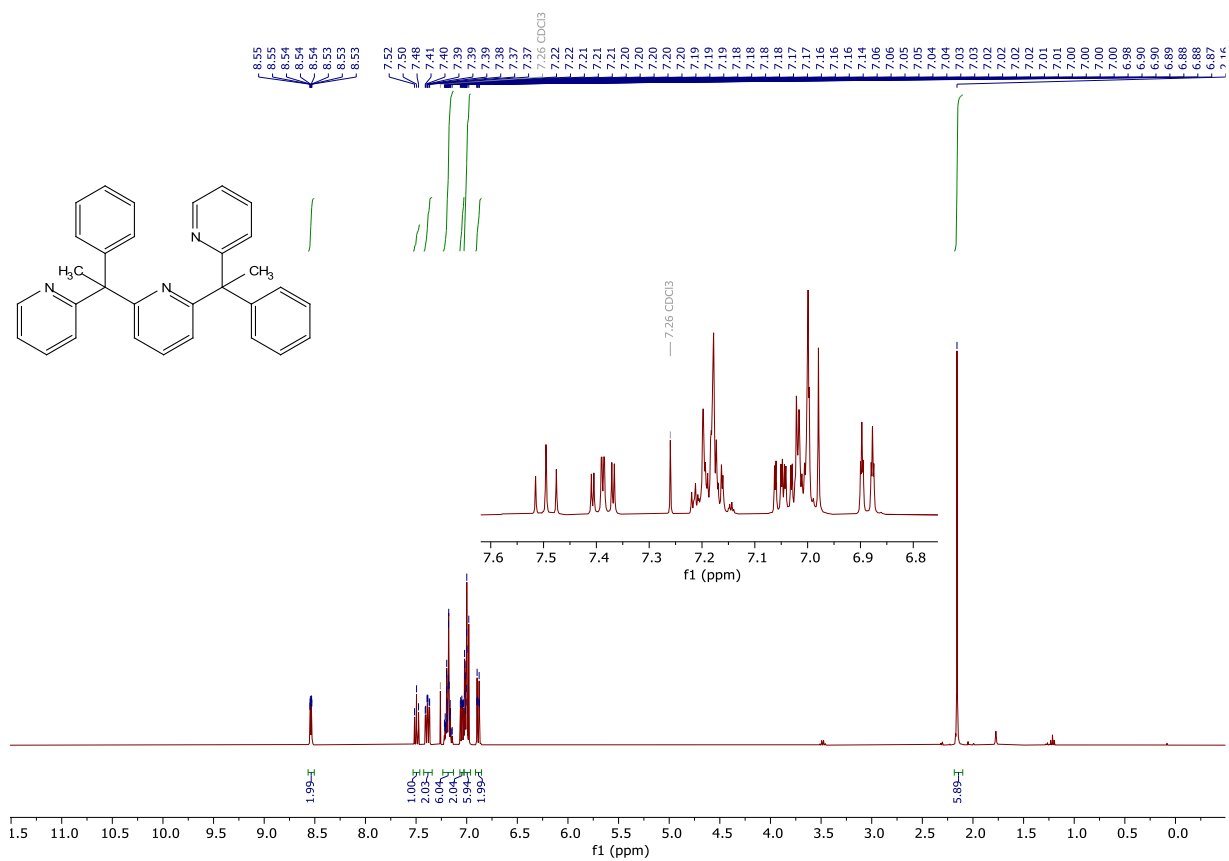
¹³C
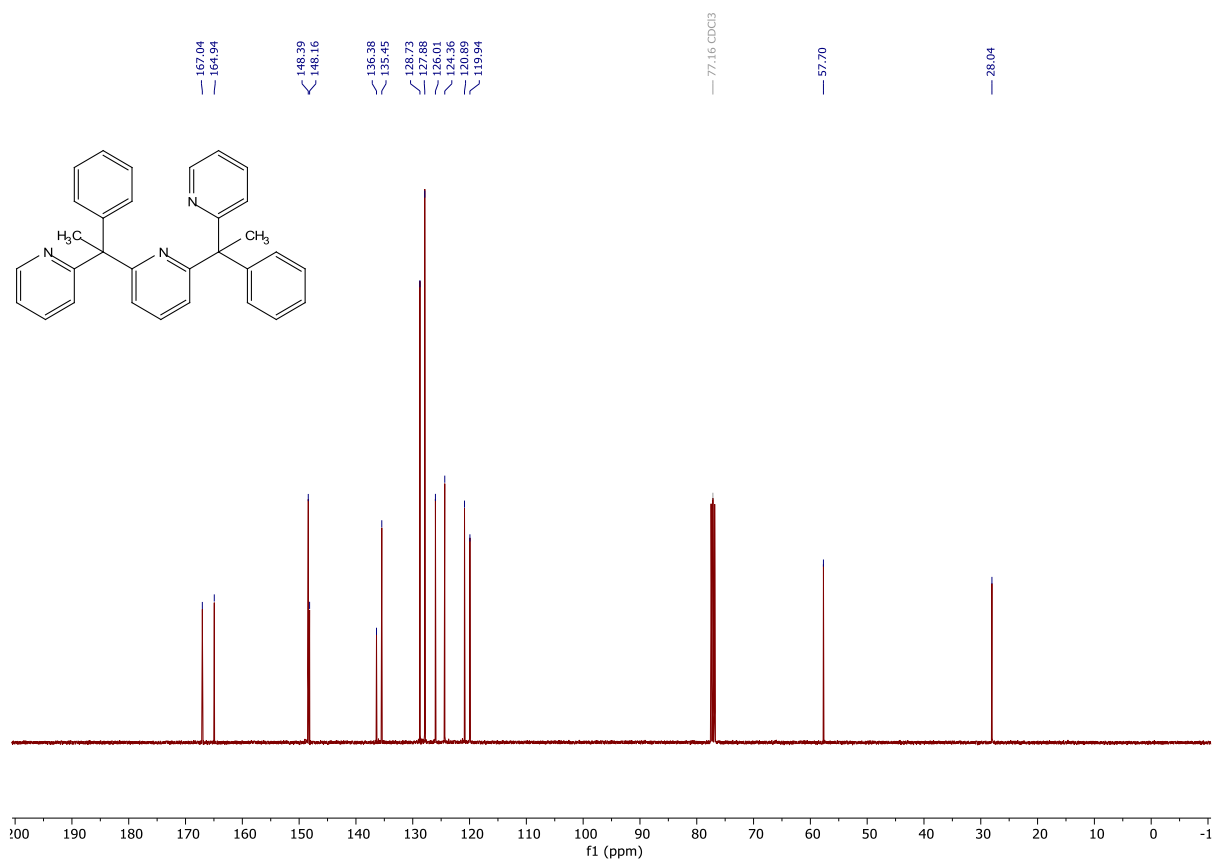
10.34. *V-21*

¹H
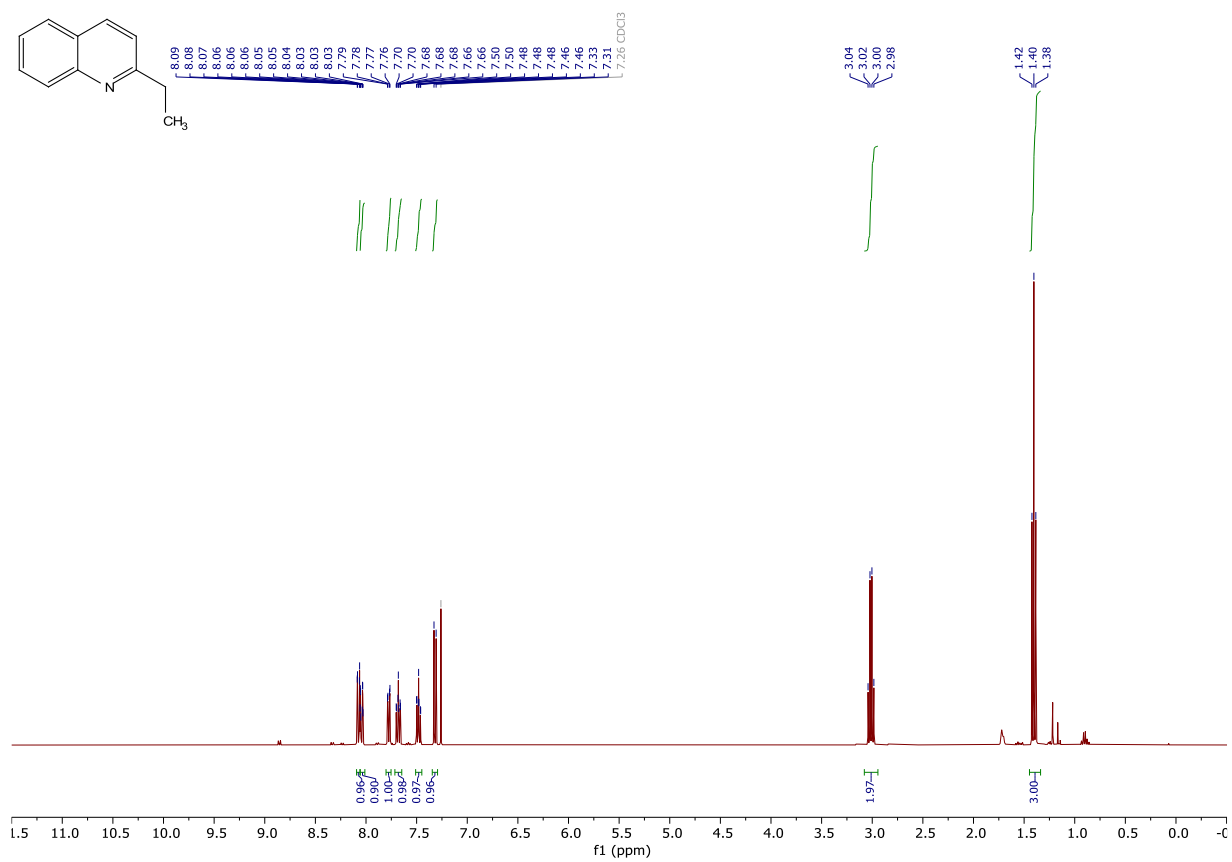
11.   NMR Spectra: Nucleobases

11.1.   *III-13*

¹H
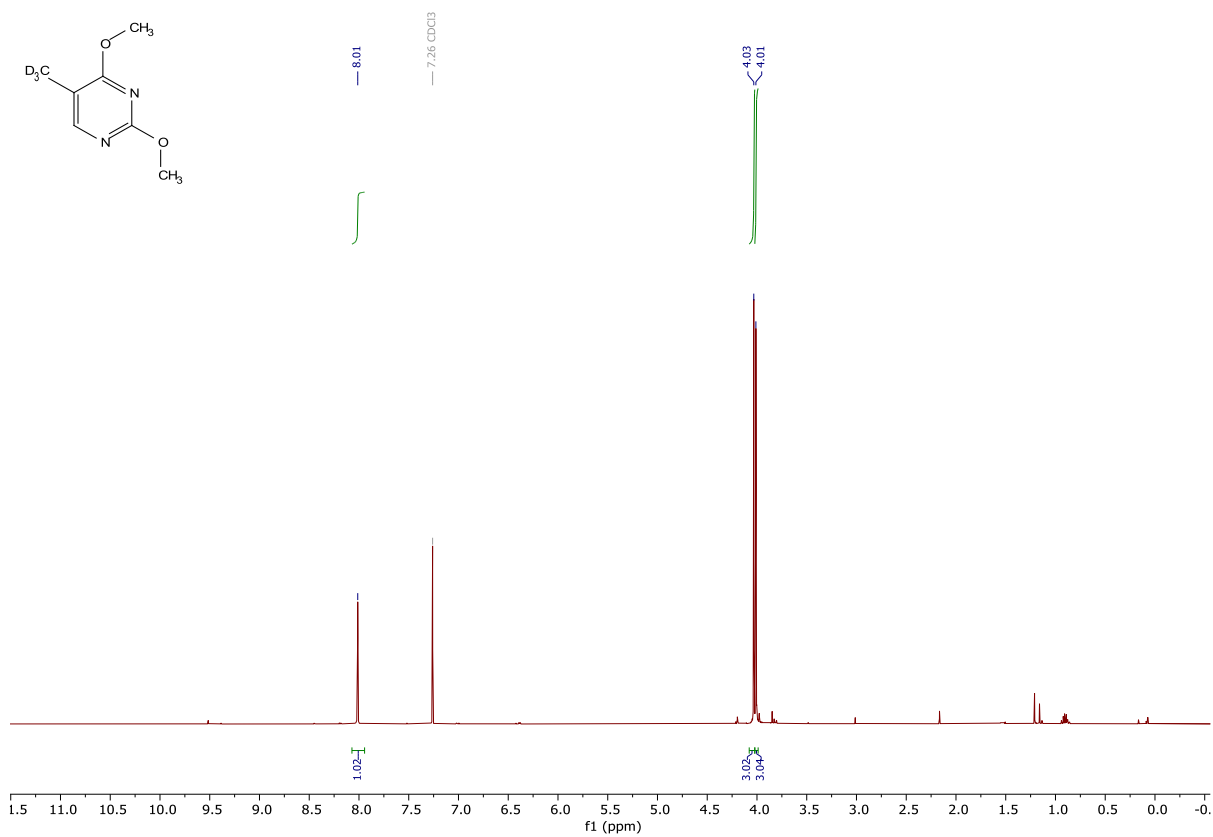
¹³C
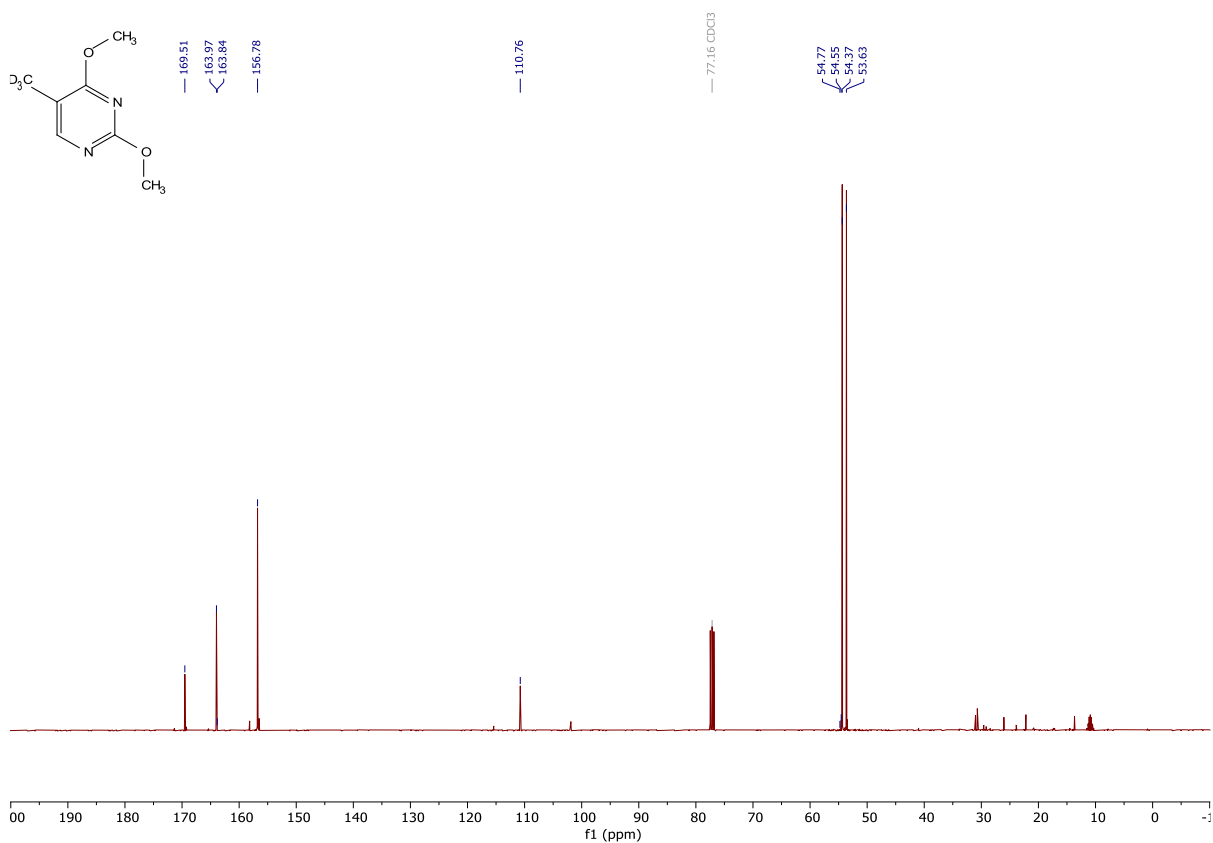
11.2. *III-14*

¹H
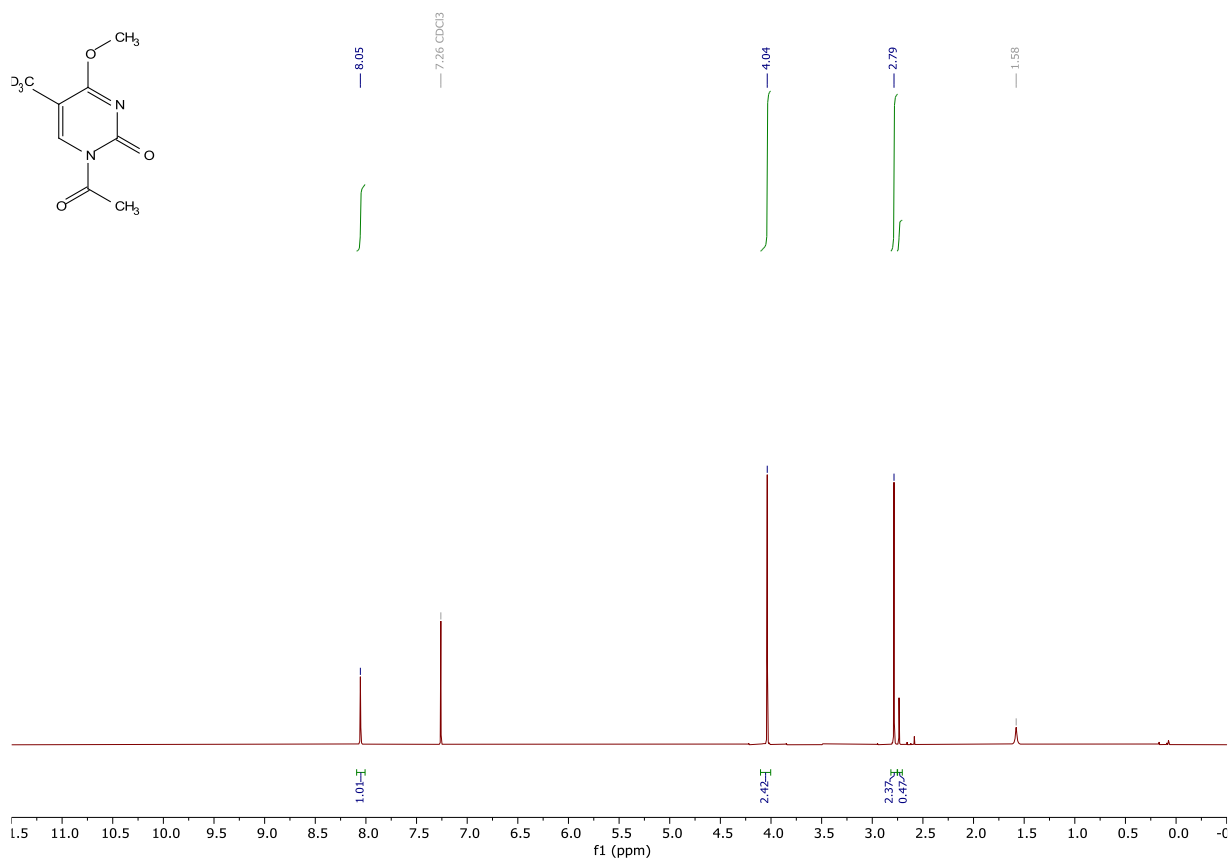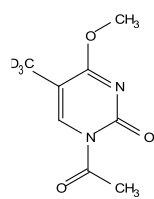
²H
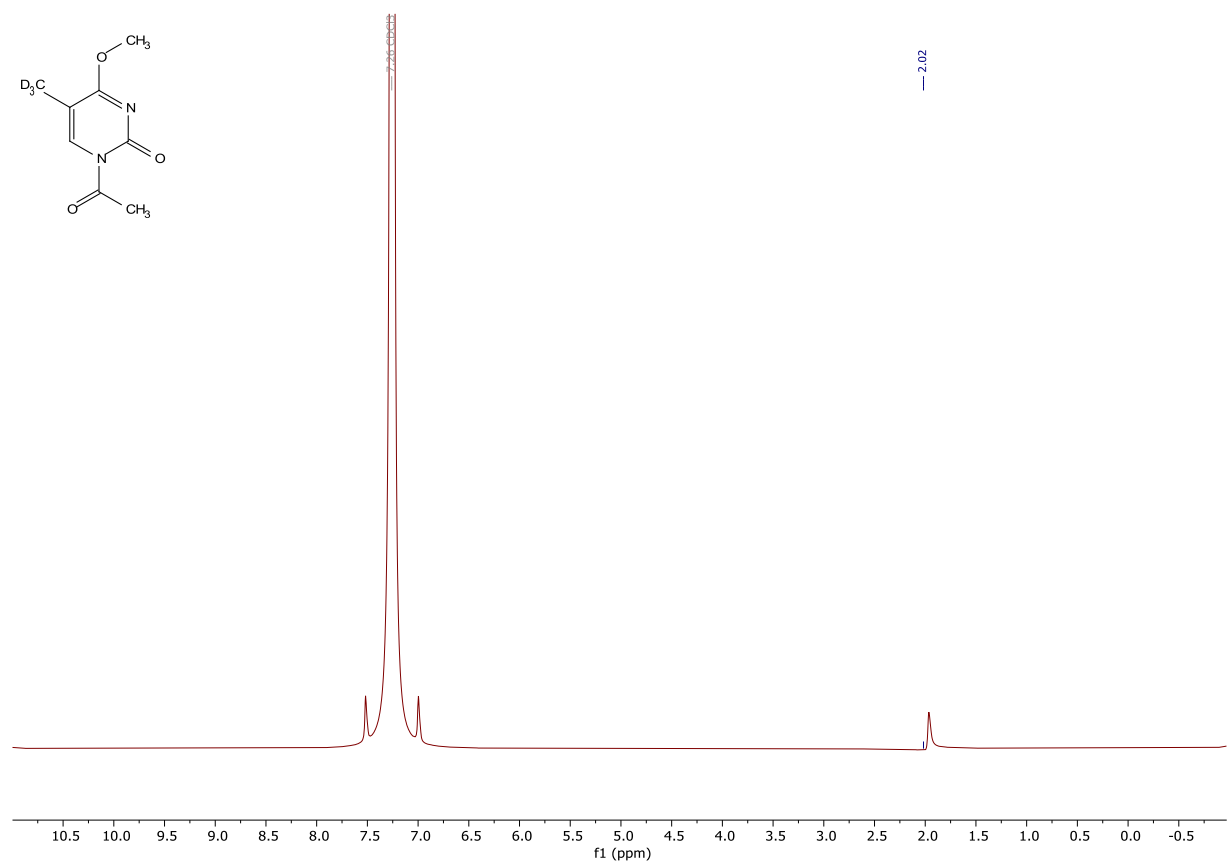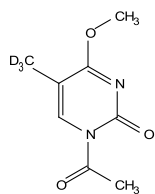
¹³C
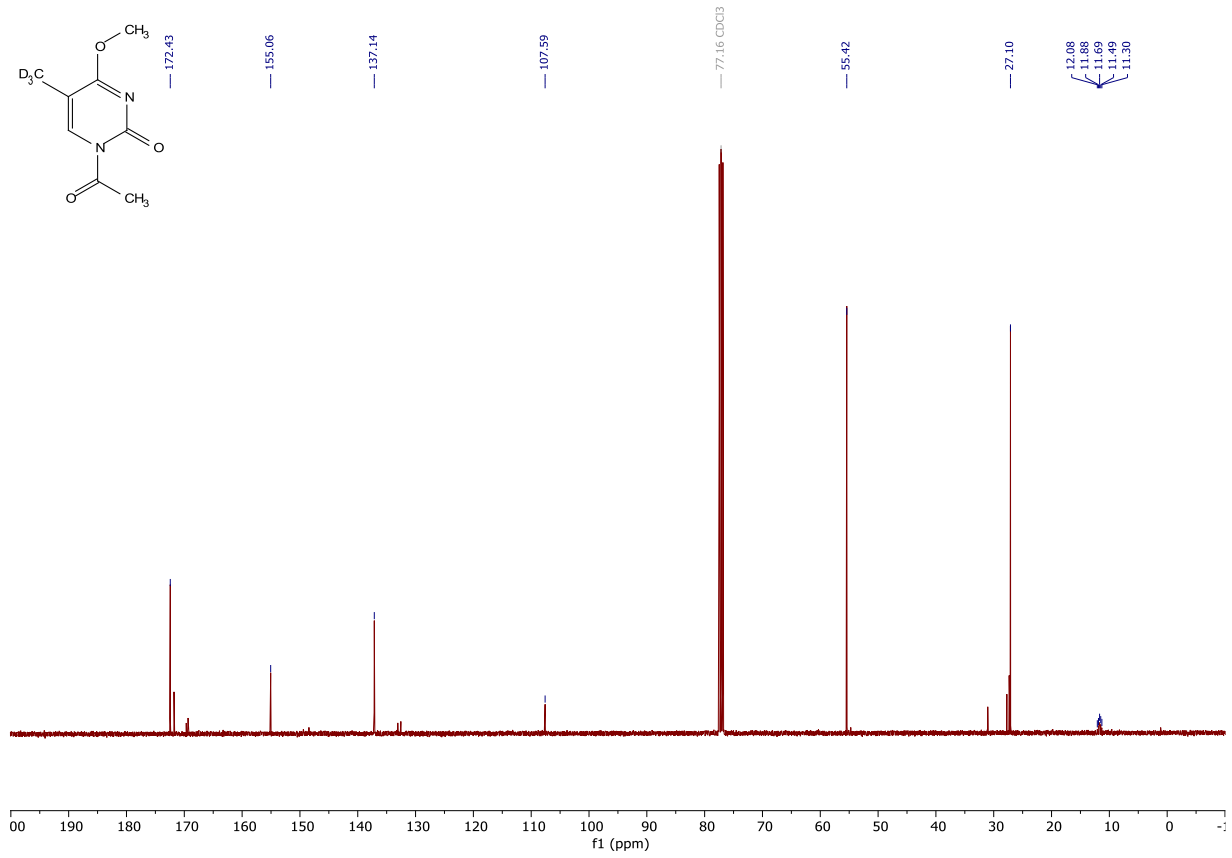
11.3. D₃-5mC

¹H
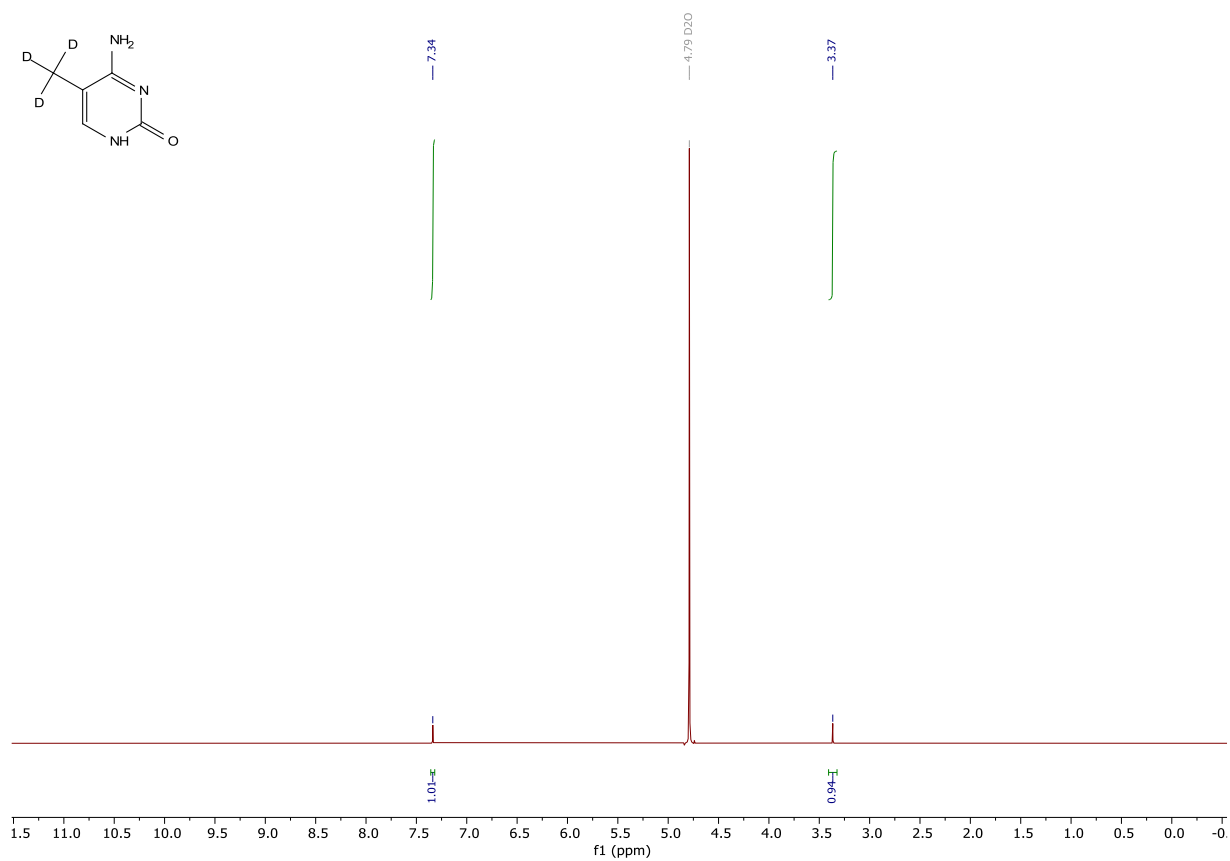
²H – D₆-DMSO
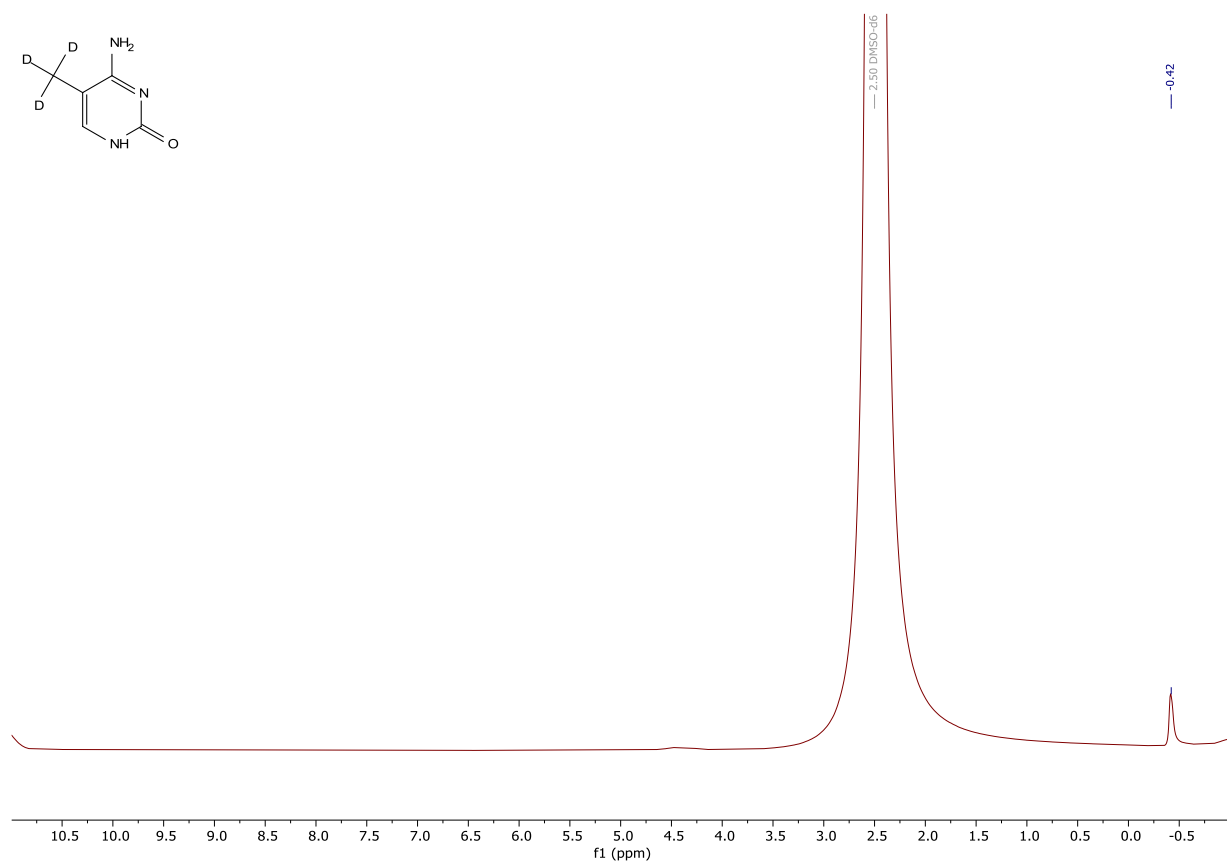
¹³C
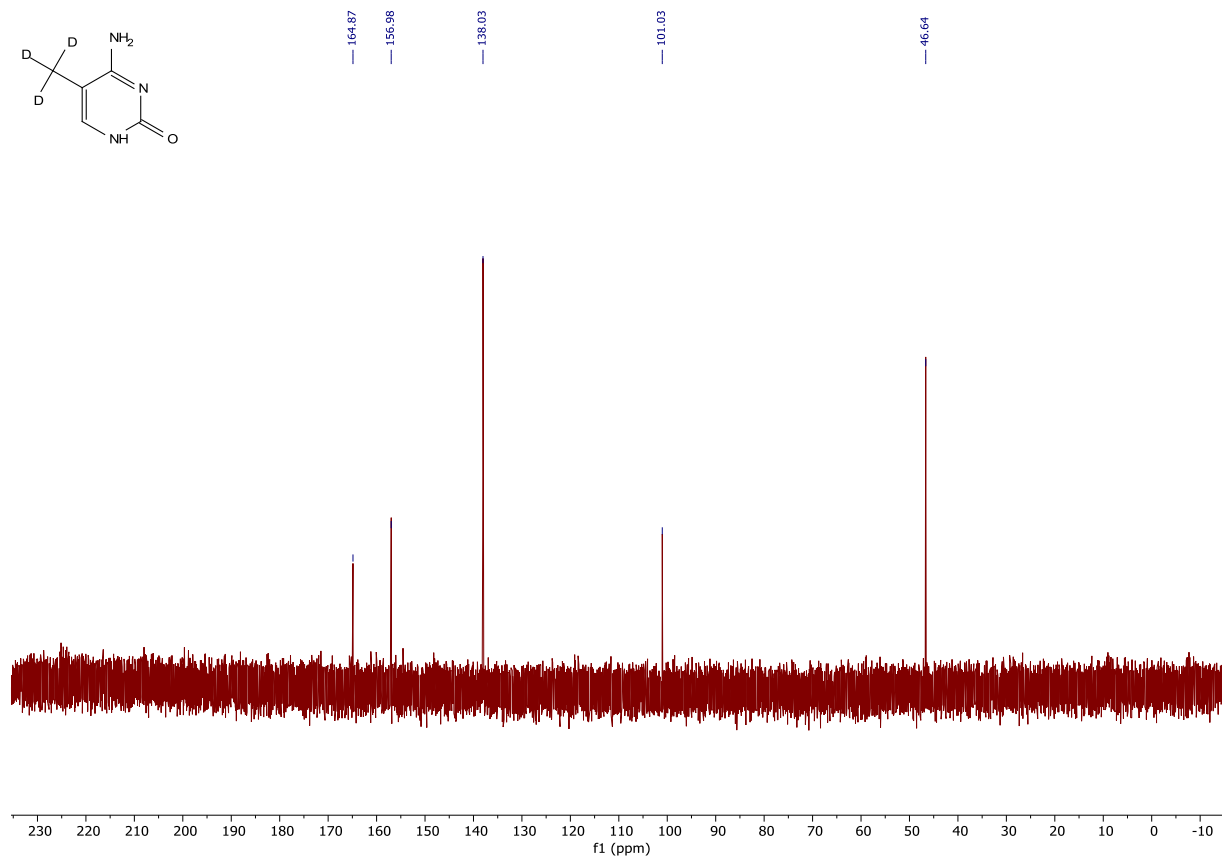
11.4.   D₃-T

¹H – D₆-DMSO
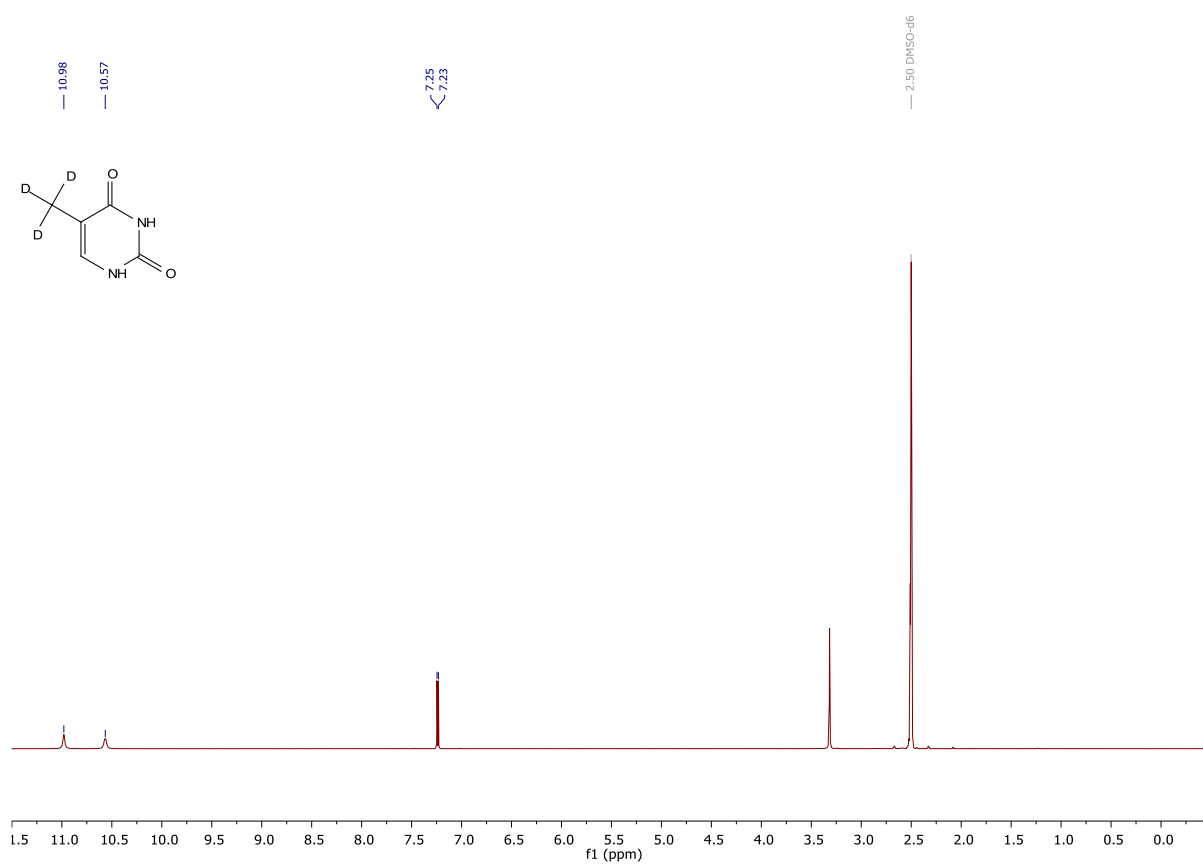
²H – D₆-DMSO
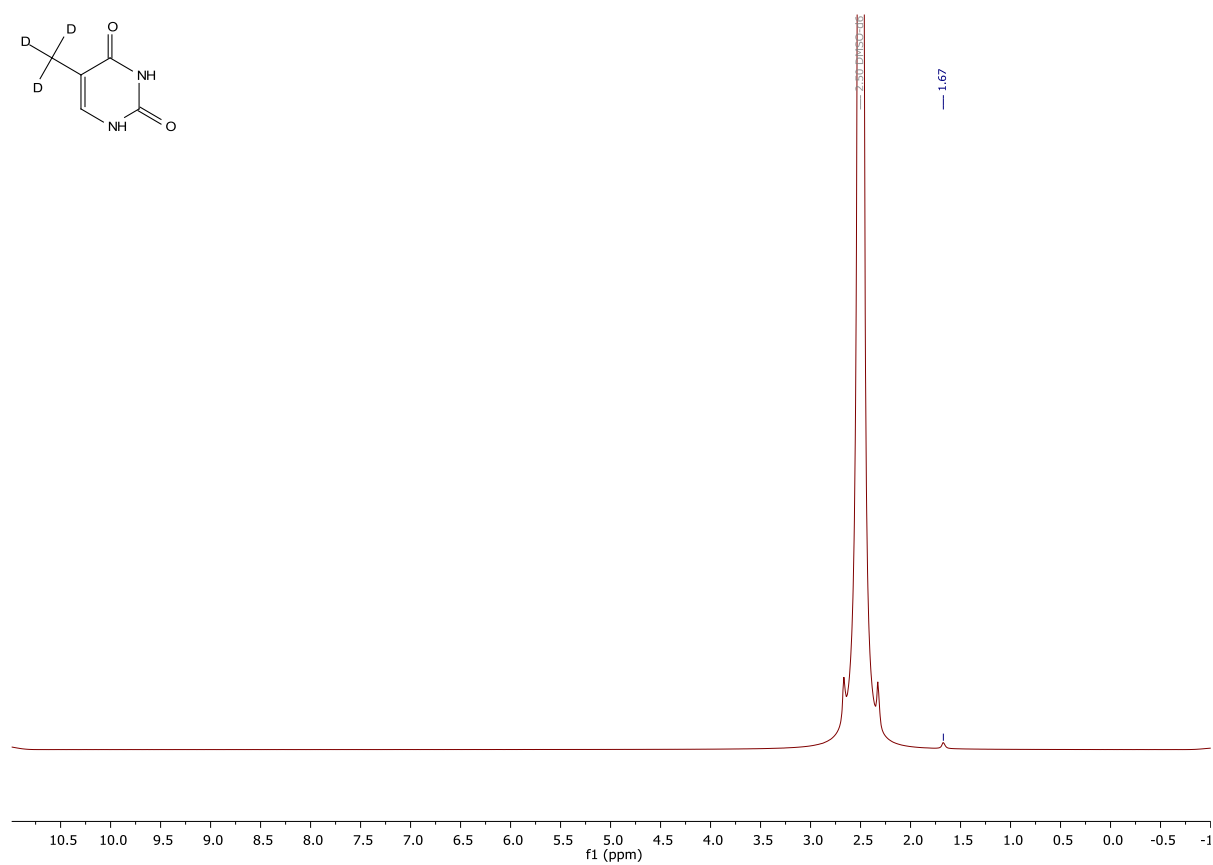
¹³C – D₆-DMSO
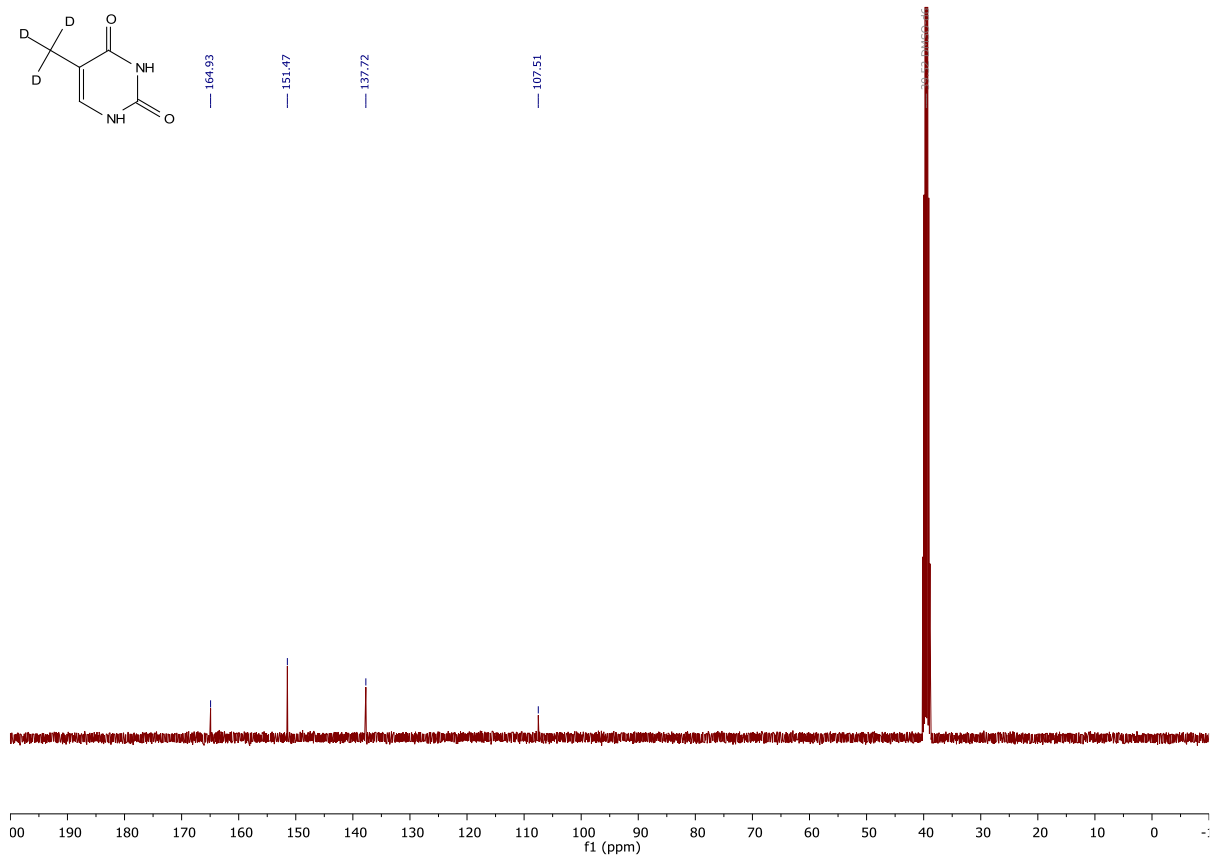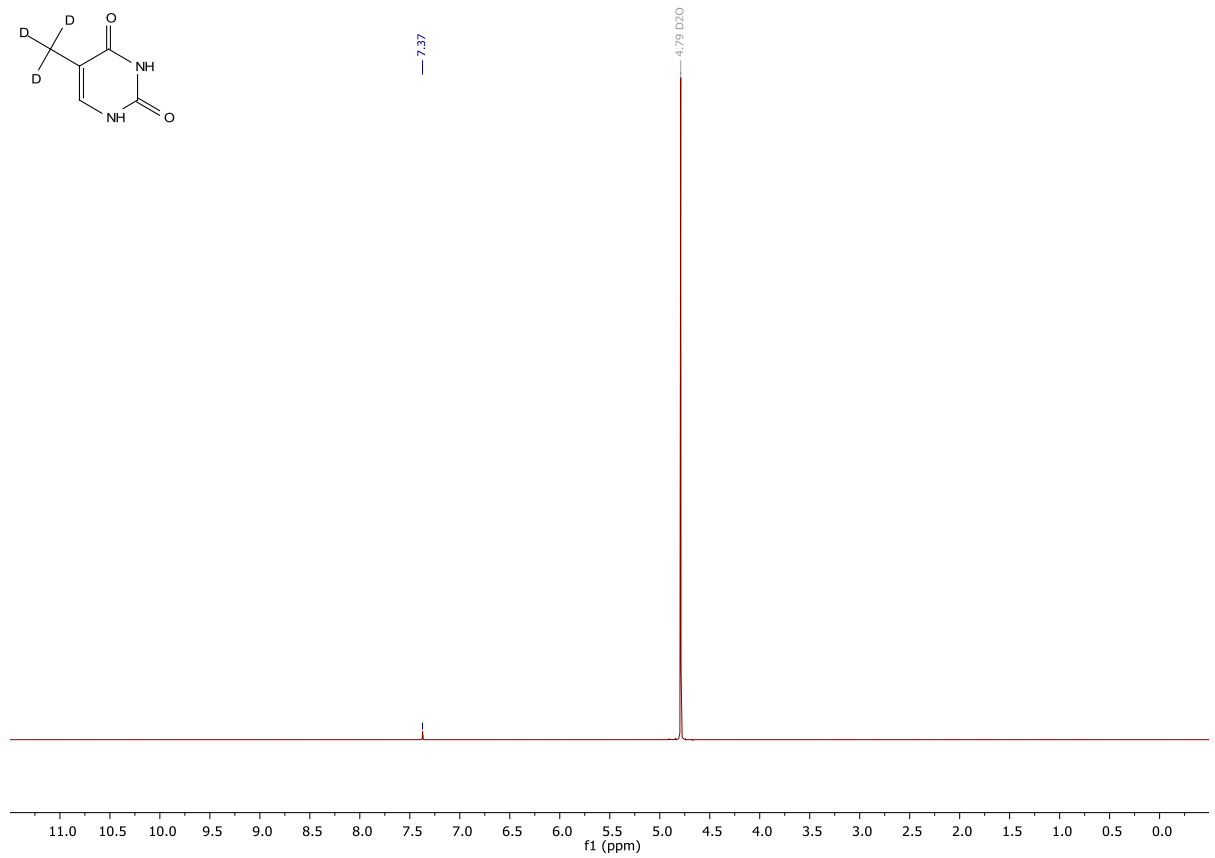
¹H – D₂O

²H – D₂O
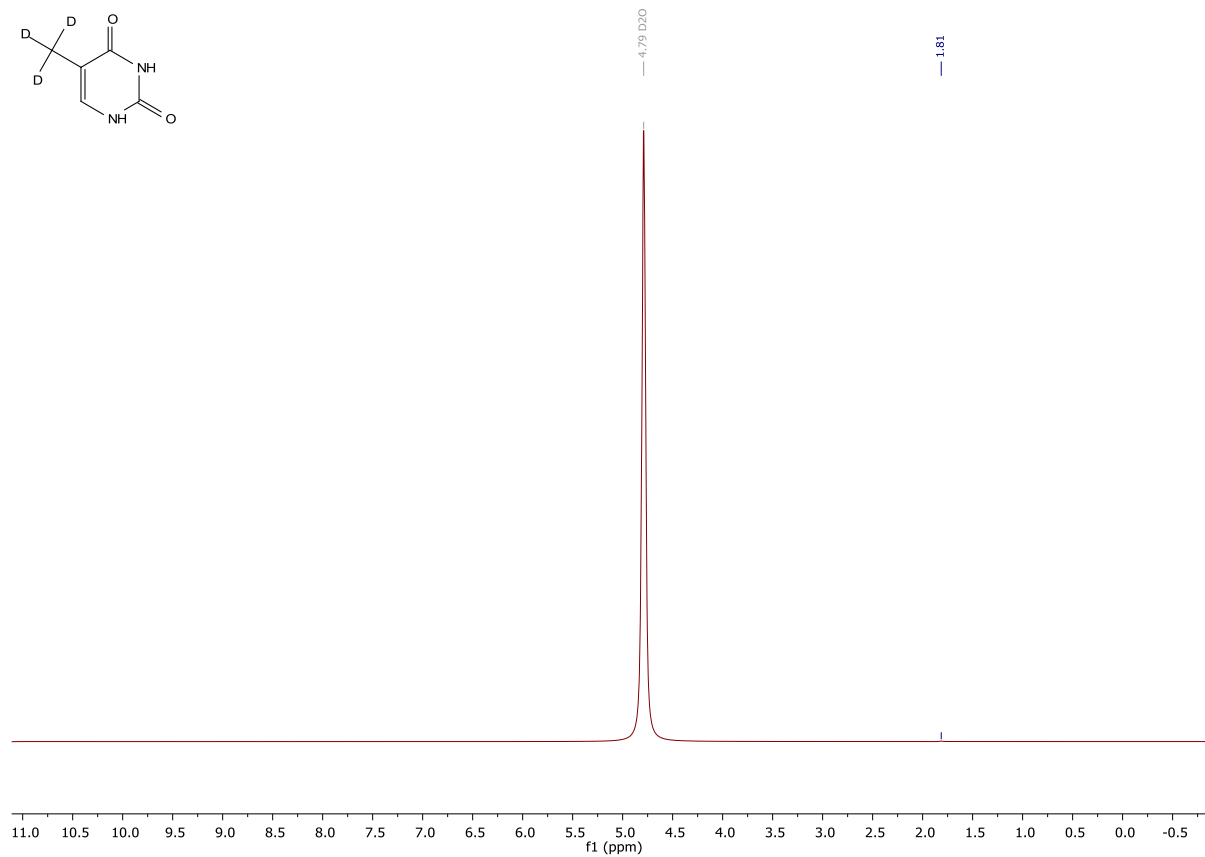
¹³C – D₂O
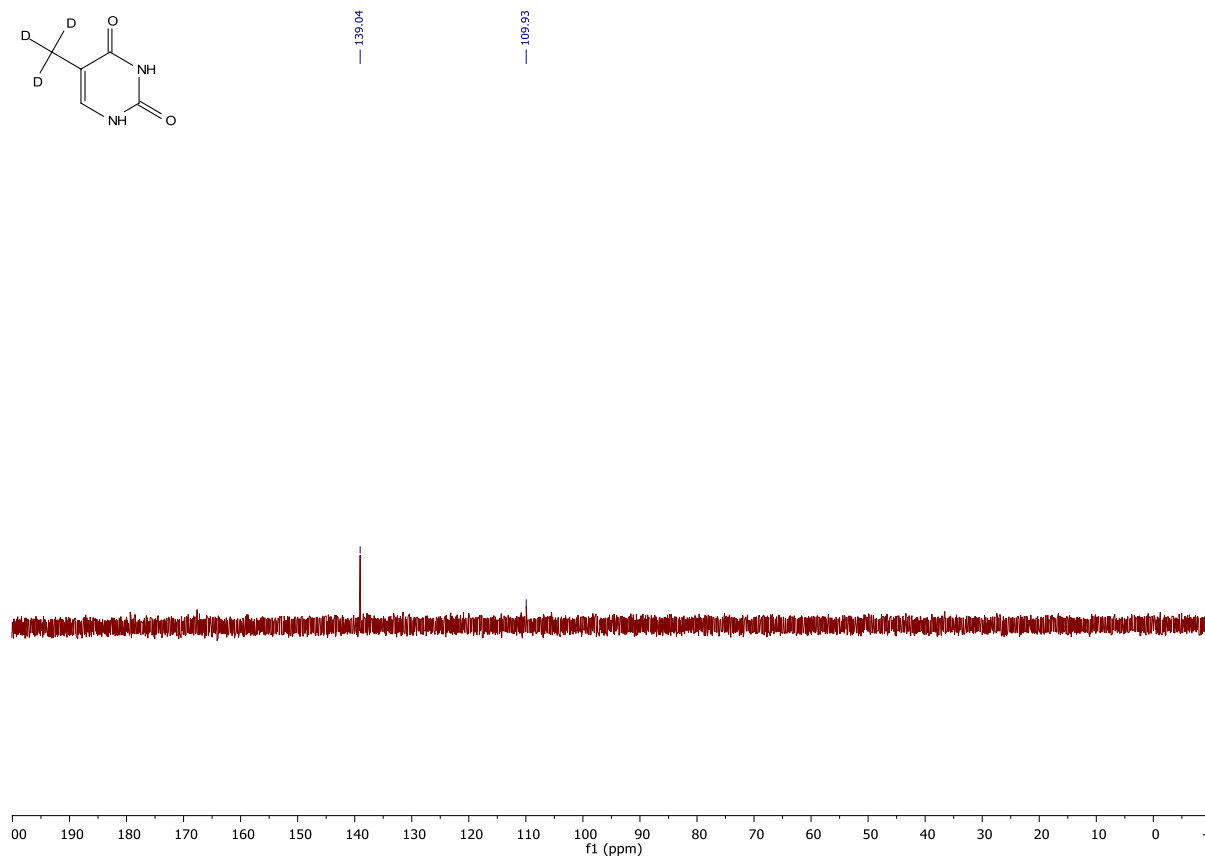
11.5. D₂-5hmC

¹H
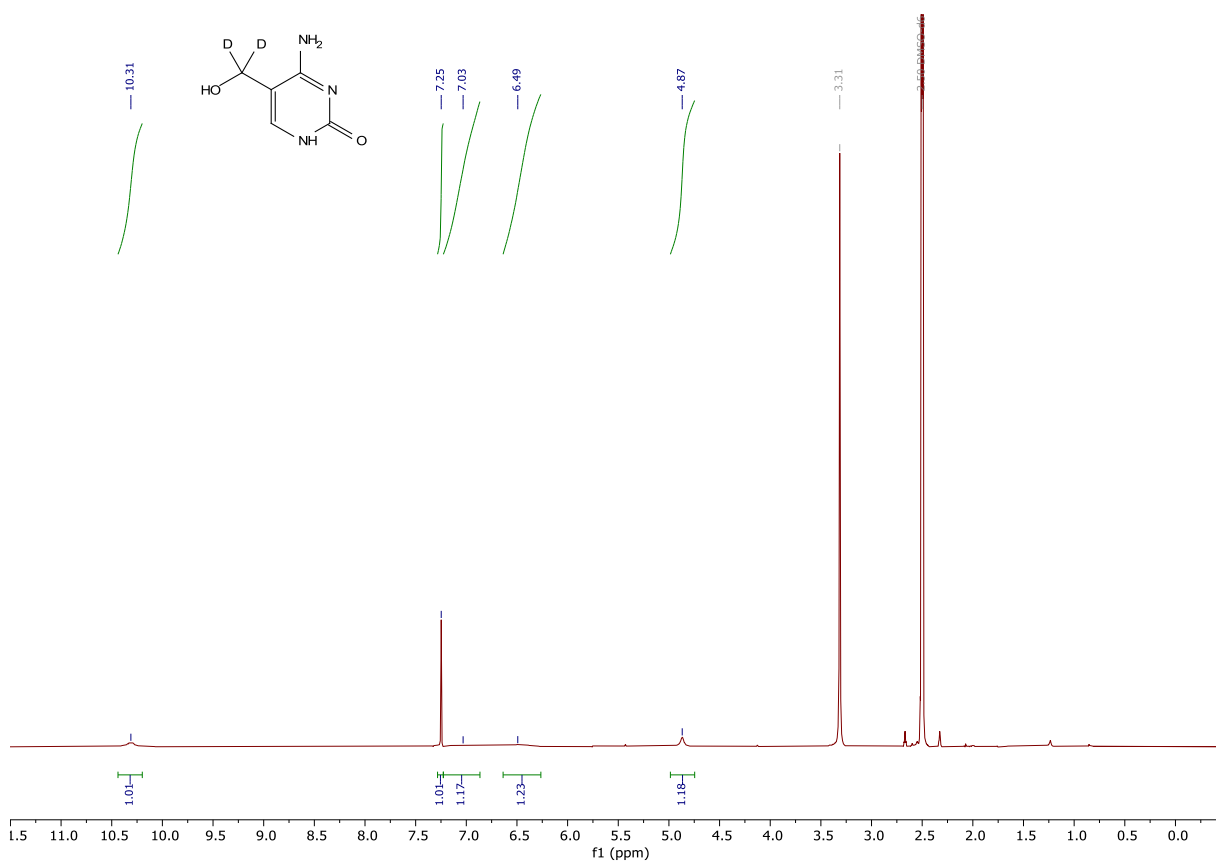
²H
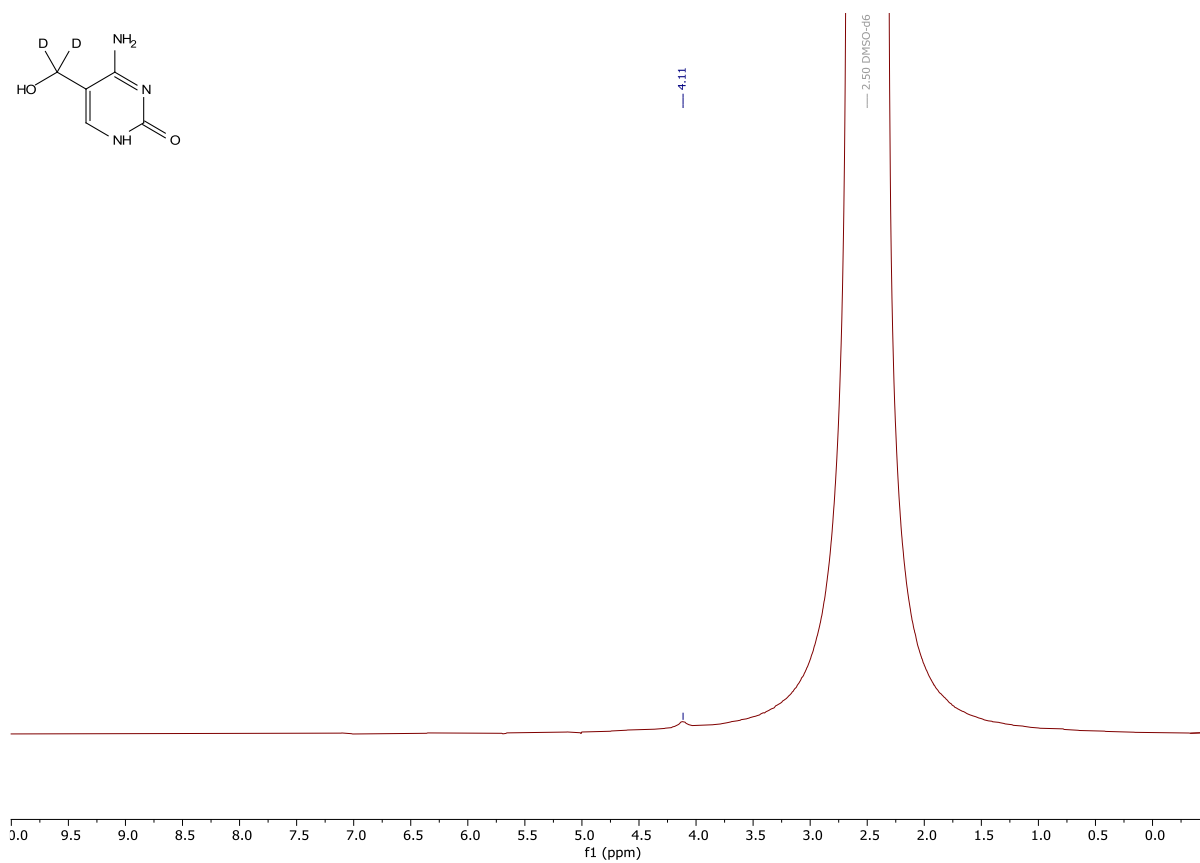
¹³C
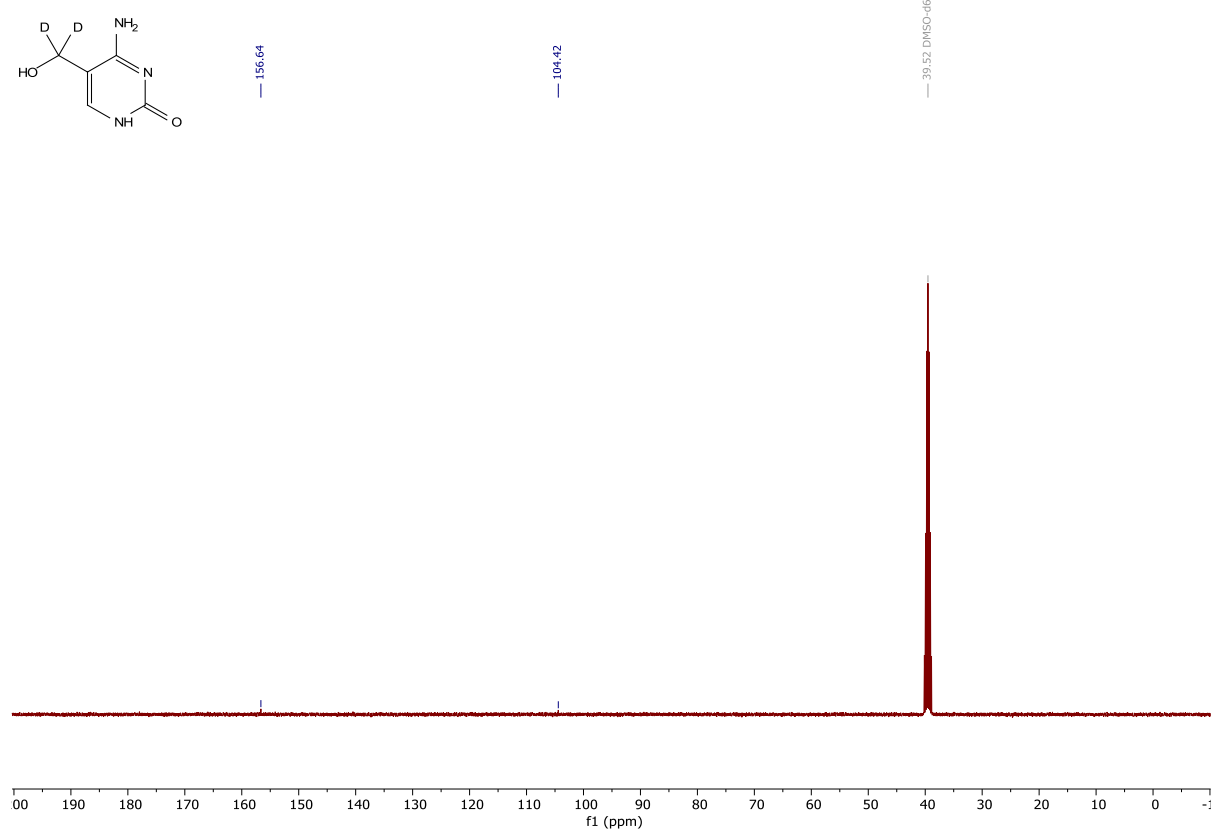
11.6. 5fC

¹H – D₆-DMSO
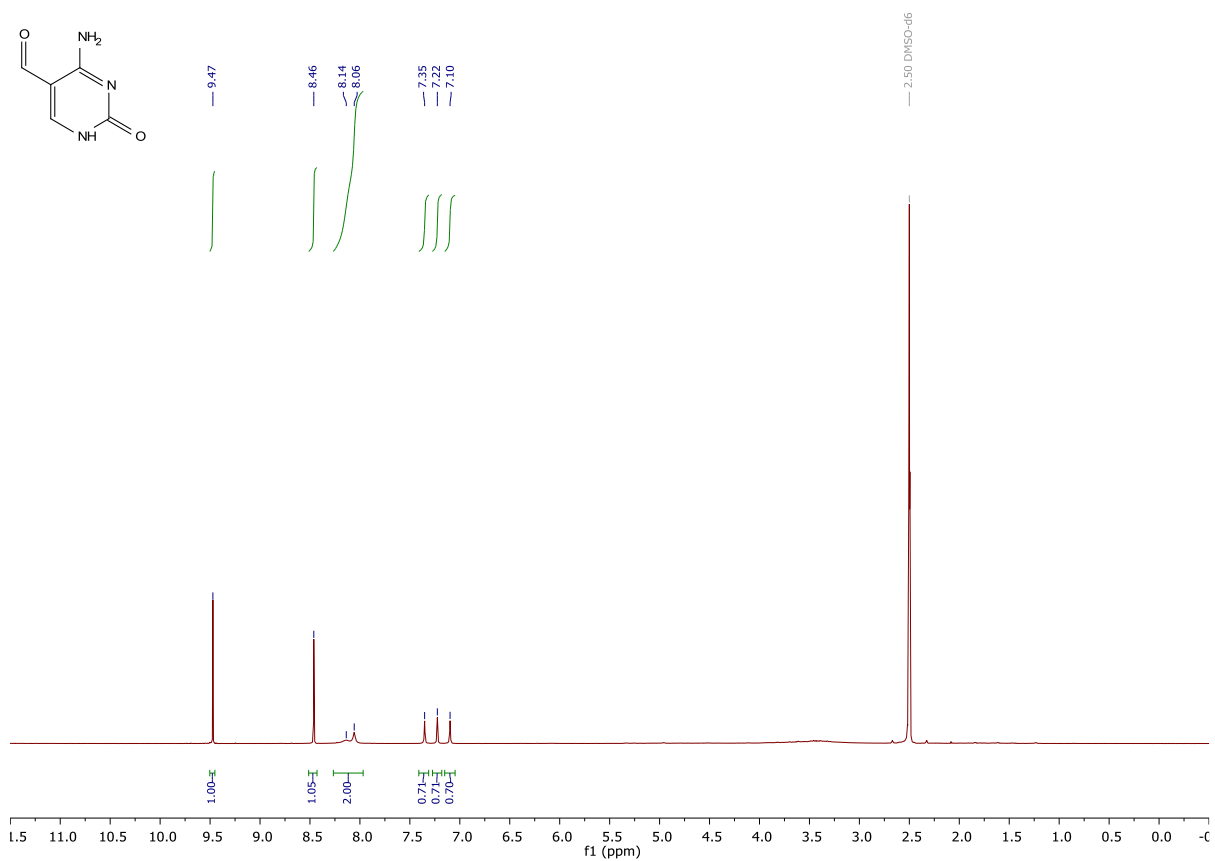
¹³C – D₆-DMSO
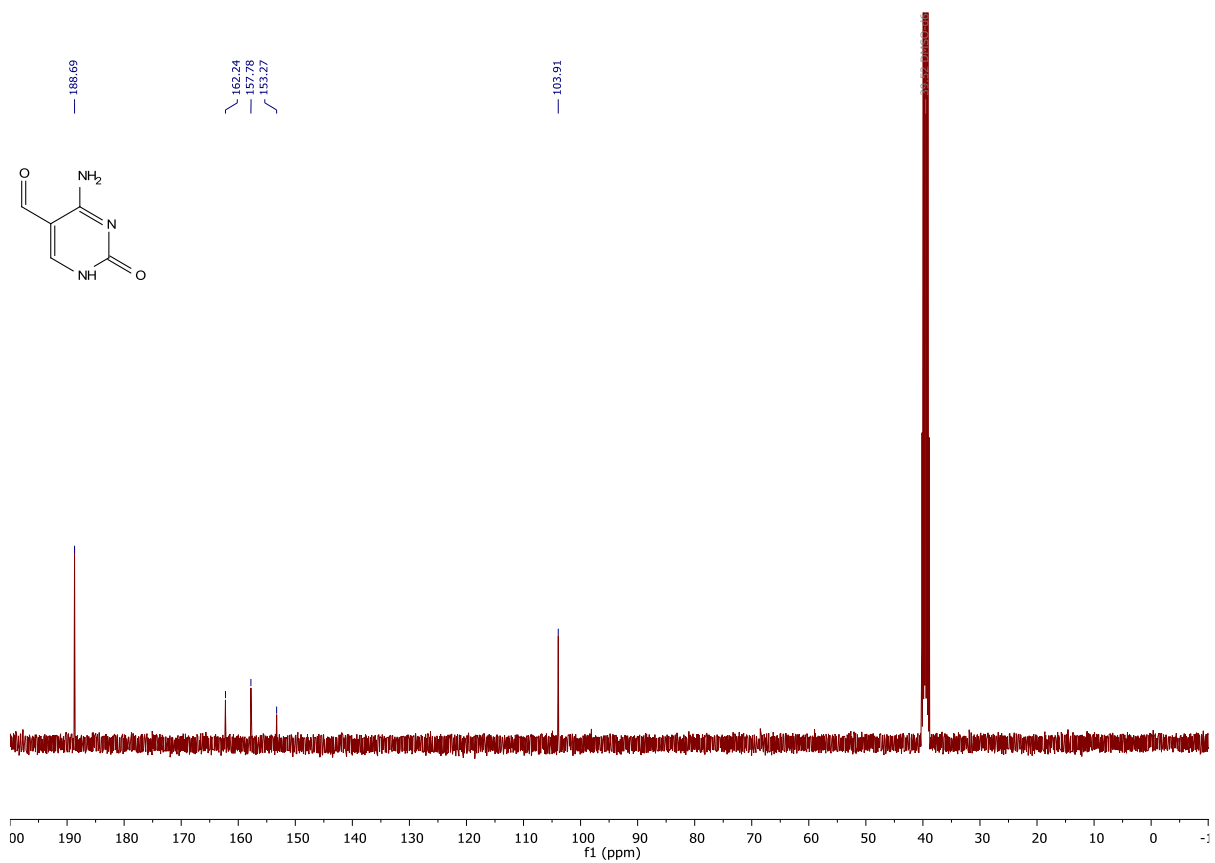
¹H – D₂O

¹³C – D₂O

11.7.   5m*i*C
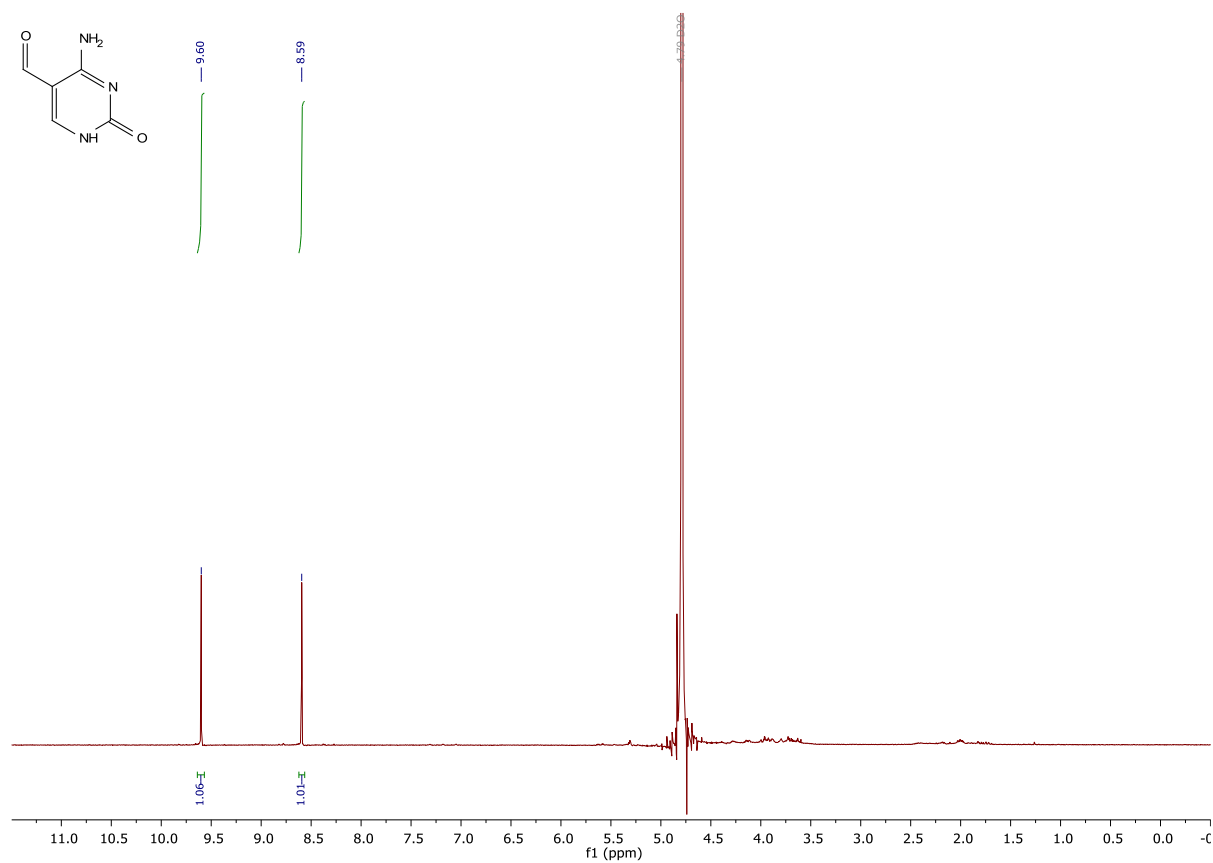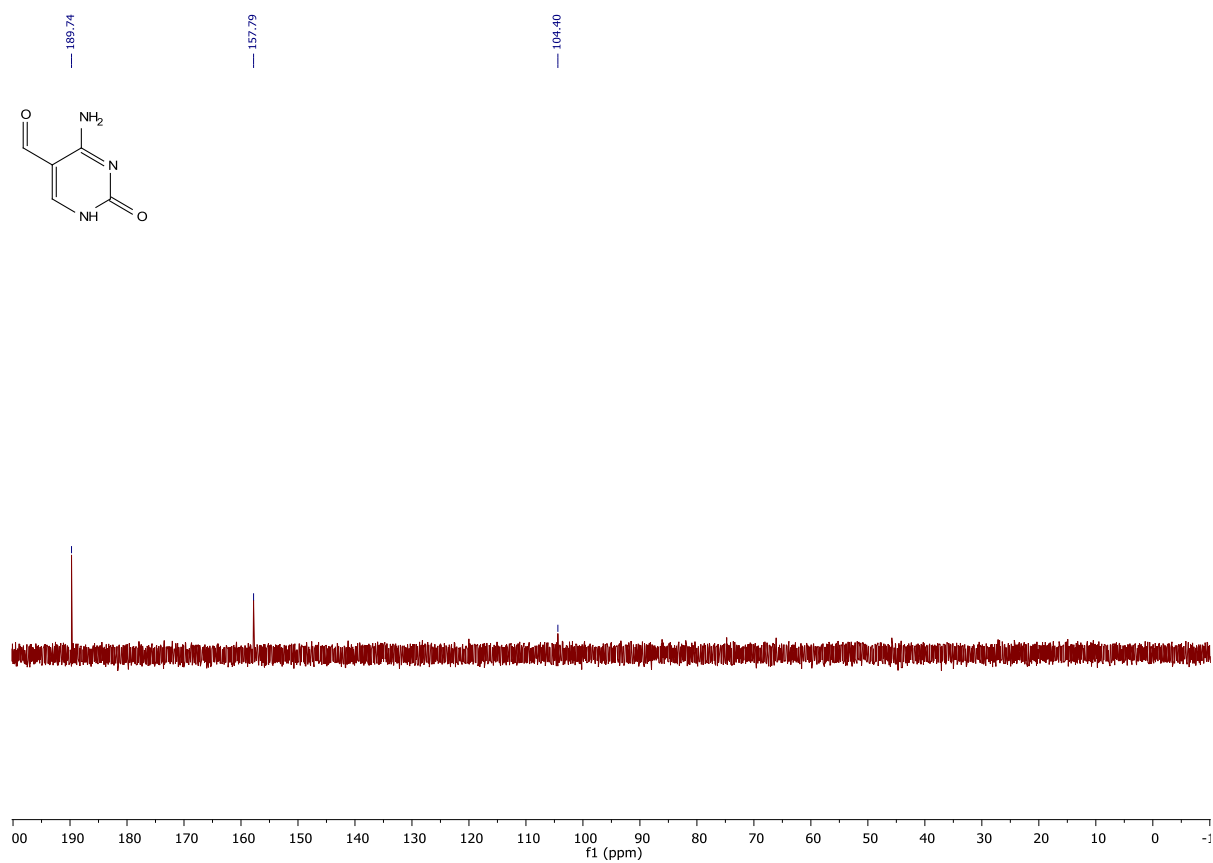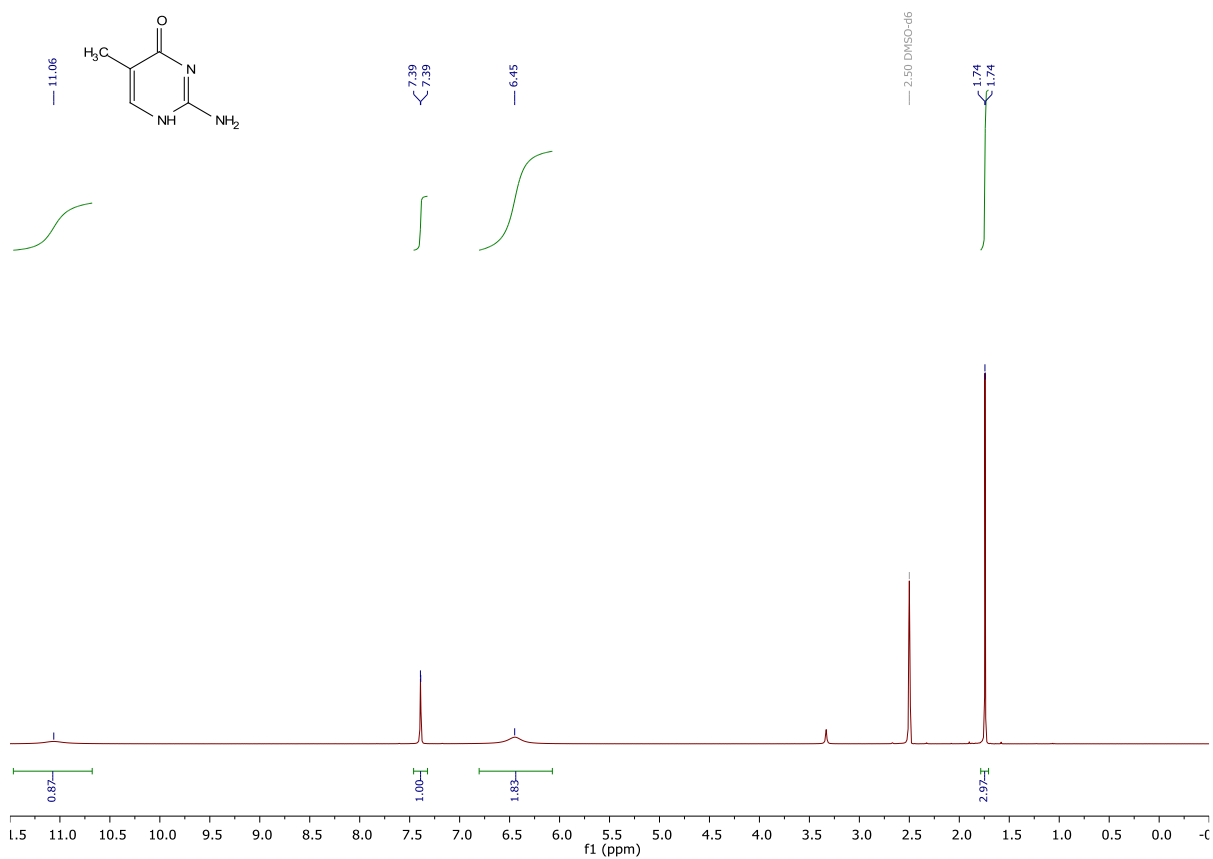
¹H – D₆-DMSO

¹³C – D₆-DMSO
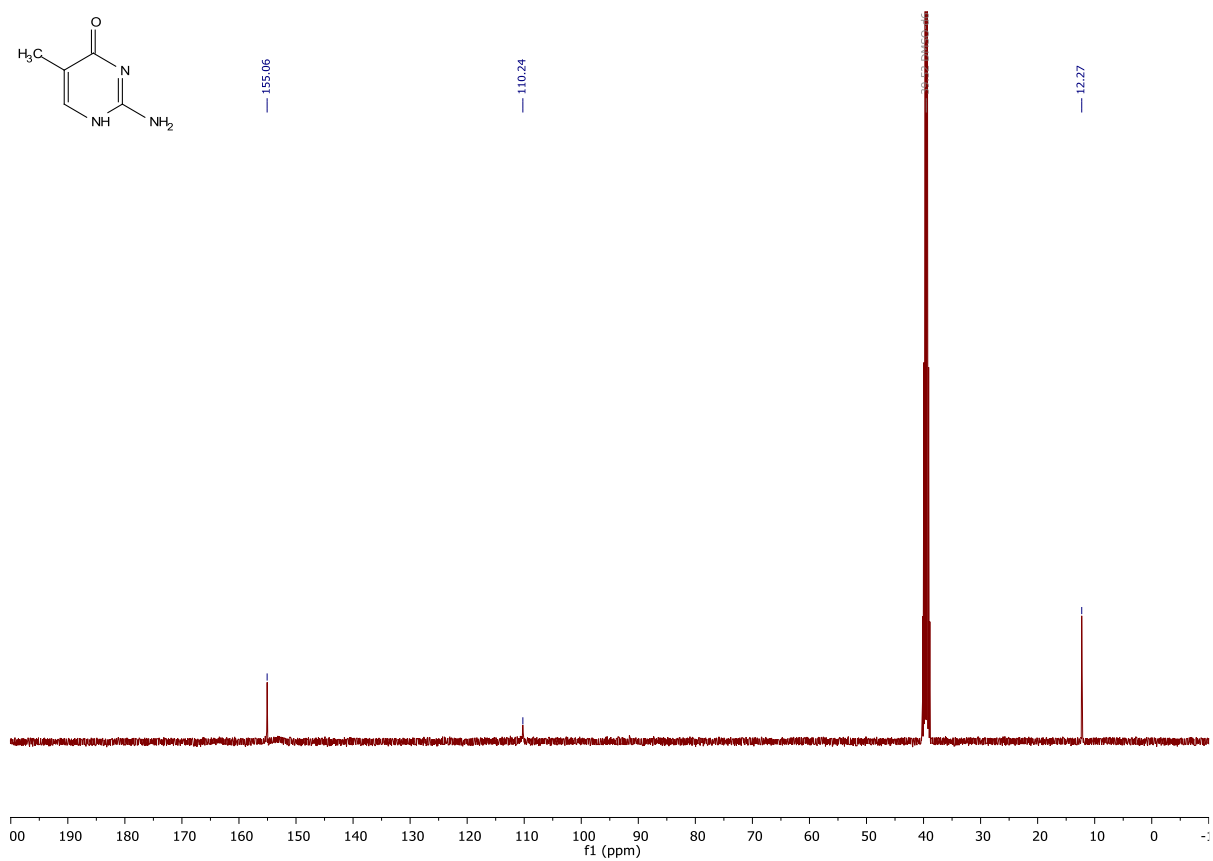
¹H – D₂O
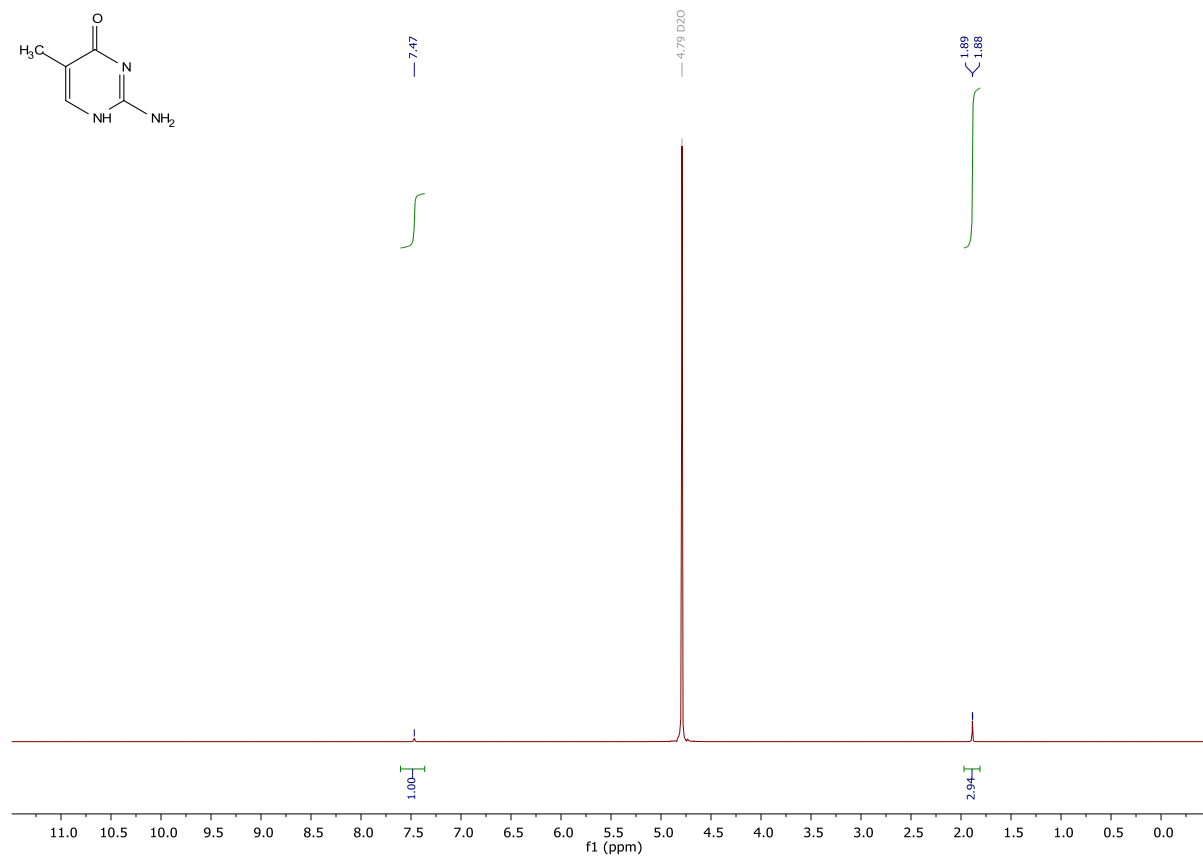
¹³C – D₂O
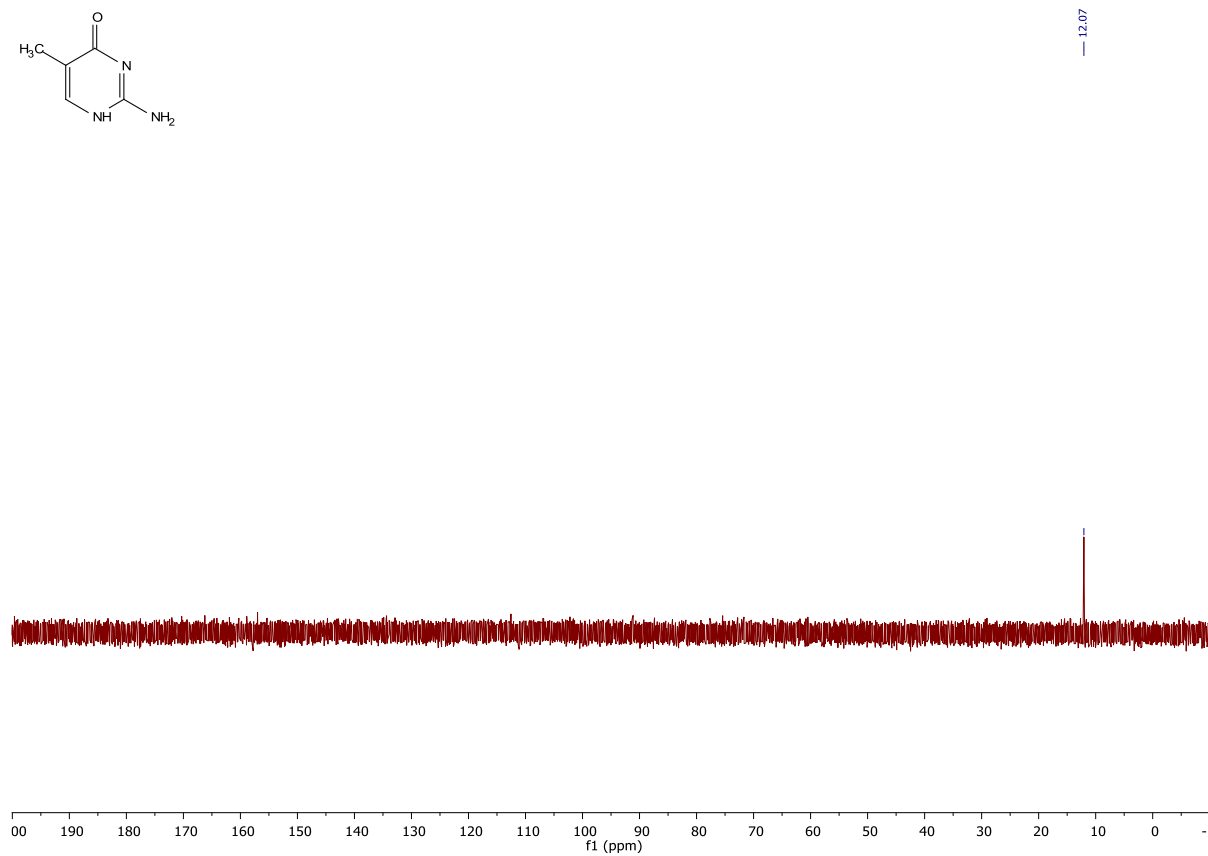
11.8. 5I*i*C

¹H
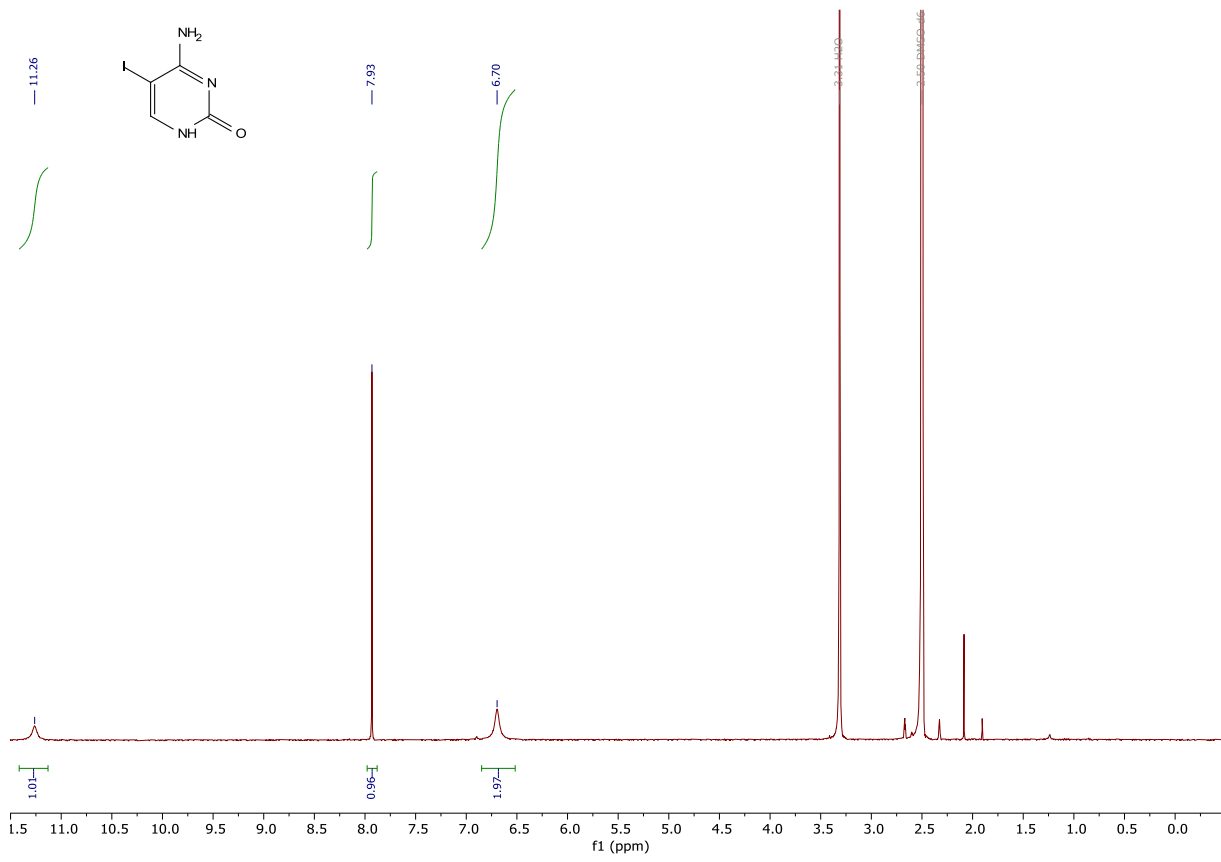
11.9. III-22

¹H
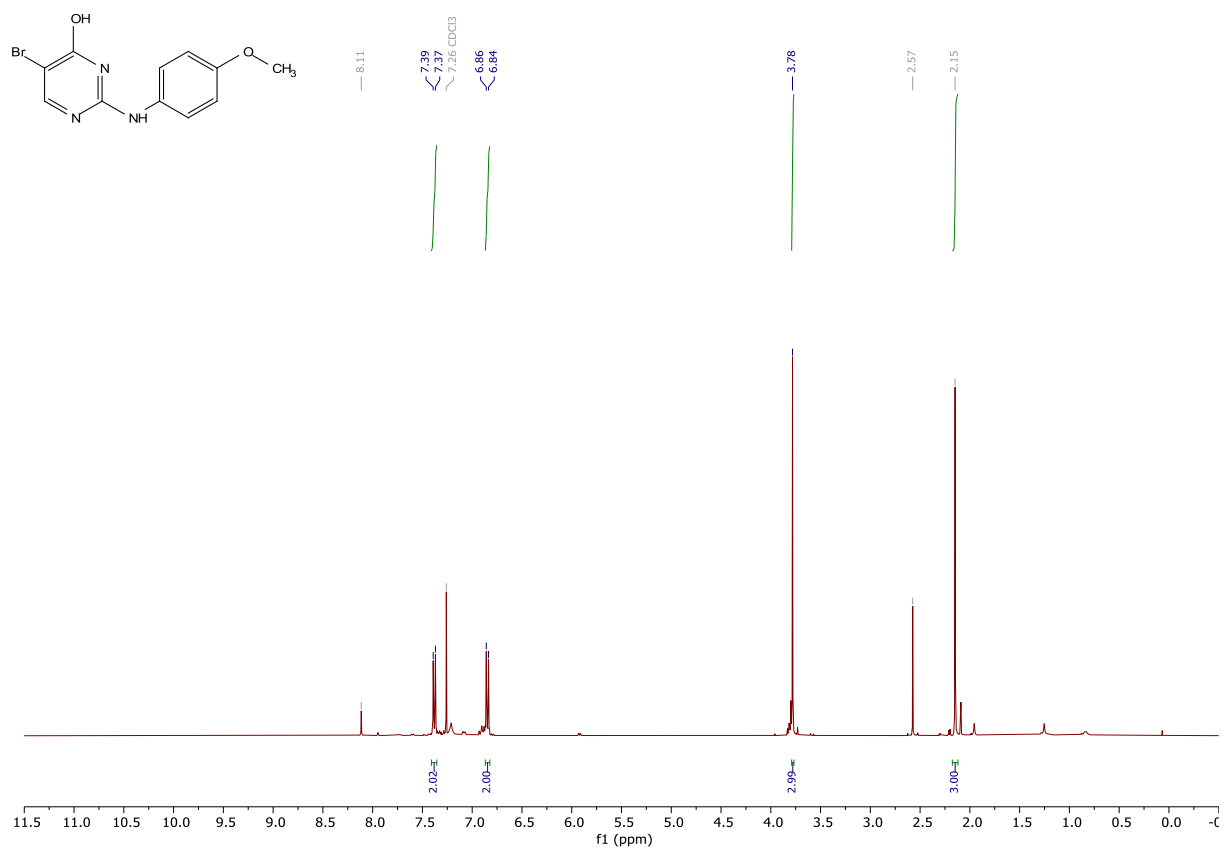
¹³C
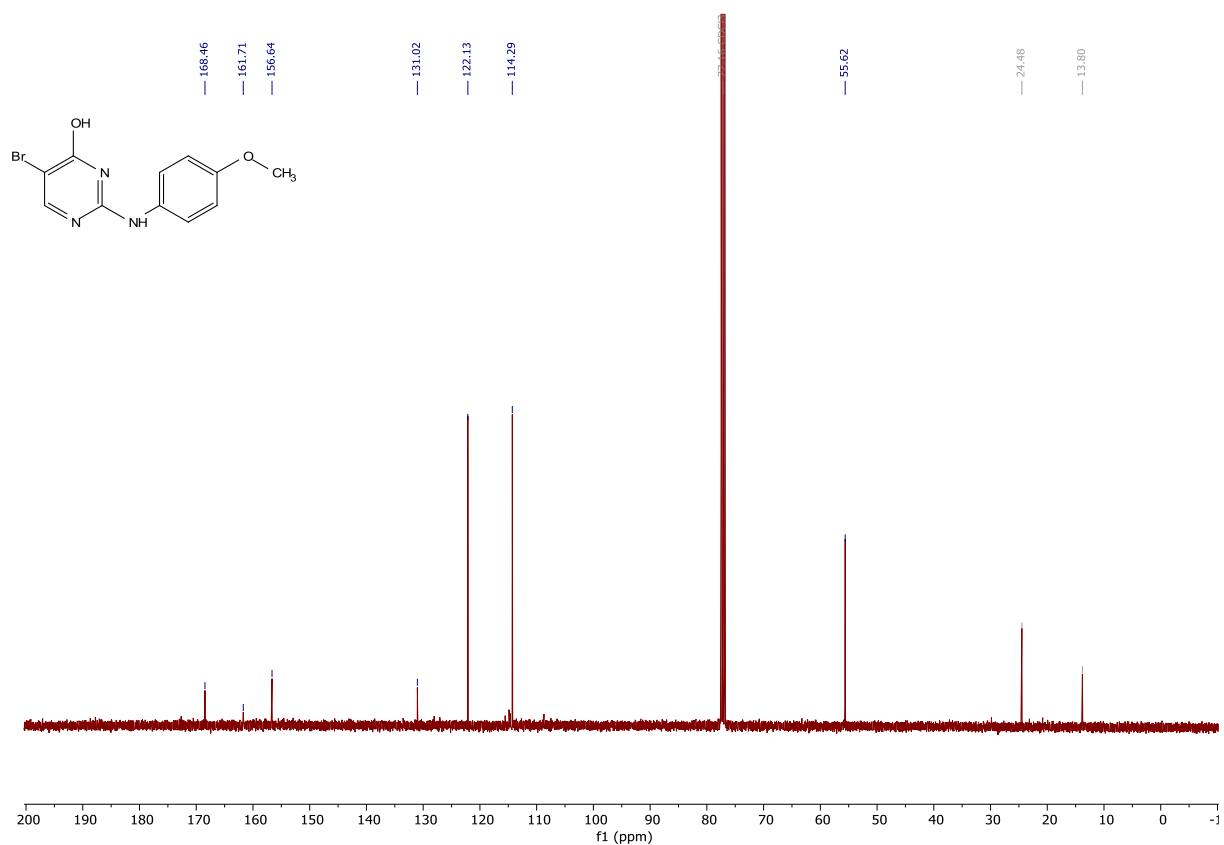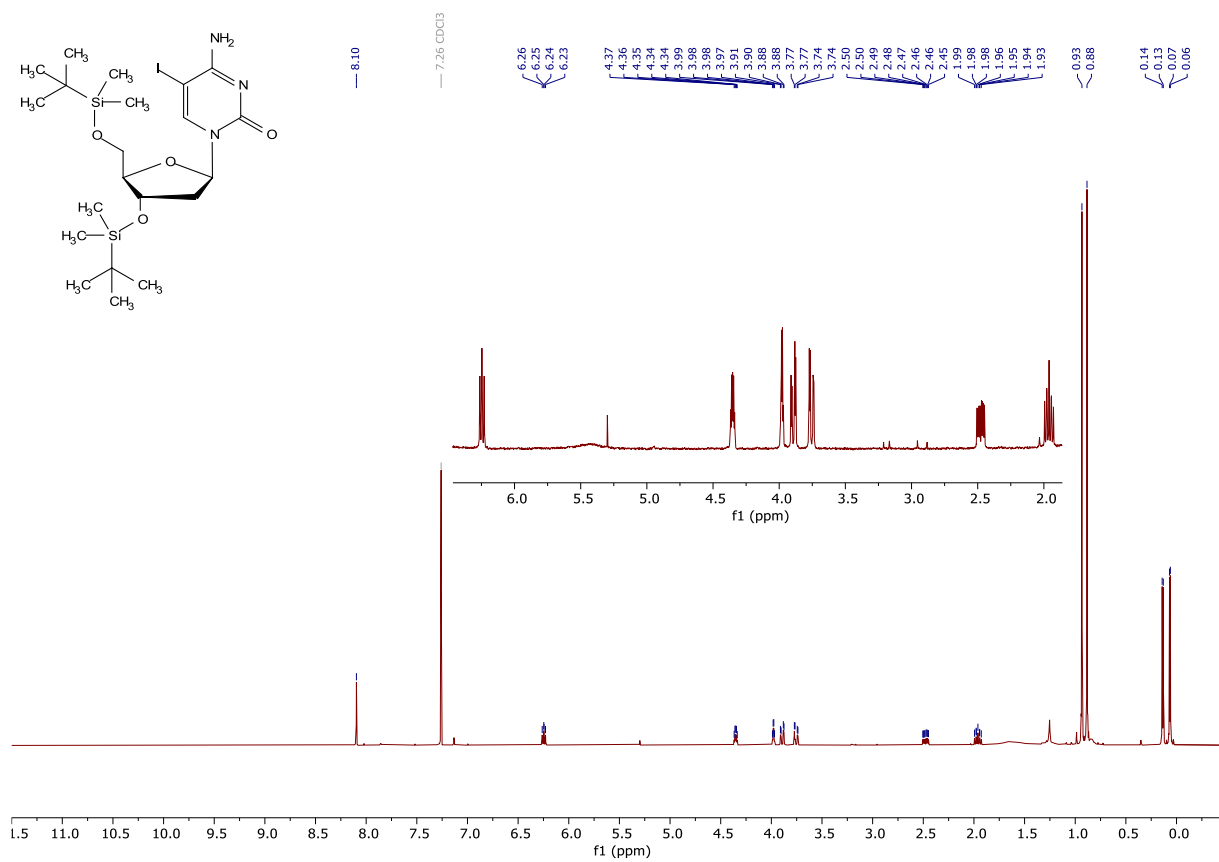
11.10. 1mU
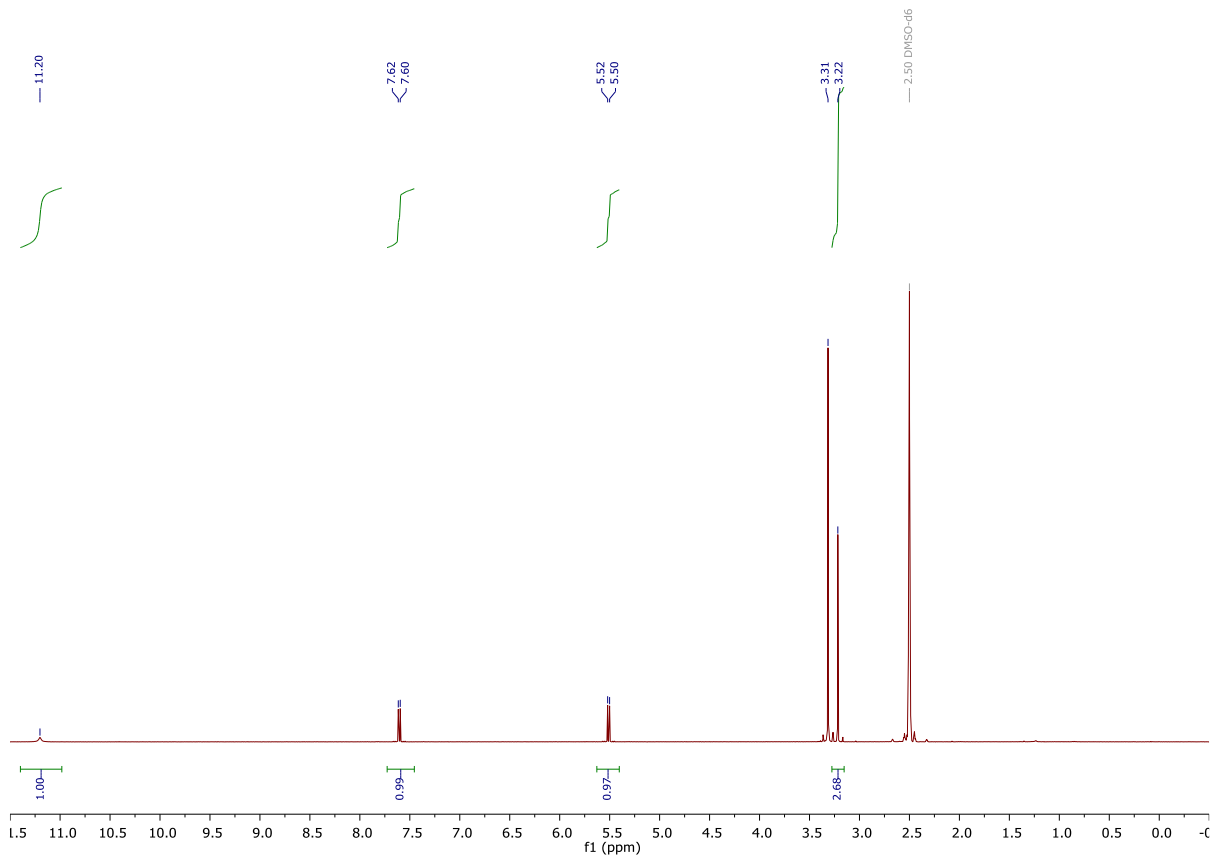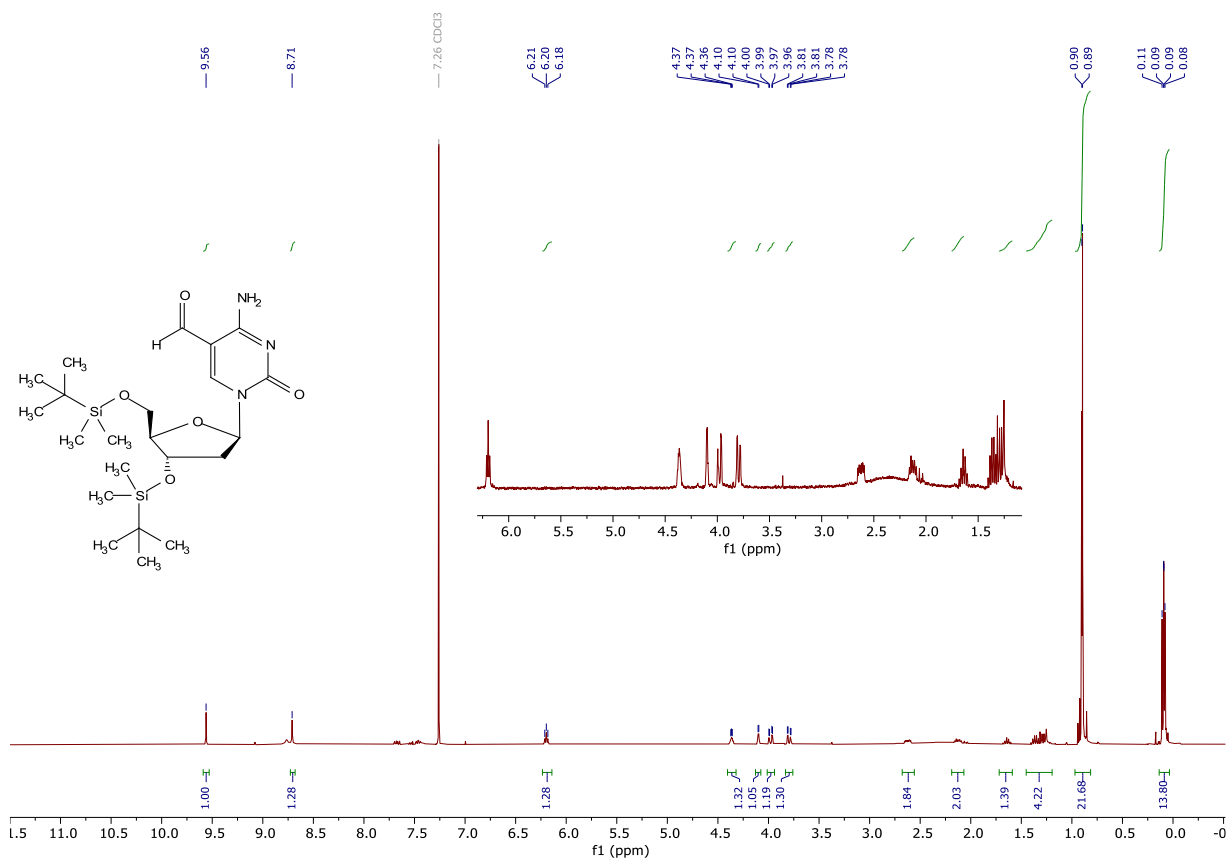
12.   NMR Spectra: Nucleosides and Dinucleotides

12.1.   *III-4*

¹H

12.2. III-5

¹H

12.3. *5fdC*

¹H – before HPLC, contains PPh₃ as impurity
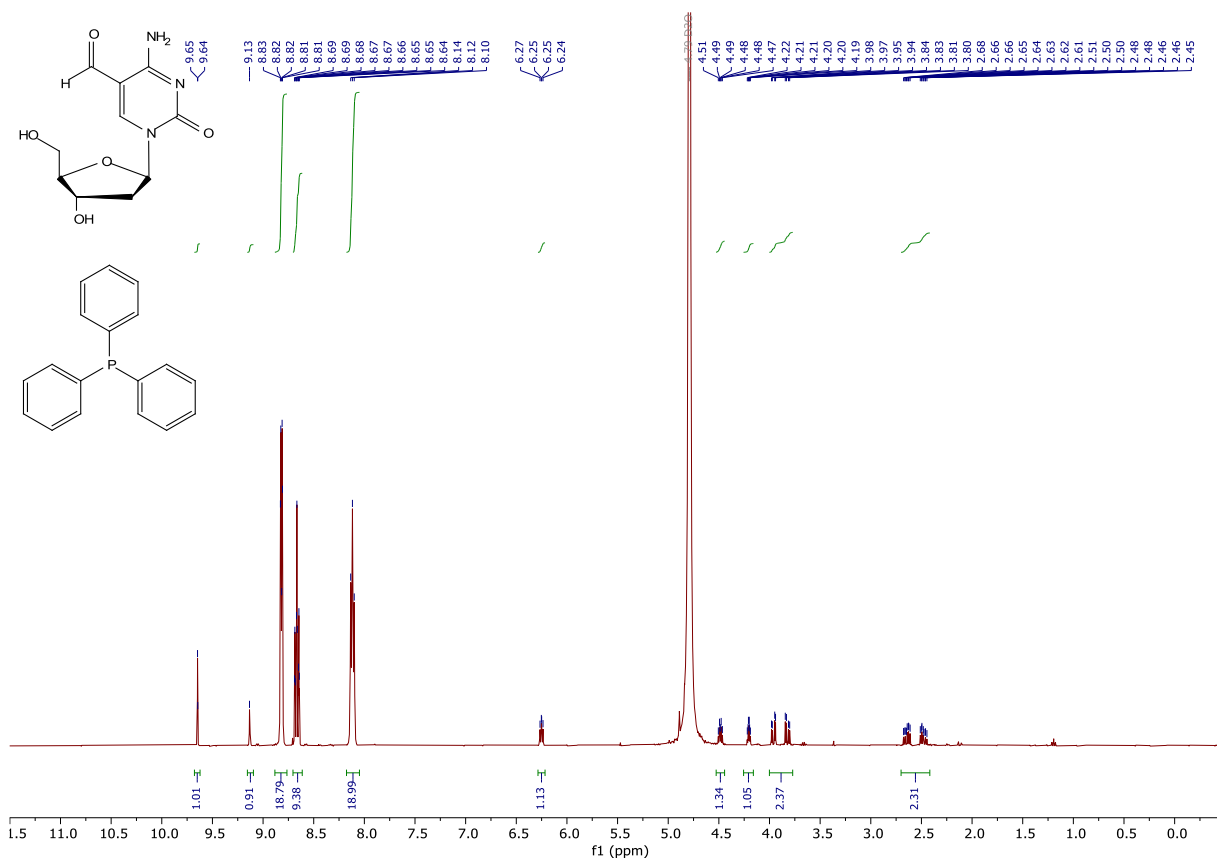
¹H – H₂O/D₂O signal suppressed
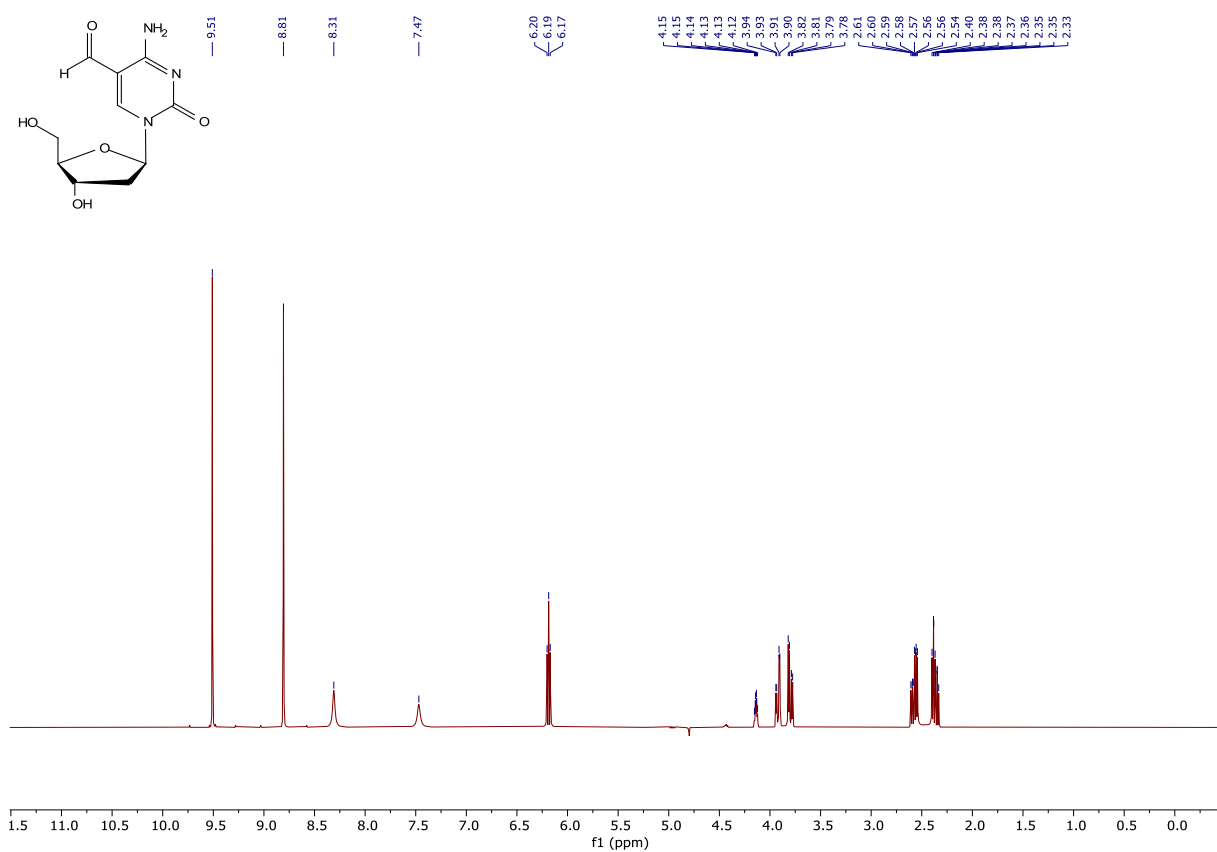
12.4. III-6

¹H
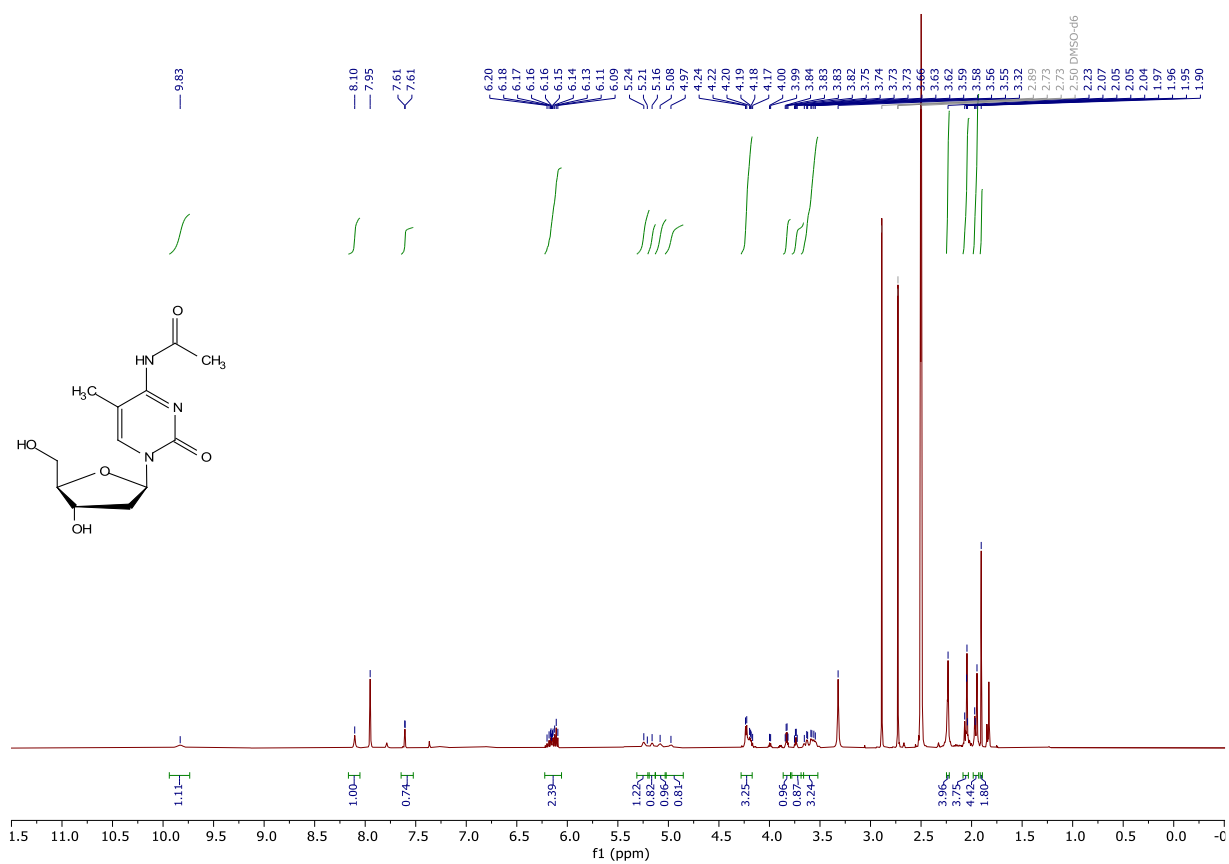
12.5. *III-7*

¹H
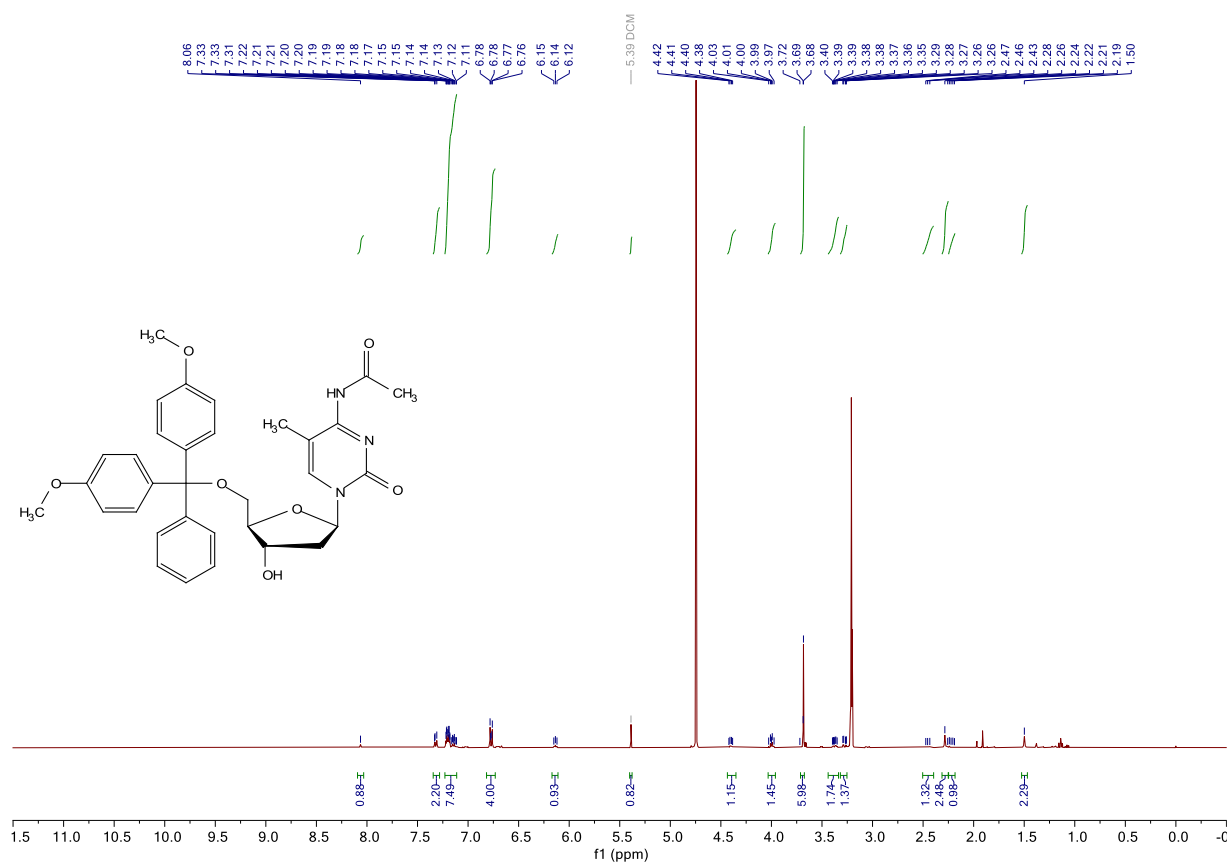
12.6. *III-8*

¹H
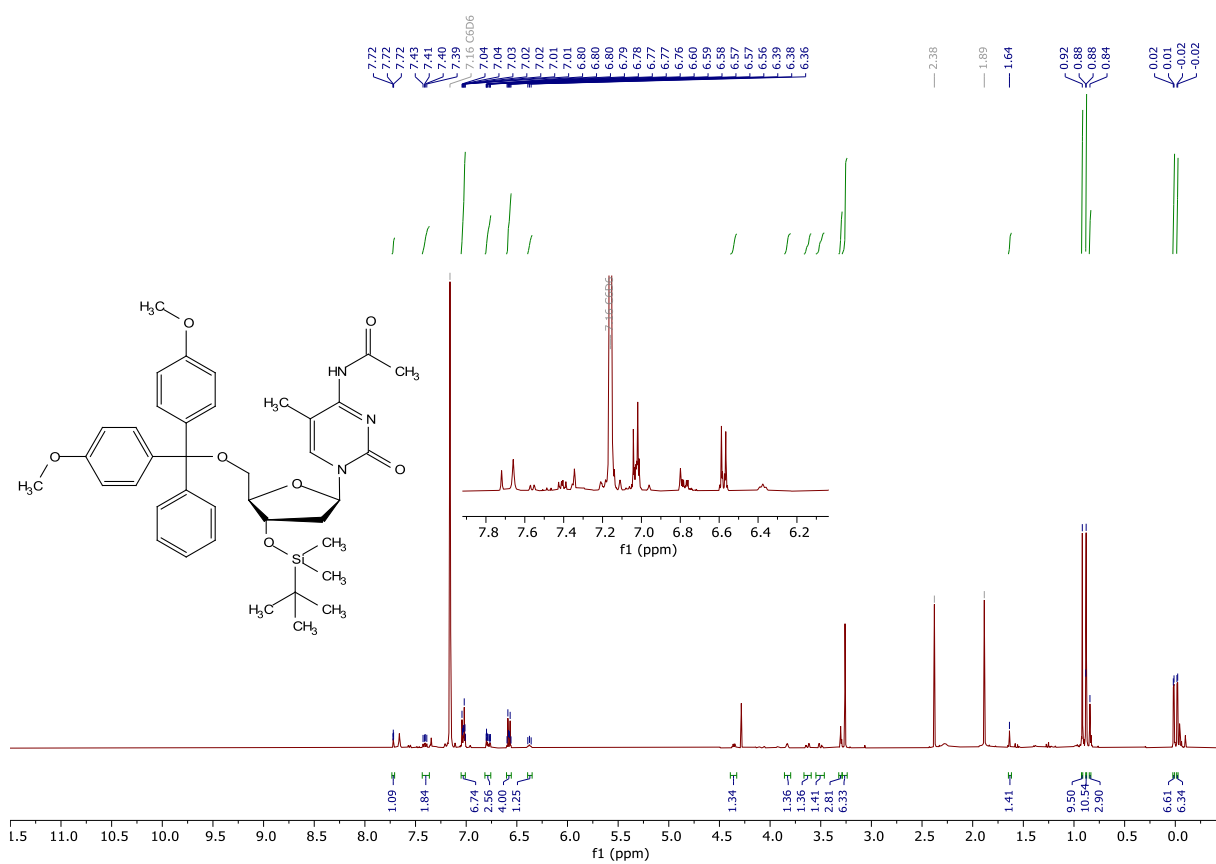
12.7.   III-6a

¹H
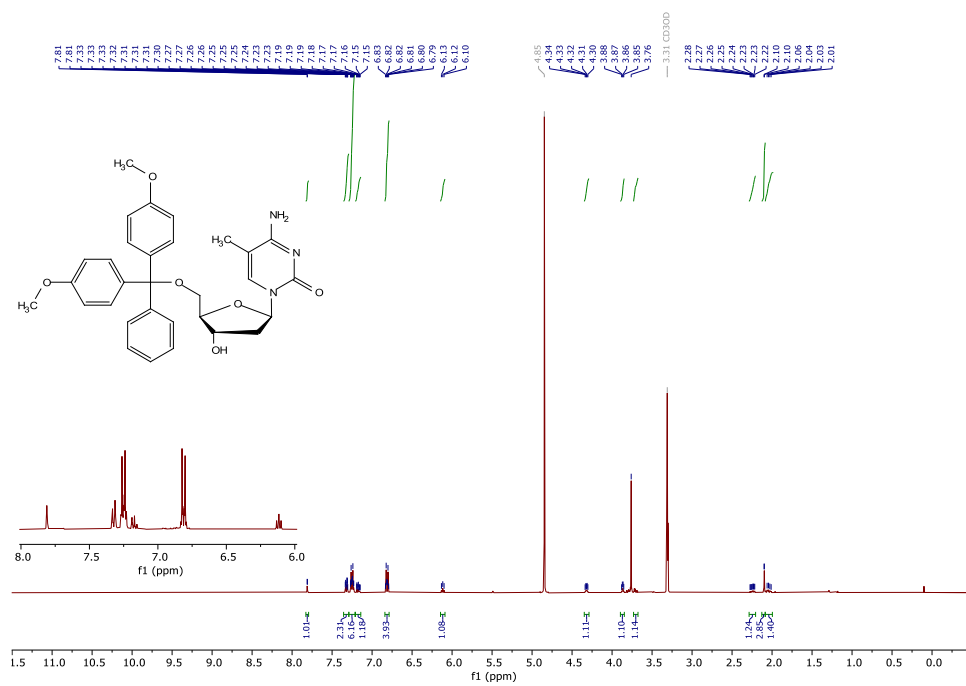
13. NMR Spectra: HPDL Project

13.1. VI-1

¹H
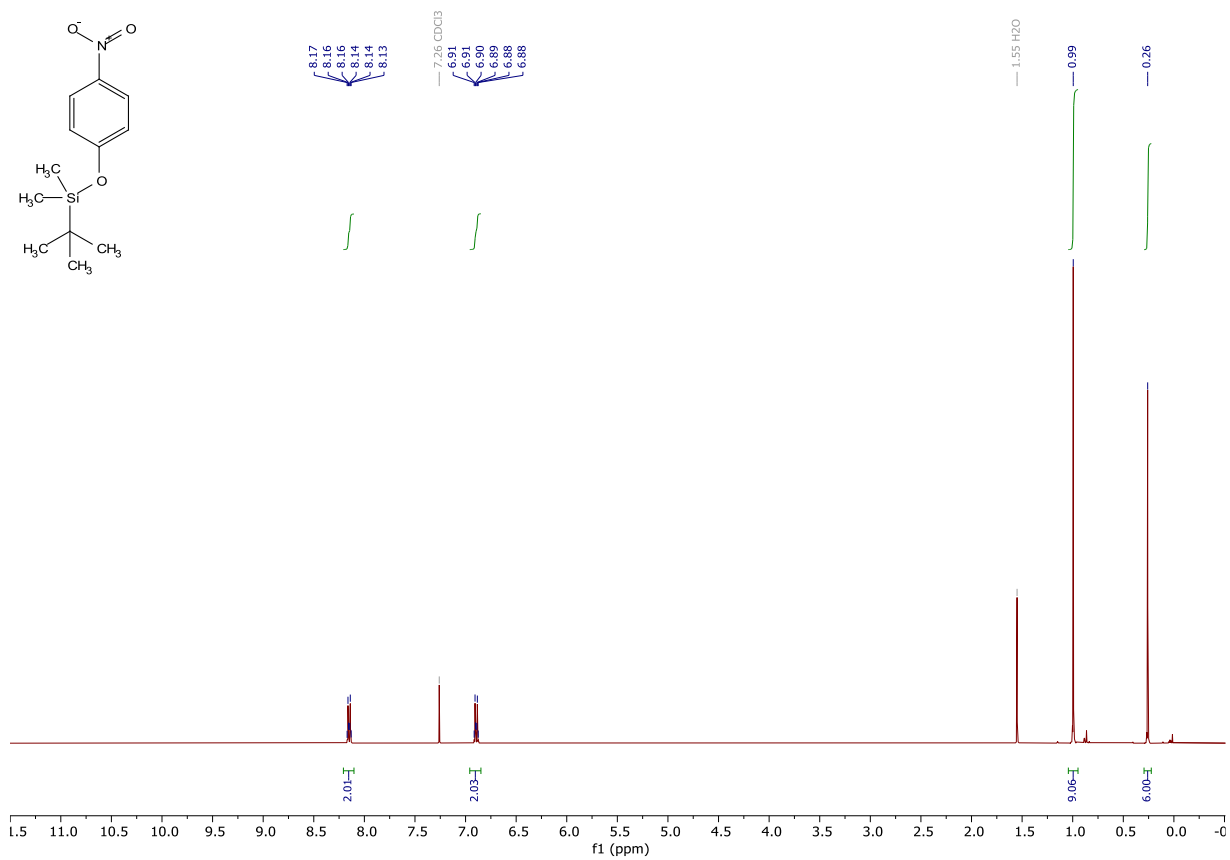
¹³C
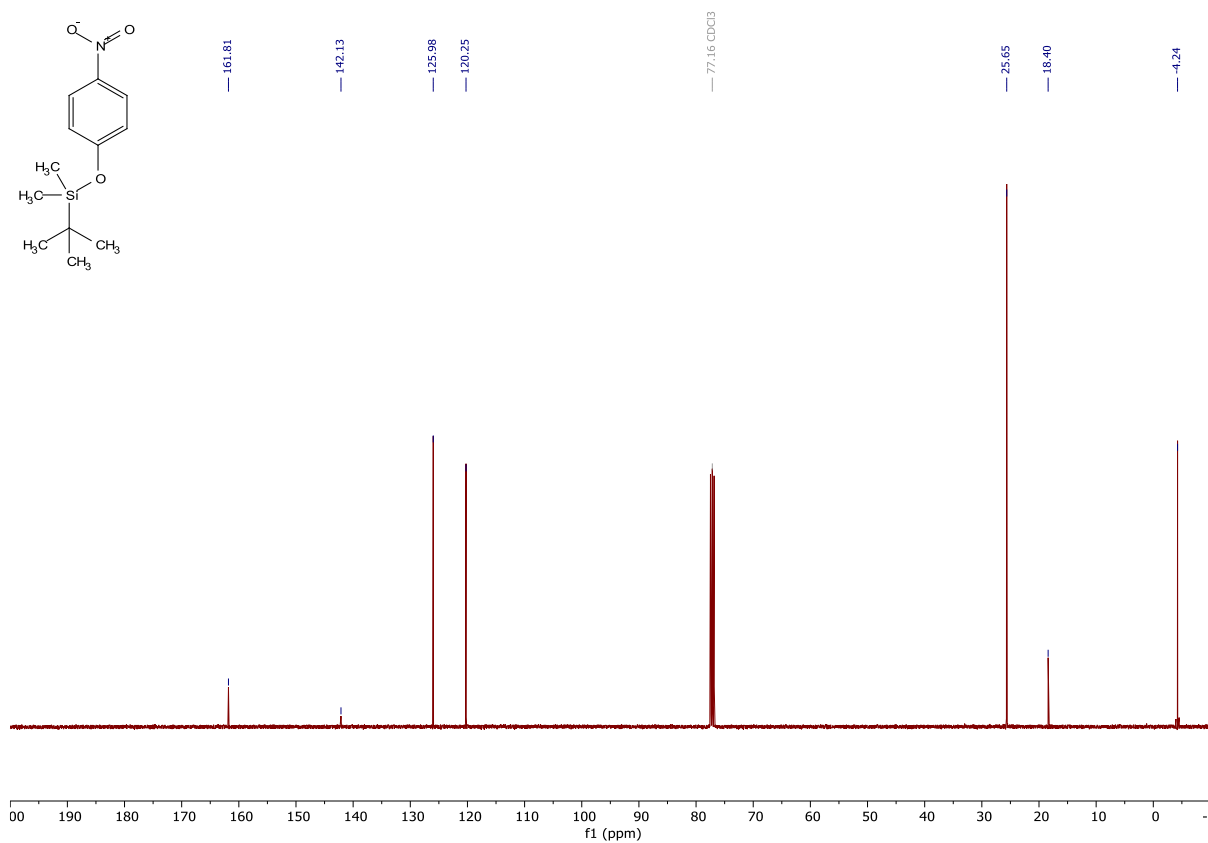
13.2. *VI-2*

¹H
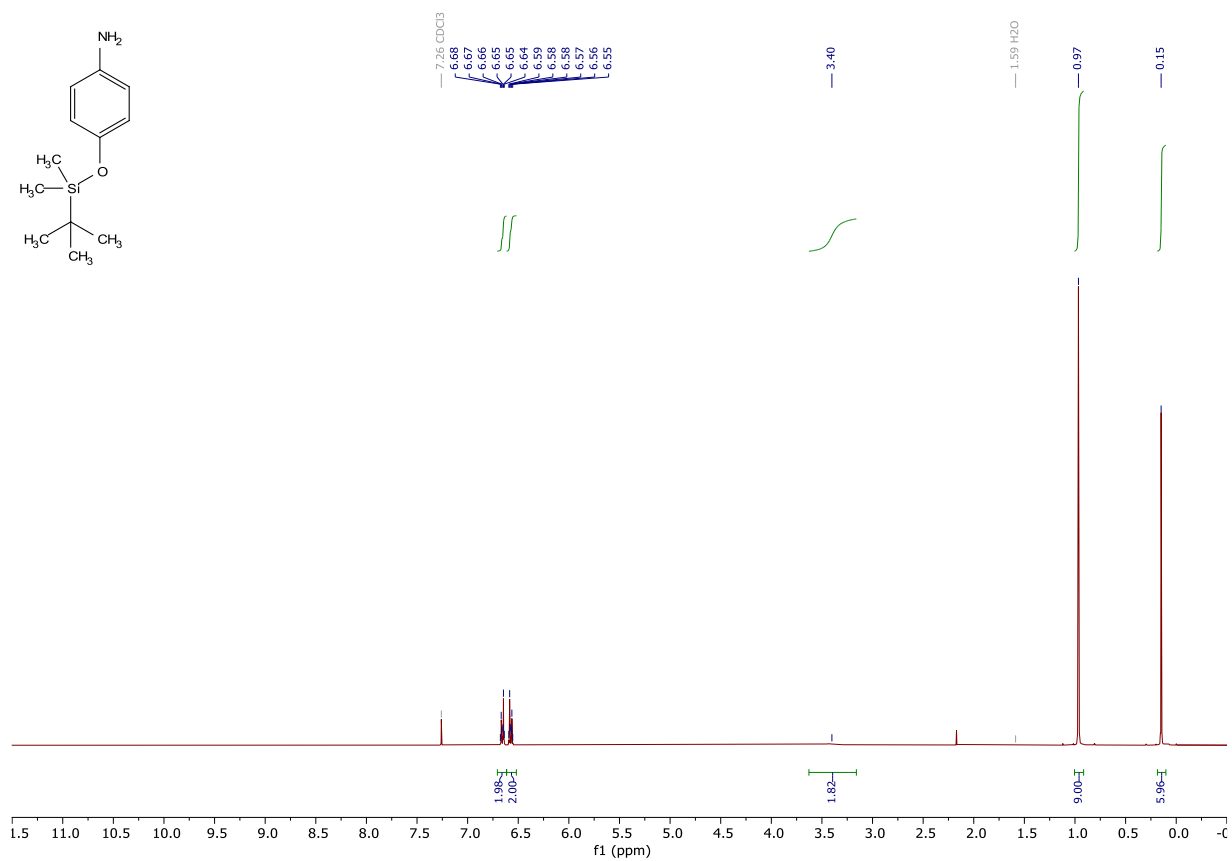
¹³C
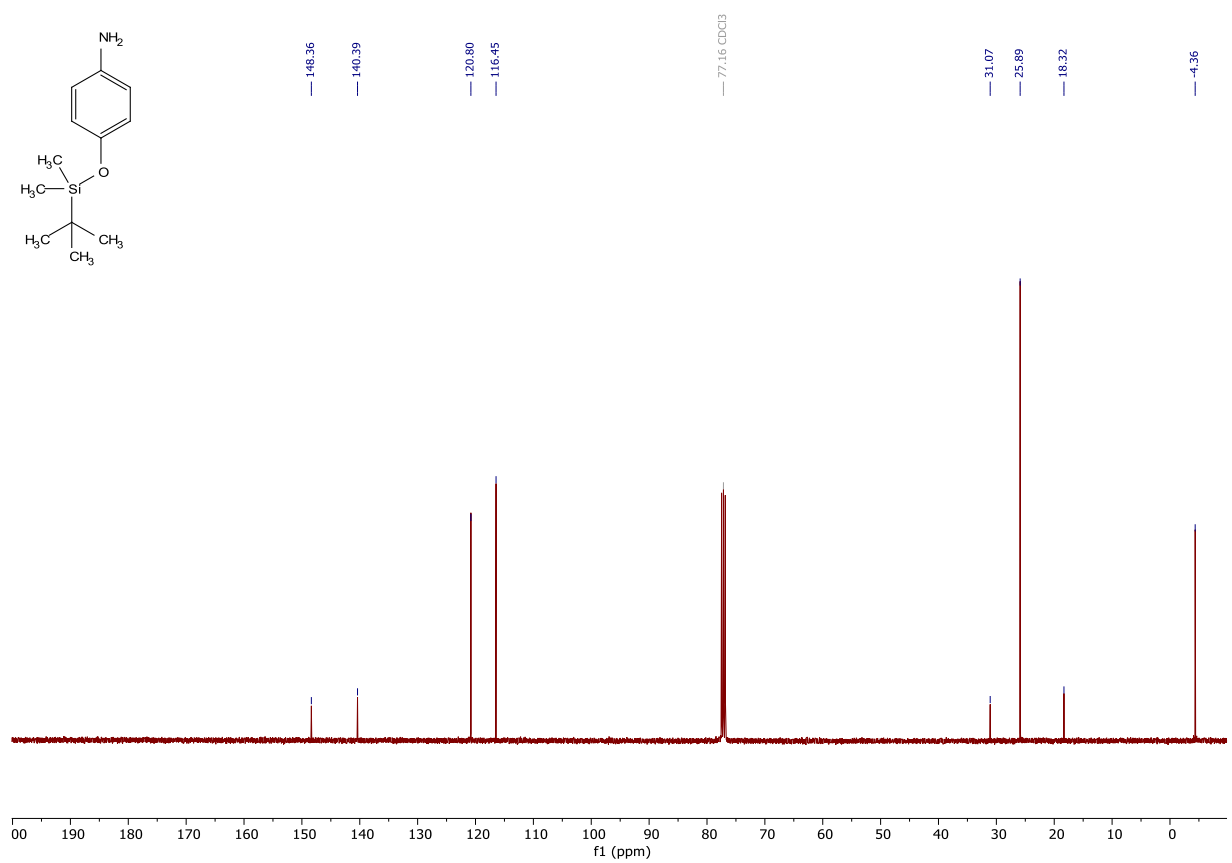
13.3. *VI-3*

¹H
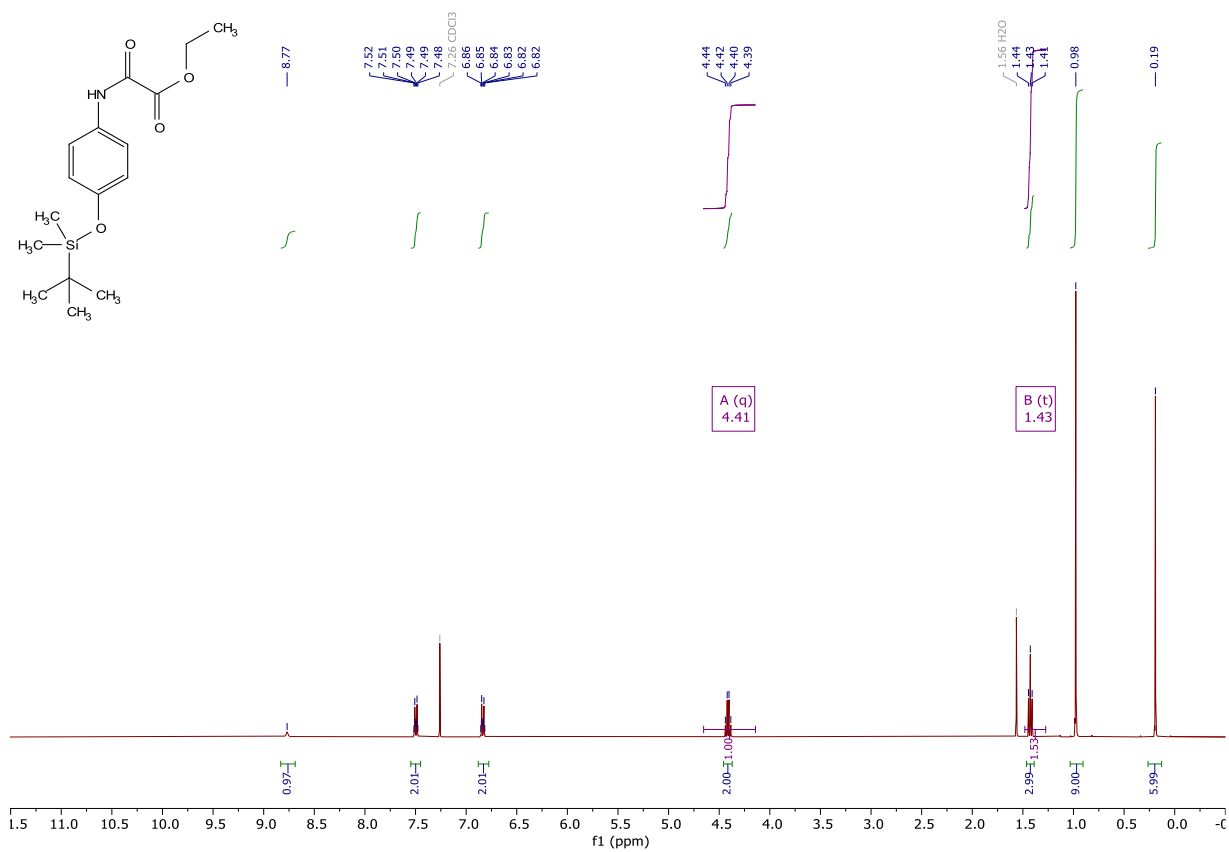
¹³C
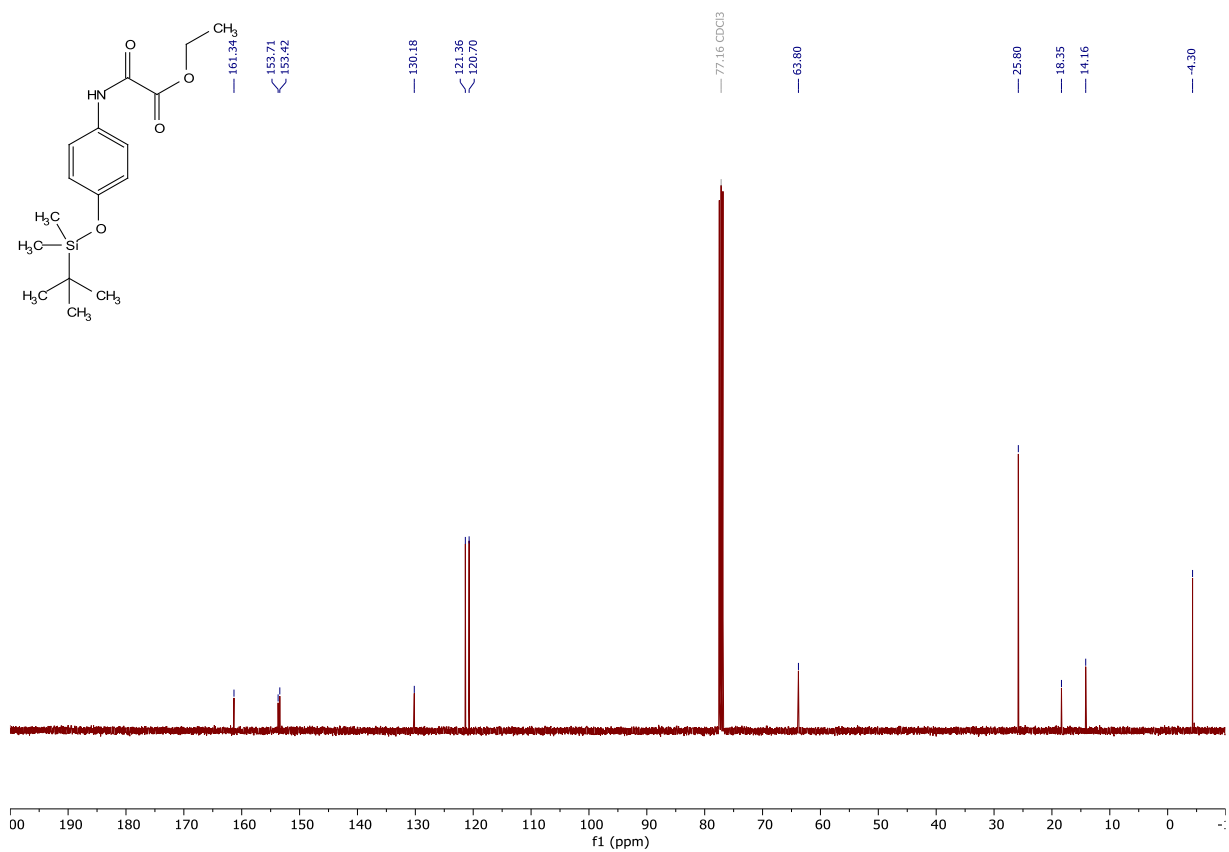
13.4. *VI-4*

¹H – CDCl₃
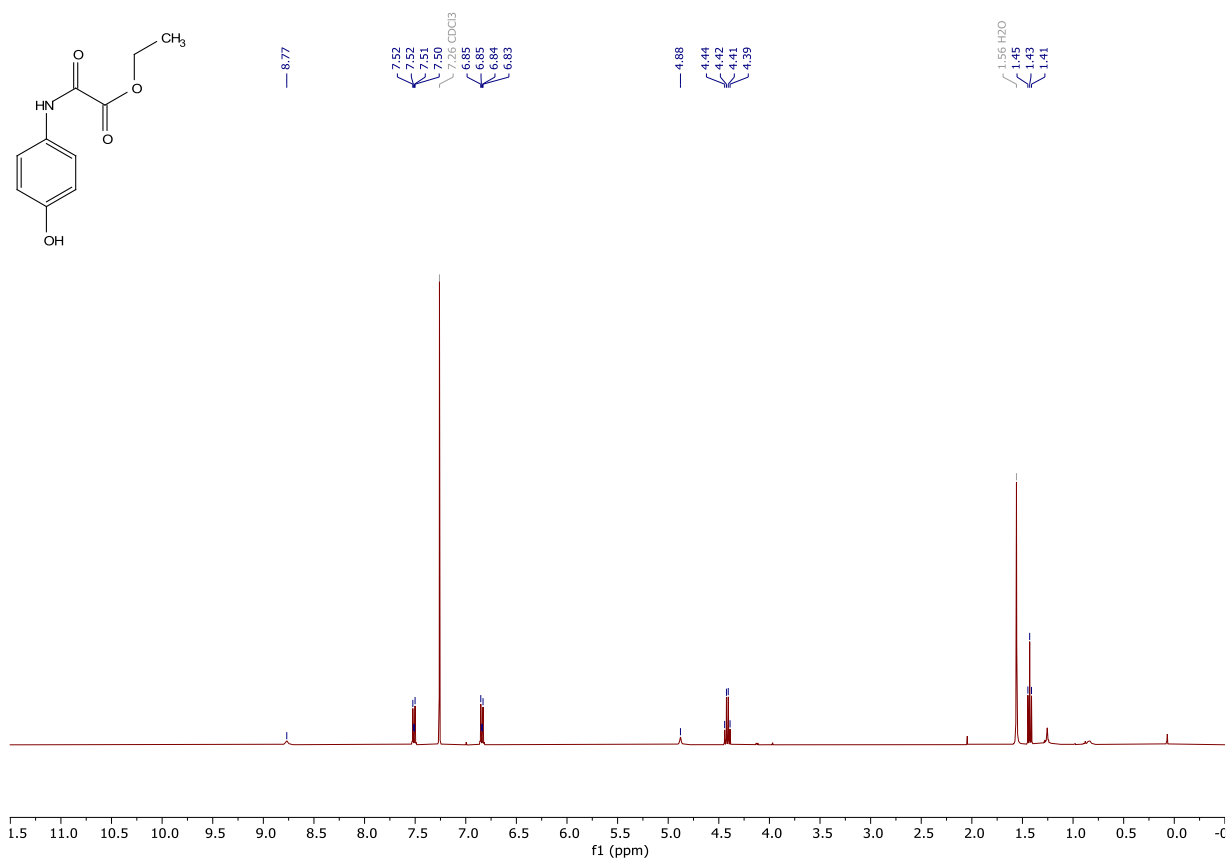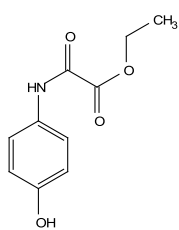
¹H – D₃-MeOD
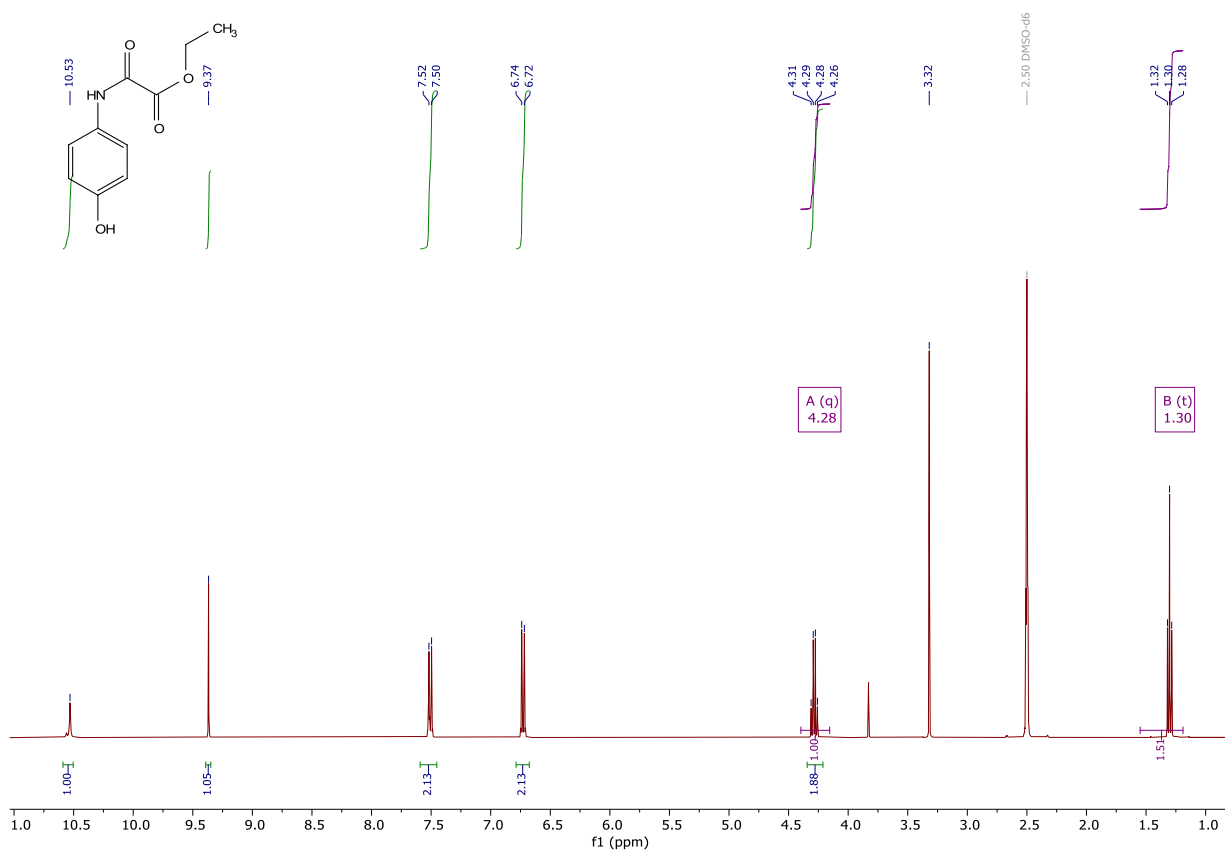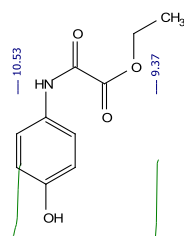
^{13}C – CDCl$_3$
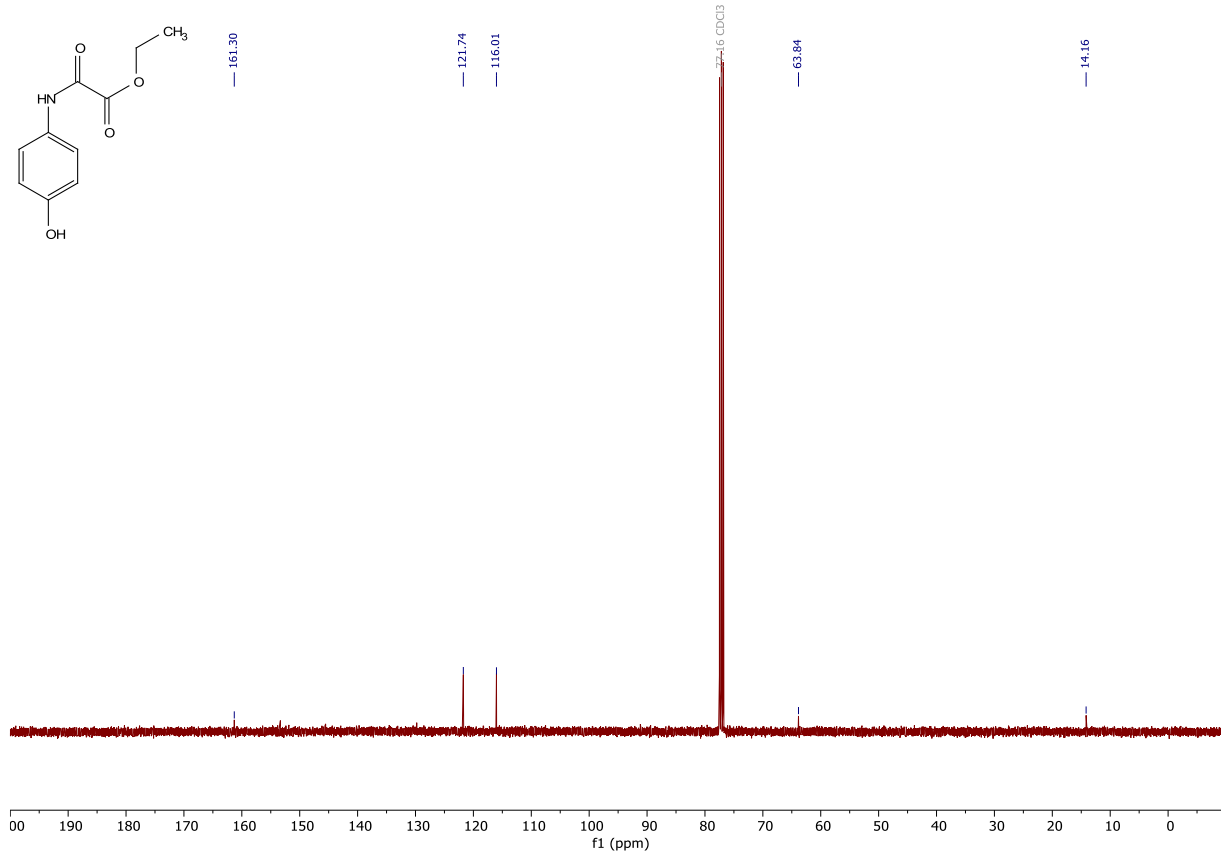
13.5. 4-HPN

¹H – D₆-DMSO
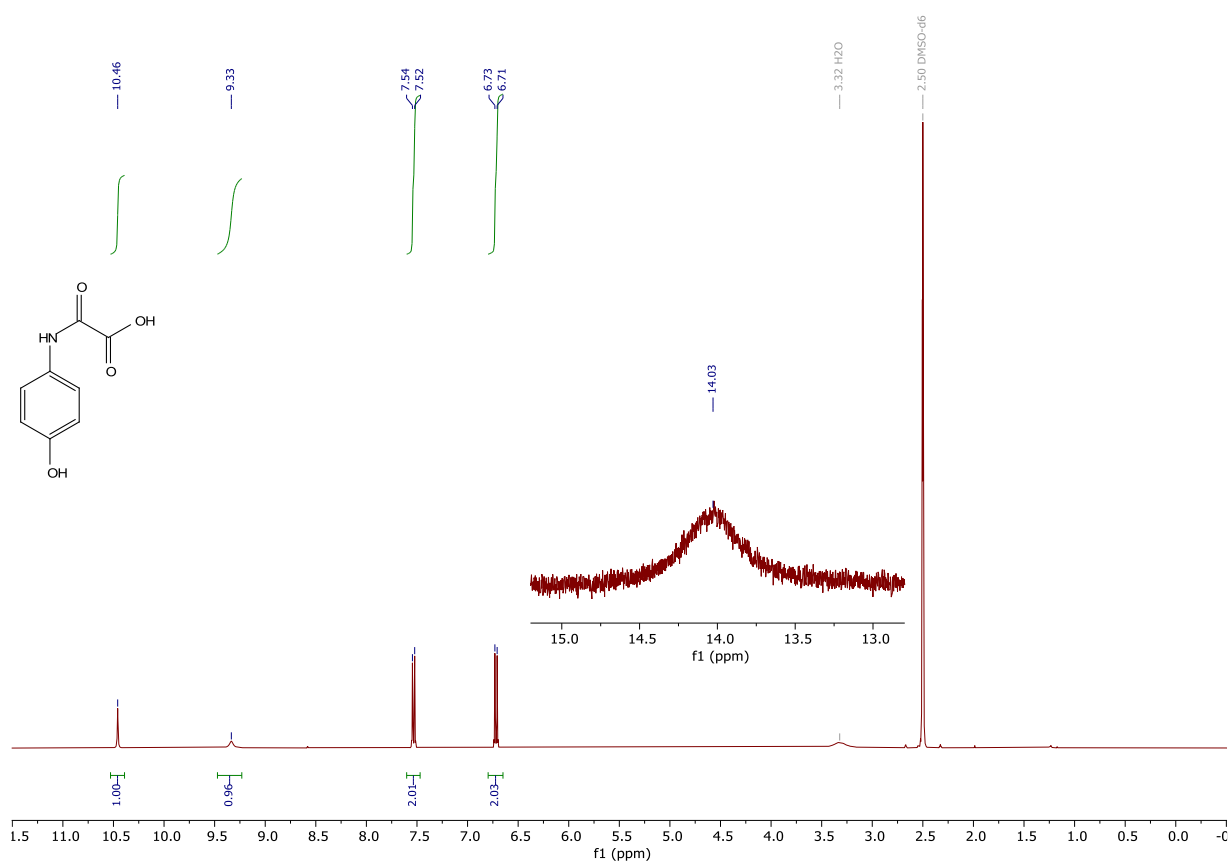
¹H – D₂O
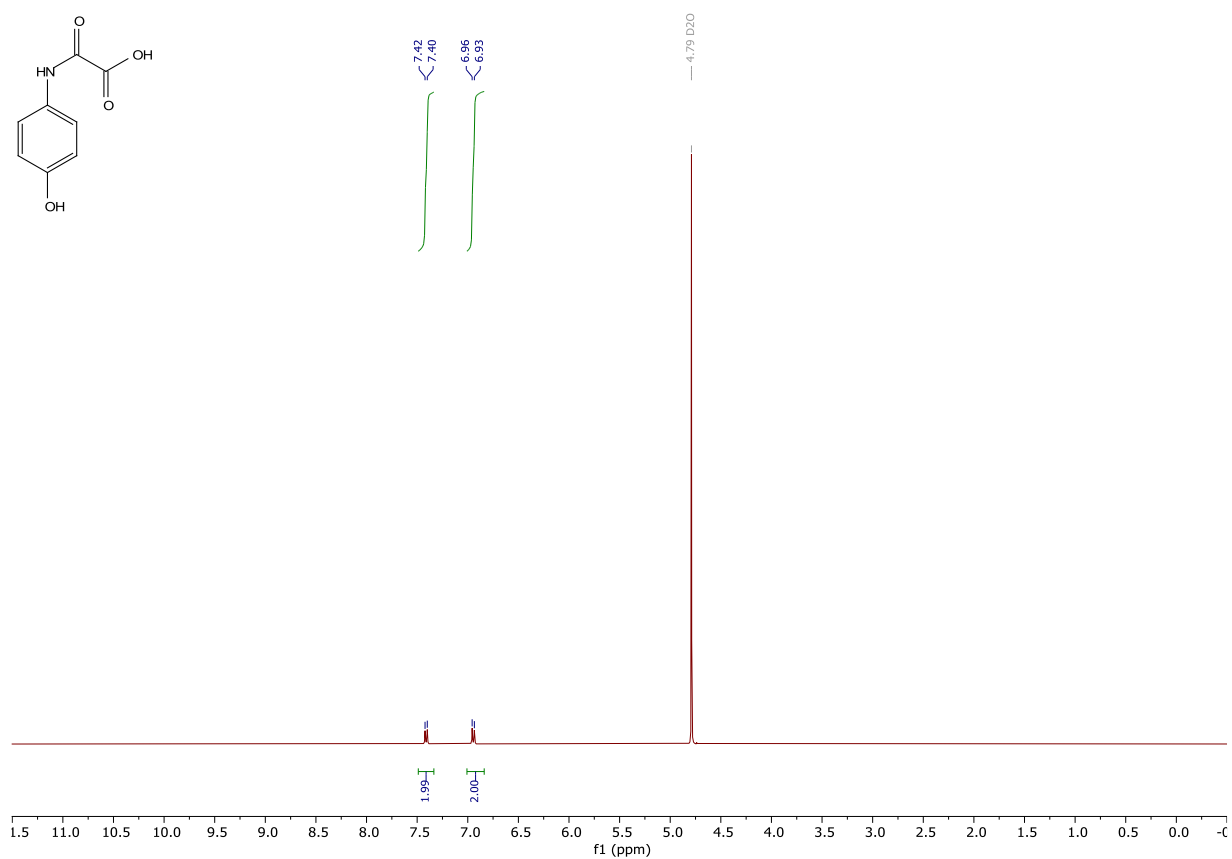
¹³C – D₆-DMSO
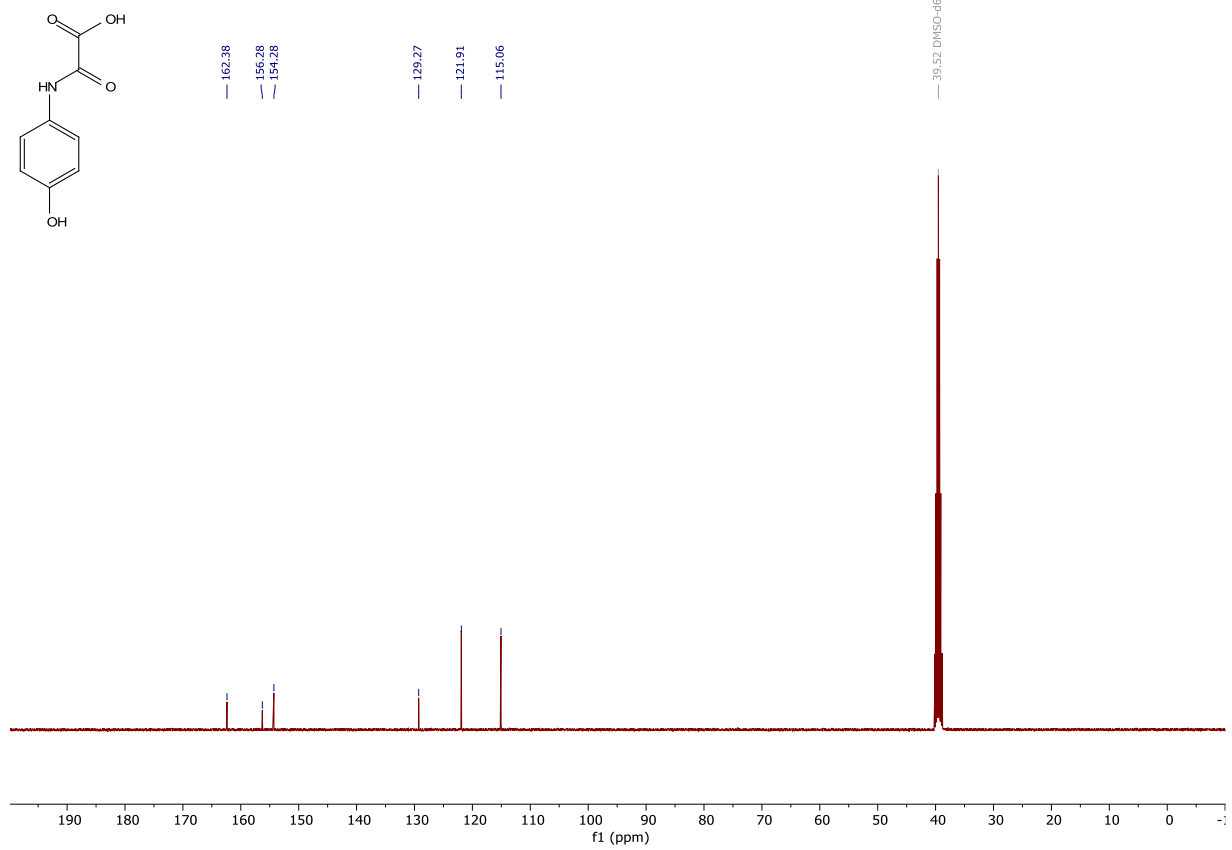
14. NMR Spectra – Miscellaneous

14.1. III-2

¹H
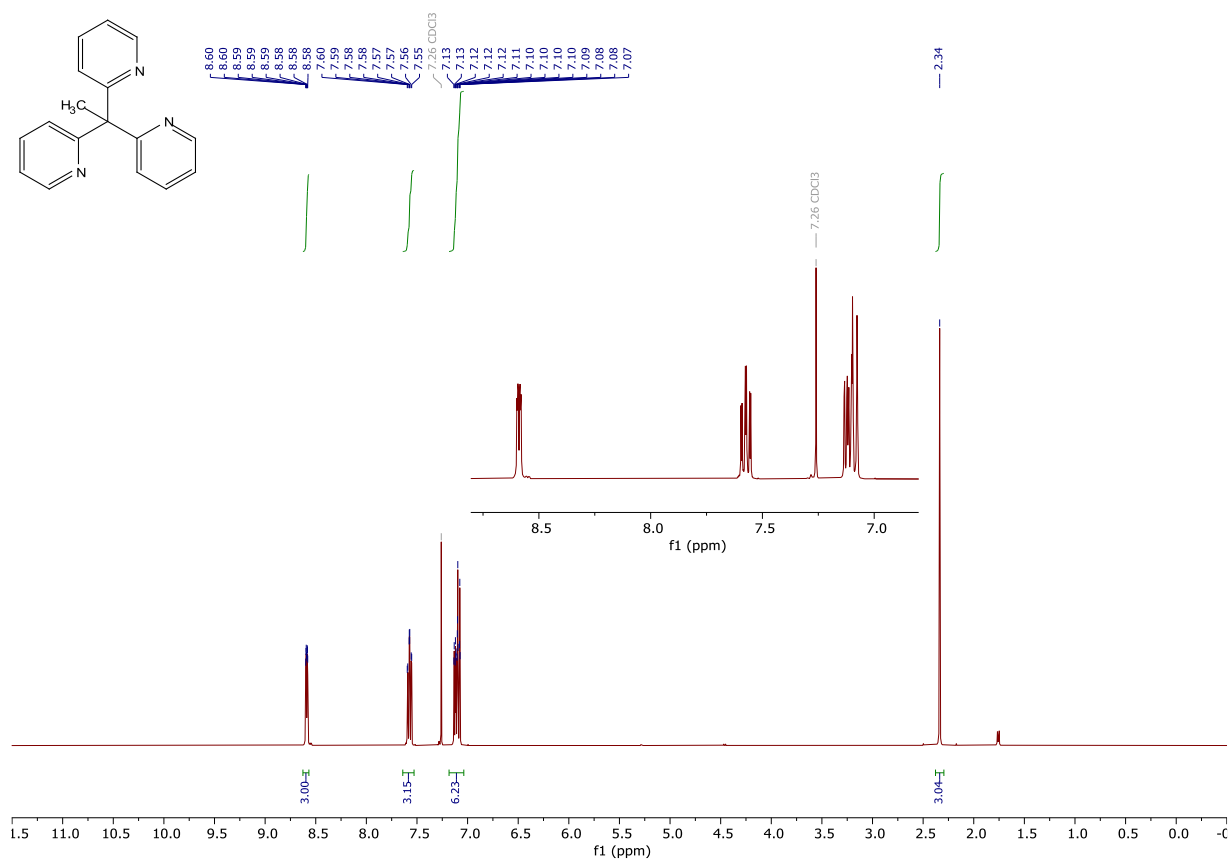
¹³C
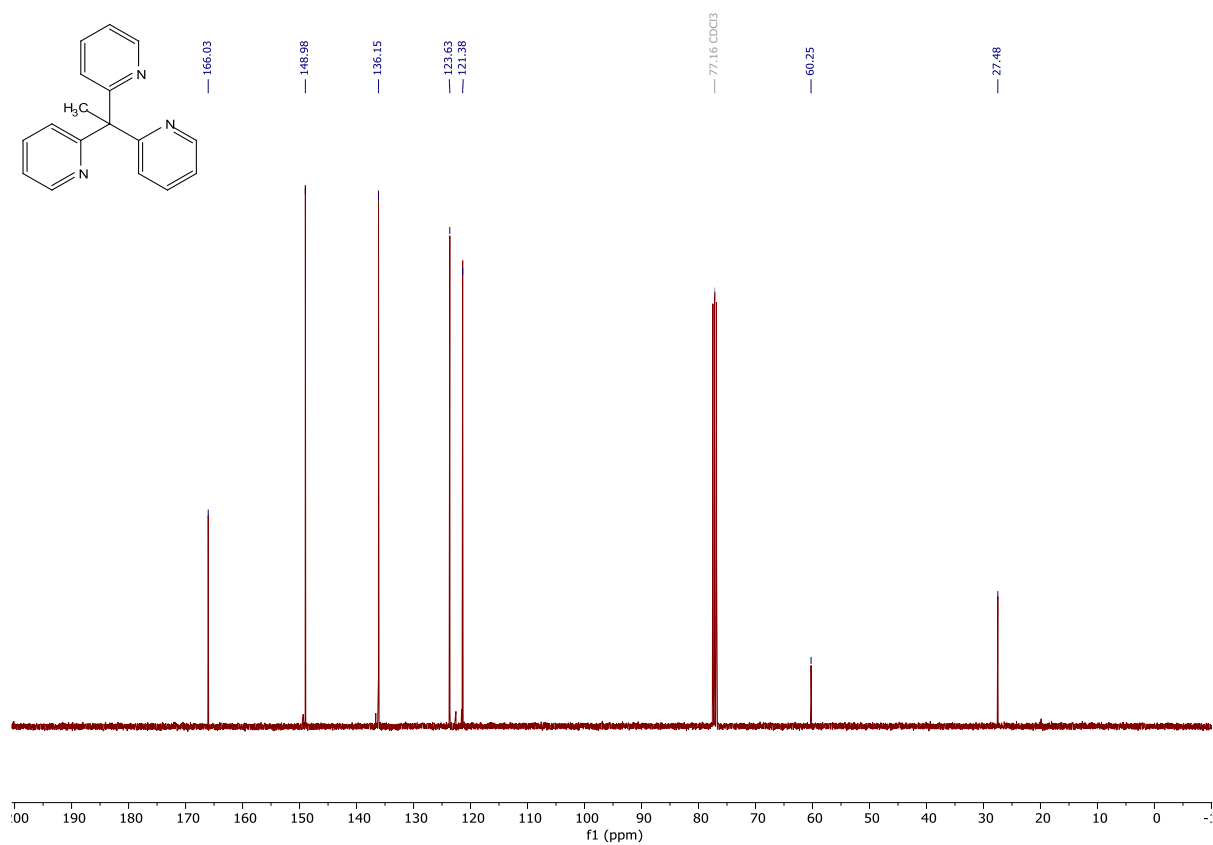
14.2. *III-3*

¹H
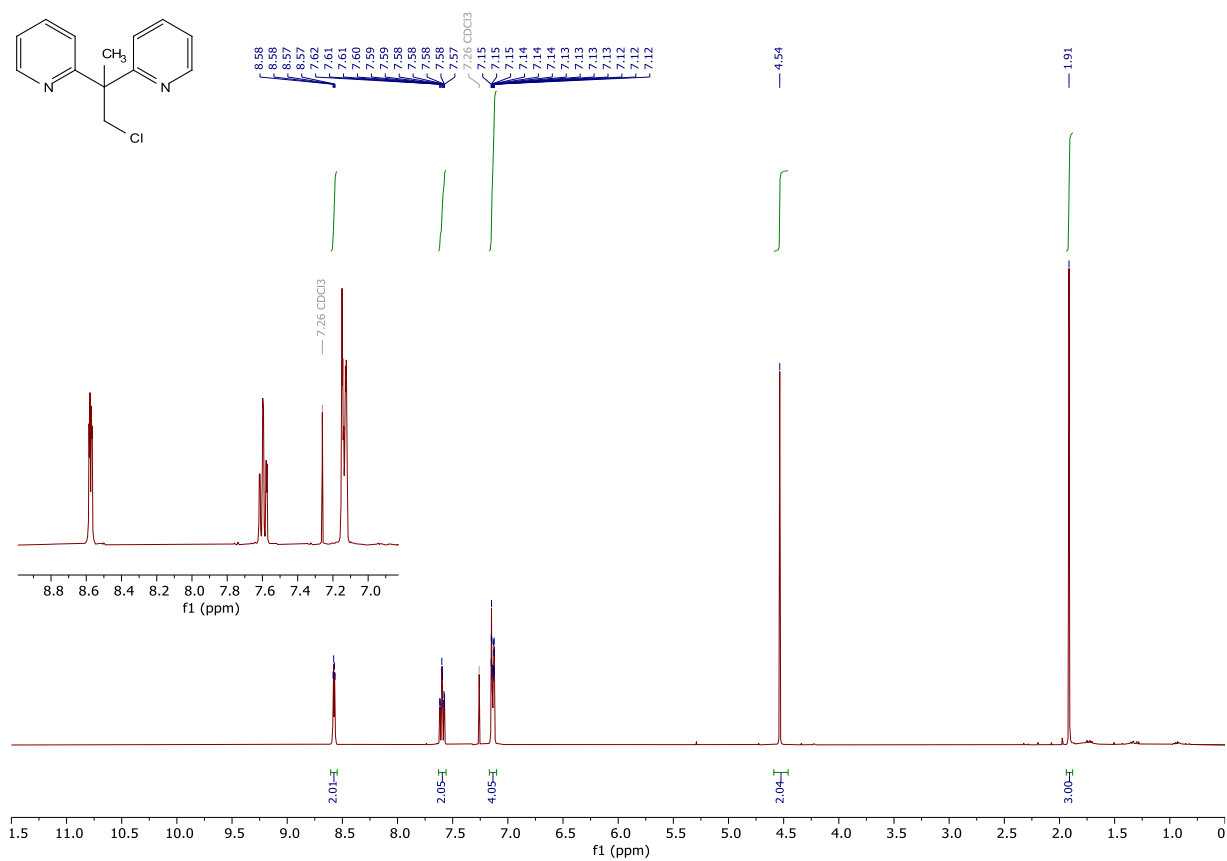
¹³C
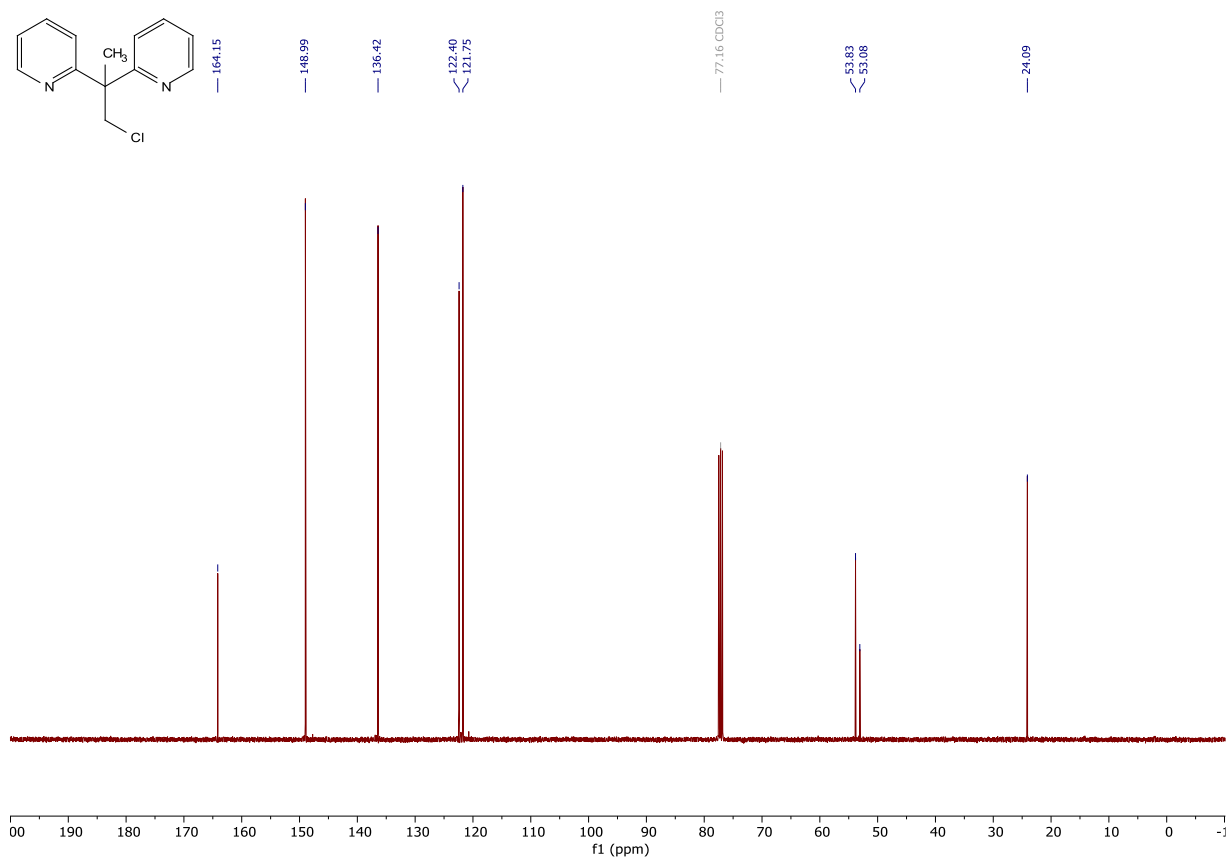
14.3. Pyocyanin

¹H
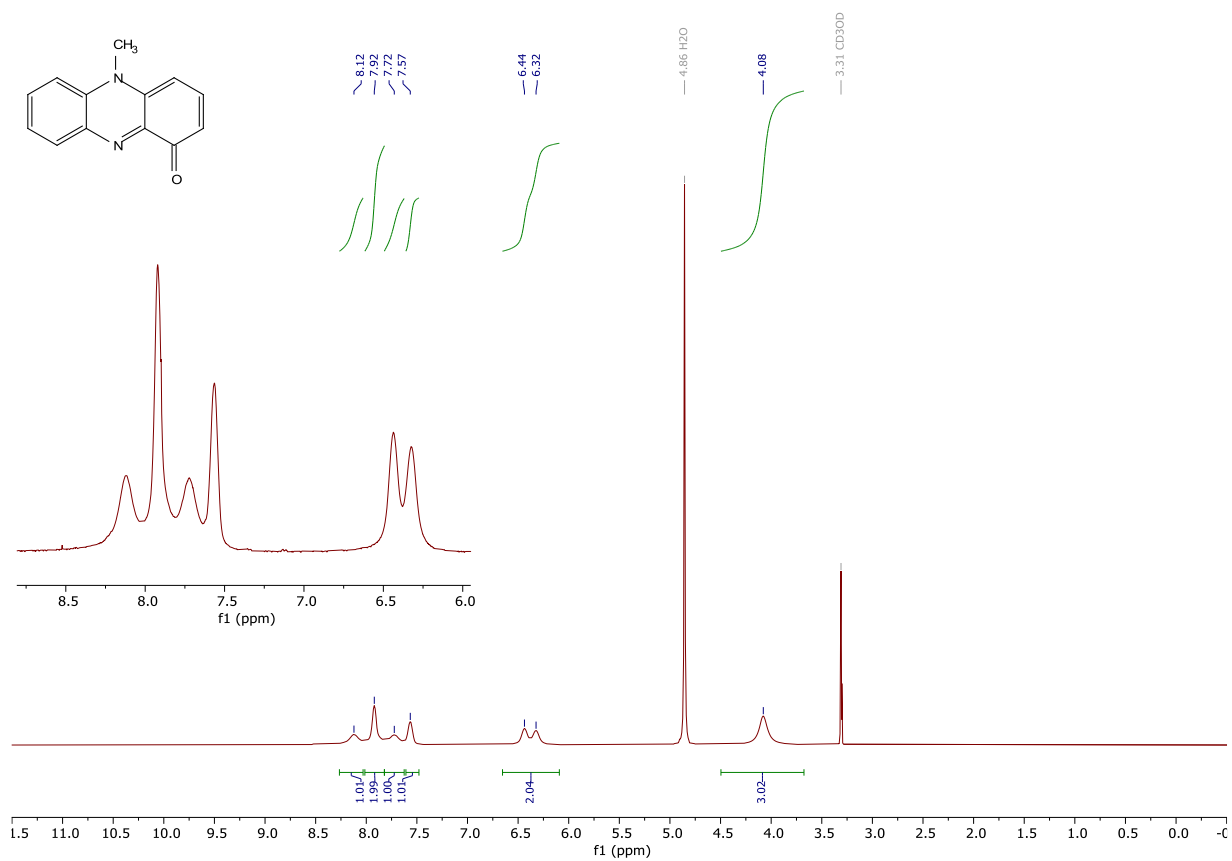
HMQC in lack of significant ¹³C signals
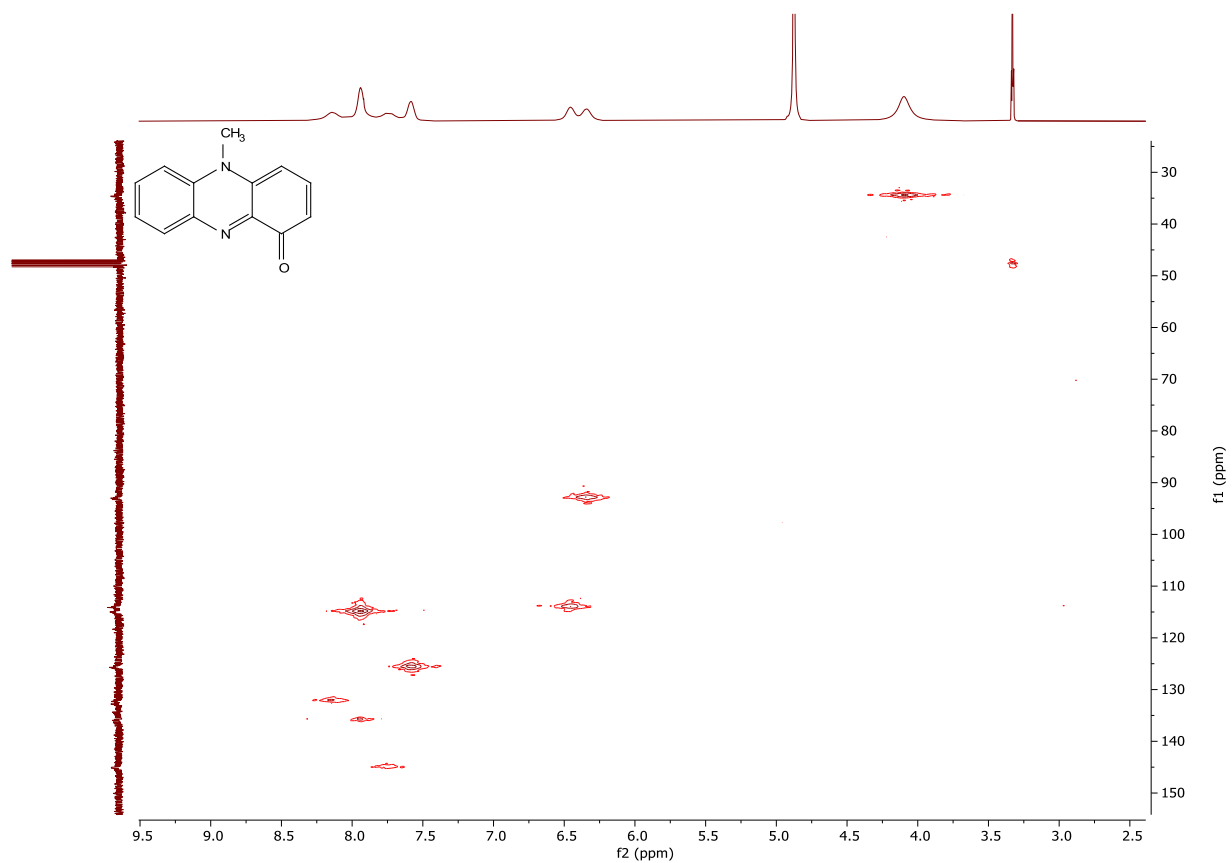
15.   Crystallography

Single crystals were analyzed and crystal structures calculated by Dr. Peter Meyer, LMU Munich.

The following colors were used in graphical representations:

Table 29: Colors used for graphical representations of crystal structures.

Element	Color	
H	white encircled/not shown	
B	cyan	
C	grey (70% black)	
N	navy	
O	red	
F	green	
P	violet	
S	yellow	
Fe	orange	

15.1. **L-1** *– Py₅Me₂H*
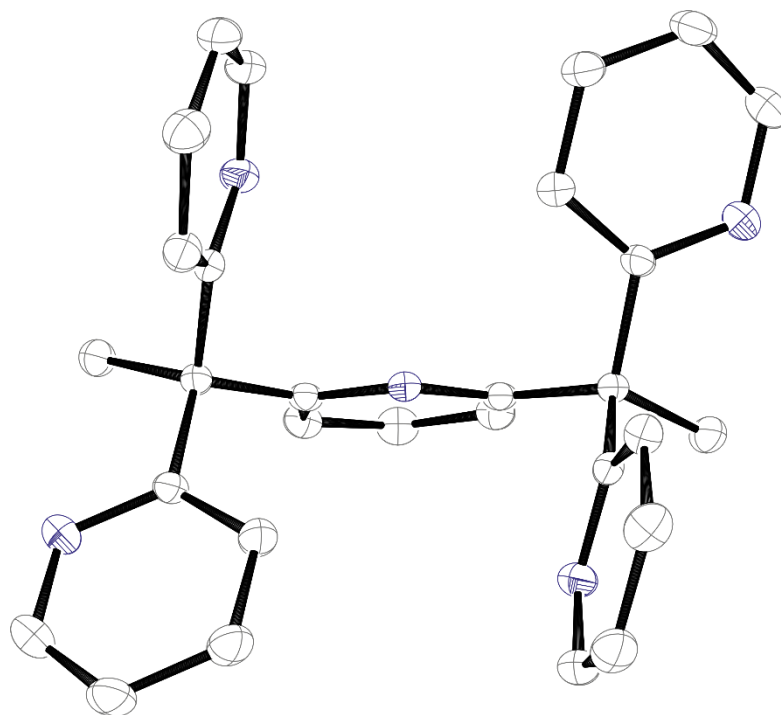
net formula	$C_{29}H_{25}N$
Mr/g mol-1	443.54
crystal size/mm	0.100 × 0.060 × 0.040
T/K	110.(2)
radiation	MoKα
diffractometer	'Bruker D8 Venture TXS'
crystal system	orthorhombic
space group	'A b a 2'
a/Å	17.8688(7)
b/Å	15.1491(5)
c/Å	8.2241(3)
α/°	90
β/°	90
γ/°	90
V/Å3	2226.23(14)
Z	4
calc. density/g cm-3	1.323
μ/mm-1	0.080
absorption correction	Multi-Scan

transmission factor range	0.96–1.00
refls. measured	21020
Rint	0.0311
mean $\sigma(I)/I$	0.0241
θ range	2.921–30.506
observed refls.	3198
x, y (weighting scheme)	0.0575, 0.7328
hydrogen refinement	constr
Flack parameter	0.5
refls in refinement	3386
parameters	156
restraints	1
$R(F$obs)	0.0377
Rw($F2$)	0.0972
S	1.052
shift/errormax	0.001
max electron density/e Å-3	0.308
min electron density/e Å-3	-0.172

*15.2. **C-1** – [Fe^{II}(mecn)(**L-1**)](OTf$_2$)$_2$ x 1.77 MeCN*
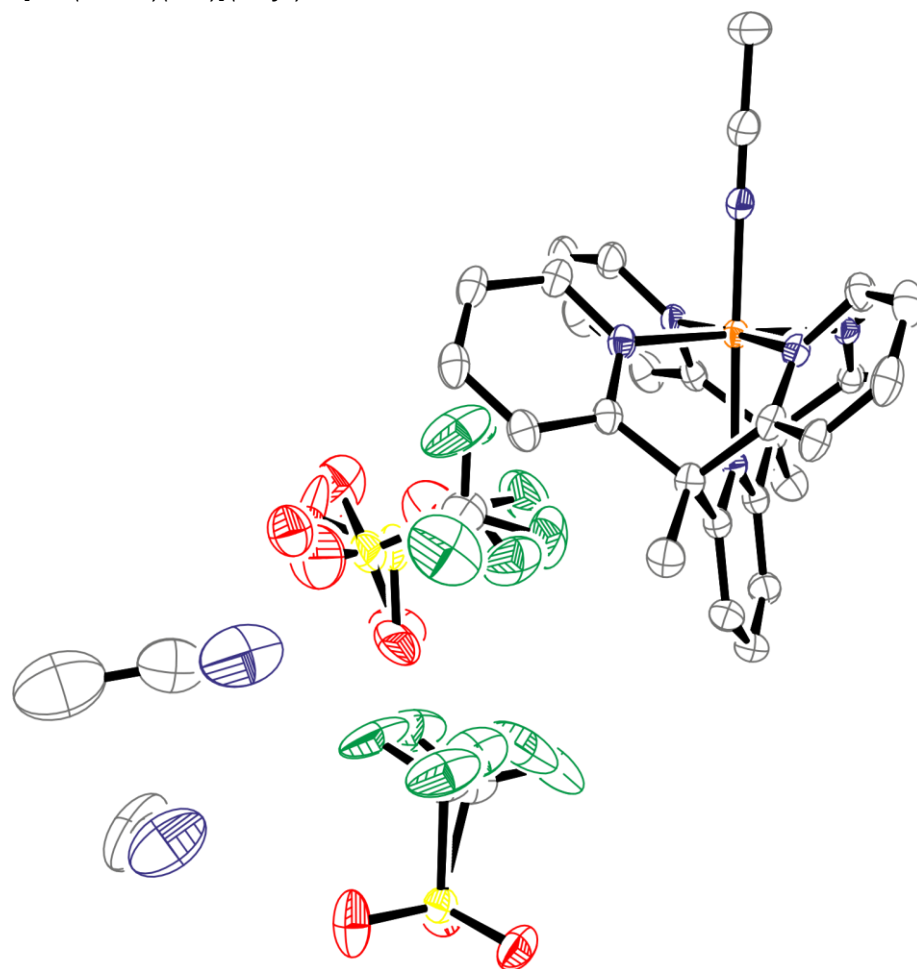
net formula	$C_{36.55}H_{33.77}F_6FeN_{7.77}O_{6.23}S_2$
M_r/g mol^{-1}	915.49
crystal size/mm	0.090 × 0.060 × 0.050
T/K	105.(2)
radiation	MoKα
diffractometer	'Bruker D8 Venture TXS'
crystal system	monoclinic
space group	'P 1 21/n 1'
a/Å	12.4626(5)
b/Å	15.6444(5)
c/Å	20.0695(8)
α/°	90
β/°	90.9620(10)
γ/°	90
V/Å^3	3912.4(3)

Z	4
calc. density/g cm⁻³	1.554
μ/mm⁻¹	0.579
absorption correction	Multi-Scan
transmission factor range	0.91–0.97
refls. measured	68611
R_{int}	0.0447
mean $\sigma(I)/I$	0.0265
θ range	2.894–27.484
observed refls.	7134
x, y (weighting scheme)	0.0488, 4.9785
hydrogen refinement	constr
refls in refinement	8953
parameters	666
restraints	168
$R(F_{obs})$	0.0431
$R_w(F^2)$	0.1241
S	1.088
shift/error$_{max}$	0.001
max electron density/e Å⁻³	0.592
min electron density/e Å⁻³	−0.497

H(C) constr, H(O) not considered in refinement (could not be located). Disorder of $CF_3SO_3^-$ has been described by split models with support of SAME, SADI, SIMU and ISOR restraints in order to improve the geometry and anisotropic displacement parameters of disordered moieties.

The formula sum is: $C_{31}H_{28}FeN_6$, $2(CF_3O_3S)$, $1.77(C_2H_3N)$, $0.23(H_2O)$.

The figure above shows the complete structure including disordered $CF_3SO_3^-$.

15.3. **C-1** *– [Fe^{II}(mecn)(**L-1**)](OTf)$_2$ x 1 H$_2$O*
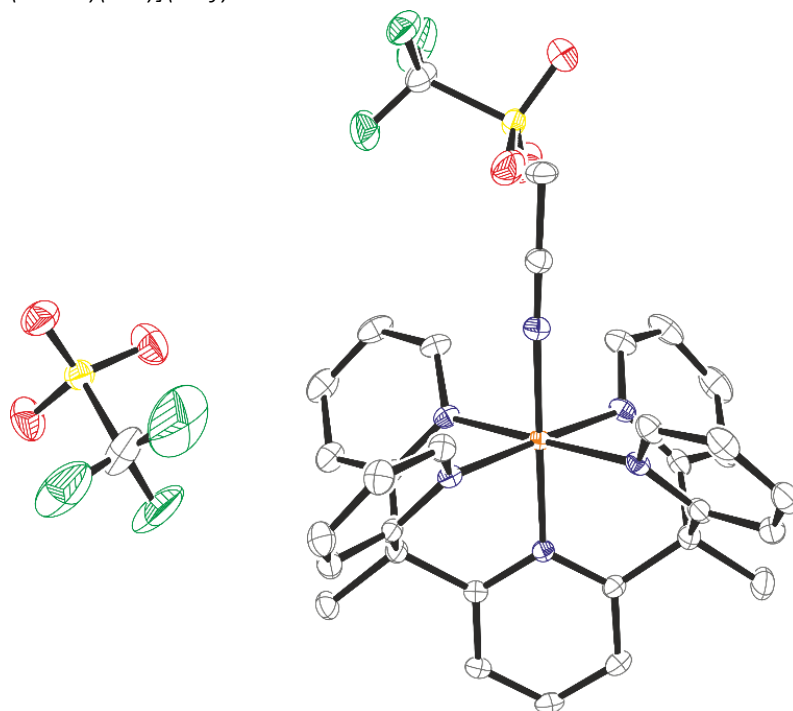
net formula	$C_{33}H_{30}F_6FeN_6O_7S_2$
M_r/g mol^{-1}	856.60
crystal size/mm	0.090 × 0.050 × 0.020
T/K	102.(2)
radiation	MoKα
diffractometer	'Bruker D8 Venture TXS'
crystal system	monoclinic
space group	'P 1 21/c 1'
a/Å	12.7429(9)
b/Å	21.8306(14)
c/Å	12.3023(9)
α/°	90
β/°	92.029(2)
γ/°	90
V/Å^3	3420.2(4)
Z	4
calc. density/g cm^{-3}	1.664
μ/mm^{-1}	0.656
absorption correction	Multi-Scan
transmission factor range	0.94–0.99

refls. measured	59523
R_{int}	0.0476
mean $\sigma(I)/I$	0.0299
θ range	2.458–27.482
observed refls.	6491
x, y (weighting scheme)	0.0519, 7.1950
hydrogen refinement	H(C) constr, H(O) refall
refls in refinement	7838
parameters	507
restraints	1
$R(F_{obs})$	0.0467
$R_w(F^2)$	0.1254
S	1.045
shift/error$_{max}$	0.001
max electron density/e Å–3	1.026
min electron density/e Å–3	–0.744

H-O-distances restrained to be equal within a standard deviation of 0.01 Å.

15.4.   C-1a – *[Fe^{II}(mecn)(**L-1**)](PF$_6$)$_2$ x 1.5 Et$_2$O*
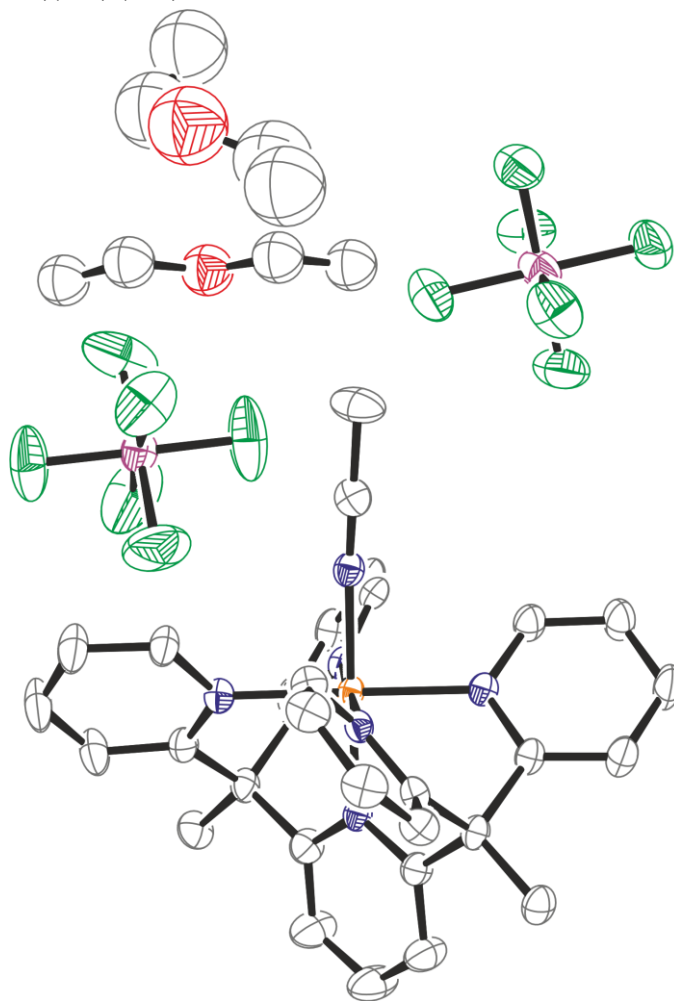
net formula	C$_{74}$H$_{86}$F$_{24}$Fe$_2$N$_{12}$O$_3$P$_4$
M_r/g mol^{-1}	1883.12
crystal size/mm	0.100 × 0.080 × 0.070
T/K	102.(2)
radiation	MoKα
diffractometer	'Bruker D8 Venture TXS'
crystal system	triclinic
space group	'P -1'
a/Å	12.7125(10)
b/Å	12.9566(9)
c/Å	15.2856(11)
$α$/°	92.383(2)
$β$/°	114.233(2)
$γ$/°	116.706(2)

$V/\text{Å}^3$	1970.4(3)
Z	1
calc. density/g cm^{-3}	1.587
μ/mm^{-1}	0.563
absorption correction	Multi-Scan
transmission factor range	0.85–0.96
refls. measured	28641
R_{int}	0.0569
mean $\sigma(I)/I$	0.0550
θ range	3.025–26.372
observed refls.	6731
x, y (weighting scheme)	0.0958, 5.0592
hydrogen refinement	constr
refls in refinement	8041
parameters	508
restraints	26
$R(F_{obs})$	0.0667
$R_w(F^2)$	0.1978
S	1.058
shift/error$_{max}$	0.001
max electron density/e Å^{-3}	1.470
min electron density/e Å^{-3}	–1.478

One of the two diethyl ether moieties in the asymmetric unit is disordered. A split model has been applied with support of geometrical restraints for all 1,2- and 1,3-distances of both ether molecules (SADI). The ether molecules have been refined isotropically with one common Uiso for all non-H atoms for each of the two moieties. The site occupation factor of the disordered ether moiety has been fixed to 0.5 due to placement over a center of inversion. The ISOR restraint has been applied to create a more round, isotropic ellipsoid for F12. DELU has been applied for the P2-F12 bond in order to avoid an Hirshfeld error.

15.5. **C-3** *– [Fe^{II}(py)(**L-1**)](OTf)$_2$ x H$_2$O*
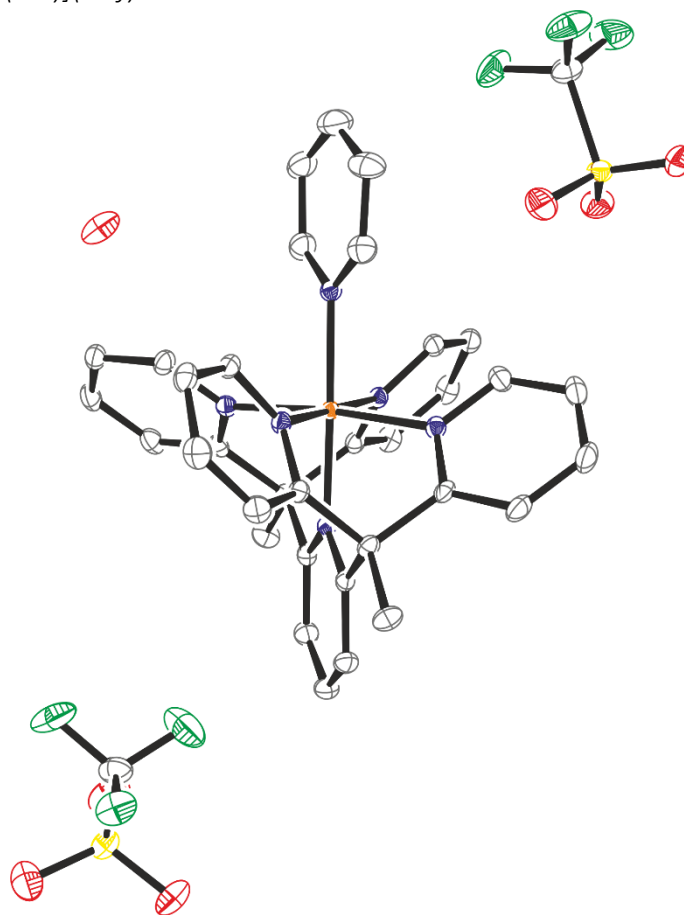
net formula	C$_{36}$H$_{32}$F$_6$FeN$_6$O$_7$S$_2$
M_r/g mol^{-1}	894.64
crystal size/mm	0.060 × 0.050 × 0.040
T/K	106.(2)
radiation	MoKα
diffractometer	'Bruker D8 Venture TXS'
crystal system	triclinic
space group	'P -1'
a/Å	11.2316(4)
b/Å	11.2625(4)
c/Å	15.8071(6)
α/°	93.0370(10)
β/°	102.2290(10)
γ/°	111.6970(10)
V/Å^3	1796.63(11)
Z	2

calc. density/g cm^{-3}	1.654
μ/mm^{-1}	0.628
absorption correction	Multi-Scan
transmission factor range	0.94–0.97
refls. measured	32421
R_{int}	0.0369
mean $\sigma(I)/I$	0.0344
θ range	2.665–27.484
observed refls.	7112
x, y (weighting scheme)	0.0325, 2.1859
hydrogen refinement	mixed
refls in refinement	8227
parameters	535
restraints	8
$R(F_{obs})$	0.0372
$R_w(F^2)$	0.0911
S	1.032
shift/error$_{max}$	0.001
max electron density/e Å^{-3}	0.727
min electron density/e Å^{-3}	−0.449

15.6. **C-4** *– [Fe^{III}(**L-1**)(OH)](F)$_{0.19}$(NO$_3$)$_{1.81}$ x 3.14 H$_2$O*

net formula	C$_{29}$H$_{32.30}$F$_{0.19}$FeN$_{6.81}$O$_{9.57}$
M_r/g mol^{-1}	688.81
crystal size/mm	0.100 × 0.030 × 0.020
T/K	105.(2)
radiation	MoKα
diffractometer	'Bruker D8 Venture TXS'
crystal system	monoclinic
space group	'P 1 21/m 1'
a/Å	8.8350(3)
b/Å	13.5080(5)

c/Å	12.2575(6)
α/°	90
β/°	100.2270(10)
γ/°	90
V/Å³	1439.61(10)
Z	2
calc. density/g cm⁻³	1.589
μ/mm⁻¹	0.597
absorption correction	Multi-Scan
transmission factor range	0.92–0.99
refls. measured	26165
R_{int}	0.0358
mean $\sigma(I)/I$	0.0231
θ range	3.016–28.280
observed refls.	3212
x, y (weighting scheme)	0.0561, 1.7023
hydrogen refinement	constr
refls in refinement	3725
parameters	252
restraints	6
$R(F_{obs})$	0.0411
$R_w(F^2)$	0.1206
S	1.060
shift/error$_{max}$	0.001
max electron density/e Å⁻³	0.575
min electron density/e Å⁻³	−0.517

H(C) constr, H(O): some have been located from the difference map, but not further refined (xyz fixed, U(H)= 1.5U(O), some hydrogen atoms could not be located at all.

The 2+ charge of the cation is balanced by 1.81 NO_3^- and 0.19 F⁻. ISOR has been applied to improve the anisotropic displacement parameters of F. The formula sum is: $C_{29}H_{26}FeN_5O^{2+}$, 1.81(NO_3^-), 0.19(F⁻), 3.14(H_2O). Symmetry code i = x, -y+1/2, z.

The figure above shows the cation as well as the nitrate and fluoride ion, the co-crystallized water molecules have been omitted.

15.7. C-4 – [Fe^{III}(L-1)(OH)](OTf)$_2$

This structure was obtained by David Schmidl in our collaborative project on the formation of **C-4** by comproportionation of **C-2** and **C-6** and is shown here only for comparison.
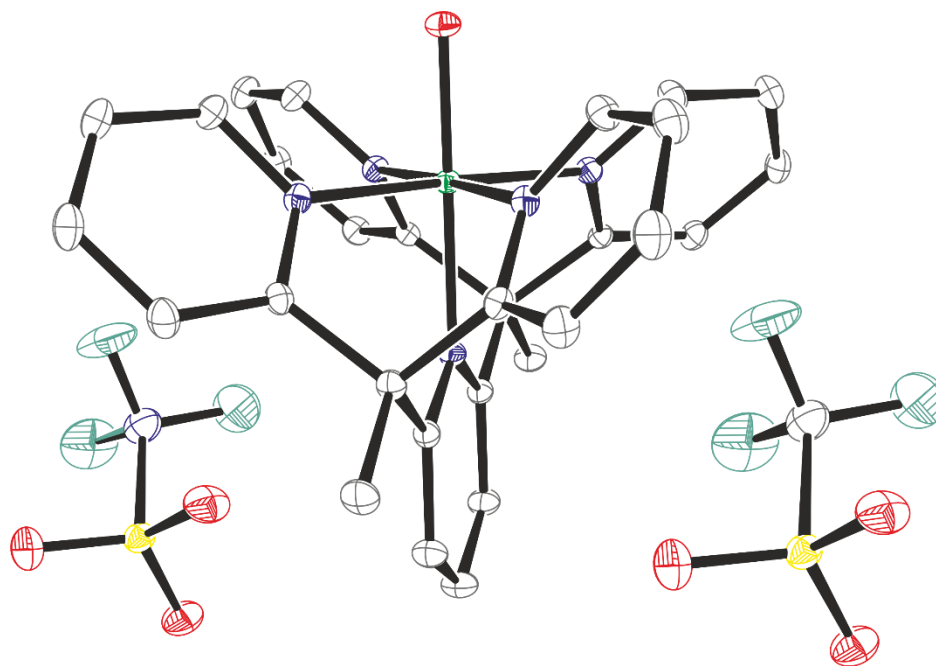
net formula	$C_{31}H_{32}F_6FeN_5O_{10}S_2$
M_r/g mol^{-1}	868.58
crystal size/mm	0.080 × 0.070 × 0.050
T/K	102.(2)
radiation	MoKα
diffractometer	'Bruker D8 Venture TXS'
crystal system	monoclinic
space group	'P 1 2$_1$/m 1'
a/Å	8.7261(7)
b/Å	20.0584(15)
c/Å	9.7491(8)
α/°	90
β/°	95.056(3)
γ/°	90
V/Å^3	1699.8(2)
Z	2
calc. density/g cm^{-3}	1.697
μ/mm^{-1}	0.666
absorption correction	Multi-Scan

transmission factor range	0.93–0.97
refls. measured	32523
R_{int}	0.0436
mean $\sigma(I)/I$	0.0297
θ range	3.171–30.506
observed refls.	4828
x, y (weighting scheme)	0.0404, 1.4634
hydrogen refinement	mixed
refls in refinement	5307
parameters	283
restraints	3
$R(F_{obs})$	0.0330
$R_w(F^2)$	0.0923
S	1.064
shift/error$_{max}$	0.001
max electron density/e Å^{-3}	0.857
min electron density/e Å^{-3}	−0.499

15.8.   **C-5** – *[Fe^{IV}(**L-1**)(O)][Ce(NO$_3$)$_6$]*
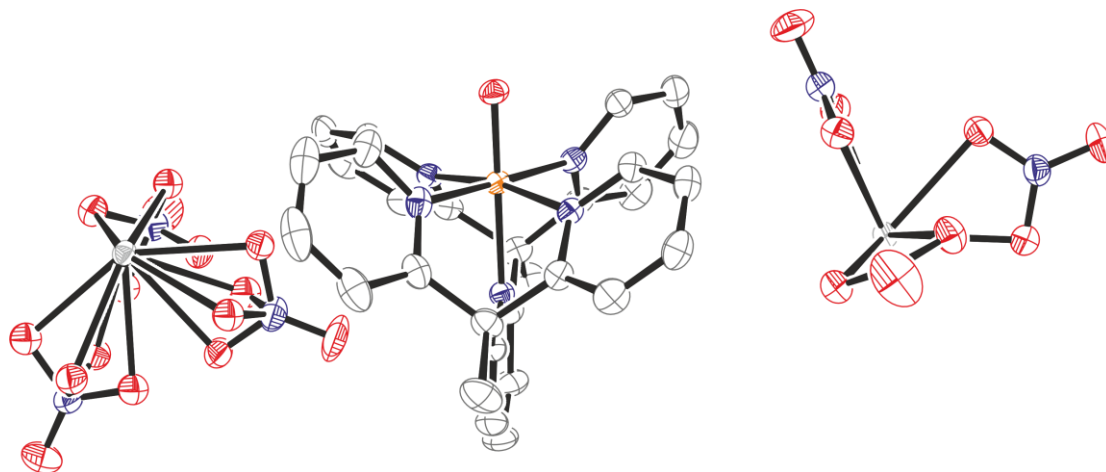
net formula	C$_{29}$H$_{25}$CeFeN$_{11}$O$_{19}$
M_r/g mol^{-1}	1027.57
crystal size/mm	0.120 × 0.080 × 0.070
T/K	173.(2)
radiation	MoKα
diffractometer	'Bruker D8 Venture TXS'
crystal system	triclinic
space group	'P -1'
a/Å	11.9336(6)
b/Å	12.0211(6)
c/Å	14.1914(7)
α/°	98.760(2)
β/°	90.028(2)
γ/°	117.223(2)
V/Å^3	1783.50(16)
Z	2
calc. density/g cm^{-3}	1.913
μ/mm^{-1}	1.769
absorption correction	Multi-Scan
transmission factor range	0.84–0.89
refls. measured	41068
R_{int}	0.0405
mean $\sigma(I)/I$	0.0312
θ range	2.613–27.484

observed refls.	7000
x, y (weighting scheme)	0.0191, 1.0812
hydrogen refinement	constr
Flack parameter	?
refls in refinement	8181
parameters	580
restraints	0
$R(F_{obs})$	0.0236
$R_w(F^2)$	0.0555
S	1.015
shift/error$_{max}$	0.001
max electron density/e Å^{-3}	0.412
min electron density/e Å^{-3}	−0.349

All hydrogen atoms have been calculated in ideal geometry riding on their parent atoms. The nitrate-O-atoms bound to Ce2 are disordered and have been described by a split model. The site occupation factors of the two disordered parts refined to 0.86 and 0.14. The disordered atoms of the minor part have been refined isotropically. The figures have been drawn at the 50% ellipsoid probability level. The less-occupied moieties of disordered parts have been omitted for the figures. In the figure above, each of the two depicted Ce-complexes has been completed by symmetry. There is one Ce-complex per Fe-complex.

15.9. **C-11** – *[Fe^{II}(OH$_2$)(Py$_5$Me$_2$-CH$_2$-OH)](BF$_4$)$_2$ x 2 H$_2$O*
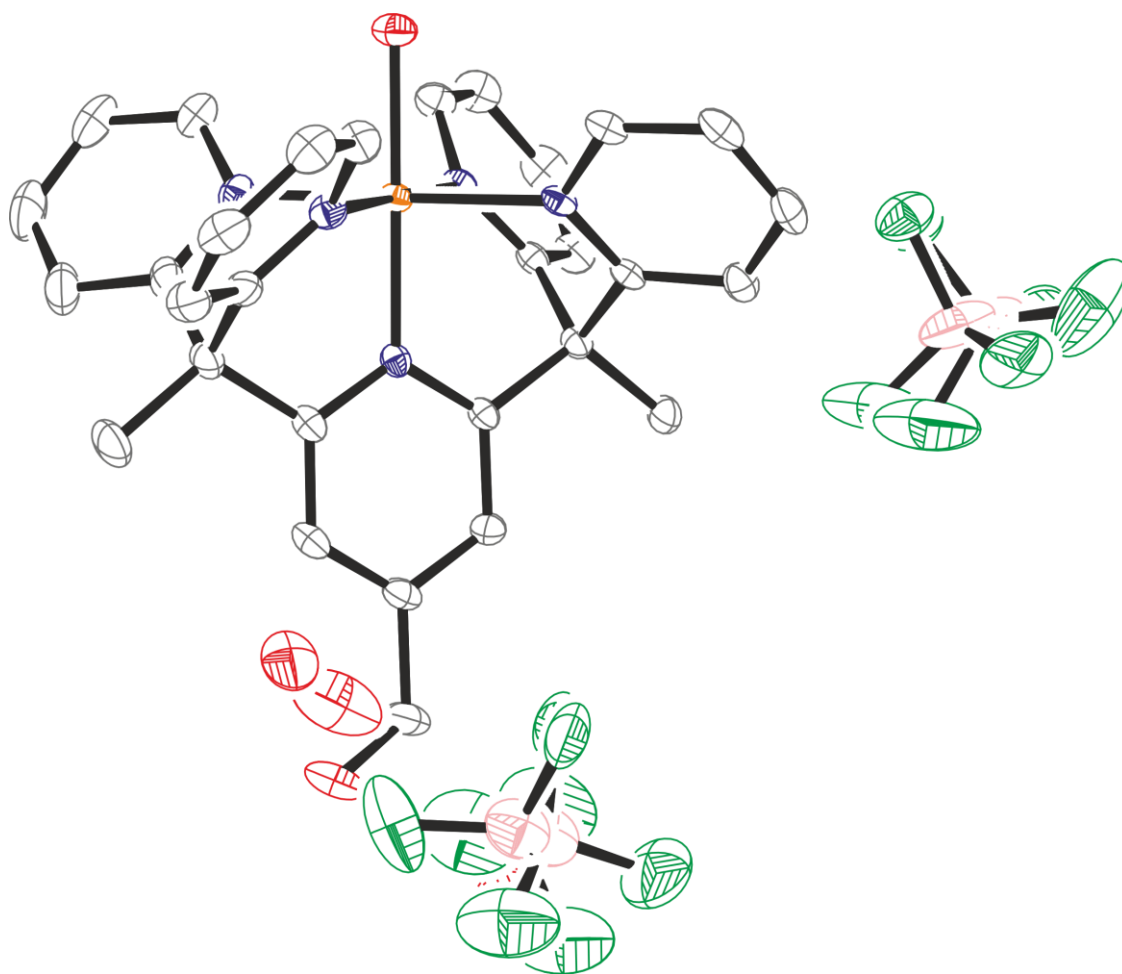
net formula	C$_{30}$H$_{33}$B$_2$F$_8$FeN$_5$O$_4$
M_r/g mol^{-1}	757.08
crystal size/mm	0.080 × 0.070 × 0.020
T/K	103.(2)
radiation	MoKα
diffractometer	'Bruker D8 Venture TXS'
crystal system	monoclinic
space group	'P 1 21/n 1'
a/Å	12.0040(10)
b/Å	15.7007(12)
c/Å	16.7040(15)
α/°	90
β/°	94.593(3)
γ/°	90

$V/Å^3$	3138.1(5)
Z	4
calc. density/g cm^{-3}	1.602
μ/mm^{-1}	0.575
absorption correction	Multi-Scan
transmission factor range	0.93–0.99
refls. measured	56443
R_{int}	0.0514
mean $\sigma(I)/I$	0.0300
θ range	2.869–27.484
observed refls.	5780
x, y (weighting scheme)	0.0581, 7.8317
hydrogen refinement	constr
refls in refinement	7198
parameters	554
restraints	462
$R(F_{obs})$	0.0553
$R_w(F^2)$	0.1470
S	1.052
shift/error$_{max}$	0.001
max electron density/e Å^{-3}	1.415
min electron density/e Å^{-3}	–1.208

H(C) constr, H(hydroxyl-O), constr H(Fe-bound O) located from difference map, than xyz noref, U(H)=1.5U(O) H(free water O) not considered SADI applied for all B-F and F-F distances respectively, SIMU and ISOR applied for some disordered atoms in order to improve the vibration ellipsoids. The highest remaining electron density is quite close to an F atom and could not be assigned properly. In the structure above two disordered BF_4^- moieties are shown.

15.10. **C-12** *– [Fe^{II}(mecn)(Py$_5$Me$_2$-CH$_2$-OBn)](OTf)$_2$ x 0.27 H$_2$O x 0.87 MeCN*
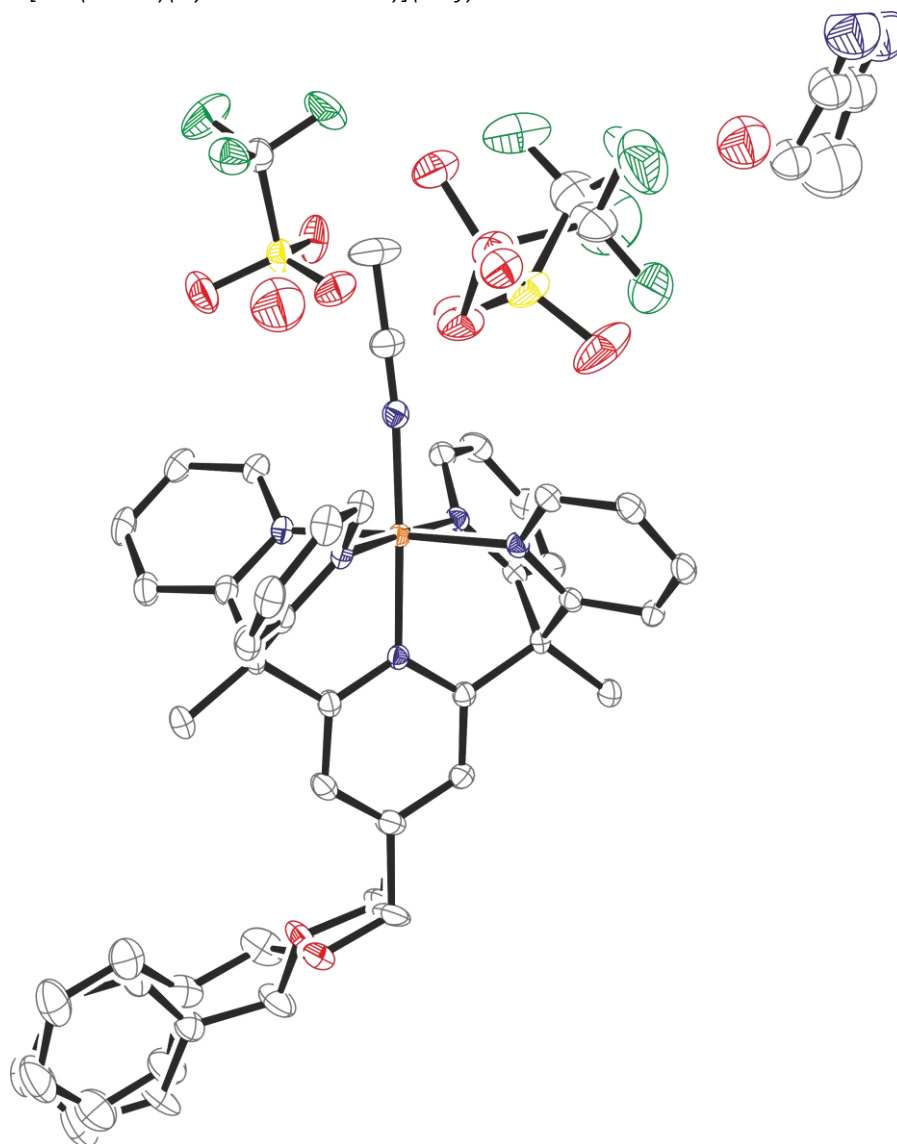
net formula	$C_{42.73}H_{39.13}F_6FeN_{6.87}O_{7.27}S_2$
M_r/g mol^{-1}	999.11
crystal size/mm	0.100 × 0.070 × 0.040
T/K	106.(2)
radiation	MoKα
diffractometer	'Bruker D8 Venture TXS'
crystal system	triclinic
space group	'P -1'
a/Å	12.2739(9)
b/Å	12.9156(9)
c/Å	15.2059(11)
α/°	76.088(2)

$\beta/°$	86.640(2)
$\gamma/°$	69.476(2)
$V/\text{Å}^3$	2190.4(3)
Z	2
calc. density/g cm^{-3}	1.515
μ/mm^{-1}	0.525
absorption correction	Multi-Scan
transmission factor range	0.92–0.98
refls. measured	39511
R_{int}	0.0473
mean $\sigma(I)/I$	0.0449
θ range	2.987–27.878
observed refls.	8326
x, y (weighting scheme)	0.0361, 1.9395
hydrogen refinement	constr
refls in refinement	10386
parameters	739
restraints	151
$R(F_{obs})$	0.0404
$R_w(F^2)$	0.1054
S	1.051
shift/error$_{max}$	0.001
max electron density/e Å^{-3}	0.474
min electron density/e Å^{-3}	−0.431

The several disorders have been described by split models. The refinement of the sof ratio of the two parts of the disordered CH_2-OBn moiety led to 0.56/0.44. The disordered 6-membered ring has been refined as perfect ring (AFIX 66). The SAME instruction has been applied for the geometry of a disordered $CF_3SO_3^-$. The geometry of $CF_3SO_3^-$ with S1 has been used as model. The sof ratio refined to 0.66/0.34. A disordered CH_3CN (modelled with SAME using the moiety with N6 as model) shares the same site with two water O-atoms. Their hydrogen atoms could not be located and have not been considered in the refinement.

In the structure above, the disordered CH_2-O-Bn moiety, a disordered $CF_3SO_3^-$ moiety and a disordered CH_3CN moiety are shown.

15.11. **V-11** *– PY3*
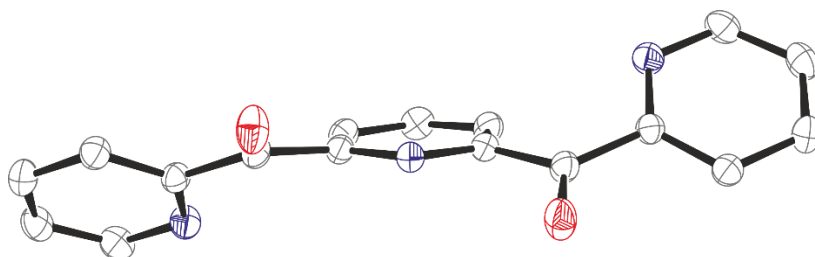
net formula	$C_{17}H_{11}N_3O_2$
M_r/g mol^{-1}	289.29
crystal size/mm	0.080 × 0.060 × 0.050
T/K	173.(2)
radiation	MoKα
diffractometer	'Bruker D8 Venture TXS'
crystal system	monoclinic
space group	'C 1 2/c 1'
a/Å	13.0900(13)
b/Å	9.1109(8)
c/Å	12.1438(10)
α/°	90
β/°	110.662(3)
γ/°	90
V/Å^3	1355.1(2)
Z	4
calc. density/g cm^{-3}	1.418
μ/mm^{-1}	0.096
absorption correction	Multi-Scan
transmission factor range	0.96–0.99
refls. measured	11556
R_{int}	0.0425
mean $\sigma(I)/I$	0.0300
θ range	2.979–27.483
observed refls.	1356
x, y (weighting scheme)	0.0499, 0.7917
hydrogen refinement	constr

Flack parameter	?
refls in refinement	1550
parameters	101
restraints	0
$R(F_{obs})$	0.0377
$R_w(F^2)$	0.1044
S	1.065
shift/error$_{max}$	0.001
max electron density/e Å^{-3}	0.261
min electron density/e Å^{-3}	−0.202

15.12. **C-20** *– [Fe^{II}(mecn)(**L-7**)](OTf)$_2$ x 1.35 MeCN*
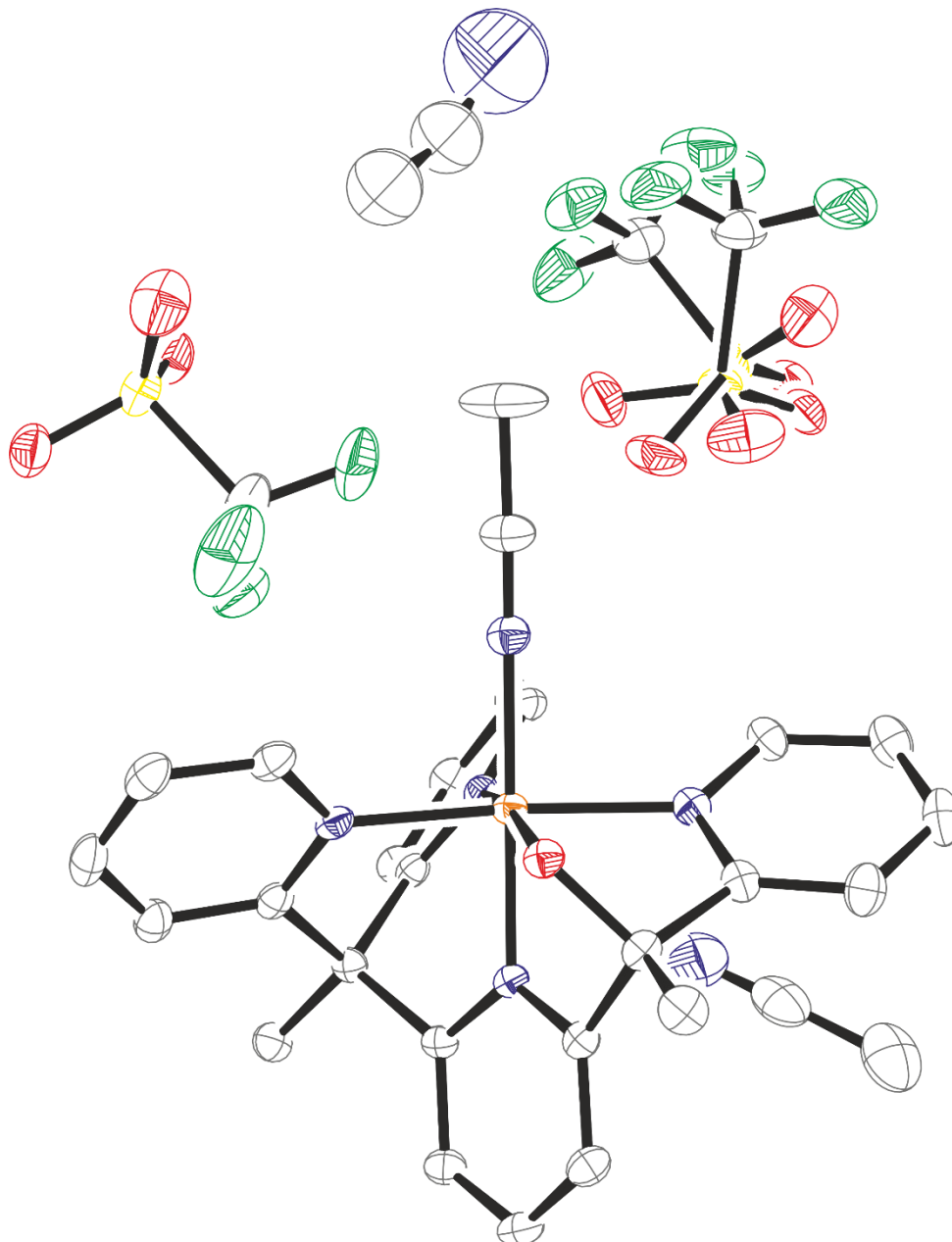
net formula	C$_{30.35}$H$_{27.53}$F$_6$FeN$_{6.18}$O$_7$S$_2$
M_r/g mol^{-1}	824.77
crystal size/mm	0.080 × 0.040 × 0.020
T/K	107.(2)
radiation	MoKα
diffractometer	'Bruker D8 Venture TXS'
crystal system	triclinic
space group	'P -1'
a/Å	8.3563(6)

b/Å	12.8792(9)
c/Å	33.076(2)
α/°	100.124(2)
β/°	90.772(2)
γ/°	100.855(2)
V/Å³	3437.6(4)
Z	4
calc. density/g cm⁻³	1.594
μ/mm⁻¹	0.649
absorption correction	Multi-Scan
transmission factor range	0.96–0.99
refls. measured	102439
R_{int}	0.0452
mean $\sigma(I)/I$	0.0299
θ range	2.485–27.103
observed refls.	12380
x, y (weighting scheme)	0.0458, 9.0402
hydrogen refinement	constr
refls in refinement	15179
parameters	1104
restraints	290
$R(F_{obs})$	0.0506
$R_w(F^2)$	0.1316
S	1.038
shift/error$_{max}$	0.001
max electron density/e Å⁻³	1.700
min electron density/e Å⁻³	–0.984

Two $CF_3SO_3^-$ moieties are disordered, split models have been applied, sof ratios refined to 0.65/0.35 and 0.58/0.42 respectively. The site of one of the two acetonitrile moieties is not fully occupied but is related to one of the disordered $CF_3SO_3^-$ moieties with SOF of 0.35. This acetonitrile has been refined isotropically. The anisotropic vibration ellipsoids of several of the disordered atoms have been improved by use of ISOR, SIMU and DELU.

One of two formula units is depicted above, showing one acetonitrile unit and a disordered $CF_3SO_3^-$ moiety.

15.13. **L-8** – *Py₄PhMe₂H*
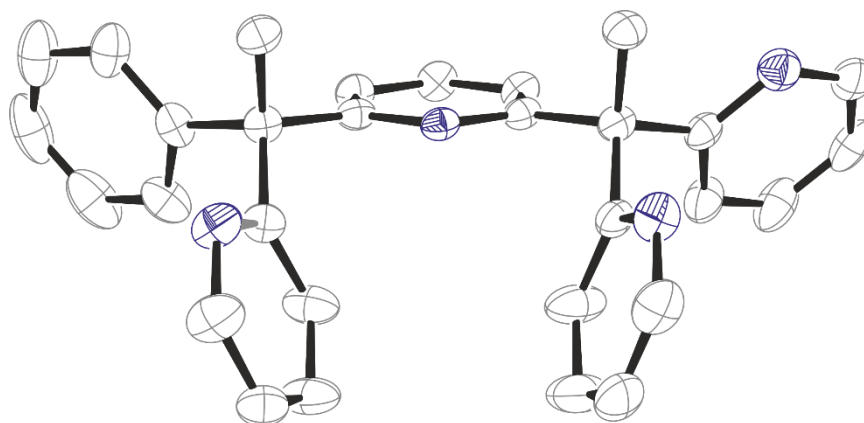
net formula	$C_{30}H_{26}N_4$
Mr/g mol-1	442.55
crystal size/mm	0.100 × 0.090 × 0.070
T/K	104.(2)
radiation	MoKα
diffractometer	'Bruker D8 Venture TXS'
crystal system	monoclinic
space group	'P 1 21/n 1'
a/Å	12.3816(5)
b/Å	14.4243(4)
c/Å	14.0203(4)
α/°	90
β/°	112.5330(10)
γ/°	90
V/Å3	2312.81(13)
Z	4
calc. density/g cm-3	1.271
μ/mm-1	0.076
absorption correction	Multi-Scan
transmission factor range	0.96–0.99
refls. measured	39790
Rint	0.0462
mean σ(I)/I	0.0278
θ range	3.129–27.101

observed refls.	4017
x, y (weighting scheme)	0.0663, 1.7397
hydrogen refinement	constr
refls in refinement	5084
parameters	355
restraints	67
$R(F\text{obs})$	0.0576
$R\text{w}(F2)$	0.1579
S	1.029
shift/errormax	0.001
max electron density/e Å-3	0.443
min electron density/e Å-3	-0.330

The disorder in a ring has been described by a split model. The sof ratio refined to 0.83/0.17. The geometrical SAME restraint has been applied for the minor occupied ring using the main part as structure model. ISOR, SIMU and DELU restraints have been applied to improve the anisotropic vibration ellipsoids and to avoid Hirshfeld errors.

15.14. C-22 – [Fe^{II}(OH$_2$)(L-8)][Fe^{II}(Py$_4$PhMe$_2$H)(F)](BF$_4$)$_3$ x H$_2$O
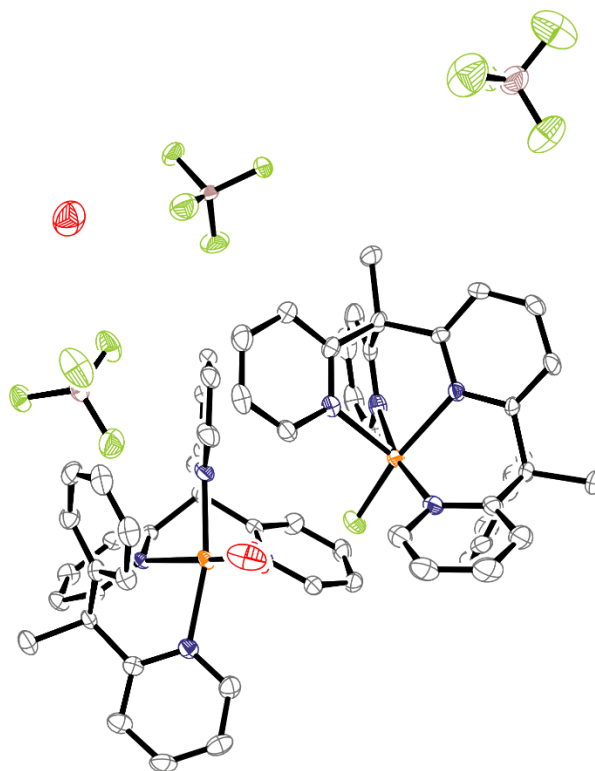
net formula	C$_{60}$H$_{57.04}$B$_3$F$_{13}$Fe$_2$N$_8$O$_{2.52}$
M_r/g mol^{-1}	1321.60
crystal size/mm	0.100 × 0.070 × 0.050
T/K	105.(2)
radiation	MoKα
diffractometer	'Bruker D8 Venture TXS'
crystal system	triclinic
space group	'P -1'
a/Å	12.2386(15)
b/Å	13.7989(17)
c/Å	19.826(3)
α/°	88.252(4)
β/°	72.104(2)
γ/°	65.096(2)
V/Å^3	2870.9(6)
Z	2
calc. density/g cm^{-3}	1.529
μ/mm^{-1}	0.601

absorption correction	Multi-Scan
transmission factor range	0.82–0.97
refls. measured	11369
R_{int}	0.0691
mean $\sigma(I)/I$	0.0551
θ range	2.567–26.369
observed refls.	9526
x, y (weighting scheme)	0.0530, 4.3715
hydrogen refinement	constr
refls in refinement	11369
parameters	853
restraints	30
$R(F_{obs})$	0.0525
$R_w(F^2)$	0.1368
S	1.086
shift/error$_{max}$	0.001
max electron density/e $Å^{-3}$	0.570
min electron density/e $Å^{-3}$	−0.515

The figure above does not show the less-occupied part of a disordered BF_4^-. Refined as a 2-component twin. BASF 0.39. A split model has been applied to describe the disorder of one of the BF_4^- moieties. In order to gain a good geometry for the spilt moieties, the SAME instruction has been used with BF_4^- containing B1 acting as model. A further water molecule has the same sof as the main disordered BF_4^-. The hydrogen atoms bound to water O-atoms could not be located and have not been considered in the refinement.

15.15. III-2
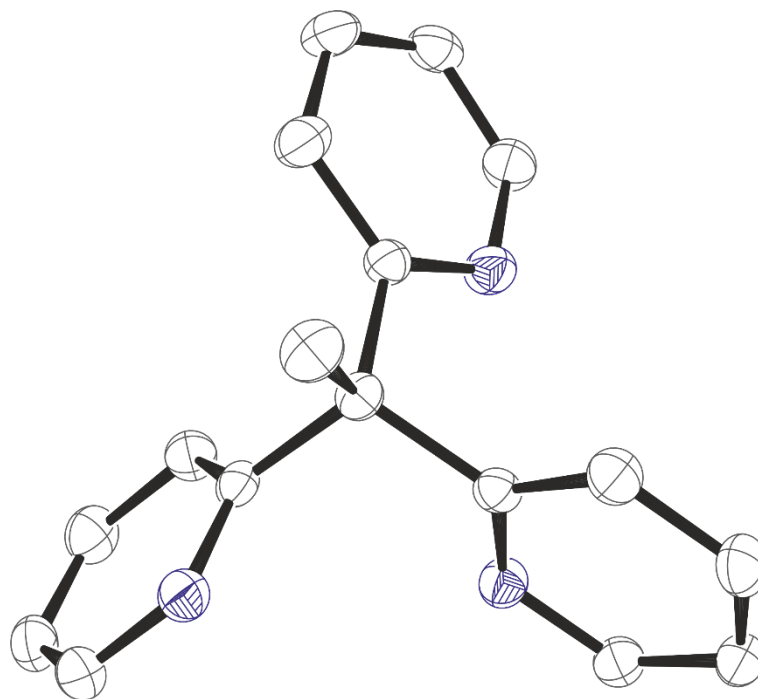
net formula	$C_{17}H_{15}N_3$
M_r/g mol^{-1}	261.32
crystal size/mm	0.130 × 0.080 × 0.050
T/K	173.(2)
radiation	MoKα
diffractometer	'Bruker D8 Venture TXS'
crystal system	monoclinic
space group	'P 1 2₁/c 1'
a/Å	9.2748(10)
b/Å	9.0412(10)
c/Å	15.8220(18)
α/°	90
β/°	95.458(4)
γ/°	90
V/Å³	1320.7(3)
Z	4
calc. density/g cm^{-3}	1.314
μ/mm^{-1}	0.080
absorption correction	Multi-Scan

transmission factor range	0.96–1.00
refls. measured	31831
R_{int}	0.0597
mean $\sigma(I)/I$	0.0341
θ range	2.598–27.481
observed refls.	2507
x, y (weighting scheme)	0.0373, 0.5557
hydrogen refinement	constr
Flack parameter	?
refls in refinement	3017
parameters	182
restraints	0
$R(F_{obs})$	0.0403
$R_w(F^2)$	0.1016
S	1.046
shift/error$_{max}$	0.001
max electron density/e Å^{-3}	0.223
min electron density/e Å^{-3}	−0.194

XI. Bibliography

[1]   H. M. Hanauske-Abel, V. Günzler, *Journal of Theoretical Biology* **1982**, *94*, 421–455.

[2]   J. C. Price, E. W. Barr, B. Tirupati, Bollinger J. Martin, C. Krebs, *Biochemistry* **2003**, *42*, 7497–7508.

[3]   J. C. Price, E. W. Barr, T. E. Glass, C. Krebs, J. M. Bollinger, *J. Am. Chem. Soc.* **2003**, *125*, 13008–13009.

[4]   D. A. Proshlyakov, T. F. Henshaw, G. R. Monterosso, M. J. Ryle, R. P. Hausinger, *J. Am. Chem. Soc.* **2004**, *126*, 1022–1023.

[5]   J. C. Price, E. W. Barr, L. M. Hoffart, C. Krebs, J. M. Bollinger, *Biochemistry* **2005**, *44*, 8138–8147.

[6]   C. Krebs, J. C. Price, J. Baldwin, L. Saleh, M. T. Green, J. M. Bollinger, *Inorg. Chem.* **2005**, *44*, 742–757.

[7]   M. Tahiliani, K. P. Koh, Y. Shen, W. A. Pastor, H. Bandukwala, Y. Brudno, S. Agarwal, L. M. Iyer, D. R. Liu, L. Aravind, A. Rao, *Science* **2009**, *324*, 930–935.

[8]   L. Hu, J. Lu, J. Cheng, Q. Rao, Z. Li, H. Hou, Z. Lou, L. Zhang, W. Li, W. Gong, M. Liu, C. Sun, X. Yin, J. Li, X. Tan, P. Wang, Y. Wang, D. Fang, Q. Cui, P. Yang, C. He, H. Jiang, C. Luo, Y. Xu, *Nature* **2015**, *527*, 118–122.

[9]   R. A. Husain, M. Grimmel, M. Wagner, J. C. Hennings, C. Marx, R. G. Feichtinger, A. Saadi, K. Rostásy, F. Radelfahr, A. Bevot, M. Döbler-Neumann, H. Hartmann, L. Colleaux, I. Cordts, X. Kobeleva, H. Darvish, S. Bakhtiari, M. C. Kruer, A. Besse, A. C.-H. Ng, D. Chiang, F. Bolduc, A. Tafakhori, S. Mane, S. G. Firouzabadi, A. K. Huebner, R. Buchert, S. Beck-Woedl, A. J. Müller, L. Laugwitz, T. Nägele, Z.-Q. Wang, T. M. Strom, M. Sturm, T. Meitinger, T. Klockgether, O. Riess, T. Klopstock, U. Brandl, C. A. Hübner, M. Deschauer, J. A. Mayr, P. E. Bonnen, I. Krägeloh-Mann, S. B. Wortmann, T. B. Haack, *Am. J. Hum. Genet.* **2020**, *107*, 364–373.

[10]   S. G. Ghosh, S. Lee, R. Fabunan, G. Chai, M. S. Zaki, G. Abdel-Salam, T. Sultan, T. Ben-Omran, J. R. Alvi, J. McEvoy-Venneri, V. Stanley, A. Patel, D. Ross, J. Ding, M. Jain, D. Pan, P. Lübbert, B. Kammerer, N. Wiedemann, N. M. Verhoeven-Duif, J. J. Jans, D. Murphy, M. B. Toosi, F. Ashrafzadeh, S. Imannezhad, E. G. Karimiani, K. Ibrahim, E. R. Waters, R. Maroofian, J. G. Gleeson, *Genet. Med.* **2021**, *23*, 524–533.

[11]   M. Wiessner, R. Maroofian, M.-Y. Ni, A. Pedroni, J. S. Müller, R. Stucka, C. Beetz, S. Efthymiou, F. M. Santorelli, A. A. Alfares, C. Zhu, A. Uhrova Meszarosova, E. Alehabib, S. Bakhtiari, A. R. Janecke, M. G. Otero, J. Y. H. Chen, J. T. Peterson, T. M. Strom, P. De Jonghe, T. Deconinck, W. De Ridder, J. De Winter, R. Pasquariello, I. Ricca, M. Alfadhel, B. P. van de Warrenburg, R. Portier, C. Bergmann, S. Ghasemi Firouzabadi, S. C. Jin, K. Bilguvar, S. Hamed, M. Abdelhameed, N. A. Haridy, S. Maqbool, F. Rahman, N. Anwar, J. Carmichael, A. Pagnamenta, N. W. Wood, F. Tran Mau-Them, T. Haack, P. network Genomics England Research Consortium, M. Di Rocco, I. Ceccherini, M. Iacomino, F. Zara, V. Salpietro, M. Scala, M. Rusmini, Y. Xu, Y. Wang, Y. Suzuki, K. Koh, H. Nan, H. Ishiura, S. Tsuji, L. Lambert, E. Schmitt, E. Lacaze, H. Küpper, D. Dredge, C. Skraban, A. Goldstein, M. J. H. Willis, K. Grand, J. M. Graham Jr, R. A. Lewis, F. Millan, Ö. Duman, N. Dündar, G. Uyanik, L. Schöls, P. Nürnberg, G. Nürnberg, A. Catala Bordes, P. Seeman, M. Kuchar, H. Darvish, A. Rebelo, F. Bouçanova, J.-J. Medard, R. Chrast, M. Auer-Grumbach, F. S. Alkuraya, H. Shamseldin, S. Al Tala, J. Rezazadeh Varaghchi, M. Najafi, S. Deschner, D. Gläser, W. Hüttel, M. C. Kruer, E.-J. Kamsteeg, Y. Takiyama, S. Züchner, J. Baets, M. Synofzik, R. Schüle, R. Horvath, H. Houlden, L. Bartesaghi, H.-J. Lee, K. Ampatzis, T. M. Pierson, J. Senderek, *Brain* **2021**, *144*, 1422–1434.

[12]   T. Chantarojsiri, Y. Sun, J. R. Long, C. J. Chang, *Inorg. Chem.* **2015**, *54*, 5879–5887.

[13]   N. S. W. Jonasson, L. Daumann, *Chem. Eur. J.* **2019**, *25*, 12091–12097.

[14]   D. Schmidl, N. S. W. Jonasson, E. Korytiaková, T. Carell, L. J. Daumann, *Angew. Chem. Int. Ed.* **2021**, *60*, 21457–21463.

[15]   N. S. W. Jonasson, R. Janßen, A. Menke, F. L. Zott, H. Zipse, L. Daumann, *ChemBioChem* **2021**, *n/a*, DOI 10.1002/cbic.202100420.

[16]   F. L. Hünefeld, *Der Chemismus in der thierischen Organisation: Physiologisch-chemische Untersuchungen der materiellen Veränderungen, oder des Bildungslebens im thierischen Organismus; insbesondere des Blutbildungsprocesses, der Natur der Blut körperchen und ihrer Kernchen. Ein Beitrag zur Physiologie und Heilmittellehre*, Brockhaus, **1840**.

[17]   M. Sono, M. P. Roach, E. D. Coulter, J. H. Dawson, *Chem. Rev.* **1996**, *96*, 2841–2888.

[18]   W. Buckel, R. K. Thauer, *Front. Microbiol.* **2018**, *9*, DOI 10.3389/fmicb.2018.00401.

[19]   Y. Sheng, I. A. Abreu, D. E. Cabelli, M. J. Maroney, A.-F. Miller, M. Teixeira, J. S. Valentine, *Chem. Rev.* **2014**, *114*, 3854–3918.

[20]   B. S. Perrin, T. Ichiye, *J. Biol. Inorg. Chem.* **2013**, *18*, 599–608.

[21]   J. T. Groves, *F1000Res* **2015**, *4*, 178.

[22]   E. L. Hegg, L. Que, *Eur. J. Biochem.* **1997**, *250*, 625–629.

[23]   I. J. Clifton, M. A. McDonough, D. Ehrismann, N. J. Kershaw, N. Granatino, C. J. Schofield, *J. Inorg. Biochem.* **2006**, *100*, 644–669.

[24]   A. R. Diebold, M. L. Neidig, G. R. Moran, G. D. Straganz, E. I. Solomon, *Biochemistry* **2010**, *49*, 6945–6952.

[25]   D. D. Shah, J. A. Conrad, B. Heinz, J. M. Brownlee, G. R. Moran, *Biochemistry* **2011**, *50*, 7694–7704.

[26]   D. D. Shah, J. A. Conrad, G. R. Moran, *Biochemistry* **2013**, *52*, 6097–6107.

[27]   *2-Oxoglutarate-Dependent Oxygenases*, **2015**.

[28]   A. K. White, W. W. Metcalf, *J. Biol. Chem.* **2002**, *277*, 38262–38271.

[29]   F. H. Vaillancourt, J. Yin, C. T. Walsh, *Proc. Natl. Acad. Sci. USA* **2005**, *102*, 10111–10116.

[30]   L. C. Blasiak, F. H. Vaillancourt, C. T. Walsh, C. L. Drennan, *Nature* **2006**, *440*, 368–371.

[31]   S. D. Wong, M. Srnec, M. L. Matthews, L. V. Liu, Y. Kwak, K. Park, C. B. Bell III, E. E. Alp, J. Zhao, Y. Yoda, S. Kitao, M. Seto, C. Krebs, J. M. Bollinger, E. I. Solomon, *Nature* **2013**, *499*, 320–323.

[32]   C. W. John, G. M. Swain, R. P. Hausinger, D. A. Proshlyakov, *J. Phys. Chem. B* **2019**, *123*, 7785–7793.

[33]   E. I. Solomon, T. C. Brunold, M. I. Davis, J. N. Kemsley, S.-K. Lee, N. Lehnert, F. Neese, A. J. Skulan, Y.-S. Yang, J. Zhou, *Chem. Rev.* **2000**, *100*, 235–350.

[34]   M. J. Ryle, R. Padmakumar, R. P. Hausinger, *Biochemistry* **1999**, *38*, 15278–15286.

[35]   J. Li, H.-J. Liao, Y. Tang, J.-L. Huang, L. Cha, T.-S. Lin, J. L. Lee, I. V. Kurnikov, M. G. Kurnikova, W. Chang, N.-L. Chan, Y. Guo, *J. Am. Chem. Soc.* **2020**, *142*, 6268–6284.

[36]   D. Henschler, W. R. Hoos, H. Fetz, E. Dallmeier, M. Metzler, *Biochem. Pharmacol.* **1979**, *28*, 543–548.

[37]   R. E. Miller, F. P. Guengerich, *Biochemistry* **1982**, *21*, 1090–1097.

[38]   S. P. de Visser, F. Ogliaro, S. Shaik, *Angew. Chem. Int. Ed.* **2001**, *40*, 2871–2874.

[39]   S. P. de Visser, D. Kumar, S. Shaik, *J. Inorg. Biochem.* **2004**, *98*, 1183–1193.

[40]   R. Shinkyo, L. Xu, K. A. Tallman, Q. Cheng, N. A. Porter, F. P. Guengerich, *J. Biol. Chem.* **2011**, *286*, 33021–33028.

[41]   W. Chang, M. Dey, P. Liu, S. O. Mansoorabadi, S.-J. Moon, Z. K. Zhao, C. L. Drennan, H. Liu, *Nature* **2013**, *496*, 114–118.

[42]   C. V. Sastri, M. S. Seo, M. J. Park, K. M. Kim, W. Nam, *Chem. Commun.* **2005**, 1405–1407.

[43]   K. K. Singh, M. k. Tiwari, B. B. Dhar, K. Vanka, S. Sen Gupta, *Inorg. Chem.* **2015**, *54*, 6112–6121.

[44]   J. Serrano-Plana, A. Aguinaco, R. Belda, E. García-España, M. G. Basallote, A. Company, M. Costas, *Angew. Chem. Int. Ed.* **2016**, *55*, 6310–6314.

[45]   H. M. Neu, T. Yang, R. A. Baglia, T. H. Yosca, M. T. Green, M. G. Quesne, S. P. de Visser, D. P. Goldberg, *J. Am. Chem. Soc.* **2014**, *136*, 13845–13852.

[46]   R. Zhang, N. Nagraj, D. S. P. Lansakara-P., L. P. Hager, M. Newcomb, *Org. Lett.* **2006**, *8*, 2731–2734.

[47]   J. Lu, L. Hu, J. Cheng, C. Wang, Y. Xu, C. Luo, *C. J. C. B.* **2016**, *38*, 1–6.

[48]   J. P. T. Zaragoza, T. H. Yosca, M. A. Siegler, P. Moënne-Loccoz, M. T. Green, D. P. Goldberg, *J. Am. Chem. Soc.* **2017**, *139*, 13640–13643.

[49]   M. J. Drummond, C. L. Ford, D. L. Gray, C. V. Popescu, A. R. Fout, *J. Am. Chem. Soc.* **2019**, *141*, 6639–6650.

[50]   M. T. Green, J. H. Dawson, H. B. Gray, *Science* **2004**, *304*, 1653–1656.

[51]   T. H. Yosca, J. Rittle, C. M. Krest, E. L. Onderko, A. Silakov, J. C. Calixto, R. K. Behan, M. T. Green, *Science* **2013**, *342*, 825–829.

[52]   T. H. Yosca, M. C. Langston, C. M. Krest, E. L. Onderko, T. L. Grove, J. Livada, M. T. Green, *J. Am. Chem. Soc.* **2016**, *138*, 16016–16023.

[53]   H. Kwon, J. Basran, C. M. Casadei, A. J. Fielding, T. E. Schrader, A. Ostermann, J. M. Devos, P. Aller, M. P. Blakeley, P. C. E. Moody, E. L. Raven, *Nat. Comm.* **2016**, *7*, ncomms13445.

[54]   K.-B. Cho, X. Wu, Y.-M. Lee, Y. H. Kwon, S. Shaik, W. Nam, *J. Am. Chem. Soc.* **2012**, *134*, 20222–20225.

[55]   S. Rana, A. Dey, D. Maiti, *Chem. Commun.* **2015**, *51*, 14469–14472.

[56]   Y. Fu, G. Jia, X. Pang, R. N. Wang, X. Wang, C. J. Li, S. Smemo, Q. Dai, K. A. Bailey, M. A. Nobrega, K.-L. Han, Q. Cui, C. He, *Nat. Commun.* **2013**, *4*, 1798.

[57]   J. Wu, H. Xiao, T. Wang, T. Hong, B. Fu, D. Bai, Z. He, S. Peng, X. Xing, J. Hu, P. Guo, X. Zhou, *Chem. Sci.* **2015**, *6*, 3013–3017.

[58]   J. Xiong, T.-T. Ye, C.-J. Ma, Q.-Y. Cheng, B.-F. Yuan, Y.-Q. Feng, *Nucleic Acids Res* **2019**, *47*, 1268–1277.

[59]   Y. Du, H. Chu, M. Wang, I. K. Chu, C. Lo, *J. Exp. Bot.* **2010**, *61*, 983–994.

[60]   J. Wu, X.-C. Wang, Y. Liu, H. Du, Q.-Y. Shu, S. Su, L.-J. Wang, S.-S. Li, L.-S. Wang, *Sci. Rep.* **2016**, *6*, 19245.

[61]   F. H. Vaillancourt, E. Yeh, D. A. Vosburg, S. E. O'Connor, C. T. Walsh, *Nature* **2005**, *436*, 1191–1194.

[62]   F. H. Vaillancourt, E. Yeh, D. A. Vosburg, S. Garneau-Tsodikova, C. T. Walsh, *Chem. Rev.* **2006**, *106*, 3364–3378.

[63]   P. Comba, S. Wunderlich, *Chem. Eur. J.* **2010**, *16*, 7293–7299.

[64]   Z. Gordon, T. J. Miller, C. A. Leahy, E. M. Matson, M. Burgess, M. J. Drummond, C. V. Popescu, C. M. Smith, R. L. Lord, J. Rodríguez-López, A. R. Fout, *Inorg. Chem.* **2019**, *58*, 15801–15811.

[65]   P. K. Grzyska, E. H. Appelman, R. P. Hausinger, D. A. Proshlyakov, *Proc. Natl. Acad. Sci. USA* **2010**, *107*, 3982–3987.

[66]   C. S. Foote, J. Valentine, A. Greenberg, J. F. Liebman, Eds., *Active Oxygen in Chemistry*, Springer Netherlands, **1995**.

[67]   K. Matsui, *Curr. Opin. Plant Biol.* **2006**, *9*, 274–280.

[68]   C. R. Goldsmith, T. D. P. Stack, *Inorg. Chem.* **2006**, *45*, 6048–6055.

[69]   S. Ogo, S. Wada, Y. Watanabe, M. Iwase, A. Wada, M. Harata, K. Jitsukawa, H. Masuda, H. Einaga, *Angew. Chem. Int. Ed.* **1998**, *37*, 2102–2104.

[70]   R. Gupta, A. S. Borovik, *J. Am. Chem. Soc.* **2003**, *125*, 13234–13242.

[71]   J. Mukherjee, R. L. Lucas, M. K. Zart, D. R. Powell, V. W. Day, A. S. Borovik, *Inorg. Chem.* **2008**, *47*, 5780–5786.

[72]   W.-M. Ching, A. Zhou, J. E. M. N. Klein, R. Fan, G. Knizia, C. J. Cramer, Y. Guo, L. Que, *Inorg. Chem.* **2017**, *56*, 11129–11140.

[73]   J. M. Mayer, *Acc. Chem. Res.* **1998**, *31*, 441–450.

[74]   J. Xiang, H. Li, J.-S. Wu, *Z. Anorg. Allg. Chem.* **2014**, *640*, 1670–1674.

[75]   J.-U. Rohde, J.-H. In, M. H. Lim, W. W. Brennessel, M. R. Bukowski, A. Stubna, E. Münck, W. Nam, L. Que, *Science* **2003**, *299*, 1037–1039.

[76]   P. Comba, Y. D. Lampeka, A. I. Prikhod'ko, G. Rajaraman, *Inorg. Chem.* **2006**, *45*, 3632–3638.

[77]   J. England, M. Martinho, E. R. Farquhar, J. R. Frisch, E. L. Bominaar, E. Münck, L. Que, *Angew. Chem. Int. Ed.* **2009**, *48*, 3622–3626.

[78]   Y.-M. Lee, S. N. Dhuri, S. C. Sawant, J. Cho, M. Kubo, T. Ogura, S. Fukuzumi, W. Nam, *Angew. Chem. Int. Ed.* **2009**, *48*, 1803–1806.

[79]   A. N. Biswas, M. Puri, K. K. Meier, W. N. Oloo, G. T. Rohde, E. L. Bominaar, E. Münck, L. Que, *J. Am. Chem. Soc.* **2015**, *137*, 2428–2431.

[80]   C. Cordes (née Kupper), M. Morganti, I. Klawitter, C. Schremmer, S. Dechert, F. Meyer, *Angew. Chem. Int. Ed.* **2019**, *131*, 10971–10974.

[81]   D. Kass, T. Corona, K. Warm, B. Braun-Cula, U. Kuhlmann, E. Bill, S. Mebs, M. Swart, H. Dau, M. Haumann, P. Hildebrandt, K. Ray, *J. Am. Chem. Soc.* **2020**, DOI 10.1021/jacs.9b13756.

[82]   X. Engelmann, D. D. Malik, T. Corona, K. Warm, E. R. Farquhar, M. Swart, W. Nam, K. Ray, *Angew. Chem. Int. Ed.* **2019**, *58*, 4012–4016.

[83]   A. J. Jasniewski, L. Que, *Chem. Rev.* **2018**, *118*, 2554–2592.

[84]   F. Thomas, *Nachr. Chem.* **2020**, *68*, 72–75.

[85]   M. C. White, J. Zhao, *J. Am. Chem. Soc.* **2018**, *140*, 13988–14009.

[86]   K. Feng, R. E. Quevedo, J. T. Kohrt, M. S. Oderinde, U. Reilly, M. C. White, *Nature* **2020**, *580*, 621–627.

[87]   R. G. Bergman, *Nature* **2007**, *446*, 391–393.

[88]   K. Godula, D. Sames, *Science* **2006**, *312*, 67–72.

[89]   C. O. Pabo, R. T. Sauer, *Annu. Rev. Biochem.* **1984**, *53*, 293–321.

[90]   V. B. Teif, D. A. Beshnova, Y. Vainshtein, C. Marth, J.-P. Mallm, T. Höfer, K. Rippe, *Genome Res.* **2014**, *24*, 1285–1295.

[91]   C. Dupont, D. R. Armant, C. A. Brenner, *Semin. Reprod. Med.* **2009**, *27*, 351–357.

[92]   H. Wu, Y. E. Sun, *Pediatr Res* **2006**, *59*, 21–25.

[93]   A. Chittka, L. Chittka, *PLOS Biology* **2010**, *8*, e1000532.

[94]   R. Kucharski, J. Maleszka, S. Foret, R. Maleszka, *Science* **2008**, *319*, 1827–1830.

[95]   E. Jae Yoo, Y. Kyu Jang, M. Ae Lee, P. Bjerling, J. Bum Kim, K. Ekwall, R. Hyun Seong, S. Dai Park, *Biochem. Biophys. Res. Commun.* **2002**, *295*, 970–974.

[96]   L. Mohrmann, C. P. Verrijzer, *Biochim. Biophys. Acta* **2005**, *1681*, 59–73.

[97]   J. Walfridsson, O. Khorosjutina, P. Matikainen, C. M. Gustafsson, K. Ekwall, *EMBO J.* **2007**, *26*, 2868–2879.

[98]   D. Y. Lee, J. J. Hayes, D. Pruss, A. P. Wolffe, *Cell* **1993**, *72*, 73–84.

[99]   B. D. Strahl, C. D. Allis, *Nature* **2000**, *403*, 41–45.

[100]   T. Jenuwein, C. D. Allis, *Science* **2001**, *293*, 1074–1080.

[101]   Y. Shiio, R. N. Eisenman, *Proc. Natl. Acad. Sci. U.S.A.* **2003**, *100*, 13225–13230.

[102]   A. Kuzmichev, T. Jenuwein, P. Tempst, D. Reinberg, *Mol. Cell* **2004**, *14*, 183–193.

[103]   S. B. Rothbart, B. D. Strahl, *Biochim. Biophys. Acta* **2014**, *1839*, 627–643.

[104]   V. B. Teif, K. Rippe, *Nucleic Acids Research* **2009**, *37*, 5641–5655.

[105]   S. Ciafrè, G. Ferraguti, A. Greco, A. Polimeni, M. Ralli, F. M. Ceci, M. Ceccanti, M. Fiore, *Neurosci. & Biobehav. Rev.* **2020**, *118*, 654–668.

[106]   D. B. Dunn, J. D. Smith, *Nature* **1955**, *175*, 336–337.

[107]   *Biochimica et Biophysica Acta (BBA) - Nucleic Acids and Protein Synthesis* **1976**, *435*, 206–210.

[108]   A. Janulaitis, S. Klimašauskas, M. Petrušyte, V. Butkus, *FEBS Letters* **1983**, *161*, 131–134.

[109]   K. C. Cheng, D. S. Cahill, H. Kasai, S. Nishimura, L. A. Loeb, *J. Biol. Chem.* **1992**, *267*, 166–172.

[110]   S. Kanvah, J. Joseph, G. B. Schuster, R. N. Barnett, C. L. Cleveland, U. Landman, *Acc. Chem. Res.* **2010**, *43*, 280–287.

[111]   A. B. Guliaev, B. Singer, in *Encyclopedia of Biological Chemistry* (Eds.: W.J. Lennarz, M.D. Lane), Elsevier, New York, **2004**, pp. 609–613.

[112]   K. L. Rioux, S. Delaney, *Chem. Res. Toxicol.* **2020**, *33*, 2688–2698.

[113]   J. Tost, *Mol Biotechnol* **2010**, *44*, 71–81.

[114]   *Journal of Molecular Biology* **1968**, *34*, 373–375.

[115]   A. M. Deaton, A. Bird, *Genes Dev.* **2011**, *25*, 1010–1022.

[116]   A. P. Bird, *Nature* **1986**, *321*, 209–213.

[117]   International Human Genome Sequencing Consortium, *Nature* **2001**, *409*, 860–921.

[118]   S. Saxonov, P. Berg, D. L. Brutlag, *PNAS* **2006**, *103*, 1412–1417.

[119]   R. S. Illingworth, U. Gruenewald-Schneider, S. Webb, A. R. W. Kerr, K. D. James, D. J. Turner, C. Smith, D. J. Harrison, R. Andrews, A. P. Bird, *PLOS Genetics* **2010**, *6*, e1001134.

[120]   T. Carell, M. Q. Kurz, M. Müller, M. Rossa, F. Spada, *Angew. Chem. Int. Ed.* **2017**, *57*, 4296–4312.

[121]   B. Panning, R. Jaenisch, *Cell* **1998**, *93*, 305–308.

[122]   F. Chédin, M. R. Lieber, C.-L. Hsieh, *PNAS* **2002**, *99*, 16916–16921.

[123] B. Jin, Y. Li, K. D. Robertson, *Genes Cancer* **2011**, *2*, 607–617.

[124] J. Song, M. Teplova, S. Ishibe-Murakami, D. J. Patel, *Science* **2012**, *335*, 709–712.

[125] K. E. Szulwach, P. Jin, *BioEssays* **2014**, *36*, 107–117.

[126] http://www.beatricebiologist.com/2016/06/gene-silencing/, *Beatrice the Biologist* **2016**.

[127] M. Okano, S. Xie, E. Li, *Nat Genet* **1998**, *19*, 219–220.

[128] S. Xie, Z. Wang, M. Okano, M. Nogami, Y. Li, W.-W. He, K. Okumura, E. Li, *Gene* **1999**, *236*, 87–95.

[129] R. Stein, Y. Gruenbaum, Y. Pollack, A. Razin, H. Cedar, *PNAS* **1982**, *79*, 61–65.

[130] S. Ishiyama, A. Nishiyama, Y. Saeki, K. Moritsugu, D. Morimoto, L. Yamaguchi, N. Arai, R. Matsumura, T. Kawakami, Y. Mishima, H. Hojo, S. Shimamura, F. Ishikawa, S. Tajima, K. Tanaka, M. Ariyoshi, M. Shirakawa, M. Ikeguchi, A. Kidera, I. Suetake, K. Arita, M. Nakanishi, *Molecular Cell* **2017**, *68*, 350-360.e7.

[131] E. Li, T. H. Bestor, R. Jaenisch, *Cell* **1992**, *69*, 915–926.

[132] R. M. Kohli, Y. Zhang, *Nature* **2013**, *502*, 472–479.

[133] K. Iwan, R. Rahimoff, A. Kirchner, F. Spada, A. S. Schröder, O. Kosmatchev, S. Ferizaj, J. Steinbacher, E. Parsa, M. Müller, T. Carell, *Nat. Chem. Biol.* **2018**, *14*, 72–78.

[134] A. Hofer, Z. J. Liu, S. Balasubramanian, *J. Am. Chem. Soc.* **2019**, *141*, 6420–6429.

[135] S. Ito, A. C. D'Alessio, O. V. Taranova, K. Hong, L. C. Sowers, Y. Zhang, *Nature* **2010**, *466*, 1129–1133.

[136] S. Ito, L. Shen, Q. Dai, S. C. Wu, L. B. Collins, J. A. Swenberg, C. He, Y. Zhang, *Science* **2011**, *333*, 1300–1303.

[137] Y. Feng, N.-B. Xie, W.-B. Tao, J.-H. Ding, X.-J. You, C.-J. Ma, X. Zhang, C. Yi, X. Zhou, B.-F. Yuan, Y.-Q. Feng, *CCS Chem.* **2020**, 994–1008.

[138] A. Schön, E. Kaminska, F. Schelter, E. Ponkkonen, E. Korytiaková, S. Schiffers, T. Carell, *Angew. Chem. Int. Ed.* **2020**, *59*, 5591–5594.

[139] Y.-F. He, B.-Z. Li, Z. Li, P. Liu, Y. Wang, Q. Tang, J. Ding, Y. Jia, Z. Chen, L. Li, Y. Sun, X. Li, Q. Dai, C.-X. Song, K. Zhang, C. He, G.-L. Xu, *Science* **2011**, *333*, 1303–1307.

[140] A. Maiti, A. C. Drohat, *J. Biol. Chem.* **2011**, *286*, 35334–35338.

[141] S. Cortellino, J. Xu, M. Sannai, R. Moore, E. Caretti, A. Cigliano, M. Le Coz, K. Devarajan, A. Wessels, D. Soprano, L. K. Abramowitz, M. S. Bartolomei, F. Rambow, M. R. Bassi, T. Bruno, M. Fanciulli, C. Renner, A. J. Klein-Szanto, Y. Matsumoto, D. Kobi, I. Davidson, C. Alberti, L. Larue, A. Bellacosa, *Cell* **2011**, *146*, 67–79.

[142] L. Zhang, W. Chen, L. M. Iyer, J. Hu, G. Wang, Y. Fu, M. Yu, Q. Dai, L. Aravind, C. He, *J. Am. Chem. Soc.* **2014**, *136*, 4801–4804.

[143] W. M. Rideout, G. A. Coetzee, A. F. Olumi, C. H. Spruck, P. A. Jones, *Princess Takamatsu Symposia* **1991**, *22*, 207–219.

[144] S.-G. Jin, Z.-M. Zhang, T. L. Dunwell, M. R. Harter, X. Wu, J. Johnson, Z. Li, J. Liu, P. E. Szabó, Q. Lu, G. Xu, J. Song, G. P. Pfeifer, *Cell Rep.* **2016**, *14*, 493–505.

[145] P. Melamed, Y. Yosefzon, C. David, A. Tsukerman, L. Pnueli, *Front. Cell Dev. Biol.* **2018**, *6*, DOI 10.3389/fcell.2018.00022.

[146] H. Lou, H. Li, K. J. Ho, L. L. Cai, A. S. Huang, T. R. Shank, M. R. Verneris, M. L. Nickerson, M. Dean, S. K. Anderson, *Front. Cell Dev. Biol.* **2019**, *7*, DOI 10.3389/fcell.2019.00099.

[147] W. Aik, M. A. McDonough, A. Thalhammer, R. Chowdhury, C. J. Schofield, *Curr. Opin. Struct. Biol.* **2012**, *22*, 691–700.

[148] J. Song, O. Rechkoblit, T. H. Bestor, D. J. Patel, *Science* **2011**, *331*, 1036–1040.

[149] L. M. Iyer, M. Tahiliani, A. Rao, L. Aravind, *Cell Cycle* **2009**, *8*, 1698–1710.

[150] M. Ko, J. An, H. S. Bandukwala, L. Chavez, T. Äijö, W. A. Pastor, M. F. Segal, H. Li, K. P. Koh, H. Lähdesmäki, P. G. Hogan, L. Aravind, A. Rao, *Nature* **2013**, *497*, 122–126.

[151] F. R. Traube, D. Özdemir, H. Sahin, C. Scheel, A. F. Glück, A. S. Geserich, S. Oganesian, S. Kostidis, K. Iwan, R. Rahimoff, G. Giorgio, M. Müller, F. Spada, M. Biel, J. Cox, M. Giera, S. Michalakis, T. Carell, *Nat. Commun.* **2021**, *12*, 4100.

[152] X. Lu, B. S. Zhao, C. He, *Chem. Rev.* **2015**, *115*, 2225–2239.

[153] L. Hu, Z. Li, J. Cheng, Q. Rao, W. Gong, M. Liu, Y. G. Shi, J. Zhu, P. Wang, Y. Xu, *Cell* **2013**, *155*, 1545–1555.

[154] W. G. Ruppel, **1899**, *26*, 218–232.

[155] T. B. Johnson, R. D. Coghill, *J. Am. Chem. Soc.* **1925**, *47*, 2838–2844.

[156] E. Vischer, S. Zamenhof, E. Chargaff, *J. Biol. Chem.* **1949**, *177*, 429–438.

[157] R. D. Hotchkiss, *J. Biol. Chem.* **1948**, *175*, 315–332.

[158] G. R. Wyatt, *Nature* **1950**, *166*, 237.

[159] G. R. Wyatt, S. S. Cohen, *Biochem. J.* **1953**, *55*, 774–782.

[160] M. G. Goll, T. H. Bestor, *Annu. Rev. Biochem.* **2005**, *74*, 481–514.

[161] J. E. Squires, H. R. Patel, M. Nousch, T. Sibbritt, D. T. Humphreys, B. J. Parker, C. M. Suter, T. Preiss, *Nucleic Acids Research* **2012**, *40*, 5023–5033.

[162] Q. Du, Z. Wang, V. L. Schramm, *Proc. Natl. Acad. Sci. USA* **2016**, *113*, 2916–2921.

[163] C.-X. Song, C. Yi, C. He, *Nat Biotechnol* **2012**, *30*, 1107–1116.

[164] X. Tekpli, A. Urbanucci, A. Hashim, C. B. Vågbø, R. Lyle, M. K. Kringen, A. C. Staff, I. Dybedal, I. G. Mills, A. Klungland, J. Staerk, *Epigenetics & Chromatin* **2016**, *9*, 21.

[165] X.-L. Cui, J. Nie, J. Ku, U. Dougherty, D. C. West-Szymanski, F. Collin, C. K. Ellison, L. Sieh, Y. Ning, Z. Deng, C. W. T. Zhao, A. Bergamaschi, J. Pekow, J. Wei, A. V. Beadell, Z. Zhang, G. Sharma, R. Talwar, P. Arensdorf, J. Karpus, A. Goel, M. Bissonnette, W. Zhang, S. Levy, C. He, *Nat. Commun.* **2020**, *11*, 6161.

[166] "Datei:A large blank world map with oceans marked in blue.svg – Wikipedia," can be found under https://commons.wikimedia.org/wiki/File:A_large_blank_world_map_with_oceans_marked_in _blue.svg, **n.d.**

[167] N. S. W. Jonasson, *Master Thesis "Investigation of Synthetic Iron(IV)-Oxo Complexes in Their Application as Functional Models for Ten Eleven Translocation Enzymes,"* **2018**.

[168] Y. Cheng, N. Xie, P. Jin, T. Wang, *Cell Biochemistry and Function* **2015**, *33*, 161–173.

[169] Y. Gruenbaum, R. Stein, H. Cedar, A. Razin, *FEBS Letters* **1981**, *124*, 67–71.

[170] D. M. Woodcock, P. J. Crowther, W. P. Diver, *Biochem. Biophys. Res. Commun.* **1987**, *145*, 888–894.

[171] R. Lister, M. Pelizzola, R. H. Dowen, R. D. Hawkins, G. Hon, J. Tonti-Filippini, J. R. Nery, L. Lee, Z. Ye, Q.-M. Ngo, L. Edsall, J. Antosiewicz-Bourget, R. Stewart, V. Ruotti, A. H. Millar, J. A. Thomson, B. Ren, J. R. Ecker, *Nature* **2009**, *462*, 315–322.

[172] K. E. Varley, J. Gertz, K. M. Bowling, S. L. Parker, T. E. Reddy, F. Pauli-Behn, M. K. Cross, B. A. Williams, J. A. Stamatoyannopoulos, G. E. Crawford, D. M. Absher, B. J. Wold, R. M. Myers, *Genome Res.* **2013**, *23*, 555–567.

[173] M. Frommer, L. E. McDonald, D. S. Millar, C. M. Collis, F. Watt, G. W. Grigg, P. L. Molloy, C. L. Paul, *PNAS* **1992**, *89*, 1827–1831.

[174] Y. Huang, W. A. Pastor, Y. Shen, M. Tahiliani, D. R. Liu, A. Rao, *PLOS ONE* **2010**, *5*, e8888.

[175] M. Yu, G. C. Hon, K. E. Szulwach, C.-X. Song, L. Zhang, A. Kim, X. Li, Q. Dai, Y. Shen, B. Park, J.-H. Min, P. Jin, B. Ren, C. He, *Cell* **2012**, *149*, 1368–1380.

[176] B. Xia, D. Han, X. Lu, Z. Sun, A. Zhou, Q. Yin, H. Zeng, M. Liu, X. Jiang, W. Xie, C. He, C. Yi, *Nat. Methods* **2015**, *12*, 1047–1050.

[177] F. Neri, D. Incarnato, A. Krepelova, S. Rapelli, F. Anselmi, C. Parlato, C. Medana, F. Dal Bello, S. Oliviero, *Cell Rep.* **2015**, *10*, 674–683.

[178] F. Neri, D. Incarnato, A. Krepelova, C. Parlato, S. Oliviero, *Nat Protoc* **2016**, *11*, 1191–1205.

[179] J. Ličytė, P. Gibas, K. Skardžiūtė, V. Stankevičius, A. Rukšėnaitė, E. Kriukienė, *Cell Rep.* **2020**, *32*, 108155.

[180] Y. Liu, P. Siejka-Zielińska, G. Velikova, Y. Bi, F. Yuan, M. Tomkova, C. Bai, L. Chen, B. Schuster-Böckler, C.-X. Song, *Nat. Biotechnol.* **2019**, *37*, 424–429.

[181] M. Yu, G. C. Hon, K. E. Szulwach, C.-X. Song, P. Jin, B. Ren, C. He, *Nat. Prot.* **2012**, *7*, 2159–2170.

[182] G. R. Wyatt, S. S. Cohen, *Nature* **1952**, *170*, 1072–1073.

[183] R. a J. Warren, *Annu. Rev. Microbiol.* **1980**, *34*, 137–158.

[184] S. Kriaucionis, N. Heintz, *Science* **2009**, *324*, 929–930.

[185]   D. Globisch, M. Münzel, M. Müller, S. Michalakis, M. Wagner, S. Koch, T. Brückl, M. Biel, T. Carell, *PLoS One* **2010**, *5*, e15367.

[186]   M. Münzel, D. Globisch, T. Brückl, M. Wagner, V. Welzmiller, S. Michalakis, M. Müller, M. Biel, T. Carell, *Angew. Chem. Int. Ed.* **2010**, *49*, 5375–5377.

[187]   M. Münzel, D. Globisch, T. Brückl, M. Wagner, V. Welzmiller, S. Michalakis, M. Müller, M. Biel, T. Carell, *Angew. Chem.* **2010**, *122*, 5503–5505.

[188]   A. Szwagierczak, S. Bultmann, C. S. Schmidt, F. Spada, H. Leonhardt, *Nucleic Acids Research* **2010**, *38*, e181–e181.

[189]   Z. Liutkevičiūtė, G. Lukinavičius, V. Masevičius, D. Daujotytė, S. Klimašauskas, *Nat Chem Biol* **2009**, *5*, 400–402.

[190]   T. Pfaffeneder, B. Hackner, M. Truß, M. Münzel, M. Müller, C. A. Deiml, C. Hagemeier, T. Carell, *Angew. Chem. Int. Ed.* **2011**, *50*, 7008–7012.

[191]   L. Shen, H. Wu, D. Diep, S. Yamaguchi, A. C. D'Alessio, H.-L. Fung, K. Zhang, Y. Zhang, *Cell* **2013**, *153*, 692–706.

[192]   A. R. Weber, C. Krawczyk, A. B. Robertson, A. Kuśnierczyk, C. B. Vågbø, D. Schuermann, A. Klungland, P. Schär, *Nat. Comm.* **2016**, *7*, 10806.

[193]   A. Jeltsch, *ChemBioChem* **2002**, *3*, 274–293.

[194]   R. C. A. Dubini, A. Schön, M. Müller, T. Carell, P. Rovó, *Nucleic Acids Res.* **2020**, gkaa589.

[195]   S. Ji, D. Park, K. Kropachev, M. Kolbanovskiy, I. Fu, S. Broyde, M. Essawy, N. E. Geacintov, N. Y. Tretyakova, *J. Biol. Chem.* **2019**, jbc.RA119.009834.

[196]   E. Naydenova, J. C. B. Dietschreit, C. Ochsenfeld, *J. Phys. Chem. B* **2019**, *123*, 4173–4179.

[197]   M. W. Kellinger, C.-X. Song, J. Chong, X.-Y. Lu, C. He, D. Wang, *Nat. Struct. Mol. Biol.* **2012**, *19*, 831–833.

[198]   L. Zhang, X. Lu, J. Lu, H. Liang, Q. Dai, G.-L. Xu, C. Luo, H. Jiang, C. He, *Nat. Chem. Biol.* **2012**, *8*, 328.

[199]   Y.-Q. Li, P.-Z. Zhou, X.-D. Zheng, C. P. Walsh, G.-L. Xu, *Nucleic Acids Research* **2007**, *35*, 390–400.

[200]   M. Tini, A. Benecke, S.-J. Um, J. Torchia, R. M. Evans, P. Chambon, *Molecular Cell* **2002**, *9*, 265–277.

[201]   T. P. Wu, T. Wang, M. G. Seetin, Y. Lai, S. Zhu, K. Lin, Y. Liu, S. D. Byrum, S. G. Mackintosh, M. Zhong, A. Tackett, G. Wang, L. S. Hon, G. Fang, J. A. Swenberg, A. Z. Xiao, *Nature* **2016**, *532*, 329–333.

[202]   M. J. Koziol, C. R. Bradshaw, G. E. Allen, A. S. H. Costa, C. Frezza, J. B. Gurdon, *Nat. Struct. Mol. Biol.* **2016**, *23*, 24–30.

[203]   S. Schiffers, C. Ebert, R. Rahimoff, O. Kosmatchev, J. Steinbacher, A.-V. Bohne, F. Spada, S. Michalakis, J. Nickelsen, M. Müller, T. Carell, *Angew. Chem. Int. Ed.* **2017**, *56*, 11268–11271.

[204]   M. U. Musheev, A. Baumgärtner, L. Krebs, C. Niehrs, *Nat. Chem. Biol.* **2020**, *16*, 630–634.

[205]   B. Butanis, "The Legacy of Henrietta Lacks," can be found under https://www.hopkinsmedicine.org/henriettalacks/, **n.d.**

[206]   L. Schomacher, D. Han, M. U. Musheev, K. Arab, S. Kienhöfer, A. von Seggern, C. Niehrs, *Nat. Struct. Mol. Biol.* **2016**, *23*, 116–124.

[207]   D. P. Patil, B. F. Pickering, S. R. Jaffrey, *Trends Cell Biol.* **2018**, *28*, 113–127.

[208]   M. Löffler, L. D. Fairbanks, E. Zameitat, A. M. Marinaki, H. A. Simmonds, *Trends Mol. Med.* **2005**, *11*, 430–437.

[209]   L. Wang, *Nucleosides, Nucleotides Nucleic Acids* **2016**, *35*, 578–594.

[210]   K. Bian, S. A. P. Lenz, Q. Tang, F. Chen, R. Qi, M. Jost, C. L. Drennan, J. M. Essigmann, S. D. Wetmore, D. Li, *Nucleic Acids Res.* **n.d.**, DOI 10.1093/nar/gkz395.

[211]   E. Hammam, G. Ananda, A. Sinha, C. Scheidig-Benatar, M. Bohec, P. R. Preiser, P. C. Dedon, A. Scherf, S. S. Vembar, *Nucleic Acids Res.* **n.d.**, DOI 10.1093/nar/gkz1093.

[212]   M. J. Gardner, N. Hall, E. Fung, O. White, M. Berriman, R. W. Hyman, J. M. Carlton, A. Pain, K. E. Nelson, S. Bowman, I. T. Paulsen, K. James, J. A. Eisen, K. Rutherford, S. L. Salzberg, A. Craig, S. Kyes, M.-S. Chan, V. Nene, S. J. Shallom, B. Suh, J. Peterson, S. Angiuoli, M. Pertea, J. Allen, J. Selengut, D. Haft, M. W. Mather, A. B. Vaidya, D. M. A. Martin, A. H. Fairlamb, M. J. Fraunholz, D. S. Roos, S. A. Ralph, G. I. McFadden, L. M. Cummings, G. M. Subramanian, C. Mungall, J. C.

Venter, D. J. Carucci, S. L. Hoffman, C. Newbold, R. W. Davis, C. M. Fraser, B. Barrell, *Nature* **2002**, *419*, 498–511.

[213] A. J. Lee, C. Majumdar, S. D. Kathe, R. P. Van Ostrand, H. R. Vickery, A. M. Averill, S. R. Nelson, A. H. Manlove, M. A. McCord, S. S. David, *J. Am. Chem. Soc.* **2020**, *142*, 13283–13287.

[214] R. D. Woods, V. L. O'Shea, A. Chu, S. Cao, J. L. Richards, M. P. Horvath, S. S. David, *Nucleic Acids Res.* **2016**, *44*, 801–810.

[215] L. Wang, S. Chakravarthy, G. L. Verdine, *J. Biol. Chem.* **2017**, *292*, 5007–5017.

[216] L. P. Russelburg, V. L. O'Shea Murray, M. Demir, K. R. Knutsen, S. L. Sehgal, S. Cao, S. S. David, M. P. Horvath, *ACS Chem. Biol.* **2020**, *15*, 93–102.

[217] J. W. Park, P. N. P. Lagniton, Y. Liu, R.-H. Xu, *Int. J. Biol. Sci.* **2021**, *17*, 1446–1460.

[218] Y. V. Svitkin, Y. M. Cheng, T. Chakraborty, V. Presnyak, M. John, N. Sonenberg, *Nucleic Acids Res.* **2017**, *45*, 6023–6036.

[219] J. Cohen, "What went wrong with CureVac's highly anticipated new mRNA vaccine for COVID-19?," can be found under https://www.sciencemag.org/news/2021/06/what-went-wrong-curevac-s-highly-anticipated-new-mrna-vaccine-covid-19, **2021**.

[220] E. Dolgin, *Nature* **2021**, *594*, 483–483.

[221] "CureVac Provides Update on Phase 2b/3 Trial of First-Generation COVID-19 Vaccine Candidate, CVnCoV," can be found under https://www.curevac.com/en/2021/06/16/curevac-provides-update-on-phase-2b-3-trial-of-first-generation-covid-19-vaccine-candidate-cvncov/, **2021**.

[222] WHO, Messenger RNA Encoding Full-Length SARS-Cov-2 Spike Glycoprotein, **2020**.

[223] L. Organick, S. D. Ang, Y.-J. Chen, R. Lopez, S. Yekhanin, K. Makarychev, M. Z. Racz, G. Kamath, P. Gopalan, B. Nguyen, C. N. Takahashi, S. Newman, H.-Y. Parker, C. Rashtchian, K. Stewart, G. Gupta, R. Carlson, J. Mulligan, D. Carmean, G. Seelig, L. Ceze, K. Strauss, *Nat. Biotechnol.* **2018**, *36*, 242–248.

[224] L. Ceze, J. Nivala, K. Strauss, *Nat. Rev. Genet.* **2019**, *20*, 456–466.

[225] R. Lopez, Y.-J. Chen, S. Dumas Ang, S. Yekhanin, K. Makarychev, M. Z. Racz, G. Seelig, K. Strauss, L. Ceze, *Nat. Commun.* **2019**, *10*, 2933.

[226] "Netflix-Serie 'Biohackers' auf synthetischer DNA gespeichert," can be found under https://www.forschung-und-lehre.de/forschung/netflix-serie-biohackers-auf-synthetischer-dna-gespeichert-3071/, **2021**.

[227] L. C. Meiser, P. L. Antkowiak, J. Koch, W. D. Chen, A. X. Kohll, W. J. Stark, R. Heckel, R. N. Grass, *Nat. Prot.* **2020**, *15*, 86–101.

[228] S. Hoshika, N. A. Leal, M.-J. Kim, M.-S. Kim, N. B. Karalkar, H.-J. Kim, A. M. Bates, N. E. Watkins, H. A. SantaLucia, A. J. Meyer, S. DasGupta, J. A. Piccirilli, A. D. Ellington, J. SantaLucia, M. M. Georgiadis, S. A. Benner, *Science* **2019**, *363*, 884–887.

[229] A. M. Raizis, F. Schmitt, J. P. Jost, *Anal. Biochem.* **1995**, *226*, 161–166.

[230] K. Tanaka, A. Okamoto, *Bioorg. Med. Chem. Lett.* **2007**, *17*, 1912–1915.

[231] M. J. Booth, M. R. Branco, G. Ficz, D. Oxley, F. Krueger, W. Reik, S. Balasubramanian, *Science* **2012**, *336*, 934–937.

[232] C. Nestor, A. Ruzov, R. Meehan, D. Dunican, *Biotechniques* **2010**, *48*, 317–319.

[233] S.-G. Jin, S. Kadam, G. P. Pfeifer, *Nucleic Acids Res.* **2010**, *38*, e125–e125.

[234] J. Cong, D. Kinschel, Q. Daniel, M. Safdari, E. Gabrielsson, H. Chen, P. H. Svensson, L. Sun, L. Kloo, *J. Mater. Chem. A* **2016**, *4*, 14550–14554.

[235] W. Rasheed, R. Fan, C. S. Abelson, P. O. Peterson, W.-M. Ching, Y. Guo, L. Que, *J. Biol. Inorg. Chem.* **2019**, *24*, 533–545.

[236] C. Kupper, B. Mondal, J. Serrano-Plana, I. Klawitter, F. Neese, M. Costas, S. Ye, F. Meyer, *J. Am. Chem. Soc.* **2017**, *139*, 8939–8949.

[237] G. Mukherjee, F. G. C. Reinhard, U. K. Bagha, C. V. Sastri, S. P. de Visser, *Dalton Trans.* **2020**, *49*, 5921–5931.

[238] D. Schmidl, *Master Thesis "Investigations on the Reactivity of a Functional TET Enzyme Model Against Nucleosides,"* **2020**.

[239] S. Steenken, S. V. Jovanovic, L. P. Candeias, J. Reynisson, *Chem. Eur. J.* **2001**, *7*, 2829–2833.

[240]   S. M. Ching, W. J. Tan, K. L. Chua, Y. Lam, *Bioorganic & Medicinal Chemistry* **2010**, *18*, 6657–6665.

[241]   Z. D. Smith, A. Meissner, *Nat. Rev. Genet.* **2013**, *14*, 204–220.

[242]   M. Mizuta, J. Banba, T. Kanamori, R. Tawarada, A. Ohkubo, M. Sekine, K. Seio, *J. Am. Chem. Soc.* **2008**, *130*, 9622–9623.

[243]   S. Shahsavari, J. Chen, T. Wigstrom, J. Gooding, A. Gauronskas, S. Fang, *Tetrahedron Lett.* **2016**, *57*, 3877–3880.

[244]   D. B. Gophane, S. T. Sigurdsson, *Beilstein J. Org. Chem.* **2015**, *11*, 219–227.

[245]   Y. He, J. R. Ecker, *Annu. Rev. Genomics Hum. Genet.* **2015**, *16*, 55–77.

[246]   M. V. C. Greenberg, D. Bourc'his, *Nat. Rev. Mol. Cell Biol.* **2019**, *20*, 590–607.

[247]   C. Mayer, G. R. McInroy, P. Murat, P. Van Delft, S. Balasubramanian, *Angewandte Chemie International Edition* **2016**, *55*, 11144–11148.

[248]   S. C. Jurczyk, J. T. Kodra, J. D. Rozzell, S. A. Benner, T. R. Battersby, *Helv. Chim. Acta* **1998**, *81*, 793–811.

[249]   S. C. Jurczyk, J. T. Kodra, J.-H. Park, S. A. Benner, T. R. Battersby, *Helv. Chim. Acta* **1999**, *82*, 1005–1015.

[250]   S. A. Benner, D. Hutter, A. M. Sismour, *Nucleic Acids Symposium Series* **2003**, *3*, 125–126.

[251]   Y. Doi, J. Chiba, T. Morikawa, M. Inouye, *J. Am. Chem. Soc.* **2008**, *130*, 8762–8768.

[252]   P. Stoss, E. Kaes, G. Eibel, U. Thewalt, *J. Heterocycl. Chem.* **1991**, *28*, 231–236.

[253]   R. Janßen, Unpublished Work, Ludwig-Maximilians-University Munich, **2020**.

[254]   C.-Y. Shiue, A. P. Wolf, D. N. Slatkin, *J. Label. Compd. Rad.* **1980**, *17*, 177–184.

[255]   H. Ballweg, *Tetrahedron Lett.* **1968**, *9*, 2171–2173.

[256]   J. L. Wong, D. S. Fuchs, *J. Org. Chem.* **1970**, *35*, 3786–3791.

[257]   A. Holý, I. Rosenberg, H. Dvořáková, *Collect. Czech. Chem. Commun.* **1989**, *54*, 2190–2210.

[258]   J. de Graaff, *Master Thesis "Synthesis of Substrates for the Investigation of α-Ketoglutarate-Dependent Hydroxylases and Their Iron(IV)-Oxo Model Complexes,"* **2018**.

[259]   B. Bartels, C. Garcia-Yebra, G. Helmchen, *Eur. J. Org. Chem.* **2003**, *2003*, 1097–1103.

[260]   J. P. Patel, M. L. Sowers, J. L. Herring, J. A. Theruvathu, M. R. Emmett, B. E. Hawkins, K. Zhang, D. S. DeWitt, D. S. Prough, L. C. Sowers, *Chem. Res. Toxicol.* **2015**, *28*, 2352–2363.

[261]   M. J. Booth, T. W. B. Ost, D. Beraldi, N. M. Bell, M. R. Branco, W. Reik, S. Balasubramanian, *Nat. Prot.* **2013**, *8*, 1841–1851.

[262]   W. Micklitz, B. Lippert, H. Schöllhorn, U. Thewalt, *Journal of Heterocyclic Chemistry* **1989**, *26*, 1499–1500.

[263]   I. Asimov, *J. Chem. Educ.* **1960**, *37*, A490.

[264]   J. Clayden, N. Greeves, S. G. Warren, *Organic Chemistry*, Oxford University Press, Oxford ; New YorK, **2012**.

[265]   S. Fukuzumi, Y. Morimoto, H. Kotani, P. Naumov, Y.-M. Lee, W. Nam, *Nat. Chem.* **2010**, *2*, 756–759.

[266]   Y. Umena, K. Kawakami, J.-R. Shen, N. Kamiya, *Nature* **2011**, *473*, 55–60.

[267]   K. D. Karlin, *Nat. Chem.* **2010**, *2*, 711–712.

[268]   F. A. Carroll, *Perspectives on Structure and Mechanism in Organic Chemistry*, John Wiley, Hoboken, N.J, **2010**.

[269]   R. Zhang, S. Klaine, C. Alcantar, F. Bratcher, *Journal of Inorganic Biochemistry* **2020**, *212*, 111246.

[270]   K. Nishikawa, Y. Honda, H. Fujii, *J. Am. Chem. Soc.* **2020**, *142*, 4980–4984.

[271]   D. Kumar, S. P. de Visser, P. K. Sharma, S. Cohen, S. Shaik, *J. Am. Chem. Soc.* **2004**, *126*, 1907–1920.

[272]   Md. R. Sarkar, S. D. Houston, G. P. Savage, C. M. Williams, E. H. Krenske, S. G. Bell, J. J. De Voss, *J. Am. Chem. Soc.* **2019**, *141*, 19688–19699.

[273]   D. Griller, K. U. Ingold, *Acc. Chem. Res.* **1980**, *13*, 317–323.

[274]   P. A. MacFaul, K. U. Ingold, D. D. M. Wayner, L. Que, *J. Am. Chem. Soc.* **1997**, *119*, 10594–10598.

[275] M. Ghosh, K. K. Singh, C. Panda, A. Weitz, M. P. Hendrich, T. J. Collins, B. B. Dhar, S. Sen Gupta, *J. Am. Chem. Soc.* **2014**, *136*, 9524–9527.

[276] S. Rana, J. P. Biswas, A. Sen, M. Clémancey, G. Blondin, J.-M. Latour, G. Rajaraman, D. Maiti, *Chem. Sci.* **2018**, *9*, 7843–7858.

[277] T. Heurich, V. Nesterov, G. Schnakenburg, Z.-W. Qu, S. Grimme, K. Hazin, D. P. Gates, M. Engeser, R. Streubel, *Angew. Chem. Int. Ed.* **2016**, *55*, 14439–14443.

[278] J. March, *Advanced Organic Chemistry: Reactions, Mechanisms, and Structure*, Wiley, New York, **1985**.

[279] E. V. Dehmlow, J. Wilkenloh, *Chem. Ber.* **1990**, *123*, 583–587.

[280] S.-Y. Choi, P. E. Eaton, P. F. Hollenberg, K. E. Liu, S. J. Lippard, M. Newcomb, D. A. Putt, S. P. Upadhyaya, Y. Xiong, *J. Am. Chem. Soc.* **1996**, *118*, 6547–6555.

[281] C. Wang, S. Otto, M. Dorn, E. Kreidt, J. Lebon, L. Sršan, P. Di Martino-Fumo, M. Gerhards, U. Resch-Genger, M. Seitz, K. Heinze, *Angew. Chem. Int. Ed.* **2018**, *57*, 1112–1116.

[282] T. W. Bell, L. Y. Hu, S. V. Patel, *J. Org. Chem.* **1987**, *52*, 3847–3850.

[283] P. McMorn, G. J. Hutchings, *Chem. Soc. Rev.* **2004**, *33*, 108–122.

[284] C. Bianchini, P. Barbaro, V. D. Santo, R. Gobetto, A. Meli, W. Oberhauser, R. Psaro, F. Vizza, *Adv. Synth. Catal.* **2001**, *343*, 41–45.

[285] M. J. Sabater, A. Corma, A. Domenech, V. Fornés, H. García, *Chem. Commun.* **1997**, 1285–1286.

[286] S. Feast, M. Rafiq, H. Siddiqui, R. P. K. Wells, D. J. Willock, F. King, C. H. Rochester, D. Bethell, P. C. Bulman Page, G. J. Hutchings, *Journal of Catalysis* **1997**, *167*, 533–542.

[287] K. Soai, M. Watanabe, A. Yamamoto, *J. Org. Chem.* **1990**, *55*, 4832–4835.

[288] J. A. Forni, L. F. T. Novaes, R. Galaverna, J. C. Pastre, *Catalysis Today* **2018**, *308*, 86–93.

[289] R. Munirathinam, J. Huskens, W. Verboom, *Adv. Synth. Catal.* **2015**, *357*, 1093–1123.

[290] K. Rickmeyer, *Master Thesis "Synthesis of an Immobilized Fe(IV)-Oxo Complex as a Functional Model for Ten Eleven Translocation Enzymes,"* **2018**.

[291] F. Kielinowski, *Zulassungsarbeit "Synthese Eines Immobilisierten FeIV=O Komplexes Des Py5Me2-Typs Als Funktionellen Modelkomplex Für TET-Enzyme,"* **2018**.

[292] M. Costas, M. P. Mehn, M. P. Jensen, L. Que, *Chem. Rev.* **2004**, *104*, 939–986.

[293] C. Krebs, D. Galonić Fujimori, C. T. Walsh, J. M. Bollinger, *Acc. Chem. Res.* **2007**, *40*, 484–492.

[294] S. Sinnecker, N. Svensen, E. W. Barr, S. Ye, J. M. Bollinger, F. Neese, C. Krebs, *J. Am. Chem. Soc.* **2007**, *129*, 6168–6179.

[295] D. C. Lacy, R. Gupta, K. L. Stone, J. Greaves, J. W. Ziller, M. P. Hendrich, A. S. Borovik, *J. Am. Chem. Soc.* **2010**, *132*, 12188–12190.

[296] J. England, Y. Guo, K. M. Van Heuvelen, M. A. Cranswick, G. T. Rohde, E. L. Bominaar, E. Münck, L. Que, *J. Am. Chem. Soc.* **2011**, *133*, 11880–11883.

[297] J. P. Bigi, W. H. Harman, B. Lassalle-Kaiser, D. M. Robles, T. A. Stich, J. Yano, R. D. Britt, C. J. Chang, *J. Am. Chem. Soc.* **2012**, *134*, 1536–1542.

[298] S. Shaik, H. Hirao, D. Kumar, *Acc. Chem. Res.* **2007**, *40*, 532–542.

[299] A. Decker, J.-U. Rohde, E. J. Klinker, S. D. Wong, Que Lawrence, E. I. Solomon, *J. Am. Chem. Soc.* **2007**, *129*, 15983–15996.

[300] L. Bernasconi, M. J. Louwerse, E. J. Baerends, *Eur. J. Inorg. Chem.* **2007**, *2007*, 3023–3033.

[301] C. Geng, S. Ye, F. Neese, *Angew. Chem. Int. Ed.* **2010**, *49*, 5717–5720.

[302] S. Shaik, H. Chen, D. Janardanan, *Nature Chem* **2011**, *3*, 19–27.

[303] P. Comba, S. Fukuzumi, C. Koke, B. Martin, A.-M. Löhr, J. Straub, *Angew. Chem. Int. Ed.* **2016**, *55*, 11129–11133.

[304] B. Das, A. Orthaber, S. Ott, A. Thapper, *ChemSusChem* **2016**, *9*, 1178–1186.

[305] C. R. Goldsmith, R. T. Jonas, T. D. P. Stack, *J. Am. Chem. Soc.* **2002**, *124*, 83–96.

[306] G. Casari, M. De Fusco, S. Ciarmatori, M. Zeviani, M. Mora, P. Fernandez, G. De Michele, A. Filla, S. Cocozza, R. Marconi, A. Dürr, B. Fontaine, A. Ballabio, *Cell* **1998**, *93*, 973–983.

[307] T. M. Pierson, D. Adams, F. Bonn, P. Martinelli, P. F. Cherukuri, J. K. Teer, N. F. Hansen, P. Cruz, J. C. M. for the N. C. S. Program, R. W. Blakesley, G. Golas, J. Kwan, A. Sandler, K. F. Fajardo, T. Markello, C. Tifft, C. Blackstone, E. I. Rugarli, T. Langer, W. A. Gahl, C. Toro, *PLOS Genetics* **2011**, *7*, e1002325.

[308] S. K. Sahai, R. E. Steiner, M. G. Au, J. M. Graham, N. Salamon, M. Ibba, T. M. Pierson, *Ann. Clin. Transl. Neurol.* **2018**, *5*, 1128–1133.

[309] S. Shribman, E. Reid, A. H. Crosby, H. Houlden, T. T. Warner, *Lancet Neurol.* **2019**, *18*, 1136–1146.

[310] U. Rüetschi, R. Cerone, C. Pérez-Cerda, M. C. Schiaffino, S. Standing, M. Ugarte, E. Holme, *Hum. Genet.* **2000**, *106*, 654–662.

[311] C. J. Ellaway, E. Holme, S. Standing, M. A. Preece, A. Green, E. Ploechl, M. Ugarte, F. K. Trefz, J. V. Leonard, *J. Inherit. Metab. Dis.* **2001**, *24*, 824–832.

[312] R. S. Banh, E. S. Kim, Q. Spillier, D. E. Biancur, K. Yamamoto, A. S. W. Sohn, G. Shi, D. R. Jones, A. C. Kimmelman, M. E. Pacold, *Nature* **2021**, 1–6.

[313] J. B. Dietrich, *Cell. Mol. Biol.* **1992**, *38*, 95–114.

[314] W. E. Knox, M. LeMay-Knox, *Biochem. J.* **1951**, *49*, 686–693.

[315] J. Brownlee, P. He, G. R. Moran, D. H. T. Harrison, *Biochemistry* **2008**, *47*, 2002–2013.

[316] D. Sheet, S. Bhattacharya, T. K. Paine, *Chem. Commun.* **2015**, *51*, 7681–7684.

[317] G. R. Moran, *Arch. Biochem. Biophys.* **2005**, *433*, 117–128.

[318] M. Gunsior, J. Ravel, G. L. Challis, C. A. Townsend, *Biochemistry* **2004**, *43*, 663–674.

[319] H. M. O'Hare, F. Huang, A. Holding, O. W. Choroba, J. B. Spencer, *FEBS Letters* **2006**, *580*, 3445–3450.

[320] C.-Y. Chang, S.-Y. Lyu, Y.-C. Liu, N.-S. Hsu, C.-C. Wu, C.-F. Tang, K.-H. Lin, J.-Y. Ho, C.-J. Wu, M.-D. Tsai, T.-L. Li, *Angew. Chem. Int. Ed.* **2014**, *53*, 1943–1948.

[321] H. S. Ali, R. H. Henchman, S. P. de Visser, *Chem. Eur. J.* **2021**, *27*, 1795–1809.

[322] J. A. Stefely, D. J. Pagliarini, *Trends Biochem. Sci.* **2017**, *42*, 824–843.

[323] B. Ke, *Photosynthesis: Photobiochemistry and Photobiophysics*, Kluwer Academic Publishers, Dordrecht, **2003**.

[324] B. Nowicka, J. Kruk, *Biochim. Biophys. Acta* **2010**, *1797*, 1587–1605.

[325] F. Pojer, R. Kahlich, B. Kammerer, S.-M. Li, L. Heide, *J. Biol. Chem.* **2003**, *278*, 30661–30668.

[326] T. K. Paine, S. Paria, L. Q. Jr, *Chem. Commun.* **2010**, *46*, 1830–1832.

[327] J. R. Widhalm, N. Dudareva, *Mol. Plant* **2015**, *8*, 83–97.

[328] E. Frick, Funktionelle Und Strukturelle Charakterisierung von 4-Hydroxyphenylpyruvat Dioxygenasen Und 4-Hydroxymandelat Synthasen, Albert-Ludwigs-Universität, **2014**.

[329] A. Waterhouse, M. Bertoni, S. Bienert, G. Studer, G. Tauriello, R. Gumienny, F. T. Heer, T. A. P. de Beer, C. Rempfer, L. Bordoli, R. Lepore, T. Schwede, *Nucleic Acids Res.* **2018**, *46*, W296–W303.

[330] C. Notredame, D. G. Higgins, J. Heringa, *J. Mol. Biol.* **2000**, *302*, 205–217.

[331] S. V. a. C. Samarasinghe, K. Krishnan, R. Naidu, M. Megharaj, K. Miller, B. Fraser, R. J. Aitken, *Andrology* **2018**, *6*, 532–541.

[332] S. Sligar, Role of Iron(III) in Heme Enzymes - ICBIC 2019, Interlaken, CH, **2019**.

[333] A. M. Shiller, E. W. Chan, D. J. Joung, M. C. Redmond, J. D. Kessler, *Sci. Rep.* **2017**, *7*, 10389.

[334] H. N. Vu, G. A. Subuyuj, S. Vijayakumar, N. M. Good, N. C. Martinez-Gomez, E. Skovran, *Journal of Bacteriology* **n.d.**, *198*, 1250–1259.

[335] B. Jahn, A. Pol, H. Lumpe, T. R. M. Barends, A. Dietl, C. Hogendoorn, H. J. M. Op den Camp, L. J. Daumann, *ChemBioChem* **2018**, *19*, 1147–1153.

[336] S. Masuda, Y. Suzuki, Y. Fujitani, R. Mitsui, T. Nakagawa, M. Shintani, A. Tani, *mSphere* **n.d.**, *3*, e00462-17.

[337] L. J. Daumann, *Angew. Chem. Int. Ed.* **2019**, *58*, 12795–12802.

[338] C. Anthony, L. Zatman, *Biochem. J.* **1964**, *92*, 609–614.

[339] C. Anthony, L. Zatman, *Biochem. J.* **1964**, *92*, 614–621.

[340] A. Pol, T. R. M. Barends, A. Dietl, A. F. Khadem, J. Eygensteyn, M. S. M. Jetten, H. J. M. O. den Camp, *Environmental Microbiology* **2014**, *16*, 255–264.

[341] S. Lim, S. J. Franklin, *CMLS, Cell. Mol. Life Sci.* **2004**, *61*, 2184–2188.

[342] A. Pol, K. Heijmans, H. R. Harhangi, D. Tedesco, M. S. M. Jetten, H. J. M. Op den Camp, *Nature* **2007**, *450*, 874–878.

[343] Y. Hibi, K. Asai, H. Arafuka, M. Hamajima, T. Iwama, K. Kawai, *J. Biosci. Bioeng.* **2011**, *111*, 547–549.

[344] T. Nakagawa, R. Mitsui, A. Tani, K. Sasa, S. Tashiro, T. Iwama, T. Hayakawa, K. Kawai, *PLOS ONE* **2012**, *7*, e50480.

[345] J. T. Keltjens, A. Pol, J. Reimann, H. J. M. Op den Camp, *Appl. Microbiol. Biotechnol.* **2014**, *98*, 6163–6183.

[346] F. Chu, D. A. C. Beck, M. E. Lidstrom, *PeerJ* **2016**, *4*, e2435.

[347] F. Chu, M. E. Lidstrom, *J. Bacteriol.* **2016**, *198*, 1317–1325.

[348] N. M. Good, O. N. Walser, R. S. Moore, C. J. Suriano, A. F. Huff, N. C. Martínez-Gómez, *Investigation of Lanthanide-Dependent Methylotrophy Uncovers Complementary Roles for Alcohol Dehydrogenase Enzymes*, **2018**.

[349] Y. Zheng, J. Huang, F. Zhao, L. Chistoserdova, *mBio* **2018**, *9*, e02430-17.

[350] D. R. Houck, J. L. Hanners, C. J. Unkefer, *J. Am. Chem. Soc.* **1988**, *110*, 6920–6921.

[351] Y.-J. Zheng, T. C. Bruice, *PNAS* **1997**, *94*, 11881–11886.

[352] S. Itoh, H. Kawakami, S. Fukuzumi, *J. Am. Chem. Soc.* **1997**, *119*, 439–440.

[353] A. Oubrie, H. J. Rozeboom, K. H. Kalk, A. J. J. Olsthoorn, J. A. Duine, B. W. Dijkstra, *EMBO J.* **1999**, *18*, 5187–5194.

[354] A. Oubrie, B. W. Dijkstra, *Protein Sci.* **2000**, *9*, 1265–1273.

[355] Y.-J. Zheng, Z. Xia, Z. Chen, F. S. Mathews, T. C. Bruice, *Proc. Natl. Acad. Sci. U.S.A.* **2001**, *98*, 432–434.

[356] C. Anthony, P. Williams, *Biochim. Biophys. Acta - Proteins Proteom.* **2003**, *1647*, 18–23.

[357] C. Anthony, *Arch. Biochem. Biophys.* **2004**, *428*, 2–9.

[358] M. Prejanò, T. Marino, N. Russo, *Chemistry – A European Journal* **2017**, *23*, 8652–8657.

[359] A. McSkimming, T. Cheisson, P. J. Carroll, E. J. Schelter, *J. Am. Chem. Soc.* **2018**, *140*, 1223–1226.

[360] C. Anthony, *Biochem. J.* **1996**, *320*, 697–711.

[361] M. G. GOODWIN, C. ANTHONY, *Biochem. J.* **1996**, *318*, 673–679.

[362] C. Anthony, in *Enzyme-Catalyzed Electron and Radical Transfer: Subcellular Biochemistry* (Eds.: A. Holzenburg, N.S. Scrutton), Springer US, Boston, MA, **2000**, pp. 73–117.

[363] P. Kalimuthu, L. J. Daumann, A. Pol, H. J. M. Op den Camp, P. V. Bernhardt, *Chemistry – A European Journal* **2019**, *25*, 8760–8768.

[364] S. M. Gutenthaler, M. T. Phi, H. Singer, L. J. Daumann, in *Methods in Enzymology* (Ed.: J.A. Cotruvo), Academic Press, **2021**, pp. 57–79.

[365] B. Jahn, N. S. W. Jonasson, H. Hu, H. Singer, A. Pol, N. M. Good, H. J. M. O. den Camp, N. C. Martinez-Gomez, L. J. Daumann, *J. Biol. Inorg. Chem.* **2020**, *25*, 199–212.

[366] D. J. Day, C. Anthony, in *Methods in Enzymology*, Academic Press, **1990**, pp. 210–216.

[367] H. McIlwain, *J. Chem. Soc.* **1937**, *0*, 1704–1711.

[368] G. R. Fulmer, A. J. M. Miller, N. H. Sherden, H. E. Gottlieb, A. Nudelman, B. M. Stoltz, J. E. Bercaw, K. I. Goldberg, *Organometallics* **2010**, *29*, 2176–2179.

[369] F. R. Traube, S. Schiffers, K. Iwan, S. Kellner, F. Spada, M. Müller, T. Carell, *Nature Protocols* **2019**, *14*, 283–312.

[370] S. R. Hörtner, T. Ritschel, B. Stengl, C. Kramer, W. B. Schweizer, B. Wagner, M. Kansy, G. Klebe, F. Diederich, *Angew. Chem. Int. Ed.* **2007**, *46*, 8266–8269.

[371] C. Bachmann, M. Guttentag, B. Spingler, R. Alberto, *Inorg. Chem.* **2013**, *52*, 6055–6061.

[372] B. Qian, S. Guo, J. Shao, Q. Zhu, L. Yang, C. Xia, H. Huang, *J. Am. Chem. Soc.* **2010**, *132*, 3650–3651.

[373] V. Parekh, J. A. Ramsden, M. Wills, *Tetrahedron: Asymmetry* **2010**, *21*, 1549–1556.

[374] I. Kumpina, N. Brodyagin, J. A. MacKay, S. D. Kennedy, M. Katkevics, E. Rozners, *J. Org. Chem.* **2019**, *84*, 13276–13298.

[375] B. Samanta, J. Seikowski, C. Höbartner, *Angew. Chem. Int. Ed.* **2016**, *55*, 1912–1916.

[376] P. A. Clemons, A. N. Koehler, B. K. Wagner, T. G. Sprigings, D. R. Spring, R. W. King, S. L. Schreiber, M. A. Foley, *Chem. Biol.* **2001**, *8*, 1183–1195.

[377] T. Lioux, M.-A. Mauny, A. Lamoureux, N. Bascoul, M. Hays, F. Vernejoul, A.-S. Baudru, C. Boularan, J. Lopes-Vicente, G. Qushair, G. Tiraby, *J. Med. Chem.* **2016**, *59*, 10253–10267.

[378] B. A. Fox, T. L. Threlfall, *Org. Synth.* **1964**, *44*, 34.

[379] S. Manna, S. Maity, S. Rana, S. Agasti, D. Maiti, *Org. Lett.* **2012**, *14*, 1736–1739.

[380] M. Hayashi, Y. Matsuura, Y. Watanabe, *Tetrahedron Lett.* **2004**, *45*, 1409–1411.

[381] F. Pape, J. F. Teichert, *Synthesis* **2017**, *49*, 2470–2482.

[382] T. T. da Cunha, V. M. M. Barbosa, W. X. C. Oliveira, C. B. Pinheiro, E. F. Pedroso, W. C. Nunes, C. L. M. Pereira, *Polyhedron* **2019**, *169*, 102–113.

[383] W. C. Yang, G. F. Yang, Structural Insight into the Catalyitc Mechanism of Human 4-Hydroxyphenylpyruvate Dioxygenase, PDB Entry, **2015**.

XII. Foldout Sheet

XIII. Overview of Synthetic Intermediates

Chapter III
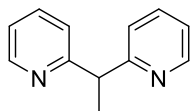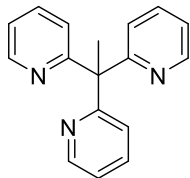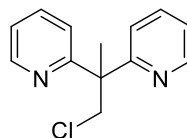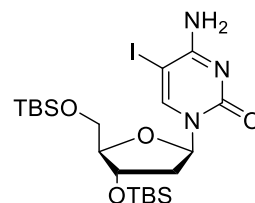
III-1   *III-2*   *III-3*   *III-4*
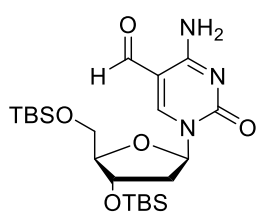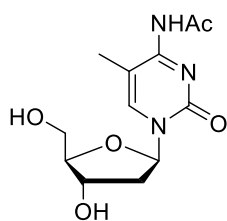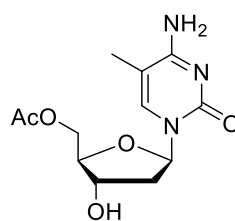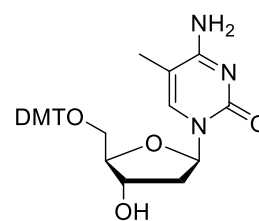
III-5   *III-6*   *III-6a*   *III-6b*
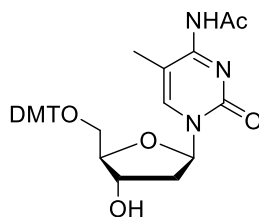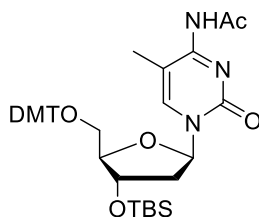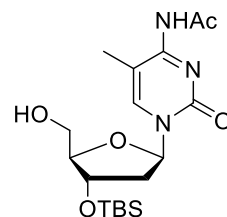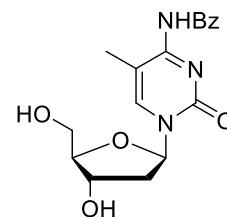
III-7   *III-8*   *III-9*   *III-12*
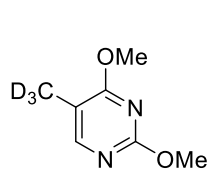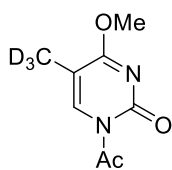
III-13   *III-14*   *III-16*   *III-17*

III-22

533
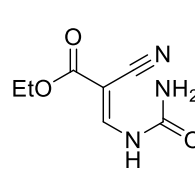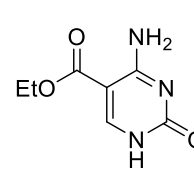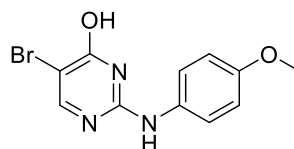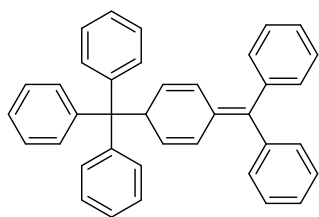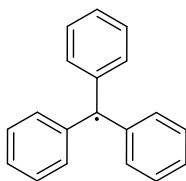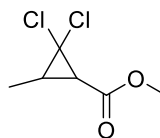
Chapter IV
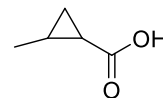
GD   IV-4   IV-5   IV-6

Chapter V

V-1   V-2   V-3   V-4

V-5   V-6   V-7

V-8

V-9

V-10

V-11

V-12

V-13

V-14

V-15

V-16

V-19

V-20

V-21

V-22
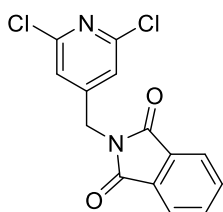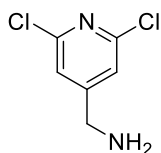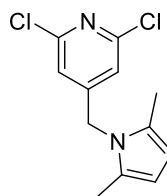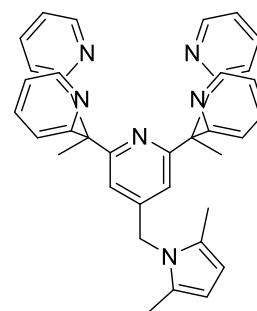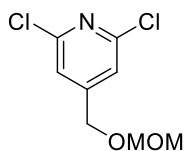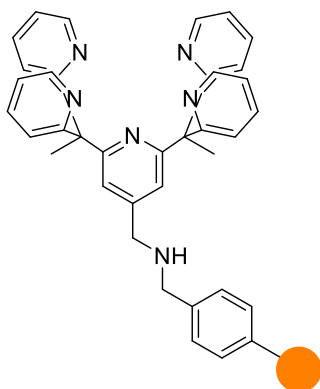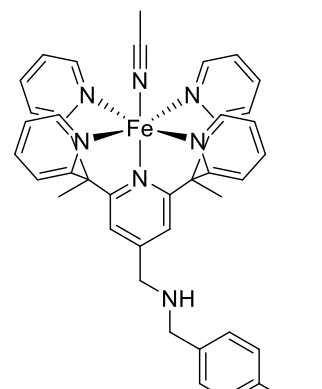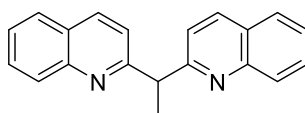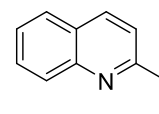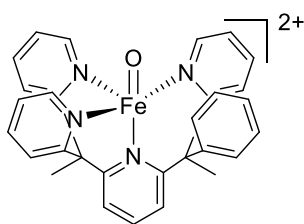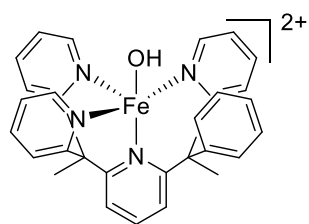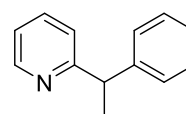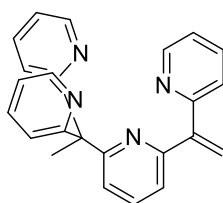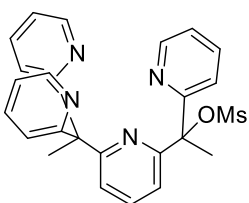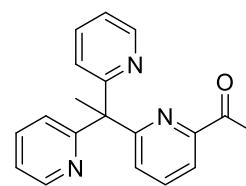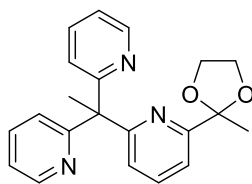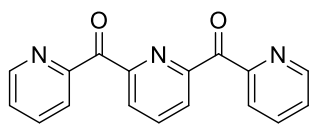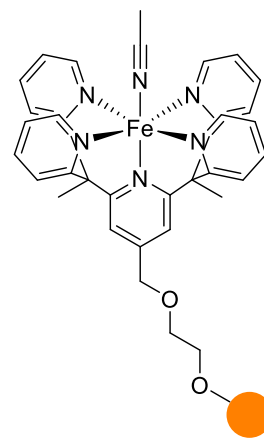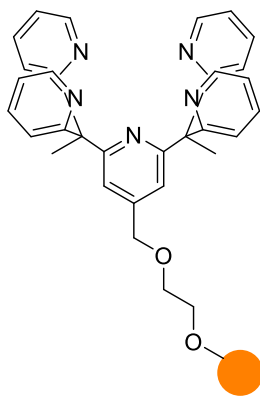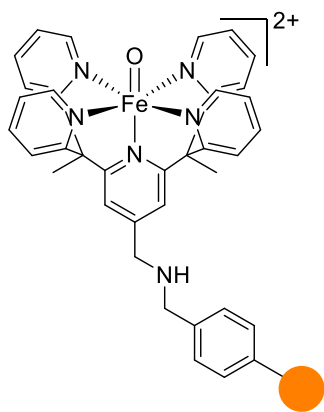
Chapter VI

VI-1   VI-2   VI-3   VI-4